EMERGING MICRO- AND NANOTECHNOLOGIES FOR MEDICAL AND PHARMACOLOGICAL APPLICATIONS

EDITED BY: Wei Tao, Jianxun Ding, Chao Wang and Jun Chen
PUBLISHED IN: Frontiers in Pharmacology

frontiers Research Topics

ISSN 1664-8714
ISBN 978-2-88966-639-3
DOI 10.3389/978-2-88966-639-3

About Frontiers

Frontiers is more than just an open-access publisher of scholarly articles: it is a pioneering approach to the world of academia, radically improving the way scholarly research is managed. The grand vision of Frontiers is a world where all people have an equal opportunity to seek, share and generate knowledge. Frontiers provides immediate and permanent online open access to all its publications, but this alone is not enough to realize our grand goals.

Frontiers Journal Series

The Frontiers Journal Series is a multi-tier and interdisciplinary set of open-access, online journals, promising a paradigm shift from the current review, selection and dissemination processes in academic publishing. All Frontiers journals are driven by researchers for researchers; therefore, they constitute a service to the scholarly community. At the same time, the Frontiers Journal Series operates on a revolutionary invention, the tiered publishing system, initially addressing specific communities of scholars, and gradually climbing up to broader public understanding, thus serving the interests of the lay society, too.

Dedication to Quality

Each Frontiers article is a landmark of the highest quality, thanks to genuinely collaborative interactions between authors and review editors, who include some of the world's best academicians. Research must be certified by peers before entering a stream of knowledge that may eventually reach the public - and shape society; therefore, Frontiers only applies the most rigorous and unbiased reviews.
Frontiers revolutionizes research publishing by freely delivering the most outstanding research, evaluated with no bias from both the academic and social point of view. By applying the most advanced information technologies, Frontiers is catapulting scholarly publishing into a new generation.

What are Frontiers Research Topics?

Frontiers Research Topics are very popular trademarks of the Frontiers Journals Series: they are collections of at least ten articles, all centered on a particular subject. With their unique mix of varied contributions from Original Research to Review Articles, Frontiers Research Topics unify the most influential researchers, the latest key findings and historical advances in a hot research area! Find out more on how to host your own Frontiers Research Topic or contribute to one as an author by contacting the Frontiers Editorial Office: frontiersin.org/about/contact

EMERGING MICRO- AND NANOTECHNOLOGIES FOR MEDICAL AND PHARMACOLOGICAL APPLICATIONS

Topic Editors:
Wei Tao, Harvard Medical School, United States
Jianxun Ding, Chinese Academy of Sciences, China
Chao Wang, Soochow University, China
Jun Chen, University of California, Los Angeles, United States

Citation: Tao, W., Ding, J., Wang, C., Chen, J., eds. (2021). Emerging Micro- and Nanotechnologies for Medical and Pharmacological Applications. Lausanne: Frontiers Media SA. doi: 10.3389/978-2-88966-639-3

Table of Contents

06 ***Editorial: Emerging Micro- and Nanotechnologies for Medical and Pharmacological Applications***
Yufen Xiao, Jun Chen, Chao Wang, Jianxun Ding and Wei Tao

08 ***Berberine-Incorporated Shape Memory Fiber Applied as a Novel Surgical Suture***
Wen-cheng Zhou, Peng-fei Tan, Xing-han Chen, Ying Cen, Chao You, Lin Tan, Hao Li and Meng Tian

21 ***Scaffold-Based Gene Therapeutics for Osteochondral Tissue Engineering***
Xin Yan, You-Rong Chen, Yi-Fan Song, Meng Yang, Jing Ye, Gang Zhou and Jia-Kuo Yu

34 ***Two-Dimensional Nanosheet-Based Photonic Nanomedicine for Combined Gene and Photothermal Therapy***
Na Yoon Kim, Sara Blake, Diba De, Jiang Ouyang, Jinjun Shi and Na Kong

48 ***Three-Dimensional Culture Promotes the Differentiation of Human Dental Pulp Mesenchymal Stem Cells Into Insulin-Producing Cells for Improving the Diabetes Therapy***
Bingbing Xu, Daoyang Fan, Yunshan Zhao, Jing Li, Zhendong Wang, Jianhua Wang, Xiuwei Wang, Zhen Guan and Bo Niu

59 ***Polymer Nanoformulation of Sorafenib and All-Trans Retinoic Acid for Synergistic Inhibition of Thyroid Cancer***
Shijie Li, Shujun Dong, Weiguo Xu, Yang Jiang and Zhongmin Li

70 ***Cell Membrane-Camouflaged Nanocarriers for Cancer Diagnostic and Therapeutic***
Shengxian Li, Jianhua Liu, Mengyao Sun, Jixue Wang, Chunxi Wang and Yinghao Sun

83 ***Dihydroartemisinin-Loaded Magnetic Nanoparticles for Enhanced Chemodynamic Therapy***
Shengdi Guo, Xianxian Yao, Qin Jiang, Kuang Wang, Yuanying Zhang, Haibao Peng, Jing Tang and Wuli Yang

94 ***Preparation and Characterization of Chitosan Nanoparticles for Chemotherapy of Melanoma Through Enhancing Tumor Penetration***
Hui Guo, Faping Li, Heping Qiu, Jianhua Liu, Sihao Qin, Yuchuan Hou and Chunxi Wang

102 ***Advances in Drug Delivery via Biodegradable Ureteral Stent for the Treatment of Upper Tract Urothelial Carcinoma***
Hongli Shan, Zhongshuai Cao, Changliang Chi, Jixue Wang, Xiaoqing Wang, Jingyan Tian and Bing Yu

109 ***Progressive 3D Printing Technology and Its Application in Medical Materials***
Daoyang Fan, Yan Li, Xing Wang, Tengjiao Zhu, Qi Wang, Hong Cai, Weishi Li, Yun Tian and Zhongjun Liu

121 ***The Use of Peripheral Blood-Derived Stem Cells for Cartilage Repair and Regeneration* In Vivo*: A Review***
You-Rong Chen, Xin Yan, Fu-Zhen Yuan, Jing Ye, Bing-Bing Xu, Zhu-Xing Zhou, Zi-Mu Mao, Jian Guan, Yi-Fan Song, Ze-Wen Sun, Xin-Jie Wang, Ze-Yi Chen, Ding-Yu Wang, Bao-Shi Fan, Meng Yang, Shi-Tang Song, Dong Jiang and Jia-Kuo Yu

136 ***Silver Nanoparticles Coated Poly(L-Lactide) Electrospun Membrane for Implant Associated Infections Prevention***
Jiaolong Wang, Lilin Zhan, Xianhua Zhang, Runfa Wu, Lan Liao and Junchao Wei

144 ***Enhanced Anti-Glioma Efficacy by Borneol Combined With CGKRK-Modified Paclitaxel Self-Assembled Redox-Sensitive Nanoparticles***
Lingyan Lv, Xinrui Li, Wei Qian, Shennan Li, Yan Jiang, Yaokun Xiong, Jianpei Xu, Wei Lv, Xiaoyan Liu, Yun Chen, Yulin Tang and Hongliang Xin

155 ***Shape Matters: Comprehensive Analysis of Star-Shaped Lipid Nanoparticles***
Shuwen Cao, Xiaodi Liu, Xiuling Li, Chunhao Lin, Wenyue Zhang, Chee Hwee Tan, Shunung Liang, Baoming Luo, Xiaoding Xu and Phei Er Saw

164 ***Facile Strategy on Hydrophilic Modification of Poly(ε-caprolactone) Scaffolds for Assisting Tissue-Engineered Meniscus Constructs* In Vitro**
Zhu-Xing Zhou, You-Rong Chen, Ji-Ying Zhang, Dong Jiang, Fu-Zhen Yuan, Zi-Mu Mao, Fei Yang, Wen-Bo Jiang, Xing Wang and Jia-Kuo Yu

175 ***Advancements in Hydrogel-Based Drug Sustained Release Systems for Bone Tissue Engineering***
Yunfan Zhang, Tingting Yu, Liying Peng, Qiannan Sun, Yan Wei and Bing Han

188 ***Locally Controlled Release of Methotrexate and Alendronate by Thermo-Sensitive Hydrogels for Synergistic Inhibition of Osteosarcoma Progression***
Hongli Shan, Ke Li, Duoyi Zhao, Changliang Chi, Qinyuan Tan, Xiaoqing Wang, Jinhai Yu and Meihua Piao

198 ***Cell-Penetrating Peptides in Diagnosis and Treatment of Human Diseases: From Preclinical Research to Clinical Application***
Jing Xie, Ye Bi, Huan Zhang, Shiyan Dong, Lesheng Teng, Robert J. Lee and Zhaogang Yang

221 ***A Lipid-Nanosphere-Small MyoD Activating RNA-Bladder Acellular Matrix Graft Scaffold [NP(saMyoD)/BAMG] Facilitates Rat Injured Bladder Muscle Repair and Regeneration [NP(saMyoD)/BAMG]***
Chongrui Jin, Nailong Cao, Jianshu Ni, Weixin Zhao, Baojun Gu and Weidong Zhu

233 ***Targeted Antitumor Mechanism of C-PC/CMC-CD55sp Nanospheres in HeLa Cervical Cancer Cells***
Guoxiang Liu, Xiaohui Xu, Liangqian Jiang, Huanhuan Ji, Feng Zhu, Bingnan Jin, Jingjing Han, Xiaolei Dong, Fanghao Yang and Bing Li

246 ***Recent Advances in Nanotechnology for Dendritic Cell-Based Immunotherapy***
Chen Qian, Li-Jun Yang and Hong Cui

255 ***Advance in Drug Delivery for Ageing Skeletal Muscle***
Yi Li, Ming Chen, Yanpeng Zhao, Ming Li, Yong Qin, Shi Cheng, Yanyu Yang, Pengbin Yin, Licheng Zhang and Peifu Tang

264 ***Delivery of microRNA-33 Antagomirs by Mesoporous Silica Nanoparticles to Ameliorate Lipid Metabolic Disorders***
Yaoye Tao, Shengjun Xu, Jianguo Wang, Li Xu, Chenzhi Zhang, Kangchen Chen, Zhengxing Lian, Junbin Zhou, Haiyang Xie, Shusen Zheng and Xiao Xu

275 ***Shear Speed-Regulated Properties of Long-Acting Docetaxel Control Release Poly (Lactic-Co-Glycolic Acid) Microspheres***
Yuhao Zheng, Fan Sheng, Zihang Wang, Guang Yang, Chenguang Li, He Wang and Zhiming Song

283 ***Development of a Hyaluronic Acid-Based Nanocarrier Incorporating Doxorubicin and Cisplatin as a pH-Sensitive and CD44-Targeted Anti-Breast Cancer Drug Delivery System***
Tao Yu, Yongshuang Li, Xueyuan Gu and Qin Li

frontiers in Pharmacology

EDITORIAL
published: 22 February 2021
doi: 10.3389/fphar.2021.648749

Editorial: Emerging Micro- and Nanotechnologies for Medical and Pharmacological Applications

Yufen Xiao[1], *Jun Chen*[2]*, *Chao Wang*[3]*, *Jianxun Ding*[4]* and *Wei Tao*[1]*

[1]Center for Nanomedicine and Department of Anesthesiology, Brigham and Women's Hospital, Harvard Medical School, Boston, MA, United States, [2]Department of Bioengineering, University of California, Los Angeles, Los Angeles, CA, United States, [3]Jiangsu Key Laboratory for Carbon-Based Functional Materials and Devices, Institute of Functional Nano & Soft Materials (FUNSOM), Soochow University, Suzhou, China, [4]Key Laboratory of Polymer Ecomaterials, Changchun Institute of Applied Chemistry, Chinese Academy of Sciences, Changchun, China

Keywords: bioengineering, microtechnology, nanotechnology, pharmaceutics, controlled drug delivery, biomedical application

Editorial on the Research Topic

Emerging Micro- and Nanotechnologies for Medical and Pharmacological Applications

OPEN ACCESS

Edited and reviewed by:
Salvatore Salomone, University of Catania, Italy

***Correspondence:**
Jun Chen
jun.chen@ucla.edu
Chao Wang
cwang@suda.edu.cn
Jianxun Ding
jxding@ciac.ac.cn
Wei Tao
wtao@bwh.harvard.edu

Specialty section:
This article was submitted to Experimental Pharmacology and Drug Discovery, a section of the journal Frontiers in Pharmacology

Received: *01 January 2021*
Accepted: *13 January 2021*
Published: *22 February 2021*

Citation:
Xiao Y, Chen J, Wang C, Ding J and Tao W (2021) Editorial: Emerging Micro- and Nanotechnologies for Medical and Pharmacological Applications. Front. Pharmacol. 12:648749. doi: 10.3389/fphar.2021.648749

New features may emerge when a bulky material was engineered into micro-/nanoscale, which could be harnessed to bring innovations to the fields of medicine and pharmacology (Su et al.), e.g., targeted drug delivery by micro- and nanotechnologies to specifically treat human diseases (Ma et al.), like cancer (Wang et al.) and diabetes (Xiao et al.). This invited Research Topic contains 25 articles, including 15 original research papers, 9 review articles, and 1 minireview article, contributed by 199 researchers worldwide (Total views: 48,798; as of February 5, 2021), which covers a wide-range of research topics in the fields of medicine and pharmacology, including cancer diagnostics and therapy (Kim et al.), tissue engineering (Zhang et al.), diabetes treatment (Xu et al.), and others (Fan et al.).

Cancer therapies have been evolving with advances in oncology. This invited special issue covers both reviews and original research articles varying from chemodynamic therapy (CDT) and photothermal therapy (PTT) to immunotherapy. Among them, micro- and nanoparticles formed by polymers were meticulously designed and prepared. US Food and Drug Administration (FDA) approved biodegradable polymers, such as poly(ethylene glycol) (PEG), poly(lactide-*co*-glycolide) (PLGA), chitosan (CS), polylactide (PLA), and poly(ε-caprolactone) (PCL), are widely used to be self-assembled into nanoparticles. Among them, PEG, PLA, and CS can perform as hydrophilic moiety, while PLGA and PCL are hydrophobic chains. For instance, Li and co-workers developed PEG-PLGA micelle for loading sorafenib and all-trans retinoic acid to synergistically inhibit the growth of thyroid cancer *via* CDT. Injectable poly(ethylene glycol)-poly(L-valine) (PEG-PLV) hydrogel (Shan et al.) and PLGA microparticle (Zheng et al.) were developed for the sustained release of chemotherapeutics. Natural materials, like CS and hyaluronic acid (HA) nanoparticles, are also good candidates for delivering hydrophobic drugs, such as 10-hydroxycamptothecin (HCPT). HCPT-loaded CS nanoparticle developed by Guo et al. showed enhanced penetration in tumor sites and improved chemotherapy of melanoma. By applying CD55 ligand peptide, CS nanoparticle showed targeted antitumor efficacy (Liu et al.). HA was capable of encapsulating doxorubicin and cisplatin as a pH-responsive nanocarrier for the inhibition of breast cancer (Yu et al.). In order to achieve better penetration of drugs, cell-penetration peptides (CPPs) were introduced (Xie et al.). By combination with CGKRK peptide, paclitaxel prodrug nanoparticle demonstrated enhanced penetration against the blood-brain barrier (BBB) (Lv et al.). In addition to CPP modification, the shape also played an

important role in nanoparticle penetration (Cao et al.). The ultra-small nanoparticle exhibited the ability of crossing BBB with enhanced cell uptake, demonstrating potential in tumor therapeutics.

Apart from polymer materials, inorganic biomaterials and cell technology are also included in this special issue. Among them, two-dimensional (2D) nanosheets attracted the most attention due to their large surface area for high loading of drugs and excellent photothermal conversion efficiency (Kim et al.). Mesoporous silica nanoparticles also benefited from a large surface-to-volume ratio in delivering a gene to ameliorate metabolic disorders (Tao et al.). Magnetic nanoparticles held the advantages in cancer theranostic due to their role in generating reactive oxygen species (ROS) for CDT and relaxation rate for diagnosis (Guo et al.). Silver nanoparticle was generally considered as an antibacterial material (Wang et al.). Cell technology is rapidly developed because of the biocompatibility and multi-functionality of the cell. Peripheral blood-derived stem cells were capable of cartilage repair regeneration (Chen et al.). Dendritic cells were responsible for immune responses, which play a significant role in cancer immunotherapy (Qian et al.). Stem cells were progenitor cells capable of differentiating into various cell lineages, such as islet β cells to mimic the artificial pancreas (Xu et al.). By coating with cell membranes, nanocarriers could obtain the ability to escape from immune response and accurately reach targeted sites for cancer therapy (Li et al.).

In addition to the drug delivery system, tissue engineering is another crucial application of microtechnology. Several reviews summarized different platforms for tissue engineering. For example, hydrogels could be displayed as scaffolds to optimize the microenvironment for bone regeneration (Zhang et al.). Besides, hydrogels were also carriers for gene delivery to selectively upregulate or knockdown target genes for osteochondral regeneration (Yan et al.). One review article discussed the unique approaches to aged skeletal muscle loss. Another review presented by Fan et al. summarized the recent progress in 3D printing technology, one of the most exciting and precise manufacturing technologies. Original research covering the vital aspect of engineering is also included. For instance, 3D PCL scaffolds developed by Zhou et al. exhibited enhanced proliferation and adhesion of cells. The advanced surgical suture could be obtained by polyurethane fiber with antibacterial and shape memory properties (Zhou et al.). Jin et al. developed gene-loaded scaffold with adipose-derived stem cells for bladder repair. The scaffold is capable of drug loading to reach sustainable and controllable drug release at specific sites during repair (Shan et al.).

Overall, the current special issue reports a diverse intersection of micro- and nanotechnologies that showed promise potential in engineering materials for biomedical and pharmacological applications. Such an interdisciplinary investigation is building a bridge between fundamental material innovation and clinical medical translation, greatly benefiting fields of micro-/nanotechnology, bioengineering, and pharmaceutics.

AUTHOR CONTRIBUTIONS

YX, JC, CW, JD and WT contributed to writing this Editorial.

ACKNOWLEDGMENTS

The editors appreciate the contributions of all authors to this Research Topic, the constructive comments of all the reviewers, and the editorial support from Frontiers throughout the publication process.

Conflict of Interest: The authors declare that the research was conducted in the absence of any commercial or financial relationships that could be construed as a potential conflict of interest.

frontiers in Pharmacology

ORIGINAL RESEARCH
published: 09 January 2020
doi: 10.3389/fphar.2019.01506

Berberine-Incorporated Shape Memory Fiber Applied as a Novel Surgical Suture

Wen-cheng Zhou[1,2†], Peng-fei Tan[3,4†], Xing-han Chen[1,2], Ying Cen[1,2], Chao You[2,5], Lin Tan[3,4], Hao Li[5*] and Meng Tian[1,2,5*]*

[1] Department of Burns and Plastic Surgery, West China Hospital, Sichuan University, Chengdu, China, [2] Neurosurgery Research Laboratory, West China Hospital, Sichuan University, Chengdu, China, [3] College of Biomass Science and Engineering, Sichuan University, Chengdu, China, [4] Key Laboratory of Leather Chemistry and Engineering of Ministry of Education, Sichuan University, Chengdu, China, [5] Department of Neurosurgery, West China Hospital, Sichuan University, Chengdu, China

OPEN ACCESS

Edited by:
Jianxun Ding,
Changchun Institute of Applied Chemistry, China

Reviewed by:
Jun Wu,
Sun Yat-sen University, China
Lin-Sen Qing,
Chinese Academy of Sciences, China
Zhiqiang Yu,
Southern Medical University, China

***Correspondence:**
Lin Tan
tanlinou@scu.edu.cn
Hao Li
coscolh@126.com
Meng Tian
tianmong007@gmail.com

[†]These authors have contributed equally to this work

Specialty section:
This article was submitted to Experimental Pharmacology and Drug Discovery, a section of the journal Frontiers in Pharmacology

Received: *11 October 2019*
Accepted: *20 November 2019*
Published: *09 January 2020*

Citation:
Zhou W-c, Tan P-f, Chen X-h, Cen Y, You C, Tan L, Li H and Tian M (2020) Berberine-Incorporated Shape Memory Fiber Applied as a Novel Surgical Suture. Front. Pharmacol. 10:1506. doi: 10.3389/fphar.2019.01506

The surgical suture has long been used to reconnect the injured tissues to restore their structure and function. However, its utility remains challenging in many areas, such as surgical site infections and minimally invasive surgeries. Herein, we report a novel surgical suture that possesses both antibacterial activity and shape memory effect to address these issues. In detail, natural antibacterial berberine was incorporated directly into the spinning solution of shape memory polyurethane with a near body transition temperature, and then berberine-containing polyurethane (BP) fibers were prepared by a facile one-step wet-spinning method for surgical suture. The prepared BP fibers were micro-sized and characterized by their transition temperature, morphology, water contact angles, mechanical properties, *in vitro* shape memory effect, drug release, and antibacterial activity. The results showed that with the increasing amount of the incorporated berberine, the transition temperatures of the fibers were not significantly affected, remains at near body temperature, while the contact angles of the fibers were significantly decreased and the mechanical properties of the fibers were significantly weakened. The optimized fiber was selected to evaluate the cytotoxicity and *in vivo* biocompatibility before *in vivo* shape memory effect and wound healing capacity in a mouse skin suture–wound model was tested. Besides the shape memory effect, it was demonstrated that the fiber is capable of antibacterial activity and anti-inflammatory effect, and promoting wound healing. The mechanism of the antibacterial activity and anti-inflammatory effect of the fiber was discussed. Overall, it is expected that by the berberine added to the fiber for surgical suture, it will be more popular and extend the utility of the sutures in a wide range of clinical applications.

Keywords: berberine, antibacterial activity, shape memory, surgical suture, wet spinning

INTRODUCTION

As one of the most important medical devices, like wound dressing materials (Huang et al., 2019a), the surgical suture has long been used to reconnect the injured tissues to restore their structure and function (Shao et al., 2016). However, its utility remains challenging in many areas due to the increasing demands in the clinic. For example, surgical site infections (SSIs) are the second most

common healthcare-associated infections that occur during the first 3 weeks postoperatively, resulting in prolonged hospital stays, readmissions, increased morbidity and mortality, and high costs (Joseph et al., 2017). Although the underlying causes have been suggested, such as bacteria bio-adherence and formation of colonization and subsequent biofilm in the surgical site, there is no effective treatment to improve the outcomes of the patients according to clinical feedback.

Antibacterial treatment of surgical suture is a promising strategy to address SSIs as it has shown the feasibility of inhibiting bacterial growth in wounds and reducing the infection rate, such as FDA-approved triclosan-impregnated Polyglactin 910 (Byrne and Aly, 2019). Nevertheless, the wide use of triclosan has been suggested to a potential selection of bacteria and triclosan-adapted cross-resistance with antibiotics. Therefore, new alternative substances need to be employed so as to achieve good antibacterial activity. In this regard, berberine hydrochloride (BCH), which is derived from *Coptis chinensis*, was applied in this study. As a natural active pharmaceutical ingredient, it has gained considerable attention for its manifold pharmacological properties, including antibacterial activity and anti-inflammatory effect, both of which have been suggested to be beneficial to the infected wound, indicating that berberine might be a promising candidate for the treatment of surgical suture (Avila-Carrasco et al., 2019).

For the fabrication of antibacterial surgical suture, there are mainly two approaches that have been involved. The drug-coating approach has its intrinsic advantages of easy production at low cost without compromising the mechanical property of the suture matrix, whereas the major drawback lies in low drug loading and poor control over the drug release. On the contrary, the drug incorporation method such as electro-spinning is beneficial to attaining high efficient drug loading, while the production process generally needs harsh post-treatment that would inactivate the loaded drugs (Feng et al., 2019; Ding et al., 2019). For instance, commercial sutures have been commonly fabricated by melt spinning; however, the use of high temperature during the processing steps would be harmful to the activities of the loaded drugs.

Besides SSIs, the surgical suture was also challenged in difficulty in handling in minimally invasive surgery, in which knotting a suture was limited in a confined space. In this case, if the knot was fixed with a force that is too weak, scar tissue would form, leading to the formation of hernias and bacteria invasion. Instead, when the force was too strong, necrosis of the surrounding tissue may occur, resulting in patients suffering from severe pain after the surgery. One solution to overcome this obstacle would be to use a smart suture with shape memory effect triggered by the body temperature, e.g., the suture was elongated to be applied loosely in its temporary shape first, and then would shrink and tighten the knot in an adapted force at body temperature, and thus suture with shape memory effect seems to be an effective approach to improving the handling in surgery.

Herein, we report a novel surgical suture possessing both antibacterial activity and shape memory effect to address these issues. Specifically, natural antibacterial berberine was incorporated directly into the spinning solution of a shape memory polyurethane with a near body transition temperature that synthesized as our previous study (the synthesis route is shown in **Figure 1A**), and then berberine-containing polyurethane (BP) fibers were prepared by a one-step wet-spinning method for surgical suture (**Figure 1B**). The prepared BP fibers were characterized by their transition temperature,

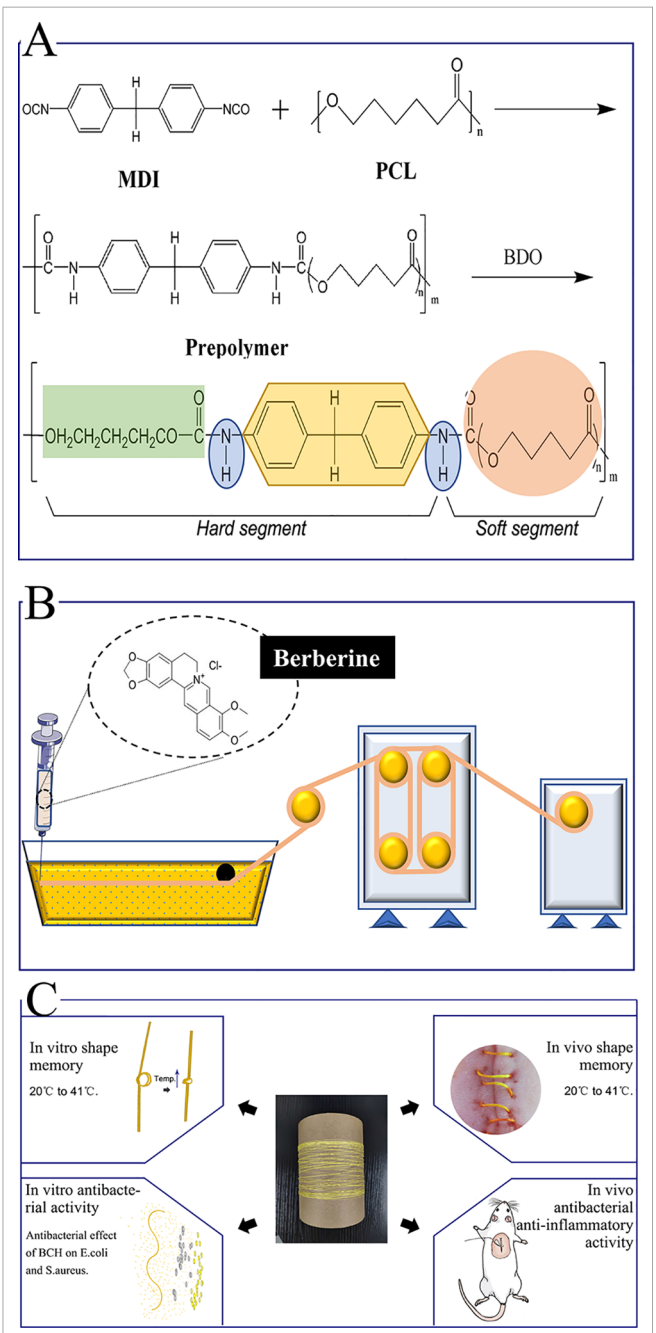

FIGURE 1 | Schematic presentation of the whole experiment. **(A)** Synthesis of the SMPU; **(B)** The one-step wet-spinning method for fiber; **(C)** *In vitro* and *in vivo* assays.

morphology, water contact angles, mechanical properties, *in vitro* shape memory effect, drug release, and antibacterial activity. The optimized fiber was selected to evaluate the cytotoxicity and *in vivo* biocompatibility before *in vivo* shape memory effect and wound healing capacity in a mouse skin suture–wound model was tested (**Figure 1C**). The mechanism of antibacterial activity and anti-inflammatory effect of the BP fiber was proposed and discussed.

MATERIALS AND METHODS

Materials

Polycaprolactone diol (PCL, Mn = 4000 g/mol) was purchased from Perstop UK Ltd. (United Kingdom). Berberine hydrochloride (BCH, 98% purity) was supplied by Aladdin Co., Ltd. (Shanghai, China). *N*,*N*-dimethylacetamide (DMAc) and other solvents were obtained from the Chengdu Kelong Reagent Company and used directly without further purification. *Escherichia coli* (ATCC8739) and *Staphylococcus aureus* (ATCC6538) were supplied by the R&D Lab of Functional Fibers of Sichuan University, China. Hematoxylin and eosin (H&E) stains were purchased from Baso Diagnostics Inc. (China). Gram's crystal violet solution (G1060) was purchased from Beijing Solarbio Science & Technology Co., Ltd. Two antibodies, interleukins (interleukin-1beta, IL-1β) and tumor necrosis factor (TNF-α), were purchased from Santa Cruz Biotechnology, Inc. (USA). Alamar Blue was purchased from Beijing Cell Chip Biotechnology Co., Ltd. (Beijing, China).

Synthesis of SMPU

Shape memory polyurethane (SMPU) was synthesized according to our previous study (Tang et al., 2019). The synthesis route is shown in **Figure 1A**. For the obtained SMPU, the thermal transition temperature (T_{trans}) based on the melting temperature (T_m) of soft segments PCL was a near body transition temperature around 41°C.

Preparation of Berberine-Containing Shape Memory Fiber for Surgical Suture

The synthesized SMPU was first softened at 60°C and then cut into small chips. A certain amount of SMPU chips were dissolved in DMAc under 60°C within 6 h to obtain a homogenous solution. Twenty percent mass concentration of SMPU was applied as the primary spinning solution, which was named SS-0. Similarly, two composite solutions were prepared, which were named SS-1 and SS-2 according to spinning solutions of 20%SMPU + 3%BCH and 20%SMPU + 6%BCH, respectively. **Table S1** summarizes the spinning parameters for preparing the fibers.

The prepared spinning solution was loaded into a syringe. The internal diameter of the syringe needle was 0.84 mm. During the process of spinning, the spinning solution was extruded from the syringe and solidified in the coagulation bath containing calculated pure water, and then the fibers passed through the drawing roller, drying rollers, and finally collected on a rotating mandrel. Three fibers were successfully obtained and named as BP-0, BP-1, and BP-2 based on the spinning solutions of SS-0, SS-1, and SS-2, respectively.

In the process of spinning, the amount of spinning solution was calculated by weighing, and the absorbance value of the coagulation bath after spinning was measured by an ultraviolet spectrophotometer. The content of berberine leaked into the coagulation bath was calculated according to the standard curve of berberine so as to calculate the actual drug load of berberine in the fiber.

Characterization of the Fibers

The surface and cross-section morphologies of the fibers were observed under scanning electron microscopy (SEM) (SU3500, Hitachi, Japan) after gold spraying. The static water contact angles of the fibers were tested with a surface contact angle tester (Harke-SPCAX1, China). Each sample was tested three times in parallel, and the average value was used as the final water contact angle to reflect the hydrophilicity and hydrophobicity of the fiber. The mechanical properties of the fibers were tested with an electronic single-yarn strength machine (YM061, China), in which the clamping distance was 50 mm, the tensile rate was 100 mm/min, and the fracture threshold was 85%. Differential scanning calorimetry (DSC) was performed on a DSC-Q200 instrument (Hitachi, Japan).

In Vitro Shape Memory Test

Shape memory performance was observed by stretching the original length of 6 cm fiber to 12 cm above its T_{trans} and fixing with deionized water at room temperature, and then heating the fibers again. The fixed ratio (R_f) and recovery rate (R_r) of the fibers were calculated using the following equations:

$$R_f = (L_2 - L_0)/(L_1 - L_0) \times 100\%$$

$$R_r = (L_1 - L_3)/(L_1 - L_0) \times 100\%$$

where L_0, L_1, L_2, and L_3 stand for the lengths of the initial shape, deformed shape, fixed shape, and recovery shape, respectively.

In Vitro Drug Release

Prior to the antibacterial and animal experiments, we investigated the release behaviors of berberine from the normal fibers and stretched ones to confirm that berberine can release from the fibers and then exhibit the antibacterial performance. In virtue of the shape memory function, the fibers can be deformed under higher temperatures and maintain the deformed shapes under lower temperatures. BP-1 and BP-2 fibers were stretched by 100% before the berberine release, and the deformed shapes were fixed at room temperature, which were named BP-1S and BP-2S, respectively. BP-1, BP-2, BP-1S, and BP-2S fibers in triplicate were put into 5-ml phosphate-buffered saline (PBS) buffer solution with different pH values, including 4.0, 7.0, and 9.0, respectively, and placed in a shaker with a constant temperature of 37°C. Three milliliters buffer solution was withdrawn at several regular intervals and an equal amount of

PBS was supplemented until the release was completed. The released amount of berberine was determined by a UV–visible spectrophotometer at 344 nm, and the accumulated release curves were plotted according to the standard curve.

Antibacterial Test

Two representative strains of *E. coli* and *S. aureus* were selected to demonstrate the antibacterial performance of the prepared fibers embedded with berberine. The test procedure was conducted as follows: 1) The bacterial strain was incubated in Luria–Bertani (LB) broth at 37°C for 12 h, and the original bacterial suspension concentration was diluted to 1×10^5–5×10^5 CFU/ml with PBS buffer with pH 7.0; 2) 20 mg BP-0, BP-1, and BP-2 fibers were individually placed inside testing vials containing 1.5 ml PBS, and then adding 1.0 ml of diluted bacterial suspension into the vials for another 12 h incubation; 3) the co-cultured bacterial suspension was diluted into several concentrations to determine the quantity of bacteria, and 100 µl of the bacterial suspension was withdrawn to spread on the LB agar plates and subsequently incubated at 37°C overnight; (4) observing and counting the colonies on LB agar plates. The bacterial suspensions without fiber were used as blank controls.

In Vitro Cytotoxicity

In vitro cytotoxicity of the fibers was assayed according to ISO 10993 part 5 guidelines 3 (Bernard et al., 2017). Extract was prepared by the incubation of 0.2 g of each fiber with 1 ml of Dulbecco's modified Eagle's medium (DMEM) supplemented with 10% fetal bovine serum (FBS), 100 µg/ml penicillin, and 100 µg/ml streptomycin for 48 h at 37°C. L929 fibroblasts were cultured until they reached approximately 80% confluency before preparing the plates for the cytotoxicity assay. The density of seeding was 5,000 cells per well in the 96-well plates. After 24 h, the culture media were discarded and replaced with the extracts. Alamar Blue assay was performed for the cytotoxicity test in accordance with the manufacturer's instruments (Mullick Chowdhury et al., 2013). Briefly, the cells were washed with PBS before adding 100 µl phenol red-free DMEM and 10 µl of Alamar Blue reagent (Bernard et al., 2017). After 4 h incubation, fluorescence measurements were recorded using a Multifunctional Fluorescent Enzyme Marker (BioTek Synergy Mx, USA) at the respective excitation and emission wavelengths of 530 and 580 nm. Six parallels were carried out in each group. All viability values were calculated relative to the blank control.

Animal Studies

Animals

The animal studies were approved by the Animal Ethical Committee of the West China Hospital of Sichuan University in compliance with Chinese national guidelines for the care and use of laboratory animals. Adult male BALB/C mice (25–30 g) were purchased from Dashuo Laboratory Animal Co., Ltd. (Chengdu, China). The mice were kept under controlled temperature and humidity with food and water *ad libitum*.

In Vivo Biocompatibility

The mice were anesthetized with intraperitoneal administration of pentobarbital sodium (3% in saline solution) at a dose of 1 ml/kg. The gluteal side of the mice was shaved and disinfected with iodine solution before surgery. The BP-1 suture, 3 cm long, was implanted into the left side of the gluteal muscle. To avoid secession of the suture construction, both ends of the suture were tied into a knot with a little space. Treatment with BP-0 suture in the right gluteal muscle was employed as control (Shao et al., 2016). After 3 and 7 days of operation, three mice in each group were sacrificed, respectively. H&E staining was performed to investigate the biocompatibility.

In Vivo Shape Memory

The *in vivo* shape memory test was performed as in the previous study, with minor modifications (Lendlein and Langer, 2002). Briefly, the sutures were first stretched twofold of their initial length and maintained for 10 min at 50°C, then cooled at room temperature and kept in ambient temperature before the following experiments. Three mice were anesthetized as before and 2-cm-long incisions were made on the back. Then the wound was sutured loosely. The shape memory effect was actuated while the temperature of antecedent trauma was increased from 20°C to 37°C, and to 41°C by a hair blower to simulate a posttraumatic hyperpyrexia process. The photos of the same wound at different temperatures were shot from vertical and lateral directions.

Mouse Skin Suture–Wound Model

The sutures were first stretched twofold of their initial length and maintained for 10 min at 50°C, then cooled at room temperature and kept in ambient temperature before use. The mouse skin suture–wound model was established as described previously, with minor modifications (Mebert et al., 2018). Briefly, the mice were anesthetized with intraperitoneal administration of pentobarbital sodium (3% in saline solution) at a dose of 1 ml/kg. The fur of the test animals was shaved carefully using an electric razor and further removed completely using a depilatory cream. Then the skin was decontaminated with alcohol and iodophor solution. A 1.5-cm-length incision was made along the mid-back of the trunk. The depth of the wound did not break into the panniculus carnosus. One wound was created per animal. The sutures were threaded onto surgical needles and the continuous suture was chosen for the closure of the wounds (Wang et al., 2018). The mice were randomly divided into four groups as follows: G I (the wound was sutured with BP-0); G II (the wound was sutured with BP-1); G III (the wound was sutured with BP-0 before bacterial inoculation); and G IV (the wound was sutured with BP-1 before bacterial inoculation). For G III and IV, *S. aureus* was inoculated by applying 10 µl of bacterial suspension (1×10^8) onto the incision site for infection (Nakagawa et al., 2017). For G I and II, the same volume (10 µl) of saline was applied as the control (Hahn et al., 2009). The wounds were photographed with a camera (Canon-IXUS230HS, Japan) and infrared thermal imaging (FLIR-T62101, Sweden) was taken every day.

For histology and immunohistochemistry, mice were euthanized after 3 and 7 days post-surgery and the skin tissues were harvested from the suture sites. The tissues were then fixed in 4% paraformaldehyde, dehydrated in graded alcohol, and embedded in paraffin. The embedded tissue blocks were sectioned at 5 μm thickness and stained with H&E, TNF-α, and IL-1β immunohistochemical staining. To identify bacteria, biopsy specimens were stained with Gram's crystal violet solution. Images of the histological section were acquired using an Olympus compound microscope (BX43, Japan) connected with an Olympus microscope camera (Sence, Japan). In order to evaluate the severity of inflammation, ImageJ software was used for image analysis and quantitative counting (Fan et al., 2018). Four random high-power fields (HPFs) were chosen from each section. Neutrophils in 10 regions of interest (ROIs) per HPF were counted. There are four sections in total randomly chosen from a mouse.

Statistical Analysis

The statistical methods were chosen according to the type of data. Two groups of unrelated data, if the variance is homogeneous, then unpaired *t* test was used. Comparisons between the multiple groups were determined by one-way ANOVA. Kruskal–Wallis was used for analyzing thermal recordings. All statistical calculations were carried out with the help of GraphPad Prism 7.0. Significance was defined as: *** for $P < 0.001$, ** for $P < 0.01$, and * for $P < 0.05$.

RESULTS AND DISCUSSION

Characterization of the Fiber for Surgical Suture

The berberine-containing shape memory fiber was fabricated by a facile scalable one-step wet-spinning approach, and the fibers were micro-sized in the range of 237–339 μm. The fibers were characterized in terms of T_m, drug loading, surface wettability, and mechanical properties, and the testing results are summarized in **Table 1** and **Figure 2**. According to the DSC curves (**Figure 2A**), the influence on the T_m after incorporating berberine is not obvious, and the prepared three types of fibers, BP-0, BP-1, and BP-2, have similar T_m which are near body temperature. Except that the T_m of pristine PCL exhibited the highest around 53°C, while that of other fibers was around 40°C, which was derived from the partial crystallization of PCL segments. In addition, with the increase of the incorporated berberine, the T_m of the fiber was decreased, indicating that the incorporated berberine also decreased the T_m of the fiber.

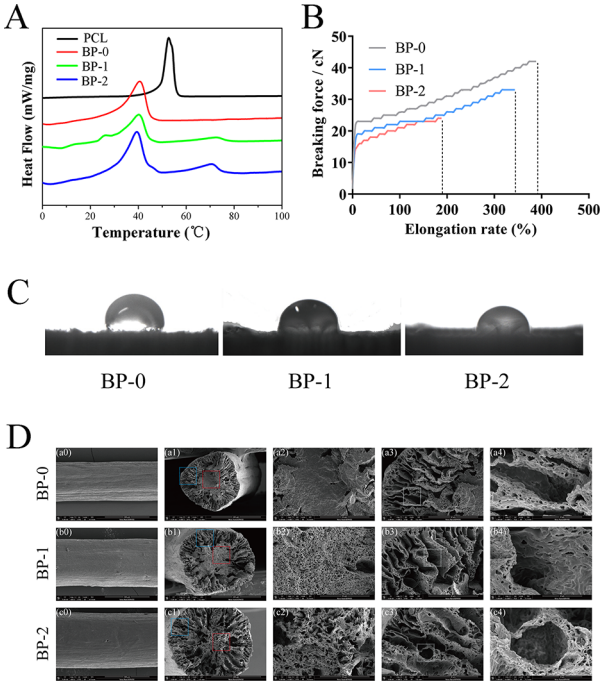

FIGURE 2 | Typical DSC curves **(A)**, stress–strain curves **(B)**, water contact angles **(C)**, and SEM images **(D)** of the fibers.

Figure 2B shows the typical tensile curves of BP-0, BP-1, and BP-2 fibers. Clearly, the content of berberine in the fiber has a significant effect on the mechanical property of the fiber, i.e., with the increase in the amount of berberine in the fibers, both breaking strength and elongation decreased, which could be ascribed to the disruption effect of berberine; in other words, the integrity of the fibers were damaged by BCH particles, and more defects were yielded when increasing the amount of BCH.

The water contact angles (WCA) of the prepared fibers were measured using a sessile drop method. As shown in **Figure 2C** and **Table 1**, the WCA of the fibers was decreased with the increase of the incorporated berberine, which was resulted from the hydrophilic nature of berberine with quaternary ammonium structure. The more berberine incorporated into the fiber, the higher the hydrophilicity of the fibers, and thus the WCA value is in the order of BP-2 < BP-1 < BP-0.

The microstructure of the fibers was observed by SEM measurements. As shown in **Figure 2D**, the surface of the obtained fibers is almost smooth, and some shallow grooves can be found. More obviously, with the increase of the incorporated berberine, the core part of the fiber became

TABLE 1 | Properties of the fibers (mean ± SD, $n = 6$).

Fiber	Diameter (μm)	T_m (°C)	Drug loading (%)	Contact angle (deg)	Breaking force (cN)	Elongation at break (%)
BP-0	237.35 ± 4.71	40.45	0	106.5 ± 0.3	42.10 ± 2.02	375.97 ± 13.68
BP-1	291.25 ± 5.09	40.36	12.70	93.3 ± 0.6	31.20 ± 2.35	287.47 ± 23.29
BP-2	339.38 ± 2.96	39.55	22.40	87.2 ± 0.8	24.40 ± 1.17	175.29 ± 7.57

looser and larger micropores were yielded, indicating that the distribution of berberine might also influence the fiber solidification and formation during the spinning process. Additionally, it could be inferred that a loose microstructure might lead to the reduction of mechanical property.

In Vitro Shape Memory

Prior to the *in vivo* application as the surgical suture, the shape memory performance was tested *in vitro*, and the testing process and the corresponding fixation and recovery ratios are shown in **Figure 3**. The whole shape memory process mainly includes four states in original shape (a), in maximum strain (b), in fixation (c), and after recovery (d), in which the fixed shape with longer length can be applied as the surgical suture, and then recover to the shorter length upon the trigger under body temperature (Lendlein and Langer, 2002). According to testing results, all the samples showed desirable R_f and R_r, which were around 90% without significant difference, and such shape memory capacity can meet the requirement for tightening wounds in practical application. More specifically, the shape memory suture with elongated length can be easily applied on the wound in a pleasant way, and then shrink and recover to the original length gradually triggered by body temperature in virtue of the thermal sensitivity.

In Vitro Drug Release

The *in situ* environment of the wound is commonly acidic due to inflammation or infection, and thus the effect of pH on the release of berberine was studied. As shown in **Figure 4**, the release profile of all fibers exhibited two stages. The first stage

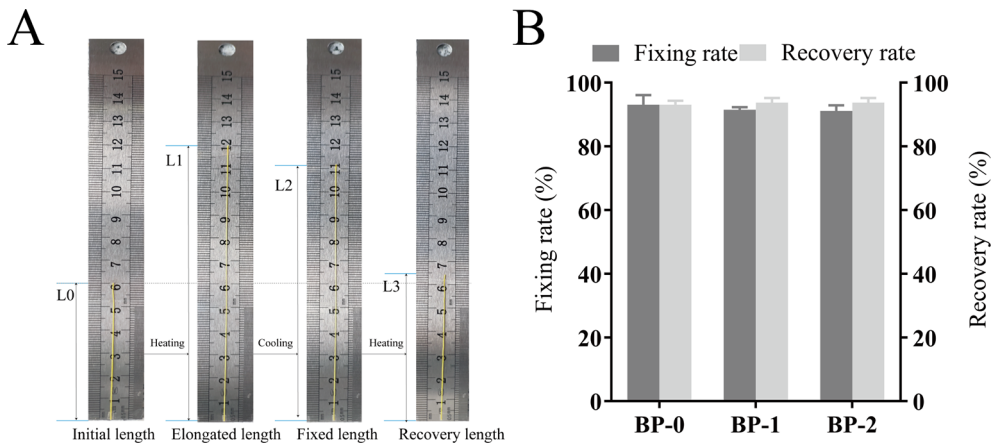

FIGURE 3 | Macroscopic pictures for demonstrating the shape memory process **(A)** and the fixation and recovery ratios of different fibers **(B)** (mean ± SD, n = 6).

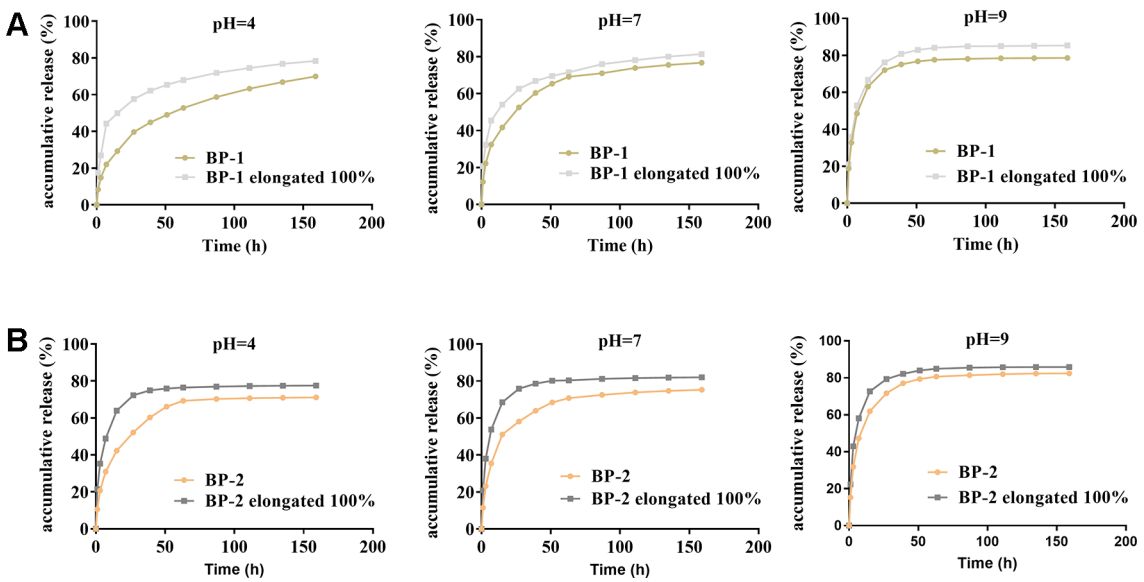

FIGURE 4 | Effects of pH and stretching on the BCH release of the fiber BP-1 (**A**) and BP-2 (**B**) (mean ± SD, n = 6).

would be one of the rapid burst releases and the second would be one of slow and extension releases. The release of berberine for all fibers was significantly affected by pH values, i.e., the release of berberine was in the order of medium at pH 4 < pH 7 < pH 9. Considering the acidic environment of the wound, the slower release of berberine probably has the advantage of release in a sustained manner.

When shape memory fiber was used as suture, the fiber was stretched, which might accelerate the release due to the increased surface area and the reduced release pathway after stretching deformation. As expected, our results showed that berberine released faster from the fiber under stretched state compared to that from original fiber, which might be beneficial to early antibacterial actions that need a high dose of berberine to kill the bacteria.

Antibacterial Activity

The antibacterial performance of berberine was tested and the results are shown in **Figure 5** and **Table S2**. Obviously, bacteria spread fully on the agar plates of BP-0 and blank control groups, and the number of bacteria colonies derived from both groups were around 10^6 CFU/ml. In contrast, few colonies can be found on the agar plates of BP-1 and BP-2 groups, indicating BP-1 and BP-2 have completely inactivated both *E. coli* and *S. aureus*.

Cytotoxicity and *In Vivo* Biocompatibility

Considering the mechanical property of the prepared fibers, BP-1 was selected as the optimized fiber for the following evaluation studies, and BP-0 was used as the control. The cytotoxicity of the BP-0 and BP-1 fibers was tested by Alamar blue assay using L929 cells. It is evident that after incubation for 1 and 3 days, the cell viability of the two fibers was around 90% (**Figure 6A**), indicating that there is almost no cytotoxicity for two sutures. The *in vivo* biocompatibility of the fibers was assayed by intramuscular implantation. As shown in **Figure 6B**, on day 3, both two fibers are surrounded by a large number of inflammatory cells, which evident a severe inflammation reaction at an early time. However, when the time prolonged to day 7, the inflammation reaction for BP-1 almost disappeared, which might be due to the pharmacological effects of berberine on anti-inflammation. In contrast, for BP-0, there was still a massive quantity of inflammatory cells around the fiber.

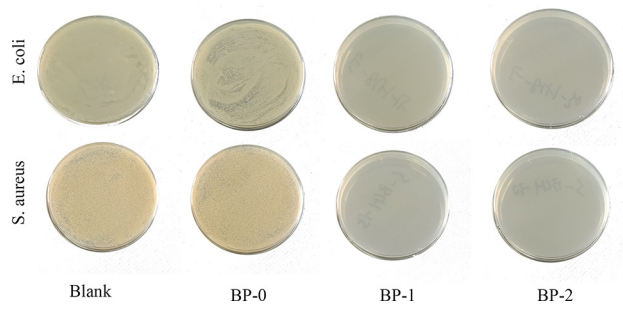

FIGURE 5 | Colony growth of the fibers against *Escherichia coli* and *Staphylococcus aureus*.

In Vivo Shape Memory

As shown in **Figure 6C**, the elongated fiber is sutured loosely in the wound and it is, as expected, gradually shrinking when the temperature rises, indicating that the *in vivo* shape memory effect of the fiber was evident. It is uneasy for a doctor to handle the tying force by using traditional surgical suture. If the force of tying is too high, it may cause necroses of the surrounding tissue. On the contrary, if the tying force is too weak, it may result in scars and even non-union. Therefore, the shape memory effect of this novel suture provides a potential therapeutic strategy that doctors could suture wounds in its slack elongated state, and then the suture would be triggered by body temperature to return to its original shape and the contraction of suture makes the knot tight in an adapted force (Zhao et al., 2019).

Mouse Skin Suture–Wound Model

Wound Healing Evaluation

The wound healing capacity of the suture was evaluated using a mouse suture–wound model. **Figure 7** shows the wound healing process of the four groups on days 1, 3, 5, 7, and 9 after the operation. On day 1, there was no distinct difference in wound condition among the four groups and no abnormality was observed in each group. In contrast, the skin around the wounds was red and swelling on day 3, indicating that the wounds were inflamed. In particular, the wounds with purulent exudate in G III and G IV were symptomatic of pyogenic infection that was a specific inflammatory caused by a bacterial infection. On day 5, it was shown that the wounds in G III and G IV have severe edema with pus scab, and the involution of these two groups was not good. However, the wounds in G IV were going to heal on day 7, and the ones in G III were still covered with pus scabs and some necrosis tissue. On day 9, the wounds in G III with scab and necrotic tissue remaining had no tendency to heal, while the other three groups have reached clinical healing. Taken together, the above results indicated that the berberine-containing suture promoted wound healing in the presence of *S. aureus* treatment condition.

The antibacterial activity of the suture was assessed by Gram staining. As shown in **Figure 8**, for G I and G II, it is normal to have no bacteria because they are not treated with *S. aureus*. On the contrary, the presence of bacteria was observed in G III (black arrow). Distinctively, G IV had no bacteria in spite of treatment with *S. aureus*, suggesting that the berberine-containing suture had antimicrobial activity.

Postoperative Thermoregulation

The wound temperature was detected by infrared thermal imaging in order to identify if the berberine-containing suture could decrease the temperature of the wound since the signs of inflammation and infection are an increase of temperature. Infrared thermal images and the time courses of the wound temperatures are shown in **Figure 9**. In all groups, the wound temperatures climbed sharply on the second day after the

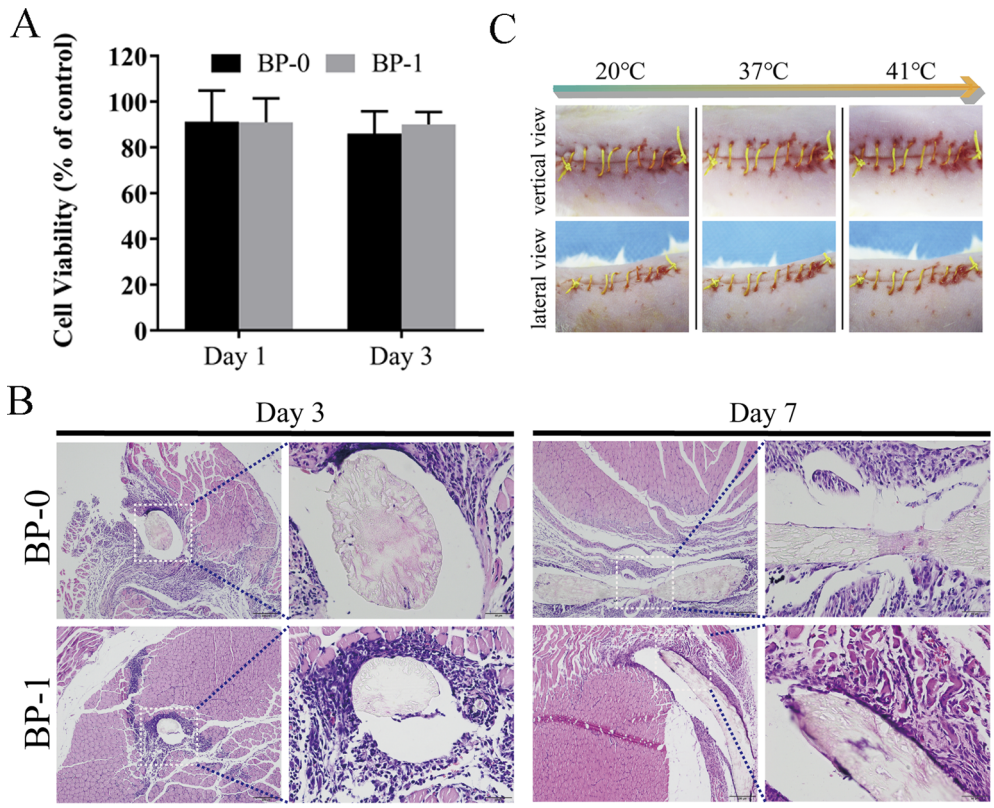

FIGURE 6 | (A) Cytotoxicity test on days 1 and 3. Data are presented as the mean ± SD (n = 6). **(B)** *In vivo* muscular biocompatibility evaluation of sutures. Representative photos of H&E-stained histological sections of the muscle tissue with BP-0 and BP-1 after implantation for 3 and 7 days. Images on the *right* were the magnified ones from the *left dotted line marked ones*. **(C)** *In vivo* shape memory assay. The photo series (20°C to 41°C) shows the shrinkage of the fiber while temperature increases (vertical and lateral views for the same temperature).

operation (**Figures 9A, B, D**) and then fluctuated around 38°C, indicating that the inflammation and infection induced the increase of the wound temperature. The recordings of the temperature were analyzed by Kruskal–Wallis test, and the results showed that there was no statistical difference in the wound temperature between G I and G II (**Figure 9C**), while the one in G IV was significantly lower than that in G III (**Figure 9E**), suggesting that the berberine-containing suture was capable of anti-inflammation and anti-infection, and thus decrease of the wound temperature. Our results are consistent with the studies of Chu et al. (Chu et al., 2014; Neag et al., 2018), who had demonstrated that berberine possesses the potential to relieve fever as an antipyretic agent.

H&E Staining

H&E staining was examined to assess the inflammatory cell response in the wound of the mice (Huang et al., 2019b). On the third day postoperatively, inflammatory cells are concentrated in the skin wound in all groups (**Figure 10A**). The severity of the inflammation was estimated by the number of neutrophils (Fan et al., 2018). As shown in **Figure 10B**, the numbers of neutrophils in G III and IV are significantly more than those in G I and G II, indicating that infection with *S. aureus* can lead to severe inflammation in the wound of the mice. When comparing G III and G IV, it was shown that the neutrophils in G IV were much more than those in G III, which suggested that berberine-containing suture could enhance the recruitment of neutrophils around the suture in the incipient process of inflammation.

When the time prolonged to day 7, both the numbers of the neutrophils in G II and G IV were significantly decreased compared to those on day 3, respectively, indicating that the inflammation is significantly suppressed on day 7. Moreover, the numbers of neutrophils in G II and G IV were also significantly less than those in G I and G III on day 7, respectively (**Figure 10C**). These tendencies proved the anti-inflammatory effect of the berberine-containing suture.

Although traditional Chinese medicine has been using berberine-containing herbs to treat inflammatory bowel disease for thousands of years, and many previous studies have revealed the anti-inflammatory properties of berberine, barely any tests have been performed for the purpose of verifying the same effect in skin tissue (Hasday et al., 2000; Küpeli et al., 2002; Doyle and Schortgen, 2016). Our study has not only demonstrated the same pharmaceutical properties in skin tissue but also showed time specificity.

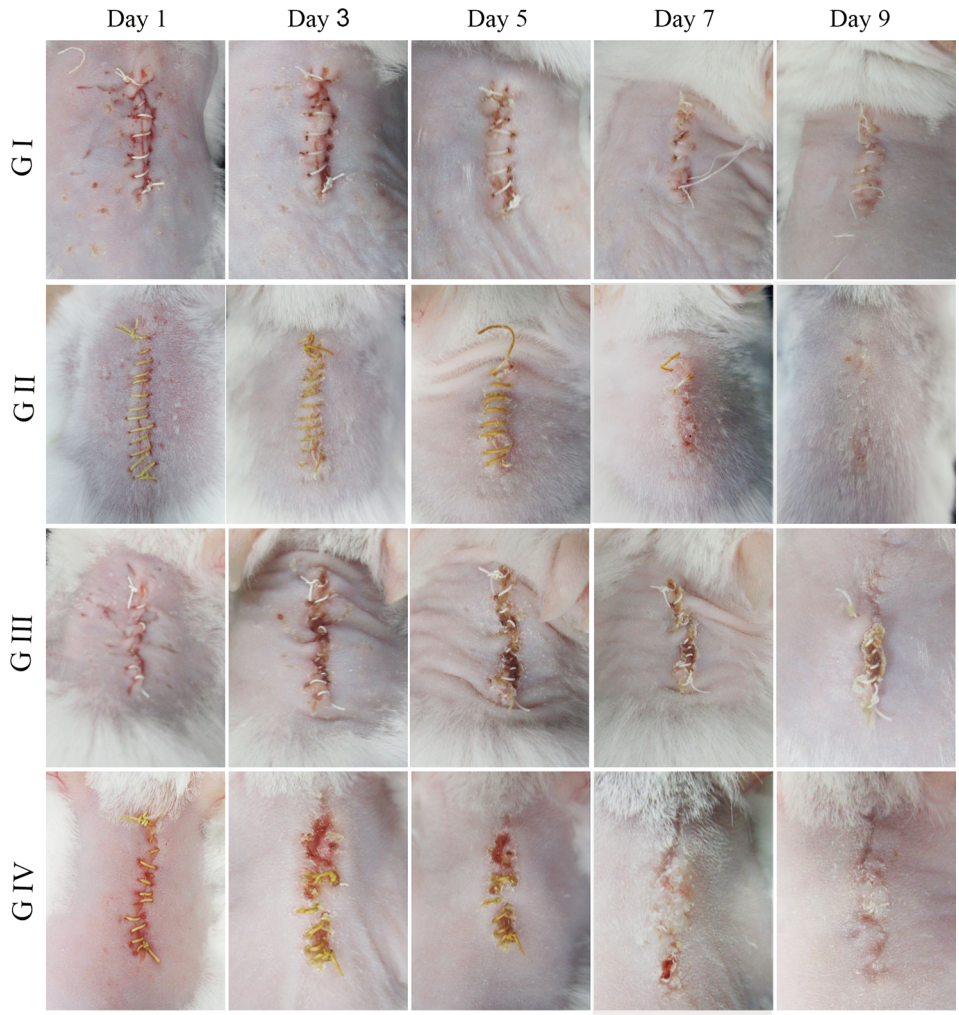

FIGURE 7 | Mouse skin suture–wound model. Representative photos from four experimental subgroups at different times postoperatively show the wound healing process.

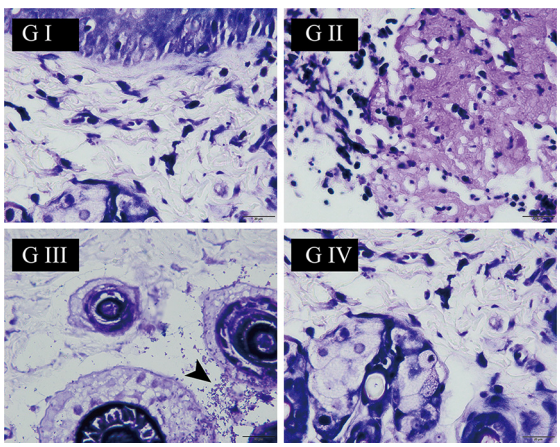

FIGURE 8 | The wound skin tissue was stained with Gram's crystal violet solution at the end of the experiment on day 9. The *black arrow* points to *Staphylococcus aureus* (the scale is 20 μm).

Immunohistochemistry Staining

To further investigate the anti-inflammation effects of the berberine-containing suture, pro-inflammatory cytokines, such as TNF-α and IL-1β, were determined to assess the inflammation by immunohistochemical staining. As shown in **Figures 11A–F**, both TNF-α and IL-1β in G III and G IV exhibited higher levels than those in G I and G II on both days 3 and 7, confirming that the infection with *S. aureus* resulted in severe inflammation, as evidenced by H&E staining. More importantly, both cytokines in G IV were always lower than those in G III on both days 3 and 7, indicating that the berberine-containing suture is capable of reducing pro-inflammatory cytokines in the course of inflammation, which is consistent with its anti-inflammation effects.

Mechanism Discussion

Based on the results from the animal study using mouse skin suture–wound model, the berberine-containing suture exhibited promotion of wound healing, antibacterial activity, decrease of

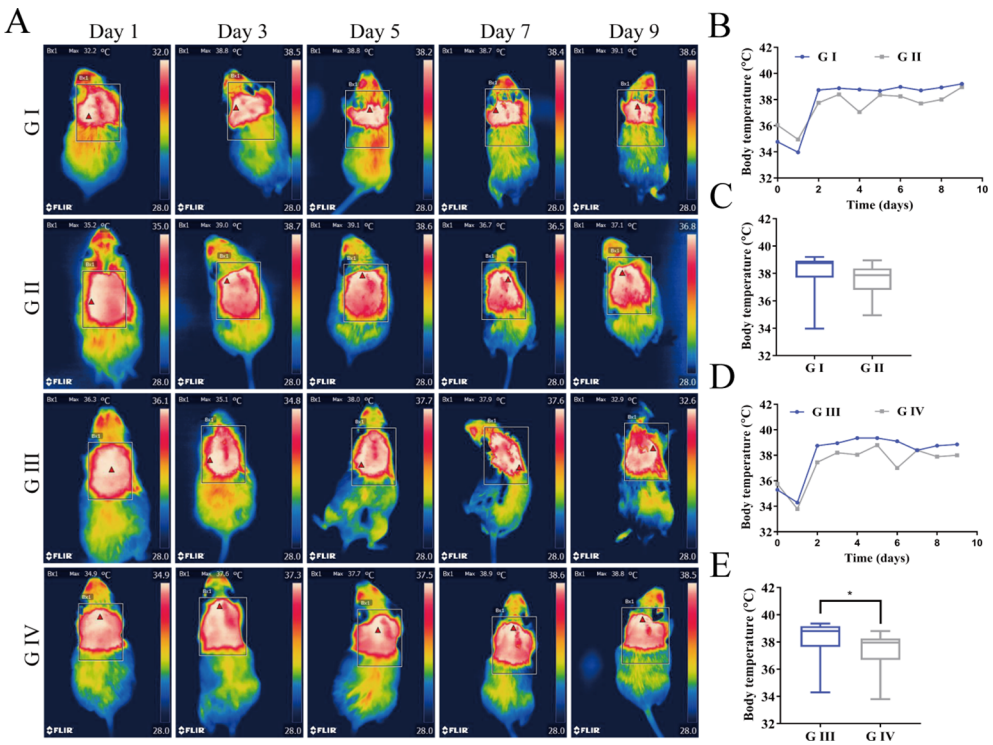

FIGURE 9 | (A) Infrared thermal images of the wounds for mice. **(B)** Time courses of the wound temperatures for G I and G II. **(C)** Comparison of the recordings of the temperature for G I and G II using Kruskal–Wallis test. **(D)** Time courses of the wound temperatures for G III and G IV. **(E)** Comparison of the recordings of the temperature for G III and G IV using Kruskal–Wallis test. (*P < 0.05).

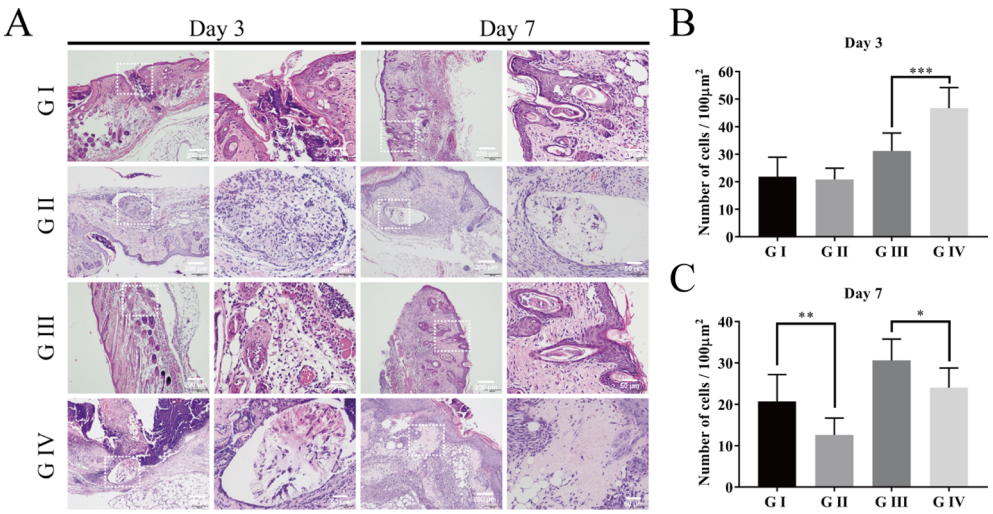

FIGURE 10 | Hematoxylin–eosin staining of the wound skin tissue. **(A)** HE staining on day 3 and day 7; Cumulative percentage of neutrophils in random regions of interest by ImageJ software on day 3 **(B)** and day 7 **(C)**. The scale bar is shown in the figure (one-way ANOVA, mean ± SD, *n* = 6) (*P < 0.05, **P < 0.001, ***P < 0.001).

wound temperature, as well as anti-inflammatory effect, all of which seem to be related to the bioactivities of berberine that was incorporated in the suture since berberine is hydrophilic and released from the suture in a sustained manner. To explain these beneficial effects of the berberine-containing suture in the mouse model, a mechanism was proposed as follows based on literature and our results.

First, the potential benefit of the berberine-containing suture in wound healing could come from the widely known antibacterial activity of the incorporated berberine. Berberine is

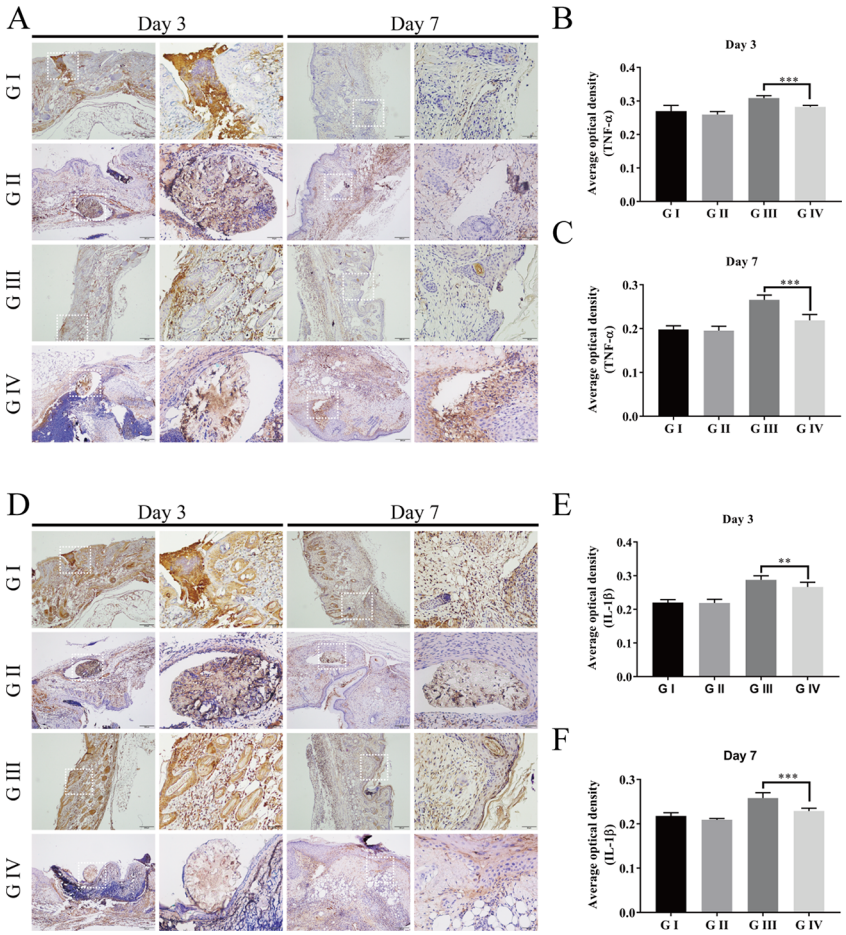

FIGURE 11 | Immunohistochemistry of the wound skin tissue. The immunohistochemical staining of pro-inflammatory cytokines TNF-α **(A)** and IL-1β **(D)** of the wound skin tissue. Average optical density of TNF-α on day 3 **(B)** and day 7 **(C)**; Average optical density of IL-1β on day 3 **(E)** and day 7 **(F)**. The scale bar is shown in the figure (one-way ANOVA, mean ± SD, $n = 6$) (**P < 0.01, ***P < 0.001).

a positively charged compound, endowing itself a property to interact directly with bacterial cell wall components, lipopolysaccharide, and cell surface proteins. In particular, Oh et al. revealed an important antibacterial mechanism that berberine possessed strong inhibition activity on sortase enzymes, leading to a remarkable reduction in the virulence and infection ability of *S. aureus* (Oh et al., 2006). The sortase enzyme is a surface protein transpeptidase relevant to anchoring the surface proteins in the cell wall of peptidoglycan in Gram-positive bacteria. For *S. aureus*, the sortase enzyme plays a pivotal role in the adhesion to the host, making them accomplices to bacterial infection. Berberine acts on *S. aureus* by inhibiting the adhesion process through deletion of two sortase enzyme isoforms, sortase A (SrtA) and sortase B (SrtB), to restrain the activities of the sortases, and thus exhibiting antibacterial activity (**Figure 12I**).

Second, our results showed that the berberine-containing suture enhanced the recruitment of neutrophils in the early stage of inflammation (**Figure 10**). The schematic diagram is shown in **Figure 12II**. In order to find out the reasons for this phenomenon, we need to see the essence of what happened. As an adaptive response to noxious conditions including infection and injury, inflammation is crucial to restoring homeostasis, even though it can affect normal physiology, resulting in a transient decline in tissue function. Inflammation is a double-edged sword for health. It is helpful for the body in reasonable amounts (Chang et al., 2018). Meanwhile, it is easy to become detrimental when of excessive duration or high intensity on account of its tissue-damaging potential (Habtemariam, 2016). Thus, it is essential for inflammation to be orchestrated in the right way. The berberine-containing suture in our study just has the ability to regulate inflammation, e.g., it can enhance the inflammation in the early stage and then suppress inflammation subsequently as well.

Besides, the expression of cytokines is significantly inhibited throughout the later stages of the inflammatory response by the berberine-containing suture (**Figure 12III**). Pro-inflammatory cytokines, such as TNF-α and IL-1β, play an important role in activating inflammation. They are fundamental in the incipient stages of inflammation. Nevertheless, it is harmful if the

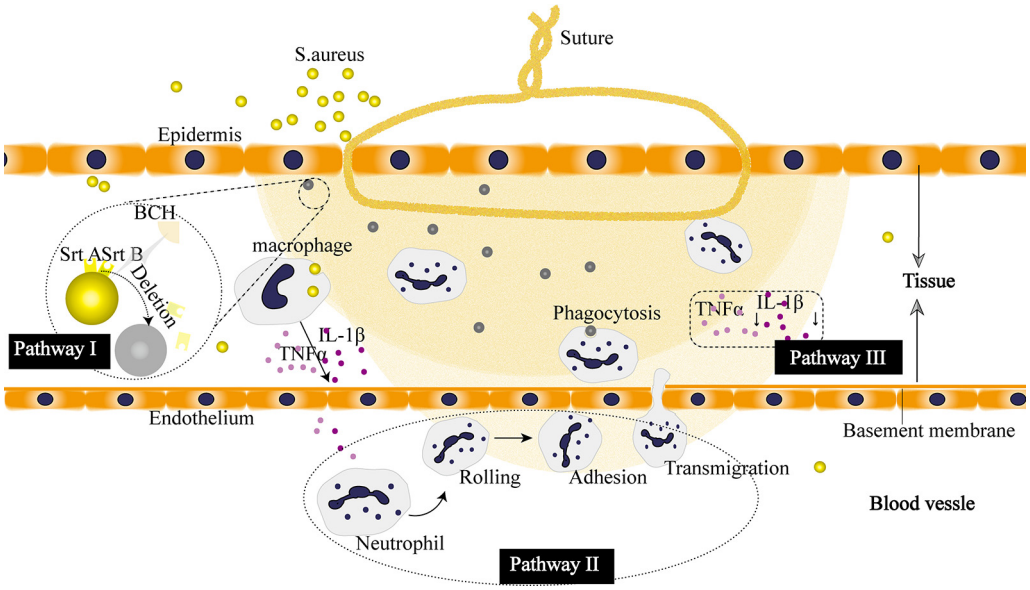

FIGURE 12 | Proposed pharmacological mechanism of the berberine released from the suture. **I** Berberine inhibits virulence and infection potential of *Staphylococcus aureus* through restraining the activities of sortase **A** (*SrtA*) and sortase **B** (*SrtB*). **II** Berberine enhances the recruitment of neutrophils. **III** Berberine plays an anti-inflammatory role by downregulating the expression of cytokines.

cytokines keep working throughout the course of inflammation. Blocking the cascade amplification of cytokines in time can reduce the damage to the tissues caused by inflammation. Lee et al. also observed that berberine was capable of suppressing inflammatory agent-induced TNF-α and IL-1β production in lung cells (Lee et al., 2007). Furthermore, their results showed that the suppression effect of berberine resulted from the inhibition of inhibitory κB-α phosphorylation and degradation.

Overall, it is interesting that berberine-containing suture is antibacterial and anti-inflammatory, plus its shape memory effect, all of which will make it attractive to extend the use of the suture in a wide range of clinical applications.

CONCLUSIONS

In summary, we report a novel berberine-containing surgical suture that possesses both antibacterial activity and shape memory effect to address clinical issues such as SSIs and difficulty in handling in minimally invasive surgery. The sutures were fabricated by a facile scalable one-step wet-spinning strategy, in which natural berberine was incorporated directly into the spinning solution of shape memory polyurethane with a T_m slightly higher than body temperature, and then were comprehensively characterized in terms of their transition temperature, morphology, water contact angles, mechanical properties, *in vitro* shape memory effect, drug release, antibacterial activity, and compatibility. The optimized fiber was further evaluated by animal studies, and the results showed that the fiber was capable of shape memory, antibacterial activity, and anti-inflammation, and thus promote wound healing. In addition, the mechanism of antibacterial activity and anti-inflammatory effect was discussed.

DATA AVAILABILITY STATEMENT

All datasets generated for this study are included in the article/ **Supplementary Material**.

ETHICS STATEMENT

The animal study was reviewed and approved by the Animal Ethical Committee of the West China Hospital of Sichuan University.

AUTHOR CONTRIBUTIONS

W-CZ: animal studies, writing the article, and results discussion. P-FT: synthesis of shape memory polyurethane, preparation of shape memory fibers, and statistical analysis. X-HC and HL performed the other experiments. LT and MT were responsible for conceptualizing and revising the manuscript. CY and YC were involved in conceptualizing and proofreading. All authors gave their final approval for the submission of the manuscript.

FUNDING

This work was sponsored by the National Natural Science Foundation of China (no. 51803128), Opening Project of Key

Laboratory of Leather Chemistry and Engineering (Sichuan University), Ministry of Education (grant no. 20826041C4159), Sichuan Science and Technology Programs (grant no. 2017SZYZF00009, no. 19YJ0126), and Strategic Project of Lu Zhou Science & Technology Bureau (grant no. 2017CDLZ-S01).

SUPPLEMENTARY MATERIAL

The Supplementary Material for this article can be found online at: https://www.frontiersin.org/articles/10.3389/fphar.2019.01506/full#supplementary-material

REFERENCES

Avila-Carrasco, L., Majano, P., Sánchez-Toméro, J. A., Selgas, R., López-Cabrera, M., et al. (2019). Natural plants compounds as modulators of Epithelial-to-Mesenchymal transition. *Front. Pharmacol.* 10, 715. doi: 10.3389/fphar.2019.00715

Bernard, M., Jubeli, E., Bakar, J., Tortolano, L., Saunier, J., et al. (2017). Biocompatibility assessment of cyclic olefin copolymers: impact of two additives on cytotoxicity, oxidative stress, inflammatory reactions, and hemocompatibility. *J. BioMed. Mater Res.* 105, 3333–3349. doi: 10.1002/jbm.a.36199

Byrne, M., and Aly, A. (2019). The surgical suture. *Aesthetic Surg. J.* 39, S67–S72. doi: 10.1093/asj/sjz036

Chang, J. B., Lane, M. E., Yang, M., and Heinrich, M. (2018). Disentangling the complexity of a Hexa-Herbal chinese medicine used for inflammatory skin conditions—predicting the active components by combining LC-MS-Based metabolite profiles and *in vitro* pharmacology. *Front. Pharmacol.* 9, 1091. doi: 10.3389/fphar.2018.01091

Chu, M., Ding, R., Chu, Z. Y., Zhang, M. B., Liu, X. Y., et al. (2014). Role of berberine in anti-bacterial as a high-affinity LPS antagonist binding to TLR4/MD-2 receptor. *BMC Complement Altern. Med.* 14, 89. doi: 10.1186/1472-6882-14-89

Ding, J., Zhang, J., Li, J., Li, D., Xiao, C., et al. (2019). Electrospun polymer biomaterials. *Prog. Polymer Sci.* 90, 1–34. doi: 10.1016/j.progpolymsci.2019.01.002

Doyle, J. F., and Schortgen, F. (2016). Should we treat pyrexia? And how do we do it? *Critical Care* 20. doi: 10.1186/s13054-016-1467-2

Fan, H., Xie, Z., Lu, Z., Tan, Z., Bi, Y., et al. (2018). Anti-inflammatory and immune response regulation of Si-Ni-San in 2,4-dinitrochlorobenzene-induced atopic dermatitis-like skin dysfunction. *J. Ethnopharmacology* 222, 1–10. doi: 10.1016/j.jep.2018.04.032

Feng, X., Li, J., Zhang, X., Liu, T., Ding, J., et al. (2019). Electrospun polymer micro/nanofibers as pharmaceutical repositories for healthcare. *J. Controlled Release* 302, 19–41. doi: 10.1016/j.jconrel.2019.03.020

Habtemariam, S. (2016). Berberine and inflammatory bowel disease: a concise review. *Pharmacol. Res.* 113, 592–599. doi: 10.1016/j.phrs.2016.09.041

Hahn, B. L., Onunkwo, C. C., Watts, C. J., and Sohnle, P. G. (2009). Systemic dissemination and cutaneous damage in a mouse model of staphylococcal skin infections. *Microb. Pathog.* 47, 16–23. doi: 10.1016/j.micpath.2009.04.007

Hasday, J. D., Fairchild, K. D., and Shanholtz, C. (2000). *The role of fever in the infected host* (France: Elsevier SAS).

Huang, J., Chen, L., Gu, Z., and Wu, J. (2019a). Red Jujube-Incorporated gelatin methacryloyl (GelMA) hydrogels with Anti-Oxidation and immunoregulation activity for wound healing. *J. BioMed. Nanotechnol.* 15, 1357–1370. doi: 10.1166/jbn.20192815

Huang, J., Chen, L., Yuan, Q., Gu, Z., and Wu, J. (2019b). Tofu-Based hybrid hydrogels with antioxidant and low immunogenicity activity for enhanced wound healing. *J. BioMed. Nanotechnol.* 15, 1371–1383. doi: 10.1166/jbn.20192814

Joseph, B., George, A., Gopi, S., Kalarikkal, N., and Thomas, S. (2017). Polymer sutures for simultaneous wound healing and drug delivery – a review. *Int. J. Pharmaceutics* 524, 454–466. doi: 10.1016/j.ijpharm.2017.03.041

Küpeli, E., Koşar, M., Yeşilada, E., and Başer, K. H. C. (2002). A comparative study on the anti-inflammatory, antinociceptive and antipyretic effects of isoquinoline alkaloids from the roots of Turkish Berberis species. *Life Sci.* 72, 645–657. doi: 10.1016/S0024-3205(02)02200-2

Lee, C., Chen, J., Hsiang, C., Wu, S., Wu, H., et al. (2007). Berberine suppresses inflammatory agents-induced interleukin-1β and tumor necrosis factor-α productions *via the* inhibition of IκB degradation in human lung cells. *Pharmacol. Res.* 56, 193–201. doi: 10.1016/j.phrs.2007.06.003

Lendlein, A., and Langer, R. (2002). Biodegradable, elastic shape-memory polymers for potential biomedical applications. *Science* 296, 1673–1676. doi: 10.1126/science.1066102

Mebert, A. M., Alvarez, G. S., Peroni, R., Illoul, C., Hélary, C., et al. (2018). Collagen-silica nanocomposites as dermal dressings preventing infection *in vivo*. *Mater. Sci. Eng.: C.* 93, 170–177. doi: 10.1016/j.msec.2018.07.078

Mullick Chowdhury, S., Lalwani, G., Zhang, K., Yang, J. Y., Neville, K., et al. (2013). Cell specific cytotoxicity and uptake of graphene nanoribbons. *Biomaterials* 34, 283–293. doi: 10.1016/j.biomaterials.2012.09.057

Nakagawa, S., Matsumoto, M., Katayama, Y., Oguma, R., Wakabayashi, S., et al. (2017). Staphylococcus aureus virulent PSMα peptides induce keratinocyte alarmin release to orchestrate IL-17-Dependent skin inflammation. *Cell Host Microbe* 22, 667–677. doi: 10.1016/j.chom.2017.10.008

Neag, M. A., Mocan, A., Echeverría, J., Pop, R. M., Bocsan, C. I., et al. (2018). Berberine: Botanical occurrence, traditional uses, extraction methods, and relevance in cardiovascular, metabolic, hepatic, and renal disorders. *Front. Pharmacol.* 9, 557. doi: 10.3389/fphar.2018.00557

Oh, K., Oh, M., Kim, J., Shin, D., and Shin, J. (2006). Inhibition of sortase-mediated Staphylococcus aureus adhesion to fibronectin *via* fibronectin-binding protein by sortase inhibitors. *Appl. Microbiol. Biotechnol.* 70, 102–106. doi: 10.1007/s00253-005-0040-8

Shao, K., Han, B., Gao, J., Jiang, Z., Liu, W., et al. (2016). Fabrication and feasibility study of an absorbable diacetyl chitin surgical suture for wound healing. *J. BioMed. Mater Res. B. Appl. Biomater.* 104, 116–125. doi: 10.1002/jbm.b.33307

Tang, J., Zhao, R., Yin, X., Wen, Y., Shi, Y., et al. (2019). Programmable release of berberine chloride hydrate from shape memory fibers prepared from core-sheath wet-spinning technology. *J. Biomed. Nanotechnol.* 15, 1432. doi: 10.1166/jbn.2019.2784

Wang, S., Yan, C., Zhang, X., Shi, D., Chi, L., et al. (2018). Antimicrobial peptide modification enhances the gene delivery and bactericidal efficiency of gold nanoparticles for accelerating diabetic wound healing. *Biomater. Sci.* 6, 2757–2772. doi: 10.1039/C8BM00807H

Zhao, W., Liu, L., Zhang, F., Leng, J., and Liu, Y. (2019). Shape memory polymers and their composites in biomedical applications. *Mater. Sci. Eng. C.* 97, 864–883. doi: 10.1016/j.msec.2018.12.054

Conflict of Interest: The authors declare that the research was conducted in the absence of any commercial or financial relationships that could be construed as a potential conflict of interest.

frontiers in Pharmacology

REVIEW
published: 14 January 2020
doi: 10.3389/fphar.2019.01534

Scaffold-Based Gene Therapeutics for Osteochondral Tissue Engineering

Xin Yan[1†], You-Rong Chen[1†], Yi-Fan Song[1†], Meng Yang[1], Jing Ye[1], Gang Zhou[2] and Jia-Kuo Yu[1]*

[1] Knee Surgery Department of the Institute of Sports Medicine, Peking University Third Hospital, Beijing, China, [2] Key Laboratory for Biomechanics and Mechanobiology of Ministry of Education, School of Biological Science and Medical Engineering, Beihang University, Beijing, China

OPEN ACCESS

Edited by:
Jianxun Ding,
Changchun Institute of Applied Chemistry (CAS), China

Reviewed by:
Da Huang,
Fuzhou University, China
Yun Qian,
Shanghai Sixth People's Hospital, China
Wuyu Zhang,
University of Louisville, United States
Dongsheng Liu,
Tsinghua University, China

****Correspondence:***
Jia-Kuo Yu
yujiakuo@126.com

[†]These authors have contributed equally to this work

Specialty section:
This article was submitted to Translational Pharmacology, a section of the journal Frontiers in Pharmacology

Received: *20 October 2019*
Accepted: *27 November 2019*
Published: *14 January 2020*

Citation:
Yan X, Chen Y-R, Song Y-F, Yang M, Ye J, Zhou G and Yu J-K (2020) Scaffold-Based Gene Therapeutics for Osteochondral Tissue Engineering. Front. Pharmacol. 10:1534. doi: 10.3389/fphar.2019.01534

Significant progress in osteochondral tissue engineering has been made for biomaterials designed to deliver growth factors that promote tissue regeneration. However, due to diffusion characteristics of hydrogels, the accurate delivery of signaling molecules remains a challenge. In comparison to the direct delivery of growth factors, gene therapy can overcome these challenges by allowing the simultaneous delivery of growth factors and transcription factors, thereby enhancing the multifactorial processes of tissue formation. Scaffold-based gene therapy provides a promising approach for tissue engineering through transfecting cells to enhance the sustained expression of the protein of interest or through silencing target genes associated with bone and joint disease. Reports of the efficacy of gene therapy to regenerate bone/cartilage tissue regeneration are widespread, but reviews on osteochondral tissue engineering using scaffold-based gene therapy are sparse. Herein, we review the recent advances in gene therapy with a focus on tissue engineering scaffolds for osteochondral regeneration.

Keywords: microRNAs, gene therapy, scaffold, tissue engineering, osteochondral regeneration

INTRODUCTION

Articular osteochondral injury is a common and frequently occurring disease in orthopedics, mainly caused by accidental trauma, sports injury or arthritis. Mature articular cartilage has a very weak ability to resist injury and disease, and has limited self-repair ability. After the articular cartilage is damaged, it cannot be effectively repaired, eventually leading to the occurrence of osteoarthritis (OA). It is expected that by 2030, OA will be the most common chronic degenerative joint disease among aging populations (Thomas et al., 2014; Tsezou, 2014). OA patients often suffer from severe pain and limited mobility. OA is also considered the leading cause of disability in the general population. The regeneration of articular cartilage that lacks self-healing ability is a major challenge in clinical treatment and clinically available methods fail to meet long-term effective regeneration requirements. This has caused concern in the field of osteochondral tissue engineering in which new tissues can be engineered to promote joint regeneration and prevent the onset of OA (Zhang et al., 2019). One promising approach is the treatment of genes delivered by tissue engineering scaffolds. By transfecting specific gene sequences into seed cells, overexpressing or silencing the original gene, the biological function of the cells could be regulated to obtain the desired effect. Gene therapy

combined with tissue engineering scaffolds provides a more precise, controlled, and sustained release of therapeutic factors compared to traditional methods of delivering growth factors directly (**Figure 1**). This review focuses on recent advances in gene therapy in the field of scaffold-based osteochondral tissue engineering. In terms of miRNAs, we focus on recent research progress related to OA in the hope that miRNA can be used in the future gene therapy approaches combined with scaffold-based osteochondral tissue engineering.

OSTEOCHONDRAL TISSUE ENGINEERING

Tissue engineering uses bionic scaffold to simulate the cell growth microenvironment and combines the body's self-healing ability to guide tissue regeneration in damaged or defective tissue sites. The cell microenvironment of tissue engineering bionics can induce cartilage or the osteogenic differentiation of stem cells, promoting their proliferation and migration, leading to endogenous osteochondral regeneration (Li et al., 2016). Osteochondral tissue engineering has evolved to enhance cell proliferation, differentiation, migration, and survival by transmitting growth factors and signaling molecules. These ligands combined with cell surface receptors of mesenchymal stem cells or mesenchymal progenitors, activate signaling pathways that promote osteochondral regeneration. However, the short half-life of recombinant proteins, such as BMPs, low bioactivity and high preparation costs lead to the exploration of new methods to deliver bioactive osteochondral regenerative compounds (Shi et al., 2014). A promising area is the use of scaffold-based gene therapy. By introducing specific gene sequences into cells, it is possible to modify or replace existing genes and regulate their epigenetic functions to achieve a desired purpose (Ginn et al., 2018). Gene-activated scaffolds provide a continuously controlled method of nucleic acid therapy to achieve a more efficient and safe release of biological agents.

Scaffold Biomaterials

To promote tissue regeneration, the osteochondral scaffold must be biocompatible, have a suitable rate of degradation, and possess a porous structure (Wang et al., 2019a). To-date, osteochondral tissue engineering biomaterials include natural polymers, synthetic polymers, metals, and inorganic materials. Natural materials are derived from animals, plants, and microorganisms and can be classified into protein, polysaccharide, polyester, and polyamide based polymers according to their chemical composition (Nooeaid et al., 2012; Liu et al., 2018). The natural biological function and ability to promote cell adhesion and proliferation are unique advantages of natural polymer materials such as collagen, gelatin, and chitosan (Nooeaid et al., 2012; Kowalczewski and Saul, 2018). The variability and low mechanical strength of different batches of natural biomaterials lead to inevitable defects (Hsu et al., 2010). In contrast, mechanical properties can be carefully controlled through structural and surface modifications using synthetic polymers (Shimomura et al., 2014). However, because of its inherent hydrophobicity and lack of binding sites, their cell adhesion ability is relatively poor (Sarasam et al., 2006; Antonova et al., 2016). Another important consideration when designing osteochondral scaffolds is that the rate of degradation of biomaterials should match the rate of tissue repair. There are significant differences in the rates at which enzymes degrade natural polymers at different transplant sites *in vivo*, depending on the activity and concentration of the enzyme under different conditions. Conversely, hydrolytically degradable synthetic polymers show minor differences between sites or patients compared to enzymatically degradable polymers. However, the by-products of degradation are toxic (Zhang et al., 2014). Bioceramics, such as calcium phosphate, are characterized by their excellent osteoinductivity. Common types of bone calcium scaffolds are hydroxyapatite, tricalcium phosphate, biphasic calcium phosphate, and multiphase bioglass. By changing the composition of $Ca_3(PO_4)_2$ ceramics, the stability and mechanical properties of the materials can be modified (Lima et al., 2019).

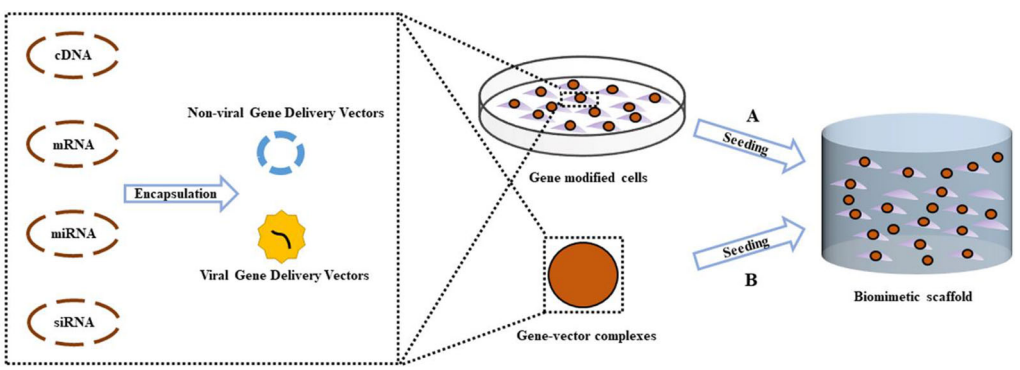

FIGURE 1 | Scheme of gene activated scaffold. Specific gene sequences were encapsulated into gene delivery vectors (Non-viral or viral), forming gene-vector complexes. **(A)** Exogenous seed cells were modified by uptake of gene–vector complexes, then were seeded into biomimetic scaffold supporting for the formation of new tissue. **(B)** The gene–vector complexes were loaded directly into the scaffold. Endogenous seed cells around the osteochondral defect migrate into the scaffold and take in specific genes in the gene–vector complexes, promoting chondrogenic or osteogenic differentiation.

However, separate scaffold biomaterials are not effective in promoting osteochondral tissue repair. To increase the number of cells and the chondrogenesis/osteogenesis of MSCs, an array of cellular factors can be applied to the scaffold to promote and maintain the production of cartilage ECM.

Biochemical Factors

Bone morphogenetic proteins (BMPs) (Reyes et al., 2014), fibroblast-growth-factor 2 (FGF-2) (Yi et al., 2012), transcriptional SOX proteins (Cao et al., 2011), nel-like molecule-1 (Nell-1) (Zhang et al., 2016b; Wang et al., 2017), and IGF-1 and IGF-2 promote cartilage formation (Wang et al., 2009) and osteogenic differentiation. In addition, as angiogenic factors, Platelet derived growth factors (PDGF), vascular endothelial growth factor (VEGF), and early growth response gene 1 (EGR-1) promote bone repair (Franses et al., 2010; Press et al., 2015; Sheng et al., 2018). As anti-angiogenic factor, chondromodulin 1 (CHM-1) not only stimulates chondrogenesis but also inhibits chondrocyte hypertrophy and endochondral ossification (Klinger et al., 2011). A common route of administration for general growth factors is intravenous injection. However, the growth factor in the blood has a short half-life. By adjusting the physicochemical properties of the scaffold to slow release of growth factors, the drawbacks of direct administration can be avoided. Although 3D scaffolds can function as sustained-release growth factors, their ability to promote perivascular tissue healing and stem cells (SCs) regeneration is limited by their localization. Scaffold-based gene therapy provides a promising approach for tissue engineering through transfecting specific nucleic acids into cells to enhance the sustained expression of the growth factors of interest or through silencing target genes associated with bone and joint disease

MicroRNAs

Cartilage

MicroRNAs (MiRNAs) are ~22 nucleotide single stranded RNAs that regulate post-transcriptional gene expression. MiRNA induces degradation of the target mRNA by binding to the 3′-untranslated region (UTR) complementary sequence on messenger RNA (mRNA), inhibiting translation, thereby suppressing corresponding protein production. Unlike small interfering RNA (siRNA), which regulates only one specific target, miRNA can regulate multiple targets. A single miRNA can regulate different targets in multiple signaling pathways, so it is more advantageous than other biomolecules in terms of functional effects. MiRNA expression profiles are significantly different during the development of articular cartilage, chondrocyte differentiation, and MSC chondrogenesis. Chondrocyte miRNA profiles differ from normal chondrocytes during their degeneration during osteoarthritis (OA). These miRNAs involved in chondrocyte differentiation or degeneration may be used in bioscaffolds in future studies to participate in the regeneration of cartilage tissue. The following is a summary of their latest.

MiRNAs regulate chondrocyte signaling and epigenetic functions (Cong et al., 2017b). Among the miRNAs, miR-210 targets the death receptor-6 (DR6) and inhibits NF-κB signaling in cultured chondrocytes and OA animal models. In addition, by inhibiting karyopherin subunit alpha-3 (KPNA3) gene expression, MiR-26a/MiR-26-b regulate the translocation of NF-κB-p65 to the nucleus (Mirzamohammadi et al., 2014), and their inhibition leads to enhanced COX-2 and MMP-3, -9, -13 expression (Yin et al., 2017). MiR-138 expression is low in OA cartilage compared to normal cartilage whilst p65 is targeted by miR-138 during OA progression (Wei et al., 2017). MiR-27a-3p levels are also lower in OA cartilage (Li et al., 2018a) while miR-139 is highly expressed and inhibits cell viability and migration by inhibiting the expression of EIF4G2 and IGF1R. MiR-139 inhibitors show the opposite effect (Hu et al., 2016).

Through its ability to target FUT1, microRNA-149-5p promotes the proliferation and survival of chondrocytes, thus preventing OA. It has also been found to be downregulated in patients with OA, leading to degenerative cartilage and disturbing homeostasis. Carriers have been employed to deliver miRNA-149-5p to MSCs to promote chondrogenesis (Celik et al., 2019). MiR-218 is highly expressed early in cartilage formation, but is stopped in synaptic-derived mesenchymal stem cells (SDSC) at the maturation stage of cartilage differentiation and miR-218 may directly regulates 15-hydroxyprostaglandin dehydrogenase expression in SDSCs (Chen et al., 2019c). MiR-320c was decreased in the later stages of chondrogenesis of adipose-derived stem cells (hADSCs) and OA chondrocytes. It inhibits degeneration of OA chondrocytes by directly targeting beta-catenin and inhibiting Wnt signaling (Hu et al., 2019). MiR-92a-3p expression was increased in MSC chondrogenic exosomes and significantly decreased in OA chondrocytes exosomes. MiR-92a-3p may be involved in regulating cartilage development by targeting WNT5A (Mao et al., 2018b). Conversely, miR-182-5p plays a negative role in BM-MSC chondrogenesis by down-regulating parathyroid hormone-like hormone (PTHLH) (Bai et al., 2019). **Table 1** summarizes the miRNAs, related to cartilage development, that have been studied in recent years.

Subchondral Bone

The subchondral bone layer below the cartilage in a joint acts as a shock absorber to absorb stress, cushion vibrations, and maintaining joint shape. Studies have shown that subchondral bone remodeling runs through the entire pathogenesis of OA (Aho et al., 2017) *via* the activities of two main cell populations, osteoblasts (OBs) that promote bone formation and osteoclasts (OCs) that promote bone resorption. OBs originate from MSC precursors mainly through BMPs, Wnt, TGF-β signals. OCs originate from peripheral blood mononuclear cell (PBMC) precursors mainly by the effects of RANKL/OPG ratio. Bone remodeling and osteoclast differentiation are controlled by miRNAs (Taipaleenmaki, 2018). MiR-135-5p promotes osteogenesis through its ability to enhance the activity of alkaline phosphatase (ALP), upregulate calcification molecules, and target the Hypoxia inducible factor 1 alpha inhibitor (HIF1AN) (Yin et al., 2019). Conversely, MiR-145 suppresses human jaw bMSC osteogenic differentiation through WNT/β-catenin signaling and semaphorin3A (SEMA3A) targeting (Jin et al., 2019). Similarly, MiR-494 suppresses osteoblast

TABLE 1 | Summary of the miRNAs associated with cartilage development and homeostasis.

miRNA	Targets gene	*In vitro*/*in vivo*	Cells/*vivo* model	Biological effect	Reference
miR-9-5p	Tnc	*In vitro*, *in vivo*	Mice chondrocytes, mice	Regulates cartilage homeostasis	(Chen et al., 2019a)
miR-10a-5p	HOXA1	*In vitro*, *in vivo*	Mice chondrocytes, mice	Regulates cartilage homeostasis	(Ma et al., 2019b)
miR-16-5p	SMAD3	*In vitro*	Human chondrocytes	Regulates cartilage homeostasis	(Li et al., 2015)
miR-21-5p	FGF18	*In vitro*, *in vivo*	Human chondrocytes, mice	Regulates cartilage homeostasis	(Wang et al., 2019b)
miR-27a	PI3K	*In vitro*	SW1353	Regulates cartilage homeostasis	(Cai et al., 2019)
miR-30a	DLL4	*In vitro*	Rat MSC	Enhance chondrogenesis	(Tian et al., 2016)
miR-34a	Cyr61	*In vitro*	Human chondrocytes	Regulates cartilage homeostasis	(Yang et al., 2018a)
miR-92a-3p	ADAMTS4/5	*In vitro*	Human MSC	Enhance chondrogenesis	(Mao et al., 2017a)
	HDAC2	*In vitro*	Human MSC	Enhance chondrogenesis	(Mao et al., 2017b)
miR-93	TCF4	*In vitro*, *in vivo*	Human chondrocytes, rabbit	Regulates cartilage homeostasis	(Xue et al., 2019)
	TLR4	*In vitro*, *in vivo*	Mice chondrocytes, mice	Regulates cartilage homeostasis	(Ding et al., 2019)
miR-95-5p	HDAC2/8	*In vitro*	Human chondrocytes	Regulates cartilage homeostasis	(Mao et al., 2018a)
miR-98	Bcl-2	*In vivo*	Rats	Regulates cartilage homeostasis	(Wang et al., 2016)
miR-107	HMGB-1	*In vitro*, *in vivo*	Human chondrocytes, rabbit	Regulates cartilage homeostasis	(Lin et al., 2019)
miR-127-5p	Runx2	*In vitro*	Rat BMSCs	Enhance chondrogenesis	(Xue et al., 2017)
miR-138	HIF-2α	*In vitro*	Human chondrocytes	Inhibit chondrogenesis	(Seidl et al., 2016)
miR-140-5p	Smad3	*In vitro*	Mandibular condylar chondrocytes	Regulates cartilage homeostasis	(Li et al., 2019c)
miR-145	MKK4	*In vitro*, *in vivo*	Rat chondrocytes, rat	Regulates cartilage homeostasis	(Hu et al., 2017)
miR-145-5p	SOX9	*In vitro*	Human BMSC	Inhibit chondrogenesis	(Verbus et al., 2017)
miR–146a–5p	CXCR4	*In vitro*	Human chondrocytes	Regulates cartilage homeostasis	(Jia et al., 2019)
miR-146b	AM	*In vitro*, *in vivo*	Mice chondrocytes, mice	Regulates cartilage homeostasis	(Liu et al., 2019b)
	SOX5	*In vitro*	Human Skeletal stem cells	Inhibit chondrogenesis	(Budd et al., 2017)
miR-149-5p	FUT-1	*In vitro*	Human MSC	Enhance chondrogenesis	(Celik et al., 2019)
miR-181a-5p	SBP2	*In vitro*	SW1353	Regulates cartilage homeostasis	(Xue et al., 2018)
miR-193b-3p	HDAC3	*In vitro*, *in vivo*	hMSC, PHCs, nude mice	Enhance chondrogenesis, Regulates cartilage homeostasis	(Meng et al., 2018)
miR-221-3p	SDF1	*In vitro*	SW1353	Regulates cartilage homeostasis	(Zheng et al., 2017)
miR-222	HDAC-4	*In vitro*, *in vivo*	Human chondrocytes, mice	Regulates cartilage homeostasis	(Song et al., 2015)
miR-320	MMP-13	*In vitro*	Mice chondrocytes	Enhance chondrogenesis	(Meng et al., 2016)
miR-322	MEK1	*In vitro*, *in vivo*	Mice chondrocytes, mice	Enhance chondrogenesis	(Bluhm et al., 2017)
miR-365	HDAC4	*In vitro*, *in vivo*	Rat BMSCs, rats	Enhance chondrogenesis	(Chen and Wu, 2019)
miR-384-5p	SOX9	*In vitro*, *in vivo*	Mice chondrocytes, mice	Regulates cartilage homeostasis	(Zhang et al., 2018)
miR-410	Wnt3a	*In vitro*	Human BMSC	Enhance chondrogenesis	(Zhang et al., 2017)
miR-411	MMP-13	*In vitro*	Human chondrocytes	Regulates cartilage homeostasis	(Wang et al., 2015)
miR-483	SMAD4	*In vitro*	Human BMSC	Enhance chondrogenesis	(Anderson and McAlinden, 2017)
miR-526b-3p	SMAD7	*In vitro*	Human BMSC	Enhance chondrogenesis	(Wu et al., 2018)

Tnc, tenascin C; AM, alpha-2-macroglobulin; HMGB-1, high mobility group box 1; CXCR4, C–X–C chemokine receptor type 4; TLR4, toll–like receptor 4; SBP2, sequence binding protein 2; SW1353, human chondrosarcoma chondrocyte; HDAC2/8, histone deacetylase 2/8; hMSC, human mesenchymal stem cell; PHCs, primary human chondrocytes; Cyr61, cysteine-rich angiogenic inducer 61; MKK4, mitogen-activated protein kinase 4; CXCL12, C–X–C motif chemokine ligand 12; MEK1, mitogen-Activated Protein Kinase 1; DLL4, delta-like 4; MMP-13, metalloproteinase 13; HIF-2α, hypoxia-inducible factor 2α.

differentiation by BMPR-SMAD-RUNX2 signal simulated by microgravity (Qin et al., 2019). MiR-877-3p targets Smad7 to enhance TGF-β1 mediated MC3T3-E1 cell differentiation (He et al., 2019). MiR-200c also enhances osteogenic differentiation of hBMSCs by regulating AKT/β-Catenin signaling through the inhibition of myeloid differentiation factor 88 (Myd88) (Xia et al., 2019). In human ADSCs, miR-125a-3p could negatively modulates osteoblastic differentiation *via* targeting Smad4 and Jak1. John et al. found that miR-487b-3p suppressed osteoblast differentiation by targeting Notch-regulated ankyrin-repeat protein (Nrarp), which in turn, suppresses Runx-2 and Wnt signaling (John et al., 2019). In BMSCs, miR-206 inhibits osteogenic differentiation through regulating glutamine metabolism (Chen et al., 2019d). MiR-223 is a newly discovered miRNA that induces MC3T3-E1 differentiation *via* HDAC2 targeting (Chen et al., 2019b). A complete summary is shown in **Table 2**.

Similar to osteoblast differentiation, the expression pattern of miRNAs related with the osteoclast differentiation has also been deeply explored (Hrdlicka et al., 2019). MiR-363-3p activated by MYB enhances osteoclast differentiation and inhibits osteoblast differentiation *via* the PI3K-AKT-PTEN axis (Li et al., 2019a). MiR-1225 suppresses TNFα-induced osteoclast differentiation through Keap1-Nrf2-HO-1 signal *via* ROS generation in bone marrow-derived macrophages (BMMs) (Reziwan et al., 2019). Conversely, miR-142-5p targets PTEN and induces BMM osteoclastogenesis (Lou et al., 2019). In addition, Smad3 expression is reduced by miR-145, the mimics of which in OVX mice repress OCs (Yu et al., 2018). MiR-125a-5p promotes osteoclast differentiation through inhibiting TNFRSF1B expression (Sun et al., 2019a). Sun and colleagues showed that miR-338-3p enhances the differentiation of Ocs by targeting Mafb (Sun et al., 2019b) that is also a target for miR-199a-5p (Guo et al., 2018). Wang et al. found that miR-218 decreased osteoclastogenic differentiation *via* suppressing NF-κB signal *via* targeting TNFR1 (Wang et al., 2018b). Recent studies have shown that miR-133a promotes postmenopausal osteoporosis through enhancing OC differentiation (Li et al.,

TABLE 2 | Summary of recently identified miRNAs associated with osteogenesis.

miRNA	Targets gene	*In vitro/in vivo*	Cells/*vivo* model	Biological effect	Reference
miR-16-2-3p	WNT5A	*In vitro*	hBMSCs	Inhibit osteogenic differentiation	(Duan et al., 2018)
miR-21-5p	SMAD7	*In vitro*	MC3T3-E1	Promote osteoblast differentiation	(Li and Jiang, 2019)
miR-27b	PPAR	*In vitro*	hBMSCs	Promote osteogenic differentiation	(Seenprachawong et al., 2018)
miR-29b	BCL-2	*In vitro*	Mice BMSCs	Promote osteoclast differentiation	(Sul et al., 2019)
miR-34c	LGR4	*In vitro*	Mice BMMs	Promote osteoclast differentiation	(Cong et al., 2017a)
miR-92b-5p	ICAM-1	*In vitro*, *in vivo*	Mice BMSCs, mice	Promote osteogenic differentiation	(Li et al., 2019d)
miR-96	SOST	*In vitro*	Mice osteoblast	Promote osteoblast differentiation	(Ma et al., 2019a)
miR–100–5p	FGF21	*In vitro*, *in vivo*	Mice BMMs, mice	Inhibit osteoclast differentiation	(Zhou et al., 2019a)
miR-125a-5p	TNFRSF1B	*In vitro*	RAW 264.7 OPC	Promote osteoclast differentiation	(Sun et al., 2019a)
miR-128	SIRT6	*In vitro*	C2C12 cells	Inhibit osteoblast differentiation	(Zhao et al., 2019b)
miR-130a	PPAR	*In vitro*	hBMSCs	Promote osteogenic differentiation	(Seenprachawong et al., 2018)
miR-132-3p	Smad5	*In vitro*	MC3T3-E1	Inhibit osteoblast differentiation	(Liu et al., 2019a)
miR-135-5p	HIF1AN	*In vitro*	MC3T3-E1	Promote osteoblast differentiation	(Yin et al., 2019)
miR-139-3p	ELK1	*In vitro*	MC3T3-E1	Inhibit osteoblast differentiation	(Wang et al., 2018c)
miR-140-5p	TLR4, BMP2	*In vitro*, *in vivo*	ASCs, rats	Promote osteogenesis	(Guo et al., 2019b)
miR-141	Calcr, EphA2	*In vitro*, *in vivo*	M-BMMs, monkey	Inhibit osteoclast differentiation	(Yang et al., 2018b)
miR-142-5p	PTEN	*In vitro*	Rat BMMs	Promotes osteoclast differentiation	(Lou et al., 2019)
miR-144-3p	RANK	*In vitro*	CD14+PBMC	Inhibit osteoclast differentiation	(Wang et al., 2018a)
miR-145	SEMA3A	*In vitro*	hJBMMSCs	Inhibit osteoblastic differentiation	(Jin et al., 2019)
miR-145-5p	OPG	*In vitro*, *in vivo*	RAW-264.7, mice	Promotes osteoclast differentiation	(Chen et al., 2018)
miR-146a	M-CSF	*In vivo*	Mice with OVX	Inhibit osteoblast differentiation	(Zhao et al., 2019a)
miR-199a-5p	Mafb	*In vitro*	RAW 264.7 cells	Promote osteoclast differentiation	(Guo et al., 2018)
miR-218-5p	COL1A1	*In vitro*	Mice BMSCs	Promote osteoblastic differentiation	(Kou et al., 2019)
miR-218	Mmp9	*In vitro*	RAW264.7 cells	Inhibit osteoblastic differentiation	(Guo et al., 2019a)
miR-200c	Myd88	*In vitro*	hBMSCs	Promote osteogenic differentiation	(Xia et al., 2019)
miR-208a-3p	ACVR1	*In vitro*, *in vivo*	MC3T3-E1, mice	Inhibit osteoblastic differentiation	(Arfat et al., 2018)
miR-210	Runx2	*In vitro*	HUCB-MSC	Promote osteoblast differentiation	(Asgharzadeh et al., 2018)
miR-221	ZFPM2	*In vitro*	MC3T3-E1	Promote osteoblast differentiation	(Zheng et al., 2018)
miR–223–5p	HDAC2	*In vitro*, *in vivo*	MC3T3–E1, mice	Promote osteoblast differentiation	(Chen et al., 2019b)
miR-338-3p	IKKβ	*In vitro*	RAW264.7 cell	Inhibit osteoclast differentiation	(Niu et al., 2019)
	RANKL	*In vitro*	Mice BMCs	Inhibit osteoclast differentiation	(Zhang et al., 2016a)
miR-342-3p	ATF3	*In vitro*, *in vivo*	MC3T3–E1, mice	Promote osteoblast differentiation	(Han et al., 2018)
miR-363-3p	PTEN	*In vitro*	CD14+PBMC	Promote osteoclast differentiation	(Li et al., 2019a)
miR-367	PANX3	*In vitro*, *in vivo*	Mice osteoblast, mice	Promote osteoblast differentiation	(Jia and Zhou, 2018)
miR-376c-3p	IGF1R	*In vitro*	hBMSCs,	Inhibit osteogenic differentiation	(Camp et al., 2018)
miR-377	RANKL	*In vitro*, *in vivo*	hBMMs, mice	Inhibit osteoclast differentiation	(Li et al., 2019b)
miR-383	Satb2	*In vitro*	Rat BMSCs	Inhibit osteoblastic differentiation	(Tang et al., 2018)
miR-494	BMPR2/RUNX2	*In vitro*	C2C12 cells	Inhibit osteoblast differentiation	(Qin et al., 2019)
miR-451	YWHAZ	*In vitro*, *in vivo*	hBMSCs, mice	Inhibit osteoblast differentiation	(Pan et al., 2018)
miR-487b-3p	Nrarp	*In vitro*, *in vivo*	Mice osteoblasts, mice	Inhibit osteoblast differentiation	(John et al., 2019)
miR-874	SUFU	*In vitro*, *in vivo*	Rat osteoblasts, rat	Promote osteoblast differentiation	(Lin et al., 2018)
miR-877-3p	Smad7	*In vitro*	MC3T3-E1	Promote osteoblast differentiation	(He et al., 2019)
miR-1225	Keap1	*In vitro*, *in vivo*	BMMs, mice	Inhibit osteoclast differentiation	(Reziwan et al., 2019)
miR-let-7c	SCD-1	*In vitro*	hADSCs	Inhibit osteogenic differentiation	(Zhou et al., 2019b)

HIF1AN, hypoxia-inducible factor 1 α inhibitor; M-CSF, macrophage colony-stimulating factor; OVX, ovariectomy; SEMA3A, semaphorin 3A; h-JBMMSCs, human jaw bone marrow mesenchymal stem cells; ICAM-1, intracellular adhesion molecule-1; SOST, sclerostin; hADSCs, human adipose derived mesenchymal stem cells; Nrarp, notch-regulated ankyrin-repeat protein; PPAR, peroxisome Proliferator-Activated Receptor γ; ATF3, activating transcription factor 3; SCD-1, stearoyl-CoA desaturase 1; ZFPM2, zinc finger protein multitype 2; MC3T3-E1,the mouse osteoblast-like cells; SUFU, suppressor of fused gene; IGF1R, insulin growth factor 1 receptor; HUCB, human umbilical cord blood; Satb2, special AT-rich-sequence-binding protein 2; ACVR1, activin A receptor type I; BMMs, bone marrow-derived macrophages; TNFRSF1B, TNF receptor superfamily member 1B gene; RAW 264.7 OPC, RAW 264.7 osteoclast precursor cell; Mmp9, matrix metalloproteinase-9; OPG, osteoprotegerin; M-BMMs, monkey bone marrow-derived macrophages; Calcr, calcitonin receptors; EphA2, ephrin type-A receptor 2 precursor; LGR4, leucine-rich repeat-containing G-protein-coupled receptor 4.

2018b). The culmination of these studies highlight the potential of miRNAs to regulate OC differentiation (**Table 2**).

VECTOR BASED GENE-DELIVERY

Tissue-engineering and gene therapy have been used in the treatment of myocardial injuries (Gabisonia et al., 2019), the repair of cartilage defects (Armiento et al., 2018), and the treatment of bone defects (Chen et al., 2019e). Compared with protein-based treatment, gene therapy has two main advantages. Gene therapy is more biologically active and physiological than common recombinant approaches (Raftery et al., 2019). Since the gene fragment itself cannot be efficiently introduced into the cell, an effective vector is required. Gene vectors can be virus-based (lentiviruses or baculoviruses) or non-viral including transfection methods such as lipofectamine, electroporation, and nanoparticles. They all have their own advantages and

disadvantages, but in general, the transfection efficiency of current viral vectors is still higher than that of non-viral vectors.

Viral Vectors

Use of Adenoviruses

Adenoviral transgenic efficiency is typically close to 100% *in vitro*. Adenoviruses can transduce different human tissue cells, dividing and non-dividing. The production of high titer adenoviral vectors is simple and no integration into the genomes of human cells occur. As such, adenoviral vectors have been increasingly used in clinical trials of gene therapy and have become the most promising viral vectors, second only to retroviral vectors. In a recent study, it is found that the use of Adenoviral-BMP-2/basic fibroblast growth factor (bFGF)-modified BMMSCs combined with demineralized bone matrix promote bone formation and angiogenesis, successfully repairing canine femoral head necrosis (ONFH) (Peng and Wang, 2017). However, the biggest challenge to the effectiveness of adenoviral approaches are the immune response.

Baculovirus Approaches

Baculoviruses show no pathogenicity toward humans and can be used under normal biosafety level 2 conditions. Baculoviruses, like adenoviral, induce both dividing and non-dividing cells. In some recent studies, baculoviruses has been used. Lo and colleagues employed Cre/loxP-based baculovirus vectors in adipose-SCs to enhance bone healing (Lo et al., 2017). Fu and coworkers highlighted the ability of baculoviruses to induce osteogenesis through allogeneic-MSCs (Fu et al., 2015). Despite this promise, the transient expression profiles of baculoviruses limit their use. In an attempt to overcome this issue, Chen and coworkers developed baculoviruses hybridized with the miR-155 scaffolds and the sleeping beauty transposon to sustainably inhibit transgene expression for extended time periods (Chen et al., 2011).

Lentiviruses

The advantage of lentiviral vectors are the high levels of foreign gene integration into the host chromosome in cells typically difficult to transfect, including primary cell cultures. Lentiviral vectors can be combined with chondroitin sulfate-hyaluronic acid-silk fibrin composite scaffolds and applied to bone-ligament connections to promote tissue engineering (Sun et al., 2014). In addition, Brunger et al. developed an independent bioactive scaffold that is capable of inducing stem cell differentiation and cartilage ECM formation using lentiviruses (Brunger et al., 2014). Despite the great progress in the study of lentiviral vector, it is still far from clinical application. First, the titer of recombinant virus is still not up to the level of *in vivo* application. Second, due to the complex biological properties of HIV, it is difficult to establish a stable HIV vector like the commonly used mouse retroviral vector, and the established packaging cells are not ideal.

Non-Viral Gene Delivery Vectors

Commercialized cationic lipids such as Lipofectamine 2000, Lipofectamine 3000, Lipofectamine RNAiMAX, and SiPORT NeoFx are widely used in biomaterial-based gene therapy. In recent studies, using lipofectamine 2000, Anti-miR-221 was transfected into adipose-MSCs which were seeded into synthetic nHA/PCL scaffolds. The results indicate that this method provides an effective way to promote osteogenesis of AT-MSCs (Hoseinzadeh et al., 2016). Macmillan et al. combined lipofectamine-complexed plasmids encoding BMP-2 and TGF-β1 with HA microparticles for delivery to the MSCs of three healthy pig donors. This study provides a promising approach to gene therapy that regulates stem cell growth and development to treat bone defects (McMillan et al., 2018).

Although the toxicity of liposomes are well-known, more efficient transfection methods to replace them have not emerged. Recently, to enhance the interaction between cells and nucleic acids, Raftery et al. developed a new cell penetrating peptide, GET, combined with a variety of collagen scaffolds, which showed good regeneration potential. GET is suitable for all three germ layer cell transfections with efficiencies comparable to Lipofectamine 3000 and minimal cytotoxicity. These findings suggest that GET can be combined with scaffold delivery systems, to provide new solutions to a variety of tissue engineering regenerative indications (Raftery et al., 2019).

GENE THERAPY IN SCAFFOLD BASED OSTEOCHONDRAL TISSUE REPAIR

Gene therapy for osteochondral tissue repair is divided into two phases: one to locate the gene to the target area directly, either through encapsulation onto a scaffold, or through a specific gene vector (*in vivo*). Alternatively, the target gene is loaded into the cells by the vectors *in vitro*, and genetically modified cells are administered to the target lesion area, with or without a scaffold (*ex vivo*). However, the main obstacle to the treatment of focal defects with non-scaffolds is that the genetically modified cells or gene vectors with intra-articular injections are diluted by the joint fluid and fail to reach the target lesion area. To avoid this drawback, a promising approach is to deliver modified cells or gene vectors using different types of scaffolds. When the scaffold is degraded, the contents are slowly released to the target area. Gene therapy combined with scaffolds increases the efficiency and duration of transfected genes, forming an efficient system to promote osteochondral regeneration. We herein summarize and discuss these gene therapy-binding scaffolds discovered from 2006 to 2019 in the contest of seeding cell types (**Figure 2**).

Gene Modified BMSCs

MSCs are the most widely studied due to their high availability and proliferative/differentiation ability. The microenvironment typically dictates the fate of MSCs. BMSCs are more commonly employed than those derived from adipose tissue (AMSCs), particularly for osteochondral therapy. In one study, BMSCs were transfected with hIGF-1 cDNA and mixed with calcium alginate gels for transplantation into 6 mm osteochondral defects and were found to improve the repair (Leng et al., 2012).

In view of the role of TGF-β in promoting cartilage repair, in addition to the inhibition of inflammatory and immune responses, pcDNA-TGF-β gene-modified BMSCs were seeded onto

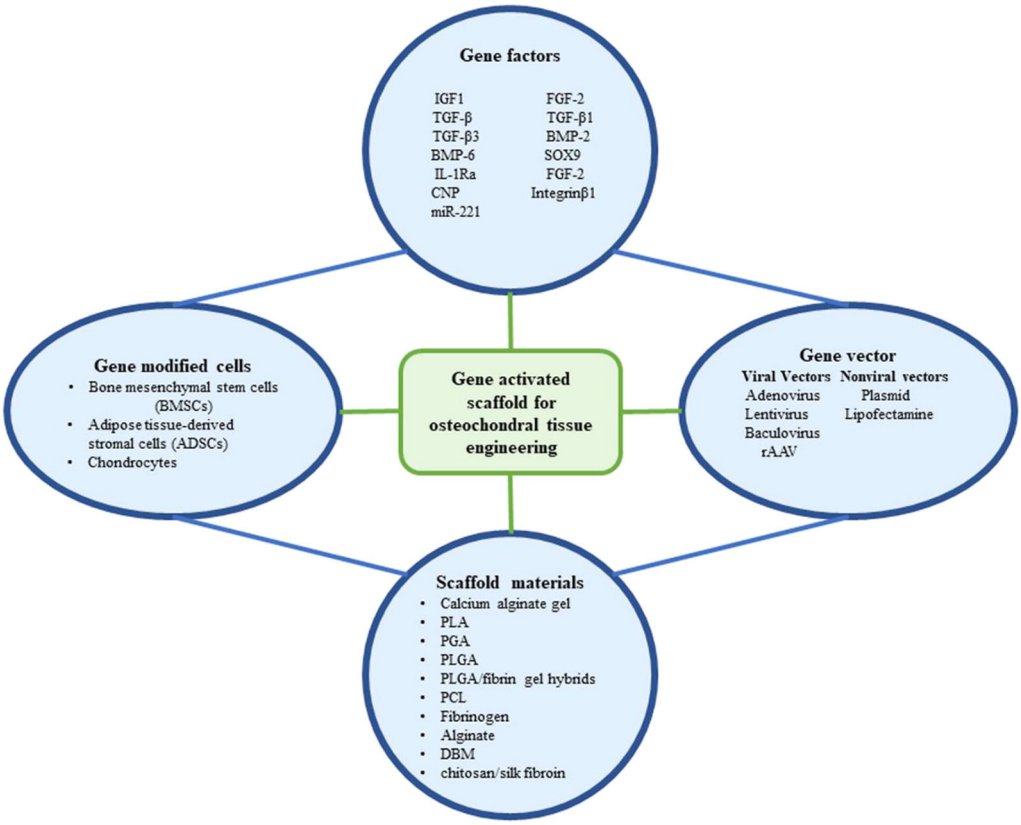

FIGURE 2 | The components that have been utilized in gene activated scaffold for osteochondral tissue engineering.

biodegradable poly-L-lysine coated polylactic acid (PLA) scaffolds which were transplanted into New Zealand rabbit articular cartilage full-thickness defects. *In vitro*, after 2 weeks of cell seeding, the cartilage matrix formed and filled with the attachment holes of the scaffold. *In vivo*, 24 weeks after transplantation, the hyaline cartilage repaired the cartilage defect area, trabecular bone and dense bone repair in the subchondral area and the quality of the regenerated tissue improved over time (Guo et al., 2006). Similarly, BMSCs were transduced with pDNA-TGF-β1 and loaded into PLGA/fibrin gel hybrids which were implanted into rabbit articular cartilage models, resulting in the regeneration of new cartilage tissue with similar thickness, cell arrangements, color, and abundant glycosaminoglycans to normal cartilage (Li et al., 2014). Moreover, TGF-β1-gene engineered rat BMSCs induced cartilage regeneration in rats (He et al., 2012), and their transfer onto PGA scaffolds using adenoviral approaches induced chondrogenic differentiation both *in vitro* and *in vivo* (Xia et al., 2009). Robust collagen II staining was observed in adenovirus-mediated-BMP-2 and TGF-β3 infected cells. DBM compounds with BMP-2 and TGF-β3 infected BMSC scaffolds showed high biocompatibility and the capacity to regeneration cartilage in pig models (Wang et al., 2014).

SOX9 is a transcription factor of the SOX (Sry-type HMG box) protein family that promotes cartilage formation and the phenotypes of chondrocytes. Adenoviral vectors have been used to transfect SOX9 into rabbit BMSCs which effectively induced their differentiation into chondrocytes on PGA scaffolds and improved the repair of cartilage defects (Cao et al., 2011). More recently, Venkatesan et al. designed 3D fibrin-polyurethane scaffolds in a hydrodynamic environment that provided a favorable growth environment for rAAV-infected SOX9-modified hBMCs and promoted their differentiation into chondrocytes. Interestingly, the expression of SOX9 lasted 21 days, the longest time point evaluated (Venkatesan et al., 2018).

Cartilage engineering can also be mediated through gene activation matrices. Rowland et al. engineered lentiviral particles expressing a doxycycline-inducible IL-1 receptor antagonist (IL-1Ra) on a cartilage-derived matrix to prevent IL-1 mediated inflammation. Similar scaffolds have been employed for site directed chondrogenic and osteogenic differentiation using BMSC populations that overexpress either chondrogenic, BMP2, or TGF-β3 transgenes. The ability to regulate IL-1Ra expression afforded protection to the cartilage-matrix in the presence of IL-1, leading to enhanced bone production and cartilage formation. When inflammation is absent, cartilage-derived matrix hemispheres expressing TGF-β3 and BMP-2 were also fused to the bilayers of osteochondral constructs to promote healing (Rowland et al., 2018). Yang and

coworkers also transfected BMSCs with adenoviruses expressing C-type natriuretic peptides and seeded the cells onto silk/chitosan scaffolds to promote chondrogenesis in rat cartilage defect models (Yang et al., 2019).

Despite advances in the development of osteochondral repair scaffolds, their combination with miRNAs remains in the early stages. MiR-221 can induce BMSCs toward chondrogenesis in the absence of TGF-β and could repair osteochondral defects following its subcutaneous implantation into mouse models, promoting Collagen type II positive tissue expression that was negative for collagen type X (a well characterized marker of hypertrophy). The potential of hMSCs silenced for miR-221 to suppress collagen type X represents an exciting development with clear therapeutic potential for cartilage repair in the clinic (Lolli et al., 2016).

Gene Modified ADSCs

It is now well accepted that ADSCs have clinical utility. An advantage is their ability to be collected *via* lipoaspiration, a non-invasive harvesting process. Lu and coworkers developed baculoviruses for FLPo/Frt expression of genetically engineered rabbit ADSCs. The cells were transfected with TGF-β3/BMP-6 and added to PLGA-GCH scaffolds for implantation to cartilage defects in weight-bearing areas, promoting regeneration. The designed neo-cartilages had defined cartilage-specific-structures in the absence of degeneration or hypertrophy (Lu et al., 2014). In other studies, the inguinal fat of rats were transduced with SOX *via* retroviral approaches and ADSCs were collected and seeded into fibrin gels and implanted onto defects in the femur patellar groove. These approaches significantly increased type II collagen expression, GAG levels, and improved cartilage healing (Lee and Im, 2012). Upon seeding the ADSCs into large PCL-scaffolds immobilized with Dox-inducible lentiviruses expressing IL-1Ra, controlled tissue growth and biomimetic cartilage properties were maintained (Moutos et al., 2016).

Gene Modified Chondrocytes

Isolated cartilage cells can be obtained through enzymatic digestion and can embed into cartilage lacuna, preventing immune cell invasion and organ rejection. However, the cells dedifferentiate overtime and their propensity for cartilage production becomes impaired, limiting their use in clinical application. The use of 3D cultures can mimic the microenvironment of the extracellular matrix permitting the maintenance of phenotypic stability. In this regard, neonatal male foals chondrocytes transduced with IGF-1-adenoviruses and embedded into fibrinogen were implanted into equine defects and conferred high levels of IGF-1 expression and cartilage healing (Goodrich et al., 2007). Griffin and colleagues used a comparable approach with rAAV5 and implanted the carriers into equine femurs, also showing improved graft healing (Griffin et al., 2016). FGF-2 and IGF-I plasmid vectors have also been delivered into Lapine articular chondrocytes. The cells were encapsulated into alginate scaffolds and transplanted onto rabbit knee joint defects for a period of three weeks, in which enhanced IGF-I/FGF-2 levels improved the defects with no adverse effects to the synovial membrane, highlighting the utility of these approaches to promote cartilage repair (Orth et al., 2011).

FGF-2 is mitogenic in articular chondrocytes and when transfected into articular chondrocytes and encapsulated in alginate scaffolds, FGF-2 expression was maintained for over 21 days and improved cartilage defects in the knee joints of rabbits. No adverse effects were again evident in the synovial membrane following histological assessments but type II collagen expression was enhanced (Kaul et al., 2006).

Mechanical movements activate integrin β1-signaling and enhance the proliferative capacity of chondrocytes, increasing matrix synthesis. Liang and co-workers seeded integrin β1-transfected chondrocytes onto PLGA scaffolds which produced higher levels of GAG and type II collagen after lentiviral-integrin β1 transfection compared to mechanically stressed sham controls. The opposing phenotype was observed in the cells silenced for integrin β1, suggesting that in addition to mechanical stimulation, the overexpression of integrin β1 enhances cartilage regeneration (Liang et al., 2015) (**Table 3**).

CONCLUSION AND FUTURE DIRECTIONS

In summary, osteochondral defects are not a single cartilage or bone injury, but involve complex multi-structural components. The healing of these components is challenging. To-date, there is no technology that can form a natural cartilage structures in the joints. Osteochondral tissue engineering shows good potential for osteochondral repair and OA treatment, but several problems remain. For example, at the seed cell level, chondrocytes have poor availability and dedifferentiation properties. Unacceptable outcomes such as chondrocyte hypertrophy and endochondral ossification are often accompanied by an inability to control the differentiation of chondrogenic SCs. Also, due to its unique layered structure, osteochondral tissue theoretically requires a multi-phase structure to simulate the native layered structure, but this is difficult to achieve. Recent studies have shown that a combination of gene vectors, genes, seed cells, and scaffolds are more likely to obtain hyaline cartilage, with the combined changes between them primarily based on lesion size, location, and structure.

Genes have been transfected into MSCs or chondrocytes to improve their phenotypic properties. In general, cartilage gene therapy enables seed cells to continuously encode growth factors, transcription factors, or anti-inflammatory cytokines, thereby inducing cartilage differentiation and inhibiting the progression of inflammatory diseases (**Figure 2**). Studies have shown that multiple combinations of genes encoding growth factors, transcription factors, or anti-adverse response cytokines are more advantageous than single genes for improving healing and reducing adverse effects. To minimize hypertrophy, ossification, and host immune responses, complex gene delivery vectors must be designed to increase safety and more sustained gene protein release. miRNAs regulate chondrogenesis and arthritis. The expression of a specific miRNA mimetic or miRNA inhibitor permits the manipulation of the expression profiles of the cellular miRNAs and their epigenetic features. On this basis, combined

TABLE 3 | Summary of gene therapy in scaffold based osteochondral tissue repair.

Cells	Gene	Scaffold	Gene vector	Approach	*Vitro* or *vivo* model	Reference
BMSCs	IGF1	Calcium alginate gel	Plasmid	*Ex vivo*	Rabbit knee osteochondral defect	(Leng et al., 2012)
	TGF-β	PLA	Plasmid	*Ex vivo*	Rabbit knee full-thickness defects	(Guo et al., 2006)
	TGF-β1	PLGA/fibrin gel hybrids	Plasmid	*Ex vivo*	Rabbit knee full-thickness defects	(Li et al., 2014)
	TGF-β1	PGA	Adenovirus	*In vitro*, *ex vivo*	Mice subcutaneous tissue	(Xia et al., 2009)
	BMP-2, TGF-β3	DBM	Adenovirus	*In vitro*, *ex vivo*	Pig knee full-thickness defects	(Wang et al., 2014)
	SOX9	PGA	Adenovirus	*In vitro*, *ex vivo*	Rabbit knee full-thickness defects	(Cao et al., 2011)
	SOX9	Fibrin-polyurethane	rAAV	*In vitro*	Hydrodynamic culture conditions	(Venkatesan et al., 2018)
	IL-1Ra, BMP-2, TGF-β3	CDM	Lentiviral	*In vitro*	Joint organoid model	(Rowland et al., 2018)
	CNP	Chitosan/silk fibroin	Adenovirus	*Ex vivo*	Rat knee full-thickness defects	(Yang et al., 2019)
	miR-221	Alginate	Lipofectamine	*In vitro*, *ex vivo*	Mice knee osteochondral defects	(Lolli et al., 2016)
ADSCs	TGF-β3/BMP-6	PLGA-GCH	Baculovirus	*Ex vivo*	Rat knee full-thickness defects	(Lu et al., 2014)
	SOX trio	Fibrin gel	Retrovirus	*In vitro*, *ex vivo*	Rat knee osteochondral defect, OA	(Lee and Im, 2012)
	eGFP, IL-1Ra	PCL	Lentiviral	*In vitro*	Cultured in chondrogenic conditions	(Moutos et al., 2016)
Chondrocytes	IGF-1	Fibrinogen	Adenovirus	*Ex vivo*	Equine knee osteochondral defect	(Goodrich et al., 2007)
	IGF-1	Fibrin	rAAV5	*Ex vivo*	Equine knee full-thickness defects	(Griffin et al., 2016)
	IGF-I, FGF-2	Alginate	Plasmid	*Ex vivo*	Rabbit knee osteochondral defect	(Orth et al., 2011)
	FGF-2	Alginate	Plasmid	*In vitro*, *ex vivo*	Rabbit knee osteochondral defect	(Kaul et al., 2006)
	Integrin β1	PLGA	Lentiviral	*In vitro*	Cultured under periodic mechanical stress	(Liang et al., 2015)

IGF, Insulin-like growth factor; TGF, Transforming growth factor; BMP, Bone morphogenetic protein; PLGA, Poly lactide-co-glycolide; DBM, Demineralized bone matrix; PGA, polyglycolic; GCH, gelatin, chondroitin-6-sulfate and hyaluronic acid; IL-1Ra, IL-1 receptor antagonist; eGFP, enhanced green fluorescent protein.

with 3D biological scaffold printing technology, it is more conducive to accurately control cell differentiation and optimize the biochemical and biomechanical properties of regenerated tissues. However, the use of 3D delivery systems to miRNA-activated scaffolds is in its infancy. Moreover, in terms of scaffolds, 3D multiphase structural scaffolds are complex, and not conducive to the control of each phase, including degradation rates and shear forces. Therefore, the two-phase scaffold divided into a cartilage phase and a bone phase is simpler than multi-phase scaffolds and ideal for osteochondral scaffolds (Seo et al., 2014). We propose that to make full use of the integrated fusion bilayer scaffold, each genetically modified cell line (overexpression or knockout of miRNA) can edit specific signaling molecules that facilitate tissue regeneration in each layer.

AUTHOR CONTRIBUTIONS

XY, Y-RC, and Y-FS proposed and wrote the manuscript. MY, JY, and GZ collected and analyzed the information. J-KY supervised the conception and writing of the manuscript.

FUNDING

The research was supported by the National Natural Science Foundation of China (Grant Nos. 51773004, 81630056, 51920105006, 51803188, 31670982) and the National Key Research and Development Program (Grant No. 2016YFC1100704).

REFERENCES

Aho, O. M., Finnila, M., Thevenot, J., Saarakkala, S., and Lehenkari, P. (2017). Subchondral bone histology and grading in osteoarthritis. *PloS One* 12 (3), e0173726. doi: 10.1371/journal.pone.0173726

Anderson, B. A., and McAlinden, A. (2017). miR-483 targets SMAD4 to suppress chondrogenic differentiation of human mesenchymal stem cells. *J. Orthop. Res.* 35 (11), 2369–2377. doi: 10.1002/jor.23552

Antonova, L. V., Seifalian, A. M., Kutikhin, A. G., Sevostyanova, V. V., Krivkina, E. O., Mironov, A. V., et al. (2016). Bioabsorbable bypass grafts biofunctionalised with RGD have enhanced biophysical properties and endothelialisation tested *in vivo*. *Front. Pharmacol.* 7, 136. doi: 10.3389/fphar.2016.00136

Arfat, Y., Basra, M. A. R., Shahzad, M., Majeed, K., Mahmood, N., and Munir, H. (2018). miR-208a-3p suppresses osteoblast differentiation and inhibits bone formation by targeting ACVR1. *Mol. Ther. Nucleic Acids* 11, 323–336. doi: 10.1016/j.omtn.2017.11.009

Armiento, A. R., Alini, M., and Stoddart, M. J. (2018). Articular fibrocartilage—why does hyaline cartilage fail to repair? *Adv. Drug Deliv. Rev.* 146, 289–305. doi: 10.1016/j.addr.2018.12.015

Asgharzadeh, A., Alizadeh, S., Keramati, M. R., Soleimani, M., Atashi, A., Edalati, M., et al. (2018). Upregulation of miR-210 promotes differentiation of mesenchymal stem cells (MSCs) into osteoblasts. *Bosn. J. Basic Med. Sci.* 18 (4), 328–335. doi: 10.17305/bjbms.2018.2633

Bai, M., Yin, H., Zhao, J., Li, Y., and Wu, Y. (2019). miR-182-5p overexpression inhibits chondrogenesis by down-regulating PTHLH. *Cell Biol. Int.* 43 (3), 222–232. doi: 10.1002/cbin.11047

Bluhm, B., Ehlen, H. W. A., Holzer, T., Georgieva, V. S., Heilig, J., Pitzler, L., et al. (2017). miR-322 stabilizes MEK1 expression to inhibit RAF/MEK/ERK pathway activation in cartilage. *Development* 144 (19), 3562–3577. doi: 10.1242/dev.148429

Brunger, J. M., Huynh, N. P., Guenther, C. M., Perez-Pinera, P., Moutos, F. T., Sanchez-Adams, J., et al. (2014). Scaffold-mediated lentiviral transduction for functional tissue engineering of cartilage. *Proc. Natl. Acad. Sci. U.S.A.* 111 (9), E798–E806. doi: 10.1073/pnas.1321744111

Budd, E., de Andres, M. C., Sanchez-Elsner, T., and Oreffo, R. O. C. (2017). MiR-146b is down-regulated during the chondrogenic differentiation of human bone marrow derived skeletal stem cells and up-regulated in osteoarthritis. *Sci. Rep.* 7, 46704. doi: 10.1038/srep46704

Cai, C., Min, S., Yan, B., Liu, W., Yang, X., Li, L., et al. (2019). MiR-27a promotes the autophagy and apoptosis of IL-1beta treated-articular chondrocytes in osteoarthritis through PI3K/AKT/mTOR signaling. *Aging (Albany NY)* 11 (16), 6371–6384. doi: 10.18632/aging.102194

Camp, E., Pribadi, C., Anderson, P. J., Zannettino, A. C. W., and Gronthos, S. (2018). miRNA-376c-3p mediates TWIST-1 inhibition of bone marrow-derived stromal cell osteogenesis and can reduce aberrant bone formation of TWIST-1 haploinsufficient calvarial cells. *Stem Cells Dev.* 27 (23), 1621–1633. doi: 10.1089/scd.2018.0083

Cao, L., Yang, F., Liu, G., Yu, D., Li, H., Fan, Q., et al. (2011). The promotion of cartilage defect repair using adenovirus mediated Sox9 gene transfer of rabbit bone marrow mesenchymal stem cells. *Biomaterials* 32 (16), 3910–3920. doi: 10.1016/j.biomaterials.2011.02.014

Celik, E., Bayram, C., and Denkbas, E. B. (2019). Chondrogenesis of human mesenchymal stem cells by microRNA loaded triple polysaccharide nanoparticle system. *Mater. Sci. Eng. C. Mater. Biol. Appl.* 102, 756–763. doi: 10.1016/j.msec.2019.05.006

Chen, J., and Wu, X. (2019). Cyclic tensile strain promotes chondrogenesis of bone marrow-derived mesenchymal stem cells by increasing miR-365 expression. *Life Sci.* 232, 116625. doi: 10.1016/j.lfs.2019.116625

Chen, C. L., Luo, W. Y., Lo, W. H., Lin, K. J., Sung, L. Y., Shih, Y. S., et al. (2011). Development of hybrid baculovirus vectors for artificial MicroRNA delivery and prolonged gene suppression. *Biotechnol. Bioeng.* 108 (12), 2958–2967. doi: 10.1002/bit.23250

Chen, Y., Wang, X., Yang, M., Ruan, W., Wei, W., Gu, D., et al. (2018). miR-145-5p increases osteoclast numbers *in vitro* and aggravates bone erosion in collagen-induced arthritis by targeting osteoprotegerin. *Med. Sci. Monit.* 24, 5292–5300. doi: 10.12659/MSM.908219

Chen, H., Yang, J., and Tan, Z. (2019a). Upregulation of microRNA-9-5p inhibits apoptosis of chondrocytes through downregulating Tnc in mice with osteoarthritis following tibial plateau fracture. *J. Cell Physiol.* 234 (12), 23326–23336. doi: 10.1002/jcp.28900

Chen, J., He, G., Wang, Y., and Cai, D. (2019b). MicroRNA223 promotes osteoblast differentiation of MC3T3E1 cells by targeting histone deacetylase 2. *Int. J. Mol. Med.* 43 (3), 1513–1521. doi: 10.3892/ijmm.2018.4042

Chen, S., Xu, Z., Shao, J., Fu, P., and Wu, H. (2019c). MicroRNA-218 promotes early chondrogenesis of mesenchymal stem cells and inhibits later chondrocyte maturation. *BMC Biotechnol.* 19 (1), 6. doi: 10.1186/s12896-018-0496-0

Chen, Y., Yang, Y. R., Fan, X. L., Lin, P., Yang, H., Chen, X. Z., et al. (2019d). miR-206 inhibits osteogenic differentiation of bone marrow mesenchymal stem cells by targetting glutaminase. *Biosci. Rep.* 39 (3), BSR20181108. doi: 10.1042/BSR20181108

Chen, Z., Wang, Z., and Gu, Z. (2019e). Bioinspired and biomimetic nanomedicines. *Acc. Chem. Res.* 52 (5), 1255–1264. doi: 10.1021/acs.accounts.9b00079

Cong, F., Wu, N., Tian, X., Fan, J., Liu, J., Song, T., et al. (2017a). MicroRNA-34c promotes osteoclast differentiation through targeting LGR4. *Gene* 610, 1–8. doi: 10.1016/j.gene.2017.01.028

Cong, L., Zhu, Y., and Tu, G. (2017b). A bioinformatic analysis of microRNAs role in osteoarthritis. *Osteoarthr. Cartil.* 25 (8), 1362–1371. doi: 10.1016/j.joca.2017.03.012

Ding, Y., Wang, L., Zhao, Q., Wu, Z., and Kong, L. (2019). MicroRNA93 inhibits chondrocyte apoptosis and inflammation in osteoarthritis by targeting the TLR4/NFkappaB signaling pathway. *Int. J. Mol. Med.* 43 (2), 779–790. doi: 10.3892/ijmm.2018.4033

Duan, L., Zhao, H., Xiong, Y., Tang, X., Yang, Y., Hu, Z., et al. (2018). miR-16-2* interferes with WNT5A to regulate osteogenesis of mesenchymal stem cells. *Cell Physiol. Biochem.* 51 (3), 1087–1102. doi: 10.1159/000495489

Franses, R. E., McWilliams, D. F., Mapp, P. I., and Walsh, D. A. (2010). Osteochondral angiogenesis and increased protease inhibitor expression in OA. *Osteoarthr. Cartil.* 18 (4), 563–571. doi: 10.1016/j.joca.2009.11.015

Fu, T. S., Chang, Y. H., Wong, C. B., Wang, I. C., Tsai, T. T., Lai, P. L., et al. (2015). Mesenchymal stem cells expressing baculovirus-engineered BMP-2 and VEGF enhance posterolateral spine fusion in a rabbit model. *Spine J.* 15 (9), 2036–2044. doi: 10.1016/j.spinee.2014.11.002

Gabisonia, K., Prosdocimo, G., Aquaro, G. D., Carlucci, L., Zentilin, L., Secco, I., et al. (2019). MicroRNA therapy stimulates uncontrolled cardiac repair after myocardial infarction in pigs. *Nature* 569 (7756), 418–422. doi: 10.1038/s41586-019-1191-6

Ginn, S. L., Amaya, A. K., Alexander, I. E., Edelstein, M., and Abedi, M. R. (2018). Gene therapy clinical trials worldwide to 2017: an update. *J. Gene Med.* 20 (5), e3015. doi: 10.1002/jgm.3015

Goodrich, L. R., Hidaka, C., Robbins, P. D., Evans, C. H., and Nixon, A. J. (2007). Genetic modification of chondrocytes with insulin-like growth factor-1 enhances cartilage healing in an equine model. *J. Bone Joint Surg. Br.* 89 (5), 672–685. doi: 10.1302/0301-620X.89B5.18343

Griffin, D. J., Ortved, K. F., Nixon, A. J., and Bonassar, L. J. (2016). Mechanical properties and structure–function relationships in articular cartilage repaired using IGF-I gene-enhanced chondrocytes. *J. Orthop. Res.* 34 (1), 149–153. doi: 10.1002/jor.23038

Guo, X., Zheng, Q., Yang, S., Shao, Z., Yuan, Q., Pan, Z., et al. (2006). Repair of full-thickness articular cartilage defects by cultured mesenchymal stem cells transfected with the transforming growth factor beta1 gene. *Biomed. Mater.* 1 (4), 206–215. doi: 10.1088/1748-6041/1/4/006

Guo, K., Zhang, D., Wu, H., Zhu, Q., Yang, C., and Zhu, J. (2018). MiRNA-199a-5p positively regulated RANKL-induced osteoclast differentiation by target Mafb protein. *J. Cell Biochem.* 120 (5), 7024–7031. doi: 10.1002/jcb.27968

Guo, J., Zeng, X., Miao, J., Liu, C., Wei, F., Liu, D., et al. (2019a). MiRNA-218 regulates osteoclast differentiation and inflammation response in periodontitis rats through Mmp9. *Cell Microbiol.* 21 (4), e12979. doi: 10.1111/cmi.12979

Guo, P. Y., Wu, L. F., Xiao, Z. Y., Huang, T. L., and Li, X. (2019b). Knockdown of MiR-140-5 promotes osteogenesis of adipose-derived mesenchymal stem cells by targeting TLR4 and BMP2 and promoting fracture healing in the atrophic nonunion rat model. *Eur. Rev. Med. Pharmacol. Sci.* 23 (5), 2112–2124. doi: 10.26355/eurrev_201903_17255

Han, Y., Zhang, K., Hong, Y., Wang, J., Liu, Q., Zhang, Z., et al. (2018). miR-342-3p promotes osteogenic differentiation *via* targeting ATF3. *FEBS Lett.* 592 (24), 4051–4065. doi: 10.1002/1873-3468.13282

He, C. X., Zhang, T. Y., Miao, P. H., Hu, Z. J., Han, M., Tabata, Y., et al. (2012). TGF-beta1 gene-engineered mesenchymal stem cells induce rat cartilage regeneration using nonviral gene vector. *Biotechnol. Appl. Biochem.* 59 (3), 163–169. doi: 10.1002/bab.1001

He, G., Chen, J., and Huang, D. (2019). miR-877-3p promotes TGF-beta1-induced osteoblast differentiation of MC3T3-E1 cells by targeting Smad7. *Exp. Ther. Med.* 18 (1), 312–319. doi: 10.3892/etm.2019.7570

Hoseinzadeh, S., Atashi, A., Soleimani, M., Alizadeh, E., and Zarghami, N. (2016). MiR-221-inhibited adipose tissue-derived mesenchymal stem cells bioengineered in a nano-hydroxy apatite scaffold. *In Vitro Cell Dev. Biol. Anim.* 52 (4), 479–487. doi: 10.1007/s11626-015-9992-x

Hrdlicka, H. C., Lee, S. K., and Delany, A. M. (2019). MicroRNAs are critical regulators of osteoclast differentiation. *Curr. Mol. Biol. Rep.* 5 (1), 65–74. doi: 10.1007/s40610-019-0116-3

Hsu, F. Y., Hung, Y. S., Liou, H. M., and Shen, C. H. (2010). Electrospun hyaluronate–collagen nanofibrous matrix and the effects of varying the concentration of hyaluronate on the characteristics of foreskin fibroblast cells. *Acta Biomater.* 6 (6), 2140–2147. doi: 10.1016/j.actbio.2009.12.023

Hu, W., Zhang, W., Li, F., Guo, F., and Chen, A. (2016). miR-139 is up-regulated in osteoarthritis and inhibits chondrocyte proliferation and migration possibly *via* suppressing EIF4G2 and IGF1R. *Biochem. Biophys. Res. Commun.* 474 (2), 296–302. doi: 10.1016/j.bbrc.2016.03.164

Hu, G., Zhao, X., Wang, C., Geng, Y., Zhao, J., Xu, J., et al. (2017). MicroRNA-145 attenuates TNF-alpha-driven cartilage matrix degradation in osteoarthritis *via* direct suppression of MKK4. *Cell Death Dis.* 8 (10), e3140. doi: 10.1038/cddis.2017.522

Hu, S., Mao, G., Zhang, Z., Wu, P., Wen, X., Liao, W., et al. (2019). MicroRNA-320c inhibits development of osteoarthritis through downregulation of canonical Wnt signaling pathway. *Life Sci.* 228, 242–250. doi: 10.1016/j.lfs.2019.05.011

Jia, H. L., and Zhou, D. S. (2018). Downregulation of microRNA-367 promotes osteoblasts growth and proliferation of mice during fracture by activating the PANX3-mediated Wnt/beta-catenin pathway. *J. Cell Biochem.* 120 (5), 8247–8258. doi: 10.1002/jcb.28108

Jia, D., Li, Y., Han, R., Wang, K., Cai, G., He, C., et al. (2019). miR146a5p expression is upregulated by the CXCR4 antagonist TN14003 and attenuates SDF1induced cartilage degradation. *Mol. Med. Rep.* 19 (5), 4388–4400. doi: 10.3892/mmr.2019.10076

Jin, Y., Hong, F., Bao, Q., Xu, Q., Duan, R., Zhu, Z., et al. (2019). MicroRNA-145 suppresses osteogenic differentiation of human jaw bone marrow mesenchymal stem cells partially *via* targeting semaphorin 3A. *Connect Tissue Res.*, 1–9. doi: 10.1080/03008207.2019.1643334

John, A. A., Prakash, R., and Singh, D. (2019). miR-487b-3p impairs osteoblastogenesis by targeting Notch-regulated ankyrin-repeat protein (Nrarp). *J. Endocrinol.* 241 (3), 249–263. doi: 10.1530/JOE-19-0015

Kaul, G., Cucchiarini, M., Arntzen, D., Zurakowski, D., Menger, M. D., Kohn, D., et al. (2006). Local stimulation of articular cartilage repair by transplantation of encapsulated chondrocytes overexpressing human fibroblast growth factor 2 (FGF-2) *in vivo*. *J. Gene Med.* 8 (1), 100–111. doi: 10.1002/jgm.819

Klinger, P., Surmann-Schmitt, C., Brem, M., Swoboda, B., Distler, J. H., Carl, H. D., et al. (2011). Chondromodulin 1 stabilizes the chondrocyte phenotype and inhibits endochondral ossification of porcine cartilage repair tissue. *Arthritis Rheumatol.* 63 (9), 2721–2731. doi: 10.1002/art.30335

Kou, J., Zheng, X., Guo, J., Liu, Y., and Liu, X. (2019). MicroRNA-218-5p relieves postmenopausal osteoporosis through promoting the osteoblast differentiation of bone marrow mesenchymal stem cells. *J. Cell Biochem.* 121 (2), 1216–1226. doi: 10.1002/jcb.29355

Kowalczewski, C. J., and Saul, J. M. (2018). Biomaterials for the delivery of growth factors and other therapeutic agents in tissue engineering approaches to bone regeneration. *Front. Pharmacol.* 9, 513. doi: 10.3389/fphar.2018.00513

Lee, J. M., and Im, G. I. (2012). SOX trio-co-transduced adipose stem cells in fibrin gel to enhance cartilage repair and delay the progression of osteoarthritis in the rat. *Biomaterials* 33 (7), 2016–2024. doi: 10.1016/j.biomaterials.2011.11.050

Leng, P., Ding, C. R., Zhang, H. N., and Wang, Y. Z. (2012). Reconstruct large osteochondral defects of the knee with hIGF-1 gene enhanced mosaicplasty. *Knee* 19 (6), 804–811. doi: 10.1016/j.knee.2012.03.009

Li, L., and Jiang, D. (2019). Hypoxia-responsive miRNA-21-5p inhibits Runx2 suppression by targeting SMAD7 in MC3T3-E1 cells. *J. Cell Biochem.* 120 (10), 16867–16875. doi: 10.1002/jcb.28944

Li, B., Li, F., Ma, L., Yang, J., Wang, C., Wang, D., et al. (2014). Poly(lactide-co-glycolide)/fibrin gel construct as a 3D model to evaluate gene therapy of cartilage *in vivo*. *Mol. Pharm.* 11 (7), 2062–2070. doi: 10.1021/mp5000136

Li, L., Jia, J., Liu, X., Yang, S., Ye, S., Yang, W., et al. (2015). MicroRNA-16-5p controls development of osteoarthritis by targeting SMAD3 in chondrocytes. *Curr. Pharm. Des.* 21 (35), 5160–5167. doi: 10.2174/1381612821666150909094712

Li, X., Ding, J., Zhang, Z., Yang, M., Yu, J., Wang, J., et al. (2016). Kartogenin-incorporated thermogel supports stem cells for significant cartilage regeneration. *ACS Appl. Mater. Interfaces* 8 (8), 5148–5159. doi: 10.1021/acsami.5b12212

Li, X., He, P., Li, Z., Wang, H., Liu, M., Xiao, Y., et al. (2018a). Interleukin1 beta mediated suppression of microRNA27a3p activity in human cartilage *via* MAPK and NFkappaB pathways: a potential mechanism of osteoarthritis pathogenesis. *Mol. Med. Rep.* 18 (1), 541–549. doi: 10.3892/mmr.2018.8970

Li, Z., Zhang, W., and Huang, Y. (2018b). MiRNA-133a is involved in the regulation of postmenopausal osteoporosis through promoting osteoclast differentiation. *Acta Biochim. Biophys. Sin. (Shanghai)* 50 (3), 273–280. doi: 10.1093/abbs/gmy006

Li, M., Luo, R., Yang, W., Zhou, Z., and Li, C. (2019a). miR-363-3p is activated by MYB and regulates osteoporosis pathogenesis *via* PTEN/PI3K/AKT signaling pathway. *In Vitro Cell Dev. Biol. Anim.* 55 (5), 376–386. doi: 10.1007/s11626-019-00344-5

Li, W., Wang, X., Chang, L., and Wang, F. (2019b). MiR-377 inhibits wear particle-induced osteolysis *via* targeting RANKL. *Cell Biol. Int.* 43 (6), 658–668. doi: 10.1002/cbin.11143

Li, W., Zhao, S., Yang, H., Zhang, C., Kang, Q., Deng, J., et al. (2019c). Potential novel prediction of TMJ-OA: MiR-140-5p regulates inflammation through Smad/TGF-beta signaling. *Front. Pharmacol.* 10, 15. doi: 10.3389/fphar.2019.00015

Li, Y., Feng, C., Gao, M., Jin, M., Liu, T., Yuan, Y., et al. (2019d). MicroRNA-92b-5p modulates melatonin-mediated osteogenic differentiation of bone marrow mesenchymal stem cells by targeting ICAM-1. *J. Cell Mol. Med.* 23 (9), 6140–6153. doi: 10.1111/jcmm.14490

Liang, W., Zhu, C., Liu, F., Cui, W., Wang, Q., Chen, Z., et al. (2015). Integrin beta1 gene therapy enhances *in vitro* creation of tissue-engineered cartilage under periodic mechanical stress. *Cell Physiol. Biochem.* 37 (4), 1301–1314. doi: 10.1159/000430253

Lima, A. C., Ferreira, H., Reis, R. L., and Neves, N. M. (2019). Biodegradable polymers: an update on drug delivery in bone and cartilage diseases. *Expert. Opin. Drug Deliv.* 16 (8), 795–813. doi: 10.1080/17425247.2019.1635117

Lin, J. C., Liu, Z. G., Yu, B., and Zhang, X. R. (2018). MicroRNA-874 targeting SUFU involves in osteoblast proliferation and differentiation in osteoporosis rats through the Hedgehog signaling pathway. *Biochem. Biophys. Res. Commun.* 506 (1), 194–203. doi: 10.1016/j.bbrc.2018.09.187

Lin, S. S., Yuan, L. J., Niu, C. C., Tu, Y. K., Yang, C. Y., and Ueng, S. W. N. (2019). Hyperbaric oxygen inhibits the HMGB1/RAGE signaling pathway by upregulating Mir-107 expression in human osteoarthritic chondrocytes. *Osteoarthr. Cartil.* 27 (9), 1372–1381. doi: 10.1016/j.joca.2019.05.011

Liu, H., Cheng, Y., Chen, J., Chang, F., Wang, J., Ding, J., et al. (2018). Component effect of stem cell-loaded thermosensitive polypeptide hydrogels on cartilage repair. *Acta Biomater.* 73, 103–111. doi: 10.1016/j.actbio.2018.04.035

Liu, M., Sun, F., Feng, Y., Sun, X., Li, J., Fan, Q., et al. (2019a). MicroRNA-132-3p represses Smad5 in MC3T3-E1 osteoblastic cells under cyclic tensile stress. *Mol. Cell Biochem.* 458 (1-2), 143–157. doi: 10.1007/s11010-019-03538-3

Liu, X., Liu, L., Zhang, H., Shao, Y., Chen, Z., Feng, X., et al. (2019b). MiR-146b accelerates osteoarthritis progression by targeting alpha-2-macroglobulin. *Aging (Albany NY)* 11 (16), 6014–6028. doi: 10.18632/aging.102160

Lo, S. C., Li, K. C., Chang, Y. H., Hsu, M. N., Sung, L. Y., Vu, T. A., et al. (2017). Enhanced critical-size calvarial bone healing by ASCs engineered with Cre/loxP-based hybrid baculovirus. *Biomaterials* 124, 1–11. doi: 10.1016/j.biomaterials.2017.01.033

Lolli, A., Narcisi, R., Lambertini, E., Penolazzi, L., Angelozzi, M., Kops, N., et al. (2016). Silencing of antichondrogenic microRNA-221 in human mesenchymal stem cells promotes cartilage repair *in vivo*. *Stem Cells* 34 (7), 1801–1811. doi: 10.1002/stem.2350

Lou, Z., Peng, Z., Wang, B., Li, X., Li, X., and Zhang, X. (2019). miR-142-5p promotes the osteoclast differentiation of bone marrow-derived macrophages *via* PTEN/PI3K/AKT/FoxO1 pathway. *J. Bone Miner. Metab.* 37 (5), 815–824. doi: 10.1007/s00774-019-00997-y

Lu, C. H., Yeh, T. S., Yeh, C. L., Fang, Y. H., Sung, L. Y., Lin, S. Y., et al. (2014). Regenerating cartilages by engineered ASCs: prolonged TGF-beta3/BMP-6 expression improved articular cartilage formation and restored zonal structure. *Mol. Ther.* 22 (1), 186–195. doi: 10.1038/mt.2013.165

Ma, S., Wang, D. D., Ma, C. Y., and Zhang, Y. D. (2019a). microRNA-96 promotes osteoblast differentiation and bone formation in ankylosing spondylitis mice through activating the Wnt signaling pathway by binding to SOST. *J. Cell Biochem.* 120 (9), 15429–15442. doi: 10.1002/jcb.28810

Ma, Y., Wu, Y., Chen, J., Huang, K., Ji, B., Chen, Z., et al. (2019b). miR-10a-5p promotes chondrocyte apoptosis in osteoarthritis by targeting HOXA1. *Mol. Ther. Nucleic Acids* 14, 398–409. doi: 10.1016/j.omtn.2018.12.012

Mao, G., Wu, P., Zhang, Z., Zhang, Z., Liao, W., Li, Y., et al. (2017a). MicroRNA-92a-3p regulates aggrecanase-1 and aggrecanase-2 expression in chondrogenesis and IL-1beta-induced catabolism in human articular chondrocytes. *Cell Physiol. Biochem.* 44 (1), 38–52. doi: 10.1159/000484579

Mao, G., Zhang, Z., Huang, Z., Chen, W., Huang, G., Meng, F., et al. (2017b). MicroRNA-92a-3p regulates the expression of cartilage-specific genes by directly targeting histone deacetylase 2 in chondrogenesis and degradation. *Osteoarthr. Cartil.* 25 (4), 521–532. doi: 10.1016/j.joca.2016.11.006

Mao, G., Hu, S., Zhang, Z., Wu, P., Zhao, X., Lin, R., et al. (2018a). Exosomal miR-95-5p regulates chondrogenesis and cartilage degradation *via* histone deacetylase 2/8. *J. Cell Mol. Med.* 22 (11), 5354–5366. doi: 10.1111/jcmm.13808

Mao, G., Zhang, Z., Hu, S., Zhang, Z., Chang, Z., Huang, Z., et al. (2018b). Exosomes derived from miR-92a-3p-overexpressing human mesenchymal stem cells enhance chondrogenesis and suppress cartilage degradation *via* targeting WNT5A. *Stem. Cell Res. Ther.* 9 (1), 247. doi: 10.1186/s13287-018-1004-0

McMillan, A., Nguyen, M. K., Gonzalez-Fernandez, T., Ge, P., Yu, X., Murphy, W. L., et al. (2018). Dual non-viral gene delivery from microparticles within 3D high-density stem cell constructs for enhanced bone tissue engineering. *Biomaterials* 161, 240–255. doi: 10.1016/j.biomaterials.2018.01.006

Meng, F., Zhang, Z., Chen, W., Huang, G., He, A., Hou, C., et al. (2016). MicroRNA-320 regulates matrix metalloproteinase-13 expression in chondrogenesis and interleukin-1beta-induced chondrocyte responses. *Osteoarthr. Cartil.* 24 (5), 932–941. doi: 10.1016/j.joca.2015.12.012

Meng, F., Li, Z., Zhang, Z., Yang, Z., Kang, Y., Zhao, X., et al. (2018). MicroRNA-193b-3p regulates chondrogenesis and chondrocyte metabolism by targeting HDAC3. *Theranostics* 8 (10), 2862–2883. doi: 10.7150/thno.23547

Mirzamohammadi, F., Papaioannou, G., and Kobayashi, T. (2014). MicroRNAs in cartilage development, homeostasis, and disease. *Curr. Osteoporos. Rep.* 12 (4), 410–419. doi: 10.1007/s11914-014-0229-9

Moutos, F. T., Glass, K. A., Compton, S. A., Ross, A. K., Gersbach, C. A., Guilak, F., et al. (2016). Anatomically shaped tissue-engineered cartilage with tunable and inducible anticytokine delivery for biological joint resurfacing. *Proc. Natl. Acad. Sci. U. S. A.* 113 (31), E4513–E4522. doi: 10.1073/pnas.1601639113

Niu, D., Gong, Z., Sun, X., Yuan, J., Zheng, T., Wang, X., et al. (2019). miR-338-3p regulates osteoclastogenesis *via* targeting IKKbeta gene. *In Vitro Cell Dev. Biol. Anim.* 55 (4), 243–251. doi: 10.1007/s11626-019-00325-8

Nooeaid, P., Salih, V., Beier, J. P., and Boccaccini, A. R. (2012). Osteochondral tissue engineering: scaffolds, stem cells and applications. *J. Cell Mol. Med.* 16 (10), 2247–2270. doi: 10.1111/j.1582-4934.2012.01571.x

Orth, P., Kaul, G., Cucchiarini, M., Zurakowski, D., Menger, M. D., Kohn, D., et al. (2011). Transplanted articular chondrocytes co-overexpressing IGF-I and FGF-2 stimulate cartilage repair *in vivo*. *Knee Surg. Sports Traumatol. Arthrosc.* 19 (12), 2119–2130. doi: 10.1007/s00167-011-1448-6

Pan, J., Huang, C., Chen, G., Cai, Z., and Zhang, Z. (2018). MicroRNA-451 blockade promotes osteoblastic differentiation and skeletal anabolic effects by promoting YWHAZ-mediated RUNX2 protein stabilization. *Medchemcomm* 9 (8), 1359–1368. doi: 10.1039/c8md00187a

Peng, W. X., and Wang, L. (2017). Adenovirus-mediated expression of BMP-2 and BFGF in bone marrow mesenchymal stem cells combined with demineralized bone matrix for repair of femoral head osteonecrosis in beagle dogs. *Cell Physiol. Biochem.* 43 (4), 1648–1662. doi: 10.1159/000484026

Press, T., Viale-Bouroncle, S., Felthaus, O., Gosau, M., and Morsczeck, C. (2015). EGR1 supports the osteogenic differentiation of dental stem cells. *Int. Endod. J.* 48 (2), 185–192. doi: 10.1111/iej.12299

Qin, W., Liu, L., Wang, Y., Wang, Z., Yang, A., and Wang, T. (2019). Mir-494 inhibits osteoblast differentiation by regulating BMP signaling in simulated microgravity. *Endocrine* 65 (2), 426–439. doi: 10.1007/s12020-019-01952-7

Raftery, R. M., Walsh, D. P., Blokpoel Ferreras, L., Mencia Castano, I., Chen, G., LeMoine, M., et al. (2019). Highly versatile cell-penetrating peptide loaded scaffold for efficient and localised gene delivery to multiple cell types: from development to application in tissue engineering. *Biomaterials* 216, 119277. doi: 10.1016/j.biomaterials.2019.119277

Reyes, R., Delgado, A., Sanchez, E., Fernandez, A., Hernandez, A., and Evora, C. (2014). Repair of an osteochondral defect by sustained delivery of BMP-2 or TGFbeta1 from a bilayered alginate-PLGA scaffold. *J. Tissue Eng. Regener. Med.* 8 (7), 521–533. doi: 10.1002/term.1549

Reziwan, K., Sun, D., Zhang, B., and Zhao, Z. (2019). MicroRNA-1225 activates Keap1-Nrf2-HO-1 signalling to inhibit TNFalpha-induced osteoclastogenesis by mediating ROS generation. *Cell Biochem. Funct.* 37 (4), 256–265. doi: 10.1002/cbf.3394

Rowland, C. R., Glass, K. A., Ettyreddy, A. R., Gloss, C. C., Matthews, J. R. L., Huynh, N. P. T., et al. (2018). Regulation of decellularized tissue remodeling *via* scaffold-mediated lentiviral delivery in anatomically-shaped osteochondral constructs. *Biomaterials* 177, 161–175. doi: 10.1016/j.biomaterials.2018.04.049

Sarasam, A. R., Krishnaswamy, R. K., and Madihally, S. V. (2006). Blending chitosan with polycaprolactone: effects on physicochemical and antibacterial properties. *Biomacromolecules* 7 (4), 1131–1138. doi: 10.1021/bm050935d

Seenprachawong, K., Tawornsawutruk, T., Nantasenamat, C., Nuchnoi, P., Hongeng, S., and Supokawej, A. (2018). miR-130a and miR-27b enhance osteogenesis in human bone marrow mesenchymal stem cells *via* specific down-regulation of peroxisome proliferator-activated receptor gamma. *Front. Genet.* 9, 543. doi: 10.3389/fgene.2018.00543

Seidl, C. I., Martinez-Sanchez, A., and Murphy, C. L. (2016). Derepression of MicroRNA-138 contributes to loss of the human articular chondrocyte phenotype. *Arthritis Rheumatol.* 68 (2), 398–409. doi: 10.1002/art.39428

Seo, S. J., Mahapatra, C., Singh, R. K., Knowles, J. C., and Kim, H. W. (2014). Strategies for osteochondral repair: focus on scaffolds. *J. Tissue Eng.* 5, 2041731414541850. doi: 10.1177/2041731414541850

Sheng, J., Liu, D., Kang, X., Chen, Y., Jiang, K., and Zheng, W. (2018). Egr-1 increases angiogenesis in cartilage *via* binding Netrin-1 receptor DCC promoter. *J. Orthop. Surg. Res.* 13 (1), 125. doi: 10.1186/s13018-018-0826-x

Shi, S., Chan, A. G., Mercer, S., Eckert, G. J., and Trippel, S. B. (2014). Endogenous versus exogenous growth factor regulation of articular chondrocytes. *J. Orthop. Res.* 32 (1), 54–60. doi: 10.1002/jor.22444

Shimomura, K., Moriguchi, Y., Murawski, C. D., Yoshikawa, H., and Nakamura, N. (2014). Osteochondral tissue engineering with biphasic scaffold: current strategies and techniques. *Tissue Eng. Part B. Rev.* 20 (5), 468–476. doi: 10.1089/ten.TEB.2013.0543

Song, J., Jin, E. H., Kim, D., Kim, K. Y., Chun, C. H., and Jin, E. J. (2015). MicroRNA-222 regulates MMP-13 *via* targeting HDAC-4 during osteoarthritis pathogenesis. *BBA Clin.* 3, 79–89. doi: 10.1016/j.bbacli.2014.11.009

Sul, O. J., Rajasekaran, M., Park, H. J., Suh, J. H., and Choi, H. S. (2019). MicroRNA-29b enhances osteoclast survival by targeting BCL-2-modifying factor after lipopolysaccharide stimulation. *Oxid. Med. Cell Longev.* 2019, 6018180. doi: 10.1155/2019/6018180

Sun, L., Li, H., Qu, L., Zhu, R., Fan, X., Xue, Y., et al. (2014). Immobilized lentivirus vector on chondroitin sulfate-hyaluronate acid-silk fibroin hybrid scaffold for tissue-engineered ligament–bone junction. *BioMed. Res. Int.* 2014, 816979. doi: 10.1155/2014/816979

Sun, L., Lian, J. X., and Meng, S. (2019a). MiR-125a-5p promotes osteoclastogenesis by targeting TNFRSF1B. *Cell Mol. Biol. Lett.* 24, 23. doi: 10.1186/s11658-019-0146-0

Sun, Q., Zhang, B., Zhu, W., Wei, W., Ma, J., and Tay, F. R. (2019b). A potential therapeutic target for regulating osteoporosis *via* suppression of osteoclast differentiation. *J. Dent.* 82, 91–97. doi: 10.1016/j.jdent.2019.01.015

Taipaleenmaki, H. (2018). Regulation of bone metabolism by microRNAs. *Curr. Osteoporos. Rep.* 16 (1), 1–12. doi: 10.1007/s11914-018-0417-0

Tang, J., Zhang, Z., Jin, X., and Shi, H. (2018). miR-383 negatively regulates osteoblastic differentiation of bone marrow mesenchymal stem cells in rats by targeting Satb2. *Bone* 114, 137–143. doi: 10.1016/j.bone.2018.06.010

Thomas, E., Peat, G., and Croft, P. (2014). Defining and mapping the person with osteoarthritis for population studies and public health. *Rheumatol. (Oxford)* 53 (2), 338–345. doi: 10.1093/rheumatology/ket346

Tian, Y., Guo, R., Shi, B., Chen, L., Yang, L., and Fu, Q. (2016). MicroRNA-30a promotes chondrogenic differentiation of mesenchymal stem cells through inhibiting Delta-like 4 expression. *Life Sci.* 148, 220–228. doi: 10.1016/j.lfs.2016.02.031

Tsezou, A. (2014). Osteoarthritis year in review 2014: genetics and genomics. *Osteoarthr. Cartil.* 22 (12), 2017–2024. doi: 10.1016/j.joca.2014.07.024

Venkatesan, J. K., Gardner, O., Rey-Rico, A., Eglin, D., Alini, M., Stoddart, M. J., et al. (2018). Improved chondrogenic differentiation of rAAV SOX9-modified human MSCs seeded in fibrin-polyurethane scaffolds in a hydrodynamic environment. *Int. J. Mol. Sci.* 19 (9), 2635. doi: 10.3390/ijms19092635

Verbus, E. A., Kenyon, J. D., Sergeeva, O., Awadallah, A., Yuan, L., Welter, J. F., et al. (2017). Expression of miR-145-5p during chondrogenesis of mesenchymal stem cells. *J. Stem Cell Res. (Overl Park)* 1 (3), 1–10. doi: 10.33425/2639-9512.1017

Wang, X., Wenk, E., Zhang, X., Meinel, L., Vunjak-Novakovic, G., and Kaplan, D. L. (2009). Growth factor gradients *via* microsphere delivery in biopolymer scaffolds for osteochondral tissue engineering. *J. Control Release* 134 (2), 81–90. doi: 10.1016/j.jconrel.2008.10.021

Wang, X., Li, Y., Han, R., He, C., Wang, G., Wang, J., et al. (2014). Demineralized bone matrix combined bone marrow mesenchymal stem cells, bone morphogenetic protein-2 and transforming growth factor-beta3 gene promoted pig cartilage defect repair. *PloS One* 9 (12), e116061. doi: 10.1371/journal.pone.0116061

Wang, G., Zhang, Y., Zhao, X., Meng, C., Ma, L., and Kong, Y. (2015). MicroRNA-411 inhibited matrix metalloproteinase 13 expression in human chondrocytes. *Am. J. Transl. Res.* 7 (10), 2000–2006.

Wang, J., Chen, L., Jin, S., Lin, J., Zheng, H., Zhang, H., et al. (2016). MiR-98 promotes chondrocyte apoptosis by decreasing Bcl-2 expression in a rat model of osteoarthritis. *Acta Biochim. Biophys. Sin. (Shanghai)* 48 (10), 923–929. doi: 10.1093/abbs/gmw084

Wang, C., Hou, W., Guo, X., Li, J., Hu, T., Qiu, M., et al. (2017). Two-phase electrospinning to incorporate growth factors loaded chitosan nanoparticles into electrospun fibrous scaffolds for bioactivity retention and cartilage regeneration. *Mater. Sci. Eng. C. Mater. Biol. Appl.* 79, 507–515. doi: 10.1016/j.msec.2017.05.075

Wang, C., He, H., Wang, L., Jiang, Y., and Xu, Y. (2018a). Reduced miR-144-3p expression in serum and bone mediates osteoporosis pathogenesis by targeting RANK. *Biochem. Cell Biol.* 96 (5), 627–635. doi: 10.1139/bcb-2017-0243

Wang, W., Yang, L., Zhang, D., Gao, C., Wu, J., Zhu, Y., et al. (2018b). MicroRNA-218 negatively regulates osteoclastogenic differentiation by repressing the nuclear factor-kappaB signaling pathway and targeting tumor necrosis factor receptor 1. *Cell Physiol. Biochem.* 48 (1), 339–347. doi: 10.1159/000491740

Wang, Y., Wang, K., Hu, Z., Zhou, H., Zhang, L., Wang, H., et al. (2018c). MicroRNA-139-3p regulates osteoblast differentiation and apoptosis by targeting ELK1 and interacting with long noncoding RNA ODSM. *Cell Death Dis.* 9 (11), 1107. doi: 10.1038/s41419-018-1153-1

Wang, C., Feng, N., Chang, F., Wang, J., Yuan, B., Cheng, Y., et al. (2019a). Injectable cholesterol-enhanced stereocomplex polylactide thermogel loading chondrocytes for optimized cartilage regeneration. *Adv. Health Mater.* 8 (14), e1900312. doi: 10.1002/adhm.201900312

Wang, X. B., Zhao, F. C., Yi, L. H., Tang, J. L., Zhu, Z. Y., Pang, Y., et al. (2019b). MicroRNA-21-5p as a novel therapeutic target for osteoarthritis. *Rheumatol. (Oxford)* 58 (8), 1485–1497. doi: 10.1093/rheumatology/kez102

Wei, Z. J., Liu, J., and Qin, J. (2017). miR-138 suppressed the progression of osteoarthritis mainly through targeting p65. *Eur. Rev. Med. Pharmacol. Sci.* 21 (9), 2177–2184.

Wu, Z., Qiu, X., Gao, B., Lian, C., Peng, Y., Liang, A., et al. (2018). Melatonin-mediated miR-526b-3p and miR-590-5p upregulation promotes chondrogenic differentiation of human mesenchymal stem cells. *J. Pineal Res.* 65 (1), e12483. doi: 10.1111/jpi.12483

Xia, W., Jin, Y. Q., Kretlow, J. D., Liu, W., Ding, W., Sun, H., et al. (2009). Adenoviral transduction of hTGF-beta1 enhances the chondrogenesis of bone marrow derived stromal cells. *Biotechnol. Lett.* 31 (5), 639–646. doi: 10.1007/s10529-009-9930-7

Xia, P., Gu, R., Zhang, W., Shao, L., Li, F., Wu, C., et al. (2019). MicroRNA-200c promotes osteogenic differentiation of human bone mesenchymal stem cells through activating the AKT/beta-catenin signaling pathway *via* downregulating Myd88. *J. Cell Physiol.* 234 (12), 22675–22686. doi: 10.1002/jcp.28834

Xue, Z., Meng, Y., and Ge, J. (2017). miR-127-5p promotes chondrogenic differentiation in rat bone marrow mesenchymal stem cells. *Exp. Ther. Med.* 14 (2), 1481–1486. doi: 10.3892/etm.2017.4711

Xue, J., Min, Z., Xia, Z., Cheng, B., Lan, B., Zhang, F., et al. (2018). The hsa-miR-181a-5p reduces oxidation resistance by controlling SECISBP2 in osteoarthritis. *BMC Musculoskelet. Disord.* 19 (1), 355. doi: 10.1186/s12891-018-2273-6

Xue, H., Tu, Y., Ma, T., Wen, T., Yang, T., Xue, L., et al. (2019). miR-93-5p attenuates IL-1beta-induced chondrocyte apoptosis and cartilage degradation in osteoarthritis partially by targeting TCF4. *Bone* 123, 129–136. doi: 10.1016/j.bone.2019.03.035

Yang, B., Ni, J., Long, H., Huang, J., Yang, C., and Huang, X. (2018a). IL-1beta-induced miR-34a up-regulation inhibits Cyr61 to modulate osteoarthritis chondrocyte proliferation through ADAMTS-4. *J. Cell Biochem.* 119 (10), 7959–7970. doi: 10.1002/jcb.26600

Yang, S., Zhang, W., Cai, M., Zhang, Y., Jin, F., Yan, S., et al. (2018b). Suppression of bone resorption by miR-141 in aged rhesus monkeys. *J. Bone Miner. Res.* 33 (10), 1799–1812. doi: 10.1002/jbmr.3479

Yang, S., Qian, Z., Liu, D., Wen, N., Xu, J., and Guo, X. (2019). Integration of C-type natriuretic peptide gene-modified bone marrow mesenchymal stem cells with chitosan/silk fibroin scaffolds as a promising strategy for articular cartilage regeneration. *Cell Tissue Bank* 20 (2), 209–220. doi: 10.1007/s10561-019-09760-z

Yi, O., Kwon, H. J., Kim, H., Ha, M., Hong, S. J., Hong, Y. C., et al. (2012). Effect of environmental tobacco smoke on atopic dermatitis among children in Korea. *Environ. Res.* 113, 40–45. doi: 10.1016/j.envres.2011.12.012

Yin, X., Wang, J. Q., and Yan, S. Y. (2017). Reduced miR26a and miR26b expression contributes to the pathogenesis of osteoarthritis *via the* promotion of p65 translocation. *Mol. Med. Rep.* 15 (2), 551–558. doi: 10.3892/mmr.2016.6035

Yin, N., Zhu, L., Ding, L., Yuan, J., Du, L., Pan, M., et al. (2019). MiR-135-5p promotes osteoblast differentiation by targeting HIF1AN in MC3T3-E1 cells. *Cell Mol. Biol. Lett.* 24, 51. doi: 10.1186/s11658-019-0177-6

Yu, F. Y., Xie, C. Q., Sun, J. T., Peng, W., and Huang, X. W. (2018). Overexpressed miR-145 inhibits osteoclastogenesis in RANKL-induced bone marrow-derived macrophages and ovariectomized mice by regulation of Smad3. *Life Sci.* 202, 11–20. doi: 10.1016/j.lfs.2018.03.042

Zhang, H., Zhou, L., and Zhang, W. (2014). Control of scaffold degradation in tissue engineering: a review. *Tissue Eng. Part B. Rev.* 20 (5), 492–502. doi: 10.1089/ten.TEB.2013.0452

Zhang, X. H., Geng, G. L., Su, B., Liang, C. P., Wang, F., and Bao, J. C. (2016a). MicroRNA-338-3p inhibits glucocorticoid-induced osteoclast formation through RANKL targeting. *Genet. Mol. Res.* 15 (3), gmr.15037674. doi: 10.4238/gmr.15037674

Zhang, Y., Dong, R., Park, Y., Bohner, M., Zhang, X., Ting, K., et al. (2016b). Controlled release of NELL-1 protein from chitosan/hydroxyapatite-modified TCP particles. *Int. J. Pharm.* 511 (1), 79–89. doi: 10.1016/j.ijpharm.2016.06.050

Zhang, Y., Huang, X., and Yuan, Y. (2017). MicroRNA-410 promotes chondrogenic differentiation of human bone marrow mesenchymal stem cells through down-regulating Wnt3a. *Am. J. Transl. Res.* 9 (1), 136–145.

Zhang, W., Cheng, P., Hu, W., Yin, W., Guo, F., Chen, A., et al. (2018). Inhibition of microRNA-384-5p alleviates osteoarthritis through its effects on inhibiting apoptosis of cartilage cells *via the* NF-kappaB signaling pathway by targeting SOX9. *Cancer Gene Ther.* 25 (11-12), 326–338. doi: 10.1038/s41417-018-0029-y

Zhang, Y., Yu, J., Ren, K., Zuo, J., Ding, J., and Chen, X. (2019). Thermosensitive hydrogels as scaffolds for cartilage tissue engineering. *Biomacromolecules* 20 (4), 1478–1492. doi: 10.1021/acs.biomac.9b00043

Zhao, J., Huang, M., Zhang, X., Xu, J., Hu, G., Zhao, X., et al. (2019a). MiR-146a deletion protects from bone loss in OVX mice by suppressing RANKL/OPG and M-CSF in bone microenvironment. *J. Bone Miner. Res.* 34 (11), 2149–2161. doi: 10.1002/jbmr.3832

Zhao, J., Liu, S., Zhang, W., Ni, L., Hu, Z., Sheng, Z., et al. (2019b). MiR-128 inhibits the osteogenic differentiation in osteoporosis by down-regulating SIRT6 expression. *Biosci. Rep.* 39 (9), BSR20191405. doi: 10.1042/BSR20191405

Zheng, X., Zhao, F. C., Pang, Y., Li, D. Y., Yao, S. C., Sun, S. S., et al. (2017). Downregulation of miR-221-3p contributes to IL-1beta-induced cartilage degradation by directly targeting the SDF1/CXCR4 signaling pathway. *J. Mol. Med. (Berl.)* 95 (6), 615–627. doi: 10.1007/s00109-017-1516-6

Zheng, X., Dai, J., Zhang, H., and Ge, Z. (2018). MicroRNA-221 promotes cell proliferation, migration, and differentiation by regulation of ZFPM2 in osteoblasts. *Braz. J. Med. Biol. Res.* 51 (12), e7574. doi: 10.1590/1414-431X20187574

Zhou, L., Song, H. Y., Gao, L. L., Yang, L. Y., Mu, S., and Fu, Q. (2019a). MicroRNA1005p inhibits osteoclastogenesis and bone resorption by regulating fibroblast growth factor 21. *Int. J. Mol. Med.* 43 (2), 727–738. doi: 10.3892/ijmm.2018.4017

Zhou, Z., Lu, Y., Wang, Y., Du, L., Zhang, Y., and Tao, J. (2019b). Let-7c regulates proliferation and osteodifferentiation of human adipose-derived mesenchymal stem cells under oxidative stress by targeting SCD-1. *Am. J. Physiol. Cell Physiol.* 316 (1), C57–C69. doi: 10.1152/ajpcell.00211.2018

Conflict of Interest: The authors declare that the research was conducted in the absence of any commercial or financial relationships that could be construed as a potential conflict of interest.

frontiers in Pharmacology

REVIEW
published: 21 January 2020
doi: 10.3389/fphar.2019.01573

Two-Dimensional Nanosheet-Based Photonic Nanomedicine for Combined Gene and Photothermal Therapy

Na Yoon Kim[1,2], *Sara Blake*[1], *Diba De*[1], *Jiang Ouyang*[1], *Jinjun Shi*[1] *and Na Kong*[1]*

[1] Center for Nanomedicine and Department of Anesthesiology, Brigham and Women's Hospital, Harvard Medical School, Boston, MA, United States, [2] Department of Chemical Engineering, Northeastern University, Boston, MA, United States

Two-dimensional (2D) nanosheets are characterized by their ultra-thin structure which sets them apart from their bulk materials. Due to this unique 2D structure, they have a high surface-to-volume ratio that can be beneficial for the delivery of various drugs including therapeutic DNAs and RNAs. In addition, various 2D materials exhibit excellent photothermal conversion efficiency when exposed to the near infrared (NIR) light. Therefore, this 2D nanosheet-based photonic nanomedicine has been gaining tremendous attention as both gene delivering vehicles and photothermal agents, which create synergistic effects in the treatment of different diseases. In this review, we briefly provide an overview of the following two parts regarding this type of photonic nanomedicine: (1) mechanism and advantages of nanosheets in gene delivery and photothermal therapy, respectively. (2) mechanism of synergistic effects in nanosheet-mediated combined gene and photothermal therapies and their examples in a few representative nanosheets (e.g., graphene oxide, black phosphorus, and translational metal dichalcogenide). We also expect to provide some deep insights into the possible opportunities associated with the emerging 2D nanosheets for synergistic nanomedicine research.

Keywords: 2D nanosheet, gene therapy, photothermal therapy, graphene oxide, black phosphorus, translational metal dichalcogenide

OPEN ACCESS

Edited by:
Chao Wang,
Soochow University, China

Reviewed by:
Tianjiao Ji,
Boston Children's Hospital and Harvard Medical School, United States
Guosheng Song,
Hunan University, China
Tianfeng Chen,
Jinan University, China

***Correspondence:**
Na Kong
kongna.zju@gmail.com

Specialty section:
This article was submitted to Experimental Pharmacology and Drug Discovery, a section of the journal Frontiers in Pharmacology

Received: *30 October 2019*
Accepted: *04 December 2019*
Published: *21 January 2020*

Citation:
Kim NY, Blake S, De D, Ouyang J, Shi J and Kong N (2020) Two-Dimensional Nanosheet-Based Photonic Nanomedicine for Combined Gene and Photothermal Therapy. Front. Pharmacol. 10:1573. doi: 10.3389/fphar.2019.01573

INTRODUCTION

Two-dimensional (2D) nanosheets have gained great attention in the science community since the finding of graphene in 2004 (Novoselov, 2004). Since then, various 2D nanosheets consisted of different elements other than carbon have been additionally discovered, such as transition metal dichalcogenide, metal-organic framework, emerging monoelemental nanosheets (e.g., black phosphorus) and MXenes (Furukawa et al., 2013; Brent et al., 2014; Manzeli et al., 2017; Tao et al., 2019). 2D nanosheets have unique properties that can be useful in various fields of biomedical research, including nucleic acid delivery for gene therapy. Some 2D nanosheets are made of elements widely present in the human body, such as phosphorus, which makes them interesting as a delivery vehicle with potential biocompatibility and safety (Choi et al., 2018). So far, extensive studies on the

use of 2D nanosheets in drug delivery have been done, and the variety of their applications have been demonstrated; these include gene delivery, small molecule drug delivery (Tao et al., 2017b; Ji et al., 2018 Tao et al., 2018), photothermal therapy (PTT) (Tao et al., 2017a; Xie et al., 2018; Ouyang et al., 2019), photodynamic therapy (PDT) (Ji et al., 2019), bioimaging (e.g., magnetic resonance imaging (MRI), X-ray Computed Tomography (CT), and photoacoustic imaging), and so on (Kurapati et al., 2016). This review will focus on 2D nanosheet-mediated combined gene and photothermal therapy. Although there has been a review article about combined photothermal and gene therapy mediated by nanomaterials in general (Kim et al., 2016c), this is the first review article on specific 2D nanosheet-mediated combine gene and photothermal therapy to our knowledge. Both gene therapy and PTT have gained great attention as new approaches to treat different diseases such as cancers and cardiovascular diseases (Kosuge et al., 2012; Shi et al., 2017; Rosenblum et al., 2018; Shi et al., 2019). 2D nanosheets' superior ability to perform both gene and photothermal therapy simultaneously can synergistically increase their therapeutic effects through different mechanisms. **Scheme 1** summarizes the content of this article. The structure of our article composes by the following two parts: (i) discussion on the mechanism and advantages of using nanosheets in gene therapy and photothermal therapy; and (ii) discussion on the mechanism and cases of nanosheet-mediated combined gene and photothermal therapy. We expect that this review to provide some perspectives for the furture applications of emerging 2D nanosheets in synergistic nanomedicine research.

Gene Therapy

Mechanism

Successful gene delivery to a therapeutic target is a crucial step in gene therapy. Generally, gene delivery using nanomaterials follows the same path: cellular uptake and endosomal escape. One kind of endocytosis, pinocytosis has been considered a major way for nanomaterials to be taken up by cells (Sahay et al., 2010). Pinocytosis is a mechanism that cells use to uptake small molecules in the extracellular fluid and can be divided into four types: micropinocytosis, clathrin-mediated, caveolin-mediated, and clathrin-and-caveolae independent endocytosis (Conner and Schmid, 2003). Study done by Huang et al. provides a unique insight of what type of pinocytosis occurs during cellular graphene oxide-based sheet uptake. Huang et al. (2012) studied the cellular uptake of gold nanoparticle-loaded graphene oxide, 100–200 nm, in the presence of inhibitors of different

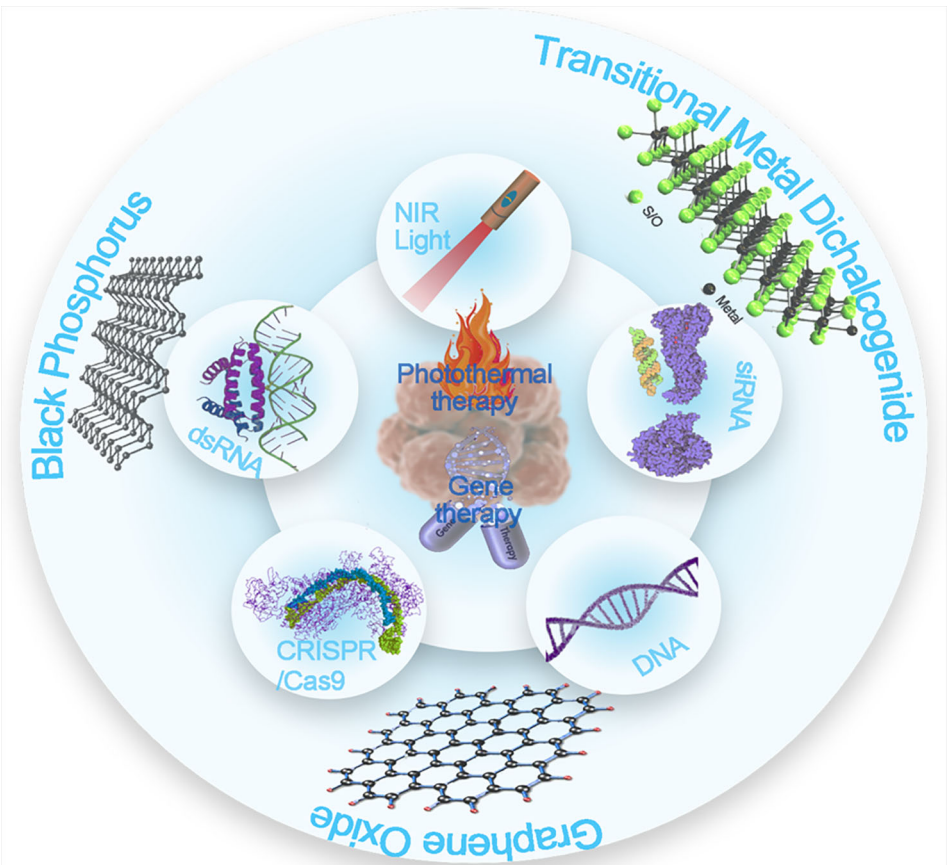

SCHEME 1 | Overview of the types of 2D nanosheets that perform combined gene and photothermal therapy.

endocytic mechanisms, such as amiloride (actin inhibitor), chlorpromazine (clathrin inhibitor), methyl-beta-cyclodextrin (caveolae inhibitor), and sodium azide (interfere endocytosis by depleting ATP). The surface-enhanced Raman scattering (SERS) analysis on Ca Ski cells showed that graphene oxide nanosheet uptake was substantially decreased when cells were treated with chlorpromazine, and sodium azide, while only a slight decrease in cellular uptake was observed in the groups treated with amiloride and methyl-beta-cyclodextrin. The results indicated that cellular uptake of graphene oxide nanosheets was clathrin and energy (ATP) dependent. According to Linares et al, macropinocytosis was a general mechanism for internalizing graphene oxide modified with fluorescein isothiocyanate and polyethylene glycolamine (PEG) FITC-PEG-GOs for Saos-2 osteoblasts, HepG2 hepatocytes, and RAW 264.7 (Linares et al., 2014). Interestingly, Mu et al. reported that large nanosheets can be uptaken by cells through phagocytosis as well (Mu et al., 2012). They synthesized protein-coated GO nanosheets with a diameter of 0.86 μm and an average height of 5.2 nm, and the formed GO nanosheets were mainly taken up by phagocytosis than clathrin-mediated endocytosis. The studies above demonstrated various possible pathways cells can uptake nanosheets, which is the first step in gene delivery.

Another important aspect of nanosheet-mediated gene delivery is its ability to perform endosomal escape. When nanosheets enter cells through endocytosis, the endocytic vesicles are formed, and the nanosheets will be sequentially passed to early endosome, late endosome/multivesicular body, and eventually to the lysosome, where proteins and nucleic acid are hydrolyzed by enzymes (Luzio et al., 2014). Based on the understanding of this process, two requirements in gene delivery cargo can be reasonably concluded: a gene carrier should be able to protect loaded genetic materials from degradation and be capable of escaping the endosome before they get to lysosome so the genetic materials can be safely delivered to the site of action, such as the cytoplasm for siRNA/mRNA or the nucleus for DNA. Numerous studies have proven that nanosheets can perform both roles successfully in different cell lines (Bao et al., 2011; Kou et al., 2014). Cationic polymers, such as polyethyleneimine (PEI) that are commonly used to load genes on 2D nanosheets causes 'proton sponge effect', which induces the endosomal escape (Boussif et al., 1995). As Behr and Varkouhi reported, the cationic polymers induce proton accumulation in the endosome, which causes osmotic swelling and endosome rupture (Varkouhi et al., 2011). Through this mechanism, the gene carrying 2D nanosheets can successfully escape the endosome and perform transfection at the site of action, either in the cytoplasm or nucleus.

Loading Efficiency

One of the distinctive characteristics of nanosheets is its high surface to volume ratio due to its extremely thin structure. This allows nanosheets to load more drugs or genes than any other drug delivery methods. According to Peng et al. (2018), doxorubicin and indocyanine green loaded Gd3+ doped monolayered-double-hydroxide nanosheets showed an extremely high drug loading of 797.36% and the encapsulation efficiency of 99.67%, which is the highest drug loading content that was among reported drug delivery systems at the time.

Nanosheets' unique geometry allows efficient loading of genetic materials. Ji et al. reported an interesting statistic that compared the DNA loading efficiency of nanoparticles and nanosheets that were made of the same material, silica (Ji et al., 2017). The loading efficiency of silica nanoparticles was 3.3% while the loading efficiency of silica nanosheets was 34%. More studies on silica spheres are also worth noting (Li et al., 2017). The fact that the loading efficiency of silica nanosheets was more than ten times that of nanoparticles implies that the geometry of nanosheets plays an important role in increased loading capacity of genetic materials.

The gene loading capacity of nanosheets can also be significantly increased *via* chemical modifications. One of the most commonly used polymers to load genetic materials to nanosheets is polyethyleneimine (PEI). Polyethyleneimine is a branched polymer that has a positive charge, which makes it capable of electrostatically attracting negatively charged genetic materials like DNA and RNA. For example, Kou at el. reported MoS2 nanosheets modified with PEI and polyethylene glycol (PEG), Mos2-PEG-PEI, as a siRNA delivery vehicle (Kou et al., 2014) successful loading of siRNA to MoS2-PEG-PEI nanosheets was confirmed with an agarose gel electrophoresis assay. Teimouri et al. also reported graphene oxide nanosheets modified with different kinds of cationic polymers, such as polypropylenimine (PPI) and polyamidoamine (PAMAM) (Teimouri et al., 2016). Graphene oxides modified with either polymers, PPI or PAMAM, successfully performed transfection of murine neuroblastoma cells using plasmid GFP DNA. However, the transfection efficiency of PEI modified nanosheets were higher than those of PPI or PAMAM modified sheets.

Different Genetic Materials (DNA, dSRNA (siRNA), Oligonucleotides, Aptamers, CRISPR)

Since the discovery of nanosheets, it has been reported that numerous genetic materials can be loaded to nanosheets and delivered to the living cells for transfection. **Table 1** shows the

TABLE 1 | Representative examples of genetic materials that were reported to be successfully delivery by nanosheets.

Material	Cell	Different Genetic Materials	Reference
Layered double hydroxide clay nanosheets	*Arabidopsis* seedlings	dsRNA	(Mitter et al., 2017)
Black phosphorus nanosheets	MCF-7	CRISPR/Cas9	(Zhou et al., 2018)
Graphene oxide nanosheets	HeLa	siRNA, plasmid, oligonucleotides	(Dowaidar et al., 2017)
Graphene oxide nanosheets	MCF-7	DNA/RNA aptamer	(Wang et al., 2013)
Silica nanosheets	Human embryonic kidney cells	DNA	(Ji et al., 2012)

representative examples of genetic materials that were reported to be successfully delivery by nanosheets. Mitter et al. reported dsRNA carrying layered double hydroxide (LDH) clay nanosheets that achieved sustained release of the genes on a plant, *Arabidopsis* seedlings, for more than 30 days (Mitter et al., 2017). Zhou et al. reported for the first time, the delivery and release of CRISPR/Cas9 complex through black phosphorus nanosheets (Zhou et al., 2018). The delivered Cas9N3-BPs showed successful genome editing and gene silencing both *in vitro* and *in vivo*. Various genetic materials could be delivered at once as well. Plasmid (pGL3), slice correction oligonucleotides (SC) or small interfering RNA (siRNA), was successfully loaded to cell penetrating peptide (PepFect 14) modified graphene oxide nanosheets, and great transfection efficacy was demonstrated on HeLa cells and U-87 MG-luc2 cells (Dowaidar et al., 2017). The delivery of siRNA could also open up the possibility of further applications of 2D nanosheets in immunotherapy *via* gene modulations (Xu et al., 2014; Li et al., 2016; Kwak et al., 2017). Wang et al. reported DNA/RNA aptamer loaded graphene oxide nanosheets that can sense ATP, GTP, adenosine derivatives, and guanosine derivatives (Wang et al., 2013). The loaded aptamers were labelled with fluorescent dye, and the successful delivery of the aptamers was shown *via* the analysis of fluorescence. Huang at el. reported a way to achieve transfection *via* naked DNA on silica glass nanosheets (Huang et al., 2015). This method had unique advantages in a sense that no vector was needed, and naked DNA was able to be transferred into cells that were known to be difficult to transfect, which like stem cells. Ji et al. introduced a new DNA delivery substrate using silica upright nanosheets (Ji et al., 2012). GFP reporter DNA complex was immobilized on the silica surface, which allowed a successful transfection on the embryonic kidney cell (HEK293XL). As demonstrated above, various kinds of genetic materials, such as DNA, RNA, aptamers, CRISPR/Cas9 complex, were successfully loaded to nanosheets and performed gene therapy on cells.

Photothermal Therapy

Mechanism

Photothermal therapy (PPT) is a recently developed therapy that uses heat produced by optical materials upon near-infrared (NIR, 700–1,000 nm) irradiation. Small sized nanosheets tend to accumulate at tumor sites when injected intravenously in animal models due to the enhanced permeability and retention effect (EPR effect) (Fang et al., 2011). Upon NIR irradiation, nanosheets absorb photons, the light energy is converted to heat energy, and the high temperature (about 42 degree Celsius) at tumour sites will cause tumor cell death (Shanmugam et al., 2014). As human tissues don't easily absorb NIR irradiation but nanosheets have excellent optical properties that effectively absorb the NIR irradiation, the PPT using nanosheets can effectively induce local temperature, which leads to selective killing of tumor cells (Zhang et al., 2019; Song et al., 2016; Song et al., 2019; Yin et al., 2019). Various studies have shown that previous studies have demonstrated that variety of nanosheets (graphene based, black phosphorous, transition-metal dichalcogenides, transition metal oxide, and MXenes) can effectively perform photothermal therapy selectively on cancer cells both *in vivo* and *in vitro* (Zhang et al., 2016; Ren et al., 2016; Yang et al., 2018).

Photothermal Conversion Efficiency and Stability

Photothermal conversion efficiency is a value that shows us how effectively a material converts light energy to thermal energy. This is an important factor in PPT because materials with high photothermal conversion efficiency can effectively produce heat to kill cancers with a certain NIR irradiation. One of the most commonly used equations to calculate photothermal conversion efficiency is the following (Liu et al., 2013):

$$\eta = \frac{hA\Delta T_{max} - Q_s}{I(1 - 10^{-A_\lambda})}$$

where η is the heat transfer coefficient, A is the container surface area, ΔT_{max} is the maximum temperature change in the solution, A_λ is the 808nm light absorbance, and I is the laser power. However, so far, the limited photothermal conversion efficiency of PTT performing particles has been a challenge. For example, an organic photothermal agent, indocyanine green (ICG) dye, reported 3.37% photothermal conversion efficiency and 8.99% when it was in liposomal forms (Yoon et al., 2017). Based on recently reported studies, many of the synthesized nanosheets have exhibited high photothermal conversion efficiency. Fu et al. reported 2D MOS2 nanosheets that had a photothermal conversion efficiency of 62% (Fu et al., 2018). As Ren has reported in SnS nanosheets, the nanosheet structure (36.1%) enhances photothermal conversion efficiency when compared to that of the bulk (24%) (Ren et al., 2016). Wang et al. explains their MnO2 nanosheets' high photothermal conversion efficiency through the concept of oxygen vacancy where the photogenerated electron can be trapped and enhance the photothermal conversion (Wang et al., 2019).

SYNERGISTIC EFFECTS OF 2D NANOSHEETS IN COMBINED GENE IN PHOTOTHERMAL THERAPY

Mechanism of Synergistic Effects of Combined Gene and Photothermal Therapy

The concept of synergistic effects between gene and photothermal therapy is based on the fact that nanosheets can perform two functions simultaneously. There are two main ways that the synergistic effects are achieved: (1) therapeutic effects from gene therapy and photothermal therapy occurring simultaneously or (2) increased therapeutic effects of gene therapy through thermal effects. Many cancer related studies demonstrated the first type of synergistic effects through the delivery of therapeutic genetic materials, meant to silence genes responsible for cancer proliferation promotion or chemo resistance, in combination with photothermal therapies that kill cancer cells via high temperature. The multi-functioning

nanosheets that can perform both therapies showed higher tumor inhibitory affects when compared to the single therapy treated groups. The second type of synergistic effects is achieved through mild heat that promotes transfection through mechanisms like inducing endosomal escape or enhancing cell membrane permeability. This improves the rate and extent of transfection which leads to more effective delivery of genes. The cases of both types of synergistic effects are further discussed in detail below. To our knowledge, nanosheet-mediated combined gene and photothermal therapies were reported in three groups of nanosheets: graphene oxide, black phosphorus, and transitional metal dichalcogenide.

Nanosheet-Mediated Combined Gene and Photothermal Therapy

Graphene Oxide

Graphene is the first discovered 2D nanomaterial that is made of carbon. Since the discovery, more members of the graphene family have been discovered, such as graphene oxide (GO), reduced graphene oxide(rGO), and few-layer graphene (Ge et al., 2018). Graphene oxide especially gained significant attention in drug delivery due to its hydrophilic nature and versatile surface chemistry, which can increase its biocompatibility (Reina et al., 2017). According to the distribution and biocompatibility study done by Zhang et al., graphene oxide showed good biocompatibility with red blood cells, which demonstrated their potential for intravenous drug delivery (Zhang, 2011).

To our knowledge, the first study to report GO based nanocarriers that performed both gene and photothermal therapy was by Feng et al. (2013). This study was meaningful in a sense that this was the first attempt to utilize GO nanosheet's optical and thermal properties to enhance the effectiveness of gene delivery. GO nanosheets were modified with PEG and PEI *via* amide bonds, which formed a nano GO-conjugate, (NGO-PEG-PEI) (**Figure 1A**). As shown in **Figure 1B**, the transfection capability of NGO-PEG-PEI in the serum condition was tested by measuring the transfection efficiency of EGFP pDNA loaded NGO-PEG-PEI nanocomposites in HeLa cells at various serum (FBS) concentrations. While the transfection efficiency of the groups transfected with GO-PEI or PEI decreased drastically as the serum concentration increased from 0 to 10%, 20%, and 30%, the NGO-PEG-PEI nanocomposites consistently showed good transfection efficiency in the presence of serum, which demonstrates NGO-PEG-PEI nanocomposite's superior transfection capability and protection of the loaded genetic material in the serum condition. NGO-PEG-PEI nanocomposite was capable of not only delivering pDNA but also delivering siRNA. As shown in **Figures 1C** and **D**, MDA-MB cells were treated with Plk1 siRNA loaded NGO-PEG-PEI nanocomposites, and the Plk1 mRNA and protein levels were analyzed through qRT-PCR and western blot. According to the Plk1 mRNA quantification results, the siRNA loaded NGO-PEG-PEI with different N/P ratios (5, 10, 20) consistently showed a lower expression of Plk mRNA expression than the lipofectatmine mediated transfected group. The suppression of Plk mRNA and protein expression was more obvious with the NIR irradiation. Especially in the NGO-PEG-PEI treated groups that had high N/P ratios (10 and 20), the suppression of Plk mRNA and protein expression were significantly enhanced with NIR irradiation. It was noted that low power density NIR light enhanced transfection efficiency through (808 nm laser at 50 W cm^{-2} for 20 min) increasing intracellular uptake of NGO-PEG-PEI. The local heating of the cell membrane led to enhanced membrane permeability (Tian et al., 2011).

Another group that extensively studied GO nanosheet's potential to create synergistic effect from combining the photothermal effect and gene delivery was Kim's group. As illustrated in **Figure 1E**. Kim's group reported a reduced graphene oxide (rGO)-based gene delivery carrier modified with BPEI (low molecular-weight branched polyethyleneimine) and PEG, PEG-BPEI-rGO nanocomposites (Kim and Kim, 2014). For the evaluation of transfection efficacy of PEG-BPEI-rGO nanocomposites, luciferase gene expression assays were performed on PC-3 and NIH/3T3 cells using plasmid DNA (pDNA) carrying PEG-BPEL-rGO nanocomposites (**Figures 2F**, **G**) In both cell lines, the group exposed to the NIR irradiation (808 nm, 6 W/cm^2, 20 min) showed 2–3-fold higher transfection efficiency than the group treated with PEG-BPEI-rGO without irradiation. The paper claimed that the NIR irradiation increased the temperature of intracellular PEG-BPEI-rGO, which induced the rupture of the endosomal membrane and lead to a higher release of DNA for transfection. The PEG-BPEI-rGO mediated gene delivery has a unique advantage as it achieves photothermally controlled gene delivery upon the NIR irradiation.

A different study performed by Kim's group introduced GO nanocarriers modified with BPEI and PEG *via* disulfide linkage, ssPEG-PEI-GO (Kim et al., 2016a). The main difference from the previous reported PEG-BPEL-rGO is that the disulfide bonds in ssPEG-PEI-GO nanocarriers enhanced their ability to be taken up by cancer cells and decreased their ability to be taken up by macrophages. **Figures 1I** and **J** showed cellular uptake of nanocarriers measured in PC3 (cancer cell) and Raw 264.7 (macrophage) with and without the presence of DTT, which reduces disulfide bonds. It is noted that the uptake of ssPEG-PEI-GO was higher than the unmodified GD in cancer cell but lower in macrophage, which showed its tumor targeting ability. **Figures 1K** and **L** evaluated ssPEG-PEI-GO nanocarrier's transfection efficiency. After PC3 cells were treated with pDNA carrying ssPEG-PEI-GO nanocarriers, the transfection efficiency with and without NIR irradiation was measured *via* luciferase assay. The transfection efficiency was increased up to five times with NIR irradiation compared to the group without irradiation, which confirms a photothermally enhanced transfection. The mechanism of photothermally enhanced transfection efficiency could be explained by two factors: NIR irradiation-induced endosomal disruption and reductive environment-induced gene release. **Figure 1H** showed an interesting confocal fluorescence images taken after the nanocarrier, pDNA, and endosome were labelled as FITC (green) TOTO (Red), and Lysotracker (yellow), respectively. Upon 10 minutes of NIR

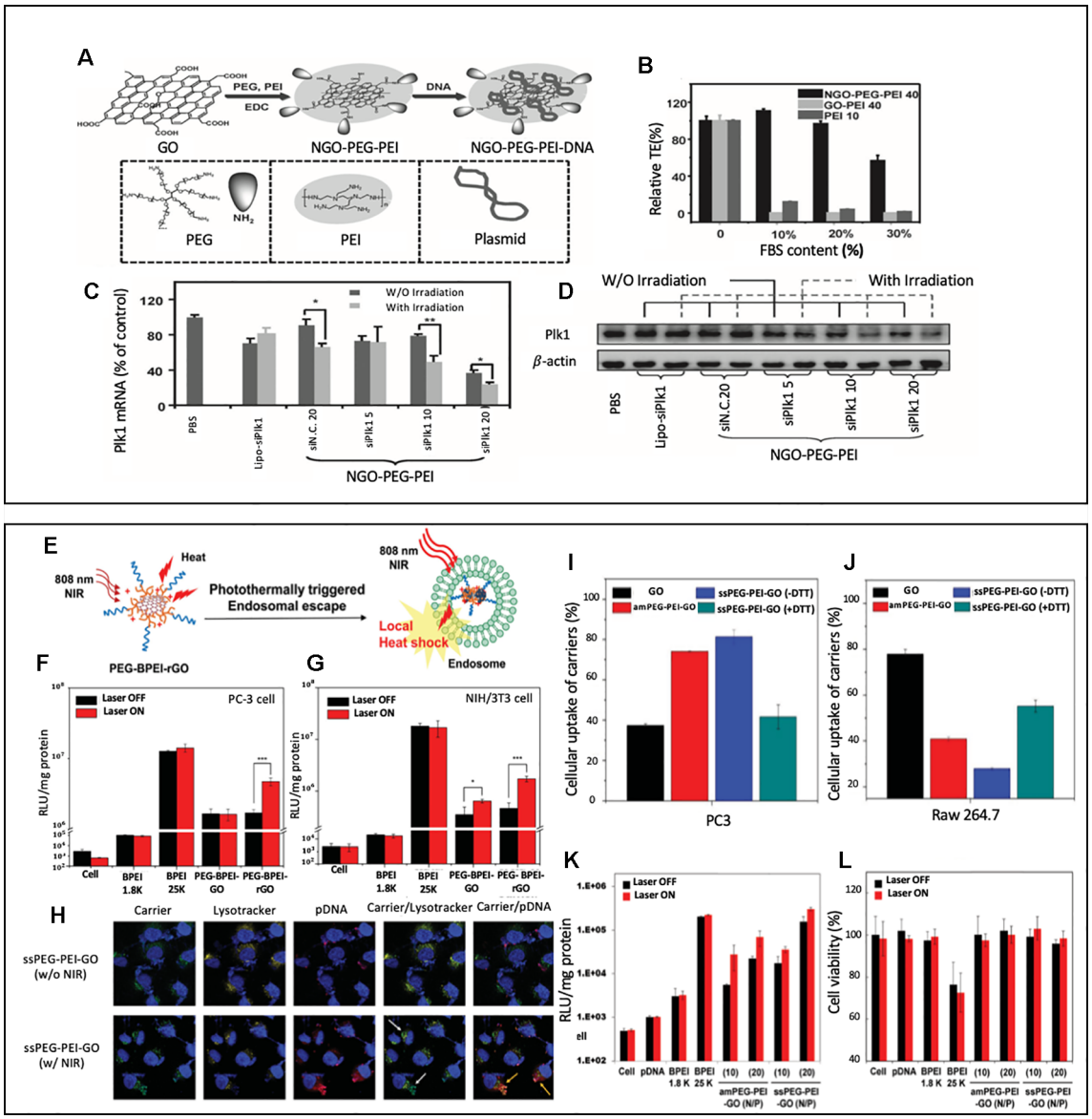

FIGURE 1 | (A) A schematic illustration showing the synthesis of NGO-PEG-PEI/pDNA complex **(B)** Transfection efficiencies of NGO-PEP-PEI, GO-PEI and bare PEI transfected HeLa cells with various FBS contents **(C, D)** The expression levels of Plk1 mRNA **(C)** and protein **(D)** as determined by qRT-PCR and western blotting, respectively, in MDA-MB-435s cells after transfection. Reprinted with permission (Feng et al., 2013). Copyright 2013, John Wiley and Sons. **(E)** Schematic illustration of photothermal transfection mechanism. **(F, G)** Transfection of the BPEI (1.8 K and 25 K), PEG-BPEI-GO and PEG– BPEI–rGO with/without NIR irradiation in PC-3 and NIH/3T3 cell lines. Reprinted with permission (Kim and Kim, 2014). Copyright 2014, John Wiley and Sons. **(H)** Confocal fluorescence microscopic images of PC-3 cells treated with GO nanocarrier/pDNA complexes at various conditions. Nuclei (blue). Carrier and pDNA (green). TOTO (red). endo/lysosomes (yellow). Relative cellular uptake of GO, amPEG-PEI-GO, ssPEG-PEI-GO, and DTT-treated ssPEG-PEI-GO in **(I)** PC-3 and **(J)** Raw 264.7 cells. **(K)** transfection efficiency and **(L)** cytotoxicity of ssPEG-PEI-GO by luciferase assay and MTT assay. Gene transfection and cell viability of the GO nanocarriers were performed at N/P ratios of 2, 5, 10, and 20 with or without NIR irradiation in PC-3 cell lines. Reprinted with permission (Kim et al., 2016a) Copyright 2016, John Wiley and Sons.

irradiation (808 nm laser at W cm^{-2}), the endosomal escape of the carrier (green) and the following dissociation of pDNA (red) from the carrier was confirmed in confocal fluorescence images. This study had a significance in a sense that new chemical modifications using disulfide linkages were done on GO nanosheets to enhance the uptake by cancer cells while decreasing the uptake by macrophages.

Multifunctional GO nanosheets that can not only perform gene and photothermal therapy together but also have targeting ability for cancer was introduced by Yin et al. Their functionalized graphene oxide nanosheets (GO nanosheets) were able to perform tumor targeting, siRNA delivery, and photothermal therapy simultaneously (Yin et al., 2017). GO nanosheets were functionalized with folic acid (FA-mPEG-NH-

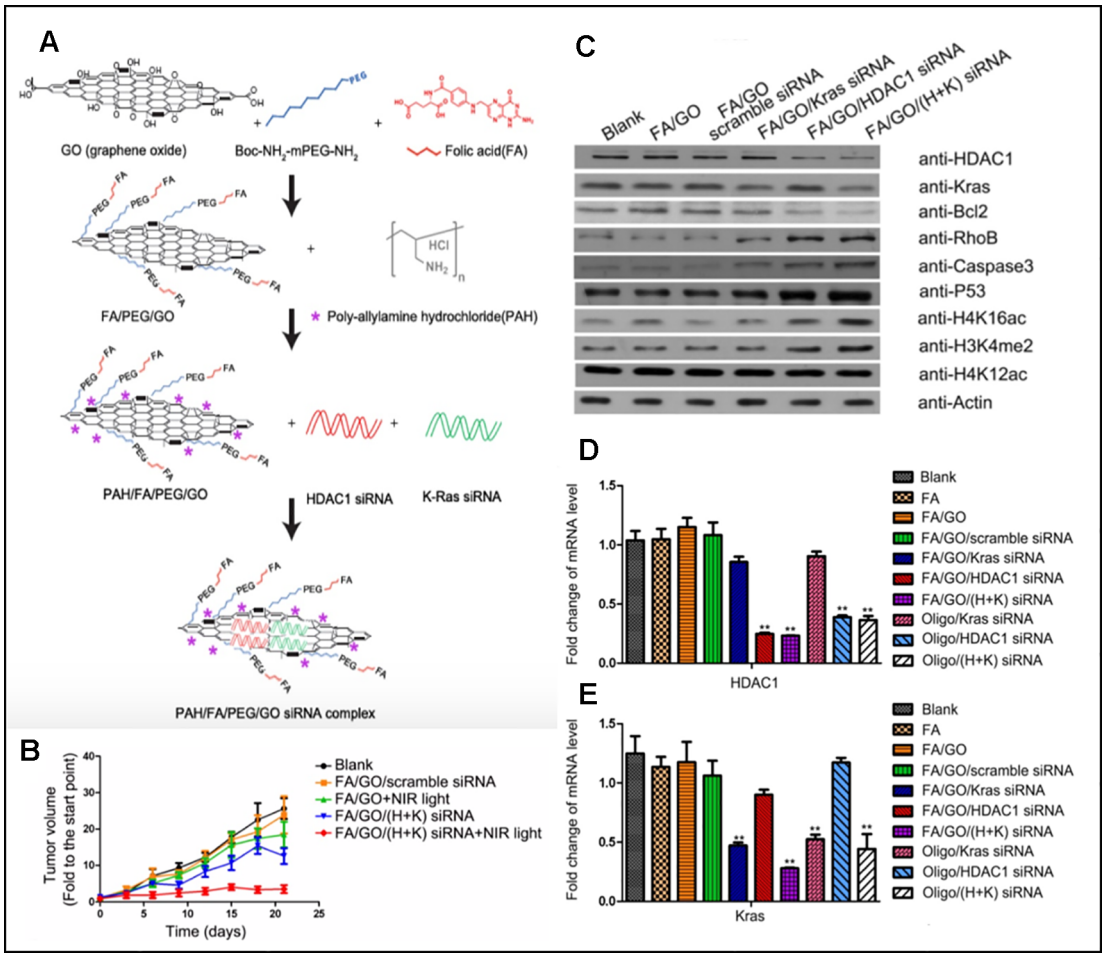

FIGURE 2 | (A) Schematic overview of the FA/PEG/GO synthesis and gene loading process using engineered GO-based nanocarriers. **(B)** Relative changes in tumor volume over time. **(C**, **D**, and **E)** Target gene expression in MIA PaCa-2 cells treated with different nanoformulations *via* western blot for relative protein levels and RT-PCR for relative mRNA levels (Yin et al., 2017). Copyright 2017, Ivyspring International Publisher.

Boc) for targeting of folate receptor-expressing cancer and coated with Poly-allylamine hydrochloride (PAH) (**Figure 2A**). PAH is a cationic polymer which can attract negatively charged siRNA *via* electrostatic interaction. Two types of siRNAs for oncogenes, HDAC1 siRNA and K-Ras siRNA, were loaded to GO nanosheets. After PaCa-2 pancreatic cancer cells were treated with synthesized GO sheet, the successful delivery of siRNA and gene silencing were confirmed by analysing the mRNA level of Kras and HDAC1 with RT-PCR and the protein levels with western blots (**Figures 2C–E**). It was noted that the transfection efficiency of nanosheets was higher than that of Oligofectamine, a commercial transfection agent. MIA PaCa-2 cells were planted subcutaneously to athymic nude mice for *in vivo* studies. Mice were treated with different treatments on a regular basis and were sacrificed on Day21 of the experiment. According to **Figure 2B**, mice with no treatment showed about 25 fold of initial tumor volume, FA/GO+NIR light treated group showed 18 fold of initial tumor volume, FA/GO/(HDAC1+Kas) siRNA treated group showed 10 fold of initial tumor volume, and mice treated with FA/GO/(HDAC1+Kas) siRNA+ NIR light showed almost no increase in tumor volume. These results clearly demonstrated the synergistic effect caused by the additive therapeutic effects from both gene therapy and photothermal therapy in suppressing tumor growth.

Black Phosphorous

Black phosphorous (BP) is a relatively new type of 2D nanosheet that has been extensively studied within the past few years since its discovery in 2014 (Li et al., 2014). It has been considered to have great potential for biomedical applications due to its biocompatibility. Phosphorus is a bone constituent that is present in our body and BP nanosheets can be degraded to phosphate and phosphonate, both are non-toxic to human body (Qian et al., 2017).

To our knowledge, the first reported study of combined gene and photothermal therapy using BP nanosheets was by Wang et al.

(2018). BP nanosheets were utilized as siRNA carriers by modifying BP nanosheets with positively charged polyethyleneimine (PEI), which allowed BP nanosheets to easily react with negatively charged siRNA molecules and form (BP-PEI-siRNA) (**Figure 3A**). Survivin protein expression in MCF-7 cells was significantly decreased after the cells were treated with BP-PEI-siRNA, which was confirmed by western blot analysis (**Figures 3F**, **E**). Both *in vitro* study and *in vivo* study were performed using MCF-7 cells to assess the synergistic effects of the combined siRNA therapy and NIR irradiation at 808 nm (PTT). In the *in vitro* cell viability study, shown in **Figure 3G**, the cell viability of MCF-7 cells was measured after 24 h treatment with BP-PEI+NIR light, BP-PEI-siRNA, and BP-PEI-siRNA + NIR light, which were about 70%, 50%, and 30%, respectively. **Figure 3B** showed the *in vivo* tumor growth study on MCF-7 bearing nude mice, the mice were divided into different treatment groups, and the relative volume of tumor (V/Vo) was measured on Day 20 of the treatment. On Day 20, the control group's relative tumor volume was 13 times of the initial volume while BP-PEI-siRNA+NIR treated group's relative tumor volume was only 2. NIR or siRNA treatment alone using BP-PEI+NIR or BP-PEI-siRNA showed antitumor effects to some extent (eight and six times of initial tumor volume on Day20), but significantly less effective than the combined gene and photothermal therapy. The body weights of all groups were comparable, which indicates the non-toxicity of the nanosheets (**Figure 3C**). **Figure 3D** also demonstrated the non-toxicity of the nanosheet treatment upto 50μg/mL *in vitro*. Wang's study held significance as it is the first reported study of combined gene and photothermal therapy using BP nanosheets to our knowledge and showed promising results of gene and photothermal therapy in both *in vitro* and *in vivo*. Due to the biodegradable nature of BP, clinical translation of nanocarriers consist of BP is promising.

Due to unique optical properties of BP nanosheets, not only photothermal therapy but also photodynamic therapy could be performed through using different wavelengths of light. Chen

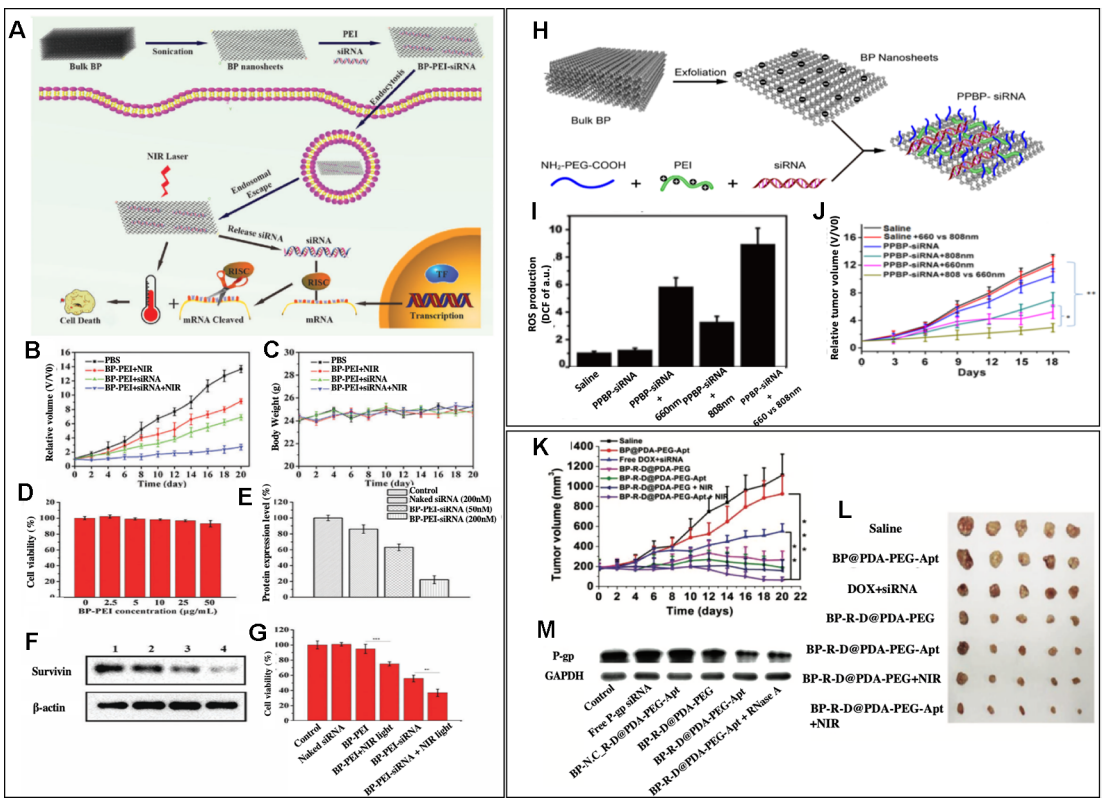

FIGURE 3 | (A) Schematic illustration of the BP nanosheet-based siRNA delivery system for synergistic photothermal and gene therapy of cancer cells. **(B, C)** Growth curves of tumors and body weight of nude mice in different groups after various treatments (n = 5 for each group). **(D)** Cell viability assay after treating with different concentrations of BP-PEI for 24 h. **(E, F)** Western blot analysis of the survivin expression in MCF-7 cells. Lane 1: control; lane 2: naked siRNA (200 nM); lane 3: BP-PEI- siRNA (50 nM) and lane 4: BP-PEI-siRNA (200 nM). **(G)** Cell viability assay after treating with different formulations for 24 h. NIR light (808 nm NIR laser with a power density of 1.0 W cm^2) was utilized to treat BP-PEI and BP-PEI-siRNA for 10 min. Reprinted with permission. (Wang et al., 2018) Copyright 2018, Royal Society of Chemistry. **(H)** Schematic illustration of the preparation of a BP nanosheet-based platform for siRNA delivery. **(I)** ROS production at the tumor site after different treatments (n = 3) **(J)** Tumor growth curves of subcutaneous HeLa xenograft in the different groups were measured. Compared with the curves in the 808 nm group and the two PBS groups, the tumor growth curve in the trimodal combined treatment group shows a significant difference (*p <0.05, **p <0.01, n = 5, respectively). Reprinted with permission (Chen et al., 2018). Copyright 2018, American Chemical Society. **(K)** Inhibition of tumor growth after different treatments. **(L)** Morphology of tumors removed from the sacrificed mice in all groups at the end point of study. **(M)** Western blot analysis. (Zeng et al., 2018). Copyright 2018, John Wiley and Sons.

et al. reported BP nanosheets modified with NH2-PEG-COOH and PEI (PPBP) that can simultaneously perform gene therapy, PDT, and PTT (Chen et al., 2018). **Figure 3H** schematically showed the synthesis of siRNA loaded PPBPs. siRNA of human telomerase reverse transcriptase (hTERT), a gene that is closely related to tumor growth and metastasis, was loaded to PPBP nanosheets, which formed PPBP-siRNA (**Figure 3H**). HeLa cells were transfected with PPBP-siRNA for 48h, and an effective hTERT mRNA and protein suppression was shown *via* RT-PCR and western blot, respectively. PPBP-siRNA's great potential in PDT and PPT were also tested *in vitro*. The increased expression of a heat shock protein, Hsp70, upon exposure to 808 nm demonstrated PPBP-siRNA's ability to induce heat stress and perform PTT. PPBP-siRNA's ability to perform PDT was also confirmed by the intracellular ROS measurement after the irradiation at 660 nm (**Figure 3I**). An effective antitumor effect of gene, PDT, and PTT therapy was also confirmed *in vivo*, as shown in **Figure 3J**. HeLa tumor-bearing BALC/c nude mice were divided into different groups with different treatments, and the relative tumor volume (V/Vo) was measured until Day 18 of the treatment. On Day 18, the relative tumor volume of the control group, PPBP-siRNA treated group, PPBP-siRNA +808 nm group, PPBP-siRNA+ 660 nm group, and PPBP-siRNA + 808 nm + 660 nm group were 12, 10, 6, 4, 2 times of the initial tumor volume, respectively. PPBP-siRNA + 808 nm + 660 nm treated group showed the best antitumor effect in the *in vivo* study, which confirms an excellent synergistic effect of gene, PTT, and PDT therapy against cancer. This study highlighted BP nanosheets' advantageous characteristics in terms of its multifunctionality.

Fully utilizing the advantage of nanosheet's high loading capacity, Zeng et al. reported BP nanosheets that carry both chemodrug and genetic material and perform a photothermal therapy (Zeng et al., 2018). BP nanosheet-mediated chemo/gene/photothermal therapy showed a unique platform to overcome drug resistance in cancer. BP nanosheets were synthesized from bulk BP using a liquid exfoliation technique. Glycoprotein (P-gp) siRNA, which could downregulate permeability related glycoprotein on cancer cells and therefore help overcome drug resistance, was adsorbed onto the surface of BP nanosheets and doxorubicin (DOX) was loaded to BP nanosheets *via* electrostatic interactions. BP nanosheets were further modified by polydopamine (PDA) coating, and an aptamer conjugate, NH2-PEG-Apt was added to the PDA coating for tumor targeting purposes. The aptamer used was AS1411, which binds to nucleolin (NCL) overexpressed in cancer cells. The synthesized nanocomplex was called BP-R-D@PDA-PEG-Apt. The western blot analysis confirmed a successful downregulation of P-gp in BP-R-D@PDA-PEG-Apt treated MCF-7/MDR cells (**Figure 3M**). The antitumor efficacy of huhjBP-R-D@PDA-PEG-Apt was performed in a subcutaneous xenograft tumor model mice. As shown in **Figures 3K** and **L**, the DOX+siRNA group showed significantly less tumor growth inhibition compared to BP-R-D@PDA-PEG treated group, which indicated an important role of P-gp siRNA in overcoming drug resistance. Also, it was noted that NIR treated groups (BP-R-D@PDA-PEG-Apt +NIR and BP-R-D@PDA-PEG + NIR) consistently showed superior tumor growth inhibition effect than the groups treated with the same materials without NIR irradiation (BP-R-D@PDA-PEG-Apt and BP-R-D@PDA-PEG). While the saline treated group's tumor volume reached five times of the initial volume on Day 22 of the treatment, the tumor volume of the BP-R-D@PDA-PEG-Apt treated group was less than half of the initial tumor volume, which is less than ten time smaller than the control group. This showed great potential of black phosphorus nanosheets as a muti-platform to perform numerous therapies and overcome drug resistance simultaneously for maximized therapeutic effects.

Transitional Metal Dichalcogenide

Transitional metal dichalcogenides are semiconductors that can be named as MX2, where M is a transition metal and X is a chalcogen (Manzeli et al., 2017). The typical transition metal atom (M) includes Mo or W and chalcogen atom (X) includes Se and Se. Biomedical applications of transitional metal dichalcogenide have been hampered due to their low water solubility, non-uniformity, and colloidal stability, but extensive interest in TMD lead to the discoveries of new methods of synthesis, exfoliation, and surface modification that makes them more biocompatible (Agarwal and Chatterjee, 2018).

One of the first reported MoS2 nanosheets that performed gene and photothermal therapy was reported by Kim et al. (2016b). They reported MoS2 nanosheets modified with PEI and PEG polymers *via* disulfide bonds. As shown in **Figures 4A** and **B**, lipoic acid conjugated to PEI, LA-PEI, was first synthesized and mixed with PEG-SH and single-layered MOS2 to synthesize MOS2-PEI-PEGs. The positive PEI polymer allowed electrostatic interatcion mediated loading of pDNA to the nanosheets, and the PEG polymers improved the biocompatibility and stability of nanosheets. Utilizing the MoS2 nanosheet's excellent photothermal conversion, photothermally triggered gene release in the cells was achieved upon the NIR irradiation. HCT116 cells were treated with luciferase gene loaded MoS2-PEI-PEG, and the luciferase reporter gene expression assay was carried out upon a mild NIR irradiation at 808 nm (2.5 W/cm^2) for 0, 10 or 20 min. As the exposure time to NIR light increased, the increase in protein expression was observed in the MoS2-PEI-PEG cell (**Figure 4C**). An increased transfection upon the NIR irradiation was due to the local heat generation at the endosome, which causes the endosomal escape of the nanosheets. After the endosomal escape of pDNA-MoS2-PEI- PEG, polymer detachment and gene release were followed upon the exposure to the intracellular GSH that led to a reduction of disulfide bond of the nanosheets. The role of GSH in triggered gene release was confirmed by repeating the luciferase reporter gene expression assay in the presence of DEM, a chemical that inhibits GSH activity. According to **Figure 4D**, 8-10-fold reduction in protein expression was resulted, which confirmed the crucial role of GSH in triggered gene release. This study introduced a great potential of MoS2 nanosheets in performing photothermally controlled gene delivery.

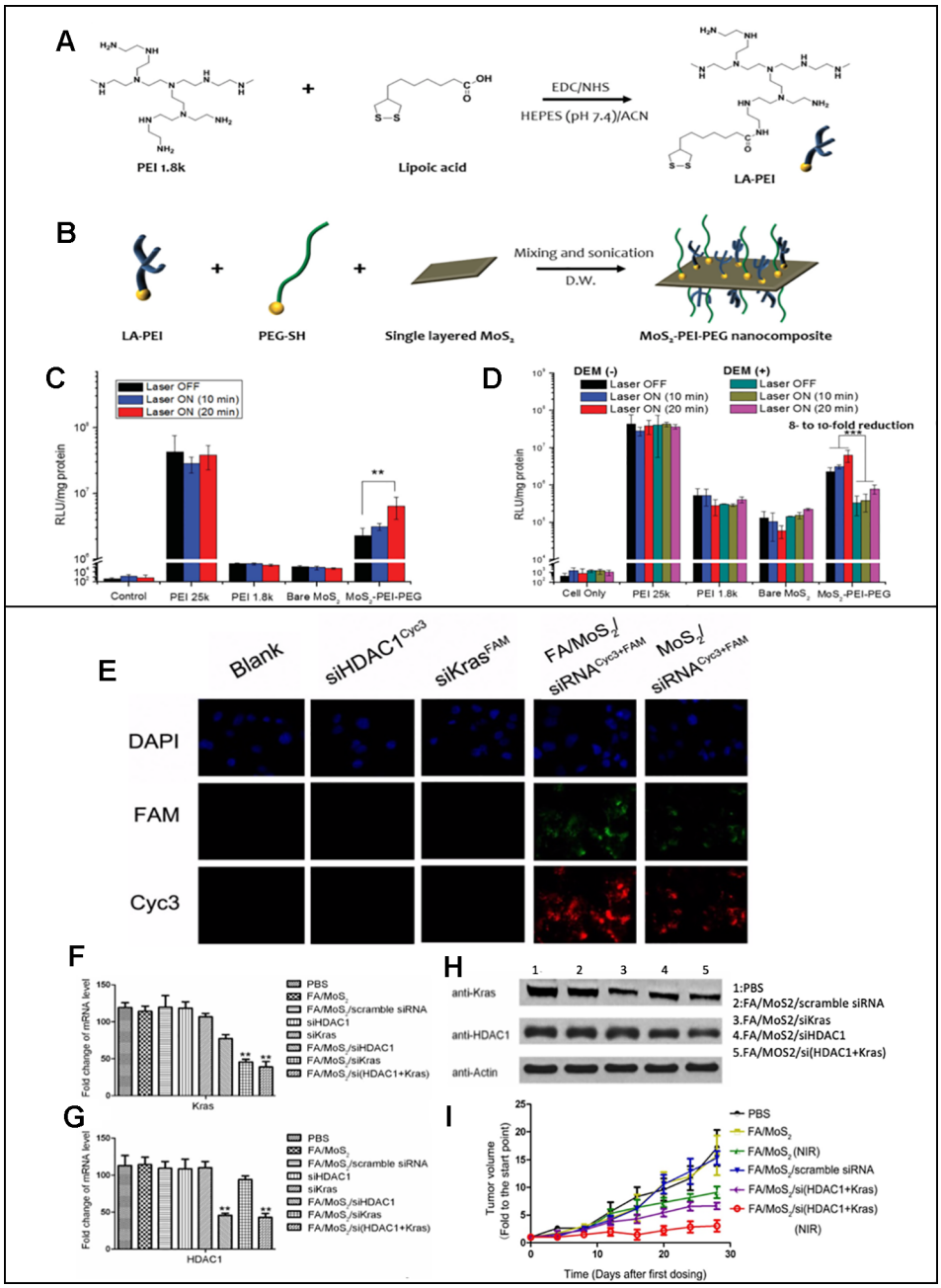

FIGURE 4 | (A) Synthesis of LA–PEI through EDC/NHS amide coupling reaction. **(B)** Modification of MoS2 surface with LA–PEI and thiolated PEG (PEG–SH) by disulfide bond formation. Luciferase reporter gene expression assay of PEI 25k, PEI 1.8k, bare MoS2, and MoS2–PEI–PEG polyplexes in the absence and presence of NIR irradiation in **(C)** HCT 116 cells and **(D)** B16F1 cells at N/P ratio of 10. Reprinted with permission (Kim et al., 2016b). Copyright 2016, John Wiley and Sons **(E)** Fluorescent images of Panc-1 cells treated with different MoS2/siRNA nanocomplex formulations four hours after treatment. Nucleus (blue), FAM (green) and Cyc3 (red). **(F, G)** mRNA relative expression levels detected by RT-PCR. **(H)** Protein relative expression levels detected by Western Blotting. **(I)** Relative changes in tumor volume versus time of mice in different treatment groups (Yin et al., 2018). Copyright 2018, Ivyspring International Publisher.

While Kim et al. reported *in vitro* studies only, both *in vitro* and *in vivo* studies on the MoS2-mediated gene and photothermal combinatorial therapy was reported by Yin et al. (2018) MoS2 nanosheets modified with lipoic acid (LA), folic acid polyethyleneglycol polymer (FA-PEG), and polyallylamine hydrochloride (PAH). HDAC1 siRNAs and KRAS siRNAs were loaded to the modified MoS2 nanosheets. The overexpression of HDAC1 and mutant KRAS were known to cause proliferation of pancreatic cancer cells, and therefore silencing the two genes was used as an anti-cancer strategy in this study. As shown in

TABLE 2 | List of reported nanosheets that perform combined gene and photothermal therapy.

Material	Modified form	Functions of modification	Cell	Testing	Gene	Synergy mechanism	Reference
Graphene	GO-PEI-PEG	PEI (positive charge) PEG (stabilization)	HeLa	*In vitro*	Plk1 siRNA	PTT increase cell permeability which leads to effective transfection	(Feng et al., 2013)
	rGO-BPEI-PEG	BPE (positive charge) PEG (stabilization)	PC3 NIH/3T3	*In vitro*	Luciferase labelled pDNA	PTT facilitates endosomal escape	(Kim and Kim, 2014)
	GO-PEI-ssPEG	PEI (Positive charge) ssPEG (stabilization)	PC3 Raw 264.7	*In vitro*	Luciferase labelled pDNA	PTT facilitates endosomal escape	(Kim et al., 2016a)
	GO-PAH-PEG-FA	PAH (Positive charge) FA (targeting) PEG (stabilization)	MIA PaCa-2	*In vitro* *In vivo*	HDAC1 siRNA K-Ras siRNA	Synergistic effects in reducing tumor growth	(Yin et al., 2017)
Black Phosphorous (BP)	BP-PEI-PEG	PEI (positive charge) PEG (stabilization)	HeLa L549	*In vitro* *In vivo*	hTERT siRNA	PDT+PTT+genetherapy synergistic in reduced tumor growth ROS produced by PDT allows selective release of siRNA	(Chen et al., 2018)
	BP-PEI	PEI (positive charge)	MCF-7	*In vitro* *In vivo*	Survivin siRNA	Synergistic in reducing tumor growth	(Wang et al., 2018)
	BP-PDA-PEG	PDA (photothermal effects and stability) PEG (stabilization)	MCF-7 MCF-7/ADR	*In vitro* *In vivo*	P-gp siRNA AS1411 Aptamer (for targeting)	Drug+PTT+gene therapy: PTT induced drug release	(Zeng et al., 2018)
Transition Metal Oxide (TMO)	MoS2-PEI-PEG	PEI (positive charge) PEG (stabilization)	HCT116 B16F1	*In vitro*	Luciferase pDNA	PTT facilitates endosomal escape	(Kim et al., 2016b)
	MoS2-FA-PEG-PAH	PAH (positive charge) FA-PEG (binding to MoS2 and stabilization)	Panc-1	*In vitro* *In vivo*	HDAC1 siRNA K-Ras siRNA	Synergistic effects in reducing tumor growth	(Yin et al., 2018)

Figure 4E, the fluorescence microscopy images were used to confirm a successful MoS2 mediated transfection of cyc3 labelled HDAC1 siRNA (red) and FAM labelled KRAS siRNA (green) in Panc-1 cells. The intensity of the fluorescence was stronger when MoS2 was modified with FA, which indicated effective targeted delivery of nanosheets. Decreased expressions of FAM and KRAS mRNA and protein were demonstrated *via* RT-PCR and western blot results (**Figures 4F–H**). Synergistic anti-cancer effects of gene and PTT was also shown *in vivo*. In animal studies, C57B1/6 mice were planted with Panc-1 cells and treated with different FA/MoS2 mediated therapies for 28 days. As shown in **Figure 4I**, for the groups treated with FA/MoS2 + NIR, FA/MoS2/si(HDAC1+Kras) and FA/MoS2/si(HDAC1 +Kras) (NIR), the final tumor volumes were 8, 6, and 3 times of that of the original tumor volume while the control group's was 20 times of the original tumor. This study demonstrated that MoS2 nanosheet-mediated gene and photothermal therapy is a platform that was effective not only *in vitro* but also *in vivo*.

CONCLUSION

2D nanosheets have unique and novel chemical properties that allow them to simultaneously perform photothermal and gene therapy. **Table 2** summarizes the examples of 2D nanosheet-mediated combined gene and photothermal therapy, mentioned in this review. Their high drug loading capacity for different therapeutics including nucleic acids and high photothermal conversion efficacy are advantageous in performing combined gene and photothermal therapies, which are shown to produce synergistic therapeutic effects through various examples. The limitations of nanosheet-mediated gene and photothermal therapy is that it is a relatively new concept, and there are not many reported cases that will help understand this field. The review paper was also limited to three groups of nanosheets that had the most reported cases of this synergistic therapy. Also, the mechanisms of synergistic effects were explained in two ways in the paper: additive therapeutic effects coming from both gene and photothermal therapy and increased therapeutic effect of gene therapy due to the temperature increase caused by the photothermal therapy. These two explanations are well studied and supported by other studies as well, but there could be more mechanisms behind the effect. The future researcher studying this field could focus on studying the exact and detailed pathways on the cause of the synergistic effects. The clinical transition of 2D nanosheets is yet to come as they are relatively new materials that require further studies in cytotoxicity, pharmacokinetics and biocompatibility. Future studies should address issues regarding validating the safety of nanosheets as drug delivery vehicles, identifying the specific need for both therapies, and assessing the side effects that could possibly arise from the interaction between the gene and photothermal treatment. The toxicity of 2D nanosheets largely varies based on numerous factors, including composition, size, shape, surface modification, and chemicals used in the synthesis process (Gurunathan and Kim, 2016). Through the optimization of these factors in designing nanosheets, biocompatible nanosheets are possible to be synthesized, which have been reported in numerous cases

(Wang et al., 2015; Qu et al., 2017; Kaur et al., 2018). Considering the fact that multifunctional therapeutic modalities has been proposed as a way to tackle the problem of drug resistance in cancer, and both gene therapy and photothermal therapy have gained great attention in the past decade, 2D nanosheet-mediated combined gene and photothermal therapies may propose a possible alternative therapeutic modality in the future. Hopefully, this timely review would encourage future researchers to fully explore the potential of the 2D nanosheet-mediated combined gene and photothermal therapy.

AUTHOR CONTRIBUTIONS

Conceptualization: NK and NYK. Writing—original draft: NYK and NK. Writing—review and editing: SB, DD, and JO. Supervision: NK and JS.

FUNDING

This study is supported by the NEU CaNCURE program (NCI R25CA174650, NYK).

REFERENCES

Agarwal, V., and Chatterjee, K. (2018). Recent advances in the field of transition metal dichalcogenides for biomedical applications. *Nanoscale* 10 (35), 16365–16397. doi: 10.1039/C8NR04284E

Bao, H., Pan, Y., Ping, Y., Sahoo, N. G., Wu, T., Li, L., et al. (2011). Chitosan-functionalized graphene oxide as a nanocarrier for drug and gene delivery. *Small* 7 (11), 1569–1578. doi: 10.1002/smll.201100191

Boussif, O., Lezoualc'h, F., Zanta, M. A., Mergny, M. D., Scherman, D., Demeneix, B., et al. (1995). A versatile vector for gene and oligonucleotide transfer into cells in culture and in vivo: polyethylenimine. *Proc. Natl. Acad. Sci.* 92 (16), 7297–7301. doi: 10.1073/pnas.92.16.7297

Brent, J. R., Savjani, N., Lewis, E. A., Haigh, S. J., Lewis, D. J., and O'Brien, P. (2014). Production of few-layer phosphorene by liquid exfoliation of black phosphorus. *Chem. Commun.* 50 (87), 13338–13341. doi: 10.1039/C4CC05752J

Chen, L., Chen, C., Chen, W., Li, K., Chen, X., Tang, X., et al. (2018). Biodegradable black phosphorus nanosheets mediate specific delivery of HTERT SiRNA for synergistic cancer therapy. *ACS Appl. Mater. Interfaces* 10 (25), 21137–21148. doi: 10.1021/acsami.8b04807

Choi, J. R., Yong, K. W., Choi, J. Y., Nilghaz, A., Lin, Y., Xu, J., et al. (2018). Black phosphorus and its biomedical applications. *Theranostics* 8 (4), 1005–1026. doi: 10.7150/thno.22573

Conner, S. D., and Schmid, S. L. (2003). Regulated portals of entry into the cell. *Nature* 422 (6927), 37–44. doi: 10.1038/nature01451

Dowaidar, M., Abdelhamid, H. N., Hällbrink, M., Zou, X., and Langel, Ü (2017). Graphene oxide nanosheets in complex with cell penetrating peptides for oligonucleotides delivery. *Biochim. Biophys. Acta (BBA) Gen. Subj.* 1861 (9), 2334–2341. doi: 10.1016/j.bbagen.2017.07.002

Fang, J., Nakamura, H., and Maeda, H. (2011). The EPR effect: unique features of tumor blood vessels for drug delivery, factors involved, and limitations and augmentation of the effect. *Adv. Drug Deliv. Rev.* 63 (3), 136–151. doi: 10.1016/j.addr.2010.04.009

Feng, L., Yang, X., Shi, X., Tan, X., Peng, R., Wang, J., et al. (2013). Polyethylene glycol and polyethylenimine dual-functionalized nano-graphene oxide for photothermally enhanced gene delivery. *Small* 9 (11), 1989–1997. doi: 10.1002/smll.201202538

Fu, C., Tan, L., Ren, X., Wu, Q., Shao, H., Ren, J., et al. (2018). Interlayer expansion of 2D MoS2 nanosheets for highly improved photothermal therapy of tumors in vitro and in vivo. *Chem. Commun.* 54 (99), 13989–13992. doi: 10.1039/C8CC08279K

Furukawa, H., Cordova, K. E., O'Keeffe, M., and Yaghi, O. M. (2013). The chemistry and applications of metal-organic frameworks. *Science* 341 (6149), 1230444. doi: 10.1126/science.1230444

Ge, Z., Yang, L., Xiao, F., Wu, Y., Yu, T., Chen, J., et al. (2018). Graphene family nanomaterials: properties and potential applications in dentistry. *Int. J. Biomater.* 2018 December, 1–12. doi: 10.1155/2018/1539678

Gurunathan, S., and Kim, J.-H. (2016). Synthesis, toxicity, biocompatibility, and biomedical applications of graphene and graphene-related materials. *Int. J. Nanomed.* May, 1927. doi: 10.2147/IJN.S105264

Huang, J., Zong, C., Shen, H., Liu, M., Chen, B., Ren, B., et al. (2012). Mechanism of cellular uptake of graphene oxide studied by surface-enhanced raman spectroscopy. *Small* 8 (16), 2577–2584. doi: 10.1002/smll.201102743

Huang, N.-C., Ji, Q., Ariga, K., and Hsu, S. (2015). Nanosheet transfection: effective transfer of naked DNA on silica glass. *NPG Asia Mater.* 7 (6), e184–e184. doi: 10.1038/am.2015.43

Ji, Q., Yamazaki, T., Hanagata, N., Lee, M. V., Hill, J. P., and Ariga, K. (2012). Silica-based gene reverse transfection: an upright nanosheet network for promoted DNA delivery to cells. *Chem. Commun.* 48 (68), 8496. doi: 10.1039/c2cc34289h

Ji, Q., Yamazaki, T., Sun, J., Górecka, Ż, Huang, N.-C., Hsu, S., et al. (2017). Spongelike porous silica nanosheets: from 'soft' molecular trapping to DNA delivery. *ACS Appl. Mater. Interfaces* 9 (5), 4509–4518. doi: 10.1021/acsami.6b15082

Ji, X., Kong, N., Wang, J., Li, W., Xiao, Y., Gan, S. T., et al. (2018). A novel top-down synthesis of ultrathin 2D boron nanosheets for multimodal imaging-guided cancer therapy. *Adv. Mater.* 30 (36), 1803031. doi: 10.1002/adma.201803031

Ji, X., Kang, Y., Ouyang, J., Chen, Y., Artzi, D., Zeng, X., et al. (2019). Synthesis of ultrathin biotite nanosheets as an intelligent theranostic platform for combination cancer therapy. *Adv. Sci.* August, 1901211. doi: 10.1002/advs.201901211

Kaur, J., Singh, M., Dell'Aversana, C., Benedetti, R., Giardina, P., Rossi, M., et al. (2018). Biological interactions of biocompatible and water-dispersed MoS2 nanosheets with bacteria and human cells. *Sci. Rep.* 8 (1), 16386. doi: 10.1038/s41598-018-34679-y

Kim, H., and Kim, W. J. (2014). Photothermally controlled gene delivery by reduced graphene oxide-polyethylenimine nanocomposite. *Small* 10 (1), 117–126. doi: 10.1002/smll.201202636

Kim, H., Kim, J., Lee, M., Choi, H. C., and Kim, W. J. (2016a). Stimuli-regulated enzymatically degradable smart graphene-oxide-polymer nanocarrier facilitating photothermal gene delivery. *Adv. Healthc. Mater.* 5 (15), 1918–1930. doi: 10.1002/adhm.201600246

Kim, J., Kim, H., and Kim, W. J. (2016b). Single-layered MoS_2-PEI-PEG nanocomposite-mediated gene delivery controlled by photo and redox stimuli. *Small* 12 (9), 1184–1192. doi: 10.1002/smll.201501655

Kim, J., Kim, J., Jeong, C., and Kim, W. J. (2016c). Synergistic nanomedicine by combined gene and photothermal therapy. *Adv. Drug Deliv. Rev. Deliv. Multimodal Ther. Synergistic Ther.* 98 (March), 99–112. doi: 10.1016/j.addr.2015.12.018

Kosuge, H., Sherlock, S. P., Kitagawa, T., Dash, R., Robinson, J. T., Dai, H., et al. (2012). Near infrared imaging and photothermal ablation of vascular inflammation using single-walled carbon nanotubes. *J. Am. Heart Assoc.* 1 (6). doi: 10.1161/JAHA.112.002568

Kou, Z., Wang, X., Yuan, R., Chen, H., Zhi, Q., Gao, L., et al. (2014). A promising gene delivery system developed from PEGylated MoS2 nanosheets for gene therapy. *Nanoscale Res. Lett.* 9 (1), 587. doi: 10.1186/1556-276X-9-587

Kurapati, R., Kostarelos, K., Prato, M., and Bianco, A. (2016). Biomedical uses for 2D materials beyond graphene: current advances and challenges ahead. *Adv. Mater.* 28 (29), 6052–6074. doi: 10.1002/adma.201506306

Kwak, G., Kim, D., Nam, G., Wang, S. Y., Kim, I.-S., Kim, S. H., et al. (2017). Programmed cell death protein ligand-1 silencing with polyethylenimine–dermatan sulfate complex for dual inhibition of melanoma growth. *ACS Nano* 11 (10), 10135–10146. doi: 10.1021/acsnano.7b04717

Li, L., Yu, Y., Ye, G. J., Ge, Q., Ou, X., Wu, H., et al. (2014). Black phosphorus field-effect transistors. *Nat. Nanotechnol.* 9 (5), 372–377. doi: 10.1038/nnano.2014.35

Li, S.-Y., Liu, Y., Xu, C.-F., Shen, S., Sun, R., Du, X.-J., et al. (2016). Restoring anti-tumor functions of T Cells *via* nanoparticle-mediated immune checkpoint modulation. *J. Controlled Release* 231 (June), 17–28. doi: 10.1016/j.jconrel.2016.01.044

Li, C., Hu, J., Li, W., Song, G., and Shen, J. (2017). Combined bortezomib-based chemotherapy and P53 gene therapy using hollow mesoporous silica nanospheres for P53 mutant non-small cell lung cancer treatment. *Biomater. Sci.* 5 (1), 77–88. doi: 10.1039/C6BM00449K

Linares, J., Matesanz, M. C., Vila, M., Feito, M. J., Gonçalves, G., Vallet-Regí, M., et al. (2014). Endocytic mechanisms of graphene oxide nanosheets in osteoblasts, hepatocytes and macrophages. *ACS Appl. Mater. Interfaces* 6 (16), 13697–13706. doi: 10.1021/am5031598

Liu, Y., Ai, K., Liu, J., Deng, M., He, Y., and Lu, L. (2013). Dopamine-melanin colloidal nanospheres: an efficient near-infrared photothermal therapeutic agent for in vivo cancer therapy. *Adv. Mater.* 25 (9), 1353–1359. doi: 10.1002/adma.201204683

Luzio, J. P., Hackmann, Y., Dieckmann, N. M. G., and Griffiths, G. M. (2014). The biogenesis of lysosomes and lysosome-related organelles. *Cold Spring Harbor Perspect. In Biol.* 6 (9), a016840–a016840. doi: 10.1101/cshperspect.a016840

Manzeli, S., Ovchinnikov, D., Pasquier, D., Yazyev, O. V., and Kis, A. (2017). 2D transition metal dichalcogenides. *Nat. Rev. Mater.* 2 (8), 17033. doi: 10.1038/natrevmats.2017.33

Mitter, N., Worrall, E. A., Robinson, K. E., Li, P., Jain, R. G., Taochy, C., et al. (2017). Clay nanosheets for topical delivery of RNAi for sustained protection against plant viruses. *Nat. Plants* 3 (2), 16207. doi: 10.1038/nplants.2016.207

Mu, Q., Su, G., Li, L., Gilbertson, B. O., Yu, L. H., Zhang, Q., et al. (2012). Size-dependent cell uptake of protein-coated graphene oxide nanosheets. *ACS Appl. Mater. Interfaces* 4 (4), 2259–2266. doi: 10.1021/am300253c

Novoselov, K. S. (2004). Electric field effect in atomically thin carbon films. *Science* 306 (5696), 666–669. doi: 10.1126/science.1102896

Ouyang, J., Feng, C., Ji, X., Li, L., Gutti, H. K., Kim, N. Y., et al. (2019). 2D monoelemental germanene quantum dots: synthesis as robust photothermal agents for photonic cancer nanomedicine. *Angew. Chem. Int. Ed.* 58 (38), 13405–13410. doi: 10.1002/anie.201908377

Peng, L., Mei, X., He, J., Xu, J., Zhang, W., Liang, R., et al. (2018). Monolayer nanosheets with an extremely high drug loading toward controlled delivery and cancer theranostics. *Adv. Mater.* 30 (16), 1707389. doi: 10.1002/adma.201707389

Qian, X., Gu, Z., and Chen, Y. (2017). Two-dimensional black phosphorus nanosheets for theranostic nanomedicine. *Mater. Horiz.* 4 (5), 800–816. doi: 10.1039/C7MH00305F

Qu, G., Liu, W., Zhao, Y., Gao, J., Xia, T., Shi, J., et al. (2017). Improved biocompatibility of black phosphorus nanosheets by chemical modification. *Angew. Chem. Int. Ed.* 56 (46), 14488–14493. doi: 10.1002/anie.201706228

Reina, G., González-Domínguez, J. M., Criado, A., Vázquez, E., Bianco, A., and Prato, M. (2017). Promises, facts and challenges for graphene in biomedical applications. *Chem. Soc. Rev.* 46 (15), 4400–4416. doi: 10.1039/C7CS00363C

Ren, Q., Li, B., Peng, Z., He, G., Zhang, W., Guan, G., et al. (2016). SnS nanosheets for efficient photothermal therapy. *New J. Chem.* 40 (5), 4464–4467. doi: 10.1039/C5NJ03263F

Rosenblum, D., Joshi, N., Tao, W., Karp, J. M., and Peer, D. (2018). Progress and challenges towards targeted delivery of cancer therapeutics. *Nat. Commun.* 9 (1), 1410. doi: 10.1038/s41467-018-03705-y

Sahay, G., Alakhova, D. Y., and Kabanov, A. V. (2010). Endocytosis of nanomedicines. *J. Controlled Release* 145 (3), 182–195. doi: 10.1016/j.jconrel.2010.01.036

Shanmugam, V., Selvakumar, S., and Yeh, C.-S. (2014). Near-infrared light-responsive nanomaterials in cancer therapeutics. *Chem. Soc Rev.* 43 (17), 6254–6287. doi: 10.1039/C4CS00011K

Shi, J., Kantoff, P. W., Wooster, R., and Farokhzad, O. C. (2017). Cancer nanomedicine: progress, challenges and opportunities. *Nat. Rev. Cancer* 17 (1), 20–37. doi: 10.1038/nrc.2016.108

Shi, S., Kong, N., Feng, C., Shajii, A., Bejgrowicz, C., Tao, W., et al. (2019). Drug delivery strategies for the treatment of metabolic diseases. *Adv. Healthc. Mater.* 8 (12), 1801655. doi: 10.1002/adhm.201801655

Song, G., Hao, J., Liang, C., Liu, T., Gao, M., Cheng, L., et al. (2016). Degradable molybdenum oxide nanosheets with rapid clearance and efficient tumor homing capabilities as a therapeutic nanoplatform. *Angew. Chem. Int. Ed.* 55 (6), 2122–2126. doi: 10.1002/anie.201510597

Song, G., Zheng, X., Wang, Y., Xia, X., Chu, S., and Rao, J. (2019). A magneto-optical nanoplatform for multimodality imaging of tumors in mice. *ACS Nano* 13 (7), 7750–7758. doi: 10.1021/acsnano.9b01436

Tao, W., Ji, X., Xu, X., Islam, M. A., Li, Z., Chen, S., et al. (2017a). Antimonene quantum dots: synthesis and application as near-infrared photothermal agents for effective cancer therapy. *Angew. Chem. Int. Ed.* 56 (39), 11896–11900. doi: 10.1002/anie.201703657

Tao, W., Zhu, X., Yu, X., Zeng, X., Xiao, Q., Zhang, X., et al. (2017b). Black phosphorus nanosheets as a robust delivery platform for cancer theranostics. *Adv. Mater.* 29 (1), 1603276. doi: 10.1002/adma.201603276

Tao, W., Ji, X., Zhu, X., Li, L., Wang, J., Zhang, Y., et al. (2018). Two-dimensional antimonene-based photonic nanomedicine for cancer theranostics. *Adv. Mater.* 30 (38), 1802061. doi: 10.1002/adma.201802061

Tao, W., Kong, N., Ji, X., Zhang, Y., Sharma, A., Ouyang, J., et al. (2019). Emerging two-dimensional monoelemental materials (xenes) for biomedical applications. *Chem. Soc. Rev.* 48 (11), 2891–2912. doi: 10.1039/C8CS00823J

Teimouri, M., Nia, A. H., Abnous, K., Eshghi, H., and Ramezani, M. (2016). Graphene oxide–cationic polymer conjugates: synthesis and application as gene delivery vectors. *Plasmid* 84–85 (March), 51–60. doi: 10.1016/j.plasmid.2016.03.002

Tian, B., Wang, C., Zhang, S., Feng, L., and Liu, Z. (2011). Photothermally enhanced photodynamic therapy delivered by nano-graphene oxide. *ACS Nano* 5 (9), 7000–7009. doi: 10.1021/nn201560b

Varkouhi, A. K., Scholte, M., Storm, G., and Haisma, H. J. (2011). Endosomal escape pathways for delivery of biologicals. *J. Controlled Release* 151 (3), 220–228. doi: 10.1016/j.jconrel.2010.11.004

Wang, Y., Li, Z., Weber, T. J., Hu, D., Lin, C.-T., Li, J., et al. (2013). In situ live cell sensing of multiple nucleotides exploiting DNA/RNA aptamers and graphene oxide nanosheets. *Anal. Chem.* 85 (14), 6775–6782. doi: 10.1021/ac400858g

Wang, S., Li, K., Chen, Y., Chen, H., Ma, M., Feng, J., et al. (2015). Biocompatible PEGylated MoS2 nanosheets: controllable bottom-up synthesis and highly efficient photothermal regression of tumor. *Biomaterials* 39 (January), 206–217. doi: 10.1016/j.biomaterials.2014.11.009

Wang, H., Zhong, L., Liu, Y., Xu, X., Xing, C., Wang, M., et al. (2018). A black phosphorus nanosheet-based SiRNA delivery system for synergistic photothermal and gene therapy. *Chem. Commun. (Cambridge England)* 54 (25), 3142–3145. doi: 10.1039/c8cc00931g

Wang, L., Guan, S., Weng, Y., Xu, S.-M., Lu, H., Meng, X., et al. (2019). Highly efficient vacancy-driven photothermal therapy mediated by ultrathin MnO_2 nanosheets. *ACS Appl. Mater. Interfaces* 11 (6), 6267–6275. doi: 10.1021/acsami.8b20639

Xie, Z., Wang, D., Fan, T., Xing, C., Li, Z., Tao, W., et al. (2018). Black phosphorus analogue tin sulfide nanosheets: synthesis and application as near-infrared photothermal agents and drug delivery platforms for cancer therapy. *J. Mater. Chem. B* 6 (29), 4747–4755. doi: 10.1039/C8TB00729B

Xu, Z., Wang, Y., Zhang, L., and Huang, L. (2014). Nanoparticle-delivered transforming growth factor-β SiRNA enhances vaccination against advanced melanoma by modifying tumor microenvironment. *ACS Nano* 8 (4), 3636–3645. doi: 10.1021/nn500216y

Yang, X., Wang, D., Shi, Y., Zou, J., Zhao, Q., Zhang, Q., et al. (2018). Black phosphorus nanosheets immobilizing Ce6 for imaging-guided photothermal/photodynamic cancer therapy. *ACS Appl. Mater. Interfaces* 10 (15), 12431–12440. doi: 10.1021/acsami.8b00276

Yin, F., Hu, K., Chen, Y., Yu, M., Wang, D., Wang, Q., et al. (2017). SiRNA delivery with PEGylated graphene oxide nanosheets for combined photothermal and genetherapy for pancreatic cancer. *Theranostics* 7 (5), 1133–1148. doi: 10.7150/thno.17841

Yin, F., Anderson, T., Panwar, N., Zhang, K., Tjin, S. C., Ng, B. K., et al. (2018). Functionalized MoS_2 nanosheets as multi-gene delivery vehicles for *in vivo* pancreatic cancer therapy. *Nanotheranostics* 2 (4), 371–386. doi: 10.7150/ntno.27308

Yin, B., Wang, Y., Zhang, C., Zhao, Y., Wang, Y., Teng, L., et al. (2019). Oxygen-embedded quinoidal acene based semiconducting chromophore nanoprobe for amplified photoacoustic imaging and photothermal therapy. *Anal. Chem.* November, acs.analchem.9b04429. doi: 10.1021/acs.analchem.9b04429

Yoon, H.-J., Lee, H.-S., Lim, J.-Y., and Park, J.-H. (2017). Liposomal indocyanine green for enhanced photothermal therapy. *ACS Appl. Mater. Interfaces* 9 (7), 5683–5691. doi: 10.1021/acsami.6b16801

Zeng, X., Luo, M., Liu, G., Wang, X., Tao, W., Lin, Y., et al. (2018). Polydopamine-modified black phosphorous nanocapsule with enhanced stability and photothermal performance for tumor multimodal treatments. *Adv. Sci.* 5 (10), 1800510. doi: 10.1002/advs.201800510

Zhang, C., Yong, Y., Song, L., Dong, X., Zhang, X., Liu, X., et al. (2016). Multifunctional WS2 @Poly(Ethylene Imine) nanoplatforms for imaging guided gene-photothermal synergistic therapy of cancer. *Adv. Healthc. Mater.* 5 (21), 2776–2787. doi: 10.1002/adhm.201600633

Zhang, H., Chen, G., Yu, B., and Cong, H. (2019). Emerging advanced nanomaterials for cancer photothermal therapy. *Rev. Adv. Mater. Sci.* 53 (2), 131–146. doi: 10.1515/rams-2018-0010

Zhang, X. (2011). "Distribution and biocompatibility studies of graphene oxide in mice after intravenous administration." Translated by Xiaoyong Zhang, Jilei Yin, Cheng Peng, Weiqing Hu, Zhiyong Zhu, Wenxin Li, Chunhai Fan, and Qing Huang. *Carbon* 49 (3), 986–995. doi: 10.1016/j.carbon.2010.11.005

Zhou, W., Cui, H., Ying, L., and Yu, X.-F. (2018). Enhanced cytosolic delivery and release of crispr/cas9 by black phosphorus nanosheets for genome editing. *Angew. Chem. Int. Ed.* 57 (32), 10268–10272. doi: 10.1002/anie.201806941

Conflict of Interest: The authors declare that the research was conducted in the absence of any commercial or financial relationships that could be construed as a potential conflict of interest.

frontiers in Pharmacology

ORIGINAL RESEARCH
published: 24 January 2020
doi: 10.3389/fphar.2019.01576

Three-Dimensional Culture Promotes the Differentiation of Human Dental Pulp Mesenchymal Stem Cells Into Insulin-Producing Cells for Improving the Diabetes Therapy

Bingbing Xu[1,2,3†], Daoyang Fan[3†], Yunshan Zhao[4], Jing Li[5], Zhendong Wang[6], Jianhua Wang[1], Xiuwei Wang[1], Zhen Guan[1] and Bo Niu[1,2]*

[1] Department of Translational Medicine, Capital Institute of Pediatrics, Beijing, China, [2] Graduate School of Peking Union Medical College, Beijing, China, [3] Knee Surgery Department of the Institute of Sports Medicine, Beijing Key Laboratory of Sports Injuries, Peking University Third Hospital, Beijing, China, [4] Institute of General Surgery, Chinese PLA General Hospital, Beijing, China, [5] Laboratory of Translational Medicine, Chinese PLA General Hospital, Beijing, China, [6] Department of Biochemistry and Molecular Biology, School of Basic Medical Sciences, Shanxi Medical University, Taiyuan, China

Introduction: Diabetes is a metabolic disease with a high incidence and serious harm to human health. Islet β-cell function defects can occur in the late stage of type 1 diabetes and type 2 diabetes. Studies have shown that stem cell is a promising new approach in bioengineering regenerative medicine. In the study of stem cell differentiation, three-dimensional (3D) cell culture is more capable of mimicking the microenvironment of cell growth *in vivo* than two-dimensional (2D) cell culture. The natural contact between cells and cells, and cells and extracellular matrix can regulate the development process and promote the formation of the artificial regenerative organs and organization. Type IV, VI collagen and laminin are the most abundant extracellular matrix components in islets. Matrigel, a basement membrane matrix biomaterial rich in laminin and collagen IV.

Materials and Methods: We used Matrigel biomaterial to physically embed human dental pulp stem cells (hDPSCs) to provide vector and 3D culture conditions for cells, and we explored and compared the preparation methods and preliminary mechanisms of differentiation of hDPSCs into insulin-producing cells (IPCs) under 2D or 3D culture conditions.We first designed and screened the strategy by mimicking the critical events of pancreatogenesis *in vivo*, and succeeded in establishing a new method for obtaining IPCs from hDPSCs. Activin A, Noggin, and small molecule compounds were used to synergistically induce hDPSCs to differentiate into definitive endoderm-like cells, pancreatic progenitor like cells and IPCs step by step under 2D culture conditions. Then, we used Matrigel to simulate the microenvironment *in vivo*, induced hDPSCs to differentiate into IPCs in Matrigel, evaluated and compared the efficiency between 2D and 3D culture conditions.

OPEN ACCESS

Edited by:
Jianxun Ding
Changchun Institute of Applied Chemistry (CAS), China

Reviewed by:
Yun-Long Wu,
Xiamen University, China
Xing Wang,
Institute of Chemistry (CAS), China
Dongdong Yao,
Northwestern Polytechnical University, China

***Correspondence:**
Bo Niu
niub2006@126.com

†These authors have contributed equally to this work

Specialty section:
This article was submitted to Translational Pharmacology, a section of the journal Frontiers in Pharmacology

Received: *01 November 2019*
Accepted: *05 December 2019*
Published: *24 January 2020*

Citation:
Xu B, Fan D, Zhao Y, Li J, Wang Z, Wang J, Wang X, Guan Z and Niu B (2020) Three-Dimensional Culture Promotes the Differentiation of Human Dental Pulp Mesenchymal Stem Cells Into Insulin-Producing Cells for Improving the Diabetes Therapy. Front. Pharmacol. 10:1576. doi: 10.3389/fphar.2019.01576

Results: The results showed that the synergistic combination of growth factors and small molecule compounds and 3D culture promoted the differentiation of hDPSCs into IPCs, significantly enhancing the release of insulin and C-peptide from IPCs.

Discussion: Significant support is provided for obtaining a large number of functional IPCs for disease modeling and final cell therapy in regenerative medicine.

Keywords: diabetes mellitus, regenerative medicine, human dental pulp stem cells, insulin-producing cells, Matrigel biomaterial

INTRODUCTION

Diabetes is a global public health problem that seriously threatens the health of more than 400 million people, and the prevalence has been increasing (Stokes and Preston, 2017). At present, the main treatments for diabetes include diet control, regular blood glucose testing, oral hypoglycemic chemotherapy and insulin supplementation. However, such treatment methods can not reconstruct the physiological blood sugar regulation function of the body, and can not avoid the occurrence of severe hypoglycemia and long-term complications (Nathan, 1993). Another treatment method is to replace endogenous β cells by islet transplantation. Islet transplantation can reduce the dependence of patients with exogenous insulin, and effectively control blood sugar levels and reduce the occurrence of complications by increasing the number of islet cells with endocrine function to treat or even cure diabetes (Shapiro et al., 2000; Bellin et al., 2012; Hering et al., 2016). Although islet transplantation has been successfully used in clinical practice, the limited supply of islets and the side effects of immunosuppressive therapy have largely hampered the widespread use of this therapy (Porat and Dor, 2007), prompting us to search for alternative sources of islet cells.

Human mesenchymal stem cells (MSCs)-derived β cells are the most promising alternative source of cells for use in diabetic cell replacement therapy and other applications, such as mimicking disease and studying pancreas development (Millman and Pagliuca, 2017). Studies have shown that liver stem cells (Yang et al., 2002), umbilical cord blood (Koblas et al., 2009), bone marrow (Chen et al., 2004), adipose tissue-derived MSCs (Li et al., 2013) have the potential to differentiate into insulin-producing cells (IPCs). However, the scarcity of tissue sources, the highly invasive procedures for acquiring tissues, and the considerable risk of morbidity at the donor site limit their use. The human dental pulp stem cells (hDPSCs) are rich in source, easy to obtain, non-invasively separated, donors have no discomfort, and there is no ethical controversy in research and development applications, which is undoubtedly an attractive source of MSCs.

Recent studies have shown that some small molecule compounds can regulate the different developmental stages of islet beta cells by regulating embryonic developmental pathways. Lithium chloride (LiCl), in place of recombinant Wnt 3a protein, activates typical Wnt signaling and promotes differentiation of ESCs into DE cells (Li et al., 2011). Retinoic acid can promote the expression of pancreatic endocrine progenitor cells and further differentiate into islet β cells (Oström et al., 2008; Cai et al., 2010); A83-01 is a selective inhibitor of transforming growth factor-β (TGF-β) type 1 receptor ALK5 kinase, which blocks phosphorylation of Smad2, inhibits TGF-β-induced epithelial–mesenchymal transition and promotes the expression of pancreatic progenitor cells; LDE225 is an FDA-approved drug for cancer patients and is an inhibitor of the Hedgehog pathway (Rimkus et al., 2016), which replaces FGF2 protein to exclude Hedgehog signaling and promotes pancreatic lineage formation (Kim and Hebrok, 2001; Li et al., 2014); 2-Phospho-L-ascorbic acid trisodium salt (pVc) promotes differentiation and maturation of ESCs and fibroblasts to insulin-secreting cells (Li et al., 2014); SB203580 is a p38 mitogen-activated protein kinase inhibitor that improves insulin-secreting cell function by promoting differentiation and maturation of insulin-secreting cells (Li et al., 2014; Wei et al., 2018).

Studies have reported different sources of cells such as mouse ESCs (Li et al., 2011), human MSCs (Wang et al., 2010), Human induced pluripotent stem cells (hiPS) (Kunisada et al., 2012) and mouse fibroblasts (Li et al., 2014), all can be induced to differentiate into IPCs by small molecule compounds. But so far hDPSCs have not been reported, so we designed and screened the strategy by mimicking the critical events of pancreatogenesis *in vivo*. Activin A, Noggin and small molecule compounds were used to synergistically induce hDPSCs to differentiate into definitive endoderm-like cells, pancreatic progenitorlike cells and IPCs step by step under 2D culture conditions. The efficiency of induction was assessed by methods such as reverse transcription quantitative polymerase chain reaction, immunocytochemical staining, and insulin secretion function assays.

Three-dimensional (3D) cell culture technology refers to the use of different methods and materials to simulate the growth environment *in vivo*, so that cells can grow and migrate in a 3D space, and promote cell differentiation, which is conducive to its function (Wang et al., 2019). A series of evidence suggests that the extracellular matrix (ECM) provides a spatial and temporally controlled environmental support for stem cell differentiation and tissue maturation, responsible for structural and biochemical support, regulates molecular signaling and tissue repair in many organ structures, including the pancreas. In islets, type IV and VI collagen and laminin are the most abundant molecules in ECM compared to other ECM molecules. Some ECM molecules are involved in the survival, function, and insulin production of beta cells, while other ECM molecules regulate the sensitivity of islet cells to cytokines (Llacua et al., 2018).

In the study of stem cell differentiation, 3D cell culture is more capable of mimicking the microenvironment of cell growth *in vivo* than 2D cell culture. The natural contact between cells and cells, between cells and ECM can regulate the development process and promote the formation of artificial organs and Organizational (Zhang et al., 2019a; Zhang et al., 2019b); 3D cell culture can perfectly reproduce the process of embryo development *in vivo*, and facilitate the further study of its molecular mechanism (Gelain et al., 2006; Albrecht et al., 2006). In the 3D microenvironment, human embryonic stem cells are more efficiently differentiated into pancreatic endocrine cells, more pronounced response to glucose (Wang et al., 2017).

The Matrigel biomaterial basement membrane matrix is derived from mouse sarcoma, the main component of which is laminin, followed by collagen IV, heparan sulfate proteoglycan and nestin (Kleinman et al., 1986; Wang et al., 2017). At room temperature (RT), Matrigel polymerizes to form a biologically active 3D matrix that mimics the structure, composition, physical properties and functions of the cell basement membrane *in vivo*, facilitating cell culture and differentiation *in vitro*. Matrigel can be used for the study of cell morphology, biochemical function, migration, infection and gene expression, and is suitable as a matrix material for the differentiation of hDPSCs into IPCs. By simulating the *in vivo* microenvironment, we first cultured hDPSCs in Matrigel rich in laminin and collagen IV to induce the differentiation of hDPSCs into insulin-secreting cells, and we compared the difference between 2D induction and 3D induction.

Our protocol can efficiently produce functional IPCs under both 2D and 3D culture conditions. Our results highlight the synergistic approach between growth factors and small molecule compounds and the important role of Matrigel in inducing hDPSCs to differentiate into IPCs. Significant support is provided for obtaining a large number of functional IPCs for disease modeling and final cell therapy in regenerative medicine.

MATERIALS AND METHODS

Materials

Dulbecco's modified Eagle's medium/nutrient mixture F-12 (DMEM-F12), penicillin/streptomycin, and fetal bovine serum (FBS) were purchased from Gibco. Anti-human CD34-PE, CD44-FITC, CD45-FITC, CD73-PE, CD90-FITC, and HLA-DR-FITC were obtained from BD Biosciences. Adipogenic induction medium and osteogenic induction medium Cyagen. Primary antibodies (Sox17, Cxcr4, Pdx1, and Glucagon) and fluorescent secondary antibodies were purchased from Abcam. Primary antibodies (Nkx6.1, Insulin, Somatostatin) were purchased from CST. A83-01 and SB203580 were purchased from Tocris. LDE225 were obtained from Selleck. Activin, Noggin human and other small molecule compounds were purchased from Sigma. Matrigel were purchased from Corning.

Isolation and Culture of Human Dental Pulp Stem Cells

Sound intact deciduous tooth were extracted from 20 donors (ages 8–12-year old of children) who were undergoing a continuous extraction for occlusion treatment. Written informed consents were obtained from donors and guardians. The experiments involving human tissue were approved by Capital Institute of Pediatrics and were all carried out in accordance with the ethical standards of the local ethical committee.

The deciduous teeth were washed two to three times with physiological saline. The teeth crown was fixed with hemostatic forceps and the teeth root was crushed with a rongeur to expose the pulp. The pulp tissue was minced into small fragments before digestion in a solution of 0.05% *(w/v)* collagenase P for 30 min at 37°C, 180 rpm in a constant temperature shaker, and then filtered through a 100 μm nylon cell strainer. The next procedures, culture conditions and media were applied as described for human endometrial stem cells.

Flow Cytometry Analysis

For phenotypic identification of the hDPSCs at P4, cells (1×10^6) were digested with 0.25% (w/v) trypsin, washed twice with phosphate-buffered saline (PBS) and divided into aliquots. The cells were centrifuged, resuspended and stained with the following antibodies for 15 min at RT: anti-human CD34-PE, CD44-FITC, CD45-FITC, CD73-PE, CD90-FITC, and HLA-DR-FITC (BD Biosciences, USA). After washing, the cells were resuspended and then analyzed using flow cytometry instrument (FC500; Beckman Coulter, USA).

In Vitro Multilineage Differentiation Assay for Human Dental Pulp Stem Cells

hDPSCs at P4 were differentiated into adipocytes and osteoblasts as follows *in vitro*. For adipogenic and osteogenic differentiation, hDPSCs were reseeded in the standard culture medium into 6-well culture plates at 2×10^4 cells per well. The cells were incubated until they are 100% confluent or post-confluent. hDPSCs were exposed to adipogenic induction medium for 28 days. hDPSCs were exposed to osteogenic induction medium (Cyagen) for 28 days. The medium was replaced with fresh induction medium every 3 days. After 7 or 28 days, cells were fixed with 4% (w/v) paraformaldehyde solution. To assess adipogenic differentiation, cells were stained with oil red O working solution. To assess osteogenic differentiation, cells were stained with alizarin red working solution. Control cells were cultured in standard culture medium over the same period of time. The stained plates were visualized under light microscope (Leica DM IL LED Fluo, Leica Microsystems Inc, Germany) and captured images using Leica Application Suite Version 4.5.0 software.

In Vitro Differentiation Assay of Human Dental Pulp Stem Cells Into Insulin-Producing Cells

Differentiation of hDPSCs into IPCs was carried out in 3 stages by Method 1 (M 1). At stage 1, for differentiation into DELCs, hDPSCs was treated with the DMEM/F12 medium supplemented with 1.92 nM Activin A, 1 mM LiCl, 180 ng/ml Noggin, 280 μM pVc, β-ME, and 1% FBS for 6 days. At stage 2, for differentiation into PPLCs, the cells were cultured in induction medium comprising DMEM/F12 and 2 μM retinoic acid, 1 μM A83-01, 2 μM LDE225, 280 μM pVc, and 1% FBS for 1 day on day 6. After 1 day, the cells were treated with the DMEM/F12 medium containing 1 μM A83-01, 2 μM LDE225, 280 μM pVc, and 1% FBS for 3 days. At stage 3, for differentiation into IPCs, the cells were cultured in induction medium comprising DMEM/F12, 5 μM SB, 280 μM pVc, ITS, 1 mM nicotinamide, 1× non-essential amino acids, and 1% FBS for 10 days. The study compared the new method 1 (M 1) with method 2(M 2); The M 2 came from Govindasamy et al. (Govindasamy et al., 2011), slightly modified as M 2. Undifferentiated hDPSCs with the same culture days were used as controls. Fresh induced differentiation medium changed every 2 days.

RNA Isolation and RT-qPCR Analysis

Cultured hDPSCs in P4 were collected and total RNA were extracted with Trizol Reagent (Invitrogen). cDNA was synthesized from RNA using All-In-One RT MasterMix Kit (abmGood, Canada). qPCR was performed using EvaGreen qPCR MasterMix Kit (abmGood, Canada). Thermal cycling conditions were 95°C for 10 min and 40 cycles of 95°C for 15 s, 60°C for 60 s. The sequences of primers were listed in **Table 1**. The gene expression level of glyceraldehyde 3-phosphate dehydrogenase (GAPDH) was served as an internal reference.

TABLE 1 | The sequences of primers.

Primers	Sequences
Sox17-Forward	5'-GGCGCAGCAGAATCCAGA-3'
Sox17-Reverse	5'-CCACGACTTGCCCAGCAT-3'
Foxa2-Forward	5'-AAGACCTACAGGCGCAGCTA-3'
Foxa2-Reverse	5'-CCTTCAGGAAACAGTCGTTGA-3'
Cxcr4-Forward	5'-AACTGAGAAGCATGACGGACAAGTAC-3'
Cxcr4-Reverse	5'-GCTGTAGAGGTTGACTGTGTAGATGAC-3'
Pdx1-Forward	5'-TGATACTGGATTGGCGTTGT-3'
Pdx1-Reverse	5'-GAATGGCTTTATGGCAGATTA-3'
Nkx6.1-Forward	5'-GGCCTGTACCCCTCATCAAG-3'
Nkx6.1-Reverse	5'-CCGGAAAAAGTGGGTCTCGT-3'
Neurod1- Forward	5'-GACGACCTCGAAGCCATGAACG-3'
Neurod1- Reverse	5'-CCTCCTCTTCCTCTTCTTCCTCCTC-3'
Ngn3- Forward	5'-GGCTGTGGGTGCTAAGGGTA-3'
Ngn3- Reverse	5'-CAGGGAGAAGCAGAAGGAACAA-3'
Pax4-Forward	5'-GTATGGCTTGGAATGAGGCAGGAG-3'
Pax4-Reverse	5'-GCAATCACAGGAAGGAGGAAGGAG-3'
Insulin-Forward	5'-CAGCCGCAGCCTTTGTGA-3'
Insulin-Reverse	5'-GTGTAGAAGAAGCCTCGTTCC-3'
Glucagon-Forward	5'-AAGAGGTCGCCATTGTTG-3'
Glucagon-Reverse	5'-TAGCAGGTGATGTTGTGAAG-3'
Gapdh-Forward	5'-CAGGAGGCATTGCTGATGAT-3'
Gapdh-Reverse	5'-GAAGGCTGGGGCTCATTT-3'

Immunocytochemistry Analysis

Undifferentiated DPSCs or IPCs were fixed for 30 min in 4% paraformaldehyde, treated with 0.1% Triton-PBS for optimal penetration of cell membranes, and incubated at RT for 30 min, treated with blocking solution (5% BSA) RT for 30 min. And the primary antibodies were incubated overnight at 4°C, washed with PBST for three times, and then incubated with secondary antibodies at 37°C for 40 min. Slides were counterstained with 4′,6′-diamidino-2-phenylindole dihydrochloride (DAPI) for 5 min. Fluorescent images were captured by Leica TCS SP8 microscope. The dilutions of antibodies are according to the instructions.

Insulin and C-Peptide Release Assay

Cells were washed five times and pre-incubated for 90 min at 37° C in the freshly prepared Krebs' Ringer bicarbonate 4-(2-hydroxyethyl)-1-piperazineethanesulfonic acid (HEPES) buffer (KRBH; 4.7 mM KCl, 118 mM NaCl, 25 mM $NaHCO_3$, 1.1 mM KH_2PO_4, 2.5 mM $MgSO_4$, 3.4 mM $CaCl_2$, 10 mM HEPES, and 2 mg/ml BSA, pH 7.4) containing 2.8 mM glucose. The supernatant was then collected and replaced with Krebs' Ringer bicarbonate HEPES buffer supplemented with 16.7 mM D-glucose at 37°C for another 90 min. The Supernatant was also collected to detect the release of insulin and C-peptide by Roche Cobas 6000 automatic electrochemiluminescence analyzer. The multiple stimulation of each culture was calculated by dividing the concentration of insulin or C-peptide in the stimulation supernatant by the concentration of insulin or C-peptide in the basal supernatant.

Statistical Analysis

Parametric data are presented as the means ± standard deviation (SD). GraphPad Prism version 5.0 (California, USA) was used for the statistical analyses. All statistical comparisons between two groups were performed using the two-sided, nonpaired *t*-test. Differences were considered significant at $p < 0.05$.

RESULTS AND DISCUSSION

Morphology and Multilineage Differentiation Potential

hDPSCs exhibited typical MSC morphology, and shared the similar fibroblast-like, spindle shape and expressed high capacity to adhere to plastic culture flasks (**Figure 1A**).

To investigate the differentiation potential of the hDPSCs, the cells were directed toward the osteogenic and adipogenic lineages at P4 (**Figure 1A**). By direct observation under the microscope, lipid droplets began to appear in hDPSCs on about day 21. After 28 days of induction with adipogenic induction medium, adipogenic differentiation was evaluated by cytoplasmic lipid droplets and Oil Red O staining. Only very small lipid granules were detected in hDPSCs on day 28. After 28 days of induction with osteogenic induction medium, osteogenic differentiation was verified by calcium deposition and alizarin red staining. hDPSCs possessed an osteogenic phenotype and also

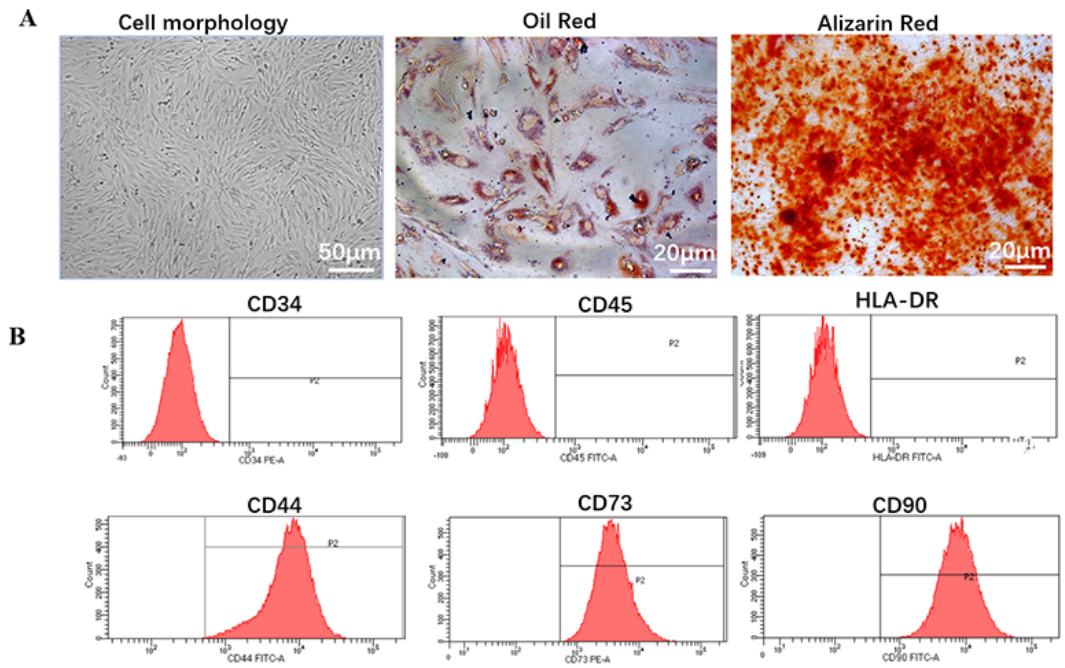

FIGURE 1 | Biology characteristic of hDPSCs. **(A)** Morphology and multilineage differentiation of hDPSCs. All MSCs exhibited a similar fibroblast-like, spindle-shaped morphology (left panel, scale bar: 50 μm) and were induced to differentiate toward adipogenic lineage verified by Oil Red O (middle panel, scale bar: 20 μm) and osteogenic lineage verified by Alizarin Red (right panel, scale bar: 20 μm). Shown is one representative of 3 independent experiments. **(B)** Flow cytometric analysis of the expression of surface markers on hDPSCs. hDPSCs showed high expression of MSC-specific surface markers (CD44, CD73, and CD90), and low expression of leucocyte marker (CD45), hematopoietic cell marker (CD34), or monocyte/macrophage marker (HLA-DR). Shown is one representative of 3 independent experiments.

differentiated into osteocytes. Therefore, we suggested that hDPSCs can differentiate into two abovementioned lineages.

Immunophenotype

We investigated hDPSCs immunophenotype at P4 using flow cytometry instrument. A series of classical MSCs phenotypic markers as defined by the International Society for Cellular Therapy criteria were examined, including CD34, CD44, CD45, CD73, CD90, and HLA-DR. hDPSCs showed high expression of MSC-specific surface markers (CD44, CD73, and CD90), and low expression of leucocyte marker (CD45), hematopoietic cell marker (CD34) and monocyte/macrophage marker (HLA-DR) (**Figure 1B**).

Differentiation of Dental Pulp Stem Cells Into Insulin-Producing Cells in 2-Dimensional Cultures

During the first phase of induction, human dental pulp mesenchymal stem cells were transformed from the original fibroblast-like morphology (**Figure 2A**) to a sparse long spindle shape (**Figure 2B**). During the second phase of induction, the cells gradually changed from long fusiform to short fusiform, elliptical and round, and voids appeared between cells in the local area, and the cells had a tendency to aggregate (**Figure 2C**). During the third phase of induction, the tendency of cell aggregation is more obvious, and cell clusters gradually form between cells, and the number of cell clusters gradually increases (**Figure 2D**). Dithizone staining showed that the cells after induction were scarlet and the undifferentiated cells cannot be stained. Dithizone can specifically chelate zinc ions, indicating that the cytoplasm of cells is rich in zinc ions specific to islet β cells (**Figure 2E**).

After induction at different stages, undifferentiated hDPSCs with the same culture days were used as controls, RT-qPCR analysis revealed mRNA expression levels of the definitive endoderm marker genes FOXA2, CXCR4, and SOX17, pancreatic progenitor marker genes Pdx1 and Nkx6.1, pancreatic cell marker genes PDX1, NKX6.1, NGN3, NEUROD1, PAX4, Insulin and Glucagon, all were maintained at different higher levels in Method 1 than that of Method 2 (**Figure 3A**). The results were further confirmed by immunofluorescence staining. The protein level identified by immunofluorescence was consistent with the level of RT-qPCR levels. After identification and analysis by immunofluorescence observation and software image-ProPlus6.0, we found that the proportion of Cxcr4+/Sox17+cells was approximately 26% after the first phase of induction, that of Method 2 was 20% (**Figure 3B**). About 35% of cells were Pdx1+/Nkx6.1+cells after the second phase of induction, which was also higher than that of Method 2(21%) (**Figure 3C**). After induction in the third stage,

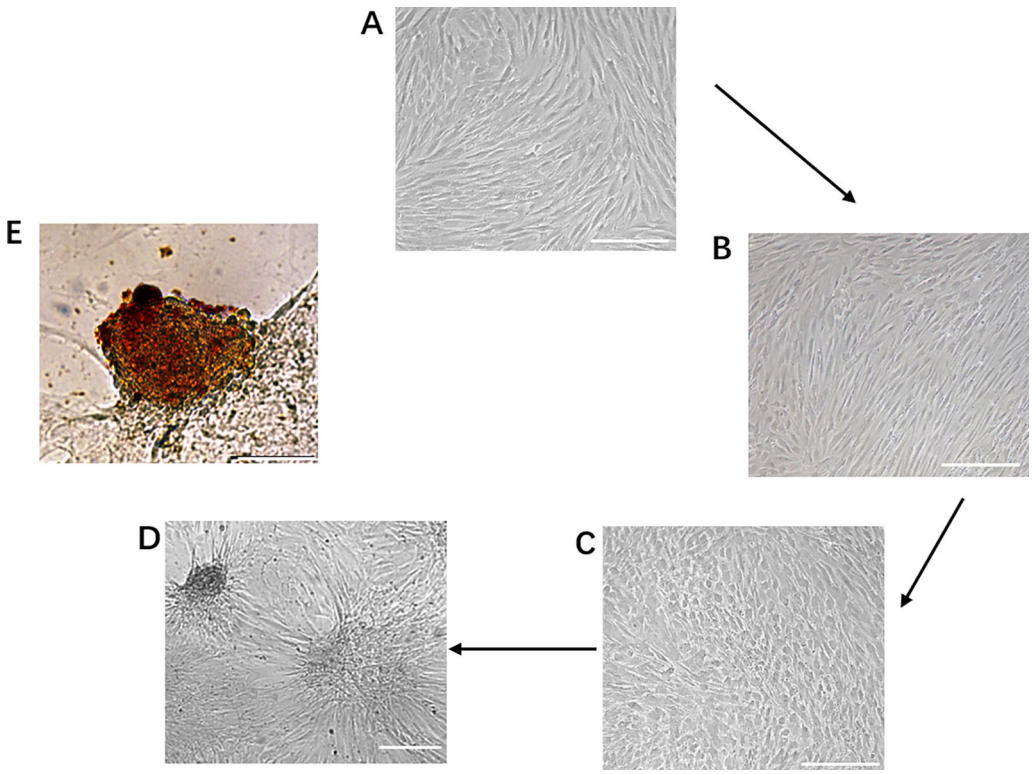

FIGURE 2 | Generation of IPCs from hDPSCs. **(A–D)** Phenotypic changes in hDPSCs during the 19-day differentiation procedure. Scale bars: 50 μm. **(E)** Dithizone staining. Dithizone staining showed that the day 19 IPCs were scarlet. Dithizone can specifically chelate zinc ions, indicating that the cytoplasm of the day 19 IPCs is rich in zinc ions specific to islet β cells. Scale bars: 25 μm.

the proportion of Insulin+/PDX1+cells was approximately 36%. However, only 15% of cells were Pdx1+/Nkx6.1+cells in Method 2 (**Figure 3D**).

In addition to the discovery of Insulin+/PDX1+cells, we also found that the induced cells contained some Glucagon+ cells, and a small number of cells simultaneously expressed insulin and glucagon in the M 1 and M2 (**Figure 4A**); In addition, we observed that cells in M 1 forming a cell aggregate like islet-like cells in the differentiated culture were colocalized with Insulin and Glucagon expression, and cells in M 1 at the edge of the cell cluster were Glucagon positive (**Figure 4A**).These cells that simultaneously express insulin and glucagon are often described as immature or fetal-like endocrine cells. Finally, we also found that the cells induced by the M 1 contained very small amounts of Somatostatin-positive cells (**Figure 4B**).

Differentiation of Dental Pulp Stem Cells Into IPCs in Three-Dimensional Culture

We used Matrigel to physically embed hDPSCs to provide vector and three-dimensional culture conditions for cells. HE staining analysis showed that DPSCs grew in small globular cell clusters during the differentiation process, and the cells grew well (**Figure 5A**).

RT-qPCR analysis showed that the mRNA levels of islet cell marker genes PDX1, NGN3, and Insulin in the third induction stage of the 3D group were significantly higher than those in the 2D group, which was statistically significant. The mRNA level of Glucagon was also higher than that of the 2D group, but the difference was not significant (**Figure 5B**). Immunocytochemistry analysis showed that cells in the cell mass were highly expressed Pdx1 and Insulin (**Figure 5C**).

Static Stimulation and Insulin/C-Peptide Content of Insulin-Producing Cells

IPCs in the 2D group were exposed to 2.8 mM glucose and 16.7 mM glucose, respectively. The total insulin and C-peptide release contents of IPCs when exposed to 2.8 mM glucose were 539.2 ± 60.68 μU/2×10^5 cells (**Figure 6A**) and 84.82 ± 10.73 pmol/2×10^5 cells (**Figure 6C**), respectively; When stimulated with 16.7mM glucose, the total insulin and C-peptide release contents were 729.6 ± 90.87 μU/2×10^5 cells (**Figure 6A**) and 120.89 ± 10.84 pmol/2×10^5 cells (**Figure 6C**), respectively, confirming their ability to respond to glucose *in vitro*.

The total insulin release contents and C-peptide release contents of IPCs when exposed to 16.7 mM glucose in the 3D group (2273.06 ± 104.4 μU/2×10^5 cells, 315.26 ± 43.07 pmol/2×10^5 cells) was significantly higher than that in the low concentration 2.8 mM glucose-stimulated group (686.16 ± 98.37 μU/2×10^5 cells, 104.74 ± 8.95 pmol/2×10^5 cells), which was statistically significant (**Figures 6A, C**). The total insulin

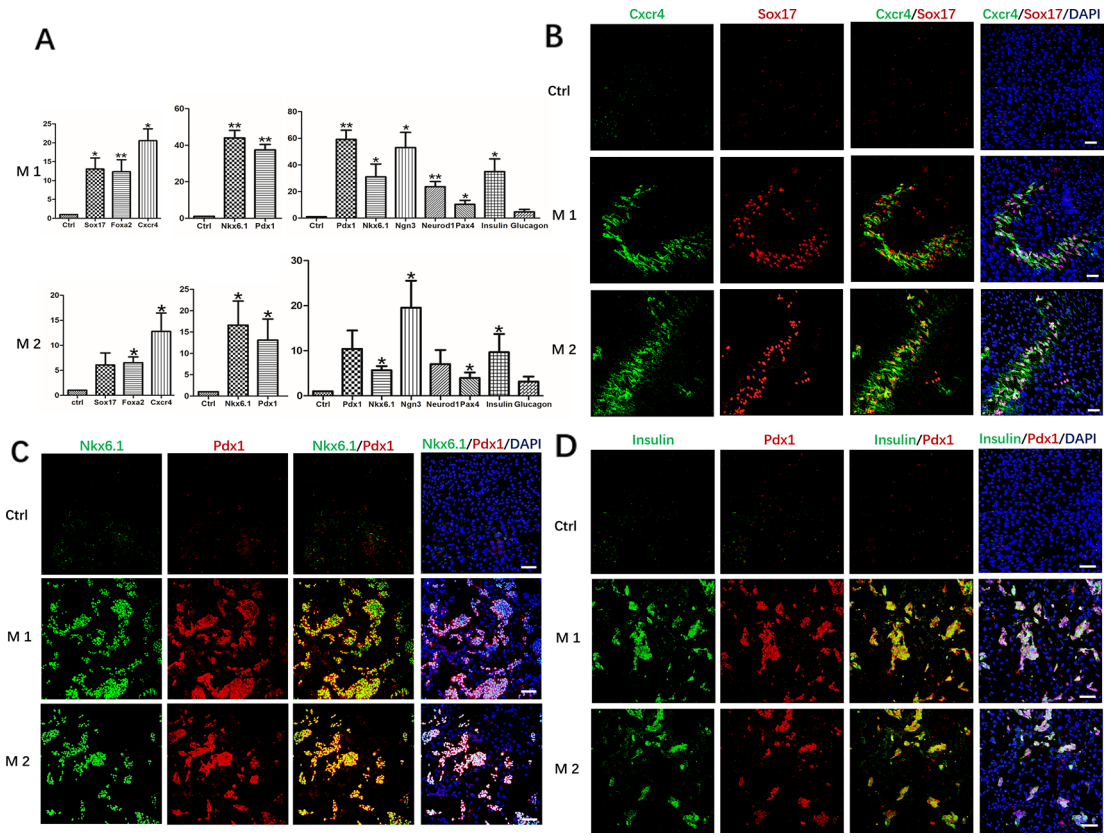

FIGURE 3 | Expression of marker genes at three differentiation stages of cells. **(A)** RT-PCR was performed to analyze the status of marker genes during the differentiation process. Results were the average of three independent experiments. *$p < 0.05$, **$p < 0.01$. **(B)** Immunostaining of definitive endoderm markers Cxcr4 and Sox17 on day 5. **(C)** Immunostaining of definitive endoderm markers pancreatic progenitor markers Pdx1 and Nkx6.1 on day 9. **(D)** Immunostaining of pancreatic cell markers Pdx1 and Insulin on day 19. Undifferentiated DPSCs were used as controls. Scale bars: 100 μm.

release contents and C-peptide release contents of IPCs when exposed to 16.7 mM glucose in the 3D group was significantly higher than that in 2D group, which was statistically significant (**Figures 6A, C**).Fold stimulation of insulin and C-peptide release over the respective basal condition for glucose in the 3D group (3.35 ± 0.35, 3.00 ± 0.18) was significantly higher than that in 2D group (1.36 ± 0.18, 1.43 ± 0.08), which was statistically significant (**Figures 6B, D**). The results of insulin and C-peptide release assay further indicated that the IPCs in the 3D group were more sensitive to glucose response. The 3D culture conditions promoted insulin synthesis in IPCs, and the insulin release function was more mature.

CONCLUSIONS

hDPSCs are a promising source of stem cells in tissue engineering therapy because they are less expensive to acquire and ease of harvest than the costly and invasive techniques required to isolate other mesenchymal stem cells (Han et al., 2019). DPSCs usually come from deciduous teeth, third molars, extra or orthodontic teeth, without adversely affecting the health of permanent dental pulp tissue (Shoi et al., 2014; Ledesma-Martínez et al., 2016). The morphology of hDPSCs showed typical morphology of MSCs, which was relatively uniform in morphology, similar to the fusiform shape of fibroblasts, and showed high adhesion to plastic culture flasks (**Figure 1A**). In this study, we successfully isolated and cultured the homogeneous hDPSCs, and confirmed the adherent cells obtained in this study were human dental pulp mesenchymal stem cells, which provide an experimental basis for the next hDPSCs as ideal seed cells for disease cell therapy.

Many embryonic development-related signaling pathways, including Wnt, Nodal, BMP4 Hedgehog, FGF, Notch, and TGF-β signaling pathways (Oliverkrasinski and Stoffers, 2008; Fuming et al., 2011), regulate different aspects of pancreatic and endocrine cell development. We use Activin A, Noggin, and a combination of small molecule compounds to design and screen strategies by simulating *in vivo* embryonic pancreatic developmental pathways. The hDPSCs were induced to differentiate into definitive endoderm-like cells, pancreatic progenitor-like cells and IPCs under 2D culture conditions. After the comparation of M 1 and M 2, the results showed that we successfully established a new system suitable for

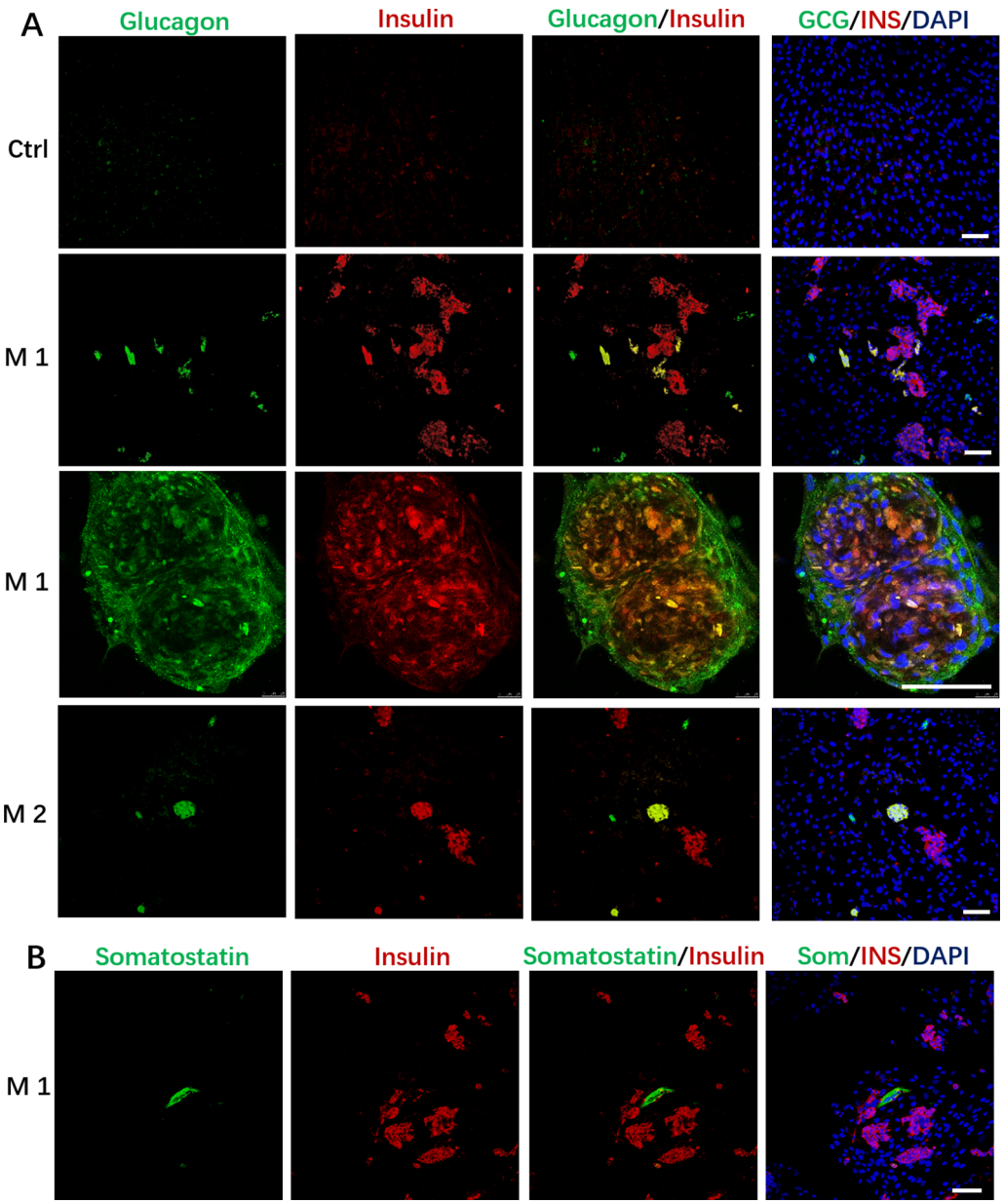

FIGURE 4 | Immunostaining of islet markers on day 19. **(A)** Immunostaining of islet cell markers Glucagon and Insulin on day 19. Cells in M 1 forming a cell aggregate like islet-like cells in the differentiated culture were colocalized with Insulin and Glucagon expression, and cells in M 1 at the edge of the cell aggregate were Glucagon positive. **(B)** Immunostaining of islet cell markers Somatostatin and Insulin on day 19 in M 1. Scale bars: 100 μm. Undifferentiated DPSCs were used as controls.

inducing hDPSCs to differentiate into IPCs, which laid the foundation for subsequent research.

We physically encapsulated hDPSCs using Matrigel, a basement membrane matrix rich in laminin and collagen IV, to provide vectors and 3D culture conditions for hDPSCs. In addition, culture and induction of the differentiation of hDPSCs into insulin-secreting cells in Matrigel rich in laminin and collagen IV has not been studied.

The 3D environment not only allows the connection between the cell and the basement membrane, but also allows the cells to acquire oxygen, hormones and nutrients, as well as to remove waste. In a 3D environment of an organism, cell movement usually follows a chemical signal or molecular gradient, which is critical for the development of the organism. In 2D cultures based on "culture dishes," cells isolated directly from higher organisms often alter their metabolism and gene expression

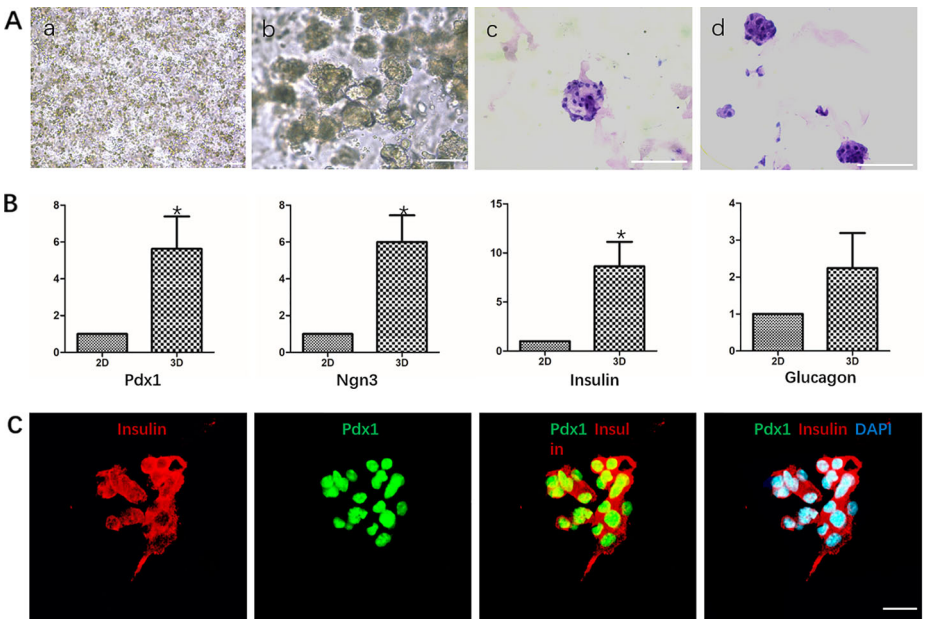

FIGURE 5 | Differentiation of hDPSCs into IPCs in Matrigel. **(A)** Analysis of the growth morphology of hDPSCs in Matrigel. a. Matrigel physical embedded cells before induction; b. Growth status of cells in Matrigel after induction; c-d. HE staining analysis of different cell aggregates after induction. Scale bars: 20 μm. **(B)** Gene expression analysis Pdx1, Nkx6.1, Insulin and Glucagon by qPCR. Cells in 2D group were used as control. Results are the average of three independent experiments. *$p < 0.05$. **(C)** Immunostaining of pancreatic cell markers Pdx1 and Insulin on day 19. Scale bars: 20 μm.

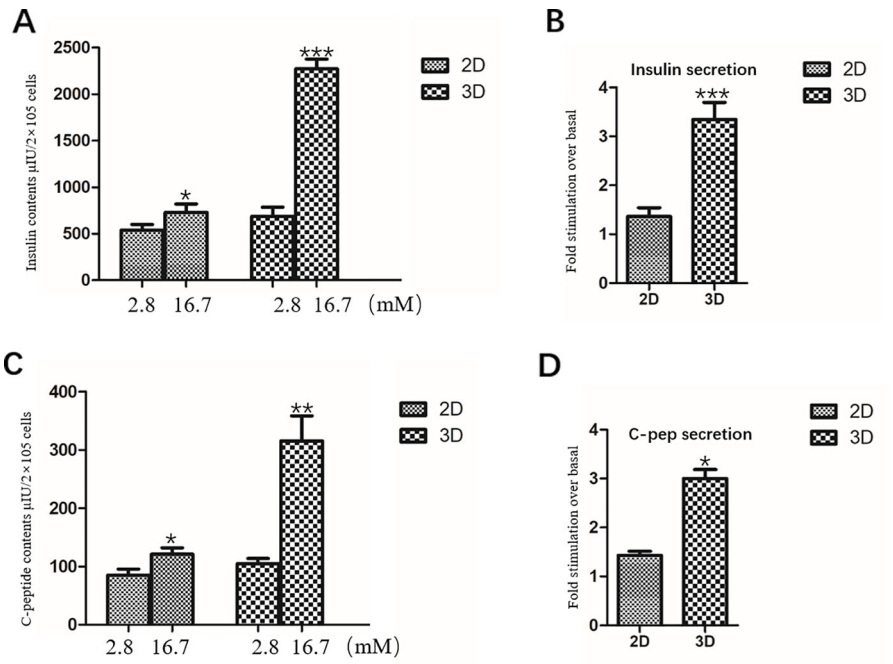

FIGURE 6 | Insulin and C-peptide Release Assay in 2D and 3D group. **(A)** The total release insulin contents of IPCs when exposed to 2.8 and 16.7 mM glucose in the 2D group and 3D group. **(B)** Fold stimulation of insulin release over the respective basal condition for glucose in the 2D group and 3D group. **(C)** The total release C-peptide contents of IPCs when exposed to 2.8 and 16.7 mM glucose in the 2D group and 3D group. **(D)** Fold stimulation of C-peptide release over the respective basal condition for glucose in the 2D group and 3D group. Results are the average of three independent experiments. *$p < 0.05$, **$p < 0.01$, ***$p < 0.001$.

patterns. Cells grown in a 2D environment may significantly reduce the production of specific ECM proteins and often undergo morphological changes (Gelain et al., 2006). Although 2D cell culture technology is beneficial to molecular level research, it ignores the role of tissue space microenvironment. This limits their potential to predict true biological cellular responses, leading to inconsistent outcomes in many *in vitro* and *in vivo* experiments (Pampaloni et al., 2007). In the 3D microenvironment, human embryonic stem cells differentiated into pancreatic endocrine cells with higher efficiency and more obvious response to glucose (Wang et al., 2017).

We identified IPCs obtained in Matrigel using 2D cultured IPCs as controls. The results of RT-qPCR showed that the mRNA expression levels of islet cell marker genes Pdx1, Ngn3 and Insulin in the 3D group were significantly higher than those in the 2D group. Immunofluorescence staining of frozen sections showed that cells in the cell mass were highly expressed Pdx1 and Insulin. The results indicate that 3D culture promoted the differentiation of hDPSCs into IPCs at the gene and protein levels, respectively. Glucose-stimulated insulin/C peptide release assay detects the function of IPCs in the 3D group. Glucose-stimulated insulin/C peptide release assay detects the function of IPCs in the 3D group. The 3D group IPCs responded significantly to high glucose stimulation, releasing significantly more insulin than the 2D group, and the stimulation index was about 2 times that of the 2D group. It is indicated that IPCs induced by 3D group are more sensitive and mature to glucose response. In summary, Matrigel-3D cell culture promoted the differentiation of hDPSCs into IPCs at the gene and protein levels, while significantly enhancing the release of insulin and C-peptide by IPCs.

DATA AVAILABILITY STATEMENT

The datasets generated for this study are available on request to the corresponding author.

ETHICS STATEMENT

Written informed consent was obtained from the donors and guardians. The experiments involving human tissue were approved by the Capital Institute of Pediatrics.

AUTHOR CONTRIBUTIONS

BX and BN conceived and designed the experiments. BX performed the experiments, analyzed the data and drafted the manuscript. YZ and JL collected human tooth samples. BX, YZ, JL, and DF carried out isolation and culture of MSCs from human dental pulp, immunophenotype analysis by flow cytometry of MSCs. BX and ZW participated in RNA isolation, qPCR analysis, immunocytochemistry analysis and insulin and C-peptide release assay. JW, DF, XW, ZG, and BN revised the manuscript. All authors read and approved the final manuscript.

FUNDING

This work was supported by the National Natural Science Foundation of China (No.81741023) and Beijing Municipal Natural Science Foundation (No.7182025).

REFERENCES

Albrecht, D. R., Underhill, G. H., Wassermann, T. B., Sah, R. L., and Bhatia, S. N. (2006). Probing the role of multicellular organization in three-dimensional microenvironments. *Nat. Methods* 3 (5), 369–375. doi: 10.1038/nmeth873

Bellin, M. D., Barton, F. B., Heitman, A., Harmon, J. V., Kandaswamy, R., Balamurugan, A. N., et al. (2012). Potent induction immunotherapy promotes long-term insulin independence after islet transplantation in type 1 diabetes. *Am. J. Transplant.* 12 (6), 1576–1583. doi: 10.1111/j.1600-6143.2011.03977.x

Cai, J., Yu, C., Liu, Y., Chen, S., Guo, Y., Yong, J., et al. (2010). Generation of homogeneous PDX1(+) pancreatic progenitors from human ES cell-derived endoderm cells. *J. Mol. Cell Biol.* 2 (1), 50–60. doi: 10.1093/jmcb/mjp037

Chen, L. B., Jiang, X. B., and Yang, L. (2004). Differentiation of rat marrow mesenchymal stem cells into pancreatic islet beta-cells. *World J. Gastroenterol.* 10 (20), 3016–3020. doi: 10.3748/wjg.v10.i20.3016

Fuming, L., Zhiying, H., Yangfang, L., et al. (2011). Combined activin A/LiCl/Noggin treatment improves production of mouse embryonic stem cell-derived definitive endoderm cells. *J. Cell. Biochem.* 112 (4), 1022–1034

Gelain, F., Bottai, D., Vescovi, A., and Zhang, S. (2006). Designer self-assembling peptide nanofiber scaffolds for adult mouse neural stem cell 3-dimensional cultures. *PloS One* 1, e119. doi: 10.1371/journal.pone.0000119

Govindasamy, V., Ronald, V. S., Abdullah, A. N., Nathan, K. R., Ab Aziz, Z. A., Abdullah, M., et al. (2011). Differentiation of dental pulp stem cells into islet-like aggregates[J]. *J. Dental Res.* 90 (5), 646–652. doi: 10.1177/0022034510396879

Han, Y., Li, X., Zhang, Y., Han, Y., Chang, F., and Ding, J. (2019). Mesenchymal stem cells for regenerative Medicine. *Cells* 8 (8), 886. doi: 10.3390/cells8080886

Hering, B. J., Clarke, W. R., Bridges, N. D., Eggerman, T. L., Alejandro, R., Bellin, M. D., et al. (2016). Phase 3 Trial of Transplantation of human islets in type 1 diabetes complicated by severe hypoglycemia. *Diabetes Care* 39 (7), 1230–1240. doi: 10.2337/dc15-1988

Kim, S. K., and Hebrok, M. (2001). Intercellular signals regulating pancreas development and function. *Genes Dev.* 15 (2), 111–127. doi: 10.1101/gad.859401

Kleinman, H. K., McGarvey, M. L., Hassell, J. R., Star, V. L., Cannon, F. B., Laurie, G. W., et al. (1986). Basement membrane complexes with biological activity. *Biochemistry* 25 (2), 312–318. doi: 10.1021/bi00350a005

Koblas, T., Zacharovova, K., Berkova, Z., Leontovic, I., Dovolilová, E., Zámecník, L., et al. (2009). *In vivo* differentiation of human umbilical cord blood-derived cells into insulin-producing beta cells. *Folia biol.* 55 (6), 224–232.

Kunisada, Y., Tsubooka-Yamazoe, N., Shoji, M., and Hosoya, M. (2012). Small molecules induce efficient differentiation into insulin-producing cells from human induced pluripotent stem cells. *Stem Cell Res.* 8 (2), 274–284. doi: 10.1016/j.scr.2011.10.002

Ledesma-Martínez, E., Mendoza-Núñez, V. M., and Santiago-Osorio, E. (2016). Mesenchymal stem cells derived from dental pulp: a review. *Stem Cells Int.* 3, 4709572. doi: 10.1155/2016/4709572

Li, F., He, Z., Li, Y., Liu, P., Chen, F., Wang, M., et al. (2011). Combined activin A/LiCl/Noggin treatment improves production of mouse embryonic stem cell-derived definitive endoderm cells. *J. Cell. Biochem.* 112 (4), 1022–1034. doi: 10.1002/jcb.22962

Li, J., Zhu, L., Qu, X., Li, J., Lin, R., Liao, L., et al. (2013). Stepwise differentiation of human adipose-derived mesenchymal stem cells toward definitive endoderm and pancreatic progenitor cells by mimicking pancreatic development *in vivo*. *Stem Cells Dev.* 22 (10), 1576–1587. doi: 10.1089/scd.2012.0148

Li, K., Zhu, S., Russ, H., Xu, S., Xu, T., Zhang, Y., et al. (2014). Small molecules facilitate the reprogramming of mouse fibroblasts into pancreatic lineages. *Cell Stem Cell* 14 (2), 228–236. doi: 10.1016/j.stem.2014.01.006

Yang, L., Li, S., Hatch, H., Ahrens, K., Cornelius, J. G., Petersen, B. E., et al. (2002). *In vitro* trans-differentiation of adult hepatic stem cells into pancreatic endocrine hormone-producing cells. *Proc. Natl. Acad. Sci. U.S.A.* 99 (12), 8078–8083. doi: 10.1073/pnas.122210699

Llacua, L. A., Faas, M. M., and Vos, P. D. (2018). Extracellular matrix molecules and their potential contribution to the function of transplanted pancreatic islets. *Diabetologia* 61 (6), 1261–1272. doi: 10.1007/s00125-017-4524-8

Millman, J. R., and Pagliuca, F. W. (2017). Autologous pluripotent stem cell-derived β-like cells for diabetes dellular therapy. *Diabetes* 66 (5), 1111–1120. doi: 10.2337/db16-1406

Nathan, D. M. (1993). Long-term complications of diabetes mellitus. *New Engl. J. Med.* 328 (23), 1676–1685. doi: 10.1056/NEJM199306103282306

Oliverkrasinski, J. M., and Stoffers, D. A. (2008). On the origin of the β cell. *Genes Dev.* 22 (15), 1998. doi: 10.1101/gad.1670808

Oström, M., Loffler, K. A., Edfalk, S., Selander, L., Dahl, U., Ricordi, C., et al. (2008). Retinoic acid promotes the generation of pancreatic endocrine progenitor cells and their further differentiation into beta-cells. *PloS One* 3 (7), e2841. doi: 10.1371/journal.pone.0002841

Pampaloni, F., Reynaud, E. G., and Stelzer, E. H. K. (2007). The third dimension bridges the gap between cell culture and live tissue. *Nat. Rev. Mol. Cell Biol.* 8 (10), 839–845. doi: 10.1038/nrm2236

Porat, S., and Dor, Y. (2007). New sources of pancreatic beta cells. *Curr. Diabetes Rep.* 7 (4), 304–308. doi: 10.1007/s11892-007-0049-8

Rimkus, T. K., Carpenter, R. L., Qasem, S., Chan, M., and Lo, H. W. (2016). Targeting the sonic hedgehog signaling pathway: review of smoothened and GLI inhibitors. *Cancers* 8 (2), 22. doi: 10.3390/cancers8020022

Shapiro, A. M., Lakey, J. R., Ryan, E. A., Korbutt, G. S., Toth, E., Warnock, G. L., et al. (2000). Islet transplantation in seven patients with type 1 diabetes mellitus using a glucocorticoid-free immunosuppressive regimen. *New Engl. J. Med.* 343 (4), 230–238. doi: 10.1056/NEJM200007273430401

Shoi, K., Aoki, K., Ohya, K., Takagi, Y., and Shimokawa, H. (2014). Characterization of pulp and follicle stem cells from impacted supernumerary maxillary incisors. *Pediatr. Dentistry* 36 (3), 79.

Stokes, A., and Preston, S. H. (2017). Deaths attributable to diabetes in the United States: comparison of data sources and estimation approaches. *PloS One* 12 (1), e0170219. doi: 10.1371/journal.pone.0170219

Wang, H. S., Shyu, J. F., Shen, W. S., Hsu, H. C., Chi, T. C., Chen, C. P., et al. (2010). Transplantation of insulin-producing cells derived from umbilical cord stromal mesenchymal stem cells to treat NOD mice. *Cell Transplant.* 20 (3), 455–466.

Wang, W., Jin, S., and Ye, K. (2017). Development of islet organoids from H9 human embryonic stem cells in biomimetic 3D scaffolds. *Stem Cells Dev.* 26 (6), 394–404. doi: 10.1089/scd.2016.0115

Wang, C., Feng, N., Chang, F., Wang, J., Yuan, B., Cheng, Y., et al. (2019). Injectable cholesterol-enhanced stereocomplex polylactide thermogel loading chondrocytes for optimized cartilage regeneration. *Adv. Healthcare Mater.* 8 (14), 1900312. doi: 10.1002/adhm.201900312

Wei, X., Gu, N., Feng, N., Guo, X., and Ma, X. (2018). Inhibition of p38 mitogen-activated protein kinase exerts a hypoglycemic effect by improving beta cell function *via* inhibition of beta cell apoptosis in db/db mice. *J. Enzyme Inhib. Med. Chem.* 33 (1), 1494–1500. doi: 10.1080/14756366.2018.1477138

Zhang, Y., Yu, J., Ren, K., Zuo, J., Ding, J., and Chen, X. (2019a). Thermosensitive Hydrogels as Scaffolds for Cartilage Tissue Engineering. *Biomacromolecules* 20 (4), 1478–1492. doi: 10.1021/acs.biomac.9b00043

Zhang, Y., Liu, X., Zeng, L., Zhang, J., Zuo, J., Zou, J., et al. (2019b). Polymer Fiber Scaffolds for Bone and Cartilage Tissue Engineering. *Adv. Funct. Mater.* 29 (36), 1903279. doi: 10.1002/adfm.201970246

Conflict of Interest: The authors declare that the research was conducted in the absence of any commercial or financial relationships that could be construed as a potential conflict of interest.

frontiers in Pharmacology

ORIGINAL RESEARCH
published: 03 February 2020
doi: 10.3389/fphar.2019.01676

Polymer Nanoformulation of Sorafenib and All-Trans Retinoic Acid for Synergistic Inhibition of Thyroid Cancer

Shijie Li[1], *Shujun Dong*[2*], *Weiguo Xu*[3*], *Yang Jiang*[4] *and Zhongmin Li*[4*]

[1] Department of Thyroid Surgery, China-Japan Union Hospital of Jilin University, Changchun, China, [2] VIP Integrated Department, School and Hospital of Stomatology, Jilin University, Changchun, China, [3] Key Laboratory of Polymer Ecomaterials, Changchun Institute of Applied Chemistry, Chinese Academy of Sciences, Changchun, China, [4] Department of Gastrointestinal Colorectal and Anal Surgery, China-Japan Union Hospital of Jilin University, Changchun, China

OPEN ACCESS

Edited by:
Chao Wang,
Soochow University, China

Reviewed by:
Ruinan Yang,
Pharmaceutical Product Development, United States
Wuyu Zhang,
University of Louisville, United States

***Correspondence:**
Zhongmin Li
lizhongmin1211@126.com
Weiguo Xu
wgxu@ciac.ac.cn
Shujun Dong
dsj@jlu.edu.cn

Specialty section:
This article was submitted to Experimental Pharmacology and Drug Discovery, a section of the journal Frontiers in Pharmacology

Received: 20 November 2019
Accepted: 23 December 2019
Published: 03 February 2020

Citation:
Li S, Dong S, Xu W, Jiang Y and Li Z (2020) Polymer Nanoformulation of Sorafenib and All-Trans Retinoic Acid for Synergistic Inhibition of Thyroid Cancer. Front. Pharmacol. 10:1676. doi: 10.3389/fphar.2019.01676

Part of differentiated thyroid cancer will relapse or develop into dedifferentiated thyroid cancer after standard therapy, such as surgery or radionuclide therapy. Sorafenib (SOR) is recommended for the treatment of advanced or radioiodine-refractory thyroid cancer. The monotherapy using SOR is often hampered by its modest efficacy, serve systemic toxicity, and high occurrence of drug resistance. In order to enhance the antitumor effect of SOR and reduce its side effects, SOR and all-trans retinoic acid (ATRA), a differentiation-promoting drug, were loaded into poly(ethylene glycol)–poly(lactide-*co*-glycolide) (PEG–PLGA) polymer micelles in this study. The drug-loaded micelles, PM/(SOR+ATRA), exhibited relatively slow drug release and effective cell uptake. Compared with other treatment groups, the PM/(SOR+ATRA) treatment group showed the most significant antitumor effect and minimal systemic toxicity toward the FTC-133 thyroid cancer-bearing BALB/c nude mouse model. Immunofluorescence analysis confirmed that PM/(SOR +ATRA) could significantly promote apoptosis and re-differentiation of tumor cells. All the results demonstrated that polymer micelles loaded with SOR and ATRA could treat thyroid cancer more effectively and safely.

Keywords: sorafenib, all-trans retinoic acid, drug delivery system, polymer micelles, thyroid cancer

INTRODUCTION

As the most common endocrine malignancy, thyroid cancer has become more and more prevalent in recent years (James et al., 2018). Differentiated thyroid cancer (DTC), which originates from follicular epithelial cells, accounts for more than 95% of thyroid cancer and usually has a good prognosis (Cabanillas et al., 2016). Surgery and postoperative thyrotropin suppression therapy or radionuclide therapy (I^{131}) are currently the standard treatment for DTC (Haugen et al., 2016). However, approximately 30% of these patients will relapse after the standard treatment (Kim et al., 2018b). The recurrent DTC tends to lose the ability to absorb iodine, thereby losing the option of radioactive iodine therapy. Multi-targeted kinase inhibitors such as sorafenib (SOR) are the first-line treatment of radioiodine-refractory DTC (RAIR-DTC) or advanced thyroid cancer, and they

can significantly improve the progression-free survival of patients (Kim et al., 2018a). SOR exhibits an excellent antitumor effect on various thyroid cancer cell lines, including dedifferentiated subtypes, leading to tumor cell apoptosis and cell cycle arrest (Broecker-Preuss et al., 2015). Nevertheless, drug resistance and serious adverse events, including hand-foot skin reactions, diarrhea, and hypertension, limit the clinical application of SOR (Wei et al., 2019). Studies have shown that patients with DTC have a higher incidence of adverse events to SOR compared to patients with renal and hepatocellular cancer, and about half of the patients need to reduce the dose to control drug toxicity in phase 2 and 3 trials (Jean et al., 2016). Therefore, how to improve the antitumor effect and reduce the adverse events of SOR is an urgent problem to be solved.

In addition, some DTCs will dedifferentiate into more aggressive types after standard treatment. Studies have shown that most of the anaplastic thyroid cancer or poorly differentiated thyroid cancer is derived from the dedifferentiation of DTC (Ma et al., 2018). These dedifferentiated thyroid cancers have become a serious clinical problem due to their lack of response to conventional treatments such as radiotherapy or chemotherapy. Differentiation therapy, which enables dedifferentiated tumor cells to continue to differentiate and mature by using differentiation inducers, is a promising strategy to treat dedifferentiated thyroid cancer. All-trans retinoic acid (ATRA), an intermediate metabolite of vitamin A, has the ability to inhibit cell proliferation and metastasis and promote cell differentiation and apoptosis (Cui et al., 2016). ATRA has been widely used in the differentiation therapy of various diseases, such as acute promyelocytic leukemia (Burnett et al., 2015), breast cancer (Coyle et al., 2018), and advanced thyroid cancer (Cristiano et al., 2017). Studies have proved that ATRA could promote the re-differentiation of thyroid cancer cells, which was characterized by high expression of sodium iodide symporter (NIS) and increased cell uptake of ^{131}I (Arisi et al., 2014).

Synergistic drug combinations are promising cancer treatment strategies, which can improve the therapeutic effect by integrating the functions of multiple drugs (Lehar et al., 2009; Stathias et al., 2018). However, there are still some problems in the clinical application, including poor specificity of drug distribution and serious systemic side effects (Boutros et al., 2016). Nanotechnology has provided a promising method for the targeted delivery of multiple drugs to tumor tissues, which can effectively solve the problems encountered in combination therapy with free drugs (Zhang et al., 2016a; Yang et al., 2017). Nanocarriers are characterized by good biocompatibility, high drug loading efficiency, prolonged circulation time *in vivo*, increased aggregation in tumor tissues, surface modification to actively target specific tissues and cells, stimuli-sensitive behavior for controlled drug release, and simultaneous delivery of different drugs for combination therapy (Feng et al., 2017; Xu et al., 2017; Guo et al., 2018; Zhang et al., 2018a; Feng et al., 2019; Wang et al., 2019). In recent years, a variety of multifunctional nanomaterials have been developed for co-delivery of multiple drugs, such as polymer nanoparticles (Zhao et al., 2016), micelles (Wang et al., 2018; Yang et al., 2019), liposomes (Yao et al., 2015), inorganic nanoparticles (Zhang et al., 2016b), and nanogels (Liu et al., 2015; Zhang et al., 2018b). These delivery systems can deliver drugs to tumor tissues more effectively and safely, thus improving the therapeutic effect.

In this study, we speculated that the re-differentiation effect induced by ATRA could enhance the antitumor efficiency of SOR, and the nanocarriers could further enhance the therapeutic effect. First, SOR and ATRA-loaded poly(ethylene glycol)–poly (lactide-*co*-glycolide) (PEG–PLGA) polymer micelles were fabricated and characterized. Then their antitumor efficiency toward FTC-133 thyroid cancer-bearing BALB/c nude mouse model was investigated. In addition, the systemic side effects were also assessed. The results demonstrated that ATRA significantly enhanced the antitumor efficiency of SOR against FTC-133 tumor cells *in vitro* and *in vivo*, and PEG–PLGA co-loaded with SOR and ATRA showed the most obvious tumor inhibition effect. Therefore, co-delivery of SOR and ARTA with nanocarriers is an effective treatment for thyroid cancer.

MATERIALS AND METHODS

Materials

PEG [number-average molecular weight (M_n) = 2,000 Da] and PLGA [L-lactide (LA):glycolide (GA) = 80:20; viscosity-average molecular weight (M_η) = 60,000 Da] were obtained from Changchun SinoBiomaterials Co., Ltd. (Changchun, P. R. China). SOR (99%) and ATRA (98.5%) were obtained from Zhejiang Hisun Pharmaceutical Co., Ltd. (Taizhou, P. R. China). Stannous 2-ethylhexanoate [$Sn(Oct)_2$, 95%] was provided by Sigma-Aldrich, Inc. (St. Louis, MO, USA). 4′,6-Diamidino-2-phenylindole (DAPI) and 3-(4,5-dimethylthiazol-2-y1)-2,5-diphenyltetrazolium bromide (MTT) were provided by Sigma-Aldrich (Shanghai, P. R., China). The primary and secondary antibodies of caspase-3, phosphorylated extracellular regulated protein kinases 2 (p-ERK2), thyroglobulin (Tg), and NIS were obtained from Abcam (Cambridge, MA, USA). Clear 6-well and 96-well cell culture plates were provided by Corning Costar Co. (Cambridge, MA, USA).

Preparation of Drug-Loaded Polymer Micelles

PEG–PLGA copolymer was prepared according to our previous procedure (Li et al., 2013). SOR and ATRA were encapsulated into PEG–PLGA micelles through a nanoprecipitation method. Typically, PEG–PLGA copolymer (12.5 mg) and SOR (2.5 mg) were dissolved by 100.0 μL of dimethyl sulfoxide (DMSO), respectively. Then these two kinds of solutions were mixtured. After that, 0.90 mL of Milli-Q water was added into the mixed solution. The mixture was then stirred evenly at room temperature for 2 h and subsequently dialyzed with deionized water for 12 h. SOR-loaded PEG–PLGA polymer micelles (PM/SOR) were obtained after the product was lyophilized. For the synthesis of ATRA-loaded PEG–PLGA polymer micelles (PM/ATRA), 31.25 mg of PEG–PLGA copolymer and 6.25 mg of

ATRA were dissolved in 100.0 μL of DMSO, respectively. And then, the synthesis process is the same as PM/SOR. SOR and ATRA-loaded PEG–PLGA polymer micelles [PM/(SOR +ATRA)] were prepared in the same way.

Characterizations of Drug-Loaded Polymer Micelles

The sizes of PM/SOR, PM/ATRA, and PM/(SOR+ATRA) were analyzed by dynamic laser scattering (DLS) using a Wyatt QELS equipment (Wyatt Technology Corp., Santa Barbara, CA, USA). The morphology of drug-loaded PEG–PLGA micelles was observed by a JEOL JEW-1011 transmission electron microscope (TEM; Tokyo, Japan).

In Vitro Drug Release

The drug release behavior of drug-loaded PEG–PLGA micelles (*i.e.*, PM/SOR, PM/ATRA, and PM/(SOR+ATRA) was studied through a dialysis approach. In brief, 1.0 mg of drug-loaded PLGA micelles were dissolved in 10.0 mL of phosphate-buffered saline (PBS) at pH 7.4, and then they were placed in dialysis bags [molecular weight cut-off (MWCO) = 3,500 Da], respectively. The dialysis bags were put into 100.0 mL of corresponding PBS at 37°C and kept vibrating at 80 rpm. At predetermined time intervals, 2.0 mL of external release medium was extracted for detection, and then the same amount of PBS was added. The amount of released SOR and ATRA was calculated by measuring the UV-vis absorbance at 269.0 and 343.5 nm, respectively.

In Vitro Cell Uptake

The *in vitro* cell uptake of drugs was evaluated in FTC-133 human thyroid cancer cells. In brief, the FTC-133 cells at a density of 2.0×10^5 cells mL^{-1} were inoculated on a six-well plate and cultured at 37°C for 24 h. After that, each well was washed twice using PBS and incubated in FBS-absent Dulbecco's Modified Eagle Medium (DMEM) with different concentrations of SOR, ATRA, SOR+ATRA, PM/SOR, PM/ATRA, and PM/(SOR+ATRA). In the control group, cells were incubated with PBS. After 2 h of incubation, the medium was taken away, and each well was washed three times using PBS. Subsequently, 1 mL of lysate was added into each well and cultured at room temperature for 20 min. Finally, the cells were suspended and centrifuged at 3,000 rpm for 5 min. 500 μL of supernatant was collected and determined by measuring the UV-vis absorbance at 269.0 and 343.5 nm, respectively.

In Vitro Cytotoxicity Test

MTT assay was used to test the cytotoxicity of SOR and ATRA on FTC-133 cells and HepG2 cells. The concentration of SOR was 0.0015–100.0 μmol L^{-1} and the concentration ATRA was 0.0031–200.0 μmol L^{-1}. In brief, the FTC-133 cells at a density of 4.0×10^3 cells mL^{-1} were inoculated on a 96-well plate in 180.0 μL of DMEM and cultured at 37°C for 24 h. After that, 20.0 μL of various concentrations of SOR or ATRA solutions were placed into each well and incubated for 72 h. And then, 20.0 μL of MTT (5.0 mg mL^{-1}) was added to each well. After 4 h of incubation, the medium was taken away, followed by the addition of 150.0 μL of DMSO. After 5 min of vibration, the absorbance of the medium was measured at 490 nm by a Bio-Rad 680 microplate reader. Furthermore, the antitumor activity of the combination of SOR and ATRA with SOR at 18.0 μmol L^{-1} and ATRA ranging from 2.8 to 70.0 μmol L^{-1} was also evaluated on FTC-133 cells according to the above protocol. The cytotoxicity of SOR and ATRA to HepG2 cells was assessed using the same procedure. The cell viability was calculated using Equation (1).

$$Cell \quad viability \quad (\%) = \frac{A_{sample}}{A_{control}} \times 100\,\% \tag{1}$$

A_{sample} and $A_{control}$ represented the absorbances of sample and control wells, respectively.

In Vivo Antitumor Efficacy Assessment

BALB/c nude mice (male, 8–12 weeks) were provided by the Animal Center of Jilin University and maintained at Changchun Institute of Applied Chemistry, Chinese Academy of Sciences. The animal studies were approved, and all the experiments were carried out under the supervision of the Animal Care and Use Committee at Jilin University.

FTC-133 cells (1×10^6 cells mL^{-1}) were inoculated in the right axillary of male BALB/c nude mice to establish the tumor-bearing mouse model. Once the tumor volume increased to approximately 100 mm^3, the tumor-bearing mice were randomized into seven groups (n = 5 per group). These seven groups were treated with natural saline (as a control), SOR, ATRA, SOR+ATRA, PM/SOR, PM/ATRA, or PM/(SOR +ATRA) at equivalent SOR dose of 10.0 mg (kg BW) $^{-1}$ and ATRA dose of 25.0 mg (kg BW) $^{-1}$ by tail vein injection every 4 days for three times. Tumor size and body weight of each mouse were measured and recorded every day. Tumor volume was calculated using Equation (2).

$$V(mm^3) = \frac{L \times S^2}{2} \tag{2}$$

L and S (mm) represented the largest and smallest axial lengths of tumors, respectively.

Histology Analysis and Immunofluorescence Assays

The mice were sacrificed using conventional cervical dislocation after 12 days of treatment. Tumors and major organs including heart, liver, spleen, lung, and kidney were resected and fixed with 10% neutral buffered formalin overnight and stained with hematoxylin and eosin staining (H&E) for histological observation and immunofluorescence analyses (*i.e.*, caspase-3, Tg, NIS, and p-ERK2). The histological and immunofluorescence changes were assessed using a microscope (Nikon Eclipse *Ti*, Optical Apparatus Co., Ardmore, PA, USA). The tumor necrosis area and the fluorescent images were further quantitatively analyzed by Image J software (National Institutes of Health, USA). The fluorescence intensity of the control group was set as "1".

Statistical Analysis

Data were presented as mean ± standard deviation (SD). Statistical analyses were carried out by Student's t-test with the statistical

software SPSS (Version 21.0, SPSS Inc., Chicago, IL, USA). $^{*}P < 0.05$ was considered statistically significant, and $^{**}P < 0.01$ and $^{***}P < 0.001$ were considered highly statistically significant.

RESULTS AND DISCUSSION

Synthesis and Characterization of Drug-Loaded PEG–PLGA Micelles

PEG–PLGA copolymers were prepared as our previously reported procedure (Li et al., 2013). Briefly, PEG–PLGA copolymers were fabricated through the ring-opening polymerization (ROP) of lactide and glycolide with PEG or tetrahydroxyl-functionalized PEG serving as the initiator and $Sn(Oct)_2$ serving as the catalyst. As shown in **Scheme 1**, SOR and ATRA were encapsulated into PEG–PLGA micelles by nanoprecipitation. DLS and TEM characterized the size and morphology of drug loaded micelles. The hydrodynamic radius (R_h) of PM/SOR, PM/ATRA, and PM/(SOR+ATRA) measured by DLS in PBS were about 77.4, 67.1, and 85.1 nm, respectively (**Figure 1A**). Furthermore, TEM showed that all the drug-loaded micelles had uniform spherical morphology and the diameters were about 140.4, 120.8, and 161.4 nm, respectively (**Figure 1B**). All the diameters were less than 200 nm, which was beneficial to their successful accumulation at the tumor site through the enhanced permeability and retention (EPR) effect (Schroeder et al., 2012). Because the size of vascular interendothelial pore is varied, the diameter is a key factor related to the pharmacokinetics and biodistribution of nanoparticles administered intravenously. If the diameters are more than 200 nm, nanoparticles will accumulate in the liver and spleen and be processed by the mononuclear phagocyte system (MPS) cells, which will cause severe loss. However, nanoparticles less than 20 nm in diameter usually have short blood circulation time and high permeation rate, so that they cannot effectively accumulate at the tumor site (Bi et al., 2017).

In Vitro Drug Release and Cell Uptake

Encapsulation of free drugs in nanocarriers by physical loading or chemical conjugating has been demonstrated to achieve controlled drug release and increase cell uptake effectively (Li et al., 2018). In this study, the *in vitro* drug release behavior of drug-loaded micelles was detected in PBS at pH 7.4 and 37°C. The relationship between UV absorption and drug concentration was determined by standard curve method, which showed good concentration dependence and provided a basis for measuring

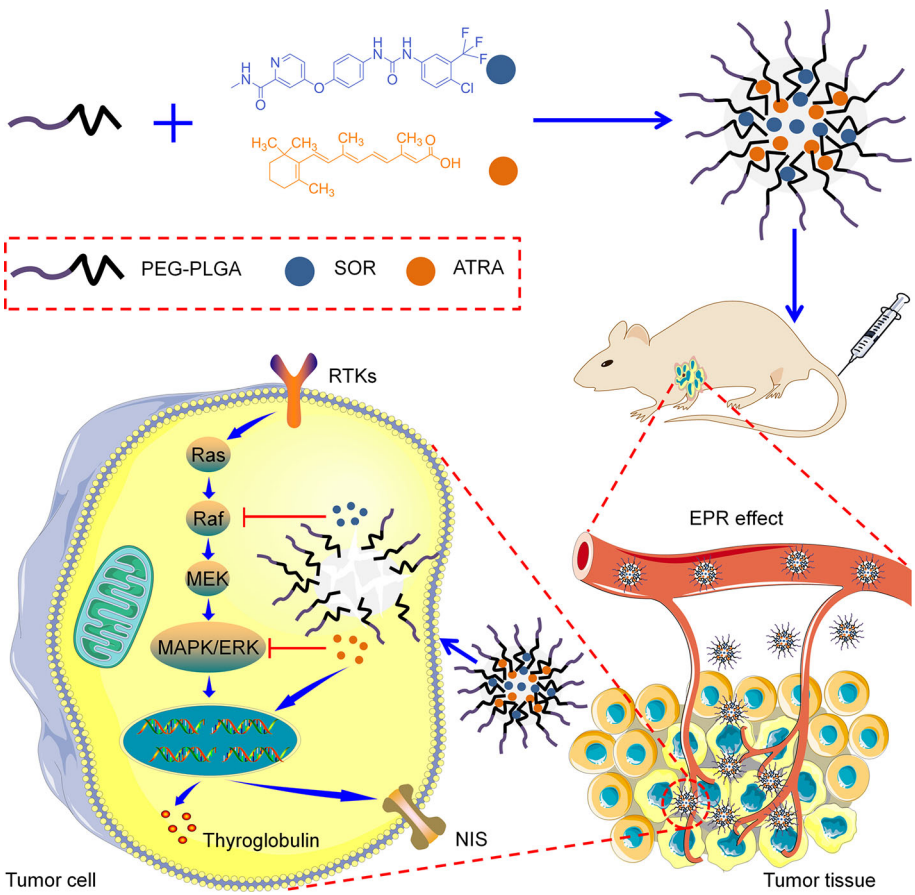

SCHEME 1 | Schematic illustration of the preparation and proposed mechanism of the PEG–PLGA micelles loaded with SOR and ATRA.

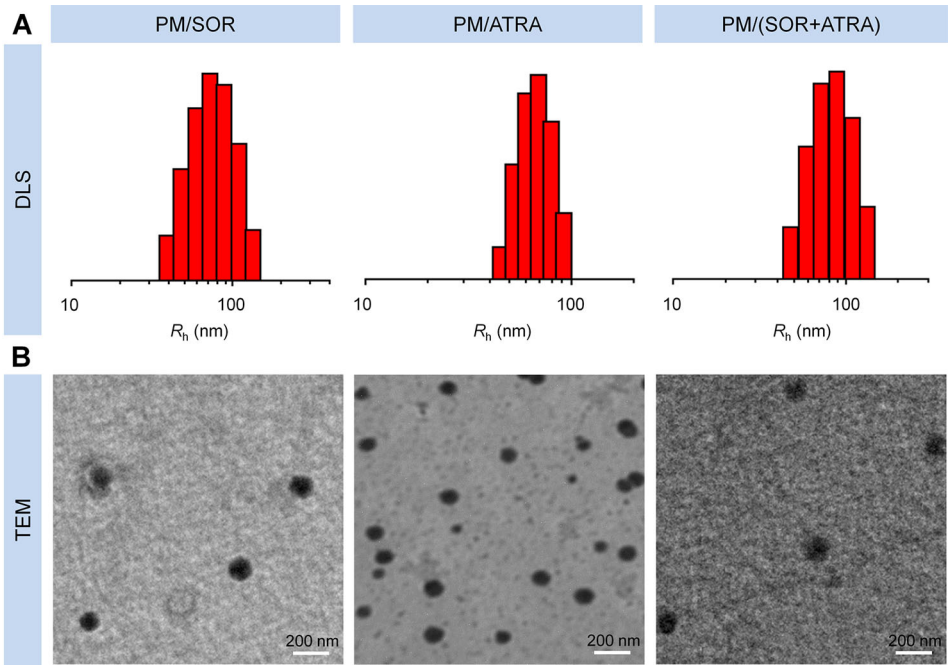

FIGURE 1 | Characterization of drug-loaded PEG–PLGA micelles. **(A)** DLS and **(B)** TEM analyses of PM/SOR, PM/ATRA, and PM/(SOR+ATRA). Scale bar = 200 nm.

drug release (**Figure S1**). All the drug-loaded micelles showed slow and sustained drug release, which was shown in **Figure 2A**. In detail, about 61.3% and 62.4% of SOR were released from PM/SOR and PM/(SOR+ATRA) after 72 h of incubation, respectively. Similarly, about 56.3% and 63.9% of ATRA were released from PM/ATRA and PM/(SOR+ATRA) after 72 h of incubation. It was worth noting that a small number of loaded drugs was not released at the end of 72 h, which might be related to the hydrophobic interaction between drugs and micelles, as reported by other studies (Shen et al., 2017). The results verified that the PEG–PLGA micelles could realize the controlled release of two different drugs.

The cell uptake of drug-loaded micelles by FTC-133 cells was evaluated by cytolysis. It could be seen from **Figures 2B, C** that after co-incubation for 2 h, the contents of SOR and ATRA in cells treated with PM/(SOR+ATRA) were about 28.2% and 55.4% higher than those in cells treated with SOR+ATRA, respectively ($P < 0.001$). The contents of SOR and ATRA in cells treated with PM/SOR and PM/ATRA were also significantly higher than those treated with free single or combined drugs ($P < 0.001$). However, there was no obvious difference in intracellular drug content between single drug-loaded micelles and two drugs-loaded micelles. These results indicated that drug-loaded micelles could effectively deliver SOR and ATRA into tumor cells.

In Vitro Cytotoxicity Test

The synergistic antitumor effects of SOR and ATRA on FTC-133 cells were determined by MTT assay. At first, the half-maximal inhibitory concentrations (IC_{50}s) of free SOR and ATRA were tested. The cell viability of FTC-133 cells treated with SOR and ATRA was shown in **Figures 2D, E**. The IC_{50}s of free SOR and ATRA were 17.9 μmol L^{-1} and 13.9 μmol L^{-1}, respectively. To confirm the optimal concentration of SOR and ATRA in synergistic antitumor therapy, we fixed the concentration of SOR at IC_{50} with the concentration of ATRA ranged from 0.2 to 5.0 times of IC_{50}. The antitumor effect of SOR combined with ATRA gradually increased as the increase of ATRA concentration, which was shown in **Figure 2F**. The combination of 18.0 μmol L^{-1} SOR and 70.0 μmol L^{-1} ATRA showed the most apparent antitumor effect, and the mass ratio of SOR to ATRA was about 0.4. These results verified the synergistic antitumor effect of SOR and ATRA and provided a reference for the subsequent antitumor animal experiments of drug-loaded micelles. As shown in **Figure S2**, similar antitumor effects were observed in human hepatocellular carcinoma HepG2 cells, suggesting that the combination of SOR and ATRA can also be used for the treatment of other malignant tumors.

In Vivo Antitumor Efficacy Evaluation

The antitumor efficacy of the drug-loaded micelles was further confirmed in the FTC-133 thyroid cancer-bearing BALB/c nude mice. According to the results of MTT, the combination of SOR and ATRA provided the best tumor inhibition effect when the mass ratio of SOR and ATRA was about 0.4, so we chose the therapeutic dosage of SOR and ATRA to be 10.0 mg (kg BW)$^{-1}$ and 25.0 mg (kg BW)$^{-1}$, respectively. It could be seen from **Figure 3A** that all drug formulations showed different degrees of

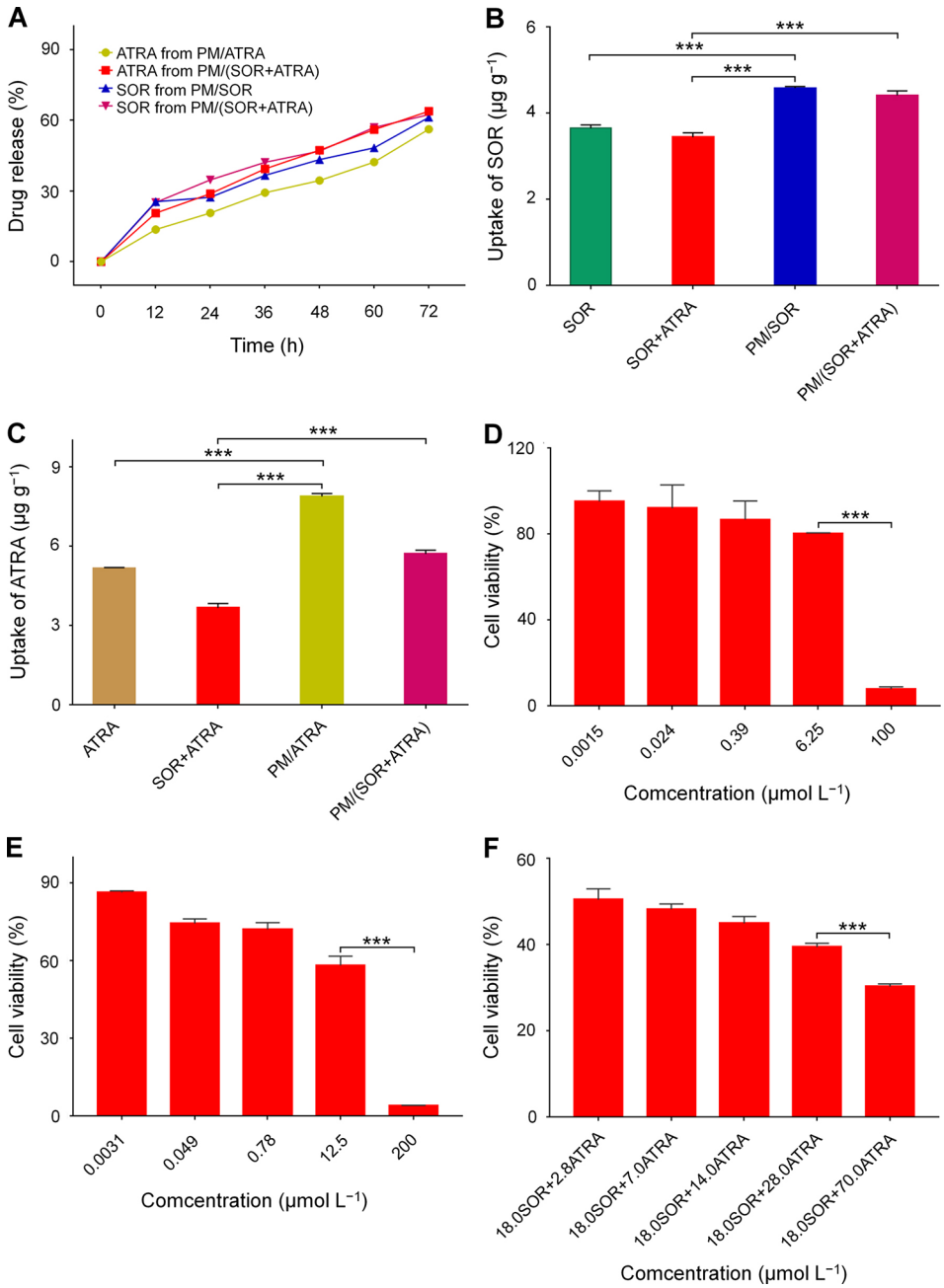

FIGURE 2 | *In vitro* characterization of SOR, ATRA, and drug-loaded PEG–PLGA polymer micelles. **(A)** Release behavior of SOR and ATRA in PBS. Cell uptake of **(B)** SOR and **(C)** ATRA by FTC-133 cells after co-incubation for 2 h. *In vitro* cytotoxicity of **(D)** SOR, **(E)** ATRA, and **(F)** SOR + ATRA on FTC-133 cells. Data are presented as mean ± SD ($n = 3$; ***$P < 0.001$).

inhibition on tumor growth, while the tumors in the control group grew rapidly. Notably, the PM/(SOR+ATRA) treatment group exhibited the most significant tumor inhibition effect. The outstanding antitumor effect of PM/(SOR+ATRA) might be attributed to prolonged circulation time, increased aggregation at the tumor site, efficient uptake of tumor cells, and controlled drug release.

The antitumor efficiency of different treatment groups was further evaluated by H&E staining. It could be seen from **Figure 3C** that the tumor cells showed uniform spherical or spindled morphology with a clear nucleus in the control group. In addition, there was almost no apoptotic tissue, suggesting that the proliferation of tumor cells was not affected. In contrast, tumor cells exhibited varying degrees of nucleus pyknotic and

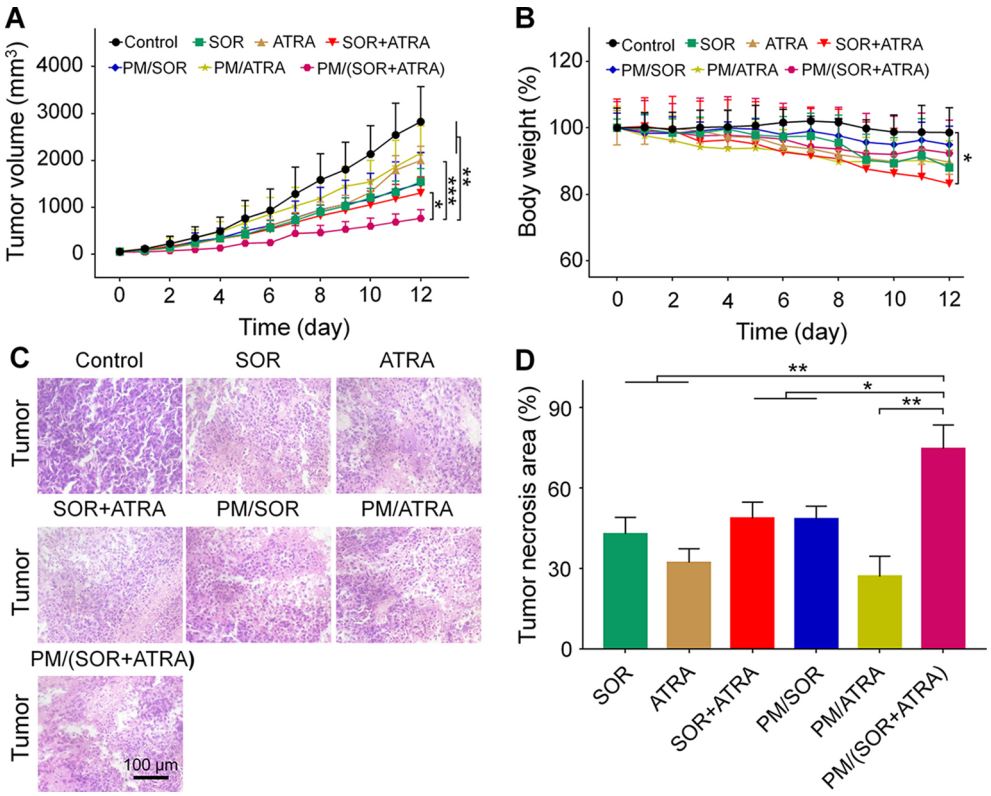

FIGURE 3 | *In vivo* behaviors of different formulations in the FTC-133 thyroid carcinoma-bearing BALB/c mouse model. **(A)** Tumor volumes. **(B)** Body weight of mice treated with different formulations, and the body weight of the mice on day 0 was set to 1. **(C)** H&E staining and **(D)** tumor necrosis area of the tumor tissues obtained from the mouse models treated with different formulations. Data are presented as mean ± SD (in **A**, **B**, $n = 5$, in **C**, **D**, $n = 3$; $^{*}P < 0.05$, $^{**}P < 0.01$, $^{***}P < 0.001$). Scale bar = 100 μm.

cataclastic in the treatment groups, demonstrating that the drugs caused different degrees of apoptosis. The most obvious tumor necrosis was seen in the PM/(SOR+ATRA) treatment group. A quantitative assessment was used to evaluate the necrotic areas. As can be seen from **Figure 3D**, the necrotic areas of SOR, ATRA, SOR+ATRA, PM/SOR, PM/ATRA, and PM/(SOR +ATRA) groups were 43.0, 32.3, 48.8, 48.5, 27.1, and 74.7%, respectively. It was obvious that the tumor necrosis area was the largest in the PM/(SOR+ATRA) treatment group. The results were consistent with the tumor inhibition effect.

Antitumor Mechanism Study

To validate the possible mechanisms of the combined application of SOR and ATRA, immunofluorescence staining and semi-quantitative analysis were performed. As can be seen from **Figures 4A, B**, the highest level of caspase-3 was expressed in tumor tissues treated with PM/(SOR+ATRA), which verified the advantages of PEG–PLGA micelles delivery and the combined application of SOR and ATRA. DTC cells express several differentiation biomarkers, including Tg and NIS, which are closely related to iodine uptake, thyroid hormone synthesis, and the DTC phenotypes (Bastos et al., 2015). In order to elucidate whether the combination of SOR and ATRA has the potential to induce redifferentiation of thyroid cancer cells, we analyzed the expression levels of Tg and NIS by immunofluorescence staining. Compared with other groups, the PM/(SOR+ATRA) treatment group expressed significantly higher levels of Tg (**Figures 4A, C**) and NIS (**Figures 5A, B**), indicating that SOR combined with ATRA appeared to be a promising differentiation therapy strategy. The expression of Tg and NIS in the group treated with PM/(SOR+ATRA) was 7.2 times and 67.9 times that of the control group, respectively. Mitogen-activated protein kinase (MAPK)/ERK signaling pathway plays an important role in the development of thyroid carcinoma, including cell proliferation and cell survival (Zaballos et al., 2019). The expression of p-ERK2 in the PM/(SOR+ATRA) treatment group was lower than that in other groups (**Figures 5A, C**), indicating that PM/(SOR+ATRA) could effectively inhibit cell proliferation. The above results indicated that PM/(SOR+ATRA) could significantly enhance the apoptosis, promote the differentiation, and inhibit the cell proliferation of FTC-133 thyroid cancer.

In Vivo Security Assessment

Serious side effects often hinder the clinical application of antitumor drugs, so security assessment plays an essential role

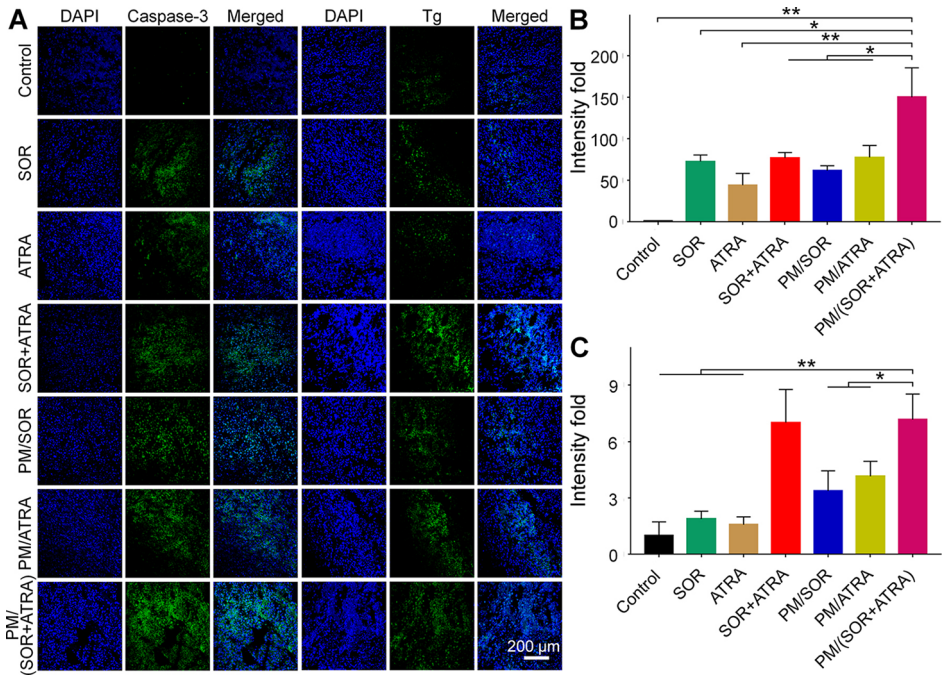

FIGURE 4 | Immunofluorescence staining and semi-quantitative analyses of tumor tissues obtained from the mouse models treated with different formulations. **(A)** Immunofluorescence staining and relative positive areas of **(B)** caspase-3, **(C)** Tg from the semi-quantitative analysis. Data are presented as mean ± SD (n = 3; $^{*}P < 0.05$, $^{**}P < 0.01$). Scale bar = 200 μm.

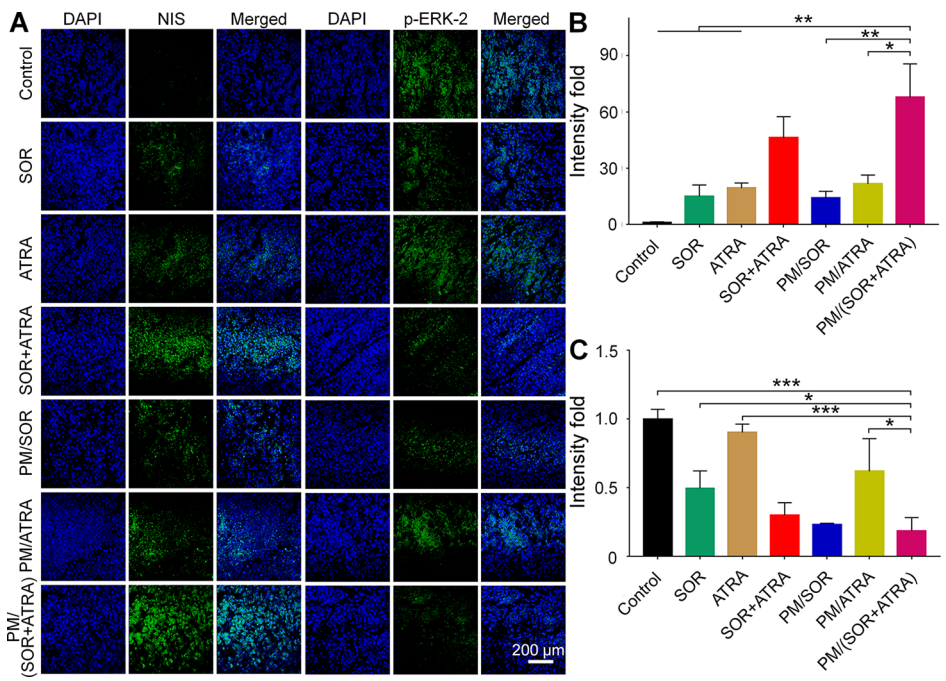

FIGURE 5 | Immunofluorescence staining and semi-quantitative analyses of tumor tissues obtained from the mouse models treated with different formulations. **(A)** Immunofluorescence staining and relative positive areas of **(B)** NIS and **(C)** p-ERK2 from the semi-quantitative analysis. Data are presented as mean ± SD (n = 3; $^{*}P < 0.05$, $^{**}P < 0.01$, $^{***}P < 0.001$). Scale bar = 200 μm.

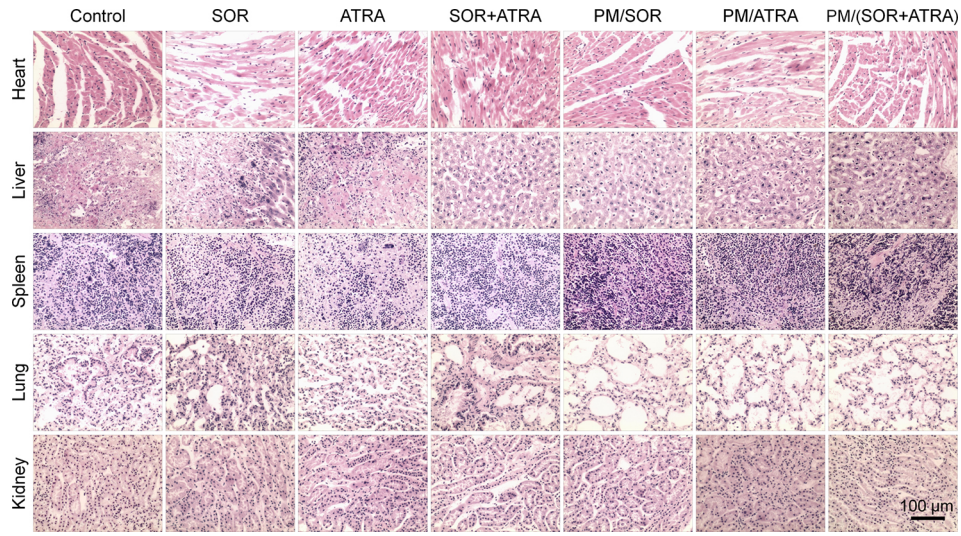

FIGURE 6 | Histological analysis of major organs (*i.e.*, heart, liver, spleen, lung, and kidney) obtained from the mouse models treated with different formulations. Scale bar = 100 μm.

in clinical practice. The change of body weight is an essential indicator of drug toxicity. **Figure 3B** showed the body weight of mice in different treatment groups. It was worth noting that the free SOR+ATRA treatment group showed the most apparent weight loss (about 16.8%). By contrast, mice in the PM/(SOR+ATRA) treatment group showed only a slight weight loss. In order to further assess the safety of different drug formulations, the main organs (*i.e.*, heart, liver, spleen, lung, and kidney) were collected for H&E analyses. As can be seen from **Figure 6**, various degrees of pulmonary fibrosis, hepatic necrosis, and hypersplenism were observed in the SOR, ATRA, and SOR+ATRA treatment groups. On the contrary, the above pathological changes were slight in the PM/SOR, PM/ATRA, and PM/(SOR+ATRA) treatment groups. All the results further confirmed the satisfactory safety of the drug-loaded micelles.

CONCLUSIONS

The combination of drugs with different mechanisms is a challenging and promising method to solve the limitation of single antitumor drugs. In addition, nanocarriers play a crucial role in enhancing the efficacy of antitumor drugs and reducing their side effects. In this work, we investigated the combination of SOR and ATRA loaded by PEG–PLGA micelles in the treatment of thyroid cancer. The drug-loaded micelles exhibited relatively slow drug release and effective cell uptake. In addition, compared with other treatment groups, the PM/(SOR+ATRA) treatment group had the highest tumor inhibition rate in the FTC-133 thyroid cancer-bearing BALB/c nude mouse model without showing severe systemic toxicity. The expression of NIS and Tg was significantly increased in the groups treated with SOR and ATRA, suggesting that the re-differentiation of thyroid cancer cells may be beneficial for antitumor therapy. All the results verified that the combination of SOR and ATRA and the application of nanocarriers might be an effective treatment for thyroid cancer. Furthermore, the combination of molecular targeted therapy and differentiation therapy may be applied to treat other undifferentiated or poorly differentiated types of malignant tumors, such as liver cancer, colorectal cancer, and gastric cancer.

DATA AVAILABILITY STATEMENT

All datasets generated for this study are included in the article/**Supplementary Material**.

ETHICS STATEMENT

The animal study was reviewed and approved by the Animal Care and Use Committee at Jilin University.

AUTHOR CONTRIBUTIONS

ZL and WX proposed and designed the experiments. SL carried out the experiments with the help of ZL, SD, and YJ. SL and ZL drafted the manuscript and interpreted the data. WX, SD, and YJ revised the manuscript.

FUNDING

The work was financially supported by the National Natural Science Foundation of China (Grant Nos. 51603204, 51873207,

51803006, and 51673190) and the Science and Technology Development Program of Jilin Province (Grant Nos. 20190201068JC, 20170101182JC and 20190701004GH). Thanks for the financial support of the Changchun Saikede Medical Device Co, Ltd (Jilin, China).

SUPPLEMENTARY MATERIALS

The Supplementary Material for this article can be found online at: https://www.frontiersin.org/articles/10.3389/fphar.2019.01676/full#supplementary-material

REFERENCES

Arisi, M. F., Starker, R. A., Addya, S., Huang, Y., and Fernandez, S. V. (2014). All trans-retinoic acid (ATRA) induces re-differentiation of early transformed breast epithelial cells. *Int. J. Oncol.* 44 (6), 1831–1842. doi: 10.3892/ijo.2014.2354

Bastos, A. U., Oler, G., Nozima, B. H., Moyses, R. A., and Cerutti, J. M. (2015). BRAF V600E and decreased NIS and TPO expression are associated with aggressiveness of a subgroup of papillary thyroid microcarcinoma. *Eur. J. Endocrinol.* 173 (4), 525–540. doi: 10.1530/EJE-15-0254

Bi, C., Miao, X. Q., Chow, S. F., Wu, W. J., Yan, R., Liao, Y. H., et al. (2017). Particle size effect of curcumin nanosuspensions on cytotoxicity, cellular internalization, *in vivo* pharmacokinetics and biodistribution. *Nanomedicine* 13 (3), 943–953. doi: 10.1016/j.nano.2016.11.004

Boutros, C., Tarhini, A., Routier, E., Lambotte, O., Ladurie, F. L., Carbonnel, F., et al. (2016). Safety profiles of anti-CTLA-4 and anti-PD-1 antibodies alone and in combination. *Nat. Rev. Clin. Oncol.* 13 (8), 473–486. doi: 10.1038/nrclinonc.2016.58

Broecker-Preuss, M., Muller, S., Britten, M., Worm, K., Schmid, K. W., Mann, K., et al. (2015). Sorafenib inhibits intracellular signaling pathways and induces cell cycle arrest and cell death in thyroid carcinoma cells irrespective of histological origin or BRAF mutational status. *BMC Cancer* 15, 184. doi: 10.1186/s12885-015-1186-0

Burnett, A. K., Russell, N. H., Hills, R. K., Bowen, D., Kell, J., Knapper, S., et al. (2015). Arsenic trioxide and all-trans retinoic acid treatment for acute promyelocytic leukaemia in all risk groups (AML17): results of a randomised, controlled, phase 3 trial. *Lancet Oncol.* 16 (13), 1295–1305. doi: 10.1016/S1470-2045(15)00193-X

Cabanillas, M. E., McFadden, D. G., and Durante, C. (2016). Thyroid cancer. *Lancet* 388 (10061), 2783–2795. doi: 10.1016/S0140-6736(16)30172-6

Coyle, K. M., Dean, C. A., Thomas, M. L., Vidovic, D., Giacomantonio, C. A., Helyer, L., et al. (2018). DNA methylation predicts the response of triple-negative breast cancers to all-trans retinoic acid. *Cancers* 10 (11), 397. doi: 10.3390/cancers10110397

Cristiano, M. C., Cosco, D., Celia, C., Tudose, A., Mare, R., Paolino, D., et al. (2017). Anticancer activity of all-trans retinoic acid-loaded liposomes on human thyroid carcinoma cells. *Colloids Surf. B-Biointerfaces* 150, 408–416. doi: 10.1016/j.colsurfb.2016.10.052

Cui, J., Gong, M., He, Y., Li, Q., He, T., and Bi, Y. (2016). All-trans retinoic acid inhibits proliferation, migration, invasion and induces differentiation of hepa1-6 cells through reversing EMT *in vitro*. *Int. J. Oncol.* 48 (1), 349–357. doi: 10.3892/ijo.2015.3235

Feng, X. R., Ding, J. X., Gref, R., and Chen, X. S. (2017). Poly(beta-cyclodextrin)-mediated polylactide-cholesterol stereocomplex micelles for controlled drug delivery. *Chin. J. Polym. Sci.* 35 (6), 693–699. doi: 10.1007/s10118-017-1932-7

Feng, X., Xu, W., Li, Z., Song, W., Ding, J., and Chen, X. (2019). Immunomodulatory Nanosystems. *Adv. Sci. (Weinh)* 6 (17), 1900101. doi: 10.1002/advs.201900101

Guo, H., Li, F. P., Xu, W. G., Chen, J. J., Hou, Y. C., Wang, C. X., et al. (2018). Mucoadhesive cationic polypeptide nanogel with enhanced penetration for efficient intravesical chemotherapy of bladder cancer. *Adv. Sci.* 5 (6), 1800004. doi: 10.1002/advs.201800004

Haugen, B. R., Alexander, E. K., Bible, K. C., Doherty, G. M., Mandel, S. J., Nikiforov, Y. E., et al. (2016). 2015 American thyroid association management guidelines for adult patients with thyroid nodules and differentiated thyroid cancer: the American thyroid association guidelines task force on thyroid nodules and differentiated thyroid cancer. *Thyroid* 26 (1), 1–133. doi: 10.1089/thy.2015.0020

James, B. C., Mitchell, J. M., Jeon, H. D., Vasilottos, N., Grogan, R. H., and Aschebrook-Kilfoy, B. (2018). An update in international trends in incidence rates of thyroid cancer, 1973-2007. *Cancer Causes Control* 29 (4-5), 465–473. doi: 10.1007/s10552-018-1023-2

Jean, G. W., Mani, R. M., Jaffry, A., and Khan, S. A. (2016). Toxic effects of Sorafenib in patients with differentiated thyroid carcinoma compared with other cancers. *Jama Oncol.* 2 (4), 529–534. doi: 10.1001/jamaoncol.2015.5927

Kim, M., Kim, T. H., Shin, D. Y., Lim, D. J., Kim, E. Y., Kim, W. B., et al. (2018a). Tertiary care experience of sorafenib in the treatment of progressive Radioiodine-Refractory differentiated thyroid carcinoma: a Korean Multicenter Study. *Thyroid* 28, 686–686. doi: 10.1089/thy.2017.0356.correx

Kim, T. M., Kim, J. H., Yoo, R. E., Kim, S. C., Chung, E. J., Hong, E. K., et al. (2018b). Persistent/recurrent differentiated thyroid cancer: clinical and radiological characteristics of persistent disease and clinical recurrence based on computed tomography analysis. *Thyroid* 28 (11), 1490–1499. doi: 10.1089/thy.2018.0151

Lehar, J., Krueger, A. S., Avery, W., Heilbut, A. M., Johansen, L. M., Price, E. R., et al. (2009). Synergistic drug combinations tend to improve therapeutically relevant selectivity. *Nat. Biotechnol.* 27 (7), 659–666. doi: 10.1038/nbt.1549

Li, D., Sun, H., Ding, J., Tang, Z., Zhang, Y., Xu, W., et al. (2013). Polymeric topology and composition constrained polyether–polyester micelles for directional antitumor drug delivery. *Acta Biomater.* 9 (11), 8875–8884. doi: 10.1016/j.actbio.2013.06.041

Li, J. N., Xu, W. G., Li, D., Liu, T. J., Zhang, Y. S., Ding, J. X., et al. (2018). Locally deployable nanofiber patch for sequential drug delivery in treatment of primary and advanced orthotopic hepatomas. *Acs Nano* 12 (7), 6685–6699. doi: 10.1021/acsnano.8b01729

Liu, X. G., Wang, J. M., Xu, W. G., Ding, J. X., Shi, B., Huang, K. X., et al. (2015). Glutathione-degradable drug-loaded nanogel effectively and securely suppresses hepatoma in mouse model. *Int. J. Nanomed.* 10, 6587–6602. doi: 10.2147/IJN.S90000

Ma, B., Xu, W. B., Wei, W. J., Wen, D., Lu, Z. W., Yang, S. W., et al. (2018). Clinicopathological and survival outcomes of well-differentiated thyroid carcinoma undergoing dedifferentiation: a retrospective study from FUSCC. *Int. J. Endocrinol.* 2018. doi: 10.1155/2018/2383715

Schroeder, A., Heller, D. A., Winslow, M. M., Dahlman, J. E., Pratt, G. W., Langer, R., et al. (2012). Treating metastatic cancer with nanotechnology. *Nat. Rev. Cancer* 12 (1), 39–50. doi: 10.1038/nrc3180

Shen, K. X., Li, D., Guan, J. J., Ding, J. X., Wang, Z. T., Gu, J. K., et al. (2017). Targeted sustained delivery of antineoplastic agent with multicomponent polylactide stereocomplex micelle. *Nanomedicine Biol. Med.* 13 (3), 1279–1288. doi: 10.1016/j.nano.2016.12.022

Stathias, V., Jermakowicz, A. M., Maloof, M. E., Forlin, M., Walters, W., Suter, R. K., et al. (2018). Drug and disease signature integration identifies synergistic combinations in glioblastoma. *Nat. Commun.* 9 (1), 5315. doi: 10.1038/s41467-018-07659-z

Wang, J. X., Xu, W. G., Li, S. X., Qiu, H. P., Li, Z. B., Wang, C. X., et al. (2018). Polylactide-cholesterol stereocomplex micelle encapsulating chemotherapeutic agent for improved antitumor efficacy and safety. *J. Biomed. Nanotechnol.* 14 (12), 2102–2113. doi: 10.1166/jbn.2018.2624

Wang, Q. L., Zhang, P., Li, Z. M., Feng, X. R., Lv, C. Y., Zhang, H. Y., et al. (2019). Evaluation of polymer nanoformulations in hepatoma therapy by established rodent models. *Theranostics* 9 (5), 1426–1452. doi: 10.7150/thno.31683

Wei, W. J., Hardin, H., and Luo, Q. Y. (2019). Targeting autophagy in thyroid cancers. *Endocr. Relat. Cancer* 26 (4), R181–R194. doi: 10.1530/ERC-18-0502

Xu, W. G., Ding, J. X., and Chen, X. S. (2017). Reduction-responsive polypeptide micelles for intracellular delivery of antineoplastic agent. *Biomacromolecules* 18 (10), 3291–3301. doi: 10.1021/acs.biomac.7b00950

Yang, R. N., Mondal, G., Wen, D., and Mahato, R. I. (2017). Combination therapy of paclitaxel and cyclopamine polymer-drug conjugates to treat advanced prostate cancer. *Nanomedicine Biol. Med.* 13 (2), 391–401. doi: 10.1016/j.nano.2016.07.017

Yang, R. N., Chen, H., Guo, D. W., Dong, Y. X., Miller, D. D., Li, W., et al. (2019). Polymeric micellar delivery of novel microtubule destabilizer and hedgehog signaling inhibitor for treating chemoresistant prostate cancer. *J. Pharmacol. Exp. Ther.* 370 (3), 864–875. doi: 10.1124/jpet.119.256623

Yao, Y., Su, Z., Liang, Y., and Zhang, N. (2015). pH-Sensitive carboxymethyl chitosan-modified cationic liposomes for sorafenib and siRNA co-delivery. *Int. J. Nanomed.* 10, 6185–6197. doi: 10.2147/IJN.S90524

Zaballos, M. A., Acuna-Ruiz, A., Morante, M., Crespo, P., and Santisteban, P. (2019). Regulators of the RAS-ERK pathway as therapeutic targets in thyroid cancer. *Endocr. Relat. Cancer* 26 (6), R319–R344. doi: 10.1530/ERC-19-0098

Zhang, R. X., Wong, H. L., Xue, H. Y., Eoh, J. Y., and Wu, X. Y. (2016a). Nanomedicine of synergistic drug combinations for cancer therapy - Strategies and perspectives. *J. Control Release* 240, 489–503. doi: 10.1016/j.jconrel.2016.06.012

Zhang, W., Shen, J., Su, H., Mu, G., Sun, J. H., Tan, C. P., et al. (2016b). Co-delivery of cisplatin prodrug and chlorin e6 by mesoporous silica nanoparticles for chemo-photodynamic combination therapy to combat drug resistance. *ACS Appl. Mater. Interfaces* 8 (21), 13332–13340. doi: 10.1021/acsami.6b03881

Zhang, Y., Cai, L. L., Li, D., Lao, Y. H., Liu, D. Z., Li, M. Q., et al. (2018a). Tumor microenvironment-responsive hyaluronate-calcium carbonate hybrid nanoparticle enables effective chemotherapy for primary and advanced osteosarcomas. *Nano Res.* 11 (9), 4806–4822. doi: 10.1007/s12274-018-2066-0

Zhang, Y., Wang, F., Li, M. Q., Yu, Z. Q., Qi, R. G., Ding, J. X., et al. (2018b). Self-stabilized hyaluronate nanogel for intracellular codelivery of doxorubicin and cisplatin to osteosarcoma. *Adv. Sci.* 5 (5), 1700821. doi: 10.1002/advs.201700821

Zhao, L., Xiao, C. S., Wang, L. Y., Gai, G. Q., and Ding, J. X. (2016). Glucose-sensitive polymer nanoparticles for self-regulated drug delivery. *Chem. Commun.* 52 (49), 7633–7652. doi: 10.1039/c6cc02202b

Conflict of Interest: The authors declare that the research was conducted in the absence of any commercial or financial relationships that could be construed as a potential conflict of interest.

frontiers in Pharmacology

REVIEW
published: 04 February 2020
doi: 10.3389/fphar.2020.00024

Cell Membrane-Camouflaged Nanocarriers for Cancer Diagnostic and Therapeutic

Shengxian Li[1], *Jianhua Liu*[1], *Mengyao Sun*[1], *Jixue Wang*[1], *Chunxi Wang*[1]* *and Yinghao Sun*[1,2]*

[1] Department of Urology, the First Hospital of Jilin University, Changchun, China, [2] Department of Urology, Shanghai Changhai Hospital, Second Military Medical University, Shanghai, China

Cell membrane (CM)-camouflaged nanocarriers (CMNPs) are the tools of a biomimetic strategy that has attracted significant attention. With a wide range of nanoparticle cores and CMs available, various creative CMNP designs have been studied for cancer diagnosis and therapy. The various functional CM molecules available allow CMNPs to demonstrate excellent properties such as prolonged circulation time, immune escape ability, reduced systemic toxicity, and homologous targeting ability when camouflaged with CMs derived from various types of natural cells including red and white blood cells, platelets, stem cells, and cancer cells. In this review, we summarize various CMNPs employed for cancer chemotherapy, immunotherapy, phototherapy, and *in vivo* imaging. We also predict future challenges and opportunities for fundamental and clinical studies.

Keywords: biological membrane, nanoparticle, drug delivery, cancer treatment, imaging

OPEN ACCESS

Edited by:
Chao Wang,
Soochow University, China

Reviewed by:
Quanyin Hu,
Massachusetts Institute of Technology, United States
Bing Feng,
École Polytechnique Fédérale de Lausanne, Switzerland

***Correspondence:**
Chunxi Wang
chunxi_wang@126.com
Yinghao Sun
sunyhsmmu@126.com

Specialty section:
This article was submitted to Experimental Pharmacology and Drug Discovery, a section of the journal Frontiers in Pharmacology

Received: *30 November 2019*
Accepted: *08 January 2020*
Published: *04 February 2020*

Citation:
Li S, Liu J, Sun M, Wang J, Wang C and Sun Y (2020) Cell Membrane-Camouflaged Nanocarriers for Cancer Diagnostic and Therapeutic. Front. Pharmacol. 11:24. doi: 10.3389/fphar.2020.00024

INTRODUCTION

Cancer is a worldwide health problem and is currently the most important hindrance to life expectancy improvement. In 2015, the World Health Organization (WHO) estimated that cancer is the first or second most common cause of death among people under age 70 in most countries (Bray et al., 2018). According to updated nationwide cancer statistics from the National Central Cancer Registry of China (NCCRC), there were 3.8 million new cancer cases (crude incidence rate: 278.07/100,000) and 2.3 million cancer deaths (crude incidence rate: 278.07/100,000) (Chen et al., 2018). Cancer cells exhibit uncontrollably rapid proliferation *via* growth signal self-sufficiency, resisting growth inhibitory, and escaping from apoptotic signals (Saez-Rodriguez et al., 2015). Cancer cells can escape from immune surveillance and metastasize from origin sites to other organs. They can even generate adaptive strategies in response to effective treatments *via* further gene mutation (Gatenby and Brown, 2018). Chemotherapy, radiotherapy, and immunotherapy are presently the main clinical cancer treatment methods. Other treatment strategies such as phototherapy and gene therapy are also being developed. However, these treatment strategies have demonstrated unsatisfactory results due to poor pharmacokinetics, low permeability, low targeting ability, and severe side-effects.

Due to the previously mentioned shortcomings of cancer treatment strategy, nanoparticle (NP)-based drug delivery systems (DDSs) have been widely studied for tumor diagnosis and treatment (Dan et al., 2007). Particles 1–1,000 nm in size are defined as nanoparticles and offer good drug delivery

characteristics. Nanoparticles 10–100 nm in size are proven to offer the highest delivery efficacy (Narain et al., 2017). Various types of nanomaterials such as polymers, liposomes, and metals have been developed for the delivery of therapeutic agents for cancer treatment. The cooperation between payload and nanomaterial can produce effective drug delivery *via* passive or active targeting strategies and can offer high drug loading capacities, increased circulation times, and reduced systemic toxicities. In the passive approach, a nanoparticle-based DDS can deliver therapeutic agents effectively *via* the enhanced permeation and retention (EPR) effect. An active antitumor agent approach can be used when the nanomaterials are synthesized to exhibit environmentally responsive characteristics or targeting ligands. Meanwhile, the cooperation of varying payloads *via* nanoparticle-based DDS can elicit diversification effects, like the implementation of chemoimmunotherapy (Fang et al., 2018).

However, the foreign nature of nanoparticles makes it easy for the immune system to recognize and eliminate them easily. In order to achieve more efficient drug delivery with a low clearance rate, biomimetic nanoparticles have been designed to prolong circulation time and evade clearance by the immune system. PEGylation has been widely used to decrease nanoparticle elimination. However, it has been reported that anti-PEG antibodies can be produced after repeated administration of PEGylated nanoparticles, and this might promote the elimination these nanoparticles (Lubich et al., 2016). In contrast, lipids are a major part of the cell membrane (CM). They have been used to produce biomimetic liposomes in order to mimic biological membranes. However, these liposomes lack structural integrity and stability. This restricts their application as DDSs (Maurer et al., 2001).

A range of new biomimetic nanoparticle-based DDSs have recently been developed to combine the benefits of natural and synthetic nanomaterials (Kroll et al., 2017; Bose et al., 2018). CMs are natural-source ingredients that can be coated onto nanoparticles to produce CM-coated nanoparticles (CMNPs) with cell-like behaviors. The nanoparticle core can protect various therapeutic cargos *via* its high structural integrity and stability. In addition, CMs can provide CMNPs with prolonged circulation time, targeting ability, and other source cell properties. For instance, red blood cell (RBC) membrane could be used for immune evasion and prolonging circulation time. White blood cell (WBC) membranes could be employed to camouflage nanoparticle for evading opsonization and reticuloendothelial system (RES) clearance and targeting inflamed sites. Cancer cell membrane (CCM) could act as the tumor-targeting navigator and the source of tumor-associated antigens (TAAs). In **Table 1**, we summarize various CM-coated nanoparticles developed for cancer diagnosis and treatment. In this review, we provide an overview of CMNP-based DDSs as tumor diagnostic and therapeutic agents and discuss potential clinical applications (**Scheme 1**).

CHEMOTHERAPY

Chemotherapy is a class of traditional cancer treatments with broad clinical implementation. Classic chemotherapy can interfere with cell proliferation to achieve cancer treatment. Systemic toxicity and low bioavailability have always been disadvantages that limit further application of chemotherapy. Furthermore, many chemotherapeutic drugs are hydrophobic, which can lead to poor absorption and bioavailability. New chemotherapeutics and existing chemotherapeutics with new formulations have recently been developed to address these limitations (Qi et al., 2017; Guo et al., 2018). Application of nanomaterials as chemotherapeutic DDSs has also been studied frequently. Therapeutic efficacy has been enhanced using nanoparticle-based DDSs. Various CMs have been coated onto nanoparticle surfaces in order to improve the biocompatibility, targeting ability, and circulation time of nanoparticles loaded with chemotherapeutic drugs.

CCM is commonly coated on nanoparticles to endow them with prolonged blood circulation, effective immune escape, and homologous targeting ability. Xu et al. prepared CCM-coated NPs by coating poly(lactide-co-glycolide)-doxorubicin (PLGA-DOX) NPs with HepG2 cell-derived CCM. The resulting CCM-coated nanoparticle size and zeta potential were approximately 100 nm and −29.49 mV, respectively. Due to the tumor specificity derived from homologous binding to CCM molecules, these biomimetic nanoparticles significantly enhanced the cellular endocytosis of DOX toward HepG2 cells when compared to nanoparticles without CCM *in vitro*. Compared to free DOX, the CCM-coated NPs exhibited enhanced antitumor efficacy and reduced system toxicity in HepG2 xenograft mouse models. They benefited from prolonged circulation, immune evasion, and enhanced DOX accumulation at the tumor site (Xu et al., 2019). Tian et al. produced polymer NPs that were co-loaded with hemoglobin (Hb) and DOX and camouflaged with CCM. The resulting nanoparticles exhibited high tumor-targeting capacities. In addition, the nanoparticles could suppress the expression of a series of genes such as hypoxia-inducible factor-1α to abate the exocytosis of DOX, a property that may lead to safe, efficient chemotherapy (Tian et al., 2017).

Blood cells include erythrocytes, leukocytes, and platelets and also serve as possible membrane vehicles for CM-coated NPs. Several studies consider blood cell membrane-coated NPs for cancer chemotherapy. Zhang et al. reported RBC membrane (RBM)-coated, DOX-loaded poly(lactic acid) (PLA) NPs. In this study, the authors compared two strategies (physical encapsulation and chemical conjugation) for loading DOX into the PLA NPs. For physical encapsulation, DOX was loaded into the PLA NPs *via* nanoprecipitation. In chemical conjugation, ring-opening polymerization was performed to produce a DOX-PLA polymer conjugate. The resulting DOX-PLA polymer conjugate was added to an aqueous phase to produce nanoparticles. The chemical conjugation strategy led to higher drug loading and more sustained drug release. Furthermore, RBM-coated DOX-loaded NPs exhibited higher toxicity toward acute myeloid leukemia cells than free DOX (Aryal et al., 2013). WBC membranes were shown to act as camouflaged surfaces that help to evade opsonization and RES clearance, as well as inflamed site-targeting navigators. This characteristic may

TABLE 1 | The antitumor application of various CM-coated nanoparticles.

Therapeutic strategies	Membrane coat	Core nanoparticle	Tumor model	Reference
Chemotherapy	CCM derived from HepG2 cell	PLGA-DOX	HepG2 cell	(Xu et al., 2019)
	CCM derived from MCF-7 cell	PLGA-DOX and Hb	MCF-7 cell	(Tian et al., 2017)
	RBM	PLA-DOX	Kasumi-1 cell	(Aryal et al., 2013)
	Monocyte cell membrane	PLGA-DOX	MCF-7 breast cancer cell	(Krishnamurthy et al., 2016)
	Macrophage membrane	Cationic 2-aminoethyldiisopropyl group (PPiP)-functionalized PEGylated poly(β-amino ester)-PTX	MDA-MB-231 breast cancer cell	(Zhang et al., 2018)
	PM	Nanovehicle-DOX and tumor necrosis factor (TNF)-related apoptosis inducing ligand (TRAIL)	MDA-MB-231 breast cancer cell	(Hu et al., 2015)
	Composite cell membrane (derived from leukocytes and HN12 tumor cell)	Liposomal nanoparticles-PTX	HN12 head and neck tumor cell and B16 melanoma cell	(He et al., 2018)
	4T1 cell- derived CCM	MSN-DOX and ICG	4T1 breast cancer cell	(Ding et al., 2019)
	RBM	MB and Pt loaded gelatin nanogel core (MPNGs)	4T1 breast cancer cell	(Zhai et al., 2018)
	RBM	Hollow mesoporous PB nanoparticles-DOX	4T1 breast cancer cell	(Chen et al., 2017a)
Immunotherapy	Composite cell membrane (derived from leukocytes and platelet)	IMBs	Blood samples of breast cancer patients	(Rao et al., 2018)
	Neutrophil membrane	PLGA nanoparticles-Carfilzomib	4T1 breast cancer cell	(Kang et al., 2017)
	CCM derived from B16-OVA cell	PLGA nanoparticle-R837	B16-OVA cancer cell	(Yang et al., 2018)
	CCM derived from RM-1 cell	PLGA nanoparticle-R837	RM-1 prostate cancer cell	(Li et al., 2019)
	RBM	BPQDs	4T1 breast cancer cell	(Liang et al., 2019)
	CCM derived from surgical 4T1 tumors	BPQDs	4T1 breast cancer cell	(Ye et al., 2019)
Photothermal therapy	Macrophage membrane	Fe_3O_4 nanoparticle	MCF-7 human breast cancer cell	(Meng et al., 2018)
	Composite cell membrane (derived from RBCs and MCF-7 cancer cell)	Melanin nanoparticle	MCF-7 human breast cancer cell	(Jiang et al., 2019)
	HA-decorated RBM	PB nanoparticle-CS-6	MDA-MB-231 cell	(Liu et al., 2019)
	Composite cell membrane (derived from RBCs and B16-F10 melanoma cell)	Hollow copper sulfide nanoparticles-DOX	B16-F10 melanoma cell	(Wang et al., 2018)
	RBM	Poly(caprolactone)-ester endcap polymer (PCL) nanoparticle-PTX	4T1 breast cancer cell	(Su et al., 2016)
	RBM	Hollow mesoporous PB nanoparticles-DOX	4T1 breast cancer cell	(Chen et al., 2017a)
	Anti-EpCam antibody-modified RBM	Gold nanoparticle-PTX	4T1 breast cancer cell	(Zhu et al., 2018)
	RBM	BPQDs	4T1 breast cancer cell	(Liang et al., 2019)
Photodynamic therapy	RBM	$NaYF_4$:Yb/Er UCNP	B16 melanoma cell	(Ding et al., 2015)
	PM	PLGA nanoparticle-verteporfin	4T1 breast cancer cell	(Xu et al., 2018)
	STM	β-NaYF4:Yb^{3+}, Er^{3+} UCNP	HeLa human cervical cancer cell	(Gao et al., 2016)
	CCM derived from 4T1 cancer cell	C16-K(PpIX)RRKK-PEG-COOH	4T1 breast cancer cell	(Qiu et al., 2018)
	CCM derived from SGC7901 cell	CM/SLN/Ce6	SGC7901 cell	(Yang et al., 2019)
	RBM	Methoxypoly(ethylene glycol)-block-poly(D,L-lactide) (PEG-bPDLLA)-PTX and TPC	HeLa human cervical cancer cell	(Pei et al., 2018)
	CCM derived from 4T1 cancer cell	MOF-GOx and catalase	4T1 breast cancer cell	(Li et al., 2017)
	CCM derived from SMMC-7721 cell	Polyethyleneimine (PEI)-modified, styrene (St), and acrylic acid (AA)-crosslinked SPIO NP	SMMC-7721 cell	(Li et al., 2018a)
	Activated fibroblast	Poly-(cyclopentadithiophene-alt-benzothiadiazole) nanoparticle	4T1 breast cancer cell	(Li et al., 2018b)
In vivo imaging	RBM	Fe_3O_4 NP	–	(Rao et al., 2016b)
	STM	SPIO NP	TRAMP-C1 mouse prostate cancer cell	(Lai et al., 2015)
	RBM	^{99m}Tc-labeled EMs	–	(Gangadaran et al., 2018)
	CCM derived from 4T1 cancer cell	^{89}Zr-labeled multicompartment membrane-derived liposomes-tetrakis(4-carboxyphenyl) porphyrin	4T1 breast cancer cell	(Yu et al., 2018)
	CCM derived from MDA-MB-435 human breast cancer cell, DU 145 human prostate cancer cell, CAL 27 human squamous cancer cell, and HCT 116 human colorectal cancer cell	β-$NaYF_4$:Er^{3+}, Yb^{3+} UCNP	MDA-MB-435 human breast cancer cell, DU 145 human prostate cancer cell, CAL 27 human squamous cancer cell, and HCT 116 human colorectal cancer cell	(Rao et al., 2016a)
	CCM derived from HeLa cancer cell	Two-photon excited (TPE)-NIR nanoprobe	HeLa human cervical cancer cell	(Lv et al., 2018)
	CCM derived from MCF-7 cancer cell	PLGA nanoparticle-ICG	MCF-7 human breast cancer cell	(Chen et al., 2016b)
	RBM	RBM nanoparticle-DOX	HeLa human cervical cancer cell	(Xiao et al., 2019)

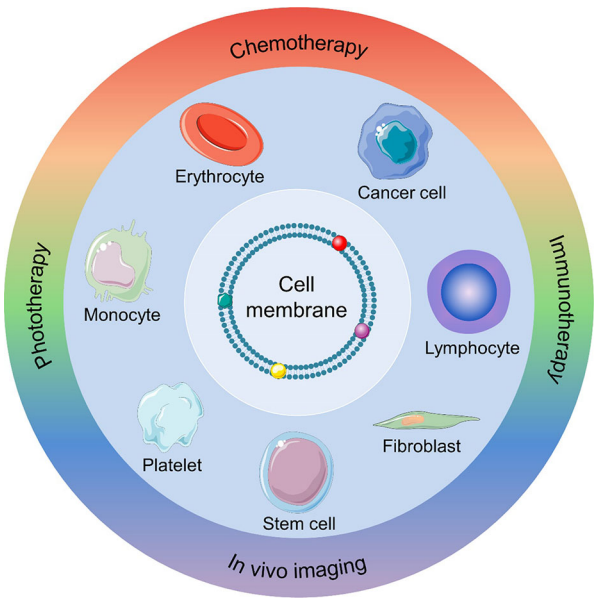

SCHEME 1 | Schematic illustration of a nanocarrier-assisted cell membrane designed for cancer diagnosis and treatment.

endow WBC membrane-coated NPs with the ability to target some tumors (Fang et al., 2018). Thus, numerous WBC membrane-coated NPs have been developed for cancer chemotherapy, including monocyte cell membrane-coated PLGA NPs (Krishnamurthy et al., 2016), macrophage membrane-coated NPs (Zhang et al., 2018), platelet membrane (PM)-coated core-shell nanovehicles (Hu et al., 2015), and composite CM (derived from leukocytes and tumor cells)-camouflaged liposomal NPs (He et al., 2018). For instance, it was reported that macrophage-membrane-coated NPs could perform step-by-step release of Paclitaxel (PTX) in response to the tumor microenvironment, resulting in tumor-targeting chemotherapy. Macrophage membranes with membrane molecules that exhibit inflammatory tumor-homing abilities were coated onto the nanoparticles. After injection, the macrophage membrane-coated nanocarriers could evade immune clearance and achieve tumor targeting. In an extracellular microenvironment, the nanoparticles could discharge from the outer membrane and further be taken up by cancer cells with help from the targeting peptide on the nanoparticle surface. Then, PTX could be released from the nanoparticles in response to the acidic environment of the endosome. This macrophage-membrane-coated nanoparticle exhibited potent antitumor efficacy (**Figure 1**) (Zhang et al., 2018).

Use of CM-coated NPs to co-deliver chemotherapy drugs and photothermal agents has been studied for cooperative cancer therapy. Ding et al. exploited CCM to enhance the tumor-targeting ability of anticancer drug-loaded mesoporous silica nanoparticles (MSNs). MSNs were co-loaded with indocyanine green (ICG) and DOX, which are a near-infrared photothermal agent and a chemotherapy drug, respectively. CCM was coated onto drug-loaded MSNs to produce CCM-coated MSNs. The CCMs reduced drug leakage during delivery and accumulated at the tumor site efficiently. The photothermal effect of ICG led to CCM fusion and thus accelerated DOX release. This type of CCM-coated MSN could achieve synergistic treatment *via* chemotherapy and photothermal therapy (Ding et al., 2019). Similarly, Zhai et al. developed a cytotoxic T lymphocyte (CTL)-inspired nanovesicle (MPV) with a RBC membrane-derived shell. The CM-coated MPV possessed a gelatin nanogel core, which was co-loaded with methylene blue (MB) and cisplatin (Pt). The CM-coated MPV could achieve deep tumor penetration and produce hyperthermia when stimulated *via* laser irradiation. In addition, photoacoustic imaging (PAI) could be employed to monitor MPV accumulation after injection. Local irradiation could then be used at the time of maximum accumulation at tumor sites. The combination of localized hyperthermia and chemotherapy led by CM-coated MPV inhibited tumor progression while maintaining low systemic toxicity (Zhai et al., 2018). RBM-decorated hollow mesoporous Prussian blue (PB) NPs were also employed for cooperative cancer therapy. These nanoparticles also encapsulated a large quantity of DOX. The authors found that this type of nanoparticle exhibited synergistic photothermal-chemotherapeutic anticancer properties with low toxicity and high efficacy (Chen et al., 2017a).

IMMUNOTHERAPY

Cancer immunotherapy can inhibit tumor progression by stimulating immune responses (Li et al., 2018c). In 1986, recombinant interferon-α (IFN-α) became the first immunotherapeutic agent marketed for hairy cell leukemia. After 6 years, recombinant interleukin-2 (IL-2) was also proven effective for metastatic renal cancer by the US Food and Drug Administration (FDA) (Ribas and Wolchok, 2018). Unfortunately, the short half-life of IL-2 can result in serious adverse effects such as vascular leak syndrome. Recent cancer immunotherapy strategies have focused on inducing specific antitumor immune responses. Sipuleucel-T (an autologous active cellular immunotherapy) has been used clinically since 2010. Checkpoint blockade cancer immunotherapies such as cytotoxic T lymphocyte antigen 4 antibody (anti-CTLA-4) and programmed cell death 1 antibody (anti-PD-1) were also demonstrated for clinical applications (Riley et al., 2019). Even though substantial advances have been achieved in cancer immunotherapy, exploring a preventive or therapeutic agent that controls modulation of the immune system, low systemic toxicity, and high antitumor efficiency remains a challenge in cancer immunotherapy applications. This is because such therapeutic agents exhibit serious adverse effects such as nonspecific inflammation and autoimmunity (Qian et al., 2018; Riley et al., 2019). Several strategies have been used to improve therapeutic efficacy and reduce side effects in order to manage cancer immunotherapy in a more controlled

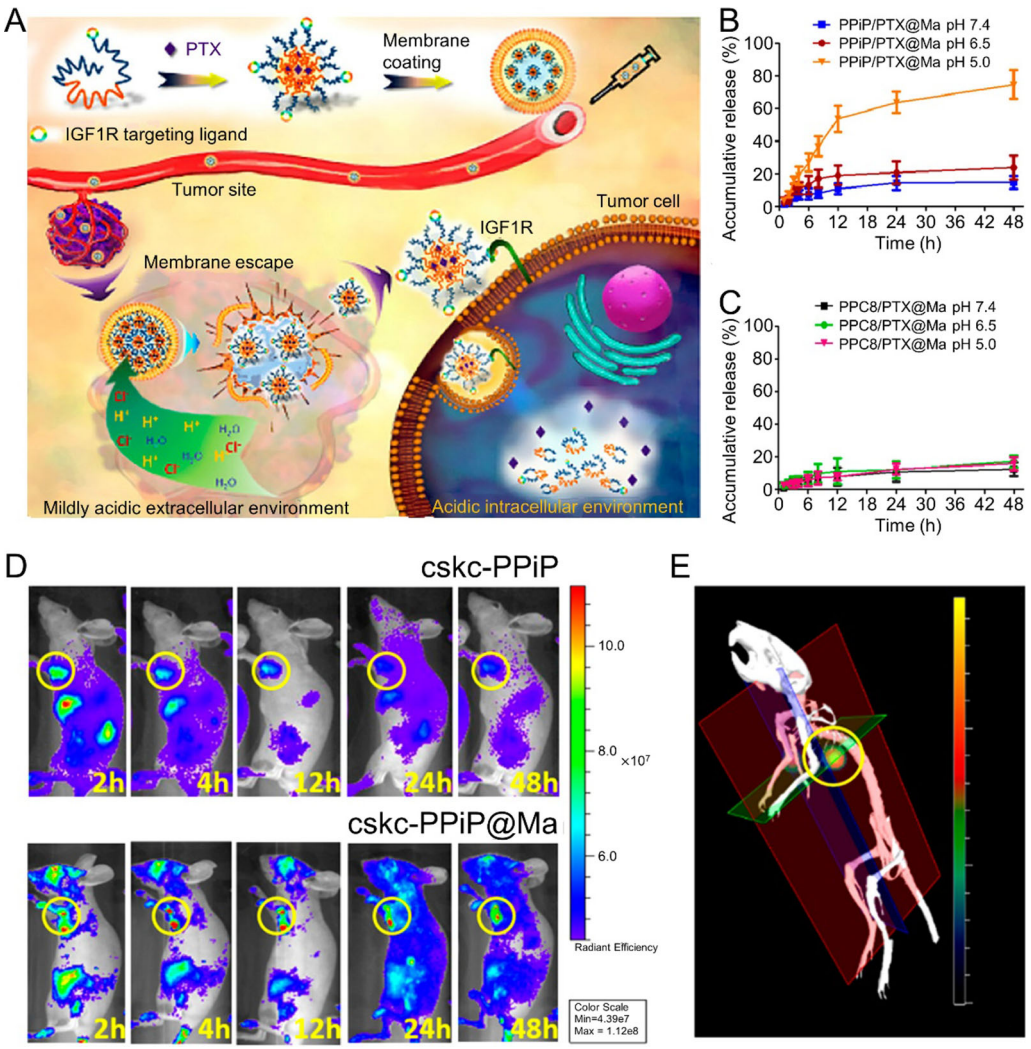

FIGURE 1 | (A) Schematic illustrations of membrane-coated nanoparticle synthesis, membrane escape, and drug-release mechanisms. Cumulative drug-release profile of **(B)** PPiP/PTX@Ma and **(C)** PPC8/PTX@Ma in various pH environments. **(D)** *In Vivo* imaging system images of mice after injection of near-infrared probe-loaded cskc-PPiP and cskc-PPiP@Ma at different times. **(E)** 3D reconstruction of the 48 h fluorescence signal of a cskc-PPiP@Ma group. Reproduced with permission from (Zhang et al., 2018). Copyright @ American Chemical Society.

manner. Nanoparticle-based DDS can protect immune-related components during circulation and deliver TAAs and immune-modulating agents efficiently. Furthermore, some types of nanoparticle-based DDSs can achieve controlled drug release in response to stimuli like pH in order to harness immunotherapy and reduce systemic toxicity (Li et al., 2018c; Qian et al., 2018). A range of CMs can be used on nanoparticle surfaces to enhance the delivery efficacies of antigens and immune-modulating molecules. In the study reported by Lang et al., platelet and WBC membranes were blended and then coated onto immunomagnetic beads (IMBs). The resulting nanoparticles (HM-IMBs) were modified with anti-epithelial cell adhesion molecules (anti-EpCAMs). The PLT-WBC hybrid membranes could enhance tumor cell binding ability and reduce the homologous leukocyte interaction of the resulting nanoparticles. This can be employed to isolate circulating tumor cells efficiently. Upon testing spiked blood samples, it was found the HM-IMBs exhibited a cell separation efficiency of 91.77%, which compares favorably to 66.68% for IMBs. The cell purity of the HM-IMBs was 96.98%, which is much higher than that of the IMBs (66.53%). HM-IMBs also proved effective in detection of PIK3CA gene mutations (Rao et al., 2018). Similarly, neutrophil-membrane-coated PLGA NPs (NM-NPs) were also developed. The authors found that NM-NPs exhibited enhanced circulating tumor cell (CTC)-capture efficiency *in vivo*. Carfilzomib-loaded NM-NPs could deplete CTCs during circulation and prevent early metastasis (Kang et al., 2017).

CCM not only acts on the nanoparticle surface to enhance cargo delivery efficacy but also can be the source of multiple tumor-specific antigens, which are the components of antitumor

vaccines. Yang et al. developed CCM-coated PLGA NPs that were loaded with imiquimod (R837). The resulting CCM-coated nanoparticles were further modified with mannose moiety. This nanovaccine exhibited improved uptake by antigen present cells (APCs), which can induce a potent antitumor immune response. When acting as a therapeutic vaccine, the nanovaccine exhibited efficient therapeutic efficacy when combined with checkpoint-blockade therapy (**Figure 2**) (Yang et al., 2018). Furthermore, Manolova et al. found that the nanoparticle size could influence *in vivo* particle migration (Manolova et al., 2008). Li et al. prepared immunoadjuvant-loaded multiantigenic NPs (MANPs/R837) with various diameters. Smaller CCM-coated PLGA NPs exhibited more efficient delivery of antigens and R837 to APCs in draining lymph nodes (LNs) to induce a stronger antitumor immune response. When combined with checkpoint blockade therapy such as the anti-PD1 strategy, MANPs/R837 (especially smaller MANPs/R837) exhibited enhanced tumor progression inhibition (Li et al., 2019).

Synergistic treatment that combines immunotherapy with photothermal therapy or chemotherapy *via* nanoparticle-based DDSs has developed rapidly. Antitumor immune response can be induced *via* photothermal therapy, which can generate TAAs near ablated tumor cells. When photothermal therapy was combined with immunotherapy *via* nanoparticle-based DDSs, potent vaccine-like behavior by therapeutic agents could elicit the elimination of residual and metastatic tumor cells (Chen et al., 2016a). For instance, Liang et al. reported a biomimetic black phosphorus quantum dot (BPQD) formulation that could induce tumor ablation *via* near-infrared (NIR) laser irradiation to elicit an antitumor immune response that further inhibited tumor progression, metastasis, and rechallenge. RBMs were coated onto BPQDs (BPQD-RMNVs) to prolong circulation time and promote tumor accumulation. Moreover, the combination of BPQD-RMNVs and the PD-1 antibody could induce an enhanced antitumor immune response to eliminate cancer cells (Liang et al., 2019). In another study, the authors obtained CCMs *via* surgical removal of tumors. The resulting CCMs were then coated onto BPQDs to get BPQD-CCNVs. BPQD-CCNVs, granulocyte-macrophage colony-stimulating factor (GM-CSF), and lipopolysaccharide (LPS) were loaded into a thermosensitive hydrogel (Gel-BPQD-CCNVs). Dendritic cells (DCs) could be recruited by the GM-CSF released from Gel-BPQD-CCNVs to uptake TAAs. NIR irradiation and LPS could then induce DC maturation.

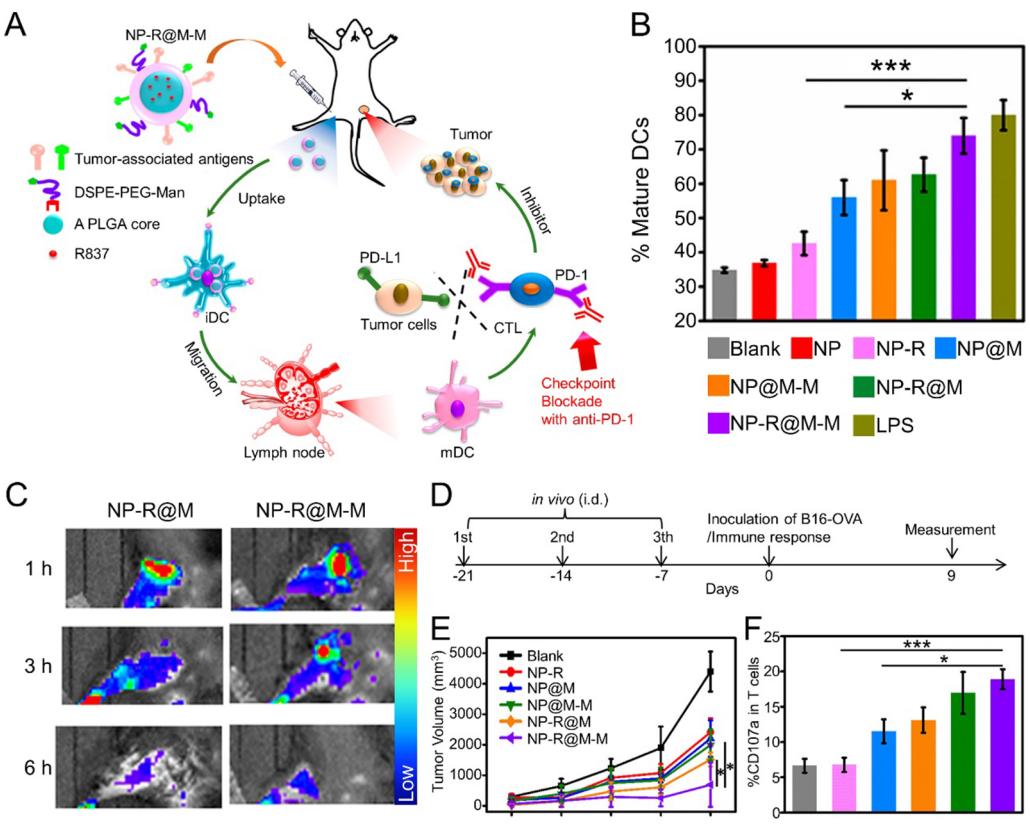

FIGURE 2 | (A) Schematic illustration to demonstrate the structures of CCM-coated, R837-loaded, mannose-modified PLGA nanoparticles (NP-R@M-M) and their immune-stimulant functions as a nanovaccine. **(B)** *In vitro* DC activation by various nanovaccine formulations. **(C)** *In vivo* fluorescence images of mouse hind legs after intradermal injection of fluorescent-labeled NP-R@M or NP-R@M-M at three different times. **(D)** Schematic illustration of a tumor challenge experimental design. **(E)** B16-OVA tumor volume curves after pretreatment with various nanovaccine formulations ($n \geq 5$). **(F)** Percentages of CD107a+ cells among all T cells. (***$P < 0.001$, *$P < 0.05$). Reproduced with permission from (Yang et al., 2018). Copyright @ American Chemical Society.

The mature DCs traveled through lymphatic capillaries to LNs to induce a potent antitumor immune response. This synergistic treatment strategy could be combined with checkpoint blockade treatment to improve the antitumor efficacies of tumor-specific CD 8+ T cells (Ye et al., 2019). Similarly, chemoimmunotherapy was proven efficient for cancer treatment. In chemoimmunotherapy, low doses of chemotherapeutic agents can induce immunogenic cell death (ICD) of tumor cells to release TAAs, thus avoiding severe side effects. Immunomodulatory agents can enhance antigen presentation and induce APC and cytotoxic CD8+ T cell maturation. Thus, use of nanoparticle-based DDSs to perform a combination of chemotherapy and immunotherapy was studied and proven efficient (Calleja et al., 2017; Feng et al., 2019). It was reported that a dual pH-responsive multifunctional DDS based on poly(L-histidine) and hyaluronic acid was designed for the delivery of resiquimod (R848, a TLR7/8 agonist) and DOX to achieve synergistic effects of immunotherapy and chemotherapy against breast cancer (Liu et al., 2018). Furthermore, excellent treatment effects might be achieved when CMs are employed to improve the delivery efficacies of synergistic therapeutic nano-agents.

PHOTOTHERAPY

Phototherapy is an effective, noninvasive cancer treatment strategy (Chen et al., 2017b). Phototherapy can be initiated *via* laser irradiation to induce selective, localized therapeutic effects. Photothermal therapy (PTT) and photodynamic therapy (PDT) are the two major categories of phototherapy (Vijayan et al., 2018).

Photothermal Therapy

PTT uses heat ablation generated *via* light-absorbing agents to execute a new, minimally invasive cancer treatment strategy with low systemic toxicity (Chen et al., 2016a). With the development of nanotechnology, it was found that nanoparticle-based DDS could improve therapeutic agent tumor accumulation and the bioavailabilities of water-insoluble cargos. Thus, a large range of nanoparticle-based DDSs have been employed to enhance the delivery efficacies of the light-absorbing agents needed for PTT. CM-coated NPs were recently employed to further improve PTT agent delivery and enhance the therapeutic efficacy of PTT. Meng et al. developed a macrophage membrane-coated magnetic iron oxide NP (Fe_3O_4@MM NP) that exhibited excellent biocompatibility, prolonged circulation time, tumor-targeting ability, and effective PTT for breast cancer *in vivo* (Meng et al., 2018). RBC-cancer cell hybrid membranes can also be employed to camouflage melanin NPs, producing Melanin@RBC-M in order to improve therapeutic PTT efficacy. RBMs can prolong nanoparticle circulation times and CCMs can endow nanoparticles with tumor-targeting abilities. The authors studied the delivery efficacy of Melanin@RBC-M formulations with various RBM-to-CCM ratios. The *in vivo* biodistribution and therapeutic efficiency were investigated after intravenous injection of various therapeutic formulations into MCF-7 tumor-bearing athymic nude mice. Melanin@RBC-M with a 1:1 membrane protein weight ratio of RBMs to CCMs exhibited better delivery efficacy and a more potent PTT effect than formulations with other membrane protein weight ratios. Moreover, the authors found that Melanin@RBC-M exhibited an enhanced photoacoustic signal when the nanoparticle size increased from 64 to 148 nm. The photoacoustic amplitude increased linearly with the nanoparticle concentration in the 680 to 800 nm excitation wavelength range. This phenomenon could be employed to quantify Melanin@RBC-M *in vivo* (Jiang et al., 2019).

In addition, PTT can be used therapeutically in combination with chemotherapy or immunotherapy. Liu et al. used hyaluronic acid (HA)-decorated, RBM-camouflaged PB NPs to carry gamabufotalin (CS-6). The study showed that RBM can prolong the circulation time to about 10 h and enhance immune evasion ability. This nanotherapeutic agent could accumulate at tumor sites efficiently because of the HA. Meanwhile, CS-6 exhibited potent antitumor efficacy by inhibiting the expression of HSP70, which can weaken the PTT effect. The resulting nanoparticles exhibited synergistic photothermal-chemotherapy leading to potent *in vivo* antitumor efficacy (Liu et al., 2019). In another study, RGD peptide [c(RGDyC)]-modified platelet vesicles were employed to co-load melanin nanoparticles (MNPs) and DOX to achieve chemo-photothermal therapy for drug-resistant tumors (Jing et al., 2018). In addition, numerous CM-coated NPs have been developed for cancer photothermal-chemotherapy including RBC-melanoma cell hybrid membrane-coated, DOX-loaded hollow copper sulfide nanoparticles (Wang et al., 2018); RBC-camouflaged, PTX-loaded polymeric NPs (Su et al., 2016); RBC-mimetic hollow mesoporous PB NPs (Chen et al., 2017a); and RBC-coated, PTX-loaded gold nanocages (Zhu et al., 2018). Furthermore, synergistic treatment using PTT and immunotherapy was investigated. Liang et al. prepared RBM-coated BPQD (BPQD-RMNV) for combined cancer photothermal- and immunotherapy. Cancer progression and metastasis were substantially delayed *via* improved infiltration of CD8+ T cells into the tumor site when the BPQD-RMNV-mediated treatment was combined with checkpoint blocked therapy (Liang et al., 2019).

Photodynamic Therapy

PDT can generate singlet oxygen to kill cancer cells when a photosensitizer (PS) is excited by a specific wavelength of light (Feng et al., 2017). RBM (Ding et al., 2015), PM (Xu et al., 2018), stem-cell membrane (Gao et al., 2016), and CCM (Qiu et al., 2018)-coated NP delivery systems were employed to carry PDT agents for cancer treatment. Ding and his colleagues developed an RBM-camouflaged upconversion NP (UCNP). The inner cores were loaded with merocyanine 540 (MC540) and the RBM surface was decorated with targeting moieties including folate (FA) and the triphenylphosphonium (TPP) cation. This formulation could generate $^1O_2$ under 980 nm irradiation. Meanwhile, the resulting RBM-coated nanovectors could

improve singlet oxygen infiltration relative to PDT agents with other surface coatings because of the unique nature of RBC as an oxygen (O_2) carrier. The combination of the RBM coating and targeting ability significantly enhanced the PDT therapeutic efficiency (Ding et al., 2015). In another study, a PM-coated, verteporfin-loaded photodynamic NP (NP-Ver@P) was developed. P-selectin on a platelet surface could specifically bind with the CD44 receptor that is heavily expressed on cancer cell surfaces. Thus, PM could endow the nanoparticle with long circulation times, good targeting ability, and a higher tumor uptake rate than RBM. Under 680–730 nm solar irradiation, NP-Ver@P exhibited a therapeutic effect against tumors without damaging skin at tumor sites (Xu et al., 2018). CCM-coated NPs have attracted significant attention due to their homologous targeting capabilities. Yang reported coating CCM onto chlorins e6 (Ce6)-loaded silica NPs (CM/SLN/Ce6). CM/SLN/Ce6 exhibited excellent stability in physiological conditions and homologous targeting ability. The aforementioned features make CM/SLN/Ce6 a promising cancer-targeting PDT platform (Yang et al., 2019).

Cooperative therapy that combines PDT with other cancer treatment strategies has been studied widely. Pei et al. reported RBM-coated NPs (RBC(M(TPC-PTX))) for PDT combined with chemotherapy. Reactive oxygen species (ROS)-responsive PTX dimer (PTX_2-TK) and 5,10,15,20-tetraphenylchlorin (a type of photosensitizer, TPC) were used to compose the inner core. Light could cause TPC to generate ROS for PDT. The resulting ROS could also elicit PTX_2-TK cleavage, releasing PTX for chemotherapy. In this platform, PDT and chemotherapy were integrated to achieve high drug loading capabilities and light-induced drug release. Synergetic treatment with PDT and chemotherapy improved antitumor efficacy and on-demand PTX release reduced systemic toxicity (**Figure 3**) (Pei et al., 2018). In another study, a CCM-coated porphyrin metal-organic framework (MOF) was used to load glucose oxidase (GO_x) and catalase. After accumulating at tumor sites efficiently, the resulting nanoparticles could enhance singlet oxygen production and intracellular glucose decomposition by catalyzing endogenous hydrogen peroxide (H_2O_2) to produce O_2. Furthermore, this O_2 could promote singlet oxygen production. Induced cooperative therapy using PDT and starvation treatment could inhibit tumor progression efficiently (Li et al., 2017). Furthermore, MR/NIR fluorescence dual-modal imaging could be combined with PDT *via* a CCM-coated nanoparticle delivery system. In a study reported by Li et al., Ce6-loaded magnetic nanobeads were camouflaged using CCM to get SSAP-Ce6@CCM, which exhibited excellent PDT efficacy and MR/NIR fluorescence imaging ability under 670 nm laser irradiation. SSAP-Ce6@CCM might be a promising theranostic platform for tumor treatment (Li et al., 2018a). Li et al. reported a cancer-associated fibroblast cell membrane-coated polymer NP (AF-SPN). AF-SPN demonstrated homologous targeting ability derived from the activated fibroblast cell membrane and used it to target cancer-associated fibroblasts. The AF-SPN core structure is made from poly(cyclopentadithiophene-alt-benzothiadiazole), which is an NIR-absorbing, semiconducting polymer. Thus, AF-SPN can accumulate at tumor sites to induce enhanced NIR fluorescence and PTT and PDT effects for cancer treatment (Li et al., 2018b).

IN-VIVO IMAGING

In addition to acting as therapeutic drug delivery systems, CM-based NPs are also employed in biomedical imaging applications such as magnetic resonance imaging (MRI), computed tomography (CT), and fluorescence imaging.

Fe_3O_4 NPs are a type of novel functional material with low systemic toxicity, high stability, good biocompatibility, and the ability to act as magnetic resonance imaging (MRI) contrast agents (Ren et al., 2016). The delivery efficacies of Fe_3O_4 NPs improve when combined with a CM-based membrane. Rao prepared magnetic Fe_3O_4 NPs camouflaged with RBM (Fe_3O_4@RBC NP). RBM clearly reduced the Fe_3O_4 NP RES uptake. Fe_3O_4@RBC NPs exhibited excellent potential for MRI and drug delivery applications (Rao et al., 2016b). In addition to MRI applications, superparamagnetic iron oxide NPs (SPIO NPs) were also used for magnetic hyperthermia therapy by their photothermal conversion abilities. Lai et al. prepared stem cell membrane (STM)-coated SPIO NPs for tumor theranostic applications. STM-SPIO NPs acted as potential MRI agents and exhibited excellent magnetization (65.9 emu g^{-1}) and dose-dependent T2-weighted imaging contrast (R2 = 653.3 s^{-1} mM^{-1}) *in vitro*. Furthermore, STM-SPIO NPs also exhibited magnetic hyperthermia capabilities for cancer treatment (Lai et al., 2015).

Radiolabeled nanocarriers derived from CMs have been studied frequently for non-invasive imaging. Radiolabeled exosome mimetics (EMs) made from RBCs have been used for *in vivo* imaging. RBC-EMs were labeled with technetium-99m (^{99m}Tc- RBC-EMs) and exhibited nearly 100% radiochemical purity until 2 h had passed. Furthermore, ^{99m}Tc- RBC-Ems exhibited higher liver and spleen uptakes, but no thyroid uptake, unlike free ^{99m}Tc (Gangadaran et al., 2018). In another study, Yu et al. developed ^{89}Zr-labeled multicompartment membrane-derived liposomes (MCLs). MCLs derived from CCMs were loaded with tetrakis(4-carboxyphenyl) porphyrin. The resulting ^{89}Zr-Df-MCLs were used for non-invasive quantitative tracing *via* positron emission tomography (PET) imaging and PDT *in vivo*. ^{89}Zr-Df-MCLs demonstrated good radiochemical stability, tumor-targeting ability, and long-term, effective PDT, as well as low systemic toxicity. Specifically, ^{89}Zr-Df-MCLs achieved rapid, highly sensitive LN localization (Yu et al., 2018).

Fluorescence imaging is one of the most efficient cancer imaging strategies used in biological studies and clinical applications (Rao et al., 2016a). Rao and his colleagues prepared a CCM-cloaked UCNP (CC-UCNP) that exhibited prolonged blood circulation, immune escape ability, and homologous targeting ability. CC-UCNPs could convert NIR fluorescence into visible light and be used for *in vivo* tumor imaging. They also exhibited potential for tumor diagnosis and

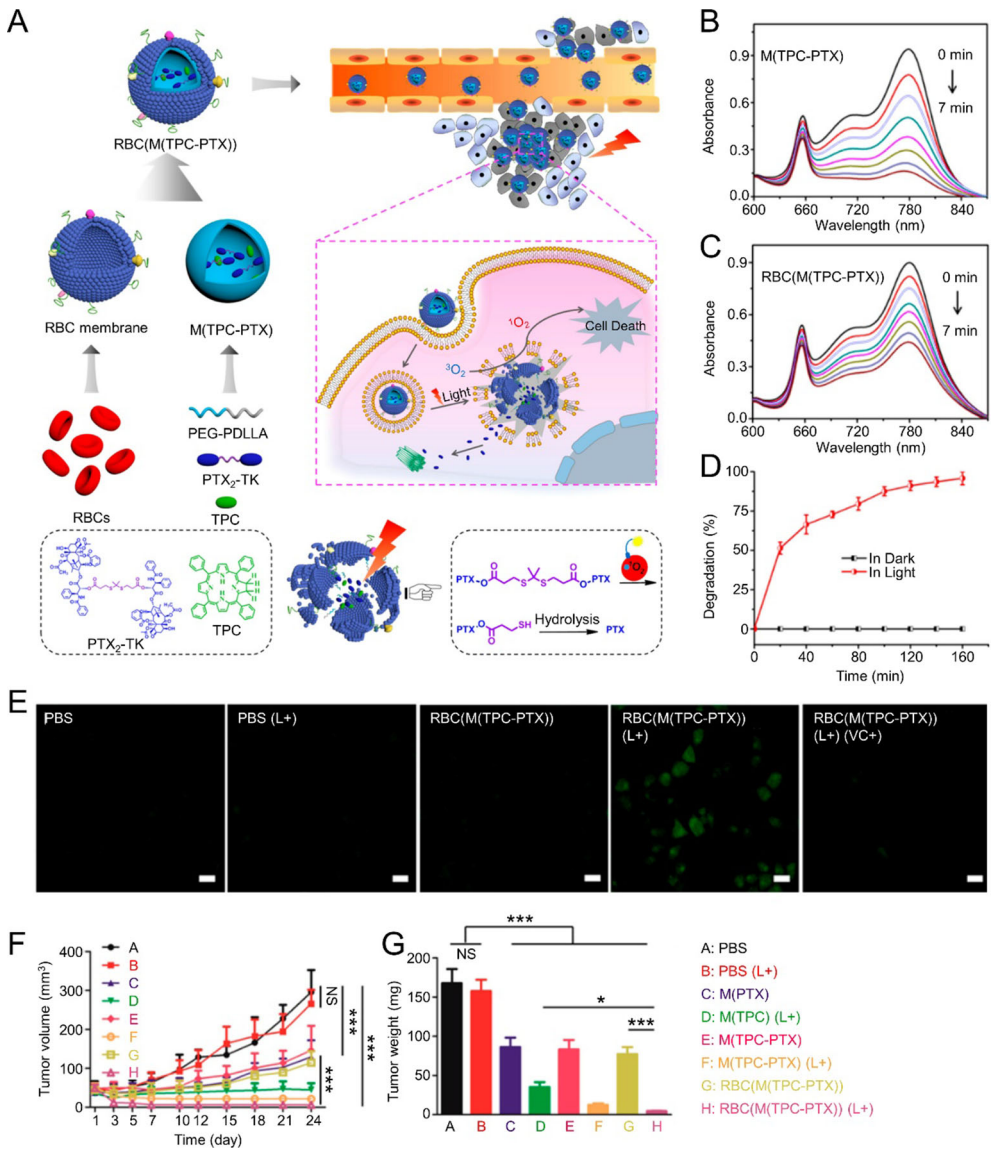

FIGURE 3 | (A) Schematic illustration of RBC(M(TPC-PTX)) light-triggered, on-demand drug release for a combination of PDT and chemotherapy. Time-dependent UV absorption spectra of ICG in **(B)** M(TPC-PTX) and **(C)** RBC(M(TPC-PTX)) solutions under 638 nm irradiation (100 mW/cm^2) for 7 min. **(D)** Degradation of PTX_2-TK in RBC(M(TPC-PTX)) under 638 nm irradiation (100 mW/cm^2) over time. **(E)** Generation of intracellular ROS in HeLa cells incubated with various therapeutic formulations. Scale bar = 20 μm. **(F)** Tumor volume curves after treatment with various therapeutic strategies (n = 6). **(G)** Quantitative analysis of tumor weights among various groups. (***P < 0.001, *P < 0.05). Reproduced with permission from (Pei et al., 2018). Copyright @ American Chemical Society.

treatment (**Figure 4**) (Rao et al., 2016a). Biomimetic fluorescent nanoprobes were developed in another study. These could convert NIR radiation ($\lambda_{max} \approx 720$ nm) into 800 nm light. The nanoprobes exhibited ideal NIR-incoming-NIR-outgoing fluorescence features. The CCM surface imparted the nanoprobes with excellent biocompatibilities and homologous targeting abilities (Lv et al., 2018). Fluorescence imaging could be combined with other treatment strategies using the CM-based delivery system. Chen et al. reported a CCM-camouflaged, ICG-loaded NP as a theranostic nanoplatform (ICNPs). The ICNPs exhibited tumor-targeting abilities derived from the CCM, fluorescence and PAI, and PTT. Benefiting from fluorescence-photoacoustic dual imaging and PTT, ICNPs could achieve real-time tumor monitoring with high spatial resolution and effective tumor treatment (Chen et al., 2016b). In addition to ICG, PB (Xiao et al., 2019), and Ce6 (Li et al., 2018a) were tested in combination with other agents using CM-based nanoplatforms in order to support a theranostic strategy. For instance, Xiao et al. developed RBM-coated, DOX-loaded PB NPs that were modified with FA. The resulting nanoparticles could achieve chemo-photothermal therapy alongside tumor fluorescence and PAI (Xiao et al., 2019).

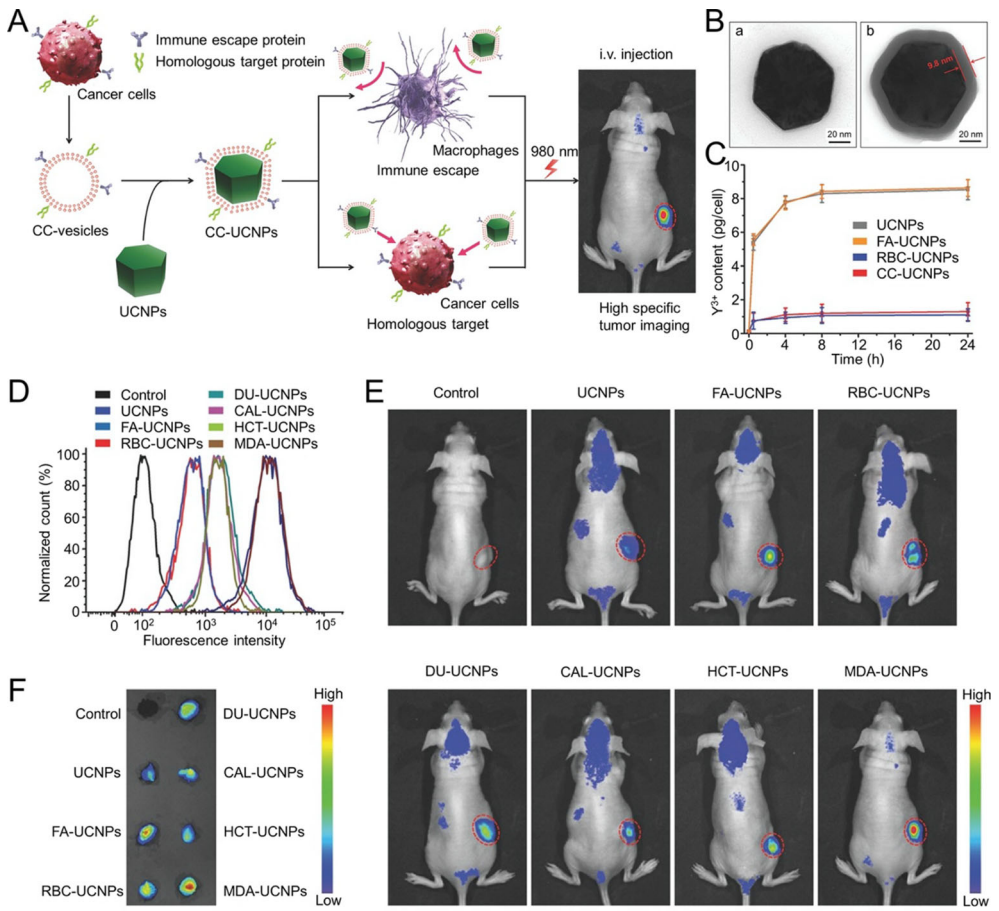

FIGURE 4 | (A) Schematic illustration of CC-UCNP preparation and application. **(B)** TEM images of (a) UCNPs and (b) CC-UCNPs. **(C)** Quantitative analysis of various nanoparticle uptakes at various times. **(D)** Flow cytometry analysis of MDA-MB-435 cells after incubation with various Cy5-labeled nanoparticles. **(E)** *In vivo* upconversion luminescence (UCL) images of MDA-MB-435-bearing mice 24 h after intravenous injection of various nano-formulations (tumor sites are indicated by red circles). **(F)** *Ex vivo* UCL images of tumors 24 h after injection. Reproduced with permission from (Rao et al., 2016a).

CONCLUSIONS

CM-based nanoparticle delivery systems have been explored in order to improve on the limitations of traditional nanomedicines. These systems exhibit excellent potential in cancer theranostic applications including chemotherapy, immunotherapy, phototherapy, and *in vivo* imaging. Various CM coatings have attracted significant attention due to the natural features derived from their source cells. CM coatings have been derived from various cells, including RBCs, macrophages, monocytes, neutrophils, platelets, stem cells, and cancer cells. A top-down strategy was used to develop the CM-coating nanoplatform, in which the natural functions of existing cells can be directly transferred to make the ultimate nanomedicine (Narain et al., 2017). RBM can endow RBM-coated NPs with prolonged circulation times, immune evasion, and reduced RES uptake (Gao et al., 2017). WBC membrane-coated NPs exhibit macrophage internalization inhibition because of the WBC membrane (Zhang et al., 2018). CCM-coated NPs have been proven to possess tumor-targeting abilities for drug delivery and vaccine-like functions (Fang et al., 2014; Ding et al., 2019).

Despite current progress in the field of CM-based nanoplatforms for cancer diagnosis and treatment, many challenges remain before they can be used in clinical applications. First, complex, inefficient CM-based nanomedicine preparation processes restrict their development. Coating techniques should be reformed for higher throughputs to satisfy the needs of future clinical applications. In addition, some of the specific functional proteins and structural units in CMs remain uncertain. For example, there are various proteins on the surfaces of CCM-based NPs. Only a few of them act as cancer-specific antigens for cancer immunotherapy. Others are common in human cells. The ability to identify these cancer-specific antigens and remove unwanted antigens or even enrich the expression of cancer-specific antigens through transgenic technology might allow CCM-based NPs to provide better therapeutic effects. Some types of cells such as fibroblasts, which have been used in

nanoparticle engineering, have proven difficult to amplify and apply practically in clinical settings. Finally, cancer cell heterogeneity can be a significant factor behind insufficient cancer treatment of CCM-based NPs. Thus, CCMs derived from autologous tumors may serve to provide specific CCM-based NPs for cancer treatment.

In conclusion, research on CM-based nanoplatforms for cancer diagnosis and treatment is still in its infancy. Numerous challenges must be overcome before the translation from bench to bedside. More innovative, efficacious CM-based nanoplatform strategies will be developed to support cancer treatments that benefit human health.

AUTHOR CONTRIBUTIONS

SL and JL produced the first draft. MS and JW revised the manuscript. CW and YS proposed the outline of the article and revised the draft before submission. In addition, all authors provided final approval of the manuscript.

FUNDING

This work was financially supported by the National Natural Science Foundation of China (Grant Nos. 5177030177).

REFERENCES

Aryal, S., Hu, C.-M. J., Fang, R. H., Dehaini, D., Carpenter, C., Zhang, D.-E., et al. (2013). Erythrocyte membrane-cloaked polymeric nanoparticles for controlled drug loading and release. *Nanomedicine* 8, 1271–1280. doi: 10.2217/nnm.12.153

Bose, R. J. C., Paulmurugan, R., Moon, J., Lee, S.-H., and Park, H. (2018). Cell membrane-coated nanocarriers: the emerging targeted delivery system for cancer theranostics. *Drug Discovery Today* 23, 891–899. doi: 10.1016/j.drudis.2018.02.001

Bray, F., Ferlay, J., Soerjomataram, I., Siegel, R. L., Torre, L. A., and Jemal, A. (2018). Global cancer statistics 2018: GLOBOCAN estimates of incidence and mortality worldwide for 36 cancers in 185 countries. *CA Cancer J. Clin.* 68, 394–424. doi: 10.3322/caac.21492

Calleja, P., Irache, J. M., Zandueta, C., Martinez-Oharriz, C., and Espuelas, S. (2017). A combination of nanosystems for the delivery of cancer chemoimmunotherapeutic combinations: 1-Methyltryptophan nanocrystals and paclitaxel nanoparticles. *Pharmacol. Res.* 126, 77–83. doi: 10.1016/j.phrs.2017.09.004

Chen, Q., Xu, L., Liang, C., Wang, C., Peng, R., and Liu, Z. (2016a). Photothermal therapy with immune-adjuvant nanoparticles together with checkpoint blockade for effective cancer immunotherapy. *Nat. Commun.* 7, 13193. doi: 10.1038/ncomms13193

Chen, Z., Zhao, P., Luo, Z., Zheng, M., Tian, H., Gong, P., et al. (2016b). Cancer cell membrane-biomimetic nanoparticles for homologous-targeting dual-modal imaging and photothermal therapy. *ACS Nano.* 10, 10049–10057. doi: 10.1021/acsnano.6b04695

Chen, W., Zeng, K., Liu, H., Ouyang, J., Wang, L., Liu, Y., et al. (2017a). Cell membrane camouflaged hollow prussian blue nanoparticles for synergistic photothermal-/chemotherapy of cancer. *Adv. Funct. Mater.* 27, 1605795. doi: 10.1002/adfm.201605795

Chen, X., Lee, D., Yu, S., Kim, G., Lee, S., Cho, Y., et al. (2017b). In vivo near-infrared imaging and phototherapy of tumors using a cathepsin B-activated fluorescent probe. *Biomaterials* 122, 130–140. doi: 10.1016/j.biomaterials.2017.01.020

Chen, W., Sun, K., Zheng, R., Zeng, H., Zhang, S., Xia, C., et al. (2018). Cancer incidence and mortality in China, 2014. *Chin. J. Cancer Res.* 30, 1–12. doi: 10.21147/j.issn.1000-9604.2018.01.01

Dan, P., Karp, J. M., Hong, S., Farokhzad, O. C., Margalit, R., and Langer, R. (2007). Nanocarriers as an emerging platform for cancer therapy. *Nat. Nanotechnol.* 2, 751. doi: 10.1038/nnano.2007.387

Ding, H., Lv, Y., Ni, D., Wang, J., Tian, Z., Wei, W., et al. (2015). Erythrocyte membrane-coated NIR-triggered biomimetic nanovectors with programmed delivery for photodynamic therapy of cancer. *Nanoscale* 7, 9806–9815. doi: 10.1039/C5NR02470F

Ding, Y., Zhu, Y., Wei, S., Zhou, J., and Shen, J. (2019). Cancer cell membrane as gate keeper of mesoporous silica nanoparticles and photothermal-triggered membrane fusion to release the encapsulated anticancer drug. *J. Mater. Sci.* 54, 12794–12805. doi: 10.1007/s10853-019-03788-y

Fang, R. H., Hu, C.-M. J., Luk, B. T., Gao, W., Copp, J. A., Tai, Y., et al. (2014). cancer cell membrane-coated nanoparticles for anticancer vaccination and drug delivery. *Nano. Lett.* 14, 2181–2188. doi: 10.1021/nl500618u

Fang, R. H., Kroll, A. V., Gao, W., and Zhang, L. (2018). Cell membrane coating nanotechnology. *Adv. Mater.* 30, 1706759. doi: 10.1002/adma.201706759

Feng, L., Tao, D., Dong, Z., Chen, Q., Chao, Y., Liu, Z., et al. (2017). Near-infrared light activation of quenched liposomal Ce6 for synergistic cancer phototherapy with effective skin protection. *Biomaterials* 127, 13–24. doi: 10.1016/j.biomaterials.2016.11.027

Feng, X., Xu, W., Li, Z., Song, W., Ding, J., and Chen, X. (2019). Immunomodulatory nanosystems. *Adv. Sci.* 6, 1900101. doi: 10.1002/advs.201900101

Gangadaran, P., Hong, C. M., Oh, J. M., Rajendran, R. L., Kalimuthu, S., Son, S. H., et al. (2018). In vivo non-invasive imaging of radio-labeled exosome-mimetics derived from red blood cells in mice. *Front. Pharmacol.* 9, 817. doi: 10.3389/fphar.2018.00817

Gao, C., Lin, Z., Wu, Z., Lin, X., and He, Q. (2016). Stem-cell-membrane camouflaging on near-infrared photoactivated upconversion nanoarchitectures for in vivo remote-controlled photodynamic therapy. *ACS Appl. Mater. Interfaces* 8, 34252–34260. doi: 10.1021/acsami.6b12865

Gao, L., Wang, H., Nan, L., Peng, T., Sun, L., Zhou, I., et al. (2017). Erythrocyte membrane-wrapped ph sensitive polymeric nanoparticles for non-small cell lung cancer therapy. *Bioconjugate Chem.* 28, 2591–2598. doi: 10.1021/acs.bioconjchem.7b00428

Gatenby, R., and Brown, J. (2018). The evolution and ecology of resistance in cancer therapy. *Cold Spring Harbor Perspect. Med.* 8, a033415. doi: 10.1101/cshperspect.a033415

Guo, H., Li, F., Xu, W., Chen, J., Hou, Y., Wang, C., et al. (2018). Mucoadhesive cationic polypeptide nanogel with enhanced penetration for efficient intravesical chemotherapy of bladder cancer. *Adv. Sci.* 5, 1800004. doi: 10.1002/advs.201800004

He, H., Guo, C., Wang, J., Korzun, W. J., Wang, X.-Y., Ghosh, S., et al. (2018). Leutusome: a biomimetic nanoplatform integrating plasma membrane components of leukocytes and tumor cells for remarkably enhanced solid tumor homing. *Nano. Lett.* 18, 6164–6174. doi: 10.1021/acs.nanolett.8b01892

Hu, Q., Sun, W., Qian, C., Wang, C., Bomba, H. N., and Gu, Z. (2015). Anticancer platelet-mimicking nanovehicles. *Adv. Mater.* 27, 7043–704+. doi: 10.1002/adma.201503323

Jiang, Q., Liu, Y., Guo, R., Yao, X., Sung, S., Pang, Z., et al. (2019). Erythrocyte-cancer hybrid membrane-camouflaged melanin nanoparticles for enhancing photothermal therapy efficacy in tumors. *Biomaterials* 192, 292–308. doi: 10.1016/j.biomaterials.2018.11.021

Jing, L., Qu, H., Wu, D., Zhu, C., Yang, Y., Jin, X., et al. (2018). Platelet-camouflaged nanococktail: Simultaneous inhibition of drug-resistant tumor growth and metastasis *via a* cancer cells and tumor vasculature dual-targeting strategy. *Theranostics* 8, 2683–2695. doi: 10.7150/thno.23654

Kang, T., Zhu, Q., Wei, D., Feng, J., Yao, J., Jiang, T., et al. (2017). Nanoparticles coated with neutrophil membranes can effectively treat cancer metastasis. *ACS Nano.* 11, 1397–1411. doi: 10.1021/acsnano.6b06477

Krishnamurthy, S., Gnanasammandhan, M. K., Xie, C., Huang, K., Cui, M. Y., and Chan, J. M. (2016). Monocyte cell membrane-derived nanoghosts for targeted cancer therapy. *Nanoscale* 8, 6981–6985. doi: 10.1039/C5NR07588B

Kroll, A. V., Fang, R. H., and Zhang, L. (2017). Biointerfacing and applications of cell membrane-coated nanoparticles. *Bioconjugate Chem.* 28, 23–32. doi: 10.1021/acs.bioconjchem.6b00569

Lai, P.-Y., Huang, R.-Y., Lin, S.-Y., Lin, Y.-H., and Chang, C.-W. (2015). Biomimetic stem cell membrane-camouflaged iron oxide nanoparticles for theranostic applications. *Rsc Adv.* 5, 98222–98230. doi: 10.1039/C5RA17447C

Li, S. Y., Cheng, H., Xie, B. R., Qiu, W. X., Zeng, J. Y., Li, C. X., et al. (2017). Cancer cell membrane camouflaged cascade bioreactor for cancer targeted starvation and photodynamic therapy. *ACS Nano.* 11, 7006–7018. doi: 10.1021/acsnano.7b02533

Li, J., Wang, X., Zheng, D., Lin, X., Wei, Z., Zhang, D., et al. (2018a). Cancer cell membrane-coated magnetic nanoparticles for MR/NIR fluorescence dual-modal imaging and photodynamic therapy. *Biomater. Sci.* 6, 1834–1845. doi: 10.1039/C8BM00343B

Li, J., Zhen, X., Lyu, Y., Jiang, Y., Huang, J., and Pu, K. (2018b). Cell membrane coated semiconducting polymer nanoparticles for enhanced multimodal cancer phototheranostics. *ACS Nano.* 12, 8520–8530. doi: 10.1021/acsnano.8b04066

Li, S., Feng, X., Wang, J., He, L., Wang, C., Ding, J., et al. (2018c). Polymer nanoparticles as adjuvants in cancer immunotherapy. *Nano. Res.* 11, 5769–5786. doi: 10.1007/s12274-018-2124-7

Li, S., Feng, X., Wang, J., Xu, W., Islam, M. A., Sun, T., et al. (2019). multiantigenic nanoformulations activate anticancer immunity depending on size. *Adv. Funct. Mater.* 29, 1903391. doi: 10.1002/adfm.201903391

Liang, X., Ye, X., Wang, C., Xing, C., Miao, Q., Xie, Z., et al. (2019). Photothermal cancer immunotherapy by erythrocyte membrane-coated black phosphorus formulation. *J. Control Release* 296, 150–161. doi: 10.1016/j.jconrel.2019.01.027

Liu, Y., Qiao, L., Zhang, S., Wan, G., Chen, B., Zhou, P., et al. (2018). Dual pH-responsive multifunctional nanoparticles for targeted treatment of breast cancer by combining immunotherapy and chemotherapy. *Acta Biomaterialia* 66, 310–324. doi: 10.1016/j.actbio.2017.11.010

Liu, B., Wang, W., Fan, J., Long, Y., Xiao, F., Daniyal, M., et al. (2019). RBC membrane camouflaged prussian blue nanoparticles for gamabutolin loading and combined chemo/photothermal therapy of breast cancer. *Biomaterials* 217, 119301. doi: 10.1016/j.biomaterials.2019.119301

Lubich, C., Allacher, P., De La Rosa, M., Bauer, A., Prenninger, T., Horling, F. M., et al. (2016). The mystery of antibodies against polyethylene glycol (PEG) - what do we know? *Pharm. Res.* 33, 2239–2249. doi: 10.1007/s11095-016-1961-x

Lv, Y., Liu, M., Zhang, Y., Wang, X., Zhang, F., Li, F., et al. (2018). Cancer cell membrane-biomimetic nanoprobes with two-photon excitation and near-infrared emission for intravital tumor fluorescence imaging. *ACS Nano.* 12, 1350–1358. doi: 10.1021/acsnano.7b07716

Manolova, V., Flace, A., Bauer, M., Schwarz, K., Saudan, P., and Bachmann, M. F. (2008). Nanoparticles target distinct dendritic cell populations according to their size. *Eur. J. Immunol.* 38, 1404–1413. doi: 10.1002/eji.200890018

Maurer, N., Fenske, D. B., and Cullis, P. R. (2001). Developments in liposomal drug delivery systems. *Expert Opin. Biol. Ther.* 1, 923–947. doi: 10.1517/14712598.1.6.923

Meng, Q.-F., Rao, L., Zan, M., Chen, M., Yu, G.-T., Wei, X., et al. (2018). Macrophage membrane-coated iron oxide nanoparticles for enhanced photothermal tumor therapy. *Nanotechnology* 29, 134004. doi: 10.1088/1361-6528/aaa7c7

Narain, A., Asawa, S., Chhabria, V., and Patil-Sen, Y. (2017). Cell membrane coated nanoparticles: next-generation therapeutics. *Nanomedicine* 12, 2677–2692. doi: 10.2217/nnm-2017-0225

Pei, Q., Hu, X., Zheng, X., Liu, S., Li, Y., Jing, X., et al. (2018). Light-activatable red blood cell membrane-camouflaged dimeric prodrug nanoparticles for synergistic photodynamic/chemotherapy. *ACS Nano.* 12, 1630–1641. doi: 10.1021/acsnano.7b08219

Qi, S. S., Sun, J. H., Yu, H. H., and Yu, S. Q. (2017). Co-delivery nanoparticles of anti-cancer drugs for improving chemotherapy efficacy. *Drug Deliv.* 24, 1909–1926. doi: 10.1080/10717544.2017.1410256

Qian, H., Liu, B., and Jiang, X. (2018). Application of nanomaterials in cancer immunotherapy. *Mater. Today Chem.* 7, 53–64. doi: 10.1016/j.mtchem.2018.01.001

Qiu, W.-X., Zhang, M.-K., Liu, L.-H., Gao, F., Zhang, L., Li, S.-Y., et al. (2018). A self-delivery membrane system for enhanced anti-tumor therapy. *Biomaterials* 161, 81–94. doi: 10.1016/j.biomaterials.2018.01.037

Rao, L., Bu, L.-L., Cai, B., Xu, J.-H., Li, A., Zhang, W.-F., et al. (2016a). Cancer cell membrane-coated upconversion nanoprobes for highly specific tumor imaging. *Adv. Mater.* 28, 3460–346+. doi: 10.1002/adma.201506086

Rao, L., Xu, J.-H., Cai, B., Liu, H., Li, M., Jia, Y., et al. (2016b). Synthetic nanoparticles camouflaged with biomimetic erythrocyte membranes for reduced reticuloendothelial system uptake. *Nanotechnology* 27, 085106. doi: 10.1088/0957-4484/27/8/085106

Rao, L., Meng, Q.-F., Huang, Q., Wang, Z., Yu, G.-T., Li, A., et al. (2018). Platelet-leukocyte hybrid membrane-coated immunomagnetic beads for highly efficient and highly specific isolation of circulating tumor cells. *Adv. Funct. Mater.* 28, 1803531. doi: 10.1002/adfm.201803531

Ren, X., Zheng, R., Fang, X., Wang, X., Zhang, X., Yang, W., et al. (2016). Red blood cell membrane camouflaged magnetic nanoclusters for imaging-guided photothermal therapy. *Biomaterials* 92, 13–24. doi: 10.1016/j.biomaterials.2016.03.026

Ribas, A., and Wolchok, J. D. (2018). Cancer immunotherapy using checkpoint blockade. *Science* 359, 1350–1355. doi: 10.1126/science.aar4060

Riley, R. S., June, C. H., Langer, R., and Mitchell, M. J. (2019). Delivery technologies for cancer immunotherapy. *Nat. Rev. Drug Discovery* 18, 175–196. doi: 10.1038/s41573-018-0006-z

Saez-Rodriguez, J., Macnamara, A., and Cook, S. (2015). Modeling signaling networks to advance new cancer therapies. *Annu. Rev. Biomed. Eng.* 17, 143–163. doi: 10.1146/annurev-bioeng-071813-104927

Su, J., Sun, H., Meng, Q., Yin, Q., Zhang, P., Zhang, Z., et al. (2016). Bioinspired nanoparticles with NIR-controlled drug release for synergetic chemophotothermal therapy of metastatic breast cancer. *Adv. Funct. Mater.* 26, 7495–7506. doi: 10.1002/adfm.201603381

Tian, H., Luo, Z., Liu, L., Zheng, M., Chen, Z., Ma, A., et al. (2017). Cancer cell membrane-biomimetic oxygen nanocarrier for breaking hypoxia-induced chemoresistance. *Adv. Funct. Mater.* 27, 1703197. doi: 10.1002/adfm.201703197

Vijayan, V., Uthaman, S., and Park, I.-K. (2018). Cell membrane-camouflaged nanoparticles: a promising biomimetic strategy for cancer theragnostics. *Polymers* 10, 983. doi: 10.3390/polym10090983

Wang, D., Dong, H., Li, M., Cao, Y., Yang, F., Zhang, K., et al. (2018). Erythrocyte-cancer hybrid membrane camouflaged hollow copper sulfide nanoparticles for prolonged circulation life and homotypic-targeting photothermal/chemotherapy of melanoma. *ACS Nano.* 12, 5241–5252. doi: 10.1021/acsnano.7b08355

Xiao, F., Fan, J., Tond, C., Xiao, C., Wang, Z., Liu, B., et al. (2019). An erythrocyte membrane coated mimetic nano-platform for chemo-phototherapy and multimodal imaging. *Rsc Adv.* 9, 27911–27926. doi: 10.1039/C9RA05867B

Xu, L., Gao, F., Fan, F., and Yang, L. (2018). Platelet membrane coating coupled with solar irradiation endows a photodynamic nanosystem with both improved antitumor efficacy and undetectable skin damage. *Biomaterials* 159, 59–67. doi: 10.1016/j.biomaterials.2017.12.028

Xu, L., Wu, S., and Wang, J. (2019). Cancer cell membrane-coated nanocarriers for homologous target inhibiting the growth of hepatocellular carcinoma. *J. Bioact. Compat. Polym.* 34, 58–71. doi: 10.1177/0883911518819107

Yang, R., Xu, J., Xu, L., Sun, X., Chen, Q., Zhao, Y., et al. (2018). Cancer cell membrane-coated adjuvant nanoparticles with mannose modification for effective anticancer vaccination. *ACS Nano.* 12, 5121–5129. doi: 10.1021/acsnano.7b09041

Yang, J., Teng, Y., Fu, Y., and Zhang, C. (2019). Chlorins e6 loaded silica nanoparticles coated with gastric cancer cell membrane for tumor specific photodynamic therapy of gastric cancer. *Int. J. Nanomed.* 14, 5061–5071. doi: 10.2147/IJN.S202910

Ye, X., Liang, X., Chen, Q., Miao, Q., Chen, X., Zhang, X., et al. (2019). Surgical tumor-derived personalized photothermal vaccine formulation for cancer immunotherapy. *ACS Nano.* 13, 2956–2968. doi: 10.1021/acsnano.8b07371

Yu, B., Goel, S., Ni, D., Ellison, P. A., Siamof, C. M., Jiang, D., et al. (2018). Reassembly of Zr-89-labeled cancer cell membranes into multicompartment membrane-derived liposomes for PET-trackable tumor-targeted theranostics. *Adv. Mater.* 30, 1704934. doi: 10.1002/adma.201704934

Zhai, Y., Ran, W., Su, J., Lang, T., Meng, J., Wang, G., et al. (2018). Traceable bioinspired nanoparticle for the treatment of metastatic breast cancer *via* NIR-trigged intracellular delivery of methylene blue and cisplatin. *Adv. Mater.* 30, 1802378. doi: 10.1002/adma.201802378

Zhang, Y., Gai, K., Li, C., Guo, Q., Chen, Q., He, X., et al. (2018). Macrophage-membrane-coated nanoparticles for tumor-targeted chemotherapy. *Nano. Lett.* 18, 1908–1915. doi: 10.1021/acs.nanolett.7b05263

Zhu, D.-M., Xie, W., Xiao, Y.-S., Suo, M., Zan, M.-H., Liao, Q.-Q., et al. (2018). Erythrocyte membrane-coated gold nanocages for targeted photothermal and chemical cancer therapy. *Nanotechnology* 29, 084002. doi: 10.1088/1361-6528/aa9ca1

Conflict of Interest: The authors declare that the research was conducted in the absence of any commercial or financial relationships that could be construed as a potential conflict of interest.

frontiers in Pharmacology

ORIGINAL RESEARCH
published: 10 March 2020
doi: 10.3389/fphar.2020.00226

Dihydroartemisinin-Loaded Magnetic Nanoparticles for Enhanced Chemodynamic Therapy

Shengdi Guo[1], Xianxian Yao[1], Qin Jiang[1], Kuang Wang[1], Yuanying Zhang[1], Haibao Peng[2], Jing Tang[3]* and Wuli Yang[1]**

[1] State Key Laboratory of Molecular Engineering of Polymers, Department of Macromolecular Science, Fudan University, Shanghai, China, [2] Department of Pharmaceutical Sciences, Shanghai University of Traditional Chinese Medicine, Shanghai, China, [3] Department of Materials Science and Engineering, Stanford University, Stanford, CA, United States

Recently, chemodynamic therapy (CDT) has represented a new approach for cancer treatment with low toxicity and side effects. Nonetheless, it has been a challenge to improve the therapeutic effect through increasing the amount of reactive oxygen species (ROS). Herein, we increased the amount of ROS agents in the Fenton-like reaction by loading dihydroartemisinin (DHA) which was an artemisinin (ART) derivative containing peroxide groups, into magnetic nanoparticles (MNP), thereby improving the therapeutic effect of CDT. Blank MNP were almost non-cytotoxic, whereas three MNP loading ART-based drugs, MNP-ART, MNP-DHA, and MNP-artesunate (MNP-AS), all showed significant killing effect on breast cancer cells (MCF-7 cells), in which MNP-DHA were the most potent. What's more, the MNP-DHA showed high toxicity to drug-resistant breast cancer cells (MCF-7/ADR cells), demonstrating its ability to overcome multidrug resistance (MDR). The study revealed that MNP could produce ferrous ions under the acidic condition of tumor microenvironment, which catalyzed DHA to produce large amounts of ROS, leading to cell death. Further experiments also showed that the MNP-DHA had significant inhibitory effect on another two aggressive breast cancer cell lines (MDA-MB-231 and MDA-MB-453 cells), which indicated that the great potential of MNP-DHA for the treatment of intractable breast cancers.

Keywords: chemodynamic therapy, reactive oxygen species, multidrug resistance, dihydroartemisinin, magnetic nanoparticle, breast cancer

OPEN ACCESS

Edited by:
Wei Tao,
Harvard Medical School,
United States

Reviewed by:
Zhongliang Wang,
Xidian University, China
Peihong Ni,
Soochow University, China

****Correspondence:***
Haibao Peng
haibaopeng@gmail.com
Jing Tang
jingtang@stanford.edu
Wuli Yang
wlyang@fudan.edu.cn

Specialty section:
This article was submitted to Experimental Pharmacology and Drug Discovery, a section of the journal Frontiers in Pharmacology

Received: *18 December 2019*
Accepted: *19 February 2020*
Published: *10 March 2020*

Citation:
Guo S, Yao X, Jiang Q, Wang K, Zhang Y, Peng H, Tang J and Yang W (2020) Dihydroartemisinin-Loaded Magnetic Nanoparticles for Enhanced Chemodynamic Therapy. Front. Pharmacol. 11:226. doi: 10.3389/fphar.2020.00226

INTRODUCTION

Chemodynamic therapy (CDT) is a tumor therapeutic strategy which generates abundant reactive oxygen species (ROS) in tumor sites *via* the Fenton reaction or Fenton-like reaction (Tang et al., 2019; Yan et al., 2019). Generally, specific nanomaterials produce ions as catalysts, which cleave the endoperoxide linkages in ROS agents to produce ROS (Bokare and Choi, 2014). In the classical Fenton reaction, the catalyst is ferrous ions produced under the acidic condition of tumor microenvironment and the ROS agent is the excessive hydrogen peroxide (H_2O_2) in cancer cells (Li et al., 2015; Chen et al., 2017). The overproduction of ROS is cytotoxic, which could damage membrane and oxidize lipids in cells, further leading to antitumor performance *via* apoptosis and/or ferroptosis (Reed and Pellecchia, 2012; Yue et al., 2018; Wan et al., 2019; Xu X. et al., 2019).

Owing to the fact that CDT needs to be activated by the stimulation of the tumor's endogenous microenvironment, for example, low pH and elevated H_2O_2 concentration, the overproduction of ROS is almost exclusively achieved at the tumor site and consequently CDT has very low toxicity and side effects on normal tissues (Breunig et al., 2008; Chen et al., 2017, 2019). Compared with other treatment strategies displaying non-negligible dark toxicity, like chemotherapy, radiotherapy, photodynamic therapy, and sonodynamic therapy, CDT has the advantage that it is highly selective and specific (Osaki et al., 2011; Tang et al., 2013, 2018; Song et al., 2016; Cho et al., 2017; Men et al., 2018; An et al., 2019; Yang et al., 2019). However, the generation of ROS will be limited to the conditions of the tumor site, so the ideas of inducing preferential cancer cell death through exogenous ROS generating agents have gained considerable momentum.

Since the efficiency of ROS production by Fenton or Fenton-like reaction is dependent on catalysts and ROS agents, a series of studies have enhanced intracellular ROS production mainly in two aspects. On one hand, varieties of materials increasing the amount of ROS are developed from the perspective of catalysts (Zheng et al., 2017; Ma et al., 2019). Increasing the number of catalyst ions is a straightforward method to promote the efficiency of CDT. Shi group reported the facile synthesis of amorphous iron nanoparticles, which could be rapidly ionized to release Fe^{2+} ions in an acidic tumor microenvironment for CDT (Zhang C. et al., 2016). Besides iron ions, many other metal ions, including Mn^{2+}, Cu^{2+}, and Co^{2+} ions, could also show Fenton-like activities (Ember et al., 2009; Xu et al., 2011; Bokare and Choi, 2014; Poyton et al., 2016). Due to the GSH depletion property of MnO_2, Chen group used MnO_2-coated mesoporous silica nanoparticles to destroy tumor cells, resulting in GSH depletion-enhanced CDT (Lin et al., 2018). On the other hand, despite the concentration of H_2O_2 in tumor cells is higher than normal tissues, the amount of H_2O_2 is still too low to achieve good therapeutic effect (Szatrowski and Nathan, 1991). Therefore, from the perspective of ROS agents, it is viable to raise the efficiency of ROS production *via* increasing the amount of ROS agents in cancer cells (Huo et al., 2017). Ge group constructed integrated multifunctional polymeric nanoparticles in which ascorbyl palmitate molecules can selectively generate H_2O_2 in tumor tissues, sequentially improving the therapeutic effect of CDT (Wang et al., 2018).

In addition, it is also a feasible way to load drugs whose treatment principles are based on Fenton or Fenton-like reactions into materials to increase the quantity of ROS agents. Many reports have shown that artemisinin (ART) and its derivatives, as frontline drugs against malarial infections, achieve antimalarial effects by Fenton-like reaction, the specific process of which is that under the catalysis of ferrous heme the weak endoperoxide linkages (R-O-O-R′) in drugs break resulting in the formation of toxic ROS (Olliaro et al., 2001; Krishna et al., 2004; Golenser et al., 2006; Tu, 2011). Currently, ART and its derivatives have also been used as tumor therapeutic agents for cancers *via* CDT (Wang et al., 2016; Wang L.L. et al., 2019; Yao et al., 2018; Sun et al., 2019). What's more, it has been found that ART and its derivatives showed sensitivity against multidrug resistance (MDR) cancer cells, as that some common ART-based drugs were not transported by P-glycoprotein (P-gp), which mediates cellular MDR by actively pumping antitumor drugs outside the cancer cells (Kruh and Belinsky, 2003; Szakacs et al., 2006; Prasad et al., 2012; Zhong et al., 2016; Wang Y. et al., 2019). Therefore, ART and its derivatives exhibit the potential to overcome tumor MDR.

In this work, as shown in **Scheme 1**, ART and its two derivatives, dihydroartemisinin (DHA) and artesunate (AS), were loaded into magnetite nanoparticles (MNP) respectively, used for CDT enhancement. After loading these drugs, the non-cytotoxic MNP showed high toxicity to breast cancer cells. Subsequently, dihydroartemisinin-loaded magnetic nanoparticles (MNP-DHA) with the best inhibitory effect exhibited the ability to effectively kill MCF-7/ADR cancer cells, and the mechanism of MNP-DHA achieving therapeutic effect was investigated. Further experiments indicated that MNP-DHA possessed excellent

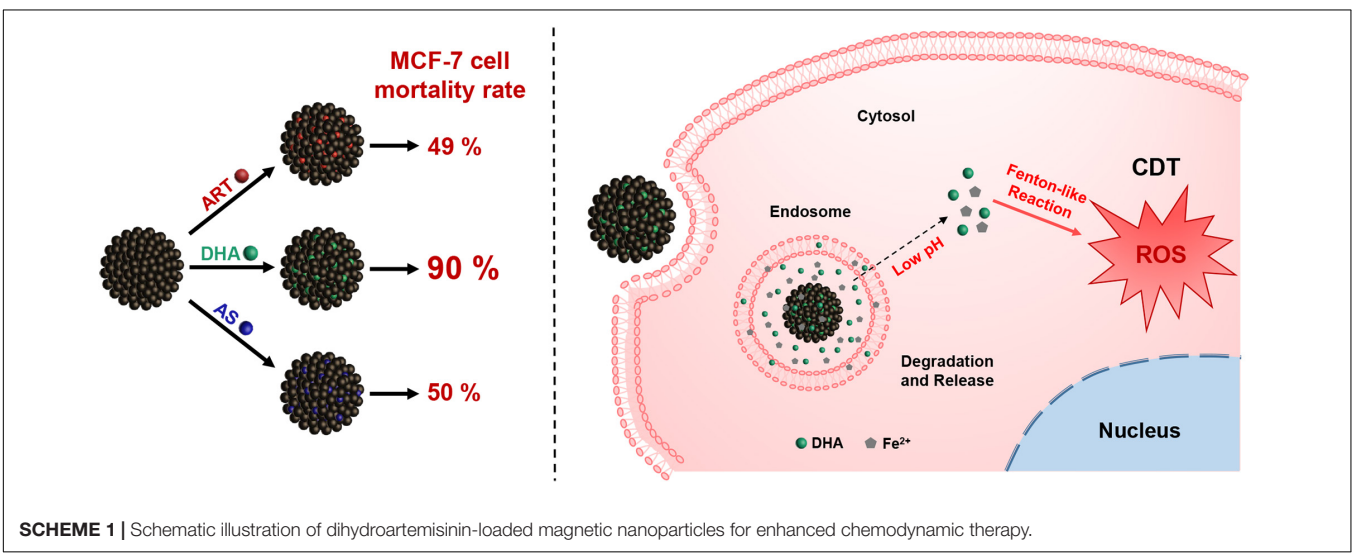

SCHEME 1 | Schematic illustration of dihydroartemisinin-loaded magnetic nanoparticles for enhanced chemodynamic therapy.

inhibition ability for other intractable breast cancer cells and had a good application prospect.

MATERIALS AND METHODS

Materials

Iron (III) chloride hexahydrate ($FeCl_3 \cdot 6H_2O$), sodium acetate anhydrous (NaOAc), trisodium citrate dihydrate ($Na_3Cit \cdot 2H_2O$), ethanol, sodium hydroxide (NaOH), and dimethyl sulfoxide (DMSO) were purchased from Shanghai Chemical Reagents Company. Doxorubicin hydrochloride (DOX), artemisinin (ART), dihydroartemisinin (DHA), artesunate (AS), 1,3-diphenylisobenzofuran (DPBF), sodium dihydngen phosphate anhydrous (NaH_2PO_4) and sodium phosphate dibasic anhydrous (Na_2HPO_4) were purchased from Shanghai Aladdin Chemistry Company. 2′,7′-dichlorofluorescein diacetate (DCFH-DA) and cell Counting Kit-8 (CCK-8) were purchased from Keygen Biotech Company (Nanjing, China). FerroOrange was purchased from Dojindo Molecular Technologies Company. Roswell Park Memorial Institute-1640 (RPMI-1640) medium, Dulbecco's modified Eagle's (DMEM) medium, penicillin/streptomycin solution, fetal bovine serum (FBS), and trypsin-ethylene diamine tetraacetic acid (Trypsin-EDTA, 0.05%) were purchased from Gibco BRL (Grand Island, NY, United States). The water used in the experiment was deionized water.

Characterization

The morphology of nanoparticles was tested by a Tecnai G2 20 TWIN transmission electron microscope (TEM) at an accelerating voltage of 200 kV and a Zeiss Ultra 55 field emission scanning electron microscope (FESEM) equipped with a fieldemission gun operated at 5 kV (Kong et al., 2014). Magnetic characterization curves were measured by a Quantum vibrating sample magnetometer (VSM) at 300 K. Dynamic light scattering (DLS) data, including the size, zeta potential and light scattering intensity of the nanoparticles were measured at 25°C on a Zetasizer Nano ZS90 analyzer (Malvern Instrument Ltd). Fourier transform infrared (FT-IR) spectra were obtained *via* a FT-IR spectrometer (Thermofisher Nicolet 6700). Ultraviolet spectrophotometer (UV-Vis) spectra were recorded at 25°C on a Perkin-Elmer Lambda 750 spectrophotometer. The concentration of metal ions was obtained on a P-4010 inductively coupled plasma-atomic emission spectrometry (ICP-AES). Confocal laser scanning microscopy (CLSM) images were acquired using a Nikon C2 + laser scanning confocal microscope. Flow cytometry analysis was operated on a flow cytometer (Beckman Coulter Gallios) at 37°C.

Synthesis of Magnetic Nanoparticles

Magnetic nanoparticles (MNP) were prepared *via* a modified solvothermal reaction (Wang K. et al., 2019). $FeCl_3 \cdot 6H_2O$ (1.8 g), $Na_3Cit \cdot 2H_2O$ (1.2 g) and NaOAc (4.8 g) were dissolved in 88 mL ethylene glycol with sonicated in an ultrasonic bath for 10 min, then the mixture was stirred vigorously for 30 min. The resulting solution was then transferred into a autoclave, which was sealed and heated for 12 h at 200°C. After cooling down to room temperature, separated by a magnet, the product was washed alternately with ethanol and deionized water for three times, then redispersed in water for subsequent use.

Preparation and Release Study of Drug-Loaded MNP *in vitro*

Three drugs were loaded into MNP, including ART, DHA, AS, respectively. 6 mg of MNP were added into 2 mL of deionized water and then sonicated for 5 min to form a homogeneous dispersion. Then 1.5 mg of ART dissolved in 1 mL of ethanol was added to the dispersion and the dispersion was shaken up for 24 h at room temperature. Subsequently, liquid of the dispersion was removed by rotary evaporation at 40°C. The product was washed with water for three times *via* a magnet and then collected for further use. After treating with NaOH-containing ethanol solution at 50°C for 30 min, the unloaded ART in the collected supernatant was converted to a UV active compound and detected by a UV-visible spectrometry at an excitation wavelength of 292 nm. According to the following formulation, the drug loading contents (LC) were calculated: LC (%) = (the drug loaded in MNP weight)/(total nanoparticles weight) × 100%.

The methods of loading DHA and AS into MNP were similar to the above method, except the mass ratio of MNP and the drug, and the volume ratio of water and ethanol. When loading DHA into MNP, 10 mg of MNP were added into 2 mL of deionized water and then 3 mg of DHA dissolved in 2 mL of ethanol was added to the dispersion. When loading AS into MNP, 10 mg of MNP were added into 4.95 mL of deionized water and then 3 mg of AS dissolved in 0.05 mL of ethanol was added to the dispersion. Furthermore, the method of converting drugs to UV active compounds was different between different drugs. In order to be measured at the wavelength of 238 nm, DHA was treated with ethanol solution containing NaOH at 60°C for 30 min and AS was treated with NaOH solution (0.1 M) at 83°C for 1 h. The stability of drug-loaded nanoparticles in phosphate buffer saline (PBS, pH 7.4) and serum-containing culture medium was detected *via* monitoring the hydrodynamic size and polydispersity index (PDI) by DLS (Xie et al., 2018).

The drug release behaviors were studied *via* an incubator shaker at 37°C (Ma et al., 2012). Sealed in a 1.4×10^4 Dalton dialysis bag, 2 mL of drug-loaded MNP were immersed into 200 mL of PBS (pH 7.4) and incubated under oscillation. At predetermined time intervals, 2 mL of release solution was withdrawn and replaced by an equal volume of fresh buffer. Through UV-visible spectrometry, the concentration of drug released from nanoparticles was obtained. Cumulative drug release was calculated as a percentage of the total drug loaded in MNP and plotted over time. All measurements were performed three times.

Cell Culture

Human embryonic kidney cell line (HEK-293T cells, normal cells), human breast cancer cell line (MCF-7, MDA-MB-231, and MDA-MB-453 cells, tumor cells), and human breast

drug-resistant cancer cell line (MCF-7/ADR cells, tumor cells) were purchased from Chinese Science Academy. HEK-293T, MCF-7, and MDA-MB-231 cells were cultured in DMEM supplemented with 10% (v/v) FBS and 1% antibiotics (penicillin/streptomycin, 100 U/mL). MDA-MB-453 and MCF-7/ADR cells were cultured in RPMI-1640 containing 10% (v/v) FBS, 1% antibiotics (penicillin/streptomycin, 100 U/mL), and DOX (0.5 mg/mL) was added to the cell culture medium of MCF-7/ADR cells. Cells were incubated in an atmosphere of 5% CO_2 at 37°C.

Cytotoxicity Assays

The cytotoxicity of nanoparticles was tested on cells using a standard CCK-8 assay (Jiang et al., 2017; Yao et al., 2019). Cells were incubated in 96 pore plates at an initial density of 1×10^4/well for 24 h at 37°C and under 5% CO_2 atmosphere. Then different concentrations of MNP, drugs and drug-loaded MNP (100 μL/well) dispersions were added in each well and coincubated with cells for 24 h, respectively. At last, CCK-8/culture medium (10 μL/100 μL) was added into each well for another 1 h incubation. The absorbance at 450 nm of each well was measured using a BioTek enzyme-linked immunosorbent assay reader. All measurements were repeated in triplicate.

Acid-Responsive Behaviors

To investigate the acid degradation performance of MNP, the concentrations of iron ions generated *via* MNP at PBS (pH 7.4 and 5.0) were measured by an inductively coupled plasma spectrometer (ICP). MNP (200 μg/mL) were sealed in a 1.4×10^4 Dalton dialysis bag and incubated in 200 mL of PBS (pH 7.4 and 5.0) at 37°C under oscillation, respectively (Li et al., 2012b). At different time points, 2 mL of release solution was removed and replaced with an equal volume of fresh solution. The histogram of iron ion concentration at different times was plotted. Each measurement was repeated three times.

Detection of Cellular Fe^{2+} Ions Generation

To clarify Fe^{2+} ions generation *via* the nanoparticles in cells, CLSM measurement was performed. MCF-7/ADR cells were seeded in confocal dishes at the density of 1×10^5 cells/mL, cultured for 24 h, and then MNP, DHA, MNP-DHA dispersions (200 μg/mL) were added into dishes, respectively. Meanwhile, a dish without adding samples was prepared as a control group. After incubated for 6 h, the culture medium was removed and cells were washed with PBS three times. Then FerroOrange (1 μM, an intracellular Fe^{2+} ions probe, Ex: 543 nm, Em: 580 nm) dispersed in serum-free medium was added to the cells, and cells were incubated for 30 min in a 37°C incubator equilibrated with 95% air and 5% CO_2. Finally, the fluorescence images of cells were captured using a C2 + confocal microscope.

Detection of ROS Generation *in vitro*

In order to measure the generation of ROS, DPBF was selected as the ROS trapper, which can be oxidized by ROS resulting in fluorescence quenching (Ding et al., 2018). Typically, DPBF (10 μM), $FeSO_4 \cdot 7H_2O$ (100 μM) and DHA (100 μM) were dissolved in ethanol quickly, and the above mixture was measured by the UV-vis spectrophotometer for 0, 2, 5, 10, 20, 30, 60, 90, and 120 min at the wavelength of 410 nm, respectively.

The production of ROS in MCF-7 and MCF-7/ADR cells was detected by CLSM and flow cytometry (Yang et al., 2019). DCFH-DA, as a ROS probe, was used to assess intracellular ROS generation ability. Cells were seeded in confocal dishes at a density of 1×10^5 cells/mL and incubated for 24 h to allow cell attachment. Then cells were incubated with different materials, respectively and the plate without adding samples was as a control group. After incubated for 6 h, the culture medium was removed and cells stained with 1 mL of DCFH-DA (10 μM) dissolved in PBS at 37°C for 30 min. Afterward, PBS containing DCFH-DA was removed and cells were rinsed three times with fresh PBS. The fluorescence images of cells were captured using a C2 + confocal microscope.

Besides, using a flow cytometer ROS production was quantitatively measured. Cells were seeded onto a 6-well plate at a density of 1×10^5 cells/mL and treated as the similar steps above to be dyed. Then cells were digested and transferred into centrifuge tubes. Cells were separated *via* centrifugation for 5 min at 1000 rpm and redispersed in PBS (0.5 mL). The fluorescence intensity of DCF was tested by the flow cytometry.

RESULTS AND DISCUSSION

Preparation and Characterization of Drug-Loaded MNP

The synthesis method of MNP was slightly modified based on the published solvothermal method (Deng et al., 2005). The detailed morphological and structural features of MNP were examined by TEM, demonstrating the rough surface and the uniform morphology with the particle size of ∼180 nm (**Figure 1A**). Meanwhile, FESEM images also showed the spherical structure of MNP (**Figure 1B**). In addition, the magnetic hysteresis curves showed no evident remanence and coercivity, suggesting superparamagnetic property of MNP (**Figure 1C**). The inset photo that MNP were separated *via* a magnet also revealed MNP had very good magnetism (Li et al., 2012a; Peng et al., 2017).

As shown in **Figure 1D** and **Supplementary Table S1**, the hydrodynamic diameter (Dh) of MNP was 200 nm with a narrow PDI of 0.013. After loading drugs, including ART, DHA and AS, the average sizes of MNP-ART, MNP-DHA, and MNP-AS were 212, 204, and 204 nm, and the PDI were 0.065, 0.026, and 0.092, respectively, which implied that the load of drugs didn't affect the stability of nanoparticles. Furthermore, the particle size, as shown by DLS, was larger than that shown by TEM and SEM, which was probably due to the interaction between nanoparticles and surrounding water molecules. The particle size of MNP in serum-containing culture medium increased slightly with time (**Supplementary Figure S1**), but didn't change much, and all were below 250 nm within 5 days. The increase in particle size was due to the adsorption of proteins in the dispersion on MNP surface (Kim et al., 2003). The PDI values within 5 days were very small, all less than 0.12, indicating

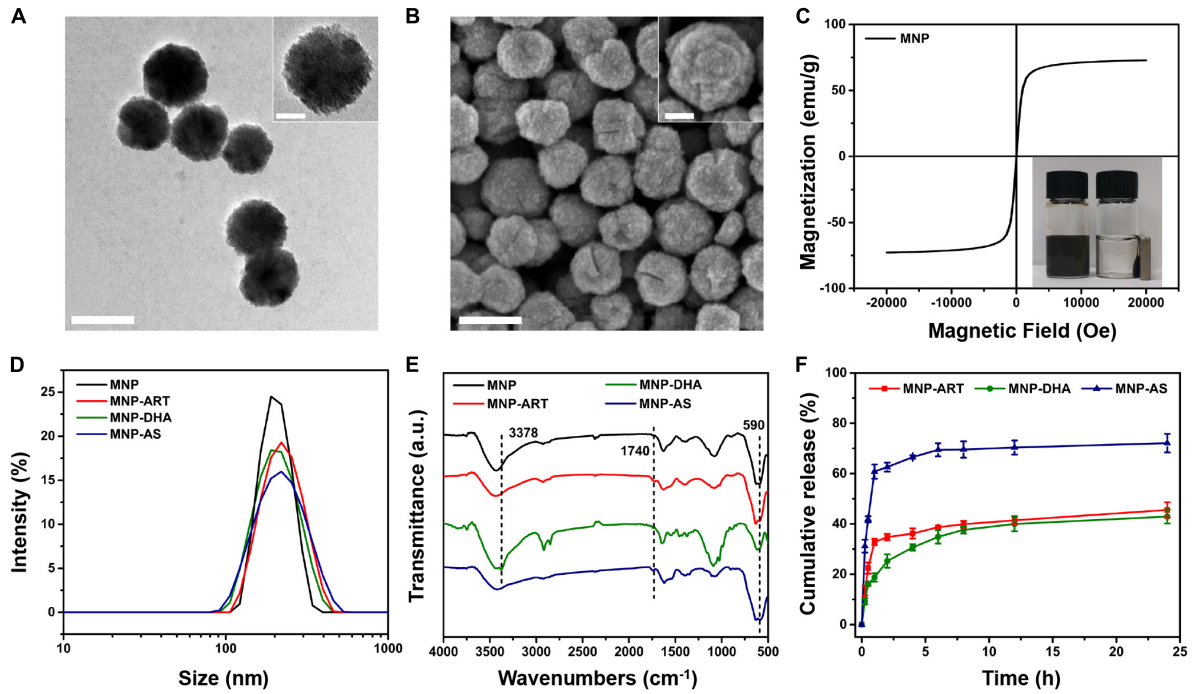

FIGURE 1 | TEM images of **(A)** MNP. FESEM images of **(B)** MNP. The scale bars represent 200 nm and the scale bars of insets are 50 nm. **(C)** Magnetic hysteresis curves of MNP. **(D)** DLS curves of MNP, MNP-ART, MNP-DHA, and MNP-AS in PBS (pH 7.4). **(E)** FT-IR spectra of MNP, MNP-ART, MNP-DHA, and MNP-AS. **(F)** Cumulative drug release from MNP-ART, MNP-DHA, and MNP-AS in PBS (pH 7.4).

that the particle size distribution was even, and proteins were slightly adsorbed. Therefore, the MNP also had good stability in serum-containing culture medium.

The FT-IR spectra demonstrated the successful loading of drugs (**Figure 1E** and **Supplementary Figure S2**). The characteristic peak at 590 cm^{-1} was attributed to Fe-O bond (Sanati et al., 2019). After ART loading, the spectrum of the MNP-ART exhibited new band in the 1740 cm^{-1} region, which belongs to C = O in δ-lactone of ART. In the same way, the absorption peaks at 3378 and 1740 cm^{-1} belong to O–H of DHA and C = O of AS, respectively (Ding et al., 2018; Kumar et al., 2019). The loading ratios of the three drugs were further measured by the UV-vis spectra. According to the standard curves of three drugs (**Supplementary Figure S3**), the LC could be calculated that ART, DHA, and AS were loaded in MNP with contents of 15.3, 15.3 and 15.7%, respectively. By the way, the LC of three drugs were all very close to 15%, which was deliberately controlled *via* adjusting the mass ratio of MNP to the drug, and with the similar drug LC, latter experiments could be more comparable. In addition, the TEM images illustrated that the morphology of the nanoparticles barely changed after loading drugs, which indicated that the drug-loaded nanoparticles were still stable (**Supplementary Figure S4**).

In order to understand the drug release behavior, the drug release profiles of drug-loaded MNP were investigated. As shown in **Figure 1F**, the cumulative release of ART was about 45.5% and DHA was about 42.9% over 24 h, which confirmed that the capacities of MNP to hold ART and DHA in physiological environment were similar. Actually, the solubility of DHA was slightly lower than ART, so during the first 2 h of the release process, ART exhibited a distinct rapid release behavior, which DHA didn't (Wang et al., 2007; Ansari et al., 2011). In addition, the cumulative release of AS reached 72.1% over 24 h, indicating that AS was more hydrophilic than ART and DHA, which was consistent with the reported work (Xu R.J. et al., 2019). Similarly, AS also had obvious burst release behavior in the first 2 h. This was actually one of the reasons why we selected MNP-DHA as the optimal system for subsequent experiments.

In vitro Biocompatibility and Cytotoxicity Assays

The cytotoxicity of nanoparticles to different cells was assessed using CCK-8 assays (Jiang et al., 2017). After incubation with blank MNP for 24 h, there was no obvious toxic effect on HEK-293T cells, and cell viability retained above 90% even with a high concentration up to 200 μg/mL, which indicated good biocompatibility of blank MNP (**Supplementary Figure S5**).

To evaluate the cytotoxicity of ART and its derivatives to cancer cells, MCF-7 cells were incubated with blank MNP, the drugs and the drug-loaded MNP for 24 h, respectively. As shown in **Figures 2A–C**, all CCK-8 assays displayed dose dependent cell viability. Cells treated by blank MNP still remained high viability at the concentration of 200 μg/mL. From the results of free-drug groups, the inhibitory effects of ART and AS to cancer cells were also not good enough at various concentrations.

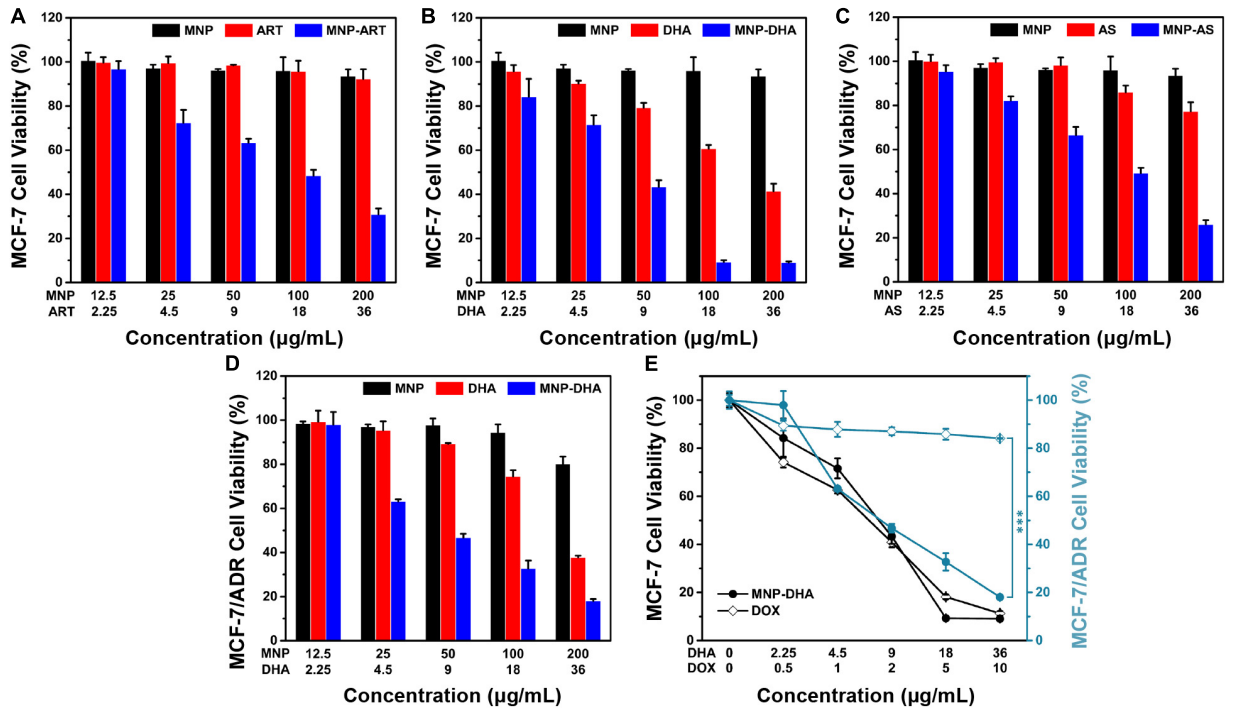

FIGURE 2 | MCF-7 cell viability after incubated with MNP, free drugs, and MNP-drug dispersions at different concentrations for 24 h, respectively: **(A)** ART, **(B)** DHA, **(C)** AS. **(D)** MCF-7/ADR cell viability after incubated with MNP, free DHA, and MNP-DHA suspensions at different concentrations for 24 h. **(E)** A comparison of the inhibitory effect of MCF-7 and MCF-7/ADR cells treated with free DOX and MNP-DHA.

However, simultaneous delivery of drugs and MNP into cancer cells all exhibited sharply enhanced cytotoxicity. For instance, in the blank MNP group, the cell viability decreased by only 4% at a concentration of 100 μg/mL, and at free ART, DHA, and AS concentrations of 18 μg/mL, the cell viability decreased by 4, 39, and 14%, respectively, while in the corresponding concentrations of MNP-ART, MNP-DHA, and MNP-AS groups, the cell viability was reduced by approximately 49, 90, and 50%, respectively, which is far greater than the sum of cell viability reduced by the two agents alone. What's more, the inhibitory effect of MNP-ART on MCF-7 cells at 48 h was more evident than at 24 h, but the difference was not significant (**Supplementary Figure S6**). This finding showed that ART and its derivatives had a particularly significant enhancement to MNP of inhibitory effects on cell viability, even exceeding the killing effect of the agent itself.

The MNP-DHA, which had the best effect on inhibiting cancer cell viability in three MNP loading ART-based drugs, was selected for subsequent experiments. After calculation, the half inhibitory concentration (IC_{50}) of free DHA was 26.10 μg/mL, which was significantly reduced after loading into MNP, changing to 7.76 μg/mL. It was shown that MNP-DHA had a better effect on killing cancer cells than free DHA, which meant the enhancement effects of materials and drugs is mutual, and further demonstrated that the combined use of DHA and MNP was an excellent strategy for enhancing killing cells effects.

According to previous reports, ART and its derivatives were sensitive to drug-resistant tumor cells, so we tried to use MNP-DHA to carry out cytotoxicity experiments on MCF-7/ADR cell lines (Zhong et al., 2016; Hu et al., 2019). As shown in **Figure 2D**, only 33% cell viability was obtained after treatment by MNP-DHA at a concentration of 100 μg/mL. The results showed that MNP-DHA also had a great killing effect to MCF-7/ADR cells. To compare the therapeutic effects on drug-resistant cancer cells between MNP-DHA and DOX, the cytotoxicity of DOX on the MCF-7 and MCF-7/ADR cell lines was evaluated. After treatment of cells with free DOX for 24 h, MCF-7 cell viability decreased rapidly, while the viability of MCF-7/ADR cells showed little change (**Figure 2E**). Whereas, whether MCF-7 or MCF-7/ADR cells, their survival rate became very low after treatment with MNP-DHA for 24 h. Consistent with published studies, the results showed that DHA wasn't a P-gp substrate, as a consequence, DHA could bypass P-gp mediated MDR (Crowe et al., 2006; Wang Y. et al., 2019). This finding demonstrated that the proposed MNP-DHA could overcome the MDR of MCF-7/ADR cells and induce high cytotoxicity.

In vitro Study of Fe^{2+} Ions Generation

The participation of a large number of ferrous ions was essential for the high efficiency of CDT, so it was necessary to evaluate the dissolving process of MNP in an acidic environment (PBS, pH 5.0), which simulated the acidic condition in the tumor microenvironment (Breunig et al., 2008; Hao et al., 2010; Wang et al., 2016; Zhang H. et al., 2016). The acid degradation experiments were carried out in PBS of different acidity (pH 7.4 and 5.0). Certified by the ICP-AES, the released iron ions increased with continuously degradation of MNP and as the pH

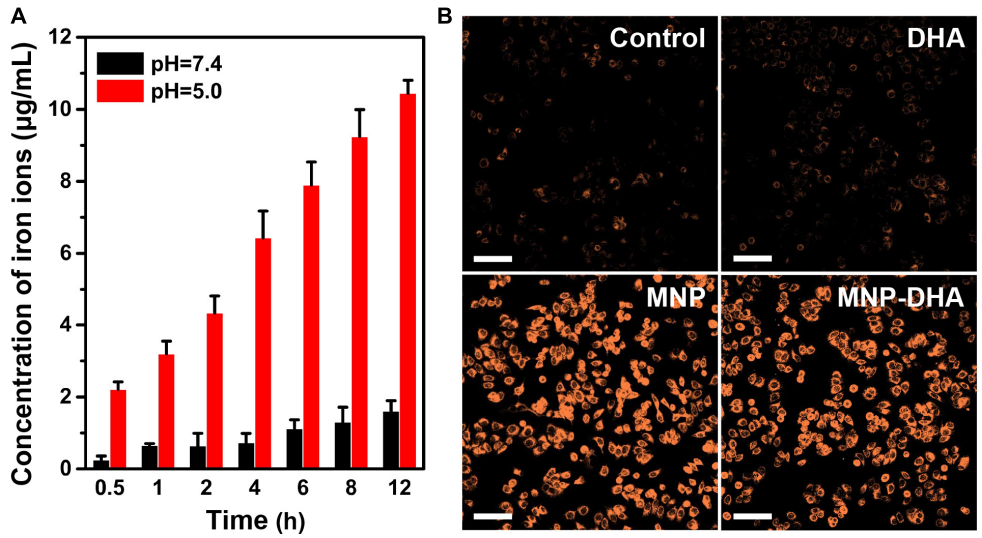

FIGURE 3 | (A) The quantitative analysis of iron ions released from pH-sensitive MNP at different pH (7.4 and 5.0) environment. **(B)** CLSM images of MCF-7/ADR cells collected to visualize the intracellular Fe^{2+} ions generation using the Fe^{2+} ions fluorescent probe Ferrorange. The scale bars are 100 μm.

value of PBS decreased, MNP exhibited more severe degradation. After 12 h, the Fe concentration in the pH 7.4 buffer solution was only 1.61 μg/mL, while the concentration of iron ions in the pH 5.0 buffer solution reached up to 10.45 μg/mL (**Figure 3A**), implying that MNP could be degraded into abundant iron ions in the microenvironment of tumors. Therefore, in theory, the drugs (DHA) would be released faster and more under acidic conditions than neutral condition (pH 7.4).

The generation of Fe^{2+} ions was corroborated using a Fe^{2+} ions probe known as Ferrorange, which could react with Fe^{2+} ions to produce a bright fluorescent substance. Compared with the control and free DHA groups, the cells treated with MNP and MNP-DHA emitted a much stronger orange fluorescence (**Figure 3B**), indicating an enormous amount of Fe^{2+} ions generated *via* MNP.

In vitro CDT Mechanism of MNP-DHA

It was well-known that endoperoxide linkages could be cleaved with ferrous ions to generate ROS *via* a Fenton-like route, which further caused apoptosis or ferroptosis of cells (Efferth et al., 2004; Ooko et al., 2015). To understand the enhanced mechanism of DHA to CDT, an assessment of the ROS generation ability produced by the reaction of DHA with Fe^{2+} ions was investigated first. A classical ROS trapper, DPBF, was used to measure ROS generation. As the generation of ROS increased, the absorbance of DPBF decreased (Ding et al., 2018). As shown in **Figure 4A**, at the beginning of the reaction, DPBF solution had a strong absorption at 412 nm. With the reaction time increasing, the absorbance of DPBF gradually decreased, indicating that ROS was produced gradually through the interaction of DHA and Fe^{2+} ions over time.

Afterward, we compared the ROS yielding ability of different groups by means of flow cytometry and CLSM, including control, blank MNP, free DHA, and MNP-DHA group. A fluorescent probe DCFH-DA was chosen to test intracellular ROS generation, which enable to produce fluorescent 2′,7′-dichlorofluorescein (DCF) under the combined actions of cellular esterase and ROS (Yuan et al., 2014). The quantitative fluorescence analysis was measured by flow cytometry (**Figures 4B,C**). Incubated with or without MNP, the MCF-7, and MCF-7/ADR cells showed no significant difference in the fluorescence intensity of DCF, due to the fact that the concentration of H_2O_2 in cells was not enough to produce a large amount of ROS with ferrous ions. After incubation with free DHA, the fluorescence intensity of the cells became a little higher, on account of the reaction of naturally existed Fe^{2+} ions with DHA. After treatment with MNP-DHA, a significant enhancement of DCF fluorescence in both MCF-7 and MCF-7/ADR cells was clearly observed, owing to the ROS generation from Fe^{2+} ions and DHA brought by DHA-loaded nanoparticles. The experiments suggested that more intracellular ROS were produced after treated by MNP-DHA.

The results of fluorescence imaging agreed well with flow cytometry. As shown in **Figure 4D**, whether the cell line used in the experiments was MCF-7 or MCF-7/ADR, the fluorescence observed in control and MNP group was faintest. The fluorescence slightly increased in free DHA group, indicating that moderately amount of ROS was generated. In the MNP-DHA group, the fluorescence was greatly enhanced, which was the strongest of the four groups. Therefore, the results verified that the effect of DHA from MNP-DHA on enhancing the production efficiency of intracellular ROS was very significant.

Cytotoxicity Assays of Other Breast Cancer Cells

In consideration of the high cytotoxicity of MNP-DHA, we tried to use this combination to conduct toxicity experiments on other canonical lethal breast cancer cell lines that were triple negative (MDA-MB-231) and human epidermal growth factor receptor

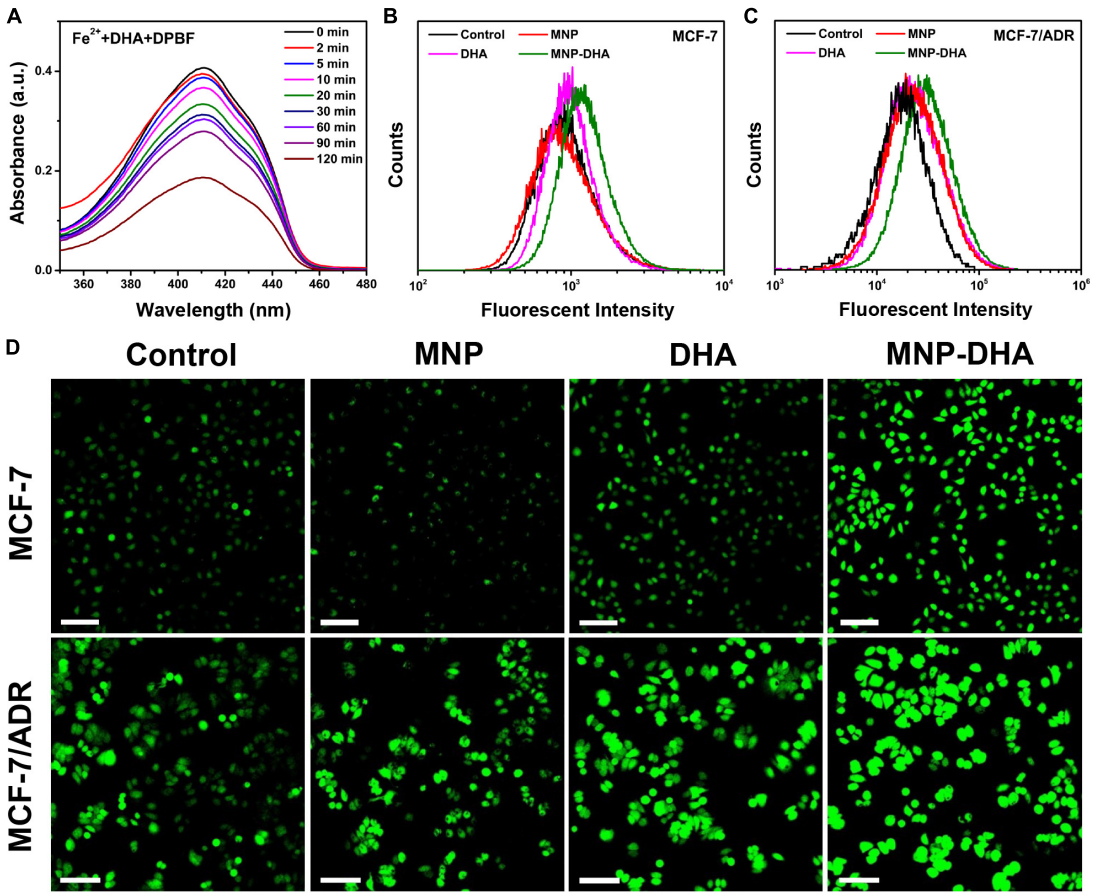

FIGURE 4 | (A) The absorption spectra of DPBF at the presence of DHA and Fe^{2+} ions at different time. Flow cytometry analyses of ROS generation in **(B)** MCF-7 and **(C)** MCF-7/ADR cells detected by DCFH-DA. **(D)** CLSM images of MCF-7/ADR cells treated under different conditions to evaluate ROS production based on DCF fluorescence intensity using the fluorescent probe DCFH-DA. The scale bars are 100 μm.

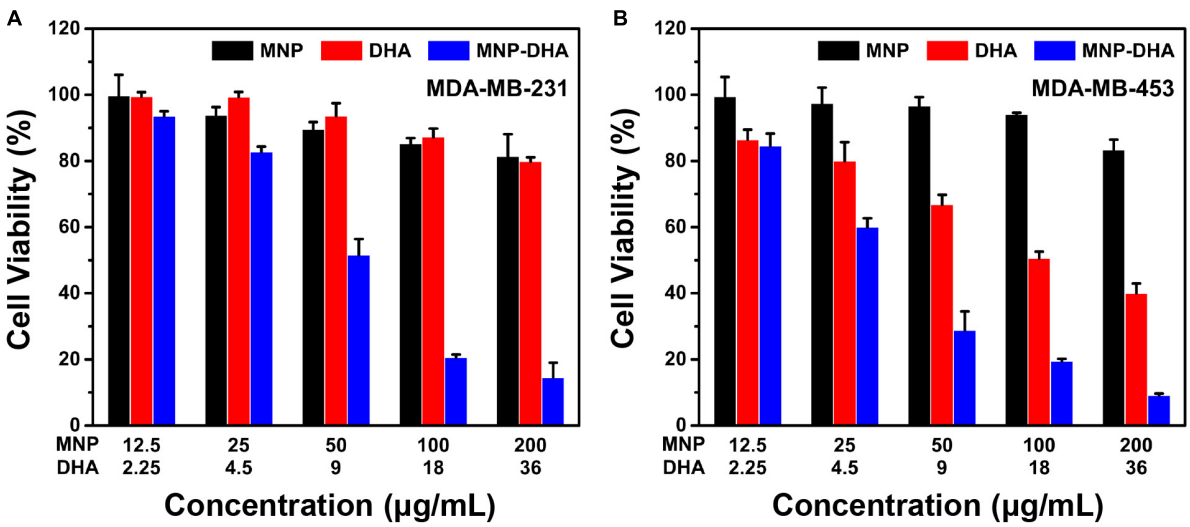

FIGURE 5 | Cell viability of **(A)** MDA-MB-231, and **(B)** MDA-MB-453 after 24 h incubation with MNP, free DHA, and MNP-DHA suspensions at different concentrations.

(HER2) overexpressing (MDA-MB-453) (Neve et al., 2006; Lee et al., 2012). Triple-negative breast cancer, defined by the lack of estrogen receptor, progesterone receptor and HER2, frequently developed resistance to chemotherapy over long-term treatment (Kim et al., 2018; Raninga et al., 2020). HER2 was overexpressed in 25–30% of breast cancers which was a considerable proportion, and patients with breast cancers that overexpress HER2 had much lower overall survival and disease-free survival due to high metastasis (Baselga et al., 1998; Slamon et al., 2001; Büyükköroğlu et al., 2016). As a consequence, it was of great significance to develop novel therapies for these tumors. As shown in **Figure 5**, after mixing with 100 μg/mL of MNP-DHA for 24 h, the viability of MDA-MB-231 cells decreased to 21% and the viability of MDA-MB-453 cells reduced to 19%. This finding made it possible to treat other types of refractory breast cancers *via* MNP-DHA, nonetheless the specific mechanism needed further research.

CONCLUSION

In summary, we successfully improved the therapeutic effect of CDT *via* loading the drugs containing peroxide groups into MNP. Among three MNP loading ART-based drugs, MNP-DHA had the strongest inhibitory effect on breast cancer cells. MNP-DHA were capable of specifically performing the Fenton-like reaction in the tumor microenvironment, thereby producing a large amount of ROS to kill tumor cells. In addition, MNP-DHA could overcome the P-gp mediated tumor MDR and could be used to treat other aggressive breast tumors. Altogether, the proposed nanoparticles may provide an effective solution for improving the efficacy of CDT treatment and have a good prospect in the treatment of aggressive breast cancers.

DATA AVAILABILITY STATEMENT

All datasets generated for this study are included in the article/**Supplementary Material**.

AUTHOR CONTRIBUTIONS

SG and WY designed the research. SG, KW, and YZ conducted the experiments. SG, XY, and QJ analyzed the data. SG, WY, JT, and HP wrote the manuscript. WY, JT, and HP supervised the work. All authors have approved the final version of the manuscript.

FUNDING

This work was supported by the National Natural Science Foundation of China (Grant Nos. 51933002 and 51873041) and the National Key R&D Program of China (Grant No. 2016YFC1100300).

ACKNOWLEDGMENTS

We thank Yongbin Cao, Ruihong Xie, Xuechun Zhang, and Jingbo Lin at Fudan for their helpful discussions.

SUPPLEMENTARY MATERIAL

The Supplementary Material for this article can be found online at: https://www.frontiersin.org/articles/10.3389/fphar.2020.00226/full#supplementary-material

REFERENCES

An, L., Wang, J.-W., Liu, J.-D., Zhao, Z.-M., and Song, Y.-J. (2019). Design, preparation, and characterization of novel calix[4]arene bioactive carrier for antitumor drug delivery. *Front. Chem.* 7:732. doi: 10.3389/fchem.2019.00732

Ansari, M. T., Batty, K. T., Iqbal, I., and Sunderland, V. B. (2011). Improving the solubility and bioavailability of dihydroartemisinin by solid dispersions and inclusion complexes. *Arch. Pharm. Res.* 34, 757–765. doi: 10.1007/s12272-011-0509-1

Baselga, J., Norton, L., Albanell, J., Kim, Y. M., and Mendelsohn, J. (1998). Recombinant humanized anti-HER2 antibody (Herceptin (TM)) enhances the antitumor activity of paclitaxel and doxorubicin against HER2/neu overexpressing human breast cancer xenografts. *Cancer Res.* 58, 2825–2831.

Bokare, A. D., and Choi, W. (2014). Review of iron-free fenton-like systems for activating H2O2 in advanced oxidation processes. *J. Hazard Mater.* 275, 121–135. doi: 10.1016/j.jhazmat.2014.04.054

Breunig, M., Bauer, S., and Goepferich, A. (2008). Polymers and nanoparticles: intelligent tools for intracellular targeting? *Eur. J. Pharm. Biopharm.* 68, 112–128. doi: 10.1016/j.ejpb.2007.06.010

Büyükköroğlu, G., Şenel, B., Gezgin, S., and Dinh, T. (2016). The simultaneous delivery of paclitaxel and Herceptin© using solid lipid nanoparticles: In vitro evaluation. *J. Drug Deliv. Sci. Technol.* 35, 98–105. doi: 10.1016/j.jddst.2016.06.010

Chen, Q., Liang, C., Sun, X., Chen, J., Yang, Z., Zhao, H., et al. (2017). H2O2-responsive liposomal nanoprobe for photoacoustic inflammation imaging and tumor theranostics via in vivo chromogenic assay. *Proc. Natl. Acad. Sci. U.S.A.* 114, 5343–5348. doi: 10.1073/pnas.1701976114

Chen, Y., Deng, J., Liu, F., Dai, P., An, Y., Wang, Z., et al. (2019). Energy-free, singlet oxygen-based chemodynamic therapy for selective tumor treatment without dark toxicity. *Adv. Healthc. Mater.* 8:e1900366. doi: 10.1002/adhm.201900366

Cho, M. H., Choi, E. S., Kim, S., Goh, S. H., and Choi, Y. (2017). Redox-responsive manganese dioxide nanoparticles for enhanced mr imaging and radiotherapy of lung cancer. *Front. Chem.* 5:109. doi: 10.3389/fchem.2017.00109

Crowe, A., Ilett, K. F., Karunajeewa, H. A., Batty, K. T., and Davis, T. M. (2006). Role of P glycoprotein in absorption of novel antimalarial drugs. *Antimicrob. Agents Chemother.* 50, 3504–3506. doi: 10.1128/AAC.00708-06

Deng, H., Li, X., Peng, Q., Wang, X., Chen, J., and Li, Y. (2005). Monodisperse magnetic single-crystal ferrite microspheres. *Angew. Chem. Int. Ed. Engl.* 44, 2782–2785. doi: 10.1002/anie.200462551

Ding, Y., Wan, J., Zhang, Z., Wang, F., Guo, J., and Wang, C. (2018). Localized Fe(II)-induced cytotoxic reactive oxygen species generating nanosystem for enhanced anticancer therapy. *ACS Appl. Mater. Interfaces* 10, 4439–4449. doi: 10.1021/acsami.7b16999

Efferth, T., Benakis, A., Romero, M. R., Tomicic, M., Rauh, R., Steinbach, D., et al. (2004). Enhancement of cytotoxicity of artemisinins toward cancer cells by ferrous iron. *Free Radic. Biol. Med.* 37, 998–1009. doi: 10.1016/j.freeradbiomed.2004.06.023

Ember, E., Rothbart, S., Puchta, R., and van Eldik, R. (2009). Metal ion-catalyzed oxidative degradation of orange II by H2O2. High catalytic activity of simple manganese salts. *New J. Chem.* 33, 34–49. doi: 10.1039/b813725k

Golenser, J., Waknine, J. H., Krugliak, M., Hunt, N. H., and Grau, G. E. (2006). Current perspectives on the mechanism of action of artemisinins. *Int. J. Parasitol.* 36, 1427–1441. doi: 10.1016/j.ijpara.2006.07.011

Hao, R., Xing, R., Xu, Z., Hou, Y., Gao, S., and Sun, S. (2010). Synthesis, functionalization, and biomedical applications of multifunctional magnetic nanoparticles. *Adv. Mater.* 22, 2729–2742. doi: 10.1002/adma.201000260

Hu, Y., Li, N., Zhang, J., Wang, Y., Chen, L., and Sun, J. (2019). Artemisinin-indole and artemisinin-imidazole hybrids: synthesis, cytotoxic evaluation and reversal effects on multidrug resistance in MCF-7/ADR cells. *Bioorg. Med. Chem. Lett.* 29, 1138–1142. doi: 10.1016/j.bmcl.2019.02.021

Huo, M., Wang, L., Chen, Y., and Shi, J. (2017). Tumor-selective catalytic nanomedicine by nanocatalyst delivery. *Nat. Commun.* 8:357. doi: 10.1038/s41467-017-00424-8

Jiang, Q., Luo, Z., Men, Y., Yang, P., Peng, H., Guo, R., et al. (2017). Red blood cell membrane-camouflaged melanin nanoparticles for enhanced photothermal therapy. *Biomaterials* 143, 29–45. doi: 10.1016/j.biomaterials.2017.07.027

Kim, C., Gao, R., Sei, E., Brandt, R., Hartman, J., Hatschek, T., et al. (2018). Chemoresistance evolution in triple-negative breast cancer delineated by single-cell sequencing. *Cell* 173, 879–893.e13. doi: 10.1016/j.cell.2018.03.041

Kim, D. K., Mikhaylova, M., Zhang, Y., and Muhammed, M. (2003). Protective coating of superparamagnetic iron oxide nanoparticles. *Chem. Mater.* 15, 1617–1627. doi: 10.1021/cm021349j

Kong, B., Tang, J., Wu, Z. X., Wei, J., Wu, H., Wang, Y. C., et al. (2014). Ultralight mesoporous magnetic frameworks by interfacial assembly of prussian blue nanocubes. *Angew. Chem.-Int. Ed.* 53, 2888–2892. doi: 10.1002/anie.201308625

Krishna, S., Uhlemann, A. C., and Haynes, R. K. (2004). Artemisinins: mechanisms of action and potential for resistance. *Drug Resist. Updat.* 7, 233–244. doi: 10.1016/j.drup.2004.07.001

Kruh, G. D., and Belinsky, M. G. (2003). The MRP family of drug efflux pumps. *Oncogene* 22, 7537–7552. doi: 10.1038/sj.onc.1206953

Kumar, R., Singh, M., Meena, J., Singhvi, P., Thiyagarajan, D., Saneja, A., et al. (2019). Hyaluronic acid – Dihydroartemisinin conjugate: Synthesis, characterization and in vitro evaluation in lung cancer cells. *Int. J. Biol. Macromol.* 133, 495–502. doi: 10.1016/j.ijbiomac.2019.04.124

Lee, M. J., Ye, A. S., Gardino, A. K., Heijink, A. M., Sorger, P. K., MacBeath, G., et al. (2012). Sequential application of anticancer drugs enhances cell death by rewiring apoptotic signaling networks. *Cell* 149, 780–794. doi: 10.1016/j.cell.2012.03.031

Li, D., Tang, J., Guo, J., Wang, S. L., Chaudhary, D., and Wang, C. C. (2012a). Hollow-core magnetic colloidal nanocrystal clusters with ligand-exchanged surface modification as delivery vehicles for targeted and stimuli-responsive drug release. *Chem. A Eur. J.* 18, 16517–16524. doi: 10.1002/chem.201202249

Li, D., Tang, J., Wei, C., Guo, J., Wang, S. L., Chaudhary, D., et al. (2012b). Doxorubicin-conjugated mesoporous magnetic colloidal nanocrystal clusters stabilized by polysaccharide as a smart anticancer drug vehicle. *Small* 8, 2690–2697. doi: 10.1002/smll.201200272

Li, R., Jin, X., Megharaj, M., Naidu, R., and Chen, Z. (2015). Heterogeneous fenton oxidation of 2,4-dichlorophenol using iron-based nanoparticles and persulfate system. *Chem. Eng. J.* 264, 587–594. doi: 10.1016/j.cej.2014.11.128

Lin, L. S., Song, J., Song, L., Ke, K., Liu, Y., Zhou, Z., et al. (2018). Simultaneous fenton-like ion delivery and glutathione depletion by MNO_2 -based nanoagent to enhance chemodynamic therapy. *Angew. Chem. Int. Ed. Engl.* 57, 4902–4906. doi: 10.1002/anie.201712027

Ma, B., Wang, S., Liu, F., Zhang, S., Duan, J., Li, Z., et al. (2019). Self-assembled copper-amino acid nanoparticles for in situ glutathione "AND" H2O2 sequentially triggered chemodynamic therapy. *J. Am. Chem. Soc.* 141, 849–857. doi: 10.1021/jacs.8b08714

Ma, W. F., Wu, K. Y., Tang, J., Li, D., Wei, C., Guo, J., et al. (2012). Magnetic drug carrier with a smart pH-responsive polymer network shell for controlled delivery of doxorubicin. *J. Mater. Chem.* 22, 15206–15214. doi: 10.1039/c2jm31721d

Men, Y., Peng, S., Yang, P., Jiang, Q., Zhang, Y., Shen, B., et al. (2018). Biodegradable zwitterionic nanogels with long circulation for antitumor drug delivery. *ACS Appl. Mater. Interfaces* 10, 23509–23521. doi: 10.1021/acsami.8b03943

Neve, R. M., Chin, K., Fridlyand, J., Yeh, J., Baehner, F. L., Fevr, T., et al. (2006). A collection of breast cancer cell lines for the study of functionally distinct cancer subtypes. *Cancer Cell* 10, 515–527. doi: 10.1016/j.ccr.2006.10.008

Olliaro, P. L., Haynes, R. K., Meunier, B., and Yuthavong, Y. (2001). Possible modes of action of the artemisinin-type compounds. *Trends Parasitol.* 17, 122–126. doi: 10.1016/S1471-4922(00)01838-9

Ooko, E., Saeed, M. E., Kadioglu, O., Sarvi, S., Colak, M., Elmasaoudi, K., et al. (2015). Artemisinin derivatives induce iron-dependent cell death (ferroptosis) in tumor cells. *Phytomedicine* 22, 1045–1054. doi: 10.1016/j.phymed.2015.08.002

Osaki, T., Tajima, M., Okamoto, Y., Takagi, S., Tsuka, T., Imagawa, T., et al. (2011). Sonodynamic antitumor effect of benzoporphyrin derivative monoacid ring A on KLN205 Cells. *J. Cancer Ther.* 02, 99–104. doi: 10.4236/jct.2011.22011

Peng, H. B., Tang, J., Zheng, R., Guo, G. N., Dong, A. G., Wang, Y. J., et al. (2017). Nuclear-targeted multifunctional magnetic nanoparticles for photothermal therapy. *Adv. Healthc. Mater.* 6, doi: 10.1002/adhm.201601289

Poyton, M. F., Sendecki, A. M., Cong, X., and Cremer, P. S. (2016). Cu(2+) binds to phosphatidylethanolamine and increases oxidation in lipid membranes. *J. Am. Chem. Soc.* 138, 1584–1590. doi: 10.1021/jacs.5b11561

Prasad, P., Cheng, J., Shuhendler, A., Rauth, A. M., and Wu, X. Y. (2012). A novel nanoparticle formulation overcomes multiple types of membrane efflux pumps in human breast cancer cells. *Drug Deliv. Transl Res.* 2, 95–105. doi: 10.1007/s13346-011-0051-1

Raninga, P. V., Lee, A. C., Sinha, D., Shih, Y. Y., Mittal, D., Makhale, A., et al. (2020). Therapeutic cooperation between auranofin, a thioredoxin reductase inhibitor and anti-PD-L1 antibody for treatment of triple-negative breast cancer. *Int. J. Cancer* 146, 123–136. doi: 10.1002/ijc.32410

Reed, J. C., and Pellecchia, M. (2012). Ironing out cell death mechanisms. *Cell* 149, 963–965. doi: 10.1016/j.cell.2012.05.009

Sanati, A. M., Kamari, S., and Ghorbani, F. (2019). Application of response surface methodology for optimization of cadmium adsorption from aqueous solutions by Fe3O4@SiO2@APTMS core–shell magnetic nanohybrid. *Surf. Interfaces* 17:100374. doi: 10.1016/j.surfin.2019.100374

Slamon, D. J., Leyland-Jones, B., Shak, S., Fuchs, H., Paton, V., Bajamonde, A., et al. (2001). Use of chemotherapy plus a monoclonal antibody against HER2 for metastatic breast cancer that overexpresses HER2. *N. Engl. J. Med.* 344, 783–792. doi: 10.1056/Nejm200103153441101

Song, G., Liang, C., Yi, X., Zhao, Q., Cheng, L., Yang, K., et al. (2016). Perfluorocarbon-loaded hollow Bi2Se3 nanoparticles for timely supply of oxygen under near-infrared light to enhance the radiotherapy of cancer. *Adv. Mater.* 28, 2716–2723. doi: 10.1002/adma.201504617

Sun, X., Yan, P., Zou, C., Wong, Y. K., Shu, Y., Lee, Y. M., et al. (2019). Targeting autophagy enhances the anticancer effect of artemisinin and its derivatives. *Med. Res. Rev.* 39, 2172–2193. doi: 10.1002/med.21580

Szakacs, G., Paterson, J. K., Ludwig, J. A., Booth-Genthe, C., and Gottesman, M. M. (2006). Targeting multidrug resistance in cancer. *Nat. Rev. Drug Discov.* 5, 219–234. doi: 10.1038/nrd1984

Szatrowski, T. P., and Nathan, C. F. (1991). Production of large amounts of hydrogen-peroxide by human tumor-cells. *Cancer Res.* 51, 794–798.

Tang, J., Kong, B., Wu, H., Xu, M., Wang, Y. C., Wang, Y. L., et al. (2013). Carbon nanodots featuring efficient FRET for real-time monitoring of drug delivery and two-photon imaging. *Adv. Mater.* 25, 6569–6574. doi: 10.1002/adma.201303124

Tang, J., Qin, N., Chong, Y., Diao, Y. P., Yiliguma, Wang, Z. X., et al. (2018). Nanowire arrays restore vision in blind mice. *Nat. Commun.* 9:786. doi: 10.1038/s41467-018-03212-0

Tang, Z., Liu, Y., He, M., and Bu, W. (2019). Chemodynamic therapy: tumour microenvironment-mediated fenton and fenton-like reactions. *Angew. Chem. Int. Ed. Engl.* 58, 946–956. doi: 10.1002/anie.201805664

Tu, Y. (2011). The discovery of artemisinin (qinghaosu) and gifts from Chinese medicine. *Nat. Med.* 17, 1217–1220. doi: 10.1038/nm.2471

Wan, X., Zhong, H., Pan, W., Li, Y., Chen, Y., Li, N., et al. (2019). Programmed release of dihydroartemisinin for synergistic cancer therapy using a CaCO3 mineralized metal-organic framework. *Angew. Chem. Int. Ed. Engl.* 58, 14134–14139. doi: 10.1002/anie.201907388

Wang, D., Zhou, J., Chen, R., Shi, R., Xia, G., Zhou, S., et al. (2016). Magnetically guided delivery of DHA and Fe ions for enhanced cancer therapy based on pH-responsive degradation of DHA-loaded Fe3O4@C@MIL-100(Fe) nanoparticles. *Biomaterials* 107, 88–101. doi: 10.1016/j.biomaterials.2016.08.039

Wang, K., Yang, P., Guo, R., Yao, X., and Yang, W. (2019). Photothermal performance of MFe2O4 nanoparticles. *Chin. Chem.* Lett. 30, 2013–2016. doi: 10.1016/j.cclet.2019.04.005

Wang, L. L., Kong, L., Liu, H., Zhang, Y., Zhang, L., Liu, X., et al. (2019). Design and synthesis of novel artemisinin derivatives with potent activities against colorectal cancer in vitro and in vivo. *Eur. J. Med. Chem.* 182:111665. doi: 10.1016/j.ejmech.2019.111665

Wang, Y., Li, Y., Shang, D., and Efferth, T. (2019). Interactions between artemisinin derivatives and P-glycoprotein. *Phytomedicine* 60, 152998. doi: 10.1016/j.phymed.2019.152998

Wang, L. H., Song, Y. T., Chen, Y., and Cheng, Y. Y. (2007). Solubility of artemisinin in ethanol plus water from (278.2 *to* 343.2) K. *J. Chem. Eng. Data* 52, 757–758. doi: 10.1021/je0603426

Wang, Y., Yin, W., Ke, W., Chen, W., He, C., and Ge, Z. (2018). Multifunctional polymeric micelles with amplified fenton reaction for tumor ablation. *Biomacromolecules* 19, 1990–1998. doi: 10.1021/acs.biomac.7b01777

Xie, R., Tian, Y., Peng, S., Zhang, L., Men, Y., and Yang, W. (2018). Poly(2-methacryloyloxyethyl phosphorylcholine)-based biodegradable nanogels for controlled drug release. *Polym. Chem.* 9, 4556–4565. doi: 10.1039/c8py00948a

Xu, A., Li, X., Ye, S., Yin, G., and Zeng, Q. (2011). Catalyzed oxidative degradation of methylene blue by in situ generated cobalt (II)-bicarbonate complexes with hydrogen peroxide. *Appl. Catal. B Environ.* 102, 37–43. doi: 10.1016/j.apcatb.2010.11.022

Xu, R. J., Han, T., Shen, L., Zhao, J. G., and Lu, X. A. (2019). Solubility determination and modeling for artesunate in binary solvent mixtures of methanol, ethanol, isopropanol, and propylene glycol plus water. *J. Chem. Eng. Data* 64, 755–762. doi: 10.1021/acs.jced.8b00988

Xu, X., Feng, Y., Chen, X., Wang, Q., Meng, T., and Liu, A. (2019). Antitumor effects of seleno-beta-lactoglobulin on human breast cancer MCF-7 and MDA-MB-231 cells in vitro. *Toxicol. In Vitro* 61:104607. doi: 10.1016/j.tiv.2019.104607

Yan, K. C., Sedgwick, A. C., Zang, Y., Chen, G. R., He, X. P., Li, J., et al. (2019). Sensors, imaging agents, and theranostics to help understand and treat reactive oxygen species related diseases. *Small Methods* 3:1900013. doi: 10.1002/smtd.201900013

Yang, P., Men, Y., Tian, Y., Cao, Y., Zhang, L., Yao, X., et al. (2019). Metal-organic framework nanoparticles with near-infrared dye for multimodal imaging and guided phototherapy. *ACS Appl. Mater. Interfaces* 11, 11209–11219. doi: 10.1021/acsami.9b01286

Yao, X., Yang, P., Jin, Z., Jiang, Q., Guo, R., Xie, R., et al. (2019). Multifunctional nanoplatform for photoacoustic imaging-guided combined therapy enhanced by CO induced ferroptosis. *Biomaterials* 197, 268–283. doi: 10.1016/j.biomaterials.2019.01.026

Yao, Y., Guo, Q., Cao, Y., Qiu, Y., Tan, R., Yu, Z., et al. (2018). Artemisinin derivatives inactivate cancer-associated fibroblasts through suppressing TGF-beta signaling in breast cancer. *J. Exp. Clin. Cancer Res.* 37:282. doi: 10.1186/s13046-018-0960-7

Yuan, Y., Liu, J., and Liu, B. (2014). Conjugated-polyelectrolyte-based polyprodrug: targeted and image-guided photodynamic and chemotherapy with on-demand drug release upon irradiation with a single light source. *Angew. Chem. Int. Ed. Engl.* 53, 7163–7168. doi: 10.1002/anie.201402189

Yue, J., Liang, L., Shen, Y., Guan, X., Zhang, J., Li, Z., et al. (2018). Investigating dynamic molecular events in melanoma cell nucleus during photodynamic therapy by SERS. *Front. Chem.* 6:665. doi: 10.3389/fchem.2018.00665

Zhang, C., Bu, W., Ni, D., Zhang, S., Li, Q., Yao, Z., et al. (2016). Synthesis of iron nanometallic glasses and their application in cancer therapy by a localized fenton reaction. *Angew. Chem. Int. Ed. Engl.* 55, 2101–2106. doi: 10.1002/anie.201510031

Zhang, H., Chen, Q., Zhang, X., Zhu, X., Chen, J., Zhang, H., et al. (2016). An Intelligent and tumor-responsive Fe(2+) donor and Fe(2+)-dependent drugs cotransport system. *ACS Appl. Mater. Interfaces* 8, 33484–33498. doi: 10.1021/acsami.6b11839

Zheng, D. W., Lei, Q., Zhu, J. Y., Fan, J. X., Li, C. X., Li, C., et al. (2017). Switching apoptosis to ferroptosis: metal-organic network for high-efficiency anticancer therapy. *Nano Lett.* 17, 284–291. doi: 10.1021/acs.nanolett.6b04060

Zhong, H., Zhao, X., Zuo, Z., Sun, J., Yao, Y., Wang, T., et al. (2016). Combating P-glycoprotein-mediated multidrug resistance with 10-O-phenyl dihydroartemisinin ethers in MCF-7 cells. *Eur J Med. Chem.* 108, 720–729. doi: 10.1016/j.ejmech.2015.10.040

Conflict of Interest: The authors declare that the research was conducted in the absence of any commercial or financial relationships that could be construed as a potential conflict of interest.

frontiers in Pharmacology

ORIGINAL RESEARCH
published: 13 March 2020
doi: 10.3389/fphar.2020.00317

Preparation and Characterization of Chitosan Nanoparticles for Chemotherapy of Melanoma Through Enhancing Tumor Penetration

*Hui Guo, Faping Li, Heping Qiu, Jianhua Liu, Sihao Qin, Yuchuan Hou and Chunxi Wang**

Department of Urology, the First Hospital of Jilin University, Changchun, China

OPEN ACCESS

Edited by:
Chao Wang,
Soochow University, China

Reviewed by:
Yang Li,
Harvard Medical School, United States
Wuyu Zhang,
University of Louisville, United States
Kun Zhou,
Boston Children's Hospital, United States

***Correspondence:**
Chunxi Wang
chunxi_wang@126.com

Specialty section:
This article was submitted to Experimental Pharmacology and Drug Discovery, a section of the journal Frontiers in Pharmacology

Received: *24 October 2019*
Accepted: *04 March 2020*
Published: *13 March 2020*

Citation:
Guo H, Li F, Qiu H, Liu J, Qin S, Hou Y and Wang C (2020) Preparation and Characterization of Chitosan Nanoparticles for Chemotherapy of Melanoma Through Enhancing Tumor Penetration. Front. Pharmacol. 11:317. doi: 10.3389/fphar.2020.00317

The poor solubility and permeability of most chemotherapeutic drugs lead to unsatisfactory bioavailability combined with insufficient drug concentration. In this study, positively charged nanoparticles based on chitosan were developed and synthesized to enhance tumor penetration capability of 10-Hydroxycamptothecin (HCPT) in order to improve the chemotherapeutic effect of melanoma. The HCPT encapsulated nanoparticles were noted as NPs/HCPT. NPs/HCPT was characterized by dynamic light scattering and *zeta* potential measurements. In addition, cell uptake, *in vitro* cytotoxicity, apoptosis and *in vivo* antitumor activity of NPs/HCPT were further investigated. The average diameter of NPs/HCPT was approximately 114.6 ± 4.1 nm. The viability of murine melanoma cell lines (B16F10 and B16F1) was significantly decreased due to interaction with NPs/HCPT. Moreover, NPs/HCPT significantly inhibited the progression of tumors. These investigations implied that cationic NPs/HCPT could be potentially applied as a promising drug delivery nanosystem.

Keywords: chitosan, nanoparticle, penetrability, melanoma, chemotherapy

INTRODUCTION

Nowadays, one of the major causes of death all over the world is cancer due to its high heterogeneity (Bray et al., 2018). Chemotherapy is the preferred treatment for most cancer patients due to its universality and excellent efficacy (Al-Batran et al., 2019). Unfortunately, the poor solubility and permeability of most chemotherapeutic drugs lead to unsatisfactory bioavailability combined with insufficient drug concentration (Jia et al., 2018). Nanotechnology provides promising application prospects in encapsulating hydrophobic drugs, enhancing drug penetration depth, and targeting drug delivery (Fan et al., 2017). It has been reported that the physicochemical properties of nanoparticles, such as size, shape, and charge, are more meaningful to promote the accumulation of nanoparticles in tumor tissues than the surface modification of active targeting of nanoparticles (Danhier, 2016). Chitosan (CS) has been extensively investigated as an efficient drug delivery biopolymer due to its intriguing biocompatibility, biodegradability, anti-microbial activity, anti-inflammatory property, and nontoxicity (Nezakati et al., 2018; Zhao et al., 2018). This cationic

polysaccharide is soluble in dilute acid and can adhere to the negatively charged biological membranes by electrostatic interaction, thus improving bioavailability and facilitating cell endocytosis (Kwak et al., 2019). In addition, CS has been reported to open the tight junction between epithelial cells, thereby enhancing the permeability of carried drugs (Sheng et al., 2015).

In this work, a positively charged drug delivery system based on CS was designed to enhance tumor penetration capability of 10-Hydroxycamptothecin (HCPT) in order to improve the chemotherapeutic effect of melanoma. As a broad-spectrum anticancer drug, HCPT is a commonly applied topoisomerase I inhibitor, which has promising antitumor property. The mechanism is mainly attributed to the effectively inhibition of DNA replication and RNA transcription in tumor cells (Guo et al., 2018; Li et al., 2018). HCPT was encapsulated into the core of nanoparticles (i.e., NPs/HCPT), which significantly improved the aqueous dispersibility and permeability. The positively charged NPs/HCPT could penetrate deep into the tumor and promote the internalization by tumor cells. The sustained release of HCPT from NPs/HCPT in the cytoplasm maintained an effective drug concentration, thus effectively inhibiting the proliferation of cancer cells. A comprehensive study was provided to further understand the application of NPs/HCPT in melanoma chemotherapy.

MATERIALS AND METHODS

Materials

CS (degree of deacetylation of 80% and molecular weight of 50 kDa) was supplied by Sigma-Aldrich (Shanghai, P. R. China). 10-Hydroxycamptothecin (HCPT) was obtained from Beijing Huafeng United Technology Co., Ltd. (Beijing, P. R. China). Dulbecco's modified Eagle's medium (DMEM) and fetal bovine serum (FBS) were provided by Gibco (Grand Island, NY, USA). Penicillin and streptomycin were purchased from Huabei Pharmaceutical Co., Ltd. (Shijiazhuang, P. R. China). Trypsin and methyl thiazolyl tetrazolium (MTT) were supplied by Sigma-Aldrich (Shanghai, P. R. China). Annexin V-FITC and Propidium iodide (PI) were bought from Shanghai Qihai Futai Biotechnology Co., Ltd. (Shanghai, P. R. China). Acetic acid (HAc) and dimethyl sulphoxide (DMSO) were obtained from Shanghai Aladdin Bio-Chem Technology Co., Ltd. (Shanghai, P. R. China). N,N-dimethylformamide (DMF) was supplied by Sigma-Aldrich (Shanghai, P. R. China). The purified deionized water was produced by the Milli-Q plus system (Millipore Co., Billerica, MA, USA). All the other reagents were analytical grade and used as received without further purification.

Cell Culture

Murine melanoma cell lines (B16F10 and B16F1) were obtained from Changchun Institute of Applied Chemistry (Jilin, China) and incubated in DMEM with 10% FBS, 100 μg ml^{-1} streptomycin and 100 μg ml^{-1} penicillin at 37°C in a 5% CO_2 incubator.

Preparation of HCPT Loaded Nanoparticles

The NPs/HCPT was fabricated according to the previous method with slight modification (Guo et al., 2018). Briefly, 25.0 mg of CS was prepared in 10.0 ml of HAc solution (pH 3.0), and then a solution of DMF containing 7.0 mg of HCPT was slowly added into the CS solution with stirring for 12 h at room temperature. The excess HCPT, which was not encapsulated inside the CS NPs, was removed by dialysis at room temperature. The whole process of purification was performed in darkness. Finally, NPs/HCPT was obtained by lyophilization.

Degree of Drug Loading

To quantify the amount of HCPT entrapped in the prepared NPs, accurately measured volumes of freeze-dried NPs/HCPT were dissolved in HAc solution (pH 3.0). Consequently, the concentration of HCPT was assayed spectrophotometrically at wavelength of 371 nm using ultraviolet-visible (UV-vis). The drug loading content (DLC) and drug loading efficiency (DLE) of NPs/HCPT were expressed as percentages with respect to the standard curve method, and calculated according to the following equations.

$$\mathrm{DLC}(\%) = \frac{\text{Amount of drug in nanogel}}{\text{Amount of loading nanogel}} \times 100\% \quad (1)$$

$$\mathrm{DLE}(\%) = \frac{\text{Amount of drug in nanogel}}{\text{Total amount of feeding drug}} \times 100\% \quad (2)$$

Particle Size and Zeta Potential Distribution

The particle size of NPs/HCPT was determined by dynamic light scattering (DLS) analyzer in a WyattQELS instrument with a vertically polarized He-Ne laser (DAWN EOS, Wyatt Technology Co., Santa Barbara, CA, USA). The concentration of NPs/HCPT for DLS was 100.0 μg ml^{-1}. Before measurement, the samples were properly diluted in aqueous solution and filtered through a 0.45-μm filter. The *zeta* potential of NPs/HCPT was determined by a *zeta* potential analyzer (Brookhaven, USA). 100.0 μg ml^{-1} of NPs/HCPT dispersed in aqueous solution after sonication was detected as a sample. The dispersion was measured in triplicate and the results were reported as means values ± standard deviation (SD).

In Vitro Drug Release Studies

The *in vitro* release profiles of HCPT from NPs/HCPT were performed in phosphate-buffered saline (PBS; pH 7.4, containing 0.1% Tween-80 (w/v)). Briefly, precisely weighed free HCPT (0.1 mg) or freeze-dried NPs/HCPT (1.0 mg) were suspended in 10.0 ml of release medium and then transferred into a dialysis cellulose bag (molecular weight cutoff (MWCO) = 3.5 kDa). The end-sealed dialysis bag was placed into a glass bottle containing 110.0 ml of release medium. The glass bottles were continuously shaken at 37°C. At experimental time intervals, aliquots of 2.0 ml were withdrawn and replenished with an

equivalent amount of release medium. The samples were acidified with 1.0 N HCl, and analyzed by high-performance liquid chromatography (HPLC; λ_{abs} = 371 nm). The mobile phase consisted of 67:33 mix-tures of acetonitrile and aqueous buffer. The aqueous buffer was a mixture of 75 mmol L^{-1} ammonium acetate, 5 mmol L^{-1} triethylamine, and 0.5% (V/V) acetic acid. The flow rate was set at 1.0 ml/min.

Cell Uptake and Distribution Studies

The cell uptake and intracellular distribution of NPs/HCPT were visualized by confocal laser scanning microscopy (CLSM). Typically, B16F10 cells were seeded into 6-well plates at a density of 2.0×10^5 cells per well at 37°C containing 5% (v/v) carbon dioxide atmosphere. After 24 h of culture, the growth medium was discarded and the cells were incubated with either free HCPT or NPs/HCPT (HCPT concentration of 1.5 μg ml^{-1}) for 2 h and 6 h. Afterward, the cells were carefully rinsed with PBS and fixed with 4% paraformaldehyde for 20 min at room temperature. At last, the obtained samples were washed with PBS for three times. The cell uptake and intracellular distribution of NPs/HCPT were confirmed by CLSM. In order to qualitatively understand the cell uptake of NPs/HCPT at different time points, B16F10 cells were cultured with either free HCPT or NPs/HCPT (HCPT concentration of 1.5 μg ml^{-1}) for a consistent period of time, and then washed, lysed, dissolved, and then measured at 384 nm with a microplate reader (Tecan, Durham, USA). The experiment was repeated three times (Wei et al., 2010).

In Vitro Cytotoxicity Assay

Cytotoxicity evaluation of NPs/HCPT was detected on melanoma cell lines (B16F10 and B16F1) by MTT assay. Briefly, B16F10 or B16F1 cells were seeded in 96-well plates at a density of 8.0×10^3 cells per well. After 24 h, the cells were incubated with prepared solutions, including free HCPT and NPs/HCPT, for further 24 h or 48 h. The equivalent HCPT concentrations in culture medium ranged from 0 to 10.0 μg ml^{-1}. After incubation period, 20.0 μl of MTT solution was added to each well and the cells were incubated at 37°C in 5% (v/v) CO_2 atmosphere for approximately 4 h. Subsequently, the supernatant was removed and 200.0 μl of DMSO was added to dissolve the formazan crystals. The absorbance of obtained MTT-products was read using a Bio-Rad 680 microplate reader (Bio-Rad Laboratories, Hercules, CA, USA) at 490 nm. The untreated cells were used as a control. The cytotoxicity of empty NPs was studied on B16F1at the highest concentration of 20.0 μg ml^{-1}. All experiments were performed in triplicate. The cell viability (%) was evaluated using the Equation 3 below.

$$\text{Cell Viability}(\%) = \frac{A\text{sample}}{A\text{control}} \times 100\,\% \quad (3)$$

In Equation 3, A_{sample} and $A_{control}$ referred to the absorbance of the sample and control well, respectively.

Cell Apoptosis Analysis

The apoptosis percentage of B16F10 cells was evaluated by flow cytometry (FCM) analysis after treatment with NPs/HCPT for 24 h. Briefly, 3.0×10^5 viable cells dispersed in 1.8 ml of DMEM medium were seeded in 6-well plates and allowed to attach overnight. Then 0.2 ml of growth medium containing different HCPT formulations was added with an equivalent HCPT concentration of 3.0 μg ml^{-1}. The untreated cells were used as a control. After 24 h of incubation, the cells were harvested by trypsinization and collected by centrifugation at 1,000 rpm for 5 min. Subsequently, 0.5 ml of 1× Annexin V Binding Buffer was applied to resuscitate the obtained cells. Finally, the samples were double-labeled with Annexin V-FITC and propidium iodide (PI) on ice in the dark, and then analyzed by FCM.

In Vivo Antitumor Activity Against Melanoma

Female C57BL/6 mice weighing 20–22 g were purchased from the Laboratory Animal Center of Jilin University. All animals received care in compliance with the guidelines outlined in the Guide for the Care and Use of Laboratory Animals, and all procedures were approved by the Animal Care and Use Committee of Jilin University. 1.0×10^5 B16F10 cells dispersed in 0.1 ml of PBS were inoculated subcutaneously in the left flank of the mice. When the tumors reached approximately 50 mm^3, mice were randomly divided into three groups: control, free HCPT, and NPs/HCPT (n = 5). Different HCPT formulations were intravenously administered to mice at a dose of 5.0 mg/kg every 3 days for four times. The body weight was also measured every 3 days during the process of the treatment.

Statistical Analyses

The results were presented as means ± SD of three replicate independent experiments. Statistical analysis was performed using Student's t-test. $P < 0.05$ was considered statistically significance.

RESULTS AND DISCUSSION

HCPT Encapsulation and NPs/HCPT Characterizations

The drug-loaded NPs/HCPT was fabricated by dialysis method, which was shown in **Figure 1**. Electrostatic forces may be the most important reason for drug encapsulation (Zhang et al., 2018). The simple preparation method predicted its good practicality. The average DLC of NPs/HCPT was 18.3 ± 0.9 wt.%. The DLE of NPs/HCPT was determined up to 80.2 ±1.5 wt.% (**Table 1**). The resulting NPs/HCPT exhibited an ideal diameter of 114.6 ± 4.1 nm, which was determined by DLS (**Figure 2**). The average diameter of NPs/HCPT ranged from 10 to 200 nm, resulting in the optimal tumor accumulation due to the enhanced permeability and retention (EPR) effect (Blanco et al., 2015). Furthermore, the *zeta* potential of NPs/HCPT was approximately 15.9 ± 2.4 mV (**Table 1**). A positive surface charge implied an enhanced interaction with the cell membranes, which was essential for increasing cell uptake and membrane permeation (Todorova et al., 2014). Apparently, NPs/HCPT is

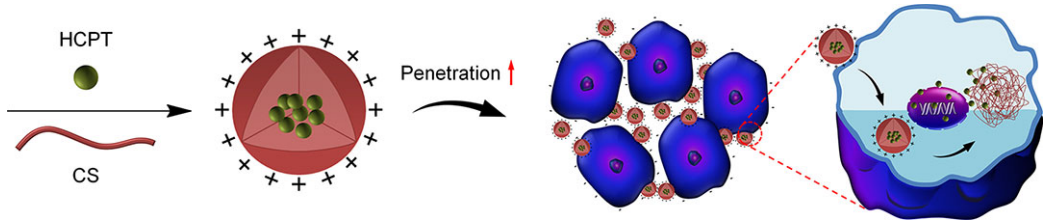

FIGURE 1 | Schematic design of preparation and enhancement on the permeability of NPs/10-Hydroxycamptothecin (HCPT).

TABLE 1 | Characterizations of NPs/10-Hydroxycamptothecin (HCPT).

Diameter (nm)	DLC (wt.%)	DLE (wt.%)	*zeta* Potential (mV)
114.6 ± 4.1	18.3 ± 0.9	80.2 ± 1.5	15.9 ± 2.4

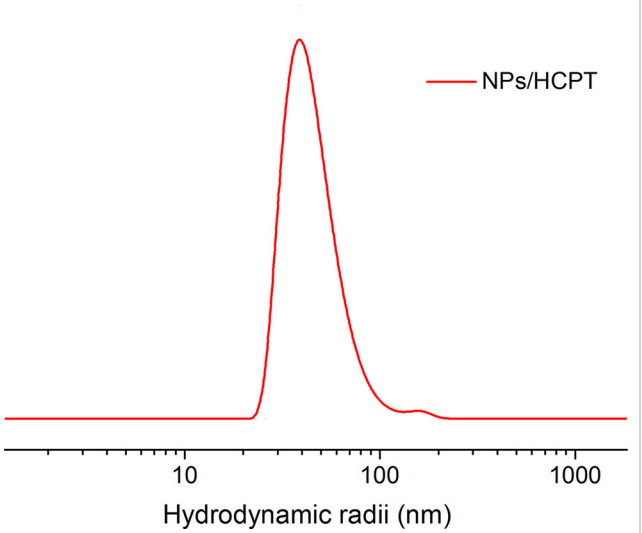

FIGURE 2 | Hydrodynamic radii of NPs/10-Hydroxycamptothecin (HCPT).

an excellent drug delivery platform due to the attractive electrostatic forces between the NPs/HCPT and biomembranes.

In Vitro HCPT Release

The *in vitro* HCPT release kinetics from the NPs/HCPT was shown in **Figure 3**, which was evaluated in PBS (pH 7.4, containing 0.1% Tween-80 (w/v)). Both free HCPT and NPs/HCPT displayed sustained release patterns. During the release process, free HCPT exhibited a very rapid release rate. However, the release of HCPT from the NPs/HCPT was decreased due to the encapsulation of CS. The prolonged and sustained drug release of NPs/HCPT indicated a relatively high level of HCPT concentration within cells, which was the key to enhance the anti-tumor activity *in vitro* and *in vivo*.

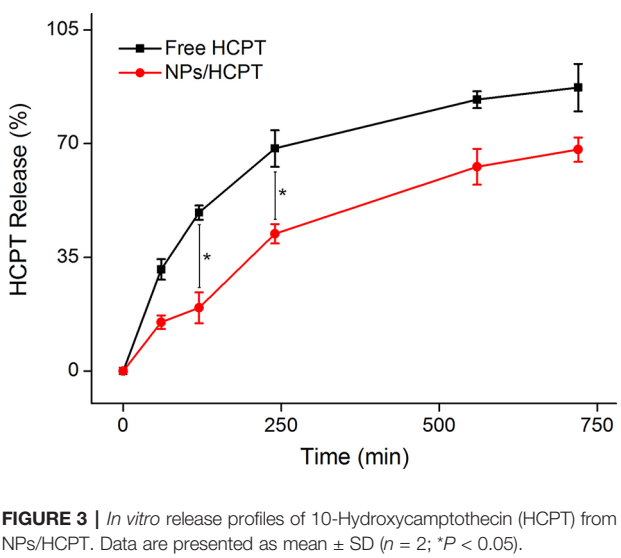

FIGURE 3 | *In vitro* release profiles of 10-Hydroxycamptothecin (HCPT) from NPs/HCPT. Data are presented as mean ± SD (n = 2; $^*P < 0.05$).

Cell Uptake and Intracellular Distribution of NPs/HCPT

NPs/HCPT treated B16F10 cells were visualized under CLSM to assess cell uptake of NPs/HCPT. Free HCPT treated cells revealed higher intracellular HCPT accumulation after 2 h of incubation, as compared to NPs/HCPT, which was depicted in **Figure 4A**. This phenomenon was due to the different ways in which drugs were transported into cells. It is reported that small molecules such as HCPT enter cells through simple diffusion (Xu et al., 2015; Zhao et al., 2017), while nanoparticles may be internalized by cells through endocytosis (Guo et al., 2017). However, with the incubation time prolonged to 6 h, the accumulation of free HCPT within B16F10 cells reduced, while the accumulation of NPs/HCPT within B16F10 cells increased significantly (**Figure 4B**). The relative optical density of intracellular HCPT was quantified with ImageJ software (National Institutes of Health, Bethesda, Maryland, USA). The HCPT fluorescence of free HCPT was 2.7 times higher than that of NPs/HCPT at 2 h. Conversely, the HCPT fluorescence of NPs/HCPT was 2.3 times higher than that of free HCPT at 6 h, which is depicted in **Figure 4C**. For further quantitative confirmation, the cell uptake of NPs/HCPT at different time points was

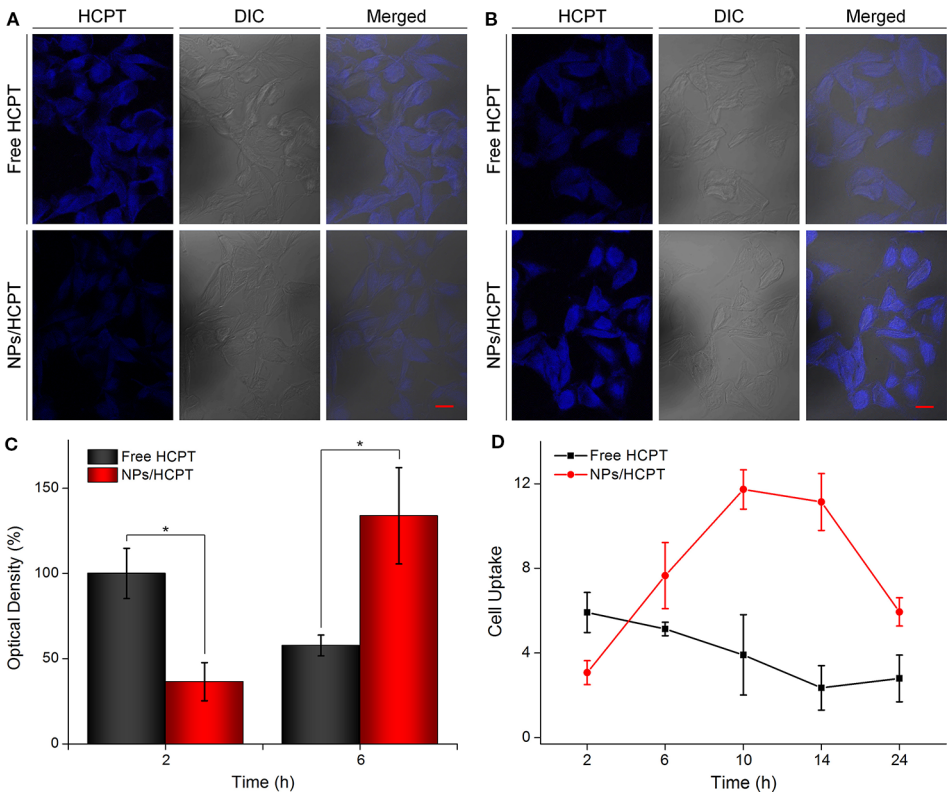

FIGURE 4 | Cell uptake and intracellular distribution of NPs/10-Hydroxycamptothecin (HCPT). **(A)** Confocal microscopy images of B16F10 cells after incubation with free HCPT or NPs/HCPT for 2 h (scale bar, 20 μm). **(B)** Confocal microscopy images of B16F10 cells after incubation with free HCPT or NPs/HCPT for 6 h (scale bar, 20 μm). **(C)** Quantitative analysis of optical density of HCPT fluorescence intensity after 2 h or 6 h of treatment with free HCPT or NPs/HCPT. **(D)** Cell uptake of B16F10 cells treated with free HCPT or NPs/HCPT at a HCPT concentration of 1.5 μg ml^{-1}. Data are presented as mean ± SD (n = 3; *P < 0.05).

performed by a microplate reader. As depicted in **Figure 4D**, the cell uptake of free HCPT decreased with time, while the internalization of NPs/HCPT increased first and then decreased, reaching a peak value at 10 h. The accumulation of NPs/HCPT in cells increased with time, suggesting that NPs/HCPT could be actively internalized by B16F10 cells in a time-dependent manner.

NPs/HCPT Decreased the Cell Viability of Melanoma Cell Lines Dependent on Time and Concentration

The inhibitory effect of NPs/HCPT on the cell viability of B16F10 was evaluated using the MTT assay. The results showed that NPs/HCPT inhibited the growth of B16F10 cells in a time and concentration-dependent manner. Concretely, the inhibition percentage of B16F10 cells in different conditions was displayed in **Figures 5A, B**. It was observed that there were obvious differences in cell viability between the two groups after incubation with different concentrations of free HCPT or NPs/HCPT for 24 and 48 h. Moreover, the viability of B16F10 cells treated with NPs/HCPT was found to be lower than that of free HCPT after 24 h and 48 h of incubation. By a non-linear regression analysis, it was calculated that NPs/HCPT showed a half maximal inhibitory concentration (IC_{50}) of 2.4 μg ml^{-1} in B16F10 cells at 48 h. In comparison, the IC_{50} of free HCPT was 6.7 μg ml^{-1} at 48 h. At the same treatment time of 24 h, free HCPT and NPs/HCPT demonstrated well pronounced cytotoxicity against B16F1, which was similar to that on B16F10 cells at concentrations (**Figure 5C**). The empty NPs did not show significant cytotoxic effect in B16F1 after 24 h exposure, which was displayed in **Figure 5D**. The apparently higher cytotoxicity of NPs/HCPT was directly attributed to the increase of intracellular HCPT concentration, which was due to the positive surface of NPs/HCPT enhanced cells internalization through endocytosis (Kim et al., 2010; Chen et al., 2018). NPs/HCPT is superior to free HCPT in inhibiting tumor cells, suggesting that CS as a drug release platform can improve the cytotoxicity of HCPT.

NPs/HCPT Induced Apoptosis in B16F10 Cells

Concerning the effect of NPs/HCPT on B16F10 cell viability, we speculated whether the reduced cell viability of B16F10 was the result of apoptotic cell death induced by NPs/HCPT. Thus, the apoptotic percentage of B16F10 cells induced by 3.0 μg ml^{-1} of free HCPT or NPs/HCPT was evaluated by Annexin V-FITC/PI double staining and FCM analysis. As showed in **Figure 5E**, an even higher percentage of apoptotic cells induced by NPs/HCPT

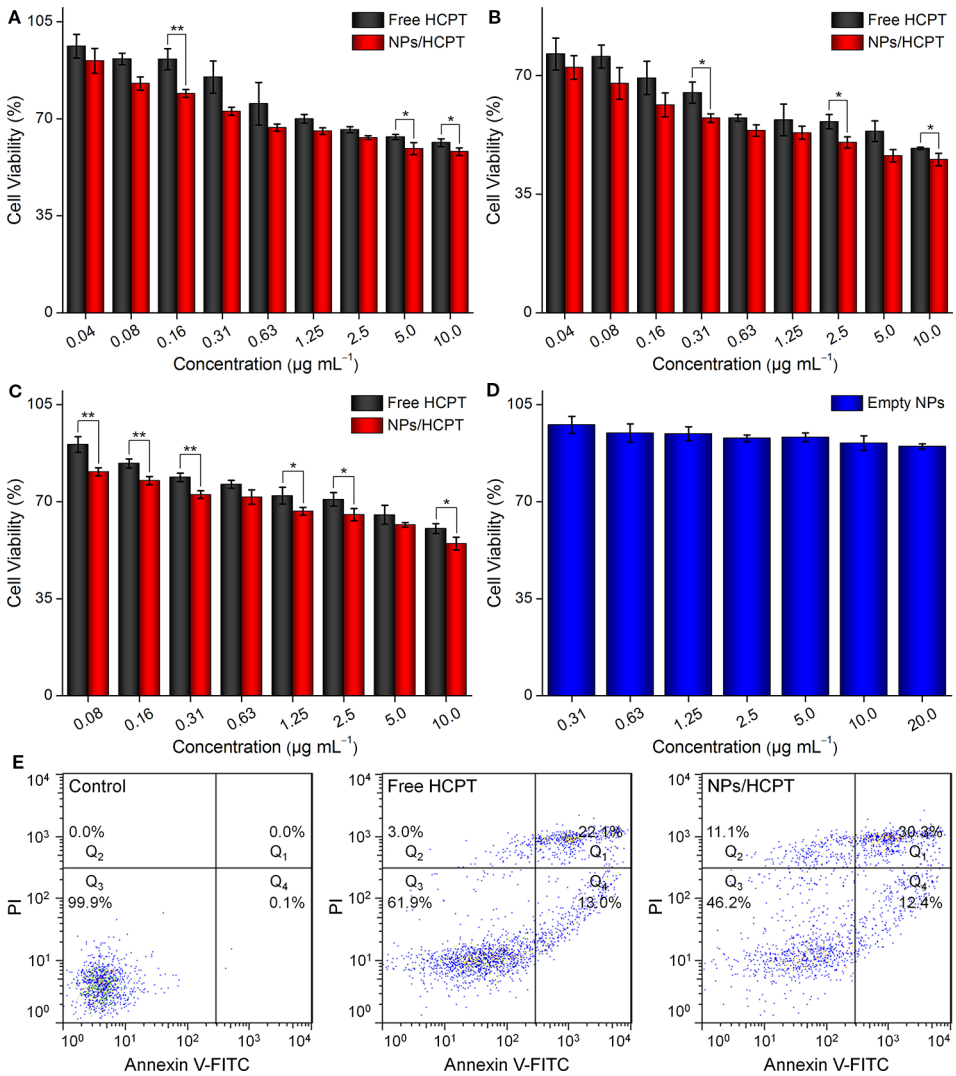

FIGURE 5 | Cell cytotoxicity. **(A)** Viabilities of B16F10 cells incubated with different concentrations of free 10-Hydroxycamptothecin (HCPT) or NPs/HCPT for 24 h. **(B)** Viabilities of B16F10 cells incubated with different concentrations of free HCPT or NPs/HCPT for 48 h. **(C)** Viabilities of B16F1 cells incubated with different concentrations of free HCPT or NPs/HCPT for 24 h. **(D)** Viabilities of B16F1 cells incubated with empty NPs for 24 h. **(E)** The percentage of apoptotic cells was analyzed by flow cytometry (FCM) with Annexin V-FITC and Propidium iodide (PI) staining after different treatments for 24 h. Data are presented as mean ± SD ($n = 3$; $^{*}P < 0.05$, $^{**}P < 0.01$).

were observed, as compared to that of free HCPT. These results indicated that NPs/HCPT not only possessed the function of inhibiting tumor, but also performed well in the delivery of HCPT into cancer cells. Therefore, as a nanoscale carrier for HCPT, NPs/HCPT has the potential to become an excellent drug delivery system for cancer therapy.

In Vivo Antitumor Activity of NPs/HCPT

The *in vivo* antitumor activity of NPs/HCPT was further confirmed in tumor-bearing mice. As exhibited in **Figure 6A**, free HCPT and NPs/HCPT inhibited the progression of tumors as compared with PBS. Moreover, NPs/HCPT showed a higher antitumor efficacy than that of free HCPT. All the tumor-bearing mice treated with NPs/HCPT showed no distinct difference in body weight during the process of the treatment, suggesting negligible toxicity (**Figure 6B**). The results indicated that NPs/HCPT exhibited an advantage of biological safety and excellent antitumor activity.

CONCLUSIONS

In this work, cationic CS-based nanoparticles were prepared to enhance tumor penetration capability of HCPT for the potential chemotherapy of melanoma. The aqueous dispersibility of hydrophobic HCPT was significantly improved. The resulting

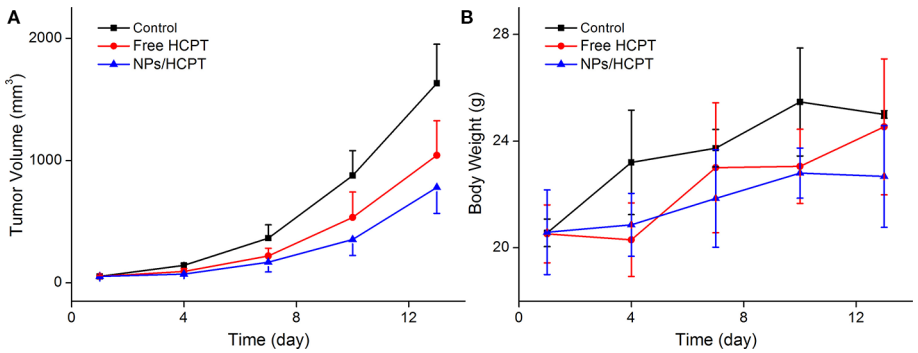

FIGURE 6 | Tumor inhibition *in vivo*. **(A)** Time profiles of tumor growth in different mice after four treatments of phosphate-buffered saline (PBS), free 10-Hydroxycamptothecin (HCPT), or NPs/HCPT. **(B)** Body weight of tumor-bearing mice during the process of treatment. Data are presented as mean ± SD (n = 5).

NPs/HCPT exhibited an ideal diameter of 114.6 ± 4.1 nm, which was the optimal tumor accumulation size for the EPR effect. The positive surface charge and sustained release behavior ensured a high intracellular drug concentration. The MTT assay and FCM analysis suggested that NPs/HCPT exhibited a greater cytotoxicity in comparison to free HCPT. Furthermore, NPs/HCPT significantly inhibited the progression of tumors in animal models. These investigations implied that NPs/HCPT could be effectively applied to improve the chemotherapeutic effect of melanoma.

DATA AVAILABILITY STATEMENT

All datasets generated for this study are included in the article.

AUTHOR CONTRIBUTIONS

CW and YH conceived the idea. HG carried out the experiments. FL, HQ, and SQ took part in the experiments and the discussion of the results. HG, JL, and FL drafted the manuscript. All authors read and approved the final manuscript.

FUNDING

The study was financially supported by the Science and Technology Development Program of Jilin Province (Nos. 20180101167JC).

REFERENCES

Al-Batran, S. E., Homann, N., Pauligk, C., Goetze, T. O., Meiler, J., Kasper, S., et al. (2019). Perioperative chemotherapy with fluorouracil plus leucovorin, oxaliplatin, and docetaxel versus fluorouracil or capecitabine plus cisplatin and epirubicin for locally advanced, resectable gastric or gastro-oesophageal junction adenocarcinoma (FLOT4): a randomised, phase 2/3 trial. *Lancet* 393 (10184), 1948–1957. doi: 10.1016/S0140-6736(18)32557-1

Blanco, E., Shen, H., and Ferrari, M. (2015). Principles of nanoparticle design for overcoming biological barriers to drug delivery. *Nat. Biotechnol.* 33 (9), 941–951. doi: 10.1038/nbt.3330

Bray, F., Ferlay, J., Soerjomataram, I., Siegel, R. L., Torre, L. A., and Jemal, A. (2018). Global cancer statistics 2018: GLOBOCAN estimates of incidence and mortality worldwide for 36 cancers in 185 countries. *CA Cancer J. Clin.* 68 (6), 394–424. doi: 10.3322/caac.21492

Chen, F., Ma, K., Madajewski, B., Zhuang, L., Zhang, L., Rickert, K., et al. (2018). Ultrasmall targeted nanoparticles with engineered antibody fragments for imaging detection of HER2-overexpressing breast cancer. *Nat. Commun.* 9 (1), 4141. doi: 10.1038/s41467-018-06271-5

Danhier, F. (2016). To exploit the tumor microenvironment: Since the EPR effect fails in the clinic, what is the future of nanomedicine? *J. Control Release* 244 (Pt A), 108–121. doi: 10.1016/j.jconrel.2016.11.015

Fan, W., Yung, B., Huang, P., and Chen, X. (2017). Nanotechnology for Multimodal Synergistic Cancer Therapy. *Chem. Rev.* 117 (22), 13566–13638. doi: 10.1021/acs.chemrev.7b00258

Guo, H., Xu, W., Chen, J., Yan, L., Ding, J., Hou, Y., et al. (2017). Positively charged polypeptide nanogel enhances mucoadhesion and penetrability of 10-hydroxycamptothecin in orthotopic bladder carcinoma. *J. Control Release* 259, 136–148. doi: 10.1016/j.jconrel.2016.12.041

Guo, H., Li, F., Xu, W., Chen, J., Hou, Y., Wang, C., et al. (2018). Mucoadhesive Cationic Polypeptide Nanogel with Enhanced Penetration for Efficient Intravesical Chemotherapy of Bladder Cancer. *Adv. Sci. (Weinh)* 5 (6), 1800004. doi: 10.1002/advs.201800004

Jia, X., Zhang, Y., Zou, Y., Wang, Y., Niu, D., He, Q., et al. (2018). Dual Intratumoral Redox/Enzyme-Responsive NO-Releasing Nanomedicine for the Specific, High-Efficacy, and Low-Toxic Cancer Therapy. *Adv. Mater.* 30 (30), e1704490. doi: 10.1002/adma.201704490

Kim, B., Han, G., Toley, B. J., Kim, C. K., Rotello, V. M., and Forbes, N. S. (2010). Tuning payload delivery in tumour cylindroids using gold nanoparticles. *Nat. Nanotechnol.* 5 (6), 465–472. doi: 10.1038/nnano.2010.58

Kwak, S. Y., Lew, T. T. S., Sweeney, C. J., Koman, V. B., Wong, M. H., Bohmert-Tatarev, K., et al. (2019). Chloroplast-selective gene delivery and expression in planta using chitosan-complexed single-walled carbon nanotube carriers. *Nat. Nanotechnol.* 14 (5), 447–455. doi: 10.1038/s41565-019-0375-4

Li, J., Xu, W., Li, D., Liu, T., Zhang, Y. S., Ding, J., et al. (2018). Locally Deployable Nanofiber Patch for Sequential Drug Delivery in Treatment of Primary and Advanced Orthotopic Hepatomas. *ACS Nano* 12 (7), 6685–6699. doi: 10.1021/acsnano.8b01729

Nezakati, T., Seifalian, A., Tan, A., and Seifalian, A. M. (2018). Conductive Polymers: Opportunities and Challenges in Biomedical Applications. *Chem. Rev.* 118 (14), 6766–6843. doi: 10.1021/acs.chemrev.6b00275

Sheng, J., Han, L., Qin, J., Ru, G., Li, R., Wu, L., et al. (2015). N-trimethyl chitosan chloride-coated PLGA nanoparticles overcoming multiple barriers to oral insulin absorption. *ACS Appl. Mater. Interf.* 7 (28), 15430–15441. doi: 10.1021/acsami.5b03555

Todorova, N., Chiappini, C., Mager, M., Simona, B., Patel, I. I., Stevens, M. M., et al. (2014). Surface presentation of functional peptides in solution determines cell internalization efficiency of TAT conjugated nanoparticles. *Nano Lett.* 14 (9), 5229–5237. doi: 10.1021/nl5021848

Wei, W., Yue, Z. G., Qu, J. B., Yue, H., Su, Z. G., and Ma, G. H. (2010). Galactosylated nanocrystallites of insoluble anticancer drug for liver-targeting therapy: an in vitro evaluation. *Nanomed. (Lond.)* 5 (4), 589–596. doi: 10.2217/nnm.10.27

Xu, W., Ding, J., Xiao, C., Li, L., Zhuang, X., and Chen, X. (2015). Versatile preparation of intracellular-acidity-sensitive oxime-linked polysaccharide-doxorubicin conjugate for malignancy therapeutic. *Biomaterials* 54, 72–86. doi: 10.1016/j.biomaterials.2015.03.021

Zhang, Y., Cai, L., Li, D., Lao, Y.-H., Liu, D., Li, M., et al. (2018). Tumor microenvironment-responsive hyaluronate-calcium carbonate hybrid nanoparticle enables effective chemotherapy for primary and advanced osteosarcomas. *Nano Res.* 11 (9), 4806–4822. doi: 10.1007/s12274-018-2066-0

Zhao, K., Li, D., Xu, W., Ding, J., Jiang, W., Li, M., et al. (2017). Targeted hydroxyethyl starch prodrug for inhibiting the growth and metastasis of prostate cancer. *Biomaterials* 116, 82–94. doi: 10.1016/j.biomaterials.2016.11.030

Zhao, X., Guo, B., Wu, H., Liang, Y., and Ma, P. X. (2018). Injectable antibacterial conductive nanocomposite cryogels with rapid shape recovery for noncompressible hemorrhage and wound healing. *Nat. Commun.* 9 (1), 2784. doi: 10.1038/s41467-018-04998-9

Conflict of Interest: The authors declare that the research was conducted in the absence of any commercial or financial relationships that could be construed as a potential conflict of interest.

frontiers in Pharmacology

REVIEW
published: 17 March 2020
doi: 10.3389/fphar.2020.00224

Advances in Drug Delivery via Biodegradable Ureteral Stent for the Treatment of Upper Tract Urothelial Carcinoma

Hongli Shan[1], Zhongshuai Cao[1], Changliang Chi[2], Jixue Wang[2], Xiaoqing Wang[2], Jingyan Tian[2]* and Bing Yu[2]**

[1] Department of Clinical Laboratory, The First Hospital of Jilin University, Changchun, China, [2] Department of Urology, The First Hospital of Jilin University, Changchun, China

OPEN ACCESS

Edited by:
Chao Wang,
Soochow University, China

Reviewed by:
Lesan Yan,
Wuhan University of Technology, China
Tianjiao Ji,
Harvard Medical School, United States

***Correspondence:**
Xiaoqing Wang
wangxiaoq@jlu.edu.cn
Jingyan Tian
tjy@jlu.edu.cn
Bing Yu
1161449482@qq.com

Specialty section:
This article was submitted to Experimental Pharmacology and Drug Discovery, a section of the journal Frontiers in Pharmacology

Received: 09 January 2020
Accepted: 18 February 2020
Published: 17 March 2020

Citation:
Shan H, Cao Z, Chi C, Wang J, Wang X, Tian J and Yu B (2020) Advances in Drug Delivery via Biodegradable Ureteral Stent for the Treatment of Upper Tract Urothelial Carcinoma. Front. Pharmacol. 11:224. doi: 10.3389/fphar.2020.00224

Drug eluting ureteral stent is an effective means for local drug delivery to the urinary tract. It can potentially solve a variety of upper urinary tract problems, such as stent-related urinary tract infections and discomfort, ureteral stricture, and neoplastic diseases. However, the release of drug elutes on the surface of biostable stents is unsustainable and uncontrollable. With the development of biomaterial science, the emergence of biodegradable ureteral stents (BUSs) provides a new approach for local drug delivery in the urinary tract. The drugs can be continuously released in a controlled manner from a drug-eluting BUS, when the stent degrades. Especially for the delivery of anti-tumor drugs, the stents can obviously improve the therapeutic effectiveness of the drugs by prolonging the contact duration of the drug and tumor cells. In addition, a secondary stent removal procedure can be avoided. The purpose of this review article is to provide an overview of anti-tumor drug-eluting BUSs and discuss the biomaterials and drug delivery systems of BUS that are currently being developed to deliver anti-tumor drugs for upper tract urothelial carcinoma.

Keywords: local drug delivery, ureteral stent, chemotherapy, biodegradable, upper tract urothelial carcinoma

INTRODUCTION

For patients with low-risk upper tract urothelial carcinoma (UTUC), kidney-sparing surgery is recommended as the preferred treatment by the European Association of Urology (EAU) guidelines (Roupret et al., 2018). After kidney-sparing surgery, the recurrence of carcinoma and the side effects caused by indwelling ureteral stent were the main urgent problems to be solved (Zigeuner and Pummer, 2008). Local chemotherapy can obviously avoid the recurrence of carcinoma, which has been used as a routine adjuvant treatment after UTUC (Babjuk et al., 2017). However, due to the characteristics of impermeable urothelium and the continuous washing of urine, the effectiveness of local chemotherapy was limited. Therefore, it is needed to realize the controlled and sustained drug release in the upper tract, which can overcome the above problems (Mosayyebi et al., 2018).

With the rapid development of nanodrug loading technology, many localized cancers can be treated by direct deposition of nanoparticle-based drugs in the target area (Ji and Kohane, 2019). Some local nanodrug loading systems have been developed and become powerful tools to reduce recurrence and progression of non-muscle invasive bladder cancer in the past decades

(Guo et al., 2019). For UTUC, the anti-tumor drug-loaded biodegradable ureteral stent might be an optional and effective method to solve the clinical problems. Incorporating coating and eluting as drug loading technologies with multiple advantages in the design of drug-loaded stents is not fully studied. In the field of cardiovascular disease, the drug-eluting degradable stents have been widely designed and studied (Waksman and Pakala, 2010; Wang et al., 2014). In addition, engineered nanomedicines have been reported to enhance the tumor penetration in local chemotherapy (Ding et al., 2019a). However, the researches of drug-eluting biodegradable stents in the urinary system are still scarce. In our review, we summarize the studies about drug-eluting biodegradable ureteral stents (BUSs) and discuss biomaterials and drug delivery systems of BUS that are currently being developed in delivering anti-tumor drugs.

BIOMATERIALS FOR BUS

The degradable drug-loaded ureteral stents have been getting more and more attention because of their advantages of no need for cystoscopy, no "forgotten stent" problem, and low incidence of infection and hematuria (Beysens and Tailly, 2018). The biomaterials used in BUS should be biocompatible, and have moderate mechanical strength to maintain intact tubular structure and well-controlled degradation rate, such as n polymers in nature, synthetic polymers, and some metals.

Natural Origin Polymers

There are various polymeric biodegradable materials in nature with great potential to be selected as a material of BUS, such as collagen, gelatin, alginate, fibrin, silk, and so on. Their own characteristics, such as biocompatibility, microstructure, mechanical strength, degradation rate, and the effect of anti-infection should be carefully considered in the design of BUS. It is fortunate that many natural origin polymers can meet these conditions and have been widely used in design of BUS (Auge et al., 2002; Nady and Kandil, 2018). Lingeman et al. (2003) designed proprietary alginate polymer-based BUS and applied in 88 patients. This stent could maintain intact within 48 h and begin to degrade after that. The *in vivo* results indicated that the alginate-based stent could effectively facilitate the urinary drainage and exhibited excellent biocompatibility. It is noted that there was a 3.4% insufficient degradation of the stent, which needed a second intervention to remove the fragments. Barros et al. (2015b) fabricated a hollow ureteral stent, consisting of alginate, gellan gum, and templated gelation. Moreover, critical point carbon dioxide drying was used in the process of building. The *in vivo* degraded experiment indicated that this stent exhibited the fastest biodegradation rate than the control group. Moreover, the stent could effectively reduce the bacterial adhesion and showed excellent biocompatibility properties (Barros et al., 2018).

Synthetic Polymers

Over the last decades, synthetic polymers have been designed to fabricate biodegradable drug carriers and are widely applied in tissue engineering, nanodrug delivery systems, and diagnosis of disease. Various kinds of synthetic polymers have been used to prepare matrix and implant forms because of their distinctive advantages, such as excellent biocompatibility, controlled biodegradation rate, ideal mechanical strength, and hydrophobicity/hydrophilicity (Kim et al., 2014; Kapoor et al., 2015). Alpha hydroxy acids, such as polylactic acid (PLA), polyglycolic acid, poly (lactide-co-glycolide) (PLGA), polycaprolactone (PCL), polyethylene glycol, poly (lactide-co-caprolactone), polydioxanone, etc., were the most commonly used synthetic polymers (Wang L. et al., 2018). Moreover, it is noted that all these polymers were approved by the U.S. Food and Drug Administration (FDA) as biomaterials (Wang et al., 2015b) and Lumiaho et al. (2007) fabricated a biodegradable ureteral stent by using PLA as the basic material. After implanting in porcine model, the results indicated that the ureteral stent exhibited satisfactory drainage characteristics and excellent antireflux effect. However, the stent degraded in blocks and caused poor drainage of ureter. Uriprene, a novel biodegradable stent constructed by PLGA, was designed to gradually degrade from distal to proximal end to avoid ureteral obstruction by fragments. Moreover, a third-generation stent that can degrade in a short time has also been designed. The *in vivo* results indicated that this stent could degrade by 90% within 28 days and played excellent drainage effect (Chew et al., 2010, 2013). The authors of this review fabricated a nanostructured PLGA ureteral stent by double-needle electrospinning. The *in vivo* animal experiment exhibited that the stent could completely degrade within 10 weeks post-insertion, and degrade from distal to proximal. Moreover, compared to a commercial stent, this stent showed less impact on epithelial cells (Wang et al., 2015a).

Metals

In terms of mechanical strength, metallic stents have obvious advantages over polymer counterparts. Some metals are suitable for fabricating biodegradable stents since they are what the body contains itself (Chew et al., 2010, 2013). For example, magnesium (Mg) is suitable for constructing medical devices due to its lightweight and biodegradable properties, especially in the cardiovascular field. In the urology field, Mg-based alloy exhibited excellent biodegradability and could effectively inhibit the growth of bacteria.

Lock et al. (2014) evaluated the antibacterial and biodegradable properties of magnesium and its alloys for potential biodegradable ureteral stent applications. The results showed that magnesium alloys decreased *E. coli* viability and reduced the colony formation units in an artificial urine solution when compared with commercial polyurethane stent.

Tian et al. (2019) investigated the cytocompatibility and degradation behaviors of four promising Mg-based alloys *in vitro*. The results indicated that the degradation rates of these Mg-based alloys should be further reduced for the sake of reducing the side effects of the soluble or insoluble degradation substances.

ANTI-TUMOR DRUG-ELUTING BUS

With the rapid development of nanotechnology, nanodrug delivery systems have been widely researched to delivery therapeutic agents, which could efficiently improve the delivery efficacy (Chen et al., 2017; Wang J. et al., 2018). For non-muscle invasive bladder cancer, one effective way to prevent cancer recurrence is intravesical instillation chemotherapeutic drugs after transurethral resection of the bladder cancer (Babjuk et al., 2017). Because of the same biological characteristics as bladder cancer, UTUC could also be treated by local chemotherapy. However, the particularity of the upper urinary tract anatomy limited the application of local chemotherapy and there are currently no effective local chemotherapy methods.

The biodegradable anti-tumor drug-loaded ureteral stents had been widely researched and had been demonstrated that they could improve the situation of chemotherapy of UTUC. It can last for a long-term effective loaded anti-tumor agent release in the ureter when the stent degrades. The drugs could permeate through the ureter, effectively affecting the cancer cells. It may also solve the problems of secondary removal simultaneously. However, reports on the application of drug-eluting techniques for biodegradable stents in urinary system are limited.

Barros et al. (2016) fabricated a biodegradable ureteral stent, which was impregnated by supercritical fluid CO_2. Furthermore, four different kinds of anti-tumor agents, including paclitaxel, doxorubicin, epirubicin (EPI), and gemcitabine, were loaded into the stent. The *in vitro* anti-tumor experiment indicated that these drug-eluted stents could efficiently suppress the growth of urothelial cancer cell (T24 cells). In addition, all these drug-eluted stents showed minimal toxicity toward the non-cancer cells (HUVEC cells). These results indicated that the impregnated BUSs could be used as proper anti-tumor drug carriers and potentially be an effective intravesical drug delivery system for UTUC therapy. In their next study, the researchers used different membranes to research the permeability of the loaded anti-tumor agents, including single paclitaxel and doxorubicin, and their release from the prepared BUS. The results demonstrated that the release performances of paclitaxel and doxorubicin from the BUS could be kept for a long time in the *ex vivo* ureter and only a small amount of the drugs can across the different permeable membranes with a permeability of 3% for paclitaxel and 11% for doxorubicin. All these results demonstrated that most drugs in these BUS could remain in the *ex vivo* ureter tissue, which were effective to suppress the growth of tumor cells and not affect the non-tumor cells (Barros et al., 2017). We also fabricated an anti-tumor drug-loaded biodegradable ureteral stent to suppress the recurrence of UTUC after kidney-sparing surgery (Wang et al., 2019). In our research, different kinds of degradable PCL/PLGA scaffolds consisting of different proportions of PCL and loading EPI were prepared by electrospinning. The results indicated that the PCL/PLGA scaffolds could sustain the release of loaded drugs and exhibited controlled degradation. Moreover, the drug release and degradation rates of scaffolds were slowed down with the increase of PCL. The anti-tumor activity demonstrated that the scaffolds could efficiently suppress the growth of bladder tumor cells both *in vitro* and *in vivo*. Moreover, their *in vivo* application showed no apparent systemic toxicity. Our results demonstrated that these electrospun polyester scaffolds could be effectively used for local inhibition of recurrence of UTUC after surgery.

DESIGN OF DRUG DELIVERY SYSTEM FOR BUS

Compared with systematic administration, *in situ* administration can effectively improve the drug concentration at the targeted sites. In local drug delivery of upper urinary tract, the key goal is to keep an effective drug treatment concentration and long-term maintenance at upper urinary tract. The second goal is to reduce the effect of drugs on non-tumor tissues, so as to reduce the toxicity of drugs to the body. The particular local anatomy and microenvironment of the upper urinary tract are potential barriers to local delivery (Weiser and Saltzman, 2014; Mittal et al., 2018). Some previous researches had coated drugs to the surface of biostable stents, and the results were not satisfactory due to the uncontrolled drug release. However, drug-eluting BUS could sustain a long-term effective drug release during the process of stent degradation, and at the same time avoid a secondary removal procedure. There are many drug delivery systems for loading drugs, including hot melt extrusion, soaking the polymers into drug solution, CO_2 impregnation, nanofibers, and nanoparticles.

Traditional Drug Delivery Systems

Drug delivery systems, such as hot melt extrusion, solvent-casting, and soaking the polymers into a drug solution, are traditional drug delivery systems. It contains numerous limitations, such as bad drug control release, lack of targeting, poor water solubility, and susceptibility to drug resistance (Tiwari et al., 2012; Edgar and Wang, 2017; Pandit et al., 2017). Lim et al. (2018) designed a bilayer swellable drug-eluting ureteral stent used for treating urothelial diseases. The drug mitomycin C was directly mixed with lactide-co-caprolactone pellets and dissolved in dichloromethane. After that, the mixed solution was coated onto the surface of the ureteral stent. To achieve sustainable drug release at the ureteric diseased site, the researchers further coated a layer of hydrogel on the surface of the stent. The results indicated that the drug could be continuously delivered over 1 month. The *in vivo* results also demonstrated the improved drug release performance and the advantage in transporting into explanted porcine ureteric tissues under a simulated dynamic fluid flow.

CO_2 Impregnation

The CO_2 impregnation has attracted growing interest and applied in various fields, which allows loading a drug into an already manufactured implant. It is noted that CO_2 in its supercritical state can dissolve well into various polymer matrices. In addition, it has low critical coordinates (Champeau et al., 2015). Barros et al. (2015a) first used this technique in preparing a ketoprofen-eluting BUS. These BUSs were fabricated by alginate or gellan gum–based polymers, and the stent was impregnated with ketoprofen. The results showed the release of ketoprofen in the

first 72 h was very promising, which was in accordance with the time needed for anti-inflammatory treatment after operation. The *in vitro* release results indicated that the temperature had an obvious effect on the impregnation yield. The same research group also used the same methods to load paclitaxel and doxorubicin into a natural origin polymer-based BUS for the treatment of UTUC. The results indicated that the release of paclitaxel and doxorubicin from the BUS could affect the tumor cells and not affect the non-tumor cells (Barros et al., 2016). However, the impregnation process also had some drawbacks, including the drug must have sufficient solubility in CO_2, low drug loading rate and drug loading efficiency, and the stent shape changes after drug loading (**Figure 1**; Ugaonkar et al., 2011; Champeau et al., 2015).

Electrospun Nanofibers

Electrospinning can converse polymeric solution/melt into solid nanofibers through the application of electrical force. The drug-loaded electrospun nanofibers have been getting more and more attention because of their distinctive properties, including high encapsulation efficiency for drug loading, controlled residence time, desirable delivery of encapsulated drug at a predictable rate, better stability, high surface contact area, degradability, and satisfactory softness and flexibility (Zamani et al., 2013; Ding et al., 2019c). Moreover, electrospun nanofibers have a nanosized diameter and a structure mimicking that of extracellular matrix proteins. Interestingly, the occurrence of degradation of extracellular matrix proteins also plays an important role in tumor metastasis (Alizadeh et al., 2018; Feng et al., 2019a). Therefore, the local and continuous delivery of chemotherapy agents can improve the concentration of agents in tumor tissue, delay and control the drug release at cytotoxic concentrations, thus significantly reducing the toxicity to normal tissues of the body, reducing the frequency of drug use, and avoiding the damage to normal vascular endothelium. Li et al. (2018) developed a local drug delivery system consisting of an emulsion-electrospun polymer patch for the treatment of primary and advanced orthotopic hepatomas. The anti-tumor drugs could realize sustained release, and could efficiently suppress the tumor growth and invasiveness in animal models.

The authors of this review first used two types of electrospinning technique to develop a series of epirubicin (EPI)-loaded PCL/PLGA nanofiber ureteral stent with adjustable rates of drug release and degradation for local chemotherapy of UTUC. First, the EPI-loaded PCL/PLGA fibers were developed by general electrospinning technique, and the drug was dispersed in the fibers, both the inside and the surface. The nanofibers showed sustained drug release and controlled degradation, and satisfactory anti-tumor effects both *in vitro* and *in vivo*. Moreover, all of them exhibited no apparent systemic toxicity (Wang et al., 2019).

However, early drug release of the fibers was relatively fast, which may affect anti-tumor effects. Emulsion-electrospinning technology was used to generated a core–sheath structured EPI-loaded PCL/PLGA nanofiber capsules. The core–sheath structures of these fibers were confirmed by a confocal laser scanning microscope, and the EPI was loaded in the inner layer of the fiber. The EPI release was more sustained than that of fibers generated by general electrospinning. The nanofiber capsules effectively inhibited the growth of tumor cells both *in vitro* and *in vivo*, with no apparent systemic toxicity (**Figure 2**; Sun et al., 2019). Although nanofibers have exhibited great potential in drug delivering, before using this technology as a mainstream drug delivery method, they still face some challenges, including low drug loading efficiency, instability of active ingredients, initial sudden release of drugs, number of residual solvents, and industrialization (Luo et al., 2012; Thakkar and Misra, 2017).

Nanoparticle-Based Drug Delivery Systems

Nanoparticle-based drug delivery systems have been widely used as an effective means for local drug-controlled release systems, and have been widely used in various fields of biomedicine (Feng et al., 2019b; He et al., 2019). Various

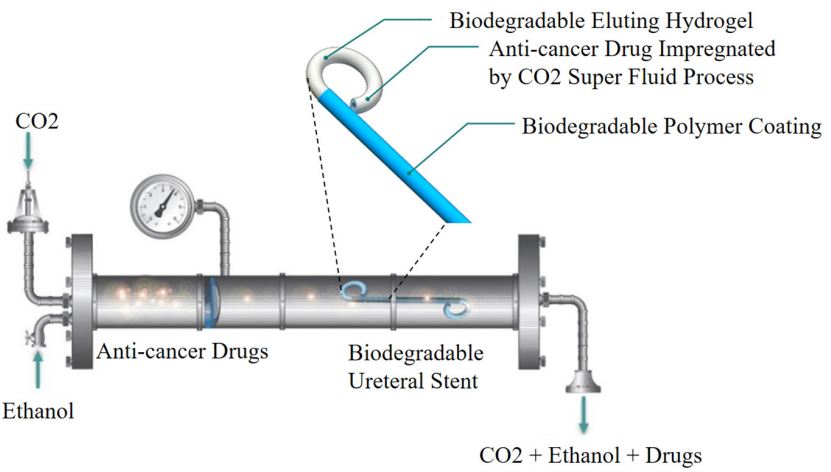

FIGURE 1 | Schematic representation of CO_2 impregnation drug-eluting BUS. Reprinted from Barros et al. (2016) under open access license.

nanoparticle-based drug delivery systems, such as liposomes, nanogels, self-assembling peptides, micelles, water-soluble polymers, and carbon nanotubes have been successfully applied to targeted treatment of cancer. Nanoparticle-based drug carriers can improve the therapeutic effects of the loaded drugs by using active targeting for the site-specific delivery, and protecting normal cells from damage (Park, 2014; Ashfaq et al., 2017).

Because of the particularity of urinary tract diseases, there are many challenges to realize *in situ* delivery of drugs. First, the dilution and washing of urine reduce the bioavailability of drugs in the urinary tract. In addition, the limited drug exposure time will influence the treatment effect. Furthermore, when drugs enter tumor cells, they will be blocked by high resistance and tight connection of drugs into superficial cells, and by high resistance and tight connection of superficial cells and semirigid and asymmetric urothelial membrane (Tyagi et al., 2016; Mittal et al., 2018). In order to overcome these problems, higher doses of drugs are usually needed to achieve effective therapeutic concentration in the target tissue. Nanoparticle-based drug delivery systems with cytotoxic agents of favorable size and capable of adhering to urothelium can potentially prolong the duration of action and decrease toxicity (Tyagi et al., 2016; Ding et al., 2019b).

Erdogar et al. (2014) designed a chitosan- and PCL-based core–shell nanoparticles to deliver mitomycin C, and evaluated the anti-tumor efficacy of the delivery system in bladder tumor model. The results indicated that the drug-loaded nanoparticles treatment group showed the longest survival rate compared to other groups. Histopathological results indicated that the cationic nanoparticles were mainly localized and accumulated in the bladder tissue, and no mitomycin C was quantified in blood. In another study, the delivery of docetaxel to bladder tumor was enhanced by mucoadhesive nanoparticles formed by hyperbranched polyglycerols. Nanoparticles improved the permeability of docetaxel across urothelium and enhanced

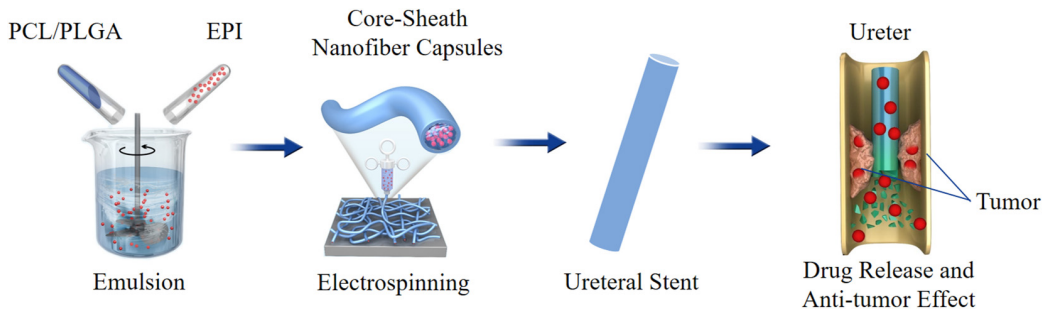

FIGURE 2 | Schematic illustration of preparation and antitumor effect of EPI-loaded BUS.

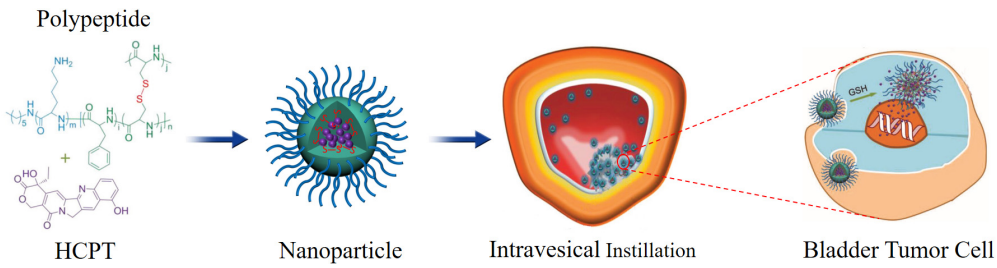

FIGURE 3 | Schematic illustration of chemical structure of polypeptide/HCPT nanoparticles and its metabolic process. Reproduced from Guo et al. (2018) under open access license.

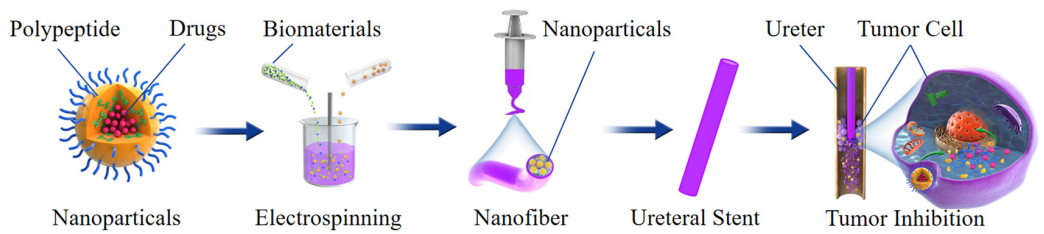

FIGURE 4 | Schematic illustration of preparation, structure and antitumor effect of a nanoparticles-based drug-eluting BUS.

the uptake into the animal tumor cells (Mugabe et al., 2011). Guo et al. (2018) designed a novel disulfide-cross linked polypeptide nanoparticles of poly (l-lysine)-poly (l-phenylalanine-co-l-cystine) to efficiently deliver HCPT to treat orthotopic bladder tumor. The results indicated that these positively charged HCPT-loaded nanoparticles could efficiently adhere to the negatively charged tumor cell membrane and internalized into the cytoplasm through the electrostatic interaction. After that, the high concentration of glutathione in bladder tumor cells could efficiently trigger the cleavage of the disulfide bond, which caused the fast release of loaded HCPT. The results showed that this nanosystem could efficiently improve the retention time and enhance the tumor tissue permeability of HCPT (**Figure 3**).

Based on the above technology, the nanoparticles can also be loaded on the BUS to deliver anti-tumor drugs. For example, an anti-tumor drug can be loaded into polypeptide nanoparticles; then, the drug-loaded nanoparticles are mixed with the biomaterials to fabricate ureteral stents by electrospinning. With the degradation of the ureteral stent, the nanoparticles will continuously release drugs; it can extend the exposure time and enhance the penetration of the nanoparticles into the urothelium. When the nanoparticles are phagocytosed by cells, endogenous stimuli cause the structural changes of the nanoparticles, and the drug will be rapidly released in the cells, which could improve the drug delivery efficiency and reduce toxicity (**Figure 4**).

CONCLUSION

The use of drug-eluting BUS in urology clinical practice not only provides local chemotherapy but also opens new treatment options. Various advancements in biomaterials, design, and drug delivery systems of BUS in this paper are reviewed. With the most appropriate biomaterial, design, and drug delivery technique, an optimal anti-tumor drug delivery stent could be developed in the future. However, there is no ideal stent, and we wish that our review can provide a summary of the technological challenges that need to be overcome in the development of constructing drug-eluted BUS. Future research should focus on how to use nanoparticle-based BUS to deliver local treatment drugs effectively.

AUTHOR CONTRIBUTIONS

XW, JT, and BY: conceptualization. HS, ZC, CC, and BY: literature and data review. HS and JW: writing – original draft. XW and JT: writing – review and editing.

REFERENCES

Alizadeh, N., Akbari, V., Nurani, M., and Taheri, A. (2018). Preparation of an injectable doxorubicin surface modified cellulose nanofiber gel and evaluation of its anti-tumor and anti-metastasis activity in melanoma. *Biotechnol. Prog.* 34, 537–545. doi: 10.1002/btpr.2598

Ashfaq, U. A., Riaz, M., Yasmeen, E., and Yousaf, M. Z. (2017). Recent advances in nanoparticle-based targeted drug-delivery systems against cancer and role of tumor microenvironment. *Crit. Rev. Ther. Drug. Carrier Syst.* 34, 317–353. doi: 10.1615/CritRevTherDrugCarrierSyst.2017017845

Auge, B. K., Ferraro, R. F., Madenjian, A. R., and Preminger, G. M. (2002). Evaluation of a dissolvable ureteral drainage stent in a Swine model. *J. Urol.* 168, 808–812. doi: 10.1016/s0022-5347(05)64748-9

Babjuk, M., Bohle, A., Burger, M., Capoun, O., Cohen, D., and Comperat, E. M. (2017). EAU guidelines on non-muscle-invasive urothelial carcinoma of the bladder: update 2016. *Eur. Urol.* 71, 447–461. doi: 10.1016/j.eururo.2016.05.041

Barros, A. A., Browne, S., Oliveira, C., Lima, E., Duarte, A. R., Healy, K. E., et al. (2016). Drug-eluting biodegradable ureteral stent: new approach for urothelial tumors of upper urinary tract cancer. *Int. J. Pharm.* 513, 227–237. doi: 10.1016/j.ijpharm.2016.08.061

Barros, A. A., Oliveira, C., Reis, R. L., Lima, E., and Duarte, A. R. (2015a). Ketoprofen-eluting biodegradable ureteral stents by CO2 impregnation: in vitro study. *Int. J .Pharm.* 495, 651–659. doi: 10.1016/j.ijpharm.2015.08.040

Barros, A. A., Rita, A., Duarte, C., Pires, R. A., Sampaio-Marques, B., and Ludovico, P. (2015b). Bioresorbable ureteral stents from natural origin polymers. *J. Biomed. Mater. Res. B Appl. Biomater.* 103, 608–617. doi: 10.1002/jbm.b.33237

Barros, A. A., Oliveira, C., Reis, R. L., Lima, E., and Duarte, A. R. C. (2017). In vitro and ex vivo permeability studies of paclitaxel and doxorubicin from drug-eluting biodegradable ureteral stents. *J. Pharm. Sci.* 106, 1466–1474. doi: 10.1016/j.xphs.2017.02.023

Barros, A. A., Oliveira, C., Ribeiro, A. J., Autorino, R., Reis, R. L., Duarte, A. R. C., et al. (2018). In vivo assessment of a novel biodegradable ureteral stent. *World J. Urol.* 36, 277–283. doi: 10.1007/s00345-017-2124-3

Beysens, M., and Tailly, T. O. (2018). Ureteral stents in urolithiasis. *Asian J. Urol.* 5, 274–286. doi: 10.1016/j.ajur.2018.07.002

Champeau, M., Thomassin, J. M., Tassaing, T., and Jerome, C. (2015). Drug loading of polymer implants by supercritical CO2 assisted impregnation: a review. *J. Control Release* 209, 248–259. doi: 10.1016/j.jconrel.2015.05.002

Chen, J., Ding, J., Xu, W., Sun, T., Xiao, H., Zhuang, X., et al. (2017). Receptor and microenvironment dual-recognizable nanogel for targeted chemotherapy of highly metastatic malignancy. *Nano Lett.* 17, 4526–4533. doi: 10.1021/acs.nanolett.7b02129

Chew, B. H., Lange, D., Paterson, R. F., Hendlin, K., Monga, M., Clinkscales, K. W., et al. (2010). Next generation biodegradable ureteral stent in a yucatan pig model. *J. Urol.* 183, 765–771. doi: 10.1016/j.juro.2009.09.073

Chew, B. H., Paterson, R. F., Clinkscales, K. W., Levine, B. S., Shalaby, S. W., and Lange, D. (2013). In vivo evaluation of the third generation biodegradable stent: a novel approach to avoiding the forgotten stent syndrome. *J. Urol.* 189, 719–725. doi: 10.1016/j.juro.2012.08.202

Ding, J., Chen, J., Gao, L., Jiang, Z., Zhang, Y., Li, M., et al. (2019a). Engineered nanomedicines with enhanced tumor penetration. *Nano Today* 29:100800. doi: 10.1021/acsami.5b07116

Ding, J., Feng, X., Jiang, Z., Xu, W., Guo, H., Zhuang, X., et al. (2019b). Polymer-mediated penetration-independent cancer therapy. *Biomacromolecules* 20, 4258–4271. doi: 10.1021/acs.biomac.9b01263

Ding, J., Zhang, J., Li, J., Li, D., Xiao, C., Xiao, H., et al. (2019c). Electrospun polymer biomaterials. *Progr. Polym. Sci.* 90, 1–34.

Edgar, J. Y. C., and Wang, H. (2017). Introduction for design of nanoparticle based drug delivery systems. *Curr. Pharm. Des.* 23, 2108–2112. doi: 10.2174/1381612822666161025154003

Erdogar, N., Iskit, A. B., Eroglu, H., Sargon, M. F., Mungan, N. A., and Bilensoy, E. (2014). Cationic core-shell nanoparticles for intravesical chemotherapy in tumor-induced rat model: safety and efficacy. *Int. J. Pharm.* 471, 1–9. doi: 10.1016/j.ijpharm.2014.05.014

Feng, X., Li, J., Zhang, X., Liu, T., Ding, J., and Chen, X. (2019a). Electrospun polymer micro/nanofibers as pharmaceutical repositories for healthcare. *J. Control Release* 302, 19–41. doi: 10.1016/j.jconrel.2019.03.020

Feng, X., Xu, W., Li, Z., Song, W., Ding, J., and Chen, X. (2019b). Immunomodulatory nanosystems. *Adv. Sci.* 6:1900101. doi: 10.1002/advs.201900101

Guo, H., Hou, Y., and Ding, J. (2019). Nanomedicines for intravesical chemotherapy in bladder Cancer. *Curr. Pharm. Des.* 25, 371–373. doi: 10.2174/1381612825041905160806 07

Guo, H., Li, F., Xu, W., Chen, J., Hou, Y., Wang, C., et al. (2018). Mucoadhesive cationic polypeptide nanogel with enhanced penetration for efficient intravesical chemotherapy of bladder cancer. *Adv. Sci.* 5:1800004. doi: 10.1002/advs.201800004

He, L., Liu, J., Li, S., Feng, X., Wang, C., Zhuang, X., et al. (2019). Polymer nanoplatforms at work in prostate cancer therapy. *Adv. Ther.* 2:1800122. doi: 10.2217/nnm-2018-0238

Ji, T., and Kohane, D. S. (2019). Nanoscale systems for local drug delivery. *Nano Today* 28:100765. doi: 10.1016/j.nantod.2019.100765

Kapoor, D. N., Bhatia, A., Kaur, R., Sharma, R., Kaur, G., and Dhawan, S. (2015). PLGA: a unique polymer for drug delivery. *Ther. Deliv.* 6, 41–58. doi: 10.4155/tde.14.91

Kim, J. K., Kim, H. J., Chung, J. Y., Lee, J. H., Young, S. B., and Kim, Y. H. (2014). Natural and synthetic biomaterials for controlled drug delivery. *Arch. Pharm. Res.* 37, 60–68. doi: 10.1007/s12272-013-0280-6

Li, J., Xu, W., Li, D., Liu, T., Zhang, Y. S., Ding, J., et al. (2018). Locally deployable nanofiber patch for sequential drug delivery in treatment of primary and advanced orthotopic hepatomas. *ACS Nano* 12, 6685–6699. doi: 10.1021/acsnano.8b01729

Lim, W. S., Chen, K., Chong, T. W., Xiong, G. M., Birch, W. R., and Pan, J. (2018). A bilayer swellable drug-eluting ureteric stent: Localized drug delivery to treat urothelial diseases. *Biomaterials* 165, 25–38. doi: 10.1016/j.biomaterials.2018.02.035

Lingeman, J. E., Preminger, G. M., Berger, Y., Denstedt, J. D., Goldstone, L., and Segura, J. W. (2003). Use of a temporary ureteral drainage stent after uncomplicated ureteroscopy: results from a phase II clinical trial. *J. Urol.* 169, 1682–1688. doi: 10.1097/01.ju.0000055600.18515.a1

Lock, J. Y., Wyatt, E., Upadhyayula, S., Whall, A., Nunez, V., Vullev, V. I., et al. (2014). Degradation and antibacterial properties of magnesium alloys in artificial urine for potential resorbable ureteral stent applications. *J. Biomed. Mater. Res. A* 102, 781–792. doi: 10.1002/jbm.a.34741

Lumiaho, J., Heino, A., Kauppinen, T., Talja, M., Alhava, E., Valimaa, T., et al. (2007). Drainage and antireflux characteristics of a biodegradable self-reinforced, self-expanding X-ray-positive poly-L,D-lactide spiral partial ureteral stent: an experimental study. *J. Endourol.* 21, 1559–1564. doi: 10.1089/end.2005.0085

Luo, C. J., Stoyanov, S. D., Stride, E., Pelan, E., and Edirisinghe, M. (2012). Electrospinning versus fibre production methods: from specifics to technological convergence. *Chem. Soc. Rev.* 41, 4708–4735. doi: 10.1039/c2cs35083a

Mittal, R., Pan, D. R., Parrish, J. M., Huang, E. H., Yang, Y., and Patel, A. P. (2018). Local drug delivery in the urinary tract: current challenges and opportunities. *J. Drug Target.* 26, 658–669. doi: 10.1080/1061186X.2017.1419356

Mosayyebi, A., Manes, C., Carugo, D., and Somani, B. K. (2018). Advances in ureteral stent design and materials. *Curr. Urol. Rep.* 19:35.

Mugabe, C., Matsui, Y., So, A. I., Gleave, M. E., Baker, J. H., and Minchinton, A. I. (2011). In vivo evaluation of mucoadhesive nanoparticulate docetaxel for intravesical treatment of non-muscle-invasive bladder cancer. *Clin. Cancer Res.* 17, 2788–2798. doi: 10.1158/1078-0432.CCR-10-2981

Nady, N., and Kandil, S. H. (2018). Novel blend for producing porous chitosan-based films suitable for biomedical applications. *Membranes* 8:2 doi: 10.3390/membranes8010002

Pandit, V., Kumar, A., Ashawat, M. S., Verma, C. P., and Kumar, P. (2017). Recent advancement and technological aspects of pulsatile drug delivery system - a laconic review. *Curr. Drug Targets* 18, 1191–1203. doi: 10.2174/1389450117666160208144343

Park, K. (2014). Controlled drug delivery systems: past forward and future back. *J. Control Release* 190, 3–8. doi: 10.1016/j.jconrel.2014.03.054

Roupret, M., Babjuk, M., Comperat, E., Zigeuner, R., and Sylvester, R. J. (2018). European association of urology guidelines on upper urinary tract urothelial carcinoma: 2017 Update. *Eur. Urol.* 73, 111–122. doi: 10.1016/j.eururo.2017.07.036

Sun, Y., Shan, H., Wang, J., Wang, X., Yang, X., and Ding, J. (2019). Laden nanofiber capsules for local malignancy chemotherapy. *J. Biomed. Nanotechnol.* 15, 939–950. doi: 10.1166/jbn.2019.2745

Thakkar, S., and Misra, M. (2017). Electrospun polymeric nanofibers: new horizons in drug delivery. *Eur. J. Pharm. Sci.* 107, 148–167. doi: 10.1016/j.ejps.2017.07.001

Tian, Q., Zhang, C., Deo, M., Rivera-Castaneda, L., Masoudipour, N., Guan, R., et al. (2019). Responses of human urothelial cells to magnesium-zinc-strontium alloys and associated insoluble degradation products for urological stent applications. *Mater. Sci. Eng. C Mater. Biol. Appl.* 96, 248–262. doi: 10.1016/j.msec.2018.11.018

Tiwari, G., Tiwari, R., Sriwastawa, B., Bhati, L., Pandey, S., Pandey, P., et al. (2012). Drug delivery systems: an updated review. *Int. J. Pharm. Investig.* 2, 2–11.

Tyagi, P., Kashyap, M., Hensley, H., and Yoshimura, N. (2016). Advances in intravesical therapy for urinary tract disorders. *Expert. Opin. Drug. Deliv.* 13, 71–84. doi: 10.1517/17425247.2016.1100166

Ugaonkar, S., Needham, T. E., and Bothun, G. D. (2011). Solubility and partitioning of carbamazepine in a two-phase supercritical carbon dioxide/polyvinylpyrrolidone system. *Int. J. Pharm.* 403, 96–100. doi: 10.1016/j.ijpharm.2010.10.031

Waksman, R., and Pakala, R. (2010). Biodegradable and bioabsorbable stents. *Curr. Pharm. Des.* 16, 4041–4051. doi: 10.2174/138161210794454905

Wang, J., Wang, G., Shan, H., Wang, X., Wang, C., Zhuang, X., et al. (2019). Gradiently degraded electrospun polyester scaffolds with cytostatic for urothelial carcinoma therapy. *Biomater. Sci.* 7, 963–974. doi: 10.1039/c8bm01317a

Wang, J., Xu, W., Li, S., Qiu, H., Li, Z., Wang, C., et al. (2018). Polylactide-cholesterol stereocomplex micelle encapsulating chemotherapeutic agent for improved antitumor efficacy and safety. *J. Biomed. Nanotechnol.* 14, 2102–2113. doi: 10.1166/jbn.2018.2624

Wang, L., Yang, G., Xie, H., and Chen, F. (2018). Prospects for the research and application of biodegradable ureteral stents: from bench to bedside. *J. Biomater. Sci. Polym. Ed.* 29, 1657–1666. doi: 10.1080/09205063.2018.1498184

Wang, X., Shan, H., Wang, J., Hou, Y., Ding, J., Chen, Q., et al. (2015a). Characterization of nanostructured ureteral stent with gradient degradation in a porcine model. *Int. J. Nanomed.* 10, 3055–3064. doi: 10.2147/IJN.S80810

Wang, X., Zhang, L., Chen, Q., Hou, Y., Hao, Y., Wang, C., et al. (2015b). A nanostructured degradable ureteral stent fabricated by electrospinning for upper urinary tract reconstruction. *J. Nanosci. Nanotechnol.* 15, 9899–9904. doi: 10.1166/jnn.2015.10747

Wang, Y., Liu, S., Luo, Y., Wang, F., Liu, H., Li, L., et al. (2014). Safety and efficacy of degradable vs. permanent polymer drug-eluting stents: a meta-analysis of 18,395 patients from randomized trials. *Int. J. Cardiol.* 173, 100–109. doi: 10.1016/j.ijcard.2014.02.023

Weiser, J. R., and Saltzman, W. M. (2014). Controlled release for local delivery of drugs: barriers and models. *J. Control Release* 190, 664–673. doi: 10.1016/j.jconrel.2014.04.048

Zamani, M., Prabhakaran, M. P., and Ramakrishna, S. (2013). Advances in drug delivery via electrospun and electrosprayed nanomaterials. *Int. J. Nanomed.* 8, 2997–3017. doi: 10.2147/IJN.S43575

Zigeuner, R., and Pummer, K. (2008). Urothelial carcinoma of the upper urinary tract: surgical approach and prognostic factors. *Eur. Urol.* 53, 720–731. doi: 10.1016/j.eururo.2008.01.006

Conflict of Interest: The authors declare that the research was conducted in the absence of any commercial or financial relationships that could be construed as a potential conflict of interest.

frontiers in Pharmacology

REVIEW
published: 20 March 2020
doi: 10.3389/fphar.2020.00122

Progressive 3D Printing Technology and Its Application in Medical Materials

Daoyang Fan[1,2†], Yan Li[1,2†], Xing Wang[3,4], Tengjiao Zhu[1,2], Qi Wang[5], Hong Cai[1,2], Weishi Li[1,2], Yun Tian[1,2*] and Zhongjun Liu[1,2*]*

[1] Department of Orthopedic, Peking University Third Hospital, Beijing, China, [2] Engineering Research Center of Bone and Joint Precision Medicine, Ministry of Education, Beijing, China, [3] Beijing National Laboratory for Molecular Sciences, State Key Laboratory of Polymer Physics & Chemistry, Institute of Chemistry, Chinese Academy of Sciences, Beijing, China, [4] University of Chinese Academy of Sciences, Beijing, China, [5] Department of Pediatrics, Peking University Third Hospital, Beijing, China

OPEN ACCESS

Edited by:
Wei Tao,
Harvard Medical School,
United States

Reviewed by:
Yang Han,
Ludwig Maximilian University of Munich, Germany
Jianxun Ding,
Changchun Institute of Applied Chemistry (CAS), China

***Correspondence:**
Xing Wang
wangxing@iccas.ac.cn
Yun Tian
tiany@bjmu.edu.cn
Zhongjun Liu
zjliu@bjmu.edu.cn

[†]These authors have contributed equally to this work

Specialty section:
This article was submitted to Translational Pharmacology, a section of the journal Frontiers in Pharmacology

Received: *01 December 2019*
Accepted: *28 January 2020*
Published: *20 March 2020*

Citation:
Fan D, Li Y, Wang X, Zhu T, Wang Q, Cai H, Li W, Tian Y and Liu Z (2020) Progressive 3D Printing Technology and Its Application in Medical Materials. Front. Pharmacol. 11:122. doi: 10.3389/fphar.2020.00122

Three-dimensional (3D) printing enables patient-specific anatomical level productions with high adjustability and resolution in microstructures. With cost-effective manufacturing for high productivity, 3D printing has become a leading healthcare and pharmaceutical manufacturing technology, which is suitable for variety of applications including tissue engineering models, anatomical models, pharmacological design and validation model, medical apparatus and instruments. Today, 3D printing is offering clinical available medical products and platforms suitable for emerging research fields, including tissue and organ printing. In this review, our goal is to discuss progressive 3D printing technology and its application in medical materials. The additive overview also provides manufacturing techniques and printable materials.

Keywords: additive manufacturing, 3D printing, functional biomaterials, tissue engineering, 3D pharmacological models, medical apparatus

INTRODUCTION

As an additive manufacturing (AM) technique, three-dimensional (3D) printing enables customized fabrication of 3D constructs based on computer aided design (CAD) software or images obtained from computed tomography (CT) and magnetic resonance imaging (MRI). Firstly developed in the 1980s, 3D printing technology was called rapid prototype technology and has been well applied in a variety of industries with different printing techniques and materials (Liaw and Guvendiren, 2017). With the rapid development of 3D printer, the overall 3D printing market grew to $9.9 billion in 2018 and is expected to reach $34.8 billion in 2024 (MarketsandMarkets, 2019). The medical 3D printing market is expected to maintain significant growth due to the huge potential demand for costumed medical products. Currently, with the expiry of many 3D printing patents (including stereolithography and selective laser sintering), 3D printers and products are becoming cheaper and easy to access (Rahman et al., 2018).

3D printing technology has been widely applied in a variety of industries including aviation (Wong, 2016), geoscience (Ishutov et al., 2018), education (Smith and Jones, 2018), clothing (Markstedt et al., 2017), medical (Mitsouras et al., 2015; Giannopoulos et al., 2016), and pharmaceuticals (Orsi et al., 2015; Norman et al., 2017; Trenfield et al., 2018). Among these

medical and pharmaceutical industries, orthopedic and dental applications are favorable to embrace the 3D printing technology (MarketsandMarkets, 2019). It is related to the demand for the patient-specific design and fabrication of the final devices (such as joint prosthesis, surgical guides, and dental restorations) (Eltorai et al., 2015; Tahayeri et al., 2018). Personalized devices manufactured preoperationally are benefited for the efficiency and accuracy (Konta et al., 2017). For medical education and surgical planning, 3D anatomical models are printed subtly with microscopic anatomy structures (Mukherjee et al., 2017; Ganguli et al., 2018). Tissue and organ printing is an emerging field that mainly focused on regenerative medicine and tissue engineering by both academy and industry (Murphy and Atala, 2014). Based on it, preclinical patient-specific disease models are used for drug testings and screenings. 3D printing technology is merging with traditional pharmaceuticals for the development of dose-customized drugs (Norman et al., 2017).

In this review, recent techniques and applications of 3D printing in medical materials are well summarized. Common AM techniques and printable materials are presented for better understanding of their potential, limitations, and applications. Medical applications including tissue engineering, anatomical models, apparatus, and instruments with 3D printing technology are also provided and summarized. We finally demonstrate our concluding remarks and future outlook on 3D printing in medical materials (**Figure 1**).

CURRENT AM TECHNOLOGIES AND PRINTABLE MATERIALS

There are about two dozen AM techniques, among which only some techniques are widely applied in medical industry. The main reason is the specific fabrication process and raw material to meet the high-quality requirements for medical devices. Four common AM techniques are powder-based printing (Brunello et al., 2016), vat polymerization-based printing (Stefaniak et al., 2019), droplet-based printing (Graham et al., 2017), and extrusion-based printing (Taylor et al., 2018).

Powder-Based Printing

Powder-based 3D printing is a promising technique with excellent ability for customized fabrication with a variety of external shapes, internal structures, and porosities. There are four common powder-based printing techniques: selective laser sintering (SLS), selective laser melting (SLM), direct metal laser sintering (DMLS), and electron beam melting (EBM) (**Figure 2**)

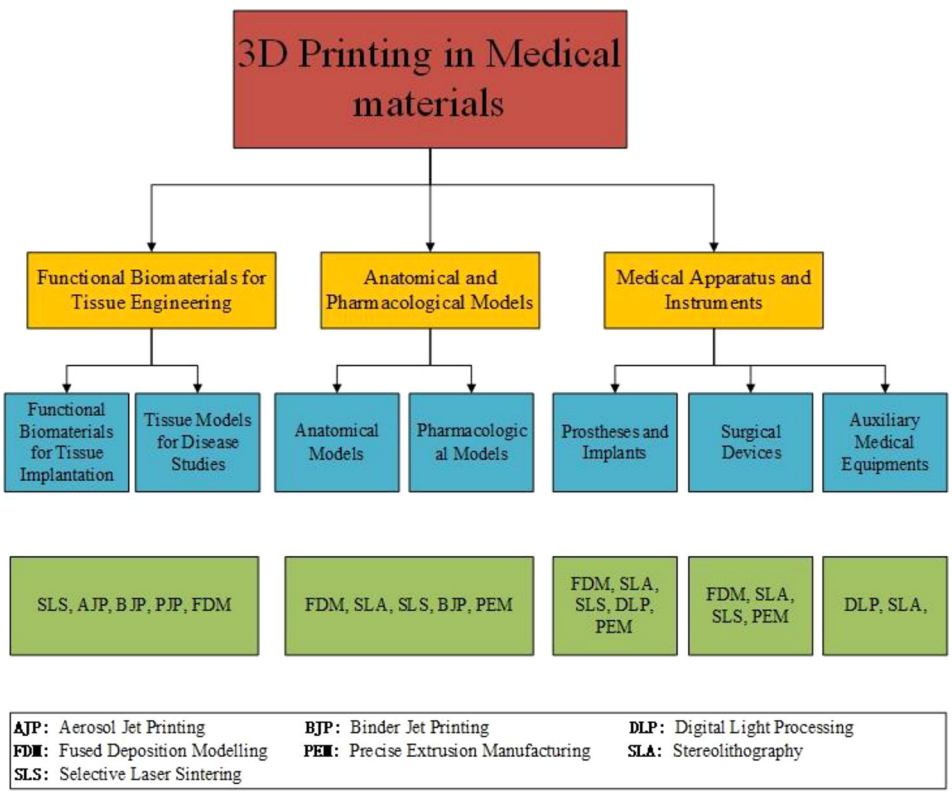

FIGURE 1 | Progressive 3d printing technology and its application in medical materials. Chart showing the application area (yellow boxes) with corresponding products (blue boxes) and primary 3D printing techniques (green boxes).

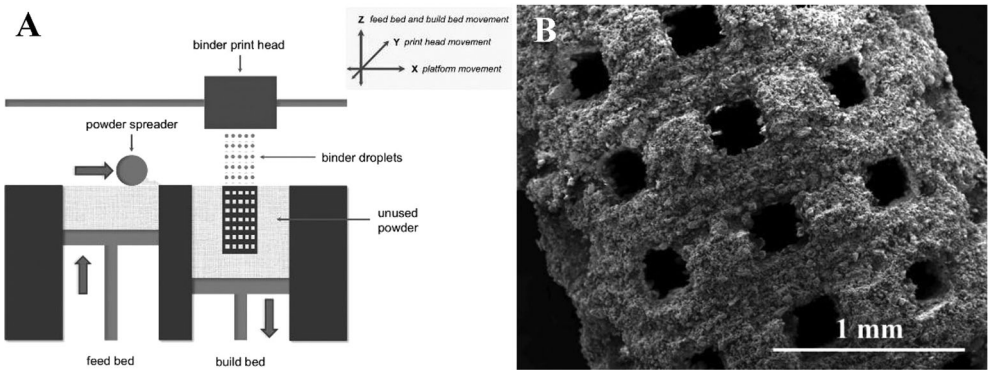

FIGURE 2 | Printing process of powder-based printing and related products. **(A)** Schematic diagram. **(B)** Products manufactured by powder-based printing method. Reproduced, with permission, from (Brunello et al., 2016).

(Brunello et al., 2016). Every technique is based on localized heating to generate melted metallic powder, which would be used to fabricate the customized products. There are obvious differences in both printing process and product characters among these four powder-based printing techniques. For SLS and DMLS, powder particles are bounded with laser instead of spray solution. In the printing process, the laser draws specific patterns on one layer of the powder bed (Fina et al., 2017). The roller in the printer distributes a new layer of powder onto the surface once the printing of the previous layer is completed. After being built layer-by-layer, printed objects are collected underneath the powder bed. As a specific kind of SLS, DMLS utilizes metal exclusively. Different from sintering techniques, SLM and EBM fully melt powder with laser and electron beam respectively (Wysocki et al., 2018). For the work of electron beam, the powder bed in the EBM printer maintains high working temperature (> 870 K). It directly affects the quality of the fabrication especially in the details of microstructure. Comparatively, products printed with SLM maintain higher tribological, mechanical, and corrosion properties. With the differences between sintering and melting, the surfaces of products printed with sintering techniques (SLS and DMLS) are rough as powders are not completely melted.

Although the sintering techniques produce products with rough surfaces, they can process with a large variety of materials including plastic powder, ceramic powder, and metal alloys. As the high working temperature, material with volatile constituents (Mg, Zn, Bi, etc.) are not feasible for EBM, while SLM can treat a much wider spectrum of metallic alloys including Ti-based, Al-based, Fe-based, Ni-based, Cu-based, Co-based, and their composites. However, the melting process brings a big advantage that it can produce fully dense parts without post-treatment steps such as infiltration or thermal process.

Vat Polymerization-Based Printing

Vat-polymerization based printing technique is based on light curing resin material and light selective hardening polymerization molding. It is widely used for fabricating complex devices with functional parts such as valves, lenses and fluidic interconnects (Carve and Wlodkowic, 2018). In the process, a vat of photosensitive polymer resin is selectively exposed to a specifically controlled beam of leaser or light (Credi et al., 2016; Credi et al., 2018). The polymer is polymerized after spatially localized irradiation to fabricate the specific constructions (Credi et al., 2016; Wang et al., 2018a). Common process includes digital light processing (DLP), stereolithography (SLA), and multiphoton polymerization (MPP) (**Figure 3**) (Carve and Wlodkowic, 2018). SLA was the first AM technology applied in medicine in 1994 (Dittmann et al., 1994). A spot laser irradiates the resin localized in a single x-y direction in SLA (Zanchetta et al., 2016), whereas a digital illuminant irradiates the whole x-y plan in DLP (Osman et al., 2017). For both SLA and DLP, the print platform moves parallelly to the z-axis while the final product is fabricated layer-by-layer (Zanchetta et al., 2016; Osman et al., 2017). Differently in MPP, the photosensitive polymer resin is irradiated by a femtosecond laser beam thoroughly in multi directions, resulting that it is not a layer-by-layer technology (Wollhofen et al., 2018). Products printed with vat polymerization technology need to be exposed to light after printing to enhance stability (Credi et al., 2016; Carve and Wlodkowic, 2018).

Droplet-Based Printing

Material jetting technology is a process where droplets of liquid materials are ejected and polymerized throughout hundreds of jets. The polymerization only occurs selectively by directed UV for designed structures (Revilla-Leon and Ozcan, 2019). Material jetting technology includes aerosol jet printing (AJP), binder jet printing (BJP), and poly jet printing (PJP) (**Figure 4**). During AJP, composite in aerosol suspension droplets is carried *via* N_2 gas and ejected onto the substrate layer by layer (Yuan et al., 2017). Multi materials including metals, polymers, and ceramics can be used in AJP with a low printing temperature, which is benefit for biomanufacturing (Mahajan et al., 2013). Binder jet printing (BJP) is similar with SLS except that BJP do not need

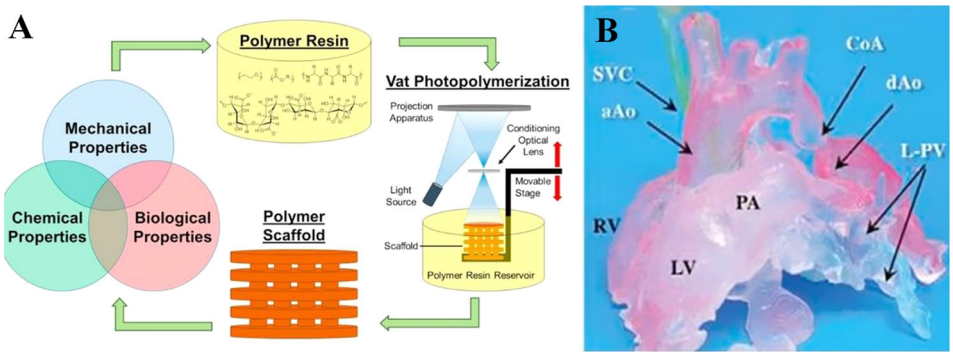

FIGURE 3 | Polymer scaffold fabricated with SLA approach. **(A)** Schematic diagram. **(B)** Products manufactured by vat-polymerization based printing method. Reproduced, with permission, from (Mondschein et al., 2017).

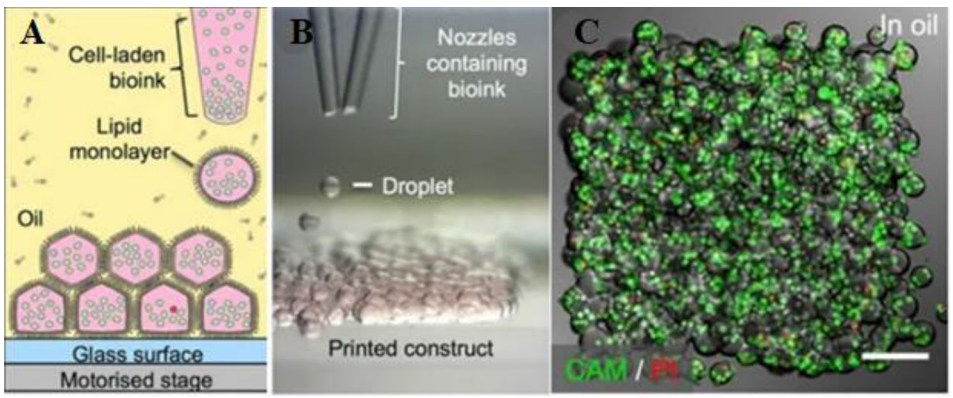

FIGURE 4 | 3D printing of droplet-based printing. **(A)** Schematic diagram of droplet-based cell printing. **(B)** Bright-field micrographs of patterned cell junctions containing two cell types. **(C)** Confocal fluorescence micrographs of cell constructs printed under oil. Reproduced, with permission, from (Brunello et al., 2016).

thermoplastic excipient (Hong et al., 2016). The binder in BJP should meet specific ranges of surface tension (35–40 mJ/N) and viscosity (5–20 Pa·s) (Kim D. H. et al., 2018). In PJP, polymer resin drops are cured by UV light immediately without time consuming postprocessing (Revilla-Leon and Ozcan, 2019). With high resolution, PJP is capable of printing refined structures (Carve and Wlodkowic, 2018).

Extrusion-Based Printing

Extrusion-based printing was firstly developed by S. Scott Crump in 1988, commonly referred as fused deposition modeling (FDM) or fused filament fabrication (FFF) (Placone and Engler, 2018). FDM is a mature technology based on the extrusion of thermoplastic or composite materials drawn through the hot extrusion head (with one/multiple extrusion nozzles) (Paxton et al., 2017). Fused materials were deposited layer by layer with the horizontal and vertical movement of nozzles controlled by numerically-controlled machine tool (Ozbolat and Hospodiuk, 2016). Extrusion-based printing widely applied in metal printing, polymer printing, and bioprinting (**Figure 5**) (Ning and Chen, 2017). The printing techniques have been recently developed to precision extrusion deposition (PED) (Fedore et al., 2017), precise extrusion manufacturing (PEM) (Jamroz et al., 2018), and multiple heads deposition extrusion (MHDS) (Serex et al., 2018). Multiple bioprinting applications in vascular models, soft-tissue models, and bone models manufactured with extrusion-based printing technology have been well-developed in recent years (Ahlfeld et al., 2017; Paxton et al., 2017; Ahlfeld et al., 2018). One major advantage of its bioprinting application is that the hydrogels of extrusion-based printing is capable to fabricate products with high cell density ($> 1 \times 10^6$ cells ml^{-1}) (Petta et al., 2018; Taylor et al., 2018; Chen et al., 2019).

APPLICATIONS IN MEDICAL MATERIALS

AM technologies have been widely applied in medical materials, especially in tissue engineering, medical models, medical

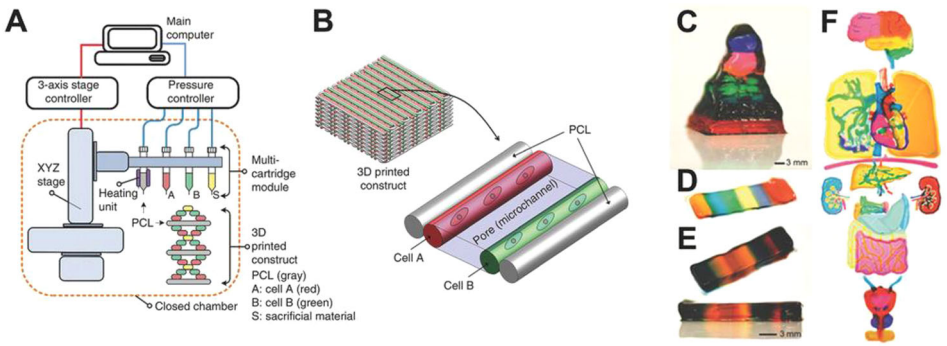

FIGURE 5 | 3D printing of extrusion-based multi-layer printing. **(A)** Schematic diagram of extrusion-based printing. **(B)** Multi materials printed with two cell types. **(C–F)** Available complex organs printed with extrusion-based printing techniques. Reproduced, with permission, from (Placone and Engler, 2018).

instruments, and drug formulations. A variety of printing technologies and products have lightened the broad market of medical and chemical applications of 3D printing.

Functional Biomaterials for Tissue Engineering

Tissue engineering with 3D printing has been focused on two parts, functional biomaterials for tissue implantation and tissue models for disease studies. In this section, functional biomaterials manufactured with AM technologies would be the focus. Tissue scaffolds are important component of 3D printing tissue engineering as they can provide structural supports for cell attachment, proliferation and migration (**Figure 6**). Tissue engineering scaffolds and basic medical scaffolds are considered different especially in biological activity and application purposes (Yang et al., 2018). Good bioactivity, excellent biocompatibility, and appropriate mechanical property are three basic requirements for an ideal tissue engineering scaffold. While basic medical scaffolds are usually applied for filling tissue coloboma or fixation without requirement for bioactivity. Implantable tissue engineering scaffolds are required to be degradable where scaffolds would be replaced by palingenetic tissues (Wang et al., 2018b). To induce tissue or bone growth inside the scaffolds, traditional procedures including molding, freeze drying, and electrospinning have been applied in the manufacture.

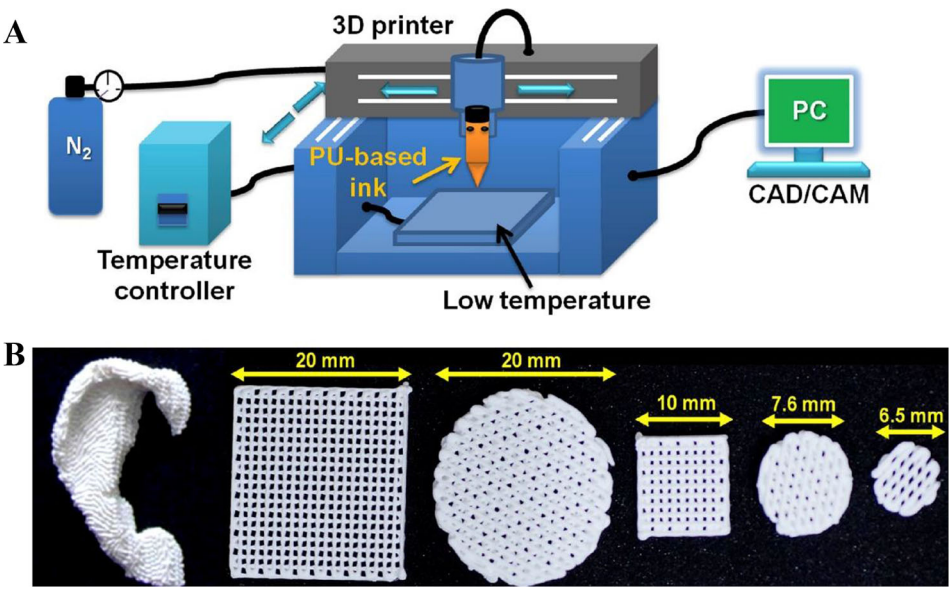

FIGURE 6 | Functional biomaterials and related printing technique. **(A)** Schematic of a 3D printing platform for performing a water-based biological scaffold. **(B)** Appearance of 3D printed brackets in various shapes and sizes. Reproduced, with permission, from (Hung et al., 2016).

However, none of the traditional procedures can fabricate scaffolds with customized mechanics, architecture and porosity. With the development of AM, scaffolds with high resolution, customized design, and high porosity have been successful in medical applications.

Tissue engineering scaffolds are fabricated in two major methods, printing with cells mixed in ink or gel and seeding cells onto scaffolds post printing. The most common methods applied in scaffolds fabrication are vat polymerization, SLS, BJ, and FDM. Inkjet printing and extrusion-based printing are the two popular bioprinting technologies, while bio-scaffolds are fabricated based on or without scaffolds. For bioprinting techniques based on scaffolds, hydrogels or polymers laden with cells are cured with AJP, BJP, PJP, and vat polymerization. For bioprinting techniques without scaffolds, hydrogels filled with high cell density ($> 1 \times 10^6$ cells ml^{-1}) are applied directly relying on cell-cell interactions. Cells in such density need to fuse and mature in the bioreactor for a period of time.

Only a few companies have launched commercial tissue engineering scaffolds. Organogenesis Inc, one of the world's most famous FDA-approved 3D printed medical device supplier, introduced their GINTUIT™, a tissue engineering product approved in 2012 for oral soft tissue repair and regeneration. It is a commercialized cell and gene therapy product combined fibroblasts and keratinocytes in bovine collagen. In 2016, another famous supplier, Stryker released the product Tritanium® LP, a titanium lumber posterior cage. The lumber cage is fabricated with abundant porous by DMLS technology with titanium alloy. The inner porous are helpful for blood vessel and bone growth inside the lumber cage.

With widespread concerns from various industries, bioprinting and tissue engineering have made significant progress and wide applications. Applications covered profuse tissues including tooth, bone, cartilage, ear, blood vessel, liver, kidney, and myocardium (Zhu et al., 2019). In 2017, Monica M. Laronda et al. from Northwestern university claimed successful fabrication of a bioprosthetic ovary created using 3D printed microporous scaffolds restoring ovarian function in sterilized mice (Laronda et al., 2017). Recently, Byoung Soo Kim and his colleges developed human skin with PJP 3D printing system (Ahn et al., 2016). This printed skin showed favorable biological characteristics, including stable dermis and epidermal layers. Manufactured skin substitutes can significantly improve skin healing of the wound area.

Anatomical and Pharmacological Models

To date, 3D printed tissue models play a significant role in the studies of mechanism of disease, pharmacological testing for new drugs, effectiveness of preclinical therapy, and anatomical structures of complicated organs (**Figures 7** and **8**). For these studies, conventional methods take plenty of mice and other experiment animals for building animal models. Typically, patient derived xenograft (PDX) models for medical studies always cost a large amount of immunodeficient mice to engraft disease cells. This kind of process takes a great mass of time and money. To overcome the disadvantage, tissue models were developed, firstly by traditional fabrication technologies without 3D printing. However, products by traditional methods revealed inaccurate models with unrealistic tissue status. With the application of 3D printing, biomimetic tissue models with high resolution are fabricated more efficiently at a lower cost than in the past. In this part, 3D printed tissue models of skin, liver, and tumor would be discussed.

The liver is a complex organ with multiple functions which have biotransformation effects on many non-nutritive substances

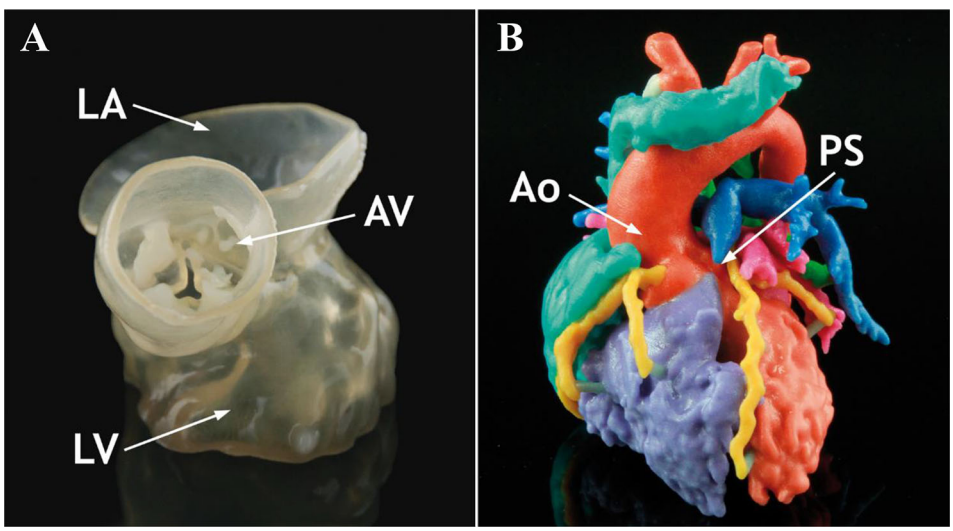

FIGURE 7 | Anatomical 3D models of heart in normal and pathological state. **(A)** Normal anatomical 3D printed heart model. **(B)** Tetralogy of Fallot anatomical 3D printed heart model. Reproduced, with permission, from (Bartel et al., 2018).

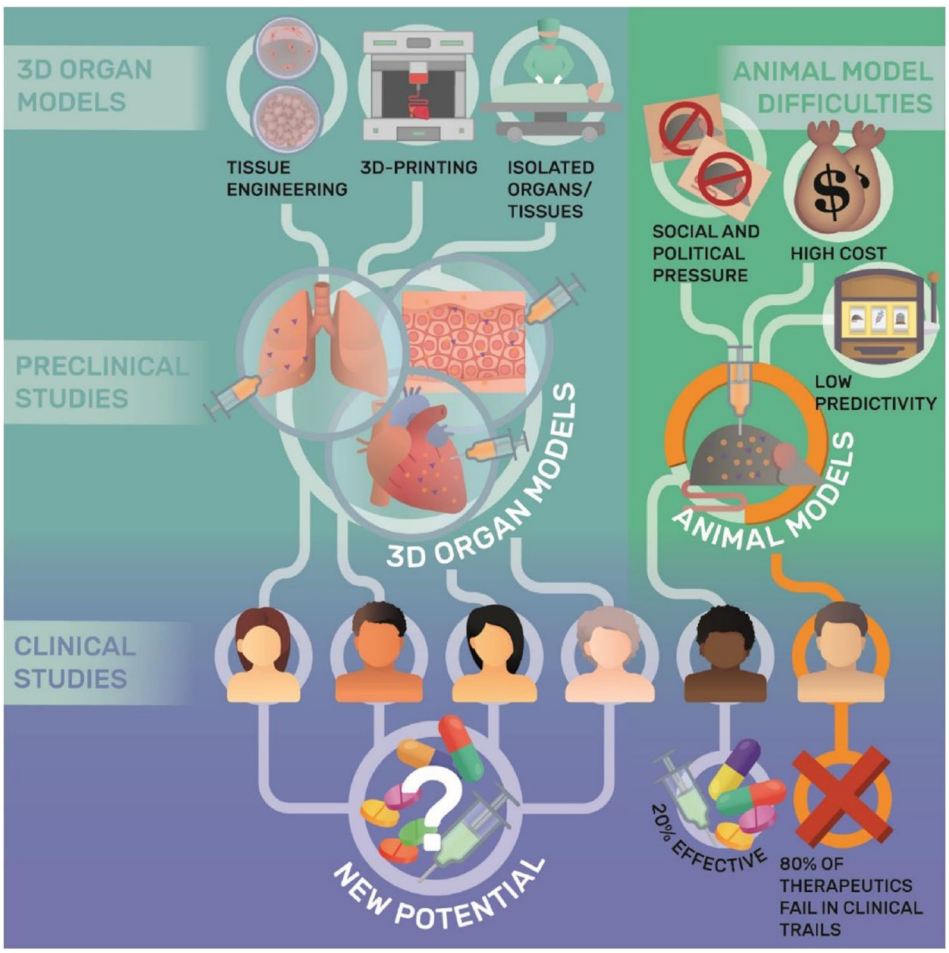

FIGURE 8 | Applications and limitations of 3D organ models in pharmacological research. Reproduced, with permission, from (Weinhart et al., 2019).

(such as various drugs, poisons, and certain metabolites) in the body. They are completely decomposed by metabolism or excreted in the original form. With highly sensitive to drug toxicity, liver tissue engineering models were developed to take drug screening and testing. Reproducing the complex structures with 3D printing technology is the basic step for mimicking hepatic functions. To date, multiple fabrications of liver tissue models were accomplished with several 3D printing technologies. Ho-Joon Lee et al. developed multicellular 3D liver with multi-functions encapsulated in hybrid hydrogel (Lee et al., 2017). HepaRG cells alone or with supporting cells were encapsulated in semi-IPNs (hydrogel) and printed with vat polymerization technology. Fabricated 3D liver model was verified to be functional maturation with a dynamic 3D microenvironment, which is important for disease modeling and drug testing. Huanhuan Joyce Chen et al. fabricated a 3D scaffold co-cultured with human intestinal cells (hIECs) and liver cells to mimic a two-organ body-on-chip situation (Chen et al., 2018). The hIECs and liver cells in this scaffold were verified to maintain high viability and differentiable. While hIECs differentiated into human gastrointestinal cells, liver cells developed into lobule-like structures. Two organs on chip 3D model significantly improved the studies on human response and Inter-organ relationships. The two 3D liver models above were well fabricated and suitable for short-term studies. To realize long-term studies with functional liver tissue models, Hassan Rashidi et al. developed a stable 3D liver tissue model with certain function, which is testified for 1 year (Rashidi et al., 2018). Mimicking realistic conditions, hexagonal scaffolds were fabricated with polycaprolactone embraced with self-aggregated pluripotent stem cells (PSCs) spheroids. Embedding with PSCs-loaded implants, two mice models of tyrosinemia were claimed to heal without any infection. Emerging 3D liver tissue models are helping solving problems in an efficient and cost-effective way that we cannot imagine before.

As one of the largest organs in human body, skin covers the whole-body surface and plays an important role in protecting, excreting, regulating body temperature, and feeling external stimuli. For patients with extensive skin wounds, clinical therapies would be complicated and important. To test the

efficacy and safety of treatment, skin tissue models reveal an irreplaceable role. Byoung Soo Kim et al. fabricated a 3D printing skin tissue model with skin-derived extracellular matrix (S-dECM) bioink (Kim B. S. et al., 2018). Embraced *in vivo* with endothelial progenitor cells (EPCs) and adipose-derived stem cells (ASCs), 3D printing skin model accelerated wound healing especially in reepithelization and neovascularization. John W. Wills et al. adapted nanoparticles in 3D reconstructed skin micronucleus (RSMN) assay (Wills et al., 2016). After normalizing the dose between the total nanoparticle mass and the cell number between 2D/3D assays, the 3D dose response was compared to the 2D micronucleus assay. Due to the protective properties of the 3D cell microstructure and the mixed barrier effect, tested silica particles revealed no (gene) toxicity for live cells in the 3D model comparing to the 2D assay. Plenty results suggested 3D skin model can more accurately reflect the toxicity of nanoparticle drugs on human skin function than traditional methods.

Tumor is a new pathological organism formed by the proliferation of local tissue cells under the action of various tumorigenic factors, and has an extremely complex microenvironment and microstructure. It is significant to mimic *in vivo* tumor environment with stroma and micro structures for the accuracy of testing new theories and therapies (Costa et al., 2016). Jizhao Li et al. developed a 3D cell model with human lung cancer A549 cells applied in scaffolds fabricated with silk fibroin protein and chitosan (Li et al., 2018). By resembling pathological conditions, the 3D tumor model provide a valuable biomaterial platform for *in-vitro* test of antitumor drugs for non-small cell lung cancer. Yu Zhao et al. fabricated a 3D *in vitro* cervical tumor model with 3D printing of Hela cells in hydrogel grid structure by a layer-by-layer fashion (Zhao et al., 2014). With higher proliferation rate and matrix metalloproteinase protein expression, 3D cervical model fabricated with novel 3D printing technology is helping cervical tumor studies. Therefore, with the development of 3D printing tissue models, it is credible for the promising future that studies will be done more efficiently without sacrifices from experimental animals.

Medical Apparatus and Instruments

AM is a promising and novel technology for the production of medical apparatus and instruments comparing with traditional manufacturing techniques. Directed by patient's clinical images, custom-designed medical apparatus and surgical guides are fabricated efficiently and accurately. It brings anatomically fit to patients and surgical safety to surgeons. Besides, AM is capable of manufacturing complex microstructures which are not possible for conventional techniques (**Figure 9**). With these advantages, AM allows fast production with high resolution, few leftover material and low costs. In this section, discussion is focused on (i) prostheses and implants and (Heidari Keshel et al., 2016) auxiliary medical equipment.

Medical implants and orthoses/prostheses (O&P) have been fabricated with traditional methods for decades. As with long term application, conservative implants revealed problems including anatomical mismatching, incompetent binding

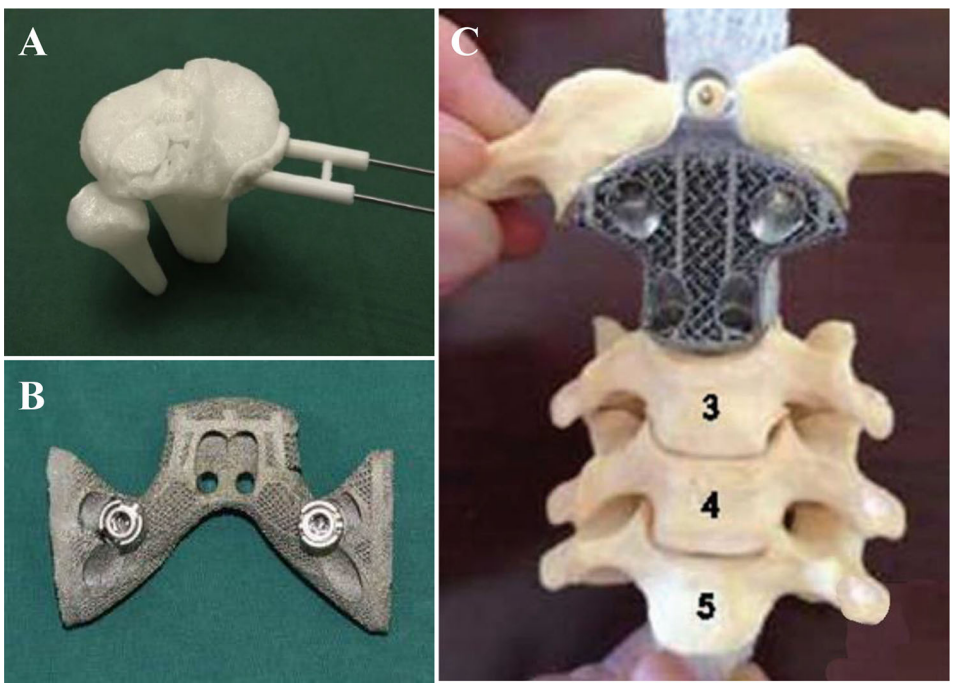

FIGURE 9 | Medical apparatus and instruments by 3D printing. **(A)** 3D printed guide template for surgery simulation. **(B, C)** 3D printed titanium apparatus for cervical spine and pelvic surgery respectively. Reproduced, with permission, from (Xu et al., 2016; Wei et al., 2017; Nie et al., 2019).

strength and initial stability, poor bone ingrowth and long-term stability, and low cost-efficiency (Wang et al., 2019). All these problems have been solved with AM technology, which is capable to fabricate implants with proper surface and mechanical properties. Powder-based 3D printing techniques (SLM, SLS, and EBM) are widely applied in implants and O&P manufacturing as they are compatible with a wide range of printing materials, such as titanium alloy, zinc alloy, cobalt–chrome alloy, and polyetheretherketone (PEEK). With outstanding mechanical properties and biocompatibility, 3D printed implants have been applied in plenty of surgical majors, including tracheobronchial (Zopf et al., 2014; Han et al., 2018), dentofacial, cardiovascular, orthopedic, and spine. For severe tracheobronchomalacia patients, a 3D printed self-expandable, metallic tracheobronchial stent fabricated with SLS technology was implanted into patient's collapse bronchus and rebuilt airway efficiently (Han et al., 2018). The printing technology offer a great opportunity of reconstruction and support for tracheobronchial diseases, which was difficult for conservative implants to be fabricated anatomically fitted. Besides self-expandable stent, a 3D printed bioresorbable stent was fabricated with SLS technique (Zopf et al., 2014). Printed bioresorbable stents were embedded into severe tracheobronchomalacia pig model, significant resolution of symptoms was observed. The stent was resorbed over time and was considered as a "4D" functional material. In maxillofacial and craniofacial surgeries, complex anatomy structures and irregular shapes of defects are the two most severe challenges. Conventionally, craniofacial prostheses are fabricated with hand-curved wax model for the anatomic defect with low precision. With 3D printing techniques, patient-customized prostheses are fabricated with guidance from CT or MRI images in which details for defects are well recorded. *Kyle K et al.* demonstrated the first application case of 3D printing in complex fetal craniofacial anomalies and perinatal management (VanKoevering et al., 2015). Researchers from Saint Louis University School of Medicine reviewed 315 patients who underwent 3D printing assisted maxillofacial and craniofacial surgeries (Jacobs and Lin, 2017). Fabrications with 3D printing techniques were mainly focused on contour models, surgical guides, splints, and implants. These objects were mainly fabricated in factory and laboratory with an average time and cost of 18.9 h and $1,353.31 respectively. Without lab or proficiency with printing software, low-cost 3D maxillofacial models could be fabricated with a cost of only $90 (Legocki et al., 2017). While commercial models can be manufactured with serializable materials and advanced virtual planning, this low-cost method can generate models with high-fidelity as educational and surgical planning tools. Cardiac diseases have been widely studied with the assistance of 3D printing technology as it offers high-resolution reduction of pathological status (Vukicevic et al., 2017). Variety of printing techniques including material jetting (Olivieri et al., 2015; Lind et al., 2017; Lau et al., 2018; Su et al., 2018), FDM (Mahmood et al., 2015; Son et al., 2015), SLS, and SLA have been applied in the studies of structural heart disease, congenital heart disease, coronary arteries, and systemic vasculature. Benefiting from 3D printing techniques, advanced visualization (Mahmood et al., 2015; Olivieri et al., 2015), diagnosis (Son et al., 2015), planning of surgeries, interventions (Lind et al., 2017), education (Lau et al., 2018; Su et al., 2018), and researches (Mahmood et al., 2015; Lind et al., 2017) in cardiovascular diseases are developing rapidly.

CONCLUSION

This paper reviews the advancements of 3D printing technologies applied in medical materials in recent years. With the superiority of patient-specific designs, high complexity, favorable productivity, and cost-effective manufacturing methods, 3D printing has been becoming widely accepted manufacturing technologies in the medical applications. The main applications of 3D printing in medicine include tissue engineering models, anatomical models, pharmacological designs and validation models, medical apparatus and instruments. Orthopedics is one of the most advanced fields that integrate 3D printing to produce end-use products such as restorations, spine models, and surgical navigation boards. Orthopedics is a pioneer in medical devices. Currently, there are many multiple 3D printed medical products on the market, including implantable craniofacial implants, acetabular cups, knee implants, spinal cages, and surgical instruments. In addition, about 99% of hearing aid housings are custom made through 3D printing. Pre-surgery printed anatomical models have revolutionized the way surgeons and medical students were trained for surgery. To date, researchers have printed about 16 different types of tissues, providing tissue models for high-throughput screening for new drugs. It is believed that 3D printing is affecting clinical and related basic research in an increasingly broader manner.

AUTHOR CONTRIBUTIONS

DF and YL contributed equally to this reviewed manuscript. XW, YT and ZL conceived and designed the content of the manuscript. DF, YL and XW collected the researched literatures, arranged the outline of collected documents and wrote the articles. TZ, QW, HC, and WL made important suggestions and helped revising the manuscript. All authors reviewed and commented on the entire manuscript.

FUNDING

This research was funded by the Ministry of Science and Technology of China (2016YFB1101501 and 2018YFE0104200) and National Natural Science Foundation of China (NSFC, 51973226).

REFERENCES

Ahlfeld, T., Cidonio, G., Kilian, D., Duin, S., Akkineni, A. R., Dawson, J. I., et al. (2017). Development of a clay based bioink for 3D cell printing for skeletal application. *Biofabrication* 9 (3), 034103. doi: 10.1088/1758-5090/aa7e96

Ahlfeld, T., Doberenz, F., Kilian, D., Vater, C., Korn, P., Lauer, G., et al. (2018). Bioprinting of mineralized constructs utilizing multichannel plotting of a self-setting calcium phosphate cement and a cell-laden bioink. *Biofabrication* 10 (4), 045002. doi: 10.1088/1758-5090/aad36d

Ahn, S. H., Lee, J., Park, S. A., and Kim, W. D. (2016). Three-dimensional bio-printing equipment technologies for tissue engineering and regenerative medicine. *Tissue Eng. Regener. Med.* 13 (6), 663–676. doi: 10.1007/s13770-016-0148-1

Bartel, T., Rivard, A., Jimenez, A., Mestres, C. A., and Muller, S. (2018). Medical three-dimensional printing opens up new opportunities in cardiology and cardiac surgery. *Eur. Heart J.* 39 (15), 1246–1254. doi: 10.1093/eurheartj/ehx016

Brunello, G., Sivolella, S., Meneghello, R., Ferroni, L., Gardin, C., Piattelli, A., et al. (2016). Powder-based 3D printing for bone tissue engineering. *Biotechnol. Adv.* 34 (5), 740–753. doi: 10.1016/j.biotechadv.2016.03.009

Carve, M., and Wlodkowic, D. (2018). 3D-Printed chips: compatibility of additive manufacturing photopolymeric substrata with biological applications. *Micromachines (Basel)* 9 (2), E91. doi: 10.3390/mi9020091

Chen, H. J., Miller, P., and Shuler, M. L. (2018). A pumpless body-on-a-chip model using a primary culture of human intestinal cells and a 3D culture of liver cells. *Lab. Chip* 18 (14), 2036–2046. doi: 10.1039/c8lc00111a

Chen, Y. R., Zhou, Z. X., Zhang, J. Y., Yuan, F. Z., Xu, B. B., Guan, J., et al. (2019). Low-molecular-weight heparin-functionalized chitosan-chondroitin sulfate hydrogels for controlled release of TGF-beta3 and *in vitro* neocartilage formation. *Front. Chem.* 7, 745. doi: 10.3389/fchem.2019.00745

Costa, E. C., Moreira, A. F., de Melo-Diogo, D., Gaspar, V. M., Carvalho, M. P., and Correia, I. J. (2016). 3D tumor spheroids: an overview on the tools and techniques used for their analysis. *Biotechnol. Adv.* 34 (8), 1427–1441. doi: 10.1016/j.biotechadv.2016.11.002

Credi, C., Fiorese, A., Tironi, M., Bernasconi, R., Magagnin, L., Levi, M., et al. (2016). 3D Printing of cantilever-type microstructures by stereolithography of ferromagnetic photopolymers. *ACS Appl. Mater Interfaces* 8 (39), 26332–26342. doi: 10.1021/acsami.6b08880

Credi, C., Griffini, G., Levi, M., and Turri, S. (2018). Biotinylated photopolymers for 3d-printed unibody lab-on-a-chip optical platforms. *Small* 14 (1), 1702831. doi: 10.1002/smll.201702831

Dittmann, W., Bill, J., Wittenberg, G., Reuther, J., and Roosen, K. (1994). [Stereolithography as a new method of reconstructive surgical planning in complex osseous defects of the cranial base. *Tech. note]. Zentralbl Neurochir* 55 (4), 209–211.

Eltorai, A. E., Nguyen, E., and Daniels, A. H. (2015). Three-dimensional printing in orthopedic surgery. *Orthopedics* 38 (11), 684–687. doi: 10.3928/01477447-20151016-05

Fedore, C. W., Tse, L. Y. L., Nam, H. K., Barton, K. L., and Hatch, N. E. (2017). Analysis of polycaprolactone scaffolds fabricated *via* precision extrusion deposition for control of craniofacial tissue mineralization. *Orthod. Craniofac. Res.* 20 Suppl 1, 12–17. doi: 10.1111/ocr.12159

Fina, F., Goyanes, A., Gaisford, S., and Basit, A. W. (2017). Selective laser sintering (SLS) 3D printing of medicines. *Int. J. Pharm.* 529 (1-2), 285–293. doi: 10.1016/j.ijpharm.2017.06.082

Ganguli, A., Pagan-Diaz, G. J., Grant, L., Cvetkovic, C., Bramlet, M., Vozenilek, J., et al. (2018). 3D printing for preoperative planning and surgical training: a review. *BioMed. Microdevices* 20 (3), 65. doi: 10.1007/s10544-018-0301-9

Giannopoulos, A. A., Mitsouras, D., Yoo, S. J., Liu, P. P., Chatzizisis, Y. S., and Rybicki, F. J. (2016). Applications of 3D printing in cardiovascular diseases. *Nat. Rev. Cardiol.* 13 (12), 701–718. doi: 10.1038/nrcardio.2016.170

Graham, A. D., Olof, S. N., Burke, M. J., Armstrong, J. P. K., Mikhailova, E. A., Nicholson, J. G., et al. (2017). High-resolution patterned cellular constructs by droplet-based 3D printing. *Sci. Rep.* 7 (1), 7004. doi: 10.1038/s41598-017-06358-x

Han, Y., Yang, S., Huang, W., Wang, Z., and Li, H. (2018). A hem-o-lok-induced tracheoesophageal fistula cured by temporary airway stenting modified with three-dimensional printing. *Ann. Thorac. Surg.* 106 (4), e219–e221. doi: 10.1016/j.athoracsur.2018.04.037

Heidari Keshel, S., Rostampour, M., Khosropour, G., Bandbon, B. A., Baradaran-Rafii, A., and Biazar, E. (2016). Derivation of epithelial-like cells from eyelid fat-derived stem cells in thermosensitive hydrogel. *J. Biomater. Sci. Polym. Ed.* 27 (4), 339–350. doi: 10.1080/09205063.2015.1130406

Hong, D., Chou, D. T., Velikokhatnyi, O. I., Roy, A., Lee, B., Swink, I., et al. (2016). Binder-jetting 3D printing and alloy development of new biodegradable Fe-Mn-Ca/Mg alloys. *Acta Biomater.* 45, 375–386. doi: 10.1016/j.actbio.2016.08.032

Hung, K. C., Tseng, C. S., Dai, L. G., and Hsu, S. H. (2016). Water-based polyurethane 3D printed scaffolds with controlled release function for customized cartilage tissue engineering. *Biomaterials* 83, 156–168. doi: 10.1016/j.biomaterials.2016.01.019

Ishutov, S., Hasiuk, F. J., Jobe, D., and Agar, S. (2018). Using resin-based 3D printing to build geometrically accurate proxies of porous sedimentary rocks. *Ground Water* 56 (3), 482–490. doi: 10.1111/gwat.12601

Jacobs, C. A., and Lin, A. Y. (2017). A new classification of three-dimensional printing technologies: systematic review of three-dimensional printing for patient-specific craniomaxillofacial surgery. *Plast. Reconstr. Surg.* 139 (5), 1211–1220. doi: 10.1097/PRS.0000000000003232

Jamroz, W., Szafraniec, J., Kurek, M., and Jachowicz, R. (2018). 3D Printing in pharmaceutical and medical applications - recent achievements and challenges. *Pharm. Res.* 35 (9), 176. doi: 10.1007/s11095-018-2454-x

Kim, B. S., Kwon, Y. W., Kong, J. S., Park, G. T., Gao, G., Han, W., et al. (2018). 3D cell printing of *in vitro* stabilized skin model and *in vivo* pre-vascularized skin patch using tissue-specific extracellular matrix bioink: a step towards advanced skin tissue engineering. *Biomaterials* 168, 38–53. doi: 10.1016/j.biomaterials.2018.03.040

Kim, D. H., Lee, J., Bae, J., Park, S., Choi, J., Lee, J. H., et al. (2018). Mechanical analysis of ceramic/polymer composite with mesh-type lightweight design using binder-Jet 3D printing. *Materials (Basel)* 11 (10), E1941. doi: 10.3390/ma11101941

Konta, A. A., Garcia-Pina, M., and Serrano, D. R. (2017). Personalised 3D printed medicines: which techniques and polymers are more successful? *Bioengineering. (Basel)* 4 (4), E79. doi: 10.3390/bioengineering4040079

Laronda, M. M., Rutz, A. L., Xiao, S., Whelan, K. A., Duncan, F. E., Roth, E. W., et al. (2017). A bioprosthetic ovary created using 3D printed microporous scaffolds restores ovarian function in sterilized mice. *Nat. Commun.* 8, 15261. doi: 10.1038/ncomms15261

Lau, I. W. W., Liu, D., Xu, L., Fan, Z., and Sun, Z. (2018). Clinical value of patient-specific three-dimensional printing of congenital heart disease: quantitative and qualitative assessments. *PLoS One* 13 (3), e0194333. doi: 10.1371/journal.pone.0194333

Lee, H. J., Son, M. J., Ahn, J., Oh, S. J., Lee, M., Kim, A., et al. (2017). Elasticity-based development of functionally enhanced multicellular 3D liver encapsulated in hybrid hydrogel. *Acta Biomater.* 64, 67–79. doi: 10.1016/j.actbio.2017.09.041

Legocki, A. T., Duffy-Peter, A., and Scott, A. R. (2017). Benefits and limitations of entry-level 3-dimensional printing of maxillofacial skeletal models. *JAMA Otolaryngol Head Neck Surg.* 143 (4), 389–394. doi: 10.1001/jamaoto.2016.3673

Li, J., Zhou, Y., Chen, W., Yuan, Z., You, B., Liu, Y., et al. (2018). A novel 3D in vitro tumor model based on silk fibroin/chitosan scaffolds to mimic the tumor microenvironment. *ACS Appl. Mater. Interfaces* 10 (43), 36641–36651. doi: 10.1021/acsami.8b10679

Liaw, C. Y., and Guvendiren, M. (2017). Current and emerging applications of 3D printing in medicine. *Biofabrication* 9 (2), 024102. doi: 10.1088/1758-5090/aa7279

Lind, J. U., Busbee, T. A., Valentine, A. D., Pasqualini, F. S., Yuan, H., Yadid, M., et al. (2017). Instrumented cardiac microphysiological devices *via* multimaterial three-dimensional printing. *Nat. Mater* 16 (3), 303–308. doi: 10.1038/nmat4782

Mahajan, A., Frisbie, C. D., and Francis, L. F. (2013). Optimization of aerosol jet printing for high-resolution, high-aspect ratio silver lines. *ACS Appl. Mater. Interfaces* 5 (11), 4856–4864. doi: 10.1021/am400606y

Mahmood, F., Owais, K., Taylor, C., Montealegre-Gallegos, M., Manning, W., Matyal, R., et al. (2015). Three-dimensional printing of mitral valve using echocardiographic data. *JACC Cardiovasc. Imaging* 8 (2), 227–229. doi: 10.1016/j.jcmg.2014.06.020

MarketsandMarkets (2019). 3D printing market by offering, process, application, vertical, technology, and geography - global forecast to 2024. Retrieved from https://www.marketsandmarkets.com/Market-Reports/3d-printing-market-1276.html.

Markstedt, K., Escalante, A., Toriz, G., and Gatenholm, P. (2017). Biomimetic inks based on cellulose nanofibrils and cross-linkable xylans for 3d printing. *ACS Appl. Mater. Interfaces* 9 (46), 40878–40886. doi: 10.1021/acsami.7b13400

Mitsouras, D., Liacouras, P., Imanzadeh, A., Giannopoulos, A. A., Cai, T., Kumamaru, K. K., et al. (2015). Medical 3D printing for the radiologist. *Radiographics* 35 (7), 1965–1988. doi: 10.1148/rg.2015140320

Mondschein, R. J., Kanitkar, A., Williams, C. B., Verbridge, S. S., and Long, T. E. (2017). Polymer structure-property requirements for stereolithographic 3D printing of soft tissue engineering scaffolds. *Biomaterials* 140, 170–188. doi: 10.1016/j.biomaterials.2017.06.005

Mukherjee, P., Cheng, K., Flanagan, S., and Greenberg, S. (2017). Utility of 3D printed temporal bones in pre-surgical planning for complex BoneBridge cases. *Eur. Arch. Otorhinolaryngol.* 274 (8), 3021–3028. doi: 10.1007/s00405-017-4618-4

Murphy, S. V., and Atala, A. (2014). 3D bioprinting of tissues and organs. *Nat. Biotechnol.* 32 (8), 773–785. doi: 10.1038/nbt.2958

Nie, W., Gu, F., Wang, Z., Wu, R., Yue, Y., and Shao, A. (2019). Preliminary application of three-dimension printing technology in surgical management of bicondylar tibial plateau fractures. *Injury* 50 (2), 476–483. doi: 10.1016/j.injury.2018.12.019

Ning, L., and Chen, X. (2017). A brief review of extrusion-based tissue scaffold bio-printing. *Biotechnol. J.* 12 (8), 1600671. doi: 10.1002/biot.201600671

Norman, J., Madurawe, R. D., Moore, C. M., Khan, M. A., and Khairuzzaman, A. (2017). A new chapter in pharmaceutical manufacturing: 3D-printed drug products. *Adv. Drug Delivery Rev.* 108, 39–50. doi: 10.1016/j.addr.2016.03.001

Olivieri, L. J., Krieger, A., Loke, Y. H., Nath, D. S., Kim, P. C., and Sable, C. A. (2015). Three-dimensional printing of intracardiac defects from three-dimensional echocardiographic images: feasibility and relative accuracy. *J. Am. Soc. Echocardiogr.* 28 (4), 392–397. doi: 10.1016/j.echo.2014.12.016

Orsi, G., De Maria, C., Montemurro, F., Chauhan, V. M., Aylott, J. W., and Vozzi, G. (2015). Combining inkjet printing and sol-gel chemistry for making pH-sensitive surfaces. *Curr. Top. Med. Chem.* 15 (3), 271–278. doi: 10.2174/1568026614666141229114738

Osman, R. B., Alharbi, N., and Wismeijer, D. (2017). Build angle: does it influence the accuracy of 3d-printed dental restorations using digital light-processing technology? *Int. J. Prosthodont.* 30 (2), 182–188. doi: 10.11607/ijp.5117

Ozbolat, I. T., and Hospodiuk, M. (2016). Current advances and future perspectives in extrusion-based bioprinting. *Biomaterials* 76, 321–343. doi: 10.1016/j.biomaterials.2015.10.076

Paxton, N., Smolan, W., Bock, T., Melchels, F., Groll, J., and Jungst, T. (2017). Proposal to assess printability of bioinks for extrusion-based bioprinting and evaluation of rheological properties governing bioprintability. *Biofabrication* 9 (4), 044107. doi: 10.1088/1758-5090/aa8dd8

Petta, D., Armiento, A. R., Grijpma, D., Alini, M., Eglin, D., and D'Este, M. (2018). 3D bioprinting of a hyaluronan bioink through enzymatic-and visible light-crosslinking. *Biofabrication* 10 (4), 044104. doi: 10.1088/1758-5090/aadf58

Placone, J. K., and Engler, A. J. (2018). Recent advances in extrusion-based 3D printing for biomedical applications. *Adv. Healthc Mater* 7 (8), e1701161. doi: 10.1002/adhm.201701161

Rahman, Z., Barakh Ali, S. F., Ozkan, T., Charoo, N. A., Reddy, I. K., and Khan, M. A. (2018). Additive manufacturing with 3D printing: progress from bench to bedside. *AAPS J.* 20 (6), 101. doi: 10.1208/s12248-018-0225-6

Rashidi, H., Luu, N. T., Alwahsh, S. M., Ginai, M., Alhaque, S., Dong, H., et al. (2018). 3D human liver tissue from pluripotent stem cells displays stable phenotype *in vitro* and supports compromised liver function *in vivo*. *Arch. Toxicol.* 92 (10), 3117–3129. doi: 10.1007/s00204-018-2280-2

Revilla-Leon, M., and Ozcan, M. (2019). Additive manufacturing technologies used for processing polymers: current status and potential application in prosthetic dentistry. *J. Prosthodont.* 28 (2), 146–158. doi: 10.1111/jopr.12801

Serex, L., Bertsch, A., and Renaud, P. (2018). Microfluidics: a new layer of control for extrusion-based 3d printing. *Micromachines (Basel)* 9 (2), E86. doi: 10.3390/mi9020086

Smith, M. L., and Jones, J. F. X. (2018). Dual-extrusion 3D printing of anatomical models for education. *Anat. Sci. Educ.* 11 (1), 65–72. doi: 10.1002/ase.1730

Son, K. H., Kim, K. W., Ahn, C. B., Choi, C. H., Park, K. Y., Park, C. H., et al. (2015). Surgical Planning by 3D Printing for Primary Cardiac Schwannoma Resection. *Yonsei Med. J.* 56 (6), 1735–1737. doi: 10.3349/ymj.2015.56.6.1735

Stefaniak, A. B., Bowers, L. N., Knepp, A. K., Luxton, T. P., Peloquin, D. M., Baumann, E. J., et al. (2019). Particle and vapor emissions from vat polymerization desktop-scale 3-dimensional printers. *J. Occup. Environ. Hyg.* 16 (8), 519–531. doi: 10.1080/15459624.2019.1612068

Su, W., Xiao, Y., He, S., Huang, P., and Deng, X. (2018). Three-dimensional printing models in congenital heart disease education for medical students: a controlled comparative study. *BMC Med. Educ.* 18 (1), 178. doi: 10.1186/s12909-018-1293-0

Tahayeri, A., Morgan, M., Fugolin, A. P., Bompolaki, D., Athirasala, A., Pfeifer, C. S., et al. (2018). 3D printed versus conventionally cured provisional crown and bridge dental materials. *Dent. Mater.* 34 (2), 192–200. doi: 10.1016/j.dental.2017.10.003

Taylor, S. L., Ibeh, A. J., Jakus, A. E., Shah, R. N., and Dunand, D. C. (2018). NiTi-Nb micro-trusses fabricated *via* extrusion-based 3D-printing of powders and transient-liquid-phase sintering. *Acta Biomater.* 76, 359–370. doi: 10.1016/j.actbio.2018.06.015

Trenfield, S. J., Awad, A., Goyanes, A., Gaisford, S., and Basit, A. W. (2018). 3D Printing pharmaceuticals: drug development to frontline care. *Trends Pharmacol. Sci.* 39 (5), 440–451. doi: 10.1016/j.tips.2018.02.006

VanKoevering, K. K., Morrison, R. J., Prabhu, S. P., Torres, M. F., Mychaliska, G. B., Treadwell, M. C., et al. (2015). Antenatal three-dimensional printing of aberrant facial anatomy. *Pediatrics* 136 (5), e1382–e1385. doi: 10.1542/peds.2015-1062

Vukicevic, M., Mosadegh, B., Min, J. K., and Little, S. H. (2017). Cardiac 3D Printing and its Future Directions. *JACC Cardiovasc. Imaging* 10 (2), 171–184. doi: 10.1016/j.jcmg.2016.12.001

Wang, X., Gao, P., Yang, Y., Guo, H., and Wu, D. (2018a). Dynamic and programmable morphology and size evolution *via a* living hierarchical self-assembly strategy. *Nat. Commun.* 9 (1), 2772. doi: 10.1038/s41467-018-05142-3

Wang, X., Yang, Y., Fan, L., Yang, F., and Wu, D. (2018b). POSS-embedded supramolecular hyperbranched polymers constructed from a 1→7 branching monomer with controllable morphology transitions. *China Chem.* 61, 3, 311–318. doi: 10.1007/s11426-017-9168-3

Wang, S. J., Jiang, D., Zhang, Z. Z., Chen, Y. R., Yang, Z. D., Zhang, J. Y., et al. (2019). Biomimetic nanosilica-collagen scaffolds for in situ bone regeneration: toward a cell-free, one-step surgery. *Adv. Mater.* 31 (49), e1904341. doi: 10.1002/adma.201904341

Wei, R., Guo, W., Ji, T., Zhang, Y., and Liang, H. (2017). One-step reconstruction with a 3D-printed, custom-made prosthesis after total en bloc sacrectomy: a technical note. *Eur. Spine J.* 26 (7), 1902–1909. doi: 10.1007/s00586-016-4871-z

Weinhart, M., Hocke, A., Hippenstiel, S., Kurreck, J., and Hedtrich, S. (2019). 3D organ models-Revolution in pharmacological research? *Pharmacol. Res.* 139, 446–451. doi: 10.1016/j.phrs.2018.11.002

Wills, J. W., Hondow, N., Thomas, A. D., Chapman, K. E., Fish, D., Maffeis, T. G., et al. (2016). Genetic toxicity assessment of engineered nanoparticles using a 3D *in vitro* skin model (EpiDerm). *Part Fibre Toxicol.* 13 (1), 50. doi: 10.1186/s12989-016-0161-5

Wollhofen, R., Axmann, M., Freudenthaler, P., Gabriel, C., Rohrl, C., Stangl, H., et al. (2018). Multiphoton-Polymerized 3D Protein Assay. *ACS Appl. Mater. Interfaces* 10 (2), 1474–1479. doi: 10.1021/acsami.7b13183

Wong, J. Y. (2016). 3D printing applications for space missions. *Aerosp Med. Hum. Perform.* 87 (6), 580–582. doi: 10.3357/AMHP.4633.2016

Wysocki, B., Idaszek, J., Zdunek, J., Rozniatowski, K., Pisarek, M., Yamamoto, A., et al. (2018). The influence of selective laser melting (SLM) process parameters on in-vitro cell response. *Int. J. Mol. Sci.*, 19 (6), E1619. doi: 10.3390/ijms19061619

Xu, N., Wei, F., Liu, X., Jiang, L., Cai, H., Li, Z., et al. (2016). Reconstruction of the upper cervical spine using a personalized 3d-printed vertebral body in an adolescent with ewing sarcoma. *Spine (Phila Pa 1976)* 41 (1), E50–E54. doi: 10.1097/BRS.0000000000001179

Yang, Y., Wang, X., Yang, F., Wang, L., and Wu, D. (2018). Highly elastic and ultratough hybrid ionic-covalent hydrogels with tunable structures and mechanics. *Adv. Mater.* 30 (18), e1707071. doi: 10.1002/adma.201707071

Yuan, B., Zhou, S. Y., and Chen, X. S. (2017). Rapid prototyping technology and its application in bone tissue engineering. *J. Zhejiang Univ. Sci. B* 18 (4), 303–315. doi: 10.1631/jzus.B1600118

Zanchetta, E., Cattaldo, M., Franchin, G., Schwentenwein, M., Homa, J., Brusatin, G., et al. (2016). Stereolithography of SiOC ceramic microcomponents. *Adv. Mater.* 28 (2), 370–376. doi: 10.1002/adma.201503470

Zhao, Y., Yao, R., Ouyang, L., Ding, H., Zhang, T., Zhang, K., et al. (2014). Three-dimensional printing of Hela cells for cervical tumor model *in vitro*. *Biofabrication* 6 (3), 035001. doi: 10.1088/1758-5082/6/3/035001

Zhu, C., Xia, Y., Zai, Y., Dai, Y., Liu, X., Bian, J., et al. (2019). Adsorption and desorption behaviors of HPEI and thermoresponsive HPEI based gels on anionic and cationic dyes. *Chem. Eng. J.* 369, 863–873. doi: 10.1016/j.cej.2019.03.169

Zopf, D. A., Flanagan, C. L., Wheeler, M., Hollister, S. J., and Green, G. E. (2014). Treatment of severe porcine tracheomalacia with a 3-dimensionally printed, bioresorbable, external airway splint. *JAMA Otolaryngol. Head Neck Surg.* 140 (1), 66–71. doi: 10.1001/jamaoto.2013.5644

Conflict of Interest: The authors declare that the research was conducted in the absence of any commercial or financial relationships that could be construed as a potential conflict of interest.

The handling editor and reviewer JD declared their involvement as co-editors in the Research Topic, and confirm the absence of any other collaboration.

frontiers in Pharmacology

REVIEW
published: 03 April 2020
doi: 10.3389/fphar.2020.00404

The Use of Peripheral Blood-Derived Stem Cells for Cartilage Repair and Regeneration *In Vivo*: A Review

You-Rong Chen[1†], Xin Yan[1†], Fu-Zhen Yuan[1†], Jing Ye[1], Bing-Bing Xu[1], Zhu-Xing Zhou[1], Zi-Mu Mao[1], Jian Guan[1], Yi-Fan Song[1], Ze-Wen Sun[1,2], Xin-Jie Wang[1], Ze-Yi Chen[1], Ding-Yu Wang[1], Bao-Shi Fan[1,2], Meng Yang[1,2], Shi-Tang Song[1], Dong Jiang[1] and Jia-Kuo Yu[1]**

[1] Knee Surgery Department of the Institute of Sports Medicine, Peking University Third Hospital, Beijing, China, [2] School of Clinical Medicine, Weifang Medical University, Weifang, China

OPEN ACCESS

Edited by:
Jianxun Ding,
Chinese Academy of Sciences, China

Reviewed by:
Jiashu Sun,
National Center for Nanoscience and Technology (CAS), China
Yan Huang,
Nantong University, China
Jan H. Spaas,
ANACURA Group, Belgium

***Correspondence:**
Jia-Kuo Yu
yujiakuo@126.com
Dong Jiang
bysyjiangdong@126.com

[†]These authors have contributed equally to this work

Specialty section:
This article was submitted to Translational Pharmacology, a section of the journal Frontiers in Pharmacology

Received: 05 January 2020
Accepted: 17 March 2020
Published: 03 April 2020

Citation:
Chen Y-R, Yan X, Yuan F-Z, Ye J, Xu B-B, Zhou Z-X, Mao Z-M, Guan J, Song Y-F, Sun Z-W, Wang X-J, Chen Z-Y, Wang D-Y, Fan B-S, Yang M, Song S-T, Jiang D and Yu J-K (2020) The Use of Peripheral Blood-Derived Stem Cells for Cartilage Repair and Regeneration In Vivo: A Review. Front. Pharmacol. 11:404. doi: 10.3389/fphar.2020.00404

Background: Peripheral blood (PB) is a potential source of chondrogenic progenitor cells that can be used for cartilage repair and regeneration. However, the cell types, isolation and implantation methods, seeding dosage, ultimate therapeutic effect, and *in vivo* safety remain unclear.

Methods: PubMed, Embase, and the Web of Science databases were systematically searched for relevant reports published from January 1990 to December 2019. Original articles that used PB as a source of stem cells to repair cartilage *in vivo* were selected for analysis.

Results: A total of 18 studies were included. Eight human studies used autologous nonculture-expanded PB-derived stem cells (PBSCs) as seed cells with the blood cell separation isolation method, and 10 animal studies used autologous, allogenic or xenogeneic culture-expanded PB-derived mesenchymal stem cells (PB-MSCs), or nonculture-expanded PBSCs as seed cells. Four human and three animal studies surgically implanted cells, while the remaining studies implanted cells by single or repeated intra-articular injections. 121 of 130 patients (in 8 human clinical studies), and 230 of 278 animals (in 6 veterinary clinical studies) using PBSCs for cartilage repair achieved significant clinical improvement. All reviewed articles indicated that using PB as a source of seed cells enhances cartilage repair *in vivo* without serious adverse events.

Conclusion: Autologous nonculture-expanded PBSCs are currently the most commonly used cells among all stem cell types derived from PB. Allogeneic, autologous, and xenogeneic PB-MSCs are more widely used in animal studies and are potential seed cell types for future applications. Improving the mobilization and purification technology, and shortening the culture cycle of culture-expanded PB-MSCs will obviously promote the researchers' interest. The use of PBSCs for cartilage repair and regeneration *in vivo* are safe. PBSCs considerably warrant further investigations due to their superiority and safety in clinical settings and positive effects despite limited evidence in humans.

Keywords: peripheral blood, stem cell, cartilage, *in vivo*, review

INTRODUCTION

Articular cartilage covering the surface of joints plays a very important role in bearing loads, absorbing mechanical shocks, and enabling synovial joints to articulate with low friction (Chen et al., 2017). Acute trauma, repetitive joint use, and degenerative joint disease may lead to cartilage and osteochondral injuries (Saw et al., 2011; Fu et al., 2014a). Articular cartilage has a very limited regenerative and self-healing potential due to its avascular, aneural, and alymphatic characteristics and a low number of progenitor cells (Redondo et al., 2018). Many attempts have been made to identify the ideal treatment for cartilage lesions, including bone marrow stimulation (BMS) techniques (Jin et al., 2011), osteochondral autografts and allografts (Makris et al., 2015), and cell-based cartilage repair procedures, including autologous chondrocyte implantation (ACI) (Riboh et al., 2017), mesenchymal stem cell (MSC)-based therapy (Fu et al., 2014a; Li et al., 2016) and tissue-engineered cartilaginous grafts (Zhao et al., 2018; Ding et al., 2019; Wang et al., 2019; Zhang et al., 2019). Since BMS techniques, osteochondral transplantation, and ACI have limitations and shortcomings, such as fibrocartilage regeneration, donor site complications, graft failure, dedifferentiation of seed cells, and two-stage invasive surgical procedures (Fortier et al., 2010; Andriolo et al., 2017; Riboh et al., 2017), MSCs, which are multipotent progenitor cells with an intrinsic potential for multilineage differentiation, self-renewal, low immunogenicity, anti-inflammatory activity, and immunomodulatory effects by suppressing the graft-versus-host reaction, may be obtained from multiple tissues of individual patients, and these cells are easily cultured, amplified, and purified (Goldberg et al., 2017; Guadix et al., 2017). MSCs are widely used in cartilage repair and regeneration as seed cells without concerns regarding increasing the risk of cancer (Hernigou et al., 2013; Liu et al., 2018; Han et al., 2019). An increasing number of studies have suggested that peripheral blood (PB) is a potential alternative source of MSCs, which have shown similar chondrogenic differentiation potential with bone marrow-derived MSCs (BM-MSCs) in both *in vitro* and *in vivo* studies (Fu et al., 2014a; Wang et al., 2016a). PB-derived stem cells (PBSCs) can be obtained by a minimally invasive procedure with fewer complications than bone marrow (BM) harvesting, which has been reportedly associated with haemorrhage, chronic pain, neurovascular injury, and even death (Bain, 2003). Moreover, PBSCs also have the ability to be used in autologous transplantation, which greatly benefits patients in clinical applications and facilitates the development of a one-stage surgical solution and other cell-based therapies (Spaas et al., 2012; Hopper et al., 2015a; Saw et al., 2015).

Although increasing evidence has shown that PBSCs are a potential alternative source of chondrogenic progenitor cells for cartilage repair, reviews describing the application of PBSCs for cartilage repair and regeneration *in vivo* are lacked. The purpose of this review was to evaluate the treatment efficacy and safety of using PBSCs for cartilage regeneration *in vivo* and attempt to clarify treatment details about cell types, isolation methods, optimal dosages, and implantation methods.

Abbreviations: PBSCs, Peripheral blood-derived stem cells; PB-MSCs, Peripheral blood-derived mesenchymal stem cells; DGC, Density gradient centrifugation; PA, Plastic adherence; BMS, Bone marrow stimulation; ACI, Autologous chondrocyte implantation; BM-MSCs, Bone marrow-derived mesenchymal stem cells; PRISMA, Preferred Reporting Items for Systematic Reviews and Meta-analyses; RCT, Randomized controlled trial; HTO, High tibial osteotomy; DBM, Decalcified bone matrix; ICRS, International Cartilage Repair Society; OA, Osteoarthritis; IA, Intra-articular; hG-CSF, Human granulocyte colony stimulating factor; HA, Hyaluronic acid; CPM, Continuous passive motion; PRP, Platelet-rich plasma; MHC, Major histocompatibility complex; COMP, Cartilage oligomeric matrix protein; GAG, Glycosaminoglycan; MRI, Magnetic Resonance Imaging; CT, Computed Tomography; KOOS, Knee injury and osteoarthritis outcome score; VAS, Visual Analogue Scale; WOMAC, The Western Ontario and McMaster Universities Osteoarthritis Index; IKDC, The International Knee Documentation Committee Knee Uation Form; ECM, extracellular matrix; GFP, green fluorescent protein; CFDA-SE, carboxyfluorescein diacetate succinimidyl ester; RalA, v-ral simian leukemia viral oncogene homolog A; SOX9, sex determining region Y-box 9; ACAN, aggrecan; CFUF, colony-forming unit fibroblast.

METHOD

This review was conducted in accordance with Preferred Reporting Items for Systematic Reviews and Meta-Analyses (PRISMA) guidelines and a PRISMA checklist using PubMed, EMBASE, and Web of Science to search for relevant studies published from 1 January 1990 to 31 December 2019 (Charlesworth et al., 2019). The search terms used in the selection were "(peripheral OR blood OR circulating OR circulation) AND (mesenchymal OR stem cell OR stromal cell OR progenitor cell OR mononuclear cell OR primitive cell) AND (cartilage OR chondrogenesis OR chondral OR osteochondral OR osteoarthritis) AND (vivo OR human OR patient OR animal OR mouse OR rat OR rabbit OR dog OR sheep OR pig OR horse OR ovine)".

YRC, XY, and FZY independently screened study titles and abstracts from the beginning. Only original research studies published in full English that used PB as the source of chondrogenic progenitor cells for cartilage repair were included in the analysis. Both print journals and e-published journals were eligible for inclusion and screening. However, all non-English language studies, review articles, letters, editorials, conference, patents, and meeting abstracts and studies not involving cartilage regeneration were excluded. Duplicates were excluded. In addition, studies of primary cells that were not derived from the PB and studies that were not related to *in vivo* animal or human experiments or only used non-PB sources were excluded. Disagreements between the authors were resolved by discussion and consensus.

To avoid the omission of relevant studies, we investigated all reference lists of the eligible studies for studies that were likely not identified by the initial retrieval criteria. Unpublished studies were not included in this review. A flowchart of the literature search is shown in **Figure 1**. We reviewed human studies first, and then reviewed the animal studies according to the order of the publication date. Preoperative characteristics of patients and animals, treatment details, and the treatment efficacy and safety of PBSCs were assessed.

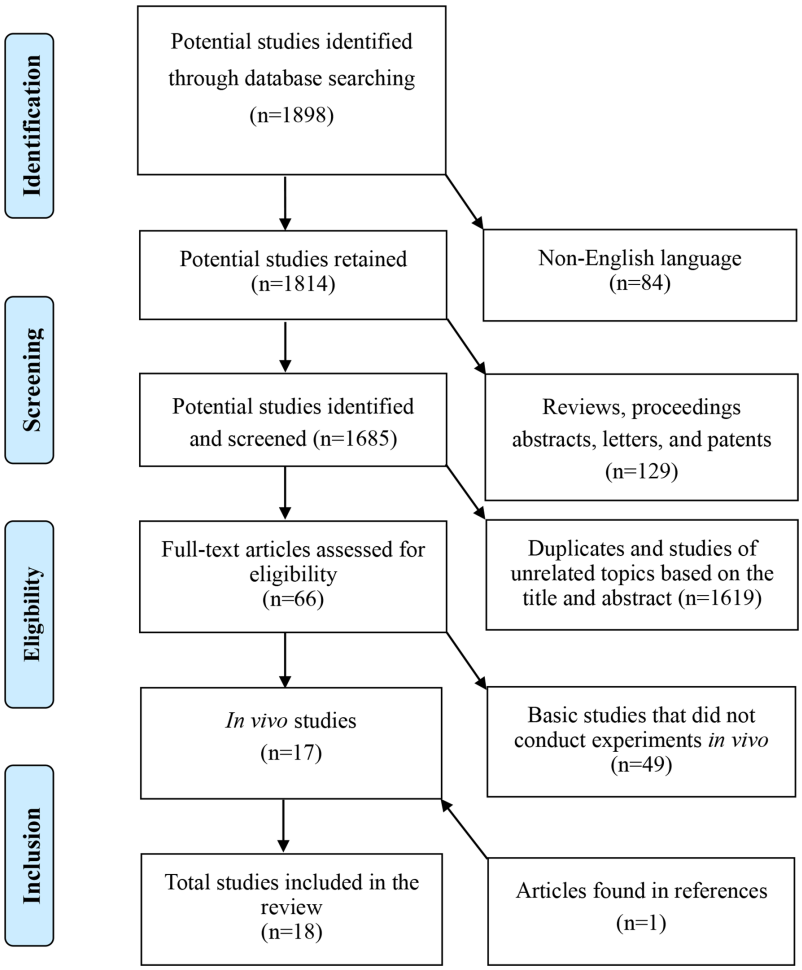

FIGURE 1 | A flowchart of the literature search.

RESULTS

Description of the Included Studies

Overall, 1,898 publications were retrieved from the initial search. A total of 1,685 potential studies were retained for further identification after 84 non-English language studies and 129 review articles, letters, editorials, conference, and meeting abstracts were excluded. Furthermore, 1,619 duplicates and studies of unrelated topics based on the title and abstract, and 49 basic studies that did not conduct experiments *in vivo* were excluded. We identified 17 *in vivo* studies consisting of 7 human trials and 10 animal studies published between 1990 and 2019 using this retrieval strategy. All reference lists of the 17 included studies were investigated, and an additional human trial (Jancewicz et al., 2004) was identified and included in this review. Finally, data from the 18 studies [8 human studies (Jancewicz et al., 2004; Saw et al., 2011; Skowroński et al., 2012; Saw et al., 2013; Skowroński and Rutka, 2013; Turajane et al., 2013; Fu et al., 2014a; Saw et al., 2015) and 10 animal studies (Spaas et al., 2012; Broeckx et al., 2014a; Broeckx et al., 2014b; Fu et al., 2014a; Deng et al., 2015; Hopper et al., 2015b; Zhao et al., 2018; Daems et al., 2019; Broeckx et al., 2019a; Broeckx et al., 2019b) published by investigators from seven countries or regions] were analyzed.

Among the 18 studies, 7 were case reports [6 in humans (Jancewicz et al., 2004; Saw et al., 2011; Skowroński et al., 2012; Turajane et al., 2013; Fu et al., 2014a; Saw et al., 2015) and 1 in horses (Spaas et al., 2012)], 1 was a human comparative study (Skowroński and Rutka, 2013), 1 was a human randomized controlled trial (RCT) (Saw et al., 2013), 1 was a preliminary study (in horses) (Broeckx et al., 2014a), 1 was a pilot study (in horses) (Broeckx et al., 2014b), 4 involved animal models [rabbits (Fu et al., 2014b), sheep (Hopper et al., 2015b), rats (Deng et al., 2015), and pigs (Zhao et al., 2018), 1 was a prospective placebo-controlled study (in dog) (Daems et al., 2019), and 2 were randomized, double-blinded, placebo-controlled proof-of-concept study (in horses) (Broeckx et al., 2019a; Broeckx et al., 2019b) (**Table 1**).

TABLE 1 | Preoperative characteristics of patients and animals.

	Study ID	Species (no. of subjects)	Study design	The age/ weight of patients or animals	Clinical or imaging examination	Types of defects or diseases	Location of lesions	The defect size/ICRS grade
Human studies	(Jancewicz et al., 2004)	Human (9)	Case report	N/A	N/A	Osteochondral defects	Talus	0.5×0.7 cm with 0.5-1.0 cm depth ICRS IV
	(Skowroński et al., 2012)	Human (52)	Case report	16-55 years old	N/A	Cartilage lesions	Patella (22), medial femoral condyle (38), lateral femoral condyle (6)	4 to 12 cm^2 (mean 6.2 cm^2), ICRS grade III and IV
	(Skowroński and Rutka, 2013)	Human (46)	Comparative study	7-52 years old (average age: 26 years)	N/A	Osteochondral lesions	Medial femoral condyle	>4 cm^2, > 6 mm deep, ICRS grade IV
	(Turajane et al., 2013)	Human (5)	Case report	52-59 years old (median age: 56 years)	Varus deformity (1.20 ± 0.84°); Kellegan Lawrence stages 1-3	Early-stage OA	Medial condyle (4), patellofemoral (1)	ICRS grade III and IV
	(Saw et al., 2011)	Human (5)	Case report	19-52 years old	N/A	Chondral defects	Knee	ICRS grade III and IV
	(Saw et al., 2013)	Human (50)	RCT	22-50 years old	N/A	Chondral defects	Knee	ICRS grade III and IV
	(Saw et al., 2015)	Human (8)	Case report	50-56 years old	Varus deformity	End-stage OA (bone-on-bone lesions)	Medial compartment of the knee joint	ICRS grade IV
	(Fu et al., 2014a)	Human (1)	Case report	19 years old	N/A	Full-thickness cartilage defects	Lateral femoral trochlea	4 cm^2 ICRS grade IV
Animal studies	(Spaas et al., 2012)	Horse (1)	Case report	5 years old	Severe unilateral forelimb lameness; new periarticular bone formation	Degenerative joint disease	Pastern joint	N/A
	(Broeckx et al., 2014a)	Horse (50)	Preliminary study	N/A	Mild to moderate clinical lameness; positive flexion test	Degenerative joint disease	Fetlock joint	N/A
	(Broeckx et al., 2014b)	Horse (165)	Pilot study	N/A	Clinical lameness; locomotory disorder; positive flexion test	Degenerative joint disease	Stifle joint (30), fetlock joint (58), coffin joint (43), pastern joint (34)	N/A
	(Fu et al., 2014b)	New Zealand white rabbit (30)	Animal models	4 months old	N/A	Full-thickness osteochondral defects	Trochlear groove of the distal femur	5 mm in diameter and 1-2 mm in depth
	(Hopper et al., 2015b)	Mountain sheep (24)	Animal models	3-5 years old	N/A	Full-thickness osteochondral defects	Medial femoral condyle (MFC)	6.0 mm in diameter and 8 mm in depth
	(Deng et al., 2015)	SD rat (28)	Animal models	12 weeks old	N/A	Papain-induced OA model	Knee joints	N/A
	(Zhao et al., 2018)	Diannan small-ear pig (12)	Animal models	N/A (average weight: 15 kg)	N/A	Chondral defects	Medial and lateral femoral condyles (MFC and LFC)	7 mm in diameter and 4 mm in depth

(Continued)

TABLE 1 | Continued

Study ID	Species (no. of subjects)	Study design	The age/ weight of patients or animals	Clinical or imaging examination	Types of defects or diseases	Location of lesions	The defect size/ICRS grade
(Broeckx et al., 2019a)	Horse (12)	A randomized, double-blind, placebo-controlled proof-of-concept study	Median age: 8.5 years old	Mild cartilage changes and normal synovium (arthroscopic examination)	Surgically induced osteoarthritis	The right fetlock joint	Mild cartilage changes (superficial wear line, partial erosion, minor irregularity or thinner cartilage spots)
(Broeckx et al., 2019b)	Horse (75)	A randomized, multicenter, double-blinded, and placebo-controlled study	3-23 years old	Grade 2 or 3 lameness on the AAEP scale; mild-to-moderate response to flexion test; mild-to-moderate joint swelling	Degenerative joint disease	Fetlock joint	Early staged fetlock degenerative joint disease lasting for at least 2 months
(Daems et al., 2019)	Dog (6)	A prospective placebo-controlled study	5-10 years old	Stable pain and lameness lasting for over 1 month	OA	Humeroradial joint	Mild to severe OA

N/A, not available; ICRS, International Cartilage Repair Society; RCT, randomized controlled trial; OA, osteoarthritis; AAEP, American Association of Equine Practitioners.

Preoperative Characteristics of the Patients and Animals

The age of the patients ranged from 7 to 59 years in the 8 human studies (Jancewicz et al., 2004; Saw et al., 2011; Skowroński et al., 2012; Saw et al., 2013; Skowroński and Rutka, 2013; Turajane et al., 2013; Fu et al., 2014a; Saw et al., 2015). Lesions were mainly located in the tibial plateaus (Saw et al., 2011; Saw et al., 2013), patella (Saw et al., 2011; Skowroński et al., 2012; Saw et al., 2013), femoral condyles (Saw et al., 2011; Skowroński et al., 2012; Saw et al., 2013; Skowroński and Rutka, 2013; Turajane et al., 2013; Saw et al., 2015), femoral trochlea (Saw et al., 2011; Saw et al., 2013; Turajane et al., 2013; Fu et al., 2014a), intercondylar notch (Saw et al., 2011), and talus of the ankle joint (Jancewicz et al., 2004). The types of lesions included cartilage defects (Saw et al., 2011; Skowroński et al., 2012; Saw et al., 2013; Fu et al., 2014a), osteochondral defects (Jancewicz et al., 2004; Skowroński and Rutka, 2013), and early- and late-stage osteoarthritis (Turajane et al., 2013; Saw et al., 2015). The International Cartilage Repair Society (ICRS) scores were all grade III–IV (Jancewicz et al., 2004; Saw et al., 2011; Skowroński et al., 2012; Saw et al., 2013; Skowroński and Rutka, 2013; Turajane et al., 2013; Fu et al., 2014a; Saw et al., 2015).

Types of lesions included spontaneous and induced osteoarthritis (Spaas et al., 2012; Broeckx et al., 2014a; Broeckx et al., 2014b; Deng et al., 2015; Daems et al., 2019; Broeckx et al., 2019a; Broeckx et al., 2019b), cartilage defects (Zhao et al., 2018), and osteochondral defects (Fu et al., 2014b; Hopper et al., 2015b) in the 10 animal studies. The lesions were in the knee joint (Broeckx et al., 2014a; Fu et al., 2014b; Deng et al., 2015; Hopper et al., 2015b; Zhao et al., 2018), fetlock joint (Broeckx et al., 2014a; Broeckx et al., 2014b; Broeckx et al., 2019a; Broeckx et al., 2019b), pastern joint (Broeckx et al., 2014a), coffin joint (Broeckx et al., 2014b), and humeroradial joint (Daems et al., 2019). The preoperative characteristics of the patients and animals, such as the age, clinical and imaging examination, types of defects and diseases, location of lesions, and defect size/ICRS grade are shown in **Table 1**.

Stem Cell Types and Isolation Methods

Eight human studies (Jancewicz et al., 2004; Saw et al., 2011; Skowroński et al., 2012; Saw et al., 2013; Skowroński and Rutka, 2013; Turajane et al., 2013; Fu et al., 2014a; Saw et al., 2015) and 1 animal (Hopper et al., 2015b) study used autologous nonculture-expanded condensed PBSCs, 1 animal study (Deng et al., 2015) used allogenic condensed PBSCs, 1 animal study (Spaas et al., 2012) used autologous culture-expanded PB-MSCs, 6 animal studies (Broeckx et al., 2014a; Broeckx et al., 2014b; Fu et al., 2014b; Zhao et al., 2018; Broeckx et al., 2019a; Broeckx et al., 2019b) used allogenic culture-expanded PB-MSCs, and 1 animal study (Daems et al., 2019) used xenogeneic culture-expanded PB-MSCs as seed cells for cartilage repair and regeneration.

All 8 human studies (Jancewicz et al., 2004; Saw et al., 2011; Skowroński et al., 2012; Saw et al., 2013; Skowroński and Rutka, 2013; Turajane et al., 2013; Fu et al., 2014a; Saw et al., 2015) with 130 patients used a blood cell separator to collect PBSCs. One animal study (Deng et al., 2015) with 28 Sprague-Dawley (SD)

rats used the density gradient centrifugation (DGC) method to isolate PBSCs. Eight animal studies (Spaas et al., 2012; Broeckx et al., 2014a; Broeckx et al., 2014b; Hopper et al., 2015b; Zhao et al., 2018; Daems et al., 2019; Broeckx et al., 2019a; Broeckx et al., 2019b) with 272 horses, 24 mountain sheep, 12 Diannan small-ear pigs, and 6 dogs used the DGC and plastic adherence (PA) methods to isolate PB-MSCs and PBSCs. Furthermore, one animal study (Fu et al., 2014b) with 30 New Zealand White rabbits used the erythrocyte lysis and PA methods to isolate PB-MSCs.

Cell density, Dosage, and Implantation Methods

The seeding dosage in 5 human studies (Saw et al., 2011; Saw et al., 2013; Skowroński and Rutka, 2013; Fu et al., 2014a; Saw et al., 2015) and 1 animal study (Deng et al., 2015) using nonculture-expanded PBSCs as seed cells ranged from 5.0×10^6 to 3.5×10^7 cells/ml (or cells/injection), and the seeding dosage in 2 human studies (Skowroński et al., 2012; Turajane et al., 2013) and 1 animal study (Hopper et al., 2015b) was less than 5.0×10^6 cells/ml (or cells/injection). In 5 animal studies using PB-MSCs as seed cells, the seeding dosage in 3 studies ranged from 1×10^6 to 5.0×10^6 cells/ml (or cells/injection) (Spaas et al., 2012; Fu et al., 2014b; Daems et al., 2019; Broeckx et al., 2019a; Broeckx et al., 2019b). One human study (Jancewicz et al., 2004) and 3 animal studies(Broeckx et al., 2014a; Broeckx et al., 2014b; Zhao et al., 2018) did not mention the cell seeding dosage.

Four human studies (Jancewicz et al., 2004; Skowroński et al., 2012; Skowroński and Rutka, 2013; Fu et al., 2014a) and 3 animal studies (Fu et al., 2014b; Hopper et al., 2015b; Zhao et al., 2018) implanted cells by surgery, while the remaining 4 human studies (Saw et al., 2011; Saw et al., 2013; Turajane et al., 2013; Saw et al., 2015) and 7 animal studies (Spaas et al., 2012; Broeckx et al., 2014a; Broeckx et al., 2014b; Deng et al., 2015; Daems et al., 2019; Broeckx et al., 2019a; Broeckx et al., 2019b) implanted cells by single or repeated intra-articular injections.

Other Therapies and Postoperative Rehabilitation

All human studies used a variety of other treatments, such as intra-articular debridement (Jancewicz et al., 2004; Saw et al., 2011; Skowroński et al., 2012; Saw et al., 2013; Skowroński and Rutka, 2013; Turajane et al., 2013; Fu et al., 2014a; Saw et al., 2015), the modified sandwich technique (Jancewicz et al., 2004; Skowroński and Rutka, 2013), BMS (Saw et al., 2011; Skowroński et al., 2012; Saw et al., 2013; Saw et al., 2015), high tibial osteotomy (HTO) (Saw et al., 2011; Saw et al., 2015), and patellofemoral realignment (Fu et al., 2014a), to promote cartilage repair and regeneration while implanting cells. Strict rehabilitation programmes and passive or active exercises (Saw et al., 2011; Saw et al., 2013; Skowroński and Rutka, 2013; Turajane et al., 2013; Fu et al., 2014a; Saw et al., 2015) were followed to avoid early weight bearing, joint stiffness, and adhesion.

The animal studies used other treatments, such as decalcified bone matrix (DBM) scaffolds (Fu et al., 2014a; Zhao et al., 2018), collagen-glycosaminoglycan (GAG) scaffolds (Hopper et al., 2015b), platelet-rich plasma (PRP) injections (Broeckx et al., 2014a; Broeckx et al., 2014b), and equine allogeneic plasma (EAP) (Broeckx et al., 2019a; Broeckx et al., 2019b), while implanting cells. Except for 2 studies (Broeckx et al., 2019a; Broeckx et al., 2019b), there were no strict rehabilitation plans in the other animal studies.

Table 2 summarizes the details of the application of PBSCs to cartilage repair and regeneration in humans and animals.

Efficacy and Safety of Treatment

We assessed the adverse events and the clinical, radiographic, and histologic results to determine the treatment efficacy and safety (**Table 3**).

The follow-up time of the 8 human trials ranged from 6 months to 7.5 years. The clinical evaluation results of 5 studies showed that Magee score (Jancewicz et al., 2004), KOOS scales (Skowroński et al., 2012; Skowroński and Rutka, 2013; Turajane et al., 2013), Lysholm scales (Skowroński et al., 2012; Skowroński and Rutka, 2013), WOMAC scales (Turajane et al., 2013), IKDC 2000 subjective score (Fu et al., 2014a) or Tegner score (Fu et al., 2014a) were improved, VAS scales (Skowroński et al., 2012; Skowroński and Rutka, 2013) were relieved, and Skowroski et al. (Skowroński et al., 2012; Skowroński and Rutka, 2013) reported 90 and 92% of patients with good results in 2012 and 2013, respectively. One study (Saw et al., 2013) reported that there was no IKDC score difference compared to the control group. One study (Saw et al., 2015) reported lower limb line recovery, and one study (Saw et al., 2011) did not report clinical evaluation results.

Five animal studies (Spaas et al., 2012; Broeckx et al., 2014a; Broeckx et al., 2014b; Broeckx et al., 2019a; Broeckx et al., 2019b) on horses reported improved visual gait, objective pressure plate analysis, short- and long-term clinical evolution scores, and relief of visual and objective lameness, flexion pain, and joint effusion.

Radiological examination, which is a non-invasive examination method, was widely used to evaluate the efficacy of cartilage repair and regeneration. Seven human studies used MRI (Jancewicz et al., 2004; Skowroński et al., 2012; Saw et al., 2013; Skowroński and Rutka, 2013; Fu et al., 2014a), X-ray (Saw et al., 2011; Saw et al., 2015) or CT (Fu et al., 2014a) to evaluate the repair effect and reported improved MRI morphologic scores, regenerative tissue with the same signal as normal cartilage, subchondral bone recovery, or reappearance of the medial compartment. However, radiological examination was rarely used in the animal studies. Three animal studies (Spaas et al., 2012; Daems et al., 2019; Broeckx et al., 2019a) reported no significant radiographic changes.

Four human studies (Saw et al., 2011; Saw et al., 2013; Fu et al., 2014a; Saw et al., 2015) evaluated cartilage repair with the method of second-look arthroscopy and suggested that cartilage regeneration was comparable to BM-MSCs with improved ICRS macroscopic scores, cartilage regeneration similar to normal cartilage tissue, or significantly fewer wear lines and synovial hyperaemia.

Histopathological examination is the gold standard for evaluation. Four human studies (Saw et al., 2011; Saw et al., 2013; Turajane et al., 2013; Saw et al., 2015) reported high-

TABLE 2 | Treatment Details of PBSCs for Cartilage Repair and Regeneration in Humans and Animals.

	Study ID	Cell types	Cell sources and blood volume (ml)	Isolation methods	Cellular constituent characterization	Cell dose	Cell stage (passage number)	Method of delivery	Surgical procedures	Rehabilitation
Human studies	(Jancewicz et al., 2004)	PBSCs	Autologous G-CSF-activated PB	Blood cell separation	$CD34^+$	N/A	Fresh condensed stem cells (P0)	Surgical implantation	Debridement +sandwich technique	N/A
	(Skowroński et al., 2012)	PBSCs	Autologous G-CSF-activated PB, 40-80 ml	Blood cell separation	N/A	8×10^5 - 3.2×10^6 cells/ml	Fresh condensed stem cells (P0)	Surgical implantation	Debridement + BMS + PBSC suspension with collagen membrane cover +treatment of co-existing pathologies	N/A
	(Skowroński and Rutka, 2013)	PBSCs	Autologous G-CSF-activated PB, 40 ml	Blood cell separation	N/A	1.25×10^6 - 5.2×10^6 cells/ml	Fresh condensed stem cells (P0)	Surgical implantation	Debridement +modified sandwich technique	Passive and active exercises, non-weight to full-weight bearing
	(Turajane et al., 2013)	PBSCs	Autologous hG-CSF-activated PB	Leukapheresis	$CD34^+$: 0.34% to 1.04%; $CD105^+$: 0.75% to 0.88%; chondrogenic differentiation	TNC: 2.67-5.99×10^3 cells/injection	Fresh or cryopreserved condensed stem cells (P0)	Repeated IA injections (3 times)	Debridement +BMS +repeated IA injections (PBSCs+ GFAP +hG-CSF +HA)	Non-weight bearing (ambulation with axillary crutch)
	(Saw et al., 2011)	PBSCs	Autologous G-CSF-mobilized PB	Apheresis	(i) Fresh PBSCs: $CD34^+$: 1.86%; $CD105^+$: 7.24%; (ii) Frozen PBSCs: $CD34^+$: 1.22%; $CD105^+$: 8.39%	2.0×10^7 cells/injection ($CD105^+$cells)	Fresh or cryopreserved condensed progenitor cells (P0)	Repeated IA injections (2 times)	Debridement +BMS +HTO(1)+repeated IA injections	CPM+ crutch-assisted partial to full weight bearing
	(Saw et al., 2013)	PBSCs	Autologous G-CSF-mobilized PB	Apheresis	(i) Fresh PBSCs: $CD34^+$: 1.86%; $CD105^+$: 7.24%; (ii) Frozen PBSCs: $CD34^+$: 1.22%; $CD105^+$: 8.39%	2.0×10^7 cells/injection ($CD105^+$cells)	Fresh or cryopreserved condensed stem cells (P0)	Repeated IA injections (8 times)	Debridement +BMS +repeated IA injections	CPM+ crutch-assisted partial to full weight bearing
	(Saw et al., 2015)	PBSCs	Autologous G-CSF-mobilized PB	Apheresis	(i) Fresh PBSCs: $CD34^+$: 1.86%; $CD105^+$: 7.24%; (ii) Frozen PBSCs: $CD34^+$: 1.22%; $CD105^+$: 8.39%	$1.0\text{-}2.0\times10^7$ cells/injection ($CD105^+$cells)	Cryopreserved condensed stem cells (P0)	Repeated IA injections (7 times)	Debridement +BMS +HTO+repeated IA injections	CPM, crutch-assisted partial to full weight bearing
	(Fu et al., 2014a)	PBSCs	Autologous rhG-CSF-mobilized PB	Blood cell separation	N/A	3.496×10^7 cells/ml	Fresh condensed stem cells (P0)	Surgical implantation	Debridement +PBSCs with autologous periosteum flap cover+ patellofemoral realignment	Strict rehabilitation programme
Animal studies	(Spaas et al., 2012)	PB-MSCs	Autologous PB, 10 ml	DGC and PA	$CD29^+$, $CD44^+$, $CD90^+$, $CD79\alpha^-$, MHC II^-, trilineage differentiation	2.5×10^6 cells/injection	Culture-expanded cells (P1, P3)	Repeated IA injections (2 times)	N/A	N/A
	(Broeckx et al., 2014a)	PB-MSCs (native or chondrogenic induction)	Allogeneic PB 50 ml	DGC and PA	(i) Native: $CD29^+$, $CD44^+$, $CD90^+$, $CD105^+$; $CD45^-$, $CD79a^-$, MHC II^- and a monocyte/macrophage marker; trilineage differentiation; $p63^-$, low in MHC I, $Ki67^+$, Col II^+, and $Vimentin^+$.	N/A	Culture-expanded cells (P4)	Single IA injection	PB-MSCs with or without PRP	N/A

(Continued)

TABLE 2 | Continued

Study ID	Cell types	Cell sources and blood volume (ml)	Isolation methods	Cellular constituent characterization	Cell dose	Cell stage (passage number)	Method of delivery	Surgical procedures	Rehabilitation
				(ii) Chondrogenic induction: aggrecan$^+$, Col II$^+$, COMP$^+$, p63$^+$ and GAG$^+$; decrease in Ki67.					
(Broeckx et al., 2014b)	PB-MSCs (native or chondrogenic-induced)	Allogeneic PB 50 ml	DGC and PA	(i) Native: CD29$^+$, CD44$^+$, CD90$^+$, CD105$^+$; CD45$^-$, CD79a$^-$, MHC II$^-$ and a monocyte/macrophage marker; trilineage differentiation; p63$^-$, low in MHC I, Ki67$^+$, Col II$^+$, and Vimentin$^+$.	N/A	Culture-expanded cells (P4)	Single IA injection	PB-MSCs with PRP	N/A
				(ii) Chondrogenic induction: aggrecan$^+$, Col II$^+$, COMP$^+$, p63$^+$ and GAG$^+$; decrease in Ki67.					
(Fu et al., 2014b)	PB-MSCs	Allogeneic G-CSF-/AMD3100-mobilized PB, 10 ml	Erythrocyte lysis and PA	CD44/CD29$^+$, CD45/MHC II$^-$, trilineage differentiation	4×10^6 cells/scaffold	Culture-expanded cells (P3)	Surgical implantation	Establishment of animal model + cell-DBM scaffold complex implantation	Free movement
(Hopper et al., 2015b)	PBSCs	Autologous PB	DGC and PA cultured under hypoxia	Stro-1$^+$, CD44$^+$, CD90$^+$, CD106$^+$, CD105$^+$, CD146$^+$ and CD166$^+$; CD34$^-$/CD45$^-$; trilineage differentiation	2.0×10^5; cells/scaffold	Fresh concentrated stem cells	Surgical implantation	Establishment of animal model + cell-collagen-GAG scaffold complex implantation	Full weight bearing
(Deng et al., 2015)	PBSCs	Allogeneic G-CSF-mobilized PB, 200–500 µl	DGC	CD34$^+$ cells (2.8%), CD34$^-$ cells (97.2%)	5×10^6 cells/injection	Cryopreserved condensed stem cells (P0)	Single IA injection	Establishment of animal model + single IA injection (PBSCs+HA)	N/A
(Zhao et al., 2018)	PB-MSCs	Allogeneic G-CSF-/AMD3100-mobilized PB, 20 ml	DGC and PA	CD34$^-$/CD45$^-$; CD44$^+$/CD90$^+$	N/A	Culture-expanded cells (P3)	Surgical implantation	Establishment of animal model + cell-DBM - cytokine scaffold complex implantation	N/A
(Broeckx et al., 2019a)	Chondrogenic-induced PB-MSCs	Allogeneic PB	DGC and PA	Aggrecan$^+$, Col II$^+$, COMP$^+$, p63$^+$ and GAG$^+$; decrease in Ki67.	2×10^6 cells/injection	Culture-expanded chondrogenic-induced cells	Single IA injection	PB-MSCs with EAP	Rested in a box for 1 week after surgery and exercised on a treadmill for the remainder of the study period
(Broeckx et al., 2019b)	Chondrogenic-induced PB-MSCs	Allogeneic PB 50 ml	DGC and PA	Chondrogenic induction: CD29$^+$, CD44$^+$, CD90$^+$, CD45$^-$, MHC II$^-$, and a 4.4-fold COMP expression	2×10^6 cells/injection	Culture-expanded chondrogenic-induced cells (P10)	Single IA injection	PB-MSCs with EAP	A strict rehabilitation protocol
(Daems et al., 2019)	Chondrogenic-induced PB-MSCs	Xenogeneic PB 50 ml	DGC and PA	Chondrogenic induction: CD44$^+$, CD90$^+$, MHC II$^-$, and a 4.4-fold COMP expression	1×10^6 cells/injection	Culture-expanded chondrogenic-induced cells (P10)	Single IA injection	PB-MSCs only	Subjected to home confinement and leash walking in the first 10 days after treatment

PBSCs, peripheral blood-derived stem cells; G-CSF, granulocyte colony-stimulating factor; PB, peripheral blood; N/A, not available; TNC, total nucleated cells; IA, intra-articular; GFAP, growth factor addition/preservation; hG-CSF, human granulocyte colony stimulating factor; HA, hyaluronic acid; BMS, bone marrow stimulus; HTO, High Tibial Osteotomy; CPM, continuous passive motion; DGC, density gradient centrifugation; PA, plastic adherence; PB-MSCs, peripheral blood mesenchymal stem/stromal cells; PRP, Platelet-rich plasma; MHC, major histocompatibility complex; Col, collagen; COMP, cartilage oligomeric matrix protein; GAG, glycosaminoglycan; DBM, decalcified bone matrix; ciMSCs, chondrogenic induced mesenchymal stem cells; EAP, equine allogeneic plasma.

TABLE 3 | Efficacy and safety of treatment.

	Study ID	Follow-up period	Clinical outcomes	Radiology	Second-look arthroscopy/ gross morphology evaluation	Histological assessment	Adverse effects
Human studies	(Jancewicz et al., 2004)	6 months to 3 years	Improved Magee score	MRI: regenerative tissue with same signals as normal cartilage	N/A	N/A	Longer bone healing (1 patient)
	(Skowroński et al., 2012)	6 years	(i) Improved KOOS and Lysholm scales, relief of VAS scale; (ii) Approximately 90% of patients with good results	MRI: defects were refilled with regenerative tissue	N/A	N/A	(i) Intra-articular adhesions (1 patient); (ii) Joint pain with intermittent exudates and movement limitations (1 patient)
	(Skowroński and Rutka, 2013)	5 years	(i) Improved KOOS and Lysholm scales, relief of VAS scale; (ii) 92% of patients with good results	MRI: satisfactory reconstruction of the cartilaginous surface and good regenerative integration	N/A	N/A	None
	(Turajane et al., 2013)	6 months	Improved WOMAC and KOOS scales	N/A	N/A	Succeeded in regenerating articular cartilage	Mild swelling and discomfort
	(Saw et al., 2011)	10-26 months	N/A	X-ray: reappearance of medial articulation (1)	Regenerated articular cartilage with a smooth surface and excellent integration with the surrounding native cartilage	Regenerated full-thickness articular hyaline cartilage	Minimal discomfort from PBSCs harvesting and IA injection
	(Saw et al., 2013)	18 months	No IKDC score difference compared to the control group	Improved MRI morphologic scores	Regenerated articular cartilage with a smooth surface and excellent integration with the surrounding native cartilage	Improved total ICRS II histologic scores	Deep vein thrombosis (1 patient in the control group)
	(Saw et al., 2015)	15-58 months	Restoration of lower limb alignment	X-ray: reappearance of the medial compartment	Smooth regenerated articular cartilage and excellent integration with the surrounding native cartilage	(i) Improved ICRS II scores; (ii) High-quality cartilage regeneration resembling hyaline cartilage	None
	(Fu et al., 2014b)	7.5 years	Improved IKDC 2000 subjective score, Lysholm score and Tegner score	(i) CT: subchondral bone recovery; (ii) MRI: near normal cartilage-like tissue regeneration	Regenerated articular cartilage with a smooth surface, but with a slightly yellowish and shallow morphology	N/A	None
Animal studies	(Spaas et al., 2012)	4 months	Improved visual gait and objective pressure plate analysis	X-ray and B-ultrasound: no considerable changes	N/A	N/A	None
	(Broeckx et al., 2014a)	12 months	(i) Improved short- and long-term clinical evolution scores; (ii) Relief from clinical lameness, flexion pain and joint effusion	N/A	N/A	N/A	None
	(Broeckx et al., 2014b)	18 weeks	(i) Improved short- and long-term clinical evolution scores; (ii) Relief from clinical lameness and locomotor disorder	N/A	N/A	N/A	Moderate flare reaction (without long-term effects, 3 horses)
	(Fu et al., 2014b)	24 weeks	N/A	N/A	Cartilage regeneration comparable to BM-MSCs	Improved histological grading scale	N/A
	(Hopper et al., 2015b)	26 weeks	N/A	N/A	Improved ICRS macroscopic scores	Improved modified O'Driscoll score	None

(Continued)

TABLE 3 | Continued

Study ID	Follow-up period	Clinical outcomes	Radiology	Second-look arthroscopy/ gross morphology evaluation	Histological assessment	Adverse effects
(Deng et al., 2015)	6 weeks	N/A	N/A	N/A	Decreased cellular necrosis, apoptosis, loss of chondrogenic proteins, and modified Mankin scores	N/A
(Zhao et al., 2018)	12 weeks	N/A	N/A	Cartilage regeneration similar to normal cartilage tissue	Improved O'Driscoll score	N/A
(Broeckx et al., 2019a)	11 weeks	Improvements in visual and objective lameness;	No significant radiographic changes	Significantly less wear lines and synovial hyperaemia	(i) A significantly higher GAG concentration in the synovial fluid; (ii) Significantly enhanced Alcian Blue uptake and area % of COMP and Collagen II in the cartilage adjacent to the osteochondral fragment	None
(Broeckx et al., 2019b)	3 weeks-1 year	(i) Improved short- and long-term clinical evolution scores; (ii) Relief from clinical lameness, flexion pain and joint effusion	N/A	N/A	N/A	Nasal discharge (2 horse in the IVP group and 1 in the CP group)
(Daems et al., 2019)	12 weeks	Relief from pain and lameness	No significant radiographic changes	N/A	N/A	One of the six dogs had vomiting and/or diarrhea twice (one after placebo treatment and one after MSCs treatment)

quality cartilage regeneration resembling hyaline cartilage and/or improved total ICRS II histologic scores. Five animal studies (Fu et al., 2014b; Deng et al., 2015; Hopper et al., 2015b; Zhao et al., 2018; Broeckx et al., 2019a) reported an improved histological grading scale, modified O'Driscoll score, modified Mankin scores, O'Driscoll score, or significantly higher Alcian blue uptake.

In eight human studies, the major adverse events included longer bone healing (1 patient) (Jancewicz et al., 2004), intra-articular adhesions (1 patient) (Skowroński et al., 2012), joint pain with intermittent exudates and motion limitation (1 patient) (Skowroński et al., 2012), mild swelling (Turajane et al., 2013), and minimal discomfort during PBSCs harvesting and intra-articular (IA) injection (Saw et al., 2011). No serious adverse events occurred during the isolation and treatment of PBSCs. In one human study (Saw et al., 2013), a case of deep vein thrombosis occurred in the control group. In animal studies, moderate flare reactions (3 in 165 horses) (Broeckx et al., 2014a), nasal discharge (3 in 75 horses) (Broeckx et al., 2019), and vomiting and diarrhea (1 in 6 dogs) (Daems et al., 2019) occurred without long-term effects.

DISCUSSION

Researchers have conducted investigations of PBSCs in cartilage repair and regeneration because of the advantages of PBSCs and limitations of chondrogenic progenitor cells from other sources, such as bone marrow (Bain, 2003), synovial membranes (Murata et al., 2018), and adipose tissue (Kuroda et al., 2015). Increasing evidence has shown that PB-MSCs have a similar potential for proliferation and trilineage differentiation as BM-MSCs and might be a promising source of seed cells for cartilage repair (Wang et al., 2016b) since Fernández et al. (Fernandez et al., 1997) reported the presence of stromal cells in hG-CSF-mobilized PB from patients with breast cancer for the first time in 1997. However, PBSCs were not used to treat chondral defects and promote cartilage regeneration *in vivo* until 2004, as reported by investigators in Poland (Jancewicz et al., 2004).

For the first time, this review comprehensively evaluated the feasibility, efficacy, and safety of using PBSCs for cartilage repair and regeneration *in vivo* by analyzing the preoperative characteristics, therapeutic details, outcomes, and adverse events reported in currently published literature. This review might provide new insights and strategies for further foundational research and clinical applications of PBSCs.

Autologous nonculture-expanded PBSCs are easy to harvest and manipulate from G-CSF-activated PB without the concerns of disease transmission, immune rejection, and ethical issues (Fu et al., 2014a; Saw et al., 2015). PBSCs are currently the most commonly used cell type for cartilage repair in all stem cell types derived from PB. It has been demonstrated that nonculture-expanded PBSCs comprise haematopoietic stem cells (HSCs), fibrocytes, a population of MSCs/mesenchymal progenitor cells (MSCs/MPCs), white blood cells, platelets, growth factors, and a small percentage of red blood cells (Stroncek et al., 1997; Cesselli

et al., 2009). When PBSCs are being cultured, other impure cell types except MSCs/MPCs are not present anymore. To a certain degree, the cell composition of nonculture-expanded PBSCs is similar to that of the bone marrow-derived buffy coat (BMBC), which is separated from bone marrow using a Ficoll gradient centrifugation system. The bone marrow-derived buffy coat has been widely used as a source of MSCs for cartilage repair and regeneration and has achieved good to excellent results (Fortier et al., 2010; Jin et al., 2011). Several possible mechanisms of action of PBSCs might contribute to cartilage repair. Hopper et al. (Hopper et al., 2015a; Hopper et al., 2015c) found that PBSCs stimulate the upregulation of eight genes associated with chondrogenic differentiation of knee infrapatellar fat pad-derived MSCs, increase the total number of MSCs, increase native chondrocyte migration, and accelerate the rate of cell movement. Exogenous MSCs, HSCs, and growth factors in PBSCs initiate cartilage regeneration and augment endogenous MSC recruitment from bone marrow to subchondral drilling sites (Khaldoyanidi, 2008; Onuora, 2015; Saw et al., 2015). Deng et al. (2015) suggested that PBSCs prevent the progression of papain-induced knee OA in a rat model by reducing articular surface fibrillation, irregularity, and erosion, and by inhibiting chondrocyte necrosis and loss of chondrogenic proteins. HSCs and non-HSCs, such as MSCs, endothelial progenitor cells, and very small embryonic-like (VSEL) cells, contained in PBSCs might play an important role through a paracrine mechanism (Kucia et al., 2007; Onuora, 2015). Although the term "PBSCs" had different expressions in different studies, such as PB progenitor cells (PBPCs) (Saw et al., 2011) and PB mononuclear cells (PBMCs) (Hopper et al., 2015b), we found that the cell acquisition method and cell composition were basically the same. For the convenience of expression, "PBSCs" was used uniformly in this paper.

The transplantation of autologous culture-expanded PB-MSCs requires two procedures for obtaining patient cells and transplanting the cells after cultivation, which prolongs hospital stays, increases costs and risks contamination related to *in vitro* culture, possibly limiting the clinical application of autologous PB-MSCs (Saw et al., 2013; Fu et al., 2014b). Moreover, an age-related decline in MSC numbers, proliferation, and clonogenicity, which lead to more difficult culture *in vitro* and a longer culture cycle than MSCs from other tissue sources, might be another significant cause for the lack of clinical applications of autologous culture-expanded PB-MSCs (Kassis et al., 2006; Bourzac et al., 2010; Chong et al., 2012; Spaas et al., 2013; Wang et al., 2016b). For example, MSCs derived from bone marrow, synovium or adipose tissue reached 80–90% confluence within 7 to 14 days (Zhang et al., 2014; Jin et al., 2016; Shimomura et al., 2016). However, MSCs derived from PB did not achieve the same confluence until about 21 days after primary culture (Chen et al., 2019). It takes longer to obtain the culture-expanded PB-MSCs than other tissue-derived MSCs. The presence of MSCs in human PB is debatable and their identification may be hampered, among others, by: (i) their low frequency in PB of healthy individuals, and (ii) the large biological variations related to donor age, pathology, disease status, and corresponding treatment regimens (Fox et al., 2007; Moll et al., 2019). Most investigators agree that their frequency in blood is low in healthy individuals, but that the amounts of circulating MSCs may increase under special mobilization conditions, thus supporting the notion that MSCs can be transiently found circulating in blood (Moll et al., 2020). Jain et al. provide evidence that MSCs can be found in PB and apheresis product of patients treated with a typical G-CSF-based HSCs mobilization regimen by using flow cytometry (Jain et al., 2020). However, a systematic review strongly indicated the existence of MSCs in the PB of animals (Wang et al., 2016b), this might be because researchers could improve the success rate of PB-MSCs in animal studies by optimizing mobilization and culture procedures, prolonging the culture time, and increasing the number of animals and the frequency of blood drawn (Pitchford et al., 2009; To et al., 2011; Spaas et al., 2013). To et al. noted in a baboon model that MSC mobilization and colony-forming unit fibroblast (CFUF) in PB in response to G-CSF did only occur when adding stem cell factor (To et al., 2011). Pitchford et al. found, that MSCs/CFU-F were not found in mice PB post-mobilization with G-CSF, but when adding vascular endothelial growth factor and CXCR4-antagonist (Pitchford et al., 2009). Spaas et al. systematically studied the isolation and culture methods, cell characteristics, and clinical safety of equine PB-MSCs, and applied them to many veterinary clinical studies, such as promoting cartilage repair, cutaneous wound healing, and healing of tendon and ligament lesions (Spaas et al., 2013; Beerts et al., 2017; Martinello et al., 2018; Broeckx et al., 2019a). Allogenic or xenogeneic MSCs banks, improving the mobilization and purification techniques, and shortening the culture cycle might effectively account for deficiencies in autologous MSCs, reduce the burden on both patients and treatment providers, and promote the development of single-stage procedures (Moroni and Fornasari, 2013; Pescador et al., 2017).

MSCs inhibit immune responses and are not restricted by the HLA system through immune evasion and immune privilege mechanisms (Paterson et al., 2014; Vega et al., 2015). Moreover, the strong immunomodulatory and immunosuppressive properties of MSCs may play an important role in modifying graft-versus-host reactions during allogenic transplantations (Le Blanc and Ringden, 2007). Two animal studies used allogenic native and chondrogenic-induced PB-MSCs as a treatment for degenerative joint disease in horses and significantly improved the short- and long-term effects without serious adverse events (Broeckx et al., 2014a; Broeckx et al., 2014b). Vega et al. (2015) performed an RCT to assess the feasibility and safety of treating osteoarthritis with allogeneic MSCs in humans, and they concluded that allogeneic MSCs might be a convenient and effective alternative to autologous MSCs for the treatment of OA in the knee without serious transplantation-related adverse events. A number of published papers have indicated that transplanted MSCs influence the local microenvironment of cartilage by paracrine actions, such as the secretion of various growth factors, cytokines, and chemokines, to exert anti-inflammatory, anti-apoptotic, and anti-fibrotic effects on

chondrocytes(Kuroda et al., 2015; Mancuso et al., 2019). Another possible mechanism of action of MSCs in cartilage repair and regeneration is that transplanted progenitor cells migrate to damaged cartilage areas and differentiate into chondrocytes and osteocytes (Cesselli et al., 2009). The fate of MSCs injected into the articular cavity can be monitored by labelling with green fluorescent protein (GFP) or carboxyfluorescein diacetate succinimidyl ester (CFDA-SE) (Guest et al., 2008; Sato et al., 2012). Murphy et al. found that the implantation of MSCs into the knee joints of goats with OA showed a strong and sustained effect in promoting cartilage repair. However, further tracing the labelled MSCs showed that the cell retention rate was very low, usually about 3%, and most cells disappeared within a few days (Murphy et al., 2003). This suggests that MSCs may not directly differentiate into chondrocytes to participate in tissue repair *in vivo*, but promote cartilage regeneration through other mechanisms. In recent years, more and more researchers believed that exosomes secreted by MSCs played an important role in cartilage repair and regeneration (Marote et al., 2016; Yan and Wu, 2019; Jin et al., 2020; Liu et al., 2020). Exosomes are generally considered as communication vectors between cells, and carry a large number of complex nucleic acids (mRNA and miRNA lncRNA), proteins and lipids that can regulate and restore extracellular matrix (ECM) homeostasis (Colombo et al., 2014). For example, MSCs exosomes with overexpressing of miR-140-5p blocked other Wnt signals *in vitro* by inhibiting v-ral simian leukemia viral oncogene homolog A (RalA) and activating sex determining region Y-box 9 (SOX9), and regulate the expression of Col II and aggrecan (ACAN) *in vivo* to promote cartilage regeneration (Tao et al., 2017). It may also be an important mechanism for PBSCs to promote cartilage repair.

Blood cell separation is the most commonly used method for collecting PBSCs. It is a developed and simple technique that has been widely used in the treatment of systemic blood diseases. In a monocyte suspension isolated by blood cell separation, $CD105^+$ cells have been shown to be more abundance than $CD34^+$ cells, and the proportion of $CD105^+$ cells increased after cryopreservation (Saw et al., 2011). However, there is no study on the subsequent isolation and culture of PB-MSCs from PBSCs collected by blood cell separation. The current standard methods of PB-MSC isolation are DGC (such as Ficoll, Lymphoprep, and Percoll) and PA (Bourzac et al., 2010).

As one of the most fundamental parameters that might influence the outcome of cartilage repair (Gupta et al., 2016), the optimal density or dosage of PBSCs used for cartilage regeneration in different methods and species has not been fully investigated. Skowroński et al. (Skowroński and Rutka, 2013) reported a slightly poorer outcome of cartilage repair in a group treated with a bone marrow concentrate than a group treated with fresh condensed PBSCs, and they attributed this result to the lower cell count in the suspension obtained from bone marrow. The main concern of using nonculture-expanded PBSCs to promote tissue regeneration is the low content of MSCs within harvests. The number of HSCs (with a $CD34^+$ surface marker) and MSCs (with a $CD105^+$ surface marker) were quantified by flow cytometry in a study carried out by Saw et al. (Saw et al., 2011). The flow cytometry result showed that the proportion of $CD105^+$ cells in fresh PBSC suspension was 7.24% (2.32×10^6 cells/ml). Interestingly, the proportion of $CD105^+$ cells reached 8.39% (2.69×10^6 cells/ml) after cryopreservation. However, the $CD105^+$ cell counts vary between different studies. Turajane et al. (Turajane et al., 2013) reported that a proportion of $CD105^+$ cells ranging from 0.75 to 0.88%. The difference of the proportion of $CD105^+$ cells in the two studies was probably due to the younger patients in the previous study and the older patients in the latter.

To increase the yield of MSCs from autologous PB, repeated intra-articular injections were implemented in some studies (Saw et al., 2011; Saw et al., 2013; Turajane et al., 2013; Saw et al., 2015), and they speculated that this method is more efficacious than a single injection for the enhancement of cartilage repair on the basis of a suggestion from an animal study (Saw et al., 2009). However, repeated IA injections of culture-expanded allogeneic MSCs is not recommended due to a significant adverse response that might be initiated by immune recognition of allogeneic MSCs after a second exposure (Joswig et al., 2017).

Currently, the optimal seeding density of MSCs also remains unknown. A systematic review showed that the dose of MSCs for cartilage repair varies from 2×10^6–7.7×10^7 cells in human clinical studies (Goldberg et al., 2017). Gupta et al. (Gupta et al., 2016) found that an MSC dose of 2.5×10^7 with the IA injection method for treating OA showed the best improvement for relieving pain and the lowest adverse events compared with other higher dose groups. They hypothesized that a higher cell dosage causes cell aggregation and subsequent cell death due to limited space in the knee joint. A prospective RCT demonstrated that an intra-articular injection of cultured MSCs with a mean dose of 1.46×10^7 cells for treating OA is effective in improving clinical and magnetic resonance observation of cartilage repair tissue (MOCART) scores after a 2-year follow-up (Wong et al., 2013). Given the limited evidence of clinical application of PB-MSCs in cartilage repair and regeneration, the optimal therapeutic dose of PB-MSCs remains to be further studied.

Moreover, a number of studies have reported concomitant procedures, such as abrasion arthroplasty (Beckmann et al., 2015), autologous bone grafting to restore bone mass (Sadlik et al., 2017), treatment of co-existing pathologies (Wong et al., 2013), and BMS (Jin et al., 2011), PRP (Broeckx et al., 2019a) and HA (Charlesworth et al., 2019) to repair cartilage defects. Thus, the abovementioned methods are recommended to supplement PBSCs for cartilage repair and regeneration. A rigorous postoperative rehabilitation programme is required to protect grafts and avoid the effusion of PBSC suspensions (Skowroński and Rutka, 2013; Fu et al., 2014a).

Compared with other tissue-derived MSCs, the culture of PB-MSCs was relatively difficult, which resulted in less reports of its application *in vivo*, but it does not affect its application prospects. On the contrary, it is ethically more suitable for clinical application due to its unique advantages, such as minimally invasive sample acquisition procedure, repeatable sampling, and high recognition of patients (Fu et al., 2014a; Fu et al., 2014b;

Wang et al., 2016a; Chen et al., 2019). In this review, we have summarized all the currently published researches on the use of PBSCs for cartilage repair and regeneration *in vivo*. Although only 5 human and veterinary clinical studies (Saw et al., 2013; Skowroński and Rutka, 2013; Daems et al., 2019; Broeckx et al., 2019a; Broeckx et al., 2019b) had a control group, the results were still very useful for readers, and can reflect the progress and problems in this field to a certain extent.

CONCLUSION

This review evaluated the use of PBSCs in cartilage repair and regeneration *in vivo* for the first time. Autologous PBSCs are easy to obtain and are free of transmittable diseases, infection risks, and medical ethical restrictions. They are currently the most commonly used cell type for cartilage repair among all stem cell types derived from PB. Blood cell separation technology is developed, simple, and convenient, making it the most commonly used method to obtain PBSC suspensions. Allogeneic culture-expanded PB-MSCs are more widely used in animal research and are potential seed cell types for cartilage repair and regeneration in the future. DGC and PA are the most commonly used methods for PB-MSC isolation. Improving the purification technology and shortening the culture cycle of culture-expanded PB-MSCs will obviously promote the researchers' interest. PBSCs are safe in cartilage repair and regeneration. Although all reviewed articles indicated that using PB as a cell source enhances cartilage repair and regeneration *in vivo* by the IA injection and surgery implantation methods, we should maintain a prudent attitude towards the positive therapeutic effect of PBSCs considering the deficiency of studies with a high level of evidence, incomplete assessment system of outcomes, and combined use of multiple other treatments. In summary, the use of PBSCs in cartilage repair and regeneration warrants considerable efforts for further investigations due to its superiorities and safety in clinical settings and positive effects despite limited evidence in human.

AUTHOR CONTRIBUTIONS

Conception and design: J-KY and DJ. Analysis and interpretation of the data: Y-RC, XY, and F-ZY. Drafting of the article: Y-RC, XY, and F-ZY. Information collection and sorting: JY, B-BX, Z-XZ, Z-MM, and JG. Manuscript editing and proofreading: Y-FS, Z-WS, X-JW, and Z-YC. D-YW, B-SF, MY, and S-TS provided oversight. Critical revision of the article for important intellectual content: J-KY and DJ. All authors read and approved the final manuscript.

FUNDING

This work was supported by the National Natural Science Foundation of China (Grant Nos. 51773004, 81630056, 51920105006, 31670982) and National Key Research and Development Program (Grant No. 2016YFC1100704).

REFERENCES

Andriolo, L., Merli, G., Filardo, G., Marcacci, M., and Kon, E. (2017). Failure of Autologous Chondrocyte Implantation. *Sports Med. Arthrosc Rev.* 25, 10–18. doi: 10.1097/JSA.0000000000000137

Bain, B. J. (2003). Bone marrow biopsy morbidity and mortality. *Br. J. Haematol.* 121, 949–951. doi: 10.1111/j.1365-2257.2004.00630.x

Beckmann, R., Lippross, S., Hartz, C., Tohidnezhad, M., Ferreira, M. S., Neuss-Stein, S., et al. (2015). Abrasion arthroplasty increases mesenchymal stem cell content of postoperative joint effusions. *BMC Musculoskelet Disord.* 16, 250. doi: 10.1186/s12891-015-0705-0

Beerts, C., Suls, M., Broeckx, S. Y., Seys, B., Vandenberghe, A., Declercq, J., et al. (2017). Tenogenically Induced Allogeneic Peripheral Blood Mesenchymal Stem Cells in Allogeneic Platelet-Rich Plasma: 2-Year Follow-up after Tendon or Ligament Treatment in Horses. *Front. Vet. Sci.* 4, 158. doi: 10.3389/fvets.2017.00158

Bourzac, C., Smith, L. C., Vincent, P., Beauchamp, G., Lavoie, J. P., and Laverty, S. (2010). Isolation of equine bone marrow-derived mesenchymal stem cells: a comparison between three protocols. *Equine Vet. J.* 42, 519–527. doi: 10.1111/j.2042-3306.2010.00098.x

Broeckx, S., Suls, M., Beerts, C., Vandenberghe, A., Seys, B., Wuertz-Kozak, K., et al. (2014a). Allogenic mesenchymal stem cells as a treatment for equine degenerative joint disease: a pilot study. *Curr. Stem Cell Res. T.* 9, 497. doi: 10.2174/1574888x09666140826110601

Broeckx, S., Zimmerman, M., Crocetti, S., Suls, M., Mariën, T., Ferguson, S. J., et al. (2014b). Regenerative Therapies for Equine Degenerative Joint Disease: A Preliminary Study. *PLoS One* 9, e85917. doi: 10.1371/journal.pone.0085917

Broeckx, S. Y., Martens, A. M., Bertone, A. L., Van Brantegem, L., Duchateau, L., Van Hecke, L., et al. (2019a). The use of equine chondrogenic-induced mesenchymal stem cells as a treatment for osteoarthritis: A randomised, double-blinded, placebo-controlled proof-of-concept study. *Equine Vet. J.* 51, 787–794. doi: 10.1111/evj.13089

Broeckx, S. Y., Seys, B., Suls, M., Vandenberghe, A., Mariën, T., Adriaensen, E., et al. (2019b). Equine Allogeneic Chondrogenic Induced Mesenchymal Stem Cells Are an Effective Treatment for Degenerative Joint Disease in Horses. *Stem Cells Dev.* 28, 410–422. doi: 10.1089/scd.2018.0061

Cesselli, D., Beltrami, A. P., Rigo, S., Bergamin, N., D'Aurizio, F., Verardo, R., et al. (2009). Multipotent progenitor cells are present in human peripheral blood. *Circ. Res.* 104, 1225–1234. doi: 10.1161/CIRCRESAHA.109.195859

Charlesworth, J., Fitzpatrick, J., Perera, N., and Orchard, J. (2019). Osteoarthritis-a systematic review of long-term safety implications for osteoarthritis of the knee. *BMC Musculoskelet Disord.* 20, 151. doi: 10.1186/s12891-019-2525-0

Chen, S., Fu, P., Wu, H., and Pei, M. (2017). Meniscus, articular cartilage and nucleus pulposus: a comparative review of cartilage-like tissues in anatomy, development and function. *Cell Tissue Res.* 370, 53–70. doi: 10.1007/s00441-017-2613-0

Chen, Y. R., Zhou, Z. X., Zhang, J. Y., Yuan, F. Z., Xu, B. B., Guan, J., et al. (2019). Low-Molecular-Weight Heparin-Functionalized Chitosan-Chondroitin Sulfate Hydrogels for Controlled Release of TGF-beta3 and in vitro Neocartilage Formation. *Front. Chem.* 7, 745. doi: 10.3389/fchem.2019.00745

Chong, P. P., Selvaratnam, L., Abbas, A. A., and Kamarul, T. (2012). Human peripheral blood derived mesenchymal stem cells demonstrate similar characteristics and chondrogenic differentiation potential to bone marrow

derived mesenchymal stem cells. *J. Orthop. Res.* 30, 634–642. doi: 10.1002/jor.21556

Colombo, M., Raposo, G., and Thery, C. (2014). Biogenesis, secretion, and intercellular interactions of exosomes and other extracellular vesicles. *Annu. Rev. Cell Dev. Biol.* 30, 255–289. doi: 10.1146/annurev-cellbio-101512-122326

Daems, R., Van Hecke, L., Schwarzkopf, I., Depuydt, E., Broeckx, S. Y., David, M., et al. (2019). A Feasibility Study on the Use of Equine Chondrogenic Induced Mesenchymal Stem Cells as a Treatment for Natural Occurring Osteoarthritis in Dogs. *Stem Cells Int.* 2019, 1–11. doi: 10.1155/2019/4587594

Deng, M., Wei, S., Yew, T., Lee, P., Yang, T., Chu, H., et al. (2015). Cell Therapy with G-CSF-Mobilized Stem Cells in a Rat Osteoarthritis Model. *Cell Transplant* 24, 1085–1096. doi: 10.3727/096368914X680091

Ding, J., Zhang, J., Li, J., Li, D., Xiao, C., Xiao, H., et al. (2019). Electrospun polymer biomaterials. *Prog. Polym. Sci.* 90, 1–34. doi: 10.1016/j.progpolymsci.2019.01.002

Fernandez, M., Simon, V., Herrera, G., Cao, C., Del, F. H., and Minguell, J. J. (1997). Detection of stromal cells in peripheral blood progenitor cell collections from breast cancer patients. *Bone Marrow Transplant.* 20, 265–271. doi: 10.1038/sj.bmt.1700890

Fortier, L. A., Potter, H. G., Rickey, E. J., Schnabel, L. V., Foo, L. F., Chong, L. R., et al. (2010). Concentrated bone marrow aspirate improves full-thickness cartilage repair compared with microfracture in the equine model. *J. Bone Joint Surg. Am.* 92, 1927–1937. doi: 10.2106/JBJS.I.01284

Fox, J. M., Chamberlain, G., Ashton, B. A., and Middleton, J. (2007). Recent advances into the understanding of mesenchymal stem cell trafficking. *Br. J. Haematol.* 137, 491–502. doi: 10.1111/j.1365-2141.2007.06610.x

Fu, W. L., Ao, Y., Ke, X., Zheng, Z., Gong, X., Jiang, D., et al. (2014a). Repair of large full-thickness cartilage defect by activating endogenous peripheral blood stem cells and autologous periosteum flap transplantation combined with patellofemoral realignment. *Knee* 21, 609–612. doi: 10.1016/j.knee.2013.10.010

Fu, W. L., Zhou, C. Y., and Yu, J. K. (2014b). A new source of mesenchymal stem cells for articular cartilage repair: MSCs derived from mobilized peripheral blood share similar biological characteristics in vitro and chondrogenesis *in vivo* as MSCs from bone marrow in a rabbit model. *Am. J. Sports Med.* 42, 592–601. doi: 10.1177/0363546513512778

Goldberg, A., Mitchell, K., Soans, J., Kim, L., and Zaidi, R. (2017). The use of mesenchymal stem cells for cartilage repair and regeneration: a systematic review. *J. Orthop. Surg. Res.* 12, 39. doi: 10.1186/s13018-017-0534-y

Guadix, J. A., Zugaza, J. L., and Galvez-Martin, P. (2017). Characteristics, applications and prospects of mesenchymal stem cells in cell therapy. *Med. Clin. (Barc)* 148, 408–414. doi: 10.1016/j.medcli.2016.11.033

Guest, D. J., Smith, M. R., and Allen, W. R. (2008). Monitoring the fate of autologous and allogeneic mesenchymal progenitor cells injected into the superficial digital flexor tendon of horses: preliminary study. *Equine Vet. J.* 40, 178–181. doi: 10.2746/042516408X276942

Gupta, P. K., Chullikana, A., Rengasamy, M., Shetty, N., Pandey, V., Agarwal, V., et al. (2016). Efficacy and safety of adult human bone marrow-derived, cultured, pooled, allogeneic mesenchymal stromal cells (Stempeucel(R)): preclinical and clinical trial in osteoarthritis of the knee joint. *Arthritis Res. Ther.* 18, 301. doi: 10.1186/s13075-016-1195-7

Han, Y., Li, X., Zhang, Y., Han, Y., Chang, F., and Ding, J. (2019). Mesenchymal Stem Cells for Regenerative Medicine. *Cells* 8, 886. doi: 10.3390/cells8080886

Hernigou, P., Homma, Y., Flouzat-Lachaniette, C. H., Poignard, A., Chevallier, N., and Rouard, H. (2013). Cancer risk is not increased in patients treated for orthopaedic diseases with autologous bone marrow cell concentrate. *J. Bone Joint Surg. Am.* 95, 2215–2221. doi: 10.2106/JBJS.M.00261

Hopper, N., Henson, F., Brooks, R., Ali, E., Rushton, N., and Wardale, J. (2015a). Peripheral blood derived mononuclear cells enhance osteoarthritic human chondrocyte migration. *Arthritis Res. Ther.* 17, 199. doi: 10.1186/s13075-015-0709-z

Hopper, N., Wardale, J., Brooks, R., Power, J., Rushton, N., and Henson, F. (2015b). Peripheral Blood Mononuclear Cells Enhance Cartilage Repair in *in vivo* Osteochondral Defect Model. *PLoS One* 10, e0133937. doi: 10.1371/journal.pone.0133937

Hopper, N., Wardale, J., Howard, D., Brooks, R., Rushton, N., and Henson, F. (2015c). Peripheral blood derived mononuclear cells enhance the migration and chondrogenic differentiation of multipotent mesenchymal stromal cells. *Stem Cells Int.* 2015, 323454. doi: 10.1155/2015/323454

Jain, A., Khadwal, A., Sachdeva, M., Bose, P., Lad, D., Bhattacharya, S., et al. (2020). Variables affecting the presence of mesenchymal stromal cells in peripheral blood and their relationship with apheresis products. *Br. J. Haematol.* doi: 10.1111/bjh.16412

Jancewicz, P., Dzienis, W., Pietruczuk, M., Skowroński, J., and Bielecki, M. (2004). Osteochondral defects of the talus treated by mesenchymal stem cell implantation–early results. *Roczniki Akademii Medycznej w Bialymstoku (1995)* 49 (Suppl 1), 25.

Jin, L. H., Choi, B. H., Kim, Y. J., Park, S. R., Jin, C. Z., and Min, B. H. (2011). Implantation of bone marrow-derived buffy coat can supplement bone marrow stimulation for articular cartilage repair. *Osteoarthritis Cartilage* 19, 1440–1448. doi: 10.1016/j.joca.2011.07.012

Jin, G., Park, J., Wall, I., and Kim, H. (2016). Isolation and culture of primary rat adipose derived stem cells using porous biopolymer microcarriers. *Tissue Eng. Regen. Med.* 13, 242–250. doi: 10.1007/s13770-016-0040-z

Jin, Z., Ren, J., and Qi, S. (2020). Human bone mesenchymal stem cells-derived exosomes overexpressing microRNA-26a-5p alleviate osteoarthritis via down-regulation of PTGS2. *Int. Immunopharmacol.* 78, 105946. doi: 10.1016/j.intimp.2019.105946

Joswig, A. J., Mitchell, A., Cummings, K. J., Levine, G. J., Gregory, C. A., Smith, R. R., et al. (2017). Repeated intra-articular injection of allogeneic mesenchymal stem cells causes an adverse response compared to autologous cells in the equine model. *Stem Cell Res. Ther.* 8, 42. doi: 10.1186/s13287-017-0503-8

Kassis, I., Zangi, L., Rivkin, R., Levdansky, L., Samuel, S., Marx, G., et al. (2006). Isolation of mesenchymal stem cells from G-CSF-mobilized human peripheral blood using fibrin microbeads. *Bone Marrow Transplant.* 37, 967–976. doi: 10.1038/sj.bmt.1705358

Khaldoyanidi, S. (2008). Directing stem cell homing. *Cell Stem Cell* 2, 198–200. doi: 10.1016/j.stem.2008.02.012

Kucia, M., Halasa, M., Wysoczynski, M., Baskiewicz-Masiuk, M., Moldenhawer, S., Zuba-Surma, E., et al. (2007). Morphological and molecular characterization of novel population of CXCR4+ SSEA-4+ Oct-4+ very small embryonic-like cells purified from human cord blood: preliminary report. *Leukemia* 21, 297–303. doi: 10.1038/sj.leu.2404470

Kuroda, K., Kabata, T., Hayashi, K., Maeda, T., Kajino, Y., Iwai, S., et al. (2015). The paracrine effect of adipose-derived stem cells inhibits osteoarthritis progression. *BMC Musculoskelet Disord.* 16, 236. doi: 10.1186/s12891-015-0701-4

Le Blanc, K., and Ringden, O. (2007). Immunomodulation by mesenchymal stem cells and clinical experience. *J. Intern. Med.* 262, 509–525. doi: 10.1111/j.1365-2796.2007.01844.x

Li, X., Ding, J., Zhang, Z., Yang, M., Yu, J., Wang, J., et al. (2016). Kartogenin-Incorporated Thermogel Supports Stem Cells for Significant Cartilage Regeneration. *ACS Appl. Mater. Interfaces* 8, 5148–5159. doi: 10.1021/acsami.5b12212

Liu, H., Cheng, Y., Chen, J., Chang, F., Wang, J., Ding, J., et al. (2018). Component effect of stem cell-loaded thermosensitive polypeptide hydrogels on cartilage repair. *Acta Biomater.* 73, 103–111. doi: 10.1016/j.actbio.2018.04.035

Liu, C., Li, Y., Yang, Z., Zhou, Z., Lou, Z., and Zhang, Q. (2020). Kartogenin enhances the therapeutic effect of bone marrow mesenchymal stem cells derived exosomes in cartilage repair. *Nanomedicine (Lond)* 15, 273–288. doi: 10.2217/nnm-2019-0208

Makris, E. A., Gomoll, A. H., Malizos, K. N., Hu, J. C., and Athanasiou, K. A. (2015). Repair and tissue engineering techniques for articular cartilage. *Nat. Rev. Rheumatol.* 11, 21–34. doi: 10.1038/nrrheum.2014.157

Mancuso, P., Raman, S., Glynn, A., Barry, F., and Murphy, J. M. (2019). Mesenchymal Stem Cell Therapy for Osteoarthritis: The Critical Role of the Cell Secretome. *Front. Bioeng. Biotechnol.* 7, 9. doi: 10.3389/fbioe.2019.00009

Marote, A., Teixeira, F. G., Mendes-Pinheiro, B., and Salgado, A. J. (2016). MSCs-Derived Exosomes: Cell-Secreted Nanovesicles with Regenerative Potential. *Front. Pharmacol.* 7, 231. doi: 10.3389/fphar.2016.00231

Martinello, T., Gomiero, C., Perazzi, A., Iacopetti, I., Gemignani, F., DeBenedictis, G. M., et al. (2018). Allogeneic mesenchymal stem cells improve the wound healing process of sheep skin. *BMC Vet. Res.* 14, 202. doi: 10.1186/s12917-018-1527-8

Moll, G., Ankrum, J. A., Kamhieh-Milz, J., Bieback, K., Ringden, O., Volk, H. D., et al. (2019). Intravascular Mesenchymal Stromal/Stem Cell Therapy Product Diversification: Time for New Clinical Guidelines. *Trends Mol. Med.* 25, 149–163. doi: 10.1016/j.molmed.2018.12.006

Moll, G., Drzeniek, N., Kamhieh-Milz, J., Geissler, S., and Reinke, P. (2020). Editorial comment: variables affecting the presence of mesenchymal stromal cells in the peripheral blood and their relationship with apheresis product. *Br. J. Haematol.* doi: 10.1111/bjh.16389

Moroni, L., and Fornasari, P. M. (2013). Human mesenchymal stem cells: a bank perspective on the isolation, characterization and potential of alternative

sources for the regeneration of musculoskeletal tissues. *J. Cell. Physiol.* 228, 680–687. doi: 10.1002/jcp.24223

Murata, Y., Uchida, S., Utsunomiya, H., Hatakeyama, A., Nakashima, H., Chang, A., et al. (2018). Synovial Mesenchymal Stem Cells Derived From the Cotyloid Fossa Synovium Have Higher Self-renewal and Differentiation Potential Than Those From the Paralabral Synovium in the Hip Joint. *Am. J. Sports Med.* 46, 2942–2953. doi: 10.1177/0363546518794664

Murphy, J. M., Fink, D. J., Hunziker, E. B., and Barry, F. P. (2003). Stem cell therapy in a caprine model of osteoarthritis. *Arthritis Rheum.* 48, 3464–3474. doi: 10.1002/art.11365

Onuora, S. (2015). PBMCs stimulate chondrocyte migration and cartilage repair. *Nat. Rev. Rheumatol.* 11, 563–563. doi: 10.1038/nrrheum.2015.118

Paterson, Y. Z., Rash, N., Garvican, E. R., Paillot, R., and Guest, D. J. (2014). Equine mesenchymal stromal cells and embryo-derived stem cells are immune privileged in vitro. *Stem Cell Res. Ther.* 5, 90. doi: 10.1186/scrt479

Pescador, D., Ibanez-Fonseca, A., Sanchez-Guijo, F., Brinon, J. G., Arias, F. J., Muntion, S., et al. (2017). Regeneration of hyaline cartilage promoted by xenogeneic mesenchymal stromal cells embedded within elastin-like recombinamer-based bioactive hydrogels. *J. Mater. Sci. Mater. Med.* 28, 115. doi: 10.1007/s10856-017-5928-1

Pitchford, S. C., Furze, R. C., Jones, C. P., Wengner, A. M., and Rankin, S. M. (2009). Differential mobilization of subsets of progenitor cells from the bone marrow. *Cell Stem Cell* 4, 62–72. doi: 10.1016/j.stem.2008.10.017

Redondo, M. L., Naveen, N. B., Liu, J. N., Tauro, T. M., Southworth, T. M., and Cole, B. J. (2018). Preservation of Knee Articular Cartilage. *Sports Med. Arthrosc. Rev.* 26, e23–e30. doi: 10.1097/JSA.0000000000000226

Riboh, J. C., Cvetanovich, G. L., Cole, B. J., and Yanke, A. B. (2017). Comparative efficacy of cartilage repair procedures in the knee: a network meta-analysis. *Knee Surg. Sports Traumatol. Arthrosc.* 25, 3786–3799. doi: 10.1007/s00167-016-4300-1

Sadlik, B., Gobbi, A., Puszkarz, M., Klon, W., and Whyte, G. P. (2017). Biologic Inlay Osteochondral Reconstruction: Arthroscopic One-Step Osteochondral Lesion Repair in the Knee Using Morselized Bone Grafting and Hyaluronic Acid-Based Scaffold Embedded With Bone Marrow Aspirate Concentrate. *Arthrosc. Tech.* 6, e383–e389. doi: 10.1016/j.eats.2016.10.023

Sato, M., Uchida, K., Nakajima, H., Miyazaki, T., Guerrero, A. R., Watanabe, S., et al. (2012). Direct transplantation of mesenchymal stem cells into the knee joints of Hartley strain guinea pigs with spontaneous osteoarthritis. *Arthritis Res. Ther.* 14, R31. doi: 10.1186/ar3735

Saw, K. Y., Hussin, P., Loke, S. C., Azam, M., Chen, H. C., Tay, Y. G., et al. (2009). Articular cartilage regeneration with autologous marrow aspirate and hyaluronic Acid: an experimental study in a goat model. *Arthroscopy* 25, 1391–1400. doi: 10.1016/j.arthro.2009.07.011

Saw, K., Anz, A., Merican, S., Tay, Y., Ragavanaidu, K., Jee, C. S. Y., et al. (2011). Articular Cartilage Regeneration With Autologous Peripheral Blood Progenitor Cells and Hyaluronic Acid After Arthroscopic Subchondral Drilling: A Report of 5 Cases With Histology. *Arthroscopy: J. Arthroscopic Related Surg.* 27, 493–506. doi: 10.1016/j.arthro.2010.11.054

Saw, K., Anz, A., Siew-Yoke Jee, C., Merican, S., Ching-Soong Ng, R., Roohi, S. A., et al. (2013). Articular Cartilage Regeneration With Autologous Peripheral Blood Stem Cells Versus Hyaluronic Acid: A Randomized Controlled Trial. *Arthroscopy: J. Arthroscopic Related Surg.* 29, 684–694. doi: 10.1016/j.arthro.2012.12.008

Saw, K., Anz, A., Jee, C. S., Ng, R. C., Mohtarrudin, N., and Ragavanaidu, K. (2015). High Tibial Osteotomy in Combination With Chondrogenesis After Stem Cell Therapy: A Histologic Report of 8 Cases. *Arthroscopy: J. Arthroscopic Related Surg.* 31, 1909–1920. doi: 10.1016/j.arthro.2015.03.038

Shimomura, K., Moriguchi, Y., Nansai, R., Fujie, H., Ando, W., Horibe, S., et al. (2016). Comparison of 2 Different Formulations of Artificial Bone for a Hybrid Implant With a Tissue-Engineered Construct Derived From Synovial Mesenchymal Stem Cells: A Study Using a Rabbit Osteochondral Defect Model. *Am. J. Sports Med.* 45, 666–675. doi: 10.1177/0363546516668835

Skowroński, J., and Rutka, M. (2013). Osteochondral lesions of the knee reconstructed with mesenchymal stem cells - results. *Ortopedia Traumatologia Rehabilitacja* 15, 1–1. doi: 10.5604/15093492.1058409

Skowroński, J., Rutka, M., and Skowroński, R. (2012). Cartilage lesions of the knee treated with blood mesenchymal stem cells - results. *Ortopedia Traumatologia Rehabilitacja* 14, 1–10. doi: 10.5604/15093492.1012404

Spaas, J. H., Oosterlinck, M., Broeckx, S., Dumoulin, M., Saunders, J., Van Soom, A., et al. (2012). Treatment of equine degenerative joint disease with autologous peripheral blood-derived mesenchymal stem cells: A case report. *Vlaams Diergen. Tijds.* 81, 11–15. doi: 10.1080/00480169.2012.658737

Spaas, J. H., De Schauwer, C., Cornillie, P., Meyer, E., Van Soom, A., and Van de Walle, G. R. (2013). Culture and characterisation of equine peripheral blood mesenchymal stromal cells. *Vet. J.* 195, 107–113. doi: 10.1016/j.tvjl.2012.05.006

Stroncek, D. F., Clay, M. E., Smith, J., Herr, G., Ilstrup, S., Kunkel, L. A., et al. (1997). Composition of peripheral blood progenitor cell components collected from healthy donors. *Transfusion* 37, 411–417. doi: 10.1046/j.1537-2995.1997.37497265342.x

Tao, S. C., Yuan, T., Zhang, Y. L., Yin, W. J., Guo, S. C., and Zhang, C. Q. (2017). Exosomes derived from miR-140-5p-overexpressing human synovial mesenchymal stem cells enhance cartilage tissue regeneration and prevent osteoarthritis of the knee in a rat model. *Theranostics* 7, 180–195. doi: 10.7150/thno.17133

To, L. B., Levesque, J. P., Herbert, K. E., Winkler, I. G., Bendall, L. J., Hiwase, D. K., et al. (2011). Mobilisation strategies for normal and malignant cells. *Pathology* 43, 547–565. doi: 10.1097/PAT.0b013e32834a9eb8

Turajane, T., Chaweewannakorn, U., Larbpaiboonpong, V., Aojanepong, J., Thitiset, T., Honsawek, S., et al. (2013). Combination of intra-articular autologous activated peripheral blood stem cells with growth factor addition/ preservation and hyaluronic acid in conjunction with arthroscopic microdrilling mesenchymal cell stimulation Improves quality of life and regenerates articular cartilage in early osteoarthritic knee disease. *J. Med. Assoc. Thailand* 96, 580. doi: 10.1109/JPROC.2015.2471838

Vega, A., Martin-Ferrero, M. A., Del, C. F., Alberca, M., Garcia, V., Munar, A., et al. (2015). Treatment of Knee Osteoarthritis With Allogeneic Bone Marrow Mesenchymal Stem Cells: A Randomized Controlled Trial. *Transplantation* 99, 1681–1690. doi: 10.1097/TP.0000000000000678

Wang, S. J., Jiang, D., Zhang, Z. Z., Huang, A. B., Qi, Y. S., Wang, H. J., et al. (2016a). Chondrogenic Potential of Peripheral Blood Derived Mesenchymal Stem Cells Seeded on Demineralized Cancellous Bone Scaffolds. *Sci. Rep.* 6, 36400. doi: 10.1038/srep36400

Wang, S. J., Yin, M. H., Jiang, D., Zhang, Z. Z., Qi, Y. S., Wang, H. J., et al. (2016b). The Chondrogenic Potential of Progenitor Cells Derived from Peripheral Blood: A Systematic Review. *Stem Cells Dev.* 25, 1195–1207. doi: 10.1089/scd.2016.0055

Wang, C., Feng, N., Chang, F., Wang, J., Yuan, B., Cheng, Y., et al. (2019). Injectable Cholesterol-Enhanced Stereocomplex Polylactide Thermogel Loading Chondrocytes for Optimized Cartilage Regeneration. *Adv. Healthc. Mater.* 8, e1900312. doi: 10.1002/adhm.201900312

Wong, K. L., Lee, K. B., Tai, B. C., Law, P., Lee, E. H., and Hui, J. H. (2013). Injectable cultured bone marrow-derived mesenchymal stem cells in varus knees with cartilage defects undergoing high tibial osteotomy: a prospective, randomized controlled clinical trial with 2 years' follow-up. *Arthroscopy* 29, 2020–2028. doi: 10.1016/j.arthro.2013.09.074

Yan, L., and Wu, X. (2019). Exosomes produced from 3D cultures of umbilical cord mesenchymal stem cells in a hollow-fiber bioreactor show improved osteochondral regeneration activity. *Cell Biol. Toxicol.* 35, 471–484. doi: 10.1007/s10565-019-09504-5

Zhang, W., Zhang, F., Shi, H., Tan, R., Han, S., Ye, G., et al. (2014). Comparisons of rabbit bone marrow mesenchymal stem cell isolation and culture methods in vitro. *PloS One* 9, e88794. doi: 10.1371/journal.pone.0088794

Zhang, Y., Yu, J., Ren, K., Zuo, J., Ding, J., and Chen, X. (2019). Thermosensitive Hydrogels as Scaffolds for Cartilage Tissue Engineering. *Biomacromolecules* 20, 1478–1492. doi: 10.1021/acs.biomac.9b00043

Zhao, D., Li, Y., Zhou, X., and Yang, Z. (2018). Peripheral Blood Mesenchymal Stem Cells Combined with Modified Demineralized Bone Matrix Promote Pig Cartilage Defect Repair. *Cells Tissues Organs*. 206, 1–9. doi: 10.1159/000493210

Conflict of Interest: The authors declare that the research was conducted in the absence of any commercial or financial relationships that could be construed as a potential conflict of interest.

The handling editor declared a past co-authorship with one of the authors JK-Y.

frontiers in Pharmacology

ORIGINAL RESEARCH
published: 08 April 2020
doi: 10.3389/fphar.2020.00431

Silver Nanoparticles Coated Poly(L-Lactide) Electrospun Membrane for Implant Associated Infections Prevention

Jiaolong Wang[1,2], *Lilin Zhan*[1,2], *Xianhua Zhang*[1,2], *Runfa Wu*[1,2], *Lan Liao*[1,2]* *and Junchao Wei*[1,2,3]*

[1] School of Stomatology, Nanchang University, Nanchang, China, [2] The Key Laboratory of Oral Biomedicine, Nanchang, China, [3] College of Chemistry, Nanchang University, Nanchang, China

OPEN ACCESS

Edited by:
Jianxun Ding,
Chinese Academy of Sciences, China

Reviewed by:
Dilyana Paneva Paneva,
Institute of Polymers (BAS), Bulgaria
Tairong Kuang,
Zhejiang University of Technology, China
Yixia Yin,
Wuhan University of Technology, China

***Correspondence:**
Lan Liao
Liaolan5106@ncu.edu.cn
Junchao Wei
weijunchao@ncu.edu.cn

Specialty section:
This article was submitted to Experimental Pharmacology and Drug Discovery, a section of the journal Frontiers in Pharmacology

Received: 31 December 2019
Accepted: 20 March 2020
Published: 08 April 2020

Citation:
Wang J, Zhan L, Zhang X, Wu R, Liao L and Wei J (2020) Silver Nanoparticles Coated Poly(L-Lactide) Electrospun Membrane for Implant Associated Infections Prevention. Front. Pharmacol. 11:431. doi: 10.3389/fphar.2020.00431

Bacterial infection has been a critic problem for implant infections. Poly(L-lactide) (PLLA) membrane has great potential for Guided bone regeneration (GBR), however, PLLA lack antibacterial property and thus may face bacterial infections. In this work, a mussel inspired method was used to treat PLLA membrane with dopamine and formed polydopamine (PDA) coated PLLA (PLLA@PDA), and then silver Nanoparticles (AgNPs) was immobilized on the surface of PLLA *via* the reduction effect of PDA. The XPS results showed that the silver element contents may be tuned from 1.6% to 15.4%. The AgNPs coated PLLA (PLLA@Ag) showed good antibacterial property (98.3% bactericidal efficiency may be obtained) and good biocompatibility, implying that the PLLA@Ag membrane have potential application as antibacterial GBR membrane, which may enhance the application of PLLA.

Keywords: poly(L-lactide), electrospun, antibacterial, Ag nanoparticles, guided bone regeneration

INTRODUCTION

Guided bone regeneration (GBR), is a common and promising augmentation technique to regain sufficient width and height of the jawbone at oral implant sites, and has been an important surgical procedure to heal peri-implantitis defects (Lundgren et al., 1994; Wang et al., 2016; Spinell et al., 2019). A critical factor that determines the success of GBR technique is the GBR membrane, which can prevent epithelial or undesirable tissues migration into the defective area (Wang et al., 2016). Up to now, various materials, such as collagen, polytetrafluoraethylene, have been widely used as GBR membrane. Polylactic acid, an important biodegradable polymer, due to its good biocompatibility, suitable mechanical strength, and controllable degradation, has been approved by Food and Drug Administration (FDA) and used on clinic (Santoro et al., 2016; Tyler et al., 2016; Hamad et al., 2018), showing great potential as GBR membrane (Wang et al., 2016).

Bacterial infection has been a common headache in our daily life or clinics. Bacterial adhere on the surface of medical materials, resulting in infections or even failure of materials or surgery operation (Chen et al., 2016; Behzadi et al., 2017; Jensen et al., 2017; Shen et al., 2019), as for GBR technique, bacterial infection has been a major reason for failure of GBR *in vivo* (Slutzkey et al., 2015). And thus, it is definitely needed to develop an effectively antibacterial GBR membrane, which

can regain sufficient bone, and reduce bacterial infections (Shi et al., 2019; Wang et al., 2019). Recently, GBR membranes with antibacterial activity have been prepared by the addition of antimicrobial agents, such as doxycycline (Kutan et al., 2016), metronidazole (Xue et al., 2014a; Xue et al., 2014b), chlorhexidine (Qian et al., 2018), and so on, showing great potential for bone regeneration. However, antimicrobial resistance has limited the applications of these organic antimicrobial agents, as Rams et al. Reported, 71.7% of 120 peri-implantitis patients appeared resistance to one or more antibiotics (Rams et al., 2014). Therefore, it is essential to develop GBR materials with alternative antibacterial agents.

Owing to the broad-spectrum antibacterial and few drug resistance properties, silver nanoparticles (AgNPs) have been widely used as antibacterial agent or surface coating in dental instrument, contact lenses, cardiovascular stent, implant, et al. (Le Ouay and Stellacci, 2015; Qiao et al., 2019; Shakya et al., 2019). However, during the synthesis process, toxic reducing agent are always used, which may increase the cytotoxicity or potential risk of environment pollution (Duan et al., 2015). Hence, it is essential to design a novel, ecosystem friendly way to prepare AgNPs loaded antibacterial GBR membranes.

Inspired by the adhesion property of mussel, polydopamine (PDA) has been coated onto various surfaces *via* the self-polymerization of dopamine (Lee et al., 2007; Xin et al., 2018). PDA contains many catechol, amino, and quinone groups, which can be used to connect other molecules or functional particles on PDA treated surfaces (Huang et al., 2017; Lin et al., 2017). Furthermore, due to the reduction effect of catechol groups, AgNPs can be synthesized *via* the in-situ reduce reaction of silver ion, and thus this mussel inspired method have been widely used to immobilize AgNPs on various matrix, such as cellulose paper (Islam et al., 2018), mesoporous silica (Song et al., 2018), and polymer electrospun fibers (Wang et al., 2017).

Although PLLA has showed many potential applications as GBR membrane, it is much important to prepare antibacterial PLLA, which can prevent the implant associated infections. In this work, poly(L-lactide) (PLLA) electrospun nanofibers membrane was prepared as a GBR membrane model. Mussel inspired method was used to prepare AgNPs coated PLLA membranes (PLLA@Ag), which can combine the antibacterial property of AgNPs and bioproperties of PLLA. The modified PLLA membranes showed superior antibacterial property and good biocompatibility, showing great potential for clinic application as GBR membrane.

MATERIALS AND METHODS

Materials

Poly(L-lactic acid) (HISUN Biological material co., LTD, PLLA revode 190), Dopamine Hydrochloride (purity 98%) (Aladdin Industrial Corporation), silver nitrate (Sinopharm Chemical Reagent co., LTD), Tris (hydroxymethyl) aminomethane (Sinopharm Chemical Reagent co., LTD), Tris (hydroxymethyl) aminomethane hydrochloride (AlfaAesar Chemical Reagent co., LTD), Cell Counting Kit-8 (CCK-8) (Beijing Zoman Biotechnology Co.,Ltd.), and all other materials used in this work were used as received, without further purification.

Preparation of PLLA Nanofiber Membrane

PLLA membranes were prepared *via* the electrospinning method. Briefly, PLLA was dissolved in volume ratio of 4:1 chloroform/N, N-dimethyl formamide (DMF) mixture under stirring for 24 h at room temperature to obtain a homogeneous electrospinning solution. The electrospinning using the following parameters: cylinder collector speed of 300 rpm, fixed spinning distance of 20 cm, flow rate of 1.2 ml/h, and spinning voltage for 18 KV. The obtained membranes were collected at room temperature and then dried under vacuum for at least 48 h to remove the remained solvent completely.

Preparation of AgNPs-Loaded PLLA Nanofiber Membrane (PLLA@Ag)

PLLA@Ag was prepared by a simple *in situ* reduction method. Briefly, square PLLA membranes (1 cm X 1 cm) were immersed into the 10 mL dopamine Tris-HCl buffer solution (pH = 8.5, 2mg/ml) for 24 h, followed by washing twice with water and drying under vacuum. Then these PLLA nanofiber membranes with PDA grafted on their surface (PLLA@PDA) were immersed into 10 ml silver nitrate solution (25 mmol/L) for different time intervals (1 h, 3 h, 6 h, 9 h, 24 h), washed and dried, resulting in PLLA nanofiber membrane loaded with different amount of AgNPs (PLLA@Ag). The corresponding membranes were denoted as PLLA@Ag1, PLLA@Ag3, PLLA@Ag6, PLLA@Ag9, and PLLA@Ag24.

Characterization

The morphology of electrospun membranes were observed with a field-emission scanning electron microscope (FE-SEM, JSM -6701F, JEOL, Japan). X-ray photoelectron spectrometer (XPS, ESCALAB 250, Thermo-fisher, USA) was carried out to analyse surface elements of membranes. X-ray diffractometer (XRD, D8 Focus, Bruker, Germany) was used to investigate the crystalline phase of membranes. The surface contact angle of the membranes was measured using a static contact angle meter (JC2000A, Powereach, China)

Antibacterial Activity Test

The antibacterial activity against Staphylococcus aureus (*S. aureus*) (ATCC 25586) of PLLA, PLLA@PDA, and PLLA@Ag samples was tested using agar diffusion assays as well as modified colony counting method. In agar diffusion assays, disk-shaped samples (5 mm in diameter) were prepared and sterilized through ultraviolet irradiation for 1 h (30 min each side), before placing on the cultured blood agar plates. 100 µl aliquot of approximately $3*10^8$ cfu/ml bacterial suspension was spread onto an agar plate. Disk-shaped samples were placed on agar plates (repeat three times for every sample). Then the plates were incubated for different times at 37°C. The bacterial growth on the plate was visualized directly and the diameter of the inhibition zone was measured on days 1 day, 3 days, 7 days, and 14 days.

In modified colony counting method, sections (1 cm × 1 cm) of nanofiber membrane were placed in a sterilized flask containing 100 µl of test organisms and incubated at 37°C for 4 h in a laboratory shaker at 200 rpm. After 4 h incubation, serial dilutions of the liquid were made in PBS. Dilution of 10^4, 10^5, and 10^6 were used for colony counting method. 50 µl of every dilution was spread on to the agar plate and then incubated at 37°C for 24 h. After incubation, the number of viable colonies were counted manually. The percent reduction in number of colonies in PLLA (in their different) treated sample as compared to the untreated samples gives the antibacterial activity of the treated samples.

The bactericidal efficiency of the membranes was calculated by the following formula:

$$\text{Bacteridical efficiency}\,(\%) = \frac{A - B}{A} * 100\,\%$$

where A is the average number of the colonies of untreated group and B is the average number of the colonies of the treated samples.

Cytotoxicity Test

Cell proliferation was determined using a cell counting kit (CCK-8) assay. All the nanofiber membranes were cut into squares (1 cm × 1 cm), sterilized under UV light (30 min each side), immersed in 70% ethanol for 30 min, and then washed twice with sterile PBS. The sterile membranes were incubated in 1mL Dulbecco's modified eagles medium (DMEM) for 48 h at 37°C under a 5% CO2 humidified atmosphere, and then the supernatant was filtered by Millipore® membrane to obtain the extract liquid. The extract liquid was serially diluted into 50%, 25%, 12.5%, and 6.25%, respectively.

Next, osteoblast MC3T3-E1 cells (1×10^4 cells/ml) were seeded into each well (100 µl/well) and incubated at 37°C under 5% CO_2 atmosphere for 24 h to make them proliferate and adhere on the wall. And then, 100 µl extract liquid and the corresponding dilutions were added into each well to replace the media, and cultured for 48 h. 20 µl of CCK-8 buffer was added to each well, and cells were incubated at 37°C for an additional 2 h. The absorbance was measured at λ= 450 nm on a plate reader.

Another cell line (fibroblast L929) was also used to do the same experiments according to the above the procedure.

Statistical Analysis

The obtained data were presented as mean ± SD. Statistics differences were checked by One-Way Analysis of Variance, and the significance was set at $P < 0.05$.

RESULTS AND DISCUSSION

Characterizations of Nanofiber Membranes

Electrospinning has been a versatile technique to prepare nonwoven membranes used for bone tissue engineering or bone regenerative (Ding et al., 2019; Feng et al., 2019). In this work, we firstly prepared PLLA membrane *via* electrospinning method, and then mussel inspired method was used to prepare silver coated PLLA membrane. To observe the change of electrospun fibers, SEM were used to observe the morphology of different samples. The PLLA membranes show porous structure, and the fibers surface are smooth (**Figure 1A**). When the PLLA membranes were immersed in basic dopamine solution, dopamine will self-polymerize and form polydopamine (PDA) on the surface of PLLA fibers. As shown in **Figure 1B**, the morphology of PLLA@PDA membrane are almost the same with that of PLLA (**Figure 1A**). The PDA layers have strong interaction with metal ions and can also reduce silver ion (Ag^+) to AgNPs (Wu et al., 2015; Wang et al., 2017). When PLLA@PDA was immersed in $AgNO_3$ solution, the Ag^+ will bind to PDA and be reduced to AgNPs, with the increase of reaction time, the AgNPs particle size or amount will increase. As shown in **Figure 1C**, only a few particles were anchored on the surface of PLLA fibers, when the reaction time was 3 h, much more AgNPs appeared on the surface of fibers. If the reaction time was 6 hours, it can be seen that, the surface of PLLA fibers were nearly coated with AgNPs. After 24 h, the AgNPs will aggregate heavily on the surface of PLLA fibers (**Figures 1H, I**).

To further analyze the change of surface composition of PLLA membrane, XPS measurements were carried out. The PLLA surface consist of C and O elements. When PDA were coated on the surface of PLLA fibers, a new element, N will appear, as shown in **Figure 2**, in the spectrum of PLLA@PDA, a weak peak centered at 399.0 eV was found, which was the characteristic signal of N element, strongly confirming the formation of PDA coating on PLLA fibers. When AgNPs were formed on the surface of PLLA@PDA, XPS will show signals of AgNPs, as shown in **Figure 2**, all the PLLA@Ag samples showed two individual peaks at 368.7 eV and 374.7 eV with a spin-orbit separation of 6 eV, which proves the existence of the AgNPs. According to the quantitative results of XPS, the Ag Content (At. %) of PLLA@Ag1, PLLA@Ag3, PLLA@Ag6, PLLA@Ag9, and PLLA@Ag24 membranes were 1.6%, 4.9%, 7.9%, 8.2%, and 15.4%, respectively, implying that the AgNPs' content can be easily tuned by tuning the reaction time.

The XRD patterns of various samples are shown in **Figure 3**. As for neat PLLA electrospun nanofibers membrane, a weak peak appeared at 16.6°, corresponding to (200)/(100) planes, however, PLLA is a semi-crystalline polymer, most of the fibers are in amorphous state (**Figure 3**). The XRD pattern of PLLA@PDA nanofibers has no difference with that of PLLA, suggesting that dopamine self-polymerization does not affect the structure of PLLA nanofibers. When PLLA@PDA was immersed into the solution of $AgNO_3$, Ag^+ will be quickly chelated, then the Ag^+ will be reduced to Ag^0 and formed AgNPs on the surface of PLLA fibers. As shown in the XRD patterns (**Figure 3**), new sharp peaks appear at 38.26°, 44.37°, 64.65°, and 77.61° in the patterns of all PLLA@Ag samples, and these peaks are assigned to the characteristic crystalline planes of (111), (200), (220), and (311) of the *fcc* structured Ag, correspondent with the data of

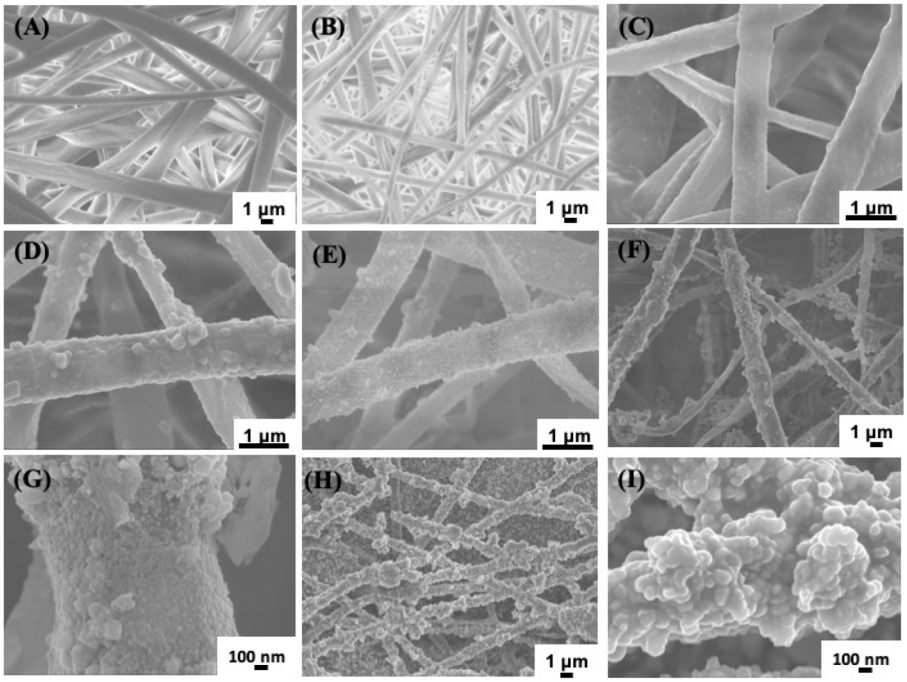

FIGURE 1 | SEM images of different samples. Poly(L-lactide) (PLLA) **(A)**, PLLA@PDA **(B)**, PLLA@Ag1 **(C)**, PLLA@Ag3 **(D)**, PLLA@Ag6 **(E)**, PLLA@Ag9 **(F**, **G)**, and PLLA@Ag 24 **(H**, **I)**.

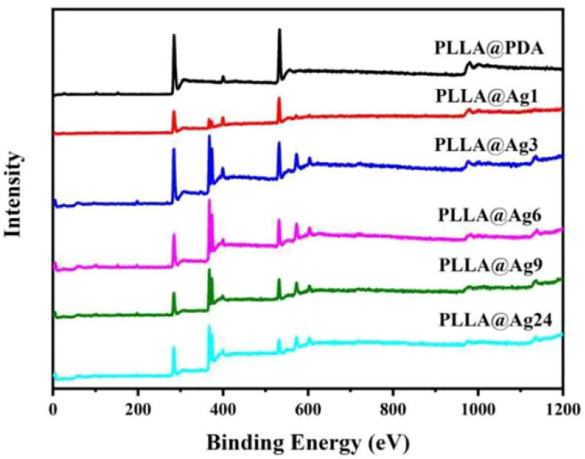

FIGURE 2 | X-ray photoelectron spectrometer (XPS) curves of poly(L-lactide) (PLLA)@PDA, PLLA@Ag1, PLLA@Ag3, PLLA@Ag6, PLLA@Ag9, PLLA@24.

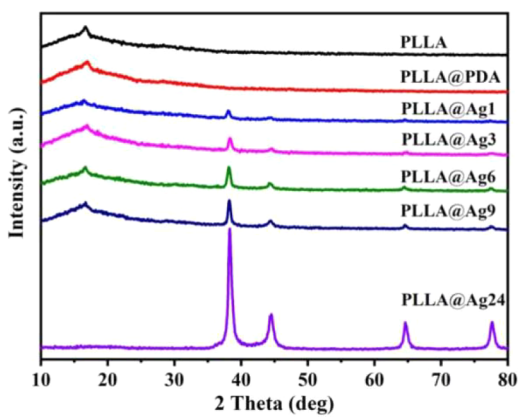

FIGURE 3 | X-ray diffractometer (XRD) patterns of poly(L-lactide) (PLLA) @PDA, PLLA@Ag1, PLLA@Ag3, PLLA@Ag6, PLLA@Ag9, PLLA@24.

JCPDS No. 04-0783 (2θ = 38.096°, 44.257°, 64.406°, and 77.452°). With the increase of reaction time (from 1hour to 24 h), the intensity of peaks increased, demonstrating that the amount of AgNPs is time-dependent. Furthermore, these results can clearly verify that it is an effective method to prepare silver coated PLLA membranes.

Antibacterial Activity

Antibacterial property is very critical for GBR membranes. Concerning the perspective of PLLA membrane used as GBR membrane, it is an valuable thing to endow PLLA membrane with antibacterial property. Due to the excellent antibacterial property of AgNPs, the prepared PLLA@Ag must have antibacterial property. Up to now, many researches have proved that AgNPs or AgNPs coated materials showed

excellent antibacterials to both the Gram-positive *S. aureus* and Gram-negative *E. coli* (Wu et al., 2015; Wang et al., 2017). On considering that *S. aureus* is an important bacterial related with stomatologic problem, such as maxillofacial infections and peri-implantitis (Persson and Renvert, 2014), and thus in this work, *S.aureus* was selected as the bacterial representative to assess the antibacterial activity *via* observation the growth of *S. aureus* on the agar plate. As shown in **Figure 4A**, Bacterial inhibition zones are clearly observed around PLLA@Ag membrane (PLLA@Ag 24 was used in **Figure 4A**), whereas, PLLA and PLLA@PDA did not show any inhibition zone (**Figure 4A** a, b). **Figures 4B–F** showed the bacterial inhibition effect of PLLA@Ag1, PLLA@Ag3, PLLA@Ag6, PLLA@Ag9, and PLLA@Ag24, respectively, and the results clearly showed that the prepared PLLA@Ag have effective antibacterial effect. PLLA@Ag1 membrane presented only 7.19 ± 0.18 mm diameter and kept less than 7 days (**Table 1**). By contrast, all the other PLLA@Ag membranes showed much better antibacterial activity. It is worth mentioning that the inhibition zones are still obvious even after 14 days except the results for PLLA@Ag1. However, from the results of PLLA@Ag3,

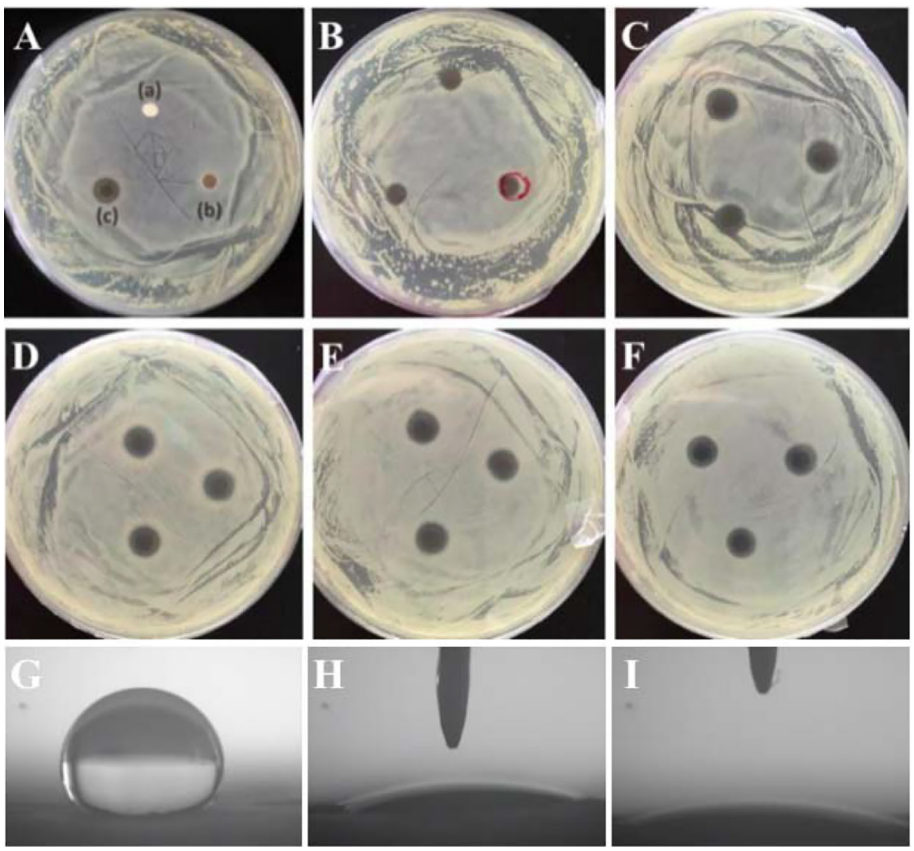

FIGURE 4 | (A–F) showed the antibacterial activity of electrospun membranes against *S. aureus*. poly(L-lactide) (PLLA) (A-a), PLLA@PDA (A-b), PLLA@Ag24 (A-c). **(B–F)** are the corresponding results of PLLA@Ag1 **(B)**, PLLA@Ag3 **(C)**, PLLA@Ag6 **(D)**, PLLA@Ag9 **(E)**, and PLLA@Ag24 **(F)**, respectively. **(G–I)** are the contact angle images of PLLA, PLLA@PDA and PLLA@Ag 24, respectively.

TABLE 1 | The average diameter of inhibition zone and bactericidal efficiency of different samples.

Sample	Inhibition zone diameter (mm)				Bactericidal efficiency (%)
	1 day	3 days	7 days	14 days	
PLLA@Ag1	7.19 ± 0.18	7.13 ± 0.11*	0	0	32
PLLA@Ag3	8.84 ± 0.34	8.45 ± 0.27	8.42 ± 0.19	8.59 ± 0.37	97.9
PLLA@Ag6	9.07 ± 0.21	8.93 ± 0.21	8.97 ± 0.04	8.93 ± 0.13	98.3
PLLA@Ag9	8.92 ± 0.22	8.72 ± 0.06	8.54 ± 0.12	8.96 ± 0.17	96.6
PLLA@Ag24	9.50 ± 0.09	8.97 ± 0.07	9.02 ± 0.06	8.61 ± 0.16	97.0

PLLA@Ag6, PLLA@Ag9, and PLLA@Ag24, the increase of AgNPs amount did not result in higher inhibition zones (**Figures 4C–F**), while this was consistent with bactericidal efficiency results calculated from the modified colonies counting tests (**Table 1**). All the bactericidal efficiency of PLLA@Ag membranes were more than 95% against the targeted bacteria, except PLLA@Ag1 membranes (only 32%). Hence, it can be concluded that the incorporation of AgNPs endowed PLLA membrane antibacterial property.

Although the mechanism for AgNPs antimicrobial activity is still controversial, it is no doubt that the presence of AgNPs could act as Ag^+ reservoir, and provide continuously a high enough concentration of silver species in their surroundings to maintain its antibacterial activity for several days (Le Ouay and Stellacci, 2015). Herein, because of the strong interactions between AgNPs and PDA coating, the AgNPs would not easily detached from the PLLA matrix, and thus the prepared PLLA@Ag can have a long-time antibacterial activity.

Up to now, commercial polylactide membrane (including PLLA and PDLLA) and their blend with other polymers or functional agents have been used as GBR membrane in clinic (Wang et al., 2016), however, the bacterial infections have been a challenge for commercial GBR membrane. And thus, the prepared PLLA@Ag membrane showed some advantages over the pure PLLA membrane. Furthermore, the surface of materials may have great affection on their properties, many methods have been designed to modify polymer membranes used as GBR membrane, such as antibiotic coating, polymer coatings (Florjanski et al., 2019). In this work, we prepared AgNPs coated PLLA membrane *via* a mild mussel inspired method, the most important results maybe endowing the antibacterial properties to PLLA. Besides, the surface wettability were also improved, as shown in **Figure 4**, the surface of PLLA membrane was hydrophobic (**Figure 4G**), while PLLA@PDA (**Figure 4H**) and PLLA@Ag24 (**Figure 4I**) are hydrophilic. In addition, the PDA may also promote the biomineralization of hydroxyapatite. And thus, compared with the PLLA membrane, the PLLA@Ag membrane have many advantages. However, the potential *in vivo* toxicity of PLLA@Ag should be further investigated.

Cytotoxicity Test

PLLA is a biocompatible polymer, while PDA is also biocompatible, and thus the PDA coated PLLA fiber membrane also showed low toxicity. As shown in **Figures 5A, B**, the cell viability of both MC3T3 and L929 cell line treated with different amount of PLLA@PDA are much better, with a cell viability more than 100%. Generally, AgNPs showed low toxicity and have been widely used as antibacterial agent. When AgNPs were immobilized on the surface of PLLA@PDA fibers, it can combine the biocompatibility of PLLA@PDA and antibacterial property of AgNPs, and thus PLLA@Ag can work as antibacterial GBR membrane. Besides, the biocompatibility of PLLA@Ag is an important factor that determines the application of PLLA@Ag. As shown in **Figure 5**, the cell viability of MC3T3 on PLLA@Ag1 and PLLA@Ag3 are about 120%, respectively, however, with the increase of AgNPs amount, the samples will show toxicity. For example, the MC3T3 cell viability of PLLA@Ag6, PLLA@Ag9, and PLLA@Ag24 membranes were lower than that of PLLA@Ag1 and PLLA@Ag2 (**Figure 5A**). To further test the biocompatibility of PLLA@Ag membrane, L929 cells were used, it is interesting to find that almost all the nanofiber membranes presented good cytocompatibility on L929 (**Figure 5B**). However, when the sample concentration was too high, for example, when 100% extract were used, the cell viability of PLLA@Ag24 was only 53.32% (**Figure 5B**), much lower than that of other samples. From results in **Figure 5**, it can be concluded that the biocompatibility of PLLA@AgNPs membrane are very good, the samples prepared in this work may have potential application as GBR membrane.

CONCLUSIONS

In this work, AgNPs was immobilized on the surface of PLLA nanofibers *via* the simple mussel inspired method to obtain antibacterial PLLA nanocomposites (PLLA@Ag). The *in vitro* test showed that the PLLA@Ag have excellent antibacterial property, more interestingly, the PLLA@Ag can have long term antibacterial effect, even after 2 weeks, the prepared sample can

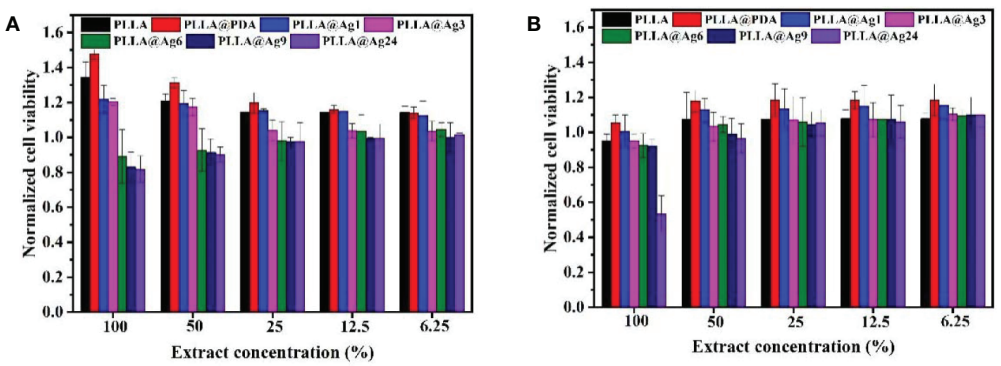

FIGURE 5 | Cell viability of different samples against MC3T3 Cells **(A)** and L929 Cells **(B)**.

still prevent the growth of bacterial. The cytotoxcity test showed that the PLLA@Ag sample showed little toxicity, when MC3T3 cell was used, all the samples showed a little toxicity when compared with PLLA. However, when L929 cells were used, the samples showed comparable biocompatibility with PLLA.

The method used in this work was simple and versatile, and may be used to immobilize AgNPs on other materials, besides, due to the various *in vivo* application of PLLA, such as GBR membrane, the PLLA@Ag may also have broad applications as implants that can prevent infections.

DATA AVAILABILITY STATEMENT

The datasets generated for this study are available on request to the corresponding authors.

AUTHOR CONTRIBUTIONS

JWe and LL proposed this project. JWa prepared all the materials. LZ carried out the antibacterial test and cytotoxicity test. XZ and RW help to analyze the results. JWa and JWe wrote the manuscript. JWa and LZ have the same contribution to this work.

FUNDING

This research was funded by the National Natural Science Foundation of China (Nos. 51663017 and 81660444), Jiangxi Key Research and Development Program (NO.20181BBG78014), Natural Science Foundation of Jiangxi Province (NO.20171BAB205050).

REFERENCES

Behzadi, S., Luther, G. A., Harris, M. B., Farokhzad, O. C., and Mahmoudi, M. (2017). Nanomedicine for safe healing of bone trauma: Opportunities and challenges. *Biomaterials* 146, 168–182. doi: 10.1016/j.biomaterials.2017.09.005

Chen, Z., Klein, T., Murray, R. Z., Crawford, R., Chang, J., Wu, C., et al. (2016). Osteoimmunomodulation for the development of advanced bone biomaterials. *Mater. Today* 19, 304–321. doi: 10.1016/j.mattod.2015.11.004

Ding, J., Zhang, J., Li, J., Li, D., Xiao, C., Xiao, H., et al. (2019). Electrospun polymer biomaterials. *Prog. Polym. Sci.* 90, 1–34. doi: 10.1016/j.progpolymsci.2019.01.002

Duan, H., Wang, D., and Li, Y. (2015). Green chemistry for nanoparticle synthesis. *Chem. Soc Rev.* 44, 5778–5792. doi: 10.1039/C4CS00363B

Feng, X., Li, J., Zhang, X., Liu, T., Ding, J., and Chen, X. (2019). Electrospun polymer micro/nanofibers as pharmaceutical repositories for healthcare. *J. Controlled Rel.* 302, 19–41. doi: 10.1016/j.jconrel.2019.03.020

Florjanski, W., Orzeszek, S., Olchowy, A., Grychowska, N., Wieckiewicz, W., Malysa, A., et al. (2019). Modifications of Polymeric Membranes Used in Guided Tissue and Bone Regeneration. *Polymers* 11 (5), 782. doi: 10.3390/polym11050782

Hamad, K., Kaseem, M., Ayyoob, M., Joo, J., and Deri, F. (2018). Polylactic acid blends: The future of green, light and tough. *Prog. Polym. Sci.* 85, 83–127. doi: 10.1016/j.progpolymsci.2018.07.001

Huang, J., Xu, Y., Xiao, Y., Zhu, H., Wei, J., and Chen, Y. (2017). Mussel-Inspired, Biomimetics-Assisted Self-Assembly of Co3O4 on Carbon Fibers for Flexible Supercapacitors. *Chemelectrochem* 4 (9), 2269–2277. doi: 10.1002/celc.201700369

Islam, M. S., Akter, N., Rahman, M. M., Shi, C., Islam, M. T., Zeng, H. B., et al. (2018). Mussel-Inspired Immobilization of Silver Nanoparticles toward Antimicrobial Cellulose Paper. *ACS Sustain. Chem. Eng.* 6 (7), 9178–9188. doi: 10.1021/acssuschemeng.8b01523

Jensen, L. K., Koch, J., Aalbæk, B., Moodley, A., Bjarnsholt, T., Kragh, K. N., et al. (2017). Early implant-associated osteomyelitis results in a peri-implanted bacterial reservoir. *APMIS* 125, 38–45. doi: 10.1111/apm.12597

Kutan, E., Duygu-Capar, G., Ozcakir-Tomruk, C., Dilek, O. C., Ozen, F., Erodogan, O., et al. (2016). Efficacy of doxycycline release collagen membrane on surgically created and contaminated defects in rat tibiae: A histopathological and microbiological study. *Arch. Biol.* 63, 15–21. doi: 10.1016/j.archoralbio.2015.11.001

Le Ouay, B., and Stellacci, F. (2015). Antibacterial activity of silver nanoparticles: A surface science insight. *Nano Today* 10, 339–354. doi: 10.1016/j.nantod.2015.04.002

Lee, H., Dellatore, S. M., Miller, W. M., and Messersmith, P. B. (2007). Mussel-Inspired Surface Chemistry for Multifunctional Coatings. *Science* 318 (5849), 426–430. doi: 10.1126/science.1147241

Lin, J., Ding, J., Dai, Y., Wang, X., Wei, J., and Chen, Y. (2017). Antibacterial zinc oxide hybrid with gelatin coating. *Mater. Sci. Eng. C Mater. Biol. Appl.* 81, 321–326. doi: 10.1016/j.msec.2017.08.009

Lundgren, D., Sennerby, L., Falk, H., Friberg, B., and Nyman, S. (1994). The use of a new bioresorbable barrier for guided bone regeneration in connection with implant installation. Case reports. *Clin. Implants Res.* 5, 177–184. doi: 10.1034/j.1600-0501.1994.050309.x

Persson, G. R., and Renvert, S. (2014). Cluster of Bacteria Associated with Peri-Implantitis. *Clin. Implant Dentistry Related Res.* 16 (6), 783–793. doi: 10.1111/cid.12052

Qian, Y., Zhou, X., Sun, H., Yang, J., Chen, Y., Li, C., et al. (2018). Biomimetic Domain-Active Electrospun Scaffolds Facilitating Bone Regeneration Synergistically with Antibacterial Efficacy for Bone Defects. *ACS Appl. Mater. Interf.* 10, 3248–3259. doi: 10.1021/acsami.7b14524

Qiao, Z., Yao, Y., Song, S., Yin, M., and Luo, J. (2019). Silver nanoparticles with pH induced surface charge switchable properties for antibacterial and antibiofilm applications. *J. Mater. Chem. B* 7, 830–840. doi: 10.1039/C8TB02917B

Rams, T. E., Degener, J. E., and van Winkelhoff, A. J. (2014). Antibiotic resistance in human peri-implantitis microbiota. *Clin. Implants Res.* 25, 82–90. doi: 10.1111/clr.12160

Santoro, M., Shah, S. R., Walker, J. L., and Mikos, A. G. (2016). Poly(lactic acid) nanofibrous scaffolds for tissue engineering. *Adv. Drug Deliv. Rev.* 107, 206–212. doi: 10.1016/j.addr.2016.04.019

Shakya, S., He, Y., Ren, X., Guo, T., Maharjan, A., Luo, T., et al. (2019). Ultrafine Silver Nanoparticles Embedded in Cyclodextrin Metal-Organic Frameworks with GRGDS Functionalization to Promote Antibacterial and Wound Healing Application. *Small* 15, 1901065. doi: 10.1002/smll.201901065

Shen, X., Zhang, Y., Ma, P., Sutrisno, L., Luo, Z., Hu, Y., et al. (2019). Fabrication of magnesium/zinc-metal organic framework on titanium implants to inhibit bacterial infection and promote bone regeneration. *Biomaterials* 212, 1–16. doi: 10.1016/j.biomaterials.2019.05.008

Shi, R., Ye, J., Li, W., Zhang, J., Li, J., Wu, C., et al. (2019). Infection-responsive electrospun nanofiber mat for antibacterial guided tissue regeneration membrane. *Mater. Sci. Eng. C Mater. Biol. Appl.* 100, 523–534. doi: 10.1016/j.msec.2019.03.039

Slutzkey, S., Kozlovsky, A., Artzi, Z., and Matalon, S. (2015). Collagen barrier membranes may accelerate bacterial growth in vitro: A potential clinical risk to regenerative procedures. *Quintessence Int.* 46, 43–50. doi: 10.3290/j.qi.a32821

Song, Y., Jiang, H., Wang, B., Kong, Y., and Chen, J. (2018). Silver-Incorporated Mussel-Inspired Polydopamine Coatings on Mesoporous Silica as an Efficient Nanocatalyst and Antimicrobial Agent. *ACS Appl. Mater. Interf.* 10 (2), 1792–1801. doi: 10.1021/acsami.7b18136

Spinell, T., Saliter, J., Hackl, B., Unger, K., Hickel, R., and Folwaczny, M. (2019). In-vitro cytocompatibility and growth factor content of GBR/GTR membranes. *Dent. Mater.* 35, 963–969. doi: 10.1016/j.dental.2019.03.011

Tyler, B., Gullotti, D., Mangraviti, A., Utsuki, T., and Brem, H. (2016). Polylactic acid (PLA) controlled delivery carriers for biomedical applications. *Adv. Drug Deliv. Rev.* 107, 163–175. doi: 10.1016/j.addr.2016.06.018

Wang, J., Wang, L., Zhou, Z., Lai, H., Xu, P., Liao, L., et al. (2016). Biodegradable Polymer Membranes Applied in Guided Bone/Tissue Regeneration: A Review. *Polymers* 8, 115. doi: 10.3390/polym8040115

Wang, J., Wang, L., Zhou, Z., Liao, L., Wang, X., Wei, J., et al. (2017). Preparation of silver coated poly(L-lactide) nanofiber membranes via the combination of mussel-inspired approach and layer-by-layer assembly method. *J. Controlled Rel.* 259, E62–E62. doi: 10.1016/j.jconrel.2017.03.144

Wang, Y., Jiang, Y., Zhang, Y., Wen, S., Wang, Y., and Zhang, H. (2019). Dual functional electrospun core-shell nanofibers for anti-infective guided bone regeneration membranes. *Mater. Sci. Eng. C Mater. Biol. Appl.* 98, 134–139. doi: 10.1016/j.msec.2018.12.115

Wu, C., Zhang, G., Xia, T., Li, Z., Zhao, K., Deng, Z., et al. (2015). Bioinspired synthesis of polydopamine/Ag nanocomposite particles with antibacterial activities. *Mater. Sci. Eng. C Mater. Biol. Appl.* 55, 155–165. doi: 10.1016/j.msec.2015.05.032

Xin, X., Li, P., Zhu, Y., Shi, L., Yuan, J., and Shen, J. (2018). Mussel-Inspired Surface Functionalization of PET with Zwitterions and Silver Nanoparticles for the Dual-Enhanced Antifouling and Antibacterial Properties. *Langmuir* 35 (5), 1788–1797. doi: 10.1021/acs.langmuir.8b01603

Xue, J., He, M., Liu, H., Niu, Y., Crawford, A., Coates, P. D., et al. (2014a). Drug loaded homogeneous electrospun PCL/gelatin hybrid nanofiber structures for anti-infective tissue regeneration membranes. *Biomaterials* 35, 9395–9405. doi: 10.1016/j.biomaterials.2014.07.060

Xue, J., He, M., Niu, Y., Liu, H., Crawford, A., Coates, P., et al. (2014b). Preparation and in vivo efficient anti-infection property of GTR/GBR implant made by metronidazole loaded electrospun polycaprolactone nanofiber membrane. *Int. J. Pharm.* 475, 566–577. doi: 10.1016/j.ijpharm.2014.09.026

Conflict of Interest: The authors declare that the research was conducted in the absence of any commercial or financial relationships that could be construed as a potential conflict of interest.

frontiers in Pharmacology

ORIGINAL RESEARCH
published: 30 April 2020
doi: 10.3389/fphar.2020.00558

Enhanced Anti-Glioma Efficacy by Borneol Combined With CGKRK-Modified Paclitaxel Self-Assembled Redox-Sensitive Nanoparticles

Lingyan Lv[1,2†], Xinrui Li[2,3†], Wei Qian[4†], Shennan Li[2], Yan Jiang[2], Yaokun Xiong[5], Jianpei Xu[2], Wei Lv[1], Xiaoyan Liu[1], Yun Chen[2], Yulin Tang[3*] and Hongliang Xin[2*]*

[1] Department of Pharmacy, The Affiliated Jiangyin Hospital of Southeast University Medical College, Jiangyin, China, [2] School of Pharmacy, Nanjing Medical University, Nanjing, China, [3] Department of Pharmacy, Sir Run Run Hospital, Nanjing Medical University, Nanjing, China, [4] Department of Pharmacy, Zhangjiagang Hospital of Traditional Chinese Medicine, Affiliated Nanjing University of Chinese Medicine, Zhangjiagang, China, [5] School of Pharmacy, Jiangxi University of Traditional Chinese Medicine, Nanchang, China

The serious therapeutic obstacles to glioma treatment include poor penetration across the blood-brain barrier (BBB) and low accumulation of therapeutic drugs at tumor sites. In this study, borneol combined with CGKRK peptide (a ligand of the heparan sulfate which overexpress on the glioma cells) modified paclitaxel prodrug self-assembled redox-responsive nanoparticles (CGKRK-PSNPs) were hypothesized to enhance the BBB penetration ability and active tumor targeting efficiency, respectively. The resulting CGKRK-PSNPs possessed a spherical shape with a small particle size (105.61 ± 1.53 nm) and high drug loading for PTX (54.18 ± 1.13%). The drug release behavior proved that CGKRK-PSNPs were highly sensitive to glutathione (GSH) redox environment. The *in vitro* cell experiments suggested that CGKRK-PSNPs significantly increased the cellular uptake and cytotoxicity of U87MG cells, meanwhile CGKRK-PSNPs showed the low cytotoxicity against BCEC cells. Combined with borneol, CGKRK-PSNPs exhibited enhanced transportation across *in vitro* BBB model. In intracranial U87MG glioma-bearing nude mice, the higher accumulation of CGKRK-PSNPs combined with borneol was observed through real-time fluorescence image. Moreover, the *in vivo* anti-glioma results confirmed that CGKRK-PSNPs combined with borneol could improve the anti-glioma efficacy with the prolonged medium survival time (39 days). In conclusion, the collaborative strategy of CGKRK-PSNPs combined with borneol provided a promising drug delivery routine for glioblastoma therapy.

OPEN ACCESS

Edited by:
Chao Wang,
Soochow University, China

Reviewed by:
Zhaowei Chen,
Fuzhou University, China
Wei Wang,
China Pharmaceutical University, China
Huile Gao,
Sichuan University, China

***Correspondence:**
Yun Chen
ychen@njmu.edu.cn
Yulin Tang
ylt1964@sina.com
Hongliang Xin
xhl@njmu.edu.cn

†These authors have contributed equally to this work

Specialty section:
This article was submitted to Experimental Pharmacology and Drug Discovery, a section of the journal Frontiers in Pharmacology

Received: *29 February 2020*
Accepted: *14 April 2020*
Published: *30 April 2020*

Citation:
Lv L, Li X, Qian W, Li S, Jiang Y, Xiong Y, Xu J, Lv W, Liu X, Chen Y, Tang Y and Xin H (2020) Enhanced Anti-Glioma Efficacy by Borneol Combined With CGKRK-Modified Paclitaxel Self-Assembled Redox-Sensitive Nanoparticles. Front. Pharmacol. 11:558. doi: 10.3389/fphar.2020.00558

Keywords: borneol, blood-brain barrier penetration, paclitaxel, redox-responsive nanoparticles, CGKRK peptide

INTRODUCTION

Glioblastoma multiforme (GBM) is the most common and malignant tumor in glioma. It accounts for 50% of primary gliomas in adults with only a 10% probability of 5 years survival (Sasmita et al., 2018). Despite aggressive surgery, radiotherapy, and chemotherapy, the prognosis of GBM has not improved significantly in recent years. The blood-brain barrier (BBB) and blood-brain tumor barrier (BBTB) act as two physical barriers to prevent most chemotherapeutic drugs entering into the brain, which restrict chemotherapy effects (Jain, 2018). In the past few decades, targeted drug delivery vehicles, such as nanoparticle, liposome, and dendrimer, have revolutionized the diagnosis and treatment of glioma (Li and Xie, 2017). However, these nanocarriers still have some drawbacks limiting the clinical applications, for example, the low drug loading, premature release of drug into the blood circulation, without active targeting, and poor permeability to cross the BBB (Hernández-Pedro et al., 2013). The utilization of natural cells as vehicles to encapsulate therapeutic cargoes for drug delivery applications has achieved some progress (Chen et al., 2020). Overall, multidisciplinary technology should be taken together to promote the development of advanced drug delivery systems for cancer therapy (Gao, 2017; Qian et al., 2018).

Borneol (Bor) is widely used in traditional Chinese medicine, which can assist other drugs enter the brain. Studies have reported that Bor could open the intercellular tight junctions and improve the permeation of drugs across the BBB, therefore enhance their concentration in the brain (Guo et al., 2019; Meng et al., 2019). However, there is a great risk for anti-glioma drugs because they will cause serious side effects to normal brain tissue due to lacking of active targeting ability (Han et al., 2018).

CGKRK peptide, which was discovered using *in vivo* phage display technique, was demonstrated it could target tumor cells and tumor neovascular through binding to the specific receptor heparan sulfate (Lv et al., 2016; Griffin et al., 2017; Zhang et al., 2019). It was reported that CGKRK peptide could specifically target tumor vasculature in high-grade glioma and not to normal vessels (Treps, 2018). Agemy et al. (2013) have demonstrated that CGKRK peptide could effectively penetrate tumor cells and tumor blood vessel endothelial cells.

In order to realize precise release of drugs at tumor sites and reduce toxicity to normal brain tissue, tumor microenvironment-responsive drug delivery systems have been arisen widespread attention (for example ROS, pH, redox, and lysosomal enzymes) (Song et al., 2017; Tao and He, 2018; Zhang et al., 2018). The redox-responsive drug carrier is connected by disulfide bond between the carrier and drug molecule, or formed by two block copolymers linked by disulfide bond with drug molecule self-assemble in solvent (Raza et al., 2018). Studies have demonstrated that the disulfide bond is very stable under normal physiological conditions, but it can be cleaved into thiols by GSH (Han et al., 2019; Yu et al., 2020). The concentration of GSH in cancerous cells is about 1,000 times higher than in plasma (Tian et al., 2018; Zhu et al., 2018), and is several times higher than that in normal cells (Liu et al., 2011). In addition, tumor tissue is more reductive than normal tissue due to hypoxia. Therefore, disulfide bond is widely used in GSH trigger system. Our group have studied disulfide bond paclitaxel prodrug (PTX-SS-C_{18}) conjugate self-assembled nanoparticles (PSNPs) used as "carrier-free" system to accurately triggered-release PTX in tumor cells by the intracellular GSH (Jiang et al., 2017).

In this study, we integrated the Bor as a "guide" drug to open the BBB with CGKRK modified PTX-SS-C_{18} conjugate self-assembled active targeted nanoparticles to enhance the anti-glioma efficacy. As shown in **Figure 1**, Bor was intragastrically administrated for 0.5 h in advance to open the tight junctions of BBB reversibly. Then CGKRK-PSNPs were injected *via* tail vein and penetrated across the BBB to accumulate at tumor sites with the assistance of Bor and active glioma target ability. Lastly, CGKRK-PSNPs could be internalized into glioma cells through heparan sulfate-mediated endocytosis, and the PTX was responsively released to the intracellular GSH. The morphology, particle size, and drug release kinetics of CGKRK-PSNPs *in vitro* were all characterized. In addition, cellular uptake and cytotoxic assay were investigated in both BCEC and U87MG cells. Meanwhile, the effect of Bor was evaluated using BBB model *in vitro*. Finally, the intracranial glioma mice model was established to study glioma targeting and anti-glioma efficacy of CGKRK-PSNPs combined with Bor *in vivo*.

MATERIALS AND METHODS

Materials

Paclitaxel (purity > 99.9%) was purchased from Zelang Medical Technology Co., Ltd. (Nanjing, China). DiR (1,1′-dioctadecyl-3,3,3′,3′-tetramethyl indotricarbocyanine iodide) (purity > 95.0%), Dithiodiglycolic acid (purity > 96.0%), 1-Octadecanol (purity > 99.0%), Glutathione(purity > 98.0%) and were obtained from Aladdin Reagent Database Inc. (Shanghai, China). CGKRK peptides (purity > 95%) were purchased from GL Biochem Co., Ltd. (Shanghai, China), Maleimide-PEG2000-DSPE (purity > 99%) and MeO-PEG2000-DSPE (purity > 99%) were purchased from Avanti Polar Lipids, Inc. (Alabama, USA). Bor (purity > 97.0%), glutathione-reduced ethyl ester (purity > 90.0%), and Coumarin-6 (purity ≥ 99%) were provided by Sigma-Aldrich (St. Louis, MO, USA). 3-(4, 5-Dimethylthiazol-2-yl)-2, 5-diphenyltetrazolium bromide (MTT) (purity >99%) and BCA kit were purchased from Beyotime Biotechnology Co., Ltd. (Nantong, China). Penicillin-streptomycin, DMEM medium, fetal bovine serum (FBS), and 0.25% (w/v) trypsin solution were purchased from Gibco BRL (MD, USA). The other chemical reagents were of analytical grade and used as received.

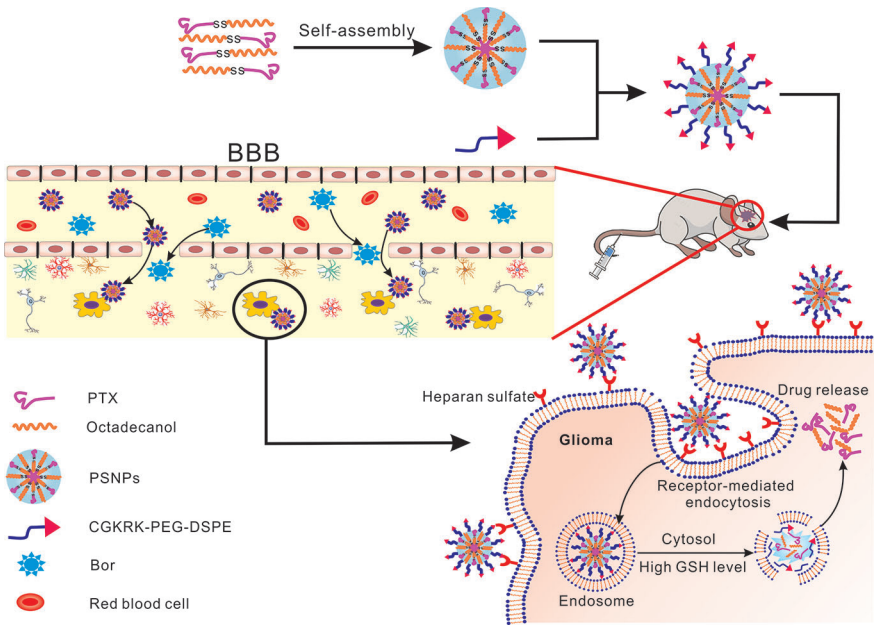

FIGURE 1 | Schematic of borneol combined with CGKRK modified PTX-SS-C_{18} conjugate self-assembled targeted nanoparticles (CGKRK-PSNPs) for glioma treatment.

Preparation and Characterization of CGKRK-PSNPs

CGKRK-PEG-DSPE was synthesized and characterized as follows. Briefly, 10 mg of CGKRK peptide and 4 mg of Mal-PEG_{2000}-DSPE were dissolved in 1 ml of PB (0.2 M, pH 7.4) buffer and 1 ml of DMF, respectively. Both of the abovementioned solution were dripped slowly into 8 ml of PB buffer to react with magnetic stirring under nitrogen. The excessive unreacted CGKRK peptide and DMF were removed through dialysis (MWCO 1.0 kDa) against distilled water. Finally, the solution was freeze-dried to obtain CGKRK-PEG-DSPE, which was characterized by ^{1}H NMR.

PTX-SS-C_{18}, PSNPs, and PEG-PSNPs were synthesized and characterized by previously described method (Jiang et al., 2017). The chemical reaction processes of PTX-SS-C_{18} were shown in **Figure S1**. CGKRK-PSNPs were prepared using ethanol injection method. In brief, 5 mg of PTX-SS-C_{18} was dissolved in 500 μl of anhydrous ethanol and then injected into 10 ml distilled water containing 1 mg CGKRK-PEG-DSPE under 650 rpm stirring for 5 min. After evaporating ethanol at 60°C with a vacuum rotary evaporator, the self-assemble CGKRK-PSNPs were filtrated through 0.45 and 0.22 μm microporous membrane, respectively.

For coumarin-6 or DiR-labeled nanoparticles, both coumarin-6 and DiR were dissolved in anhydrous ethanol using the same method as above.

Transmission electronic microscopy (TEM) (JEOL USA, Wilmington, DE, USA) was used to observe the morphology of nanoparticles. Dynamic light scattering (DLS) (Zs90, Malvern, U.K.) was applied to characterize the particle size and zeta potential of nanoparticles.

In Vitro Reduction-Triggered Drug Release

The *in vitro* release profile of PTX from CGKRK-PSNPs was performed by ultrafiltration centrifugation method. First, PEG-PSNPs and CGKRK-PSNPs were diluted to 4 ml release media, which containing 30 μg of PTX to achieve sink condition. The release medium were phosphate buffer saline (PBS) solutions at pH 7.4 with 1 μM GSH and HAc-NaAc buffer at pH 5.0 with 10 mM GSH containing 0.5% (w/v) Tween-80. The mixtures were kept in 10-ml tubes shaking with a speed of 150 rpm at 37°C. At predetermined time points, the solutions were immediately transferred to ultrafiltration centrifuge tube (MWCO = 30 kDa), centrifuging at 4,000 rpm for 10 min to obtain free PTX. Taking filtrate to measure the concentration of PTX by HPLC analysis.

In Vitro Cellular Uptake

The cellular uptake of PEG-PSNPs and CGKRK-PSNPs was detected qualitatively using fluorescent microscopy. The U87MG cells were implanted at 5×10^4 cells/well in a 24-well plate. After incubation for 24 h, the cells were exposed to coumarin-6-labeled nanoparticles at the coumarin-6 concentrations of 5, 10, and 30 ng/ml for 1 h at 37°C and 4°C, respectively. Afterward, the cells were rinsed with cold PBS thrice and immobilized with 4% formaldehyde for 15 min. Finally, the samples were observed and photographed with fluorescent microscopy (Imager A1, Zeiss, Germany).

HPLC analysis was utilized to further investigate quantitative cell uptake of nanoparticles in U87MG cells. 1×10^5 of U87MG cells per well were inoculated in a 24-well plate. After 24 h, the cells were incubated with PEG-PSNPs and CGKRK-PSNPs at PTX concentrations ranged from 10 to 100 μg/ml for 1 h at 37°C or 4°C, respectively. After washed with cold PBS, the cells were lysed by 400 μl of 1% TritonX-100 per well, and then shook for

10 min. Next, the samples were centrifuged at 8000 rpm for 10 min. In order to determine the total cell protein content, an aliquot of the cell lysate from each well was analyzed using BCA protein assay. The PTX concentration of each well was measured by HPLC.

For the competition assay, after 24 h of cell culture, CGKRK peptide was added to the wells at a concentration of 200 μg/ml at 37°C for 30 min. Next, the cells were washed twice with PBS, and then added the media containing coumarin-6-labeled CGKRK-PSNPs or CGKRK-PSNPs, followed the preceding steps for both qualitative and quantitative assays.

In Vitro Cytotoxicity

The MTT assay was used to evaluate the cytotoxicity of PEG-PSNPs and CGKRK-PSNPs in U87MG and BCEC cells. First, 5×10^3 cells/well of U87MG and BCEC cells were cultured in the 96-well plate for 24 h. Then, the cells were treated with Taxol®, PEG-PSNPs and CGKRK-PSNPs at different PTX concentration (0.01, 0.1, 1, 5, 10 μg/ml), respectively. After 48 h, 20 μl/well of MTT (5 mg/ml) reagents were added to incubate another 4 h. Subsequently, the mixture was removed, and each well was supplemented with 200 μl of DMSO shaking in the darkness for 10 min to dissolve formazan crystals completely. Finally, the cell viability was measured using a microplate reader (Thermo Multiskan MK3, USA) with the excitation wavelength at 490 nm.

In order to verify the redox response of drug release of PSNPs in cells, the U87MG and BCEC cells were seeded as described above and pretreated with or without 10 mM glutathione monoester (GSH-OEt). After incubation for 2 h at 37°C, the cells were washed twice with PBS to remove extracellular residual GSH-OEt, and then 1 and 5 μg/ml of different PTX formulations were added into the cells for 48 h. U87MG and BCEC cells without GSH-OEt pretreatment were used as the control, respectively. The cell cytotoxicity was evaluated by the MTT method.

BBB Penetration *In Vitro*

BCEC cell monolayer was used to establish the BBB model *in vitro*. In briefly, 1×10^5 BCEC cells were seeded into transwell filters with the polycarbonate membrane of 3 μm pore size for 10 days. The BBB transport model was evaluated by measuring transepithelial electrical resistance (TEER) value. Afterward, 200 μl of coumarin-6-labeled PEG-PSNPs and CGKRK-PSNPs with or without Bor (10 μg/ml) were added into upper compartment, respectively. After incubation for 0.5, 1, 1.5, 2, 2.5, 3, and 4 h, 200-μl samples were taken from basal chamber and supplied with the equal volume of culture medium. The coumarin-6 concentration of sample was determined using microplate reader of multi-wavelength.

In Vivo Imaging Analysis

Four to 5 weeks male Balb/c nude mice weighing approximately 20 g were obtained from BK Lab Animal Ltd. (Shanghai, China). All animal experiments were approved by the laboratory animal ethics committee of Nanjing Medical University. The operational procedures were performed according to protocols evaluated.

The real-time fluorescence imaging analysis was used to evaluate the biodistribution of CGKRK-PSNPs *in vivo*. Intracranial U87MG tumor-bearing mice were established as described previously (Xin et al., 2011; Wang et al., 2014). After 18 days, the glioma-bearing mice were randomly dived into 4 groups. The mice in groups 2 and 4 were given 100 μl of DiR-labeled PEG-PSNPs and CGKRK-PSNPs *via* tail vein, respectively. For groups 1 and 3, besides PEG-PSNPs and CGKRK-PSNPs, 25 mg/kg Bor solution was administrated intragastrically before 0.5 h. Next, the mice were scanned using an *in vivo* imaging system (Caliper, USA) at 4 h to acquire the fluorescent images. Afterward, all mice were sacrificed, and their organs were harvested for *ex vivo* fluorescent imaging.

In Vivo Anti-Glioma Efficacy

To evaluate the *in vivo* anti-glioma activity of different PTX formulations, intracranial glioma bearing nude mice were randomly divided into six groups and administered with saline, Taxol®, PEG-PSNPs, PEG-PSNPs with Bor, CGKRK-PSNPs, and CGKRK-PSNPs with Bor every other day for four times at a PTX dose of 10 mg/kg, respectively. For nanoparticles with Bor group, the mice were orally administrated with 25 mg/kg Bor 0.5 h before intravenous injection of nanoparticles suspension. Next, the survival time of each mice was recorded to plot Kaplan-Meier survival curves.

Statistical Analysis

All the results were expressed as mean± standard deviation (SD). One-way ANOVA was utilized for statistical evaluation. Statistical analysis was performed with SPSS 20.0 software. Differences were considered significant when $^*P < 0.05$, $^{**}P < 0.01$, $^{***}P < 0.001$, respectively.

RESULTS AND DISCUSSION

Characterization of Nanoparticles

The structures of Mal-PEG_{2000}-DSPE and CGKRK-PEG-DSPE were determined by ^{1}H NMR (**Figure 2**). The methylene protons of PEG in Mal-PEG_{2000}-DSPE was at 3.6 ppm (**Figure 2A**), and the maleimide group has a characteristic peak at 6.7 ppm (**Figure 2A**) before reaction. However, after reaction with CGKRK peptide, the maleimide peak (δ 6.7) disappeared in the ^{1}H NMR spectra of CGKRK-PEG-DSPE (**Figure 2B**), whereas the PEG segment was still presented at 3.6 ppm (**Figure 2B**). It suggested that CGKRK peptide was conjugated with Mal-PEG_{2000}-DSPE.

PTX-SS-C_{18} compound was synthesized and characterized according to our previous study (Jiang et al., 2017). The CGKRK-PSNPs were prepared *via* ethanol injection method. The physical characterizations of nanoparticles including particle size, polymer dispersion index (PDI), zeta potential, and loading capacity (LC) were shown in **Table 1**. The mean particle size of PEG-PSNPs and CGKRK-PSNPs were 96.57 ± 1.25 nm and 105.61 ± 1.53 nm, respectively, with a narrow distribution (PDI < 0.2). Typically, nanoparticles with a particle size of 20 to 200 nm could passively extravasate and accumulate at malignant sites through the enhanced permeability and retention (EPR) effects

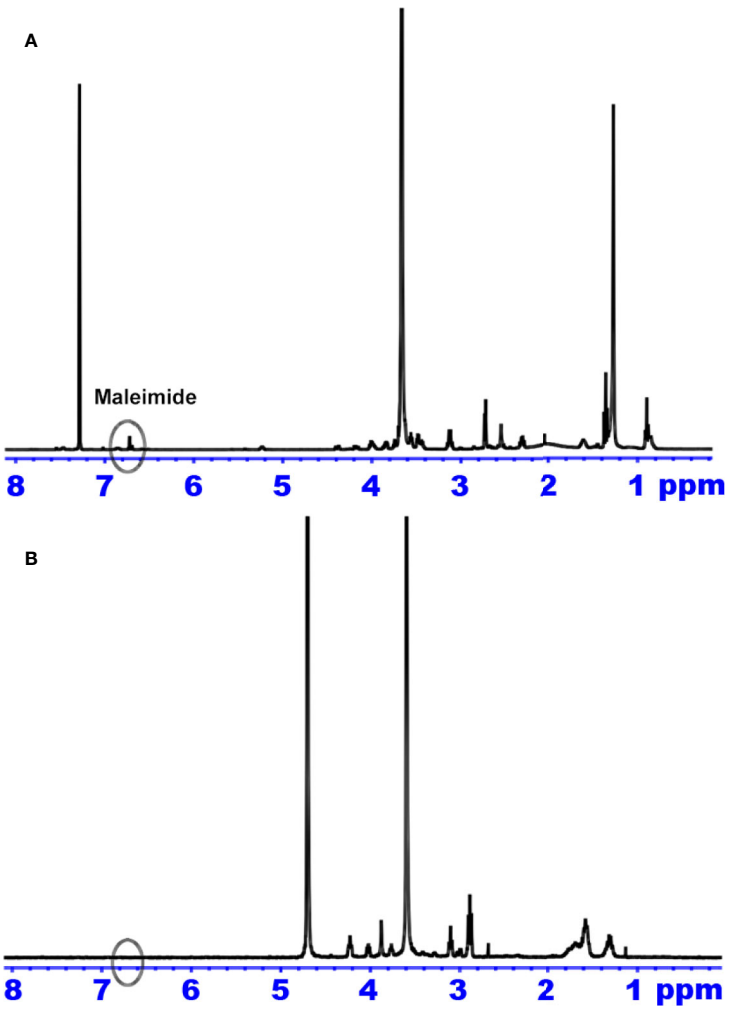

FIGURE 2 | ^{1}H NMR spectrum of Mal-PEG$_{2000}$-DSPE **(A)** and CGKRK-PEG-DSPE **(B)**.

(Deshantri et al., 2018). After modified with CGKRK peptide, the particles size had a slight increase but still close to 100 nm, which was beneficial for tumor drug delivery. All the nanoparticles showed negative zeta potential (about −30 mV). The LC of PEG-PSNPs and CGKRK-PSNPs were 55.41 ± 1.27% and 54.18 ± 1.13%, respectively, which was superior to traditional PTX nanoformulations with less than 10% (w/w) (Zhang et al., 2013; Nehate et al., 2014).

TABLE 1 | Characterizations of various nanoparticles.

	PEG-PSNPs	CGKRK-PSNPs
Particle size (nm)	96.57 ± 1.25	105.61 ± 1.53
Polydispersity index (PDI)	0.14 ± 0.05	0.16 ± 0.06
Zeta potential (-mV)	−30.6 ± 1.32	−28.4 ± 1.21
Loading capacity (LC %)	55.41 ± 1.27	54.18 ± 1.13

Data are represented with mean ± SD (n=3).

The morphology of CGKRK-PSNPs was observed by TEM (**Figure 3A**). CGKRK-PSNPs showed spherical shape, and the diameter was about 100 nm, which was in line with the size distribution (**Figure 3B**).

In Vitro Reduction-Triggered Drug Release

In previous reports, the intracellular GSH concentration in tumor cells is about 2 to 10 mM, while in the plasma is almost 1 to 2 μM (Maggini et al., 2016). In this study, 10 mM GSH was used to mimic the intracellular redox condition. The *in vitro* PTX release behavior was shown in **Figure 4**, when exposed to 1 μM GSH (pH = 7.4) solution, it showed that the nanoparticles remained stable with no PTX release over 24 h. By contrast, when the GSH concentration was adjusted to 10 mM, more than 50% of PTX was released before 5 h. After 24 h, PEG-PSNPs and CGKRK-PSNPs showed the cumulative release of PTX were 74.37% and 74.92%, respectively. These results suggested that CGKRK-PSNPs were highly sensitive to redox environment,

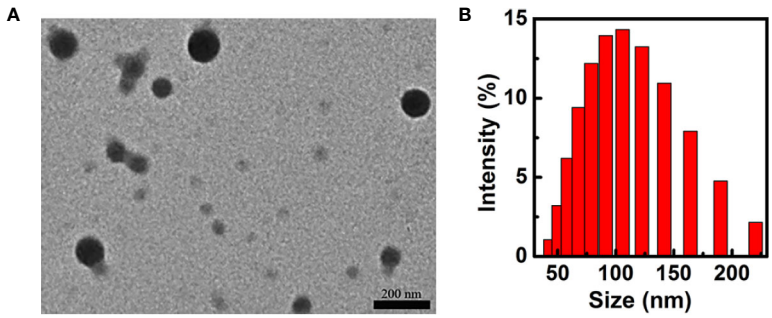

FIGURE 3 | TEM images **(A)** and particle size and size distribution **(B)** of CGKRK-PSNPs.

which indicating the disulfide bond could rapidly be cleaved in cancer cells to release PTX. The reduction-responsive PTX-SS-C_{18} conjugate self-assembled targeted nanoparticles provided a great potential to improve the anti-tumor effect.

In Vitro Cellular Uptake

The cellular uptake assay was performed qualitatively by fluorescent microscopy with coumarin-6 as the fluorescence probe. As shown in **Figure 5A**, the fluorescence intensity of U87MG cells treated with PEG-PSNPs and CGKRK-PSNPs was increased with the increasing concentration of coumarin-6 ranging from 5 to 30 ng/ml, suggesting concentration-dependent cellular uptake of nanoparticles. From **Figures 5Aa–f**, it was shown that CGKRK-PSNPs exhibited stronger fluorescence intensity as compared to that of PEG-PSNPs at all the detected concentrations after 1 h incubation. Besides, the competition assay showed that CGKRK-PSNPs group that pre-incubated with free CGKRK peptide exhibited much weaker fluorescence intensity than that of untreated ones at the same concentration of coumarin-6, respectively (**Figures 5Ag–i**). Moreover, the fluorescence intensity of CGKRK-PSNPs decreased when the incubation temperature dropped from 37°C to 4°C (**Figures 5Aj–l**).

The quantitative results were fully consistent with qualitative fluorescence intensity (**Figure 5B**). The cellular association of CGKRK-PSNPs was 1.4, 1.44, 1.31, and 1.29 folds higher than that of PEG-PSNPs on U87MG cells at the PTX concentration of 10, 20, 50, and 100 μg/ml at 37°C, respectively. In competition assay, the cellular uptake of CGKRK-PSNPs was 1.74, 1.95, 1.76, and 1.71 folds higher than that of pretreated with free CGKRK peptide at 37°C, respectively. In addition, the cellular uptake of CGKRK-PSNPs at 37°C was 2.33, 2.44, 2.28, and 2.59 folds higher than that of 4°C, respectively.

Based on qualitative and quantitative experiment results, it indicated that CGKRK peptide acted as a positive targeting role in CGKRK-PSNPs cellular uptake through heparan sulfate receptor-mediated endocytosis in U87MG cells.

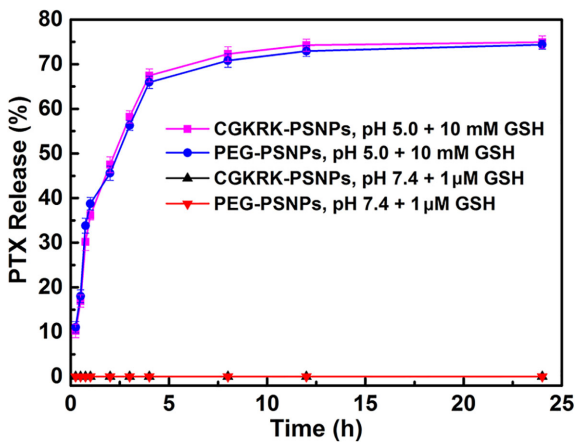

FIGURE 4 | Reduction-triggered PTX release from CGKRK-PSNPs with 1 μM GSH or 10 mM GSH (n = 3).

In Vitro Cytotoxicity

The *in vitro* anti-proliferation of different PTX formulations against U87MG and BCEC cells was evaluated using the MTT assay. The results (**Figure 6A**) showed that all the PTX formulations inhibited U87MG cells viability in a concentration dependent manner with the increasing concentration of PTX ranging from 0.01 to 10 μg/ml. In line with the cellular uptake results, CGKRK-PSNPs displayed significantly stronger cytotoxicity as compared to PEG-PSNPs. As shown in **Figures 6A, B**, Taxol® exhibited much lower cell viability than nanoparticles, because they could passively transport into cells and diffused to cytosol rapidly (Tian et al., 2018), whereas nanoparticles needed to be internalized by endocytosis and then the disulfide bond would be cleaved to release PTX under high concentration of GSH (Feng et al., 2018). In BCEC cells (**Figure 6B**), PEG-PSNPs and CGKRK-PSNPs displayed negligible cytotoxicity at all the detected concentrations, which suggested that the GSH concentration was too low to cleave disulfide bond in normal cells. These results implied that CGKRK-PSNPs could improve the cellular uptake *via* receptor-mediated endocytosis and then further enhance the cytotoxicity to tumor cells, meanwhile the redox-responsive characteristic of CGKRK-PSNPs realized precise release of PTX in tumor cells, avoiding the cytotoxic side effects to normal cells.

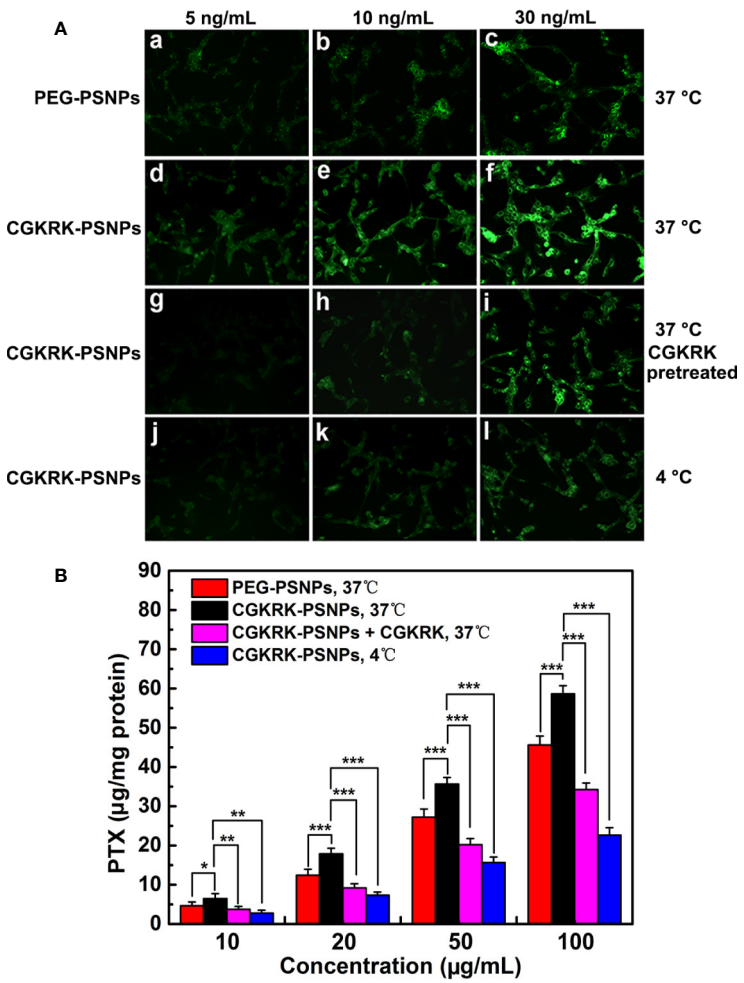

FIGURE 5 | Cellular uptake of coumarin-6-labeled PEG-PSNPs **(a–c)** and CGKRK-PSNPs **(d–l)** at 37°C **(a–i)** and 4°C **(j–l)** after incubation for 1 h at the coumarin-6 concentration of 5 **(a, d, g, j)**, 10 **(b, e, h, k)**, and 30 ng/ml **(c, f, i, l)** in U87MG and CGKRK pretreated U87MG cells **(g–i)** was examined by fluorescent microscopy **(A)**. Original magnification: ×20. U87MG uptake of PEG-PSNPs and CGKRK-PSNPs at different conditions after incubation for 1 h at the PTX concentrations from 10 to 100 μg/ml (n = 3) **(B)**. ***$P < 0.001$, **$P < 0.01$, *$P < 0.05$.

To further investigate whether PTX release from nanoparticles triggered by different intracellular GSH concentration, exogenous GSH was artificially added into the cell as external enhancers to increase the intracellular concentration of GSH (Zhang et al., 2016; Wang et al., 2017). It was reported that GSH-OEt could generate the high intracellular concentration of GSH by ethyl ester hydrolyzation in cytoplasm (Liu et al., 2011). The cytotoxicity of the redox-responsive nanoparticles was further analyzed by MTT assay against U87MG and BCEC cells. Before the addition of various PTX formulations, the cells were firstly pretreated with 10 mM GSH-OEt for 2 h. It proved that GSH-OEt did not affect the viability and endocytosis ability of the cells at the tested concentration (Zhang et al., 2016). Cells without pretreatment were used as the control. As shown in **Figures 6C, D**, PEG-PSNPs and CGKRK-PSNPs exhibited significant higher inhibitory effect on both U87MG and BCEC cells pretreated by GSH-OEt when compared with the control cells. It was noted that CGKRK-PSNPs showed significant cytotoxicity than PEG-PSNPs to the pretreated U87MG cells (**Figure 6C**). At the same time, the proliferation of U87MG or BCEC cells incubated with Taxol® was not affected after adding GSH-OEt to the cell culture media at PTX dose of 1 and 5 μg/ml. These results demonstrate that the GSH concentration in tumor cells can accelerate PTX release from PSNPs, and then increase the cytoplasm uptake of PTX, afterward enhance proliferation inhibition to tumor cells. Therefore, it indicates that CGKRK-PSNP is a promising site-specific delivery carrier for tumor treatment.

BBB Penetration *In Vitro*

The BBB maintains the brain microenvironment homeostasis due to its unique structure and cellular composition, which consists of capillary endothelium with its tight junctions, basal lamina, the end-feet of astrocytes and pericytes (Seo et al., 2019).

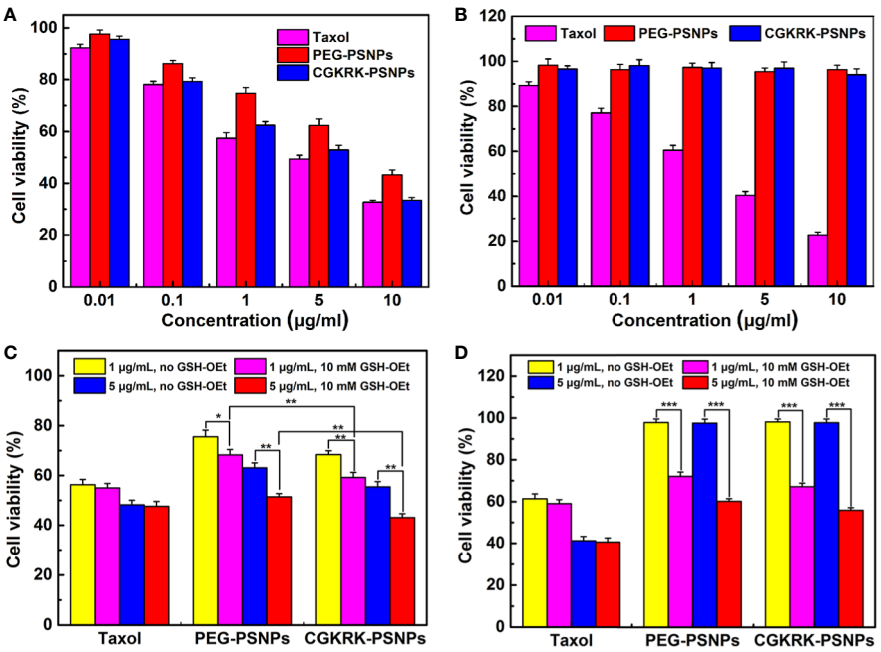

FIGURE 6 | Cytotoxicity of Taxol®, PEG-PSNPs, and CGKRK-PSNPs in U87MG cells **(A)** and BCEC cells **(B)** after incubation for 48 h (n = 6). Viability of GSH-OEt pretreated or non-pretreated U87MG cells **(C)** and BCEC cells **(D)** incubated with Taxol®, PEG-PSNPs and CGKRK-PSNPs for 48 h. ***$P < 0.001$, **$P < 0.01$, *$P < 0.05$.

This special physical barrier prevents most pharmaceutical anti-tumor drugs from entering the brain. In this study, we used BCEC cells to establish the *in vitro* BBB model to investigate the penetration efficiency of CGKRK-PSNPs with the assistance of Bor. As shown in **Figure 7**, the BBB permeability of CGKRK-PSNPs combined with Bor was significantly higher than the other groups after incubated for 3 h. The transport behavior of different nanoparticles displayed a time-dependent profile. After 4 h incubation, the transportation ratios were 19.33% and 13.11% for PEG-PSNPs (with or without Bor), 23.85% and 18.38% for CGKRK-PSNPs (with or without Bor), respectively. The results suggested that Bor could enhance the migration efficiency of both PEG-PSNPs and CGKRK-PSNPs penetrating the *in vitro* BBB. At all the determined time points, the permeability of CGKRK-PSNPs was higher than PEG-PSNPs, which might be due to BCEC as one kind of vascular endothelial cells, there was also a certain expression of heparin sulfate receptor on surface.

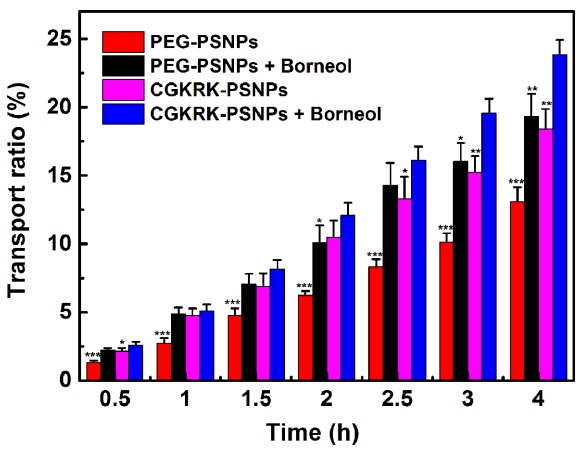

FIGURE 7 | The transport ratios of PEG-PSNPs and CGKRK-PSNPs (with or without borneol) across the BBB model *in vitro*. ***$P < 0.001$, **$P < 0.01$, *$P < 0.05$ significantly lower than that of CGKRK-PSNPs with borneol.

In Vivo Imaging Analysis

In order to estimate the brain targeting capability of CGKRK-PSNPs combined with Bor, U87MG glioma-bearing nude mice were imaged using DiR as the fluorescent marker. As shown in **Figure 8A**, the fluorescence intensity of CGKRK-PSNPs and PEG-PSNPs with Bor was higher compared with that without Bor, respectively, which indicted that Bor could improve the BBB penetration. When combined with Bor, the fluorescence signal of CGKRK-PSNPs group was slightly higher than PEG-PSNPs group. In addition, the images of *ex vivo* brains and the semi-quantitative results (**Figures S2** and **8B**) also confirmed that CGKRK-PSNPs combined with Bor exhibited the highest accumulation than other three groups at the glioma sections. Taken together, the enhanced glioma site distribution of CGKRK-PSNPs combined with Bor was attributed to the CGKRK peptide-mediated endocytosis and Bor for BBB penetration enhancement.

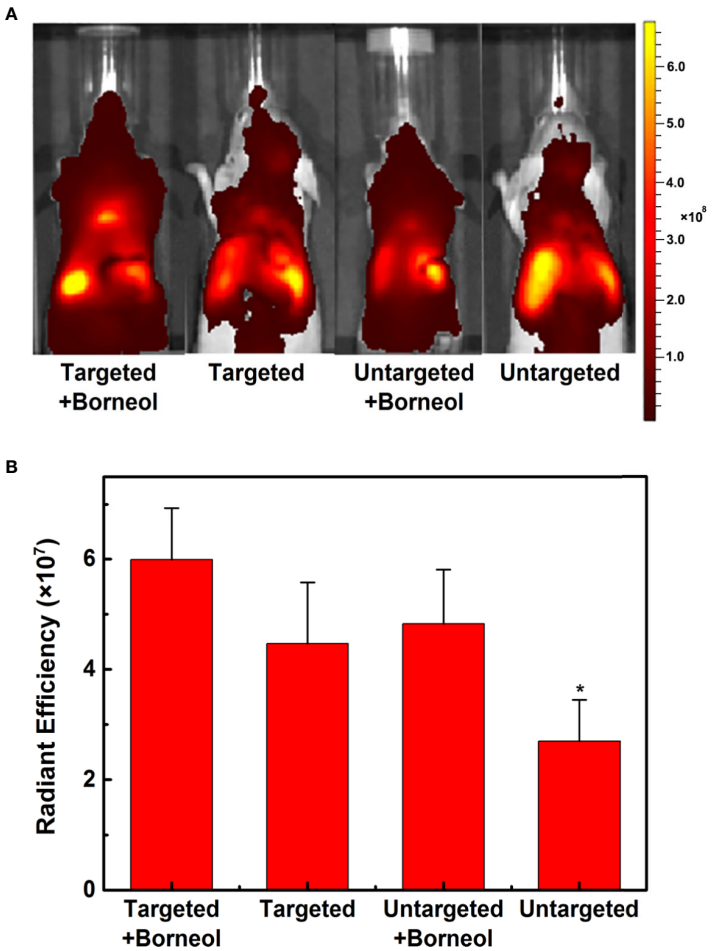

FIGURE 8 | *In vivo* fluorescence imaging of U87MG glioma-bearing nude mice after administration with DiR-labeled CGKRK-PSNPs with borneol, DiR-labeled CGKRK-PSNPs, DiR-labeled PEG-PSNPs with borneol, and DiR-labeled PEG-PSNPs **(A)**. The corresponding semi-quantitative radiant efficiency of brains **(B)**. *$P < 0.05$ significantly lower than that of CGKRK-PSNPs with borneol.

In Vivo Anti-Glioma Efficacy

The anti-glioma efficacy of CGKRK-PSNPs combined with Bor was investigated on intracranial U87MG glioma mice models. As shown in **Figure 9** and **Table 2**, the medium survival time of mice treated with CGKRK-PSNPs combined with Bor (39 days) was longer when compared to saline (18 days, $P < 0.001$), Taxol® (20 days, $P < 0.001$), PEG-PSNPs (27 days, $P < 0.001$), PEG-PSNPs with Bor (32 days) and CGKRK-PSNPs (33 days). These results confirmed that CGKRK-PSNPs combined with Bor had great advantage in improving anti-glioma efficacy.

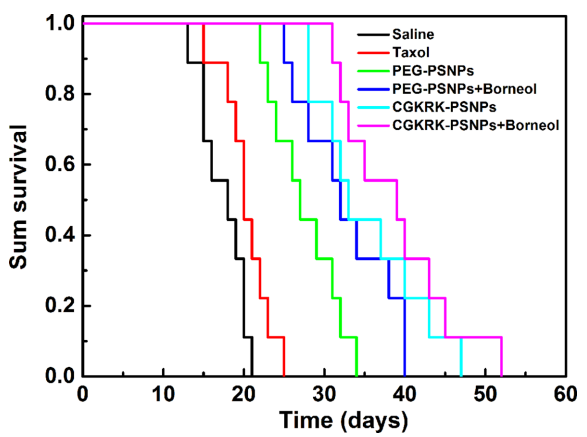

FIGURE 9 | Kaplan-Meier survival curve of U87MG glioma-bearing mice treated with different PTX formulations at a dose of 10mg/kg PTX on day 2, 4, 6, and 8 post implantation (n = 9).

CONCLUSIONS

In summary, CGKRK peptide modified redox-sensitivity nanoparticles were successfully developed in this study. *In vitro* release study showed that CGKEK-PSNPs kept stable under physiological conditions and disassembled rapidly with high

TABLE 2 | *In vivo* anti-glioma efficacy of different PTX formulations on intracranial U87MG glioma mice model (n = 9).

Groups	Dose (mg/kg)	MST[a] (days)	Median (days)	Compare with saline[b]	Compare with Taxol[b]	Compare with PEG-PSNPs[b]
Saline	——	17.4 ± 0.9	18	——	——	——
Taxol	10	20.3 ± 1.0	20	*	——	——
PEG-PSNPs	10	27.6 ± 1.4	27	***	***	——
PEG-PSNPs +borneol	10	32.7 ± 1.9	32	***	***	*
CGKRK-PSNPs	10	35.4 ± 2.2	33	***	***	**
CGKRK-PSNPs +borneol	10	38.9 ± 2.3	39	***	***	***

[a]*MST, mean survival time.*
[b]**P < 0.05, **P < 0.01, ***P < 0.001 of log-rank analysis.*

concentration of GSH. Compared with PEG-PSNPs, CGKEK-PSNPs displayed enhanced cellular uptake and cytotoxicity against U87MG cells. Nevertheless, both of them showed negligible cytotoxicity on BCEC cells. *In vitro* BBB model, CGKEK-PSNPs combined with Bor significantly improved the BBB penetration ability. Furthermore, CGKEK-PSNPs combined with Bor exhibited higher accumulation at the glioma site and extended survival time in U87MG glioma-bearing mice. In conclusion, the strategy that combined Bor with receptor-mediated redox-responsive drug delivery system displayed a great potential for glioma treatment.

DATA AVAILABILITY STATEMENT

The datasets generated for this study are available on request to the corresponding authors.

ETHICS STATEMENT

The animal study was reviewed and approved by Nanjing Medical University.

AUTHOR CONTRIBUTIONS

YC, YT, and HX designed the experiments. LL, XinL, and WQ performed the experiments. LL and HX wrote the main manuscript. SL, YJ, and YX analyzed the data. JX, WL, and XiaL prepared the figures and tables. All authors reviewed the manuscript.

FUNDING

This work was supported by the grants from National Natural Science Foundation of China (81973255), Six Talent Peaks Project of Jiangsu Province (SWYY-051), the grants from the Suzhou Science and Technology Plan Project (SYSD2018219), Science and Technology Development Foundation of Nanjing Medical University (2017NJMU216) and Science and Technology Plan Project of Jiangxi Province Education Department (GJJ170736).

SUPPLEMENTARY MATERIAL

The Supplementary Material for this article can be found online at: https://www.frontiersin.org/articles/10.3389/fphar.2020.00558/full#supplementary-material

REFERENCES

Agemy, L., Kotamraju, V. R., Friedmann-Morvinski, D., Sharma, S., Sugahara, K. N., and Ruoslahti, E. (2013). Proapoptotic peptide-mediated cancer therapy targeted to cell surface p32. *Mol. Ther.* 21, 2195–2204. doi: 10.1038/mt.2013.191

Chen, Z. W., Wen, D., and Gu, Z. (2020). Cargo-encapsulated cells for drug delivery. *Sci. China Life Sci.* 63, 599–601. doi: 10.1007/s11427-020-1653-y

Deshantri, A. K., Moreira, A. V., Ecker, V., Mandhane, S. N., Schiffelers, R. M., Buchner, M., et al. (2018). Nanomedicines for the treatment of hematological malignancies. *J. Control. Release* 287, 194–215. doi: 10.1016/j.jconrel.2018.08.034

Feng, R. Y., Chen, Q., Zhou, P., Wang, Y. S., and Yan, H. (2018). Nanoparticles based on disulfide-containing poly (β-amino ester) and zwitterionic fluorocarbon surfactant as a redox-responsive drug carrier for brain tumor treatment. *Nanotechnology* 29, 495101. doi: 10.1088/1361-6528/aae122

Gao, H. L. (2017). Perspectives on Dual Targeting Delivery Systems for Brain Tumors. *J. Neuroimmune Pharmacol.* 12, 6–16. doi: 10.1007/s11481-016-9687-4

Griffin, J. I., Cheng, S. K. K., Hayashi, T., Carson, D., Saraswathy, M., Nair, D. P., et al. (2017). Cell-penetrating peptide CGKRK mediates efficient and widespread targeting of bladder mucosa following focal injury. *Nanomedicine* 13, 1925–1932. doi: 10.1016/j.nano.2017.04.004

Guo, X. Y., Wu, G. J., Wang, H., and Chen, L. K. (2019). Pep-1&borneol-Bifunctionalized Carmustine-Loaded Micelles Enhance Anti-Glioma Efficacy Through Tumor-Targeting and BBB-Penetrating. *J. Pharm. Sci.* 108, 1726–1735. doi: 10.1016/j.xphs.2018.11.046

Han, S. P., Zheng, H. Y., Lu, Y. P., Sun, Y., Huang, A. H., Fei, W. D., et al. (2018). A Novel Synergetic Targeting Strategy for Glioma Therapy Employing Borneol Combination with Angiopep-2-modified, DOX-loaded PAMAM Dendrimer. *J. Drug Targeting* 26, 86–94. doi: 10.1080/1061186X.2017.1344849

Han, L., Hu, L., Liu, F., Wang, X., Huang, X., Liu, B., et al. (2019). Redox-sensitive micelles for targeted intracellular delivery and combination chemotherapy of paclitaxel and all-trans-retinoid acid. *Asian J. Pharm. Sci.* 14, 531–542. doi: 10.1016/j.ajps.2018.08.009

Hernández-Pedro, N. Y., Rangel-López, E., Magaña-Maldonado, R., de la Cruz, V. P., del Angel, A. S., Pineda, B., et al. (2013). Application of Nanoparticles on Diagnosis and Therapy in Gliomas. *BioMed. Res. Int.* 2013, 351031. doi: 10.1155/2013/351031

Jain, K. K. (2018). A Critical Overview of Targeted Therapies for Glioblastoma. *Front. Oncol.* 8, 1–19. doi: 10.3389/fonc.2018.00419

Jiang, Y., Wang, X. Z., Liu, X., Lv, W., Zhang, H. J., Zhang, M. W., et al. (2017). Enhanced Antiglioma Efficacy of Ultrahigh Loading Capacity Paclitaxel Prodrug Conjugate Self-Assembled Targeted Nanoparticles. *ACS Appl. Mater. Interf.* 9, 211–217. doi: 10.1021/acsami.6b13805

Li, R., and Xie, Y. (2017). Nanodrug delivery systems for targeting the endogenous tumor microenvironment and simultaneously overcoming multidrug

resistance properties. *J. Control. Release* 251, 49–67. doi: 10.1016/j.jconrel.2017.02.020

Liu, J. Y., Pang, Y., Huang, W., Huang, X. H., Meng, L. L., Zhu, X. Y., et al. (2011). Bioreducible micelles self-assembled from amphiphilic hyperbranched multiarm copolymer for glutathione-mediated intracellular drug delivery. *Biomacromolecules* 12, 1567–1577. doi: 10.1021/bm200275j

Lv, L. Y., Jiang, Y., Liu, X., Wang, B. Y., Lv, W., Zhao, Y., et al. (2016). Enhanced Antiglioblastoma Efficacy of Neovasculature and Glioma Cells Dual Targeted Nanoparticles. *Mol. Pharm.* 13, 3506–3517. doi: 10.1021/acs.molpharmaceut.6b00523

Maggini, L., Cabrera, I., Ruiz-Carretero, A., Prasetyanto, E. A., Robinet, E., and De Cola, L. (2016). Breakable mesoporous silica nanoparticles for targeted drug delivery. *Nanoscale* 8, 7240–7247. doi: 10.1039/c5nr09112h

Meng, L. W., Chu, X. Y., Xing, H. Y., Liu, X., Xin, X., Chen, L. Q., et al. (2019). Improving glioblastoma therapeutic outcomes via doxorubicin-loaded nanomicelles modifed with borneol. *Int. J. Pharm.* 567, 118485–118500. doi: 10.1016/j.ijpharm.2019.118485

Nehate, C., Jain, S., Saneja, A., Khare, V., Alam, N., Dubey, R. D., et al. (2014). Paclitaxel formulations: challenges and novel delivery options. *Curr. Drug Deliv.* 11, 666–686. doi: 10.2174/1567201811666140609154949

Qian, W. B., Qian, M., Wang, Y., Huang, J. F., Chen, J., Ni, L. C., et al. (2018). Combination Glioma Therapy Mediated by a Dual-Targeted Delivery System Constructed Using OMCN-PEG-Pep22/DOX. *Small* 14, e1801905. doi: 10.1002/smll.201801905

Raza, A., Hayat, U., Rasheed, T., Bilal, M., and Iqbal, H. M. N. (2018). Redox-responsive nano-carriers as tumor-targeted drug delivery systems. *Eur. J. Med. Chem.* 157, 705–715. doi: 10.1016/j.ejmech.2018.08.034

Sasmita, A. O., Wong, Y. P., and Ling, A. P. K. (2018). Biomarkers and therapeutic advances in glioblastoma multiforme. *Asia-Pac J. Clin. Oncol.* 14, 40–51. doi: 10.1111/ajco.12756

Seo, S., Kim, H., Sung, J. H., Choi, N., Lee, K., and Kim, H. N. (2019). Microphysiological systems for recapitulating physiology and function of blood-brain barrier. *Biomaterials* 232, 119732. doi: 10.1016/j.biomaterials.2019.119732

Song, Q. L., Yin, Y. J., Shang, L. H., Wu, T. T., Zhang, D., Kong, M., et al. (2017). Tumor Microenvironment Responsive Nanogel for the Combinatorial Antitumor Effect of Chemotherapy and Immunotherapy. *Nano Lett.* 17, 6366–6375. doi: 10.1021/acs.nanolett.7b03186

Tao, W., and He, Z. (2018). ROS-responsive drug delivery systems for biomedical applications. *Asian J. Pharm. Sci.* 13, 101–112. doi: 10.1016/j.ajps.2017.11.002

Tian, C. H., Asghar, S., Xu, Y. R., Chen, Z. P., Zhang, J. W., Ping, Q. N., et al. (2018). Tween80-modified hyaluronic acid-ss-curcumin micelles for targeting glioma: Synthesis, characterization and their in vitro evaluation. *Int. J. Biol. Macromol.* 120, 2579–2588. doi: 10.1016/j.ijbiomac.2018.09.034

Treps, L. (2018). EnLIGH Tenment of tumor vessel normalization and immunotherapy in glioblastoma. *J. Pathol.* 246, 3–6. doi: 10.1002/path.5103

Wang, B. Y., Lv, L. Y., Wang, Z. Y., Zhao, Y., Wu, L., Fang, X. L., et al. (2014). Nanoparticles functionalized with Pep-1 as potential glioma targeting delivery system via Interleukin 13 receptor 2-mediated endocytosis. *Biomaterials* 35, 5897–5907. doi: 10.1016/j.biomaterials.2014.03.068

Wang, X. L., He, C. Y., Yang, Q. L., Tan, L. J., Liu, B. Y., Zhu, Z. G., et al. (2017). Dynamic covalent linked triblock copolymer micelles for glutathione-mediated intracellular drug delivery. *Mater. Sci. Eng. C* 77, 34–44. doi: 10.1016/j.msec.2017.03.240

Xin, H. L., Jiang, X. Y., Gu, J. J., Sha, X. Y., Chen, L. C., Law, K., et al (2011). Angiopep-conjugated poly(ethylene glycol)-co-poly(ϵ-caprolactone) nanoparticles as dual-targeted drug delivery system for brain glioma. *Biomaterials* 32, 4293–4305. doi: 10.1016/j.biomaterials.2011.02.044

Yu, X., Xieripu, A., Xu, Q., Zulipikaer, A., Song, Y., Cai, L., et al. (2020). GSH-responsive curcumin/doxorubicin encapsulated Bactrian camel serum albumin nanocomposites with synergistic effect against lung cancer cells. *J. Biomed. Res.* 34, 54–66. doi: 10.7555/JBR.33.20190036

Zhang, Z., Mei, L., and Feng, S. S. (2013). Paclitaxel Drug Delivery Systems. *Expert Opin. Drug Deliv.* 10, 325–340. doi: 10.1517/17425247.2013.752354

Zhang, Y., Han, L., Zhang, Y., Chang, Y. Q., Chen, X. W., He, R. H., et al. (2016). Glutathione-mediated mesoporous carbon as a drug delivery nanocarrier with carbon dots as a cap and fluorescent tracer. *Nanotechnology* 27, 355102. doi: 10.1088/0957-4484/27/35/355102

Zhang, P. F., Wang, J. Q., Chen, H., Zhao, L., Chen, B. B., Chu, C. C., et al. (2018). Tumor microenvironment-responsive ultra-small-nanodrug generators with enhanced tumor delivery and penetration. *J. Am. Chem. Soc* 140, 14980–14989. doi: 10.1021/jacs.8b09396

Zhang, J., Zeng, Y., Su, M., Yu, M., Zhang, Y., Cheng, H., et al. (2019). Multifunctional Ferritin Nanoparticles as Theranostics for Imaging-Guided Tumor Phototherapy. *J. Biomed. Nanotechnol.* 15, 1546–1555. doi: 10.1166/jbn.2019.2788

Zhu, X. F., Zhou, H., Liu, Y. N., Wen, Y. Y., Wei, C. F., Yu, Q. Q., et al. (2018). Transferrin/aptamer conjugated mesoporous ruthenium nanosystem for redoxcontrolled and targeted chemo-photodynamic therapy of glioma. *Acta Biomater.* 82, 143–157. doi: 10.1016/j.actbio.2018.10.012

Conflict of Interest: The authors declare that the research was conducted in the absence of any commercial or financial relationships that could be construed as a potential conflict of interest.

frontiers in Pharmacology

ORIGINAL RESEARCH
published: 30 April 2020
doi: 10.3389/fphar.2020.00539

Shape Matters: Comprehensive Analysis of Star-Shaped Lipid Nanoparticles

Shuwen Cao[1,2†], Xiaodi Liu[1,2,3†], Xiuling Li[1,2], Chunhao Lin[1,2], Wenyue Zhang[1,2,3], Chee Hwee Tan[4], Shunung Liang[4], Baoming Luo[3], Xiaoding Xu[1,2] and Phei Er Saw[1,2*]*

[1] Guangdong Provincial Key Laboratory of Malignant Tumor Epigenetics and Gene Regulation, Sun Yat-sen Memorial Hospital, Sun Yat-sen University, Guangzhou, China, [2] Medical Research Center, Sun Yat-sen Memorial Hospital, Sun Yat-sen University, Guangzhou, China, [3] The Ultrasound Department, Sun Yat-sen Memorial Hospital, Sun Yat-sen University, Guangzhou, China, [4] The First Clinical Medical School of Guangzhou University of Chinese Medicine, Guangzhou University of Chinese Medicine, Guangzhou, China

OPEN ACCESS

Edited by:
Chao Wang,
Soochow University, China

Reviewed by:
Yanlan Liu,
Hunan University, China
Yujing Li,
National Center for Nanoscience and Technology (CAS), China

***Correspondence:**
Xiaoding Xu
xuxiaod5@mail.sysu.edu.cn
Phei Er Saw
caipeie@mail.sysu.edu.cn

[†]These authors have contributed equally to this work

Specialty section:
This article was submitted to Experimental Pharmacology and Drug Discovery, a section of the journal Frontiers in Pharmacology

Received: 10 March 2020
Accepted: 07 April 2020
Published: 30 April 2020

Citation:
Cao S, Liu X, Li X, Lin C, Zhang W, Tan CH, Liang S, Luo B, Xu X and Saw PE (2020) Shape Matters: Comprehensive Analysis of Star-Shaped Lipid Nanoparticles. Front. Pharmacol. 11:539. doi: 10.3389/fphar.2020.00539

The research of lipid nanoparticles (LNPs) has been ongoing for more than three decades, and more research are still being carried out today. Being the first Food and Drug Administration (FDA)-approved nanomedicine, LNPs not only provide various advantages, but also display some unique properties. The unique lipid bilayer structure of LNPs allows it to encapsulate both fat-soluble and water-soluble molecules, hence enabling a wide range of possibilities for the delivery of therapeutic agents with different physical and chemical properties. The ultra-small size of some LNPs confers them the ability to cross the blood brain barrier (BBB), thus obtaining superiority in the treatment of diseases of the central nervous system (CNS). The ability of tumor targeting is one of the basic requirements to be an excellent delivery system, where the LNPs have to reach the interior of the tumor. Factors that influence tumor extravasation and the permeability of LNPs are size, surface charge, lipid composition, and shape. The effect of size, surface charge, and lipid composition on the cellular uptake of LNPs is no longer recent news, while increasing numbers of researchers are interested in the effect of shape on the uptake of LNPs and its consequential effects. In our study, we prepared three lipid nanostars (LNSs) by mixing phosphatidylcholine (PC) with different backbone lengths (C14:C4 or C16:C6 or C18:C8) at a 3:1 ratio. Although several star-shaped nanocarriers have been reported, these are the first reported star-shaped LNPs. These LNSs were proven to be safe, similar in size with their spherical controls (~100 nm), and stable at 37°C. The release rate of these LNSs are inversely related to the length of the lipid backbone. Most importantly, these LNSs exhibited greatly enhanced cellular uptake and *in vivo* tumor extravasation compared with their spherical controls. Based on the different uptake and pharmacokinetic characteristics displayed by these LNSs, numerous route formulations could be taken into consideration, such as *via* injection or transdermal patch. Due to their excellent cellular uptake and *in vivo* tumor accumulation, these LNSs show exciting potential for application in cancer therapy.

Keywords: star, shape, nanocarrier, nanoparticle, lipid, uptake, permeability

INTRODUCTION

Current strategies for cancer therapy include chemotherapy, surgery, angiogenesis, and monoclonal antibody therapy. However, tumors either quickly become resistant to these treatment modalities, or severe side effects occur, leading to discontinuity of the treatment or significant degradation to quality of life (Zugazagoitia et al., 2016). Along with the advent of nanoparticles, cancer diagnosis and therapy has emerged into a new era. The enhanced permeation and retention (EPR) effect was first reported by Maeda and Matsumura in 1986, stating that the blood vessels in tumor areas are formed fortuitously and thus inconsecutively due to the rapid growth of blood vessels stimulated by growth factors secreted by tumor cells (Matsumura and Maeda, 1986). The pores between endothelial cells allow nanoparticles to passively accumulate in tumors, which provides a new avenue for tumor targeting therapy. Over the past decades, various nanomedicine have been designed and approved to be reliable for cancer therapy, among them, lipid nanoparticles (LNPs) are the most time-honored nanomedicine and also the pioneer to be applied clinically (Shi et al., 2017). Liposomal doxorubicin modified by poly(ethylene glycol) (Doxil) was the first nanomedicine approved by the US Food and Drug Administration for cancer therapy. As the oldest and still widely researched nanomedicine, LNPs provide various advantages that other nanomedicines offer, such as specificity (Flayhan et al., 2018) and multi-functionality (Han et al., 2014; Ma et al., 2015). Meanwhile, LNPs possess some unique advantages compared with other nanomedicine. LNPs have an aqueous inner part, and a surrounding of one or more concentric lipid bilayers. This unique structure allows LNPs to encapsulate both fat-soluble and water-soluble molecules, hence providing a wide range of possibilities to deliver therapeutic reagents with different physical and chemical properties (Khan et al., 2008). Unlike polymeric nanoparticles, the diameter of LNPs range from 1 to 200 nm. Due to their sub-micron ultra-small size, LNPs are not only physically stable in structure, but are also able to pass through the blood-brain barrier (BBB) to enter the central nervous system (CNS), gaining widespread attention among various nanoparticles for the treatment of CNS diseases (Saw et al., 2017a; Mendes M et al., 2018). Other superiorities of LNPs include facilitated industrial production, suitable bioavailability (Din et al., 2015), biocompatibility (Eiras et al., 2017), improved drug absorption (Wang et al., 2017), and delayed dissolution (Xu et al., 2010).

To be an excellent delivery system, LNPs have to reach the core of tumors. Clearly, passively targeting the tumor by the EPR effect is insufficient, as the physical and chemical properties of the LNPs itself may affect its permeability. The extravasation ability of the nanocarrier is largely dependent on its size. The accumulation of nano-scale particles in the tumor tissue is not only due to the EPR effect, but also size of nanoparticles shows significant influence on the cell penetration. Although there is no conclusive ideal size for maximal cellular uptake of nanocarriers, research has reported that nanoparticles with certain sizes exhibit a better ability to be internalized, for example 50 nm Au nanoparticles show better permeability into HeLa cells compared to any other sizes (Chithrani et al., 2006). The surface charge of the nanocarrier accounts for another well-established factor in its ability to be taken up by tumor cells. Positively charged nanocarriers usually show better permeability than those neutral or negatively charged nanocarriers of the same size (Jiang et al., 2015). The lipid composition of the nanocarrier also largely affects its ability to be internalized. The lipid headgroups, the length of the lipid tail and even the saturability of the lipid carries an impact on the internalization ability of LNPs. Receptor-targeting headgroup shows the best cellular uptake, followed by the cationic amine headgroups. Generally, the longer the lipid tail, the better the displayed uptake of LNPs. Whereas within the same length of the lipid tail, unsaturated lipids demonstrated superior internalization ability (Hare, 1975). Recently, increasing amounts of research reports that the shape of nanocarriers carries some sort of performance effect on its extravasation ability (Jurney et al., 2017; Xie et al., 2017), while the importance of the shape remains unclear.

In our study, we chose phosphatidylcholine (PC) with six different lengths of backbone (C4, C14, C6, C16, C8, C18) to prepare the spherical LNPs (by C14 or C16 or C18 only) or lipid nanostars (LNSs) (by mixing C14:C4 or C16:C6 or C18:C8 at the ratio of 3:1). LNPs synthesized with PC have been reported by numerous articles, whereas the preparation of the LNSs by mixing PC with long and short backbones at certain ratios is first reported in this article. We further investigated the *in vitro* permeability and the *in vivo* extravasation in tumors to reveal the importance of the shape on the uptake of nanocarriers by tumors.

MATERIALS AND METHODS

Materials

1,2-Distearoyl-sn-glycero-3-phosphocholine (18:0 PC; DHPC), 1,2-dipalmitoyl-sn-glycero-3-phosphocholine (16:0 PC; DPPC), 1,2-dimyristoyl-sn-glycero-3-phosphocholine (14:0 PC; DMPC), 1,2-dioctanoyl-sn-glycero-3-phosphocholine (08:0 PC; DOPC), 1,2-dihexanoyl-sn-glycero-3-phosphocholine (06:0 PC; DHPC), 1,2-dibutyryl-sn-glycero-3-phosphocholine (04:0 PC; DBPC), 1,2-dioleoyl-sn-glycero-3-phosphoethanolamine-N-(lissamine rhodamine B sulfonyl) (ammonium salt) (18:1 Liss Rhod PE), 1,2-dipalmitoyl-sn-glycero-3-phosphoethanolamine-N-(lissamine rhodamine B sulfonyl) (ammonium salt) (16:0 Liss Rhod PE), and 1,2-dimyristoyl-sn-glycero-3-phosphoethanolamine-N-(lissamine rhodamine B sulfonyl) (ammonium salt) (DMPE-Rh) were purchased from Avanti Polar Lipids (AL, USA). Phosphate buffer saline (PBS), cell culture media, and fetal bovine serum (FBS) was purchased from Gibco (MA, USA). HepG2 cells were purchased from ATCC (VA, USA). All chemicals and reagents were received and used according to the manufacturer's protocol.

METHODS

Synthesis of Various Nanostars

After various combinations of lipid chains at various ratios (data not shown), we successfully synthesized three types of nanostars by using three distinct combinations of lipids (**Table 1**).

Size Distribution and Zeta Potential

The particle size and zeta potential of LNSs and LNPs were determined by dynamic light scattering (DLS) analysis using Malvern Panalytical, MA, USA. The data for each sample were obtained from three replicates.

Transmission Electron Microscopy Analysis

Five µl aliquots of all LNSs (10 mg/ml) were dropped onto a transmission electron microscopy (TEM) grade carbon-only mesh copper grid. Particles were left on the grid at ambient temperature for 5 min. Each grid was washed five times with distilled water. The specimens were then negatively stained using 2% uranyl acetate and left at ambient temperature for 2 min. Grids were then washed thrice with distilled water and air-dried. The specimens were visualized using a TECNAI F20 electron microscope (Philips Electronic Instruments Corp., Mahwah, NJ).

Stability of Lipid Nanostars

To determine the stability of LNSs, we synthesized LNSs as mentioned above at 10 mg/ml. The LNSs were then kept in a closed vial at 37°C. At pre-determined time points (1, 2, 4, 8, 12, 24, and 48 h), the size of LNSs were measured by DLS and recorded.

In Vitro Release Profile of Lipid Nanostars

Rhodamine-labeled LNSs (n=3) were dispersed in 1 ml of PBS (pH 7.4) and then transferred to a Float-A-Lyzer G2 dialysis device (MWCO 100 kDa, Spectrum, USA) that was immersed in PBS (pH 7.4) at 37°C. At predetermined intervals (1, 2, 4, 8, 12, 24, 48, 72, 96 h), 5 µl of the NP solution was withdrawn from inside of the dialysis device and mixed with 95 µl of dimethyl sulfoxide (DMSO). After thorough mixing, the fluorescence intensity of rhodamine in each well representing each LNSs was determined by Synergy HT Multi-Mode Microplate Reader (BioTek, USA).

TABLE 1 | Long chain vs. short chain lipid used in this study and their hydrodynamic sizes and zeta potential.

Long chain lipid	Short chain lipid	Long/short chain lipid ratio	Name	Hydrodynamic size (DLS) (nm)	Zeta Potential (mV)
18 C	8 C	3:1	$LNS_{18:8}$	121.8±13.2	-15.02±3.0
16 C	6 C	3:1	$LNS_{16:6}$	95.0±0.7	-12.4±2.7
14 C	4 C	3:1	$LNS_{14:4}$	81.9±6.0	-12.2±5.3
18 C	–	–	LNP_{18}	95.0±0.7	-13.8±1.2
16 C	–	–	LNP_{16}	74.4±8.6	-13.8±1.9
14 C	–	–	LNP_{14}	72.6±7.4	-12.0±1.5

Cell Culture

The human liver carcinoma cells HepG2 and mice triple negative breast cancer cell line 4T1 were purchased from ATCC and was cultured and used according to the protocols given by the provider. The cells were maintained at 37°C in a humidified cell culture chamber equipped with 5% CO_2. Cells were maintained in RPMI-1640 medium supplemented with 10% fetal bovine serum (FBS), 100 U/ml penicillin, and 100 µg/ml streptomycin.

Cellular Toxicity of Lipid Nanostars

To rule out possible cytotoxicity of LNSs toward cells, we performed a cytotoxicity analysis. HepG2 cells were grown at 5,000 cells per well in a 96-well plate. The cells were then treated with LNSs at a concentration range of 0.1–50 mg/ml. LNSs were co-incubated with the cells for 4 h, before washing off with PBS and undergoing further incubation for 48 h. Cell viability was determined *via* alamarBlue assay as previously described (Saw et al., 2017a; Saw et al., 2017b).

In Vitro Cellular Uptake

To visualize the *in vitro* uptake and internalization of nanoparticles, LNSs and LNPs were labeled with fluorescent rhodamine labeled lipid (please see **Table 2**) at 0.5 wt. % of lipid content. HepG2 cells were grown to ~80% confluence on glass coverslips (12 x 12 mm; Fisher Scientific, Texas, USA). Prior to the addition of 200 µg/ml of fluorescently-labeled LNSs or LNPs, the medium was replaced with serum-free medium. After 1 h incubation at 37°C, cells were washed three times with PBS and fixed with 4% (w/v) paraformaldehyde (PFA). Coverslips with fixed cells were mounted onto glass slides with Dako® mounting media and examined using an Olympus Fluoview 1000 confocal microscope (Olympus Imaging Co., Tokyo, Japan). For 3D spheroid culture, HepG2 cells were obtained from monolayer culture using the protocol described previously (Saw et al., 2017a).

In Vivo Biodistribution Analysis

To visualize the *in vivo* biodistribution of all nanoparticles, LNSs and LNPs were fluorescently labeled with rhodamine labeled lipid (please see Table S1) at 2 wt. % of lipid content. 4T1 cells were subcutaneously implanted into Balb/c mice to generate the xenograft model. Ten milligrams of fluorescently labeled LNSs or LNPs were intravenously *(i.v.)* injected per mouse when the

TABLE 2 | Rhodamine labeled lipid used in LNSs and LNPs for in vitro uptake experiment and in vivo Biodistribution analysis.

Nanoparticles	Rhodamine labeled lipid*
$LNS_{18:8}$	18:1 Liss Rhod PC
$LNS_{16:6}$	16:0 Liss Rhod PC
$LNS_{14:4}$	14:0 Liss Rhod PC
LNP_{18}	18:1 Liss Rhod PC
LNP_{16}	16:0 Liss Rhod PC
LNP_{14}	14:0 Liss Rhod PC

**for in vitro experiments, rhodamine labeled lipid was used at 0.5 wt. %; for in vivo BioD analysis, rhodamine labeled lipid was used at 2 wt. %.*

tumor size was around 100 mm^3. After 24 h, the mice were sacrificed and the major organs, muscle, and tumor were observed by IVIS® Imaging system (PerkinElmer, UK).

Immunogenicity of Lipid Nanostars After Intravenous Injection

To evaluate the immunogenicity of all nanoparticles, LNSs and LNPs were intravenously injected into Balb/c mice at a dosage of 10 mg per mouse. After 24 h, the mice were anesthetized with isoflurane, and blood was collected and centrifuged at 3,000 rpm for 15 min after standing at room temperature for 15 min. The aspartate transaminase (AST), alanine transaminase (ALT), urea, and creatinine in the serum was analyzed by the Department of Biochemistry, Sun Yat-sen Memorial Hospital.

RESULTS

Characterization of the Lipid Nanostars

To investigate the size and surface charge of the LNPs, dynamic light scattering (DLS) was utilized. Despite the shape, the size of six LNPs increased slightly (LNPs: from 72.6 ± 7.4 to 95.0 ± 0.7 nm, LNSs: from 81.9 ± 6.0 to 121.8 ± 13.2 nm) as the length of the lipid backbone increased, however no statistical significance was observed. In addition, the size was similar between LNPs and LNSs when they share the same backbone length (**Figure 1A**). The same trend could be seen in zeta potential results, where the above six LNPs and LNSs were negatively charged (~−12 mV to −15 mV) with no significant difference (**Figure 1B**). The transmission electron microscope (TEM) results showed that the $LNS_{14:4}$, $LNS_{16:6}$, and $LNS_{18:8}$ were star-shaped, and well distributed in water (**Figure 1C**).

Stability and Release Profile of the Lipid Nanostars

To check if the LNSs were stable, the size of three LNPs were measured by DLS. The diameter of the LNSs was stable at around 100 nm during the first 48 h at 37°C (**Figure 2A**). Then the release profiles of the LNSs were measured at 37°C. As shown in **Figure 2B**, the longer the lipid backbone, the slower the release of the encapsulated rhodamine. $LNS_{14:4}$ rapidly released all the encapsulated rhodamine in 12 h, while ~30% of the encapsulated rhodamine remained in $LNS_{16:6}$ at 12 h and was slowly released

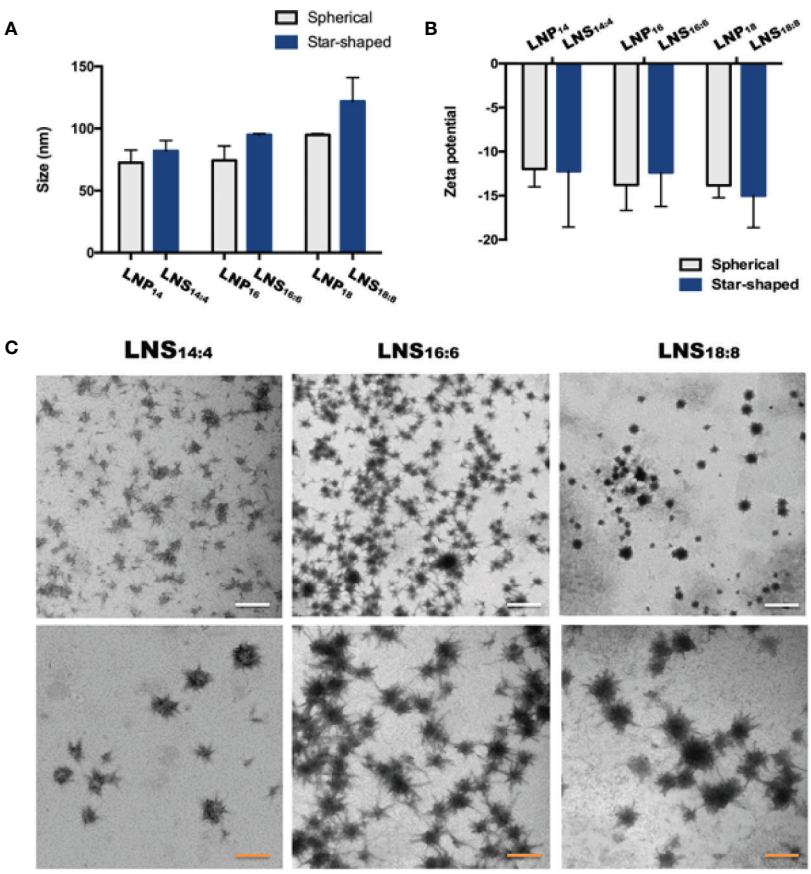

FIGURE 1 | Characterization of the lipid nanostars (LNSs). Size **(A)** and zeta potential **(B)** of the lipid nanoparticles (LNPs) (gray) and LNSs (blue); transmission electron microscopy (TEM) image **(C)** of the LNSs (the write scale bar shows 200 nm, the orange scale bar shows 50 nm).

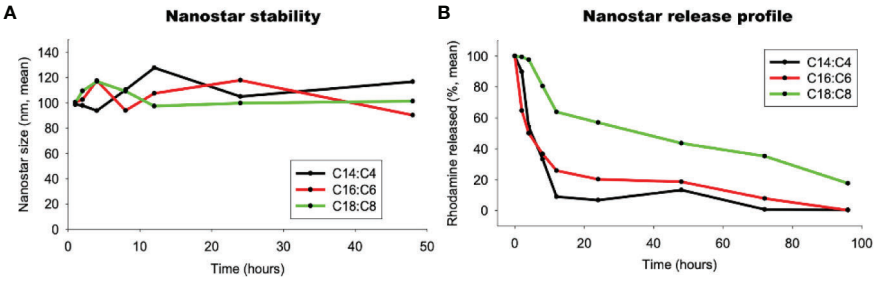

FIGURE 2 | Stability **(A)** and release profile **(B)** of the lipid nanostars (LNSs).

in the following 84 h. Moreover, $LNS_{18:8}$ retained ~60% of the encapsulated rhodamine at 12 h, and ~20% was left even at 96 h.

In Vitro and *In Vivo* Uptake of the Lipid Nanoparticles and Lipid Nanostars

To investigate the *in vitro* uptake of the LNPs and LNSs by cancer cells, the human liver cancer HepG2 cells were treated by Rhod-labeled LNPs or LNSs for 4 h, and then observed by confocal laser scanning microscope (CLSM). The results showed that for LNPs, LNP_{16} had the best cellular uptake, while LNP_{14} had the least. However, all the LNSs exhibited significantly enhanced cellular uptake compared with any of the observed LNPs (**Figure 3A**). To further investigate the permeability of the LNPs, HepG2 cells were utilized to measure the uptake in 3D sphere culture. Despite the length of the lipid backbone, the LNPs were mainly accumulated at the outer part of the tumor sphere while LNSs could deeply penetrate into the inner part of the tumor sphere. Still, LNP_{16} showed the best permeability in LNPs, and $LNS_{16:6}$ demonstrated the greatest permeability among the LNSs (**Figure 3B**). To investigate the *in vivo* extravasation in tumors, mice breast cancer 4T1 cells were utilized to build up the xenograft tumor model, and 10 mg of rhodamine-labeled LNPs or LNSs were intravenously injected into each mouse. After 24 h, the tumors were observed by IVIS®

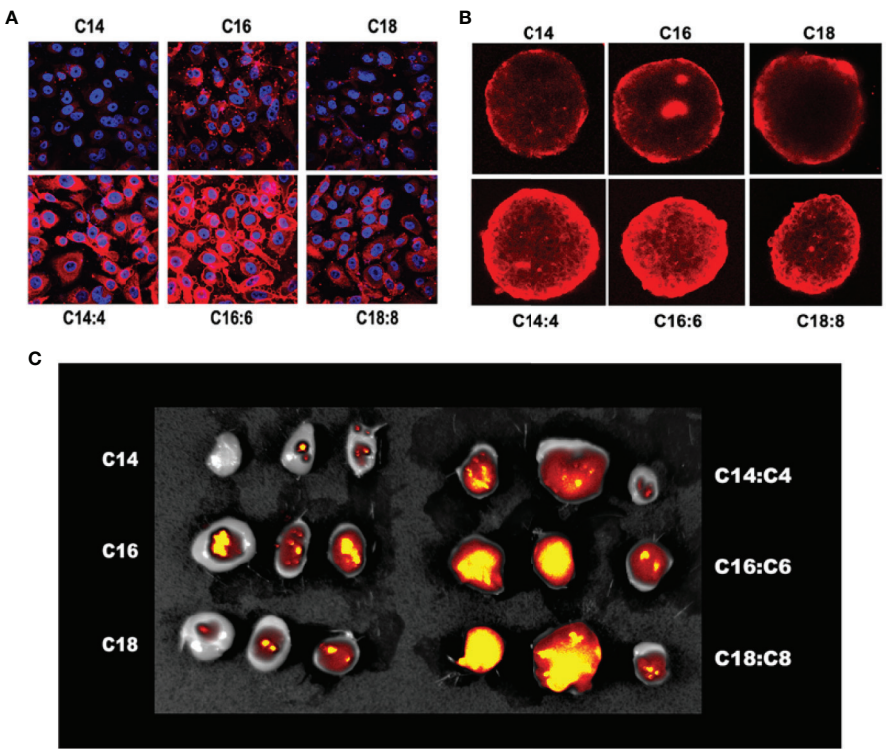

FIGURE 3 | *In vitro* and *in vivo* uptake of the lipid nanoparticles (LNPs) and lipid nanostars (LNSs). The 2D cellular uptake **(A)** of the LNPs (up) and LNSs (down); The 3D cellular uptake **(B)** of the LNPs (up) and LNSs (down); The *in vivo* tumor accumulation **(C)** of the LNPs (left) and LNSs (right); the scale bar shows 50 μm.

Imaging system. Along with the *in vitro* uptake results, LNP_{16} demonstrated the best tumor accumulation among the LNPs, while LNP_{14} performed the least. However, all the LNSs exhibited better tumor extravasation than any of the LNPs, in addition, $LNS_{16:6}$ and $LNS_{18:8}$ showed better extravasation than $LNS_{14:4}$ (**Figure 3C**).

Biodistribution of the Lipid Nanoparticles and Lipid Nanostars

To investigate the biodistribution of the LNPs and LNSs, 10 mg of rhodamine-labeled LNPs or LNSs was intravenously injected into 4T1 tumor bearing mice. After 24 h, the major organs along with the tumor and muscle were observed by IVIS. As **Figure 4** showed, those LNPs mainly accumulated in the liver, kidney, lung, and tumors, while accumulation in other organs was hardly observed. However, LNSs tend to display higher accumulation in the liver and tumors compared with the spherical nanoparticles that share the same lipid backbone length. Especially for $LNS_{14:4}$ and $LNS_{18:8}$, tumor accumulation increased significantly (**Figures 4A, C**). For $LNS_{16:6}$ and $LNS_{18:8}$, liver accumulation increased but does not show statistical significance (**Figures 4B, C**).

In Vitro and *In Vivo* Toxicity of the Lipid Nanostars

To check the *in vitro* safety of the LNSs, HepG2 cells were treated with different concentrations of each LNSs for 4 h followed by 48 h post-incubation before cell viability was measured. As the

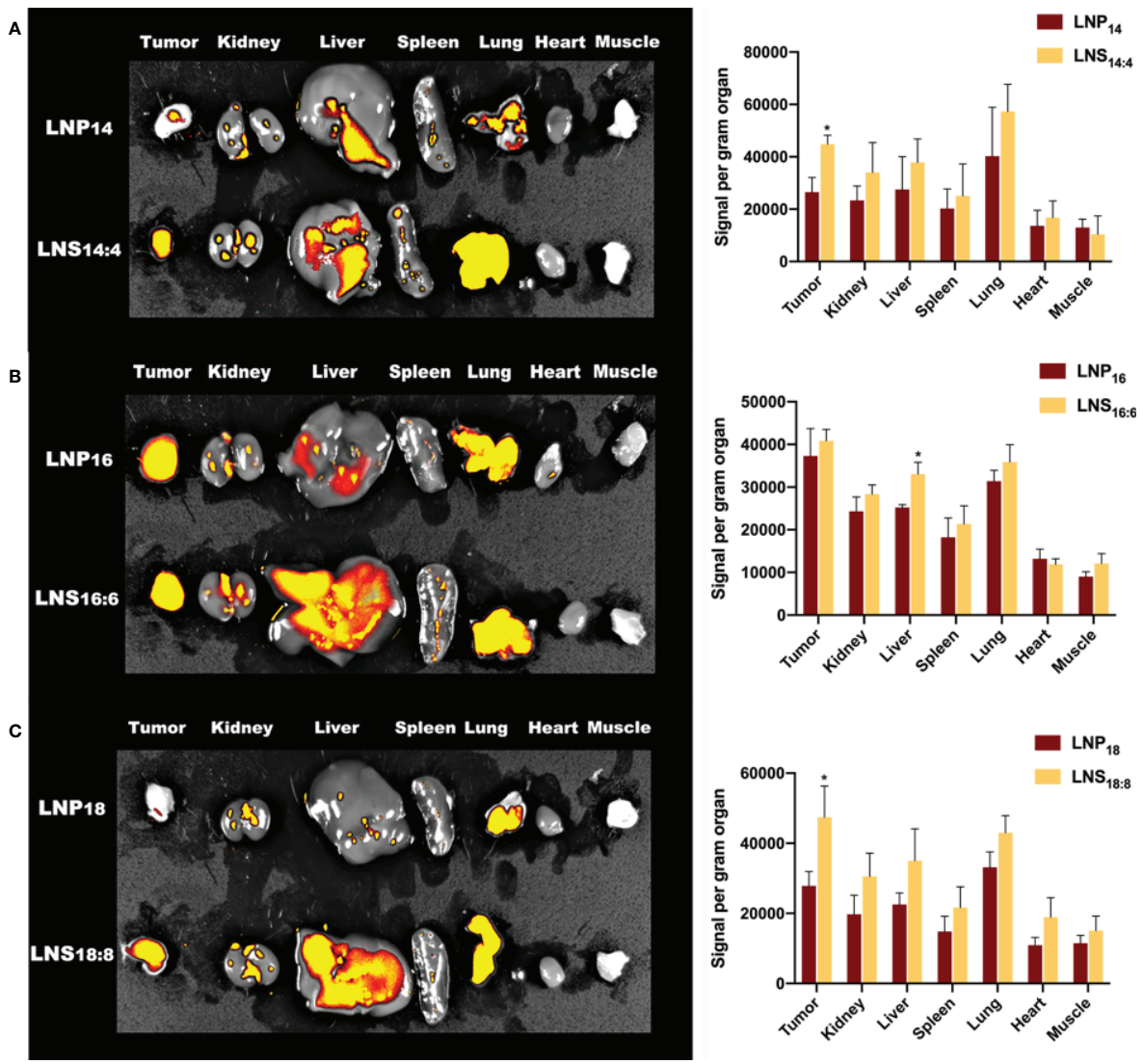

FIGURE 4 | Biodistribution of the lipid nanoparticles (LNPs) and lipid nanostars (LNSs). The image (left) and quantification (right) of *in vivo* biodistribution (BioD) of the LNPs (up) and LNSs (down) prepared by the lipid with backbone of C14/C4 **(A)**, C16/C6 **(B)**, C18/C8 **(C)**. *$p < 0.05$, compared with relevant spherical control group.

results showed, although the cell viability values fluctuated slightly, there was no significant difference. Treatment of cells with three types of LNSs revealed that these LNSs were non-toxic over the concentration range of 0.1 mg/ml to 50 mg/ml (**Figure 5A**). To further evaluate the *in vivo* safety, the LNPs or LNSs were injected intravenously at a dose of 10 mg per mouse into Balb/c mice. After 24 h, serum from mice was taken for blood biochemical examination to evaluate their liver and renal function, and the major organs was taken for HE staining to investigate the tissue damage. Compared to the control group, the ALT, AST, and urea values showed no significant changes, whereas the creatinine value of all the groups treated with LNPs decreased significantly, revealing that the liver and renal function of the mice remained normal after injection of LNPs or LNSs (**Figure 5B**). Similarly, the HE staining showed no significant tissue damage of the major organs of LNPs or LNSs treated mice (**Figure 5C**).

DISCUSSION

PCs is widely used to prepare LNPs (Chakraborty et al., 2015), however not all the PCs are suitable for nanocarrier preparation. In order to prepare qualified nanocarriers, certain lengths of backbone were required (Abumanhal-Masarweh et al., 2019). For example, PC with the backbone length of C14, C16, or C18 were used most frequently (Abumanhal-Masarweh et al., 2019), while those with short backbones (C4, C6, or C8) could hardly form nanoparticles. However, no one has reported whether mixing PCs with different lengths of backbone could be made into nanoparticles. Hence we tried series of fumulation, and finally successfully synthesized three nanoparticles by mixing long backbone PCs (C14, C16, and C18) with short backbone PCs (C4, C6, and C8) at the weight ratio of 3:1. The shape of traditional LNPs are spherical. Surprisingly, when we used PC with different lengths of backbone (C14:C4 or C16:C6 or C18:C8) at the ratio of 3:1 to prepare the nanoparticles, it demonstrated star-like shapes by TEM observation. This might be due to certain amounts of long chain PC being required to stabilize the structure of LNSs, whereas the radial arrangement of short chain PC formed the star-like shape. Due to the slightly increased backbone length of PC, the size increased slightly while no significant change could be seen. As expected, the shape exhibited no significant effect on both the size and zeta potential of the LNSs compared with their spherical controls. Since the samples used for TEM observation were dry whereas the samples were in aqueous solution for DLS detection, the size measured by DLS were bigger than as showed in TEM images due to the layer

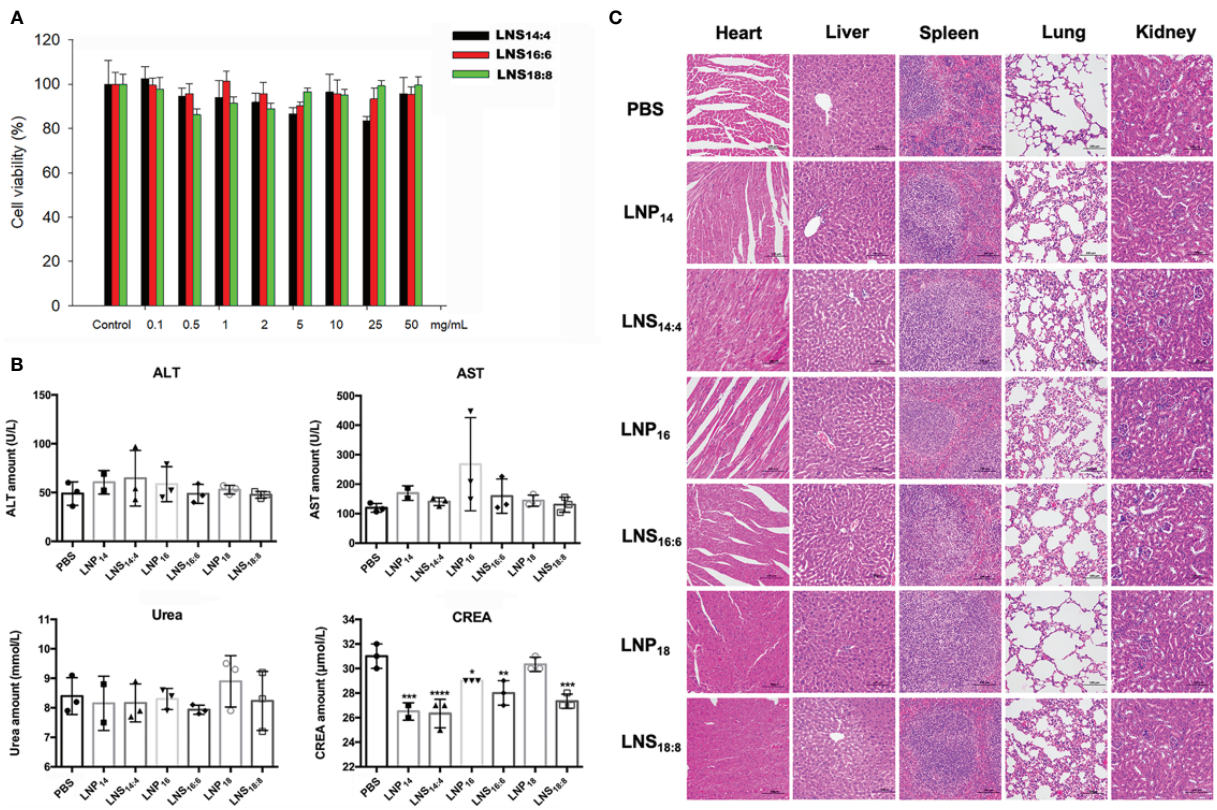

FIGURE 5 | *In vitro* and *in vivo* toxicity of lipid nanostars (LNSs). The cell viability of HepG2 cells treated with different concentrations of the LNSs **(A)**. The serum biochemistry examination of the mice injected with 10 mg of lipid nanoparticles (LNPs) and LNSs **(B)**. The HE staining of the major organs of the mice injected with 10 mg of LNPs and LNSs **(C)**. *p < 0.05; **p < 0.01; ***p < 0.005; ****p < 0.001, compared with PBS group.

of hydration around the LNPs (Naha et al., 2015; Kumar et al., 2018).

These LNSs were then studied to investigate their stability and release profiles. As mentioned above, the LNSs prepared by PC with longer backbones exhibited slower release profiles, while the size of all the LNSs remained stable after 48 h at 37°C. This result suggested that the PC with longer chains provided better interweaving with the short chain PC, resulting in stronger inter-molecular interaction. The releasing of the encapsulated rhodamine might be due to the loss of the interwoven short chain PC (C4, C6, or C8) in the LNSs.

In recent years, research regarding the effect of shape on the uptake of nanoparticles has been increasing in popularity. Anisotropic gold nanoparticles with different shapes exhibited significant different cellular uptake (Xie et al., 2017). Similar results were also reported on other inorganic nanoparticles (Karaman et al., 2012; Dai et al., 2015), carbon nanotubes (Smith et al., 2012; Zhang et al., 2017), polymeric nanoparticles (Jurney et al., 2017), and folate nanocarriers (Tahmasbi Rad et al., 2019). Consistent with these findings, our result showed that LNSs obtained significantly enhanced cellular uptake and *in vivo* tumor extravasation ability compared with their spherical controls which shared the same length of lipid backbone. One of the explanations of this phenomenon might be that the radial arrangement of long chain lipids interwoven with short chain lipids constructed arm-like structures around the surface of LNSs. These lipid "arms," unlike the sphere structures, effectively increased the surface area of the LNSs, thus largely enhancing membrane fusion. Other theories also indicates that the lipid arms of LNSs might increase the odds for it to avoid the steric effect caused by the protein on the cell surface to make direct contact with the cell membrane. Moreover, due to the inherent advantages of lipid nanocarriers, LNSs exhibits lower toxicity than inorganic nanostars meanwhile provide more possibilities to encapsulate therapeutic reagents with different solubility than polymeric nanostars.

Advantages usually come with disadvantages. As illustrated by our biodistribution results, the LNSs experienced increased accumulation in the liver, possibly due to its enhanced surface area. Thus, the question remain whether LNSs were hepatotoxic. However, the results of the serum biochemical examination reassuringly revealed no hepatotoxic effects nor renal toxicity, where the decreased creatinine value suggested enhanced renal clearance. Additionally, increased liver accumulation and renal clearance generally implied worse pharmacokinetic characteristics. However, depending on the pharmacokinetic performance, different formulations could be designed based on its remarkable cellular uptake and *in vivo* tumor extravasation, such as transdermal formulations.

CONCLUSION

As a conclusion, we first prepared three LNSs by mixing PC with different backbone lengths (C14:C4 or C16:C6 or C18:C8) at the ratio of 3:1, and then confirmed that they exhibited largely enhanced cellular uptake and *in vivo* tumor extravasation compared with their spherical controls. Among them, $LNS_{16:6}$ showed the best cellular uptake and *in vivo* tumor extravasation, while the characteristics of $LNS_{14:4}$ was increased the most. The enhanced cellular uptake and *in vivo* extravasation might have been induced by the arm-like structures around the surface due to the enlarged surface area of LNSs or the avoidance of the steric effect caused by the protein on the cell surface. Further in-depth investigation is needed to clarify the mechanism, and further research on that topic is being carried out by our team. These LNSs were proven to be safe, similar in size with their spherical controls (~100 nm), and stable at 37°C. The release rate of these LNSs were inversely related to the length of the lipid backbone ($LNS_{18:8}$ showed the slowest release profile, while $LNS_{14:4}$ showed the fastest). Additionally, numerous formulations could be considered depending on the different uptake and pharmacokinetic characteristics displayed by these LNSs, for example injection or transdermal patch. Due to the excellent cellular uptake and *in vivo* tumor accumulation, these LNSs display exciting application potential in the field of tumor therapeutics.

DATA AVAILABILITY STATEMENT

All datasets generated for this study are included in the article/ Supplementary Material.

ETHICS STATEMENT

The animal study was reviewed and approved by Sun Yat-sen Memorial Hospital.

AUTHOR CONTRIBUTIONS

PS and XX designed and oversee all experiments. SC and XLiu carried out all experiments. XLi, CL, and WZ helped in *in vivo* experiments, CT and SL analyzed the data, and BL revised and critically analyzed the manuscript.

FUNDING

This work was supported by the National Natural Science Foundation of China (81874226 and 81803020), the International Scientific and Technological Cooperation Program from Guangdong Science and Technology Department (2018A050506033), the Thousand Talents Program for Distinguished Young Scholars, the grant from Guangzhou Science and Technology Bureau (201704020131), The Three Million for Three Years Project of SYSMH, Special Funds for the Cultivation of Guangdong College Students' Scientific and Technological Innovation (pdjh2019a0001) and grant from Guangdong Science and Technology Department (2017B030314026).

REFERENCES

Abumanhal-Masarweh, H., da Silva, D., Poley, M., Zinger, A., Goldman, E., Krinsky, N., et al. (2019). Tailoring the lipid composition of nanoparticles modulates their cellular uptake and affects the viability of triple negative breast cancer cells. *J. Control Release* 307, 331–341. doi: 10.1016/j.jconrel.2019.06.025

Chakraborty, A., Mucci, N. J., Tan, M. L., Steckley, A., Zhang, T., Forrest, M. L., et al. (2015). Phospholipid composition modulates carbon nanodiamond-induced alterations in phospholipid domain formation. *Langmuir* 31 (18), 5093–5104. doi: 10.1021/la504923j

Chithrani, B. D., Ghazani, A. A., and Chan, W. C. (2006). Determining the size and shape dependence of gold nanoparticle uptake into mammalian cells. *Nano Lett.* 6 (4), 662–668. doi: 10.1021/nl052396o

Dai, L., Banta, G. T., Selck, H., and Forbes, V. E. (2015). Influence of copper oxide nanoparticle form and shape on toxicity and bioaccumulation in the deposit feeder, Capitella teleta. *Mar Environ. Res.* 111, 99–106. doi: 10.1016/j.marenvres.2015.06.010

Din, F. U., Mustapha, O., Kim, D. W., Rashid, R., Park, J. H., Choi, J. Y., et al. (2015). Novel dual-reverse thermosensitive solid lipid nanoparticle-loaded hydrogel for rectal administration of flurbiprofen with improved bioavailability and reduced initial burst effect. *Eur. J. Pharm. Biopharm* 94, 64–72. doi: 10.1016/j.ejpb.2015.04.019

Eiras, F., Amaral, M. H., Silva, R., Martins, E., Lobo, J. M. S., and Silva, A. C. (2017). Characterization and biocompatibility evaluation of cutaneous formulations containing lipid nanoparticles. *Int. J. Pharm.* 519 (1-2), 373–380. doi: 10.1016/j.ijpharm.2017.01.045

Flayhan, A., Mertens, H. D. T., Ural-Blimke, Y., Martinez Molledo, M., Svergun, D. I., and Low, C. (2018). Saposin Lipid Nanoparticles: A Highly Versatile and Modular Tool for Membrane Protein Research. *Structure* 26 (2), 345–355 e5. doi: 10.1016/j.str.2018.01.007

Han, Y., Zhang, Y., Li, D., Chen, Y., Sun, J., and Kong, F. (2014). Transferrin-modified nanostructured lipid carriers as multifunctional nanomedicine for codelivery of DNA and doxorubicin. *Int. J. Nanomed.* 9, 4107–4116. doi: 10.2147/IJN.S67770

Hare, J. D. (1975). Distinctive alterations of nucleoside, sugar and amino acid uptake of sulfhydryl reagents in cultured mouse cells. *Arch. Biochem. Biophys.* 170 (2), 347–352. doi: 10.1016/0003-9861(75)90128-9

Jiang, Y., Huo,, S., Mizuhara, T., Das, R., Lee, Y. W., Hou, S., et al. (2015). The Interplay of Size and Surface Functionality on the Cellular Uptake of Sub-10 nm Gold Nanoparticles. *ACS Nano* 9 (10), 9986–9993. doi: 10.1021/acsnano.5b03521

Jurney, P., Agarwal, R., Singh, V., Choi, D., Roy, K., Sreenivasan, S. V., et al. (2017). Unique size and shape-dependent uptake behaviors of non-spherical nanoparticles by endothelial cells due to a shearing flow. *J. Control Release* 245, 170–176. doi: 10.1016/j.jconrel.2016.11.033

Karaman, D. S., Desai, D., Senthilkumar, R., Johansson, E. M., Ratts, N., Oden, M., et al. (2012). Shape engineering vs organic modification of inorganic nanoparticles as a tool for enhancing cellular internalization. *Nanoscale Res. Lett.* 7 (1), 358. doi: 10.1186/1556-276X-7-358

Khan, D. R., Rezler, E. M., Lauer-Fields, J., and Fields, G. B. (2008). Effects of drug hydrophobicity on liposomal stability. *Chem. Biol. Drug Des.* 71 (1), 3–7. doi: 10.1111/j.1747-0285.2007.00610.x

Kumar, R., Singh, A., Garg, N., and Siril, P. F. (2018). Solid lipid nanoparticles for the controlled delivery of poorly water soluble non-steroidal anti-inflammatory drugs. *Ultrason Sonochem.* 40 (Pt A), 686–696. doi: 10.1016/j.ultsonch.2017.08.018

Ma, Y., Zhang, X., Xu, X., Shen, L., Yao, Y., Yang, Z., et al. (2015). STAT3 Decoy Oligodeoxynucleotides-Loaded Solid Lipid Nanoparticles Induce Cell Death and Inhibit Invasion in Ovarian Cancer Cells. *PloS One* 10 (4), e0124924. doi: 10.1371/journal.pone.0124924

Matsumura, Y., and Maeda, H. (1986). A new concept for macromolecular therapeutics in cancer chemotherapy: mechanism of tumoritropic accumulation of proteins and the antitumor agent smancs. *Cancer Res.* 46 (12 Pt 1), 6387–6392.

Mendes M, M. A., Cova, T., Gonçalves, L., Almeida, A. J., Sousa, J. J., do Vale, M. L. C., et al. (2018). Modeling of ultra-small lipid nanoparticle surface charge for targeting glioblastoma. *Europe J. Pharmaceut. Sci.* 117, 255–269. doi: 10.1016/j.ejps.2018.02.024

Naha, P. C., Chhour, P., and Cormode, D. P. (2015). Systematic in vitro toxicological screening of gold nanoparticles designed for nanomedicine applications. *Toxicol. Vitro* 29 (7), 1445–1453. doi: 10.1016/j.tiv.2015.05.022

Saw, P. E., Yu, M., Choi, M., Lee, E., Jon, S., and Farokhzad, O. C. (2017a). Hyper-cell-permeable micelles as a drug delivery carrier for effective cancer therapy. *Biomaterials* 123, 118–126. doi: 10.1016/j.biomaterials.2017.01.040

Saw, P. E., Yu, M., Choi, M., Lee, E., Jon, S., and Farokhzad, O. C. (2017b). A drug-delivery strategy for overcoming drug resistance in breast cancer through targeting of oncofetal fibronectin. *Nanomedicine* 13 (2), 713–722. doi: 10.1016/j.nano.2016.10.005

Shi, J., Kantoff, P. W., Wooster, R., and Farokhzad, O. C. (2017). Cancer nanomedicine: progress, challenges and opportunities. *Nat. Rev. Cancer* 17 (1), 20–37. doi: 10.1038/nrc.2016.108

Smith, B. R., Kempen, P., Bouley, D., Xu, A., Liu, Z., Melosh, N., et al. (2012). Shape matters: intravital microscopy reveals surprising geometrical dependence for nanoparticles in tumor models of extravasation. *Nano Lett.* 12 (7), 3369–3377. doi: 10.1021/nl204175t

Tahmasbi Rad, A., Chen, C. W., Aresh, W., Xia,, Y., Lai, P. S., and Nieh, M. P. (2019). Combinational Effects of Active Targeting, Shape, and Enhanced Permeability and Retention for Cancer Theranostic Nanocarriers. *ACS Appl. Mater Interf.* 11 (11), 10505–10519. doi: 10.1021/acsami.8b21609

Wang, T., Shen, L., Zhang, Z., Li, H., Huang, R., Zhang, Y., et al. (2017). A novel core-shell lipid nanoparticle for improving oral administration of water soluble chemotherapeutic agents: inhibited intestinal hydrolysis and enhanced lymphatic absorption. *Drug Delivery* 24 (1), 1565–1573. doi: 10.1080/10717544.2017.1386730

Xie, X., Liao, J., Shao, X., Li, Q., and Lin, Y. (2017). The Effect of shape on Cellular Uptake of Gold Nanoparticles in the forms of Stars, Rods, and Triangles. *Sci. Rep.* 7 (1), 3827. doi: 10.1038/s41598-017-04229-z

Xu, Y., Jin, X., Ping, Q., Cheng, J., Sun, M., Cao, F., et al. (2010). A novel lipoprotein-mimic nanocarrier composed of the modified protein and lipid for tumor cell targeting delivery. *J. Control Release* 146 (3), 299–308. doi: 10.1016/j.jconrel.2010.05.022

Zhang, B., Feng, X., Yin, H., Ge, Z., Wang, Y., Chu, Z., et al. (2017). Anchored but not internalized: shape dependent endocytosis of nanodiamond. *Sci. Rep.* 7, 46462. doi: 10.1038/srep46462

Zugazagoitia, J., Guedes, C., Ponce, S., Ferrer, I., Molina-Pinelo, S., and Paz-Ares, L. (2016). Current Challenges in Cancer Treatment. *Clin. Ther.* 38 (7), 1551–1566. doi: 10.1016/j.clinthera.2016.03.026

Conflict of Interest: The authors declare that the research was conducted in the absence of any commercial or financial relationships that could be construed as a potential conflict of interest.

frontiers in Pharmacology

ORIGINAL RESEARCH
published: 01 May 2020
doi: 10.3389/fphar.2020.00471

Facile Strategy on Hydrophilic Modification of Poly(ε-caprolactone) Scaffolds for Assisting Tissue-Engineered Meniscus Constructs *In Vitro*

Zhu-Xing Zhou[1†], You-Rong Chen[1†], Ji-Ying Zhang[1], Dong Jiang[1], Fu-Zhen Yuan[1], Zi-Mu Mao[1], Fei Yang[2,3], Wen-Bo Jiang[4], Xing Wang[2,3] and Jia-Kuo Yu[1]**

[1] Knee Surgery Department of the Institute of Sports Medicine, Peking University Third Hospital, Beijing, China, [2] Beijing National Laboratory for Molecular Sciences, State Key Laboratory of Polymer Physics & Chemistry, Institute of Chemistry, Chinese Academy of Sciences, Beijing, China, [3] University of Chinese Academy of Sciences, Beijing, China, [4] Clinical Translational R&D Center of 3D Printing Technology, Shanghai Ninth People's Hospital, Shanghai Jiao Tong University School of Medicine, Shanghai, China

OPEN ACCESS

Edited by:
Jianxun Ding,
Chinese Academy of Sciences, China

Reviewed by:
Wuyu Zhang,
University of Louisville, United States
Lei Zhang,
Tsinghua University, China

***Correspondence:**
Xing Wang
wangxing@iccas.ac.cn
Jia-Kuo Yu
yujiakuo@126.com

†These authors have contributed equally to this work

Specialty section:
This article was submitted to Translational Pharmacology, a section of the journal Frontiers in Pharmacology

Received: *26 October 2019*
Accepted: *25 March 2020*
Published: *01 May 2020*

Citation:
Zhou Z-X, Chen Y-R, Zhang J-Y, Jiang D, Yuan F-Z, Mao Z-M, Yang F, Jiang W-B, Wang X and Yu J-K (2020) Facile Strategy on Hydrophilic Modification of Poly(ε-caprolactone) Scaffolds for Assisting Tissue-Engineered Meniscus Constructs In Vitro. Front. Pharmacol. 11:471. doi: 10.3389/fphar.2020.00471

Poly(ε-caprolactone) (PCL) derived scaffolds have been extensively explored in the field of tissue-engineered meniscus (TEM) originating from their good biosafety and biomechanical properties. However, the poor intrinsic hydrophobicity severely hindered their wide applications for the scaffold-assisted tissue regeneration. Herein, we developed a simple strategy on surface modification of three-dimensional (3D) PCL scaffolds *via* a simply soaking treatment of sodium hydroxide (NaOH) solutions to increase the hydrophilicity and roughness of scaffolds' surfaces. We investigated the effect of hydrolysis degree mediated by NaOH solutions on mechanical properties of 3D scaffolds, considering the importance of scaffolds' resistance to internal force. We also investigated and analyzed the biological performances of mesenchymal stromal cells (MSCs) and meniscal fibrocartilage cells (MFCs) onto the scaffolds treated or untreated by NaOH solutions. The results indicated that hydrophilic modification could improve the proliferation and attachment of cells on the scaffolds. After careful screening process condition, structural fabrication, and performance optimization, these modified PCL scaffolds possessed roughened surfaces with inherent hierarchical pores, enhanced hydrophilicity and preferable biological performances, thus exhibiting the favorable advantages on the proliferation and adhesion of seeded cells for TEM. Therefore, this feasible hydrophilic modification method is not only beneficial to promote smarter biomedical scaffold materials but also show great application prospect in tissue engineering meniscus with tunable architectures and desired functionalities.

Keywords: tissue-engineered meniscus, poly(ε-caprolactone), fused deposition modeling, three-dimension printing, scaffold, hydrophilic modification, regenerative medicine

INTRODUCTION

Traumatic meniscal disorder is one of the most common types of orthopedic injuries in many people of all ages (Beals et al., 2016). It was estimated that the number of patients in need of meniscal surgery was over 1.5 million until 2014 in Europe and US (Moran et al., 2015). Traditionally, arthroscopic surgery in clinical practice was performed to relieve symptoms and improve outcomes, especially, meniscal lesions in avascular region are irreversible and difficult to be restored, which often requires partial and total meniscectomy (Rongen et al., 2014; Roos and Thorlund, 2017; Thorlund et al., 2017). Up to date, physicians and researchers have been aware of the important role of menisci in knee joints, including the protective effect on cartilage, absorbing the shock, and maintaining the stability of the knees (Badlani et al., 2013). Therefore, a number of measures are devised to save meniscal tissues or replace the irreparable meniscal issues rather than simple removal of them.

One of the intellectual strategies is meniscal regeneration enhanced by tissue-engineered technique, in which meniscal scaffolds fabricated by biocompatible materials are loaded with living seeded cells (Petri et al., 2012; Zhang et al., 2017). Materials for scaffold's fabrication in that strategy play a vital role in scaffold-guided tissue regeneration, particularly for tissue-engineered meniscus (TEM), which are not only supposed to resist the load from femur and tibia with strong mechanical properties, but also provide a suitable microenvironment for seeded cells to reside. Based on those requirements, the emerging biodegradable macromolecular materials with tunable biophysical and biochemical properties promote the development of scaffolds for TEM dramatically. In the past few decades, a number of recent studies evaluated and published the results of biocompatibilities, biomechanical properties, and replacing functions of synthetic materials for TEM (Hannink et al., 2011; Verdonk et al., 2011; Esposito et al., 2013; Lee et al., 2014; Kwak et al., 2017; Moradi et al., 2017). In those materials, poly(ε-caprolactone) (PCL), as one of the aliphatic polyesters, possesses thermal plasticity and shapeability that can be molded into different three-dimensional (3D) scaffolds with designed geometric shape, degrading into nontoxic products after implantation into host (Oh et al., 2007; Zhang et al., 2017). More importantly, it had been an FDA-approved implantable biomaterial (Neufurth et al., 2017), which suggested its fitness for the tissue-engineered applications. In our recent research, we found that 3D-printed PCL scaffolds combined with biophysical and biochemical stimuli could contribute to well-regenerated and anisotropic menisci with better mechanical properties and protective effects on cartilage (Zhang et al., 2019). Thus, PCL-based TEM attracts wide attention and exhibits a promising prospect to realize meniscal regeneration and therapeutic potential of TEM applications.

However, similar to other aliphatic polymers with the intrinsic hydrophobicity, the hydrophilicity of the PCL should be improved although it has many abovementioned advantages and bright application prospects. When it comes to hydrophobicity, it leads to the lack of recognition site attached by cells on the surface of scaffold, impeding the cellular behavior on scaffold (Neufurth et al., 2017). Some strategies of hydrophilic modification such as protein coating, cold plasma treatment, and chemical etching are conducted to achieve well-attached property for scaffold (Ma et al., 2007). Given the time-consuming, complexity, and expensiveness, some of abovementioned techniques are not practical. Therefore, a simple method on the hydrophilic development of PCL scaffolds is urgent and imperative in the field of TEM.

In this work, we devised a simple and efficient strategy of NaOH etching to facilitate seeded cells to attach and proliferate on the PCL scaffolds (**Figure 1**). Based on the fused deposition modeling (FDM) technique, 3D PCL scaffolds were well fabricated with homogeneous microstructures, such as pore size, pore interconnectivity, and satisfactory mechanical properties. Adjusting the alkali soaking time of PCL scaffolds could significantly improve their hydrophilicity and increase the roughness of surfaces without severely impairing the biomechanical properties. Notably, the rougher surfaces of PCL fibers were beneficial to the attachment, viability, and proliferation of two commonly used seeded mesenchymal stromal cells (MSCs) and meniscal fibrocartilage cells (MFCs). Overall, this universal alkali soaking strategy could be a cost-efficient method of hydrophilic modification for the construction of cell-scaffold for meniscal regeneration.

MATERIALS AND METHODS

Scaffold Fabrication and Hydrophilic Modification

3D-PCL (Mn=80,000, Sigma-Aldrich, MO, USA) scaffolds were fabricated by FDM 3D printing system as previously described (Zhang et al., 2017). Briefly, the PCL particles were added into a metal tube and melted to molten state before extrusion by a nozzle. During the fabrication process of layer-by-layer, the metal nozzle could lay down the PCL fibers at the 0°–90° direction controlled by computer-aided system. The printing parameters were set to ensure the microstructures of scaffolds to be dispersed homogenously, including pore size, thickness and space between two layers. After fabrication, the scaffolds were cut into some small cylinder examples by trephine. Those cylinder scaffolds were treated by 5 M NaOH for different time point at 0, 5, 15, and 30 min at room temperature. After soaking, the scaffolds were washed thoroughly with flowing water 12 h and rinsed by deionized water for three times.

Characterization of 3D-Printed PCL Scaffolds With or Without Hydrolysis Treatment

After being coated with a 5-nm layer of gold in a high-vacuum gold sputter coater, the scaffolds were observed under scanning electron microscopy (SEM) (JEOL USA, Inc., Peabody, MA, USA) to observe the morphology of produced scaffolds treated and untreated with 5 M NaOH. In order to measure the microstructural parameters of scaffolds, we used Image-J software (NIH Image, Bethesda, MD) to analyze mean pore sizes and road widths of samples (n = 4). The Leica DCM 3D

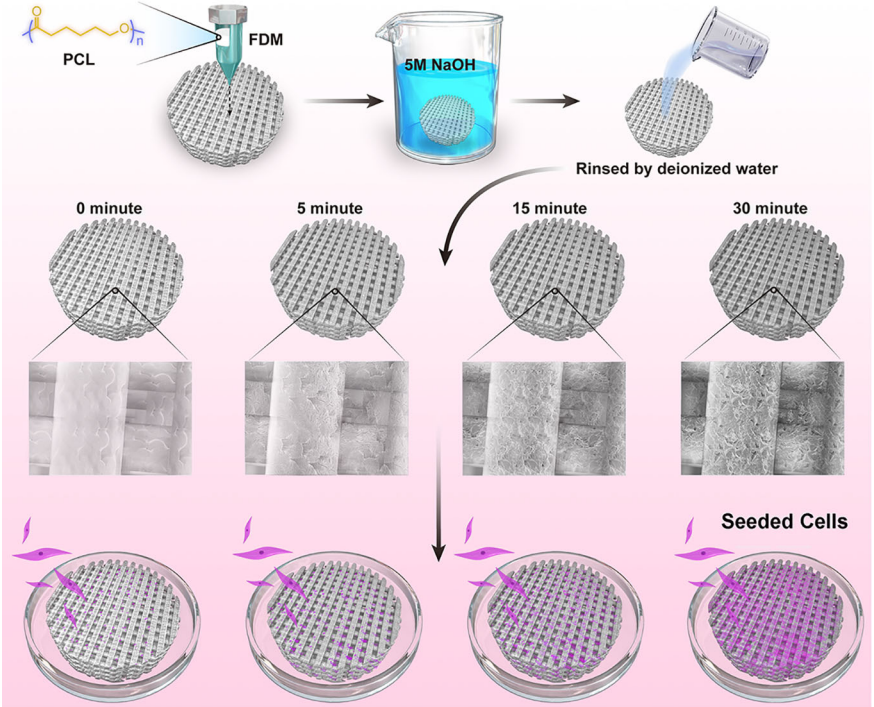

FIGURE 1 | Schematic illustration for NaOH-modified poly(ε-caprolactone) (PCL) scaffolds seeded with mesenchymal stromal cells (MSCs) and meniscal fibrocartilage cells (MFCs).

dual system (Leica, Nussloch, Germany) was used to display the surface topography and calculate the surface area roughness (Sa) of 3D PCL scaffold. Images were taken with a confocal objective with a magnification of 150×, and 10 independent sites of a sample under the same conditions were observed and analyzed (n = 3). The chemical characteristics of samples were revealed by ^{1}H nuclear magnetic resonance spectrum (^{1}H NMR) on 600 MHz Bruker AVII-600 spectrometers.

Water Contact Angle Measurements

The water contact angle was evaluated for the change of hydrophilicity of untreated and treated PCL. Considering the existing porous structure of PCL scaffold, water would penetrate the pores leading to the failed results. Therefore, static contact angle measurements were performed on the produced PCL-based membranes prepared by 5wt% of PCL chloroform solution into a poly(tetrafluoroethylene) (PTFE) mold, which were then treated with NaOH, rinsed by deionized water with abovementioned method and dried in air for 24 h. Untreated PCL membranes were prepared for 0 min group. Contact angles of deionized water drops were recorded and calculated at room temperature with Drop shape Analyzer-DSA100 (Krüss, Hamburg, Germany) (Shen et al., 2008). Twelve independent determinations at different sites of three films' (Four sites were collected in each film, n = 3) surfaces were averaged.

Degradation Experiments *In Vitro*

In this experiments, PCL scaffolds of all groups were completely immersed into phosphate buffered saline (PBS, pH=7.4) to investigate whether hydrolyzed effects applied by NaOH could accelerate the degradation rate of PCL. In brief, the dry weights of samples (n = 6) among all groups were recorded as m_0 before hydrolysis. After treatment by NaOH for different time, these samples were rinsed by distilled water thoroughly and immersed into PBS at room temperature whose dry weights were then recorded respectively as m_1 at the first day and fifteenth day after degradation in PBS. The mass loss (%) during immersion into PBS was calculated as the following formula.

$$\text{Mass loss } \% = \left[\frac{m_0 - m_1}{m_0}\right] \times 100\,\%$$

Mechanical Tests

To investigate the hydrolyzed effects mediated by 5 M NaOH on scaffolds' mechanical properties, we performed compression and tensile tests on the cylindrical samples and "dog-bone" shape samples of PCL, which were printed according to the same protocols and parameters. For compressive test, the cylindrical sample of 6 mm diameter and 2.5 mm thickness was prepared by trephine. The compressive test was conducted at a constant stress rate of 1 mm/min (n = 5). For tensile test, the "dog-bone" shape

sample of 75 mm length and 2.5 mm thickness was loaded by tensile force to ultimate failure at a rate of 2 mm/min (n = 5).

Biological Evaluation

Isolation, Culture of seeded cells

All protocols of animal experiments for isolation of MSCs and MFCs were approved by the Animal Care and Use Committee of Peking University Third Hospital. The method we used to isolate, culture and passage seeded cells was similar to the previous article published by our group (Wang S. et al., 2016). MSCs and MFCs reaching 80% to 90% confluence were trypsinized with 0.25% trypsin/0.1% ethylene diamine tetraacetic acid (EDTA, Gibco BRL Co. Ltd. Gaithersburg, MD, USA) for passage at 1:2. MFCs and MSCs were used between the second passage (P2) and the fifth passage (P5).

Cell Seeding

Scaffolds were totally immersed into 70% ethanol for 12 h to sterilize before they were rinsed in PBS three times, and then air-dried for 24 h at room temperature in a biosafety cabinet. The scaffolds were wet with 200 μl of media containing 10% fetal bovine serum (FBS) and kept in standard conditions (37°C under 5% CO_2 and 95% humidity) for 2 h prior to cell seeding. Cells were seeded on each scaffold (50 μl of medium containing around 5×10^4 cells). The cell-seeded scaffolds were incubated at standard conditions (37°C under 5% CO_2 and 95% humidity) for 2 h to allow cell attachment before the addition of 1 ml of culture media.

Cell Viability/Proliferation

We adopted the alamarBlue™ Cell Viability Reagent (Life Technologies, Carlsbad, CA, USA) to study the cell proliferation on the scaffold untreated and treated with NaOH. Briefly, cell proliferation was measured at the first and fifth day after cell seeding to PCL scaffolds, the cell-seeded PCL scaffolds were transferred to a new 48-well plate, and 10% alamarBlue™ solution (alamarBlue™: growth culture medium, 1:9; v/v) was added to each well and the control well. The plates were incubated for 4 h under standard conditions. After incubation, 150 μl of each sample was pipetted and moved to a 96-well plate, and the absorbance was measured at 570 and 600 nm respectively with a plate reader (n = 5). The cellular viability was assessed with a LIVE/DEAD Viability/Cytotoxicity assay (Invitrogen, Carlsbad, CA, USA) under Leica TCS-SP8 confocal laser microscopy (CFLM; Leica, Nussloch, Germany). All PCL scaffolds with seeded cells were cultured in complete medium for 3 days. Before the test, the samples (n = 3) were washed in PBS three times, followed by immersion in 500.0 μl of PBS with 2.0 mM calcein AM and 4.0 mM ethidium homodimer-1 reagents, and incubated for 30 min at room temperature. Excitation wavelength of 568 or 488 nm was adopted to excite the fluorescence.

Cell Morphology and Attachment

The cell morphology and attachment were observed under SEM. After a three-day culture, cell-seeded scaffolds (n = 3) were rinsed by PBS and fixed immediately in a 2.5% glutaraldehyde solution, and then dehydrated with a gradient ethanol and the critical point drying was performed in liquid CO_2 at 37°C. After being coated with gold, those samples were viewed by a scanning electron microscope. F-actin and nuclear of the cells in the 3D scaffolds (n = 3) cultured in 3 days after seeding were observed by confocal microscopy. Briefly, the samples were washed with PBS three times and fixed with 4% paraformaldehyde for 30 min and the cellular membranes were penetrated with 0.5 % Triton X-100. The cytoskeleton was stained by Acti-stain™ 488 phalloidin (100 nM; Cytoskeleton Inc., Denver, CO, USA) for 30 min at room temperature, and the nuclei were stained by RedDot™-2 (Cambridge Bioscience; #40061) working solution for 10 min.

Statistical Analysis

The data in the current work were expressed as means ± standard deviation (SD). We used SPSS statistical software (Version 20.0; SPSS Inc., Chicago, IL, USA) to perform datum analysis. A one-way analysis of variance (ANOVA) and the paired sample t test were used to analyze the results, $p < 0.05$ was considered statistically significant.

RESULTS AND DISCUSSION

Characterization of 3D PCL Scaffold

The 3D PCL scaffold was printed by FDM technique with 30 mm×30 mm×2.5 mm, and then trimmed into cylindrical test samples with a 6-mm diameter corneal trephine respectively for the following experiments. The gross view of cylindrical test sample with 6.0 mm in diameter and 2.5 mm height was illustrated in **Figure 2A**. The PCL fibers deposited layer by layer along 0°–90°, forming the micropores with square geometry, in which the top surface and cross-section of PCL fibers displayed the relatively homogenous microstructures and interconnection by the SEM observation (**Figure 2B**). We also analyzed the distribution of pore size and road width and found that the mean pore sizes of scaffolds were 236.5 μm ± 23.8 μm with the arrangement from 146.7–300.0 μm while the mean road widths were 338.1 μm ± 11.6 μm with the arrangement from 306.7–370.9 μm (**Figures 2C, D**). FDM, a 3D printing technique, melts, extrudes biomaterials and then deposits the examples with targeted geometric shape by controlling the pathway of moving nuzzle. In our previous work, we investigated the role of mean pore sizes of PCL-fabricated meniscal implants printed by FDM in promoting the meniscal regeneration (Zhang et al., 2016). As a cost-effective rapid prototype technique, it not only avoided using the toxic organic solvents for materials during the process of fabrication, but also generated relatively homogenous microstructural parameters, such as pore sizes, porosities, and road widths of fibers, reducing the differences among testing specimens effectively (Do et al., 2015). The change in chemical structures of PCL scaffolds immersed into NaOH was detected by NMR as illustrated in **Figure 3**. Compared with the original PCL, an obvious signal peak occurred at 3.7 ppm in the ^{1}H-NMR spectra, which belongs to the free hydroxyl group at the end of PCL chain, indicating the breakage of ester bond and hydrolysis of PCL under alkali conditions. In addition, the

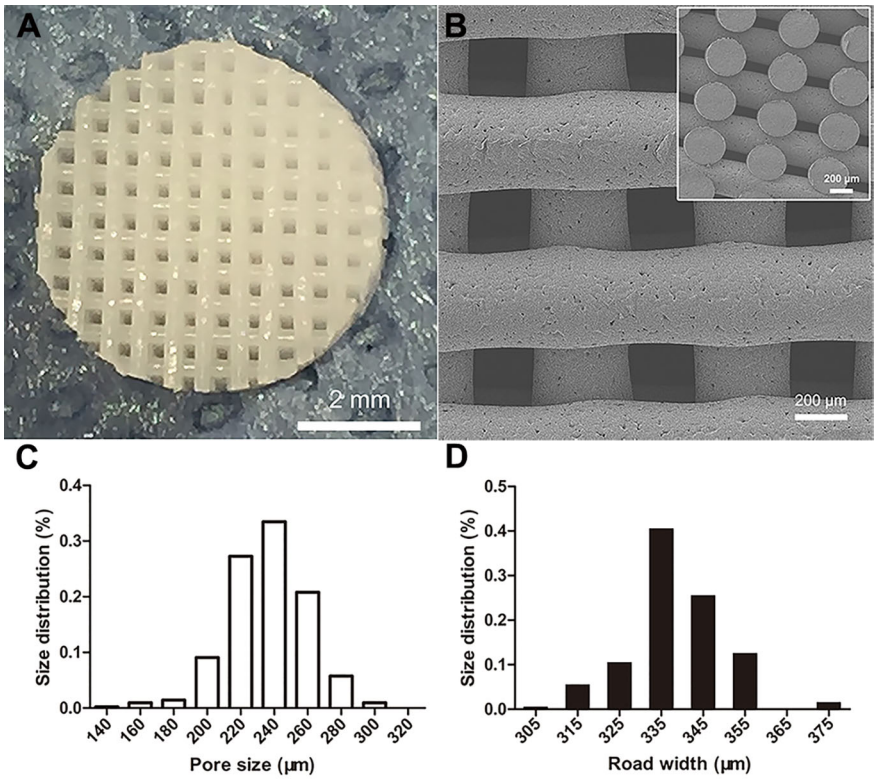

FIGURE 2 | Morphological characteristics of poly(ε-caprolactone) (PCL) scaffolds. The PCL specimen with 6.0 mm in diameter and 2.5 mm height, scale bar represented 2 mm **(A)**. The SEM image of top surface and cross-section of scaffold, scale bar represented 200 μm **(B)**. The distribution of PCL scaffolds' micropore size **(C)** and road width **(D)**.

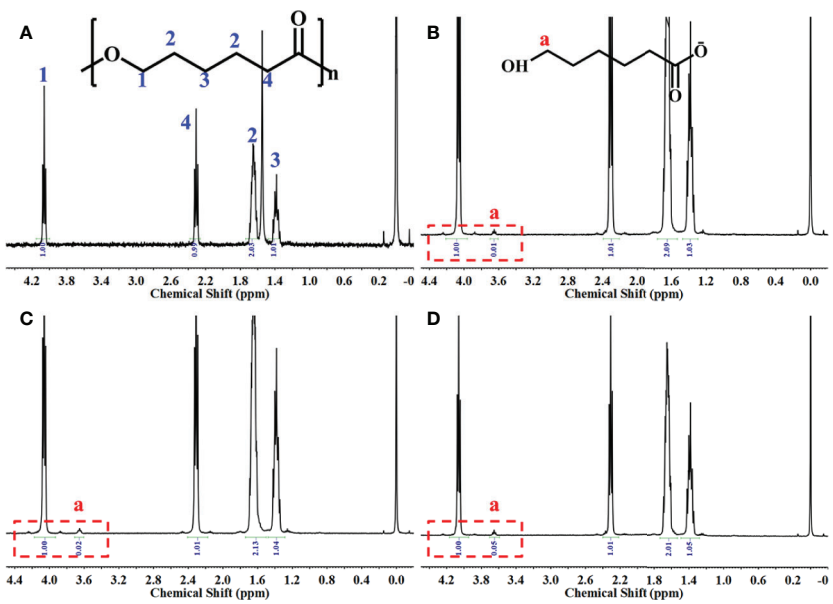

FIGURE 3 | ^{1}H-NMR spectrum of the samples. Original poly(ε-caprolactone) (PCL) scaffolds **(A)**, PCL scaffolds etched by NaOH for 5 **(B)**, 15 **(C)**, and 30 min **(D)**.

quantitative proof was clearly seen in the integral areas ratio (1: a). Along with the immersion time in NaOH for 5, 15, and 30 min, this typical area ratio was 100:1, 50:1, and 20:1, respectively, which further reflected more hydrophilic function groups exposing at the surfaces of samples as they soaked into NaOH for a longer time. Similarly, all of other samples showed the same characteristics, revealing that the hydrolyzed effect did not change the bulk chain of PCL and alkali treatment was one of the suitable strategies for PCL surface hydrophilic modification.

Water Contact Angle and Morphological Observation of PCL

Water contact angel in air could illustrate the hydrophilicity of material surface, thus, it is a direct indicator of the hydrophilic change of PCL surface before and after treatment of NaOH solutions. However, because of the porous texture of PCL scaffold, it is hard to measure the values directly. Hereby, we characterized the hydrophilic changes of films paved by the same materials and exposed into the 5 M NaOH under the same condition with scaffold to assess the hydrophilic modification result of PCL after NaOH treatment. The results of apparent static contact angles on PCL films soaked in 5 M NaOH at different time point were illustrated in **Figures 4A–D**. After the treatment of NaOH, the water contact angles of PCL films in 5, 15, and 30 min of treatment groups was 66° ± 4.4°, 55° ± 4.2°, and 39° ± 5.7°, respectively, displaying a significant reductive tendency compared to the untreated PCL films with 83° ± 7.1°. A statistical difference was detected among all alkali-treated PCL films at different time point, suggesting that the hydrophilicity of PCL surface increased with the soaking time prolonging in 5 M NaOH. (p<0.05). Due to the hydrolysis of aliphatic polyester in NaOH solutions, hydrophilic carboxyl and hydroxyl of PCL surface can be produced by cleaving the ester bonds (Wang W. et al., 2016). When the PCL-based films were soaked into 5 M NaOH for different time, the water contact angle variation indicated that the alkali treatment could effectively degrade the ester bond and dramatically etch the PCL surface to improve its hydrophilicity that was in line with the previous research (Yang et al., 2003). These results also suggested that 30 min soaking in 5 M NaOH is enough for PCL (Mn = 80000) to improve its hydrophilicity without prolonged soaking time. The SEM images in **Figures 4E–H** revealed the change of surfaces' characteristics of PCL scaffolds. 3D confocal topographical images in **Figures 5A–D** represented and analyzed the roughness of 3D scaffolds' surfaces treated by NaOH for 0, 5, 15, and 30 min. Evidently, the roughness increased dramatically because of the different treatment time soaked in NaOH solution as showed in **Figure 5E** (P<0.05). The surface of untreated PCL scaffold was relatively smooth, however, the surfaces crazed gradually with the increase of gaps, cracks, and defects, which even appeared volcanic topographical characteristics onto scaffolds etched by NaOH for 30 min. These results demonstrated that controlling the etching time of NaOH could not only modify the hydrophilicity of PCL, but also regulate the surfaces' roughness.

Degradation Experiments *In Vitro*

The results of degradative changes in mass loss (%) of original and hydrolyzed PCL scaffolds were shown in **Figure 6**. At the first day, the mass loss % of PCL scaffolds etched by NaOH for 0, 5, 15, and 30 min was 0.27%±0.19%, 8.58%±0.37%, 25.79%±1.2%, and 38.38%±0.91%, respectively. After immersion into PBS for fifteen days, the mass loss % of those samples was 0.40% ±0.35%, 9.43%±0.95%, 29.57%±1.08%, and 52.77%±1.30%, respectively. The mass loss of all samples among groups of 5, 15, and 30 min at the fifteenth day showed higher than their loss at the first day ($p < 0.05$), while no significant results were detected among untreated scaffolds between the first and second measurements ($p > 0.05$). Apparently, PCL was much more easily degraded *in vitro* after exposure to 5 M NaOH, which indicated that the surface modification of alkali applied on PCL could not only improve its hydrophilicity, but also accelerate its degradation. The main mechanism related to abovementioned phenomenon is the formation of hydroxyl and carboxyl groups at the surfaces of scaffolds. When the increasing number of hydrophilic groups exposed with materials soaked into alkali solutions much longer, more hydrogen bonds between the

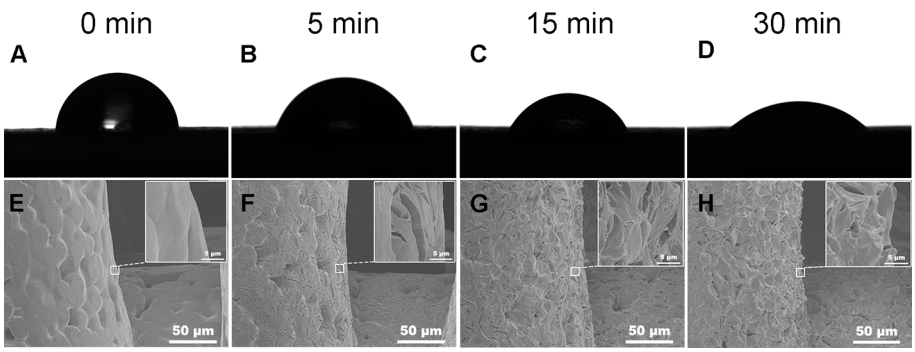

FIGURE 4 | Water contact angle in the air of poly(ε-caprolactone) (PCL) film. Samples treated by 5 M NaOH for different time **(A–D)**. Scanning electron microscopy (SEM) images of PCL scaffolds' surfaces soaked in 5 M NaOH for different time **(E–H)**. **(A, E)** 0, **(B, F)** 5, **(C, G)** 15, and **(D, H)** 30 min.

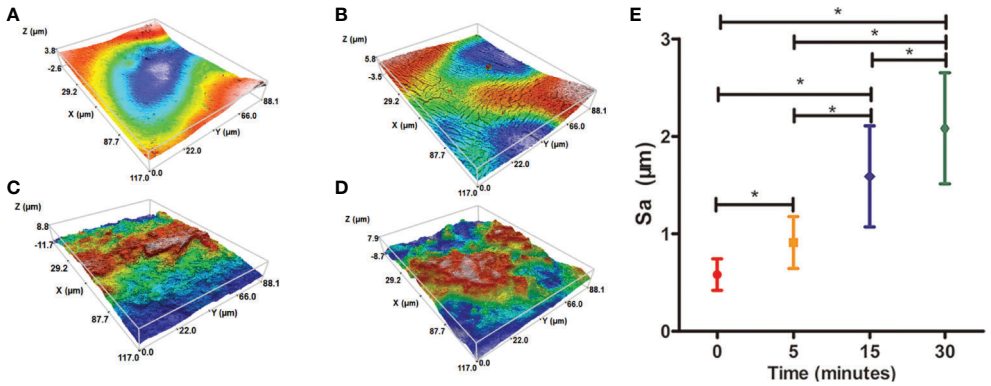

FIGURE 5 | Three-dimensional (3D) confocal topographical images of poly(ε-caprolactone) (PCL) scaffolds' surfaces treated by 5 M NaOH at different time point. **(A)** 0, **(B)** 5, **(C)** 15, and **(D)** 30 min. The results of average roughness values (Sa) of PCL scaffolds' surfaces treated by 5 M NaOH at different time point, *$P < 0.05$ **(E)**.

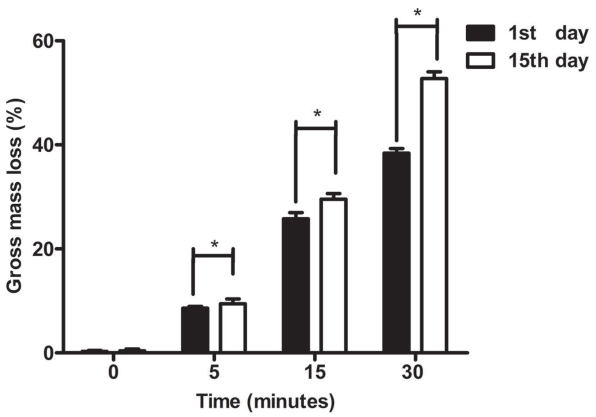

FIGURE 6 | Degradative experiments of poly(ε-caprolactone) (PCL) scaffolds. The change in mass loss (%) of PCL scaffolds modified by 5 M NaOH at different time point was detected at 1st day and 15th day. The results were analyzed by the paired sample *t* test, *$P < 0.05$.

surfaces of materials and water molecules tied and contributed to rapid degradation of PCL, forming a positive feedback during degradation process (Gupta et al., 2019).

Mechanical Properties of 3D-Printed PCL Scaffolds

The mechanical properties (Yong's moduli) of tested samples among all groups were presented in **Figure 7**. The compressive modulus of each example was calculated as the ratio of stress to strain, i.e., the slope of the stress–strain curve. As shown in **Figure 7**, PCL without etching by NaOH possessed strongest mechanical properties compared to other scaffolds in the rest groups with treatment of 5 M NaOH for 5, 15, and 30 min respectively, but no statistical difference was observed from the scaffolds in 5 min group ($p > 0.05$). PCL scaffolds soaked in 5 M NaOH for 30 min displayed the weakest compressive moduli compared to other scaffolds exposed to alkali solution, but no differences of compressive moduli were detected from scaffolds in NaOH for 15 min ($p > 0.05$). The results of tensile tests were similar to the compressive ones. Compared with PCL samples in 0 and 5 min group, the tensile moduli of scaffolds hydrolyzed by NaOH for 30 min showed the lowest ones ($p < 0.05$). Because of the hydrolyzed effect of alkali on PCL, solid content of PCL scaffold would be decreasing and bulk polyester would be degrading during the period of contacting with NaOH solution, which would inevitably compromise scaffolds' mechanical properties and alter the mechanical integrities. Fortunately, compared with the compressive moduli of the native meniscal tissues, the compressive moduli of PCL scaffolds treated by NaOH for 30 min were still higher, such as the maximum instantaneous compressive modulus of native human's meniscus was around two MPa reported in the previous research (Fischenich et al., 2015). It is, therefore, still acceptable about NaOH treatment within 30 min to satisfy the usage for PCL scaffolds.

Cellular Proliferation

The alamarBlue™ assay demonstrated that all constructs with cells (MSCs and MFCs) showed an increasing proliferative tendency during 5 days of *in vitro* culture (**Figure 8**). However, the percent of reduced alamarBlue™ of cell-scaffolds constructs among all groups on day 1 did not display significant increase ($p > 0.05$). On day 5, the percent of reduced alamarBlue™ of scaffolds treated by 5 M NaOH for 30 min with MSCs and MFCs was higher than those untreated constructs ($p<0.05$). Besides, both MSCs and MFCs in the other treated scaffolds did not show any proliferative advantage than untreated ones. Proliferative assay proved that the scaffolds with the longest soaking time in NaOH provided the best proliferative effect on MSCs and MFCs. This might be attributed to hydrolyzed effect of NaOH on PCL scaffolds, because hydrophilic function groups such as

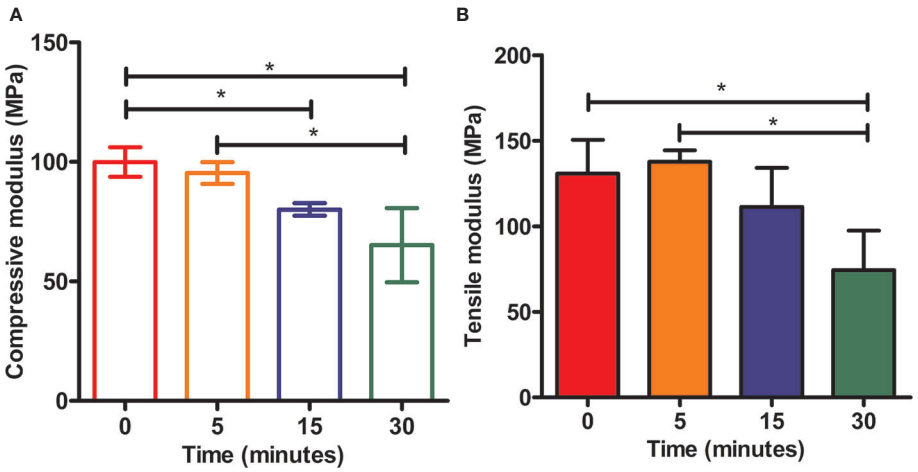

FIGURE 7 | Mechanical tests of scaffolds. Static compressive moduli **(A)** and tensile moduli **(B)** of three-dimensional (3D) poly(ε-caprolactone) (PCL) samples under the treatment of NaOH for different time, *P<0.05.

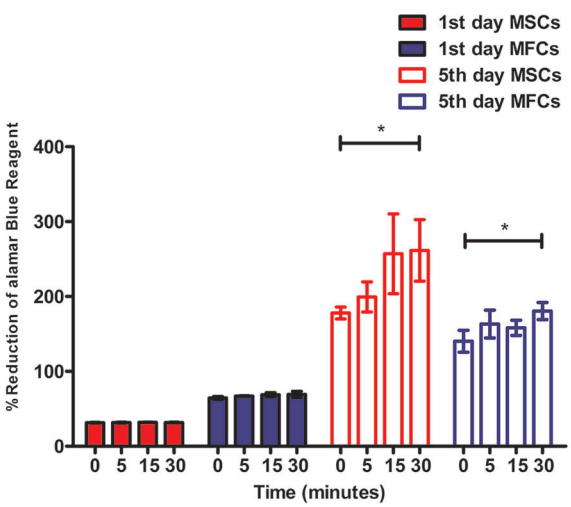

FIGURE 8 | Cellular proliferation of mesenchymal stromal cells (MSCs) and meniscal fibrocartilage cells (MFCs) onto scaffolds. Scaffolds untreated or treated by NaOH for different time (0, 5, 15, and 30 min) at 1st day and 5th day after cell seeding, *P < 0.05.

carboxyl and hydroxyl groups were exposed on the surfaces of scaffolds after treatment by NaOH. These generated functional groups might offer the adhesive recognition for seeded cells that could attach onto scaffolds rapidly and further proliferate onto them. Besides, the rougher surfaces could account for another reason why both MSCs and MFCs showed better proliferation in the scaffolds treated by NaOH for 30 min. The increasing roughness of materials' surfaces meant the larger surfaces' areas, which could extensively support more seeded cells surviving onto the PCL scaffolds.

Cellular Viability, Morphology, and Attachment

Cellular viability of seeded cells in the scaffolds untreated or treated by NaOH was evaluated *via* laser confocal microscopy after 48 h of culture. LIVE/DEAD stain showed the live cells (green) or dead cells (red) in the scaffolds. As shown in **Figure 9A**, live MSCs and MFCs were spreading and distributing on the surfaces of PCL scaffolds along the aligned PCL fibers. 3D rendering of cell-PCL constructs displayed that the number of live MSCs and MFCs on the scaffolds treated by NaOH were larger than those were on the untreated ones in a qualitative way. Especially, both MSCs and MFCs have been forming the confluent cell sheet on PCL scaffold soaked in NaOH for 30 min to portrait the structure and pore shape of scaffold clearly. Scaffolds seeded with MSCs and MFCs were observed by SEM to evaluate the cellular attachment and morphology. Extensive and firm cellular attachment was observed as shown in **Figure 9B**. Both MSCs and MFCs were spreading and distributing on the surfaces of PCL fibers, forming the interconnections among the cells. These images also reflected that MSCs appeared vary shapes, like elongated, polygonal, or spindle morphologies, which were similar to the MFCs. Successful cellular attachment suggested that the modified-PCL scaffolds could not bring about the negative effect on the survival and proliferation of cells. Generally, it was believed that hydrophilic surfaces favor cell adhesion and growth (Chen et al., 2014), which was confirmed by LIVE-DEAD assay after 48-h culture *in vitro*. Both MSCs and MFCs showed better distribution and viability in the scaffolds after treatment with NaOH solution for 30 min, compared with the other groups. Particularly, more live cells were observed on the scaffolds soaked in NaOH for 30 min. Although cell's, spreading and attachment were observed by SEM among all groups, MSCs and MFCs distributing on the surfaces of scaffolds treated by

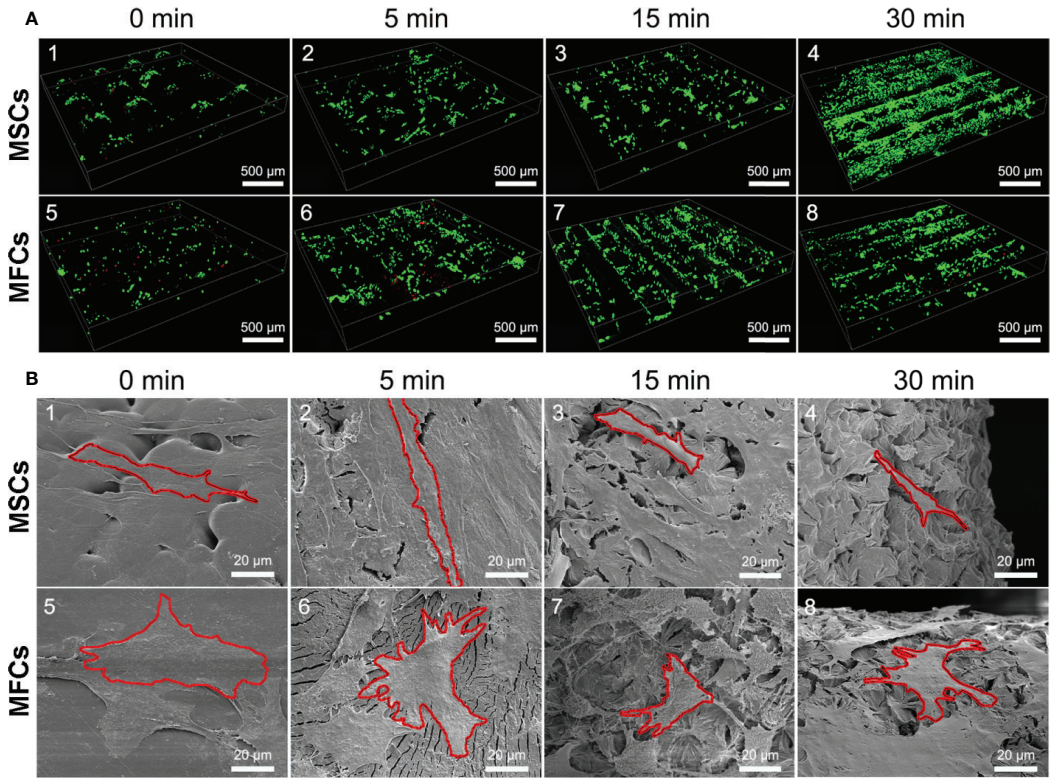

FIGURE 9 | Images of seeded cells on scaffolds detected by laser confocal microscopy and scanning electron microscopy (SEM). **(A)** Confocal images of LIVE/DEAD assay presented the cellular viability and distribution onto the PCL scaffolds at 3rd day (green, live cells, red, dead cells.). **(B)** SEM images of cellular attachment and morphology onto the surfaces of PCL scaffolds at 3rd day, red outline was added and used to isolate and label single cell in these pictures.

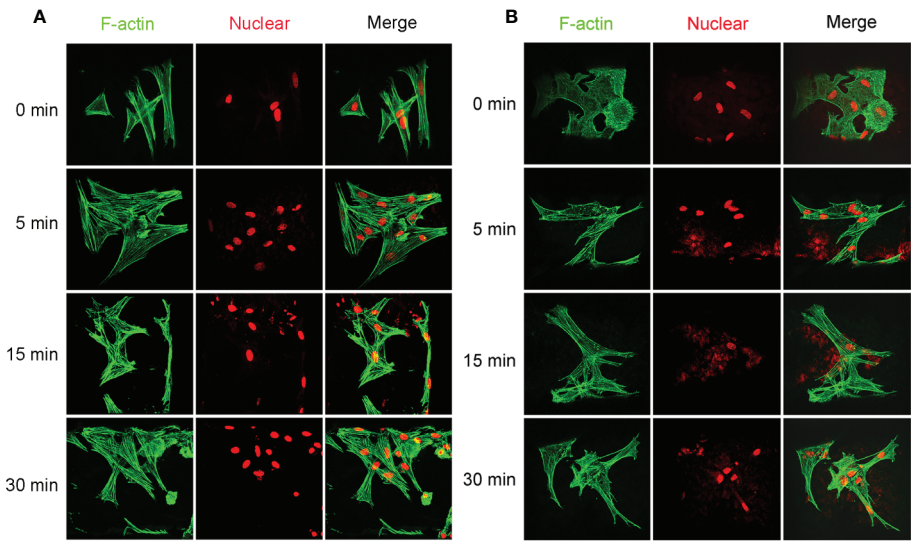

FIGURE 10 | Images of cellular skeleton and nuclear. Images of F-actin stained with Alex 488 and nuclear stained with Rot-2 of mesenchymal stromal cells (MSCs) **(A)** and meniscal fibrocartilage cells (MFCs) **(B)** seeded on the poly(ε-caprolactone) (PCL) scaffolds modified with or without 5 M NaOH, which were taken by confocal laser microscopy.

NaOH were bridging with each other and more aggregative on the scaffold filament. Besides, the area of attached single cell on the untreated scaffold was larger, leading to the loss of typical morphology of both MSCs and MFCs such as prolonged, polygons, and spindle-liked shape. The morphology of F-actin stained with Alex 488 also displayed that the slightly different shape of MSCs and MFCs seeded on the scaffolds among all groups, as shown in **Figure 10**. These phenomena indicated that transformed surface's morphology of scaffold produced by NaOH treatment had an impact on the cells surviving on its surface, which might then affect the phenotype of seeded cells and their functions. It has been reported by some studies that surface roughness of biomaterials, except for hydrophilicity, could favor the cell adhesion (Chen et al., 2014; Faia-Torres et al., 2014; Zhou et al., 2015). In other words, increased interface roughness could account for the differences of cellular proliferation and viability among scaffolds treated or untreated by NaOH.

CONCLUSIONS

In summary, we established a simple and universal method on the improvement of hydrophilicity of PCL scaffold. By means of the FDM technique and the subsequent NaOH treatment method, 3D PCL scaffolds were fabricated with uniform pore size and homogeneous pore interconnectivity and modified for wettability. This simple alkali-soaking modification not only improved the hydrophilicity, but also produced the rougher surface of PCL fiber that might maintain the typical cellular morphology, which furnished the two commonly used MSCs and MFCs with better cell attachment, viability, and proliferative capacities on the scaffold. Thus, we believe that the extrusion-based additive manufacturing system could be a promising platform for the fabrication of novel and smart scaffold, and alkali-soaking treatment could be a cost-efficient strategy on hydrophilic modification for construction of cell-scaffold for meniscal regeneration.

DATA AVAILABILITY STATEMENT

The datasets generated for this study are available on request to the corresponding authors.

ETHICS STATEMENT

The animal study was reviewed and approved by Animal Care and Use Committee of Peking University Third Hospital.

AUTHOR CONTRIBUTIONS

Z-XZ and Y-RC contributed to this study: conception and design, collection and assembly of data, analysis and interpretation of data, drafting of the manuscript. DJ and FY: assistance in analysis and interpretation of data. W-BJ, J-YZ, F-ZY, and Z-MM: technical support on analysis and interpretation. J-KY and XW: conception and design, critical revision, and final approval of the manuscript.

FUNDING

This study was supported by the National Natural Scientific Foundation of China (Grant No. 31670982, Grant No. 81630056, Grant No. 51773004 and Grant No. 51973226), the Open Research Project Funds (K2019-27), and the National Key Research and Development Program of China (Grant NO. 2016YFC1100704).

REFERENCES

Badlani, J. T., Borrero, C., Golla, S., Harner, C. D., and Irrgang, J. J. (2013). The effects of meniscus injury on the development of knee osteoarthritis: data from the osteoarthritis initiative. *Am. J. Sports Med.* 41 (6), 1238–1244. doi: 10.1177/0363546513490276

Beals, C. T., Magnussen, R. A., Graham, W. C., and Flanigan, D. C. (2016). The Prevalence of Meniscal Pathology in Asymptomatic Athletes. *Sports Med.* 46 (10), 1517–1524. doi: 10.1007/s40279-016-0540-y

Chen, C. H., Lee, M. Y., Shyu, V. B., Chen, Y. C., Chen, C. T., and Chen, J. P. (2014). Surface modification of polycaprolactone scaffolds fabricated via selective laser sintering for cartilage tissue engineering. *Mater. Sci. Eng. C. Mater. Biol. Appl.* 40, 389–397. doi: 10.1016/j.msec.2014.04.029

Do, A. V., Khorsand, B., Geary, S. M., and Salem, A. K. (2015). 3D Printing of Scaffolds for Tissue Regeneration Applications. *Adv. Healthc. Mater.* 4 (12), 1742–1762. doi: 10.1002/adhm.201500168

Esposito, A. R., Moda, M., Cattani, S. M., de Santana, G. M., Barbieri, J. A., Munhoz, M. M., et al. (2013). PLDLA/PCL-T Scaffold for Meniscus Tissue Engineering. *Biores. Open Access* 2 (2), 138–147. doi: 10.1089/biores.2012.0293

Faia-Torres, A. B., Guimond-Lischer, S., Rottmar, M., Charnley, M., Goren, T., Maniura-Weber, K., et al. (2014). Differential regulation of osteogenic differentiation of stem cells on surface roughness gradients. *Biomaterials* 35 (33), 9023–9032. doi: 10.1016/j.biomaterials.2014.07.015

Fischenich, K. M., Lewis, J., Kindsfater, K. A., Bailey, T. S., and Haut Donahue, T. L. (2015). Effects of degeneration on the compressive and tensile properties of human meniscus. *J. Biomech.* 48 (8), 1407–1411. doi: 10.1016/j.jbiomech.2015.02.042

Gupta, D., Singh, A. K., Kar, N., Dravid, A., and Bellare, J. (2019). Modelling and optimization of NaOH-etched 3-D printed PCL for enhanced cellular attachment and growth with minimal loss of mechanical strength. *Mater. Sci. Eng. C.* 98, 602–611. doi: 10.1016/j.msec.2018.12.084

Hannink, G., van Tienen, T. G., Schouten, A. J., and Buma, P. (2011). Changes in articular cartilage after meniscectomy and meniscus replacement using a biodegradable porous polymer implant. *Knee Surg. Sports Traumatol. Arthrosc.* 19 (3), 441–451. doi: 10.1007/s00167-010-1244-8

Kwak, H. S., Nam, J., Lee, J. H., Kim, H. J., and Yoo, J. J. (2017). Meniscal repair in vivo using human chondrocyte-seeded PLGA mesh scaffold pretreated with platelet-rich plasma. *J. Tissue Eng. Regener. Med.* 11 (2), 471–480. doi: 10.1002/term.1938

Lee, C. H., Rodeo, S. A., Fortier, L. A., Lu, C., Erisken, C., and Mao, J. J. (2014). Protein-releasing polymeric scaffolds induce fibrochondrocytic differentiation of endogenous cells for knee meniscus regeneration in sheep. *Sci. Transl. Med.* 6 (266), 266ra171. doi: 10.1126/scitranslmed.3009696

Ma, Z., Mao, Z., and Gao, C. (2007). Surface modification and property analysis of biomedical polymers used for tissue engineering. *Colloids Surf. B. Biointerfaces* 60 (2), 137–157. doi: 10.1016/j.colsurfb.2007.06.019

Moradi, L., Vasei, M., Dehghan, M. M., Majidi, M., Farzad Mohajeri, S., and Bonakdar, S. (2017). Regeneration of meniscus tissue using adipose mesenchymal stem cells-chondrocytes co-culture on a hybrid scaffold: In vivo study. *Biomaterials* 126, 18–30. doi: 10.1016/j.biomaterials.2017.02.022

Moran, C. J., Busilacchi, A., Lee, C. A., Athanasiou, K. A., and Verdonk, P. C. (2015). Biological augmentation and tissue engineering approaches in meniscus surgery. *Arthroscopy* 31 (5), 944–955. doi: 10.1016/j.arthro.2014.11.044

Neufurth, M., Wang, X., Wang, S., Steffen, R., Ackermann, M., Haep, N. D., et al. (2017). 3D printing of hybrid biomaterials for bone tissue engineering: Calcium-polyphosphate microparticles encapsulated by polycaprolactone. *Acta Biomater.* 64, 377–388. doi: 10.1016/j.actbio.2017.09.031

Oh, S. H., Park, I. K., Kim, J. M., and Lee, J. H. (2007). In vitro and in vivo characteristics of PCL scaffolds with pore size gradient fabricated by a centrifugation method. *Biomaterials* 28 (9), 1664–1671. doi: 10.1016/j.biomaterials.2006.11.024

Petri, M., Ufer, K., Toma, I., Becher, C., Liodakis, E., Brand, S., et al. (2012). Effects of perfusion and cyclic compression on in vitro tissue engineered meniscus implants. *Knee Surg. Sports Traumatol. Arthrosc.* 20 (2), 223–231. doi: 10.1007/s00167-011-1600-3

Rongen, J. J., van Tienen, T. G., van Bochove, B., Grijpma, D. W., and Buma, P. (2014). Biomaterials in search of a meniscus substitute. *Biomaterials* 35 (11), 3527–3540. doi: 10.1016/j.biomaterials.2014.01.017

Roos, E. M., and Thorlund, J. B. (2017). It is time to stop meniscectomy. *Br. J. Sports Med.* 51 (6), 490–491. doi: 10.1136/bjsports-2016-097273

Shen, H., Hu, X., Bei, J., and Wang, S. (2008). The immobilization of basic fibroblast growth factor on plasma-treated poly(lactide-co-glycolide). *Biomaterials* 29 (15), 2388–2399. doi: 10.1016/j.biomaterials.2008.02.008

Thorlund, J. B., Englund, M., Christensen, R., Nissen, N., Pihl, K., Jorgensen, U., et al. (2017). Patient reported outcomes in patients undergoing arthroscopic partial meniscectomy for traumatic or degenerative meniscal tears: comparative prospective cohort study. *BMJ* 356, j356. doi: 10.1136/bmj.j356

Verdonk, R., Verdonk, P., Huysse, W., Forsyth, R., and Heinrichs, E. L. (2011). Tissue ingrowth after implantation of a novel, biodegradable polyurethane scaffold for treatment of partial meniscal lesions. *Am. J. Sports Med.* 39 (4), 774–782. doi: 10.1177/0363546511398040

Wang, S. J., Zhang, Z. Z., Jiang, D., Qi, Y. S., Wang, H. J., Zhang, J. Y., et al. (2016). Thermogel-Coated Poly(epsilon-Caprolactone) Composite Scaffold for Enhanced Cartilage Tissue Engineering. *Polymers* 8 (5), 200. doi: 10.3390/Polym8050200

Wang, W., Caetano, G., Ambler, W. S., Blaker, J. J., Frade, M. A., Mandal, P., et al. (2016). Enhancing the Hydrophilicity and Cell Attachment of 3D Printed PCL/Graphene Scaffolds for Bone Tissue Engineering. *Mater. (Basel)* 9 (12), 992. doi: 10.3390/ma9120992

Yang, J., Wan, Y. Q., Tu, C. F., Cai, Q., Bei, J. Z., and Wang, S. G. (2003). Enhancing the cell affinity of macroporous poly(L-lactide) cell scaffold by a convenient surface modification method. *Polymer Int.* 52 (12), 1892–1899. doi: 10.1002/pi.1272

Zhang, Z. Z., Jiang, D., Ding, J. X., Wang, S. J., Zhang, L., Zhang, J. Y., et al. (2016). Role of scaffold mean pore size in meniscus regeneration. *Acta Biomater.* 43, 314–326. doi: 10.1016/j.actbio.2016.07.050

Zhang, Z. Z., Wang, S. J., Zhang, J. Y., Jiang, W. B., Huang, A. B., Qi, Y. S., et al. (2017). 3D-Printed Poly(epsilon-caprolactone) Scaffold Augmented With Mesenchymal Stem Cells for Total Meniscal Substitution: A 12- and 24-Week Animal Study in a Rabbit Model. *Am. J. Sports Med.* 45 (7), 1497–1511. doi: 10.1177/0363546517691513

Zhang, Z. Z., Chen, Y. R., Wang, S. J., Zhao, F., Wang, X. G., Yang, F., et al. (2019). Orchestrated biomechanical, structural, and biochemical stimuli for engineering anisotropic meniscus. *Sci. Transl. Med.* 11 (487), eaao0750. doi: 10.1126/scitranslmed.aao0750

Zhou, B., Gao, X., Wang, C., Ye, Z., Gao, Y., Xie, J., et al. (2015). Functionalized PDMS with Versatile and Scalable Surface Roughness Gradients for Cell Culture. *ACS Appl. Mater. Interfaces* 7 (31), 17181–17187. doi: 10.1021/acsami.5b04032

Conflict of Interest: The authors declare that the research was conducted in the absence of any commercial or financial relationships that could be construed as a potential conflict of interest.

frontiers in Pharmacology

REVIEW
published: 06 May 2020
doi: 10.3389/fphar.2020.00622

Advancements in Hydrogel-Based Drug Sustained Release Systems for Bone Tissue Engineering

Yunfan Zhang[1†], Tingting Yu[1†], Liying Peng[1], Qiannan Sun[1], Yan Wei[2*] and Bing Han[1*]*

[1] Department of Orthodontics, Peking University School and Hospital of Stomatology & National Engineering Laboratory for Digital and Material Technology of Stomatology & Beijing Key Laboratory of Digital Stomatology, Beijing, China, [2] Department of Geriatric Dentistry, Peking University School and Hospital of Stomatology, Beijing, China

OPEN ACCESS

Edited by:
Jianxun Ding,
Chinese Academy of Sciences, China

Reviewed by:
Juan Wang,
Sichuan University, China
Dan Wang,
Institute of Process Engineering (CAS), China
Wenjing Yu,
University of Pennsylvania, United States

***Correspondence:**
Tingting Yu
tingtingyu@bjmu.edu.cn
Yan Wei
kqweiyan@bjmu.edu.cn
Bing Han
kqbinghan@bjmu.edu.cn

[†]These authors have contributed equally to this work and share first authorship

Specialty section:
This article was submitted to Experimental Pharmacology and Drug Discovery, a section of the journal Frontiers in Pharmacology

Received: *12 March 2020*
Accepted: *20 April 2020*
Published: *06 May 2020*

Citation:
Zhang Y, Yu T, Peng L, Sun Q, Wei Y and Han B (2020) Advancements in Hydrogel-Based Drug Sustained Release Systems for Bone Tissue Engineering. Front. Pharmacol. 11:622. doi: 10.3389/fphar.2020.00622

Bone defects caused by injury, disease, or congenital deformity remain a major health concern, and efficiently regenerating bone is a prominent clinical demand worldwide. However, bone regeneration is an intricate process that requires concerted participation of both cells and bioactive factors. Mimicking physiological bone healing procedures, the sustained release of bioactive molecules plays a vital role in creating an optimal osteogenic microenvironment and achieving promising bone repair outcomes. The utilization of biomaterial scaffolds can positively affect the osteogenesis process by integrating cells with bioactive factors in a proper way. A high water content, tunable physio-mechanical properties, and diverse synthetic strategies make hydrogels ideal cell carriers and controlled drug release reservoirs. Herein, we reviewed the current advancements in hydrogel-based drug sustained release systems that have delivered osteogenesis-inducing peptides, nucleic acids, and other bioactive molecules in bone tissue engineering (BTE).

Keywords: hydrogel, sustained drug release, bone tissue engineering, growth factors, mesenchymal stem cells

INTRODUCTION

Bone defects may be caused by various events, including trauma, inflammation, neoplasm resection, congenital deformity, and degeneration (Crane et al., 1995; Spicer et al., 2012). Despite numerous solutions being applied to tackle this issue, clinical demands remain unmet.

To date, autologous bone grafts are still the gold standard and most considered therapeutic strategy for critical-sized bone defects among all restoration methods due to their remarkable osteoconductive and osteoinductive properties. However, *de novo* problems might arise, such as a limited amount of donor tissue, an excessive harvest procedure, and the possibility of postoperative infection of the donor site (Langer and Vacanti, 1993; Betz, 2002; Ahlfeld et al., 2019). Allografts or xenografts usually serve as secondary alternatives, as slower incorporation, immune rejection, and pathogen transmission might occur (Crane et al., 1995; Haugen et al., 2019). Utilizing biocompatible scaffold materials, such as mesenchymal stem cells (MSCs) and/or bioactive factors (Meijer et al., 2007), bone tissue engineering can offer more possibilities. Achieving sufficient and qualified bone formation *via* artificial composites is the grand aim of bone tissue engineering.

Compared with bone harvest operations, MSCs are relatively easy to obtain. These cells exhibit self-renewal, multipotentiality (Prockop, 1997), and immunomodulatory properties (Keating, 2008),

which are imperative for bone regeneration. In addition, bioactive factors, for example, cytokines and growth factors (GFs), play a crucial role in new bone formation. Bone morphogenetic proteins (BMPs) are a group of GFs that have been substantially investigated. Recombinant human BMP-2 and BMP-7 is commercially available for limited clinical usage (Nauth et al., 2011). However, naked GFs are vulnerable *in vivo*, and to achieve optimal osteogenic effects, a supraphysiological dose of GFs is required. Paradoxically, diffusion or uncontrolled release of GFs may lead to ectopic bone formation and other complications, including carcinogenicity (Carragee et al., 2011; de Melo Pereira and Habibovic, 2018). Hence, attaining sustained release of bioactive factors is an essential objective for scaffold design to promote the therapeutic efficacy of bone tissue engineering. The scaffold materials not only create a congenial microenvironment to promote MSC biological behaviors but also help to maintain bioactive molecules *in situ*. To date, the controlled release of bioactive factors in bone tissue engineering has been realized by a wide range of biomaterials of different natures and configurations, which provide diverse release profiles in different treatment scenarios (Lee and Shin, 2007).

Hydrogels are a category of highly hydrated 3-dimensional (3D) crosslinked homopolymer, copolymer, or macromer networks that can be cast into different shapes and sizes (Slaughter et al., 2009; Seliktar, 2012). The application of hydrogels in tissue engineering, bone tissue engineering in particular, has been garnering increasing attention. Laden with osteogenic-inducing drugs and sustained release profiles, hydrogels have been suggested to be promising bone tissue engineering biomaterials. In this review, we discuss the progress and limitations of current bone tissue engineering, the advantages of hydrogel-based bone regeneration biomaterials and recent advancements in hydrogel-based drug sustained release systems for bone tissue engineering.

THE PRESENT CHALLENGES OF BONE TISSUE ENGINEERING

To date, substantial progress has been made in bone regenerative medicine. A variety of biomimetic polymers and inorganic materials with bone-like microarchitecture have been designed with advanced manufacturing methods (Wei et al., 2011; Kim et al., 2017b; Yin et al., 2019), including 3D printing, aiming to achieve superb osteogenic properties as well as accuracy and spatial fitness of critical-sized defects. Light-cured, thermal-setting, pH- or enzyme-sensitive, and other smart biomaterials enable bone tissue engineering to serve in many on-demand circumstances. Varieties of seed cells from different origins including umbilical cord MSCs (UCMSCs), induced pluripotent stem cell-derived MSCs (iPSC-MSCs), and embryonic stem cell-derived MSCs (ESC-MSCs) are successfully applied (Xie et al., 2016; Chen et al., 2018). Multifarious drugs or bioactive factors are delivered *in situ* with different strategies and tailored release profiles, offering osteogenic-friendly environments for relevant cells. Noteworthy, it was reported that MSC-derived exosomes combining scaffolds achieved preferable osteogenesis outcomes (Li et al., 2018), indicating the promising prospect of exosomes-based cell-free bone regeneration.

MSCs from different sources, such as bone marrow and dental tissue, are available for bone tissue engineering. The stem cell niche, 3D microenvironments containing specific biophysical and biochemical signals, maintains the stemness of stem cells *in vivo* (Scadden, 2006; Jones and Wagers, 2008). However, maintaining the viability and stemness of MSCs as well as controlling stem cell fate is a fairly critical issue in regenerative medicine. Substrate-derived stimuli are able to prolong the stemness of stem cells and guide stem cell fate into specific lineages (Fisher et al., 2010; Marklein and Burdick, 2010; Lee et al., 2015). Moreover, as the proliferation and differentiation of MSCs may drive into specific lineages depending on different microenvironmental cues, biochemical stimuli, including cytokines and GFs, are used in a spatiotemporal sequence during the complex and continuous reparative procedure (Samorezov and Alsberg, 2015; Farokhi et al., 2016). Successful bone regeneration requires the proper combination of stimuli that can trigger MSC differentiation and matrix deposition. As the scaffold material itself is capable of combining substrate-derived and biochemical stimuli, biomimetic and bioinspired synthetic materials with sustained drug release systems should be designed to facilitate bone tissue regeneration. Due to the constraints of current knowledge in this field, the research is far from sufficient.

Natural bone fracture healing requires the coordinated participation of osteogenesis and angiogenesis (Collin-Osdoby, 1994; Marsell and Einhorn, 2011). Bioactive factors and signal pathway crosstalk, which mediates the interplay between epithelial cells and osteoprogenitors, has been well summarized (Ramasamy et al., 2016). Likewise, vascularization in bone substitutes is vital for successful bone tissue engineering. Insufficient blood supply may result in undernutrition, hypoxia, and inadequate cell recruitment, leading to the failure of bone tissue engineering. Varieties of assessments and solutions have been summarized (Rouwkema et al., 2008; Das and Botchwey, 2011), yet there is no convincing evidence that the strategies are ample to sustain large tissue constructs, encouraging the proposal of more promising methods.

THE PREPONDERANCE OF HYDROGELS IN BONE TISSUE ENGINEERING

Ideal bone tissue engineering scaffolds should meet the following criteria: (1) biocompatible, nontoxic and nonimmunogenic; (2) porous-structured; (3) proper mechanical properties, load-bearing ability, and sufficient dimensional stability; and (4) fully degradable, with a degradation rate that matches neotissue formation (Lee and Shin, 2007; Slaughter et al., 2009; Haugen et al., 2019). Numerous inorganic scaffolds, such as metals and bioceramics, have been applied in bone regeneration, yet their lack of cell affinity, unbalanced mechanical properties,

and rather poor degradation cannot be ignored (Pearlin et al., 2018).

According to types of raw materials, hydrogels can be briefly categorized into natural and synthetic. It is usually considered that natural hydrogels are more biocompatible and bioactive, while synthetic ones possess more tunable mechanical and degradation properties. 3D-structured, highly water-containing, and biocompatible hydrogels act as excellent extracellular matrix (ECM) analogs. The porous structure of the hydrogel enables substance exchange and cell entrance at the initial stage as well as vascular ingrowth in the follow-up stage. It has been substantially shown that cells are easily suspended within hydrogels, and the viability of the encapsulated cells is highly preserved (Gao et al., 2020; Paez et al., 2020).

MSCs are highly sensitive to physical parameters (Higuchi et al., 2013), including viscoelasticity Engler et al. (2006) and topography (Fiedler et al., 2013), in the surrounding milieus. The stiffness (elastic modulus) of the matrix is believed to contribute greatly to determining stem cell fate. As Engler et al. (2006) demonstrated, 2D-cultured MSCs exhibited osteogenic characteristics when the microenvironmental stiffness was relatively rigid, at 20–40 kPa. However, osteogenesis occurred at 11–30 kPa when MSCs were cultivated 3-dimensionally (Huebsch et al., 2010). Due to flexible synthetic strategies and the range of constituents, hydrogels possess tunable physio-mechanical properties, which could match the desirable ranges of material elasticity, porosity, and degradation rate required for bone tissue engineering (Slaughter et al., 2009). Meanwhile, photodegradable (Lunzer et al., 2018), thermal-sensitive, or pH-sensitive (GhavamiNejad et al., 2016) linkages as well as other advantageous materials could be subtly introduced into hydrogels, which may fabricate a versatile and intelligent composite system to fulfill the growing clinical demands.

On the other hand, bioactive molecules play an important role in bone regenerative medicine. During bone formation, numerous cytokines and GFs are orchestrated in a spatiotemporal manner (Farokhi et al., 2016), which would provide a suitable microenvironment for MSC proliferation and differentiation, as well as recruit progenitors from surrounding tissue and peripheral blood for further restoration. Apart from competent cell carriers, hydrogels can also be employed as promising local drug reservoirs. Multiple schemes have been applied to reach desirable and smart drug delivery kinetics (Lee and Shin, 2007; Slaughter et al., 2009). Non-covalent immobilization strategies are the most commonly used in hydrogel-based drug depots, the drug release rate was mainly determined by parameters such as crosslink density, carrier affinity for drugs, and the matrix degradation profile (Dimatteo et al., 2018). Bioactive factors also could be linked covalently to polymers by which a longer drug retention time would be achieved, and covalent linkages could be broken as reactions of specific external cues, leading an on-demand drug controlled release. Moreover, other sustained release systems like microspheres could be introduced to hydrogel matrix, enabling multiple drug molecules sustained release in sequential or spatiotemporal manners (Chen et al., 2010).

HYDROGEL-BASED DRUG SUSTAINED RELEASE SYSTEMS FOR BONE TISSUE ENGINEERING

Extensive drug and sustained release strategies have been designed for bone tissue engineering. Herein, we introduce studies on hydrogel-based controlled release systems according to the category of bioactive molecule loaded within.

Peptides

The majority of cytokines, GFs, and hormones that stimulate bone formation are peptides. These biomolecules are produced through the autocrine, paracrine, and endocrine systems, acting concertedly to regulate the complex cascade of bone-related gene expression (Lee and Shin, 2007; Farokhi et al., 2016). Hence, a well-orchestrated sustained release system of these peptides has been pursued in order to present a more biomimetic approach.

BMP

With the promoted understanding of the underlying mechanism of osteogenesis (Chen et al., 2012), BMP, as a prominent member of the TGF-β superfamily, has always been a favored candidate for bone tissue engineering applications.

Since some hydrogels are believed to possess inferior osteoconductive properties, Olthof et al. (2018) modified an oligo[poly(ethylene glycol) (PEG) fumarate] (OPF) hydrogel with bisphosphate. BMP-2 was encapsulated in poly(lactic-co-glycolic acid) (PLGA) microspheres. The additional BMP-2 and drug-laden PLGA microspheres were entrapped in the hydrogel matrix. The researchers believed that the anionic groups would produce a strong interaction between the matrix and inorganic phase of the bone as well as enhance BMP-2-induced bone formation. The hydrogel matrix could be functionalized by peptides, which might be beneficial to reduce the dose of encapsulated BMP. In addition, nanofibrous mesh-hydrogel hybrid composites have been applied to reach a proper spatiotemporal release profile (Kolambkar et al., 2011). Shekaran et al. (2014) modified a matrix metalloproteinase (MMP)-degradable peptide crosslinked PEG with an α2β1 integrin-specific peptide (GFOGER). The interaction between integrin and collagen I has been proposed to be vital in osteogenic differentiation and mineralization. It was suggested that the modified matrix is able to support cell adhesion and proliferation and upregulate osteogenic gene expression. Laden with the low dose of BMP-2, robust bone healing was achieved. Along with BMP-2, BMP-7 is considered to be a promising GF in bone formation. An injectable chitosan/β-glycerophosphate (CS/β-GP) hydrogel laden with BMP-7 and antibiotic exhibited preferable reparative effects towards infection-induced bone loss (Zang et al., 2019). Growth differentiation factor-5 (GDF-5), also known as BMP-14, regulates the development of numerous tissue and cell types, including limbs and teeth. Bae et al. (2014) mixed different concentrations of GDF-5 with a light-cured hydrogel matrix. The results showed that GDF-5 improved the osteogenic ability in a dose-dependent manner, as the strongest

augmentation was achieved by the hydrogel loaded with the highest concentration.

Apart from adsorption or physical entrapment, electrostatic, hydrophobic, or other interactions have been introduced into the systems to prolong the release of BMPs. Heparin was reported to be a strong binder to BMPs, yet the side effects were not negligible. Heparin mimics, which are usually negatively charged, are supposed to be capable of controlling BMP release. Chondroitin sulfate (Anjum et al., 2016), 2-N,6-O-sulfated chitosan (26SCS)-based nanoparticles (Cao et al., 2014), alginate sulfate (Park et al., 2018) were synthesized by researchers, and satisfactory results were achieved both *in vitro* and *in vivo*. When higher concentrations of heparin mimics were introduced, the release rate of BMP became slower. Seo et al. (2015, 2017) harnessed the ionic and hydrophobic interactions provided by polyphosphazene nanoparticles. They found that release rate of BMPs were controlled by the types and amounts of pendants. Thus, the optimal release profile and osteogenesis outcomes rely on a reasonable proportion of BMP-tethering molecules.

Genetic engineering is another option to obtain long-lasting BMP release. As Lin et al. (2019) described in a manuscript, the *BMP* gene was transduced into human bone marrow-derived stem cells (BMMSCs), obtaining a continuous (up to 56 days) and economical BMP supply. Using visible light-based projection stereolithography (VL-PSL) technology to encapsulate the transduced cells, the researchers were able to fabricate more structurally and geometrically compatible constructs for individualized bone defects, which would be conducive to achieving tissue fusion and bone tissue engineering long-term success.

Vascular Epithelial Growth Factor (VEGF)

Vascularization plays a crucial role in both bone development and bone regeneration (Collin-Osdoby, 1994; Olsen et al., 2000). Blood vessels do not solely work as substance exchange pathways; they are also regarded as highly active paracrine organs targeting various progenitors during bone formation and reconstruction (Collin-Osdoby, 1994). VEGF, a key angiogenic growth factor (Carmeliet and Jain, 2011), has been widely used in bone tissue engineering.

The cooperation between VEGF receptors and integrin adhesion receptors has been elucidated in angiogenic regulation. Garcia et al. (2016) engineered a protease-degradable, GFOGER-modified PEG hydrogel as a VEGF depot. They found that covalently linked VEGF remained highly bioactive during a prolonged release period. Whereas it was shown that a GFOGER hydrogel augmented neovascularization regardless of exogenous VEGF, micro computed tomography (micro-CT) showed delivering exogenous VEGF failed to enhance critical-sized bone repair. Heterogenous material composites are manufactured by which we can juggle both timed drug release and osteoconduction. Composed of a 3D multichannel calcium phosphate cement (CPC) and alginate/gellan gum (AlgGG) hydrogel, the CPC/AlgGG biphasic scaffold tethers VEGF *via* the interaction with heparin (Ahlfeld et al., 2019). Despite some remarkable properties observed *in vitro*, significant enhancement by VEGF on new bone formation has not been detected. Amirian et al. (2015) coated VEGF and BMP-2 separately onto gelatin-pectin-biphasic calcium phosphate composites. The results revealed that composites coated with VEGF mainly aided in woven bone formation, and the percent of new bone formation was not greater than those coated with BMP-2.

Since exclusive delivery of VEGF performed barely satisfactorily in GF-induced osteogenesis, dual or multidrug delivery is warranted. When accompanied by BMP-2, VEGF exhibited a significant improvement in bone formation compared with hydrogels encapsulating BMP-2 alone. VEGF combined with BMP-2 has been used routinely as a GF formula in bone tissue engineering. Similar loading strategies were applied by Barati et al. (2016) and Kader et al. (2019) for spatiotemporal release of BMP-2 and VEGF. MSCs and BMP-tethered nanoparticles were embedded in the outer space, while endothelial colony-forming cells (ECFCs) and VEGF-tethered nanoparticles were dispersed inside the microchannel-patterned hydrogel, as illustrated in **Figure 1**. Degradation and GF release could be tuned by altering stoichiometric ratio chain-extended molecules and proteolysis. According to the data, the release of VEGF and BMP-2 could last over 10 days and 21 days, respectively. It was observed that the patterned hydrogel dual delivery system performed significantly better than that of single delivery systems, which was attributed to paracrine crosstalk. During bone repair, VEGF expression peaks appear in the early period, while BMP peaks later. Thus, consisting of a PLGA microsphere-incorporating poly(propylene fumarate) (PPF) rod surrounded by a rapidly degrading gelatin hydrogel, the composite was designed as a GF delivery vehicle (Kempen et al., 2009). VEGF was encapsulated in the hydrogel, whereas BMP-2 was immobilized by microspheres inside the rod in order to achieve an ideal GF sequential release pattern. VEGF exhibited a large initial burst release within the first 3 days, and BMP-2 showed sustained release over 8 weeks. Likewise, although VEGF did not induce neo-bone formation, it significantly enhanced BMP-induced osteogenesis. Organic-inorganic modular scaffolds are able to optimally orchestrate dual GF release and serve as an "anatomy-structure-function" trinity system in regenerating weight-bearing bones (Bao et al., 2017). Mesoporous bioactive glass (MBG) with hollowed channels and hierarchical porous structures was introduced in a controlled release system as a scaffold (Tang et al., 2020). VEGF was carried by hydrogel inside the channel, and BMP-2 was adsorbed by the MBG scaffolds. 26SCS acted as an analog of ECM, which exhibits super-affinity to GFs. *In vitro* experiments showed that 26SCS promoted the bioactivity of BMP-2 and VEGF. It could be assumed that the VEGF hydrogel column in the hollowed channels might induce chemotaxis of vascular endothelial cells, thus regulating cell migration and vascular infiltration. Moreover, increased type H vessels and neotissue ingrowth were observed.

Fibroblast Growth Factor (FGF)

FGF signaling is a dominant regulator during bone development and fracture repair (Bourque et al., 1993; Kronenberg, 2003). However, contradictory results have implied that FGF signaling

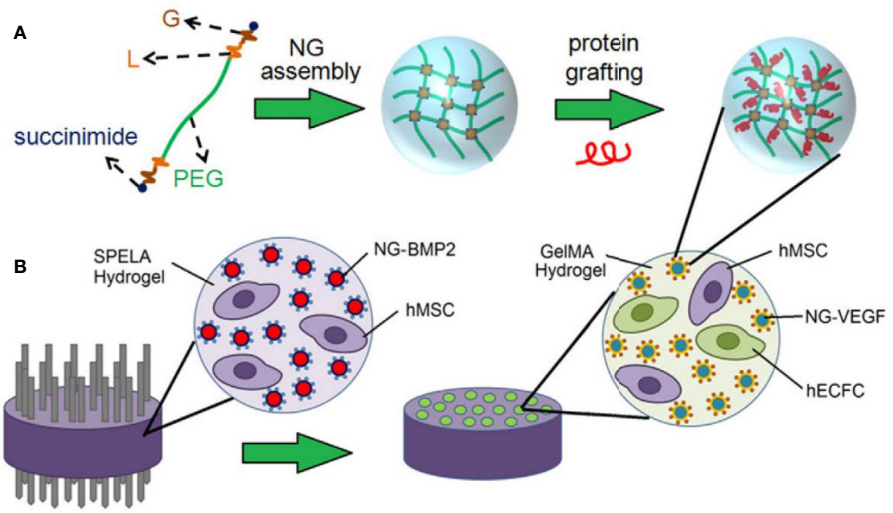

FIGURE 1 | Schematic illustration of **(A)** nanogel (NG) assembly and peptide grafting. **(B)** Achievement of BMP-2 and VEGF spatiotemporal release profiles *via* a patterned hydrogel-based sustained release system. Reprinted from a previous article by Barati et al. (2016) with permission.

may exert dual-directional effects on osteogenic procedures, probably in a dose-dependent manner (Kato et al., 1998; Quarto and Longaker, 2006). Thus, sustained release should be achieved when FGF is delivered in bone tissue engineering.

Two Japanese groups encapsulated FGF in gelatin hydrogels for controlled release (Kodama et al., 2009; Furuya et al., 2014). A longer FGF release period may improve cell proliferation, the expression levels of osteogenic markers and BMP-2 as well as bone mineral density (BMD) at defect sites. However, these enhancements vanished, and side effects occurred when a high dose of FGF was delivered (Kodama et al., 2009). In order to achieve bone-like biomechanical properties and slower release of FGF, a stiffer hydrogel matrix, poly(2-hydroxyethyl methacrylate) copolymerized with 2-vinyl pyrrolidone, was engineered (Mabilleau et al., 2008). The data suggested that in the first 4 days, the FGF release rate was approximately 1% per day, which was relevant to hydrogel swelling. Unfortunately, no significant difference between the FGF and control groups was noted in bone mass, but the poorly mineralized woven bone area was significantly larger in the FGF group.

It is a preferable strategy for other GFs to accompany FGF in order to obtain a promising outcome. Chen et al. (2016) chose gelatin microspheres as BMP-2 and basic FGF (bFGF) carriers, which were further embedded in a commercialized injectable thermal-sensitive hydrogel. The hydrogel was injected into a porous cell-loading scaffold before use. Micro-CT revealed that the dual-loaded composites achieved the best reparative results. As expected, composites loading bFGF alone regenerated less bone and neobone at the margin of the defect areas, while the dual-loaded composites showed much more central area bone formation. FGF9 has been indicated to be a stabilizing factor for neovessels, thus, Yuan et al. (2016) introduced FGF9 as an assistant for VEGF, exerting synergetic effects on angiogenesis in bone tissue engineering. A specific peptide segment was fused to VEGF and FGF9 to obtain a covalent connection with the fibrin hydrogel. *BMP-2* was transfected into BMSCs, endowing a greater osteogenic ability and resistance of the osteogenic differentiation inhibition induced by fusion with FGF9. Less bone was formed in the FGF9 groups compared to the groups treated with only VEGF, whereas VEGF/FGF9-loaded composites performed the best among the groups.

Other Peptides

Other peptides that regulate the bone regeneration cascade, including osteoprotegerin (OPG) (Jayash et al., 2017), stromal cell-derived factor-1α (SDF-1α) (Ratanavaraporn et al., 2011; Cipitria et al., 2017; Mi et al., 2017), platelet-derived growth factor (PDGF) (Wang et al., 2020), and parathyroid hormone (PTH) (Erten Taysi et al., 2019), etc., might also be worthy of an attempt. The selected studies of hydrogel-based peptide sustained release systems for bone regeneration and their findings are concluded in **Table 1**.

Nucleic Acids

Since GFs and cytokines are required for weeks during new bone formation, gene therapy might be a feasible alternative. Delivering DNA or RNA locally to increase or knockdown target gene expression, gene therapy is capable of manipulating the microenvironment and determining cell fate in bone regenerative medicine.

Fang et al. (1996) utilized collagen sponges as BMP-4 and PTH plasmid DNA carriers to regenerate nonunion rat femur defects early in 1996. Bonadio et al. (1999) confirmed that non-viral DNA delivery possesses numerous advantages compared with the protein strategy. Hydrophilic nucleic acids and hydrogels could provide stable and sequestered environments for gene delivery. Komatsu et al. (2016) demonstrated that gelatin hydrogels could transduce BMP-2 plasmid DNA efficiently, facilitating local bone regeneration.

TABLE 1 | Summary of selected studies of hydrogel-based peptide sustained release systems.

Peptide	Carrier material	Release pattern	Findings (*ex/in vivo*)	Reference
BMP-2	PLGA microspheres + bisphosphate modified oligo OPF hydrogel	Burst and sustained	Osteoconductivity and osteoinductivity were significantly improved	(Olthof et al., 2018)
BMP-2	Nanofibrous mesh + peptide modified alginate hydrogel	Spatiotemporal controlled release	Micro-CT showed more bone regeneration, superior mechanical properties of neobone were achieved	(Kolambkar et al., 2011)
BMP-2	GFOGER-modified MMP-degradable PEG-maleimide hydrogel	More than 20% BMP-2 remained after 14 days	GFOGER-modified hydrogel exhibited intrinsic osteogenic activities, micro-CT demonstrated; improved bone repair	(Shekaran et al., 2014)
BMP-2	VL-PSL-manufactured live-cell hydrogel scaffold	Sustained expression for 56 days	Micro-CT and histological evidence indicated mature and robust bone formation	(Lin et al., 2019)
BMP-7	CS/β-GP hydrogel	Release 46% in first 12 h, 84% by the end of 336 h	Radiographical and histological observation suggested better periodontal regeneration	(Zang et al., 2019)
GDF-5	Photo-cured hyaluronic acid (HA) hydrogel	Release profiles varies with the initial drug concentration, sustained release period over 25 days	Hydrogel with the highest drug concentration displayed promoted osteogenic potential both *in vitro* and *in vivo*	(Bae et al., 2014)
BMP-2 + VEGF	Acrylate-functionalized lactide-chain-extended star polyethylene glycol (SPELA) hydrogel + gelatin methacryloyl (GelMA) hydrogel + PEG nanogel	Release of VEGF and BMP-2 lasted over 10 days and 21 days, respectively (tunable release kinetics)	Patterned constructs significantly increase osteogenic and vasculogenic differentiation of precursors, bFGF expression was upregulated	(Barati et al., 2016)
VEGF + BMP-2	PLGA microsphere + PPF rod + gelatin hydrogel	A large initial burst was shown *in vivo*, which changed significantly from *ex vivo* release profiles	Micro-CT and histological section demonstrated co-delivery significantly enhanced osteogenesis and angiogenesis ectopically, but it did not reach significant results orthotopically	(Kempen et al., 2009)
VEGF + BMP-2	Hydroxyapatite (HA)/ polycaprolactone (PCL) scaffold + PLGA-PEG-PLGA hydrogel	Burst release in first 3 days, sustained release for 3 weeks	Micro-CT showed newly-formed callus in co-delivery group almost covered defect areas, histological analysis showed no significant difference between co-delivery group and autologous group	(Bao et al., 2017)
BMP-2 + VEGF	MBG-based matrix + GelMA/26SCS hydrogel	The release rates of BMP-2 and VEGF were 24.01% and 34.47% respectively within 24 h, 67.90% and 82.73% respectively in 14 days	*In vitro* osteogenic and angiogenic has been markedly improved. Ectopic bone formation in hindlimb ischemia model suggested type H vessels and neobone formation significantly increased	(Tang et al., 2020)
BMP-2 + bFGF	Gelatin microspheres + n-HA/PU40 scaffold + F-127 hydrogel	Pronounced burst release occurred in first 24 h, linear release in following 29 days	Micro-CT analysis indicated dual-delivery reached significantly higher bone volume (BV). Quantitative histological analysis showed remarkable tissue response	(Chen et al., 2016)
VEGF + FGF9	Nanocalcium sulfate + fibrin hydrogel	Addition of the peptide sequence decreased GFs release in an enzyme concentration-dependent manner	Radiographical and quantitative analysis of micro-CT showed the highest BV in dual-delivery hybrid composite. Quantification of blood vessels in explanted tissue suggested more neovessels were obtained	(Yuan et al., 2016)
Osteoprotegerin (OPG)	CS hydrogel	Lasts 28 days, release profile could be adjusted by CS molecular weight	An almost-complete recovery was observed, osteocalcin and osteopontin were upregulated	(Jayash et al., 2017)
SDF-1α	CS/carboxymethyl CS nanoparticles + CS/β-GP hydrogel	20% initial burst release, a cumulative release of 40% over 28 days	Micro-CT showed most new bone formation within the defect area	(Mi et al., 2017)
SDF-1α + BMP-2	Gelatin hydrogel	Large initial burst release of SDF-1α in first 3 days, which may due to BMP-2 combination	Better new bone formation was observed in the dual-delivery group. SDF-1α enhanced BMP-2 osteogenic effects	(Ratanavaraporn et al., 2011)
SDF-1α	RGD-modified alginate hydrogel	Sustained release over 42 days	Improvements induced by SDF-1α or hydrogel stiffness levelled within 8 weeks. Higher number of cells were recruited by SDF-1α, but the difference was not significant *in vivo*	(Cipitria et al., 2017)
PDGF-BB +BMP-9	Sericin hydrogel (genetically incorporated)	Almost 48% released within 17 days, intermittent rapid and slow release phases	Biocompatible compared with other materials and stimulated cell proliferation. Osteogenic markers were significantly upregulated, and greater bone formation when accompanied by BMP-9.	(Wang et al., 2020)
PTH	CS microsphere suspended in poloxamer hydrogel	43% of PTH released in first week, sustained release lasted over 27 days	New bone formation was found to be significantly higher compared to other groups after 10 days, but on day 21 a significant difference exists only when compared with the no treatment group	(Erten Taysi et al., 2019)

(Continued)

TABLE 1 | Continued

Peptide	Carrier material	Release pattern	Findings (*ex/in vivo*)	Reference
Abaloparatide (analog of PTH)	Photo-crosslinked methacrylated gelatin hydrogel	25% released within 24 h, remaining was released steadily over next 10 days	Drug-loaded hydrogel showed significantly higher rate of bone regeneration	(Ning et al., 2019)
Oxytocin	PLGA microsphere + poloxamer hydrogel + β-tricalcium phosphate (β-TCP) and hydroxyapatite	42% released in first week, complete release within 32 days	4 weeks after operation, the lowest residual graft and highest BMD and BV was obtained among all groups	(Akay et al., 2020)
Calcium accumulating peptide (artificially synthesized)	Gelatin-derived hydrogel	Sustained release over 7 days, collagenase accelerated release	Bone formation markers expression levels were enhanced. Micro-CT and histology showed the regenerative effect was superior to that of BMP-2 hydrogels	(Jo et al., 2018)

CS or polyethyleneimine (PEI) is usually introduced as the carrier due to the electrostatic interaction between the negatively charged nucleic acids and the polycations. It was reported that branched PEI-HA-DNA complexes were entrapped in bilayered OPF hydrogels to restore osteochondral defects (Needham et al., 2014). Moreover, BMP-2 plasmid DNA conjugated with CS nanoparticles exhibited significant augmentation in hydrogel-mediated rat calvaria bone regeneration (Li et al., 2017). Due to the low stability of liposomes and electrostatic disturbance of other charged compounds, calcium phosphate (CaP) can also be used for DNA incorporation and transfection in bone tissue engineering (Krebs et al., 2010).

MicroRNAs (miRNAs) and small interfering RNAs (siRNAs) are groups of short single-stranded RNA fragments that downregulate target gene expression post-translationally. Various miRNAs associated with bone formation have been reported (Fang et al., 2015), shedding new light on future bone tissue engineering. Nguyen et al. (2014) synthesized an 8-arm PEG *in situ*-forming hydrogel loaded with siRNA/PEI nanocomplexes. siRNA remained bioactive during the prolonged release period. The *in vitro* results showed that siNoggin and siNoggin/miRNA-20a sustained release promoted hMSC osteogenic differentiation in 3D hydrogel cultivation. As mentioned previously, a stiffer substrate may lead to MSC osteogenic differentiation. Carthew et al. (2020) incorporated PEG/gelatin norbornene hydrogels with mechanosensitive miRNAs. MSCs encapsulated in hydrogels were transfected *in situ*, which predominantly enhanced osteogenic gene expression and mineralization. Researchers presumed that the higher transfection efficacy might be ascribed to longer cell exposure times to the transfection agent.

Ions or Small Molecules

To date, a number of metal ions and artificially synthesized compounds have been found to be beneficial in bone regeneration. Achieving a sustained release pattern and longer duration of drug function may lead to promising therapeutic outcomes.

Metal Ions

Since magnesium ions (Mg^{2+}) play an important role in bone metabolism and mineralization, a variety of strategies for the sustained delivery of Mg^{2+} have been applied to hydrogel-based scaffolds. Lin et al. (2018b) coated MgO nanoparticles with PLGA and an alginate hydrogel, constructing a monodisperse core-shell delivery system. The release profile of Mg^{2+} revealed a significant suppression of the initial burst, and its release rate was stable and programmed. Enhancement of progenitor cell viability and proliferation, upregulation of osteogenic gene expression levels, and increased bone regeneration volume *in vivo* were attributed to the stable and precise Mg^{2+} supply. Bisphosphonates (BPs) possess two adjacent phosphonic groups, which are propitiously bind to divalent metal ions. Zhang and colleagues (Zhang et al., 2017) developed acrylated-BP-Mg nanoparticles to deliver Mg^{2+} as well as strengthen the acellular hydrogel composite, which serves as a matrix for *in situ* bone formation, *via* multivalent crosslinked domains. They also utilized Mg^{2+} to fulfill on-demand intelligent drug release in bone tissue engineering (Zhang et al., 2018). Intriguingly, Mg^{2+} played multiple roles in this research. First, BP-Mg nanoparticles enabled hydrogel formation and stabilized the prodrug. Second, Mg^{2+} promoted osteogenic differentiation, resulting in increased alkaline phosphatase (ALP) expression. However, and more importantly, Mg^{2+} is also a critical cofactor of ALP. ALP enzymatic hydrolysis was promoted; thus, more bioactive drug molecules were generated, which introduced positive feedback (**Figure 2**). According to the results, this strategy significantly enhanced bone regeneration.

Other metal ions, such as strontium ions (Sr^{2+}) and cobalt ions (Co^{2+}), may act synergistically in bone reconstruction. A Sr^{2+}-crosslinked RGD-alginate hydrogel combined with Sr-doped hydroxyapatite microspheres was engineered, showing a sustained release of Sr^{2+} from two sources (Lourenco et al., 2019). The researchers elaborated that this Sr-hybrid system facilitated MSC osteogenic differentiation, inhibited the functions of osteoclasts and modulated the inflammatory response. As a pro-vasculogenic factor, Co^{2+} was incorporated into the alginate hydrogel shell, while BMP-2 was laden into the collagen core (Perez et al., 2015). Co^{2+} released relatively rapidly, as expected. VEGF secretion and qPCR revealed that Co^{2+} not only stimulated angiogenesis but also elevated osteogenic gene expression. These results indicated an appealing prospect for applying metal ions bone tissue engineering in the future.

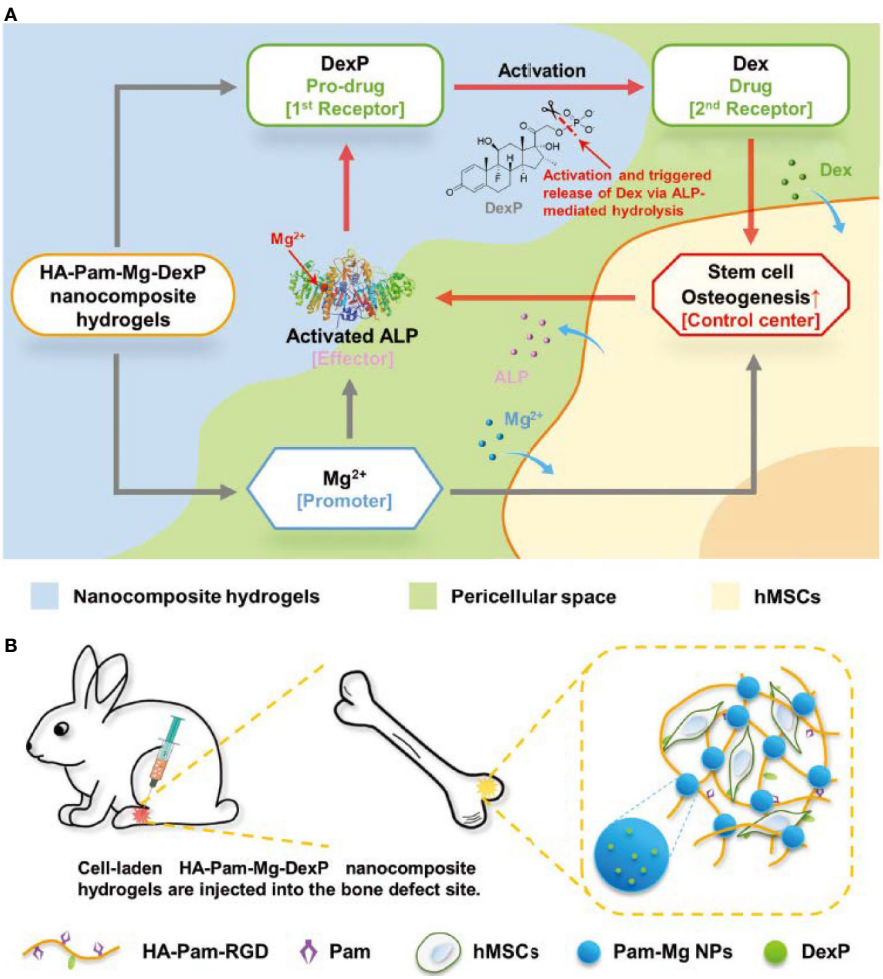

FIGURE 2 | Schematic illustration of **(A)** positive feedback mediated by a cofactor-assisted smart hydrogel drug release system and **(B)** *in situ* application to promote bone regeneration. Reprinted from a previous article by Zhang et al. (2018) with permission.

Small Molecules

A range of pharmaceutical molecules were designed or discovered to be effective in bone regeneration. Highlighted as chelating agents, BPs are utilized as antiresorptive drugs frequently in clinics. BPs mainly target osteoclasts, impeding the differentiation and maturation of osteoclast progenitors. Increasing evidence has shown that BPs directly or indirectly take part in other bone-forming mechanisms and are capable of targeting various cells (Corrado et al., 2017). Since bone healing and regeneration is known to consist of three consecutive phases of inflammation, repair, and remodeling, a proper scale of immune response is indispensable (Claes et al., 2012). However, excess or aberrant immune activation may jeopardize bone repair procedures (Claes et al., 2012; Gibon et al., 2017). Therefore, immunomodulatory drugs, such as nonsteroidal anti-inflammatory drugs (NSAIDs), have been applied in bone tissue engineering. Evidence has shown that aspirin elevates MSC osteogenic potency by inhibiting the tumor necrosis factor-α (TNF-α) and interferon-γ (IFN-γ) pathways (Liu et al., 2011). Statins are inhibitors of a key enzyme of cholesterol synthesis and are widely used to lower serum lipids. Researchers have reported that osteogenesis was enhanced concomitant with promoted *BMP-2* expression in bone cells when treating cells and rodents with statins (Mundy et al., 1999). Localized and sustained delivery of these drugs *via* hydrogels has pointed to a new direction in bone tissue engineering. Many relevant studies are listed and outlined in **Table 2**.

CONCLUSION AND FUTURE PERSPECTIVES

In this review, we summarized a series of investigations focused on hydrogel-based drug sustained release systems in bone tissue engineering. The hydrogels possess a porous microarchitecture, tunable biophysical parameters, and an adjustable degradation

TABLE 2 | Summary of selected studies on hydrogel-based small bioactive compound sustained release systems.

Drug	Carrier material	Release pattern	Findings (*ex/in vivo*)	Reference
Alendronate	Fibrin hydrogel	Steady release rate, cumulative release of approximately 45% over 10 days	Hydrogel containing 10^{-6} M showed the best augmentation in cell proliferation, osteogenic differentiation, and bone regeneration.	(Kim et al., 2017a)
Dexamethasone (Dex)	DNA- 2D silicate nanodisks (nSi) hybrid hydrogel	Release rate decreased with higher nSi concentration. Half-time of release was measured from 2.5 to 5.5 days	Drug bioactivity was preserved by the hydrogel. nSi may contribute to *in vivo* osteogenesis whereas Dex showed limited effects.	(Basu et al., 2018)
Aspirin	Thermo-sensitive alginate/ β-TCP hydrogel composite	20% drug released in the first day, 40% in 3 days, slowdown in day 5.	Percent of mineralized tissue was significantly higher compared to control group.	(Fang et al., 2018)
Aspirin	Tetra-PEG hydrogel	Released approximately 40% in first 2 days, cumulative release of 80% in 14 days	Low cytotoxicity, significantly improved expression of osteogenic markers and calvarial defect regeneration. Relatively low local inflammation status might be attributed to being laden with aspirin.	(Zhang et al., 2019)
Diclofenac	CS-coated alginate hydrogel	Released 50% and 90% in 2.5 h and 8 h, respectively	Osteoblasts grew and mineralized significantly regardless of drug exhaustion. Osteogenic genes increased over time, while osteogenic suppressing gene expression decreased.	(Lin et al., 2018a)
Tacrolimus	Type I collagen hydrogel	21 days release profile remained similar for different concentrations. Steady release rate.	More newly-formed bone and blood vessels were observed	(Nabavi et al., 2020)
Simvastatin	Maltodextrin micelle-CHO/ hydrogel composite	Slow release profile, exhibiting a slight difference according to different degrees of oxidation	Good biocompatibility, stimulated ALP activity and mineralization	(Yan et al., 2018)
Simvastatin	L-lactic acid oligomer (LAo) modified gelatin micelle/ gelatin hydrogel composite	Drug released faster as hydrogel crosslinking degree decreased. Release rate showed a good correlation with hydrogel degradation rate.	Hydrogel loaded with 10 μg of drug formed the largest area of bone	(Tanigo et al., 2010)
Rosuvastatin	chitosan/chondroitin sulfate nanoparticles+ Pluronic F127/hyaluronic acid hydrogel composite	Release rate significantly slower than control groups. 60% released from composite in 48 h	Low cytotoxicity, more calcium deposits were observed	(Rezazadeh et al., 2019)

rate, which makes them qualified bone tissue engineering scaffolds. Due to their high water content, chemical inertness and relatively sequestered and stable internal environment, they are also excellent in preserving the viabilities of the laden cells and bioactive factors. With the combination of biophysical and biochemical cues, researchers are able to facilely establish an osteo-friendly microenvironment, which would be beneficial for osteoprogenitors to obtain better bone regeneration. Thus, hydrogel-based biomaterials are strong candidates for current or future bone tissue engineering.

Evidence has shown that hydrogel-based drug sustained release systems are highly biocompatible and versatile drug deliverers, obtaining satisfactory osteogenesis results both *in vitro* and *in vivo*. The drug release profile varies according to the loading strategy, degradation ability of the matrix and drug concentration. Among these studies, physical entrapment and diffusion are the most applied drug loading and release strategies, respectively. In particular, the dispersion of drugs, ions and small molecules largely depends on hydrogel pore size and crosslinking density. Although it is quite simple and easy to operate, there are difficulties in initial burst release management. Swelling or degradation of hydrogel matrices contributes to polymer mesh size enlargement, resulting in drug release acceleration, especially for macromolecular drugs. Stronger interactions between matrices and drugs, such as electrostatic interactions and covalent bonds, and other drug reservoirs could be introduced into hydrogels, providing more efficacious drug protection and immobilization. However, negative results have been reported from sustained release systems that did not facilitate bone formation mainly because the carrier exhibited an extremely strong affinity towards the growth factor, resulting in a low level of drug concentration in the surrounding tissue (Hettiaratchi et al., 2017). Thus, optimal drug concentrations should also be determined to achieve a more reasonable and effective release profile.

As mentioned above, cells from different origins are involved in the bone formation process. A vast number of GFs and cytokines collaboratively trigger the repair cascade. Extensive studies have already been conducted on multiple bioactive factors controlled release. Spatiotemporal sequence release of bioactive factors might be a better mimic of complex regeneration procedures as well as exert extraordinary synergistic effects on bone regeneration. Various of multiple GFs delivery strategies was coherently summarized (Chen et al., 2010). Nevertheless, controlling dose ratio of drugs to maximize the synergistic effects and manipulating multiple bioactive factors release kinetics to mimic physiological release profile in different phases of bone regeneration are obstacles in nowadays bone tissue regeneration which needs further investigation.

AUTHOR CONTRIBUTIONS

YZ and TY contributed equally to this review. TY, YW, and BH designed and revised this article. YZ, TY, LP, and QS collected the literatures, arranged the outline of collected documents, and wrote the articles. All authors reviewed and commented on the entire manuscript.

FUNDING

This work was supported by the National Natural Science Foundation of China (51972005, 51672009, 51903003), National Natural Science Foundation of China Youth Fund (81922019), and National Youth Top-notch Talent Support Program (QNBJ2019-3).

REFERENCES

Ahlfeld, T., Schuster, F. P., Forster, Y., Quade, M., Akkineni, A. R., Rentsch, C., et al. (2019). 3D Plotted Biphasic Bone Scaffolds for Growth Factor Delivery: Biological Characterization In Vitro and In Vivo. *Adv. Healthc. Mater.* 8 (7), e1801512. doi: 10.1002/adhm.201801512

Akay, A. S., Arisan, V., Cevher, E., Sessevmez, M., and Cam, B. (2020). Oxytocin-loaded sustained-release hydrogel graft provides accelerated bone formation: An experimental rat study. *J. Orthop. Res.* 1–12. doi: 10.1002/jor.24607

Amirian, J., Linh, N. T., Min, Y. K., and Lee, B. T. (2015). Bone formation of a porous Gelatin-Pectin-biphasic calcium phosphate composite in presence of BMP-2 and VEGF. *Int. J. Biol. Macromol.* 76, 10–24. doi: 10.1016/j.ijbiomac.2015.02.021

Anjum, F., Lienemann, P. S., Metzger, S., Biernaskie, J., Kallos, M. S., and Ehrbar, M. (2016). Enzyme responsive GAG-based natural-synthetic hybrid hydrogel for tunable growth factor delivery and stem cell differentiation. *Biomaterials* 87, 104–117. doi: 10.1016/j.biomaterials.2016.01.050

Bae, M. S., Ohe, J. Y., Lee, J. B., Heo, D. N., Byun, W., Bae, H., et al. (2014). Photo-cured hyaluronic acid-based hydrogels containing growth and differentiation factor 5 (GDF-5) for bone tissue regeneration. *Bone* 59, 189–198. doi: 10.1016/j.bone.2013.11.019

Bao, X., Zhu, L., Huang, X., Tang, D., He, D., Shi, J., et al. (2017). 3D biomimetic artificial bone scaffolds with dual-cytokines spatiotemporal delivery for large weight-bearing bone defect repair. *Sci. Rep.* 7 (1), 7814. doi: 10.1038/s41598-017-08412-0

Barati, D., Shariati, S. R. P., Moeinzadeh, S., Melero-Martin, J. M., Khademhosseini, A., and Jabbari, E. (2016). Spatiotemporal release of BMP-2 and VEGF enhances osteogenic and vasculogenic differentiation of human mesenchymal stem cells and endothelial colony-forming cells co-encapsulated in a patterned hydrogel. *J. Control Release* 223, 126–136. doi: 10.1016/j.jconrel.2015.12.031

Basu, S., Pacelli, S., Feng, Y., Lu, Q., Wang, J., and Paul, A. (2018). Harnessing the Noncovalent Interactions of DNA Backbone with 2D Silicate Nanodisks To Fabricate Injectable Therapeutic Hydrogels. *ACS Nano.* 12 (10), 9866–9880. doi: 10.1021/acsnano.8b02434

Betz, R. R. (2002). Limitations of autograft and allograft: new synthetic solutions. *Orthopedics* 25 (5 Suppl), s561–s570.

Bonadio, J., Smiley, E., Patil, P., and Goldstein, S. (1999). Localized, direct plasmid gene delivery in vivo: prolonged therapy results in reproducible tissue regeneration. *Nat. Med.* 5 (7), 753–759. doi: 10.1038/10473

Bourque, W. T., Gross, M., and Hall, B. K. (1993). Expression of four growth factors during fracture repair. *Int. J. Dev. Biol.* 37 (4), 573–579.

Cao, L., Werkmeister, J. A., Wang, J., Glattauer, V., McLean, K. M., and Liu, C. (2014). Bone regeneration using photocrosslinked hydrogel incorporating rhBMP-2 loaded 2-N, 6-O-sulfated chitosan nanoparticles. *Biomaterials* 35 (9), 2730–2742. doi: 10.1016/j.biomaterials.2013.12.028

Carmeliet, P., and Jain, R. K. (2011). Molecular mechanisms and clinical applications of angiogenesis. *Nature* 473 (7347), 298–307. doi: 10.1038/nature10144

Carragee, E. J., Hurwitz, E. L., and Weiner, B. K. (2011). A critical review of recombinant human bone morphogenetic protein-2 trials in spinal surgery: emerging safety concerns and lessons learned. *Spine J.* 11 (6), 471–491. doi: 10.1016/j.spinee.2011.04.023

Carthew, J., Donderwinkel, I., Shrestha, S., Truong, V. X., Forsythe, J. S., and Frith, J. E. (2020). In situ miRNA delivery from a hydrogel promotes osteogenesis of encapsulated mesenchymal stromal cells. *Acta Biomater.* 101, 249–261. doi: 10.1016/j.actbio.2019.11.016

Chen, F. M., Zhang, M., and Wu, Z. F. (2010). Toward delivery of multiple growth factors in tissue engineering. *Biomaterials* 31 (24), 6279–6308. doi: 10.1016/j.biomaterials.2010.04.053

Chen, G., Deng, C., and Li, Y. P. (2012). TGF-beta and BMP signaling in osteoblast differentiation and bone formation. *Int. J. Biol. Sci.* 8 (2), 272–288. doi: 10.7150/ijbs.2929

Chen, T., Gomez, A. W., Zuo, Y., Li, X., Zhang, Z., Li, Y., et al. (2016). Osteogenic potential and synergistic effects of growth factors delivered from a bionic composite system. *J. BioMed. Mater. Res. A* 104 (3), 659–668. doi: 10.1002/jbm.a.35605

Chen, W., Liu, X., Chen, Q., Bao, C., Zhao, L., Zhu, Z., et al. (2018). Angiogenic and osteogenic regeneration in rats via calcium phosphate scaffold and endothelial cell co-culture with human bone marrow mesenchymal stem cells (MSCs), human umbilical cord MSCs, human induced pluripotent stem cell-derived MSCs and human embryonic stem cell-derived MSCs. *J. Tissue Eng. Regenerative Med.* 12 (1), 191–203. doi: 10.1002/term.2395

Cipitria, A., Boettcher, K., Schoenhals, S., Garske, D. S., Schmidt-Bleek, K., Ellinghaus, A., et al. (2017). In-situ tissue regeneration through SDF-1alpha driven cell recruitment and stiffness-mediated bone regeneration in a critical-sized segmental femoral defect. *Acta Biomater.* 60, 50–63. doi: 10.1016/j.actbio.2017.07.032

Claes, L., Recknagel, S., and Ignatius, A. (2012). Fracture healing under healthy and inflammatory conditions. *Nat. Rev. Rheumatol.* 8 (3), 133–143. doi: 10.1038/nrrheum.2012.1

Collin-Osdoby, P. (1994). Role of vascular endothelial cells in bone biology. *J. Cell Biochem.* 55 (3), 304–309. doi: 10.1002/jcb.240550306

Corrado, A., Sanpaolo, E. R., Di Bello, S., and Cantatore, F. P. (2017). Osteoblast as a target of anti-osteoporotic treatment. *Postgrad. Med.* 129 (8), 858–865. doi: 10.1080/00325481.2017.1362312

Crane, G. M., Ishaug, S. L., and Mikos, A. G. (1995). Bone tissue engineering. *Nat. Med.* 1 (12), 1322–1324. doi: 10.1038/nm1295-1322

Das, A., and Botchwey, E. (2011). Evaluation of angiogenesis and osteogenesis. *Tissue Eng. Part B. Rev.* 17 (6), 403–414. doi: 10.1089/ten.TEB.2011.0190

de Melo Pereira, D., and Habibovic, P. (2018). Biomineralization-Inspired Material Design for Bone Regeneration. *Adv. Healthc. Mater.* 7 (22), e1800700. doi: 10.1002/adhm.201800700

Dimatteo, R., Darling, N. J., and Segura, T. (2018). In situ forming injectable hydrogels for drug delivery and wound repair. *Adv. Drug Delivery Rev.* 127, 167–184. doi: 10.1016/j.addr.2018.03.007

Engler, A. J., Sen, S., Sweeney, H. L., and Discher, D. E. (2006). Matrix elasticity directs stem cell lineage specification. *Cell* 126 (4), 677–689. doi: 10.1016/j.cell.2006.06.044

Erten Taysi, A., Cevher, E., Sessevmez, M., Olgac, V., Mert Taysi, N., and Atalay, B. (2019). The efficacy of sustained-release chitosan microspheres containing recombinant human parathyroid hormone on MRONJ. *Braz. Res.* 33, e086. doi: 10.1590/1807-3107bor-2019.vol33.0086

Fang, J., Zhu, Y. Y., Smiley, E., Bonadio, J., Rouleau, J. P., Goldstein, S. A., et al. (1996). Stimulation of new bone formation by direct transfer of osteogenic plasmid genes. *Proc. Natl. Acad. Sci. U. S. A.* 93 (12), 5753–5758. doi: 10.1073/pnas.93.12.5753

Fang, S., Deng, Y., Gu, P., and Fan, X. (2015). MicroRNAs regulate bone development and regeneration. *Int. J. Mol. Sci.* 16 (4), 8227–8253. doi: 10.3390/ijms16048227

Fang, X., Lei, L., Jiang, T., Chen, Y., and Kang, Y. (2018). Injectable thermosensitive alginate/beta-tricalcium phosphate/aspirin hydrogels for bone augmentation. *J. BioMed. Mater. Res. B. Appl. Biomater.* 106 (5), 1739–1751. doi: 10.1002/jbm.b.33982

Farokhi, M., Mottaghitalab, F., Shokrgozar, M. A., Ou, K. L., Mao, C., and Hosseinkhani, H. (2016). Importance of dual delivery systems for bone tissue engineering. *J. Control Release* 225, 152–169. doi: 10.1016/j.jconrel.2016.01.033

Fiedler, J., Ozdemir, B., Bartholoma, J., Plettl, A., Brenner, R. E., and Ziemann, P. (2013). The effect of substrate surface nanotopography on the behavior of multipotnent mesenchymal stromal cells and osteoblasts. *Biomaterials* 34 (35), 8851–8859. doi: 10.1016/j.biomaterials.2013.08.010

Fisher, O. Z., Khademhosseini, A., Langer, R., and Peppas, N. A. (2010). Bioinspired materials for controlling stem cell fate. *Acc. Chem. Res.* 43 (3), 419–428. doi: 10.1021/ar900226q

Furuya, H., Tabata, Y., and Kaneko, K. (2014). Bone regeneration for murine femur fracture by gelatin hydrogels incorporating basic fibroblast growth factor with different release profiles. *Tissue Eng. Part A* 20 (9-10), 1531–1541. doi: 10.1089/ten.TEA.2012.0763

Gao, F., Li, J., Wang, L., Zhang, D., Zhang, J., Guan, F., et al (2020). Dual-enzymatically crosslinked hyaluronic acid hydrogel as a long-time 3D stem cell culture system. *BioMed. Mater.* doi: 10.1088/1748-605X/ab712e

Garcia, J. R., Clark, A. Y., and Garcia, A. J. (2016). Integrin-specific hydrogels functionalized with VEGF for vascularization and bone regeneration of critical-size bone defects. *J. BioMed. Mater. Res. A* 104 (7), 1845. doi: 10.1002/jbm.a.35777

GhavamiNejad, A., SamariKhalaj, M., Aguilar, L. E., Park, C. H., and Kim, C. S. (2016). pH/NIR Light-Controlled Multidrug Release via a Mussel-Inspired Nanocomposite Hydrogel for Chemo-Photothermal Cancer Therapy. *Sci. Rep.* 6, 33594. doi: 10.1038/srep33594

Gibon, E., Lu, L. Y., Nathan, K., and Goodman, S. B. (2017). Inflammation, ageing, and bone regeneration. *J. Orthop. Translat.* 10, 28–35. doi: 10.1016/j.jot.2017.04.002

Haugen, H. J., Lyngstadaas, S. P., Rossi, F., and Perale, G. (2019). Bone grafts: which is the ideal biomaterial? *J. Clin. Periodontol.* 46 Suppl 21, 92–102. doi: 10.1111/jcpe.13058

Hettiaratchi, M. H., Rouse, T., Chou, C., Krishnan, L., Stevens, H. Y., Li, M. A., et al. (2017). Enhanced in vivo retention of low dose BMP-2 via heparin microparticle delivery does not accelerate bone healing in a critically sized femoral defect. *Acta Biomater.* 59, 21–32. doi: 10.1016/j.actbio.2017.06.028

Higuchi, A., Ling, Q. D., Chang, Y., Hsu, S. T., and Umezawa, A. (2013). Physical cues of biomaterials guide stem cell differentiation fate. *Chem. Rev.* 113 (5), 3297–3328. doi: 10.1021/cr300426x

Huebsch, N., Arany, P. R., Mao, A. S., Shvartsman, D., Ali, O. A., Bencherif, S. A., et al. (2010). Harnessing traction-mediated manipulation of the cell/matrix interface to control stem-cell fate. *Nat. Mater.* 9 (6), 518–526. doi: 10.1038/nmat2732

Jayash, S. N., Hashim, N. M., Misran, M., and Baharuddin, N. A. (2017). Formulation and in vitro and in vivo evaluation of a new osteoprotegerin-chitosan gel for bone tissue regeneration. *J. BioMed. Mater. Res. A* 105 (2), 398–407. doi: 10.1002/jbm.a.35919

Jo, B. S., Lee, Y., Suh, J. S., Park, Y. S., Lee, H. J., Lee, J. Y., et al. (2018). A novel calcium-accumulating peptide/gelatin in situ forming hydrogel for enhanced bone regeneration. *J. BioMed. Mater. Res. A* 106 (2), 531–542. doi: 10.1002/jbm.a.36257

Jones, D. L., and Wagers, A. J. (2008). No place like home: anatomy and function of the stem cell niche. *Nat. Rev. Mol. Cell Biol.* 9 (1), 11–21. doi: 10.1038/nrm2319

Kader, S., Monavarian, M., Barati, D., Moeinzadeh, S., Makris, T. M., and Jabbari, E. (2019). Plasmin-Cleavable Nanoparticles for On-Demand Release of Morphogens in Vascularized Osteogenesis. *Biomacromolecules* 20 (8), 2973–2988. doi: 10.1021/acs.biomac.9b00532

Kato, T., Kawaguchi, H., Hanada, K., Aoyama, I., Hiyama, Y., Nakamura, T., et al. (1998). Single local injection of recombinant fibroblast growth factor-2 stimulates healing of segmental bone defects in rabbits. *J. Orthop. Res.* 16 (6), 654–659. doi: 10.1002/jor.1100160605

Keating, A. (2008). How do mesenchymal stromal cells suppress T cells? *Cell Stem Cell* 2 (2), 106–108. doi: 10.1016/j.stem.2008.01.007

Kempen, D. H., Lu, L., Heijink, A., Hefferan, T. E., Creemers, L. B., Maran, A., et al. (2009). Effect of local sequential VEGF and BMP-2 delivery on ectopic and orthotopic bone regeneration. *Biomaterials* 30 (14), 2816–2825. doi: 10.1016/j.biomaterials.2009.01.031

Kim, B. S., Shkembi, F., and Lee, J. (2017a). In Vitro and In Vivo Evaluation of Commercially Available Fibrin Gel as a Carrier of Alendronate for Bone Tissue Engineering. *BioMed. Res. Int.* 2017, 6434169. doi: 10.1155/2017/6434169

Kim, H. D., Amirthalingam, S., Kim, S. L., Lee, S. S., Rangasamy, J., and Hwang, N. S. (2017b). Biomimetic Materials and Fabrication Approaches for Bone Tissue Engineering. *Adv. Healthc. Mater.* 6 (23), 1700612. doi: 10.1002/adhm.201700612

Kodama, N., Nagata, M., Tabata, Y., Ozeki, M., Ninomiya, T., and Takagi, R. (2009). A local bone anabolic effect of rhFGF2-impregnated gelatin hydrogel by promoting cell proliferation and coordinating osteoblastic differentiation. *Bone* 44 (4), 699–707. doi: 10.1016/j.bone.2008.12.017

Kolambkar, Y. M., Boerckel, J. D., Dupont, K. M., Bajin, M., Huebsch, N., Mooney, D. J., et al. (2011). Spatiotemporal delivery of bone morphogenetic protein enhances functional repair of segmental bone defects. *Bone* 49 (3), 485–492. doi: 10.1016/j.bone.2011.05.010

Komatsu, K., Shibata, T., Shimada, A., Ideno, H., Nakashima, K., Tabata, Y., et al. (2016). Cationized gelatin hydrogels mixed with plasmid DNA induce stronger and more sustained gene expression than atelocollagen at calvarial bone defects in vivo. *J. Biomater. Sci. Polym. Ed.* 27 (5), 419–430. doi: 10.1080/09205063.2016.1139486

Krebs, M. D., Salter, E., Chen, E., Sutter, K. A., and Alsberg, E. (2010). Calcium phosphate-DNA nanoparticle gene delivery from alginate hydrogels induces in vivo osteogenesis. *J. BioMed. Mater. Res. A* 92 (3), 1131–1138. doi: 10.1002/jbm.a.32441

Kronenberg, H. M. (2003). Developmental regulation of the growth plate. *Nature* 423 (6937), 332–336. doi: 10.1038/nature01657

Langer, R., and Vacanti, J. P. (1993). Tissue engineering. *Science* 260 (5110), 920–926. doi: 10.1126/science.8493529

Lee, S. H., and Shin, H. (2007). Matrices and scaffolds for delivery of bioactive molecules in bone and cartilage tissue engineering. *Adv. Drug Delivery Rev.* 59 (4-5), 339–359. doi: 10.1016/j.addr.2007.03.016

Lee, J., Abdeen, A. A., Kim, A. S., and Kilian, K. A. (2015). Influence of Biophysical Parameters on Maintaining the Mesenchymal Stem Cell Phenotype. *ACS Biomater. Sci. Eng.* 1 (4), 218–226. doi: 10.1021/ab500003s

Li, H., Ji, Q., Chen, X., Sun, Y., Xu, Q., Deng, P., et al. (2017). Accelerated bony defect healing based on chitosan thermosensitive hydrogel scaffolds embedded with chitosan nanoparticles for the delivery of BMP2 plasmid DNA. *J. BioMed. Mater. Res. A* 105 (1), 265–273. doi: 10.1002/jbm.a.35900

Li, W., Liu, Y., Zhang, P., Tang, Y., Zhou, M., Jiang, W., et al. (2018). Tissue-Engineered Bone Immobilized with Human Adipose Stem Cells-Derived Exosomes Promotes Bone Regeneration. *ACS Appl. Mater. Interf.* 10 (6), 5240–5254. doi: 10.1021/acsami.7b17620

Lin, H. Y., Chang, T. W., and Peng, T. K. (2018a). Three-dimensional plotted alginate fibers embedded with diclofenac and bone cells coated with chitosan for bone regeneration during inflammation. *J. BioMed. Mater. Res. A* 106 (6), 1511–1521. doi: 10.1002/jbm.a.36357

Lin, Z., Wu, J., Qiao, W., Zhao, Y., Wong, K. H. M., Chu, P. K., et al. (2018b). Precisely controlled delivery of magnesium ions thru sponge-like monodisperse PLGA/nano-MgO-alginate core-shell microsphere device to enable in-situ bone regeneration. *Biomaterials* 174, 1–16. doi: 10.1016/j.biomaterials.2018.05.011

Lin, H., Tang, Y., Lozito, T. P., Oyster, N., Wang, B., and Tuan, R. S. (2019). Efficient in vivo bone formation by BMP-2 engineered human mesenchymal stem cells encapsulated in a projection stereolithographically fabricated hydrogel scaffold. *Stem Cell Res. Ther.* 10 (1), 254. doi: 10.1186/s13287-019-1350-6

Liu, Y., Wang, L., Kikuiri, T., Akiyama, K., Chen, C., Xu, X., et al. (2011). Mesenchymal stem cell-based tissue regeneration is governed by recipient T lymphocytes via IFN-gamma and TNF-alpha. *Nat. Med.* 17 (12), 1594–1601. doi: 10.1038/nm.2542

Lourenco, A. H., Torres, A. L., Vasconcelos, D. P., Ribeiro-Machado, C., Barbosa, J. N., Barbosa, M. A., et al. (2019). Osteogenic, anti-osteoclastogenic and immunomodulatory properties of a strontium-releasing hybrid scaffold for bone repair. *Mater. Sci. Eng. C. Mater. Biol. Appl.* 99, 1289–1303. doi: 10.1016/j.msec.2019.02.053

Lunzer, M., Shi, L., Andriotis, O. G., Gruber, P., Markovic, M., Thurner, P. J., et al. (2018). A Modular Approach to Sensitized Two-Photon Patterning of Photodegradable Hydrogels. *Angew. Chem. Int. Ed. Engl.* 57 (46), 15122–15127. doi: 10.1002/anie.201808908

Mabilleau, G., Aguado, E., Stancu, I. C., Cincu, C., Basle, M. F., and Chappard, D. (2008). Effects of FGF-2 release from a hydrogel polymer on bone mass and microarchitecture. *Biomaterials* 29 (11), 1593–1600. doi: 10.1016/j.biomaterials.2007.12.018

Marklein, R. A., and Burdick, J. A. (2010). Controlling stem cell fate with material design. *Adv. Mater.* 22 (2), 175–189. doi: 10.1002/adma.200901055

Marsell, R., and Einhorn, T. A. (2011). The biology of fracture healing. *Injury* 42 (6), 551–555. doi: 10.1016/j.injury.2011.03.031

Meijer, G. J., de Bruijn, J. D., Koole, R., and van Blitterswijk, C. A. (2007). Cell-based bone tissue engineering. *PloS Med.* 4 (2), e9. doi: 10.1371/journal.pmed.0040009

Mi, L., Liu, H., Gao, Y., Miao, H., and Ruan, J. (2017). Injectable nanoparticles/hydrogels composite as sustained release system with stromal cell-derived factor-1alpha for calvarial bone regeneration. *Int. J. Biol. Macromol.* 101, 341–347. doi: 10.1016/j.ijbiomac.2017.03.098

Mundy, G., Garrett, R., Harris, S., Chan, J., Chen, D., Rossini, G., et al. (1999). Stimulation of bone formation in vitro and in rodents by statins. *Science* 286 (5446), 1946–1949. doi: 10.1126/science.286.5446.1946

Nabavi, M. H., Salehi, M., Ehterami, A., Bastami, F., Semyari, H., Tehranchi, M., et al. (2020). A collagen-based hydrogel containing tacrolimus for bone tissue engineering. *Drug Delivery Transl. Res.* 10 (1), 108–121. doi: 10.1007/s13346-019-00666-7

Nauth, A., Ristevski, B., Li, R., and Schemitsch, E. H. (2011). Growth factors and bone regeneration: how much bone can we expect? *Injury* 42 (6), 574–579. doi: 10.1016/j.injury.2011.03.034

Needham, C. J., Shah, S. R., Dahlin, R. L., Kinard, L. A., Lam, J., Watson, B. M., et al. (2014). Osteochondral tissue regeneration through polymeric delivery of DNA encoding for the SOX trio and RUNX2. *Acta Biomater.* 10 (10), 4103–4112. doi: 10.1016/j.actbio.2014.05.011

Nguyen, M. K., Jeon, O., Krebs, M. D., Schapira, D., and Alsberg, E. (2014). Sustained localized presentation of RNA interfering molecules from in situ forming hydrogels to guide stem cell osteogenic differentiation. *Biomaterials* 35 (24), 6278–6286. doi: 10.1016/j.biomaterials.2014.04.048

Ning, Z., Tan, B., Chen, B., Lau, D. S. A., Wong, T. M., Sun, T., et al. (2019). Precisely Controlled Delivery of Abaloparatide through Injectable Hydrogel to Promote Bone Regeneration. *Macromol. Biosci.* 19 (6), e1900020. doi: 10.1002/mabi.201900020

Olsen, B. R., Reginato, A. M., and Wang, W. (2000). Bone development. *Annu. Rev. Cell Dev. Biol.* 16, 191–220. doi: 10.1146/annurev.cellbio.16.1.191

Olthof, M. G. L., Tryfonidou, M. A., Liu, X., Pouran, B., Meij, B. P., Dhert, W. J. A., et al. (2018). Phosphate Functional Groups Improve Oligo[(Polyethylene Glycol) Fumarate] Osteoconduction and BMP-2 Osteoinductive Efficacy. *Tissue Eng. Part A* 24 (9-10), 819–829. doi: 10.1089/ten.TEA.2017.0229

Paez, J. I., Farrukh, A., Valbuena-Mendoza, R., Wlodarczyk-Biegun, M. K., and Del Campo, A. (2020). Thiol-Methylsulfone-Based Hydrogels for 3D Cell Encapsulation. *ACS Appl. Mater. Interf.* 12 (7), 8062–8072. doi: 10.1021/acsami.0c00709

Park, J., Lee, S. J., Lee, H., Park, S. A., and Lee, J. Y. (2018). Three dimensional cell printing with sulfated alginate for improved bone morphogenetic protein-2 delivery and osteogenesis in bone tissue engineering. *Carbohydr. Polym.* 196, 217–224. doi: 10.1016/j.carbpol.2018.05.048

Pearlin, N. S., Manivasagam, G., and Sen, D. (2018). Progress of Regenerative Therapy in Orthopedics. *Curr. Osteoporos. Rep.* 16 (2), 169–181. doi: 10.1007/s11914-018-0428-x

Perez, R. A., Kim, J. H., Buitrago, J. O., Wall, I. B., and Kim, H. W. (2015). Novel therapeutic core-shell hydrogel scaffolds with sequential delivery of cobalt and bone morphogenetic protein-2 for synergistic bone regeneration. *Acta Biomater.* 23, 295–308. doi: 10.1016/j.actbio.2015.06.002

Prockop, D. J. (1997). Marrow stromal cells as stem cells for nonhematopoietic tissues. *Science* 276 (5309), 71–74. doi: 10.1126/science.276.5309.71

Quarto, N., and Longaker, M. T. (2006). FGF-2 inhibits osteogenesis in mouse adipose tissue-derived stromal cells and sustains their proliferative and osteogenic potential state. *Tissue Eng.* 12 (6), 1405–1418. doi: 10.1089/ten.2006.12.1405

Ramasamy, S. K., Kusumbe, A. P., Itkin, T., Gur-Cohen, S., Lapidot, T., and Adams, R. H. (2016). Regulation of Hematopoiesis and Osteogenesis by Blood Vessel-Derived Signals. *Annu. Rev. Cell Dev. Biol.* 32, 649–675. doi: 10.1146/annurev-cellbio-111315-124936

Ratanavaraporn, J., Furuya, H., Kohara, H., and Tabata, Y. (2011). Synergistic effects of the dual release of stromal cell-derived factor-1 and bone morphogenetic protein-2 from hydrogels on bone regeneration. *Biomaterials* 32 (11), 2797–2811. doi: 10.1016/j.biomaterials.2010.12.052

Rezazadeh, M., Parandeh, M., Akbari, V., Ebrahimi, Z., and Taheri, A. (2019). Incorporation of rosuvastatin-loaded chitosan/chondroitin sulfate nanoparticles into a thermosensitive hydrogel for bone tissue engineering: preparation, characterization, and cellular behavior. *Pharm. Dev. Technol.* 24 (3), 357–367. doi: 10.1080/10837450.2018.1484765

Rouwkema, J., Rivron, N. C., and van Blitterswijk, C. A. (2008). Vascularization in tissue engineering. *Trends Biotechnol.* 26 (8), 434–441. doi: 10.1016/j.tibtech.2008.04.009

Samorezov, J. E., and Alsberg, E. (2015). Spatial regulation of controlled bioactive factor delivery for bone tissue engineering. *Adv. Drug Delivery Rev.* 84, 45–67. doi: 10.1016/j.addr.2014.11.018

Scadden, D. T. (2006). The stem-cell niche as an entity of action. *Nature* 441 (7097), 1075–1079. doi: 10.1038/nature04957

Seliktar, D. (2012). Designing cell-compatible hydrogels for biomedical applications. *Science* 336 (6085), 1124–1128. doi: 10.1126/science.1214804

Seo, B. B., Choi, H., Koh, J. T., and Song, S. C. (2015). Sustained BMP-2 delivery and injectable bone regeneration using thermosensitive polymeric nanoparticle hydrogel bearing dual interactions with BMP-2. *J. Control Release* 209, 67–76. doi: 10.1016/j.jconrel.2015.04.023

Seo, B. B., Koh, J. T., and Song, S. C. (2017). Tuning physical properties and BMP-2 release rates of injectable hydrogel systems for an optimal bone regeneration effect. *Biomaterials* 122, 91–104. doi: 10.1016/j.biomaterials.2017.01.016

Shekaran, A., Garcia, J. R., Clark, A. Y., Kavanaugh, T. E., Lin, A. S., Guldberg, R. E., et al. (2014). Bone regeneration using an alpha 2 beta 1 integrin-specific hydrogel as a BMP-2 delivery vehicle. *Biomaterials* 35 (21), 5453–5461. doi: 10.1016/j.biomaterials.2014.03.055

Slaughter, B. V., Khurshid, S. S., Fisher, O. Z., Khademhosseini, A., and Peppas, N. A. (2009). Hydrogels in regenerative medicine. *Adv. Mater.* 21 (32-33), 3307–3329. doi: 10.1002/adma.200802106

Spicer, P. P., Kretlow, J. D., Young, S., Jansen, J. A., Kasper, F. K., and Mikos, A. G. (2012). Evaluation of bone regeneration using the rat critical size calvarial defect. *Nat. Protoc.* 7 (10), 1918–1929. doi: 10.1038/nprot.2012.113

Tang, W., Yu, Y., Wang, J., Liu, H., Pan, H., Wang, G., et al. (2020). Enhancement and orchestration of osteogenesis and angiogenesis by a dual-modular design of growth factors delivery scaffolds and 26SCS decoration. *Biomaterials* 232, 119645. doi: 10.1016/j.biomaterials.2019.119645

Tanigo, T., Takaoka, R., and Tabata, Y. (2010). Sustained release of water-insoluble simvastatin from biodegradable hydrogel augments bone regeneration. *J. Control Release* 143 (2), 201–206. doi: 10.1016/j.jconrel.2009.12.027

Wang, F., Hou, K., Chen, W., Wang, Y., Wang, R., Tian, C., et al. (2020). Transgenic PDGF-BB/sericin hydrogel supports for cell proliferation and osteogenic differentiation. *Biomater. Sci.* 8 (2), 657–672. doi: 10.1039/c9bm01478k

Wei, Y., Zhang, X., Song, Y., Han, B., Hu, X., Wang, X., et al. (2011). Magnetic biodegradable Fe3O4/CS/PVA nanofibrous membranes for bone regeneration. *BioMed. Mater.* 6 (5), 055008. doi: 10.1088/1748-6041/6/5/055008

Xie, J., Peng, C., Zhao, Q., Wang, X., Yuan, H., Yang, L., et al. (2016). Osteogenic differentiation and bone regeneration of iPSC-MSCs supported by a biomimetic nanofibrous scaffold. *Acta Biomater.* 29, 365–379. doi: 10.1016/j.actbio.2015.10.007

Yan, S., Ren, J., Jian, Y., Wang, W., Yun, W., and Yin, J. (2018). Injectable Maltodextrin-Based Micelle/Hydrogel Composites for Simvastatin-Controlled Release. *Biomacromolecules* 19 (12), 4554–4564. doi: 10.1021/acs.biomac.8b01234

Yin, S., Zhang, W., Zhang, Z., and Jiang, X. (2019). Recent Advances in Scaffold Design and Material for Vascularized Tissue-Engineered Bone Regeneration. *Adv. Healthc. Mater.* 8 (10), e1801433. doi: 10.1002/adhm.201801433

Yuan, X., Smith, R. J.Jr., Guan, H., Ionita, C. N., Khobragade, P., Dziak, R., et al. (2016). Hybrid Biomaterial with Conjugated Growth Factors and

Mesenchymal Stem Cells for Ectopic Bone Formation. *Tissue Eng. Part A* 22 (13-14), 928–939. doi: 10.1089/ten.TEA.2016.0052

Zang, S., Mu, R., Chen, F., Wei, X., Zhu, L., Han, B., et al. (2019). Injectable chitosan/beta-glycerophosphate hydrogels with sustained release of BMP-7 and ornidazole in periodontal wound healing of class III furcation defects. *Mater. Sci. Eng. C. Mater. Biol. Appl.* 99, 919–928. doi: 10.1016/j.msec.2019.02.024

Zhang, K., Lin, S., Feng, Q., Dong, C., Yang, Y., Li, G., et al. (2017). Nanocomposite hydrogels stabilized by self-assembled multivalent bisphosphonate-magnesium nanoparticles mediate sustained release of magnesium ion and promote in-situ bone regeneration. *Acta Biomater.* 64, 389–400. doi: 10.1016/j.actbio.2017.09.039

Zhang, K., Jia, Z., Yang, B., Feng, Q., Xu, X., Yuan, W., et al. (2018). Adaptable Hydrogels Mediate Cofactor-Assisted Activation of Biomarker-Responsive Drug Delivery via Positive Feedback for Enhanced Tissue Regeneration. *Adv. Sci. (Weinh)* 5 (12), 1800875. doi: 10.1002/advs.201800875

Zhang, Y., Ding, N., Zhang, T., Sun, Q., Han, B., and Yu, T. (2019). A Tetra-PEG Hydrogel Based Aspirin Sustained Release System Exerts Beneficial Effects on Periodontal Ligament Stem Cells Mediated Bone Regeneration. *Front. Chem.* 7, 682. doi: 10.3389/fchem.2019.00682

Conflict of Interest: The authors declare that the research was conducted in the absence of any commercial or financial relationships that could be construed as a potential conflict of interest.

frontiers in Pharmacology

ORIGINAL RESEARCH
published: 19 May 2020
doi: 10.3389/fphar.2020.00573

Locally Controlled Release of Methotrexate and Alendronate by Thermo-Sensitive Hydrogels for Synergistic Inhibition of Osteosarcoma Progression

Hongli Shan[1], Ke Li[2], Duoyi Zhao[2], Changliang Chi[3], Qinyuan Tan[3], Xiaoqing Wang[3], Jinhai Yu[4] and Meihua Piao[5]**

[1] Department of Clinical Laboratory, The First Hospital of Jilin University, Changchun, China, [2] Department of Orthopedics, the Fourth Affiliated Hospital of China Medical University, Shenyang, China, [3] Department of Urology, the First Hospital of Jilin University, Changchun, China, [4] Department of Gastrointestinal Surgery, The First Hospital of Jilin University, Changchun, China, [5] Department of Anesthesiology, The First Hospital of Jilin University, Changchun, China

OPEN ACCESS

Edited by:
Wei Tao,
Harvard Medical School,
United States

Reviewed by:
Chao Zhao,
University of Alabama,
United States
Gang Guo,
Sichuan University, China
Yilong Cheng,
Xi'an Jiaotong University,
China

***Correspondence:**
Jinhai Yu
jidayujinhai@126.com
Meihua Piao
pumh@jlu.edu.cn

Specialty section:
This article was submitted to Experimental Pharmacology and Drug Discovery, a section of the journal Frontiers in Pharmacology

Received: *09 February 2020*
Accepted: *15 April 2020*
Published: *19 May 2020*

Citation:
Shan H, Li K, Zhao D, Chi C, Tan Q, Wang X, Yu J and Piao M (2020) Locally Controlled Release of Methotrexate and Alendronate by Thermo-Sensitive Hydrogels for Synergistic Inhibition of Osteosarcoma Progression. Front. Pharmacol. 11:573. doi: 10.3389/fphar.2020.00573

Osteosarcoma (OS) is a serious primary bone malignant tumor that can easily affect children and adolescents. Chemotherapy is one of the important and feasible clinical treatment strategies for the treatment of OS at present, which is severely limited due to insufficient retention time, poor penetration ability, and serious side effects of current anti-tumor drug preparations. In this work, a novel injectable thermo-sensitive hydrogel ($mPEG_{45}$–PLV_{19}) loaded with methotrexate and alendronate, and the sustained release at the tumor site synergistically inhibited the progression of OS. The $mPEG_{45}$–PLV_{19} shows excellent physical and chemical properties. Compared with other treatment groups, the *in vivo* treatment of gel+ methotrexate + alendronate effectively inhibited the growth of tumor. More importantly, it significantly reduced bone destruction and lung metastasis caused by OS. Therefore, this injectable thermo-sensitive hydrogel drug delivery system has broad prospects for OS chemotherapy.

Keywords: thermo-sensitive hydrogel, local injection, controlled drug release, osteosarcoma, synergistic chemotherapy

INTRODUCTION

Osteosarcoma (OS) is a malignant bone tumor that occurs mainly in the proximal tibia and distal femur in children and adolescents (Kosei et al., 2013; Nedelcu et al., 2014; Xu et al., 2019). Even with adequate clinical treatment, 5-year overall survival for OS patients is still less than 60% (Ottaviani and Jaffe, 2009; Zhang et al., 2018a; Zhang et al., 2018b). And when OS patients have metastasis or recurrence, their 5-year survival rate drops to less than 20% (Wu et al., 2009).

Current clinical treatment for patients with OS includes preoperative chemotherapy, intraoperative resection of the lesion (including metastasis), and postoperative chemotherapy (Isakoff et al., 2015; Li et al., 2018). Systemic chemotherapy is currently one of the most important means of clinically suppressing the progression of OS. However, systemic chemotherapy is often accompanied by the

following severe problems: (1) poor selectivity of chemotherapy drugs (Chen et al., 2017; Gao et al., 2019; Sun et al., 2019; Ma et al., 2020); (2) strong side effects (Feng et al., 2019a; Feng et al., 2019b; Wang et al., 2019); (3) drug resistance (Ding et al., 2019a; Ding et al., 2019b; Ding et al., 2019c); (4) tumor recurrence, etc (Kim and Helman, 2009; Marco and Sch?Fer, 2010; Moorthi et al., 2011). Therefore, there is an urgent need for new and effective therapy for treating OS.

Hydrogels are materials of a 3D network structure formed by physical or chemical crosslinking (Du et al., 2019). Injectable hydrogels are now common in biomedical applications (Zhang W. et al., 2018). Among them, temperature-responsive hydrogels are particularly noteworthy (Du et al., 2019; Mu et al., 2019). Thermo-sensitive hydrogel is a special kind of injectable biomaterials (Huang et al., 2019; Zarrintaj et al., 2019). The solution is in a sol state and has fluidity at low temperatures, which is extremely beneficial for drug loading (Ta et al., 2008; Wang et al., 2015). The mixed solution is injected into the tumor site, and the solution rapidly changes from the sol state to the gel state upon stimulation of body temperature. Then, the hydrogel slowly degrades in the body due to the interaction between its own molecules, causing its loaded drug to slowly release from the hydrogel (Seeli and Prabaharan, 2017). Localized treatment of thermo-sensitive hydrogel has been reported to include the following advantages: (1) sustained release of drug at the tumor site; (2) reduced administration time and systemic side effects; (3) overcoming the low solubility of the chemotherapeutic drug; (4) small surgical trauma and simple operation; (5) patients' compliance and comfort level were improved (Lovett et al., 2015; Xiong et al., 2015; Wu et al., 2016).

Therefore, based on the above characteristics, a temperature-sensitive poly(L-valine) (PLV) hydrogel was developed in this work. First, a ring-opening polymerization (ROP) of L-valine N-carboxy anhydride (L-Val NCA) is initiated by terminally aminated polyethylene glycol monomethyl ether ($mPEG_{45}$-NH_2) to form $mPEG_{45}$–PLV_{19}. Secondly, the chemical structure characteristics of temperature-sensitive PLV hydrogels were identified by proton nuclear magnetic resonance spectroscopy and Fourier transform infrared spectroscopy (FT-IR). Then, the change of the state of PLV hydrogel with temperature was analyzed by tube inversion method, and the mechanical properties were further analyzed by rheological analysis. The surface morphology of PLV hydrogel was obtained by scanning electron microscopy (SEM). Thereafter, the biodegradability of PLV hydrogel was analyzed by an *in vivo* environment simulated *in vitro*. Hematoxylin and eosin staining (H&E) were used to observe the biocompatibility of PLV hydrogels. Methotrexate (Mtx) is one of the first-line chemotherapy drugs for OS, which mainly inhibits tumor cell synthesis by inhibiting dihydrofolate reductase. Alendronate (Aln) is the most important anti-resorber for the treatment of bone diseases. Aln has a high affinity for bone minerals and prevents bone destruction by inhibiting osteoclast activity. Finally, the PLV hydrogel was loaded with Mtx and alendronate Aln to inhibit orthotopic OS in mice. The Gel+Mtx +Aln group was observed to have the greatest tumor suppressive effect, with minimal lung metastasis and minimal bone destruction. In summary, the temperature-sensitive PLV hydrogel combined with Mtx and Aln as a novel drug delivery system has shown good application prospects in the local synergistic chemotherapy of OS.

MATERIALS AND METHODS

Materials

Methoxy poly(ethylene glycol) ($mPEG_{45}$, 98%) and *n*-hexylamine (99%) was purchased from Sigma-Aldrich (St. Louis, MO, USA). L-Valine (L-Val, 98%) is from GL Biochemicals Co., Ltd. (Shanghai, P. R. China). Mtx (99%) and alendronate (97%) was purchased from Sigma-Aldrich (St. Louis, MO, USA). Triphosgene (98%) was purchased from Shanghai Duodian Chemical Co., Ltd. (Shanghai, P. R. China). *p*-Toluenesulfonyl chloride (99%) was purchased from Sinopharm Chemical Reagent Co., Ltd (Shanghai, P. R. China). *n*-Hexane (99%), toluene (99%), ethyl acetate (99.8%), *N*,*N*-dimethylformamide (DMF, 99.5%), and diethyl ether (98%) were purchased at Beijing Chemical Plant (Beijing, P. R. China). Among them, *n*-hexylamine and DMF were purified by a solvent treatment system.

Synthesis of $mPEG_{45}$–PLV_{19}

L-Val NCA ROP was initiated by using $mPEG_{45}$-NH_2 as a macroinitiator to obtain $mPEG_{45}$–PLV_{19} block copolymer. Weigh a portion of $mPEG_{45}$-NH_2 2.0 g and 150.0 ml of anhydrous toluene at 130°C for 2 h to azeotropically remove water. Subsequently, the toluene was gradually taken out, and the cold trap was evacuated for 1 h to remove the residual toluene in the reaction flask. Then 2.86 g (0.02 mol) of L-Val NCA was added and mixed with 100.0 ml of DMF. The polymerization was stirred magnetically at 25°C for 3 d, next settled with 1,000.0 ml of ice diethyl ether. The obtained product was dissolved in 40.0 ml of DMF and dialyzed (molecular weight cut-off [MWCO] = 3,500 Da) for 72 h. The dialyzed water was changed every 6 h. Finally, the final product, $mPEG_{45}$-PLV_{19}, was obtained by lyophilization.

In Vitro Drug Release

The copolymer solution (500 ul, 5% wt%) was added to a 3.0 ml glass vial and incubated for 10 min at a constant temperature (37°C) to obtain an mPEG45-PLV19 hydrogel. Buffer solution (2.0 ml) was added to the top of the hydrogel at 37°C, and the medium was changed once a day. Determine the concentration of MTX or Aln released by a UV spectrophotometer.

Establishment of an Orthotopic OS Model

K7M2 cells were collected and then mixed with PBS. The mice were anesthetized with ether and depilated to fully expose the surgical site. Using a 1 ml syringe needle, the cortical layer of the right tibia was pierced vertically and the needle was inserted into the metaphysis of the tibia for approximately 3.5 mm. After the needle was removed, 2 million K7M2 cells (30 ul) were slowly injected into the bone marrow using a micro-injector. Tumor growth in the right leg of mice was monitored daily, while the

tumor volume (V) was measured by micrometers. Mice were euthanized when the experiment was over (16 d) or when the tumor size reached 1 cm^3.

In Vivo Anti-Tumor Efficacy

After inoculation of K7M2 tumors for 3–4 weeks, when the right tibia tumors of the mice were visible (volume about 200 mm^3), the mice began to receive treatment. The Mtx and the Aln dose was 50 mg/kg. The gel (5.0 wt.%) containing Mtx and Aln was injected in the sol state (4) to inoculate 100 ul to the vicinity of the mouse *in situ* tumor. Tumors were measured at the top (AP) and longitudinal (L) using a digital caliper. AP was measured at the knee joint, and L was measured along the long axis of the tibia. Estimate the size of the primary tumor (V) according to formula (Zhang W. et al., 2018) (1):

$$V(\mathrm{mm}_3) = \frac{4\pi}{3}\left(\frac{AP+L}{4}\right)^2 \quad (1)$$

Euthanasia was performed after all treatments were completed, and the hind limbs with tumors were collected and photographed.

Micro-CT

The right tibia of the mouse was collected and placed on a micro-CT specimen table to evaluate the damage of the humerus bone by radiographic analysis. The X-ray tube voltage was set to 40 kV. The data is derived from a 360° individual projection collected every 1° of rotation, rotated one week around the specimen, and then reconstructed using computer software for 3D reconstruction (Recon; PINGSENG, Shanghai, China).

RESULTS AND DISCUSSION

Fabrication and Characterization of $mPEG_{45}$-PLV_{19}

$mPEG_{45}$–PLV_{19} obtained by L-Val NCA ROP initiated by $mPEG_{45}$-NH_2 as a macromolecular initiator (**Figure S1**). **Figure 1A** showed the typical ^1H NMR spectrum of the block copolymer $mPEG_{45}$–PLV_{19}. In the ^1H NMR spectrum, the peaks at 0.91, 2.04, 3.75–3.89, and 4.36 ppm stood for valine methyl, mPEG terminal methoxy, mPEG backbone, and polymer methine, respectively. It can be seen that $mPEG_{45}$–PLV_{19} was successfully synthesized. The degree of polymerization of PLV was calculated by comparing the integral of the methyl peak of the side chain (-CH_3) with the methylene peak of polyethylene glycol (-CH_2CH_2O-).

The secondary structure of the copolymer was analyzed by FT-IR. From **Figure 1B**, there were characteristic peaks of the amide bonds at 1,548 cm^{-1} and 1,636 cm^{-1}, which also showed that copolymers had undergone the main β-sheet conformation.

Circular dichroism is the most widely used instrument for analyzing the secondary structure of proteins. It is a simple, fast, and highly accurate method for studying the conformation of proteins in dilute solutions. As shown in **Figure 1C**, the 0.5 mg/ml polymer solution has a positive absorption characteristic peak at 195 nm and a wavelength range of 180–260 nm. Negative absorption characteristic peak at 226 nm, which is absorption peak specific to the β-sheet conformation, indicating that the block copolymer $mPEG_{45}$–PLV_{19} has undergone the β-sheet conformation

Phase Diagram, Dynamics, and Morphology Analysis

The phase diagram is derived from the test tube inversion method. The block polymer was dissolved in PBS and a sol-gel transition occurred with increasing temperature. After the test tube is inverted for 30 seconds, the sample does not flow, the temperature is considered to be the phase transition temperature. **Figure 1D** showed the phase diagram of the block copolymer. The gradient concentration of $mPEG_{45}$–PLV_{19} undergoes a sol-gel phase transition under temperature stimulation, and a concentration of 5.0 wt.% is selected as the subsequent experimental gelation concentration. This concentration has fluidity under low temperature conditions, is easy to mix with drugs, is loaded with drugs, and can form a gel upon body temperature stimulation in the body environment, slowly degrades and releases drugs, and has a long-lasting effect on the affected area.

The changes of thermally induced storage modulus (G′) and loss modulus (G″) of $mPEG_{45}$–PLV_{19} were analyzed by rheological experiments. The G′ of $mPEG_{45}$-PLV_{19} increased significantly with temperature and exceeded G″ (**Figure 1E**). When the temperature is below the critical gel temperature (CGTs), G′ is less than G″, the hydrogel was in a liquid state. While the temperature continued to rise above the intersection, G′ exceeds G″, demonstrating the formation of a gel. At the same time, higher G′ also indicates that $mPEG_{45}$-PLV_{19} hydrogel has better mechanical strength The characterization of the drug-loaded gel was shown in **Figure S2**, and the results showed no significant change compared to the unloaded gel.

At the same time, the SEM image of $mPEG_{45}$–PLV_{19} hydrogel is shown in **Figure 1F**. We can observe that the $mPEG_{45}$–PLV_{19} hydrogel forms a 3D network structure with a large number of pores, which indicates that the hydrogel material can load drugs or antibodies are more suitable as carriers and have obvious advantages.

Degradation Test *In Vivo* and *In Vitro*

The biodegradability of hydrogels is an important factor for clinical application considerations. When the hydrogel is rapidly degraded, the effect of sustained release of the drug cannot be achieved. Conversely, when the hydrogel has poor degradation performance, it may cause side effects such as inflammation at the injection site. The degradation of $mPEG_{45}$-PLV_{19} hydrogel (concentration 5.0%) *in vitro* was analyzed in PBS with elastase K and PBS. As shown in **Figure 1G**, at day 20, the hydrogel mass loss in the elastase K group exceeded 40%, which was significantly higher than 20% in PBS. Degradation was significantly slower in the control group due to lack of enzyme catalysis. The results may indicate that in the absence of elastase

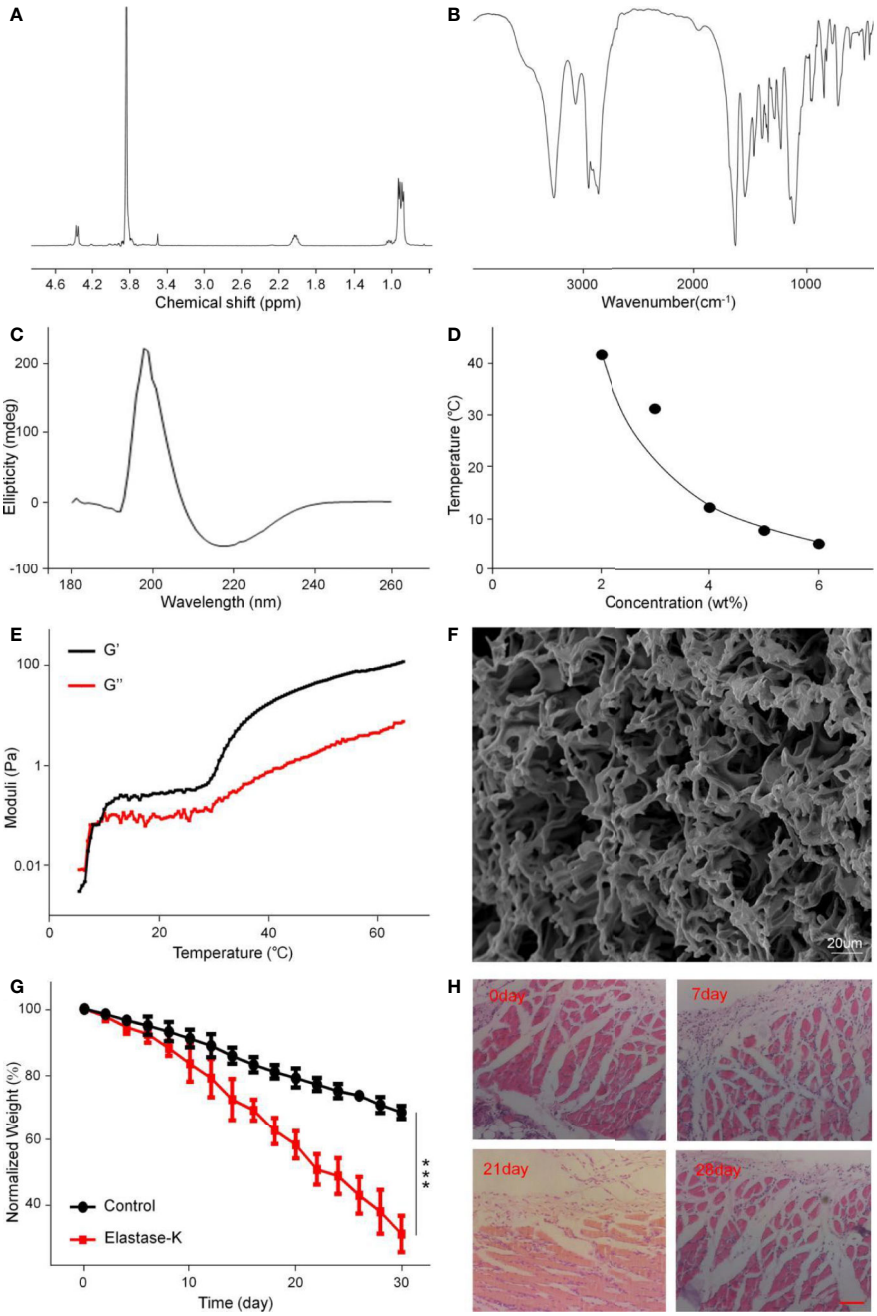

FIGURE 1 | The structural characterization, gelatinization properties, and degradation of $mPEG_{45}$–PLV_{19}. **(A)** ^1H NMR spectra of $mPEG_{45}$–PLV_{19}; **(B)** Fourier-transform infrared (FT-IR) spectra of $mPEG_{45}$–PLV_{19}; **(C)** circular chromatogram of $mPEG_{45}$–PLV_{19}; **(D)** Solution-gel phase diagrams of $mPEG_{45}$–PLV_{19}; **(E)** changes of G′ and G″ of $mPEG_{45}$–PLV_{19} in PBS solutions (5 wt. %); **(F)** scanning electron microscope (SEM) image of $mPEG_{45}$–PLV_{19} hydrogels formed at 40; **(G)** mass loss curves of *in vitro* degradation of hydrogels in PBS, and PBS with elastase-K (0.2 mg/ml) groups; **(H)** hematoxylin and eosin staining (H&E) images of the skin tissue near the hydrogels on day 0, 7, 21, and 28, respectively.

K, the mass loss of the gel is only because of the surface erosion of hydrogel. For elastase-K, hydrogel's polypeptide chain is also rapidly degraded, which accelerates gel loss. Therefore, it can be seen from the degradation rate curve that $mPEG_{45}$-PLV_{19} hydrogel has a more suitable degradation time and is suitable for *in vivo* application. It will not cause adverse reactions due to long stay at the injection site, nor will it cause rapid release of the drug due to too fast degradation.

As shown in **Figure 1H**, *in vivo* degradation experiments can be seen that $mPEG_{45}$-PLV_{19} hydrogel will produce a slight inflammatory response 7 d after implantation, which is mainly because the implantation of the material caused a xenobiotic

response of the body. As the hydrogel continued to degrade, the inflammation decreased on the 21st day, and on the 28th day, the tissue section staining was close to normal tissue. Therefore, H&E results show that this hydrogel material will produce a slight inflammatory response in the early stage of implantation, but with the increase of degradation time, the inflammation will gradually disappear without causing serious tissue lesions, indicating that this hydrogel material has good biocompatibility.

Drug Release *In Vitro* and Local Retention of Hydrogels

The *in vitro* release profile of the drug in PBS solution is shown in **Figures 2A, B**. Free Mtx and free Aln showed rapid release behavior, and the release amount reached more than 90% in a short time. However, the sustained release of the drug from the Gel+Mtx+Aln group was significantly different from the cumulative release of the free drug. Therefore, Gel+Mtx+Aln exhibited slowly release of Mtx and Aln, so as to achieve the purpose of sustained and effective drug release at the tumor site.

In **Figure 2C**, the solution rapidly turns into a gel under the influence of body temperature. A small amount of hydrogel was degraded within the first week. The volume of the hydrogel was reduced to below 50% by the second week. After 4 weeks, the hydrogel was not retained locally. This hydrogel retention effect enables sustained local release of the drug.

Evaluation of Anti-Tumor Effects *In Vivo*

Mtx is one of the first-line chemotherapy drugs for OS, which inhibits the synthesis of tumor cells mainly by inhibiting dihydrofolate reductase (Yu et al., 2019; Zhang et al., 2020). Aln is the most important anti-bone resorber for the treatment of bone diseases (Vasikaran, 2001; Rogers et al., 2015). Aln has a high affinity with bone minerals to prevent bone destruction by inhibiting osteoclast activity (Guven et al., 2020). We next evaluated the therapeutic potential of Gel+Mtx+Aln *in vivo*. Treatment was initiated when the tumor in the right leg of the mouse reached 200 mm^3. In the *in situ* OS mouse model, tumor volume in the PBS group increased significantly over time. As shown in **Figure 3A**, It is worth noting that inhibition of tumor growth was most pronounced by treatment with Gel+Mtx+Aln, however tumor growth was slightly inhibited in other group. As shown in **Figure 3B**, tumor inhibition rates also differed between groups. The inhibition rate of Mtx+Aln was only 21.2%, while the tumor inhibition rates of the gel loaded with Mtx or Aln were 33.0% and 34.8%, respectively. The tumor inhibition rate of Gel +Mtx+Aln group was 55.8%. The same results can be obtained in **Figures 3C, D**. At the end of the experiment, we isolated the right tibia of the mouse and weighed the tumor. The results showed: PBS (5.72 ± 0.24 g) > Mtx+Aln (4.77 ± 0.21 g) > Gel+Mtx (4.11 ± 0.13 g) > Gel+Aln (3.88 ± 0.30 g) > Gel+Mtx+Aln (2.11 ± 0.14 g) (**Figure 3E**), the trend was consistent with tumor volume.

The *in vivo* therapeutic effect of Gel+Mtx+Aln was further evaluated by staining with representative H&E staining of treated mouse K7M2 orthotopic OS tissue. Large and deformed cells with nuclear pyknosis and nuclear fragmentation in the staining results are tumor cells. As shown in **Figure 3F**, in Gel+Mtx+Aln, the tumor necrosis area was smaller than any other group, indicating its enhanced anti-tumor activity.

Evaluation of Anti-Bone Destruction Effect

Micro-CT is used to observe microstructures due to its unique high resolution. Skeleton is one of the most important

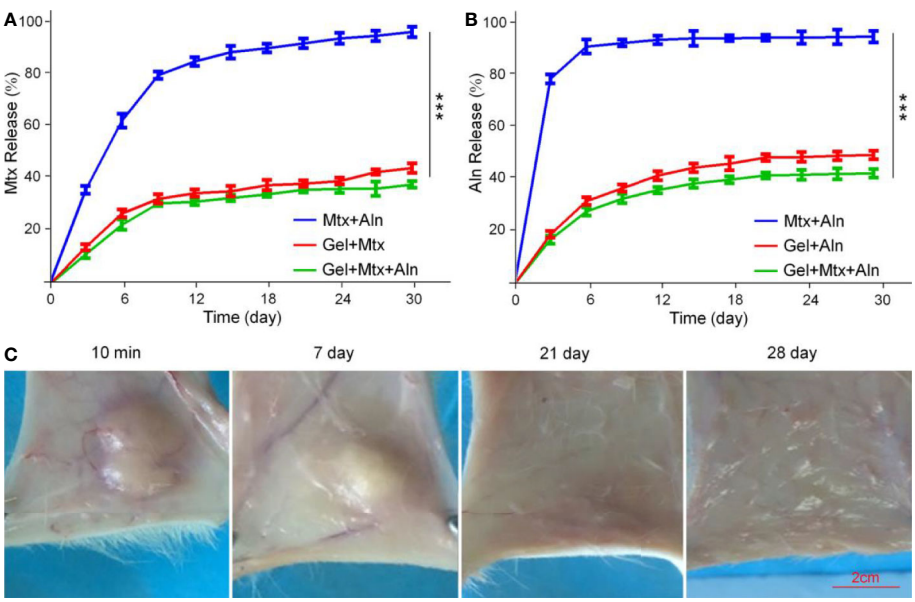

FIGURE 2 | The drugs release behavior *in vitro* and local retention of hydrogels. **(A)** *In vitro* release behavior of Mtx from Mtx+Aln, Gel+Mtx, and Gel+Mtx+Aln; **(B)** *in vitro* release behavior of Aln from Mtx+Aln, Gel+Mtx, and Gel+Mtx+Aln; **(C)** images of localized retention at 10 min, 7, 14, 21, and 28 d after injection of hydrogels. ***$P < 0.001$.

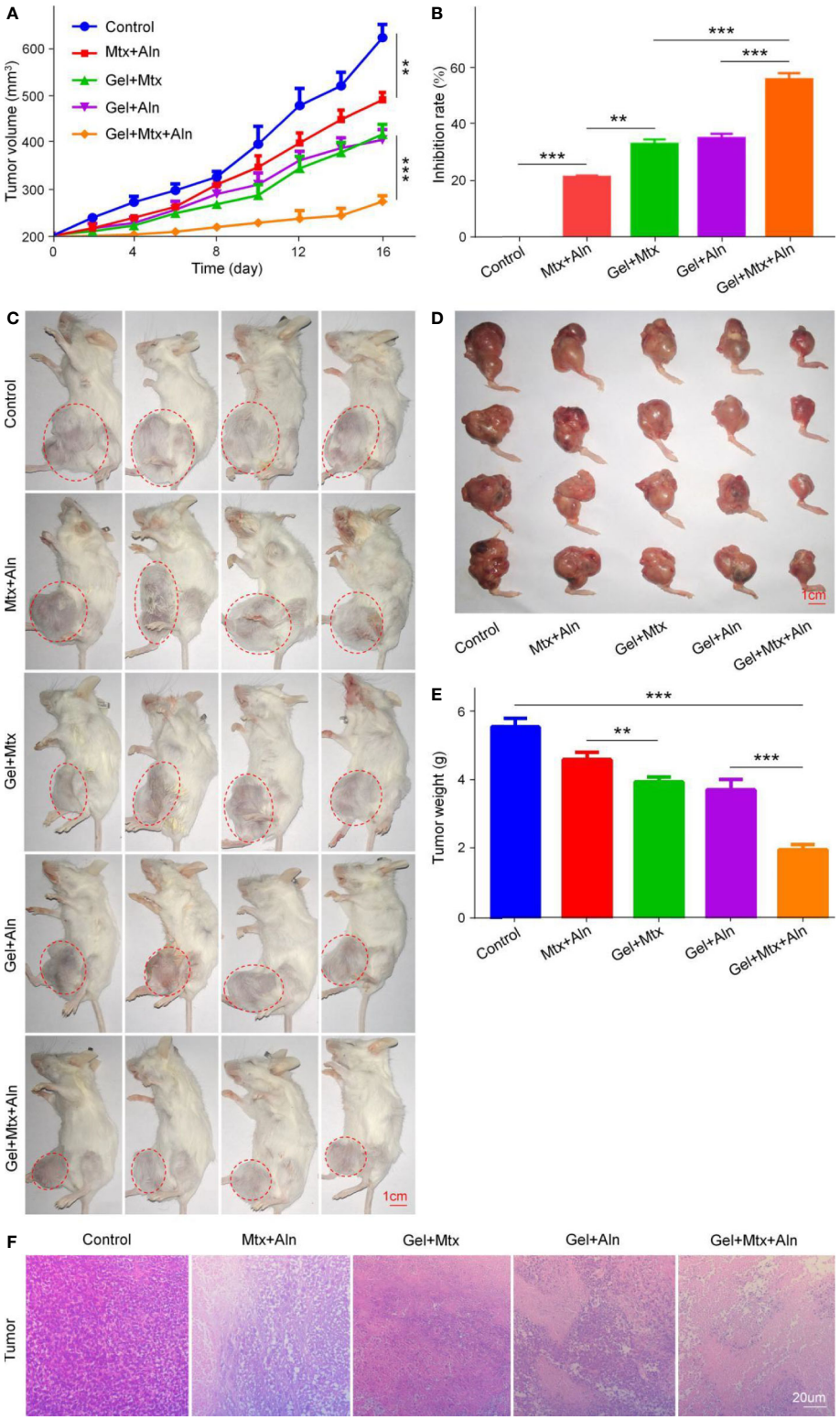

FIGURE 3 | *In vivo* antitumor efficacy of Gel+Mtx+Aln against primary OS. **(A)** Tumor growth curves; **(B)** tumor suppression rate; **(C)** the image of tumor-bearing mice; **(D)** posterior limb tumors. **(E)** Average weight of tibial primary OS tumors. **(F)** Hematoxylin and eosin staining (H&E) of primary tumor. Scale bar = 20 μm (n=4; **P < 0.01, and ***P < 0.001).

applications of micro-CT. To further confirm that Gel+Mtx+Aln has significant tumor suppressive efficacy, the extent of local OS bone destruction is assessed by micro-CT. As shown in **Figure 4A**, in the Gel+Mtx+Aln treatment group, there was no significant bone destruction in the tibia of the mouse, and there was no significant difference compared with the normal mouse tibia. In the PBS group, the surface of the tibia was extremely rough and even defective, and the bone destruction was very serious. Different degrees of bone destruction caused by OS were also clearly seen in the tibia. Micro-CT provides strong support for the remarkable anti-tumor efficacy of Gel+Mtx+Aln. Bone destruction sites in the 3D reconstructed image were set as regions of interest (ROIs), and CTAn software was used to analyze the bone volume/tissue volume (BV/TV) and the number of trabecular bone (Tb. N). The results showed that BV/TV and Tb. N were the highest in the Gel+Mtx+Aln group, indicating that the Gel+Mtx+Aln has a significant anti-bone destruction effect (**Figures 4B, C**).

Reduced Lung Metastasis of OS

The prognosis of OS has been poor for nearly 30 years. The survival rate at diagnosis without lung metastases and lung metastases varies widely, mainly because of less treatment for OS lung metastasis (Kansara et al., 2014; Friebele et al., 2015). Therefore, effective inhibition of lung metastasis is critical. At the end of the experiment, the lungs of the mice in the different treatment groups were taken out, and after 4 h of fixation with 4% paraformaldehyde, they were evaluated by apparent morphology and H&E staining of the lung sections. As shown in **Figure 5A**, compared with the other groups, the lung metastasis was the smallest in Gel+Mtx+Aln. The lungs were weighed and found in the Gel+Mtx+Aln < Gel+Aln < Gel+Mtx < Gel < PBS group (**Figure 5B**). This is closely related to the number of metastases in the lungs. At the same time, the number of metastases was the highest in the PBS group, but significantly inhibited in the Gel+Mtx+Aln group (**Figure 5C**). This fully demonstrates the efficacy of Gel+Mtx+Aln in inhibiting lung metastasis of OS.

In Vivo Safety Assessment

Studies show that many chemotherapeutic drugs have toxic side effects while treating disease, so their biological safety needs more attention. Here, the safety of the drug is evaluated by monitoring body weight and histopathological analysis of major organs. Weight loss is a comprehensive response to the systemic toxicity of chemotherapy agents. The weight loss of the Mtx

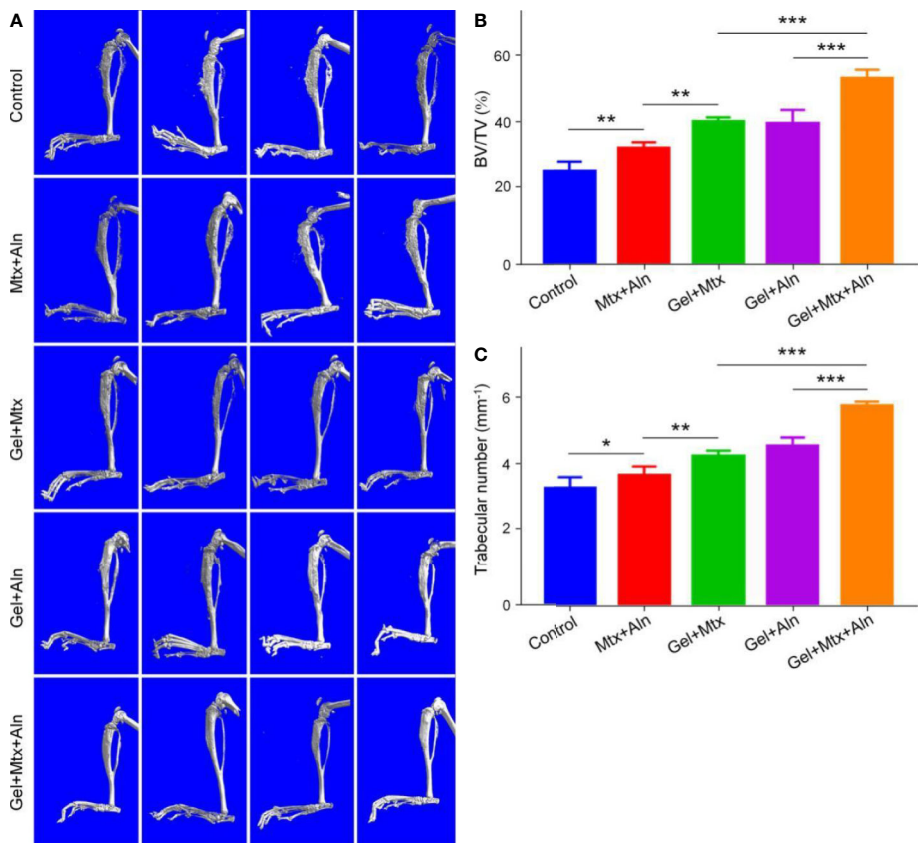

FIGURE 4 | The effect of anti-bone destruction. **(A)** 3D reconstruction of the tibia using micro-CT and **(B, C)** semi-quantitative analyses of bone destruction sites (n = 4; *P < 0.05, **P < 0.01, and ***P < 0.001).

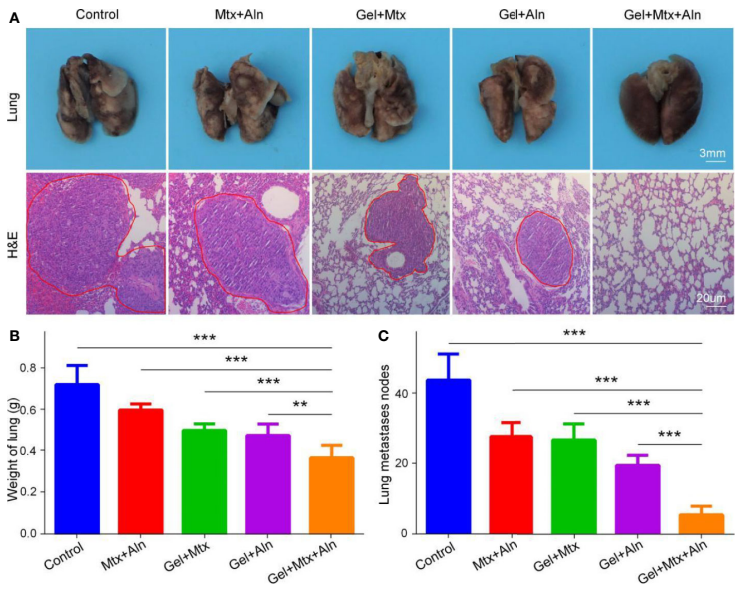

FIGURE 5 | The inhibition of pulmonary metastasis in OS. **(A)** Macroscopic appearance and hematoxylin and eosin staining (H&E) of lung metastatic; **(B)** Lung weight and **(C)** average counted lung metastases. (n = 4; 0.05, **P < 0.01, and ***P < 0.001).

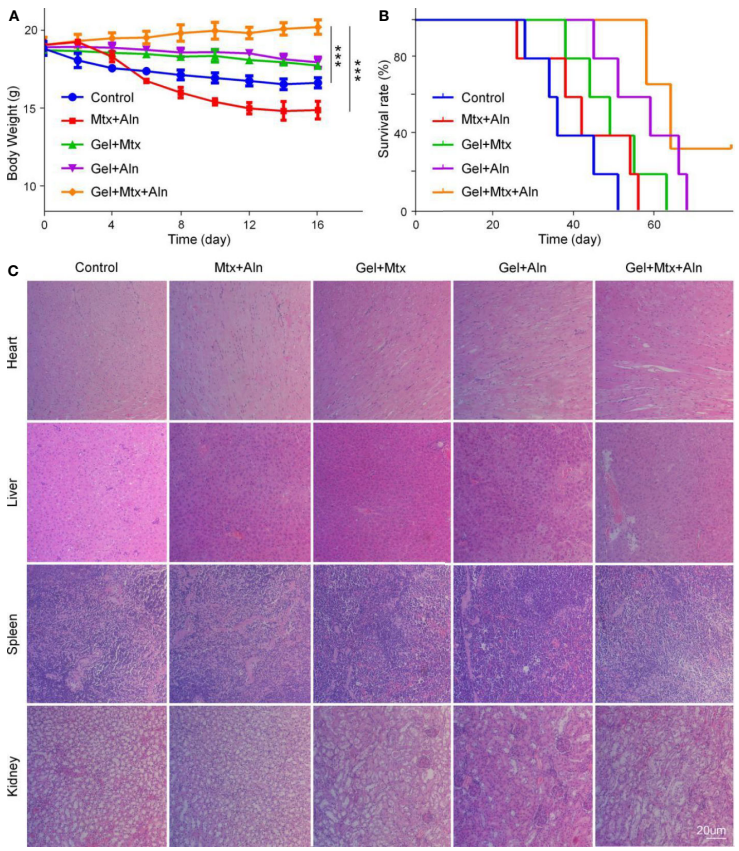

FIGURE 6 | *In vivo* safety. **(A)** Weight changes; **(B)** survival rates; **(C)** mouse organs stained with hematoxylin and eosin staining (H&E). (n = 4; **P < 0.01, and ***P < 0.001).

+Aln group is significant compared with other groups, which is related to the serious side effects of chemotherapy drugs (**Figure 6A**). However, treatment with Gel+Mtx+Aln did not affect mouse body weight, indicating that the hydrogel improved drug tolerance. Simultaneously monitoring the survival rates of different treatment groups, as shown in **Figure 6B**, the results show that Gel+Mtx+Aln has a significantly longer survival time due to its good antitumor efficacy and higher *in vivo* safety.

Histopathological results showed that Mtx+Aln treatment caused severe renal damage, showing degeneration and necrosis of renal tubular epithelial cells, nucleus pyknosis, and tubular lumen expansion. These signs of toxicity were significantly improved in the Gel+Mtx and Gel+Aln groups. In contrast, mice treated with Gel+Mtx+Aln showed no pathological changes or inflammatory cell infiltration in heart and spleen tissue sections. From **Figure 6C**, it was noted that no significant renal damage was found by Gel+Mtx+Aln, which may be because of the controlled release of the drug *in situ* in the hydrogel.

CONCLUSIONS

This study prepared a degradable, injectable compound delivery system for inhibiting the growth of OS. The drug delivery system consists of a temperature sensitive hydrogel and MTX, ALN. Specifically, the ROP of L-Val NCA elicited by $mPEG_{45}$-NH_2 produces a polypeptide hydrogel which is then thoroughly mixed by adding Mtx and Aln in the sol state. The obtained sol state is injected into the OS and becomes a gel state at body temperature. Synthetic temperature-sensitive hydrogels have stable mechanical properties, suitable degradation rates and good biocompatibility. Next we studied the advantages of Gel+Mtx +Aln as an OS treatment strategy. The results showed that the drug delivery system had a significant inhibitory effect on K7M2 OS. In summary, the $mPEG_{45}$-PLV_{19} hydrogel designed in this chapter can effectively carry MTX and ALN and may have potential application value in the treatment of OS. At the same time, there were some limitations in the application of $mPEG_{45}$–PLV_{19}. The preparation of $mPEG_{45}$-PLV_{19} hydrogel was complicated and needs further optimization. In addition, the specific injection site and dose of the hydrogel for clinical treatment remain to be explored.

DATA AVAILABILITY STATEMENT

All datasets generated for this study are included in the article/ **Supplementary Material**.

ETHICS STATEMENT

The animal study was reviewed and approved by the Animal Care and Use Committee at Jilin University.

AUTHOR CONTRIBUTIONS

KL, JY, and MP proposed and designed the experiments. HS, KL, and CC carried out the experiments with the help of QT and XW. HS and KL drafted the manuscript and interpreted the data. KL, DZ, JY, and MP revised the manuscript.

SUPPLEMENTARY MATERIAL

The Supplementary Material for this article can be found online at: https://www.frontiersin.org/articles/10.3389/fphar.2020.00573/full#supplementary-material.

REFERENCES

Chen, J., Ding, J., Wang, Y., Cheng, J., Ji, S., Zhuang, X., et al. (2017). Sequentially responsive shell-stacked nanoparticles for deep penetration into solid tumors. *Adv. Mater.* 29, 1701170. doi: 10.1002/adma.201701170

Ding, J., Chen, J., Gao, L., Jiang, Z., Zhang, Y., Li, M., et al. (2019a). Engineered nanomedicines with enhanced tumor penetration. *Nanotoday 29,* 100800. doi: 10.1016/j.nantod.2019.100800

Ding, J., Feng, X., Jiang, Z., Xu, W., Guo, H., Zhuang, X., et al. (2019b). Polymer-mediated penetration-independent cancer therapy. *Biomacromolecules* 20, 4258–4271. doi: 10.1021/acs.biomac.9b01263

Ding, J., Zhang, J., Li, J., Li, D., Xiao, C., Xiao, H., et al. (2019c). Electrospun polymer biomaterials. *Prog. Polym. Sci.* 90, 1–34. doi: 10.1016/j.progpolymsci.2019.01.002

Du, H., Liu, W., Zhang, M., Si, C., Zhang, X., and Li, B. (2019). Cellulose nanocrystals and cellulose nanofibrils based hydrogels for biomedical applications. *Carbohydr. Polym.* 209, 130–144. doi: 10.1016/j.carbpol.2019.01.020

Feng, X., Li, J., Zhang, X., Liu, T., Ding, J., and Chen, X.J.J.O.C.R. (2019a). Electrospun polymer micro/nanofibers as pharmaceutical repositories for healthcare. *J. Control. Release* 302, 19–41. doi: 10.1016/j.jconrel.2019.03.020

Feng, X., Xu, W., Li, Z., Song, W., Ding, J., and Chen, X. J. A. S. (2019b). Immunomodulatory nanosystems. *Adv. Sci.* 6, 1900101. doi: 10.1002/advs.201900101

Friebele, J. C., Peck, J., Pan, X., Abdel-Rasoul, M., and Mayerson, J. L. (2015). Osteosarcoma: A Meta-Analysis and Review of the Literature. *Am. J. Orthop. (Belle Mead N.J.)* 44, 547–553.

Gao, S., Tang, G., Hua, D., Xiong, R., Han, J., Jiang, S., et al. (2019). Stimuli-responsive bio-based polymeric systems and their applications. *J. Mater. Chem. B.* 7, 709–729. doi: 10.1039/C8TB02491J

Guven, M. N., Demirci, G., Altuncu, S., Gulyuz, U., Okay, O., Acar, H. Y., et al. (2020). Alendronate-functionalized poly(amido amine) cryogels of high-toughness for biomedical applications. *Polymer* 190, 122248. doi: 10.1016/j.polymer.2020.122248

Huang, H. Q., Qi, X. L., Chen, Y. H., and Wu, Z. H. (2019). Thermo-sensitive hydrogels for delivering biotherapeutic molecules: A review. *Saudi Pharm. J.* 27, 990–999. doi: 10.1016/j.jsps.2019.08.001

Isakoff, M. S., Bielack, S. S., Meltzer, P., and Gorlick, R. (2015). Osteosarcoma: Current Treatment and a Collaborative Pathway to Success. *J. Clin. Oncol.* 33, 3029–U3127. doi: 10.1200/JCO.2014.59.4895

Kansara, M., Teng, M. W., Smyth, M. J., and Thomas, D. M. (2014). Translational biology of osteosarcoma. *Nat. Rev. Cancer* 14, 722–735. doi: 10.1038/nrc3838

Kim, S. Y., and Helman, L. J. (2009). Strategies to Explore New Approaches in the Investigation and Treatment of Osteosarcoma. *Cancer Treat. Res.* 152, 517–528. doi: 10.1007/978-1-4419-0284-9_31

Kosei, A., Marie-FranOise, H., Verena, S., Kanji, M., Fran?Oise, R., and Dominique, H. J. C. (2013). Current therapeutic strategies and novel approaches in osteosarcoma. *Cancers* 5, 591–616. doi: 10.3390/cancers5020591

Li, S., Zhang, T., Xu, W., Ding, J., Yin, F., Xu, J., et al. (2018). Sarcoma-targeting peptide-decorated polypeptide nanogel intracellularly delivers shikonin for upregulated osteosarcoma necroptosis and diminished pulmonary metastasis. *Theranostics* 8, 1361. doi: 10.7150/thno.18299

Lovett, M. L., Wang, X., Yucel, T., York, L., Keirstead, M., Haggerty, L., et al. (2015). Silk hydrogels for sustained ocular delivery of anti-vascular endothelial growth factor (anti-VEGF) therapeutics. *Eur. J. Pharm. Biopharm.* 95, 271–278. doi: 10.1016/j.ejpb.2014.12.029

Ma, W., Sha, S. N., Chen, P. L., Yu, M., Chen, J. J., Huang, C. B., et al. (2020). A Cell Membrane-Targeting Self-Delivery Chimeric Peptide for Enhanced Photodynamic Therapy and In Situ Therapeutic Feedback. *Adv. Healthcare Mater.* 9, 1901100. doi: 10.1002/adhm.201901100

Marco, W., and Sch?Fer, B. W. (2010). Targets for cancer therapy in childhood sarcomas. *J. Cancer Treat Rev.* 36, 318–327. doi: 10.1016/j.ctrv.2010.02.007

Moorthi, C., Manavalan, R., and Kathiresan, K. (2011). Nanotherapeutics to Overcome Conventional Cancer Chemotherapy Limitations. *J. Pharm. Pharm. Sci.* 14, 67–77. doi: 10.18433/J30C7D

Mu, M., Li, X. L., Tong, A. P., and Guo, G. (2019). Multi-functional chitosan-based smart hydrogels mediated biomedical application. *Expert Opin. Drug Del.* 16, 239–250. doi: 10.1080/17425247.2019.1580691

Nedelcu, D., Andreescu, N., Boeriu, E., Stefanescu, R., Arghirescu, S., and Puiu, M. (2014). Retrospective study on osteosarcoma and ewing sarcoma - our experience. *Maedica* 9, 151–156.

Ottaviani, G., and Jaffe, N. (2009). ""The Epidemiology of Osteosarcoma,"," in *Pediatric and Adolescent Osteosarcoma*. Eds. N. Jaffe, O. S. Bruland and S. S. Bielack (Dordrecht: Springer), 3–13.

Rogers, M. J., Watts, D. J., and Russell, R.G.G.J.C. (2015). Overview of bisphosphonates. *Cancer* 80, 1652–1660. doi: 10.1002/(SICI)1097-0142(19971015)80:8+<1652::AID-CNCR15>3.0.CO;2-Z

Seeli, D. S., and Prabaharan, M. (2017). Guar gum oleate-graft-poly(methacrylic acid) hydrogel as a colon-specific controlled drug delivery carrier. *Carbohydr. Polym.* 158, 51–57. doi: 10.1016/j.carbpol.2016.11.092

Sun, Y., Ma, W., Yang, Y., He, M., Li, A., Bai, L., et al. (2019). Cancer nanotechnology: Enhancing tumor cell response to chemotherapy for hepatocellular carcinoma therapy. *Asian J. Pharm. Sci.* 14, 581–594. doi: 10.1016/j.ajps.2019.04.005

Ta, H. T., Dass, C. R., and Dunstan, D. E. (2008). Injectable chitosan hydrogels for localised cancer therapy. *J. Controlled Rel.* 126, 205–216. doi: 10.1016/j.jconrel.2007.11.018

Vasikaran, S.D.J.A.O.C.B. (2001). Bisphosphonates: an overview with special reference to alendronate. *Ann. Clin. Biochem.* 38, 608–623. doi: 10.1258/0004563011901037

Wang, J., Xu, W., Guo, H., Ding, J., Chen, J., Guan, J., et al. (2015). Selective intracellular drug delivery from pH-responsive polyion complex micelle for enhanced malignancy suppression in vivo. *Colloids Surf. B-Biointerf.* 135, 283–290. doi: 10.1016/j.colsurfb.2015.07.065

Wang, Q., Zhang, P., Li, Z., Feng, X., Lv, C., Zhang, H., et al. (2019). Evaluation of polymer nanoformulations in hepatoma therapy by established rodent models. *Theranostics* 9, 1426. doi: 10.7150/thno.31683

Wu, P. K., Chen, W. M., Chen, C. F., Lee, O. K., Haung, C. K., and Chen, T. H. (2009). Primary Osteogenic Sarcoma with Pulmonary Metastasis: Clinical Results and Prognostic Factors in 91 Patients. *Jpn. J. Clin. Oncol.* 39, 514–522. doi: 10.1093/jjco/hyp057

Wu, X., He, C., Wu, Y., and Chen, X. (2016). Synergistic therapeutic effects of Schiffs base cross-linked injectable hydrogels for local co-delivery of metformin and 5-fluorouracil in a mouse colon carcinoma model. *Biomaterials* 75, 148–162. doi: 10.1016/j.biomaterials.2015.10.016

Xiong, L., Luo, Q., Wang, Y., Li, X., Shen, Z., and Zhu, W. (2015). An injectable drug-loaded hydrogel based on a supramolecular polymeric prodrug. *Chem. Commun.* 51, 14644–14647. doi: 10.1039/C5CC06025G

Xu, J., Wang, H., Hu, Y., Zhang, Y. S., Wen, L., Yin, F., et al. (2019). Inhibition of CaMKIIα activity enhances antitumor effect of fullerene C60 nanocrystals by suppression of autophagic degradation. *Adv. Sci.* 6, 1801233. doi: 10.1002/advs.201801233

Yu, D. P., Zhang, S. S., Feng, A. L., Xu, D. G., Zhu, Q. S., Mao, Y. T., et al. (2019). Methotrexate, doxorubicin, and cisplatinum regimen is still the preferred option for osteosarcoma chemotherapy A meta-analysis and clinical observation. *Medicine* 98, e15582. doi: 10.1097/MD.0000000000015582

Zarrintaj, P., Jouyandeh, M., Ganjali, M. R., Hadavand, B. S., Mozafari, M., Sheiko, S. S., et al. (2019). Thermo-sensitive polymers in medicine: A review. *Eur. Polym. J.* 117, 402–423. doi: 10.1016/j.eurpolymj.2019.05.024

Zhang, W., Ning, C., Xu, W., Hu, H., Li, M., Zhao, G., et al. (2018). Precision-guided long-acting analgesia by Gel-immobilized bupivacaine-loaded microsphere. *Theranostics* 8, 3331. doi: 10.7150/thno.25276

Zhang, Y., Cai, L., Li, D., Lao, Y.-H., Liu, D., Li, M., et al. (2018a). Tumor microenvironment-responsive hyaluronate-calcium carbonate hybrid nanoparticle enables effective chemotherapy for primary and advanced osteosarcomas. *Nano Res.* 11, 4806–4822. doi: 10.1007/s12274-018-2066-0

Zhang, Y., Wang, F., Li, M., Yu, Z., Qi, R., Ding, J., et al. (2018b). Self-Stabilized Hyaluronate Nanogel for Intracellular Codelivery of Doxorubicin and Cisplatin to Osteosarcoma. *Adv. Sci.* 5, 1700821. doi: 10.1002/advs.201700821

Zhang, B., Zhang, Y., Li, R. Z., Li, J. Z., Lu, X. C., and Zhang, Y. (2020). The efficacy and safety comparison of first-line chemotherapeutic agents (high-dose methotrexate, doxorubicin, cisplatin, and ifosfamide) for osteosarcoma: a network meta-analysis. *J. Orthop. Surg. Res.* 15, 1–10. doi: 10.1186/s13018-020-1576-0

Conflict of Interest: The authors declare that the research was conducted in the absence of any commercial or financial relationships that could be construed as a potential conflict of interest.

frontiers in Pharmacology

REVIEW
published: 20 May 2020
doi: 10.3389/fphar.2020.00697

Cell-Penetrating Peptides in Diagnosis and Treatment of Human Diseases: From Preclinical Research to Clinical Application

*Jing Xie[1], Ye Bi[2], Huan Zhang[3], Shiyan Dong[3], Lesheng Teng[3], Robert J. Lee[4] and Zhaogang Yang[5]**

[1] School of Pharmacy and Bioengineering, Chongqing University of Technology, Chongqing, China, [2] Practice Training Center, Changchun University of Chinese Medicine, Changchun, China, [3] School of Life Sciences, Jilin University, Changchun, China, [4] Division of Pharmaceutics and Pharmacology, The Ohio State University, Columbus, OH, United States, [5] Department of Radiation Oncology, University of Texas Southwestern Medical Center, Dallas, TX, United States

OPEN ACCESS

Edited by:
Wei Tao,
Harvard Medical School,
United States

Reviewed by:
Phei Er Saw,
Sun Yat-Sen Memorial Hospital,
China
Chuang Liu,
Ningbo Institute of Materials
Technology & Engineering (CAS),
China
Wenliang Li,
Jilin Medical University, China

***Correspondence:**
Zhaogang Yang
Zhaogang.Yang@
UTSouthwestern.edu

Specialty section:
This article was submitted to
Experimental Pharmacology
and Drug Discovery,
a section of the journal
Frontiers in Pharmacology

Received: 11 March 2020
Accepted: 28 April 2020
Published: 20 May 2020

Citation:
Xie J, Bi Y, Zhang H, Dong S, Teng L,
Lee RJ and Yang Z (2020)
Cell-Penetrating Peptides in Diagnosis
and Treatment of Human Diseases:
From Preclinical Research
to Clinical Application.
Front. Pharmacol. 11:697.
doi: 10.3389/fphar.2020.00697

Cell-penetrating peptides (CPPs) are short peptides (fewer than 30 amino acids) that have been predominantly used in basic and preclinical research during the last 30 years. Since they are not only capable of translocating themselves into cells but also facilitate drug or CPP/cargo complexes to translocate across the plasma membrane, they have potential applications in the disease diagnosis and therapy, including cancer, inflammation, central nervous system disorders, otologic and ocular disorders, and diabetes. However, no CPPs or CPP/cargo complexes have been approved by the US Food and Drug Administration (FDA). Many issues should be addressed before translating CPPs into clinics. In this review, we summarize recent developments and innovations in preclinical studies and clinical trials based on using CPP for improved delivery, which have revealed that CPPs or CPP-based delivery systems present outstanding diagnostic therapeutic delivery potential.

Keywords: cell-penetrating peptides, cellular uptake, diagnosis, translocate, targeting

INTRODUCTION

Successful systemic administration of a drug usually includes a series of steps such as a long circulation, penetration of a biological barrier, uptake in recipient cells, and endosomal escape to the cytosolic space after endocytosis, each of which has its own set of constraints. In fact, a broad range of bioactive molecules have difficulty accessing the target, and penetrate the cell membrane to achieve the therapeutic effect. Because plasma membranes work as effective biochemical barriers, they play a critical role in preventing exogenous invasion (Groves, 2019). For example, peptides and oligonucleotides have been extensively evaluated in various therapeutic studies, which tend to have relatively low transmembrane efficiency, and therefore, achieving desired drug concentrations at the therapeutic site is challenging. Current strategies for delivery of macromolecules, such as nanoparticles, liposomes, viral-based vectors, microinjection, and electroporation (Kang et al.,

2016; Shi et al., 2018; Hao et al., 2019; Yang et al., 2019b; Yang et al., 2019c), may result in high toxicity, poor specificity, immunogenicity, as well as low delivery efficiency and efficacy (Swain et al., 2016). Accordingly, an approach for the delivery of macromolecules into target cells with high efficiency and efficacy is urgently needed.

Generally, it is believed that hydrophilic macromolecules can only be internalized by the classical endocytosis pathway. However, several peptides with membrane penetrating function could transport hydrophilic macromolecules to eukaryotic cells through energy-independent pathways (Lindgren et al., 2000; Gupta et al., 2005). They are termed as cell-penetrating peptides (CPPs), also known as protein transduction domains (PTDs), which are short peptides (no more than 30 residues) that have been predominantly evaluated in basic and preclinical research for the disease diagnosis and therapy including cancer, inflammation, central nervous system disorders, otoprotective, ocular disorders, and diabetes. They are not only able to translocate small macromolecular drugs, nucleic acids (Tobin et al., 1991), proteins, viruses, imaging agents across plasma membranes but also allow CPP/cargo complexes to transport across the cell membrane, by different endocytosis pathways depending on the types of CPPs (Tripathi et al., 2018). Different from other delivery strategies mentioned above, CPPs can enter the cells in a noninvasive way, as they usually do not disturb the structure of the plasma membranes and are considered safe and highly efficient. CPPs was first introduced by two research groups in 1988 (Frankel and Pabo, 1988; Green and Loewenstein, 1988). Both Frankel et al. and Green et al. observed that the HIV-trans-activator of transcription (TAT) protein could enter tissue-cultured cells, target into cell nucleus, and finally result in target gene expression. In 1991, Joliot et al. revealed that the homeodomain of Antennapedia (pAntp), a synthetic peptide with 60 amino acids long, was internalized by nerve cells (Joliot et al., 1991). Subsequently, Derossi et al. found a short peptide with 16 amino acids from the third helix of the antennapedia homeodomain (RQIKIYFQNRRMKWKK), named penetratin, was able to penetrate the plasma membrane (Derossi et al., 1994). From then on, various CPPs have been characterized from natural sources and synthetic sources (Tru Van et al., 2018).

CPPs have been successfully applied in the delivery of different types of drugs, nanoparticles, and liposomes for disease diagnosis and treatment. Although the number of CPP-based clinical trials has been greatly increased, in fact, no CPPs or CPP/cargo complexes have been approved by the US Food and Drug Administration (FDA). In this review, we will systematically summarize the latest application strategies of CPPs in various diseases diagnosis and treatment over the last 5 years and emphasize the preclinical research and clinical application of CPPs. We present a classification of CPPs and explain cellular uptake mechanisms of these peptides. We will discuss the deficiency and limitation of CPPs in clinical applications. Answering these questions will allow us to develop a more effective drug delivery system. Finally, we will discuss various new strategies for the application of CPPs in different disease diagnosis and therapy.

CLASSIFICATION OF CPPS

Currently, CPPsite 2.0 (http://crdd.osdd.net/raghava/cppsite/) database contains about 1850 kinds of CPP sequences, and the number is expected to continue to increase (Agrawal et al., 2016). CPPs are highly diverse in physicochemical and biological properties, different types of CPPs have different length, charge, solubility, and hydrophobicity (Kauffman et al., 2015). At present, CPP is often classified according to different characteristics, as shown in **Figure 1** and **Table 1**, including their origin, conformation, and physical and chemical properties.

Classification Based on Origin

Based on their origins, CPPs can be divided into protein-derived CPPs, synthetic CPPs, and chimeric CPPs. (1). Protein-derived CPPs, including the TAT protein (Vives et al., 1997) and penetratin (Derossi et al., 1994), can enter the cell because they have a specific motifs or helical structures (Traub, 2009). (2). Synthetic CPPs. In this group, polyarginine 8-10-mers are most widely studied because of their high efficiency in cellular uptake (Mitchell et al., 2000). (3). Chimeric CPPs. This group of CPPs is generally recognized as a transition from natural to synthetic CPPs since they contain sequences from two or more different naturally occurring proteins. Examples include amphipathic peptide (CADY) (20 amino acids) which combines aromatic residue (Tryptophan, W) and cationic residue (Arginine, R) (Crombez et al., 2009).

Classification Based on Conformation

Depending on their conformation, CPPs are divided into linear CPPs and cyclic CPPs. Many current studies have confirmed that cyclic CPPs offer advantages compared to their linear counterparts. Compared with linear CPPs, cyclic CPPs have higher cell permeability and higher affinity with the target receptor on the cell, so the transmembrane ability is further increased through receptor-mediated uptake (Dougherty et al., 2019). In addition, linear CPPs are usually sensitive to proteolytic hydrolysis, which results in poor pharmacokinetic properties *in vivo* (Bechara and Sagan, 2013), while cyclic CPPs generally have a higher resistance to proteolysis (Qian et al., 2016). At the same time, some cyclic CPPs can be taken up without endosome degradation and have the characteristics of targeting the nucleus (Mandal et al., 2011).

Classification Based on Physical–Chemical Character

Based on differences in physicochemical characters, CPPs can be classified into three subgroups: cationic CPPs, amphipathic CPPs, and hydrophobic CPPs. Under normal physiological pH conditions, the positive charge of cationic CPPs shows excellent affinity with the cytoplasmic membrane. The cationic CPPs combine with the cell membrane glycoprotein which is negatively charged through electrostatic interaction and then internalizes into the cell through a mechanism independent of the receptor. The key factors affecting the activity of cationic CPPs are the number and position of positively charged

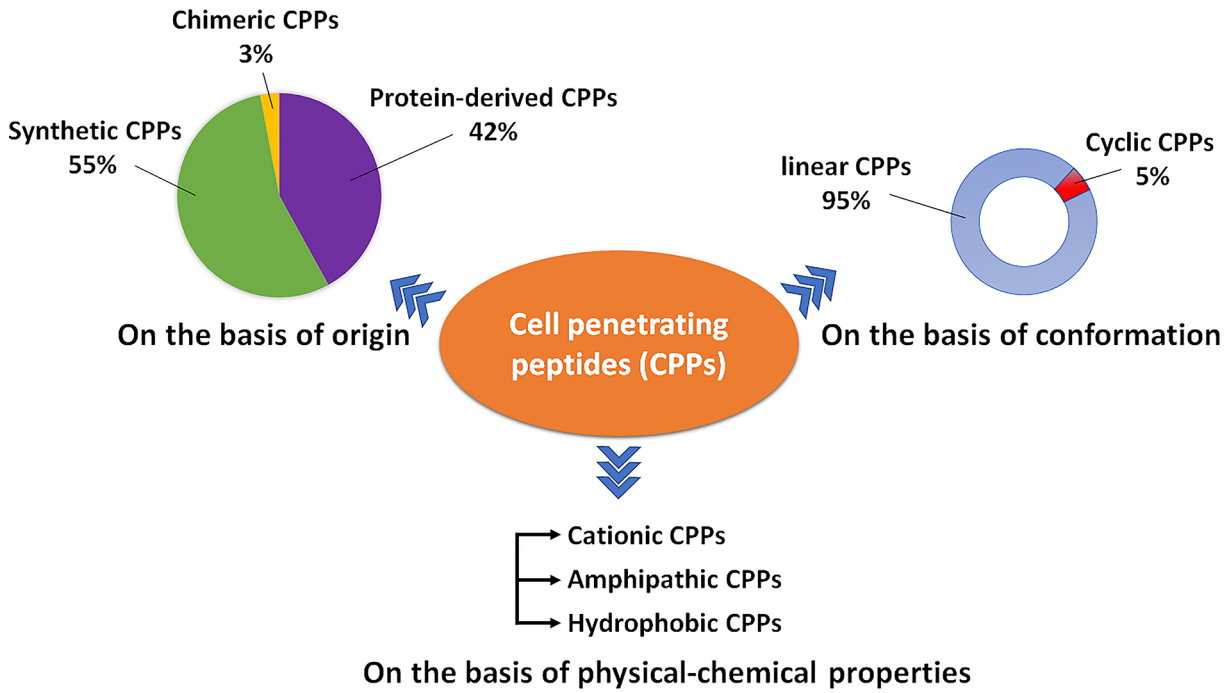

FIGURE 1 | A schematic diagram illustrating the types of CPPs.

arginines in the CPP structure (Xu et al., 2019). Most cationic CPPs usually contain more than five positively charged amino acids (Borrelli et al., 2018). The poly-arginine stretches have the highest cell uptake capacity and have therapeutic potential. The results of the study show that the internalization capacity of oligoarginine increases with its length (Chu et al., 2015), but for delivery purposes, the optimal length is R8 to R10. Higher values will have irreversible side effects on the cells and reduce overall delivery efficiency (Verdurmen and Brock, 2011). Nuclear localization signal (NLS) is a small peptide rich in arginine, lysine or proline commonly found in CPP. NLS can be transported into the cell nucleus through the classical nuclear introduction pathway (Tammam et al., 2017). Due to the limited positive charge and the limited membrane penetration ability of

TABLE 1 | Classification of the types of CPPs.

Peptide	Sequence	Length	Origin	References
Cationic CPPs				
TAT	RKKRRQRRR	9	Protein derived	(Baoum et al., 2012)
R8	RRRRRRRR	8	Synthetic	(Chu et al., 2015)
DPV3	RKKRRRESRKKRRRES	16	Protein derived	(De coupade et al., 2005)
DPV6	GRPRESGKKRKRKRLKP	17	Protein derived	(De coupade et al., 2005)
Penetratin	RQIKIWFQNRRMKWKK	16	Protein derived	(Nielsen et al., 2014)
R9-TAT	GRRRRRRRRRPPQ	13	Protein derived	(Futaki et al., 2001)
Amphipathic CPPs				
pVEC	LLIILRRRIRKQAHAHSK	18	Protein derived	(Eggimann et al., 2014)
ARF (19-31)	RVRVFVVHIPRLT	13	Protein derived	(Johansson et al., 2008)
MPG	GALFLGFLGAAGSTMGAWSQPKKKRKV	27	Chimeric	(Simeoni, 2003)
MAP	KLALKLALKALKAALKLA	18	Synthetic	(Wada et al., 2013)
Transportan	GWTLNSAGYLLGKINLKALAALAKKIL	27	Protein derived	(Pae et al., 2014)
Hydrophobic CPPs				
Bip4	VSALK	5	Protein derived	(Gomez et al., 2010)
C105Y	CSIPPEVKFNPFVYLI	16	Protein derived	(Rhee and Davis, 2006)
Melittin	GIGAVLKVLTTGLPALISWIKRKRQQ	26	Protein derived	(Hou et al., 2013)
gH625	HGLASTLTRWAHYNALIRAF	20	Protein derived	(Galdiero et al., 2015)

NLS, it is often combined with hydrophobic or amphoteric amino acid sequences to produce effective and versatile amphiphilic vectors including MPG (Lee et al., 2014) and Pep-1 (Yang et al., 2005).

Among the CPPs currently found, amphipathic CPPs are the most common, accounting for more than 40%. Amphiphilic CPPs contain polar and non-polar amino acid regions, and the non-polar regions are rich in hydrophobic amino acids (for example, alanine, valine, leucine, and isoleucine). Some amphiphilic CPPs are derived entirely from natural proteins such as pVEC, ARF (19–31). ARF (19–31) is from the N-terminal domain of the tumor suppressor gene p14ARF protein (19–31) (Johansson et al., 2008). Chimeric peptides obtained by partially covalently bonding hydrophobic fragments and NLS *via* amphiphilic CPPs, such as Pep1 (KETWWETWWTEWSQPKKRKV), MPG (GLAFLGFLGAA GSTMGAWSQPKKKRKV) are both based on the SV40 NLS (PKKRKV) (Milletti, 2012). Previous studies have shown that the same amphiphilic CPP may have different secondary structures, and their binding ability to the hydrophobic/hydrophilic interface may change under different conditions (Eiriksdottir et al., 2010). Amphiphilic CPPs, such as MAP, can interact strongly with negatively charged phospholipids, and MAP with an alpha-helical structure will spontaneously insert into the lipid monolayer. In addition, structural analysis of peptide/lipid interactions showed that MPGs with β-sheet structures are more sensitive to charge than α-helical structures (Borrelli et al., 2018).

There are relatively few numbers of hydrophobic CPPs, and their structure contains a large number of non-polar residues or only a few charged amino acids (less than 20% of the sequence). Natural hydrophobic CPPs found so far include C105Y (Rhee and Davis, 2006), Bip4 (Gomez et al., 2010), and K-FGF (Carnevale et al., 2018). Different from what is known for most amphiphilic cationic CPPs, the peptide sequence of hydrophobic CPPs does not significantly affect cell uptake (Gomez et al., 2010).

CELLULAR UPTAKE MECHANISMS OF CPPS

As we all know, it has been proven that CPPs can transport various cargoes into cells (Kristensen et al., 2016; Tashima, 2017; Derakhshankhah and Jafari, 2018). However, considerable controversies regarding the mechanism of cellular uptake still exist, which is mainly due to the properties of CPPs or transported cargoes (for instance, concentration, structure, etc.), cell types (membrane lipid composition, etc.), and the experimental conditions (such as pH and temperature) (Fretz et al., 2007; Kauffman et al., 2015; Akahoshi et al., 2016). It seems to be consensus on the internalization mechanisms of various CPPs or CPP/cargoes (Kauffman et al., 2015; Zhu and Jin, 2017; Borrelli et al., 2018; Pescina et al., 2018). The cellular uptake pathways of CPPs or CPP/cargoes have been generally divided into two types according to whether energy is required or not in the process of internalization (Chugh et al., 2010; Zhu and Jin, 2017): direct translocation and endocytosis (Tashima, 2017; Yang et al., 2019a), which will be described in this paper (**Figure 2**).

Direct Translocation

Direct translocation, also known as the non-endocytic uptake pathway, is energy-independent (Reissmann, 2014; Tashima, 2017; Derakhshankhah and Jafari, 2018). It occurs initially through electrostatic interaction or hydrogen bonding between phospholipid bilayer and CPPs or CPP/cargoes (Zhu and Jin, 2017; Pescina et al., 2018). The interaction is followed by CPPs or CPP/cargoes entrance *via* pore formation or membrane destabilization (Guidotti et al., 2017). According to the different transduced mechanisms, direct translocation is mainly divided into three models: "Barrel-Stave" model (Munjal et al., 2017), "Carpet-like" model (Guidotti et al., 2017) and Inverted-micelle model (Islam et al., 2018), which were presented in **Figure 2**.

In "Barrel-Stave" model based on pore formation, amphipathic CPPs or CPP/cargoes insert into the cell membrane, their hydrophobic regions combine with phospholipid in the cell membrane, while their hydrophilic regions combine with the hydrophilic head of the phospholipid, forming the "barrel-like" pore, and transmembrane movements are increased (Kauffman et al., 2015; Habault and Poyet, 2019). Thereafter, CPPs are delivered into the cytoplasm (Borrelli et al., 2018). Whereas, the inverted-micelle model is dependent on the invagination of a phospholipid bilayer and the formation of the inverted micelle (Guidotti et al., 2017). In this process, electrically charged CPPs or CPP/cargoes residues binds to phospholipids on the cell surface, the hydrophobic regions of CPPs or CPP/cargoes interact with the cell membrane, forming inverted micelles (Wang et al., 2014; Islam et al., 2018; Yang et al., 2019a). And then CPPs or CPP/cargoes are transported into the cell by inverted micelles. However, it is worth mentioning that the inverted-micelle model is suitable for CPPs or CPP/cargoes with hydrophobic amino acid residues (Thennarasu et al., 2010). In the "Carpet-like" model, CPPs or CPP/cargoes are transported into the cell by charge interaction between CPPs and cell membranes (Xu et al., 2019). CPPs or CPP/cargoes cover on the cell membranes surface in a carpet-like manner, their hydrophobic part interacts with the hydrophobic region of the cell membrane (Futaki et al., 2007). Once the concentration of CPPs or CPP/cargoes is high, their hydrophobic part will be flipped by the hydrophobic core of cell membrane, the cell membrane fluidity is increased (Murray et al., 2016). Finally, the cell membrane is disrupted and CPPs or CPP/cargoes are transported into the cell (Yang et al., 2019a). However, direct translocation is most suitable for CPPs or CPPs associated with small cargo enter into the cell, while large molecules weight CPPs or CPP/cargoes mainly depend on endocytosis.

Endocytosis

In addition to uptake by direct translocation, CPPs or CPP/cargoes can also be translocated into the cell *via* endocytosis. It has been shown that energy-dependence endocytosis is the

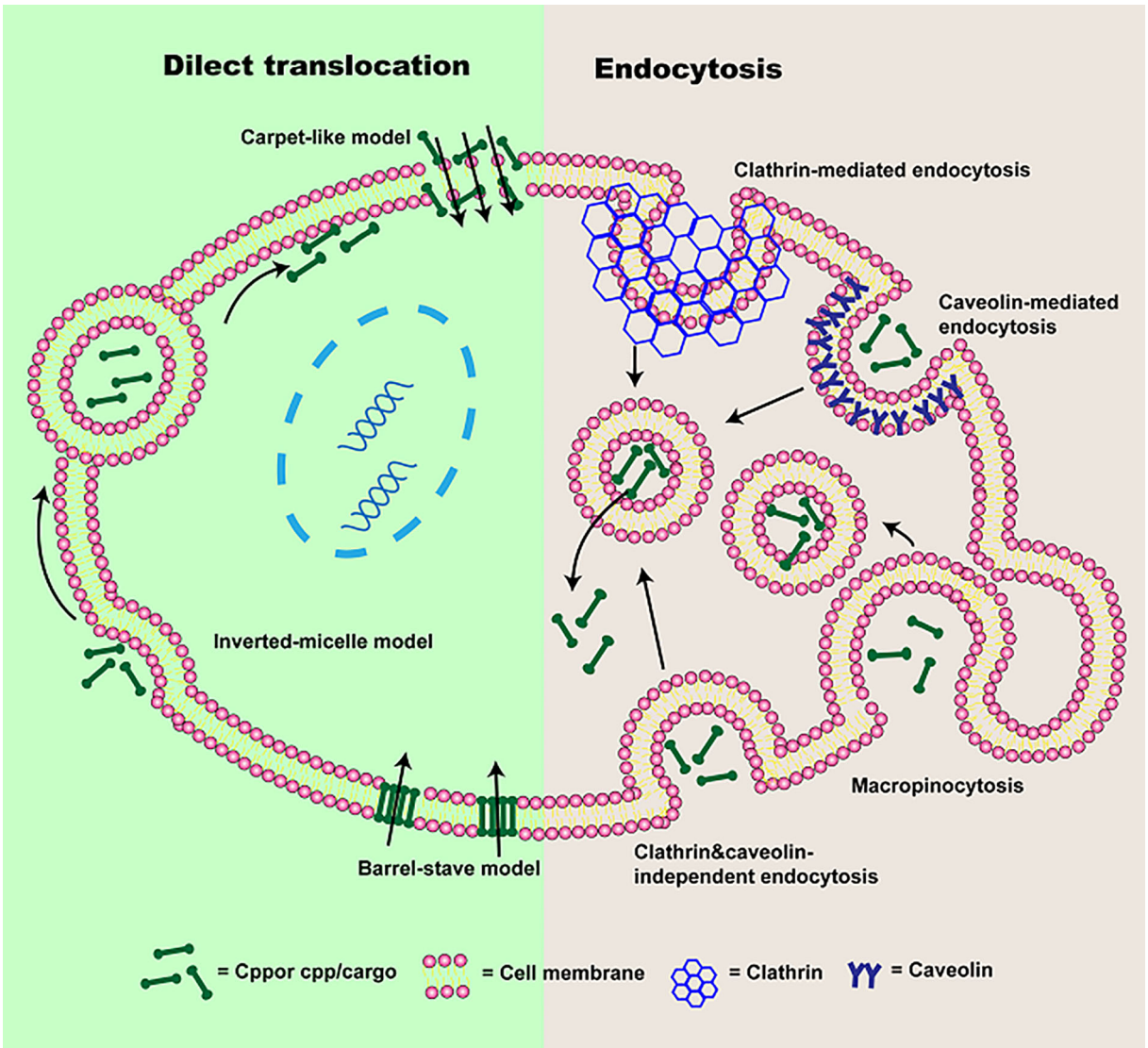

FIGURE 2 | The schematic of cellular uptake mechanisms of CPP or CPP/cargo. Two types of pathways were presented: direct translocation and endocytosis. Direct translocation is divided into three models: "Barrel-Stave" model, "Carpet-like" model, and the Inverted-micelle model. Endocytosis is composed of macropinocytosis, caveolin-mediated endocytosis, clathrin-mediated endocytosis, and clathrin- and caveolin-independent endocytosis.

prevailing cellular uptake mechanism for large molecules weight CPPs or CPP/cargoes (Borrelli et al., 2018; Yang et al., 2019a). So far, four different pathways including macropinocytosis (Wadia et al., 2004), caveolin-mediated endocytosis (Fittipaldi et al., 2003), clathrin-mediated endocytosis (Yang et al., 2016), and clathrin- and caveolin-independent endocytosis (Yang et al., 2019a) have been used to describe endocytosis, the schematic is also presented in **Figure 1**.

Macropinocytosis based on receptor-independent and lipid raft-dependent is preferred endocytic pathways for CPPs associated with large cargoes. Owing to the induction of growth factors and stimulation of actin, CPP/cargoes can be transferred into cells by mature vesicles (Xu et al., 2019). The Cellular uptake process through macropinocytosis as follow: firstly, CPP/cargoes interact with membrane proteoglycans to activate the rac protein in the cytoplasm. And F-actin organizations are triggered by signals from the rac protein. The actin microfilaments shrink, cell membrane deforms, protrusions, and endocytic vesicles are formed. At last, CPP/cargoes are endocytosed into cells (Pujals and Giralt, 2008). Clathrin-mediated endocytosis, also named as receptor-mediated endocytosis, is the process by which cells specifically uptake extracellular. CPP/cargoes firstly attach to receptors in the cell membrane, and curvature is produced after the interaction between epsin protein and cell membrane (Yang et al., 2019a). Subsequently, a pit is formed by recruiting clathrin

and hetero-tetrameric protein (AP-2) and developed into clathrin-coated vesicles containing CPP/cargoes (Richard et al., 2005). The endosome is following formed in the cytoplasm (Yang et al., 2019a). Whereas, caveolin-mediated endocytosis is similar to clathrin-mediated endocytosis, but it is related to caveolin (Aderem and Underhill, 1999). In this process, CPP/cargoes would specifically recognize receptors on the lipid rafts that is a hydrophobic region rich in cholesterol and sphingomyelin (Zhao et al., 2015). Cavin-1 connects to caveolin, a pit is generated and invaginated with the gradual increase of the number of cavin-1 and caveolin complex. The caveolin-coated vesicle is obtained, and the endosome is formed. Additionally, clathrin- and caveolin-independent is another endocytic pathway, mainly occurs in specialized cells such as macrophages (Mcclorey and Banerjee, 2018). CPP/cargoes can be recognized and tagged by opsonins. And CPP/cargoes are attached to the Fc receptor from cell membrane and actin is stimulated, the cell membrane coated CPP/cargoes are generated and subsequently, CPP/cargoes are translocated into the cytoplasm (Yang et al., 2019a). Although energy-dependence endocytosis is the main route for CPP/cargoes entrance cells, CPP/cargoes remain coated in endosomes and difficult to exert their biological activity. Therefore, in order to avoid degradation from lysosomes, CPP/cargoes must escape from endosomes. Some reports have shown that pH gradient formation, an increasing in vesicles concentration and the attraction of differently charged endosomes membrane with CPPs all cause membrane stiffening and rupture, contributing to CPP/cargoes escape from endosomes (Borrelli et al., 2018; Xu et al., 2019). However, it is still a challenge.

APPLICATION OF CPPS IN THE DIAGNOSIS AND TREATMENT OF VARIOUS DISEASES

CPPs were increasingly applied in drug delivery and disease diagnosis by precise control the transmembrane transport. Membrane translocation ability of CPPs was an important element in inflammation, central nervous system disorders, ocular disorders, and cancer treatment. Basic researches were performed to identify potential application value of CPPs combined drugs. CPPs application in preclinical studies has obtained great achievements, demonstrated the boundless potential of CPPs-based therapies. Some recent studies of CPPs to deliver cargos are underway in the clinic, detailed data were listed in **Table 2**. There was not much unambiguous evidence for CPPs modified system could work as expected. It is disappointing that no CPPs-based drugs have been approved by the FDA. In this section, we reviewed the recent development of CPP's research in the application of various diseases from the pros and cons.

Application of CPPs in Cancer Treatment

Up to now, researchers have developed more than 1800 kinds of CPPs to deliver cargos from basic research to clinics in therapeutics delivery, gene editing, and cell imaging (identified in the CPPsite 2.0 database). One trouble in cancer treatment was that tumor microenvironment or other barriers blocked drug delivery to tumor cells, especially in brain gliomas and pancreatic cancers. CPPs opened a new perspective to overcome a semipermeable hydrophobic barrier to realizing drugs' effective delivery in tissue and subcellular construction.

Most CPPs had positive side chains, interacted with a high-density anionic charge on cell membranes. Different length polyarginines were widely used in drug delivery. The cationic charge density of CPPs was an important parameter to influence the transfection efficiency of cargos. Favaro et al. designed four polyarginines fused green fluorescent protein (R3-GFP-H6, R6-GFP-H6, R7-GFP-H6, R9-GFP-H6) by *E. coli* bio-produced. Differently charged polyarginine tails impacted the folding status of the GFP variants, R7-GFP-H6, R9-GFP-H6 could self-assembly form nanoparticles in Tris Dextrose buffer. At the early stages of incubation with HeLa cells, cellular uptake of unimolecular R3-GFP-H6, R6-GFP-H6, R7-GFP-H6 through CXCR4 receptor were improved by arginine residues number in a linear way. When R7-GFP-H6 assembled nanoparticles, penetrability was higher than free R7-GFP-H6. Multivalent cationic arginine increased nanoparticle uptake, multimerization can further increase the internalization effect. Free Rn-GFP-H6 was majorly endocytic by the CXCR4-dependent pathway, oligomerization status switch to receptor-independent uptake mechanisms. The internalization ability of CPPs was also related to cargos status (Favaro et al., 2018). In addition, Kadonosono et al. found that NRP1 binding also could promote CPP/PTD extravasation (Kadonosono et al., 2015). CPPs were also used to mediate cellular uptake of extracellular vesicles except for protein and nanoparticles. Extracellular vesicles were modified by poly-arginine to improve internalization by inducing active micropinocytosis, effective cellular internalization was influenced by the number of arginine residues. Hexadeca-arginine (R16) peptide modified extracellular vesicles exhibited relatively effective anti-cancer activity (Nakase et al., 2017).

CPPs were usually used to transfer protein by covalent bonding. However, covalent CPPs technology was not the most effective strategy to transfer macromolecules as altered biological activity and or steric hindrance (Tai and Gao, 2017). Electrostatic adsorption strategy appeared to be a preponderant approach to deliver oligonucleotide. CPPs with positive charge could efficiently condensate oligonucleotide and promote cell internalization. Tian et al. used TAT to modify the tobacco mosaic virus (TMV) to design novel siRNA carriers with high gene transfection efficiency and safety, inspired by combining viral vectors with CPPs (**Figure 3**). siRNA uptake efficiency of 45% TAT modified TMV (TMV-TAT45) was threefold than TMV in HeLa at 5 h, which benefited from not only the α-helical secondary structure but also the positive charge of TAT. TAT modified TMV endowed siRNA endosomal escape property. Gene silencing efficiency of TAT- TMV was similar to PEI25k and Lipo 2000 but showed much higher safeness. siRNA@TMV-TAT45 silenced 65% fluorescent signal of GFP expression in

TABLE 2 | Examples of CPP-conjugated therapeutics under clinical development.

Compound	CPPs	Cargos	Organization	Therapeutic application	Status	Effect	ClinicalTrials.gov ID	Refs
AM-111	TAT	D-JNKI-1	Auris Medical, Inc.	Acute Inner Ear Hearing Loss	Phase 3	AM-111 exhibited effective otoprotection in idiopathic sudden sensorineural hearing loss after acute cochlear injury	NCT02561091 Completed 2017	(Staecker et al., 2019)
P28GST	P28	Glutathione-S-transferase	University Hospital, Lille	Crohn's disease patients	Phase 2	P28GST induced slight changes of overall fecal bacterial composition in Crohn's disease patients	NCT02281916 Completed 2018	(Capron et al., 2019)
P28	P28	non-HDM2-mediated Peptide Inhibitor of p53	Pediatric Brain Tumor Consortium	Central Nervous System Tumors	Phase 1	Data demonstrated that phase II adult recommended dose of p28 is well-tolerated for children with recurrent CNS malignancies.	NSC745104 Completed 2017	(Lulla et al., 2016)
P28	P28	P28	CDG Therapeutics, Inc.	Solid Tumors That Resist Standard Methods of Treatment	Phase 1	No Study Results Posted	NCT00914914 Completed 2017	ClinicalTrials.gov
XG-102	TAT-	dextrogyre peptide	Xigen SA	Postoperative Ocular Inflammation	Phase 3	Ocular inflammation postoperative effect of XG-102 with a single subconjunctival injection after ocular surgery was lower than dexamethasone eye drops	NCT02508337 Completed 2017	(Chiquet et al., 2017)
DTS-108	a highly charged oligopeptide of human origin	SN38	Drais Pharmaceuticals, Inc.	Tumor	Phase 1	Advanced or metastatic solid tumors patients could receive a DTS-108 dose of 313 mg/m^2 every 2 weeks *via* intravenous. The maximum tolerated dose of DTS-108 was 416 mg/m^2.	NA	(Coriat et al., 2016)
AVB-620	ACPPs	Cy5 and Cy7	Avelas Biosciences, Inc.	Tumor imaging	Phase 1	AVB-620 improved intraoperative cancer visualization with high safety. NOAEL in rats with single-dose was more than 110-fold of human clinical application dose.	NCT02391194 Completed 2017	(Miampamba et al., 2017; Unkart et al., 2017)

MHCC97-H/GFP tumors at day 10 post-injection *via* the tail vein. TMV-TAT provided a potentially safer approach to silence disease-causing genes (Tian et al., 2018b).

Generally, the linear structure of CPPs hardly obtains very gratifying transfection efficiency of oligonucleotides as low charge number, which resulted in a weak complexation and structural instability of nano-carrier. Yoo et al. synthesized a branched R9 using disulfide bonds and further constructed a novel bio-reducible cationic network using R9 as a vector (B-mR9), and branched structures provide powerful electrostatic adsorption of pDNA or siRNA. B-mR9 showed good biocompatibility and intracellular trafficking *in vitro*. In addition, B-mR9 exhibited a specifically targeted effect on the tumor by the EPR effect remaining for 48 h. B-mR9/siVEGF dramatically inhibited tumor growth by 56.5% versus control, and the therapeutic efficacy was superior to PEI25k and R9 vector in NCI-H460 bearing BALB/c nude mice model. CPPs derived cationic network provided a new approach to design gene delivery platform. Wang et al. also used Chol-based CPPs to assemble a pH-sensitive and biocompatible micelle system, which could co-deliver ULK1 siRNA and the AMPK activator narciclasine to effectively inhibit hepatocellular carcinoma in preclinical studies by regulating programmed cell death (Tai and Gao, 2017). Recent researches verified CPPs were to be the novel paradigm for siRNA oligonucleotides.

CPPs exhibited narrow clinical applications as positive charges inducing non-target and systemic toxicity. Penetrating capacity of cationic or amphiphilic CPPs was normally further powerful than neutral CPPs. Gao et al. discovered a novel highly hydrophobic cyclic CPPs (Cyclosporin A, CsA) with electronic neutral, which showed several folds higher penetrating capacity than PFV (PFVYLI) and pentapeptide VPT (VPTLQ) in MCF-7 cells, it was significantly more effective than conventional neutral CPPs. Efficiency and toxicity of cyclosporin A were compared to TAT by delivering a membrane-impenetrable pro-apoptotic peptide (PAD). When CsA conjugated to PAD, the uptake of PDA was improved 2.2- to 4.7-fold in the tumor cell lines tested by CsA, and cellular uptake of CsA-PAD was generally greater

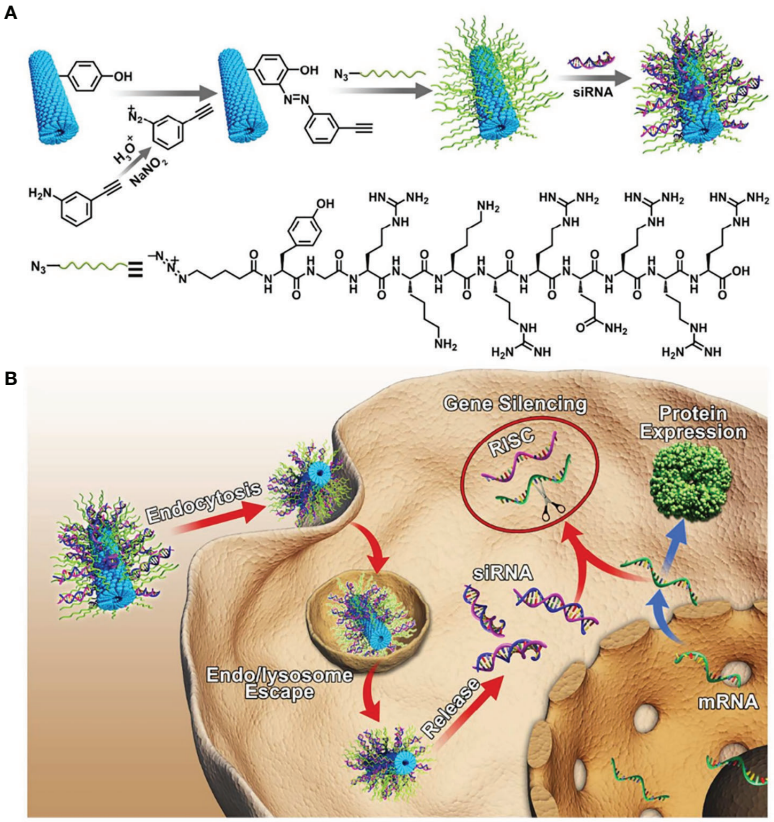

FIGURE 3 | (A) Schematic illustration for the design of siRNA loaded TMV-TAT. **(B)** Gene silencing process of TMV-TAT within the cells (Tian et al., 2018b) (with reproduction permission).

than TAT-PAD. Cytotoxicity of CsA-PAD was similar or greater than TAT-PAD in four different tumor cell lines, which depended on the cell type, but it was significantly stronger than PAD. In xenografted MCF-7 nude mice models, CsA-PAD showed comparable anti-tumor activity to TAT-PAD, but with reduced systemic toxicity. Electroneutral CPPs likely had better potential application value *in vivo* than cationic CPPs, but the accurate tissue distribution of electroneutral CPPs needs to further evaluate (Gao et al., 2017). Another strategy to reduce toxicity and non-target of positive CPPs was used polyanionic materials to coat nanoparticles, such as hyaluronic acid (HA), which was a high-affinity ligand on tumor surface-specific overexpressed marker CD44. Zhao et al. prepared a multifunctional liposome modified with TAT and HA to deliver 10-HCPT against hepatocellular carcinoma (HA/CPPs-10-HCPT-NPs), low-intensity focused ultrasound was used to precisely control drug release at tumor tissue. Zeta potential of liposome was reversed from +45.5 mV to −6.55 mV after HA modified. The penetration depth of liposome after TAT modified was improved 2.76-fold in the multicellular tumor spheroid model. Liposome combined application of HA and CPPs with the aid of ultrasound had a significantly higher tumor inhibition against hepatic carcinoma than other groups, HA-coated nano-carrier was a valuable and promising strategy for CPPs application *in vivo* (Zhao et al., 2018).

A major challenge in oncotherapy was the prognosis poor, especially for pancreatic cancer, glioma, and lymph metastasis. The curative effect of refractory tumors was a lack of significant progress because delivery systems were the inability to overcome the complex tumor microenvironment to deliver drugs reaching the treatment site. CPPs could be used as a molecular drive for cargos deep penetration of tumors. Pancreatic ductal adenocarcinoma (PDAC) had profuse collagenic fibers in the tumor stroma to resist drug penetration. Lo et al. attempted to address the target and tumor stroma penetration challenges in PDAC, two tandem peptides (pTP-PEG-iRGD and pTP-iRGD) were synthesized to prepared mixed micelle for siRNA systemic delivery. It could effectively bypass the delivery barriers of PDAC achieving tumor penetration in three-dimensional organoids and autochthonous tumors models. Furthermore, the mixed micelle complexed siRNA significantly delayed tumor growth (Lo et al., 2018). CPPs could induce cargos across the blood brain barrier (BBB) for glioma treatment. Liu et al. also prepared an anionic random-coiled polypeptide (PLG) coated CPPs (PVBLG-8) micelle to transport siRNA against glioma. PLG entangled with PVBLG-8/siRNA complex to obtain a stable structure in serum

and reversed the surface potential of micelle to negative charge. In addition, micelle could respond to low pH in the tumor extracellular microenvironment to perform the cell penetration function of PVBLG-8. This carrier exhibited excellent therapeutic advantages than several commercial transfection reagents such as poly(L-lysine) (PLL) or Lipofectamine 2000 in glioblastoma tumor spheroids and U-87 MG xenograft mice model (Liu et al., 2018). In order to further improving the target limit of CPPs in glioma application, CPPs were combined with glioma-homing peptides to specifically translocate siRNA. The bonding form of Two CPPs (PF14, PF28) with targeting moistures by either covalent conjugation or non-covalent complex were optimized to increase tumor-specific targeting and gene knockdown effect. The authors established a non-covalently complexed PF14:TG1 siRNA delivery system with specificity to U87 cells showed a two-fold gene-silencing efficiency than PF14. Gene-silencing efficiency of covalently conjugated PF32 was significantly lower than PF14:TG1, due to CPPs probably shield the interaction between targeting peptide and U87 MG receptor or hinder siRNA release into the cytosol. Data demonstrated that targeting peptide non-covalently complexed CPPs was a feasible strategy for siRNA targeting delivery against the tumor (Srimanee et al., 2018). Lymph metastasis was a crucial pathway of tumor dissemination, lymph nodes nearby were the site of original tumor metastasis and further extend to the whole body. Current treatments aiming at lymphatic metastasis *via* intravenous injection were restricted non-target and poor penetration capacity due to the blood–lymph barrier. An R9 modified cabazitaxel nanoparticle (R9-CN) with 13 nm size, and the slight positive charge was verified to possess prominent lymph target and deep penetration effect after i.v. administration for potential anti-metastasis therapy. The fluorescence signal of R9-CN maintained for at least 24 h at a high level in primary tumor sites. R9-CN clearly suppressed 1.4-fold of tumor growth rate and showed a 63.3% inhibition rate of lung metastasis than CN in a breast cancer lymphatic metastasis model. CPPs modified nanoparticles were an effective anti-metastasis platform with deep lymph penetration (Hu et al., 2018).

Application of CPPs in Inflammation

Transdermal administration is an effective means of local delivery of anti-inflammatory drugs with good compliance, stratum corneum and mucosa the main obstacles to delivery. Polyarginine peptides are commonly applied in transdermal drug delivery as efficient skin penetration ability. Gao et al. prepared lornoxicam-loaded lipid gels by R11 modified (LN-NLC-R11) to treat rat paw edema. LN-NLC-R11 significantly improved cellular uptake of NLC in HaCaT cells, remitted rat paw edema, and inhibited the inflammatory cytokines production than NLC *in vivo* (Gao et al., 2019). Due to steric hindrance, the distance between CPPs and nanoparticles will influence the efficiency of cellular internalization. The distance between CPPs and nanoparticles will influence the efficiency of cellular internalization due to steric hindrance. CPPs modified gene carriers R9Gn-chitosan/siMIF (n = 0, 4, 10) were established to inhibit pulmonary inflammation. The length of the glycine chain had little effect on the structure of the nanoparticles. Cell uptake, gene silencing efficiency, and anti-inflammatory activity *in vivo* of R9Gn-chitosan/siMIF were improved with the increasing of Gn controlled spacer arm length. R9G10-chitosan/siMIF significantly reduced the inflammation and goblet cell hyperplasia of lung tissue than R9-chitosan/siMIF in a particulate matter-induced airway inflammation mouse model (Jeong et al., 2015). Similarly, phospholipase D1 (PLD1) conjugated with TAT to enhance anti-asthmatic effect *via* intranasal administration (Lee et al., 2018). Psoriasis is a common epidermal hyperplasia disease with massive infiltration of inflammatory immune cells. Signal transducer and activator of transcription 3 (STAT3) is a key factor on the pathogenesis of psoriasis. APTstat3 is the high-affinity peptide specific to block STAT3. APTstat3 was modified by R9 (APTstat3-9R) to improve stratum corneum penetration. APTstat3-9R exhibited satisfactory results on ameliorating local psoriasis-like skin inflammation after topical treatment *via* intradermal. However, APTstat3-9R showed little skin penetrability *via* transcutaneous administration, it was blocked by the stratum corneum barrier. APTstat3-9R complexed with DMPC/DHPC to form discoidal lipid nanoparticles (DLNPs) to improve transdermal delivery with high colloidal stability (∼20 nm size) and safety. DLNPs could penetrate stratum corneum due to the lipophilicity and then move through the gaps of epidermal layers to reach dermal layers in a psoriasis-like mouse model. APTstat3-9R released from DLNPs to further act against inflammation (**Figure 4**). DLNPs effectively reduced skin edema and epidermal hyperplasia in imiquimod-induced psoriatic mice model (Kim et al., 2018). CPPs application has more advantages in the field of anti-inflammatory than anti-tumor because the local administration does not need to consider causing adverse systemic events and non-targeting.

Application of CPPs in Central Nervous System Disorders

Central nervous system disorders mainly include stroke, Parkinson's disease, and Alzheimer's disease. BBB was composed of tightly connected endothelial cells without any fenestrae, which resulted in low permeability for drug brain delivery. The therapeutic effect of incurable central nervous system disorders was hardly to meet expectations due to the obstruction of BBB (Kristensen et al., 2015). CPPs transported therapeutic agents into brain *via* adsorptive-mediated transcytosis route across BBB, and they exhibited efficient BBB translocation function in submicromolar concentration without producing cytolytic effects (Sharma et al., 2016). In addition, CPPs could bypass P-glycoprotein to increase drug brain accumulation to improve therapeutic effect. However, different types of CPPs possess inconsistent BBB penetrating power. Cho et al. established culture-based multicellular BBB spheroids model with reproducible BBB functions and features to rapid screen brain-penetrating CPPs (Cho et al., 2017). Nineteen kinds of common CPPs labeled by Cy5.5 dye were investigated for their BBB penetrating ability, with DPV 15, HoxA-13, Engrailed-2,

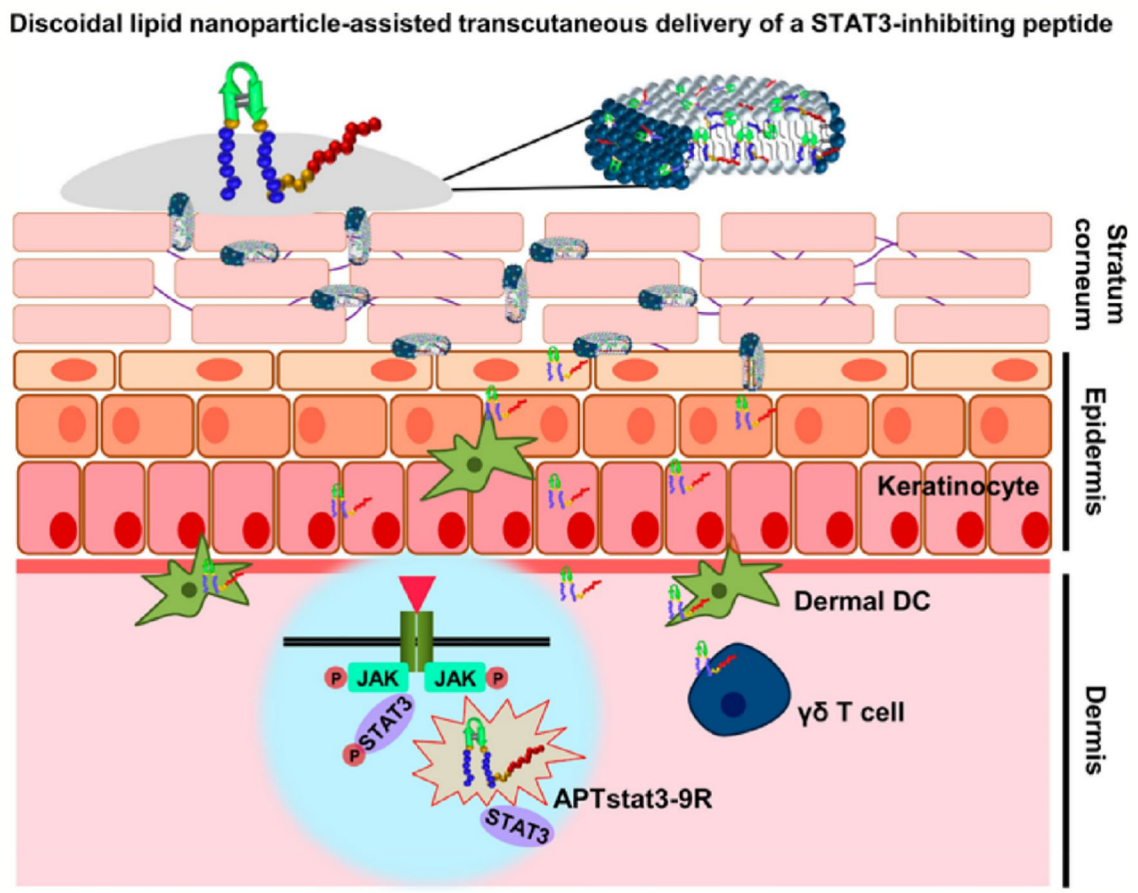

FIGURE 4 | DLNPs deliver APTstat3 for Psoriasis treatment *via* transcutaneous administration (Kim et al., 2018) (with reproduction permission).

Bip(1), and Bip(2) showed the top 5 fluorescence level inside the BBB spheroids model, and all CPPs remained relatively stable except SynB1 with higher degradation rate in working media. In nude mice model, the order of CPPs brain accumulation after tail vein injection were HoxA-13, Bip(2), Bip(1), and DPV15 from high to low. However, it was not exactly consistent with the BBB spheroids model due to the difference of CPPs' pharmacokinetics, biodistribution, and stability *in vivo* and *in vitro*. This powerful BBB model *in vitro* could serve as a valuable next generation platform to accelerate the development of central nervous system disorders therapies. CPPs' modified strategy was a key technology to overcome BBB to enhance the therapeutic effect. The application of CPPs in Central Nervous System Disorders within the last 5 years was summarized in **Table 3** with details. In conclusion, CPPs exhibited a promising prospect for central nervous system disorders treatment through promoting BBB penetration.

CPPs were effective tools for drug brain delivery against Parkinson's disease. Kang et al. synthesized a fusion CPP using TAT and mitochondria-targeting sequence (YGRKKRRQRRR LLRAALR-KAAL) named CAMP, and used it to deliver the antioxidant protein human metallothionein 1A (hMT1A) into mitochondria to target ROS damage for preventing Parkinson's disease (Kang et al., 2018). CAMP-hMT1A could effectively rescue movement impairment in a mouse model of Parkinson's disease. Kim et al. constructed a kind of PEP-1-PON1 fusion protein to transduce PON1 into cells to prevent LDL and HDL oxidation induced inflammatory, oxidized-LDL level associated with Parkinson's disease. The cellular uptake of PON1 was remarkably enhanced in neuroblastoma SH-SY5Y cells and microglial BV2 cells after PEP modified. The delivery ability of PEP-1–PON1 to cross BBB *in vivo* was evaluated after intraperitoneally injection, bio-distribution of PON1 in brain was visualized by immunohistochemistry. PEP-1–PON1 largely accumulated within the substantia nigra region of the midbrain (Kim et al., 2015). However, PON1 without CPP modified was not found to have brain delivery. PEP-1–PON1 reduced the expression of MMP-9 and protected dopaminergic neuronal against cell death in MPTP induced mice Parkinson's disease model. Ahlschwede et al. structured a chitosan modified PLGA nanoparticles to enhance the plasma half-life and provide targeting ability to cerebrovascular amyloid deposits for Alzheimer's disease treatment (Ahlschwede et al., 2019b). A cationic BBB-penetrating peptide (K16ApoE) was added by

TABLE 3 | Recently developed on CPPs application in central nervous system disorders.

CPPs	Cargos	Delivery platform/ stimuli-responsive	Disease	Model	Effect	Ref
CAMP	human metallothionein 1A (hMT1A)	Fusion protein	Parkinson's disease	A mouse model of PD	CAMP could deliver cargo to mitochondria to alleviate mitochondrial damage	(Kang et al., 2018)
TP10	dopamine	Fusion protein	Parkinson's disease	Preclinical animal model of PD	TP10-dopamine form accessed to the brain tissue and showed significant anti-parkinsonian activity	(Rusiecka et al., 2019)
TAT	ND-13	Fusion protein	Parkinson's disease	Mouse model with DJ-1 knockout	TAT modified ND-13 improved the behavioral outcome and dopaminergic system dysfunction	(Finkelstein et al., 2015)
MAP	Rasagiline (RAS)	Prodrug	Parkinson's disease	A human synucleinopathy cell model	RAS-MAP reduced protein alpha-synuclein in cells	(Vale et al., 2020)
R_9	amyloid	Fusion protein	Alzheimer's disease	Cellular level	Total Tau decreased	(Veloria et al., 2017)
RVG-9R	BACE1 siRNA	Chitosan-coated solid lipid nanoparticles	Alzheimer's disease	Cellular level	Prolong residence time in the nasal cavity and improve Nose-to-brain delivery of siRNA	(Rassu et al., 2017)
K16ApoE	Curcumin	Target nanoparticles	Alzheimer's disease	Cellular level and *in vivo* distribution	Nanoparticles could specifically accumulate in brain vasculature and also detect brain amyloid plaques.	(Ahlschwede et al., 2019a)
Penetratin	Ru(II) complex	Ru@Pen@PEG-AuNS	Alzheimer's disease	Cellular level and *in vivo* distribution	Ru@Pen@PEG-AuNS could obviously inhibit the formation of Aβ fibrils, BBB permeability was significantly increased	(Yin et al., 2016)
R_9	Cy5	ACPPs, ACPPs dendrimer/MMPs	Stroke	Cellular level and *in vivo* distribution	ACPPs could response MMP-2/-9	(Chen et al., 2016b)
R_9	NA	Fusion protein	Stroke	Rat stroke model	Poly-arginine exhibited highly neuroprotective	(Meloni et al., 2015)

physical absorption onto the nanoparticles surface to generate BBB transcytosis. The plasma AUC of targeted nanoparticles was ~23 folds higher than K16ApoE-targeted nanoparticles in DutchAβ 40 treated mice. However, the brain distribution in various regions of targeted nanoparticles increased 7 to 9 times of DutchAβ 40 treated mice after K16ApoE modified. The results illuminated that K16ApoE could induce nanoparticles accumulation in the brain to reduce plasma drug concentration. K16ApoE-modified nanoparticles showed significantly greater brain uptake and also could provide specific MRI contrast to detect brain amyloid plaques. TAT was also a brain-penetrant carrier has been used in Alzheimer's disease therapies. In addition, it has been proven TAT could bind to heparan sulfate glicosaminoglicans of extracellular cerebral deposits of amyloid to targeted treat Alzheimer's disease (Maderna et al., 2018). MMPs were involved in neurovascular impairment after stroke, Trojan horse strategies of ACPP could be used for stroke specific detection. Chen et al. designed a gelatinase-activatable CPP to detect MMPs activity in primary neurons in culture and ischemic mouse brain *in vivo*. Cell penetrating function of R9 was shielded by anion poly-glutamate, they were conjugated by MMP-2/-9 cleaved peptide linker. Cy5-conjugated ACPP responded high expression of MMPs derived by stroke to increase cellular uptake for stroke detection. In addition, CPPs also have neuroprotective effects against stroke, such as poly-arginine and arginine-rich CPPs, efficacy was improved with the content increasing of arginine. They had the capacity to reduce neuronal calcium influx induced by glutamic acid, and the neuroprotective effect needed to induce by heparan sulfate preotoglycan-mediated endocytosis (Meloni et al., 2015). CPPs were promising tools to improve drug brain delivery for central nervous system disorders therapies.

Application of CPPs in Otoprotective and Ocular

Acute sensorineural hearing loss mediated by traumatic has attracted more and more attention. The jun-N-terminal protein kinase (JNK) is related to cochlear inflammation. D-JNK-1 (AM-111) is an inhibitor of JNK pathway to treat acute cochlear injury. D-JNK-1 modified by TAT to realize rapid internalization by the local administration route. Phase 3 of AM-111 had completed at 2017, AM-111 indicated effective otoprotection in idiopathic sudden sensorineural hearing loss after acute cochlear injury (Eshraghi et al., 2018).

The eye consists of two parts, an anterior segment, including cornea, conjunctiva, aqueous humor, chambers, lens, and iris, a posterior segment, including vitreous humor, posterior sclera, choroid, retina. They co-formed a biological barrier to protect the eyes and simultaneously prevent drug delivery for eye treatments by several static, dynamic, and metabolic barriers. Topical application is appropriate for disease within eye anterior segment, local injection is suited to the disease within the eye posterior segment. The physiology of the eye is a challenge for ocular drug-efficient delivery, (1) The cornea is highly impervious to hydrophilic biomacromolecule, (2) the drug enters the systemic circulatory system after local injection. CPPs are potential tools for ocular drug delivery to improve bioavailability across barriers (Pescina et al., 2018). CPPs structure has an influence on the ocular distribution after topical delivery. Liu et al. evaluated several cationic CPPs on eye penetration, including TAT, polyarginine R8, polyserine S8, protamine, and penetratin. Penetratin had the optimized activity on cell uptake and ex vivo permeation (Liu et al., 2014). Chu et al. prepared an iRGD and TAT dual-modified choroidal neovascularization target nanoparticles *via* topical ocular

administration. The corneal permeation of nanoparticles enhanced 5.50- and 4.56-fold after iRGD and TAT, respectively, modified. Dual-modified nanoparticles had the most cellular uptake *in vitro*, and also displayed promising targeting and penetration ability *in vivo* (Chu et al., 2017). Tai et al. developed a nano-composites to deliver antisense oligonucleotide (ASO) for gene silencing of the intraocular tumor *via* topical instillation. Polyamidoamine (PG5) was used as a gene carrier by condensing ASO, and penetratin (Pene) was introduced to improve uptake efficiency. Nanoscale PG5/ASO/Pene stably bonded by electrostatic interaction. Nano-composites displayed cell penetration and gene silencing ability after modified by Pene. PG5/ASO/Pene could also significantly inhibit the tumor volume growth in subcutaneous and orthotopic nude mice tumor models (Tai et al., 2017).

Application of CPPs in Diabetes

At present, the commonly used method of insulin administration is a continuous subcutaneous injection by the patient. If oral insulin can be used instead of subcutaneous injection, the patient's pain will be greatly reduced. However, insulin is unstable in the small intestine, has poor permeability in the intestinal epithelium, and low oral bioavailability. Thus, an improved insulin delivery system should be developed. Delivery of insulin using CPP is a promising candidate. In previous studies, When TAT is covalently linked to the insulin B29 Lysine residue, it can dramatically improve insulin penetration in the Caco-2 cell culture model. The bioavailability of CPP prepared insulin was six to eight times higher compared to normal insulin (Liang and Yang, 2005). Since then, including polyarginine and penetratin, and other CPPs have been seen as potential carriers of insulin. Studies by Mariko et al. Have demonstrated that the use of insulin in combination with oligoarginine (R8) can significantly increase intestinal insulin uptake without inducing observable side effects to cell (Morishita et al., 2007). In another study, Mie Kristensen et al. Found that covalently binding penetratin to insulin can increase the epithelial penetration of insulin, because penetratin is rich in Arg and Lys residues, and has a high pI value, it is positively charged at physiological pH, which promotes electrostatic interaction with the oppositely charged components on the cell surface. And they confirmed that the existence of arginine residues in the CPP sequence is a prerequisite for enhancing insulin epithelial penetration (Kristensen et al., 2015). Polyarginine can enhance insulin transmission in the rat intestinal mucosa, thereby lowering blood glucose levels, which also depends on the length of the polyarginine peptide. In the latest study, Feng Guo et al. Covalently combined amphipathic chitosan derivative (ACS) with CPP to prepare nano delivery vehicles for oral insulin delivery. The authors claim that in pharmacodynamic studies, TAT modified nanocarriers deliver insulin Significant hypoglycemic effect (40% reduction) (Guo et al., 2019). It is foreseeable that modifying the surface of nanoparticles through CPPs is a potential method to improve the absorption and delivery of insulin.

Application of CPPs as Imaging Agents and Diagnosis

Imaging agents are essential for disease diagnosis and have the ability to trace or provide timely information on the therapeutic effect of drugs. However, it is still a great challenge to deliver imaging agents to diseased tissue due to preventing the uptake of many unnatural compounds by cell membranes (Xu et al., 2019). CPPs play a significantly important role in the delivery of imaging agents, due to their excellent permeability, high affinity, and high stability (Xu et al., 2019). Many researchers also devoted to the study of CPPs as imaging agents for diagnosis, obtaining a certain advancement in preclinical and clinical (Jiang et al., 2004; Olson et al., 2010; Miampamba et al., 2017; Unkart et al., 2017).

CPPs-Mediated Molecular Probes as Imaging Agents for Diagnosis

In order to accurately probe diseased sites, many CPPs-mediated molecular probes such as activatable CPP (ACPP) (Jiang et al., 2004), AVB-620 (Miampamba et al., 2017) have been studied for molecular imaging (Zhang et al., 2018a). Research has shown that ACPP can be activated by matrix metalloproteinase overexpressed in tumors and images for different enzymes by fluorescence resonance energy transfer (FRET) effect-based FI and PA agents (Jiang et al., 2004). Building on the work of ACPP, Miampamba et al. have designed and developed a novel intravenously administered AVB-620 by changing a ratiometric fluorescence readout from FRET using Cy5 and Cy7 as the couple fluorophores (Miampamba et al., 2017). AVB-620 was a fluorescent imaging agent for breast cancer diagnosis (Munjal et al., 2017). The experimental results indicated that AVB-620 can visualize the tumors under a fluorescence imaging camera system, which possesses high sensitivity and specificity in the diagnosis of lymph node status in metastatic murine breast cancer models, thus provide an excellent basis for clinical application (Miampamba et al., 2017). Moreover, AVB-620 was in the clinical phase I study in patients with breast cancer (Unkart et al., 2017). The result indicated that AVB-620 was safe, well-tolerated at doses for tumor-specific fluorescence detection which was obtained by intraoperative imaging of surgical specimens after administration of AVB-620 (Unkart et al., 2017). In addition, Zhu et al. also designed and synthesized CPPs-mediated molecular probes as imaging agents (Zhu et al., 2018). They firstly synthesized three thermally activated delayed fluorescence (TADF) chemicals (4CzIPN, NAI-DPAC, BTZ-DMAC) and TADF was loaded into amphiphilic CPPs (F6G6(rR)3R2) which was capable of self-assembling into nanoparticles in water to constructed TADF nanoparticles as imaging agents. They present low cytotoxicity and rapid membrane penetration (Zhu et al., 2018). The time-resolved luminescence imaging result indicated that more TADF nanoparticles were accumulated in cells and brighter fluorescence signals were observed in the cytoplasm with the increase of incubation time, illustrating the feasibility of TADF nanoparticles as imaging agents (Zhu et al.,

2018). However, TADF nanoparticles are still basic research and expected to more researches *in vitro* or *in vivo*.

CPPs-Mediated Nanoplatforms as Imaging Agents for Diagnosis

Although organic fluorophores or fluorescent proteins have been extensively applied to imaging agents and disease diagnosis, the drawbacks of low brightness, poor stability, wide emission bandwidth limit their application (Xu et al., 2019). With the emerging of nanotechnology, CPPs-mediated nanoplatforms as imaging agents for diagnosis have attracted widespread attentions (Cai and Chen, 2007; Onoshima et al., 2015; Chen et al., 2019), this is mainly because of their advantages of low cytotoxicity, good biocompatible, high cell membrane permeability, small size, large surface areas, abundant functional group on their surface, and easily modify (Onoshima et al., 2015; Sun et al., 2017). One excellent example is CPPs-mediated quantum dots (QDs) as imaging agents for biological diagnosis (Onoshima et al., 2015; Zhang et al., 2018b; Yang et al., 2020). QDs are fluorescence semiconductor nanoparticles, possessing many advantages such as low cytotoxicity, high quantum yields, excellent stability, broad emission spectra (Cai and Chen, 2007). However, CPPs-mediated QDs not only possess the advantages of QDs, but also have high cell membrane permeability (Yang et al., 2020). Zhang et al. synthesized near-infrared semiconducting polymer dots coated with a CPP (R8-Pdots) for cell tracking in deep organs, the schematic of synthetic R8-Pdots and experimental results were presented in **Figure 5** (Zhang et al., 2018b). The particle size of R8-Pdots with good dispersion is ~12 nm. R8-Pdots presented low cytotoxicity and high cell membrane permeability for MCF-7 cells. Meanwhile, a clear and strong fluorescence signal was recorded *in vitro* and *in vivo*. The results of cell tracking capability of Pdots in live mice *in vivo* indicated that MCF-7 cells labeled with R8-Pdots were visualized in real-time, which are powerful for whole-body fluorescence imaging *in vivo* (Zhang et al., 2018b). In addition, mesoporous silica nanoparticles, superparamagnetic iron oxide (SPIO) nanoparticles, Gold nanoparticles have also been explored for imaging agents and diagnosis, on account of their low cytotoxicity and easy functionalization (Grasso et al., 2019). For example, CPPs (RGE) modified, Gd-DTPA conjugated, and doxorubicin (DOX) incorporated Fe3O4@SiO2@mSiO2 nanoparticle drug delivery system (Fe3O4@SiO2@mSiO2/DOX-(Gd-DTPA)-PEG-RGE NPs) were synthesized for MRI, explored by Gao et al. The NPs could be accumulated in U87 cells and provided a T1-T2 dual-mode contrast MR imaging result, which indicates a more accurate diagnosis (Gao et al., 2018a). Gao et al. also designed a multifunctional drug-loaded nanosystem (F/A-PLGA@DOX/SPIO) as a T2-negative contrast agent for MRI and the nanosystem realized the dynamic monitoring of DOX efficacy (Gao et al., 2018b). Although

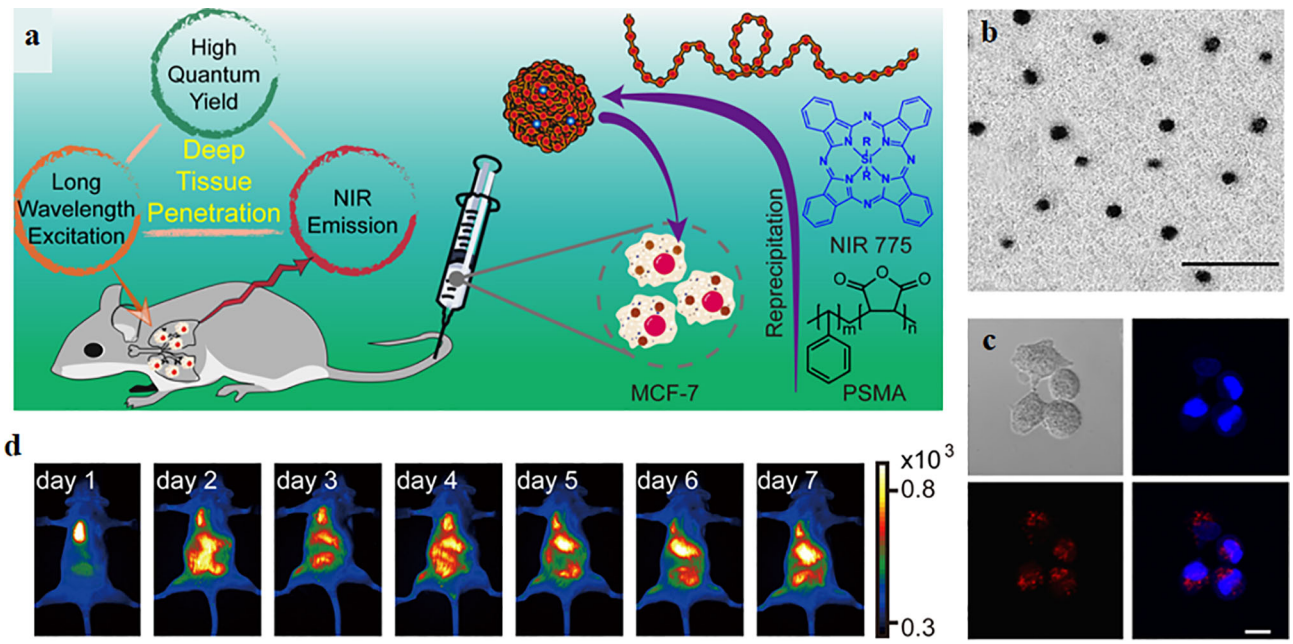

FIGURE 5 | (A) The schematic of synthetic R8-Pdots as imaging agents for whole-body cell tracking in deep organs. **(B)** The TEM image of Pdots, the scale bar is 100 nm. **(C)** Fluorescence imaging of MCF-7 cells labeled with R8-Pdots (red) and the cell nucleus was stained by Hoechst 33258. Scale bar: 20 μm. **(D)** Fluorescence imaging of the mouse *in vivo* (Zhang et al., 2018b) (with reproduction permission).

CPPs-mediated nanoplatforms as imaging agents show excellent experimental results in diagnosis, very few nanoplatforms have been translated into the clinic.

Radiolabeled CPPs as Imaging Agents for Diagnosis

Radiolabeled peptides as traditional imaging agents are the most widely utilized due to their high precision. Radiolabeled CPPs, as one of the peptide-mediated imaging agents, have also been developed for disease diagnosis. Recently, some radiolabeled CPPs such as [^{18}F]-FPPRGD2, [^{18}F]Galacto-RGD and 18F-RGD-K5 have been translated into clinical trials (Sun et al., 2017). [^{18}F]Galacto-RGD was the first applied to RGD PET tracer in human, achieving high specificity and fast metabolism in cancer patients (Chen et al., 2016a; Jackson et al., 2017). And [18F]-FPPRGD2 was the first dimeric RGD peptide approved by FDA and used for humans, indicating promising outcome in glioma (Xing et al., 2014; Chen et al., 2016a). Additionally, 18F-RGD-K5 was also applied to human, and its radiation dose was determined from whole-body PET/CT. The results indicated that the radiation dose of 18F-RGD-K5 was highest in the urinary bladder wall and can be decreased by frequent voiding. Moreover, 18F-RGD-K5 could be rapidly cleared by the renal system (Doss et al., 2012).

LIMITATIONS OF CPP-MEDIATED APPLICATION

In the past 30 years, CPPs have been increasingly used in various disease diagnosis and therapy, as one of the most useful approaches for transfection in different cell types. CPPs have been key factors in achieving therapeutic concentrations in cells and tissue that are hard to target, consequently improving their therapeutic outcome. Their success is not only dependent on their powerful transmembrane delivery characteristic but also due to their versatility. They can be simply synthesized, modified, and improved.

However, CPPs are a double-edged sword since they may induce significant adverse effects owing to various reasons. So far, no CPP-conjugated drugs have been approved by FDA and several clinical trials have been terminated. The reasons are as follows: (1) Stability tissues *in vivo* (Pujals and Giralt, 2008). The rapid clearance from blood is a drawback as a therapeutic payload may be degraded in circulation before reaching the therapeutic site caused by enzymic degradation. (2) Immunogenicity issues. CPPs, due to its polypeptide property, will increase the risk of the undesired immune response in patients, which may not only reduce the drug effect but also cause unwanted immune stress response (Jarver et al., 2010). It can be used in high-dose and frequent intervals with the purpose of increasing exposure to reduce the immunogenicity of therapeutics, but this way results in toxicity. The other way is to inject therapeutics subcutaneously which can reduce the production of anti-drug antibodies caused by the immune system (Jauset and Beaulieu, 2019). (3) Cellular toxicity. Due to off-target cellular absorption of the therapeutics by normal tissues, CPPs can be internalized by almost all types of cells. Most research reported low toxicity of CPPs, however, it should be noticed that everything can become cytotoxic at a high concentration, and many questions need to be answered before being officially applied to the patients. The cytotoxicity of CPPs is of great concern (Saar et al., 2005). For example, the MAP, as a typical CPP, is similar in the structure of the antimicrobial lytic peptides to affect microbial cells by disturbing their plasma membranes (Zorko and Langel, 2005). It has been reported that the MAP showed a fairly high toxic effect on various cell types at concentrations higher than 1 μM through carrying out a variety of cytotoxicity assays (Aguilera et al., 2009). Due to their amphipathic effect in the presence of artificial micelles, MAPs can induce the leakage of protons, proteins, metal ions, etc., which results in cell death due to the damage of the plasma membrane (Moutal et al., 2015). (4) Low specificity. It is well accepted that cationic CPPs can bind to glycosaminoglycans (Walrant et al., 2017), but it is an unknown field whether CPPs can interact with specific membrane receptors. A widespread tissue distribution of CPP-conjugated therapeutics can reduce drug efficiency due to a lower local concentration. Therefore, maximizing specific cells targeting while ignoring normal cells is crucial. (5) Endosomal degradation after entering into cytosol. The delivery of CPPs and CPP/cargo complexes to the cytosol from endosome before lysosomal degradation is another critical problem (Erazo-Oliveras et al., 2012). It is believed that drugs remain within endosomes cannot exhibit their biological function. Therefore, CPPs should be engineered that it should promote effective endosomal escape to speed up the release of the carrier from the endosome into the cytosol. Meanwhile, the foremost important methods for delivery of CPPs are not only translocated to the target tissue or organ, but also target into specific organelles in the cell, such as nucleus and mitochondria (Horton et al., 2008), to accomplish efficient treatment (Biswas and Torchilin, 2014).

In summary, in order to realize the clinical application of CPPs, to overcome CPPs associated with treatment challenges, optimized CPPs with low toxicity, high efficiency, and specificity are urgently demanded.

CPP-BASED OPTIMIZATION

As mentioned above, clinical applications of CPPs depend on the improvement of some important characters including enhancement of stability, the delay of degradation of CPPs by enzymes in the circulation, reduction of cytotoxicity, the improvement of the endosomal escape efficiency and target specificity.

Endosomal Escape Efficiency

To date, potential mechanisms for endosomal escape have been proposed. One potential explanation is based on the positively charged CPPs, which are thought to bind to negatively charged components in the endosomal membrane (Erazo-Oliveras et al., 2012). This would lead to the formation of a membrane pore

which results in the leakage of CPPs (Yang et al., 2010). Another possible reason for escape is the formation of ionic pairs between negatively charged phospholipids and positively charged CPPs (El-Sayed et al., 2009), which would partition across the endosomal membrane (Tuennemann et al., 2008).

To increase the CPPs' release from endosome, some of the most common strategies have been used as follows. For example, the use of fusogenic lipids to improve the endosomal release of CPPs. Dioleoylphosphatidyle thanolamine (DOPE) can significantly increase the release and activity of the therapeutics from endosomes. El-Sayed et al. indicated that DOPE showed a giant improvement in transfection efficacy combining into lipoplexes or TAT-pDNA complexes. DOPE changes from lamellar phase to an inverted hexagonal phase in endosomes with lower pH levels. This transformed phase promotes the fusion of the CPP/cargo complexes and the endosomal phospholipids, which causing the destabilizing of the membrane to release the CPP/cargo complexes into the intracellular space (El-Sayed et al., 2009). The "proton sponge" effect is also used to enhance the endosomal release of CPPs. When the pH of lysosome decreases, the buffering capacity of an agent can capture a large number of protons and cause Cl-influx, which results in lysosome osmotic swelling, and finally lysosome rupture to release the internalized CPP/cargo complexes to the cytoplasm. Another commonly used agent is histidine. The imidazole group of histidine can be protonated to cause lysosome osmotic swelling and rupture of the endosomes (Beloor et al., 2015), which has been extensively used to heighten the gene expression of a TAT/pDNA complex (Lo and Wang, 2008). Another effective way is to use membrane-disruptive peptides to improve the endosomal release of CPPs (Wadia et al., 2004). As we know, viruses can overcome the endosomal trap easily, so using the mechanism of the virus to realize endosomal escape is feasible by conjugating a viral fusion sequence to CPP/cargo complexes (El-Andaloussi et al., 2006). HA2 peptide originated from the hemagglutinin protein of influenza virus is a pH-sensitive fusogenic peptide. The HA2 peptide has an α-helix structure at its N-terminus, which can be inserted into lipids. At the low pH environment inside endosomes, a conformational change exposes the α-helix structure to fuse with the endosomal lipids, resulting in the endosomal release of complexes with proteins and transportan–peptide nucleic acid (PNA) complexes in the cytosol (Trabulo et al., 2010).

Organelle-Specific Delivery: Mitochondrial Delivery

Mitochondria are recognized as the powerhouses of cells, which control most, if not all, programmed cell death mechanisms. In the etiology of metabolic diseases, the dysfunction of mitochondria is thought to be the culprit causing some abnormalities in the patients (Szeto, 2006), such as hypertension, cancers, and some neurodegenerative diseases, seriously damage human health (Cerrato et al., 2015). However, very few therapeutic drugs have access to mitochondria (Borrelli et al., 2018). Cerrato et al. designed and synthesized a series of small novel CPPs targeting mitochondria to regulate intramitochondrial processes and enhance the biologic effects. Mitochondria-penetrating peptide (mtCPP-1) could transport 5(6)-carboxyfluorescein (5-FAM) into the plasma membrane and selectively concentrate into the mitochondria, which had no effect on mitochondrial membrane potential and inhibited reactive oxygen species release by two-fold compared with SS-31. Experimental data analysis showed the mitochondrial uptake increased by 35% compared with SS-31. No toxicity was detected even at higher concentrations. These results show that mtCPP-1 is a mitochondrial CPP. Kang et al. (2018) developed a cell-penetrating artificial mitochondria-targeting peptide (CAMP), which could conjugate the antioxidant protein human metallothionein 1A (hMT1A) to form CAMP-hMT1A successfully localized to the mitochondria. CAMP-hMT1A restored mitochondrial activity, tyrosine hydroxylase production, and inhibited ROS release after treating a cell Parkinson's disease model. Furthermore, CAMP-hMT1A injected into the brain of the PD mouse model protected dopaminergic neuronal degeneration and movement impairment (Dinca et al., 2016).

"Smart" Intracellular Drug Delivery Systems

CPPs modified drug or CPP/cargo complexes would concentrate widespread to other undesired targets because of their low targeting specificity, which leads to limited therapeutic efficiency and serious drug-induced toxic reaction. To overcome the obstacle of drug-induced systemic toxicity, a "smart" intracellular drug delivery system based on CPP was designed, named as "ATTEMPTS" (antibody-targeted triggered electrically modified prodrug type strategy) (Ye et al., 2015). The ATTEMPTS system has two components, one is the antibody targeting part which is consisting of antibodies-conjugated heparin, another is the CPPs modified drug component. The two components form a compact complex by electrostatic adsorption between cationic CPP and the anionic heparin. In fact, the electrical charge of the CPPs is neutralized by the heparin, and this could increase the plasma stability of CPP/cargo complexes against endogenous proteases. The whole process is illustrated in **Figure 6** (Shin et al., 2014). Intravenous injection administration, the antibody will carry the whole complexes to reach the target site (Huang et al., 2010). Then the clinical heparin antidote protamine sulfate is systemically injected to separate the CPP drug from its Target-Hep (Huang et al., 2013). Due to the fact that protamine has stronger heparin-binding affinity than CPPs, the CPP/cargo complexes would be released from the complex, and the complexes could translocate across the plasma membrane into the tumor cells by the activity of the CPPs (He et al., 2014).

Shin et al. (2014) successfully prepared a recombinant chimeric TAT–gelonin fusion toxin (TAT-Gel) by the genetic engineering method. TAT-Gel bound the anionic heparin by electrostatic interaction, when the protamine sulfate is systemically injected, and 75% of TAT-Gel was instantly

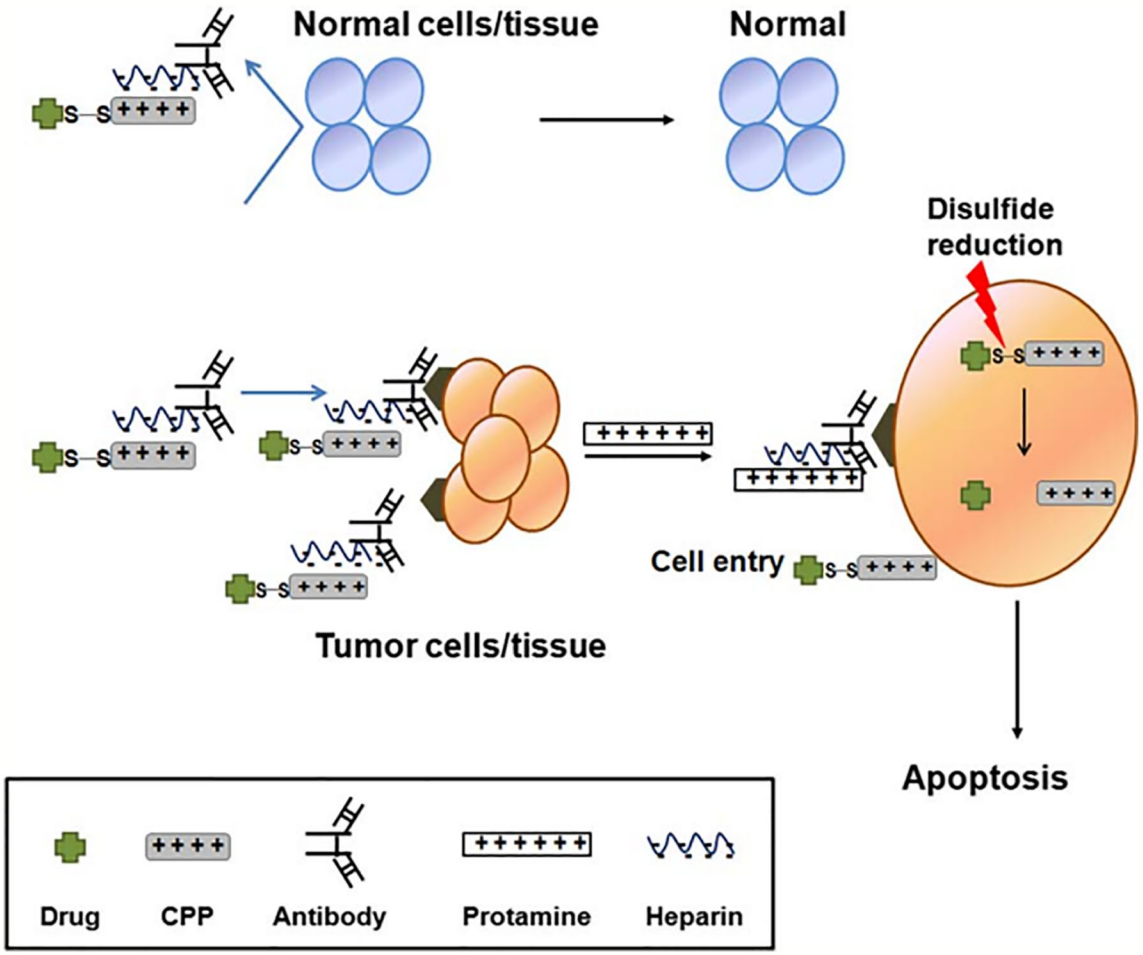

FIGURE 6 | Illustration of CPP-modified ATTEMPTS system (Shin et al., 2014) (with reproduction permission).

released in 30 min, then the CPPs translocated across the plasma membrane into the tumor cells displaying substantial tumor suppression. In addition, based on the ATTEMPTS system, TAT-Gel bound the heparin-conjugated anti-CEA mAb (T84.66) by electrostatic force, which could specifically target CEA over-expressed on colorectal cancer cells. Compared to the mice administration of TAT-gel alone, TAT-gelonin/T84.66-Hep showed a significantly augmented about 58-fold target delivery (Shin et al., 2015).

Increasing Cell Specificity Systems: Activatable CPPs

The mechanism of CPP internalization is nonspecific binding to bilayer phospholipids on the cell membrane, which severely limits the clinical application of CPPs. A possible way to enhance the specificity is achieved by the ACPP while the CPP's cell-penetrating effect is masked by a stimulus sensitive cleavable linkers (Savariar et al., 2013), such as pH-sensitive (Tang et al., 2018), enzyme-sensitive (Yang et al., 2015), temperature-sensitive, electricity, and magnetism-sensitive or light-sensitive cleavable linker. Once in the specific tissue environment, ACPP receives external stimulation, the linker will be cleaved, and the CPPs restore its normal activity.

Enzymes possess a great variety of functions inside organisms. In pathological tissues, such as inflammation or cancer locus, the expression level of specific enzymes (Quach et al., 2014) like protease, glycosidase or esterase is usually higher compared with their concentration in normal tissues (McAtee et al., 2014). Therefore, many tumor-associated enzymes have been extensively used for enzyme-sensitive disease diagnosis and therapy because of this tissue specificity concentration gradients. the combination of CPP/cargo complexes delivery with the enzyme-triggered system not only overcome the cell permeability obstacle of the conventional delivery system, but also the selectivity obstacle of the CPP-based delivery system.

The matrix metalloprotease 2 (MMP2) is overexpressed in the tumor microenvironment. Zhu et al. Designed a novel multifunctional nanocarrier, which could respond to the upregulated extracellular MMP2, enhancing tumor-specific targeting and internalization. The functionalized nanocarrier

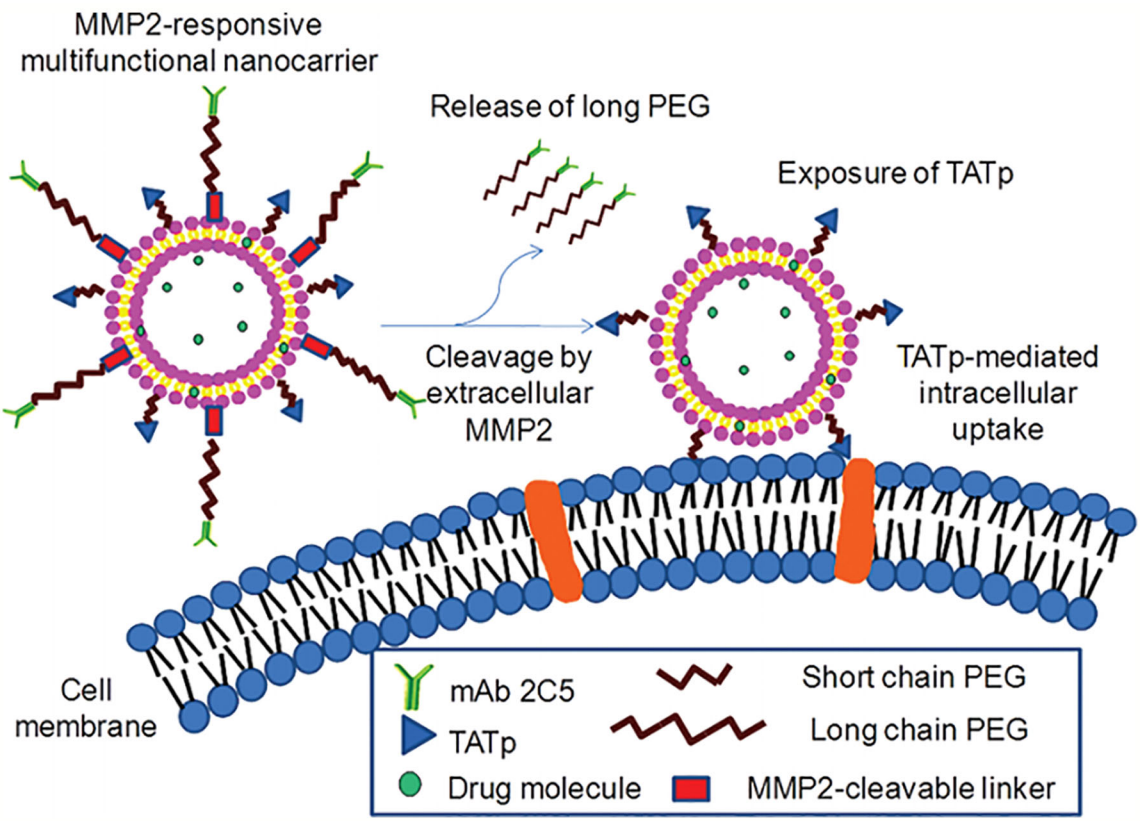

FIGURE 7 | MMP2-responsive multifunctional liposomal nanocarrier and its drug delivery strategy (Zhu et al., 2012) (with reproduction permission).

was decorated with the tumor cell-specific anti-nucleosome monoclonal antibody by using the long-chain PEG block as a steric shield for the nanocarrier (**Figure 7**). The MMP2-cleavable peptide was applied as a sensitive linker between nanoparticle lipid and long-chain PEG, and the nanoparticle was also modified with surface-attached cell-penetrating function (TATp). When the 2C5/peptide/TATp-Lip specifically targeted tumor cells, the long-chain PEG was released after the MMP2-cleavable linker was cleaved by the highly expressed extracellular MMP2, resulting in the exposure of the originally unexposed surface-attached cell-penetrating TATp, which facilitated the enhanced intracellular delivery of the system (Zhu et al., 2012).

Jiao et al. also used MMP-2–responsive peptides as the enzymatically degradable linkers to establish a gene delivery system named ch-Kn(s-s)R8-An micelles for the BBB and glioma dual-targeting. The linker conjugated angiopep-2, which can specifically bind to the low-density lipoprotein receptor-related protein-1 (LRP1) overexpressed on glioma cells. The micelles could effectively target to the glioma cells and then further migrate into the center of the tumor after the MMP2-cleavable linker was degraded by the overexpressed extracellular MMP2, resulting in the exposure of R8. This delivery system showed high gene transfection efficiency and improved uptake in glioma cells. The application of ch-K5(s-s) R8-An/Dbait with radiotherapy dramatically inhibited the tumor growth *in vitro* (Jiao et al., 2019).

pH was the most common condition to trigger CPPs activation in tumor delivery, pH-responsive anionic materials were generally used in combination. Yu et al. synthesized two kinds of polypeptide conjugated cholesterol-polyoxyethylene sorbitol oleate, (HE)5-CPSO, and (RG)5-CPSO. They were used to forming mixed micelles to deliver PTX to the brain with high tolerance. Polyanionic (HE)5 shielded the positive charge of (RG)5 to reduce non-target uptake in physiological conditions. However, the surface potential of (HE)5 reversed when they located at extracellular tumor or endosome with lower pH, the charge transition could activate (RG)5 to promote directed micellar uptake and drug release of PTX. Mixed micelles preferentially accumulated in tumor tissues and significantly inhibited 74.84% tumor growth comparing to control in a glioma mouse model (Tian et al., 2018a). Tang et al. also prepared a PEG-PLA nanoparticle to deliver PTX, which was modified by (HE)10G5R6 peptide to obtain pH-sensitive characteristics. It shared a similar strategy with the one above. (HE)10 controlled R6 screening ON/OFF through the hairpin structural transformation at different pH conditions (Tang et al., 2018).

In addition, UV-activatable CPPs are also a promising system to overcome the selectivity obstacle of the CPP-based delivery

system. Hansen et al. designed a novel method to constrain the CPPs. After radiation with UV-light, the liposomes would be triggered following uptake into cells. Tat-peptide was inserted in PEG loop to endow stealth property, both termini of Tat were linked with an alkyl chain, which one terminus was anchored to the liposomal surface and another terminus was achieved by an UV-cleavable linker that endowed CPPs in a deactivated and constrained form. Once the UV-cleavable linker cracked after UV-irradiation, the CPPs would be exposed and reinstate the activation state to transport the entire liposome into cells (Hansen et al., 2012).

As mentioned above, these ACPPs possess innovation and excitement, but the activation process is generally believed irreversible and still often occurs at off-target sites instead of the target sites. To overcome the issue that ACPPs is lack of reversibility *in vivo* targeted delivery applications. The new group of ACPPs was synthesized, termed as reversibly activatable CPPs (RACPPs). RACPPs have a high response to biostimulus, and they will revert back to original form after leaving from the specific sites of activation to avoid the nonspecific uptake of ACPPs/cargo complexes after activation. Tang et al. designed a novel pH-sensitive RACPPs (HE-CPP), which used a highly pH-sensitive masking sequence linked to a CPP *via* a polyglycine linker (HE-CPP) to mask its positive charge and prevent off-target uptake of the ACPPs/cargo complexes. The polyethyleneglycol-polylactic acid (PEG-PLA) coupled with the HE-CPP sequence to compose polymer micelles (PMs-HE-CPP), which can enhance specificity and promote encapsulated paclitaxel (PTX) targeting. PTX/PMs-HE-CPP displayed reversible charge-conversion according to the surrounding pH as well as satisfactory loading capacity, encapsulated efficiency, and size distribution (Tang et al., 2018).

CONCLUSIONS AND FUTURE PERSPECTIVES

CPPs are a hot topic for translocating drug or CPP/cargo complexes across the plasma membrane. Since the discovery of the TAT peptide in 1988, a large number of CPPs have been developed. CPPs have been widely used to deliver different kinds of therapeutics, imaging agents, and CPP/cargo complexes, including liposomes and nanoparticles, for diagnosis and treatment of several diseases. Although CPP is developing in full swing, numerous CPP-based clinical trials have been dramatically expanded. So far, in fact, no CPPs or CPP/cargo complexes have been approved by FDA. Many issues should be addressed before translating CPPs into clinics, as following: stability *in vivo*, immunogenicity, cellular toxicity, lack of specific intracellular uptake and failure to escape from endosomes. Of course, in terms of clinical applications, cost, ease of synthesis, suitable for industrial production and elimination should also be considered. In the future, the application of CPPs should be devoted to solving these issues, and numerous new CPP-based delivery systems should be evaluated. We can use strategies of fusogenic lipids, the "proton sponge" effect or membrane-disruptive peptides for the delivery of CPPs to promote efficient endosomal escape. A series small novel CPPs had been designed and synthesized to deliver not only to the target tissue or organ but also inside the specific intracellular organelles to accomplish more efficient therapy. The major obstacles to CPP-based delivery systems are the limited cell-type specificity, due to the most CPPs are uptaken by all cell types, and the short blood plasma half-life because of the presence of proteases. Novel strategies have been evaluated to improve CPPs specificity to the target site, such as the linking of CPPs with specific ligands in the form of covalent or noncovalent. The targeting ligands include an antibody, folic acid, transferrin, and RGD peptides (Xie et al., 2013; Yang et al., 2014; Zhou et al., 2014; Yang et al., 2015; Xie et al., 2016; Meng et al., 2019). The receptors of these targeted ligands are usually overexpressed in certain tumor types other than the normal tissue. In addition, "ATTEMPTS" strategy can not only improve the specificity of CPP-based delivery systems but also protect CPPs from enzyme degradation. The ACPP is another promising system to increase specificity. In this system CPPs are masked by the stimuli sensitive cleavable linker, which will be cleaved in the specific tissue environment, then the CPPs restore its normal activity, efficiently deliver CPP-based delivery systems into the cell and avoid delivery to non-targeted site.

The design of a safe, efficient, specific CPP-based delivery system as well as easy to produce and low cost have enormous potential and significant prospects in terms of clinical applications. CPPs and CPP/cargo complexes have the potential to provide more effective methods in diagnosis and treatment of human diseases, such as cancer, inflammation, central nervous system disorders, otoprotective, ocular, and diabetes. Furthermore, we strongly believe that CPP drugs or CPP/cargo complexes will enter the market within the next few years.

AUTHOR CONTRIBUTIONS

All the authors contributed to the writing of the manuscript.

REFERENCES

Aderem, A., and Underhill, D. M. (1999). Mechanisms Of Phagocytosis In Macrophages. *Annu. Rev. Immunol.* 17, 593–623. doi: 10.1146/annurev.immunol.17.1.593

Agrawal, P., Bhalla, S., Usmani, S. S., Singh, S., Chaudhary, K., Raghava, G. P., et al. (2016). CPPsite 2.0: a repository of experimentally validated cell-penetrating peptides. *Nucleic Acids Res.* 44, D1098–D1103. doi: 10.1093/nar/gkv1266

Aguilera, T. A., Olson, E. S., Timmers, M. M., Jiang, T., and Tsien, R. Y. (2009). Systemicin vivodistribution of activatable cell penetrating peptides is superior to that of cell penetrating peptides. *Integr. Biol.* 1 (5-6), 371–381. doi: 10.1039/b904878b

Ahlschwede, K. M., Curran, G. L., Rosenberg, J. T., Grant, S. C., Sarkar, G., Jenkins, R. B., et al. (2019a). Cationic carrier peptide enhances cerebrovascular targeting of nanoparticles in Alzheimer's disease brain. *Nanotechnol. Biol. Med.* 16, 258–266. doi: 10.1016/j.nano.2018.09.010

Ahlschwede, K. M., Curran, G. L., Rosenberg, J. T., Grant, S. C., Sarkar, G., Jenkins, R. B., et al. (2019b). Cationic carrier peptide enhances cerebrovascular targeting of nanoparticles in Alzheimer's disease brain. *Nanomedicine* 16, 258–266. doi: 10.1016/j.nano.2018.09.010

Akahoshi, A., Matsuura, E., Ozeki, E., Matsui, H., Watanabe, K., and Ohtsuki, T. (2016). Enhanced cellular uptake of lactosomes using cell-penetrating peptides. *Sci. Technol. Adv. Mater.* 17, 245–252. doi: 10.1080/14686996.2016.1178056

Baoum, A., Ovcharenko, D., and Berkland, C. (2012). Calcium condensed cell penetrating peptide complexes offer highly efficient, low toxicity gene silencing. *Int. J. Pharm.* 427, 134–142. doi: 10.1016/j.ijpharm.2011.08.012

Bechara, C., and Sagan, S. (2013). Cell-penetrating peptides: 20 years later, where do we stand? *FEBS Lett.* 587, 1693–1702. doi: 10.1016/j.febslet.2013.04.031

Beloor, J., Zeller, S., Choi, C. S., Lee, S. K., and Kumar, P. (2015). Cationic cell-penetrating peptides as vehicles for siRNA delivery. *Therapeutic Deliv.* 6 (4), 491–507. doi: 10.4155/tde.15.2

Biswas, S., and Torchilin, V. P. (2014). Nanopreparations for organelle-specific delivery in cancer. *Adv. Drug Deliv. Rev.* 66, 26–41. doi: 10.1016/j.addr.2013.11.004

Borrelli, A., Tornesello, A., Tornesello, M., and Buonaguro, F. (2018). Cell Penetrating Peptides as Molecular Carriers for Anti-Cancer Agents. *Molecules* 23, 295. doi: 10.3390/molecules23020295

Cai, W., and Chen, X. (2007). Nanoplatforms for Targeted Molecular Imaging in Living Subjects. *Small* 3, 1840–1854. doi: 10.1002/smll.200700351

Capron, M., Béghin, L., Leclercq, C., Labreuche, J., Dendooven, A., Standaert, A., et al. (2019). Safety of P28GST, a Protein Derived from a Schistosome Helminth Parasite, in Patients with Crohn's Disease: A Pilot Study (ACROHNEM). *J. Clin. Med.* 9, 41. doi: 10.3390/jcm9010041

Carnevale, K. J. F., Muroski, M. E., Vakil, P. N., Foley, M. E., Laufersky, G., Kenworthy, R., et al. (2018). Selective Uptake Into Drug Resistant Mammalian Cancer by Cell Penetrating Peptide-Mediated Delivery. *Bioconjugate Chem.* 29, 3273–3284. doi: 10.1021/acs.bioconjchem.8b00429

Cerrato, C. P., Pirisinu, M., Vlachos, E. N., and Langel, Ü. (2015). Novel cell-penetrating peptide targeting mitochondria. *FASEB J.* 29 (11), 4589–4599. doi: 10.1096/fj.14-269225

Chen, H., Niu, G., Wu, H., and Chen, X. (2016a). Clinical Application of Radiolabeled RGD Peptides for PET Imaging of Integrin αvβ3. *Theranostics* 6, 78–92. doi: 10.7150/thno.13242

Chen, S., Cui, J., Jiang, T., Olson, E. S., Cai, Q.-Y., Yang, M., et al. (2016b). Gelatinase activity imaged by activatable cell-penetrating peptides in cell-based andin vivomodels of stroke. *J. Cereb. Blood Flow Metab.* 37, 188–200. doi: 10.1177/0271678X15621573

Chen, Y., Fu, Y., Li, X., Chen, H., Wang, Z., and Zhang, H. (2019). Peptide-functionalized NaGdF4 nanoparticles for tumor-targeted magnetic resonance imaging and effective therapy. *RSC Adv.* 9, 17093–17100. doi: 10.1039/C9RA02135C

Chiquet, C., Aptel, F., Creuzot-Garcher, C., Berrod, J.-P., Kodjikian, L., Massin, P., et al. (2017). Postoperative Ocular Inflammation: A Single Subconjunctival Injection of XG-102 Compared to Dexamethasone Drops in a Randomized Trial. *Am. J. Ophthalmol.* 174, 76–84. doi: 10.1016/j.ajo.2016.10.012

Cho, C. F., Wolfe, J. M., Fadzen, C. M., Calligaris, D., Hornburg, K., Chiocca, E. A., et al. (2017). Blood-brain-barrier spheroids as an in vitro screening platform for brain-penetrating agents. *Nat. Commun.* 8, 15623. doi: 10.1038/ncomms15623

Chu, D., Xu, W., Pan, R., Ding, Y., Sui, W., and Chen, P. (2015). Rational modification of oligoarginine for highly efficient siRNA delivery: structure–activity relationship and mechanism of intracellular trafficking of siRNA. *Nanotechnol. Biol. Med.* 11, 435–446. doi: 10.1016/j.nano.2014.08.007

Chu, Y., Chen, N., Yu, H., Mu, H., He, B., Hua, H., et al. (2017). Topical ocular delivery to laser-induced choroidal neovascularization by dual internalizing RGD and TAT peptide-modified nanoparticles. *Int. J. Nanomed. Volume* 12, 1353–1368. doi: 10.2147/IJN.S126865

Chugh, A., Eudes, F., and Shim, Y.-S. (2010). Cell-penetrating peptides: Nanocarrier for macromolecule delivery in living cells. *IUBMB Life* 62, 183–193. doi: 10.1002/iub.297

Coriat, R., Faivre, S., Mir, O., Dreyer, C., Ropert, S., Bouattour, M., et al. (2016). Pharmacokinetics and safety of DTS-108, a human oligopeptide bound to SN-38 with an esterase-sensitive cross-linker in patients with advanced malignancies: a Phase I study. *Int. J. Nanomed. Volume* 11, 6207–6216. doi: 10.2147/IJN.S110274

Crombez, L., Aldrian-Herrada, G., Konate, K., Nguyen, Q. N., Mcmaster, G. K., Brasseur, R., et al. (2009). A New Potent Secondary Amphipathic Cell–penetrating Peptide for siRNA Delivery Into Mammalian Cells. *Mol. Ther.* 17, 95–103. doi: 10.1038/mt.2008.215

De coupade, C., Fittipaldi, A., Chagnas, V., Michel, M., Carlier, S., Tasciotti, E., et al. (2005). Novel human-derived cell-penetrating peptides for specific subcellular delivery of therapeutic biomolecules. *Biochem. J.* 390, 407–418. doi: 10.1042/BJ20050401

Derakhshankhah, H., and Jafari, S. (2018). Cell penetrating peptides: A concise review with emphasis on biomedical applications. *Biomed. Pharmacother.* 108, 1090–1096. doi: 10.1016/j.biopha.2018.09.097

Derossi, D., Joliot, A. H., Chassaing, G., and Prochiantz, A. (1994). The 3rd Helix Of The Antennapedia Homeodomain Translocates Through Biological-Membranes. *J. Biol. Chem.* 269, 10444–10450.

Dinca, A., Chien, W.-M., and Chin, M. (2016). Intracellular delivery of proteins with cell-penetrating peptides for therapeutic uses in human disease. *Int.J. Mol. Sci.* 17 (2), 263. doi: 10.3390/ijms17020263

Doss, M., Kolb, H. C., Zhang, J. J., Belanger, M. J., Stubbs, J. B., Stabin, M. G., et al. (2012). Biodistribution and Radiation Dosimetry of the Integrin Marker 18F-RGD-K5 Determined from Whole-Body PET/CT in Monkeys and Humans. *J. Nuclear Med.* 53, 787–795. doi: 10.2967/jnumed.111.088955

Dougherty, P. G., Sahni, A., and Pei, D. (2019). Understanding Cell Penetration of Cyclic Peptides. *Chem. Rev.* 119, 10241–10287. doi: 10.1021/acs.chemrev.9b00008

Eggimann, G. A., Blattes, E., Buschor, S., Biswas, R., Kammer, S. M., Darbre, T., et al. (2014). Designed cell penetrating peptide dendrimers efficiently internalize cargo into cells. *Chem. Commun. (Camb)* 50, 7254–7257. doi: 10.1039/C4CC02780A

Eiriksdottir, E., Konate, K., Langel, U., Divita, G., and Deshayes, S. (2010). Secondary structure of cell-penetrating peptides controls membrane interaction and insertion. *Biochim. Biophys. Acta* 1798, 1119–1128. doi: 10.1016/j.bbamem.2010.03.005

El-Andaloussi, S., Johansson, H. J., Lundberg, P., and Langel, Ü. (2006). Induction of splice correction by cell-penetrating peptide nucleic acids. *J. Gene Med.* 8 (10), 1262–1273. doi: 10.1002/jgm.950

El-Sayed, A., Futaki, S., and Harashima, H. (2009). Delivery of macromolecules using arginine-rich cell-penetrating peptides: ways to overcome endosomal entrapment. *AAPS J.* 11 (1), 13–22. doi: 10.1208/s12248-008-9071-2

Erazo-Oliveras, A., Muthukrishnan, N., Baker, R., Wang, T.-Y., and Pellois, J.-P. (2012). Improving the Endosomal Escape of Cell-Penetrating Peptides and Their Cargos: Strategies and Challenges. *Pharmaceuticals* 5 (11), 1177–1209. doi: 10.3390/ph5111177

Eshraghi, A. A., Aranke, M., Salvi, R., Ding, D., Coleman, J. K. M., Ocak, E., et al. (2018). Preclinical and clinical otoprotective applications of cell-penetrating peptide D-JNKI-1 (AM-111). *Hearing Res.* 368, 86–91. doi: 10.1016/j.heares.2018.03.003

Favaro, M. T. D. P., Serna, N., Sánchez-García, L., Cubarsi, R., Roldán, M., Sánchez-Chardi, A., et al. (2018). Switching cell penetrating and CXCR4-binding activities of nanoscale-organized arginine-rich peptides. *Nanotechnol. Biol. Med.* 14, 1777–1786. doi: 10.1016/j.nano.2018.05.002

Finkelstein, D. I., Lev, N., Barhum, Y., Ben-Zur, T., Aharony, I., Trifonov, L., et al. (2015). A DJ-1 Based Peptide Attenuates Dopaminergic Degeneration in Mice Models of Parkinson's Disease via Enhancing Nrf2. *PloS One* 10, e0127549. doi: 10.1371/journal.pone.0127549

Fittipaldi, A., Ferrari, A., Zoppé, M., Arcangeli, C., Pellegrini, V., Beltram, F., et al. (2003). Cell Membrane Lipid Rafts Mediate Caveolar Endocytosis of HIV-1 Tat Fusion Proteins. *J. Biol. Chem.* 278, 34141–34149. doi: 10.1074/jbc.M303045200

Frankel, A. D., and Pabo, C. O. (1988). Cellular uptake of the tat protein from human immunodeficiency virus. *Cell* 55 (6), 1189–1193. doi: 10.1016/0092-8674(88)90263-2

Fretz, M., Penning, N., Al-Taei, S., Futaki, S., Takeuchi, T., Nakase, I., et al. (2007). Temperature-, concentration- and cholesterol-dependent translocation of L- and D-octa-arginine across the plasma and nuclear membrane of CD34+ leukaemia cells. *Biochem. J.* 403, 335–342. doi: 10.1042/BJ20061808

Futaki, S., Suzuki, T., Ohashi, W., Yagami, T., Tanaka, S., Ueda, K., et al. (2001). Arginine-rich Peptides. *J. Biol. Chem.* 276, 5836–5840. doi: 10.1074/jbc.M007540200

Futaki, S., Nakase, I., Tadokoro, A., Takeuchi, T., and Jones, A. T. (2007). Arginine-rich peptides and their internalization mechanisms. *Biochem. Soc. Trans.* 35, 784–787. doi: 10.1042/BST0350784

Galdiero, S., Falanga, A., Morelli, G., and Galdiero, M. (2015). gH625: A milestone in understanding the many roles of membranotropic peptides. *Biochim. Biophys. Acta (BBA) Biomembr.* 1848, 16–25. doi: 10.1016/j.bbamem.2014.10.006

Gao, W., Yang, X., Lin, Z., He, B., Mei, D., Wang, D., et al. (2017). The use of electronic-neutral penetrating peptides cyclosporin A to deliver pro-apoptotic peptide: A possibly better choice than positively charged TAT. *J. Controlled Release* 261, 174–186. doi: 10.1016/j.jconrel.2017.06.018

Gao, L., Yu, J., Liu, Y., Zhou, J., Sun, L., Wang, J., et al. (2018a). Tumor-penetrating Peptide Conjugated and Doxorubicin Loaded T1-T2 Dual Mode MRI Contrast Agents Nanoparticles for Tumor Theranostics. *Theranostics* 8, 92–108. doi: 10.7150/thno.21074

Gao, P., Mei, C., He, L., Xiao, Z., Chan, L., Zhang, D., et al. (2018b). Designing multifunctional cancer-targeted nanosystem for magnetic resonance molecular imaging-guided theranostics of lung cancer. *Drug Deliv.* 25, 1811–1825. doi: 10.1080/10717544.2018.1494224

Gao, S., Tian, B., Han, J., Zhang, J., Shi, Y., Lv, Q., et al. (2019). Enhanced transdermal delivery of lornoxicam by nanostructured lipid carrier gels modified with polyarginine peptide for treatment of carrageenan-induced rat paw edema. *Int. J. Nanomed. Volume* 14, 6135–6150. doi: 10.2147/IJN.S205295

Gomez, J. A., Chen, J., Ngo, J., Hajkova, D., Yeh, I. J., Gama, V., et al. (2010). Cell-Penetrating Penta-Peptides (CPP5s): Measurement of Cell Entry and Protein-Transduction Activity. *Pharmaceut. (Basel)* 3, 3594–3613. doi: 10.3390/ph3123594

Grasso, G., Mercuri, S., Danani, A., and Deriu, M. A. (2019). Biofunctionalization of Silica Nanoparticles with Cell-Penetrating Peptides: Adsorption Mechanism and Binding Energy Estimation. *J. Phys. Chem. B* 123, 10622–10630. doi: 10.1021/acs.jpcb.9b08106

Green, M., and Loewenstein, P. M. (1988). Autonomous functional domains of chemically synthesized human immunodeficiency virus tat trans-activator protein. *Cell* 55 (6), 1179–1188. doi: 10.1016/0092-8674(88)90262-0

Groves, J. T. (2019). Membrane mechanics in living cells. *Developmental Cell* 48 (1), 15–16. doi: 10.1016/j.devcel.2018.12.011

Guidotti, G., Brambilla, L., and Rossi, D. (2017). Cell-Penetrating Peptides: From Basic Research to Clinics. *Trends Pharmacol. Sci.* 38, 406–424. doi: 10.1016/j.tips.2017.01.003

Guo, F., Ouyang, T., Peng, T., Zhang, X., Xie, B., Yang, X., et al. (2019). Enhanced oral absorption of insulin using colon-specific nanoparticles co-modified with amphiphilic chitosan derivatives and cell-penetrating peptides. *Biomater. Sci.* 7, 1493–1506. doi: 10.1039/C8BM01485J

Gupta, B., Levchenko, T. S., and Torchilin, V. P. (2005). Intracellular delivery of large molecules and small particles by cell-penetrating proteins and peptides. *Adv. Drug Delivery Rev.* 57, 637–651. doi: 10.1016/j.addr.2004.10.007

Habault, J., and Poyet, J.-L. (2019). Recent Advances in Cell Penetrating Peptide-Based Anticancer Therapies. *Molecules* 24, 927. doi: 10.3390/molecules24050927

Hansen, M. B., van Gaal, E., Minten, I., Storm, G., van Hest, J. C. M., and Löwik, D. W. P. M. (2012). Constrained and UV-activatable cell-penetrating peptides for intracellular delivery of liposomes. *J. Control. Release* 164 (1), 87–94. doi: 10.1016/j.jconrel.2012.10.008

Hao, F., Li, Y., Zhu, J., Sun, J., Marshall, B., Lee, R. J., et al. (2019). Polyethylenimine-based Formulations for Delivery of Oligonucleotides. *Curr. Med. Chem.* 26, 2264–2284. doi: 10.2174/0929867325666181031094759

He, H., Ye, J., Liu, E., Liang, Q., Liu, Q., and Yang, V. C. (2014). Low molecular weight protamine (LMWP): A nontoxic protamine substitute and an effective cell-penetrating peptide. *J. Control. Release* 193, 63–73. doi: 10.1016/j.jconrel.2014.05.056

Horton, K. L., Stewart, K. M., Fonseca, S. B., Guo, Q., and Kelley, S. O. (2008). Mitochondria-penetrating peptides. *Chem. Biol.* 15 (4), 375–382. doi: 10.1016/j.chembiol.2008.03.015

Hou, K. K., Pan, H., Lanza, G. M., and Wickline, S. A. (2013). Melittin derived peptides for nanoparticle based siRNA transfection. *Biomaterials* 34, 3110–3119. doi: 10.1016/j.biomaterials.2013.01.037

Hu, H., Wang, J., Wang, H., Tan, T., Li, J., Wang, Z., et al. (2018). Cell-penetrating peptide-based nanovehicles potentiate lymph metastasis targeting and deep penetration for anti-metastasis therapy. *Theranostics* 8, 3597–3610. doi: 10.7150/thno.25608

Huang, Y., Shin Park, Y., Wang, J., Moon, C., Min Kwon, Y., Sun Chung, H., et al. (2010). ATTEMPTS System: A Macromolecular Prodrug Strategy for Cancer Drug Delivery. *Curr. Pharm. Design* 16 (21), 2369–2376. doi: 10.2174/138161210791920441

Huang, Y., Jiang, Y., Wang, H., Wang, J., Shin, M. C., Byun, Y., et al. (2013). Curb challenges of the "Trojan Horse" approach: Smart strategies in achieving effective yet safe cell-penetrating peptide-based drug delivery. *Adv. Drug Deliv. Rev.* 65 (10), 1299–1315. doi: 10.1016/j.addr.2012.11.007

Islam, M. Z., Sharmin, S., Moniruzzaman, M., and Yamazaki, M. (2018). Elementary processes for the entry of cell-penetrating peptides into lipid bilayer vesicles and bacterial cells. *Appl. Microbiol. Biotechnol.* 102, 3879–3892. doi: 10.1007/s00253-018-8889-5

Jackson, I. M., Scott, P. J. H., and Thompson, S. (2017). Clinical Applications of Radiolabeled Peptides for PET. *Semin. Nuclear Med.* 47, 493–523. doi: 10.1053/j.semnuclmed.2017.05.007

Järver, P., Mäger, I., and Langel, Ü. (2010). In vivo biodistribution and efficacy of peptide mediated delivery. *Trends Pharmacol. Sci.* 31 (11), 528–535. doi: 10.1016/j.tips.2010.07.006

Jauset, T., and Beaulieu, M.-E. (2019). Bioactive cell penetrating peptides and proteins in cancer: a bright future ahead. *Curr. Opin. Pharmacol.* 47, 133–140. doi: 10.1016/j.coph.2019.03.014

Jeong, E. J., Choi, M., Lee, J., Rhim, T., and Lee, K. Y. (2015). The spacer arm length in cell-penetrating peptides influences chitosan/siRNA nanoparticle delivery for pulmonary inflammation treatment. *Nanoscale* 7, 20095–20104. doi: 10.1039/C5NR06903C

Jiang, T., Olson, E. S., Nguyen, Q. T., Roy, M., Jennings, P. A., and Tsien, R. Y. (2004). Tumor imaging by means of proteolytic activation of cell-penetrating peptides. *Proc. Natl. Acad. Sci.* 101, 17867–17872. doi: 10.1073/pnas.0408191101

Jiao, X., Yu, Y., Meng, J., He, M., Zhang, C. J., Geng, W., et al. (2019). Dual-targeting and microenvironment-responsive micelles as a gene delivery system to improve the sensitivity of glioma to radiotherapy. *Acta Pharmaceutica Sinica B* 9 (2), 381–396. doi: 10.1016/j.apsb.2018.12.001

Joliot, A., Pernelle, C., Deagostini-Bazin, H., and Prochiantz, A. (1991). Antennapedia homeobox peptide regulates neural morphogenesis. *Proceedings of the National Academy of Sciences* 88 (5), 1864–1868. doi: 10.1073/pnas.88.5.1864

Johansson, H. J., El-Andaloussi, S., Holm, T., Mäe, M., Jänes, J., Maimets, T., et al. (2008). Characterization of a Novel Cytotoxic Cell-penetrating Peptide Derived From p14ARF Protein. *Mol. Ther.* 16, 115–123. doi: 10.1038/sj.mt.6300346

Kadonosono, T., Yamano, A., Goto, T., Tsubaki, T., Niibori, M., Kuchimaru, T., et al. (2015). Cell penetrating peptides improve tumor delivery of cargos through neuropilin-1-dependent extravasation. *J. Controlled Release* 201, 14–21. doi: 10.1016/j.jconrel.2015.01.011

Kang, C., Sun, Y., Zhu, J., Li, W., Zhang, A., Kuang, T., et al. (2016). Delivery of Nanoparticles for Treatment of Brain Tumor. *Curr. Drug Metab.* 17, 745–754. doi: 10.2174/1389200217666160728152939

Kang, Y. C., Son, M., Kang, S., Im, S., Piao, Y., Lim, K. S., et al. (2018). Cell-penetrating artificial mitochondria-targeting peptide-conjugated metallothionein 1A alleviates mitochondrial damage in Parkinson's disease models. *Exp. Mol. Med.* 50, 105. doi: 10.1038/s12276-018-0124-z

Kauffman, W. B., Fuselier, T., He, J., and Wimley, W. C. (2015). Mechanism Matters: A Taxonomy of Cell Penetrating Peptides. *Trends Biochem. Sci.* 40, 749–764. doi: 10.1016/j.tibs.2015.10.004

Kim, M. J., Park, M., Kim, D. W., Shin, M. J., Son, O., Jo, H. S., et al. (2015). Transduced PEP-1-PON1 proteins regulate microglial activation and dopaminergic neuronal death in a Parkinson's disease model. *Biomaterials* 64, 45–56. doi: 10.1016/j.biomaterials.2015.06.015

Kim, J. Y., Ahn, J., Kim, J., Choi, M., Jeon, H., Choe, K., et al. (2018). Nanoparticle-Assisted Transcutaneous Delivery of a Signal Transducer and Activator of Transcription 3-Inhibiting Peptide Ameliorates Psoriasis-like Skin Inflammation. *ACS Nano* 12, 6904–6916. doi: 10.1021/acsnano.8b02330

Kristensen, M., Franzyk, H., Klausen, M. T., Iversen, A., Bahnsen, J. S., Skyggebjerg, R. B., et al. (2015). Penetratin-Mediated Transepithelial Insulin

Permeation: Importance of Cationic Residues and pH for Complexation and Permeation. *AAPS J.* 17, 1200–1209. doi: 10.1208/s12248-015-9747-3

Kristensen, M., Birch, D., and Mørck Nielsen, H. (2016). Applications and Challenges for Use of Cell-Penetrating Peptides as Delivery Vectors for Peptide and Protein Cargos. *Int. J. Mol. Sci.* 17, 185. doi: 10.3390/ijms17020185

Lee, S. H., Moroz, E., Castagner, B., and Leroux, J. C. (2014). Activatable cell penetrating peptide-peptide nucleic acid conjugate via reduction of azobenzene PEG chains. *J. Am. Chem. Soc.* 136, 12868–12871. doi: 10.1021/ja507547w

Lee, Y. Y., Lee, S. Y., Park, S.-Y., Choi, H.-J., Kim, E.-G., and Han, J.-S. (2018). Therapeutic potential of a phospholipase D1 inhibitory peptide fused with a cell-penetrating peptide as a novel anti-asthmatic drug in a Der f 2-induced airway inflammation model. *Exp. Mol. Med.* 50, 1–11. doi: 10.1038/s12276-018-0187-x

Liang, J. F., and Yang, V. C. (2005). Insulin-cell penetrating peptide hybrids with improved intestinal absorption efficiency. *Biochem. Biophys. Res. Commun.* 335, 734–738. doi: 10.1016/j.bbrc.2005.07.142

Lindgren, M., Hällbrink, M., Prochiantz, A., and Langel, U. (2000). Cell-penetrating peptides. *Trends Pharmacol. Sci.* 21, 99–103. doi: 10.1016/S0165-6147(00)01447-4

Liu, C., Tai, L., Zhang, W., Wei, G., Pan, W., and Lu, W. (2014). Penetratin, a Potentially Powerful Absorption Enhancer for Noninvasive Intraocular Drug Delivery. *Mol. Pharmaceut.* 11, 1218–1227. doi: 10.1021/mp400681n

Liu, Y., Song, Z., Zheng, N., Nagasaka, K., Yin, L., and Cheng, J. (2018). Systemic siRNA delivery to tumors by cell-penetrating α-helical polypeptide-based metastable nanoparticles. *Nanoscale* 10, 15339–15349. doi: 10.1039/C8NR03976C

Lo, J. H., Hao, L., Muzumdar, M. D., Raghavan, S., Kwon, E. J., Pulver, E. M., et al. (2018). iRGD-guided Tumor-penetrating Nanocomplexes for Therapeutic siRNA Delivery to Pancreatic Cancer. *Mol. Cancer Ther.* 17, 2377–2388. doi: 10.1158/1535-7163.MCT-17-1090

Lo, S. L., and Wang, S. (2008). An endosomolytic Tat peptide produced by incorporation of histidine and cysteine residues as a nonviral vector for DNA transfection. *Biomaterials* 29 (15), 2408–2414. doi: 10.1016/j.biomaterials.2008.01.031

Lulla, R. R., Goldman, S., Yamada, T., Beattie, C. W., Bressler, L., Pacini, M., et al. (2016). Phase I trial of p28 (NSC745104), a non-HDM2-mediated peptide inhibitor of p53 ubiquitination in pediatric patients with recurrent or progressive central nervous system tumors: A Pediatric Brain Tumor Consortium Study. *Neuro-Oncology* 18, 1319–1325. doi: 10.1093/neuonc/now047

Maderna, E., Colombo, L., Cagnotto, A., Di Fede, G., Indaco, A., Tagliavini, F., et al. (2018). In Situ Tissue Labeling of Cerebral Amyloid Using HIV-Related Tat Peptide. *Mol. Neurobiol.* 55, 6834–6840. doi: 10.1007/s12035-018-0870-x

Mandal, D., Nasrolahi Shirazi, A., and Parang, K. (2011). Cell-penetrating homochiral cyclic peptides as nuclear-targeting molecular transporters. *Angew Chem. Int. Ed Engl.* 50, 9633–9637. doi: 10.1002/anie.201102572

Mcclorey, G., and Banerjee, S. (2018). Cell-Penetrating Peptides to Enhance Delivery of Oligonucleotide-Based Therapeutics. *Biomedicines* 6, 51. doi: 10.3390/biomedicines6020051

McAtee, C. O., Barycki, J. J., and Simpson, M. A. (2014). "Emerging Roles for Hyaluronidase in Cancer Metastasis and Therapy," in *Hyaluronan Signaling and Turnover*, eds. M. A. Simpson and P Heldin (San Diego: Elsevier Academic Press Inc), p. 1–34.

Meloni, B. P., Brookes, L. M., Clark, V. W., Cross, J. L., Edwards, A. B., Anderton, R. S., et al. (2015). Poly-Arginine and Arginine-Rich Peptides are Neuroprotective in Stroke Models. *J. Cereb. Blood Flow Metab.* 35, 993–1004. doi: 10.1038/jcbfm.2015.11

Meng, F., Sun, Y., Lee, R. J., Wang, G., Zheng, X., Zhang, H., et al. (2019). Folate Receptor-Targeted Albumin Nanoparticles Based on Microfluidic Technology to Deliver Cabazitaxel. *Cancers (Basel)* 11, 1571. doi: 10.3390/cancers11101571

Miampamba, M., Liu, J., Harootunian, A., Gale, A. J., Baird, S., Chen, S. L., et al. (2017). Sensitive in vivo Visualization of Breast Cancer Using Ratiometric Protease-activatable Fluorescent Imaging Agent, AVB-620. *Theranostics* 7, 3369–3386. doi: 10.7150/thno.20678

Milletti, F. (2012). Cell-penetrating peptides: classes, origin, and current landscape. *Drug Discovery Today* 17, 850–860. doi: 10.1016/j.drudis.2012.03.002

Mitchell, D. J., Steinman, L., Kim, D. T., Fathman, C. G., and Rothbard, J. B. (2000). Polyarginine enters cells more efficiently than other polycationic homopolymers. *J. Pept. Res.* 56, 318–325. doi: 10.1034/j.1399-3011.2000.00723.x

Morishita, M., Kamei, N., Ehara, J., Isowa, K., and Takayama, K. (2007). A novel approach using functional peptides for efficient intestinal absorption of insulin. *J. Controlled Release* 118, 177–184. doi: 10.1016/j.jconrel.2006.12.022

Moutal, A., FranÃ§ois-Moutal, L., Brittain, J. M., Khanna, M., and Khanna, R. (2015). Differential neuroprotective potential of CRMP2 peptide aptamers conjugated to cationic, hydrophobic, and amphipathic cell penetrating peptides. *Front. Cell. Neurosci.* 8. doi: 10.3389/fncel.2014.00471

Munjal, A., Khandia, R., Kumar, A., Singh, G., Karthik, K., and Dhama, K. (2017). Cell Penetrating Peptides: Biomedical/Therapeutic Applications with Emphasis as Promising Futuristic Hope for Treating Cancer. *Int. J. Pharmacol.* 13, 677–689. doi: 10.3923/ijp.2017.677.689

Murray, B., Pearson, C. S., Aranjo, A., Cherupalla, D., and Belfort, G. (2016). Mechanism of Fourde NovoDesigned Antimicrobial Peptides. *J. Biol. Chem.* 291, 25706–25715. doi: 10.1074/jbc.M116.733816

Nakase, I., Noguchi, K., Aoki, A., Takatani-Nakase, T., Fujii, I., and Futaki, S. (2017). Arginine-rich cell-penetrating peptide-modified extracellular vesicles for active macropinocytosis induction and efficient intracellular delivery. *Sci. Rep.* 7, 1991. doi: 10.1038/s41598-017-02014-6

Nielsen, E. J. B., Yoshida, S., Kamei, N., Iwamae, R., Khafagy, E.-S., Olsen, J., et al. (2014). In vivo proof of concept of oral insulin delivery based on a co-administration strategy with the cell-penetrating peptide penetratin. *J. Controlled Release* 189, 19–24. doi: 10.1016/j.jconrel.2014.06.022

Olson, E. S., Jiang, T., Aguilera, T. A., Nguyen, Q. T., Ellies, L. G., Scadeng, M., et al. (2010). Activatable cell penetrating peptides linked to nanoparticles as dual probes for in vivo fluorescence and MR imaging of proteases. *Proc. Natl. Acad. Sci.* 107, 4311–4316. doi: 10.1073/pnas.0910283107

Onoshima, D., Yukawa, H., and Baba, Y. (2015). Multifunctional quantum dots-based cancer diagnostics and stem cell therapeutics for regenerative medicine. *Adv. Drug Deliv. Rev.* 95, 2–14. doi: 10.1016/j.addr.2015.08.004

Pae, J., Säälik, P., Liivamägi, L., Lubenets, D., Arukuusk, P., Langel, Ü., et al. (2014). Translocation of cell-penetrating peptides across the plasma membrane is controlled by cholesterol and microenvironment created by membranous proteins. *J. Controlled Release* 192, 103–113. doi: 10.1016/j.jconrel.2014.07.002

Pescina, S., Ostacolo, C., Gomez-Monterrey, I. M., Sala, M., Bertamino, A., Sonvico, F., et al. (2018). Cell penetrating peptides in ocular drug delivery: State of the art. *J. Controlled Release* 284, 84–102. doi: 10.1016/j.jconrel.2018.06.023

Pujals, S., and Giralt, E. (2008). Proline-rich, amphipathic cell-penetrating peptides. *Adv. Drug Deliv. Rev.* 60, 473–484. doi: 10.1016/j.addr.2007.09.012

Qian, Z., Martyna, A., Hard, R. L., Wang, J., Appiah-Kubi, G., Coss, C., et al. (2016). Discovery and Mechanism of Highly Efficient Cyclic Cell-Penetrating Peptides. *Biochemistry* 55, 2601–2612. doi: 10.1021/acs.biochem.6b00226

Quach, N. D., Arnold, R. D., and Cummings, B. S. (2014). Secretory phospholipase A2 enzymes as pharmacological targets for treatment of disease. *Biochem. Pharmacol.* 90 (4), 338–348. doi: 10.1016/j.bcp.2014.05.022

Rassu, G., Soddu, E., Posadino, A. M., Pintus, G., Sarmento, B., Giunchedi, P., et al. (2017). Nose-to-brain delivery of BACE1 siRNA loaded in solid lipid nanoparticles for Alzheimer's therapy. *Biointerfaces* 152, 296–301. doi: 10.1016/j.colsurfb.2017.01.031

Reissmann, S. (2014). Cell penetration: scope and limitations by the application of cell-penetrating peptides. *J. Pept. Sci.* 20, 760–784. doi: 10.1002/psc.2672

Rhee, M., and Davis, P. (2006). Mechanism of Uptake of C105Y, a Novel Cell-penetrating Peptide. *J. Biol. Chem.* 281, 1233–1240. doi: 10.1074/jbc.M509813200

Richard, J. P., Melikov, K., Brooks, H., Prevot, P., Lebleu, B., and Chernomordik, L. V. (2005). Cellular Uptake of Unconjugated TAT Peptide Involves Clathrin-dependent Endocytosis and Heparan Sulfate Receptors. *J. Biol. Chem.* 280, 15300–15306. doi: 10.1074/jbc.M401604200

Rusiecka, I., Ruczyński, J., Kozłowska, A., Backtrog, E., Mucha, P., Kocić, I., et al. (2019). TP10-Dopamine Conjugate as a Potential Therapeutic Agent in the Treatment of Parkinson's Disease. *Bioconjugate Chem.* 30, 760–774. doi: 10.1021/acs.bioconjchem.8b00894

Saar, K., Lindgren, M., Hansen, M., Eiríksdóttir, E., Jiang, Y., Rosenthal-Aizman, K., et al. (2005). Cell-penetrating peptides: A comparative membrane toxicity study. *Analytical Biochemistry* 345 (1), 55–65. doi: 10.1016/j.ab.2005.07.033

Savariar, E. N., Felsen, C. N., Nashi, N., Jiang, T., Ellies, L.G., Steinbach, P., et al. (2012). Real-time In Vivo Molecular Detection of Primary Tumors and Metastases with Ratiometric Activatable Cell-Penetrating Peptides. *Cancer Res.* 73 (2), 855–864. doi: 10.1158/0008-5472.can-12-2969

Sharma, G., Lakkadwala, S., Modgil, A., and Singh, J. (2016). The Role of Cell-Penetrating Peptide and Transferrin on Enhanced Delivery of Drug to Brain. *Int. J. Mol. Sci.* 17, 806. doi: 10.3390/ijms17060806

Shi, J., Ma, Y., Zhu, J., Chen, Y., Sun, Y., Yao, Y., et al. (2018). A Review on Electroporation-Based Intracellular Delivery. *Molecules* 23, 3044. doi: 10.3390/molecules23113044

Shin, M. C., Zhang, J., Min, K. A., Lee, K., Byun, Y., David, A. E., et al. (2014). Cell-penetrating peptides: Achievements and challenges in application for cancer treatment. *J. Biomed. Mater. Res. Part A* 102, 575–587. doi: 10.1002/jbm.a.34859

Shin, M. C., Zhao, J., Zhang, J., Huang, Y., He, H., Wang, M., et al (2015). Recombinant TAT-gelonin fusion toxin: Synthesis and characterization of heparin/protamine-regulated cell transduction. *J. Biomed. Mater. Res. Part A* 103 (1), 409–419. doi: 10.1002/jbm.a.35188

Simeoni, F. (2003). Insight into the mechanism of the peptide-based gene delivery system MPG: implications for delivery of siRNA into mammalian cells. *Nucleic Acids Res.* 31, 2717–2724. doi: 10.1093/nar/gkg385

Srimanee, A., Arvanitidou, M., Kim, K., Hällbrink, M., and Langel, Ü. (2018). Cell-penetrating peptides for siRNA delivery to glioblastomas. *Peptides* 104, 62–69. doi: 10.1016/j.peptides.2018.04.015

Staecker, H., Jokovic, G., Karpishchenko, S., Kienle-Gogolok, A., Krzyzaniak, A., Lin, C.-D., et al. (2019). Efficacy and Safety of AM-111 in the Treatment of Acute Unilateral Sudden Deafness—A Double-blind, Randomized, Placebo-controlled Phase 3 Study. *Otol. Neurotol.* 40, 584–594. doi: 10.1097/MAO.0000000000002229

Sun, X., Li, Y., Liu, T., Li, Z., Zhang, X., and Chen, X. (2017). Peptide-based imaging agents for cancer detection. *Adv. Drug Deliv. Rev.* 110-111, 38–51. doi: 10.1016/j.addr.2016.06.007

Swain, S., Sahu, P., Beg, S., and Babu, S. (2016). Nanoparticles for cancer targeting: current and future directions. *Current Drug Delivery* 13 (8), 1290–1302. doi: 10.2174/1567201813666160713121122

Szeto, H. H. (2006). Mitochondria-targeted peptide antioxidants: Novel neuroprotective agents. *AAPS J.* 8 (3), E521–E531. doi: 10.1208/aapsj080362

Tai, W., and Gao, X. (2017). Functional peptides for siRNA delivery. *Adv. Drug Deliv. Rev.* 110-111, 157–168. doi: 10.1016/j.addr.2016.08.004

Tai, L., Liu, C., Jiang, K., Chen, X., Wei, G., Lu, W., et al. (2017). Noninvasive delivery of oligonucleotide by penetratin-modified polyplexes to inhibit protein expression of intraocular tumor. *Nanotechnol. Biol. Med.* 13, 2091–2100. doi: 10.1016/j.nano.2017.04.011

Tammam, S. N., Azzazy, H. M. E., and Lamprecht, A. (2017). The effect of nanoparticle size and NLS density on nuclear targeting in cancer and normal cells; impaired nuclear import and aberrant nanoparticle intracellular trafficking in glioma. *J. Controlled Release* 253, 30–36. doi: 10.1016/j.jconrel.2017.02.029

Tang, B., Zaro, J. L., Shen, Y., Chen, Q., Yu, Y., Sun, P., et al. (2018). Acid-sensitive hybrid polymeric micelles containing a reversibly activatable cell-penetrating peptide for tumor-specific cytoplasm targeting. *J. Controlled Release* 279, 147–156. doi: 10.1016/j.jconrel.2018.04.016

Tashima, T. (2017). Intelligent substance delivery into cells using cell-penetrating peptides. *Bioorg. Med. Chem. Lett.* 27, 121–130. doi: 10.1016/j.bmcl.2016.11.083

Thennarasu, S., Tan, A., Penumatchu, R., Shelburne, C. E., Heyl, D. L., and Ramamoorthy, A. (2010). Antimicrobial and Membrane Disrupting Activities of a Peptide Derived from the Human Cathelicidin Antimicrobial Peptide LL37. *Biophys. J.* 98, 248–257. doi: 10.1016/j.bpj.2009.09.060

Tian, Y., Mi, G., Chen, Q., Chaurasiya, B., Li, Y., Shi, D., et al. (2018a). Acid-Induced Activated Cell-Penetrating Peptide-Modified Cholesterol-Conjugated Polyoxyethylene Sorbitol Oleate Mixed Micelles for pH-Triggered Drug Release and Efficient Brain Tumor Targeting Based on a Charge Reversal Mechanism. *ACS Appl. Mater. Interf.* 10, 43411–43428. doi: 10.1021/acsami.8b15147

Tian, Y., Zhou, M., Shi, H., Gao, S., Xie, G., Zhu, M., et al. (2018b). Integration of Cell-Penetrating Peptides with Rod-like Bionanoparticles: Virus-Inspired Gene-Silencing Technology. *Nano Lett.* 18, 5453–5460. doi: 10.1021/acs.nanolett.8b01805

Tobin, J. F., Laban, A., and Wirth, D. F. (1991). Homologous recombination in Leishmania enriettii. *Proc. Natl. Acad. Sci. U. S. A.* 88, 864–868. doi: 10.1073/pnas.88.3.864

Trabulo, S., Cardoso, A. L., Mano, M., and de Lima, M. C. P. (2010). Cell-penetrating peptides-mechanisms of cellular uptake and generation of delivery systems. *Pharmaceuticals* 3 (4), 961–993. doi: 10.3390/ph3040961

Traub, L. M. (2009). Tickets to ride: selecting cargo for clathrin-regulated internalization. *Nat. Rev. Mol. Cell Biol.* 10, 583–596. doi: 10.1038/nrm2751

Tripathi, P. P., Arami, H., Banga, I., Gupta, J., and Gandhi, S. (2018). Cell penetrating peptides in preclinical and clinical cancer diagnosis and therapy. *Oncotarget* 9, 37252–37267. doi: 10.18632/oncotarget.26442

Tru Van, N., Shin, M. C., Min, K. A., Huang, Y., Oh, E., and Moon, C. (2018). Cell-penetrating peptide-based non-invasive topical delivery systems. *J.Pharm. Investig.* 48 (1), 77–87. doi: 10.1007/s40005-017-0373-1

Tünnemann, G., Ter-Avetisyan, G., Martin, R. M., Stöckl, M., Herrmann, A., and Cardoso, M. C. (2008). Live-cell analysis of cell penetration ability and toxicity of oligo-arginines. *J.Pept. Sci.* 14 (4), 469–476. doi: 10.1002/psc.968

Unkart, J. T., Chen, S. L., Wapnir, I. L., González, J. E., Harootunian, A., and Wallace, A. M. (2017). Intraoperative Tumor Detection Using a Ratiometric Activatable Fluorescent Peptide: A First-in-Human Phase 1 Study. *Ann. Surg. Oncol.* 24, 3167–3173. doi: 10.1245/s10434-017-5991-3

Vale, N., Alves, C., Sharma, V., Lázaro, D. F., Silva, S., Gomes, P., et al. (2020). A new MAP-Rasagiline conjugate reduces α-synuclein inclusion formation in a cell model. *Pharmacol. Rep.* 72 (2), 456–464. doi: 10.1007/s43440-019-00032-x

Veloria, J. R., Li, L., Breen, G. A. M., and Goux, W. J. (2017). Novel Cell Model for Tauopathy Induced by a Cell-Permeable Tau-Related Peptide. *ACS Chem. Neurosci.* 8, 2734–2745. doi: 10.1021/acschemneuro.7b00275

Verdurmen, W. P., and Brock, R. (2011). Biological responses towards cationic peptides and drug carriers. *Trends Pharmacol. Sci.* 32, 116–124. doi: 10.1016/j.tips.2010.11.005

Vives, E., Brodin, P., and Lebleu, B. (1997). A truncated HIV-1 Tat protein basic domain rapidly translocates through the plasma membrane and accumulates in the cell nucleus. *J. Biol. Chem.* 272, 16010–16017. doi: 10.1074/jbc.272.25.16010

Wada, S.-I., Hashimoto, Y., Kawai, Y., Miyata, K., Tsuda, H., Nakagawa, O., et al. (2013). Effect of Ala replacement with Aib in amphipathic cell-penetrating peptide on oligonucleotide delivery into cells. *Bioorg. Med. Chem.* 21, 7669–7673. doi: 10.1016/j.bmc.2013.10.029

Wadia, J. S., Stan, R. V., and Dowdy, S. F. (2004). Transducible TAT-HA fusogenic peptide enhances escape of TAT-fusion proteins after lipid raft macropinocytosis. *Nat. Med.* 10, 310–315. doi: 10.1038/nm996

Walrant, A., Cardon, S., Burlina, F., and Sagan, S. (2017). Membrane crossing and membranotropic activity of cell-penetrating peptides: dangerous liaisons? *Acc. Chem. Res.* 50 (12), 2968–2975. doi: 10.1021/acs.accounts.7b00455

Wang, F., Wang, Y., Zhang, X., Zhang, W., Guo, S., and Jin, F. (2014). Recent progress of cell-penetrating peptides as new carriers for intracellular cargo delivery. *J. Controlled Release* 174, 126–136. doi: 10.1016/j.jconrel.2013.11.020

Xie, J., Teng, L., Yang, Z., Zhou, C., Liu, Y., Yung, B. C., et al. (2013). A polyethylenimine-linoleic acid conjugate for antisense oligonucleotide delivery. *BioMed. Res. Int.* 2013, 710502. doi: 10.1155/2013/710502

Xie, J., Yang, Z., Zhou, C., Zhu, J., Lee, R. J., and Teng, L. (2016). Nanotechnology for the delivery of phytochemicals in cancer therapy. *Biotechnol. Adv.* 34, 343–353. doi: 10.1016/j.biotechadv.2016.04.002

Xing, Y., Zhao, J., Conti, P. S., and Chen, K. (2014). Radiolabeled Nanoparticles for Multimodality Tumor Imaging. *Theranostics* 4, 290–306. doi: 10.7150/thno.7341

Xu, J., Khan, A. R., Fu, M., Wang, R., Ji, J., and Zhai, G. (2019). Cell-penetrating peptide: a means of breaking through the physiological barriers of different tissues and organs. *J. Control Release* 309, 106–124. doi: 10.1016/j.jconrel.2019.07.020

Yang, S.-T., Zaitseva, E., Chernomordik, L. V., and Melikov, K. (2010). Cell-penetrating peptide Induces leaky fusion of liposomes containing late endosome-specific anionic lipid. *Biophys. J.* 99 (8), 2525–2533. doi: 10.1016/j.bpj.2010.08.029

Yang, X. L., Xie, J., Niu, B., Hu, X. N., Gao, Y., Xiang, Q., et al. (2005). Structure analysis of the protein transduction domain of human Period1 and its mutant analogs. *J. Mol. Graphics Modell.* 23, 389–394. doi: 10.1016/j.jmgm.2004.11.008

Yang, Z., Yu, B., Zhu, J., Huang, X., Xie, J., Xu, S., et al. (2014). A microfluidic method to synthesize transferrin-lipid nanoparticles loaded with siRNA LOR-1284 for therapy of acute myeloid leukemia. *Nanoscale* 6, 9742–9751. doi: 10.1039/C4NR01510J

Yang, X., Yang, S., Chai, H., Yang, Z., Lee, R. J., Liao, W., et al. (2015). A Novel Isoquinoline Derivative Anticancer Agent and Its Targeted Delivery to Tumor Cells Using Transferrin-Conjugated Liposomes. *PloS One* 10, e0136649. doi: 10.1371/journal.pone.0136649

Yang, Z., Xie, J., Zhu, J., Kang, C., Chiang, C., Wang, X., et al. (2016). Functional exosome-mimic for delivery of siRNA to cancer: in vitro and in vivo evaluation. *J. Controlled Release* 243, 160–171. doi: 10.1016/j.jconrel.2016.10.008

Yang, J., Luo, Y., Shibu, M. A., Toth, I., and Skwarczynskia, M. (2019a). Cell-penetrating Peptides: Efficient Vectors for Vaccine Delivery. *Curr. Drug Deliv.* 16, 430–443. doi: 10.2174/1567201816666190123120915

Yang, Z., Ma, Y., Zhao, H., Yuan, Y., and Kim, B. Y. S. (2019b). Nanotechnology platforms for cancer immunotherapy. *WIREs Nanomed. Nanobiotechnol.* 12, e1590. doi: 10.1002/wnan.1590

Yang, Z., Shi, J., Xie, J., Wang, Y., Sun, J., Liu, T., et al. (2019c). Large-scale generation of functional mRNA-encapsulating exosomes via cellular nanoporation. *Nat. Biomed. Eng.* 4, 69–83. doi: 10.1038/s41551-019-0485-1

Yang, Y., Xia, M., Zhang, S., and Zhang, X. (2020). Cell-penetrating peptide-modified quantum dots as a ratiometric nanobiosensor for the simultaneous sensing and imaging of lysosomes and extracellular pH. *Chem. Commun.* 56, 145–148. doi: 10.1039/C9CC07596H

Ye, J., Shin, M.C., Liang, Q., He, H., and Yang, V. C. (2015). 15 years of ATTEMPTS: A macromolecular drug delivery system based on the CPP-mediated intracellular drug delivery and antibody targeting. *J. Control. Release* 205, 58–69. doi: 10.1016/j.jconrel.2014.12.002

Yin, T., Xie, W., Sun, J., Yang, L., and Liu, J. (2016). Penetratin Peptide-Functionalized Gold Nanostars: Enhanced BBB Permeability and NIR Photothermal Treatment of Alzheimer's Disease Using Ultralow Irradiance. *ACS Appl. Mater. Interf.* 8, 19291–19302. doi: 10.1021/acsami.6b05089

Zhang, P., Cui, Y., Anderson, C. F., Zhang, C., Li, Y., Wang, R., et al. (2018a). Peptide-based nanoprobes for molecular imaging and disease diagnostics. *Chem. Soc. Rev.* 47, 3490–3529. doi: 10.1039/C7CS00793K

Zhang, Z., Yuan, Y., Liu, Z., Chen, H., Chen, D., Fang, X., et al. (2018b). Brightness Enhancement of Near-Infrared Semiconducting Polymer Dots for in Vivo Whole-Body Cell Tracking in Deep Organs. *ACS Appl. Mater. Interf.* 10, 26928–26935. doi: 10.1021/acsami.8b08735

Zhao, X.-L., Chen, B.-C., Han, J.-C., Wei, L., and Pan, X.-B. (2015). Delivery of cell-penetrating peptide-peptide nucleic acid conjugates by assembly on an oligonucleotide scaffold. *Sci. Rep.* 5, 17640. doi: 10.1038/srep17640

Zhao, H., Wu, M., Zhu, L., Tian, Y., Wu, M., Li, Y., et al. (2018). Cell-penetrating Peptide-modified Targeted Drug-loaded Phase-transformation Lipid Nanoparticles Combined with Low-intensity Focused Ultrasound for Precision Theranostics against Hepatocellular Carcinoma. *Theranostics* 8, 1892–1910. doi: 10.7150/thno.22386

Zhou, C., Yang, Z., and Teng, L. (2014). Nanomedicine based on nucleic acids: pharmacokinetic and pharmacodynamic perspectives. *Curr. Pharm. Biotechnol.* 15, 829–838. doi: 10.2174/1389201015666141020155620

Zhu, P., and Jin, L. (2017). Cell Penetrating Peptides: A Promising Tool for the Cellular Upta ke of Macromolecular Drugs. *Curr. Protein Pept. Sci.* 19, 211–220. doi: 10.2174/1389203718666170710115240

Zhu, L., Kate, P., and Torchilin, V. P. (2012). Matrix Metalloprotease 2-Responsive Multifunctional Liposomal Nanocarrier for Enhanced Tumor Targeting. *ACS Nano* 6, 3491–3498. doi: 10.1021/nn300524f

Zhu, Z., Tian, D., Gao, P., Wang, K., Li, Y., Shu, X., et al. (2018). Cell-Penetrating Peptides Transport Noncovalently Linked Thermally Activated Delayed Fluorescence Nanoparticles for Time-Resolved Luminescence Imaging. *J. Am. Chem. Soc.* 140, 17484–17491. doi: 10.1021/jacs.8b08438

Zorko, M., and Langel, U. (2005). Cell-penetrating peptides: mechanism and kinetics of cargo delivery. *Adv. Drug Deliv. Rev.* 57 (4), 529–545. doi: 10.1016/j.addr.2004.10.010

Conflict of Interest: The authors declare that the research was conducted in the absence of any commercial or financial relationships that could be construed as a potential conflict of interest.

frontiers in Pharmacology

ORIGINAL RESEARCH
published: 04 June 2020
doi: 10.3389/fphar.2020.00795

A Lipid-Nanosphere-Small MyoD Activating RNA-Bladder Acellular Matrix Graft Scaffold [NP(saMyoD)/BAMG] Facilitates Rat Injured Bladder Muscle Repair and Regeneration [NP(saMyoD)/BAMG]

Chongrui Jin[1,2], *Nailong Cao*[1,2], *Jianshu Ni*[1,2], *Weixin Zhao*[3], *Baojun Gu*[1,2]* *and Weidong Zhu*[1,2]*

[1] Department of Urology, Shanghai Jiao Tong University Affiliated Sixth People's Hospital, Shanghai, China, [2] Department of Urology, Shanghai Eastern Urological Reconstruction and Repair Institute, Shanghai, China, [3] Wake Forest Institute for Regenerative Medicine, Winston-Salem, NC, United States

OPEN ACCESS

Edited by:
Jianxun Ding,
Chinese Academy of Sciences, China

Reviewed by:
Xiaoqing Wang,
First Affiliated Hospital of Jilin University, China
Weiguo Xu,
Chinese Academy of Sciences, China
Lesan Yan,
Wuhan University of Technology, China

***Correspondence:**
Baojun Gu
gubaojun@yahoo.com
Weidong Zhu
Zhuweidong-1981@163.com

Specialty section:
This article was submitted to Experimental Pharmacology and Drug Discovery, a section of the journal Frontiers in Pharmacology

Received: 11 March 2020
Accepted: 14 May 2020
Published: 04 June 2020

Citation:
Jin C, Cao N, Ni J, Zhao W, Gu B and Zhu W (2020) A Lipid-Nanosphere-Small MyoD Activating RNA-Bladder Acellular Matrix Graft Scaffold [NP(saMyoD)/BAMG] Facilitates Rat Injured Bladder Muscle Repair and Regeneration [NP(saMyoD)/BAMG]. Front. Pharmacol. 11:795. doi: 10.3389/fphar.2020.00795

Background: Bladder tissue engineering is an excellent alternative to conventional gastrointestinal bladder enlargement in the treatment of various acquired and congenital bladder abnormalities. We constructed a nanosphere-small MyoD activating RNA-bladder acellular matrix graft scaffold NP(saMyoD)/BAMG inoculated with adipose-derived stem cells (ADSC) to explore its effect on smooth muscle regeneration and bladder repair function in a rat augmentation model.

Methods: We performed many biotechniques, such as reverse transcriptase-polymerase chain reaction (RT-PCR), Western blot, MTT assay, HE staining, masson staining, and immunohistochemistry in our study. Lipid nanospheres were transfected into rat ADSCs after encapsulate saRNA-MyoD as an introduction vector. Lipid nanospheres encapsulated with saRNA-MyoD were transfected into rat ADSCs. The functional transfected rat ADSCs were called ADSC-NP(saMyoD). Then, Rat models were divided into four groups: sham group, ADSC-BAMG group, ADSC-NP(saMyoD)/BAMG group, and ADSC-NP(saMyoD)/SF(VEGF)/BAMG group. Finally, we compared the bladder function of different models by detecting the bladder histology, bladder capacity, smooth muscle function in each group.

Results: RT-PCR and Western blot results showed that ADSCs transfected with NP (saMyoD) could induce high expression of α-SMA, SM22α, and Desmin. At the same time, MTT analysis showed that NP(saMyoD) did not affect the activity of ADSC cells, suggesting little toxicity. HE staining and immunohistochemistry indicated that the rat bladder repair effect (smooth muscle function, bladder capacities) was better in the ADSC-NP(saMyoD)/BAMG group, ADSC-NP(saMyoD)/SF(VEGF)/BAMG group than in the control group.

Conclusions: Taken together, our results demonstrate that the NP(saMyoD)/SF(VEGF)/BAMG scaffold seeded with ADSCs could promote bladder morphological regeneration and improved bladder urinary function. This strategy of ADSC-NP(saMyoD)/SF(VEGF)/BAMG may has a potential to repair bladder defects in the future.

Keywords: nanospheres, adipose-derived stem cells, bladder regeneration, bladder acellular matrix graft, saRNA-MyoD

INTRODUCTION

Reconstruction of the bladder is imminent in various congenital and acquired urinary tract diseases, such as neuro-bladder, bladder cancer, and congenital bladder abnormalities (Lam Van Ba et al., 2015). Bowel segment grafting has been popular for decades as the gold standard for augmentation cystoplasty or neo-bladder creation. Due to the appropriate mechanical endurance, accessibility and anatomical vascularization of the intestinal wall, it is a justified choice for bladder reconstruction. However, there are still many adverse effects, including urolithiasis, urinary tract infections, secondary malignancies, and electrolyte imbalance (Xiao et al., 2017). In the context of the imminent need for new alternatives to entero-cystoplasty, the augmentation of tissue-engineered (TE) bladder brings a new approach to bladder reconstruction (Adamowicz et al., 2019).

The basic principle mode of TE combines biologically active seed cells with scaffold materials to form a specific active material, which is acceptable for the body to promote the regeneration of bladder tissue effectively for bladder regeneration (Ardeshirylajimi et al., 2018). Among them, scaffolds and seed cells are two core elements of tissue engineering. Bladder acellular matrix graft (BAMG) has been proposed as a preferable scaffold with the same extracellular matrix composition, mechanical properties and complexity, comparing with native tissue (Coutu et al., 2014). In our previous work, we encapsulated vascular endothelial growth factor (VEGF) with silk fibroin (SF) fiber. Then we performed coaxial electrospinning technique to develop SF(VEGF)/BAMG ford a sustained-release system of VEGF, and verified its role in stimulating the growth of urethra epitheliums and smooth muscle cells (Zhu et al., 2016).

In recent years, stem cells have been widely used in tissue engineering as seed cells (Mousa et al., 2015). Adipose tissue-derived stem cells (ADSCs) are one of the most easily acquired adult stem cells and have good proliferation and differentiation ability on the surface of BAMG (Wang et al., 2019).However, some researchers showed that only a small number of ADSCs can differentiate into smooth muscle cells, and most ADSCs remain undifferentiated (Pokrywczynska et al., 2018), so increasing myogenic differentiation of ADSCs will help to reconstruct bladder function. MyoD is a member of the MRFs (myogenic regulatory factors) family of myogenic regulators. Several studies have confirmed that terminally differentiated mature adipocytes can promote myogenic proliferation through MyoD (Kocaefe et al., 2005; Kabadi et al., 2015; Wang C. et al., 2017). At present, the commonly used method is to simply adsorb the growth factor on the material. From the related literature reports and clinical application results, this method has great deficiencies: First, the combination of associated growth factors and biological materials is challengeable, owing to its diffusion degradation and unstable function in human body (Chen et al., 2014). Therefore, it is necessary to explore the application of a new method that applies MyoD in a RNA activation (RNAa) provides a new way to promote upregulation of endogenous gene expression. However, most of the nucleic acid substances are polyanions, which are difficult to penetrate the cell membrane, less intracellular accumulation, and easily degraded by nuclease during transport. Nanogene introduction vectors have attracted extensive attention due to the advantage of low toxicity, nonimmunogenicity, large loading capacity, and ease of preparation (Yang et al., 2015). Among them, lipid nanospheres (NPs) are currently the most widely used developed carrier, compared with other inorganic nanocarriers and viral-based systems, lipid nanocarriers have good biocompatibility and biodegradability (Vargas and Shon, 2019).

Based on our previous silk fibroin NPs SF(VEGF), the lipid NPs were used as the carrier of saRNA-MyoD to form a composite scaffold with BAMG, and inoculated into ADSCs. In the rat bladder defect model repair and functional recovery, trying to explore its application value for the clinical study and try to solve the current clinical bladder reconstruction problems.

MATERIALS AND METHODS

ADSCs Isolation and Culture

Fifty- to sixty-gram Sprague Dawley (SD) rats (purchased from the Animal Center of Shanghai Jiaotong University) were anesthetized with 10% chloral hydrate, and the inguinal subcutaneous fat was excised and soaked three times with 0.25% chloramphenicol. The tissue was then minced and digested with 0.1% type I collagenase (Sigma-Aldrich Co. LLC., MO, USA) for 45 min at 37°C, filtered with a 200-mm nylon strainer (BD Falcon, Corning Inc., NY, USA) and collected by centrifugation (1,500 r/min, 10 min, 37°C). The upper layer of fat

Abbreviations: ADSC, adipose tissue-derived stem cells; ADSC-BAMG, bladder acellular matrix graft seeded with ADSCs; BAMG, bladder acellular matrix graft; NP, nanospheres; NP(saMyoD)/BAMG, nanosphere encapsulated with small MyoD activating RNA-bladder acellular matrix graft scaffold; NP(saMyoD)/SF(VEGF)/BAMG, NP(saMyoD)/BAMG combine with SF(VEGF); SF(VEGF), encapsulated vascular endothelial growth factor (VEGF) with silk fibroin (SF) fiber.

and the supernatant were removed and cultured in DMEM (Gibco, Thermo Fisher Scientific Inc.) supplemented with 10% FBS (Gibco, Thermo Fisher Scientific Inc., MA, USA) at 37°C in a 5% CO_2. Forty-eight hours later, the cells were washed with PBS and digested with 0.25% trypsin and passaged with a ratio of 1:3 upon reaching 80%–90% confluence. The culture medium was changed every 2 days. The second passage of ADSCs was identified by flow cytometry analysis of the marker of CD34, CD90, CD29, and CD105.

Synthesis and Selection of MyoD saRNA

DsRNAs targeting the MyoD promoter were designed and synthesized by Thermo Fisher Scientific Co., Ltd, China. Then, MyoD saRNA was transfected into ADSCs with Lipofectamine™ RNAiMAX (Thermo Fisher Scientific Co., Ltd, China) following the manufacturer's instruction. Seventy-two hours after transfection, cells were collected to extract total protein or RNA. The effective cells were analyzed by RT-PCR and western blot and picked with statistical analysis.

The saRNA sequences are as follows: control saRNA forward: 5′-UUCUCCGAACGUGUCACGUTT-3′; control saRNA reverse: 5′-ACGUGACACGUUCGGAGAATT-3′. MyoD saRNA forward:5′-UGCCUGGUAUCCCUACAAAtt-3′; MyoD saRNA reverse: 5′-UUUGUAGGGAUACCAGGCAtt-3′. The above sequence was labeled with green fluorescent FAM.

Preparation of NP(saMyoD)

NPs and saRNA encapsulated NPs were prepared by double emulsion method with a carrier material PEG-PLA and cationic lipid BHEM-Chol. PEG_{5000}-PLA_{25000} and BHEM-Chol are dissolved in 0.5 ml chloroform, 25 μl saRNA solution (including 200 μg saMyoD), and the initial emulsion is formed under the ultrasonic of the probe type ultrasonic breaker (output power 80 W, 30 s). The initial emulsion was added to 1.5 ml of 1% polyvinyl alcohol aqueous solution, and then emulsified again (output power 80 W, 2 min). Then the emulsion was added to 25 ml of 0.3% PVA aqueous solution and the organic solvent was volatilized under reduced pressure, centrifuged (4°C, 30,000g, 1 h). The NPs were collected and suspended twice with ultrapure water, washed by centrifugation, collected. The sample was lyophilized.

Identification NP Function *In Vitro*

Detection of Particles Size, Polydispersity Index, and Zeta Potential

Particles size, polydispersity index and Zeta potential were detected in NP(saMyoD) aqueous solution (1 mg/ml), temperature (25°C) by Nano-ZS90 (Malvern).

Measurement of Packing Efficiency and Drug Loading Capacity

1 mg NP(saMyoD) were dissolved in 500 μl TE buffer and 250 μl chloroform. Shaking for 30 min in room temperature. Then centrifuged for 10 min at 13,000 rpm/min, 4°C. At last, NP (saMyoD) were submitted to spectrophotometer to measure the concentration of siRNA. Then, the packing efficiency and drug loading capacity could be calculated.

Release *In Vitro*

NP(saMyoD) were dissolved in DEPC water to 1 mg/ml. Then dialysis in PBS (pH7.4) at 100 rpm/min. Collected the dialysate in suitable time and replenish equal volume PBS. Detect the concentration of siRNA with UV method.

Cell Transfection

ADSCs were seeded in 24-well cell culture plates at a density of 10^5/well. After overnight culture, the medium was changed to DMEM complete medium (containing 10% FBS) containing FAM-MyoD-saRNA-NPs. The concentration of the particles was 0.366 mg/ml and the FAM-saRNA was 100 nM. The experiments were divided into four groups, ADSCs transfected with PBS group NP), NP(saMyoD) group, NP(scramble) group, and empty NP (Blank) group. The cells were cultured at 37°C for 4 h and then the FAM was detected by Flow cytometry.

Cellular Viability Assay

ADSCs were incubated with both 100 mg SF(VEGF)/BAMG and 100 mg NP(saMyoD)/BAMG composite scaffold containing DMEM medium, or 200 mg each scaffolds DMEM medium for 3 days (37°C, 5% CO_2). The cytotoxicity of 1, 2, and 3 days was detected with an MTT [3-(4,5-dimethylthiazolyl-2)-2,5-diphenyltetrazolium bromide] based *In Vitro* Toxicology kit (Sigma-Aldrich, Schnelldorf, Germany) according to the manufacturer's instructions.

Preparation of Silk Fibroin NPs-VEGF

Following the former research (Wang Q. et al., 2017), 200 μl VEGF solution (20 μg/ml) and 8 ml ethanol were added into 20 ml 3% SF aqueous solution. Then, the mixture were stabilized for 5 min under low speed stirring, and frozen at −20°C for 24 h. After ultracentrifugation at 40,000g, the supernatant was removed, and the precipitated silk fibroin particles were lyophilized for further use.

Scaffold Preparation

The bladder tissue was cut longitudinally from the rat bladder, Then, carefully peeled off the bladder mucosa, and remove the muscle layer of the pulp by microscopy. After soaking in nuclease-free water for 24 h, the treated tissues were dipped in a decellularized solution (0.1% Triton X-100 and 0.15% ammonia water) for 14 days, the decellularized solution was updated every 3 days. Then, the tissues were frozen at −80°C for 24 h, vacuum dried for 24 h, and stored in 75% alcohol.

SF(VEGF) or NP(saMyoD) were dissolved in PBS to a final concentration of 1% and added to BAMG. Due to ultrasound could improve the kinetic energy of biomolecules and increase the collision frequency with BAMG (Zhang et al., 2018), the BAMG was ultrasonically shaken in SF(VEGF) and NP (saMyoD) solution for 10 min and dried under low temperature pressure. Then the SF(VEGF)/BAMG or NP (saMyoD)/BAMG composite scaffold were well prepared. To get the ADSCs well attached the composite scaffold, 100 μl third generation of ADSCs were incubated with SF(VEGF)/BAMG or NP(saMyoD)/BAMG composite scaffold at 3×10^6/ml. Two hours later serum-free medium was added, 4 h later, the cells were

incubated with medium supplemented with serum. After 24 h, the cells were washed with serum medium and washed twice with PBS to remove unadhered and dead cells.

Scaffold mechanical testing: In brief, five pieces BAMGs were picked randomly and immersed in PBS for 24 h. Then those BAMGs were fixed for tensile test with no shift. Before the test, the length and width within the framework were measured. The frame was stretched in the vertical shift in longitudinally with 10mm/min. We reaped these indexes, the initial elastic modulus (EM), ultimate tensile strength (UTS), and % elongation to failure (ETF) with instron 5542 Tensile Tester (Norwood, MA, USA).

Experimental Animals

Eight-week-old adult male SD rats were acclimatized and housed in cages with free access to food and water in temperature-controlled, pathogen-free animal room facilities (20°C–22°C, humidity 40%–70%, 12 h day/night cycle) for one week before the experiments. The animals were randomly divided into four groups (12 in each group): the sham operation group, the ADSC-BAMG group, the ADSC-saMyo/BAMG group, the ADSC-saMyoD/SF(VEGF)/BAMG group. All animal procedures were approved and supervised by the Ethical Committee of Shanghai Jiaotong University and were performed as the guidelines of the China Act on Welfare and Management of Animals.

Surgical Procedures for Bladder Augmentation

Rat bladder enlargement model was simply described as follows: rats were anesthetized by intraperitoneal injection of pentobarbital (30 mg/kg), and incised under sterile conditions with a 1-cm incision at the lower abdomen skin to expose the bladder. Cut about 40% to 60% bladder tissue in squares (Wang Q. et al., 2017). BAMG with the same size and area was sutured with the 5–0 polypropylene line to repair the defect of the bladder. BAMG was faced to the bladder cavity. Intravesical incision, normal saline was injected into the bladder from the urethra, and the abdominal cavity was closed after no clear leakage.

Western Blot Analysis

Total protein extracted from cell were loaded on to sodium dodecyl sulfate-polyacrylamide gel electrophoresis (SDS-PAGE) and then transferred onto polyvinylidene fluoride (PVDF) membranes (Millipore, Bedford, MA, USA). The membranes were incubated first with primary antibody and then with secondary antibody. GAPDH was used as a control to verify the equal loading of proteins. Western blot analysis was carried out by a standard protocol using antibodies for SM22a (ab14106, 1:800); Desmin (#5332, 1:1000); α-SMA (sc-53142, 1:800) and GAPDH (sc-32233, 1:1000)

Real-Time RT-PCR Analysis

Total RNA was extracted from cells using the Trizol reagent (Invitrogen, Thermo Fisher Scientific Inc., NY, USA) as the manufacture's protocol. The cDNA was acquired by cDNA Reverse Transcription Kit (ABI). Then, the mRNA expression of a-SMA, SM22α and Desmin were conducted by ABI Prism 7900 (Applied Biosystems, Foster City, CA, USA). All reactions were run in triplicate. The cycle threshold (Ct) method was used to calculate values. Target mRNA expression levels were normalized to the housekeeping genes of GAPDH as an internal control.

VEGF Release *In Vitro*

One hundred milligram of SF(VEGF)/BAMG was suspended in 1 ml of PBS and shakened at 37°C at 100 rpm. A 0.2 ml sample was taken daily from day 1 to day 7 and replenished with an equal volume of fresh PBS. The taken sample concentration of VEGF was measured by ELISA.

Histopathological and Immunohistochemistry Analysis

Following Rats sacrifice, the bladder tissue was harvested and kept in neutral buffered formalin 10% (v/v) for one day until paraffin embedding for histology. The tissue was sliced in a 5-μm thickness in paraffin block and stained with routine hematoxylin and eosin solutions. Images were captured with a light microscope (Olympus CKX41 microscope, Tokyo, Japan) linked to a computer.

Paraffin-embedded tissue sections were dewaxed with xylene and rehydrated through an ethanol gradient into water. Following blocking of endogenous peroxidase activity with 0.3% hydrogen peroxide for 10 min, the tissue slices were washed with PBS, and incubated with VEGF (sc-80442, 1:200), a-SMA (sc-53142, 1:100) antibody. Next, slices were incubated with biotinylated secondary antibody and then with horseradish peroxidase labeled streptavidin. Diaminobenzidine (DAB) was used as chromogen and antibodies were diluted in the recommended antibody diluting buffer.

Statistical Analysis

All data are expressed as the mean ± standard deviation. According to different data set, using a two-tailed Student's t-test or one-way analysis of variance (ANOVA) with the Bonferroni *post hoc* test in GraphPad Prism 8 (GraphPad Software Inc., San Diego, CA, USA). $P< 0.05$ indicates statistical significance.

RESULTS

Identification of Rat ADSC

In this study, we isolated and cultured rat ADSC cells, and found uniform spindle-like structure in the second generation. Optimistically, the cell began to proliferate rapidly. To identify the isolated cells were functional ADSCs, we detected cell surface specific markers with flow cytometry analysis (**Figure 1**). The results showed that 85.12% of the detected isolated cells were able to express CD90, 78.87% express CD29 and 81.54% express CD105 (Schäffler and Büchler, 2007; Yamamoto et al., 2007), but few isolated cells express CD34 (4.52%). These results strongly suggested that we had isolated and culture ADSC successfully.

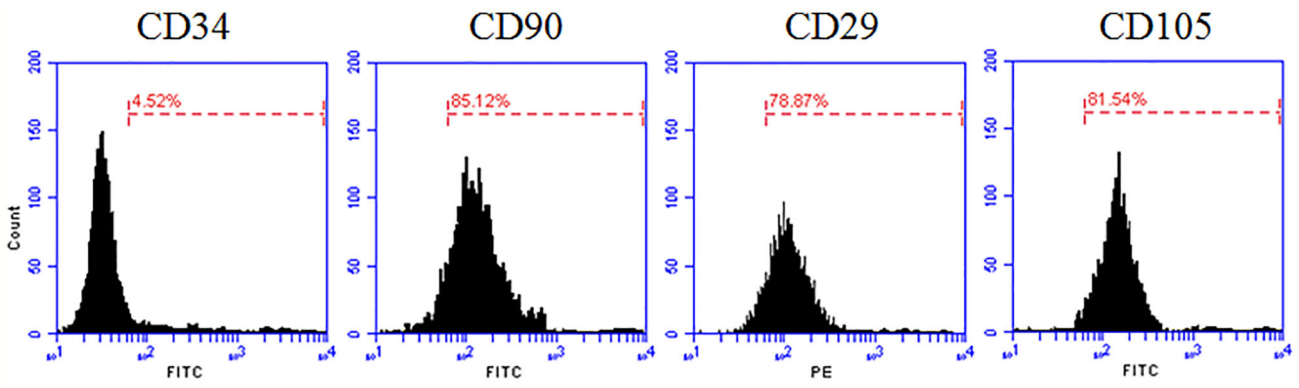

FIGURE 1 | Flow cytometry analysis of rat ADSC. Rat ADSC within two passages were harvested and detected specific cell surface antigens CD34, CD90, CD29, and CD105 by Flow cytometry.

Characterization of NP(saMyoD)

The mean diameter of NP(saMyoD) was 167 ± 7.3nm, with PDI 0.208, indicating homogeneous distribution of the particles. The NP(saMyoD) has a 12.1 mV potential voltage, instructing NP (saMyoD) could bind with negative charged cell membrane epitope. NP(saMyoD) displayed a stable diameter of within 180 nm in fetal bovine serum within 48 h, showing good stability (**Figure 2A**). In addition, NP(saMyoD) had encapsulate efficiency (92.3%) and drug loading capacity (0.667%), suggesting that siRNA could be encapsulated efficiently in NP. Besides, the release assay showed that NP(saMyoD) release effect could last for 12 days before plateau (**Figure 2B**).

NP(saMyoD) Is Able to Increase the Expression of Myod in ADSC Cells

Myogenic differentiation 1 (MoD) plays a vital role in muscle cell differentiation and muscle regeneration (Weintraub et al., 1991; Clemen et al., 1999; Gaudet et al., 2011). After isolated rat ADSCs *in vitro* efficiently, we were looking for a method to overexpression Myod in ADSCs more efficiently and keep those ADSCs well-functioned in animal body. Currently, rushing research have shed light on the application of NPs in conjunction with small molecular compounds or nucleotide in the medical area (Moghimi et al., 2001; Fan et al., 2018; Li et al., 2019). In this work, we have developed an saMyod-conjugated-hollow gold NPs NP(saMyoD) and identified its biological function. First, FAM-labeled saMyoD was used to prepare NP(saMyoD), we then transfected the compound into ADSCs. The flow cytometry results showed that NP(saMyoD) was greatly expressed in ADSCs, the same to NP(saScr) (**Figure 3A**). The quantitative results showed that about 80% of the cells could be transfected with NP(saMyoD) (**Figure 3B**). Two days after transfection, the expression of MyoD was detected by RT-PCR (**Figure 3C**) and Western Blot (**Figure 3D**). These results demonstrated that, after transfection of ADSC with NP(saMyoD), the mRNA and protein expression of MyoD increased dramatically in ADSCs transfected with NP(saMyoD) compared to other groups (**Figures 3C, D**). Meanwhile, the expression of MyoD in cells transfected with NP was similar to NP (scramble) transfected cells (**Figures 3C, D**).

Evaluate the Effect of NP(saMyoD) on ADSC

As the NP(saMyoD) transfected ADSCs showed high Myod expression level, we further investigate the function of those ADSCs. First, we examined the expression level of smooth

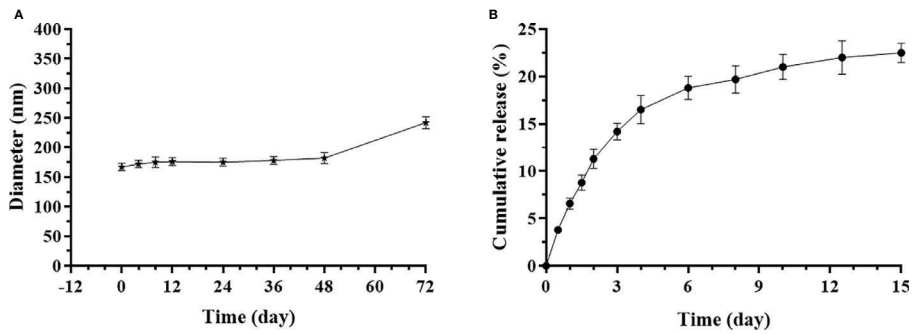

FIGURE 2 | Characterization of NP(saMyoD). **(A)** Detection of the diameter of NP in different time points. **(B)** The cumulative release curve of NP(saMyoD).

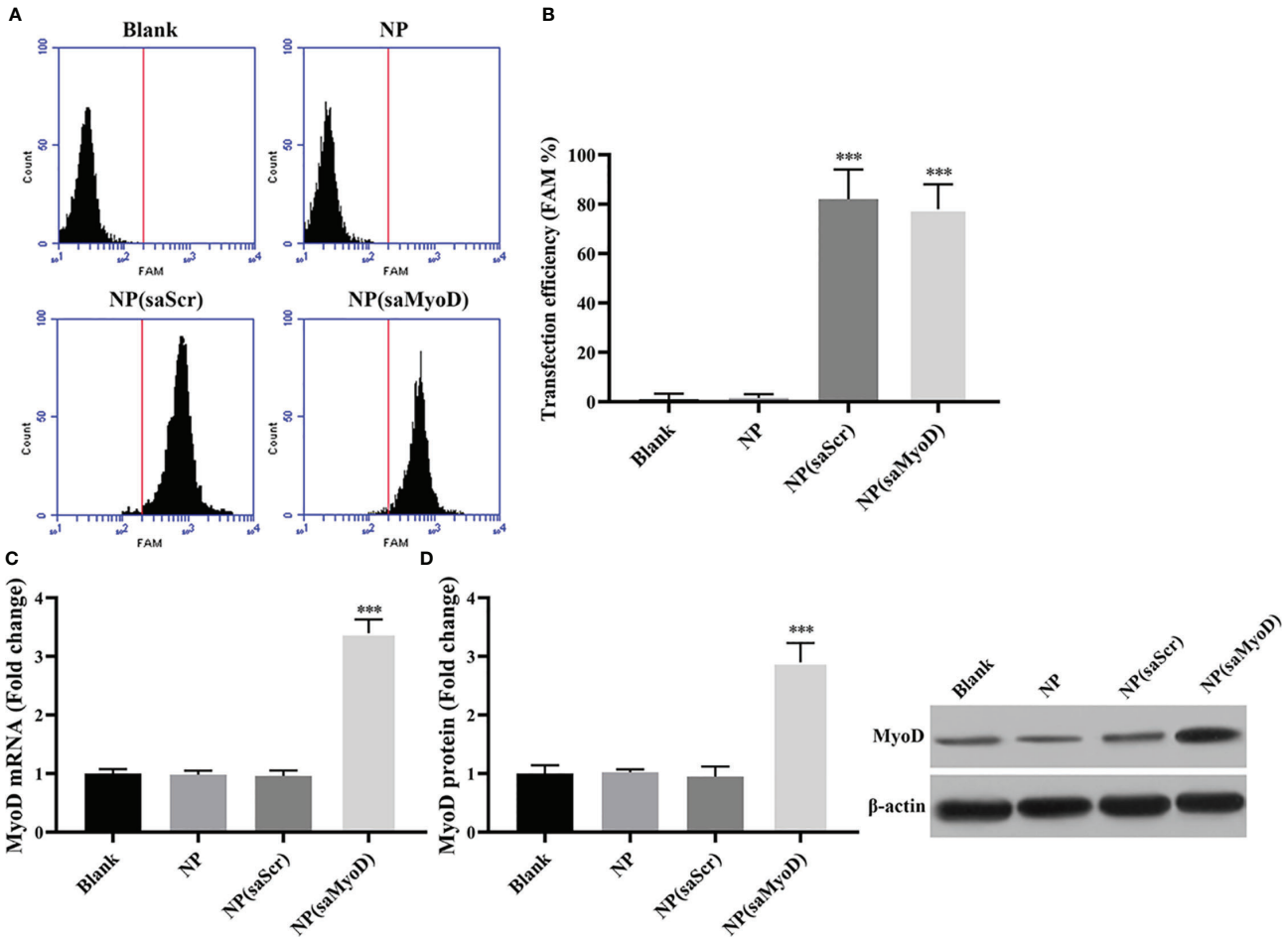

FIGURE 3 | Determination of NP(saMyoD) transfection efficiency in ADSCs. **(A)** Flow cytometry analysis of the NP(saMyoD) transfection efficiency. **(B)** Quantitative analysis of NP(saMyoD) transfection efficiency. **(C)** The mRNA expression level of MyoD. **(D)** The protein expression level of MyoD. ***$P < 0.001$, compared with the NP(saScr) group.

muscle cell markers α-SMA, SM22α, and Desmin. As shown in **Figure 4A**, compared with NP(saScr), the mRNA expression of α-SMA, SM22α, and Desmin were significantly upregulated after 14 days transfection with NP(saMyoD). The protein expression of α-SMA, SM22α, and Desmin were consistent with mRNA results (**Figure 4B**).

Evaluation of the ADSC-NP(saMyoD)/SF (VEGF)/BAMG

We have evaluated the efficiency and function of NP(saMyoD) on ADSCs, then we'd like to evaluate the SF(VEGF) scaffolds by detecting the sustained release of VEGF on SF-BAGM. The release of VEGF was increased along with the time elapsed and exhibited a burst release in the third day, and then the release ratio of VEGF was slowed down but the release period lasted for more than 7 days (**Figure 5A**). Then, we have checked other indicators in previous reports, the characterization of SF, BAMG and their composite scaffolds were measured with scanning electron microscopy (Zhu et al., 2016). These results indicated that SF-BAMG was successfully constructed and suitable for drug delivery and release regulation. We performed mechanical test for the scaffolds that we generated, the results showed the biomechanics of ADSC-NP (saMyoD)/SF(VEGF)/BAMG is UTS 0.47 ± 0.12 MPa, EM 1.02 ± 0.35 MPa (**Figure 5D**). MTT assay was performed to determine the toxic effects ofNP(saMyoD)/BAMG and SF (VEGF)/BAMG scaffolds on ADSCs. Comparing to the blank group, NP(saMyoD)/BAMG slightly inhibited the proliferation of ADSC, which is consistent with our previous study (Wang et al., 2015), but NP(saMyoD)/BAMG is not toxic accroding to the China national standards for medical devices evaluation (GB/T16886.5-2017), because the inhibition ratio is lower than 20%. The cell morphology is normal under the microscope (**Figure 5C**). SF(VEGF)/BAMG is also not toxic to ADSCs and even promotes the growth of ADSC compared to control group (**Figure 5B**).

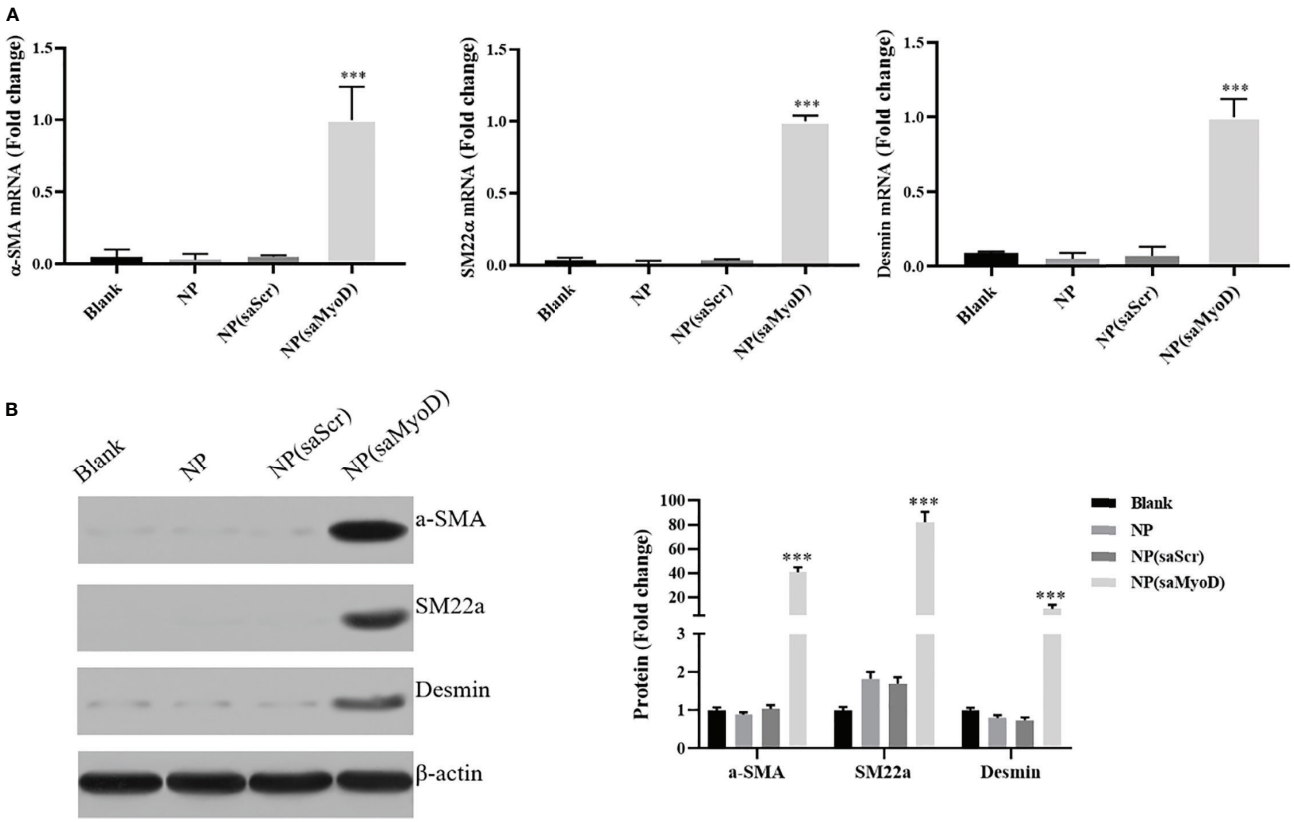

FIGURE 4 | The Expression changes of α-SMA, SM22α, and Desmin were detected. **(A)** The mRNA level of α-SMA, SM22α, and Desmin by RT-PCR. **(B)** The protein level of α-SMA, SM22α, and Desmin by Western blot. ***$P < 0.001$, compared with the NP(saScr) group.

In Vivo effect of ADSC-NP(saMyoD)/BAMG and ADSC-SF(VEGF)/BAMG

A rat model of bladder enlargement was prepared and different scaffolds were implanted. After 10 weeks, the animals were executed to test the repair function of ADSC-NP(saMyoD)/BAMG and ADSC-NP(saMyoD)/SF(VEGF)/BAMG. First, we did not found obvious deterioration in liver and renal of these groups. After detecting the stone situation of these groups, the data demonstrated the composite group showed the least stones than other groups (**Figure 6A**). Then, Bladder function was evaluated, the data showed that the bladder capacities of the ADSC-NP(saMyoD)/SF(VEGF)/BAMG groups were significantly higher than sham group (**Figure 6B**). ADSC-NP (saMyoD)/BAMG also appeared to play a role in bladder repair, but there was no statistical difference compared with sham group (**Figure 6B**). The gradually increasing bladder capacities indicated that MyoD and VEGF might improve the balance between the degradability and generation of the scaffold. The bladder compliance of three treated groups were gradually increased and the compliance of ADSC-NP(saMyoD)/SF (VEGF)/BAMG group was the max (**Figure 6C**).

The HE staining examination of bladder tissue slices in the ADSC-NP(saMyoD)/BAMG and ADSC-NP(saMyoD)/SF(VEGF)/BAMG groups illustrated in-growth of connective tissue into both the marginal and central regions of the original implantation sites. In addition, the entire urothelium regenerated well and more densely and regularly arranged smooth muscle fibers were detected in the ADSC-NP(saMyoD)/SF(VEGF)/BAMG groups (**Figure 6D**). Immunohistochemistry were performed to analyze the regeneration of bladder wall components. The results demonstrated that, comparing with ADSC-NP(saMyoD)/BAMG, there were more α-SMA and VEGF positive signal in ADSC-NP (saMyoD)/SF(VEGF)/BAMG group (**Figures 6E, F**). Thus, ADSC-NP(saMyoD)/SF(VEGF)/BAMG may better promote the growth of smooth muscle and blood vessels formation. At last, the masson dye results showed the sham group showed more collagen than ADSC-NP(saMyoD)/BAMG group, and the ADSC-NP(saMyoD)/SF (VEGF)/BAMG group just had little fibrosis, indicating that the composite scaffolds have enough ability to antifibrotic and with great safety (**Figure 6G**).

DISCUSSION

Bladder tissue engineering is an important research hotspot of urology. However, the bladder, as a complex organ, has vital

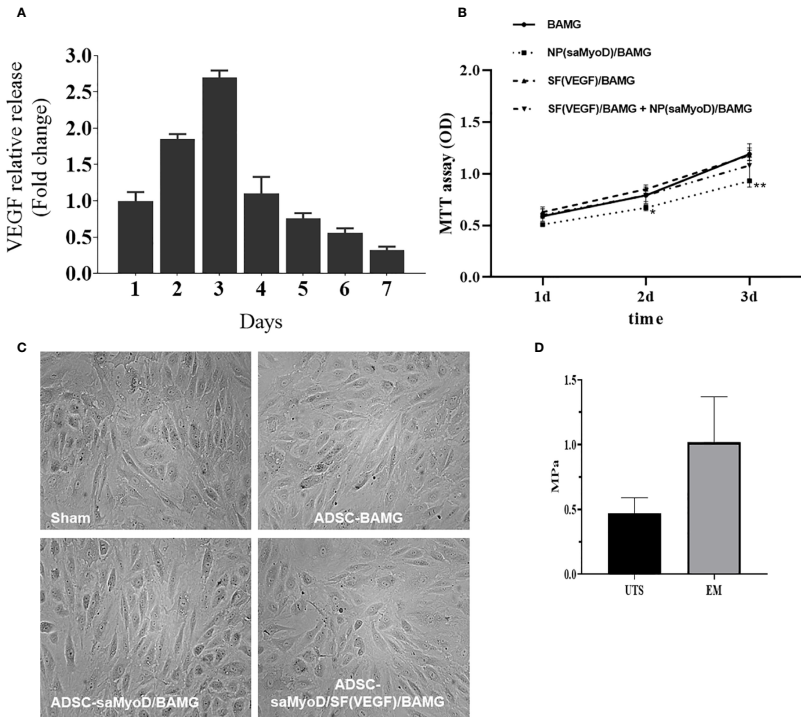

FIGURE 5 | NP(saMyoD)/BAMG and SF(VEGF)/BAMG scaffolds were evaluated. **(A)** The continuous release of VEGF on SF-BAGM. **(B)** The activity of ADSC cells by MTT assay. *$P < 0.05$, **$P < 0.01$, compared with the BAGM group. **(C)** The cell morphology of every group. **(D)** The biomechanics of ADSC-NP(saMyoD)/SF(VEGF)/BAMG.

storage and excretion function. Owing to the requirement of its good compliance, bladder tissue engineering is therefore a promising but still challenging direction to provide a safe alternative mean to gastrointestinal reconstructive techniques (Lam Van Ba et al., 2015).

In this study, based on the preprepared SF-VEGF-NPs, the appropriate MyoD saRNA molecules were screened to develop NP(saMyoD)/BAMG scaffolds. The rat bladder enlargement model was established to verify the effect of ADSCs inoculation of NP(saMyoD)/SF(VEGF)/BAMG composite scaffold to reconstruct bladder structure and functional regeneration. The results showed that NPs carrying saMyoD and VEGF promoted bladder smooth muscle regeneration and neovascularization, thereby promoting bladder defect repair.

Tissue engineering mainly includes three procedures: seed cells, scaffold materials, and regulatory factors. In this study, BAMG was selected as the scaffold material, ADSC was the seed cell, and saMyoD and VEGF were the regulatory factors. At present, there are three main types of scaffold materials for bladder tissue engineering: acellular matrix, collagen, and polymer synthetic materials. These biomaterials have been shown to have good histocompatibility with bladder epithelial cells and smooth muscle cells. The acellular matrix obtained through removing the cellular components in the original tissue by various decellularization methods is rich in collagen. The acellular matrix is nonimmunogenic, and can be degraded *in vivo*, and is increasingly utilized in tissue engineering research (Sacks and Gloeckner, 1999). BAMG, deriving from the bladder and retaining the original three-dimensional scaffold structure of the bladder, is therefore increasingly used, especially in tissue engineering reconstruction of the bladder (Zhu et al., 2011). In the previous study, we vacuum-dried the traditionally preserved BAMG to make the collagen arrangement more well-aligned and the biomechanical properties improved. We performed mechanical test for the scaffolds that we generated, the results showed the biomechanics of ADSC-NP(saMyoD)/SF(VEGF)/BAMG is UTS0.47 ± 0.12 MPa, EM1.02 ± 0.35 MPa, indicating a familiar former reported parameters (Dahms et al., 1998). It was utilized in the reconstruction of varying degree injury of rabbit bladder defects. These results showed that BAMG was an effective scaffold material for bladder defect reconstruction (Zhu et al., 2011).

Seed cells should have a wide range of properties, such as: easily obtained and cultured, well expanded *in vitro*, and with good compatibility with scaffold materials. Traditional tissue engineering techniques employ their own bladder epithelial cells and smooth muscle cells as seed cells (Yoo et al., 1998). However, many pathological conditions restrict the traditional approach of biopsy to obtain autologous adult cells as a source of seed cells (Dozmorov et al., 2007). Stem cells, with self-renewal activity, high proliferation and multi-directional differentiation potential, are ideal sources of seed cells. In recent years, stem cells, such as bone marrow mesenchymal stem cells, adipose stem cells, endothelial progenitor cells, smooth muscle progenitor

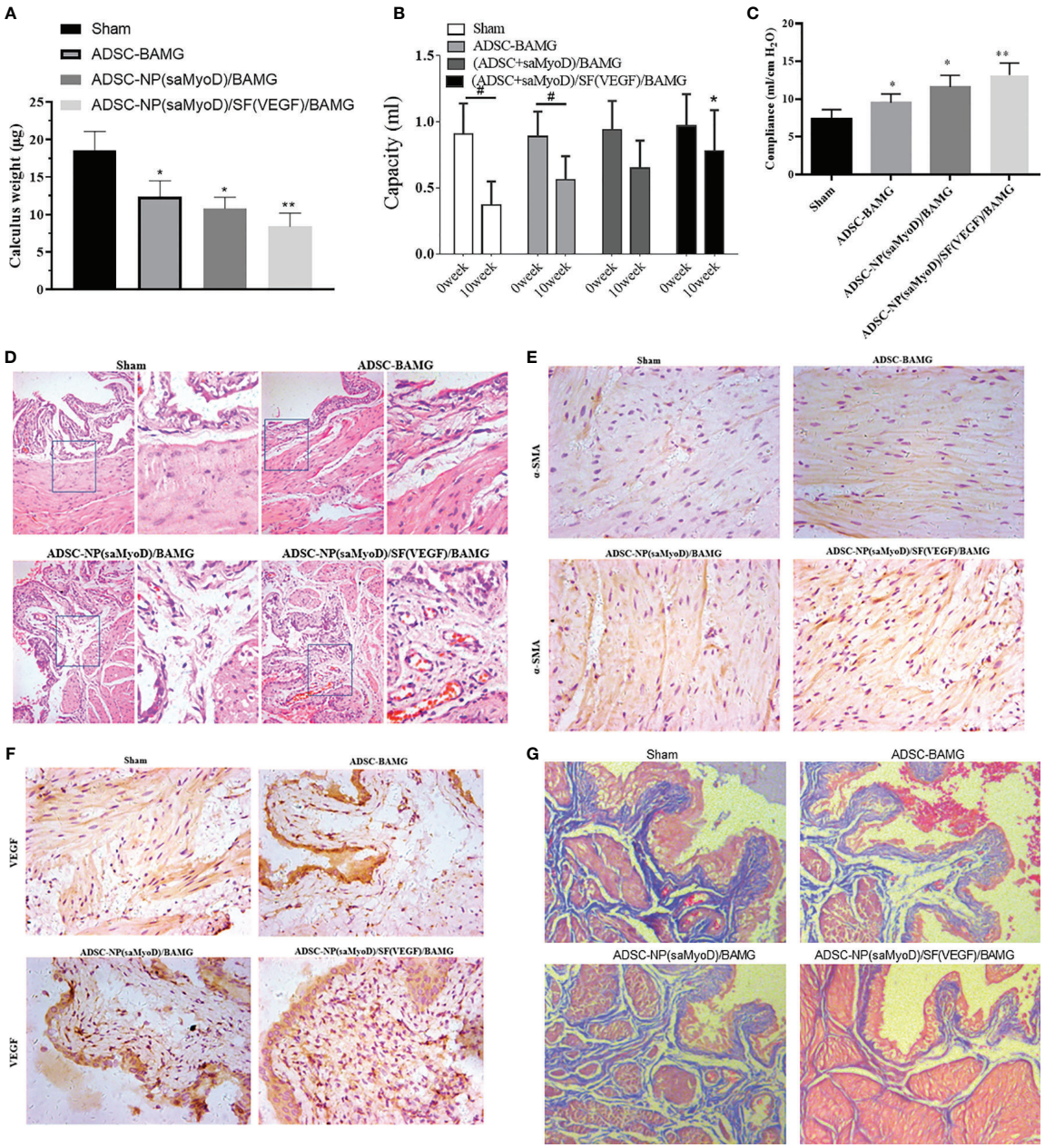

FIGURE 6 | ADSC-NP(saMyoD)/SF(VEGF)/BAMG promotes bladder repair in rat. **(A)** Calculus weight. **(B)** Bladder capacity. **(C)** Bladder compliance. **(D)** HE staining of the bladder regeneration area. **(E)** Immunohistochemistry of α-SMA in bladder tissue. **(F)** Immunohistochemistry of VEGF in bladder tissue. **(G)** Masson dye. $^{*}P < 0.05$, $^{**}P < 0.01$, compared with the sham group; $^{\#}P < 0.05$, compared with the 0 week group.

cells, have been widely used as seed cells for tissue engineering work. Among them, ADSCs are getting more and more attention (Zhang et al., 2016). Compared with other stem cells, ADSCs, extracting from human body adipose tissue with less trauma and no ethical problems, have higher proliferation rate and differentiation ability than other adult stem cells (Lue et al., 2010; Wang C. et al., 2017; Pokrywczynska et al., 2019). In addition to expressing the myogenic marker MyoD and myosin heavy chain *in vitro* culture (Mizuno et al., 2002), ADSCs have also demonstrated expresses α-actin *in vivo* experiments (Jack et al., 2005), indicating that ADSCs have the potency to form normal smooth muscle. In the previous study, we used adipose stem cells as seed cells combined with BAMG surface for the reconstruction of partial rabbit bladder defects. The results showed that adipose-derived stem cells grew well on BAMG surface, and they have good biocompatibility. In addition, we did not conduct cell tracking for the ADSCs and we could not identify whether the degradation of the scaffolds is in company

with the proliferation and differentiation of the ADSCs. But this should get great concern in the further study. And by histological examination, the resulted shown that adipose-derived stem cells can promote the regeneration of the bladder, especially the regeneration of smooth muscle tissue, which is an ideal seed cell of bladder tissue engineering.

The key to tissue engineering reconstruction of the bladder is rapid vascularization and regeneration of bladder smooth muscle. The use of composite growth factors on scaffold materials provides an option for adequate rapid vascularization and regeneration of bladder smooth muscle in tissue engineered bladders. MyoD and VEGF are key factors that promote smooth muscle regeneration and angiogenesis, respectively. This study selected MyoD as a myogenic regulatory factor. However, the current common method is to simply enrich the growth factor on the material, which is very inadequate (Kanematsu et al., 2007). Using genetic engineering technology, seed cells carrying MyoD gene, upregulate the expression of associated growth factors, further promoting the regeneration of bladder smooth muscle by continuous secretion of MyoD growth factor. MyoD can significantly improve the survival rate and functional regeneration of tissues (Lazarous et al., 1996). SaRNA displayed high specificity and low toxicity, making it a new tool for gene function research and clinical treatment (Li et al., 2006; Li, 2008; Wang et al., 2008; Portnoy et al., 2011). In this study, we designed and screened appropriate dsRNA molecules targeting MyoD and transfected them into ADSCs, and found that saMyoD induced high expression of smooth muscle markers α-SMA, SM22a and Desmin in ADSCs.

The effective delivery of the target gene by saRNA is an important part of drug efficacy. The ideal gene inducing vector should be characterized by high efficiency, stability, nontoxicity, convenient preparation and efficient targeting (El-Aneed, 2004; Hughes, 2004). In recent years, nanogene introduction vectors have attracted extensive attention due to their advantages of low toxicity, nonimmunogenicity, large loading capacity, and ease of preparation (Brannon-Peppas and Blanchette, 2004; Yang et al., 2015). Moo Rim Kang (Kang et al., 2012) performed lipid nanoparticle-mediated saRNA treatment in a mouse model of bladder cancer, urinary epithelial absorption, prolonged mouse survival, and tumor regression reached 40%. Lipid nanoparticles are currently the most developed carrier. In this study, lipid nanomaterials were selected as the saMyoD inducing vector. The bonding of saMyoD to the lipid nanomaterials allows it being maintained at the treatment site more permanently, limiting its spread and forming a targeted sustained release system. This method can reduce the potential risk of free diffusion of cytokines to the body, and can make efficient utilization of cytokines.

CONCLUSION

In this study, based on the preprepared silk fibroin-VEGF NPs, the saRNA-MyoD lipid NPs were prepared by genetic engineering, and combined with BAMG to form a composite scaffold and inoculated into ADSCs. *In vivo* studies have found that saRNA-MyoD lipid NPs and VEGF silk fibroin NPs promote sustained release of VEGF and MyoD and rapid vascularization and smooth muscle regeneration with scaffold degradation in rats. Through this study, we have further explored new bladder reconstruction materials and factors that facilitate graft smooth muscle regeneration, and desire to provide a new perspective for finding alternative materials for bladder defects.

DATA AVAILABILITY STATEMENT

All datasets generated for this study are included in the article/supplementary material.

ETHICS STATEMENT

The animal study was reviewed and approved by the Animal Care and Use Committee at Shanghai Jiao Tong University Affiliated Sixth People's Hospital.

AUTHOR CONTRIBUTIONS

These studies were conceived of and designed by all authors. Experiments were performed by CJ, BG, and WZhao with the help of WZ. Data analysis, data interpretation, manuscript preparations were done by CJ, NC, JN, WZhao, BG, and WZhu.

FUNDING

This study was supported by the National Natural Science Foundation of China (Grant no. 81200497).

REFERENCES

Adamowicz, J., Kuffel, B., Pokrywczynska, M., Vontelin Van Breda, S., and Drewa, T. (2019). Reconstructive urology and tissue engineering: converging developmental paths. *J. Tissue Eng. Regener. Med.* 13 (3). doi: 10.1002/term.2812

Ardeshirylajimi, A., Ghaderian, S. M., Omrani, M. D., and Moradi, S. L. (2018). Biomimetic scaffold containing PVDF nanofibers with sustained TGF-beta release in combination with AT-MSCs for bladder tissue engineering. *Gene* 676, 195–201. doi: 10.1016/j.gene.2018.07.046

Brannon-Peppas, L., and Blanchette, J. O. (2004). Nanoparticle and targeted systems for cancer therapy. *Adv. Drug Delivery Rev.* 56, 1649–1659. doi: 10.1016/j.addr.2004.02.014

Chen, W., Shi, C., Hou, X., Zhang, W., and Li, L. (2014). Bladder acellular matrix conjugated with basic fibroblast growth factor for bladder regeneration. *Tissue Eng. Part A* 20, 2234–2242. doi: 10.1089/ten.tea.2013.0730

Clemen, C. S., Hofmann, A., Zamparelli, C., and Noegel, A. A. (1999). Expression and localisation of annexin VII (synexin) isoforms in differentiating myoblasts. *J. Muscle Res. Cell Motil.* 20, 669–679. doi: 10.1023/A:1005524623337

Coutu, D. L., Mahfouz, W., Loutochin, O., Galipeau, J., and Corcos, J. (2014). Tissue engineering of rat bladder using marrow-derived mesenchymal stem cells and bladder acellular matrix. *PloS One* 9, e111966. doi: 10.1371/journal.pone.0111966

Dahms, S. E., Piechota, H. J., Dahiya, R., Lue, T. F., and Tanagho, E. A. (1998). Composition and biomechanical properties of the bladder acellular matrix graft: comparative analysis in rat, pig and human. *Br. J. Urol.* 82, 411–419. doi: 10.1046/j.1464-410X.1998.00748.x

Dozmorov, M. G., Kropp, B. P., Hurst, R. E., Cheng, E. Y., and Lin, H. K. (2007). Differentially expressed gene networks in cultured smooth muscle cells from normal and neuropathic bladder. *J. Smooth Muscle Res.* 43, 55–72. doi: 10.1540/jsmr.43.55

El-Aneed, A. (2004). An overview of current delivery systems in cancer gene therapy. *J. Control Release* 94, 1–14. doi: 10.1016/j.jconrel.2003.09.013

Fan, K., Xi, J., Fan, L., Wang, P., Zhu, C., Tang, Y., et al. (2018). In vivo guiding nitrogen-doped carbon nanozyme for tumor catalytic therapy. *Nat. Commun.* 9, 1440–1440. doi: 10.1038/s41467-018-03903-8

Gaudet, P., Livstone, M. S., Lewis, S. E., and Thomas, P. D. (2011). Phylogenetic-based propagation of functional annotations within the Gene Ontology consortium. *Brief Bioinform.* 12, 449–462. doi: 10.1093/bib/bbr042

Hughes, R. M. (2004). Strategies for cancer gene therapy. *J. Surg. Oncol.* 85, 28–35. doi: 10.1002/jso.20001

Jack, G. S., Almeida, F. G., Zhang, R., Alfonso, Z. C., Zuk, P. A., and Rodriguez, L. V. (2005). Processed lipoaspirate cells for tissue engineering of the lower urinary tract: implications for the treatment of stress urinary incontinence and bladder reconstruction. *J. Urol.* 174, 2041–2045. doi: 10.1097/01.ju.0000176489.96993.84

Kabadi, A. M., Thakore, P. I., Vockley, C. M., Ousterout, D. G., Gibson, T. M., Guilak, F., et al. (2015). Enhanced MyoD-induced transdifferentiation to a myogenic lineage by fusion to a potent transactivation domain. *ACS Synth. Biol.* 4, 689–699. doi: 10.1021/sb500322u

Kanematsu, A., Yamamoto, S., and Ogawa, O. (2007). Changing concepts of bladder regeneration. *Int. J. Urol.* 14, 673–678. doi: 10.1111/j.1442-2042.2007.01768.x

Kang, M. R., Yang, G., Place, R. F., Charisse, K., Epstein-Barash, H., Manoharan, M., et al. (2012). Intravesical delivery of small activating RNA formulated into lipid nanoparticles inhibits orthotopic bladder tumor growth. *Cancer Res.* 72, 5069–5079. doi: 10.1158/0008-5472.CAN-12-1871

Kocaefe, Y. C., Israeli, D., Ozguc, M., Danos, O., and Garcia, L. (2005). Myogenic program induction in mature fat tissue (with MyoD expression). *Exp. Cell Res.* 308, 300–308. doi: 10.1016/j.yexcr.2005.03.038

Lam Van Ba, O., Aharony, S., Loutochin, O., and Corcos, J. (2015). Bladder tissue engineering: a literature review. *Adv. Drug Delivery Rev.* 82-83, 31–37. doi: 10.1016/j.addr.2014.11.013

Lazarous, D. F., Shou, M., Scheinowitz, M., Hodge, E., Thirumurti, V., Kitsiou, A. N., et al. (1996). Comparative effects of basic fibroblast growth factor and vascular endothelial growth factor on coronary collateral development and the arterial response to injury. *Circulation* 94, 1074–1082. doi: 10.1161/01.CIR.94.5.1074

Li, L. C., Okino, S. T., Zhao, H., Pookot, D., Place, R. F., Urakami, S., et al. (2006). Small dsRNAs induce transcriptional activation in human cells. *Proc. Natl. Acad. Sci. U. S. A* 103, 17337–17342. doi: 10.1073/pnas.0607015103

Li, W., Yang, J., Luo, L., Jiang, M., Qin, B., Yin, H., et al. (2019). Targeting photodynamic and photothermal therapy to the endoplasmic reticulum enhances immunogenic cancer cell death. *Nat. Commun.* 10, 3349–3349. doi: 10.1038/s41467-019-11269-8

Li, L. C. (2008). The multifaceted small RNAs. *RNA Biol.* 5, 61–64. doi: 10.4161/rna.5.2.5989

Lue, J., Lin, G., Ning, H., Xiong, A., Lin, C. S., and Glenn, J. S. (2010). Transdifferentiation of adipose-derived stem cells into hepatocytes: a new approach. *Liver Int.* 30, 913–922. doi: 10.1111/j.1478-3231.2010.02231.x

Mizuno, H., Zuk, P. A., Zhu, M., Lorenz, H. P., Benhaim, P., and Hedrick, M. H. (2002). Myogenic differentiation by human processed lipoaspirate cells. *Plast. Reconstr. Surg.* 109, 199–209; discussion 210-191. doi: 10.1097/00006534-200201000-00030

Moghimi, S. M., Hunter, A. C., and Murray, J. C. (2001). Long-circulating and target-specific nanoparticles: theory to practice. *Pharmacol. Rev.* 53, 283–318.

Mousa, N. A., Abou-Taleb, H. A., and Orabi, H. (2015). Stem cell applications for pathologies of the urinary bladder. *World J. Stem Cells* 7, 815–822. doi: 10.4252/wjsc.v7.i5.815

Pokrywczynska, M., Jundzill, A., Rasmus, M., Adamowicz, J., Balcerczyk, D., Buhl, M., et al. (2018). Understanding the role of mesenchymal stem cells in urinary bladder regeneration-a preclinical study on a porcine model. *Stem Cell Res. Ther.* 9, 328. doi: 10.1186/s13287-018-1070-3

Pokrywczynska, M., Rasmus, M., Jundzill, A., Balcerczyk, D., Adamowicz, J., Warda, K., et al. (2019). Mesenchymal stromal cells modulate the molecular pattern of healing process in tissue-engineered urinary bladder: the microarray data. *Stem Cell Res. Ther.* 10, 176. doi: 10.1186/s13287-019-1266-1

Portnoy, V., Huang, V., Place, R. F., and Li, L. C. (2011). Small RNA and transcriptional upregulation. *Wiley Interdiscip. Rev. RNA* 2, 748–760. doi: 10.1002/wrna.90

Sacks, M. S., and Gloeckner, D. C. (1999). Quantification of the fiber architecture and biaxial mechanical behavior of porcine intestinal submucosa. *J. BioMed. Mater. Res.* 46, 1–10. doi: 10.1002/(SICI)1097-4636(199907)46:1<1::AID-JBM1>3.0.CO;2-7

Schäffler, A., and Büchler, C. (2007). Concise review: adipose tissue-derived stromal cells–basic and clinical implications for novel cell-based therapies. *Stem Cells (Dayton Ohio)* 25, 818–827. doi: 10.1634/stemcells.2006-0589

Vargas, K. M., and Shon, Y. S. (2019). Hybrid lipid-nanoparticle complexes for biomedical applications. *J. Mater. Chem. B.* 7, 695–708. doi: 10.1039/C8TB03084G

Wang, X., Arai, S., Song, X., Reichart, D., Du, K., Pascual, G., et al. (2008). Induced ncRNAs allosterically modify RNA-binding proteins in cis to inhibit transcription. *Nature* 454, 126–130. doi: 10.1038/nature06992

Wang, C., Chen, Z., Wu, J., Zhang, Y., Hu, J., Ge, Q., et al. (2015). Small activating RNA induces myogenic differentiation of rat adipose-derived stem cells by upregulating MyoD. *Int. Braz. J. Urol.* 41, 764–772. doi: 10.1590/S1677-5538.IBJU.2014.0400

Wang, C., Liu, W., Nie, Y., Qaher, M., Horton, H. E., Yue, F., et al. (2017). Loss of MyoD Promotes Fate Transdifferentiation of Myoblasts Into Brown Adipocytes. *EBioMedicine* 16, 212–223. doi: 10.1016/j.ebiom.2017.01.015

Wang, Q., Xiao, D. D., Yan, H., Zhao, Y., Fu, S., Zhou, J., et al. (2017). The morphological regeneration and functional restoration of bladder defects by a novel scaffold and adipose-derived stem cells in a rat augmentation model. *Stem Cell Res. Ther.* 8, 149. doi: 10.1186/s13287-017-0597-z

Wang, Y., Zhou, S., Yang, R., Zou, Q., Zhang, K., Tian, Q., et al. (2019). Bioengineered bladder patches constructed from multilayered adipose-derived stem cell sheets for bladder regeneration. *Acta Biomater.* 85, 131–141. doi: 10.1016/j.actbio.2018.12.016

Weintraub, H., Davis, R., Tapscott, S., Thayer, M., Krause, M., Benezra, R., et al. (1991). The myoD gene family: nodal point during specification of the muscle cell lineage. *Science* 251, 761–766. doi: 10.1126/science.1846704

Xiao, D., Wang, Q., Yan, H., Lv, X., Zhao, Y., Zhou, Z., et al. (2017). Adipose-derived stem cells-seeded bladder acellular matrix graft-silk fibroin enhances bladder reconstruction in a rat model. *Oncotarget* 8, 86471–86487. doi: 10.18632/oncotarget.21211

Yamamoto, N., Akamatsu, H., Hasegawa, S., Yamada, T., Nakata, S., Ohkuma, M., et al. (2007). Isolation of multipotent stem cells from mouse adipose tissue. *J. Dermatol. Sci.* 48, 43–52. doi: 10.1016/j.jdermsci.2007.05.015

Yang, X., Iyer, A. K., Singh, A., Choy, E., Hornicek, F. J., Amiji, M. M., et al. (2015). MDR1 siRNA loaded hyaluronic acid-based CD44 targeted nanoparticle systems circumvent paclitaxel resistance in ovarian cancer. *Sci. Rep.* 5, 8509. doi: 10.1038/srep08509

Yoo, J. J., Meng, J., Oberpenning, F., and Atala, A. (1998). Bladder augmentation using allogenic bladder submucosa seeded with cells. *Urology* 51, 221–225. doi: 10.1016/S0090-4295(97)00644-4

Zhang, H., Yu, N., Zhou, Y., Ma, H., Wang, J., Ma, X., et al. (2016). Construction and characterization of osteogenic and vascular endothelial cell sheets from rat adipose-derived mesenchymal stem cells. *Tissue Cell* 48, 488–495. doi: 10.1016/j.tice.2016.07.004

Zhang, D., Cao, N., Zhou, S., Chen, Z., Zhang, X., and Zhu, W. (2018). The enhanced angiogenesis effect of VEGF-silk fibroin nanospheres-BAMG

scaffold composited with adipose derived stem cells in a rabbit model. *RSC Adv.* 8, 15158–15165. doi: 10.1039/C7RA11610A

Zhu, W. D., Xu, Y. M., Feng, C., Fu, Q., and Song, L. J. (2011). Different bladder defects reconstructed with bladder acellular matrix grafts in a rabbit model. *Urol. A* 50, 1420–1425. doi: 10.1007/s00120-011-2627-2

Zhu, W., Chao, F., Zhang, X., Qiang, F., Song, L., Rong, C., et al. (2016). The Use of Vascular Endothelial Growth Factor with Silk Fibroin Scaffolds and Bladder Acellular Matrix Grafts to Support Bladder Reconstruction in Rabbit Model. *J. Tissue Eng. Regen. M.* 6, 493–499. doi: 10.1166/jbt.2016.1466

Conflict of Interest: The authors declare that the research was conducted in the absence of any commercial or financial relationships that could be construed as a potential conflict of interest.

frontiers in Pharmacology

ORIGINAL RESEARCH
published: 18 June 2020
doi: 10.3389/fphar.2020.00906

Targeted Antitumor Mechanism of C-PC/CMC-CD55sp Nanospheres in HeLa Cervical Cancer Cells

*Guoxiang Liu[1], Xiaohui Xu[1], Liangqian Jiang[2], Huanhuan Ji[1], Feng Zhu[1], Bingnan Jin[1], Jingjing Han[1], Xiaolei Dong[1], Fanghao Yang[1] and Bing Li[1,3]**

[1] Department of Genetics and Cell Biology, Basic Medical College, Qingdao University, Qingdao, China, [2] Department of Medical Genetics, Linyi People's Hospital, Linyi, China, [3] Department of Hematology, The Affiliated Hospital of Qingdao University, Qingdao, China

OPEN ACCESS

Edited by:
Wei Tao,
Harvard Medical School, United States

Reviewed by:
Xiaowei Zeng,
Sun Yat-sen University, China
Vinoth Kumar Lakshmanan,
Gulf Medical University,
United Arab Emirates

***Correspondence:**
Bing Li
libing_516@qdu.edu.cn

Specialty section:
This article was submitted to Experimental Pharmacology and Drug Discovery, a section of the journal Frontiers in Pharmacology

Received: *11 April 2020*
Accepted: *03 June 2020*
Published: *18 June 2020*

Citation:
Liu G, Xu X, Jiang L, Ji H, Zhu F, Jin B, Han J, Dong X, Yang F and Li B (2020) Targeted Antitumor Mechanism of C-PC/CMC-CD55sp Nanospheres in HeLa Cervical Cancer Cells. Front. Pharmacol. 11:906. doi: 10.3389/fphar.2020.00906

In vitro studies had shown that C-Phycocyanin (C-PC) inhibited cervical cancer HeLa cells growth. We constructed C-PC/CMC-CD55sp nanospheres using C-PC, Carboxymethyl Chitosan (CMC), and CD55 ligand peptide (CD55sp) to allow for targeted antitumor effects against HeLa cells *in vitro* and *in vivo*. The characteristics of the nanospheres were determined using FTIR, electron microscopy, and laser particle size analysis. Flow cytometry, laser confocal microscopy and small animal imaging system showed the targeting of C-PC/CMC-CD55sp nanospheres on HeLa cells. Subsequently, the proliferation and apoptosis were analyzed by Cell Counting Kit-8 (CCK-8), flow cytometry, TUNEL assay and electron microscopy. The expression of the apoptosis-related protein was determined using western blot. The stainings of Hematoxylin and Eosin (HE) were employed to evaluate the cell condition of tumor tissue sections. The cytokines in the blood in tumor-bearing nude mice was determined using ELISA. These results showed that C-PC/CMC-CD55sp nanospheres were successfully constructed and targeted HeLa cells. The constructed nanospheres were more effective than C-PC alone in inhibiting the proliferation and inducing apoptosis in HeLa cells. We also found that C-PC/CMC-CD55sp nanospheres had a significant inhibitory effect on the expression of antiapoptotic protein Bcl-2 and a promotion on the transformation of caspase 3 to cleaved caspase 3. C-PC/CMC-CD55sp nanospheres played an important role in tumor suppression, reduced the expression TGF-β, and increased IL-6 and TNF-α. This study demonstrates that the constructed new C-PC/CMC-CD55sp nanospheres exerted targeted antitumor effects *in vivo* and *in vitro* which provided a novel idea for application of C-PC, and provided experimental basis for comprehensive targeted treatment of tumors.

Keywords: C-phycocyanin, carboxymethyl chitosan, CD55 ligand peptide, targeting nanospheres, HeLa cells

INTRODUCTION

Early screening and vaccination are the most common methods to prevent cervical cancer (Torre et al., 2015), and chemotherapy is a first-line treatment option for patients with cervical cancer. Cetuximab combined with carboplatin and paclitaxel can effectively treat advanced/recurrent cervical cancer (Pignata et al., 2019). Pembrolizumab monotherapy has also been shown to exhibit lasting antitumor activity with adequate safety in patients with advanced cervical cancer (Chung et al., 2019). However, due to lack of targeting, chemotherapy drugs also affect normal cells (Cao et al., 2018). Tumor-targeted drug delivery systems represent an important advancement in cancer therapy. These formulations can deliver effective antitumor drugs specifically or selectively to tumor tissues, which allows for control of drug dosing at specific physiological sites. Specific targeting results in reduced side effects and toxicity at nontargeted sites (Schellmann et al., 2010; Chow et al., 2011; Liu F. et al., 2014; Costa Lima et al., 2017). Nanospheres have been conjugated to a monoclonal antibody against Trophoblast cell surface antigen 2 (TROP2), which is a protein abundant on the surface of HeLa cells. This formulation selectively killed cervical cancer cells through induction of apoptosis and DNA damage (Liu T. et al., 2014). Magnetically responsive bacterial polyester-based nanospheres that encapsulating etoposide and modified with concanavalin-A have been used to target cervical cancer (HeLa) cells (Erdal et al., 2012). Folic acid–conjugated albumin nanospheres have been developed to target drugs to cervical cancer cells, and to reduce side effects (Shen et al., 2011).

Rapid development of nanotechnology has allowed for construction of drug-chitosan nanospheres (Azab et al., 2007; Zhang et al., 2008). C-PC (Zheng et al., 2013), a natural photosynthetic pigment, has antiaging and antioxidative effects, and is nontoxic, safe, and water-soluble. C-PC fluoresces red, and can be used as a fluorescent marker. Li et al. (Li et al., 2010; Li et al., 2016) find that C-PC inhibits tumor growth. However, C-PC is rapidly degraded by proteases *in vivo*, which has limited its use in the pharmaceutical industry. Chitosan (Xu and Du, 2003; Narayanan et al., 2014; Snima et al., 2014; Ravindranathan et al., 2016; Qi et al., 2018) is a natural polymer material that is nontoxic, biocompatible, and biodegradable, and exerts antibacterial, antiinflammatory, wound healing, and antitumor effects. Use of chitosan has been limited by poor water solubility. CMC (Snima et al., 2012; Farag and Mohamed, 2012; Kumar Singh Yadav and Shivakumar, 2012; Maya et al., 2013; Sharif et al., 2017), formed by carboxylation of chitosan, exhibits good water solubility and biocompatibility, is nontoxic, and promotes bacteriostasis (Jiang et al., 2004). CMC has been used as a drug carrier to improve drug efficacy, reduce side effects, and significantly inhibits tumor growth (Snima et al., 2012; Anitha et al., 2014). Complement regulatory protein CD55 (Mamidi et al., 2013) is a decay accelerating factor, presents an anchored Glycosylphosphatidylinositol (GPI) moiety on cell membranes, and it is often highly expressed on the surfaces of tumor cells. This protein may be a target which can make tumor cells escape from autoimmune monitoring and immunotherapy. We synthesized CD55sp (Li et al., 2018) to target drug formulations to CD55 molecules highly expressed on the surfaces of cervical cancer HeLa cells.

In this study, C-PC/CMC-CD55sp nanospheres were constructed based on the antitumor activity of C-PC, the biocompatibility of CMC, and the targeting properties of CD55sp. These nanospheres were evaluated for antitumor efficacy, and the mechanisms of action were characterized *in vivo* and *in vitro*.

MATERIALS AND METHODS

Materials

HeLa cells were purchased from Zhongqiao Xinzhou Biotechnology (Shanghai, China). NU/NU nude mice were purchased from Weitong Lihua Laboratory Animal Technology (Beijing, China). C-PC was purchased from Binmei Biotechnology (Taizhou, China). CMC was purchased from Honghai Biotechnology (Qingdao, China). CD55sp (QVNGLGERSQQM) was purchased from Gill Biochem (Shanghai, China). Cell Counting Kit-8 (CCK-8) was purchased from Biosharp (Hefei, China). Annexin V-FITC/PI apoptosis detection kit and TUNEL kit were purchased from Yeasen Biotechnology (Shanghai, China). Enzyme-linked immunosorbent assay kits were purchased from Gene Mei (Wuhan, China). Rabbit anti-human Bcl-2, caspase 3, and goat anti-rabbit IgG antibody were purchased from Abcam (UK). A laser particle size analyzer (Nano ZS90) was purchased from Malvern Instruments (UK). A full-function micropore detector was purchased from BIO-TEK (USA). A flow cytometer (Accuri C6) was purchased from Bidi Medical Devices (Shanghai, China). A fluorescence microscope (DP80) was purchased from Olympus (Japan). Powerpac Basic was purchased from BIO-RAD (USA). Vilber Fusion Solo Chemiluminescence Imaging System (4S) was purchased from Vilber (France).

Synthesis of C-PC/CMC-CD55sp Nanospheres

Using $CaCl_2$ (1.5 mg/ml) as a cross-linking agent, C-PC/CMC nanospheres were spontaneously constructed by encapsulating C-PC (1 mg/ml) with CMC (2 mg/ml) at 4°C for 30 min in the dark. EDC (2 mg/ml) was added to the C-PC/CMC nanospheres solution. The solution was adjusted to pH 5.6 and stirred at 4°C in the dark for 1 h. C-PC/CMC-CD55sp nanospheres were prepared by combining CD55sp (0.1 mg/ml) overnight at 4°C in the dark (Wang et al., 2017). Encapsulation Efficiency (EE) and Loading Efficiency (LE) of C-PC in nanospheres were calculated as follows (Yang et al., 2017):

$$EE = \frac{\text{weight of C} - \text{PC in the nanospheres}}{\text{initial weight of C} - \text{PC}} \times 100\,\%$$

$$LE = \frac{\text{weight of C} - \text{PC in the nanospheres}}{\text{weight of the nanospheres}} \times 100\,\%$$

Nanospheres were evaluated using FTIR spectra across the range of 500–4,000 cm^{-1} (Abbas et al., 2018; Dong et al., 2018). Nanospheres morphology was observed using a transmission electron microscope (Shi et al., 2016; Nantachit et al., 2017; Tao et al., 2018). Zeta potential (surface charge) and particle size (nanospheres size) were measured using a laser particle size analyzer at 25°C (Zhang et al., 2015; Ahmad et al., 2018; Panchu et al., 2018; von Halling Laier et al., 2018).

Cell Culture and Experimental Grouping

Cell lines were cultured in MEM supplemented with 10% newborn calf serum and incubated in a humid incubator at 37° C and 5% CO_2. Cells were divided into the following four groups: Control (no drug treatment); C-PC (treated with C-PC); C-PC/CMC (treated with C-PC/CMC nanospheres); and C-PC/CMC-CD55sp (treated with C-PC/CMC-CD55sp nanospheres). The IC50 values in the C-PC/CMC-CD55sp were calculated after incubation for 24 h, and these values were used as the drug concentration for all subsequent cell experiments.

Cell Counting Kit-8

Cells were treated with different concentrations of C-PC, C-PC/CMC, and C-PC/CMC-CD55sp in a 96-well plate, and incubated for 24 h in CO_2 incubator. After the medium was aspirated, and the cells were incubated with CCK-8 mixture for 2 h. Measurement of absorbance was carried out at wavelength of 450 nm using a full-function micropore detector (Liu et al., 2013).

Flow Cytometry

In 6-well plates, cells were treated with C-PC, C-PC/CMC, or C-PC/CMC-CD55sp. The cells were digested with pancreatin without EDTA, collected, centrifuged, and washed with PBS. After resuspended in 1× binding buffer, the cells were incubated with annexin V-FITC and PI staining solution at room temperature for 15 min in the dark. Then the solutions were mixed with an appropriate amount of 1× binding buffer, and placed on ice. The samples were evaluated using flow cytometry within 1 h (Liang et al., 2017; Murata et al., 2018; Sui et al., 2018b; Zhao et al., 2018).

Laser Confocal Microscopy

Cells were pretreated with C-PC, C-PC/CMC, or C-PC/CMC-CD55sp in 24-well plates, then incubated at 37°C in a 5% CO_2 incubator for 24 h. Four percent paraformaldehyde were added to fix the cells. The cells were stained with DAPI solution for 10 min. After washing with PBS, cell slides were treated with antifade mounting medium and visualized using laser confocal microscopy (Costa Lima and Reis, 2015; Srivastav et al., 2019).

TUNEL Analysis

Cells were pretreated with C-PC, C-PC/CMC and C-PC/CMC-CD55sp in 24-well plates. The cells were then fixed using 4% paraformaldehyde. After processed successively by Proteinase K solution and 1× equilibration buffer, the cells were incubated with excess TDT incubation buffer at 37°C for 1 h in the dark. Then cell nuclei were stained using DAPI. After washing with deionized water, the samples soaked in the PBS were immediately analyzed using a fluorescence microscope (Sui et al., 2018b).

Electron Microscopy

In six-well plates, cells were treated with Control solution and C-PC/CMC-CD55sp, then scraped off the wells. After centrifugation, the precipitates were fixed using glutaraldehyde, and the cells were visualized using transmission electron microscopy (Guardiola et al., 2017).

Western Blot Analysis

In 6-well plates, cells were divided into C-PC, C-PC/CMC, and C-PC/CMC-CD55sp. After cells were lysed, the supernatants were collected. Then total protein concentrations were measured using the BCA assay. Proteins were separated using SDS-PAGE and transferred to PVDF membranes, and blocked with 5% skim milk for 1 h. The membranes were immunoblotted with the target primary antibodies at 4°C overnight. After washing with PBST, the membranes were treated with HRP-conjugated secondary antibody at room temperature for 1 h. Bands were visualized using chemiluminescence, and gray value analysis of the bands was performed using ImageJ software (Saleh et al., 2014; Lin et al., 2016).

Nude Mouse Tumor Model

Mice were inoculated with a 0.2-ml subcutaneous injection of HeLa cell suspension (1×10^7 cells/ml) under the armpit of the right forelimb. After tumor formation, the mice were also separated into control, C-PC, C-PC/CMC and C-PC/CMC-CD55sp. We injected C-PC/CMC-CD55sp into the tail veins of the mice, and the fluorescence intensity of the tumors was observed using small animal imaging system at 6 and 24 h. After 24 h, the mice were sacrificed and the fluorescence intensities of the heart, liver, spleen, kidney, and tumors were observed using small animal imaging system (Yeh et al., 2016; Li C. et al., 2017; Li W. et al., 2017; Wan et al., 2017; Song et al., 2018). An additional five mice per group were injected with doses based on body weight, and the IC50 values determined in the C-PC/CMC-CD55sp were used as the drug concentrations for each group. Mice were injected once every 2 days, and sacrificed after 20 days. Tumors and serum were collected for subsequent experiments (Li et al., 2013; Gao et al., 2016; Yeh et al., 2016; Wang et al., 2017; Sui et al., 2018a).

Hematoxylin and Eosin Staining

For histological studies, tumor tissue samples (1 cm by 1 cm) were fixed in 10% formalin for a week to prepare paraffinized blocks by routine histological techniques. The 6-μm paraffinized sections were dewaxed and hydrated, then rinsed three times with PBS (3 min each). The samples were stained with hematoxylin for 5 min, faded with 1% HCl, and rinsed six times with ddH_2O (5 min each). The samples were stained blue using a lithium carbonate saturated solution for 1 to 2 min, then rinsed three times with double-distilled water (5 min each). Stain separation was performed using 80% alcohol followed by rinsing three times with double-distilled water (5

min each). The sample were then stained with eosin for 5 min, and rinsed three times with double-distilled water (5 min each). The sections were then dehydrated, hyalinized, and mounting using resin. Field by field assessments of tissue morphology were performed using a light microscope (Abedpour et al., 2018; Baig et al., 2018; Liu et al., 2018; Wang et al., 2018; Gao et al., 2018).

Enzyme-Linked Immunosorbent Assay

We used enzyme-linked immunosorbent assay (ELISA) kits to determine levels of interleukin-6 (IL-6), tumor necrosis factor-α (TNF-α), and transforming growth factor β (TGF-β) (Chen et al., 2004; Yang et al., 2010; Shi et al, 2018). Serum was collected and tested according to the ELISA kit manufacturer's instructions. Analysis was performed within 15 min after adding the stop solution.

Statistical Analysis

Statistical analyses were performed using Prism 5.0 (GraphPad Software, Inc., La Jolla, CA, USA). Results are expressed as the mean ± SEM of three or more observations (as indicated in each experiment). The mean values for biochemical data from two groups were compared using two-tailed Student's *t*-tests. *P*-values less than 0.05 were considered statistically significant.

RESULTS

Encapsulation Efficiency and Loading Efficiency

The standard curve equation for C-PC concentration and fluorescence intensity was Y = 4.6481X-2.5841 (r^2 = 0.9993), and was linear across the range of 5–100 μg/ml (**Figures 1A, B**). The prepared C-PC/CMC nanospheres solution was centrifuged, and the fluorescence intensity of the supernatant was measured to determine the concentration. The EE was 65%. The samples were then precipitated by centrifugation, and the precipitates were freeze-dried. The net weights of the precipitates were determined using an electronic balance to determine the weights of the nanospheres. The LE was 20% (**Figure 1C**).

Characteristics of Nanospheres

In **Figure 2A**, based on FTIR spectra, we find that the peak situated at 1259 cm^{-1} in C-PC/CMC nanospheres related to C-O stretching turned to wave number 1237 cm^{-1} and 1018 cm^{-1} in C-PC/CMC-CD55sp nanospheres, and which may attribute to C-PC/CMC nanospheres modified with CD55sp resulted in the shifting and increase of peaks. In **Figure 2B**, the nanospheres were spherical and uniformly dispersed, as determined using electron microscopy. The nanospheres were dehydrated as a result of drying, which resulted in a bias in determination of particle size using electron microscopy. The relative sizes of nanospheres were compared using electron microscopy to confirm that the nanospheres contained drug. Compared with CMC nanospheres, the relative diameter of C-PC/CMC nanospheres was larger. This larger diameter may have been due to encapsulation of C-PC within the CMC nanospheres. The larger relative diameter of C-PC/CMC-CD55sp nanospheres may have been due to conjugation of CD55sp to the surface of C-PC/CMC nanospheres. As shown in **Table 1**, the particle sizes of CMC nanospheres, C-PC/CMC nanospheres, and C-PC/CMC-CD55sp nanospheres were 160.5 ± 48.06 nm, 146.6 ± 53.3 nm, and 258.9 ± 40.505 nm, respectively. The particle size of C-PC/CMC nanospheres was lower than that of CMC nanospheres, which may have been due to tighter internal bonds. Conjugation of CD55sp to the surface of C-PC/CMC nanospheres may have resulted in increased particle size. The zeta potentials of CMC nanospheres, C-PC/CMC nanospheres, and C-PC/CMC-CD55sp nanospheres were -7.66 ± 3.83 mV, -19.7 ± 2.53 mV, and -13.1 ± 3.28 mV, respectively. These values indicated that CMC and C-PC were negatively charged, and CD55sp was positively charged.

Targeting Ability of Nanospheres

To investigate cellular uptake of nanospheres into HeLa cells, C-PC was used as a fluorescent marker. The fluorescence intensity was higher in the C-PC/CMC-CD55sp group than that in the other groups, as determined using flow cytometry and laser confocal microscopy, which indicated that this formulation was targeted to HeLa cells (**Figures 3A, B**). The results showed that the nanospheres formulation enhanced the internalization of drugs into HeLa cells. To evaluate the tissue distribution of nanospheres *in vivo*, the fluorescent marker C-PC was detected in a nude mouse model. The mice were injected with C-PC/CMC-CD55sp nanospheres *via* the tail vein, and fluorescence was observed 6 h after injection, and the fluorescence intensity was increased 24 h after injection. The nanospheres accumulated in the liver, the spleen, and the tumor, with most accumulation observed in the tumor. Accumulation of the nanospheres in the liver and the spleen may have been related to drug metabolism and the reticuloendothelial phagocytosis (**Figure 3C**). These results indicated that C-PC/CMC-CD55sp nanospheres were targeted to tumors, and that CD55sp may be an effective tumor targeting factor.

Inhibition of Proliferation

In **Figure 4A**, HeLa cells proliferation decreased in a dose-dependent manner in response to treatment with C-PC, C-PC/CMC, and C-PC/CMC-CD55sp. Furthermore, treatment with C-PC/CMC-CD55sp inhibited proliferation of HeLa cells to a greater extent than the other formulations. The IC50 value for C-PC/CMC-CD55sp in HeLa cells was about 40 μg/ml. We also evaluated the antitumor effects of the nanospheres in tumor-bearing nude mice. After 20 days of observation and measurement, no nude mice in the C-PC, C-PC/CMC, or C-PC/CMC-CD55sp exhibited weight loss or showed signs of significant toxicity, and all animals survived to the end of the experiment. As shown in **Figure 4B**, tumor growth rate was inhibited by each of the drugs, and C-PC/CMC-CD55sp inhibited tumor growth to the greatest extent. The size and weight of the tumors were measured following sacrifice, and the results were consistent with those for tumor growth (**Figures 4C, D**). These results showed that C-PC, C-PC/CMC, and C-PC/

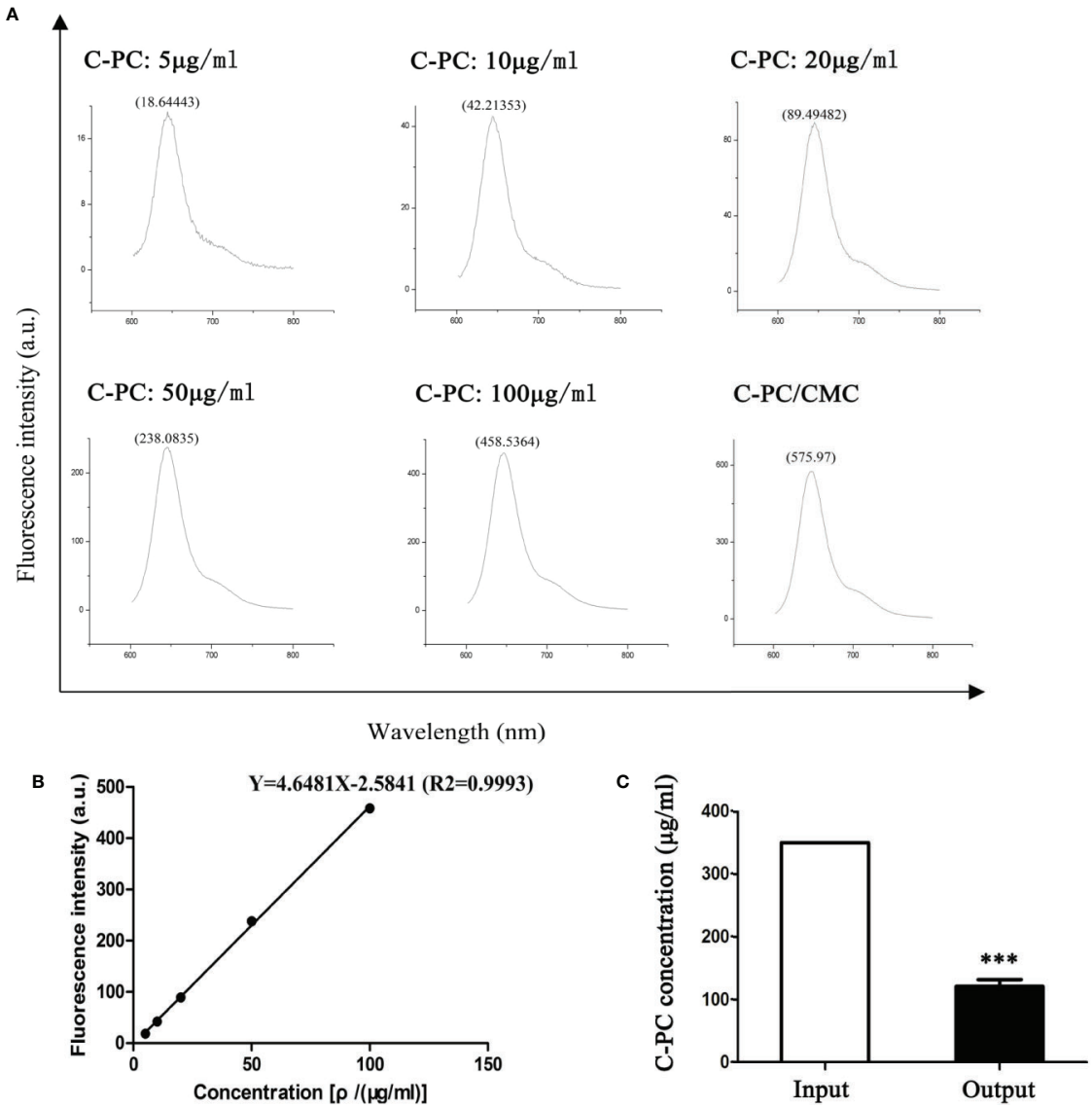

FIGURE 1 | Encapsulation Efficiency (EE) and Loading Efficiency (LE) of C-Phycocyanin (C-PC)/Carboxymethyl Chitosan (CMC) nanospheres. **(A)** Fluorescence spectrophotometry assay. The horizontal axis represents the wavelength (nm) and the vertical axis represents the fluorescence intensity (a.u.). The fluorescence intensity in response to 5, 10, 20, 50, and 100 μg/ml C-PC at 644 nm was 18.64443, 42.21353, 89.49482, 238.0835, and 458.5364, respectively. The fluorescence intensity of the supernatant of the C-PC/CMC solution was 575.97. **(B)** Standard curve. The horizontal axis represents the concentration [ρ/(μg/ml)] and the vertical axis represents the fluorescence intensity (a.u.). The concentration was linearly related to the fluorescence intensity, and the standard curve was used to determine the concentration of the supernatant of the C-PC/CMC solution. **(C)** Supernatant analysis. The initial concentration of C-PC was used as the input, and the concentration of the supernatant of the C-PC/CMC solution was the output. Results are expressed as the mean ± SEM (n = 3). ***P < 0.001.

CMC-CD55sp inhibited tumor growth, and C-PC/CMC-CD55sp induced the strongest inhibitory effect.

Apoptosis

Apoptosis is a key indicator of the antitumor ability of drugs. We found that C-PC, C-PC/CMC, and C-PC/CMC-CD55sp increased apoptosis in HeLa cells, and C-PC/CMC-CD55sp induced apoptosis to the greatest extent by TUNEL assay (**Figures 5A, B**) and flow cytometry analysis (**Figures 5C, D**). In **Figure 5E** a, ultrastructural analysis of untreated HeLa cells was used to characterize the normal morphology of the control group. In **Figure 5E** b, cells treated with C-PC/CMC-CD55sp showed apoptotic morphology, which included cytoplasm concentration, decreased cell volume, nuclear shrinkage and deepened staining, and disappearance of microvilli. As shown in **Figure 5F**, tumor tissue sections were prepared from tumor-bearing nude mice to further evaluate apoptosis. In the Control group, the tumor cells indicated by arrow 1 were closely aligned,

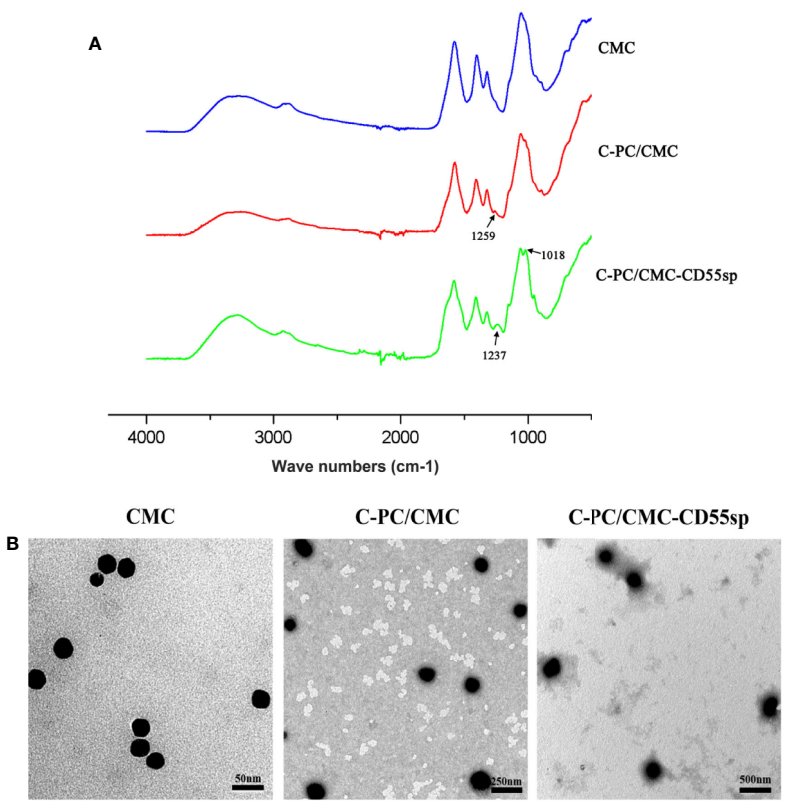

FIGURE 2 | Characterization of nanospheres. **(A)** FTIR spectra for Carboxymethyl Chitosan (CMC), C-Phycocyanin (C-PC)/CMC, and C-PC/CMC-CD55sp. **(B)** Morphology was determined using transmission electron microscopy. CMC, scale bars, 50 nm; C-PC/CMC, scale bars, 250 nm; C-PC/CMC-CD55sp, scale bars, 500 nm.

TABLE 1 | The sizes and zeta potentials of the developed nanospheres.

Nanospheres	Size (d.nm)	Zeta potential (mV)
CMC	160.5 ± 48.06	-7.66 ± 3.83
C-PC/CMC	146.6 ± 53.3	-19.7 ± 2.53
C-PC/CMC-CD55sp	258.9 ± 40.505	-13.1 ± 3.28

with clear margins and normal karyotypes. In the three treatment groups, the tumor cells indicated by arrow 2 were dispersed, and showed characteristic apoptotic changes, such as nuclear shrinkage, nuclear rupture, and nuclear dissolution. Apoptosis is tightly regulated by apoptosis-related proteins such as Bcl-2 and caspase 3. **Figures 5G, H** showed that the levels of Bcl-2 protein and cleaved caspase 3 were lower in response to treatment with nanospheres, and C-PC/CMC-CD55sp induced the most pronounced changes. These results showed that C-PC/CMC-CD55sp induced apoptosis by altering the levels of apoptosis-related proteins.

Immunoregulation

To evaluate the role of immune response in tumor killing, the levels of IL-6, TNF-α, and TGF-β were measured in mouse serum using ELISA. The levels of IL-6 and TNF-α in the C-PC, C-PC/CMC, and C-PC/CMC-CD55sp groups were higher than those in the Control group. In contrast, the levels of TGF-β were lower in the treated groups than those in the Control group, and C-PC/CMC-CD55sp induced the strongest effect (**Figure 6**). These results indicated that C-PC/CMC-CD55sp stimulated secretion of IL-6 and TNF-α, and reduced the expression of TGF-β, which might indicate that tumor cells death occurred through modulation of the immune response.

DISCUSSION

Cervical cancer is among the most common types of gynecological malignant tumors (Torre et al., 2015). Base on the epidemiological studies, there are about 500,000 new cases of cervical cancer globally each year (Torre et al., 2015). Li B. et al. (2006) showed that release of cytochrome C from mitochondria to the cytoplasm following C-PC treatment of HeLa cells was associated with apoptosis. Another study showed that CMC-co-poly (AA) had potential for targeted delivery of various antitumor drugs (Sharif et al., 2017). Li et al. (2018) also showed that CD55sp could bind to CD55 molecules on the surface of HeLa cells as a ligand peptide. Therefore, we

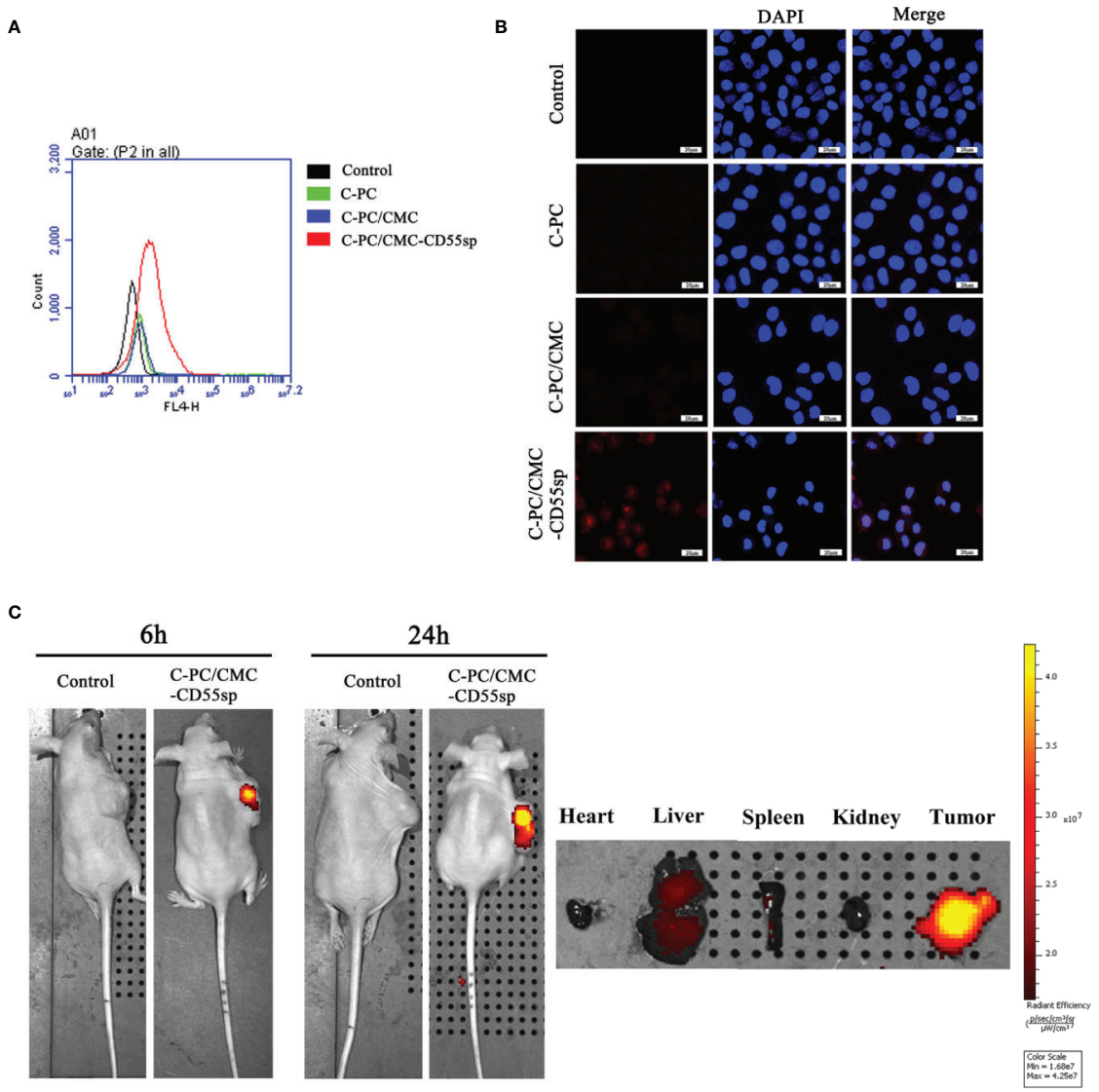

FIGURE 3 | Determination of targeting effects using flow cytometry, laser confocal microscopy, and imaging. **(A)** Flow cytometry analysis. The fluorescence intensity of HeLa cells was determined using flow cytometry. The horizontal axis represents fluorescence intensity. Fluorescence intensity represented the targeting ability of drugs. **(B)** Laser confocal microscopy. Fluorescence intensity of HeLa cells was determined using laser confocal. Blue fluorescence represents nuclei, and red fluorescence represents targeting ability. **(C)** Imaging. Fluorescence intensity in tumor tissues and organs (heart, liver, spleen, and kidney) was detected using small animal imaging system. The color scale represents fluorescence intensity. Fluorescence intensity represents the targeting ability of drugs.

constructed novel C-PC/CMC-CD55sp nanospheres with C-PC included as an anticancer drug, CMC as a carrier, and CD55sp as a targeting peptide. Targeted inhibition of proliferation and apoptosis were evaluated in HeLa cells (**Figure 7**).

The EE and LE of the nanospheres were determined (Yang et al., 2017). The nanospheres were characterized using FTIR (Abbas et al., 2018; Dong et al., 2018), electron microscopy (Shi et al., 2016; Nantachit et al., 2017; Tao et al., 2018), and laser particle size analysis (Couvreur et al., 2002; Zhang et al., 2015; Shi et al., 2016; Ahmad et al., 2018; Panchu et al., 2018; von Halling Laier et al., 2018). The results showed that C-PC/CMC-CD55sp nanospheres were successfully constructed.

Flow cytometry (Ying et al., 2018), laser confocal microscopy (Costa Lima and Reis, 2015; Srivastav et al., 2019), and small animal imaging system (Yeh et al., 2016; Li C. et al., 2017; Li W. et al., 2017; Wan et al., 2017; Song et al., 2018) showed that C-PC/CMC-CD55sp nanospheres were targeted to tumor cells. These results showed that the developed nanospheres targeted HeLa cells *in vitro* and *in vivo* in a tumor-bearing mouse model.

Cell viability was analyzed as the proportion of healthy cells in a sample, and proliferation has been shown to be an important parameter for understanding the pathways involved in cell survival or death after treatment (Adan et al., 2016). Generally, methods used to determine cell viability have also been used to

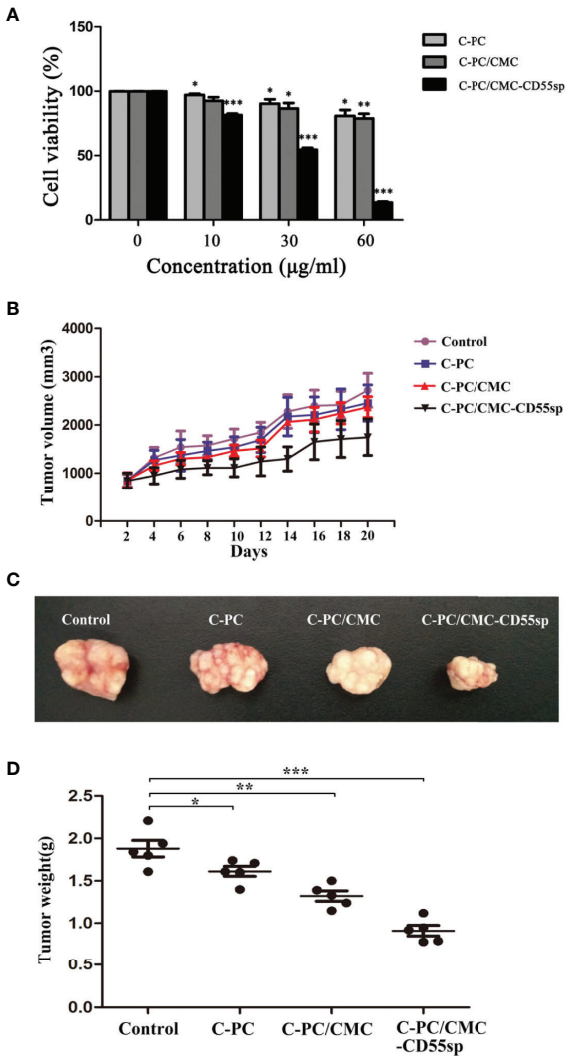

FIGURE 4 | Inhibitory effects of drugs on cell proliferation *in vitro* and *in vivo*. **(A)** Cell Counting Kit-8 (CCK-8) assay. The x-axis represents drug concentration (0, 10, 30, and 60 μg/ml), and the y-axis represents cell activity, as determined using the CCK-8 assay. Results are expressed as the mean ± SEM (n = 3). *P < 0.05, **P < 0.01, ***P < 0.001. **(B)** Tumor volume. The horizontal axis represents days and the vertical axis represents tumor volume (mm^3). **(C)** Tumor size. **(D)** Tumor weights. The vertical axis represents tumor weights (g). Results are expressed as the mean ± SEM (n = 5). *P < 0.05, **P < 0.01, ***P < 0.001.

determine cell proliferation (Adan et al., 2016). Furthermore, cell proliferation assays have been generally used for drug screening to determine whether the test molecules had induced the desired effects (Adan et al., 2016). In our study, CCK-8 was used to evaluated the effects of C-PC, C-PC/CMC, and C-PC/CMC-CD55sp on HeLa cell proliferation. The results showed that C-PC/CMC-CD55sp induced the strongest antitumor effect.

Tumorigenesis results from disruption of the balance between proliferation and apoptosis, and apoptotic signal transduction is a key factor in apoptosis. To detect nuclear DNA cleaved by activated DNases during late stages of apoptosis, TUNEL staining is typically used (Fayzullina and Martin, 2014). Flow cytometry can be used to identify apoptotic cells through binding of dye to phosphatidylserine on the cell surface of early apoptosis, and through binding of dyes to DNA of late apoptotic or necrotic cells (Wlodkowic et al., 2011; Jiang et al., 2017). Dynamic changes in compaction of nuclear chromatin are characteristic of apoptosis (Wyllie et al., 1984). During apoptosis, chromatin undergoes a phase change from a heterogeneous, genetically active network to an inert highly condensed fragmented form (Maruyama et al., 2001; Tone et al., 2007). Cell morphology, size, and changes in organelles can also be used to identify apoptotic cells (Taatjes et al., 2008). Apoptosis-related proteins such as the caspase 3 protease family (Hsu et al., 2018; Safavi et al., 2018) and the antiapoptotic protein Bcl-2 (Pihan et al., 2017; Beberok et al., 2018) play key roles in apoptosis. Using western blot, we determined the expression of cleaved caspase 3 and Bcl-2 to evaluate apoptosis in tumor cells. The results showed that C-PC/CMC-CD55sp induced apoptosis of HeLa cells to the greatest extent, which resulted in strong antitumor effects.

We detected cytokines such IL-6, TNF-α, and TGF-β in mouse serum, and showed that the developed nanospheres induced an immune response, which may have regulated tumor killing. IL-6 signaling been shown to inhibit tumor growth by mobilizing antitumor T cell immune responses (Fisher et al., 2014). IL-6, which is produced by dendritic cells in lymph nodes, has been shown to impact activation, expansion, survival, and polarization of T cells during immune responses (Hope et al., 1995). IL-6 may participate in modulation of the T cell immune response, resulting in a shift from a suppressive to a responsive state that could promote antitumor activity. Furthermore, IL-6 has been shown to play an important role in promoting T cell trafficking to lymph nodes and to tumor sites, where they become activated and exert cytotoxic effector activity (Chen et al., 2004; Appenheimer et al., 2007; Fisher et al., 2011; Fisher et al., 2014).

TNF-α is produced by monocytes and macrophages, and plays a role in cell survival, apoptosis-related inflammation, and immune activity (Shi et al., 2018). In addition, TNF-α has been shown to be an effective antitumor agent *in vitro* and *in vivo* through induction of tumor apoptosis and necrosis (Li M.O. et al., 2006). High loco-regional doses of TNF-α have been shown to induce hemorrhagic necrosis *via* selective destruction of tumor blood vessels and generation of specific T cell antitumor immunity (Lejeune, 2002; Balkwill, 2006).

TGF-β signaling plays an important role in promoting tumor initiation and progression, and its mechanisms include dysregulation of cyclin-dependent kinase inhibitors, alteration of cytoskeletal architecture, increased protease expression and extracellular matrix formation, decreased immune surveillance, and increased angiogenesis (Massague, 2008; Yang et al., 2010). Studies have shown that TGF-β had an adverse effect on antitumor immunity and inhibited host tumor immune surveillance (Li M.O. et al., 2006; Yang et al., 2010). Furthermore, TGF-β markedly suppressed the 'cytotoxic

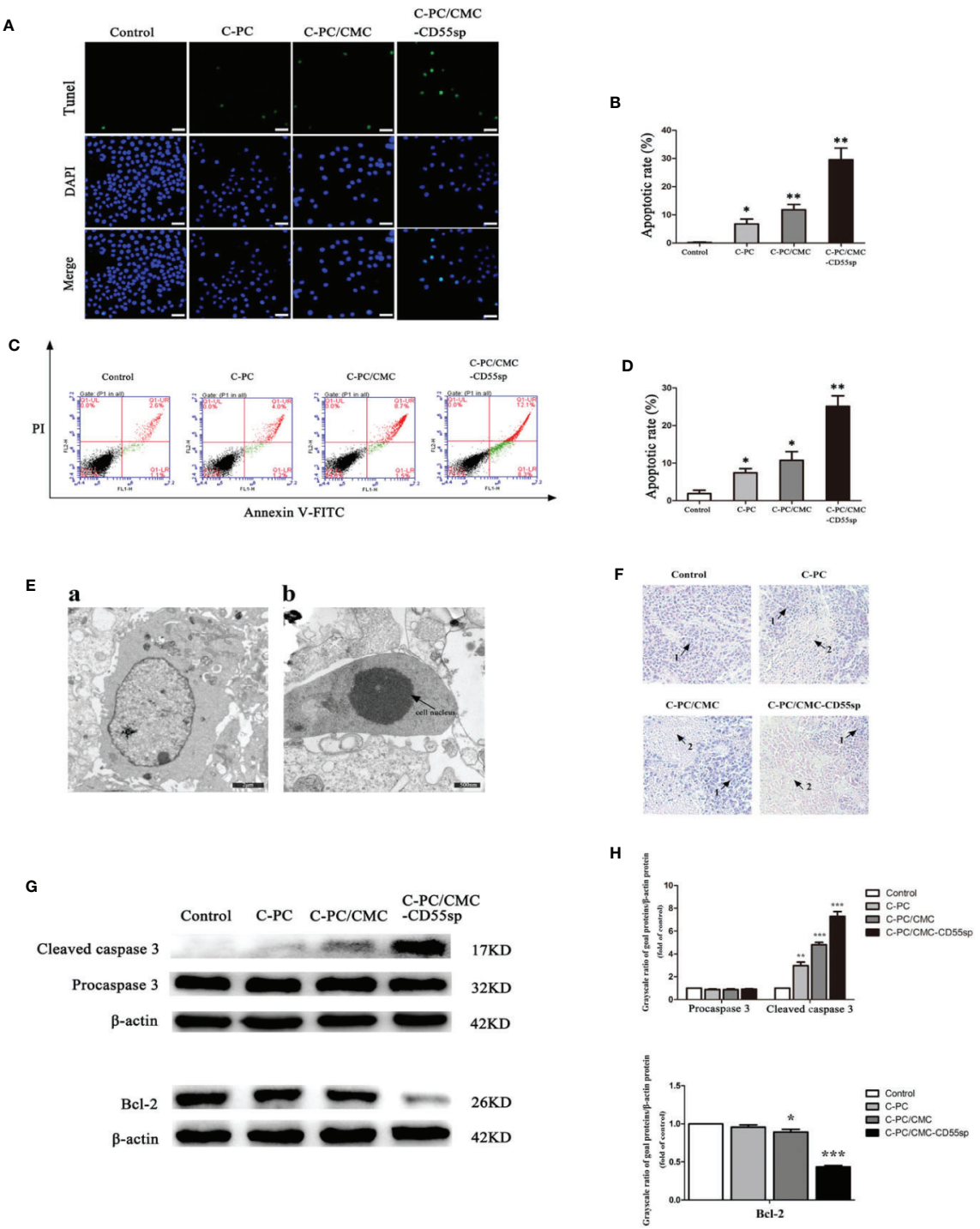

FIGURE 5 | Drug-induced apoptosis. **(A, B)** TUNEL assay. Blue fluorescence indicates nuclei, and green fluorescence indicates apoptotic cells. The percentage of apoptotic cells (%) was equal to the ratio of the number of stained cells to the total number of cells. Results are expressed as the mean ± SEM (n = 3). *P < 0.05, **P < 0.01. Scale bars, 20 μm. **(C, D)** Flow cytometry analysis. Apoptosis was evaluated using an annexin V-FITC and PI apoptosis detection kit. The apoptosis rates of cells were determined, and C-Phycocyanin (C-PC)/CMC-CD55sp nanospheres induced apoptosis to the greatest extent. Results are expressed as the mean ± SEM (n = 3). *P < 0.05, **P < 0.01. **(E)** Electron microscopy. a. Normal HeLa cells. Scale bars, 2 μm; b. Apoptotic HeLa cells. Scale bars, 500 nm. Arrows indicate nuclei. **(F)** Hematoxylin and eosin staining. (1) Normal HeLa cells; (2) apoptotic HeLa cells. **(G, H)** Western blot. Protein levels were normalized to β-actin. Results are expressed as the mean ± SEM (n = 3). *P < 0.05, **P < 0.01, ***P < 0.001.

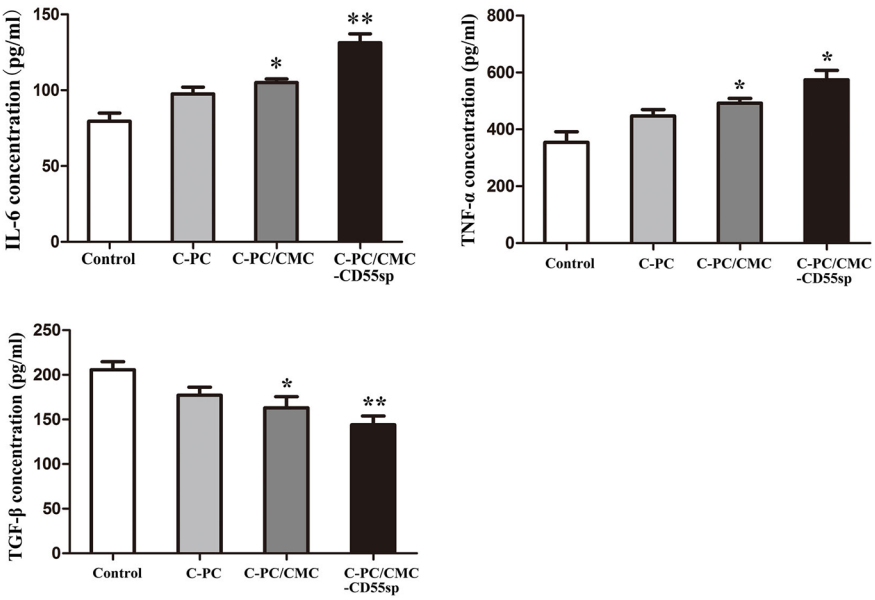

FIGURE 6 | Levels of interleukin-6 (IL-6), tumor necrosis factor-α (TNF-α), and transforming growth factor β (TGF-β) in nude mice. Enzyme-linked immunosorbent assay. The vertical axis represents concentration (pg/ml). Results are expressed as the mean ± SEM (n = 3). *P<0.05, **P<0.01.

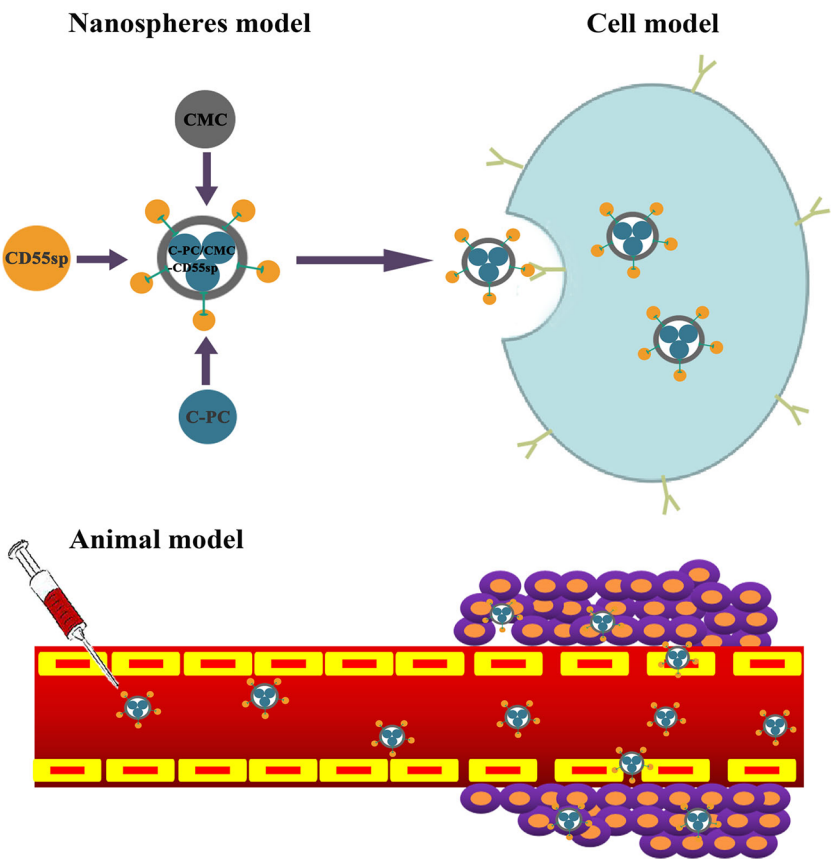

FIGURE 7 | A model for C-PC/CMC-CD55sp nanospheres in targeting tumor cells *in vivo* and *in intro*.

program' of cytotoxic T lymphocytes, which have been shown that favor tumor progression (Thomas and Massague, 2005; Yang et al., 2010). Detection of IL-6, TNF-α, and TGF-β in blood of tumor-bearing nude mice showed that C-PC/CMC-CD55sp nanospheres induced an immune response that was associated with tumor growth inhibition.

CONCLUSION

We successfully constructed C-PC/CMC-CD55sp nanospheres and confirmed their targeting properties. These nanospheres inhibited HeLa cell proliferation and promoted HeLa cell apoptosis *in vivo* and *in vitro*. Furthermore, these nanospheres inhibited tumor tissue growth through regulation of the immune response *in vivo* in nude mice.

DATA AVAILABILITY STATEMENT

The raw data supporting the conclusions of this article will be made available by the authors, without undue reservation.

ETHICS STATEMENT

The animal study was reviewed and approved by Medical Ethics Committee of Affiliated Hospital of Qingdao University.

AUTHOR CONTRIBUTIONS

GL, XX, LJ, and BL designed the study, performed the experiments, analyzed and interpreted the data. HJ, FZ, and BJ wrote and refined the manuscript. JH, XD, and FY assisted in the completion of the project. All authors contributed to the article and approved the submitted version.

FUNDING

This work was supported by grants from the National Natural Science Foundation of China (Nos. 81871231, 81471546, and 81001346), Youth Innovation and Technology Plan of Shandong Colleges (2019KJK016), and Science and Technology Project of Qingdao (No. 18-6-1-91-nsh).

REFERENCES

Abbas, S. S., Rees, G. J., Kelly, N. L., Dancer, C. E. J., Hanna, J. V., and McNally, T. (2018). Facile silane functionalization of graphene oxide. *Nanoscale* 10, 16231–16242. doi: 10.1039/c8nr04781b

Abedpour, N., Salehnia, M., and Ghorbanmehr, N. (2018). The Effects of Lysophosphatidic Acid on The Incidence of Cell Death in Cultured Vitrified and Non-Vitrified Mouse Ovarian Tissue: Separation of Necrosis and Apoptosis Border. *Cell J.* 20, 403–411. doi: 10.22074/cellj.2018.5180

Adan, A., Kiraz, Y., and Baran, Y. (2016). Cell Proliferation and Cytotoxicity Assays. *Curr. Pharm. Biotechnol.* 17, 1213–1221. doi: 10.2174/1389201017666160808160513

Ahmad, N., Ahmad, R., Alam, M. A., and Ahmad, F. J. (2018). Enhancement of oral bioavailability of doxorubicin through surface modified biodegradable polymeric nanoparticles. *Chem. Cent. J.* 12, 65. doi: 10.1186/s13065-018-0434-1

Anitha, A., Sreeranganathan, M., Chennazhi, K. P., Lakshmanan, V. K., and Jayakumar, R. (2014). In vitro combinatorial anticancer effects of 5-fluorouracil and curcumin loaded N,O-carboxymethyl chitosan nanoparticles toward colon cancer and in vivo pharmacokinetic studies. *Eur. J. Pharm. Biopharm.* 88, 238–251. doi: 10.1016/j.ejpb.2014.04.017

Appenheimer, M. M., Girard, R. A., Chen, Q., Wang, W. C., Bankert, K. C., Hardison, J., et al. (2007). Conservation of IL-6 trans-signaling mechanisms controlling L-selectin adhesion by fever-range thermal stress. *Eur. J. Immunol.* 37, 2856–2867. doi: 10.1002/eji.200636421

Azab, A. K., Kleinstern, J., Doviner, V., Orkin, B., Srebnik, M., Nissan, A., et al. (2007). Prevention of tumor recurrence and distant metastasis formation in a breast cancer mouse model by biodegradable implant of 131I-norcholesterol. *J. Control Release.* 123, 116–122. doi: 10.1016/j.jconrel.2007.07.014

Baig, M., Khan, S., Naeem, M. A., Khan, G. J., and Ansari, M. T. (2018). Vildagliptin loaded triangular DNA nanospheres coated with eudragit for oral delivery and better glycemic control in type 2 diabetes mellitus. *BioMed. Pharmacother.* 97, 1250–1258. doi: 10.1016/j.biopha.2017.11.059

Balkwill, F. (2006). TNF-alpha in promotion and progression of cancer. *Cancer Metastasis Rev.* 25, 409–416. doi: 10.1007/s10555-006-9005-3

Beberok, A., Wrzesniok, D., Rok, J., Rzepka, Z., Respondek, M., and Buszman, E. (2018). Ciprofloxacin triggers the apoptosis of human triple-negative breast cancer MDA-MB-231 cells via the p53/Bax/Bcl-2 signaling pathway. *Int. J. Oncol.* 52, 1727–1737. doi: 10.3892/ijo.2018.4310

Cao, J., Chen, Z., Chi, J., Sun, Y., and Sun, Y. (2018). Recent progress in synergistic chemotherapy and phototherapy by targeted drug delivery systems for cancer treatment. *Artif. Cells Nanomed. Biotechnol.* 46, 817–830. doi: 10.1080/21691401.2018.1436553

Chen, Q., Wang, W. C., Bruce, R., Li, H., Schleider, D. M., Mulbury, M. J., et al. (2004). Central role of IL-6 receptor signal-transducing chain gp130 in activation of L-selectin adhesion by fever-range thermal stress. *Immunity* 20, 59–70. doi: 10.1016/S1074-7613(03)00358-3

Chow, E. K., Zhang, X. Q., Chen, M., Lam, R., Robinson, E., Huang, H., et al. (2011). Nanodiamond therapeutic delivery agents mediate enhanced chemoresistant tumor treatment. *Sci. Transl. Med.* 3, 73ra21. doi: 10.1126/scitranslmed.3001713

Chung, H. C., Ros, W., Delord, J. P., Perets, R., Italiano, A., Shapira-Frommer, R., et al. (2019). Efficacy and Safety of Pembrolizumab in Previously Treated Advanced Cervical Cancer: Results From the Phase II KEYNOTE-158 Study. *J. Clin. Oncol.* 37, 1470–1478. doi: 10.1200/JCO.18.01265

Costa Lima, S. A., and Reis, S. (2015). Temperature-responsive polymeric nanospheres containing methotrexate and gold nanoparticles: A multi-drug system for theranostic in rheumatoid arthritis. *Colloids Surf. B Biointerfaces.* 133, 378–387. doi: 10.1016/j.colsurfb.2015.04.048

Costa Lima, S. A., Gaspar, A., Reis, S., and Duraes, L. (2017). Multifunctional nanospheres for co-delivery of methotrexate and mild hyperthermia to colon cancer cells. *Mater. Sci. Eng C Mater. Biol. Appl.* 75, 1420–1426. doi: 10.1016/j.msec.2017.03.049

Couvreur, P., Barratt, G., Fattal, E., Legrand, P., and Vauthier, C. (2002). Nanocapsule technology: a review. *Crit. Rev. Ther. Drug Carrier Syst.* 19, 99–134. doi: 10.1615/CritRevTherDrugCarrierSyst.v19.i2.10

Dong, H., Guo, M., Liang, Y., Fan, C., Ding, G., Zhang, W., et al. (2018). Preparation and characterization of indole-3-butyric acid nanospheres for improving its stability and utilization. *Mater. Sci. Eng C Mater. Biol. Appl.* 89, 175–181. doi: 10.1016/j.msec.2018.04.004

Erdal, E., Kavaz, D., Sam, M., Demirbilek, M., Demirbilek, M. E., Saglam, N., et al. (2012). Preparation and characterization of magnetically responsive bacterial polyester based nanospheres for cancer therapy. *J. BioMed. Nanotechnol.* 8, 800–808. doi: 10.1166/jbn.2012.1431

Farag, R. K., and Mohamed, R. R. (2012). Synthesis and characterization of carboxymethyl chitosan nanogels for swelling studies and antimicrobial activity. *Molecules* 18, 190–203. doi: 10.3390/molecules18010190

Fayzullina, S., and Martin, L. J. (2014). Detection and analysis of DNA damage in mouse skeletal muscle in situ using the TUNEL method. *J. Vis. Exp.* 52211. doi: 10.3791/52211

Fisher, D. T., Chen, Q., Skitzki, J. J., Muhitch, J. B., Zhou, L., Appenheimer, M. M., et al. (2011). IL-6 trans-signaling licenses mouse and human tumor microvascular gateways for trafficking of cytotoxic T cells. *J. Clin. Invest.* 121, 3846–3859. doi: 10.1172/jci44952

Fisher, D. T., Appenheimer, M. M., and Evans, S. S. (2014). The two faces of IL-6 in the tumor microenvironment. *Semin. Immunol.* 26, 38–47. doi: 10.1016/j.smim.2014.01.008

Gao, Z., Liu, X., Wang, Y., Deng, G., Zhou, F., Wang, Q., et al. (2016). Facile one-pot synthesis of Fe3O4@chitosan nanospheres for MRI and fluorescence imaging guided chemo-photothermal combinational cancer therapy. *Dalton Trans.* 45, 19519–19528. doi: 10.1039/c6dt03897b

Gao, S., Zhou, H., Cui, S., and Shen, H. (2018). Bottom-up synthesis of MoS2 nanospheres for photothermal treatment of tumors. *Photochem Photobiol. Sci.* 17, 1337–1345. doi: 10.1039/c8pp00198g

Guardiola, F. A., Logothetis, P., Meseguer, J., and Esteban, M. A. (2017). Evaluation of silver nanospheres on viability and innate cellular parameters of gilthead seabream (Sparus aurata L.) head-kidney leucocytes. *Fish Shellfish Immunol.* 69, 99–107. doi: 10.1016/j.fsi.2017.08.017

Hope, J. C., Cumberbatch, M., Fielding, I., Dearman, R. J., Kimber, I., and Hopkins, S. J. (1995). Identification of dendritic cells as a major source of interleukin-6 in draining lymph nodes following skin sensitization of mice. *Immunology* 86, 441–447.

Hsu, H. Y., Lin, T. Y., Hu, C. H., Shu, D. T. F., and Lu, M. K. (2018). Fucoidan upregulates TLR4/CHOP-mediated caspase-3 and PARP activation to enhance cisplatin-induced cytotoxicity in human lung cancer cells. *Cancer Lett.* 432, 112–120. doi: 10.1016/j.canlet.2018.05.006

Jiang, H. L., Park, I. K., Shin, N. R., Kang, S. G., Yoo, H. S., Kim, S. I., et al. (2004). In vitro study of the immune stimulating activity of an atrophic [correction of athrophic] rhinitis vaccine associated to chitosan microspheres. *Eur. J. Pharm. Biopharm.* 58, 471–476. doi: 10.1016/j.ejpb.2004.05.006

Jiang, L., Paone, S., Caruso, S., Atkin-Smith, G. K., Phan, T. K., Hulett, M. D., et al. (2017). Determining the contents and cell origins of apoptotic bodies by flow cytometry. *Sci. Rep.* 7, 14444. doi: 10.1038/s41598-017-14305-z

Kumar Singh Yadav, H., and Shivakumar, H. G. (2012). In Vitro and In Vivo Evaluation of pH-Sensitive Hydrogels of Carboxymethyl Chitosan for Intestinal Delivery of Theophylline. *ISRN Pharm.* 2012, 763127. doi: 10.5402/2012/763127

Lejeune, F. J. (2002). Clinical use of TNF revisited: improving penetration of anti-cancer agents by increasing vascular permeability. *J. Clin. Invest.* 110, 433–435. doi: 10.1172/jci16493

Li, B., Gao, M. H., Zhang, X. C., and Chu, X. M. (2006). Molecular immune mechanism of C-phycocyanin from Spirulina platensis induces apoptosis in HeLa cells in vitro. *Biotechnol. Appl. Biochem.* 43, 155–164. doi: 10.1042/ba20050142

Li, M. O., Wan, Y. Y., Sanjabi, S., Robertson, A. K., and Flavell, R. A. (2006). Transforming growth factor-beta regulation of immune responses. *Annu. Rev. Immunol.* 24, 99–146. doi: 10.1146/annurev.immunol.24.021605.090737

Li, B., Chu, X., Gao, M., and Li, W. (2010). Apoptotic mechanism of MCF-7 breast cells in vivo and in vitro induced by photodynamic therapy with C-phycocyanin. *Acta Biochim. Biophys. Sin. (Shanghai).* 42, 80–89. doi: 10.1093/abbs/gmp104

Li, J., Di, Y., Jin, C., Fu, D., Yang, F., Jiang, Y., et al. (2013). Gemcitabine-loaded albumin nanospheres (GEM-ANPs) inhibit PANC-1 cells in vitro and in vivo. *Nanoscale Res. Lett.* 8, 176. doi: 10.1186/1556-276x-8-176

Li, B., Gao, M. H., Lv, C. Y., Yang, P., and Yin, Q. F. (2016). Study of the synergistic effects of all-transretinoic acid and C-phycocyanin on the growth and apoptosis of A549 cells. *Eur. J. Cancer Prev.* 25, 97–101. doi: 10.1097/cej.0000000000000157

Li, C., Qian, M., Wang, S., Jiang, H., Du, Y., Wang, J., et al. (2017). Aptavalve-gated Mesoporous Carbon Nanospheres image Cellular Mucin and provide On-demand Targeted Drug Delivery. *Theranostics* 7, 3319–3325. doi: 10.7150/thno.18692

Li, W., Zhang, H., Guo, X., Wang, Z., Kong, F., Luo, L., et al. (2017). Gold Nanospheres-Stabilized Indocyanine Green as a Synchronous Photodynamic-Photothermal Therapy Platform That Inhibits Tumor Growth and Metastasis. *ACS Appl. Mater. Interfaces.* 9, 3354–3367. doi: 10.1021/acsami.6b13351

Li, G., Yin, Q., Ji, H., Wang, Y., Liu, H., Jiang, L., et al. (2018). A study on screening and antitumor effect of CD55-specific ligand peptide in cervical cancer cells. *Drug Des. Devel Ther.* 12, 3899–3912. doi: 10.2147/dddt.S182337

Liang, Y., Liu, J., Liu, T., and Yang, X. (2017). Anti-c-Met antibody bioconjugated with hollow gold nanospheres as a novel nanomaterial for targeted radiation ablation of human cervical cancer cell. *Oncol. Lett.* 14, 2254–2260. doi: 10.3892/ol.2017.6383

Lin, W. W., Chen, I. J., Cheng, T. C., Tung, Y. C., Chu, P. Y., Chuang, C. H., et al. (2016). A Secondary Antibody-Detecting Molecular Weight Marker with Mouse and Rabbit IgG Fc Linear Epitopes for Western Blot Analysis. *PloS One* 11, e0160418. doi: 10.1371/journal.pone.0160418

Liu, Q., Song, Y. J., Meng, L. J., Hu, F., Gou, L. X., Jia, C. H., et al. (2013). Role of LM23 in cell proliferation and apoptosis and its expression during the testis development. *Asian J. Androl.* 15, 539–544. doi: 10.1038/aja.2013.43

Liu, F., Li, M., Liu, C., Liu, Y., Liang, Y., Wang, F., et al. (2014). Tumor-specific delivery and therapy by double-targeted DTX-CMCS-PEG-NGR conjugates. *Pharm. Res.* 31, 475–488. doi: 10.1007/s11095-013-1176-3

Liu, T., Tian, J., Chen, Z., Liang, Y., Liu, J., Liu, S., et al. (2014). Anti-TROP2 conjugated hollow gold nanospheres as a novel nanostructure for targeted photothermal destruction of cervical cancer cells. *Nanotechnology* 25, 345103. doi: 10.1088/0957-4484/25/34/345103

Liu, Y., Chen, J., Jin, M., Li, Z., Tian, T., Li, L., et al. (2018). Relationship between changes in mitochondrial function and hippocampal neuronal apoptosis after recurrent convulsion during developmental stage. *Exp. Ther. Med.* 16, 127–132. doi: 10.3892/etm.2018.6147

Mamidi, S., Cinci, M., Hasmann, M., Fehring, V., and Kirschfink, M. (2013). Lipoplex mediated silencing of membrane regulators (CD46, CD55 and CD59) enhances complement-dependent anti-tumor activity of trastuzumab and pertuzumab. *Mol. Oncol.* 7, 580–594. doi: 10.1016/j.molonc.2013.02.011

Maruyama, R., Takemura, G., Aoyama, T., Hayakawa, K., Koda, M., Kawase, Y., et al. (2001). Dynamic process of apoptosis in adult rat cardiomyocytes analyzed using 48-hour videomicroscopy and electron microscopy: beating and rate are associated with the apoptotic process. *Am. J. Pathol.* 159, 683–691. doi: 10.1016/s0002-9440(10)61739-7

Massague, J. (2008). TGFbeta in Cancer. *Cell* 134, 215–230. doi: 10.1016/j.cell.2008.07.001

Maya, S., Kumar, L. G., Sarmento, B., Sanoj Rejinold, N., Menon, D., Nair, S. V., et al. (2013). Cetuximab conjugated O-carboxymethyl chitosan nanoparticles for targeting EGFR overexpressing cancer cells. *Carbohydr. Polym.* 93, 661–669. doi: 10.1016/j.carbpol.2012.12.032

Murata, Y., Jo, J. I., and Tabata, Y. (2018). Preparation of cationized gelatin nanospheres incorporating molecular beacon to visualize cell apoptosis. *Sci. Rep.* 8, 14839. doi: 10.1038/s41598-018-33231-2

Nantachit, N., Sunintaboon, P., and Ubol, S. (2017). EDIII-DENV3 nanospheres drive immature dendritic cells into a mature phenotype in an in vitro model. *Microbiol. Immunol.* 61, 305–317. doi: 10.1111/1348-0421.12497

Narayanan, D., Jayakumar, R., and Chennazhi, K. P. (2014). Versatile carboxymethyl chitin and chitosan nanomaterials: a review. *Wiley Interdiscip. Rev. Nanomed. Nanobiotechnol.* 6, 574–598. doi: 10.1002/wnan.1301

Panchu, S. J., Dhani, S., Chuturgoon, A., and Moodley, M. K. (2018). Laser assisted synthesis of inorganic fullerene like MoS2-Au nanohybrid and their cytotoxicity against human monocytic (THP-1) cells. *J. Photochem Photobiol. B.* 187, 10–17. doi: 10.1016/j.jphotobiol.2018.07.028

Pignata, S., Scambia, G., Lorusso, D., De Giorgi, U., Nicoletto, M. O., Lauria, R., et al. (2019). The MITO CERV-2 trial: A randomized phase II study of cetuximab plus carboplatin and paclitaxel, in advanced or recurrent cervical cancer. *Gynecol Oncol.* 153, 535–540. doi: 10.1016/j.ygyno.2019.03.260

Pihan, P., Carreras-Sureda, A., and Hetz, C. (2017). BCL-2 family: integrating stress responses at the ER to control cell demise. *Cell Death Differ.* 24, 1478–1487. doi: 10.1038/cdd.2017.82

Qi, H., Chen, Q., Ren, H., Wu, X., Liu, X., and Lu, T. (2018). Electrophoretic deposition of dexamethasone-loaded gelatin nanospheres/chitosan coating and its dual function in anti-inflammation and osteogenesis. *Colloids Surf. B Biointerfaces.* 169, 249–256. doi: 10.1016/j.colsurfb.2018.05.029

Ravindranathan, S., Koppolu, B. P., Smith, S. G., and Zaharoff, D. A. (2016). Effect of Chitosan Properties on Immunoreactivity. *Mar Drugs* 14, 91. doi: 10.3390/md14050091

Safavi, M., Shakeri, R., Ardestani, S. K., Davoodi, J., Ajdary, S., and Foroumadi, A. (2018). Caspase-dependent apoptosis induced by two synthetic halogenated flavanones, 3',7-dichloroflavanone and 3',6-dichloroflavanone, on human breast and prostate cancer cells. *In Vitro Cell Dev. Biol. Anim.* 54, 136–146. doi: 10.1007/s11626-017-0209-3

Saleh, A. M., Aljada, A., Rizvi, S. A., Nasr, A., Alaskar, A. S., and Williams, J. D. (2014). In vitro cytotoxicity of Artemisia vulgaris L. essential oil is mediated by a mitochondria-dependent apoptosis in HL-60 leukemic cell line. *BMC Complement Altern. Med.* 14, 226. doi: 10.1186/1472-6882-14-226

Schellmann, N., Deckert, P. M., Bachran, D., Fuchs, H., and Bachran, C. (2010). Targeted enzyme prodrug therapies. *Mini Rev. Med. Chem.* 10, 887–904. doi: 10.2174/138955710792007196

Sharif, Q. U., Sohail, M., Ahmad, M., Usman Minhas, M., Khan, S., Khan, S., et al. (2017). Novel polymeric composites based on carboxymethyl chitosan and poly(acrylic acid): in vitro and in vivo evaluation. *J. Mater. Sci. Mater. Med.* 28, 147. doi: 10.1007/s10856-017-5952-1

Shen, Z., Li, Y., Kohama, K., Oneill, B., and Bi, J. (2011). Improved drug targeting of cancer cells by utilizing actively targetable folic acid-conjugated albumin nanospheres. *Pharmacol. Res.* 63, 51–58. doi: 10.1016/j.phrs.2010.10.012

Shi, C., Zhu, P., Chen, N., Ye, X., Wang, Y., and Xiao, S. (2016). Preparation and sustainable release of modified konjac glucomannan/chitosan nanospheres. *Int. J. Biol. Macromol.* 91, 609–614. doi: 10.1016/j.ijbiomac.2016.05.073

Shi, F., Li, J., Ye, Z., Yang, L., Chen, T., Chen, X., et al. (2018). Antitumor effects of melanin from Lachnum YM226 and its derivative in H22 tumor-bearing mice. *Medchemcomm*. 9, 1059–1068. doi: 10.1039/c8md00035b

Snima, K. S., Jayakumar, R., Unnikrishnan, A. G., Nair, S. V., and Lakshmanan, V. K. (2012). O-carboxymethyl chitosan nanoparticles for metformin delivery to pancreatic cancer cells. *Carbohydr. Polym.* 89, 1003–1007. doi: 10.1016/j.carbpol.2012.04.050

Snima, K. S., Jayakumar, R., and Lakshmanan, V. K. (2014). In vitro and in vivo biological evaluation of O-carboxymethyl chitosan encapsulated metformin nanoparticles for pancreatic cancer therapy. *Pharm. Res.* 31, 3361–3370. doi: 10.1007/s11095-014-1425-0

Song, Z., Xu, X., Liu, M., Liu, J., Chen, J., Li, C., et al. (2018). Efficacy and mechanism of steep pulse irreversible electroporation technology on xenograft model of nude mice: a preclinical study. *World J. Surg. Oncol.* 16, 84. doi: 10.1186/s12957-018-1386-6

Srivastav, A., Chandanshive, B., Dandekar, P., Khushalani, D., and Jain, R. (2019). Biomimetic Hydroxyapatite a Potential Universal Nanocarrier for Cellular Internalization & Drug Delivery. *Pharm. Res.* 36, 60. doi: 10.1007/s11095-019-2594-7

Sui, B., Liu, X., and Sun, J. (2018a). Dual-Functional Dendritic Mesoporous Bioactive Glass Nanospheres for Calcium Influx-Mediated Specific Tumor Suppression and Controlled Drug Delivery in Vivo. *ACS Appl. Mater. Interfaces.* 10, 23548–23559. doi: 10.1021/acsami.8b05616

Sui, B., Liu, X., and Sun, J. (2018b). Dual-Functional Dendritic Mesoporous Bioactive Glass Nanospheres for Calcium Influx-Mediated Specific Tumor Suppression and Controlled Drug Delivery in Vivo. *ACS Appl. Mater. Interfaces*. 10, 23548–23559. doi: 10.1021/acsami.8b05616

Taatjes, D. J., Sobel, B. E., and Budd, R. C. (2008). Morphological and cytochemical determination of cell death by apoptosis. *Histochem. Cell Biol.* 129, 33–43. doi: 10.1007/s00418-007-0356-9

Tao, L., Jiang, J., Gao, Y., Wu, C., and Liu, Y. (2018). Biodegradable Alginate-Chitosan Hollow Nanospheres for Codelivery of Doxorubicin and Paclitaxel for the Effect of Human Lung Cancer A549 Cells. *BioMed. Res. Int.* 2018, 4607945. doi: 10.1155/2018/4607945

Thomas, D. A., and Massague, J. (2005). TGF-beta directly targets cytotoxic T cell functions during tumor evasion of immune surveillance. *Cancer Cell.* 8, 369–380. doi: 10.1016/j.ccr.2005.10.012

Tone, S., Sugimoto, K., Tanda, K., Suda, T., Uehira, K., Kanouchi, H., et al. (2007). Three distinct stages of apoptotic nuclear condensation revealed by time-lapse imaging, biochemical and electron microscopy analysis of cell-free apoptosis. *Exp. Cell Res.* 313, 3635–3644. doi: 10.1016/j.yexcr.2007.06.018

Torre, L. A., Bray, F., Siegel, R. L., Ferlay, J., Lortet-Tieulent, J., and Jemal, A. (2015). Global cancer statistics 2012. *CA Cancer J. Clin.* 65, 87–108. doi: 10.3322/caac.21262

von Halling Laier, C., Gibson, B., van de Weert, M., Boyd, B. J., Rades, T., Boisen, A., et al. (2018). Spray dried cubosomes with ovalbumin and Quil-A as a nanoparticulate dry powder vaccine formulation. *Int. J. Pharm.* 550, 35–44. doi: 10.1016/j.ijpharm.2018.08.036

Wan, D. H., Zheng, B. Y., Ke, M. R., Duan, J. Y., Zheng, Y. Q., Yeh, C. K., et al. (2017). C-Phycocyanin as a tumour-associated macrophage-targeted photosensitiser and a vehicle of phthalocyanine for enhanced photodynamic therapy. *Chem. Commun. (Camb).* 53, 4112–4115. doi: 10.1039/c6cc09541k

Wang, Y., Jiang, L., Yin, Q., Liu, H., Liu, G., Zhu, G., et al. (2017). The Targeted Antitumor Effects of C- PC/CMC-CD59sp Nanoparticles on HeLa Cells in Vitro and in Vivo. *J. Cancer.* 8, 3001–3013. doi: 10.7150/jca.21059

Wang, L., Wang, Z., Shi, J., Jiang, Q., Wang, H., Li, X., et al. (2018). Inhibition of proprotein convertase subtilisin/kexin type 9 attenuates neuronal apoptosis following focal cerebral ischemia via apolipoprotein E receptor 2 downregulation in hyperlipidemic mice. *Int. J. Mol. Med.* 42, 2098–2106. doi: 10.3892/ijmm.2018.3797

Wlodkowic, D., Telford, W., Skommer, J., and Darzynkiewicz, Z. (2011). Apoptosis and beyond: cytometry in studies of programmed cell death. *Methods Cell Biol.* 103, 55–98. doi: 10.1016/b978-0-12-385493-3.00004-8

Wyllie, A. H., Morris, R. G., Smith, A. L., and Dunlop, D. (1984). Chromatin cleavage in apoptosis: association with condensed chromatin morphology and dependence on macromolecular synthesis. *J. Pathol.* 142, 67–77. doi: 10.1002/path.1711420112

Xu, Y., and Du, Y. (2003). Effect of molecular structure of chitosan on protein delivery properties of chitosan nanoparticles. *Int. J. Pharm.* 250, 215–226. doi: 10.1016/S0378-5173(02)00548-3

Yang, L., Pang, Y., and Moses, H. L. (2010). TGF-beta and immune cells: an important regulatory axis in the tumor microenvironment and progression. *Trends Immunol.* 31, 220–227. doi: 10.1016/j.it.2010.04.002

Yang, P., Li, B., Yin, Q.-F., and Wang, Y.-J. (2017). Carboxymethyl chitosan nanoparticles coupled with CD59-specific ligand peptide for targeted delivery of C-phycocyanin to HeLa cells. *Tumor Biol.* 39, 1–9. doi: 10.1177/1010428317692267

Yeh, C. Y., Hsiao, J. K., Wang, Y. P., Lan, C. H., and Wu, H. C. (2016). Peptide-conjugated nanoparticles for targeted imaging and therapy of prostate cancer. *Biomaterials* 99, 1–15. doi: 10.1016/j.biomaterials.2016.05.015

Ying, M., Zhuang, J., Wei, X., Zhang, X., Zhang, Y., Jiang, Y., et al. (2018). Remote-Loaded Platelet Vesicles for Disease-Targeted Delivery of Therapeutics. *Adv. Funct. Mater.* 28, 1801032. doi: 10.1002/adfm.201801032

Zhang, C., Qu, G., Sun, Y., Wu, X., Yao, Z., Guo, Q., et al. (2008). Pharmacokinetics, biodistribution, efficacy and safety of N-octyl-O-sulfate chitosan micelles loaded with paclitaxel. *Biomaterials* 29, 1233–1241. doi: 10.1016/j.biomaterials.2007.11.029

Zhang, H., Hou, X., Lin, M., Wang, L., Li, H., Yuan, C., et al. (2015). The study on the preparation and characterization of gene-loaded immunomagnetic albumin nanospheres and their anti-cell proliferative effect combined with magnetic fluid hyperthermia on GLC-82 cells. *Drug Des. Devel Ther.* 9, 6445–6460. doi: 10.2147/dddt.S93481

Zhao, H., Wu, C., Gao, D., Chen, S., Zhu, Y., Sun, J., et al. (2018). Antitumor Effect by Hydroxyapatite Nanospheres: Activation of Mitochondria-Dependent Apoptosis and Negative Regulation of Phosphatidylinositol-3-Kinase/Protein Kinase B Pathway. *ACS Nano*. 12, 7838–7854. doi: 10.1021/acsnano.8b01996

Zheng, J., Inoguchi, T., Sasaki, S., Maeda, Y., McCarty, M. F., Fujii, M., et al. (2013). Phycocyanin and phycocyanobilin from Spirulina platensis protect against diabetic nephropathy by inhibiting oxidative stress. *Am. J. Physiol. Regul. Integr. Comp. Physiol.* 304, R110–R120. doi: 10.1152/ajpregu.00648.2011

Conflict of Interest: The authors declare that the research was conducted in the absence of any commercial or financial relationships that could be construed as a potential conflict of interest.

frontiers in Pharmacology

MINI REVIEW
published: 30 June 2020
doi: 10.3389/fphar.2020.00960

Recent Advances in Nanotechnology for Dendritic Cell-Based Immunotherapy

*Chen Qian, Li-Jun Yang and Hong Cui**

Department of Pediatrics, Beijing Friendship Hospital, Capital Medical University, Beijing, China

Dendritic cells (DCs) are the most important antigen-presenting cells that determine cancer immune responses by regulating immune activation and tolerance, especially in the initiation stage of specific responses. Manipulation of DCs to enhance specific antitumor immune response is considered to be a powerful tool for tumor eradication. Nanotechnology, which can incorporate multifunction components and show spatiotemporal control properties, is of great interest and is widely investigated for its ability to improve immune response activity against cancer and even for prevention and avoiding recurrence. In this mini-review, we aim to provide a general view of DC-based immunotherapy, including that involving the promising nanotechnology. Particularly we discuss: (1) manipulation or engineering of DCs for adoptive vaccination, (2) employing DCs as a combination to more existing therapeutics in tumor treatment, and (3) direct modulation of DCs *in vivo* to enhance antigen presentation efficacy and priming T cells subsequently. We comprehensively discuss the updates on the application of nanotechnology in DC-based immunotherapy and provide some insights on the challenges and opportunities of DC-based immunotherapeutics, including the potential of nanotechnology, against cancers.

Keywords: nanotechnology, dendritic cell, cancer, immunotherapy, antigen delivery, cross-presentation

OPEN ACCESS

Edited by:
Jianxun Ding,
Chinese Academy of Sciences, China

Reviewed by:
Evelien Smits,
University of Antwerp, Belgium
Xiangru Feng,
Chinese Academy of Sciences, China

***Correspondence:**
Hong Cui
Cuihong2017@126.com

Specialty section:
This article was submitted to Experimental Pharmacology and Drug Discovery, a section of the journal Frontiers in Pharmacology

Received: *17 February 2020*
Accepted: *12 June 2020*
Published: *30 June 2020*

Citation:
Qian C, Yang L-J and Cui H (2020) Recent Advances in Nanotechnology for Dendritic Cell-Based Immunotherapy. Front. Pharmacol. 11:960. doi: 10.3389/fphar.2020.00960

INTRODUCTION

Cancer therapies have been evolving with advances in oncology (Couzin-Frankel, 2013). There has been some success with the use of traditional cancer therapies such as surgery (Krook et al., 1991; Wolf, 1991; Macdonald et al., 2001; Coffey et al., 2003), chemotherapy (Liu et al., 2011; Al-Lazikani et al., 2012; Koppelmans et al., 2012; Chen et al., 2017), and radiotherapy (Sauer et al., 2004; Abe et al., 2005). However, low-specificity, drug resistance, and side effects hinder the efficacies of these tumor treatments (Lippert et al., 2008; Guth et al., 2011; Housman et al., 2014; Rothermundt, 2015; Leary et al., 2018). Inducing or boosting up the patients' own immune responses enable specific recognition and killing of tumor cells. Besides, immune response-mediated tumor eradication reduces the potential risks of toxicity and drug resistance (Beltran et al., 2011; Zhong et al., 2017). Therefore, in recent years, cancer immunotherapy is burgeoning and is considered to be the fourth important therapeutic method to deal with cancers. For example, the first tumor vaccine Sipuleucel-T was approved by the U.S. Food and Drug Administration (FDA) in 2010 for prostate cancer treatment (Higano et al., 2009; Kantoff et al., 2010). In the next year, the first immune-checkpoint

inhibitor antibody Ipilimumab (anti-CTLA4 antibody) was approved for the treatment of advanced melanoma (Robert et al., 2011). In the next few years, multiple immune-checkpoint blockage antibodies were approved in various cancers and achieved great success (Brahmer et al., 2015; Le et al., 2015; Reck et al., 2016). Encouragingly, the Nobel prize in physiology and medicine honored James P. Allison and Tasuku Honjo for their discovery of the efficacy of inhibiting negative immune regulation in cancer therapy. Additionally, Tisagenlecleucel, the first chimeric antigen receptor-T cell-based adoptive transfer treatment for pediatric and young adult acute lymphoblastic leukemia and adult diffuse large B-cell lymphoma was approved in 2018 by the FDA (June et al., 2018; Maude et al., 2018).

Although great achievements have been made in cancer immunotherapy, only some percentage of patients can benefit from those promising immunotherapeutics, mainly owing to the immunosuppressive microenvironment of the solid tumor and immune tolerance to mono-therapeutics (Albini et al., 2018; Binnewies et al., 2018; Costa et al., 2018; Feng et al., 2018; Knudson et al., 2018; Zhao et al., 2018). Therefore, maximizing the potential and ability of the immune system to overcome tumors is critical (Zhang and Bevan, 2011; Nicholson, 2016). Dendritic cells (DCs) are the initiators of specific immune responses, and when activated effectively can lead to priming of T cells to elicit immune antitumor responses for tumor destruction (Rescigno et al., 1997; Leifer, 2017). More importantly, results of whole exome sequencing and RNA sequencing present the possibility of developing DC-targeting vaccines and DC-based immunotherapy (Leitner et al., 1999; Mathan et al., 2017). Manipulating DCs by taking advantage of the controllable and modifiable features of nanotechnology shows promising antitumor responses both in vitro and in vivo.

DCS IN IMMUNE SYSTEM

DCs are originated from dedicated hematopoietic precursor cells and transformed into DC in variable stimuli in physiological environment. (Thomas and Lipsky, 1996; Ardavin et al., 2001; Ardavin, 2003; Wang et al., 2019b). Circulating blood cells such as monocytes, white blood cells may differentiate to matured DCs owing to the crosstalk among diverse signals coordination (Rutella et al., 2006; Williams et al., 2013). DCs were demonstrated to play a crucial role in mediating innate and adaptive immune responses in 1970s by Ralph Steinman and Zanvil A. Cohn, who were honored with the Noble Prize for their discovery. Since then, DCs have been documented as the most effective antigen-presenting cells that activate primary and subsequent memory immune responses (Kadowaki, 2009).

DCs as antigen-presenting cells encounter antigens and present them to T cell for priming in the form of antigen peptide-major histocompatibility complex (MHC) (Cohen et al., 2003; Zehn et al., 2004). Antigens may circulate through peripheral blood and stimulate DCs or captured by tissue resident DCs such as lymph node, spleen. Whatever, DCs' received antigens are required to migrate to the lymphoid organs which determines the subsequent T cell activation efficacy due to the abundance of T cells in the lymphoid organs (Mempel et al., 2004) (Segura and Villadangos, 2009). The success of DCs' activation requires two signals, antigens and activation stimuli. The second activation signals may be provided exogenously such as by lipopolysaccharide (Morrison and Kline, 1977), Toll-like receptor (TLR) ligands (Kawai and Akira, 2007), and antibodies targeting activation of receptors like tumor necrosis factor (Schnurr et al., 2000), proinflammatory cytokines IFN-γ, *etc* (Simmons et al., 2012; Minton, 2014). Endogenous damage-associated molecular patterns such as high mobility group proteins (Raucci et al., 2007), calreticulin (Li et al., 2015), and heat shock proteins with immunogenic features are also capable of maturing DCs (Bethke et al., 2002). Similarly, two signals are required for T cell priming; one is a specific antigen-MHC I/II complex and the other one is a costimulatory signal expressed on activated DCs. mDCs with antigen-MHC complex expression induce T cells to differentiate into Th1 or Th2 cells under the condition of variable cytokines, for example, IL-12, which is essential to activate cytotoxic T cells. In some other cases, under the condition of IL-4, it may switch immunity with antibody secretion. Mostly, these activated CD8+ T cells are fully functional, with cytotoxicity and ability to secrete IFN-γ for highly effective and specific killing of cancer cells. Other than cytotoxic T cell stimulation, matured DCs (mDCs) may also function to neutralize antibody secretion by B cells in the way of IL-10 and IL-33 secretion, driving Th2 immunity and influencing immunoglobulin subtype polarization (Segura et al., 2013). Additionally, DCs with inflammatory features induce Th17 differentiation, which promotes cytotoxic T cell responses and regresses tumor (Murugaiyan and Saha, 2009; Segura et al., 2013; Guéry and Hugues, 2015). Apart from stimulating specific adaptive immunity, mDCs can also be decorated with IL-12, IL-15, and type I IFNs which are positive to NK cell functions in innate immunity. Thus, the DCs act as a bridge between innate and adaptive immunity for host defenses (**Figure 1**). As discussed above, the immature DCs that are usually found in peripheral lymphoid tissues process antigens without activation stimuli and are capable of presenting antigen-MHC to naïve T cells, resulting in tolerance to T cell responses (Probst et al., 2005).

MANIPULATION OF DCS FOR VACCINATION

DCs that initiate adaptive immune responses, including antitumorigenesis, are of great interest worldwide, owing to their ability to be able to present tumor-associated antigens and prime subsequent antitumor responses. Because of their critical role with professional presentation expertise in the immune system, exploiting DC for vaccination is considered to provide a powerful tool to prevent and cure infections and cancers (Lizotte et al., 2016; Roden and Stern, 2018; Wang et al., 2019a; Wen et al., 2019). As initiators of adaptive

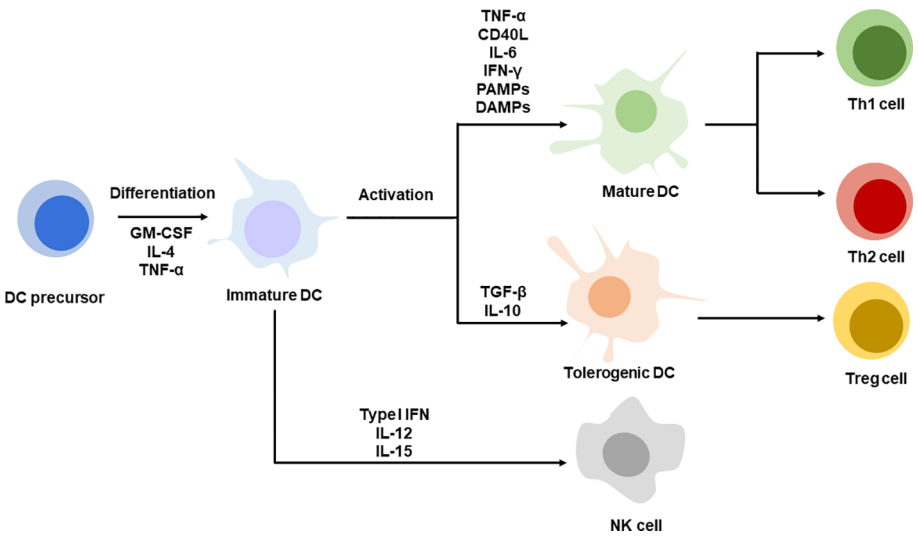

FIGURE 1 | DC differentiation and maturation. DC precursors are differentiating into immature DC. Immature DCs are activated with specific stimuli, TNF-α, CD40L, IL-6, IFN-γ, PAMPs, DAMPs promote DC maturation, corresponding to Th1 or Th2 cells priming. DCs stimulate with TGF-β, IL-10 present tolerogenic phenotype leading to Treg differentiation. Immature DC decorated with type I IFN, IL-12 and IL-15 favor NK cell function.

immunity, DCs are ideal targets for *ex vivo* education and adoptive vaccination, which can induce specific antitumor immune responses in patients *in vivo* (Lövgren et al., 2018). Conventional techniques to develop DC-based vaccines involved isolation or culture precursor cells from patients' peripheral blood, loading them with antigens *in vitro* and applying certain maturation stimuli to promote DC maturation. Precursor cells such as CD34+ hematopoietic cells, monocytes cultured with certain stimuli enabled differentiating into immature DCs. In order to differentiate and expand DCs *in vitro*, immature DCs are loaded with tumor antigens such as tumor lysates, peptides, proteins, nucleotides, or fused with tumor cells, under the condition of stimulatory molecules. Challenges remained although more techniques have been developed. Peptides can be loaded directly on MHC molecules; however, it requires clear and definite information not only on the epitopes such as sequence and conserved motif, but also on an individual's HLA configuration that determines the type of immune responses and adaptive immunity. Clinical study is ongoing to confirm the immunogenicity of peptide-loaded DC vaccination (NCT02334735). Instead of peptides, loading of proteins or lysates has also been used for numerous cancer treatments (NCT00045968). Although these require further intracellular processing, the major advantage of using whole protein processing is its potential to induce both CD4+ and CD8+ T cell responses (Constantino et al., 2016; Wang et al., 2017; Sharma et al., 2018). To realize the DC function of initiating specific antitumor immunity, DCs loaded with tumor-associated antigens require stimuli (example, CD40L or TLR agonist) for maturation. The mDCs are then transferred back to the patients to mediate specific immune response. The whole process is complicated and requires skilled operation and high cost. Most clinical studies on DC vaccines are in combination with chemotherapy (NCT03688178, NCT03657966, NCT03047525) (Kongsted et al., 2017), radiotherapy (NCT03226236,), targeted agents (Ogasawara et al., 2018; Palma et al., 2018), or immunotherapeutic regimens (NCT03546426, NCT03735290, NCT03450044, NCT03735589). Clinical studies implied that technologies that combine antigen loading and various combination agents are required and of great potential.

Nanotechnology refers to the technology utilizing nanosized materials that range from 10 to 100 nm in size; these are emerging as an ideal tool for cancer therapy. Nanomaterials with divergent compositions enable passive or active targeting, which enhances the efficacy and reduces the toxicity of treatment (Liu et al., 2018; Wang and Mooney, 2018; Feng et al., 2019). The ability of DCs to capture, process, and present antigen to induce T cell priming is essential in adaptive antitumor immunity. Therefore, nanomaterials targeting DCs are considered to be a promising tool to boost an efficient and specific anticancer immune response. Nanomaterials also incorporate multifunctional molecules together to modulate part or whole of the antigen presentation (Parvanian et al., 2017; Sangtani et al., 2017). Functional nanomaterials with lysosome escaping ability have been widely reported; these nanomaterials are favorable for antigen delivery to the cytoplasm and their intracellular digestion, which further contributes to antigen processing and presentation (Jiang et al., 2018; Zhong et al., 2019). Lipid-based nanoparticles and polymeric nanoparticles (Reichmuth et al., 2016; Zhou et al., 2016; Gulla et al., 2019; Wen et al., 2019; Lin et al., 2020), with better biocompatibility, have been reported in the development of DC targeted vaccines for anticancer and antiviral treatments. Liposome-based nanoparticles containing molecules such as trivalent influenza antigen, OVA, and heat shock

proteins, have been investigated for their ability to activate the immune system in disease treatment. Delivery of protein, peptide, and nucleic acid antigens, which can induce corresponding immune responses, to DCs *via* nanomaterials might probably increase their circulation and reduce their degradation *in vivo*, which are necessary for future approaches that aim to directly activate DCs *in vivo* (Rogel et al., 1985; Paglia et al., 1996; Ghadersohi and Sood, 2001; Goodwin and Huang, 2017; Wongso et al., 2017; Dellacherie et al., 2018). Moreover, nanomaterials (*e.g.*, gold, aluminum nanoparticles) probably enhance internalization at the single cell level (Wang et al., 2015; Li et al., 2016; Wang et al., 2016). Aluminum, which was documented as an adjuvant for Th2 stimulation, failed to generate CD8+ T cell responses (Ho et al., 2018). However, using nanosized aluminum particles (100 nm) stabilized by PEG-containing polymer showed higher internalization in antigen-presenting cells and activated CD8+ T cells for curing cancer. Thus, nanotechnology not only improves the bio- or physiochemical features of antigen formulation through antigen protection, quantity improvement, function combination, and antigen presentation pathway, but also redefines the efficacy of traditional agents or materials with potential novel functions in antitumor immunity modulation (Zupančič et al., 2017; Smith et al., 2018; Zhong et al., 2019), which are all beneficial for the subsequent adaptive immunity against cancers. Importantly, a few cases that used nanotechnology for DC vaccination have been reported. For instance, liposome based Tecemotide, AS15, DepoVax, decorating with tumor-associated antigens are in clinical trials (Berinstein et al., 2012; Butts et al., 2014; Vansteenkiste et al., 2014). Virus-like nanoparticles CYT004-MelQbG10 delivering melanoma-associated antigen peptide are in Phase II clinical trials (Speiser et al., 2010). These pre/clinical trials evidenced the potential targeting DC for antitumor immunotherapy.

IN VIVO ACTIVATION OF DC FOR ENHANCING ANTIGEN PRESENTATION

The traditional approach of activating DCs *in vitro* and transferring them back into patients is expensive, labor-dependent, and difficult to evaluate antitumor immunity generation parallelly in patients. Targeting DCs for *in vivo* activation with antitumor immunity enhancement is another promising DC-based therapeutic strategy to induce specific antitumor immune responses; this approach directly activates DCs *in vivo* and can potentially generate a large number of antitumor responses. Nanotechnology-enabled spatiotemporal delivery of formulations aimed to directly activate DCs has been demonstrated in numerous cases (**Figure 2**). These formulations can be classified into three categories: (1) those that target and activate local DC response in the tumor microenvironment in addition to chemotherapy/radiotherapy (Sau et al., 2018); (2) those that target and activate lymph node-resident DCs, and in addition, target activation receptors on DCs, thereby boosting specific T cell response (De Koker et al., 2016; Jiang et al., 2017); and (3) those that modulate intracellular antigen presentation process for higher cross-presentation efficacy (Sil et al., 2019; Wang et al., 2019a).

DC-Based Combination Therapy

Because of the heterogeneous features of variable tumors and their immune microenvironment, "cold" tumors with low immunogenicity show enrichment of immunosuppressive cells such as macrophages and myeloid-derived suppressor cells around the microenvironment to escape from the immune surveillance (Smyth et al., 2006; Dadi et al., 2016; Lussier and Schreiber, 2016; Haanen, 2017). Therefore, combination therapies aimed to change the tumor immunogenic phenotype

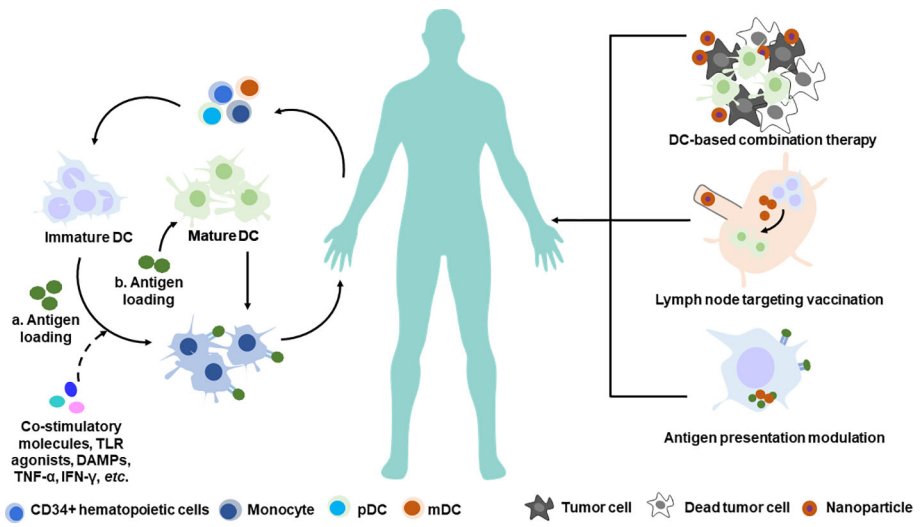

FIGURE 2 | Nanotechnology-based manipulation of DCs therapy. Conventional strategy of DC-based adoptive transfer therapy (left) and novel strategy employing nanotechnology for future DC-based immunotherapy (right). a. Antigen loading on immature DC in the scenario of DC maturation stimuli. b. Antigen loading on mature DC directly. pDC, plasmacytoid dendritic cell; mDC, myeloid dendritic cell.

provide a means to reduce the mortality associated with cancers (Da Silva et al., 2016; Nam et al., 2019). Chemo-immunotherapy approach that incorporates doxorubicin (DOX) and indoximod (IND) with phospholipid as a prodrug shows improved pharmacokinetics and accumulation in 4T1 breast tumor model. In such an approach, the chemo drugs induce tumor cell death, eliciting immunogenic reactions along with the debris being taken up by DCs, leading to further antigen presentation and naïve T cell priming. The activated T cells present cytotoxic effects on tumor cells through perforin and release of IFN-γ for robust killing of both primary and metastatic tumors. Not only does the dual-functional liposomes exert synergistic antitumor effects *via* DOX and IND components, but also the immune-checkpoint blockage combination treatment which further boosts immune responses allowing metastatic tumor eradication (Johnson et al., 2017; Lu et al., 2018). Radiotherapy is also known to promote CD8+ T cells around the tumor, however, radiation-induced immunosuppression may lead to treatment failure. Bismuth sulfide nanoparticles that conjugate immunoactive polysaccharide can increase radiotherapy sensitivity and activate DCs. Meanwhile, the nanoparticle can further enhance DC maturation and their distribution in tumor. Several studies have indicated that photodynamic therapy, which induces tumor cell lysates, is usually accompanied with damage-associated molecular pattern release that promotes DC activation, leading to specific antitumor immunity. Formulating photosensitizer is a major challenge in photodynamic therapy and further acceptance in clinic. The application of nanotechnology is a stride forward in solving this problem to some extent (Lucky et al., 2015), which favors photodynamic and DC combination therapy (Chen et al., 2016; Yu et al., 2019).

Lymph Node Targeting Vaccination

Peripheral DCs that encounter antigens are required to be trafficked to the lymph node where abundant lymphocytes are located and enabled highly efficient T cell priming. Moreover, diverse cytokines in the lymph node further promote DC maturation and exert function (Manfredi et al., 2008; Martín-Fontecha et al., 2009; Granot et al., 2017). Modifying antigens to target the lymph node and enhance lymph node-resident DC uptake was demonstrated to be a promising strategy in vaccine designing to initiate effective immune responses (Van Herck et al., 2018). Developing delivery systems with variable size can greatly influence the lymph node trafficking and DC uptake of antigens (Bachmann and Jennings, 2010; Kuai et al., 2017; Zhang et al., 2018). Proteins or subunit viral antigens within 10 nm are mostly incorporated with adjuvants to form larger-sized particles or aggregates. Supramolecular antigen formulations such as virus-like particles range from 20 to 200 nm. Virosomes with liposomes and antigens are approximately 100–200 nm (Jennings and Bachmann, 2007; Bachmann and Jennings, 2010). These antigen formulations are presented in the form of nano- or microparticles. Zhang et al. (2018) systemically investigated the influence of size and charge on the micelle-like formulations and their contributions to modulating immune responses, including lymph node accumulation, and DC internalization and immunogenicity, which provide an insight into the micelles and the generated immune responses. Lymph node accumulation and interaction properties of antigen-presenting cells are the two most important factors that influence the immunogenicity of nanoparticulated/nanoformulated antigens. Lymph node draining and DC uptake capability are both size-dependent processes, with a diameter of 10–200 nm considered to be optimal to stimulate immune response. Additionally, the authors claimed that the optimized size range was relatively independent of the materials, as the efficacy of lymph node draining and DC internalization is critically attributed to the particle size. However, variable materials with surface charges might influence the internalization capability of the antigen-presenting cells. Micelles with positive charged surface are beneficial for the enhancement of host antibody production (Reddy et al., 2007; Irvine et al., 2013). The previously published reviews provide an overview of materials on physiochemistry properties of antigen formulation in exerting effective immune responses.

Zhang et al. (2019) designed and synthesized a hybrid nanoparticle including the TLR 7/8 agonist imiquimod, TLR4 agonist monophosphoryl lipid A, polycaprolactone–polyethylene–polycaprolactone copolymer, dioleoyl-3-trimethylammonium propane, and 1,2-Distearoyl-sn-Glycero-3-Phosphoethanolamine-mannos. The hybrid nanoparticles enabled trafficking to secondary lymphoid tissues, spatiotemporal delivery and stimulation of both extracellular and intracellular TLRs, which was critical for efficient DC activation. It was demonstrated that the hybrid nanoparticles favorably enhanced the DC uptake of tumor antigen and cytokine secretion by mDCs. Additionally, homogenous tumor cells re-inoculated into C57BL/6 mice were inhibited upon treatment with the hybrid nanoparticles, highlighting the promising specific antitumor immune responses mediated by the nanoparticles.

Modulating Antigen Presentation for DC Vaccination

Antigen processing is an essential process for the final antigen presentation efficacy followed by lymph node draining accumulation and uptake by antigen-presenting cells. Thus, regulating intracellular antigen processing is important for antigen presentation and subsequent T cell priming. DCs are considered with well capacity for lysosomal proteolysis. It was documented that macrophages containing abundant lysosomal proteases enabled internalized protein degradation rapidly. In contrast, DCs with limited lysosomal capacity due to poor proteolysis degraded antigens slowly *in vivo* thus preserved antigen for an extended period. The limited proteolysis capacity benefits antigen presentation (Delamarre et al., 2005). Moderate lysosomal capacity of DCs favored antigen presentation implied us the opportunity of other pathway modulation in enhancing antigen degradation and presentation. It has been reported that inducing autophagy, an intracellular degradation and clearance process of unnecessary or dysfunctional components, is beneficial for antigen processing by DCs and leads to highly effective T cell stimulation. Wang et. al. combined a model antigen peptide $OVA_{257–264}$, autophagy inducing peptide Beclin1, and a pH sensitive polymer together by covalent

conjugation and fabricated an autophagy-inducing nanoactivator, which could induce autophagy in DCs, and evaluated the antigen-specific immune responses both *in vitro* and *in vivo* (Wang et al., 2015; Wang et al., 2019a). They demonstrated that induction of autophagy improved the antigen-presenting efficacy and T cell activation. Notably, the MHC I-$OVA_{257–264}$ complex expression was significantly decreased on combining the nanoactivator with an autophagy inhibitor. Furthermore, cross-presentation DCs and antigen-specific T cells increased, along with the appearance of specific antitumor immune responses, tumor infiltrated cytotoxic T cell accumulation, and tumor growth inhibition, indicating that the nanoactivators were capable of initiating antigen-specific immune responses *in vivo* for the eradication of established solid tumors.

CONCLUSION

Considering that DCs play a vital role in priming naïve T cell and inducing adaptive immunity, tremendous efforts have been made in manipulating DC for cancer immunotherapy. It is documented that adoptive DC transfer can elicit specific immune responses in approximately 70% patients (Draube et al., 2011). Controlled parallel studies and comparative analysis are limited but essential for outcome evaluation and further clinical translation of adoptive DC vaccination. Moreover, immunosuppressive patients and intrinsic tumor-associated factors such as inhibitory ligands and Tregs do not favorably respond to DC-based immunotherapy. Hence, there is a need to improve therapeutic efficacy by manipulating DCs independently in the primary step. Developing combination strategies are expected to be promising in the exploitation of DC vaccines (Kalinski et al., 2013). Taking the advantages of nanotechnology, manipulation, and engineering of DCs *in vitro* can be simplified and its activation efficiency can be improved, which could increase the therapeutic efficacy of adoptive DC transfer treatment. In addition, nano-engineering can allow *in vivo* DC activation, mimicking natural antigen presentation followed by priming processes. Directly activating DCs *in vivo* fully employed the moderate lysosomal proteolysis feature that degraded antigens slowly which enabled sustaining antigen presentation. Making use of nanotechnology can also allow the conjugation of DCs to extraordinary functional molecules, which can further enhance antigen presentation, mediating sophisticated crosstalk inside the antigen-presenting cells and or work together with other cells, thereby contributing to the efficacy of DC-based immunotherapy. Another challenge to conventional DC-based therapeutics is that activated DCs are required to migrate to lymph nodes and prime T cells for specific antitumor responses; however, the majority of the DCs are unable to reach the lymph nodes, leading to limited specific immune responses. In contrast, nanoparticles enable higher lymph node accumulation, contributing to highly effective lymph node draining. Emerging nano- and bio-engineering techniques that fabricate lymphoid organs are promising to provide an artificial environment for DCs and T cell priming. Thus, nanotechnology is a promising approach for DC-based therapeutics and can promote multifield development with great impact on clinical cancer treatment.

AUTHOR CONTRIBUTIONS

CQ, L-JY, and HC wrote the manuscript. HC provided advice both on the review writing and discussion.

FUNDING

This work was supported by Beijing Municipal Science & Technology Commission (Z171100001717020).

REFERENCES

Abe, O., Abe, R., Enomoto, K., Kikuchi, K., Koyama, H., Masuda, H., et al. (2005). Effects of radiotherapy and of differences in the extent of surgery for early breast cancer on local recurrence and 15-year survival: an overview of the randomised trials. *Lancet* 366, 2087–2106. doi: 10.1016/S0140-6736(05)67887-7

Albini, A., Bruno, A., Noonan, D. M., and Mortara, L. (2018). Contribution to Tumor Angiogenesis From Innate Immune Cells Within the Tumor Microenvironment: Implications for Immunotherapy. *Front. Immunol.* 9, 1–9. doi: 10.3389/fimmu.2018.00527

Al-Lazikani, B., Banerji, U., and Workman, P. (2012). Combinatorial drug therapy for cancer in the post-genomic era. *Nat. Biotechnol.* 30, 679–691. doi: 10.1038/nbt.2284

Ardavin, C., Del Hoyo, G. M., Martin, P., Anjuere, F., Arias, C. F., Marin, A. R., et al. (2001). Origin and differentiation of dendritic cells. *Trends Immunol.* 22, 691–700. doi: 10.1016/S1471-4906(01)02059-2

Ardavin, C. (2003). Origin, precursors and differentiation of mouse dendritic cells. *Nat. Rev. Immunol.* 3, 582–590. doi: 10.1038/nri1127

Bachmann, M. F., and Jennings, G. T. (2010). Vaccine delivery: a matter of size, geometry, kinetics and molecular patterns. *Nat. Rev. Immunol.* 10, 787–796. doi: 10.1038/nri2868

Beltran, H., Beer, T. M., Carducci, M. A., De Bono, J., Gleave, M., Hussain, M., et al. (2011). New Therapies for Castration-Resistant Prostate Cancer: Efficacy and Safety. *Eur. Urol.* 60, 279–290. doi: 10.1016/j.eururo.2011.04.038

Berinstein, N. L., Karkada, M., Morse, M. A., Nemunaitis, J. J., Chatta, G., Kaufman, H., et al. (2012). First-in-man application of a novel therapeutic cancer vaccine formulation with the capacity to induce multi-functional T cell responses in ovarian, breast and prostate cancer patients. *J. Trans. Med.* 10, 156. doi: 10.1186/1479-5876-10-156

Bethke, K., Staib, F., Distler, M., Schmitt, U., Jonuleit, H., Enk, A. H., et al. (2002). Different efficiency of heat shock proteins (HSP) to activate human monocytes and dendritic cells: superiority of HSP60. *J. Immunol.* 169, 6141–6148. doi: 10.4049/jimmunol.169.11.6141

Binnewies, M., Roberts, E. W., Kersten, K., Chan, V., Fearon, D. F., Merad, M., et al. (2018). Understanding the tumor immune microenvironment (TIME) for effective therapy. *Nat. Med.* 24, 541–550. doi: 10.1038/s41591-018-0014-x

Brahmer, J., Reckamp, K. L., Baas, P., Crino, L., Eberhardt, W. E. E., Poddubskaya, E., et al. (2015). Nivolumab versus Docetaxel in Advanced Squamous-Cell Non-Small-Cell Lung Cancer. *New Engl. J. Med.* 373, 123–135. doi: 10.1056/NEJMoa1504627

Butts, C., Socinski, M. A., Mitchell, P. L., Thatcher, N., Havel, L., Krzakowski, M., et al. (2014). Tecemotide (L-BLP25) versus placebo after chemoradiotherapy

for stage III non-small-cell lung cancer (START): a randomised, double-blind, phase 3 trial. *Lancet Oncol.* 15, 59–68. doi: 10.1016/S1470-2045(13)70510-2

Chen, Q., Xu, L., Liang, C., Wang, C., Peng, R., and Liu, Z. (2016). Photothermal therapy with immune-adjuvant nanoparticles together with checkpoint blockade for effective cancer immunotherapy. *Nat. Commun.* 7, 13193. doi: 10.1038/ncomms13193

Chen, W. S., Ouyang, J., Liu, H., Chen, M., Zeng, K., Sheng, J. P., et al. (2017). Black Phosphorus Nanosheet-Based Drug Delivery System for Synergistic Photodynamic/Photothermal/Chemotherapy of Cancer. *Adv Mater* 29, 1–7. doi: 10.1002/adma.201603864

Coffey, J. C., Wang, J. H., Smith, M. J. F., Bouchier-Hayes, D., Cotter, T. G., and Redmond, H. P. (2003). Excisional surgery for cancer cure: therapy at a cost. *Lancet Oncol.* 4, 760–768. doi: 10.1016/S1470-2045(03)01282-8

Cohen, C. J., Denkberg, G., Lev, A., Epel, M., and Reiter, Y. (2003). Recombinant antibodies with MHC-restricted, peptide-specific, T-cell receptor-like specificity: new tools to study antigen presentation and TCR–peptide–MHC interactions. *J. Mol. Recog* 16, 324–332. doi: 10.1002/jmr.640

Constantino, J., Gomes, C., Falcão, A., Cruz, M. T., and Neves, B. M. (2016). Antitumor dendritic cell–based vaccines: lessons from 20 years of clinical trials and future perspectives. *Trans. Res.* 168, 74–95. doi: 10.1016/j.trsl.2015.07.008

Costa, A., Kieffer, Y., Scholer-Dahirel, A., Pelon, F., Bourachot, B., Cardon, M., et al. (2018). Fibroblast Heterogeneity and Immunosuppressive Environment in Human Breast Cancer. *Cancer Cell* 33, 463–46+. doi: 10.1016/j.ccell.2018.01.011

Couzin-Frankel, J. (2013). Cancer immunotherapy. *Science* 342, 1432–1433. doi: 10.1126/science.342.6165.1432

Da Silva, C., Rueda, F., Löwik, C., Ossendorp, F., and Cruz, L. J. (2016). Combinatorial prospects of nano-targeted chemoimmunotherapy. *Biomaterials* 83, 308–320. doi: 10.1016/j.biomaterials.2016.01.006

Dadi, S., Chhangawala, S., Whitlock, B. M., Franklin, R. A., Luo, C. T., Oh, S. A., et al. (2016). Cancer immunosurveillance by tissue-resident innate lymphoid cells and innate-like T cells. *Cell* 164, 365–377. doi: 10.1016/j.cell.2016.01.002

De Koker, S., Cui, J., Vanparijs, N., Albertazzi, L., Grooten, J., Caruso, F., et al. (2016). Engineering Polymer Hydrogel Nanoparticles for Lymph Node-Targeted Delivery. *Angewandte Chemie Int. Ed* 55, 1334–1339. doi: 10.1002/anie.201508626

Delamarre, L., Pack, M., Chang, H., Mellman, I., and Trombetta, E. S. (2005). Differential Lysosomal Proteolysis in Antigen-Presenting Cells Determines Antigen Fate. *Science* 307, 1630. doi: 10.1126/science.1108003

Dellacherie, M. O., Li, A. W., Lu, B. Y., and Mooney, D. J. (2018). Covalent conjugation of peptide antigen to mesoporous silica rods to enhance cellular responses. *Bioconjug Chem.* 29, 733–741. doi: 10.1021/acs.bioconjchem.7b00656

Draube, A., Klein-Gonzalez, N., Mattheus, S., Brillant, C., Hellmich, M., Engert, A., et al. (2011). Dendritic cell based tumor vaccination in prostate and renal cell cancer: a systematic review and meta-analysis. *PloS One* 6, 1–11. doi: 10.1371/journal.pone.0018801

Feng, B., Zhou, F. Y., Hou, B., Wang, D. G., Wang, T. T., Fu, Y. L., et al. (2018). Binary Cooperative Prodrug Nanoparticles Improve Immunotherapy by Synergistically Modulating Immune Tumor Microenvironment. *Adv Mater* 30, 1–10. doi: 10.1002/adma.201803001

Feng, X., Xu, W., Li, Z., Song, W., Ding, J., and Chen, X. (2019). Immunomodulatory Nanosystems. *Adv Sci.* 6, 1900101. doi: 10.1002/advs.201900101

Ghadersohi, A., and Sood, A. K. (2001). Prostate epithelium-derived Ets transcription factor mRNA is overexpressed in human breast tumors and is a candidate breast tumor marker and a breast tumor antigen. *Clin. Cancer Res.* 7, 2731–2738.

Goodwin, T. J., and Huang, L. (2017). Investigation of phosphorylated adjuvants co-encapsulated with a model cancer peptide antigen for the treatment of colorectal cancer and liver metastasis. *Vaccine* 35, 2550–2557. doi: 10.1016/j.vaccine.2017.03.067

Granot, T., Senda, T., Carpenter, D. J., Matsuoka, N., Weiner, J., Gordon, C. L., et al. (2017). Dendritic Cells Display Subset and Tissue-Specific Maturation Dynamics over Human Life. *Immunity* 46, 504–515. doi: 10.1016/j.immuni.2017.02.019

Guéry, L., and Hugues, S. (2015). Th17 Cell Plasticity and Functions in Cancer Immunity. *BioMed. Res. Int.* 2015, 314620. doi: 10.1155/2015/314620

Gulla, S. K., Rao, B. R., Moku, G., Jinka, S., Nimmu, N. V., Khalid, S., et al. (2019). In vivo targeting of DNA vaccines to dendritic cells using functionalized gold nanoparticles. *Biomater Sci.* 7, 773–788. doi: 10.1039/C8BM01272E

Guth, U., Myrick, M. E., Schotzau, A., Kilic, N., and Schmid, S. M. (2011). Drug switch because of treatment-related adverse side effects in endocrine adjuvant breast cancer therapy: how often and how often does it work? *Breast Cancer Res. Treat* 129, 799–807. doi: 10.1007/s10549-011-1668-y

Haanen, J. B. (2017). Converting cold into hot tumors by combining immunotherapies. *Cell* 170, 1055–1056. doi: 10.1016/j.cell.2017.08.031

Higano, C. S., Schellhammer, P. F., Small, E. J., Burch, P. A., Nemunaitis, J., Yuh, L., et al. (2009). Integrated Data From 2 Randomized, Double-Blind, Placebo-Controlled, Phase 3 Trials of Active Cellular Immunotherapy With Sipuleucel-T in Advanced Prostate Cancer. *Cancer* 115, 3670–3679. doi: 10.1002/cncr.24429

Ho, N. I., Huis in 'T Veld, L. G. M., Raaijmakers, T. K., and Adema, G. J. (2018). Adjuvants Enhancing Cross-Presentation by Dendritic Cells: The Key to More Effective Vaccines? *Front. Immunol.* 9, 1–12. doi: 10.3389/fimmu.2018.02874

Housman, G., Byler, S., Heerboth, S., Lapinska, K., Longacre, M., Snyder, N., et al. (2014). Drug Resistance in Cancer: An Overview. *Cancers* 6, 1769–1792. doi: 10.3390/cancers6031769

Irvine, D. J., Swartz, M. A., and Szeto, G. L. (2013). Engineering synthetic vaccines using cues from natural immunity. *Nat. Mater* 12, 978–990. doi: 10.1038/nmat3775

Jennings, G. T., and Bachmann, M. F. (2007). Designing recombinant vaccines with viral properties: a rational approach to more effective vaccines. *Curr. Mol. Med.* 7, 143–155. doi: 10.2174/156652407780059140

Jiang, H., Wang, Q., and Sun, X. (2017). Lymph node targeting strategies to improve vaccination efficacy. *J. Controlled Release* 267, 47–56. doi: 10.1016/j.jconrel.2017.08.009

Jiang, H., Wang, Q., Li, L., Zeng, Q., Li, H., Gong, T., et al. (2018). Turning the Old Adjuvant from Gel to Nanoparticles to Amplify CD8+ T Cell Responses. *Adv Sci.* 5, 1700426. doi: 10.1002/advs.201700426

Johnson, T. S., Mcgaha, T., and Munn, D. H. (2017). "Chemo-immunotherapy: role of indoleamine 2, 3-dioxygenase in defining immunogenic versus tolerogenic cell death in the tumor microenvironment," in *Tumor Immune Microenvironment in Cancer Progression and Cancer Therapy and Cancer Therapy* (Springer), 1036, 91–104.

June, C. H., O'connor, R. S., Kawalekar, O. U., Ghassemi, S., and Milone, M. C. (2018). CAR T cell immunotherapy for human cancer. *Science* 359, 1361–1365. doi: 10.1126/science.aar6711

Kadowaki, N. (2009). The divergence and interplay between pDC and mDC in humans. *Front. Biosci* 14, 808–817. doi: 10.2741/3279

Kalinski, P., Muthuswamy, R., and Urban, J. (2013). Dendritic cells in cancer immunotherapy: vaccines and combination immunotherapies. *Expert Rev. Vaccines* 12, 285–295. doi: 10.1586/erv.13.22

Kantoff, P. W., Higano, C. S., Shore, N. D., Berger, E. R., Small, E. J., Penson, D. F., et al. (2010). Sipuleucel-T Immunotherapy for Castration-Resistant Prostate Cancer. *New Engl. J. Med.* 363, 411–422. doi: 10.1056/NEJMoa1001294

Kawai, T., and Akira, S. (2007). TLR signaling *Semin Immunon.* 19, 24–32.

Knudson, K. M., Hicks, K. C., Luo, X. L., Chen, J. Q., Schlom, J., and Gameiro, S. R. (2018). M7824, a novel bifunctional anti-PD-L1/TGF beta Trap fusion protein, promotes anti-tumor efficacy as monotherapy and in combination with vaccine. *Oncoimmunology* 7, 1–14. doi: 10.1080/2162402X.2018.1426519

Kongsted, P., Borch, T. H., Ellebaek, E., Iversen, T. Z., Andersen, R., Met, Ö, et al. (2017). Dendritic cell vaccination in combination with docetaxel for patients with metastatic castration-resistant prostate cancer: a randomized phase II study. *Cytotherapy* 19, 500–513. doi: 10.1016/j.jcyt.2017.01.007

Koppelmans, V., Breteler, M. M. B., Boogerd, W., Seynaeve, C., Gundy, C., and Schagen, S. B. (2012). Neuropsychological Performance in Survivors of Breast Cancer More Than 20 Years After Adjuvant Chemotherapy. *J. Clin. Oncol.* 30, 1080–1086. doi: 10.1200/JCO.2011.37.0189

Krook, J. E., Moertel, C. G., Gunderson, L. L., Wieand, H. S., Collins, R. T., Beart, R. W., et al. (1991). Effective surgical adjuvant therapy for high-risk rectal-carcinoma. *New Engl. J. Med.* 324, 709–715. doi: 10.1056/NEJM199103143241101

Kuai, R., Ochyl, L. J., Bahjat, K. S., Schwendeman, A., and Moon, J. J. (2017). Designer vaccine nanodiscs for personalized cancer immunotherapy. *Nat. Mater* 16, 489–496. doi: 10.1038/nmat4822

Lövgren, T., Wolodarski, M., Edbäck, U., Martell, E., Markland, K., Nyström, M., et al. (2018). Abstract CT032: Adoptive T cell transfer combined with DC vaccination in patients with metastatic melanoma. *Cancer Research* 78. doi: 10.1158/1538-7445.AM2018-CT032

Le, D. T., Uram, J. N., Wang, H., Bartlett, B. R., Kemberling, H., Eyring, A. D., et al. (2015). PD-1 Blockade in Tumors with Mismatch-Repair Deficiency. *New Engl. J. Med.* 372, 2509–2520. doi: 10.1056/NEJMoa1500596

Leary, M., Heerboth, S., Lapinska, K., and Sarkar, S. (2018). Sensitization of Drug Resistant Cancer Cells: A Matter of Combination Therapy. *Cancers* 10, 1–18. doi: 10.3390/cancers10120483

Leifer, C. A. (2017). Dendritic cells in host response to biologic scaffolds. *Semin. Immunol.* 29, 41–48. doi: 10.1016/j.smim.2017.01.001

Leitner, W. W., Ying, H., and Restifo, N. P. (1999). DNA and RNA-based vaccines: principles, progress and prospects. *Vaccine* 18, 765–777. doi: 10.1016/S0264-410X(99)00271-6

Li, Y., Zeng, X., He, L., and Yuan, H. (2015). Dendritic cell activation and maturation induced by recombinant calreticulin fragment 39-272. *Int. J. Clin. Exp. Med.* 8, 7288.

Li, F., Chen, W.-L., You, B.-G., Liu, Y., Yang, S.-D., Yuan, Z.-Q., et al. (2016). Enhanced cellular internalization and on-demand intracellular release of doxorubicin by stepwise pH-/reduction-responsive nanoparticles. *ACS Appl. Mater Interfaces* 8, 32146–32158. doi: 10.1021/acsami.6b09604

Lin, Y.-X., Wang, Y., Blake, S., Yu, M., Mei, L., Wang, H., et al. (2020). RNA Nanotechnology-Mediated Cancer Immunotherapy. *Theranostics* 10, 281. doi: 10.7150/thno.35568

Lippert, T. H., Ruoff, H. J., and Volm, M. (2008). Intrinsic and acquired drug resistance in malignant tumors. *Arzneimittelforschung-Drug Res.* 58, 261–264. doi: 10.1055/s-0031-1296504

Liu, H. Y., Chen, D., Li, L. L., Liu, T. L., Tan, L. F., Wu, X. L., et al. (2011). Multifunctional Gold Nanoshells on Silica Nanorattles: A Platform for the Combination of Photothermal Therapy and Chemotherapy with Low Systemic Toxicity. *Angewandte Chemie-International Ed* 50, 891–895. doi: 10.1002/anie.201002820

Liu, Z., Jiang, W., Nam, J., Moon, J. J., and Kim, B. Y. S. (2018). Immunomodulating Nanomedicine for Cancer Therapy. *Nano Lett.* 18, 6655–6659. doi: 10.1021/acs.nanolett.8b02340

Lizotte, P., Wen, A., Sheen, M., Fields, J., Rojanasopondist, P., Steinmetz, N., et al. (2016). In situ vaccination with cowpea mosaic virus nanoparticles suppresses metastatic cancer. *Nat. Nanotechnol* 11, 295. doi: 10.1038/nnano.2015.292

Lu, J., Liu, X., Liao, Y.-P., Wang, X., Ahmed, A., Jiang, W., et al. (2018). Breast cancer chemo-immunotherapy through liposomal delivery of an immunogenic cell death stimulus plus interference in the IDO-1 pathway. *ACS Nano* 12, 11041–11061. doi: 10.1021/acsnano.8b05189

Lucky, S. S., Soo, K. C., and Zhang, Y. (2015). Nanoparticles in Photodynamic Therapy. *Chem. Rev.* 115, 1990–2042. doi: 10.1021/cr5004198

Lussier, D. M., and Schreiber, R. (2016). Cancer immunosurveillance: immunoediting. *Immunity Patho. Tumors* 4, 396–405. doi: 10.1016/B978-0-12-374279-7.17001-8

Macdonald, J. S., Smalley, S. R., Benedetti, J., Hundahl, S. A., Estes, N. C., Stemmermann, G. N., et al. (2001). Chemoradiotherapy after surgery compared with surgery alone for adenocarcinoma of the stomach or gastroesophageal junction. *New Engl. J. Med.* 345, 725–730. doi: 10.1056/NEJMoa010187

Manfredi, A. A., Capobianco, A., Esposito, A., De Cobelli, F., Canu, T., Monno, A., et al. (2008). Maturing Dendritic Cells Depend on RAGE for In Vivo Homing to Lymph Nodes. *J. Immunol.* 180, 2270. doi: 10.4049/jimmunol.180.4.2270

Martín-Fontecha, A., Lanzavecchia, A., and Sallusto, F. (2009). "Dendritic Cell Migration to Peripheral Lymph Nodes," in *Dendritic Cells*. Eds. G. Lombardi and Y. Riffo-Vasquez (Berlin, Heidelberg: Springer Berlin Heidelberg), 31–49.

Mathan, T. S. M., Textor, J., Skold, A. E., Reinieren-Beeren, I., Van Oorschot, T., Bruning, M., et al. (2017). Harnessing RNA sequencing for global, unbiased evaluation of two new adjuvants for dendritic-cell immunotherapy. *Oncotarget* 8, 19879–19893. doi: 10.18632/oncotarget.15190

Maude, S. L., Laetsch, T. W., Buechner, J., Rives, S., Boyer, M., Bittencourt, H., et al. (2018). Tisagenlecleucel in Children and Young Adults with B-Cell Lymphoblastic Leukemia. *New Engl. J. Med.* 378, 439–448. doi: 10.1056/NEJMoa1709866

Mempel, T. R., Henrickson, S. E., and Von Andrian, U. H. (2004). T-cell priming by dendritic cells in lymph nodes occurs in three distinct phases. *Nature* 427, 154–159. doi: 10.1038/nature02238

Minton, K. (2014). IFN-dependent DC maturation. *Nat. Rev. Immunol.* 14, 67–67. doi: 10.1038/nri3618

Morrison, D. C., and Kline, L. F. (1977). Activation of the classical and properdin pathways of complement by bacterial lipopolysaccharides (LPS). *J. Immunol.* 118, 362–368.

Murugaiyan, G., and Saha, B. (2009). Protumor vs Antitumor Functions of IL-17. *J. Immunol.* 183, 4169. doi: 10.4049/jimmunol.0901017

Nam, J., Son, S., Park, K. S., Zou, W., Shea, L. D., and Moon, J. J. (2019). Cancer nanomedicine for combination cancer immunotherapy. *Nat. Rev. Mater* 4, 398–414. doi: 10.1038/s41578-019-0108-1

Nicholson, L. B. (2016). The immune system. *Essays Biochem.* 60, 275–301. doi: 10.1042/EBC20160017

Ogasawara, M., Miyashita, M., and Ota, S. (2018). Vaccination of Urological Cancer Patients With WT1 Peptide-Pulsed Dendritic Cells in Combination With Molecular Targeted Therapy or Conventional Chemotherapy Induces Immunological and Clinical Responses. *Ther. Apheresis Dialysis* 22, 266–277. doi: 10.1111/1744-9987.12694

Paglia, P., Chiodoni, C., Rodolfo, M., and Colombo, M. P. (1996). Murine dendritic cells loaded in vitro with soluble protein prime cytotoxic T lymphocytes against tumor antigen in vivo. *J. Exp. Med.* 183, 317–322. doi: 10.1084/jem.183.1.317

Palma, M., Hansson, L., Mulder, T. A., Adamson, L., Näsman-Glaser, B., Eriksson, I., et al. (2018). Lenalidomide as immune adjuvant to a dendritic cell vaccine in chronic lymphocytic leukemia patients. *Eur. J. Haematol* 101, 68–77. doi: 10.1111/ejh.13065

Parvanian, S., Mostafavi, S. M., and Aghashiri, M. (2017). Multifunctional nanoparticle developments in cancer diagnosis and treatment. *Sens. Biosensing Res.* 13, 81–87. doi: 10.1016/j.sbsr.2016.08.002

Probst, H. C., Mccoy, K., Okazaki, T., Honjo, T., and Van Den Broek, M. (2005). Resting dendritic cells induce peripheral CD8+ T cell tolerance through PD-1 and CTLA-4. *Nat. Immunol.* 6, 280–286. doi: 10.1038/ni1165

Raucci, A., Palumbo, R., and Bianchi, M. E. (2007). HMGB1: a signal of necrosis. *Autoimmunity* 40, 285–289. doi: 10.1080/08916930701356978

Reck, M., Rodriguez-Abreu, D., Robinson, A. G., Hui, R. N., Csoszi, T., Fulop, A., et al. (2016). Pembrolizumab versus Chemotherapy for PD-L1-Positive Non-Small-Cell Lung Cancer. *New Engl. J. Med.* 375, 1823–1833. doi: 10.1056/NEJMoa1606774

Reddy, S. T., Van Der Vlies, A. J., Simeoni, E., Angeli, V., Randolph, G. J., O'neil, C. P., et al. (2007). Exploiting lymphatic transport and complement activation in nanoparticle vaccines. *Nat. Biotechnol.* 25, 1159–1164. doi: 10.1038/nbt1332

Reichmuth, A. M., Oberli, M. A., Jaklenec, A., Langer, R., and Blankschtein, D. (2016). mRNA vaccine delivery using lipid nanoparticles. *Ther. Deliv* 7, 319–334. doi: 10.4155/tde-2016-0006

Rescigno, M., Winzler, C., Delia, D., Mutini, C., Lutz, M., and Ricciardi-Castagnoli, P. (1997). Dendritic cell maturation is required for initiation of the immune response. *J. Leukoc Biol.* 61, 415–421. doi: 10.1002/jlb.61.4.415

Robert, C., Thomas, L., Bondarenko, I., O'day, S., Weber, J., Garbe, C., et al. (2011). Ipilimumab plus Dacarbazine for Previously Untreated Metastatic Melanoma. *New Engl. J. Med.* 364, 2517–2526. doi: 10.1056/NEJMoa1104621

Roden, R. B., and Stern, P. L. (2018). Opportunities and challenges for human papillomavirus vaccination in cancer. *Nat. Rev. Cancer* 18, 240. doi: 10.1038/nrc.2018.13

Rogel, A., Popliker, M., Webb, C. G., and Oren, M. (1985). p53 cellular tumor antigen: analysis of mRNA levels in normal adult tissues, embryos, and tumors. *Mol. Cell. Biol.* 5, 2851–2855. doi: 10.1128/MCB.5.10.2851

Rothermundt, C. (2015). Management of side effects and adherence to oral cancer therapies in metastatic renal cell cancer. *Oncol. Res. Treat* 38, 17–17.

Rutella, S., Danese, S., and Leone, G. (2006). Tolerogenic dendritic cells: cytokine modulation comes of age. *Blood* 108, 1435–1440. doi: 10.1182/blood-2006-03-006403

Sangtani, A., Nag, O. K., Field, L. D., Breger, J. C., and Delehanty, J. B. (2017). Multifunctional nanoparticle composites: progress in the use of soft and hard nanoparticles for drug delivery and imaging. *Wiley Interdiscip. Rev: Nanomed Nanobiotechnol* 9, e1466. doi: 10.1002/wnan.1466

Sau, S., Alsaab, H. O., Bhise, K., Alzhrani, R., Nabil, G., and Iyer, A. K. (2018). Multifunctional nanoparticles for cancer immunotherapy: a groundbreaking approach for reprogramming malfunctioned tumor environment. *J. Controlled Release* 274, 24–34. doi: 10.1016/j.jconrel.2018.01.028

Sauer, R., Becker, H., Hohenberger, W., Rodel, C., Wittekind, C., Fietkau, R., et al. (2004). Preoperative versus postoperative chemoradiotherapy for rectal cancer. *New Engl. J. Med.* 351, 1731–1740. doi: 10.1056/NEJMoa040694

Schnurr, M., Then, F., Galambos, P., Scholz, C., Siegmund, B., Endres, S., et al. (2000). Extracellular ATP and TNF-α synergize in the activation and maturation of human dendritic cells. *J. Immunol.* 165, 4704–4709. doi: 10.4049/jimmunol.165.8.4704

Segura, E., and Villadangos, J. A. (2009). Antigen presentation by dendritic cells in vivo. *Curr. Opin. Immunol.* 21, 105–110. doi: 10.1016/j.coi.2009.03.011

Segura, E., Touzot, M., Bohineust, A., Cappuccio, A., Chiocchia, G., Hosmalin, A., et al. (2013). Human Inflammatory Dendritic Cells Induce Th17 Cell Differentiation. *Immunity* 38, 336–348. doi: 10.1016/j.immuni.2012.10.018

Sharma, M. D., Rodriguez, P. C., Koehn, B. H., Baban, B., Cui, Y., Guo, G., et al. (2018). Activation of p53 in immature myeloid precursor cells controls differentiation into Ly6c+ CD103+ monocytic antigen-presenting cells in tumors. *Immunity* 48, 91–106. e106. doi: 10.1016/j.immuni.2017.12.014

Sil, P., Zhao, F., Muse, G. W., Wong, S.-W., Kolb, J. P., Degraff, L. M., et al. (2019). Non-canonical autophagy in dendritic cells restricts cross-presentation and anti-tumor immunity. *bioRxiv* 789867. doi: 10.1101/789867

Simmons, D. P., Wearsch, P. A., Canaday, D. H., Meyerson, H. J., Liu, Y. C., Wang, Y., et al. (2012). Type I IFN Drives a Distinctive Dendritic Cell Maturation Phenotype That Allows Continued Class II MHC Synthesis and Antigen Processing. *J. Immunol.* 188, 3116. doi: 10.4049/jimmunol.1101313

Smith, G., Liu, Y., Tian, J.-H., Massare, M. J., Boddapati, S., Shane, E., et al. (2018). Vaccine compositions having improved stability and immunogenicity. WO/2017/041100

Smyth, M. J., Dunn, G. P., and Schreiber, R. D. (2006). Cancer immunosurveillance and immunoediting: the roles of immunity in suppressing tumor development and shaping tumor immunogenicity. *Adv. Immunol.* 90, 1–50. doi: 10.1016/S0065-2776(06)90001-7

Speiser, D. E., Schwarz, K., Baumgaertner, P., Manolova, V., Devevre, E., Sterry, W., et al. (2010). Memory and Effector CD8 T-cell Responses After Nanoparticle Vaccination of Melanoma Patients. *J. Immunother* 33, 848–858. doi: 10.1097/CJI.0b013e3181f1d614

Thomas, R., and Lipsky, P. E. (1996). Dendritic cells: origin and differentiation. *Stem Cells* 14, 196–206. doi: 10.1002/stem.140196

Van Herck, S., Deswarte, K., Nuhn, L., Zhong, Z., Portela Catani, J. P., Li, Y., et al. (2018). Lymph-node-targeted immune activation by engineered block copolymer amphiphiles–TLR7/8 agonist conjugates. *J. Am. Chem. Soc.* 140, 14300–14307. doi: 10.1021/jacs.8b08595

Vansteenkiste, J. F., Cho, B., Vanakesa, T., De Pas, T., Zielinski, M., Kim, M. S., et al. (2014). Magrit, a Double-Blind, Randomized, Placebo-Controlled Phase III Study to Assess the Efficacy of the Recmage-A3 + As15 Cancer Immunotherapeutic As Adjuvant Therapy in Patients with Resected Mage-A3-Positive Non-Small Cell Lung Cancer (Nsclc). *Ann. Oncol.* 25, iv409. doi: 10.1093/annonc/mdu347.1

Wang, H., and Mooney, D. J. (2018). Biomaterial-assisted targeted modulation of immune cells in cancer treatment. *Nat. Mater* 17, 761–772. doi: 10.1038/s41563-018-0147-9

Wang, Y., Lin, Y. X., Qiao, Z. Y., An, H. W., Qiao, S. L., Wang, L., et al. (2015). Self-Assembled Autophagy-Inducing Polymeric Nanoparticles for Breast Cancer Interference In-Vivo. *Adv Mater* 27, 2627–2634. doi: 10.1002/adma.201405926

Wang, S., Huang, P., and Chen, X. (2016). Hierarchical targeting strategy for enhanced tumor tissue accumulation/retention and cellular internalization. *Adv Mater* 28, 7340–7364. doi: 10.1002/adma.201601498

Wang, Y., Lin, Y.-X., Qiao, S.-L., An, H.-W., Ma, Y., Qiao, Z.-Y., et al. (2017). Polymeric nanoparticles enable reversing macrophage in tumor microenvironment for immunotherapy. *Biomaterials* 112, 3e163.

Wang, Y., Lin, Y.-X., Wang, J., Qiao, S.-L., Liu, Y.-Y., Dong, W.-Q., et al. (2019a). In Situ Manipulation of Dendritic Cells by an Autophagy-Regulative Nanoactivator Enables Effective Cancer Immunotherapy. *ACS Nano* 13, 7568–7577. doi: 10.1021/acsnano.9b00143

Wang, Y., Lin, Y. X., Qiao, S. L., Wang, J., and Wang, H. (2019b). Progress in Tumor-Associated Macrophages: From Bench to Bedside. *Adv Biosyst.* 3, 1800232. doi: 10.1002/adbi.201800232

Wen, R., Umeano, A. C., Kou, Y., Xu, J., and Farooqi, A. A. (2019). Nanoparticle systems for cancer vaccine. *Nanomedicine* 14, 627–648. doi: 10.2217/nnm-2018-0147

Williams, J. W., Tjota, M. Y., Clay, B. S., Vander Lugt, B., Bandukwala, H. S., Hrusch, C. L., et al. (2013). Transcription factor IRF4 drives dendritic cells to promote Th2 differentiation. *Nat. Commun.* 4, 1–12. doi: 10.1038/ncomms3990

Wolf, G. T. (1991). Induction chemotherapy plus radiation compared with surgery plus radiation in patients with advanced laryngeal-cancer. *New Engl. J. Med.* 324, 1685–1690. doi: 10.1056/NEJM199106133242402

Wongso, D., Dong, J., Ueda, H., and Kitaguche, T. (2017). Flashbody: A Next Generation Fluobody with Fluorescence Intensity Enhanced by Antigen Binding. *Anal Chem.* 89, 6719–6725. doi: 10.1021/acs.analchem.7b00959

Yu, H., Yang, Y., Jiang, T., Zhang, X., Zhao, Y., Pang, G., et al. (2019). Effective Radiotherapy in Tumor Assisted by Ganoderma lucidum Polysaccharide-Conjugated Bismuth Sulfide Nanoparticles through Radiosensitization and Dendritic Cell Activation. *ACS Appl. Mater Interfaces* 11, 27536–27547. doi: 10.1021/acsami.9b07804

Zehn, D., Cohen, C. J., Reiter, Y., and Walden, P. (2004). Extended presentation of specific MHC-peptide complexes by mature dendritic cells compared to other types of antigen-presenting cells. *Eur. J. Immunol.* 34, 1551–1560. doi: 10.1002/eji.200324355

Zhang, N., and Bevan, M. J. (2011). CD8+ T cells: foot soldiers of the immune system. *Immunity* 35, 161–168. doi: 10.1016/j.immuni.2011.07.010

Zhang, R., Smith, J. D., Allen, B. N., Kramer, J. S., Schauflinger, M., and Ulery, B. D. (2018). Peptide Amphiphile Micelle Vaccine Size and Charge Influence the Host Antibody Response. *ACS Biomater Sci. Eng.* 4, 2463–2472. doi: 10.1021/acsbiomaterials.8b00511

Zhang, L., Wu, S., Qin, Y., Fan, F., Zhang, Z., Huang, C., et al. (2019). Targeted Codelivery of an Antigen and Dual Agonists by Hybrid Nanoparticles for Enhanced Cancer Immunotherapy. *Nano Lett.* 19, 4237–4249. doi: 10.1021/acs.nanolett.9b00030

Zhao, P. F., Wang, Y. H., Kang, X. J., Wu, A. H., Yin, W. M., Tang, Y. S., et al. (2018). Dual-targeting biomimetic delivery for anti-glioma activity via remodeling the tumor microenvironment and directing macrophagemediated immunotherapy. *Chem. Sci.* 9, 2674–2689. doi: 10.1039/C7SC04853J

Zhong, L. L., Zhao, Y. L., Zhang, K., Li, X., Cui, R. J., and Yang, W. (2017). Recent advances of immune checkpoint in breast cancer. *Biomed. Research-India* 28, 7268–7273. doi: 10.1186/s12916-019-1326-5

Zhong, X., Zhang, Y., Tan, L., Zheng, T., Hou, Y., Hong, X., et al. (2019). An aluminum adjuvant-integrated nano-MOF as antigen delivery system to induce strong humoral and cellular immune responses. *J. Controlled Release* 300, 81–92. doi: 10.1016/j.jconrel.2019.02.035

Zhou, Q., Zhang, Y., Du, J., Li, Y., Zhou, Y., Fu, Q., et al. (2016). Different-sized gold nanoparticle activator/antigen increases dendritic cells accumulation in liver-draining lymph nodes and CD8+ T cell responses. *ACS Nano* 10, 2678–2692. doi: 10.1021/acsnano.5b07716

Zupančič, E., Curato, C., Paisana, M., Rodrigues, C., Porat, Z., Viana, A. S., et al. (2017). Rational design of nanoparticles towards targeting antigen-presenting cells and improved T cell priming. *J. Controlled Release* 258, 182–195. doi: 10.1016/j.jconrel.2017.05.014

Conflict of Interest: The authors declare that the research was conducted in the absence of any commercial or financial relationships that could be construed as a potential conflict of interest.

frontiers in Pharmacology

REVIEW
published: 08 July 2020
doi: 10.3389/fphar.2020.01016

Advance in Drug Delivery for Ageing Skeletal Muscle

Yi Li[1,2†], Ming Chen[1,2†], Yanpeng Zhao[1,2], Ming Li[1,2], Yong Qin[3], Shi Cheng[3], Yanyu Yang[4], Pengbin Yin[1,2*], Licheng Zhang[1,2*] and Peifu Tang[1,2]*

[1] Department of Orthopedics, General Hospital of Chinese PLA, Beijing, China, [2] National Clinical Research Center for Orthopedics, Sports Medicine & Rehabilitation, Beijing, China, [3] The Department of Orthopedic Surgery, Second Affiliated Hospital of Harbin Medical University, Harbin, China, [4] College of Materials Science and Engineering, Zhengzhou University, Zhengzhou, China

OPEN ACCESS

Edited by:
Jianxun Ding,
Chinese Academy of Sciences, China

Reviewed by:
Hua Lu,
Peking University, China
Ruinan Yang,
Pharmaceutical Product Development, United States
Xue Qu,
East China University of Science and Technology, China

***Correspondence:**
Yanyu Yang
yyyang@zzu.edu.cn
Pengbin Yin
yinpengbin@gmail.com
Licheng Zhang
zhanglcheng218@126.com

[†]These authors have contributed equally to this work

Specialty section:
This article was submitted to Translational Pharmacology, a section of the journal Frontiers in Pharmacology

Received: 13 March 2020
Accepted: 23 June 2020
Published: 08 July 2020

Citation:
Li Y, Chen M, Zhao Y, Li M, Qin Y, Cheng S, Yang Y, Yin P, Zhang L and Tang P (2020) Advance in Drug Delivery for Ageing Skeletal Muscle. Front. Pharmacol. 11:1016. doi: 10.3389/fphar.2020.01016

The age-related loss of skeletal muscle, sarcopenia, is characterized by progressive loss of muscle mass, reduction in muscle strength, and dysfunction of physical performance. It has become a global health problem leading to several adverse outcomes in the ageing population. Research on skeletal muscle loss prevention and treatment is developing quickly. However, the current clinical approaches to sarcopenia are limited. Recently, novel drug delivery systems offer new possibilities for treating aged muscle loss. Herein, we briefly recapitulate the potential therapeutic targets of aged skeletal muscle and provide a concise advance in the drug delivery systems, mainly focus on the use of nano-carriers. Furthermore, we elaborately discuss the prospect of aged skeletal muscle treatment by nanotechnology approaches.

Keywords: ageing skeletal muscle, drug delivery, extracellular vesicle, sarcopenia, skeletal muscle regeneration

INTRODUCTION

Skeletal muscles, as one of the largest organs in the body, are characterized by their mechanical activity required for posture, movement, and breathing (Fan et al., 2013; Pedersen, 2013). However, with the increasing age, skeletal muscle mass gradually declines and gradually loses function, leading to adverse outcomes in older people, such as high risk of falls and fractures, and damaged physical ability (Wilkinson et al., 2018; Cuesta-Triana et al., 2019). Current clinical approaches to age-related muscle loss are limited. At present, there are many studies on skeletal muscle regeneration which focus on muscle injuries, but research on strategies for age-related muscle loss is still relatively basic.

Conventionally, the research of skeletal muscle injuries mainly focuses on tissue engineering methods and cell therapies. These methods are suitable for the injury with obvious muscle defects (McKeon-Fischer et al., 2015). However, these methods are not suitable for age-related muscle loss, a kind of systemic skeletal muscle disease without local defect. In recent years, novel nano-carriers delivery systems offer new possibilities for treating systemic diseases. Even further, Rong, S et al. proposed a prospect that extracellular vesicles (EVs), including exosomes, may also be ideal drug carriers which could regulate muscle regeneration and protein synthesis. EV-based delivery systems may be potential strategies of age-related muscle loss in the future (Rong et al., 2020).

Therefore, this review will discuss the potential therapeutic targets of ageing skeletal muscle and provide a concise advance in the drug delivery systems, mainly focus on the use of nano-carriers.

MOLECULAR MECHANSIM OF AGEING SKELETAL MUSCLE REGENERATION

The Process of Skeletal Muscle Regeneration

Skeletal muscle regeneration includes four consecutive phases: the degeneration phase, the inflammatory phase, the phase of satellite cell differentiation, and the phase of maturation and remodeling (Barberi et al., 2013; Yin et al., 2013; Schmidt et al., 2019) (**Figure 1**). After injury, myofibers are rapid necrosis (phase of degeneration) which induce the inflammatory phase (**Figure 2**). The first inflammatory cells, neutrophils, are recruited to the damaged skeletal muscle within 6 h. Soon afterwards, macrophages begin to infiltrate the damaged skeletal muscle. Similar to the inflammation in other post injury parts, the infiltrating macrophages include M1 macrophages ($CD68^+$/$CD163^-$) and M2 macrophages ($CD68^-$/$CD163^+$). In the first 24 h, the M1 macrophages secrete pro-inflammatory cytokines such as TNFα and IL-1. Then, the M2 macrophages secrete anti-inflammatory cytokines such as IL-10 to attenuate the inflammatory response and promote satellite cells (SC) proliferation and differentiation. (Saini et al., 2016). In the third phase, unactivated satellite cells migrate to the target location and begin to differentiate into rapidly proliferating cells, myogenic progenitor cells (Souza et al., 2018). In this phase, several muscle-related proteins are detected with highly expression such as MyoD, Desmin, and Myf5 (Zammit, 2017; Schiaffino et al., 2018). In the maturation phase, myogenic progenitor cells differentiate into myocytes and newly myofibers occur. Meanwhile, devMHC (developmental myosin heavy chain), are detected with highly expression in this phase (Sutcu and Ricchetti, 2018). At the end of the maturation phase, the nuclei move towards the edge of newly myofibers which simultaneously increase in size (Ruparelia et al., 2019). However, when ageing occurs, the process of skeletal muscle regeneration is hindered. The main obstacles include changes in the satellite cells themselves and changes in the muscle regeneration microenvironment.

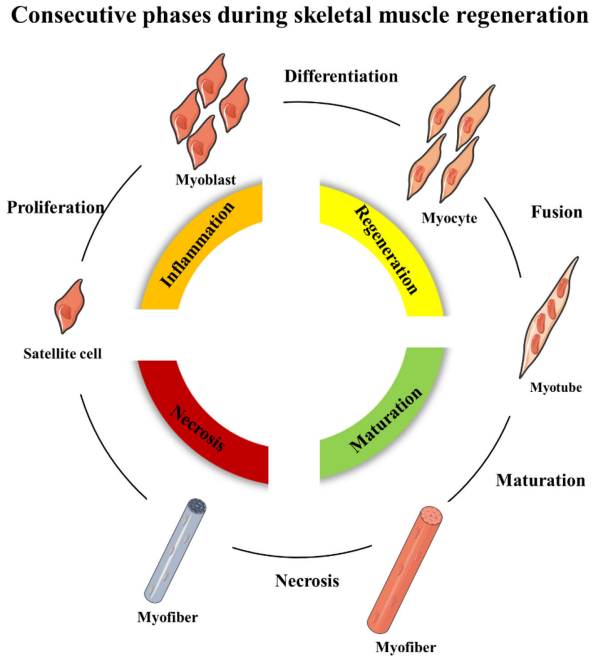

FIGURE 1 | Schematic representation of the four consecutive phases during skeletal muscle regeneration.

Changes in the Ageing Satellite Cells

Satellite cells, also called muscle stem cells, are necessary for muscle regeneration and support the repair and remodeling of muscle fibers and help maintain healthy muscle mass throughout life. With ageing, satellite cells become losing self-renewal and regenerative capacity. The number of muscle stem cells expressing high level of transcription factor Pax7 (Pax7Hi) decreased during ageing (Li H. et al., 2019). Recent studies have explored changes in satellite cells from the genetic and molecular levels. Epigenetic stress response in satellite cells

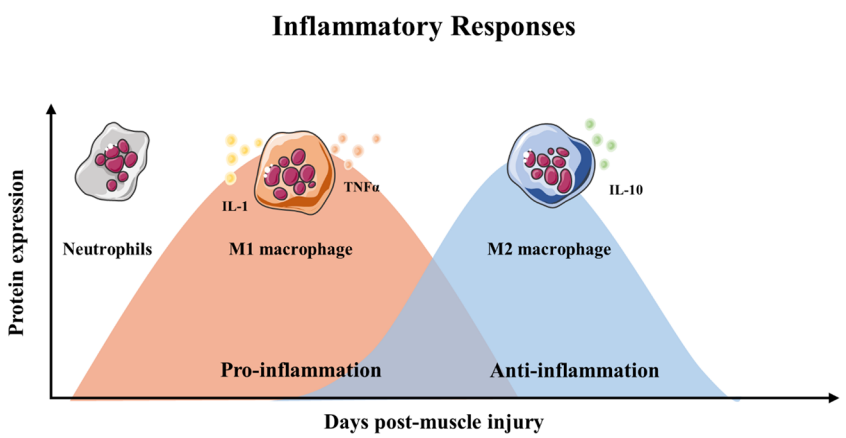

FIGURE 2 | Timeline of inflammatory responses and immune cell during muscle regeneration.

would limit muscle regeneration by Hoxa9 developmental signaling. After analyzing the whole genome of satellite cells from healthy individuals of different ages, somatic mutagenesis was identified as another age-related negative regulator (Schwörer et al., 2016; Franco et al., 2018). Several signaling pathways were found become aberrant during muscle ageing including RTK signaling, FGF signaling and p38 MAPK (Patel et al., 2019; Bae et al., 2020). Cdon-deficit satellite cells had impaired proliferation and lower regenerative capacity *via* aberrant integrin and FGFR signaling. In ageing satellite cells, the p38 α/β-MAPK signaling can activate high expression of $p16^{Ink4a}$ which could inhibit satellite cells self-renew (Almada and Wagers, 2016; Zhu et al., 2019). Emerging studies found that ageing leads to the asymmetric division of satellite cells (Garcia-Prat and Munoz-Canoves, 2017; Feige et al., 2018; Hwang and Brack, 2018). Garcia-Prat et al. found that autophagic activity is also impaired in aged satellite cells, resulting in the accumulation of impaired proteins and mitochondria, leading to the dysfunction and reduced number of satellite cells (García-Prat et al., 2016). Oxidative stressors, especially reactive oxygen species (ROS), have been thought to have a negative effect on skeletal muscle (Baraibar et al., 2013). The oxidative capacity of skeletal muscles is closely related to general physical performance. Overexpressed ROS cause oxidative stress and mitochondrial dysfunction in cells, which eventually induce apoptosis (Zhou et al., 2018; Szentesi et al., 2019).

Changes in the Aged Muscle Microenvironment

During the ageing process, the microenvironment of muscle tissue changes, which affects the process of self-repair. Immune regulation is closely related to muscle regeneration. The numbers of myeloid lineage cells in their skeletal muscles increased during ageing, including macrophages and granulocytes (Li et al., 2020). When immune cells and factors change in the muscle microenvironment, muscle regeneration will be affected (Livshits and Kalinkovich, 2019). Immune senescence includes a systemic, chronic, low-grade pro-inflammatory state which is also known as inflammageing (Wilson et al., 2017). The proportion of serum inflammatory cytokines begins to change. The proportion of pro-inflammatory cytokines, such as IL-1β, IL-6 and TNFα, are gradually increasing. In contrast, the proportion of anti-inflammatory cytokines are gradually decreased (Rezus et al., 2020). The reasons for inflammageing are complex, including changes in monocyte and lymphocyte phenotypes. Meanwhile, obesity is also involved in the process of immuneageing, in which the expression of pro-inflammatory factors such as leptin increases and the expression of anti-inflammatory factors such as adiponectin decreases (Wilson et al., 2017; Weyh et al., 2020). Lukjanenko L et al. found that fibro-adipogenic progenitors indirectly affect the functions of satellite cells during ageing. WNT1 Inducible Signaling Pathway Protein 1 (WISP1) secreted by fibro-adipogenic progenitors was a key matricellular communicator to repair regenerative capacity (Lukjanenko et al., 2019).

POTENTIAL THERAPEUTIC TARGETS OF AGEING SKELETAL MUSCLE

Currently, the only validated treatment of aged skeletal muscle is exercise, which can reverse different types of muscle ageing to some extent. However, for patients undergoing long-term bed rest or with other clinical complications, they are generally not recommended to exercise. Therefore, there is a need to develop new treatments for old patients to reduce skeletal muscle loss and restore muscle function. (Cohen et al., 2015). Many studies have identified various biological pathways and targets that may promote skeletal muscle regeneration, and some drugs have been tested in clinical trials. For example, A phase 2 randomized study involved 170 aged women diagnosed with sarcopenia and moderate physical dysfunction showed a significant increase in lean body mass but fail to improve muscle strength or function after receiving MK-0773, the selective androgen receptor modulator (SARM) (Papanicolaou et al., 2013). Another cohort involved in 400 individuals aged ≥50 years treated with total hip arthroplasty for osteoarthritis. After receiving LY2495655, a humanized monoclonal antibody targeting myostatin, no meaningful difference in muscle strength, physical performance was found compared to placebo (Woodhouse et al., 2016).To date, results from trials have shown less success for improving muscle strength or patient physical function (Rooks and Roubenoff, 2019). As research continues, new targets have emerged in recent years, giving prospect for disease treatment. Here, we summarize the latest promising targets for treating muscle ageing.

Anti-Myostatin

Myostatin (MSTN), functioning as an endogenous regulator for the skeletal muscle growth, has drawn wide attention as a novel target. Myostatin can combine with activin receptors type IIB (ActRIIB) on the myofibers membrane which regulate skeletal muscle mass and function (White and LeBrasseur, 2014). Myostatin may also directly affect skeletal muscle mass by suppressing muscle regeneration (Ge et al., 2020). Because myostatin significantly regulates muscle regeneration, it has become a promising target for preventing the decline and dysfunction of skeletal muscle function for many years (Polkey et al., 2019). Several clinical trials have shown positive results through direct inhibiting the expression of myostatin. LY2495655, a humanized MSTN antibody, could increase appendicular lean mass in a randomised, phase 2 clinical trial (Becker et al., 2015). Bimagrumab is another human monoclonal antibody which targets activin type II receptors (ActRII). A 24-week, randomized, double-blind study, which involved 40 individuals, showed that treat with bimagrumab over 16 weeks could increase muscle mass and strength in older adults with sarcopenia. However, a multicentre, double-blind, placebo-controlled study, which involved 251 individuals, evaluated the safety and efficacy of intravenous bimagrumab in inclusion body myositis. The results indicated the treatment of bimagrumab did not meet the primary endpoint as no significant difference between bimagrumab and placebo in 6-min walking distance (6MWD) (Furrer and Handschin, 2019; Hanna et al., 2019; Hardee and Lynch, 2019).

The above clinical research shows that large-scale multi-center clinical research is still needed to verify the efficacy and adaptive diseases of anti-myostatin treatment.

Anti-Inflammatory Cytokine

Since the immune cells are deeply involved in skeletal reconstruction process, the immune cells and inflammatory factors may become the target of improving aged skeletal muscle. Huang, S et al. observed the highly expression of TNF-α and decreased expression of IL-10 in soleus muscle after treating with doxorubicin, an anti-tumor drug which could cause skeletal muscle loss in cancer patients. More importantly, doxorubicin may cause the absent of M1 macrophage during the inflammatory phase (Huang S. et al., 2017). Lee, C. et al. found Magnolol, a kind of anti-cancer drug, could attenuate the imbalance of M1/M2c macrophages to inhibit muscle loss (Lee et al., 2020). Further, Liao, Z.H., et al. found that regulating the functions of Treg cells would also be an important measure to promote muscle regeneration. They treated cardiotoxin (CTX)-induced muscle injury by estrogen and the results indicated estrogen could suppress immune response and reverse phenotypes of monocytes/macrophages by regulating the function of Treg cells, and suppressing Th1 response in the inflammatory phase (Liao et al., 2019). Administration of exogenous anti-inflammatory factors may also improve skeletal muscle regeneration. Costamagna, D et al. found the IL-4 treatment would improve the performances and prolonged survival of colon carcinoma-bearing (C26) mice. IL-4 could rescue muscle mass by increasing protein synthesis and promote myogenesis (Costamagna et al., 2020). Du H et al. investigated that overexpression of ADAMTS1 in macrophages could active satellite cell and promote muscle regeneration by reduces Notch signaling (Du et al., 2017). Although a large number of studies have suggested that immune cells and immune factors play an important role in promoting muscle regeneration, the role of the immune system in ageing muscle loss is unknown. Therefore, further research is needed to further explore the immune microenvironment around ageing skeletal muscles for possible therapeutic targets.

Nucleic Acids

Nucleic acids, particularly non-encoding nucleic acid, act as a key modulator of skeletal muscle proliferation and regeneration. It is noteworthy that a group of muscle- specific miRNAs, myomiRNAs, are closely related to skeletal muscle development and regeneration, including miR-133, miR-206, miR-208b, and miR-499. Iannone, F et al. investigated that the under-expression of miR-133b may contribute to the impaired regenerative capacity of satellite cells (Iannone et al., 2020). The expression of miR-206 increased during muscle regeneration result in the inhibition of Pax3, Pax7, and c-Met. These downstream genes subsequently affect myogenic differentiation (McCarthy, 2008).

As EVs are closely related to exercise, researchers have confirmed that different types of exercise would release a large number of EVs into the blood circulation. Since the discovery of EVs can transfer functional non-encoding nucleic acid, EV-associated nucleic acid may play a key role in muscle cell-cell communication (Yin et al., 2018). Fulzele, S. et al. found a significant increase in expression of senescence-associated EVs-derived miR-34a in skeletal muscle from ageing mice. The results indicated that senescence-associated EVs secreted from skeletal muscle may directly reduce stem cell populations *via* their microRNA cargo (Fulzele et al., 2019). As the growing understanding of EVs, more therapeutic targets may be constantly discovered.

Bone-Derived Factors

Bone and muscle are closely related, and many studies have found that bone and muscle interact on each other. As emerging evidence supports the concept that bone would act as an endocrine organ, bone-secreted factors may be an important target for muscle regeneration **(Figure 3)**. Osteocalcin (OCN) is currently the most widely studied bone-derived factor. OCN regulates the uptake and catabolism of nutrients in muscle during exercise by promoting the release of interleukin-6 from myofibers. More importantly, the muscle mass increased significantly after giving exogenous OCN in older mice. These findings strongly suggest that OCN would be a promising therapeutic target for ageing muscle regeneration(Mera et al., 2016a; Mera et al., 2016b). In contrast, transforming growth factor (TGF)-β derived from bone surface was a negative regulator which contributes to muscle weakness (Waning et al., 2015). Sclerostin is mainly secreted by osteocytes and osteoblasts which is a key inhibitor of Wnt signaling. Sclerostin could inhibit myogenic differentiation by activating Wnt/β-catenin pathway *in vitro* experiment. Hesse E et al. found that sclerostin antibody would alleviate muscle weakness and improve skeletal muscle function (Huang J. et al., 2017; Hesse et al., 2019). The receptor-activator of nuclear factor κB/receptor-activator of nuclear factor κB ligand/osteoprotegerin (RANK/RANKL/OPG) is a key pathway for bone remodeling. Recent studies found that bone derived RANKL inhibitor could significantly improve skeletal muscle function and restore bone mass. OPG-deficient mice displayed reduced muscle weakness with selective atrophy of fast-twitch-type IIb myofibers. After using RANKL inhibitors, represented by Denosumab, patients have improved handgrip strength which indicate RANKL inhibitors may be an important method for treating muscle diseases (Dufresne et al., 2018; Bonnet et al., 2019; Hamoudi et al., 2020).

Although there are many therapeutic targets for ageing skeletal muscle, a very important point is how to accurately deliver functional nucleic acids or proteins. Obviously, the current clinical trials for muscle regeneration have encountered some difficulties. For example, the anti-myostatin drug has not achieved the expected effect. The results of clinical trials suggest that the exploration of functional molecules may not achieve good therapeutic effects. How to accurately deliver and release functional molecules may be another important issue to be explored. We believe that building an appropriate delivery system for muscle regeneration is another area worthy of in-depth study.

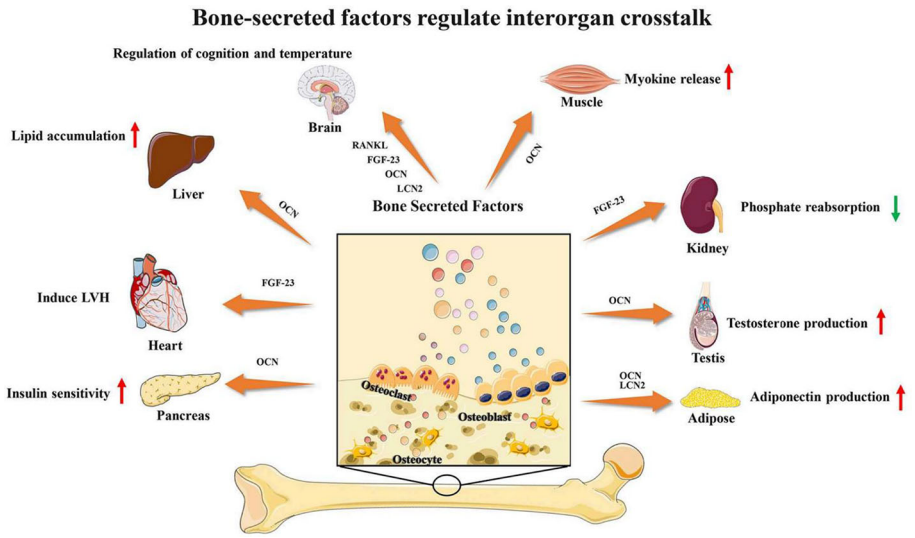

FIGURE 3 | Bone-secreted factors regulate interorgan crosstalk. Reproduced, with permission, from (Li Y. et al., 2019).

DRUG DELIVERY SYSTEM FOR AGEING SKELETAL MUSCLE REGENERATION

To treat aged skeletal muscle dysfunction, appropriate drug delivery system that loads with potential therapeutic factors would be highly desired. Here, we summarize the current promising drug delivery systems, and future studies may load different active factors on the basis of these systems.

Adeno-Associated Virus (AAV)

Adeno-associated viral (AAV) vectors are currently developing rapidly in the treatment of gene-related muscle disorders. Natural or engineered viral capsids have been successfully constructed by transferring nucleic acids, antibodies or gene-editing machinery *via* various routes of administration successfully (Lisowski et al., 2015; Naso et al., 2017). Currently, AAV appears to be the most promising vector for gene therapy, especially the treatment of Duchenne muscular dystrophy and Spinal muscular atrophy (SMA) (Groen et al., 2018; Verhaart and Aartsma-Rus, 2019). There will be more clinical trials to be performed in the future, and it will also be applied to other muscle diseases. However, the limitations of AAV are also obvious. Lacking muscle cell tropism induces the inefficiency of AAV. Lacking effective nucleic acid editing targets also makes AAV difficult to use as an effective means to promote ageing skeletal muscle regeneration. Therefore, we propose constructing novel drug delivery systems to repair skeletal muscles with complex pathogenesis.

Muscle-Targeting Delivery System

Because ageing-related muscle loss has no local lesions, drug therapy can only be administered systemically. The problem with systemic administration is the side effects in other organs, and the high concentration in liver and kidney. To solve above problems, another important strategy for building drug delivery systems is muscle-targeting delivery systems. A muscle-targeting delivery system requires a targeted motif, which can be combined with a delivery system to specifically deliver drugs to skeletal muscles. For example, skeletal muscle-related cell surface-specific proteins can serve as a targeted motif. Large molecules such as antibodies or antibody-drug conjugates would also be a potential method of targeting (Ebner et al., 2015). Several examples of muscle-targeting peptide have been reported. Samoylova TI et al. found a heptapeptide sequence, ASSLNIA, which could improve specificity for binding to skeletal muscle by screening a random phage display library (Samoylova and Smith, 1999). Then, Jativa S D et al. develop a generation 5-polyamidoamine dendrimer (G5-PAMAM) modified with ASSLNIA to synergistically enhance gene delivery to skeletal muscle cells (Jativa et al., 2019). Gao X et al. identified a novel 12-mer peptide (M12) which was shown more effective muscle-homing ability. This motif could enhance binding affinity to myoblast *in vitro*. Conjugated muscle-homing peptide with phosphorodiamidate morpholino oligomers showed significant improvement in grip strength in mdx mice (Seow et al., 2010; Gao et al., 2014). Currently, only a few studies have discovered molecules with muscle-targeting functions. Therefore, subsequent research still needs to explore more novel muscle-targeting molecules and make appropriate modifications to ameliorate ageing-related muscle loss.

Nanoparticles

The growing concern of nanoparticles is triggered by the rapid development of nanotechnology. Nanoparticles have many unique advantages including enhanced tissue targeting, nucleic acids protection from degradation, and low immunogenicity

(Nance et al., 2018; Nag et al., 2020). For example, Poussard, S et al. observed the silica nanoparticles uptake by myoblasts and promote the differentiation *in vitro* (Poussard et al., 2015). Ge. J et al. developed a kind of monodispersed gold and gold-silver nanoparticles (AuNPs and Au-AgNPs) which could support adhesion and proliferation of myoblast by motivating the p38α MAPK signaling pathway (Ge et al., 2018). Raimondo, T.M. et al. found that constructing cytokines binding gold nanoparticles could regulate the inflammatory phase by changing M2 macrophage polarization, which subsequently promote regeneration and increased newly myofibles function (Raimondo and Mooney, 2018). Nanoparticles are easy to prepare on a uniform scale and are easier to modify. There are many optional materials for nanoparticles such as metal particles or silica particles. However, the follow-up research still needs to consider the safety of nanoparticles, including material toxicity, dose toxicity, and metabolic rate. In addition, how to increase the skeletal muscle targeting of nanoparticles still needs to be explored.

Extracellular Vesicles (EVs)

EVs, 30–150 nm in diameter, have been demonstrated to transfer functional proteins, nucleic acid (e.g. mRNA, miRNA, lncRNA) to neighboring or remote cells. The membrane of EVs acts as a natural barrier to prevent degradation in the blood circulation **(Figure 4)**. EVs can be administered *via* intravenous (IV) and intranasal routes to reach the target location, depending on the therapeutic purpose. Due to these characteristics, EVs are considered ideal natural systems for drug delivery (Vader et al., 2016; Skotland et al., 2020; Rong et al., 2020).

Many studies show that EVs are closely involved in skeletal muscle metabolism and regeneration. Zanotti S et al. found that EVs derived from local fibroblasts in the Duchenne muscular dystrophy (DMD) muscle are able to induce a transfer of unactivated fibroblasts to myofibroblasts thereby motivating the fibrotic response (Zanotti et al., 2018). As mentioned above, Fulzele, S. et al. found EVs-derived miR-34a could regulate muscle metabolism (Fulzele et al., 2019). Many studies investigated that physical exercise, which is closely related with muscle regeneration, can induce rapid release of EVs into the blood circulation. Fruhbeis, C et al. found that a consecutive release of EVs would be triggered after physical exercise. During physical exercise, the released-EVs may participate in intercellular communication or remote communication which involve signaling across tissues and organs (Frühbeis et al., 2015). Guescini, M found similar results and further showed that muscle-specific miRNAs in EVs were significantly upregulated (Guescini et al., 2015). Whitham, M et al. found that exercise-related EVs tend to accumulate in the liver and can transfer inner proteins (Whitham et al., 2018). These studies have demonstrated the promising potential of EVs for therapeutic drug delivery in various muscle diseases. It is worth noting that Ran N et al. created a novel exosome-based delivery system by anchoring the inhibitory domain of myostatin propeptide. The exosome-delivery system could efficiently promote muscle function in mdx mice (Ran et al., 2020). Gao et al. also demonstrated a muscle-targeting exosome-based delivery system, which was modified by CP05, could increase dystrophin expression in mdx mice (Gao et al., 2018). These exosome-based delivery platforms may be effective delivery methods for the treatment of DMD.

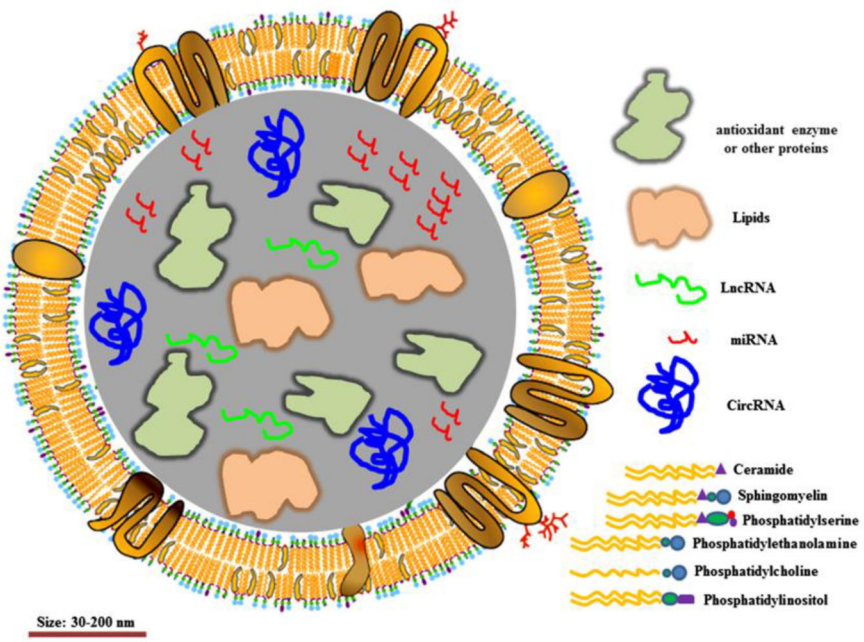

FIGURE 4 | Structure of extracellular vesicles. Reproduced, with permission, from (Rong et al., 2020).

The advantages of exosomes are good biological safety, easy absorption and metabolism. Its widespread presence in the body also makes it relatively easy to obtain. It has been found that exosomes have a natural targeting function, which makes it an ideal precision delivery system (Song et al., 2019). However, the research on exosomes is still in an early stage, and the following issues still need to be solved. First, constructing a large number of exosomes with uniform size is still difficult. Efficient loading rate also needs to be considered. In addition, the selection of cell-derived exosomes to construct a delivery system still requires further exploration. At present, there are few studies on the affinity and targeting ability of different exosomes to skeletal muscle. When the problem of exosome preparation is solved, screening the appropriate functional molecule is another key step. In summary, exosomes may be an ideal delivery system for aging skeletal muscle regeneration. Exploring the characteristics and modification of exosomes still needs further investigation.

CONCLUSION AND FUTURE DIRECTIONS

Currently there is no ideal treatment for the ageing-related loss of skeletal muscle. Nano-carrier drug delivery system is an emerging area which may provide the ultimate solution for the clinical treatment. Future research should be divided into two aspects for further exploration. Current studies on potential targets for skeletal muscle regeneration do not consider the characteristics of aging. Taking into account the changes in the muscle satellite cells and immune microenvironment in aging skeletal muscle, new therapeutic targets may be discovered. Although the nanocarrier delivery system provides a good method for the treatment of aging diseases, many safety and effectiveness issues still need to be explored. The construction of the delivery system should be carried out simultaneously with the research on the mechanism of regulating muscle regeneration. The ideal delivery system should not only play a role in promoting, but adopt multiple control methods to maximize the improvement of aging muscle loss.

AUTHOR CONTRIBUTIONS

PY, LZ, and PT made major contributions to the conception of the work. YL, MC, and YY drafted the manuscript. YZ, ML, YQ, and SC revised the manuscript.

ACKNOWLEDGMENTS

This work was supported by National Natural Science Foundation of China (81702176, 81772369, 81972115 and 51803188).

REFERENCES

Almada, A. E., and Wagers, A. J. (2016). Molecular circuitry of stem cell fate in skeletal muscle regeneration, ageing and disease. *Nat. Rev. Mol. Cell Biol.* 17 (5), 267–279. doi: 10.1038/nrm.2016.7

Bae, J. H., Hong, M., Jeong, H. J., Kim, H., Lee, S. J., Ryu, D., et al. (2020). Satellite cell-specific ablation of Cdon impairs integrin activation, FGF signalling, and muscle regeneration. *J. Cachexia Sarcopenia Muscle*. doi: 10.1002/jcsm.12563

Baraibar, M. A., Gueugneau, M., Duguez, S., Butler-Browne, G., Bechet, D., and Friguet, B. (2013). Expression and modification proteomics during skeletal muscle ageing. *Biogerontology* 14 (3), 339–352. doi: 10.1007/s10522-013-9426-7

Barberi, L., Scicchitano, B. M., De Rossi, M., Bigot, A., Duguez, S., Wielgosik, A., et al. (2013). Age-dependent alteration in muscle regeneration: the critical role of tissue niche. *Biogerontology* 14 (3), 273–292. doi: 10.1007/s10522-013-9429-4

Becker, C., Lord, S. R., Studenski, S. A., Warden, S. J., Fielding, R. A., Recknor, C. P., et al. (2015). Myostatin antibody (LY2495655) in older weak fallers: a proof-of-concept, randomised, phase 2 trial. *Lancet Diabetes Endocrinol.* 3 (12), 948–957. doi: 10.1016/S2213-8587(15)00298-3

Bonnet, N., Bourgoin, L., Biver, E., Douni, E., and Ferrari, S. (2019). RANKL inhibition improves muscle strength and insulin sensitivity and restores bone mass. *J. Clin. Invest.* 129 (8), 3214–3223. doi: 10.1172/JCI125915

Cohen, S., Nathan, J. A., and Goldberg, A. L. (2015). Muscle wasting in disease: molecular mechanisms and promising therapies. *Nat. Rev. Drug Discovery* 14 (1), 58–74. doi: 10.1038/nrd4467

Costamagna, D., Duelen, R., Penna, F., Neumann, D., Costelli, P., and Sampaolesi, M. (2020). Interleukin-4 administration improves muscle function, adult myogenesis, and lifespan of colon carcinoma-bearing mice. *J. Cachexia Sarcopenia Muscle* 11 (3), 783–801. doi: 10.1002/jcsm.12539

Cuesta-Triana, F., Verdejo-Bravo, C., Fernandez-Perez, C., and Martin-Sanchez, F. J. (2019). Effect of Milk and Other Dairy Products on the Risk of Frailty, Sarcopenia, and Cognitive Performance Decline in the Elderly: A Systematic Review. *Adv. Nutr.* 10 (suppl_2), S105–S119. doi: 10.1093/advances/nmy105

Du, H., Shih, C. H., Wosczyna, M. N., Mueller, A. A., Cho, J., Aggarwal, A., et al. (2017). Macrophage-released ADAMTS1 promotes muscle stem cell activation. *Nat. Commun.* 8 (1), 669. doi: 10.1038/s41467-017-00522-7

Dufresne, S. S., Boulanger-Piette, A., Bosse, S., Argaw, A., Hamoudi, D., Marcadet, L., et al. (2018). Genetic deletion of muscle RANK or selective inhibition of RANKL is not as effective as full-length OPG-fc in mitigating muscular dystrophy. *Acta Neuropathol. Commun.* 6 (1), 31. doi: 10.1186/s40478-018-0533-1

Ebner, D. C., Bialek, P., El-Kattan, A. F., Ambler, C. M., and Tu, M. (2015). Strategies for skeletal muscle targeting in drug discovery. *Curr. Pharm. Des.* 21 (10), 1327–1336. doi: 10.2174/1381612820666140929095755

Fan, W., Atkins, A. R., Yu, R. T., Downes, M., and Evans, R. M. (2013). Road to exercise mimetics: targeting nuclear receptors in skeletal muscle. *J. Mol. Endocrinol.* 51 (3), T87–T100. doi: 10.1530/JME-13-0258

Feige, P., Brun, C. E., Ritso, M., and Rudnicki, M. A. (2018). Orienting Muscle Stem Cells for Regeneration in Homeostasis, Aging, and Disease. *Cell Stem Cell* 23 (5), 653–664. doi: 10.1016/j.stem.2018.10.006

Frühbeis, C., Helmig, S., Tug, S., Simon, P., and Krämer-Albers, E. (2015). Physical exercise induces rapid release of small extracellular vesicles into the circulation. *J. Extracell. Vesicles* 4 (1), 28211–28239. doi: 10.3402/jev.v4.28239

Franco, I., Johansson, A., Olsson, K., Vrtačnik, P., Lundin, P., Helgadottir, H. T., et al. (2018). Somatic mutagenesis in satellite cells associates with human skeletal muscle aging. *Nat. Commun.* 9 (1), 800. doi: 10.1038/s41467-018-03244-6

Fulzele, S., Mendhe, B., Khayrullin, A., Johnson, M., Kaiser, H., Liu, Y., et al. (2019). Muscle-derived miR-34a increases with age in circulating extracellular vesicles and induces senescence of bone marrow stem cells. *Aging (Albany NY)* 11 (6), 1791–1803. doi: 10.18632/aging.101874

Furrer, R., and Handschin, C. (2019). Muscle Wasting Diseases: Novel Targets and Treatments. *Annu. Rev. Pharmacol. Toxicol.* 59, 315–339. doi: 10.1146/annurev-pharmtox-010818-021041

Gao, X., Zhao, J., Han, G., Zhang, Y., Dong, X., Cao, L., et al. (2014). Effective dystrophin restoration by a novel muscle-homing peptide-morpholino

conjugate in dystrophin-deficient mdx mice. *Mol. Ther.* 22 (7), 1333–1341. doi: 10.1038/mt.2014.63

Gao, X., Ran, N., Dong, X., Zuo, B., Yang, R., Zhou, Q., et al. (2018). Anchor peptide captures, targets, and loads exosomes of diverse origins for diagnostics and therapy. *Sci. Trans. Med.* 10 (444), t195. doi: 10.1126/scitranslmed.aat0195

García-Prat, L., Martínez-Vicente, M., Perdiguero, E., Ortet, L., Rodríguez-Ubreva, J., Rebollo, E., et al. (2016). Autophagy maintains stemness by preventing senescence. *Nature* 529 (7584), 37–42. doi: 10.1038/nature16187

Garcia-Prat, L., and Munoz-Canoves, P. (2017). Aging, metabolism and stem cells: Spotlight on muscle stem cells. *Mol. Cell Endocrinol.* 445, 109–117. doi: 10.1016/j.mce.2016.08.021

Ge, J., Liu, K., Niu, W., Chen, M., Wang, M., Xue, Y., et al. (2018). Gold and gold-silver alloy nanoparticles enhance the myogenic differentiation of myoblasts through p38 MAPK signaling pathway and promote in vivo skeletal muscle regeneration. *Biomaterials* 175, 19–29. doi: 10.1016/j.biomaterials.2018.05.027

Ge, L., Dong, X., Gong, X., Kang, J., Zhang, Y., and Quan, F. (2020). Mutation in myostatin 3'UTR promotes C2C12 myoblast proliferation and differentiation by blocking the translation of MSTN. *Int. J. Biol. Macromol.* 154, 634–643. doi: 10.1016/j.ijbiomac.2020.03.043

Groen, E. J. N., Talbot, K., and Gillingwater, T. H. (2018). Advances in therapy for spinal muscular atrophy: promises and challenges. *Nat. Rev. Neurol.* 14 (4), 214–224. doi: 10.1038/nrneurol.2018.4

Guescini, M., Canonico, B., Lucertini, F., Maggio, S., Annibalini, G., Barbieri, E., et al. (2015). Muscle Releases Alpha-Sarcoglycan Positive Extracellular Vesicles Carrying miRNAs in the Bloodstream. *PloS One* 10 (5), e125094. doi: 10.1371/journal.pone.0125094

Hamoudi, D., Bouredji, Z., Marcadet, L., Yagita, H., Landry, L. B., Argaw, A., et al. (2020). Muscle weakness and selective muscle atrophy in osteoprotegerin-deficient mice. *Hum. Mol. Genet.* 29 (3), 483–494. doi: 10.1093/hmg/ddz312

Hanna, M. G., Badrising, U. A., Benveniste, O., Lloyd, T. E., Needham, M., Chinoy, H., et al. (2019). Safety and efficacy of intravenous bimagrumab in inclusion body myositis (RESILIENT): a randomised, double-blind, placebo-controlled phase 2b trial. *Lancet Neurol.* 18 (9), 834–844. doi: 10.1016/S1474-4422(19)30200-5

Hardee, J. P., and Lynch, G. S. (2019). Current pharmacotherapies for sarcopenia. *Expert Opin. Pharmacother.* 20 (13), 1645–1657. doi: 10.1080/14656566.2019.1622093

Hesse, E., Schroder, S., Brandt, D., Pamperin, J., Saito, H., and Taipaleenmaki, H. (2019). Sclerostin inhibition alleviates breast cancer-induced bone metastases and muscle weakness. *JCI Insight* 5 (9), e125543. doi: 10.1172/jci.insight.125543

Huang, J., Romero-Suarez, S., Lara, N., Mo, C., Kaja, S., Brotto, L., et al. (2017). Crosstalk between MLO-Y4 osteocytes and C2C12 muscle cells is mediated by the Wnt/beta-catenin pathway. *JBMR Plus* 1 (2), 86–100. doi: 10.1002/jbm4.10015

Huang, S., Wu, J., Saovieng, S., Chien, W., Hsu, M., Li, X., et al. (2017). Doxorubicin inhibits muscle inflammation after eccentric exercise. *J. Cachexia Sarcopenia Muscle* 8 (2), 277–284. doi: 10.1002/jcsm.12148

Hwang, A. B., and Brack, A. S. (2018). Muscle Stem Cells and Aging. *Curr. Top. Dev. Biol.* 126, 299–322. doi: 10.1016/bs.ctdb.2017.08.008

Iannone, F., Montesanto, A., Cione, E., Crocco, P., Caroleo, M. C., Dato, S., et al. (2020). Expression Patterns of Muscle-Specific miR-133b and miR-206 Correlate with Nutritional Status and Sarcopenia. *Nutrients* 12 (2), 297. doi: 10.3390/nu12020297

Jativa, S. D., Thapar, N., Broyles, D., Dikici, E., Daftarian, P., Jiménez, J. J., et al. (2019). Enhanced Delivery of Plasmid DNA to Skeletal Muscle Cells using a DLC8-Binding Peptide and ASSLNIA-Modified PAMAM Dendrimer. *Mol. Pharm.* 16 (6), 2376–2384. doi: 10.1021/acs.molpharmaceut.8b01313

Lee, C., Jeong, H., Lee, H., Hong, M., Park, S., and Bae, H. (2020). Magnolol Attenuates Cisplatin-Induced Muscle Wasting by M2c Macrophage Activation. *Front. Immunol.* 11, 77. doi: 10.3389/fimmu.2020.00077

Li, H., Chen, Q., Li, C., Zhong, R., Zhao, Y., Zhang, Q., et al. (2019). Muscle-secreted granulocyte colony-stimulating factor functions as metabolic niche factor ameliorating loss of muscle stem cells in aged mice. *EMBO J.* 38 (24), e102154. doi: 10.15252/embj.2019102154

Li, Y., Yin, P., Guo, Z., Lv, H., Deng, Y., Chen, M., et al. (2019). Bone-Derived Extracellular Vesicles: Novel Players of Interorgan Crosstalk. *Front. Endocrinol.* 10, 846. doi: 10.3389/fendo.2019.00846

Li, J., Yi, X., Yao, Z., Chakkalakal, J. V., Xing, L., and Boyce, B. F. (2020). TNF receptor-associated factor 6 mediates TNFα-induced skeletal muscle atrophy in mice during aging. *J. Bone Miner. Res.* doi: 10.1002/jbmr.4021

Liao, Z. H., Huang, T., Xiao, J. W., Gu, R. C., Ouyang, J., Wu, G., et al. (2019). Estrogen signaling effects on muscle-specific immune responses through controlling the recruitment and function of macrophages and T cells. *Skeletal Muscle* 9 (1), 20. doi: 10.1186/s13395-019-0205-2

Lisowski, L., Tay, S. S., and Alexander, I. E. (2015). Adeno-associated virus serotypes for gene therapeutics. *Curr. Opin. Pharmacol.* 24, 59–67. doi: 10.1016/j.coph.2015.07.006

Livshits, G., and Kalinkovich, A. (2019). Inflammaging as a common ground for the development and maintenance of sarcopenia, obesity, cardiomyopathy and dysbiosis. *Ageing Res. Rev.* 56, 100980. doi: 10.1016/j.arr.2019.100980

Lukjanenko, L., Karaz, S., Stuelsatz, P., Gurriaran-Rodriguez, U., Michaud, J., Dammone, G., et al. (2019). Aging Disrupts Muscle Stem Cell Function by Impairing Matricellular WISP1 Secretion from Fibro-Adipogenic Progenitors. *Cell Stem Cell* 24 (3), 433–446. doi: 10.1016/j.stem.2018.12.014

McCarthy, J. (2008). MicroRNA-206: The skeletal muscle-specific myomiR. *Biochim. Biophys. Acta (BBA) - Gene Regul. Mech.* 1779 (11), 682–691. doi: 10.1016/j.bbagrm.2008.03.001

McKeon-Fischer, K. D., Browe, D. P., Olabisi, R. M., and Freeman, J. W. (2015). Poly(3,4-ethylenedioxythiophene) nanoparticle and poly(ε-caprolactone) electrospun scaffold characterization for skeletal muscle regeneration. *J. Biomed. Mater. Res. Part A* 103 (11), 3633–3641. doi: 10.1002/jbm.a.35481

Mera, P., Laue, K., Ferron, M., Confavreux, C., Wei, J., Galan-Diez, M., et al. (2016a). Osteocalcin Signaling in Myofibers Is Necessary and Sufficient for Optimum Adaptation to Exercise. *Cell Metab.* 23 (6), 1078–1092. doi: 10.1016/j.cmet.2016.05.004

Mera, P., Laue, K., Wei, J., Berger, J. M., and Karsenty, G. (2016b). Osteocalcin is necessary and sufficient to maintain muscle mass in older mice. *Mol. Metab.* 5 (10), 1042–1047. doi: 10.1016/j.molmet.2016.07.002

Nag, O. K., Muroski, M. E., Hastman, D. A., Almeida, B., Medintz, I. L., Huston, A. L., et al. (2020). Nanoparticle-Mediated Visualization and Control of Cellular Membrane Potential: Strategies, Progress, and Remaining Issues. *ACS Nano.* 14 (3), 2659–2677. doi: 10.1021/acsnano.9b10163

Nance, M. E., Hakim, C. H., Yang, N. N., and Duan, D. (2018). Nanotherapy for Duchenne muscular dystrophy. *Wiley Interdiscip. Rev. Nanomed. Nanobiotechnol.* 10 (2). doi: 10.1002/wnan.1472

Naso, M. F., Tomkowicz, B., Perry, W. R., and Strohl, W. R. (2017). Adeno-Associated Virus (AAV) as a Vector for Gene Therapy. *BioDrugs* 31 (4), 317–334. doi: 10.1007/s40259-017-0234-5

Papanicolaou, D. A., Ather, S. N., Zhu, H., Zhou, Y., Lutkiewicz, J., Scott, B. B., et al. (2013). A phase IIA randomized, placebo-controlled clinical trial to study the efficacy and safety of the selective androgen receptor modulator (SARM), MK-0773 in female participants with sarcopenia. *J. Nutr. Health Aging* 17 (6), 533–543. doi: 10.1007/s12603-013-0335-x

Patel, K., Simbi, B., Ritvos, O., Vaiyapuri, S., and Dhoot, G. K. (2019). Dysregulated cell signalling and reduced satellite cell potential in ageing muscle. *Exp. Cell Res.* 385 (2), 111685. doi: 10.1016/j.yexcr.2019.111685

Pedersen, B. K. (2013). Muscle as a secretory organ. *Compr. Physiol.* 3 (3), 1337–1362. doi: 10.1002/cphy.c120033

Polkey, M. I., Praestgaard, J., Berwick, A., Franssen, F. M. E., Singh, D., Steiner, M. C., et al. (2019). Activin Type II Receptor Blockade for Treatment of Muscle Depletion in Chronic Obstructive Pulmonary Disease. A Randomized Trial. *Am. J. Respir. Crit. Care Med.* 199 (3), 313–320. doi: 10.1164/rccm.201802-0286OC

Poussard, S., Decossas, M., Le Bihan, O., Mornet, S., Naudin, G., and Lambert, O. (2015). Internalization and fate of silica nanoparticles in C2C12 skeletal muscle cells: evidence of a beneficial effect on myoblast fusion. *Int. J. Nanomed.* 10, 1479–1492. doi: 10.2147/IJN.S74158

Raimondo, T. M., and Mooney, D. J. (2018). Functional muscle recovery with nanoparticle-directed M2 macrophage polarization in mice. *Proc. Natl. Acad. Sci.* 115 (42), 10648–10653. doi: 10.1073/pnas.1806908115

Ran, N., Gao, X., Dong, X., Li, J., Lin, C., Geng, M., et al. (2020). Effects of exosome-mediated delivery of myostatin propeptide on functional recovery of mdx mice. *Biomaterials* 236, 119826. doi: 10.1016/j.biomaterials.2020.119826

Rezus, E., Burlui, A., Cardoneanu, A., Rezus, C., Codreanu, C., Parvu, M., et al. (2020). Inactivity and Skeletal Muscle Metabolism: A Vicious Cycle in Old Age. *Int. J. Mol. Sci.* 21 (2), 592. doi: 10.3390/ijms21020592

Rong, S., Wang, L., Peng, Z., Liao, Y., Li, D., Yang, X., et al. (2020). The mechanisms and treatments for sarcopenia: could exosomes be a perspective research strategy in the future? *J. Cachexia Sarcopenia Muscle* 11 (2), 348–365. doi: 10.1002/jcsm.12536

Rooks, D., and Roubenoff, R. (2019). Development of Pharmacotherapies for the Treatment of Sarcopenia. *J. Frailty Aging* 8 (3), 120–130. doi: 10.14283/jfa.2019.11

Ruparelia, A. A., Ratnayake, D., and Currie, P. D. (2019). Stem cells in skeletal muscle growth and regeneration in amniotes and teleosts: Emerging themes. *WIREs Dev. Biol.* 9 (2), e365. doi: 10.1002/wdev.365

Saini, J., McPhee, J. S., Al-Dabbagh, S., Stewart, C. E., and Al-Shanti, N. (2016). Regenerative function of immune system: Modulation of muscle stem cells. *Ageing Res. Rev.* 27, 67–76. doi: 10.1016/j.arr.2016.03.006

Samoylova, T. I., and Smith, B. F. (1999). Elucidation of muscle-binding peptides by phage display screening. *Muscle Nerve* 22 (4), 460–466. doi: 10.1002/(SICI)1097-4598(199904)22:4<460::AID-MUS6>3.0.CO;2-L

Schiaffino, S., Dyar, K. A., and Calabria, E. (2018). Skeletal muscle mass is controlled by the MRF4-MEF2 axis. *Curr. Opin. Clin. Nutr. Metab. Care* 21 (3), 164–167. doi: 10.1097/MCO.0000000000000456

Schmidt, M., Schüler, S. C., Hüttner, S. S., von Eyss, B., and von Maltzahn, J. (2019). Adult stem cells at work: regenerating skeletal muscle. *Cell. Mol. Life Sci.* 76 (13), 2559–2570. doi: 10.1007/s00018-019-03093-6

Schwörer, S., Becker, F., Feller, C., Baig, A. H., Köber, U., Henze, H., et al. (2016). Epigenetic stress responses induce muscle stem-cell ageing by Hoxa9 developmental signals. *Nature* 540 (7633), 428–432. doi: 10.1038/nature20603

Seow, Y., Yin, H., and Wood, M. J. (2010). Identification of a novel muscle targeting peptide in mdx mice. *Peptides* 31 (10), 1873–1877. doi: 10.1016/j.peptides.2010.06.036

Skotland, T., Sagini, K., Sandvig, K., and Llorente, A. (2020). An emerging focus on lipids in extracellular vesicles. *Adv. Drug Delivery Rev.* S0169-409X(20)30014-4. doi: 10.1016/j.addr.2020.03.002

Song, H., Li, X., Zhao, Z., Qian, J., Wang, Y., Cui, J., et al. (2019). Reversal of osteoporotic activity by endothelial cell-secreted bone targeting and biocompatible exosomes. *Nano Lett.* 19 (5), 3040–3048. doi: 10.1021/acs.nanolett.9b00287

Souza, N., Mesquita-Ferrari, R. A., Rodrigues, M., Da, S. D., Ribeiro, B. G., Alves, A. N., et al. (2018). Photobiomodulation and different macrophages phenotypes during muscle tissue repair. *J. Cell Mol. Med.* 22 (10), 4922–4934. doi: 10.1111/jcmm.13757

Sutcu, H. H., and Ricchetti, M. (2018). Loss of heterogeneity, quiescence, and differentiation in muscle stem cells. *Stem Cell Invest.* 5, 9. doi: 10.21037/sci.2018.03.02

Szentesi, P., Csernoch, L., Dux, L., and Keller-Pintér, A. (2019). Changes in Redox Signaling in the Skeletal Muscle with Aging. *Oxid. Med. Cell. Longevity* 2019, 1–12. doi: 10.1155/2019/4617801

Vader, P., Mol, E. A., Pasterkamp, G., and Schiffelers, R. M. (2016). Extracellular vesicles for drug delivery. *Adv. Drug Deliv. Rev.* 106, 148–156. doi: 10.1016/j.addr.2016.02.006

Verhaart, I., and Aartsma-Rus, A. (2019). Therapeutic developments for Duchenne muscular dystrophy. *Nat. Rev. Neurol.* 15 (7), 373–386. doi: 10.1038/s41582-019-0203-3

Waning, D. L., Mohammad, K. S., Reiken, S., Xie, W., Andersson, D. C., John, S., et al. (2015). Excess TGF-beta mediates muscle weakness associated with bone metastases in mice. *Nat. Med.* 21 (11), 1262–1271. doi: 10.1038/nm.3961

Weyh, C., Kruger, K., and Strasser, B. (2020). Physical Activity and Diet Shape the Immune System during Aging. *Nutrients* 12 (3), 622. doi: 10.3390/nu12030622

White, T. A., and LeBrasseur, N. K. (2014). Myostatin and sarcopenia: opportunities and challenges - a mini-review. *Gerontology* 60 (4), 289–293. doi: 10.1159/000356740

Whitham, M., Parker, B. L., Friedrichsen, M., Hingst, J. R., Hjorth, M., Hughes, W. E., et al. (2018). Extracellular Vesicles Provide a Means for Tissue Crosstalk during Exercise. *Cell Metab.* 27 (1), 237–251. doi: 10.1016/j.cmet.2017.12.001

Wilkinson, D. J., Piasecki, M., and Atherton, P. J. (2018). The age-related loss of skeletal muscle mass and function: Measurement and physiology of muscle fibre atrophy and muscle fibre loss in humans. *Ageing Res. Rev.* 47, 123–132. doi: 10.1016/j.arr.2018.07.005

Wilson, D., Jackson, T., Sapey, E., and Lord, J. M. (2017). Frailty and sarcopenia: The potential role of an aged immune system. *Ageing Res. Rev.* 36, 1–10. doi: 10.1016/j.arr.2017.01.006

Woodhouse, L., Gandhi, R., Warden, S. J., Poiraudeau, S., Myers, S. L., Benson, C. T., et al. (2016). A Phase 2 Randomized Study Investigating the Efficacy and Safety of Myostatin Antibody LY2495655 versus Placebo in Patients Undergoing Elective Total Hip Arthroplasty. *J. Frailty Aging* 5 (1), 62–70. doi: 10.14283/jfa.2016.81

Yin, H., Price, F., and Rudnicki, M. A. (2013). Satellite Cells and the Muscle Stem Cell Niche. *Physiol. Rev.* 93 (1), 23–67. doi: 10.1152/physrev.00043.2011

Yin, P., Li, Y., Lv, H., Deng, Y., Meng, Y., Zhang, L., et al. (2018). Exchange of genetic material: a new paradigm in bone cell communications. *Cell. Mol. Life Sci.* 75 (11), 1989–1998. doi: 10.1007/s00018-018-2782-3

Zammit, P. S. (2017). Function of the myogenic regulatory factors Myf5, MyoD, Myogenin and MRF4 in skeletal muscle, satellite cells and regenerative myogenesis. *Semin. Cell Dev. Biol.* 72, 19–32. doi: 10.1016/j.semcdb.2017.11.011

Zanotti, S., Gibertini, S., Blasevich, F., Bragato, C., Ruggieri, A., Saredi, S., et al. (2018). Exosomes and exosomal miRNAs from muscle-derived fibroblasts promote skeletal muscle fibrosis. *Matrix Biol.* 74, 77–100. doi: 10.1016/j.matbio.2018.07.003

Zhou, T., Prather, E. R., Garrison, D. E., and Zuo, L. (2018). Interplay between ROS and Antioxidants during Ischemia-Reperfusion Injuries in Cardiac and Skeletal Muscle. *Int. J. Mol. Sci.* 19 (2), 417. doi: 10.3390/ijms19020417

Zhu, P., Zhang, C., Gao, Y., Wu, F., Zhou, Y., and Wu, W. (2019). The transcription factor Slug represses p16Ink4a and regulates murine muscle stem cell aging. *Nat. Commun.* 10 (1), 2568. doi: 10.1038/s41467-019-10479-4

Conflict of Interest: The authors declare that the research was conducted in the absence of any commercial or financial relationships that could be construed as a potential conflict of interest.

frontiers in Pharmacology

ORIGINAL RESEARCH
published: 05 August 2020
doi: 10.3389/fphar.2020.00921

Delivery of microRNA-33 Antagomirs by Mesoporous Silica Nanoparticles to Ameliorate Lipid Metabolic Disorders

Yaoye Tao[1,2], *Shengjun Xu*[1,2], *Jianguo Wang*[1,2], *Li Xu*[1,2], *Chenzhi Zhang*[1,2], *Kangchen Chen*[1,2], *Zhengxing Lian*[1,2], *Junbin Zhou*[1,2], *Haiyang Xie*[1,2], *Shusen Zheng*[1,2] *and Xiao Xu*[1,2*]

[1] *Department of Hepatobiliary and Pancreatic Surgery, First Affiliated Hospital, Zhejiang University School of Medicine, Hangzhou, China,* [2] *NHC Key Lab of Combined Multi-Organ Transplantation, Hangzhou, China*

Lipid metabolic disorders have become a major global public health concern. Fatty liver and dyslipidemia are major manifestations of these disorders. Recently, MicroRNA-33 (miR-33), a post-transcriptional regulator of genes involved in cholesterol efflux and fatty acid oxidation, has been considered as a good therapeutic target for these disorders. However, the traditional methods of gene therapy impede their further clinical transformation into a mature treatment system. To counter this problem, in this study we used mesoporous silica nanoparticles (MSNs) as nanocarriers to deliver miR-33 antagomirs developing nanocomposites miR-MSNs. We observed that the hepatocellular uptake of miR-33 antagomirs increased by ~5 times when they were delivered using miR-MSNs. The regulation effects of miR-MSNs on miR-33 and several genes involved in lipid metabolism were confirmed in L02 cells. In a high-fat diet fed mice, miR-33 intervention *via* miR-MSNs lowered the serum triglyceride levels remarkably by 18.9% and reduced hepatic steatosis. Thus, our results provide a proof-of-concept for a potential strategy to ameliorate lipid metabolic disorders.

Keywords: mesoporous silica nanoparticles, lipid metabolic disorder, non-alcoholic fatty liver disease, dyslipidemia, miR-33

OPEN ACCESS

Edited by:
Wei Tao,
Harvard Medical School, United States

Reviewed by:
Jiang Ouyang,
Central South University, China
Duo Mao,
National University of Singapore, Singapore

****Correspondence:***
Xiao Xu
zjxu@zju.edu.cn

Specialty section:
This article was submitted to Translational Pharmacology, a section of the journal Frontiers in Pharmacology

Received: *11 December 2019*
Accepted: *05 June 2020*
Published: *05 August 2020*

Citation:
Tao Y, Xu S, Wang J, Xu L, Zhang C, Chen K, Lian Z, Zhou J, Xie H, Zheng S and Xu X (2020) Delivery of microRNA-33 Antagomirs by Mesoporous Silica Nanoparticles to Ameliorate Lipid Metabolic Disorders. Front. Pharmacol. 11:921. doi: 10.3389/fphar.2020.00921

INTRODUCTION

Lipid metabolic disorders are key contributors to many illnesses, such as cardiovascular diseases (CVDs) and type 2 diabetes mellitus; they are now considered a serious threat to human health (Zhou et al., 2019). Nonalcoholic fatty liver disease (NAFLD), a manifestation of lipid metabolic disorders, is the most common cause of chronic liver disease worldwide, affecting one-third of the total adult population in the world (Younossi et al., 2016; Younossi et al., 2018). One of the primary pathological signs of NAFLD is an excess of triglyceride accumulation in hepatocytes. This condition is called steatosis and is related to dyslipidemia (Woods et al., 2015). Although simple steatosis does not have serious implications in the beginning, NAFLD, particularly its histological phenotype non-alcoholic steatohepatitis, can potentially result in cirrhosis, end-stage liver disease,

and hepatocellular carcinoma (Buzzetti et al., 2016). There are currently no approved pharmacological therapies for NAFLD and thus it has become the second leading cause for liver transplantation (LT) in the United States (Wong et al., 2015; Rotman and Sanyal, 2017). However, 30%–60% of patients who undergo LT due to NAFLD relapse in less than five years. In addition, 20%–30% of patients undergoing LT for other liver diseases also suffer from NAFLD and 40%–66% of LT patients suffer from dyslipidemia (Zheng and Wang, 2015; Pais et al., 2016). Due to the high prevalence of lipid metabolic disorders after transplantation, CVDs have become the leading cause of non-hepatic mortality in LT recipients, accounting for 11% of deaths annually. It has been found that the incidence of CVD events after LT increases over time (Lee et al., 2017; Fatourou and Tsochatzis, 2019). Therefore, new treatment modalities for lipid metabolic disorders, especially NAFLD, are urgently needed.

MicroRNA-33 (miR-33) is a post-transcriptional regulator of genes involved in cholesterol efflux and fatty acid oxidation; it is encoded within the introns of sterol regulatory element–binding proteins 1 and 2 (SREBF-1 and SREBF-2), which are key transcriptional modulators of lipid metabolism and are abundant in the liver. MiR-33 can suppress the expression of cholesterol efflux proteins, ATP-binding cassette A1 (ABCA1), and ATP-binding cassette subfamily G member 1 (ABCG1), and genes involved in fatty acid oxidation, carnitine palmitoyltransferase 1A (CPT1A), and carnitine O-octanoyltransferase (CROT) (Marquart et al., 2010; Najafi-Shoushtari et al., 2010; Rayner et al., 2010; Dávalos et al., 2011; Karunakaran et al., 2015). Moreover, miR-33 can promote the expression of SREBF-1, which is involved in the synthesis of fatty acids. Therefore, gene therapy based on miR-33, which delivers genetic material to genes for targeted therapy, has attracted the attention of researchers (Kulkarni et al., 2018). Studies on mice and nonhuman primates suggested that an miR-33 blockade results in changes in the expression of hepatic genes involved in lipid metabolism; further, it ameliorates dyslipidemia that is induced by a high-fat diet (HFD) (Rayner et al., 2011a; Rayner et al., 2011b). However, the traditional methods used in these studies yielded a limited delivery efficacy *in vivo* and inhibited further applications in clinic (He et al., 2018). One of the problems associated with the low efficiency of the traditional methods is that they require high doses of agents, with mice needing 10 mg/kg of anti-miR-33 oligonucleotides per week (Rayner et al., 2011b).

In recent times, safe, smart, and highly efficient nanomaterials have been gaining importance for their roles in treating different diseases, including NAFLD and dyslipidemia (Wang et al., 2016; Cao et al., 2018; Wan et al., 2018; Lee et al., 2019). Moreover, nanocarriers are promising carriers for gene delivery (Canup et al., 2017; Wang et al., 2018; Zai et al., 2019). Among the various types of nanoparticles (NPs) being used, mesoporous silica nanoparticles (MSNs) are promising vectors, owing to their unique characteristics of a tailored structure, large surface area, high agent-loading volume, abundant chemistry functionality, and acceptable biocompatibility (Tang et al., 2012; Zhou et al., 2018; Tao et al., 2020). Owing to these distinctive features, MSNs can serve as multifunctional and efficient platforms for gene delivery (Keasberry et al., 2017; Lin et al., 2018).

In this study, we attempted to deliver miR-33 antagomirs using MSNs to treat NAFLD and dyslipidemia. Aminated MSNs, such as MSNs-NH_2, possess a net positive charge and form a stable complex with electronegative nucleic acid miR-33 antagomirs, named miR-MSNs. Our results suggest that the designed miR-MSNs can effectively facilitate hepatocellular uptake of miR-33 antagomirs. In vivo studies showed that intervention with miR-MSNs for a period of 2 weeks, which extended the retention time of miR-33 antagomirs to maximize the effect of therapy, can significantly decrease lipid deposition in liver, thus ameliorating metabolic disorders in HFD-fed mice. Therefore, this study provides a novel strategy for efficiently combating lipid metabolic disorder using MSNs-based nanoplatforms.

MATERIALS AND METHODS

Materials

MiR-33 antagomirs and Cy5-labeled miR-33 antagomirs (Cy5-antagomirs) were purchased from GenePharma (Shanghai, China). The sequence of miR-33 antagomirs for mice is UGCAAUGCAACUACAAUGCAC; this sequence is the same for mice and humans. MSNs-NH_2 were purchased from So-Fe Biomedical (Shanghai, China). Dulbecco's Modified Eagles's Medium (DMEM) and Trypsin-EDTA (0.25%) were purchased from Thermo Fisher Scientific (Waltham, USA). Fetal bovine serum (FBS) was purchased from Wisent (Montreal, Canada). Lipofectamine 3000 (lipo3000) was purchased from Invitrogen (Grand Island, NY). Oleic acid (OA) was purchased from Sigma-Aldrich (St Louis, MO, USA). Lovastatin was obtained from Glpbio (Montclair, USA). All other solvents were of an analytical grade. Fresh double-distilled water was used in all the experiments.

Preparation of miR-MSNs

To prepare miR-MSNs, MSNs-NH_2 and miR-33 antagomirs were mixed at a ratio of 100:1 (w/w) in RNase-free H_2O. The samples were incubated at room temperature for 60 min to ensure NPs' formation. NPs morphology was observed using a transmission electron microscope (TEM, Spirit 120kV, China). In addition, particle-size distribution and zeta (ζ) potential (ZP) were measured on a Malvern Nano-ZS90 instrument (Malvern, U.K.). Elemental distribution analysis by energy dispersive spectrum (EDS) was obtained on a field emission scanning electron microscope (Nova Nano 450, FEI Company, Czech).

Cell Culture, *In Vitro* Transfection Studies and Co-Culture With Fatty Acids

Human hepatocyte L02 cells, hepatic fibroblasts LX02 cells, and mouse mononuclear macrophage leukemia RAW264.7 cells were purchased from the Cell Bank of China Science (Shanghai, China). These cells were cultured in DMEM supplemented with 10% FBS. For the transfection of miR-33 antagomirs, L02 cells were plated at a density of 2×10^5 cells per well in six-well

plates. Cells incubated overnight were transfected with 100 nM of miR-33 antagomirs using lipo3000 or miR-MSNs. Cells were then treated with OA (50 μM) for 72h and harvested for further detection.

Agarose Gel Electrophoresis

Agarose gel electrophoresis was conducted to evaluate the loading of miR-33 antagomirs in MSNs. The antagomirs or miR-MSNs (antagomirs dose was 100 pmol) were separated on 2% agarose gels containing Super Gelred (US Everbright, Jiangsu, China) and the corresponding images were obtained using a UV transilluminator system (Life Science Technologies, USA).

Cytotoxicity Study

Cells were seeded on 96-well plates at a density of 5×10^3 cells/well and incubated overnight. Later, they were treated with MSNs-NH_2 and miR-MSNs (125, 62.5, 31.25, 15.625, 7.8125, and 3.90625 μg/mL) for 72 h and the number of viable cells were measured using CCK-8 kits (MedChemExpress, USA) according to the protocol included in the user manual. Cell viability in each group was expressed as a percentage of the viability of untreated control cells.

Hemolysis Assay

700 μL of MSNs-NH_2 and miR-MSNs (200, 100, 50, 25, 12.5, and 6.25 μg/ml) solution was added to 700 μL of 2% w/v red blood cell (RBC) suspension and incubated at 37 °C for 1.5 h. Later, the mixtures were centrifuged and the supernatant was transferred to a 96-well plate (150 μL per well); hemoglobin release in these wells was measured by spectrophotometry as absorbance (A) at 540 nm. Deionized water and phosphate-buffered saline (PBS) were used as positive and negative controls, respectively. The extent of hemolysis was calculated as $(A_{sample} - A_{PBS})/(A_{water} - A_{PBS}) \times 100\%$.

In Vitro Cellular Uptake

The cellular uptake of Cy5-antagomirs of different formulations was examined using confocal laser scanning microscopy (CLSM) and flow cytometry analysis. Five groups were analyzed in this study: control, antagomirs (100 nM Cy5-antagomirs), lipo3000 +antagomirs (100 nM Cy5-antagomirs), miR-MSNs (low) (50 nM Cy5-antagomirs), and miR-MSNs (high) (100 nM Cy5-antagomirs) groups. L02 cells were initially seeded on 3a 5 mm glass-bottom cell-culture dish (Thermo Scientific Nunc, USA) at a density of 4×10^5 cells $dish^{-1}$ and incubated for 24 h. Later, Cy5-antagomirs containing different formulations (stated above) were added to the cells, which were then incubated for three more hours. After incubation, the cells were washed thrice with PBS and immediately visualized under CLSM (Olympus Fluoview FV-3000, Japan) with red channel (Cy5-antagomirs) excitation at 640 nm. ImageJ was used to quantify fluorescence intensity. In flow-cytometry experiments, L02 cells were grown on 6-well plates (3×10^5 cells per well) and exposed to Cy5-antagomirs with different formulations for 3h. The free Cy5-antagomirs containing formulations were removed by PBS washing. Subsequently, cells were harvested and centrifuged at 300 g for 5 min. Finally, cells were suspended in PBS and immediately analyzed by ACEA NovoCyteTM (ACEA Biosciences, USA).

RT-PCR Analysis

Total RNA of L02 cells was extracted using NucleoZOL reagent (Macherey-Nagel, Germany) and then reverse transcribed into cDNA using a reverse transcription reagent Kit (Guangzhou Geneseed Biotech, China). Real-time PCR analysis was conducted with ChamQ™ SYBR qPCR Master Mix (Vazyme Biotech, China).

Western Blot Analysis

Cell lysates were prepared using RIPA lysis buffer (Hangzhou Fude Biological Technology, China) containing 1 × protease cocktail inhibitor (Sigma-Aldrich, USA). Samples of the proteins were run on 8%–12% SDS-PAGE gels for immunoblotting. The primary antibodies used were SREBF1 (1:1000, Proteintech, USA), ABCA1 (1:1000, Abcam, UK), and β-actin (1:5000, Genscript, China). Matching horseradish peroxidase (HRP) conjugated secondary antibodies (1:5000, Genscript, China) were used to evaluate protein expression and the results were analyzed on a ChemiDoc Touch Imaging System (Bio-Rad Laboratories, USA).

Cell Staining With Oil Red O and Lipid Measurement

For Oil Red O staining, L02 cells were washed twice with PBS, then fixed with 10% formalin for 30 min, and stained with Oil Red for 1 h before microscopic observation. For lipid measurement, the cells were ultrasonically broken using an ultrasonic cell disruptor (Sonics, USA). The levels of total cholesterol (TC) and triglyceride (TG) in the cells were measured using assay kits (Nanjing Jiancheng Bioengineering, China) according to the manufacturer's protocol.

Animals and Treatment

All animal studies were executed with the approval of the Institutional Animal Care and Use Committee of Zhejiang University. Male C57BL/6J (4 weeks) mice were purchased from the Shanghai Experimental Animal Center, Chinese Academy of Sciences. The mice were housed in a (20 ± 1) °C temperature-controlled room with a 12 h light/dark cycle and free access to food and water. To induce NAFLD and dyslipidemia, the mice were fed with HFD (60% kcal fats, 20% kcal carbohydrates, and 20% kcal proteins, n = 30). After 2 weeks, six mice were sacrificed, and their livers were harvested. The rest of the HFD mice were randomly divided into four groups (n=6), a model control group (MC group, untreated), a lovastatin group (5 mg/kg lovastatin, twice a week), a low dose miR-MSN group (25 mg/kg miR-MSNs, twice a week), and a high dose miR-MSNs group (50 mg/kg miR-MSNs, twice a week), and treated for 2 more weeks. During the study, the animals were weighed twice a week and their plasma was obtained on Day 0, 14, 21, and 28 from their eye-socket veins. At the end of the experimental period, liver, heart, spleen, lung, and kidney tissues were harvested from these mice. The fresh tissues were divided into two portions, half of which were

immediately frozen in liquid nitrogen and stored at −80°C, and the remaining of which were fixed with 4% paraformaldehyde for histological analysis.

In Vivo Biodistribution Studies

For *in vivo* imaging, the mice were randomly divided into two groups (n = 12 in each group) and injected with a single dose of Cy5-antagomirs or miR-MSNs (0.25 mg/kg equivalent Cy5-antagomirs) *via* the tail vein. At each predetermined time point, three mice in each group were sacrificed and major organs (heart, liver, spleen, lung, and kidney) were collected for *ex vivo* imaging. Fluorescent Cy5-antagomirs was used for measuring by an *in vivo* imaging system (IVIS) (Clairvivo OPT, SHIMADZU Corporation, Japan).

Histological Staining

Mice-tissue samples embedded in paraffin wax were sectioned into 4 μm thick samples in the maximum cut area and stained with hematoxylin and eosin (HE) for microscopic observation. Hepatic fat accumulation was evaluated by Oil Red O staining. Liver-tissue samples stored at −80°C were sectioned and stained with 0.1% Oil Red to detect lipid droplets.

Serum Biochemical Analysis

Plasma levels corresponding to TC, TG, alanine aminotransferase (ALT), aspartate aminotransferase (AST), creatinine (CRE), and blood urea nitrogen (BUN) were measured using commercially available kits (Changchun Huili Biotech, China) on a Chemray 240 automatic biochemical analyzer (Rayto Life and Analytical Sciences, China), according to the manufacturer's protocol.

Statistical Analysis

All the observed analytical results are reported as mean ± standard deviation (SD). Statistical analysis was conducted on SPSS 23.0 (two-sided student's t-test or one-way ANOVA *post hoc*). *$p < 0.05$, **$p < 0.01$, and ***$p < 0.001$ were considered to be statistically significant.

RESULTS AND DISCUSSION

Preparation and Characterization of miR-MSNs

Our strategy for the design and synthesis of miR-MSNs is illustrated in **Scheme 1**. Briefly, miR-33 antagomirs were incorporated into MSNs-NH_2 by constant stirring. The particle sizes and size distributions of MSNs-NH_2 and miR-MSNs are detailed in **Table 1**; as shown in the table, the fabricated NPs exhibited hydrodynamic diameters of 110–130 nm, which means that they can theoretically escape the reticulo-endothelial system in blood circulation (Tang et al., 2012). MSNs-NH_2 exhibited an average size of (108.8 ± 0.6) nm, while miR-MSNs were (131.1 ± 5.4) nm in size (**Figures 1A, B**). Compared to MSNs-NH_2, miR-MSNs were ∼20 nm larger in size and this difference may be regarded as evidence of the successful loading of miR-33 antagomirs in the latter. The polydispersity index (PDI) of these

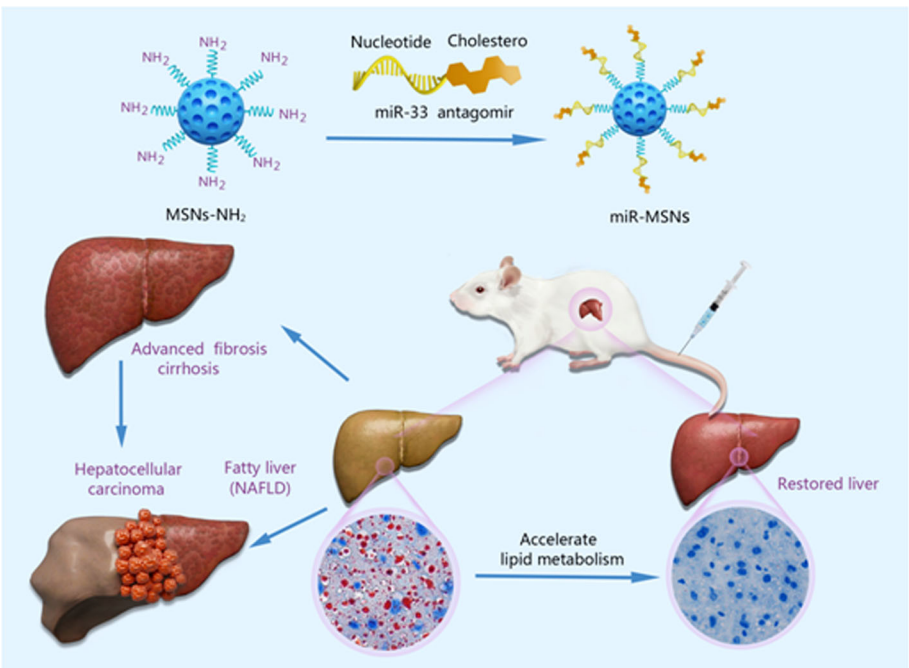

SCHEME 1 | Schematic illustration of the miR-MSNs targeting the miR-33 to treat NAFLD.

NPs was in the range of 0.154–0.227, which is acceptable. The ZP of MSNs-NH_2 was (24.8 ± 1.9) mV, which is suitable for loading miR-33 antagomirs (Keasberry et al., 2017). The low ZP of miR-MSNs is due to the incorporation of the antagomirs, which is consistent with previous reports (Xue et al., 2017; Lin et al., 2018). The morphologies of the MSNs-NH_2 and miR-MSNs were evaluated by TEM (**Figures 1A, B**). All the NPs exhibited a uniform mesoporous structure and monodispersed spherical shape. The capability of MSNs-NH_2 for miR-33 antagomirs loading could be confirmed by agarose gel electrophoresis using untreated miR-33 antagomirs as negative control (NC). There remained a considerable amount of unbonded miR-33 antagomirs at a MSNs-NH_2: miR-33 antagomirs ratio of 25:1 (w/w). When this ratio was greater than 50:1 (w/w), the NPs exhibited an adequate loading capacity (**Figure 1C**). Based on these results, we chose a 100:1 weight ratio for the follow-up experiment. EDS results showed that the distributions of Si and O are similar between MSNs-NH_2 and miR-MSNs, while miR-MSNs contain more P elements than MSNs-NH_2 (**Supplementary Figure 1**). The increase of P elements probably comes from miR-33 antagomirs incorporated in MSNs-NH_2, reflecting successful formation of miR-MSNs. The cytotoxicity of MSNs-NH_2 and miR-MSNs with respect to L02 cells was evaluated. The viability of L02 cells was greater than 82% after incubation with 125 μg/mL of MSNs-NH_2 and miR-MSNs for 72 h (**Figure 1D**). Similarly, low cytotoxicity of MSNs-NH_2 and miR-MSNs was also found in LX02 and RAW274.6 cells (**Supplementary Figure 2**). **Figure 1E** shows that hemolytic activity of MSNs-NH_2 and miR-MSNs with respect to RBCs was negligible. The low cytotoxicity and hemolytic activity of these NPs can be mainly ascribed to their well-ordered mesoporous structure and suitable particle size (Lin and Haynes, 2010). These results clearly indicate that MSNs-NH_2

TABLE 1 | Characterization of the prepared NPs.

NP	Size (nm)	PDI	ZP(mV)
MSNs-NH_2	108.8 ± 0.6	0.154 ± 0.013	24.8 ± 1.9
miR-MSNs	131.1 ± 5.4	0.227 ± 0.009	17.4 ± 0.7

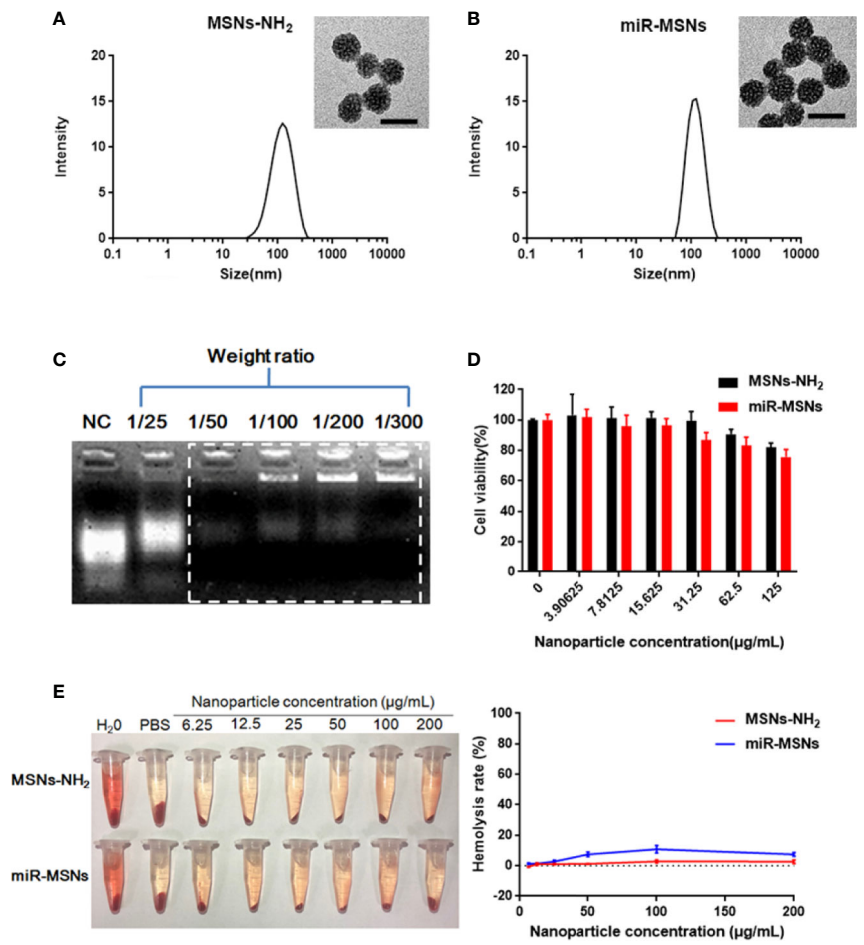

FIGURE 1 | (A) Hydrodynamic diameter of MSNs-NH_2 and the corresponding TEM image. Scale bar = 50 nm. **(B)** Hydrodynamic diameter of miR-MSNs and the corresponding TEM image. Scale bar = 50 nm. **(C)** Agarose gel electrophoresis of miR-33 antagomirs bonded with MSNs-NH_2 at different weight ratios. **(D)** Cytotoxicity of MSNs-NH_2 and miR-MSNs *via* CCK-8 assays. n=3. **(E)** Hemolysis assay and images of RBCs incubated with MSNs-NH_2 and miR-MSNs. n=3.

and miR-MSNs are biocompatible and show no significant toxicity toward tissues and cells.

In Vitro Cellular Uptake

The extent of miR-33 antagomirs internalization in L02 cells was investigated by CLSM. L02 cells in the miR-MSNs (low) group were treated with 50 nM of miR-33 antagomirs while L02 cells in the other treatment groups were treated with equivalent miR-33 antagomirs (100nM). It can be observed that the fluorescence intensity of miR-33 antagomirs in L02 cells incubated with miR-MSNs for 3 h was higher than that of the cells in other groups (**Figure 2A**). From the statistical results, it can be inferred that miR-33 antagomirs in miR-MSNs exhibited approximately a 5-fold higher uptake in L02 cells when compared to lipo3000 in equivalent miR-33 antagomirs, thus confirming our hypothesis that NPs can enhance the endocytosis of miR-33 antagomirs to a much higher extent than lipo3000 (**Figure 2B**). The enhanced uptake of miR-33 antagomirs from miR-MSNs by L02 cells was further demonstrated by flow cytometry (**Figure 2C**); these results also correspond with the results of CLSM analysis. The enhanced intracellular uptake of miR-33 antagomirs by miR-MSNs may be attributed to the distinct cellular internalization of MSNs; they can be taken up by cells *via* various routes, such as caveolae-mediated andclathrin-mediated pathways (Zhou et al., 2018).

In Vitro Regulation Effects of Lipid Metabolism

To further define the effects of miR-MSNs on lipid accumulation, we applied the well-established *in vitro* model of lipid accumulation (OA administration model). L02 cells were treated with lovastatin, miR-33 antagomirs, miR-33 antagomirs +lipo3000, or miR-MSNs and then incubated with OA for 72 h. Lovastatin, a common clinical drug for dyslipidemia, was considered as the positive control (Downs et al., 1998). The Oil Red results showed that miR-MSNs significantly inhibited lipid accumulation in L02 cells when compared to the untreated control group and other treated groups (**Figure 3A**). Furthermore, we examined TG and TC levels in L02 cells. TG levels in the miR-MSNs group was significantly lower than that in the control group and other treatment groups. Meanwhile, TC levels in the miR-MSNs group was much lower than that in the control group, but there were no significant differences between

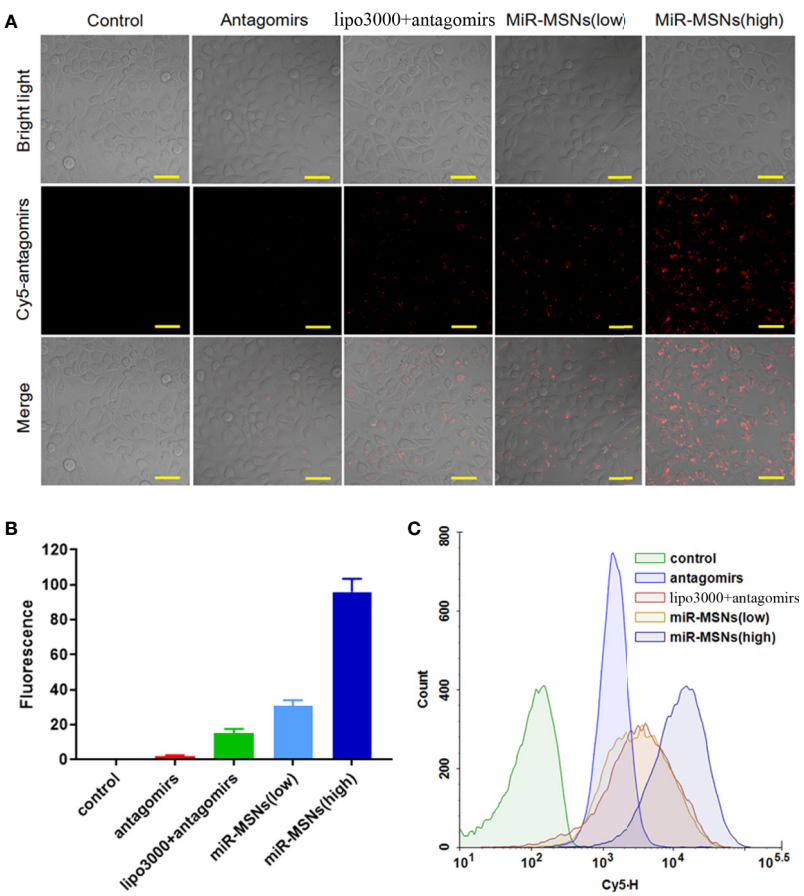

FIGURE 2 | Intracellular uptake analysis. **(A)** CLSM images of cells after incubation with different Cy5-antagomirs formulations. Scale bar = 50 μm. n=3. **(B)** Corresponding quantitative results of CLSM images. **(C)** Flow cytometric histogram profiles of L02 cells after 3 h of incubation.

other treatment groups and the control group, which indicated that miR-MSNs exhibited the best lipid-lowering effect among all the tested groups (**Figure 3B**).

In Vitro Transfection Efficiency and Altered Gene Expression

To determine the transfection efficiency of miR-33 antagomirs in miR-MSNs using an *in vitro* lipid accumulation model, L02 cells were treated with miR-33 antagomirs, miR-33 antagomirs +lipo3000, or miR-MSNs. We found a greater reduction of miR-33 in miR-MSNs–treated cells when compared to other groups (**Figure 4A**). We also observed changes in the mRNA levels of miR-33 downstream genes involved in lipid metabolism (ABCA1, CROT, SREBF1, and CPT1A). As shown in **Figure 4C**, the mRNA expression of ABCA1 and CROT was higher than that of other groups, while that of SREBF1 was lower than that of the control group. These results are consistent with previously reported results (Rayner et al., 2010; Rayner et al., 2011a; Rayner et al., 2011b). Meanwhile, the mRNA expression of CPT1A did not change after incubation, which is not consistent with *in vivo* observations of the above research. However, other studies reported that there are no marked changes in the expression of CPT1A in HepG2 cells and Huh7 cells after antagomir 33 transfection (Gerin et al., 2010; Goedeke et al., 2013). Hence, it might be inferred that the effect of anti-miR33 on CPT1A is different between cells and animals; this aspect requires further investigation. In addition, as miRNAs can affect both mRNA stability and translation, we measured two main functional protein levels (ABCA1 and SREBF1) in L02 cells. As shown in **Figure 4B**, ABCA1 was present at much higher levels in cells treated with miR-MSNs when compared to cells in other groups; meanwhile, the opposite trend was observed for SREBF1. These changes in protein expression influence lipid metabolism in a manner consistent with previous results.

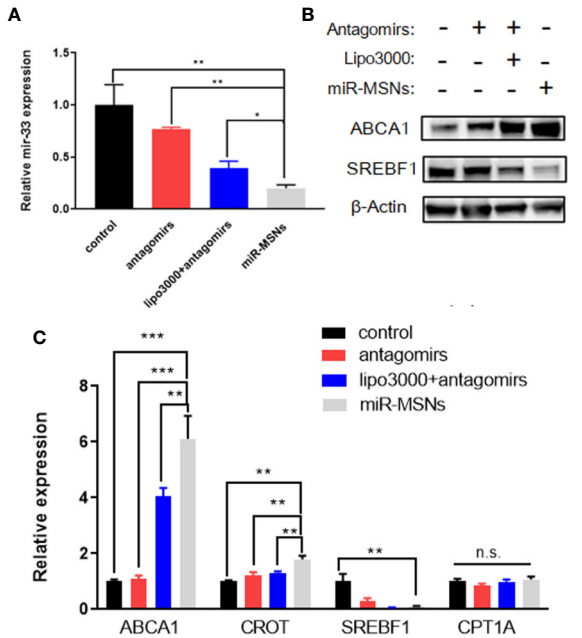

FIGURE 4 | Silencing effect of miR-33 by miR-MSNs and changes in the expression of downstream genes. **(A)** Expression of miR-33 quantified by RT-PCR. n=3. **(B)** Western blot analysis of ABCA1 and SREBF1 protein. **(C)** Expression of miR-33 downstream genes (ABCA1, CROT, SREBF1, and CPT1A) quantified by RT-PCR. n=3. *p < 0.05, **p < 0.01, ***p < 0.001. n.s., no significance.

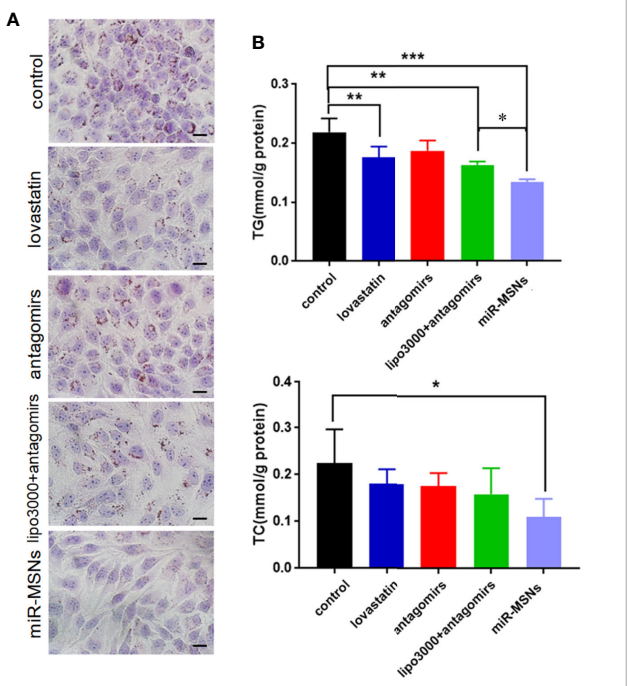

FIGURE 3 | Anti-steatosis activity of miR-MSNs in L02 cells. **(A)** Determination of lipid accumulation using Oil Red O. Scale bar = 20 μm. **(B)** TG and TC levels in the cells. n=3. *p < 0.05, **p < 0.01, and ***p < 0.001.

In Vivo Biodistribution Study

To evaluate the *in vivo* distribution of miR-33 antagomirs and delivery capacity of miR-MSNs, mice were intravenously injected with miR-MSNs *via* their tails. The distribution of miR-33 antagomirs can be tracked by ex vivo fluorescence imaging of Cy5-labled miR-33 antagomirs in different organs. As shown in **Figure 5A**, a strong fluorescence signal could be detected in liver tissues for two groups 2 h after injection. The liver fluorescence intensity of the antagomirs group gradually decreased along with time, while that of the miR-MSNs group still maintained a high level 48h after injection. Moreover, the liver fluorescence intensity of the miR-MSNs group was observed to be significantly stronger than that of the antagomirs group at each predetermined time point (**Figure 5B**). These results suggest that miR-MSNs could protect miR-33 antagomirs and prolong their retention time *in vivo*; thus, a large dosage of miR-33 antagomirs produces a good therapeutic effect. miR-MSNs are also mainly distributed in the liver and spleen, which is similar to that of MSNs (He et al., 2011).

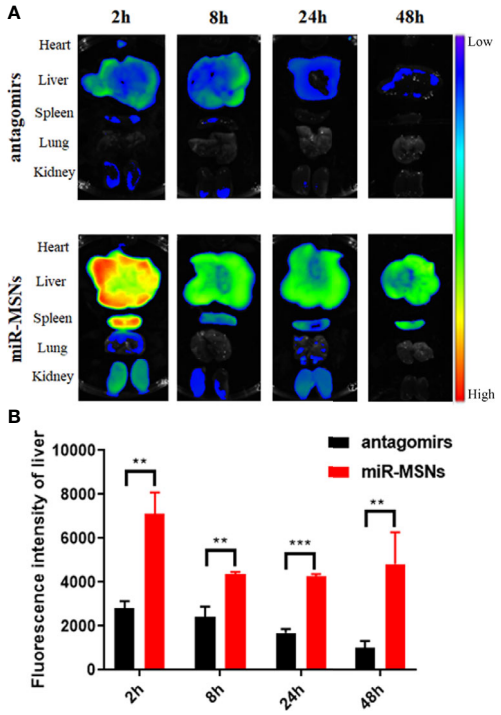

FIGURE 5 | Bio-distribution evaluation. n=3. **(A)** Ex vivo fluorescence images of major organs (heart, liver, spleen, lung, and kidney) after administration. **(B)** Quantitative analysis of the distribution of miR-33 antagomirs in the liver. **p < 0.01, and ***p < 0.001.

In Vivo Regulation Effects of Lipid Metabolism

We used HFD-fed mice models to assess the *in vivo* effects of miR-MSNs. Mice fed on HFD for two weeks were divided into four groups – MC, lovastatin, low dose miR-MSNs, and high dose miR-MSNs groups – and they were injected with PBS, 5 mg/kg lovastatin, 25 mg/kg miR-MSNs, and 50 mg/kg miR-MSNs twice a week *via* their tails. These mice were then sacrificed after 4 weeks. The mice in all four groups gained considerable body weight over the course of the study. However, the body weight of the high dose miR-MSNs group decreased significantly when compared to the MC group at Day 28. The body weight of the lovastatin and low dose miR-MSNs groups was reduced to some extent when compared to the MC group at Day 28, while no significant change was observed (**Figure 6A**). The reason for this may be the inadequate observation time; other studies reported a marked weight difference in animal models over two months of observation (Guo et al., 2019; Zai et al., 2019). To evaluate the effect of the synthesized NPs on dyslipidemia, TC and TG levels were measured on Day 0, 14, 21, and 28 (**Figure 6B**). TC and TG levels increased steadily in the MC group, indicating that our model was successful. On Day 28, TG levels in the low dose miR-MSNs group decreased significantly when compared to MC group and lovastatin groups, thus demonstrating the excellent effect of miR-MSNs on TG regulation in the serum when compared to the commercial drug. However, TC levels increased in all groups over the course of the study and there were no significant differences between the four groups at any given time point. ABCA1 is one of the main target proteins of miR-33 and its function is critical to the biogenesis of high

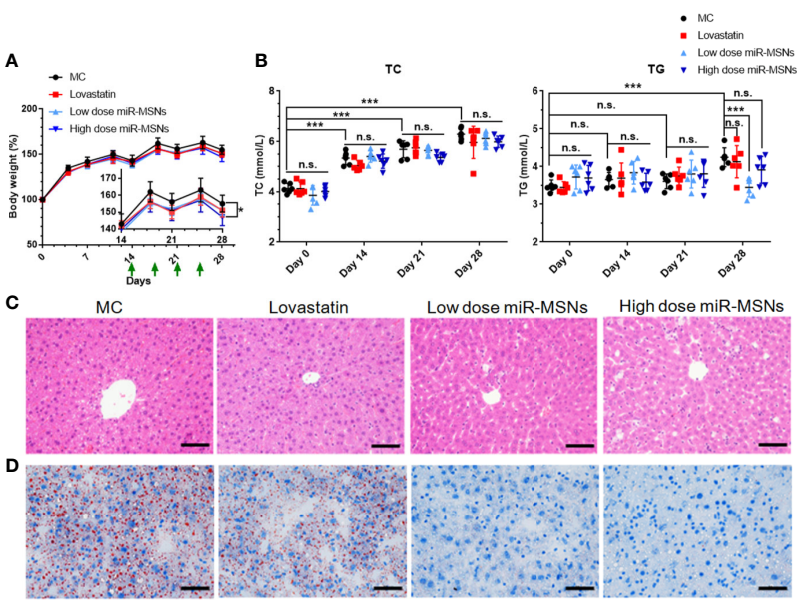

FIGURE 6 | Lipid-metabolism regulation efficacy of miR-MSNs. n=6. **(A)** Weight change curve of HFD-fed C57BL/6J during the course of the study. **(B)** Concentration of TC and TG in the serum. **(C)** Representative photographs of HE-stained liver sections. Scale bar = 50 μm. **(D)** Representative photographs of Oil Red O stained liver sections. Scale bar = 50 μm. *p < 0.05, ***p <0.001. n.s., no significance.

density lipoprotein (HDL) and the efflux of excess cholesterol in the liver (Cohen et al., 2004; Wang et al., 2004). In serum, HDL increases with interference from miR-33 (Rayner et al., 2011a; Rayner et al., 2011b). There is strong evidence that high levels of circulating HDL are associated with positive cardiovascular outcomes (Viseshakul et al., 1979; Wilson Peter et al., 1998). Therefore, the increase in HDL, a component of total serum cholesterol, in miR-MSNs-treated mice may influence the change of TC levels.

Furthermore, hepatic steatosis in the tested mice was analyzed using HE and Oil Red staining of liver tissues (**Figures 6C, D**). While the lovastatin group exhibited reduced hepatic steatosis compared to the MC group, the low dose miR-MSNs and high dose miR-MSNs groups exhibited drastically reduced lipid accumulation in the liver. In fact, on Day 28, the lipid accumulation in these groups was similar to that of the pre-treated liver on Day14. These results illustrate the excellent therapeutic effect of miR-MSNs on NAFLD and dyslipidemia.

In Vivo Safety Study

The safety of the NPs designed in this study was investigated in terms of their biocompatibility. As shown in **Figure 7**, there were no obvious histological differences in the major organs of treated and untreated mice. Except for the high dose miR-MSNs group, there were no significant differences between the treated groups and untreated group in terms of their ALT, AST, BUN, and CRE plasma levels, indicating the good tissue compatibility of the synthesized miR-MSNs. However, the rise in ALT and AST plasma levels in the high dose miR-MSNs group indicates potential liver toxicity. This finding is consistent with a previous report (Liu et al., 2011). To reduce liver toxicity, we recommend a NP dosage of 25 mg/kg for animal experiments; at this level, a similar therapeutic effect was observed. However, studies should be undertaken on the long-term *in vivo* toxicity of these NPs.

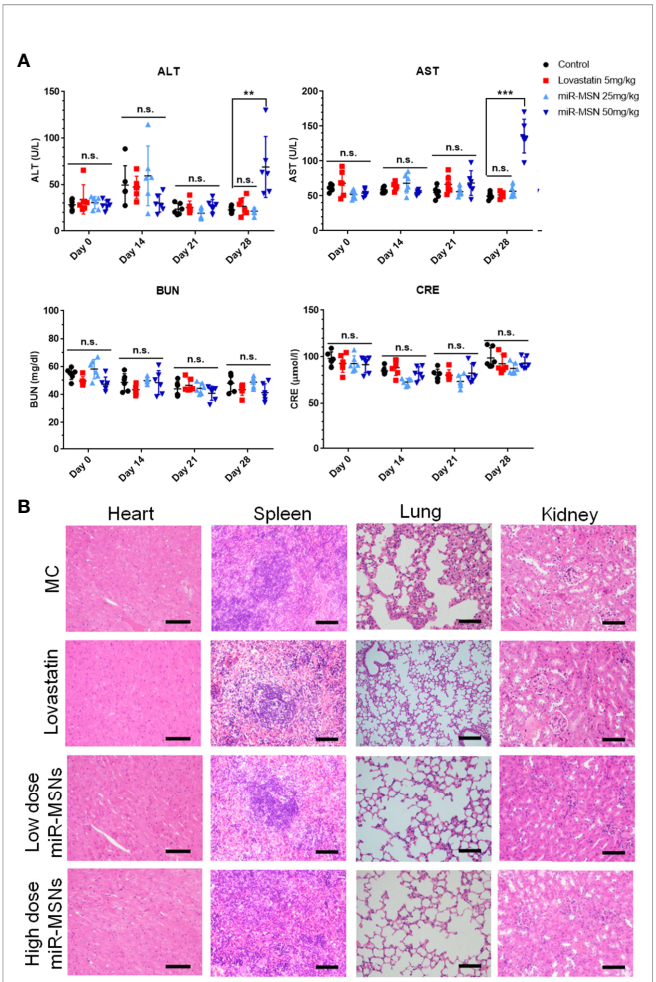

FIGURE 7 | Safety analysis. n=6. **(A)** Concentration of AST, ALT, BUN, and CRE in serum on Day28; **(B)** Representative tissue sections of mice stained with HE on Day28. Scale bar = 50 μm. **p < 0.01, ***p < 0.001. n.s., no significance.

CONCLUSION

NAFLD and dyslipidemia seriously affect public health, especially in LT recipients, who are at a high risk of metabolic diseases. These lipid metabolic disorders not only reduce patients' quality of life, but also adversely affect long-term survival. Several lipid-lowering drugs are often used in clinical settings to treat dyslipidemia. However, these drugs are not useful for treating NAFLD. Statins are one of the most common lipid-lowering drugs used for patients. Some trials even reported the prevalence of NAFLD was higher in a group with statins (Sigler et al., 2018). Therefore, in this study, we attempted to develop a therapeutic nano-system superior to statins for both NAFLD and dyslipidemia.

We successfully synthesized a novel system of miR-MSNs for delivering miR-33 antagomirs to the liver. In vitro cellular uptake assay of miR-MSN NPs, which exhibited a hydrodynamic size of ~120 nm, indicated that they entered hepatocytes specifically at a much higher efficiency than lipo3000. In vitro and *in vivo* experiments demonstrated that affected lipid metabolism, to a greater extent than lovastatin, were biocompatible and essentially nontoxic. Thus, we could conclusively prove that MSNs as delivery vehicles for miR-33 antagomirs represent a promising gene therapy system for lipid metabolic disorders. Further studies are needed to modify MSNs with hepatic-targeting ligands, such as lactobionic acid and hyaluronic acid, for enhancing the accumulation of NPs in liver.

DATA AVAILABILITY STATEMENT

The raw data supporting the conclusions of this article will be made available by the authors, without undue reservation, to any qualified researcher.

ETHICS STATEMENT

The animal study was reviewed and approved by the Institutional Animal Care and Use Committee of Zhejiang University.

AUTHOR CONTRIBUTIONS

Conceptualization, LX and XX. Investigation, YT and SX. Methodology, YT and SX. Resources, YT and CZ. Writing—original draft preparation, YT. Writing—review and editing, all authors. Visualization, YT and SX. Supervision, XX. Project administration, JW. Funding acquisition, XX and JW.

FUNDING

This work was supported by the National Natural Science Foundation of China (81801824, 81930016), China National Funds for Distinguished Young Scientists (81625003), National Major Science and Technology Projects of China (No. 2017ZX10203205), and Key Research & Development Plan of Zhejiang Province (No. 2019C03050).

ACKNOWLEDGMENTS

The authors sincerely thank the technical support provided at the Core Facilities, Zhejiang University School of Medicine and the pathological identification provided by Dr. Wen.

SUPPLEMENTARY MATERIAL

The Supplementary Material for this article can be found online at: https://www.frontiersin.org/articles/10.3389/fphar.2020.00921/full#supplementary-material

REFERENCES

Buzzetti, E., Pinzani, M., and Tsochatzis, E. A. (2016). The multiple-hit pathogenesis of non-alcoholic fatty liver disease (NAFLD). *Metabolism* 65 (8), 1038–1048. doi: 10.1016/j.metabol.2015.12.012

Canup, B. S., Song, H., Le Ngo, V., Meng, X., Denning, T. L., Garg, P., et al. (2017). CD98 siRNA-loaded nanoparticles decrease hepatic steatosis in mice. *Dig Liver Dis.* 49 (2), 188–196. doi: 10.1016/j.dld.2016.11.008

Cao, Y. N., Baiyisaiti, A., Wong, C. W., Hsu, S. H., and Qi, R. (2018). Polyurethane Nanoparticle-Loaded Fenofibrate Exerts Inhibitory Effects on Nonalcoholic Fatty Liver Disease in Mice. *Mol. Pharm.* 15 (10), 4550–4557. doi: 10.1021/acs.molpharmaceut.8b00548

Cohen, J. C., Kiss, R. S., Pertsemlidis, A., Marcel, Y. L., McPherson, R., and Hobbs, H. H. (2004). Multiple Rare Alleles Contribute to Low Plasma Levels of HDL Cholesterol. *Science* 305 (5685), 869. doi: 10.1126/science.1099870

Dávalos, A., Goedeke, L., Smibert, P., Ramírez, C. M., Warrier, N. P., Andreo, U., et al. (2011). miR-33a/b contribute to the regulation of fatty acid metabolism and insulin signaling. *Proc. Natl. Acad. Sci.* 108 (22), 9232. doi: 10.1073/pnas.1102281108

Downs, J. R., Clearfield, M., Weis, S., Whitney, E., Shapiro, D. R., Beere, P. A., et al. (1998). Primary prevention of acute coronary events with lovastatin in men and women with average cholesterol levels - Results of AFCAPS/TexCAPS. *Jama-Journal Am. Med. Assoc.* 279 (20), 1615–1622. doi: 10.1001/jama.279.20.1615

Fatourou, E. M., and Tsochatzis, E. A. (2019). Management of metabolic syndrome and cardiovascular risk after liver transplantation. *Lancet Gastroenterology Hepatology* 4 (9), 731–741. doi: 10.1016/S2468-1253(19)30181-5

Gerin, I., Clerbaux, L.-A., Haumont, O., Lanthier, N., Das, A. K., Burant, C. F., et al. (2010). Expression of miR-33 from an SREBP2 intron inhibits cholesterol export and fatty acid oxidation. *J. Biol. Chem.* 285 (44), 33652–33661. doi: 10.1074/jbc.M110.152090

Goedeke, L., Vales-Lara, F. M., Fenstermaker, M., Cirera-Salinas, D., Chamorro-Jorganes, A., Ramírez, C. M., et al. (2013). A Regulatory Role for MicroRNA 33* in Controlling Lipid Metabolism Gene Expression. *Mol. Cell. Biol.* 33 (11), 2339. doi: 10.1128/MCB.01714-12

Guo, H. H., Feng, C. L., Zhang, W. X., Luo, Z. G., Zhang, H. J., Zhang, T. T., et al. (2019). Liver-target nanotechnology facilitates berberine to ameliorate cardio-metabolic diseases. *Nat. Commun.* 10 (1), 1981. doi: 10.1038/s41467-019-09852-0

He, Q., Zhang, Z., Gao, F., Li, Y., and Shi, J. (2011). In vivo Biodistribution and Urinary Excretion of Mesoporous Silica Nanoparticles: Effects of Particle Size and PEGylation. *Small* 7 (2), 271–280. doi: 10.1002/smll.201001459

He, S., Guo, W., Deng, F., Chen, K., Jiang, Y., Dong, M., et al. (2018). Targeted delivery of microRNA 146b mimic to hepatocytes by lactosylated PDMAEMA nanoparticles for the treatment of NAFLD. *Artif. Cells Nanomedicine Biotechnol.* 46 (sup2), 217–228. doi: 10.1080/21691401.2018.1453830

Karunakaran, D., Geoffrion, M., Barrett, D., Harper, M.-E., Esau Christine, C., and Rayner Katey, J. (2015). Abstract 692: Therapeutic Inhibition of miR-33 Does Not Promote Obesity, Insulin Resistance or Hepatic Lipid Accumulation. *Arteriosclerosis Thrombosis Vasc. Biol.* 35 (suppl_1), A692–A692. doi: 10.1161/atvb.35.suppl_1.692

Keasberry, N. A., Yapp, C. W., and Idris, A. (2017). Mesoporous Silica Nanoparticles as a Carrier Platform for Intracellular Delivery of Nucleic Acids. *Biochem. (Mosc)* 82 (6), 655–662. doi: 10.1134/S0006297917060025

Kulkarni, K. M., Khot, A. M., Lokapure, S. G., and Jadhav, S. (2018). A BRIEF REVIEW ON GENE THERAPY. *Indo Am. J. Pharm. Sci.* 5 (5), 3288–3299. doi: 10.5281/zenodo.1240470

Lee, S. W., Lee, T. Y., Yang, S. S., Peng, Y. C., Yeh, H. Z., and Chang, C. S. (2017). The association of non-alcoholic fatty liver disease and metabolic syndrome in a Chinese population. *Hepatobiliary Pancreatic Dis. Int.* 16 (2), 176–180. doi: 10.1016/s1499-3872(16)60132-7

Lee, S., Han, D., Kang, H. G., Jeong, S. J., Jo, J. E., Shin, J., et al. (2019). Intravenous sustained-release nifedipine ameliorates nonalcoholic fatty liver disease by restoring autophagic clearance. *Biomaterials* 197, 1–11. doi: 10.1016/j.biomaterials.2019.01.008

Lin, Y.-S., and Haynes, C. L. (2010). Impacts of Mesoporous Silica Nanoparticle Size, Pore Ordering, and Pore Integrity on Hemolytic Activity. *J. Am. Chem. Soc.* 132 (13), 4834–4842. doi: 10.1021/ja910846q

Lin, X., Wu, M., Li, M., Cai, Z., Sun, H., Tan, X., et al. (2018). Photo-responsive hollow silica nanoparticles for light-triggered genetic and photodynamic synergistic therapy. *Acta Biomaterialia* 76, 178–192. doi: 10.1016/j.actbio.2018.07.007

Liu, T., Li, L., Teng, X., Huang, X., Liu, H., Chen, D., et al. (2011). Single and repeated dose toxicity of mesoporous hollow silica nanoparticles in intravenously exposed mice. *Biomaterials* 32 (6), 1657–1668. doi: 10.1016/j.biomaterials.2010.10.035

Marquart, T. J., Allen, R. M., Ory, D. S., and Baldán, A. (2010). miR-33 links SREBP-2 induction to repression of sterol transporters. *Proc. Natl. Acad. Sci. United States America* 107 (27), 12228–12232. doi: 10.1073/pnas.1005191107

Najafi-Shoushtari, S. H., Kristo, F., Li, Y., Shioda, T., Cohen, D. E., Gerszten, R. E., et al. (2010). MicroRNA-33 and the SREBP Host Genes Cooperate to Control Cholesterol Homeostasis. *Science* 328 (5985), 1566. doi: 10.1126/science.1189123

Pais, R., Barritt, A., Calmus, Y., Scatton, O., Runge, T., Lebray, P., et al. (2016). NAFLD and liver transplantation: Current burden and expected challenges. *J. Hepatol* 65 (6), 1245–1257. doi: 10.1016/j.jhep.2016.07.033

Rayner, K. J., Suárez, Y., Dávalos, A., Parathath, S., Fitzgerald, M. L., Tamehiro, N., et al. (2010). MiR-33 Contributes to the Regulation of Cholesterol Homeostasis. *Science* 328 (5985), 1570. doi: 10.1126/science.1189862

Rayner, K. J., Esau, C. C., Hussain, F. N., McDaniel, A. L., Marshall, S. M., van Gils, J. M., et al. (2011a). Inhibition of miR-33a/b in non-human primates raises plasma HDL and lowers VLDL triglycerides. *Nature* 478, 404. doi: 10.1038/nature10486

Rayner, K. J., Sheedy, F. J., and Esau, C. C. (2011b). Antagonism of miR-33 in Mice Promotes Reverse Cholesterol Transport and Regression of Atherosclerosis. *J. Vasc. Surg.* 54 (5), 1535. doi: 10.1016/j.jvs.2011.09.067

Rotman, Y., and Sanyal, A. J. (2017). Current and upcoming pharmacotherapy for non-alcoholic fatty liver disease. *Gut* 66 (1), 180–190. doi: 10.1136/gutjnl-2016-312431

Sigler, M. A., Congdon, L., and Edwards, K. L. (2018). An Evidence-Based Review of Statin Use in Patients With Nonalcoholic Fatty Liver Disease. *Clinical Medicine Insights: Gastroenterology* 11, 1179552218787502. doi: 10.1177/1179552218787502

Tang, F., Li, L., and Chen, D. (2012). Mesoporous silica nanoparticles: synthesis, biocompatibility and drug delivery. *Adv. Mater* 24 (12), 1504–1534. doi: 10.1002/adma.201104763

Tao, Y., Wang, J., and Xu, X. (2020). Emerging and Innovative Theranostic Approaches for Mesoporous Silica Nanoparticles in Hepatocellular Carcinoma: Current Status and Advances. *Front. Bioengineering Biotechnol.* 8:184 (184), 184. doi: 10.3389/fbioe.2020.00184

Viseshakul, D., Chularojanamontri, V., Chuprasert, S., and Benchakarn, V. (1979). The high-density lipoprotein as a protective factor against coronary heart disease in pregnant women. *J. Med. Assoc. Thailand = Chotmaihet thangphaet* 62 (7), 354–359.

Wan, S., Zhang, L., Quan, Y., and Wei, K. (2018). Resveratrol-loaded PLGA nanoparticles: enhanced stability, solubility and bioactivity of resveratrol for non-alcoholic fatty liver disease therapy. *R Soc. Open Sci.* 5 (11), 181457. doi: 10.1098/rsos.181457

Wang, N., Lan, D., Chen, W., Matsuura, F., and Tall, A. R. (2004). ATP-binding cassette transporters G1 and G4 mediate cellular cholesterol efflux to high-density lipoproteins. *Proc. Natl. Acad. Sci. United States America* 101 (26), 9774. doi: 10.1073/pnas.0403506101

Wang, J., Wang, H., Li, J., Liu, Z., Xie, H., Wei, X., et al. (2016). iRGD-Decorated Polymeric Nanoparticles for the Efficient Delivery of Vandetanib to Hepatocellular Carcinoma: Preparation and in Vitro and in Vivo Evaluation. *ACS Appl. Materials Interfaces* 8 (30), 19228–19237. doi: 10.1021/acsami.6b03166

Wang, Z., Chang, Z., Lu, M., Shao, D., Yue, J., Yang, D., et al. (2018). Shape-controlled magnetic mesoporous silica nanoparticles for magnetically-mediated suicide gene therapy of hepatocellular carcinoma. *Biomaterials* 154, 147–157. doi: 10.1016/j.biomaterials.2017.10.047

Wilson Peter, W. F., D'Agostino Ralph, B., Levy, D., Belanger Albert, M., Silbershatz, H., and Kannel William, B. (1998). Prediction of Coronary Heart Disease Using Risk Factor Categories. *Circulation* 97 (18), 1837–1847. doi: 10.1161/01.CIR.97.18.1837

Wong, R. J., Aguilar, M., Cheung, R., Perumpail, R. B., Harrison, S. A., Younossi, Z. M., et al. (2015). Nonalcoholic Steatohepatitis Is the Second Leading Etiology of Liver Disease Among Adults Awaiting Liver Transplantation in the United States. *Gastroenterology* 148 (3), 547–555. doi: 10.1053/j.gastro.2014.11.039

Woods, C. P., Hazlehurst, J. M., and Tomlinson, J. W. (2015). Glucocorticoids and non-alcoholic fatty liver disease. *J. Steroid Biochem. Mol. Biol.* 154, 94–103. doi: 10.1016/j.jsbmb.2015.07.020

Xue, H., Yu, Z., Liu, Y., Yuan, W., Yang, T., You, J., et al. (2017). Delivery of miR-375 and doxorubicin hydrochloride by lipid-coated hollow mesoporous silica nanoparticles to overcome multiple drug resistance in hepatocellular carcinoma. *Int. J. Nanomedicine* 12, 5271–5287. doi: 10.2147/IJN.S135306

Younossi, Z. M., Koenig, A. B., Abdelatif, D., Fazel, Y., Henry, L., and Wymer, M. (2016). Global epidemiology of nonalcoholic fatty liver disease-Meta-analytic assessment of prevalence, incidence, and outcomes. *Hepatology* 64 (1), 73–84. doi: 10.1002/hep.28431

Younossi, Z., Anstee, Q. M., Marietti, M., Hardy, T., Henry, L., Eslam, M., et al. (2018). Global burden of NAFLD and NASH: trends, predictions, risk factors and prevention. *Nat. Rev. Gastroenterol. Hepatol* 15 (1), 11–20. doi: 10.1038/nrgastro.2017.109

Zai, W., Chen, W., Wu, Z., Jin, X., Fan, J., Zhang, X., et al. (2019). Targeted Interleukin-22 Gene Delivery in the Liver by Polymetformin and Penetratin-Based Hybrid Nanoparticles to Treat Nonalcoholic Fatty Liver Disease. *ACS Appl. Mater Interfaces* 11 (5), 4842–4857. doi: 10.1021/acsami.8b19717

Zheng, J., and Wang, W. L. (2015). Risk factors of metabolic syndrome after liver transplantation. *Hepatobiliary Pancreatic Dis. Int.* 14 (6), 582–587. doi: 10.1016/s1499-3872(15)60037-6

Zhou, Y., Quan, G., Wu, Q., Zhang, X., Niu, B., Wu, B., et al. (2018). Mesoporous silica nanoparticles for drug and gene delivery. *Acta Pharm. Sin. B* 8 (2), 165–177. doi: 10.1016/j.apsb.2018.01.007

Zhou, L., Chen, H., Xu, Q., Han, X., Zhao, Y., Song, X., et al. (2019). The effect of di-2-ethylhexyl phthalate on inflammation and lipid metabolic disorder in rats. *Ecotoxicology Environ. Saf.* 170, 391–398. doi: 10.1016/j.ecoenv.2018.12.009

Conflict of Interest: The authors declare that the research was conducted in the absence of any commercial or financial relationships that could be construed as a potential conflict of interest.

frontiers in Pharmacology

ORIGINAL RESEARCH
published: 20 August 2020
doi: 10.3389/fphar.2020.01286

Shear Speed-Regulated Properties of Long-Acting Docetaxel Control Release Poly (Lactic-*Co*-Glycolic Acid) Microspheres

Yuhao Zheng[1], *Fan Sheng*[2], *Zihang Wang*[3], *Guang Yang*[3], *Chenguang Li*[4], *He Wang*[5] *and Zhiming Song*[1]*

[1] Department of Sports Medicine, First Hospital of Jilin University, Changchun, China, [2] Klebs Research Center, Department of Dermatology, Yanbian University Hospital, Yanji, China, [3] Department of Traumatology, First Hospital of Jilin University, Changchun, China, [4] Department of Colorectal and Anal Surgery, First Hospital of Jilin University, Changchun, China, [5] Department of Anesthesia, Yanbian University Hospital, Yanji, China

OPEN ACCESS

Edited by:
Chao Wang,
Soochow University, China

Reviewed by:
Feng Qi,
University of Missouri, United States
Lesan Yan,
Wuhan University of Technology, China
Hongliang Xin,
Nanjing Medical University, China

***Correspondence:**
Zhiming Song
szm3210@163.com

Specialty section:
This article was submitted to Experimental Pharmacology and Drug Discovery, a section of the journal Frontiers in Pharmacology

Received: 22 February 2020
Accepted: 03 August 2020
Published: 20 August 2020

Citation:
Zheng Y, Sheng F, Wang Z, Yang G, Li C, Wang H and Song Z (2020) Shear Speed-Regulated Properties of Long-Acting Docetaxel Control Release Poly (Lactic-Co-Glycolic Acid) Microspheres. Front. Pharmacol. 11:1286. doi: 10.3389/fphar.2020.01286

Advanced drug carriers for the controlled release of chemotherapeutics in the treatment of malignant tumors have drawn significant notice in recent years. In the current study, microspheres (MPs) loaded with docetaxel (DTX) were prepared using polylactic-*co*-glycolic acid copolymer (PLGA). The double emulsion solvent evaporation method is simple to perform, and results in high encapsulation efficiency. Electron micrographs of the MPs showed that controlling the shear rate can effectively control the size of the MPs. At present, most DTX sustained-release carriers cannot maintain stable and long-term local drug release. The 1.68 μm DTX-loaded microspheres (MP/DTX) with elastase was completely degraded in 14 d. This controlled degradation period is similar to a course of treatment for most cancers. The drug release profile of all kinds of MP/DTX demonstrated an initial rapid release, then slower and stable release to the end. The current study demonstrates that it is possible to create drug-loaded MPs with specific degradation times and drug release curves, which may be useful in achieving optimal treatment times and drug release rates for different diseases, and different drug delivery routes. The initial burst release reaches the effective concentration of the drug at the beginning of release, and then the drug concentration is maintained by stable release to reduce the number of injections and improve patient compliance.

Keywords: shear rate, poly (lactic-co-glycolic acid) microspheres, particle size, controlled release, docetaxel

INTRODUCTION

Advanced drug carriers for the controlled release of chemotherapeutics in the treatment of malignant tumors have attracted significant attention in recent years (Wang et al., 2019). The encapsulation matrices for chemotherapy drug delivery mainly include microspheres, hydrogels (Gao et al., 2019), electrospun fibers (Ding et al., 2019c; Feng et al., 2019), nanoparticles (Ding et al., 2019b; Sun et al., 2019), nanogels (Ding et al., 2019a), and composite biomaterials (Zheng et al., 2017). Drug release systems involving microspheres (MPs) are widely used in the treatment of

various diseases (García-González et al., 2015). MPs can be used as drug carriers in the nasal cavity and orally, and through injection, local administration and other modes of administration, and they are expected to be widely used in clinical practice in the future (He et al., 2013; Molavi et al., 2020).

The carrier material in MPs has a direct relationship with their properties. An MP carrier material must meet the following requirements: good biocompatibility, non-toxicity, ideal drug dissolution and diffusion abilities, excellent drug compatibility, suitable processing performance, simple preparation process, and low production cost (Prajapati et al., 2015). Many carrier materials can be used to prepare polymer MPs (Floyd et al., 2015; Annamalai et al., 2018). Among these, poly (lactic-co-glycolic acid) (PLGA) has attracted significant attention as a biodegradable synthetic polymer (Han et al., 2009; Kapoor et al., 2015). Using PLGA to prepare MPs has advantages compared with traditional treatment methods, and such MPs can slow the release rate of drugs and prolong the activity of drugs to improve their bioavailability (Minardi et al., 2020). PLGA is currently widely used as a drug carrier and bio-scaffold (Wu et al., 2010; Li et al., 2019), and it is also a biodegradable polymer authorized by the US Food and Drug Administration (FDA) for injection (Makadia and Siegel, 2011). The precursors of most drugs are fat-soluble. Researchers have chemically modified drugs to increase their water solubility, which affects their efficacy. PLGA MPs can contain many small molecule drugs, such as 5-fluorouracil, cisplatin, dexamethasone, docetaxel (DTX), doxorubicin, and paclitaxel (Floyd et al., 2015; Zheng et al., 2017). They have a higher drug loading rate and encapsulation rate for fat-soluble drugs. With the gradual degradation of the PLGA matrix, PLGA MPs can release a drug more stably and can achieve long-term continuous drug delivery. DTX is widely used for chemotherapy of a variety of tumors, and has a good curative effect. In the current study, DTX was used as a representative drug to study the controlled release of drugs from MPs.

DTX, also known as Taxol or Taxotere, is a new antitumor drug. The structure and effects of DTX are similar to those of paclitaxel, and it is a mitotic inhibitor. It promotes tubulin aggregation and inhibits tubulin depolymerization to prevent cells from undergoing normal mitosis, and also promotes apoptosis. In clinical practice, DTX, alone or in combination with other chemotherapeutic drugs, has begun to be used to treat breast cancer, lung cancer and other tumors, and it has a good therapeutic effect with few side effects (Ashrafizadeh et al., 2019). DTX is a fat-soluble drug with poor water solubility. DTX solution for injection contains a large amount of Tween, which is likely to cause severe allergic reactions in clinical applications (Tan et al., 2012). In addition, because of significant toxic and side effects, it is indispensable to exploit a novel DTX drug delivery system (Gong et al., 2020). Drug delivery systems for DTX mainly exploit liposomes, albumin and other nanoparticles as carriers (Gong et al., 2020). Although these nanoparticle carrier systems have unique targeting properties, improve drug stability, and reduce toxic and side effects, their release time is relatively short, whereby the shortest is 1–2 days, and the longest is approximately 2 weeks (Musumeci et al., 2006; Hwang et al., 2008). Therefore, it is necessary to develop a drug carrier with a longer release time.

The current methods for preparing MPs include solvent extraction, phase separation, solvent evaporation, spray drying, and supercritical fluid technology. In the current study, the solvent evaporation method was applied. The basic principle of this method is to prepare an emulsion of two immiscible oil-water phases through mechanical stirring or ultrasonication. The organic solvent in the interior phase is volatilized and the droplets are solidified into MPs. The emulsion solvent evaporation method is currently the most common technique for preparing MPs. The process for this technique can be separated into the following procedures: First, the polymer is dissolved in a volatile and water-soluble organic solvent (such as methylene chloride), and the drug is dissolved or dispersed in the polymer material solution. Second, the mixed solution or suspension is emulsified in the continuous phase to formulate uniformly dispersed emulsion droplets. Finally, the organic solvent is volatilized under constant stirring, and the dispersed emulsion droplets are solidified into spheres, which are then precipitated through centrifugation to obtain MPs.

The process can be a two-phase emulsion system or a multi-phase emulsion system based on the number of immiscible phases during emulsion formation (Perez et al., 2000). A two-phase emulsion system means that the emulsion is emulsified and dispersed from two immiscible phases. The most common method is the oil-in-water (O/W) method. A multi-phase emulsion system is an emulsion made by emulsifying three or more phases, such as the water-in-oil-in-water (W/O/W) method. MPs are mostly prepared through the O/W method for fat-soluble drugs or drugs with low solubility in water. The W/O/W method is used to encapsulate hydrophilic drugs, especially protein drugs (Utzinger et al., 2017). The solvent evaporation method is simple to perform, easy to control, and has outstanding reproducibility. The mild conditions in the preparation process of this method are difficult to destroy the stability and biological activity of the drug, and the drug utilization rate is high. The solubility of a drug in an organic solvent will affect the distribution of the drug in the MPs and the drug load. Because of the high solubility of DTX in the organic phase, drug-loaded PLGA MPs were directly compounded using the O/W method in the current study.

Particle size and distribution are the most critical MP variables. The main factors that affect the MP particle size are the stirring speed and the shape of the stirrer. The stirring speed has the largest effect on the average particle size of MPs. Generally, the particle size of drug-loaded MPs decreases with an increase in the stirring rate (Kim et al., 2002; Bagheri-Khoulenjani et al., 2013).

There are also many unknown factors concerning PLGA MPs, such as whether the addition of fat-soluble drugs will affect the particle size of the MPs; how to effectively control the degradation time and drug release rate of drug-loaded MPs to adapt to the course of different diseases and different routes of administration. Through several preliminary experiments, it was

difficult to form microspheres when the shear rate was less than 1,000 r/min. However, the particle size of the microspheres formed by shearing too fast was less than 1 μm, which leaded to an increase in the surface area of the microspheres, and the degradation and release rate were excessively fast. At the same time, the drug diffusion distance was too short, which also caused the drug release rate to be overquick. Therefore, we chose shear speed of 1,000 r/min to 3,500 r/min for systematic research, to prepare PLGA MPs with various drug release rates.

MATERIALS AND METHODS

Materials

PLGA (intrinsic viscosity (η) = 0.6 dL g^{-1}, LA: GA = 75:25, mol/mol) was purchased from Changchun SinoBiomaterials Co., Ltd. (Changchun, P. R. China). DTX was purchased from Beijing Huafeng United Technology Co., Ltd. (Beijing, P. R. China). Poly (vinyl alcohol) (PVA), sodium hydroxide (NaOH), sodium dodecyl sulfonate (SDS), and dichloromethane were obtained from Shanghai Chemical Reagent Co., Ltd. (Shanghai, P. R. China). Elastase was acquired from Aladdin Reagent Co., Ltd. (Shanghai, P. R. China).

Synthesis of Blank MPs and MP/DTX With Different Particle Sizes

The blank MPs and DTX-loaded MPs (MP/DTX) were compounded through the O/W solvent evaporation method. The dosage of DTX was uniformly 10%. For the preparation of MP/DTX, 135.0 mg of PLGA, and 24.0 mg of Tween-80 were dissolved in 4.5 mL of dichloromethane containing 15.0 mg of DTX. After the complete dissolution of PLGA and DTX, the mixture was slowly injected into 50.0 mL of PVA aqueous solution with a mass fraction of 1.0 wt. % over 3 min. At the same time, the PVA solution was sheared at a rotating speed of 1,000 r/min using a high-speed shearing machine. After pouring the emulsion into 100.0 ml of double distilled water and stirring for 6 h, the dichloromethane was fully volatized. Next, the products were centrifuged and collected at 2,000 r/min for 3 min, and then washed using double distilled water three times. After lyophilization, the obtained white powder was MP/DTX, created using a rotating speed of 1,000 r/min.

The shear speed of the high-speed shearing machine was adjusted to prepare MP/DTX with a rotating speed of 1,500, 2,000, 2,500, 3,000, and 3,500 r/min (all other steps were consistent with those in the procedure used to create MPs at 1,000 r/min). Blank MPs were prepared using a similar procedure without DTX.

Drug-Loading Content, Efficiency, and Solid Matter Yield of MP/DTX With Different Particle Sizes

A sodium hydroxide–sodium dodecylsulfonate (NaOH–SDS) method was used to measure the drug-loading content (DLC) and drug-loading efficiency (DLE) of the MP/DTX. Lyophilized microsphere powders (2.0 mg, three groups) were dissolved in 1.0 mL of a NaOH–SDS (5 wt.%, NaOH 0.1 mol L^{-1}) solution and shaken overnight at a constant temperature of 37°C in an oscillation box (HZQ-X100, Donglian Co., Ltd., Harbin, P. R. China). After the decomposition of MP/DTX, the clear liquid supernatant was removed, and the DTX concentration in the supernatant was measured through high-performance liquid chromatography (HPLC); (Waters 1525 system with a Waters C18 column and a Waters 2489 ultraviolet/visible (UV/vis) detector, Waters, Milford, MA, USA). A DTX standard curve was established. The elution was acetonitrile–water (60:40, V/V). And the flow rate of elution was 1.0 ml min^{-1}. The absorption wavelength (λabs) of DTX was set at 230 nm. The data was calculated by Breeze software. The mass of DTX in the MPs was calculated and the measurement was repeated three times. Then DLC, DLE, and solid matter yield were calculated using formula (1), (2), and (3).

$$\mathrm{DLC}(\%) = \frac{W_{\text{loaded drug}}\,(\mathrm{mg})}{W_{\text{loaded MP}}\,(\mathrm{mg})} \times 100\,\% \tag{1}$$

Where, $W_{\text{loaded drug}}$ and $W_{\text{loaded MP}}$ denote the weight of loaded drug and MP/DTX, respectively.

$$\mathrm{DLE}(\%) = \frac{W_{\text{loaded drug}}\,(\mathrm{mg})}{W_{\text{feeding drug}}\,(\mathrm{mg})} \times 100\,\% \tag{2}$$

Where, $W_{\text{loaded drug}}$ and $W_{\text{feeding drug}}$ denote the weight of the loaded drug in the MP/DTX and the feeding drug in the course of drug encapsulation, respectively.

$$\mathrm{Yield}(\%) = \frac{W_{\text{loading MP}}\,(\mathrm{mg})}{W_{\text{feeding solid}}\,(\mathrm{mg})} \times 100\,\% \tag{3}$$

Where, $W_{\text{feeding solid}}$ denotes the weight of the entire feeding solid in the course of drug encapsulation.

Morphology and Particle Size Measurement of Blank MPs and MP/DTX With Different Particle Sizes

Blank MPs and MP/DTX with different particle diameters were pasted to different areas of a metal plate using conductive adhesive tape, and then sprayed with gold. A scanning electron microscope was used to observe the morphology of the MPs, and 100 MPs in each group were selected and the average particle diameters were measured. Then the variance of the particle diameters was calculated.

In Vitro Degradation of MP/DTX With Different Particle Sizes

MP/DTX was added into 10 mL centrifuge tubes (30.0 mg for each group), and then 5.0 mL of PBS without or with 2.0 mg ml^{-1} of elastase was laxly put in the tubes. Then the tubes were placed into an oscillation chamber at 37°C. The vibration rate was set to 70 rpm. The tubes were centrifuged at 1,000 r min^{-1} every 7 d, and then the supernatant was aspirated. After lyophilization, the total mass of the centrifuge tubes was measured. Finally, the new buffer was replaced, and then shaking at 37°C continued. Three parallel control tubes were set up per group. When the MP

powder of each particle size had completely degraded, a line chart of the remaining mass and days was constructed.

In Vitro Release Profiles of MP/DTX With Different Particle Sizes

The dynamic direct release method was used to obtain a drug release curve of MP/DTX with different particle sizes. First, 2.0 mg of MP/DTX with different particle diameters was placed into centrifuge tubes. Then 2.0 ml of PBS without or with elastase (2.0 mg ml^{-1}) was put in the tubes. Three parallel controls per group were established. After the tubes were sealed, they were placed into an oscillation chamber at 37°C. The vibration rate was set to 70 rpm. The tubes were centrifuged at 1,000 r/min for 5 min to separate MP/DTX and the release solution every other day. The release solution was filtered through a micro-porous filter membrane, and the released drug concentration was measured through HPLC. When the MP/DTX had completely degraded, fresh buffer was added to the tubes and the previous steps were repeated. The total time of degradation and drug release was recorded for each group, and drug release curves were obtained based on the time and cumulative release.

Statistical Analyses

All the statistical data are shown as mean ± standard deviation. Differences were analyzed using the paired Student's *t*-test. Differences between experimental groups were assessed by one-way analysis of variance with statistical software SPSS 17.0 (SPSS Inc.,Chicago, IL). $P < 0.05$ was considered statistically significant, $P < 0.01$ was considered highly significant, and $P > 0.05$ was considered no significant.

RESULTS AND DISCUSSION

Morphology and Particle Size Analysis of Blank MPs and MP/DTX With Different Particle Sizes

As shown in **Figure 1**, the morphology of blank MPs and MP/DTX with different particle sizes was observed through scanning electron microscopy (SEM; Philips XL30, Eindhoven, The Netherlands). All the MPs were perfectly round spheres with smooth surfaces. The average size of the MPs was analyzed by assessing 100 MPs, using the scale bar in the **Figure 1**. The mean and variance of the particle size were calculated, and the results are shown in **Table 1**. When the emulsification speed increased from 1,000 r/min to 3,500 r/min, the average particle size of the blank MPs decreased from 8.84 μm to 1.53 μm, and the average particle size of MP/DTX decreased from 8.98 μm to 1.68 μm. This indicates that the shear rate has a prominent effect on the particle size of both blank MPs and MP/DTX ($P < 0.01$). When the shear rate is increased, the degree of dispersion of the oil phase droplets in the water phase increases, causing a smaller particle size in the formation of MPs. The particle size distribution is also narrowed to some extent. The particle size and distribution of MPs created using different shear rates were very close, regardless of whether DTX was added ($P > 0.05$). These results show that without changing the dichloromethane concentration in the PLGA solution, adding fat-soluble drugs has little impact on the particle size of the MPs.

Drug-Loading Content, Efficiency, and Solid Matter Yield of MP/DTX With Different Particle Sizes

As shown in **Table 2**, when the dosage of DTX was consistent (10 wt. %), the DLC decreased from 8.95% to 8.63% when the emulsification rate increased from 1,000 r/min to 3,500 r/min. This is because with the increase in the emulsification and dispersion rate, the surface area of the droplets increases, and the diffusion distance of the drugs decreases. A small amount of DTX is lost, so the DLC decreases (Berkland et al., 2003). However, because of the strong lipid solubility of DTX, the DLC and DLE of each group was very high without significant differences ($P > 0.05$). Moreover, the yield for each MP/DTX group was above 85%, which indicates that the loss of material during the volatilization solvent evaporation method is minimal. Therefore, these PLGA MPs demonstrate controlled size, morphology and high DLE, and are a promising platform to encapsulate and deliver drugs such as DTX.

In Vitro Degradation of MP/DTX With Different Particle Sizes

The following conclusions can be drawn from **Figure 2**. Firstly, elastase was added to mimic the *in vivo* circumstances, which promoted the degradation of the MPs. Secondly, the MPs with the smallest particle size obtained at high shear rates had the fastest degradation rate and the shortest degradation time. The 1.68 μm MP/DTX with elastase was completely degraded in about 14 d, while 2.56 μm MP/DTX, 4.85 μm MP/DTX and 8.98 μm MP/DTX with the same elastase were degraded in 21, 35 and 42 d. Most tumor chemotherapy takes about 14 days in one course of treatment. At this time, 1.68 μm MP/DTX can be applied. If it is necessary to prolong the chemotherapy time according to the condition, it can be treated by MP/DTX with a longer degradation time. Finally, all degradation curves were slower in the early stage and faster in the later stage. This is because the PLGA molecular chain contains a hydrophilic ester bond, which can hydrolyze in an aqueous medium, causing the polymer molecular chain to break. The hydrolytic cleavage of the ester bond is random, and the polymer chain was broken into low molecular weight chains. However, these low molecular weight chains still demonstrate a certain degree of polymerization and can be bonded to each other. Consequently, at this stage, the mass of the MPs did not change much. With the further degradation of the MPs, the short chain molecules continued to hydrolyze into acidic small molecule monomers such as lactic acid, and entered the aqueous medium through channels such as molecular chain gaps and pores. Finally, with the continuous loss of small molecule monomers, the MPs gradually dissolved and disintegrated until they disappeared completely. Therefore, the degradation of the MPs changed significantly in the later stage.

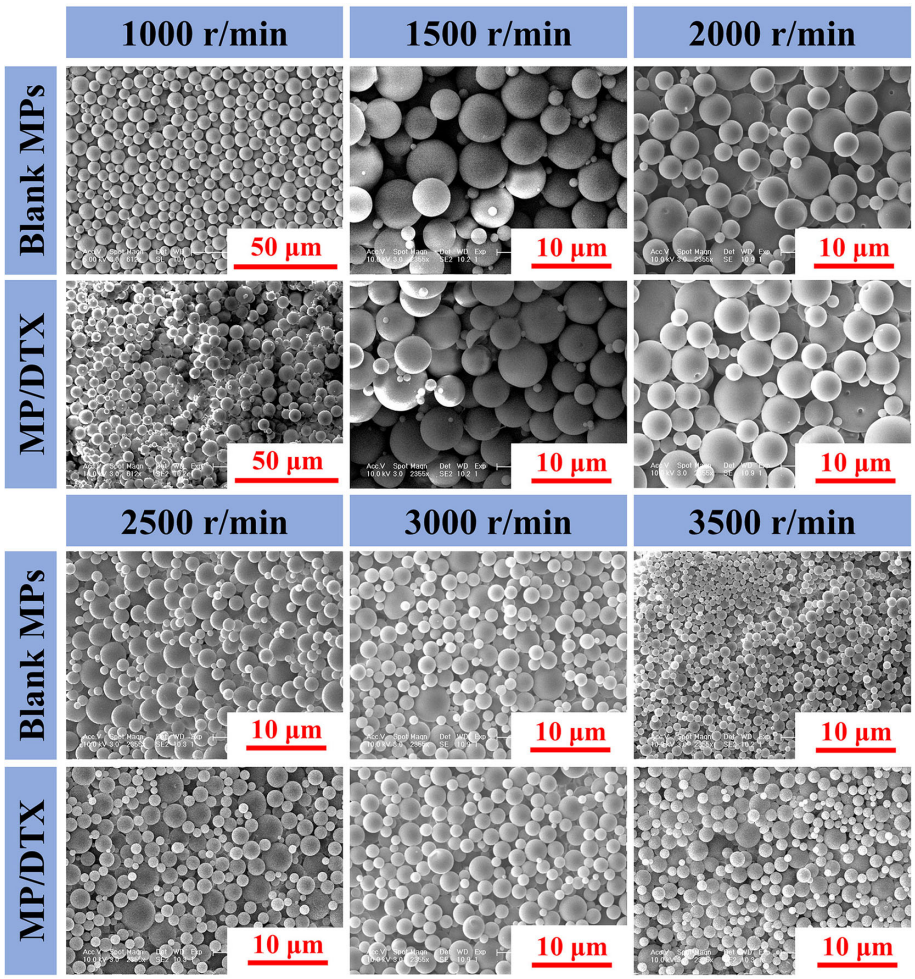

FIGURE 1 | Morphology and scale of blank microspheres (MPs) and MP/docetaxel (DTX) created using different shear speeds.

TABLE 1 | Particle sizes of blank microspheres (MPs) and MP/docetaxel (DTX) created using different shear speeds.

Shear Rate (r/min)	Particle Size of blank MPs (μm)	Particle Size of MP/DTX (μm)
1,000	8.84 ± 1.81[a,b]	8.98 ± 1.53[a,c]
1,500	6.61 ± 1.86[a,b]	6.73 ± 1.28[a,c]
2,000	4.81 ± 1.33[a,b]	4.85 ± 1.20[a,c]
2,500	3.34 ± 1.01[a,b]	3.47 ± 1.41[a,c]
3,000	2.64 ± 0.67[a,b]	2.56 ± 0.74[a,c]
3,500	1.53 ± 0.32[a,b]	1.68 ± 0.36[a,c]

Data are presented as mean ± SD (n = 100, [a]P > 0.05, [b]P < 0.01, [c]P < 0.01).

TABLE 2 | Particle sizes, drug-loading content, efficiency, and solid matter yield of microsphere (MP)/docetaxel (DTX).

Shear Rate (r/min)	Drug Loading (%)	Loading Efficiency (%)	Yield (%)
1,000	8.95 ± 0.26*	76.57 ± 4.19	85.55 ± 3.22
1,500	8.94 ± 0.38*	77.89 ± 3.58	87.12 ± 2.94
2,000	8.92 ± 0.31*	78.47 ± 2.75	87.97 ± 1.51
2,500	8.90 ± 0.19*	79.95 ± 2.59	89.83 ± 1.76
3,000	8.88 ± 0.15*	80.21 ± 1.93	90.33 ± 2.85
3,500	8.63 ± 0.29*	79.53 ± 2.69	92.15 ± 2.36

*Data are presented as mean ± SD (n = 3, *P > 0.05).*

(Mogi et al., 2000) In addition, polyester materials are also affected by their own degradation products. The degradation products were small molecules of lactic acid and glycolic acid. It was difficult for such molecules to diffuse to the outside of the matrix, which caused the accumulation of acid degradation products inside the MPs, forming a local slightly acidic environment. Hydrogen ions can catalyze the hydrolysis of ester bonds, which is called the "autocatalytic effect", which also leads to the faster degradation of MPs in the later stage (Busatto et al., 2018).

In Vitro Release Profiles of MP/DTX With Different Particle Sizes

The release performance of drug-loaded MPs *in vitro* is an important index in terms of evaluating MP performance and

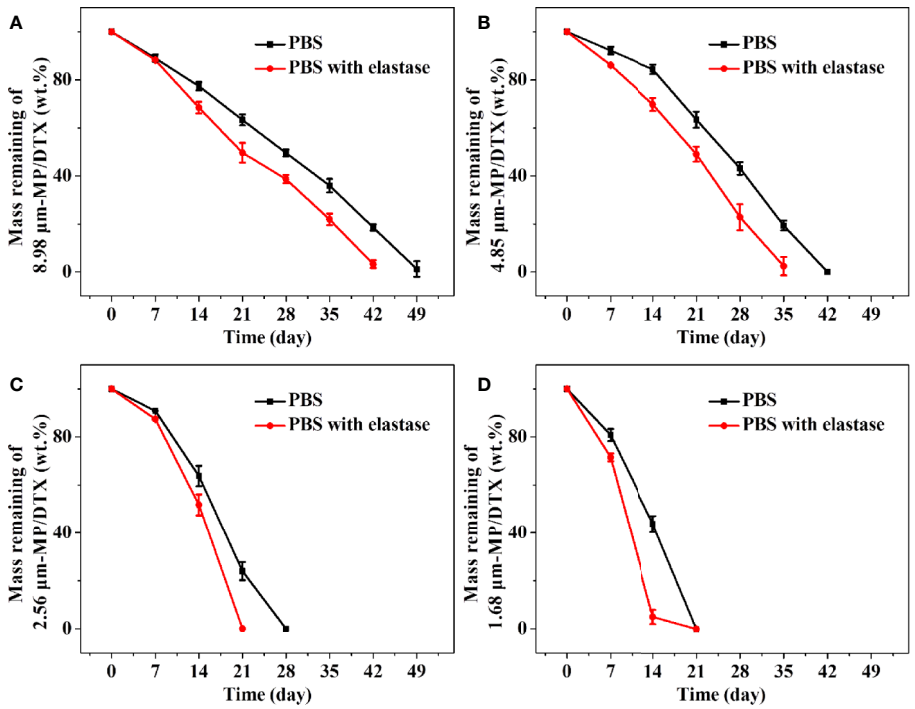

FIGURE 2 | Degradation curves of remaining masses of 8.98 μm microsphere (MP)/docetaxel (DTX) **(A)**, 4.85 μm MP/DTX **(B)**, 2.56 μm MP/DTX **(C)**, and 1.68 μm MP/DTX **(D)**. Data are presented as mean ± SD (n = 3).

effectiveness. The advantages of the method used in the current study are its simple operation and slow shaking speed. MPs are piled up on the bottom of the container. MPs in this state mimic the condition of MPs when injected subcutaneously or intramuscularly. The main disadvantage of this method is that some samples may be lost during sampling, which will increase the relative error of the *in vitro* release measurement.

As shown in **Figure 3**, the groups of MP/DTX with elastase had finished release 1 week earlier than the group without elastase, which is consistent with the results of the MP degradation experiments. The drug release profile of all kinds of MP/DTX demonstrated an initial rapid release, then slower release, and then slightly accelerated release. The degradation trend of 2.56 μm MPs in PBS was taken as an example. 47.86% of the total DTX was desorbed quickly in the first ten days. DTX was released in a smooth and slow trend from the 10th day to the 38th day. During this period, 1.01% of the total DTX was released every day. From the 38th day to the 50th day, DTX was released rapidly with an average daily release of 1.86% of the total DTX. Based on this trend, the process of drug release from the MPs can be divided into three phases: an initial burst release phase, a stable release phase, and a late accelerated release phase.

In the first stage, an initial burst release can increase the blood concentration quickly to reach the effective therapeutic concentration, which is beneficial for treatment. However, an excessive burst release may easily lead to the blood concentration approaching toxic levels, which may cause adverse reactions. This "bursting" effect can be reduced by washing the MPs multiple times during the preparation course. The surface morphology and particle size of the MPs are the main factors affecting the initial burst release (Jeyanthi et al., 1997). As shown in **Figure 3**, with the decrease in the particle size of the MP/DTX, the initial burst release increased. The cumulative DTX release of the four MP types (with elastase), from a large to small particle size, in the first 2 d was 23.70%, 27.37%, 31.45%, and 40.53%, respectively. As the particle size of the MP/DTX decreased, the surface area was larger, resulting in an increase in the contact area between MP/DTX and the degradation solution. Therefore, the smaller the MP/DTX particle size, the greater the initial burst release phenomenon. Secondly, when the hydrophilicity of the drug is low, the drug that diffused out of the MPs will adhere to the MP surface during the volatilization of the solvent (Rieger et al., 2015).

The initial burst release of the four MPs occurred in the first 2 d, and then the stable release phase began. During this process, the external liquid gradually diffused to the inside of the MPs and drove the drug to diffuse outward. At the same time, the polymer carrier was gradually degraded, which drove the diffusion of external liquids into the MPs and the diffusion of drugs outside the MPs. This process is controlled by both the diffusion process and the degradation process.

In the last stage of drug release, when the matrix degradation of the polymer reached a certain level, the MPs completely swell and disintegrated completely, so that the unreleased drugs are

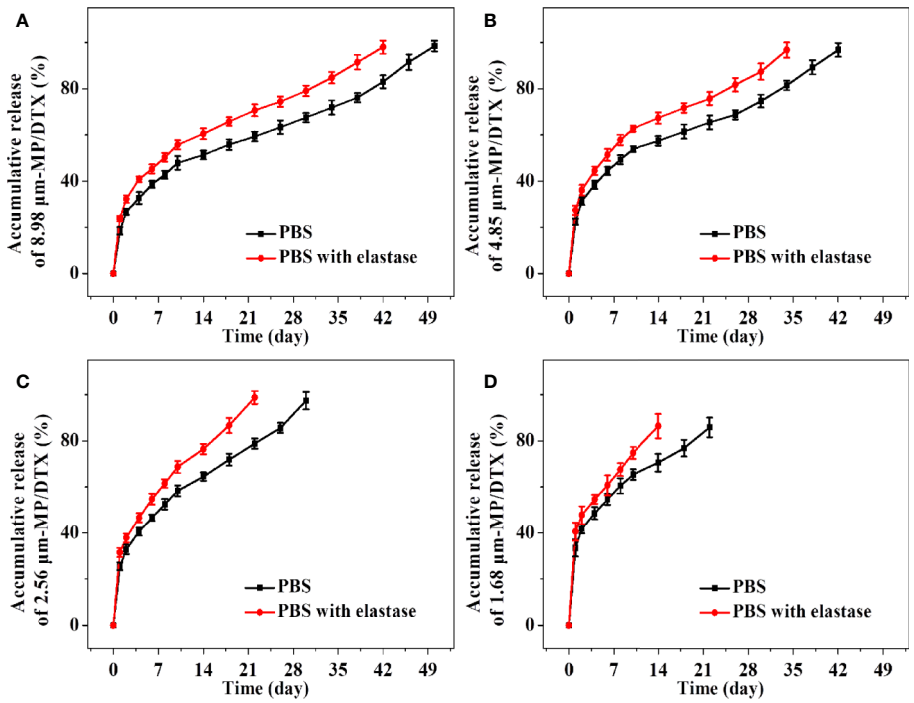

FIGURE 3 | Accumulative release amount and release time of docetaxel (DTX) for 8.98 μm microsphere (MP)/DTX **(A)**, 4.85 μm MP/DTX **(B)**, 2.56 μm MP/DTX **(C)**, and 1.68 μm MP/DTX **(D)**. Data are presented as mean ± SD (n = 3).

fully released. Although the complete disintegration of the MP/DTX accelerated the release of DTX, the external liquid had gradually diffused into the MP/DTX during the stable release phase, taking away most of the internal DTX, and the release rate did not change a lot.

CONCLUSIONS

In the current study, PLGA MPs loaded with DTX were prepared through the solvent evaporation method. By observing electron micrographs of the MPs, it was found that controlling the shear rate can effectively control the particle size of the MPs. The obtained MPs have a complete glossy surface and a standard spherical shape. These PLGA MPs also have a high drug loading rate, high yield, and they are easy to prepare and adjust the MP particle size. The degradation and release characteristics of MPs with different particle sizes were determined through degradation and release tests. It is conducive to selecting the appropriate drug-loaded MPs, which match the degradation time with the time of therapy according to the needs of different disease. This method can carry not only DTX but also other anti-tumor drugs. Simultaneously, as an excellent drug delivery vehicle, it can continuously release the drug locally in the tumor for a long time, thereby maintaining the local concentration of the drugs. Therefore, compared to systemic medicine, this drug delivery vehicle can reduce the toxic and side effects by locally releasing the drug near the tumor. This new drug delivery system will play a more effective role in chemotherapy for human tumors.

DATA AVAILABILITY STATEMENT

All datasets generated for this study are included in the article/supplementary material.

AUTHOR CONTRIBUTIONS

All authors contributed to the article and approved the submitted version.

FUNDING

The current study was financially funded by the National Natural Science Foundation of China (No. 81902227); the China Postdoctoral Science Foundation (No. 2018M631864); the National Postdoctoral Program for Innovative Talents of China (No. BX201701278); and the Department of Science and Technology of Jilin Province of China (Nos. 20190303154SF, 20200201478JC).

REFERENCES

Annamalai, R. T., Turner, P. A., Carson, W. F., Levi, B., Kunkel, S., and Stegemann, J. P. (2018). Harnessing macrophage-mediated degradation of gelatin microspheres for spatiotemporal control of BMP2 release. *Biomaterials* 161, 216–227. doi: 10.1016/j.biomaterials.2018.01.040

Ashrafizadeh, M., Ahmadi, Z., Mohamadi, N., Zarrabi, A., Abasi, S., Dehghannoudeh, G., et al. (2019). Chitosan-based advanced materials for docetaxel and paclitaxel delivery: Recent advances and future directions in cancer theranostics. *Int. J. Biol. Macromolecules* 145, 282–300. doi: 10.1016/j.ijbiomac.2019.12.145

Bagheri-Khoulenjani, S., Mirzadeh, H., Etrati-Khosroshahi, M., and Shokrgozar, M. A. (2013). Particle size modeling and morphology study of chitosan/gelatin/nanohydroxyapatite nanocomposite microspheres for bone tissue engineering. *J. Biomed. Mater. Res. Part A* 101, 1758–1767. doi: 10.1002/jbm.a.34481

Berkland, C., Kim, K., and Pack, D. W. (2003). PLG microsphere size controls drug release rate through several competing factors. *Pharm. Res.* 20, 1055–1062. doi: 10.1023/A:1024466407849

Busatto, C., Pesoa, J., Helbling, I., Luna, J., and Estenoz, D. (2018). Effect of particle size, polydispersity and polymer degradation on progesterone release from PLGA microparticles: Experimental and mathematical modeling. *Int. J. Pharm.* 536, 360–369. doi: 10.1016/j.ijpharm.2017.12.006

Ding, J., Chen, J., Gao, L., Jiang, Z., Zhang, Y., Li, M., et al. (2019a). Engineered nanomedicines with enhanced tumor penetration. *Nano Today* 29, 100800. doi: 10.1016/j.nantod.2019.100800

Ding, J., Feng, X., Jiang, Z., Xu, W., Guo, H., Zhuang, X., et al. (2019b). Polymer-Mediated Penetration-Independent Cancer Therapy. *Biomacromolecules* 20, 4258–4271. doi: 10.1021/acs.biomac.9b01263

Ding, J., Zhang, J., Li, J., Li, D., Xiao, C., Xiao, H., et al. (2019c). Electrospun polymer biomaterials. *Prog. Polymer Sci.* 90, 1–34. doi: 10.1016/j.progpolymsci.2019.01.002

Feng, X., Li, J., Zhang, X., Liu, T., Ding, J., and Chen, X. (2019). Electrospun polymer micro/nanofibers as pharmaceutical repositories for healthcare. *J. Controlled Rel. Off. J. Controlled Rel. Soc.* 302, 19–41. doi: 10.1016/j.jconrel.2019.03.020

Floyd, J. A., Galperin, A., and Ratner, B. D. (2015). Drug encapsulated polymeric microspheres for intracranial tumor therapy: A review of the literature. *Adv. Drug Deliv. Rev.* 91, 23–37. doi: 10.1016/j.addr.2015.04.008

Gao, S., Tang, G., Hua, D., Xiong, R., Han, J., Jiang, S., et al. (2019). Stimuli-responsive bio-based polymeric systems and their applications. *J. Mater. Chem. B* 7, 709–729. doi: 10.1039/C8TB02491J

García-González, C., Jin, M., Gerth, J., Alvarez-Lorenzo, C., and Smirnova, I. (2015). Polysaccharide-based aerogel microspheres for oral drug delivery. *Carbohydr. Polymers* 117, 797–806. doi: 10.1016/j.carbpol.2014.10.045

Gong, F., Wang, R., Zhu, Z., Duan, J., Teng, X., and Cui, Z. K. (2020). bDrug-interactive mPEG–PLA-Phe(Boc) micelles enhance the tolerance and anti-tumor efficacy of docetaxel. *Drug Deliv.* 27, 238–247. doi: 10.1080/10717544.2020.1718245

Han, Y., Tian, H., He, P., Chen, X., and Jing, X. (2009). Insulin nanoparticle preparation and encapsulation into poly(lactic-co-glycolic acid) microspheres by using an anhydrous system. *Int. J. Pharm.* 378, 159–166. doi: 10.1016/j.ijpharm.2009.05.021

He, P., Liu, H., Tang, Z., Deng, M., Yang, Y., Pang, X., et al. (2013). Poly(ester amide) blend microspheres for oral insulin delivery. *Int. J. Pharm.* 455, 259–266. doi: 10.1016/j.ijpharm.2013.07.022

Hwang, H. Y., Kim, I. S., Kwon, I. C., and Kim, Y. H. (2008). Tumor targetability and antitumor effect of docetaxel-loaded hydrophobically modified glycol chitosan nanoparticles. *J. Controlled Rel. Off. J. Controlled Rel. Soc.* 128, 23–31. doi: 10.1016/j.jconrel.2008.02.003

Jeyanthi, R., Mehta, R. C., Thanoo, B. C., and DeLuca, P. P. (1997). Effect of processing parameters on the properties of peptide-containing PLGA microspheres. *J. Microencapsulation* 14, 163–174. doi: 10.3109/02652049709015330

Kapoor, D. N., Bhatia, A., Kaur, R., Sharma, R., Kaur, G., and Dhawan, S. (2015). PLGA: a unique polymer for drug delivery. *Ther. Deliv.* 6, 41–58. doi: 10.4155/tde.14.91

Kim, J. C., Song, M. E., Lee, E. J., Park, S. K., Rang, M. J., and Ahn, H. J. (2002). Preparation of microspheres by an emulsification-complexation method. *J. Colloid Interface Sci.* 248, 1–4. doi: 10.1006/jcis.2001.8171

Li, S., Feng, X., Wang, J., Xu, W., Islam, M. A., Sun, T., et al. (2019). Multiantigenic Nanoformulations Activate Anticancer Immunity Depending on Size. *Adv. Funct. Mater.* 29, 1903391. doi: 10.1002/adfm.201903391

Makadia, H. K., and Siegel, S. J. (2011). Poly Lactic-co-Glycolic Acid (PLGA) as Biodegradable Controlled Drug Delivery Carrier. *Polymers* 3, 1377–1397. doi: 10.3390/polym3031377

Minardi, S., Fernandez-Moure, J. S., Fan, D., Murphy, M. B., Yazdi, I. K., Liu, X., et al. (2020). Biocompatible PLGA-Mesoporous Silicon Microspheres for the Controlled Release of BMP-2 for Bone Augmentation. *Pharmaceutics* 12, 118. doi: 10.3390/pharmaceutics12020118

Mogi, T., Ohtake, N., Yoshida, M., Chimura, R., Kamaga, Y., Ando, S., et al. (2000). Sustained release of 17 beta-estradiol from poly (lactide-co-glycolide) microspheres in vitro and in vivo. *Colloids Surf. B-Biointerf.* 17, 153–165. doi: 10.1016/S0927-7765(99)00105-8

Molavi, F., Barzegar-Jalali, M., and Hamishehkar, H. (2020). Polyester based polymeric nano and microparticles for pharmaceutical purposes: A review on formulation approaches. *J. Controlled Rel. Off. J. Controlled Rel. Soc.* 320, 265–282. doi: 10.1016/j.jconrel.2020.01.028

Musumeci, T., Ventura, C. A., Giannone, I., Ruozi, B., Montenegro, L., Pignatello, R., et al. (2006). PLA/PLGA nanoparticles for sustained release of docetaxel. *Int. J. Pharm.* 325, 172–179. doi: 10.1016/j.ijpharm.2006.06.023

Perez, M. H., Zinutti, C., Lamprecht, A., Ubrich, N., Astier, A., Hoffman, M., et al. (2000). The preparation and evaluation of poly(epsilon-caprolactone) microparticles containing both a lipophilic and a hydrophilic drug. *J. Controlled Rel.* 65, 429–438. doi: 10.1016/S0168-3659(99)00253-9

Prajapati, V. D., Jani, G. K., and Kapadia, J. R. (2015). Current knowledge on biodegradable microspheres in drug delivery. *Expert Opin. Drug Deliv.* 12, 1283–1299. doi: 10.1517/17425247.2015.1015985

Rieger, E., Dupret-Bories, A., Salou, L., Metz-Boutigue, M. H., Layrolle, P., Debry, C., et al. (2015). Controlled implant/soft tissue interaction by nanoscale surface modifications of 3D porous titanium implants. *Nanoscale* 7, 9908–9918. doi: 10.1039/C5NR01237F

Sun, Y., Ma, W., Yang, Y., He, M., Li, A., Bai, L., et al. (2019). Cancer nanotechnology: Enhancing tumor cell response to chemotherapy for hepatocellular carcinoma therapy. *Asian J. Pharm. Sci.* 14, 581–594. doi: 10.1016/j.ajps.2019.04.005

Tan, Q., Liu, X., Fu, X., Li, Q., Dou, J., and Zhai, G. (2012). Current development in nanoformulations of docetaxel. *Expert Opin. Drug Deliv.* 9, 975–990. doi: 10.1517/17425247.2012.696606

Utzinger, M., Jarzebinska, A., Haag, N., Schweizer, M., Winter, G., Dohmen, C., et al. (2017). cmRNA/lipoplex encapsulation in PLGA microspheres enables transfection via calcium phosphate cement (CPC)/PLGA composites. *J. Controlled Rel. Off. J. Controlled Rel. Soc.* 249, 143–149. doi: 10.1016/j.jconrel.2017.01.045

Wang, Q., Zhang, P., Li, Z., Feng, X., Lv, C., Zhang, H., et al. (2019). Evaluation of Polymer Nanoformulations in Hepatoma Therapy by Established Rodent Models. *Theranostics* 9, 1426–1452. doi: 10.7150/thno.31683

Wu, S. C., Chang, J. K., Wang, C. K., Wang, G. J., and Ho, M. L. (2010). Enhancement of chondrogenesis of human adipose derived stem cells in a hyaluronan-enriched microenvironment. *Biomaterials* 31, 631–640. doi: 10.1016/j.biomaterials.2009.09.089

Zheng, Y., Cheng, Y., Chen, J., Ding, J., Li, M., Li, C., et al. (2017). Injectable Hydrogel-Microsphere Construct with Sequential Degradation for Locally Synergistic Chemotherapy. *ACS Appl. Mater. Interf.* 9, 3487–3496. doi: 10.1021/acsami.6b15245

Conflict of Interest: The authors declare that the research was conducted in the absence of any commercial or financial relationships that could be construed as a potential conflict of interest.

frontiers in Pharmacology

ORIGINAL RESEARCH
published: 28 August 2020
doi: 10.3389/fphar.2020.532457

Development of a Hyaluronic Acid-Based Nanocarrier Incorporating Doxorubicin and Cisplatin as a pH-Sensitive and CD44-Targeted Anti-Breast Cancer Drug Delivery System

Tao Yu[1†], *Yongshuang Li*[2†], *Xueyuan Gu*[3] *and Qin Li*[1,3*]

[1] Center for Translational Medicine, the Fourth Affiliated Hospital of China Medical University, Shenyang, China, [2] Department of General Surgery, the Fourth Affiliated Hospital of China Medical University, Shenyang, China, [3] Centeral Laboratory, the Fourth Affiliated Hospital of China Medical University, Shenyang, China

OPEN ACCESS

Edited by:
Jianxun Ding,
Chinese Academy of Sciences, China

Reviewed by:
Weiguo Xu,
Chinese Academy of Sciences, China
Silvia Arpicco,
University of Turin, Italy

***Correspondence:**
Qin Li
qli@cmu.edu.cn

[†]*These authors have contributed equally to this work*

Specialty section:
This article was submitted to Experimental Pharmacology and Drug Discovery a section of the journal Frontiers in Pharmacology

Received: *04 February 2020*
Accepted: *14 August 2020*
Published: *28 August 2020*

Citation:
Yu T, Li Y, Gu X and Li Q (2020) Development of a Hyaluronic Acid-Based Nanocarrier Incorporating Doxorubicin and Cisplatin as a pH-Sensitive and CD44-Targeted Anti-Breast Cancer Drug Delivery System. Front. Pharmacol. 11:532457. doi: 10.3389/fphar.2020.532457

Tumor-targeting nanomaterial-based chemotherapeutic drug delivery systems have been shown to represent an efficacious approach for the treatment of cancer because of their stability in blood circulation and predictable delivery patterns, enhanced tumor-selective drug accumulation, and decreased toxicity to normal tissues. The cell-surface transmembrane glycoprotein CD44 binds to the extracellular domain of hyaluronic acid (HA), and is overexpressed in breast, ovarian, lung, and stomach cancer. In this study, an HA-based nano-carrier incorporating doxorubicin (DOX) and cisplatin (CDDP) was synthesized as a CD44-targeting anti-cancer drug delivery system, and its tumor inhibition effects against $CD44^+$ breast cancer cells were evaluated *in vitro* and *in vivo*. These dual drug-loaded HA micelles (HA-DOX-CDDP) exhibited significantly enhanced drug release under acidic conditions, and showed higher cellular uptake and stronger cellular growth inhibition than free drugs against 4T1 ($CD44^+$) breast cancer cells. In contrast, no significant differences in growth inhibition and cellular uptake were observed between HA-DOX-CDDP and free drugs in NIH-3T3 ($CD44^-$) control cells. Furthermore, HA-DOX-CDDP micelles exhibited stronger inhibitory effects and lower systemic toxicity than free drugs in a 4T1 mammary cancer-bearing mouse model, as determined using immunofluorescence and histological analyses. Therefore, HA-DOX-CDDP micelles represent a promising drug delivery system that exhibits acid-sensitive drug release, CD44-targeted delivery, and excellent biocompatibility and biodegradation. These properties resulted in excellent tumor accumulation and reduced adverse effects, indicating that HA-DOX-CDDP micelles have promising potential applications in chemotherapy for breast cancer.

Keywords: hyaluronic acid, doxorubicin, CD44, pH-sensitive, breast cancer chemotherapy

INTRODUCTION

Breast cancer is the most serious threat to female health globally because of the associated high morbidity, poor prognosis, and limited availability of effective therapies. Breast cancer chemotherapy typically involves the administration of a single anti-tumor drug, and side effects and drug resistance remain significant challenges. Combined and targeted anticancer therapies have replaced conventional medical treatments owing to their enhanced breast tumor-targeting and improved drug delivery. However, a majority of currently used drug carriers have limitations that restrict their clinical application, such as the lack of long-term safety, poor biocompatibility, high cost of manufacturing, and limited drug loading efficiency (Cheng et al., 2014; Feng et al., 2017; Freitas de Freitas et al., 2018). Therefore, the development of targeted anticancer drug delivery systems with low toxicity and good biocompatibility is critical to improve the efficacy of breast cancer chemotherapy.

Previous studies have shown that polymeric nanoparticles (NPs) can be surface-engineered to act as drug delivery vehicles to improve biocompatibility, increased cellular uptake, and specific tumor targeting, which may result in targeted drug delivery and reduced adverse effects (Bahrami et al., 2017; Mu et al., 2017; Parashar et al., 2018). Hyaluronic acid (HA), a major component of the extracellular matrix, is frequently used as a nanocarrier in the biomedical and cosmetic industries because of its excellent water-binding properties, biocompatibility, biodegradation, and receptor targeting (Papalia et al., 2017; Michaud, 2018; Wang, 2018). Previous studies show that HA can be used as tumor site-specific drug delivery vehicle towing to its high binding affinity for the CD44 receptor (a member of the cell adhesion protein family), which is over-expressed on the surface of various carcinoma cells, including breast cancer (Louhichi et al., 2018) and lung cancer (Mattheolabakis et al., 2015). In contrast, CD44 has been shown to be expressed at low levels on normal cells (Cortes-Dericks and Schmid, 2017; Li et al., 2017). Therefore, HA-modified nanoparticles or micelles are promising as potential carriers for CD44-targeted chemotherapeutic agents.

Treatments using combinations of drugs with different physico-chemical properties may have limitations such as unexpected drug release. Cisplatin (i.e. cis-diamminedichloroplatinum, CDDP), a representative chemotherapeutic drug for various types of cancers, has been extensively formulated into NPs as cross-linked micelles to increase tumor targeting ability through high delivery efficiency and enhanced permeability and retention (EPR) effect at low pH (Ganesh et al., 2013; Fan et al., 2015; Alam et al., 2017; Cai et al., 2017; Girma et al., 2018). The tumor microenvironment is generally acidic, whereas normal tissues are neutral in pH or slightly alkaline (Katheder et al., 2017; Zheng et al., 2020). Therefore, we hypothesized that the pH sensitivity of the present CDDP-crosslinked HA-modified antineoplastic nanoparticles may result in modified drug release behavior in tumor tissues, thereby leading to reduced side effects.

In the present study, HA-modified nanoparticles crosslinked with CDDP and loaded with doxorubicin (DOX) as the anticancer drug were developed as a tumor-targeting formulation for breast cancer chemotherapy. The physicochemical properties, antitumor efficacy, and mechanisms of action of the HA-DOX-CDDP micelles were investigated using $CD44^-$ normal fibroblast cells (NIH-3T3) and $CD44^+$ breast cancer cells (4T1) *in vitro*, and in mice bearing 4T1 breast tumors *in vivo*.

MATERIALS AND METHODS

Materials

Hyaluronic acid (MW = 1.0×10^5 Da) was purchased from Freda Biochem Co., Ltd (Shandong, China). Doxorubicin hydrochloride (DOX HCl) was purchased from Dalian Meilun Biotechnology Co., Ltd. (Purity 98%, Dalian, China). CDDP was purchased from Shandong Boyuan Pharmaceutical Co., Ltd. (Purity 99%, Jinan, China). Poly (ADP-ribose) polymerase (PARP) and survivin antibodies were purchased from Abcam (Cambridge, UK). Purified deionized water was prepared using a Milli-Q plus system (Millipore Co., Billerica, MA, USA).

Cell Lines and Animal Models

Murine $CD44^+$ mammary carcinoma cells (4T1) and normal $CD44^-$ fibroblast cells (NIH-3T3) were purchased from American Type Culture Collection (ATCC, Rockefeller, Maryland, USA), and cultured at 37°C in DMEM supplemented with 10% FBS, penicillin (50 U/ml) and streptomycin (50 U/ml).

Female BALB/c mice (4–5 weeks old) were purchased from the Experimental Animal Center of Jilin University, and housed in a standard environment with access to normal chow diet until they reached a weight of 18–20 g. A tumor-bearing model was generated by inoculating 1.5×10^6 4T1 cells into the abdominal mammary glands of female BALB/c mice. All animal procedures were designed to minimize animal suffering and were approved by the Institutional Animal Care and Use Committee of Jilin University.

Preparation of HA-DOX-CDDP Nanoparticles

Hyaluronic acid-DOX-CDDP nanoparticles were prepared according to previous studies (Zhang et al., 2018; Zhao et al., 2018; Wang et al., 2019). Hyaluronic acid and phosphate buffer (pH=7.4, 1:9 volume ratio) were blended in deionized water until the HA was completely dissolved. Following dissolution, the pH was adjusted to 7.0 using 0.05 M NaOH. An aqueous DOX solution (6.0mg/ml) was added dropwise into the polymer solution, then stirred overnight in the dark at room temperature. Next, a predetermined amount of CDDP was dissolved and added into the reaction mixture mentioned above, and then, incubated at 37°C for 72 h. Finally, HA-DOX-CDDP was obtained using a dialysis method with deionized water as the releasing medium for 10 h.

Characterization of HA-DOX-CDDP Nanoparticles

Dynamic light scanning (DLS) (Wyatt Technology, Santa Barbara, CA, USA) and transmission electron microscopy (TEM) (JEM-1011, JEOL, Japan) were performed to determine HA-DOX-CDDP nanoparticle size and morphology,

respectively. Five milliliters of drug-loaded nanoparticles (0.1 mg/ml) were added to a clean glass container and dissolved prior to DLS detection. Ten microliters of drug-loaded nanoparticles (at the same concentration of 0.1 mg/ml) were added to a copper wire and completely dried for TEM analysis.

In Vitro Drug Release

To determine the release characteristics of HA-DOX-CDDP in PBS (pH 5.5, pH 6.8, and pH 7.4), 1.0 mg of freeze-dried HA-DOX-CDDP micelles was used to prepare release diluent (100.0 mg/ml). The micelles were sealed with 10.0 ml of diluted solution in a dialysis bag (MW cut-off 3,500 Da) and placed in 100.0 ml of release medium, and the solution containing the dialysis bag was shaken at 70 rpm at 37°C. At 0.5, 1, 2, 4, 8, 12, 24, and 48 h, 2.0 ml of release diluent was removed and replaced with fresh diluent. The amounts of released DOX and CDDP were determined using a fluorescence spectrophotometer (UV-1800, Shimadzu, Japan) (λex = 480 nm and λem = 590 nm) and an inductively coupled plasmae mass spctrometer (ICP-MS, Xseries II, Thermoscientific, USA), respectively.

In Vitro Cellular Uptake

Cellular uptake and intracellular DOX release of HA-DOX-CDDP micelles, free DOX, and free CDDP in 4T1 and 3T3 cells were assessed using flow cytometry (FCM) (Beckman, California, USA). Cells were seeded in 6-well plates at a density of 2×10^5 cells per well, then incubated for 12 h at 37°C. The original culture medium was replaced with medium containing free DOX+CDDP or HA-DOX-CDDP at a final DOX HCl concentration of 10.0μmg/ml. In the HA-pretreated groups, cells were incubated with HA micelles for 1 h prior to treatment. Following pretreatment, the medium was replaced with medium containing HA-DOX-CDDP at the same concentration. After 6 h of incubation in a thermostatic incubator, the cells were harvested, washed in cold PBS, and centrifuged twice at 4°C for 5 min at 1,500 rpm. Finally, 500.0 μl of cell suspension was subjected to FCM analysis.

The cellular localization of DOX in 4T1 and 3T3 cells was determined using an LSM 780 confocal laser scanning microscope (CLSM) (Carl Zeiss, Jena, Germany). Cells (1.5×10^5) were incubated on cover slips in 6-well plates for 12 h, and the medium was replaced with medium containing HA-DOX-CDDP micelles, or free DOX+CDDP in DMEM at a final DOX HCl concentration of 10.0 μg/ml. Hyaluronic acid pretreatment groups were pretreated with HA, and then incubated with HA-DOX-CDDP. After incubation for 6 h, cells were fixed in 4% (W/V) PBS-buffered formaldehyde for 30 min at 15–20°C. The cells were then stained with DAPI (blue) and Alexa 488 (green) at 37°C to visualize the cell nucleus and cytoskeleton, respectively.

In Vitro Cytotoxicity Assay

The cytotoxicity of HA-DOX-CDDP was evaluated using the MTT assay. Briefly, 7×10^3 4T1 or NIH-3T3 cells per well were seeded in 96-well plates and incubated for 12 h. Two hundred microliters of culture medium was replaced with fresh medium containing free DOX+CDDP, HA-DOX-CDDP, or HA micelles at various concentrations, and each incubated for 24 or 48 h. Then, 20.0 μl of MTT (5.0 mg/ml) was added to each well, and the cells were incubated for 4 h at 37°C. Next, the medium was replaced with 150.0 μl of DMSO to dissolve the formazan crystals, and the cells were shaken for 10 min prior to analysis. Absorbance was measured at 490 nm using a microplate reader (Bio-Rad 680, Hercules, CA, USA). Cell viability was calculated using equation 1:

$$\text{Cell viability}\,(\%) = \frac{A_{\text{sample}}}{A_{\text{control}}} \times 100$$

In Eq. 1, A_{sample} and A_{control} represent the absorbances of sample and control wells, respectively.

In Vitro Analysis of Morphology of Multicellular Spheroids in 3D Suspension Cultures

A 3D cell suspension cultures model was established using HDP 1096 Perfecta 3D®96-well hanging drop plates (3D Biomatrix, USA) as described in a previous study (Xiao et al., 2018). Briefly, suspensions of 4T1 and NIH-3T3 cells were added into agarose solution preprocessed 96-well plates at 2.5×10^4 cells per well, and the cells were incubated at 37°C. After 5 days, multicellular spheroids were randomly divided into HA (control), free DOX+CDDP, and HA-DOX-CDDP groups with a final DOX HCl concentration of 10.0 μg/ml. Morphologic changes of the multicellular spheroids were visualized using CLSM after treatment for 24 h.

In Vivo Fluorescence Imaging of DOX Biodistribution

The biodistribution of DOX in major internal organs and tumor tissues following intravenous injections was assessed using fluorescence imaging *in vivo*. When tumors grew to 60–80 mm^3, the 4T1 tumor-bearing mice were injected with 0.1% normal saline (NS) as a control, HA-DOX-CDDP micelles, or DOX+CDDP *via* the lateral tail vein, at a DOX HCl dose of 5.0 mg/kg. Major organs (heart, liver, spleen, lung, and kidney) and tumors were excised 6 or 12 h post-injection, washed with NS three times, and analyzed for DOX-related fluorescence using an *in vivo* imaging system (Maestro 500 FL, Cambridge Research & Instrumentation, Inc., USA). A 150 W halogen lamp and a 450–500 nm excitation filter were used for DOX fluorescence analysis. Averaged signals with autofluorescence excluded were quantitatively analyzed using Maestro™2.4 software. Tumor volume (V) was calculated as 0.5 × length × width × height.

In Vivo Antitumor Assay

In vivo antitumor efficacies of free drugs and HA-DOX-CDDP micelle were evaluated using the 4T1-xenografted Balb/c mice. Similarly to the detections of tissue distributions, 0.1 ml of cell suspension containing 1.5×10^6 4T1 cells in NS was injected subcutaneously into the abdominal mammary gland of 4–5 weeks old mice weighing of 18–20 g. When the tumor volume increased to about 60–100 mm^3, the mice were treated with NS, combination of free DOX and CDDP, or HA-DOX-CDDP

micelle at a DOX concentration of 5.0 mg/kg^{-1} body weight by the tail-veil injections on 0, 5, 10, 15, and 20 days. In the course of treatment, tumor volumes and body weights were monitored every other day. Tumor volume (V) was calculated as 0.5 × length × width × height.

Immunofluorescence and Histological Analyses

Tumor-bearing mice were randomly divided into three groups (n=5) that received NS, DOX + CDDP, or HA-DOX-CDDP micelles *via* injection. The mice were sacrificed 8 days after the final injection. Mouse body and tumor weights were recorded at 1–2-day intervals. Tumors, major organs, and lymph nodes were washed with NS, fixed in 4% paraformaldehyde, and embedded in paraffin. Tissues in paraffin blocks were cut into ~5-μm slices for hematoxylin and eosin (H&E) staining and ~3-μm slices for immunofluorescence (PARP and survivin) analyses. Alterations in pathological histology and fluorescence intensity were detected using a Nikon microscope (Eclipse Ti, Optical Apparatus Co., Ardmore, USA) and CLSM, respectively. All image data collected were analyzed using ImageJ software (National Institutes of Health, Bethesda, Maryland).

Statistical Analysis

All experiments were performed in triplicate and results were analyzed for statistical significance using IBM SPSS 17.0 (IBM Company, Armonk, NY, USA). Differences between the groups were estimated using one-way ANOVA or t-tests, and reported as means ± standard deviations (SD). Two-tailed *P* values <0.05 were considered to indicate statistically significant results. When *P* values <0.01 or <0.001, results were considered to have statistically obvious difference.

RESULTS

Physicochemical Properties of HA-DOX-CDDP

As shown in **Figure 1**, HA-DOX and HA-DOX-CDDP were spherical (**Figures 1A, B**). The diameters from TEM microimages were about 100 nm. The hydrodynamic radius (Rh) was about 80 nm. The relative smaller size from TEM detection should be attributed shrinking of nanoparticles during preparing the samples for TEM detection (**Figure 1C**). The FT-IR spectra of HA, HA-DOX, and HA-DOX-CDDP are shown in in **Figure 1D**. The absorption peaks of HA-DOX and HA-DOX-CDDP in the FT-IR spectra were 1300–1000 cm^{-1} duo to the stretching vibration of C-O bond in DOX, but in the spectra of HA-DOX-CDDP, the characteristic absorption peak at 3300–3200 cm^{-1} was also present duo to the amines (NH2) in CDDP. The waveforms of DOX-loaded HA micelles were nearly identical, and slightly different from those of HA, which indicated that the three types of micelles had similar chemical construction.

To determine the release characteristics of HA-DOX-CDDP under physiological conditions, and in the intracellular microenvironment, *in vitro* drug release of DOX and CDDP

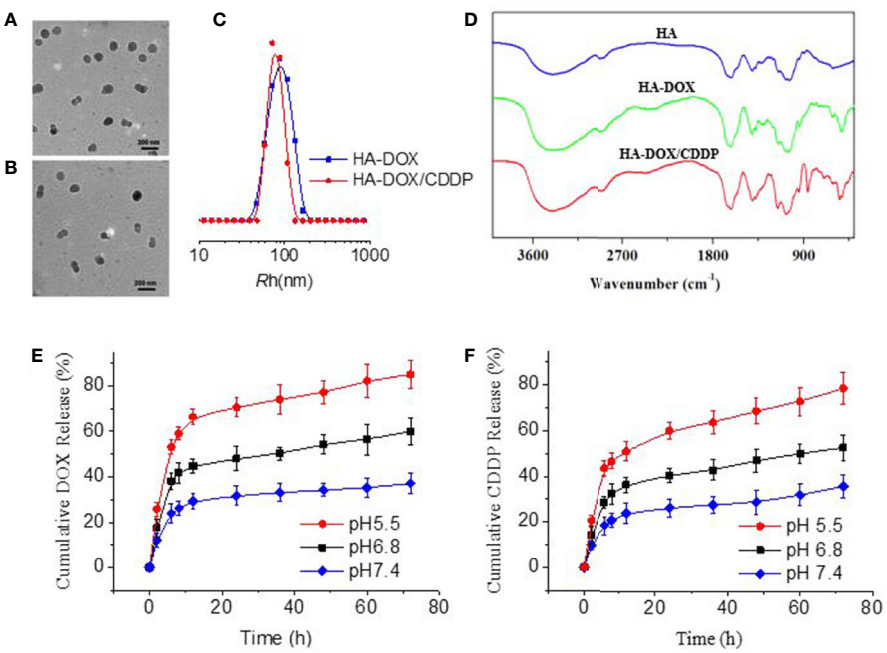

FIGURE 1 | Characterization of DOX-loaded HA micelles. **(A–B)** Transmission electron microscopy images of **(A)** HA-DOX and **(B)** HA-DOX-CDDP. Scale bars: 200 nm. **(C)** Particle size of HA-DOX and HA-DOX-CDDP. **(D)** Fourier transform IR spectra of HA, HA-DOX, and HA-DOX-CDDP. **(E)** *In vitro* DOX release profiles of HA-DOX-CDDP across a range of pH values. **(F)** *In vitro* CDDP release profiles of HA-DOX-CDDP across a range of acidic pH values.

from micelles was evaluated at pH 5.5, 6.8, and 7.4 (**Figures 1E, F**). The micelles exhibited a burst release pattern during the first 4–6 h, and then showed sustained release at different acidic conditions. Doxorubicin and CDDP release from cross-linked micelles was less than 35% at pH 7.4. However, as pH decreased to 6.8 or 5.5, DOX and CDDP release from cross-linked micelles increased to approximately 50% and 80%, respectively, after 72 h.

In Vitro Cellular Uptake

Flow cytometry and CLSM were used to investigate the internalization profiles of HA-DOX-CDDP micelles in 3T3 and 4T1 cells. After incubation with free drugs (DOX+CDDP) or HA-DOX-CDDP for 6 h, the highest levels of free drug internalization were observed in 3T3 cells. In CD44-positive 4T1 cells, HA-DOX-CDDP-treated groups exhibited significantly higher internalization than groups treated with free drugs or pretreated with HA (**Figure 2A**). In addition, the fluorescence intensity induced by HA-pretreatment was almost similar to that induced by HA-DOX-CDDP treatment in 3T3 cells, but less than that following treatment with free drugs in both 3T3 and 4T1 cells. The results obtained from FCM analysis were consistent with those obtained using CLSM (**Figure 2B**).

Inhibition of Cell Proliferation

Inhibition of cell proliferation in response to DOX-loaded HA micelles was evaluated using the MTT assay in 3T3 and 4T1 cells following 24 or 48 h of exposure (**Figure 3**). Groups treated with the free drugs (DOX+CDDP) and HA-DOX-CDDP micelles both exhibited time- and dose-dependent cytotoxicity. However, treatment with HA groups induced slightly smaller effects on cell viability, indicating low cytotoxicity against the two cell types. Compared with groups treated with free drugs, HA-DOX-CDDP-treated groups exhibited significantly more cytotoxicity toward 4T1 cells, which express high levels of CD44 receptors, following treatment at 2.5, 5, and 10 μg/ml for 24 h, or treatment at a concentration of 0.65 μg/ml or higher for 48 h (**Figure 3B**). In contrast, no significant differences in cell viability were observed following treatment with free drugs or HA-DOX-CDDP in 3T3 cells, which express low levels of CD44. HA-DOX-CDDP against the 3T3 and 4T1 cells with the IC50s of 3.07 and 1.10 μg/ml for 24 h exposure, but 2.04 and 0.34 μg/ml for 48 h exposure. Moreover, free DOX plus CDDP against the 3T3 and 4T1 cells with the IC50s of 3.45 and 1.16 μg/ml for 24 h exposure, but 3.58 and 0.56 μg/ml for 48 h exposure.

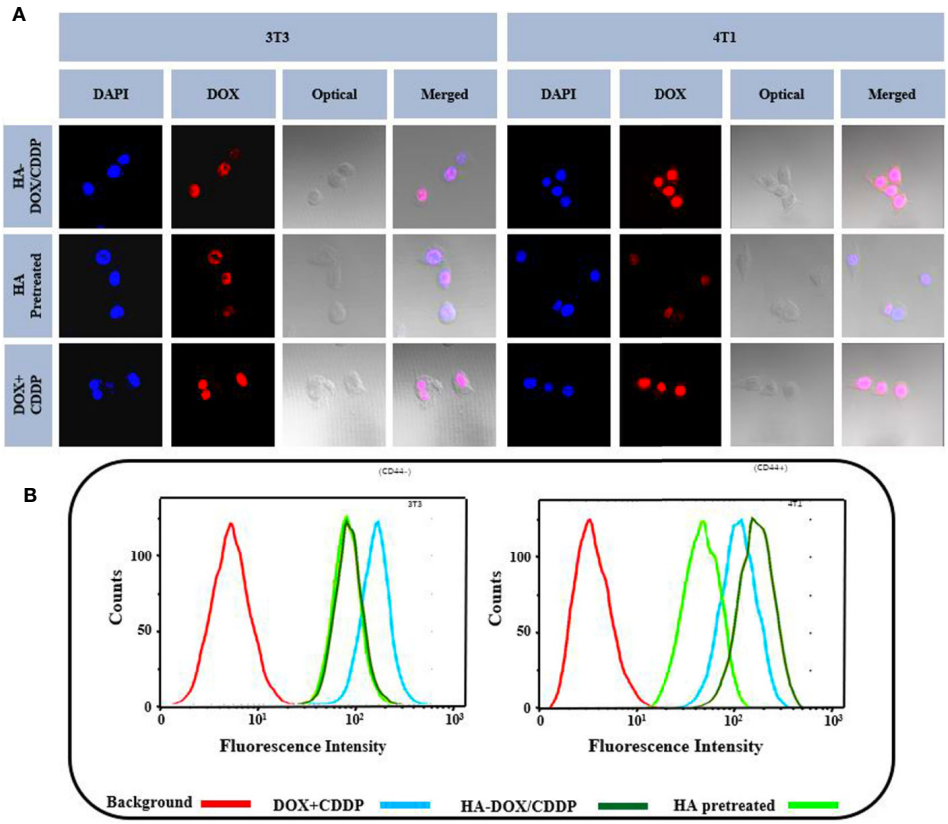

FIGURE 2 | *In vitro* cellular uptake and intracellular DOX release in 3T3 and 4T1 cells. **(A)** Confocal laser scattering microscopy and **(B)** FCM analysis were performed on 3T3 and 4T1 cells following HA pretreatment, and treatment with free DOX+CDDP and HA-DOX-CDDP.

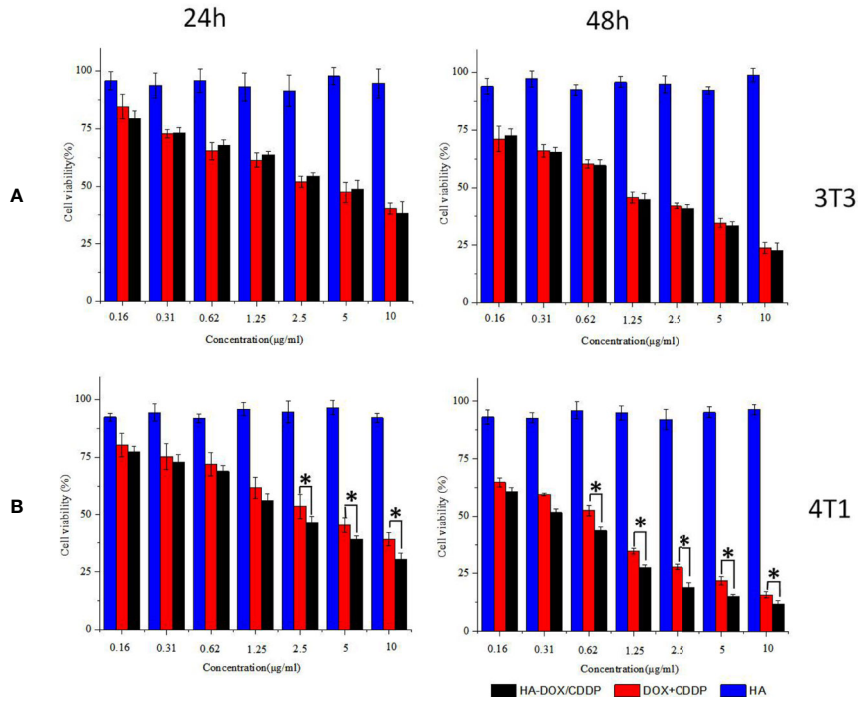

FIGURE 3 | *In vitro* cytotoxicity assay. **(A)** Cell viability of 3T3 cells treated with HA, DOX+CDDP, and HA-DOX-CDDP for 24 or 48 h. **(B)** Cell viability of 4T1 cells treated with HA, DOX+CDDP, and HA-DOX-CDDP for 24 or 48 h. Data are presented as the mean ± SD (n = 3). *$P < 0.05$ compared with the DOX+ CDDP group.

Inhibition of Cell Proliferation and HA-DOX-CDDP Penetration in 3D Cell Culture

Three-dimensional multicellular spheroid models of 3T3 and 4T1 cells were established to further evaluate the tumor inhibition effects and cellular uptake of HA-DOX-CDDP micelles (see **Figure 4**). The 4T1 spheroid volumes in the HA-DOX-CDDP treatment group were significantly smaller than those in the free drugs group ($P < 0.05$). In contrast, no significant differences in 3T3 spheroid volume were observed between the HA-DOX-CDDP and DOX+CDDP groups (**Figures 4A, B**). In addition, drug penetration was evaluated following co-incubation with drugs for 24 h. Compared with the free drugs group, the cores of the multicellular 4T1 spheroids in the HA-DOX-CDDP group showed much stronger fluorescence intensity ($P<0.05$) (**Figures 4A, C**). Consistent with the proliferation results, no significant differences in fluorescence intensity were observed between the HA-DOX-CDDP and DOX +CDDP groups in the 3T3 cell model. These results demonstrate that the nanoparticulate drug formulation showed enhanced inhibition of cell proliferation and cellular uptake *via* CD44 receptors on the surfaces of 4T1 tumor cells.

Drug Biodistribution *In Vivo*

Drug distribution in major organs and isolated tumors was evaluated 6 or 12 h after injection of free or nanoparticulate drugs (**Figure 5**). The livers and kidneys showed strong fluorescence in the HA-DOX-CDDP and free DOX+CDDP groups 6 h post-injection, and the fluorescence intensity was higher at 12 h (**Figure 5A**). These results may be attributed to the high rate of metabolism of small-molecule anticancer drugs in the liver and kidney (Wicki et al., 2015; Huang et al., 2017). The fluorescence signals in major organs were significantly weaker for the HA-DOX-CDDP group than for the free drug group at both 6 and 12 h post-injection, except in the spleen, suggesting lower levels of drug distribution in the spleen relative to the other organs and tissues. In contrast, the fluorescence intensity in tumors was 1.3- and 2.1-fold higher in the HA-DOX-CDDP group than in the free drug groups after 6 and 12 h exposure, respectively (**Figure 5B**).

In Vivo Tumor Suppression

The tumor suppression effect of NPs and free drugs *in vivo* was evaluated in BALB/c mice injected with 4T1 cells in the abdominal fat pad. Tumor volumes and body weights were calculated at the end of the experiment. As shown in **Figure 6A**, the tumors progressed rapidly with an average volume of 1600 ± 487 mm^3 in the control group. In contrast, the tumors were significantly smaller in the HA-DOX-CDDP- and DOX +CDDP-treated groups. Treatment with HA-DOX-CDDP resulted in 66% tumor inhibition compared with that in the other treatment groups. In addition, body weight decreased rapidly in the free DOX+CDDP group during the initial 10 days of treatment, then stabilized gradually. Overall, the animals in this group experienced a 19% loss in body weight (**Figure 6B**). In the HA-DOX-CDDP group, body weight decreased at a rate similar to that in the control group during the early treatment

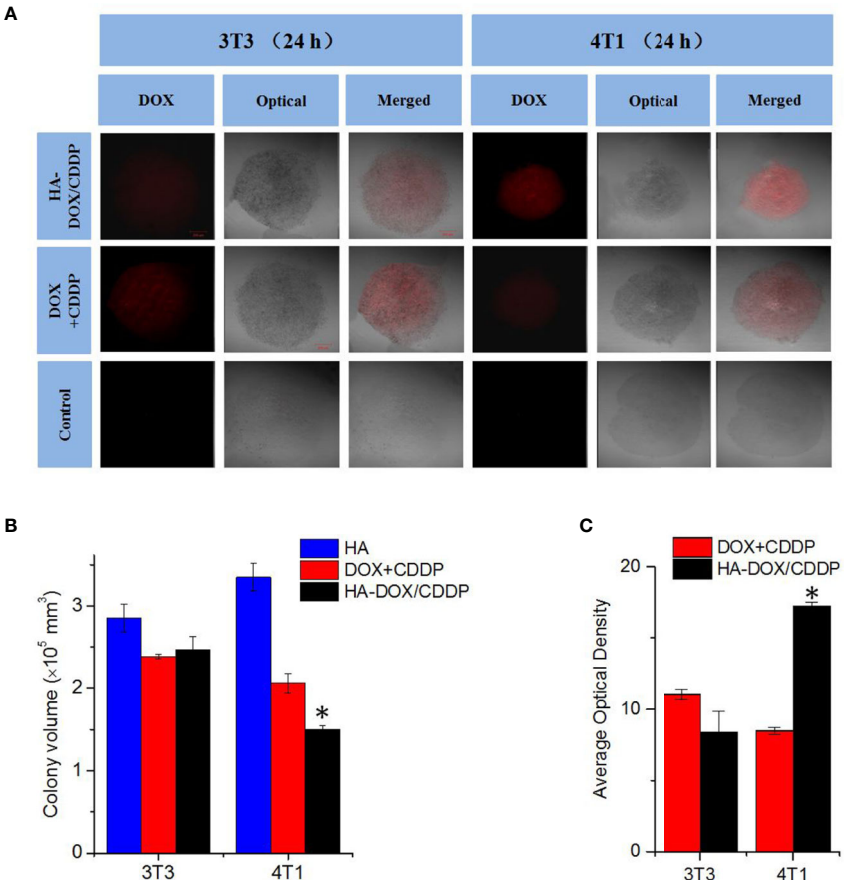

FIGURE 4 | *In vitro* multicellular spheroids in 3D suspension cultures. **(A)** Confocal laser scattering microscopy of 4T1 and 3T3 cell spheroids treated with HA, DOX+ CDDP, and HA-DOX-CDDP for 24 h. **(B)** Colony volume and **(C)** fluorescence density analyses of 4T1 and 3T3 cell spheroids treated with HA, DOX+ CDDP, and HA-DOX-CDDP for 24 h. *$P < 0.05$ compared with the DOX+ CDDP group.

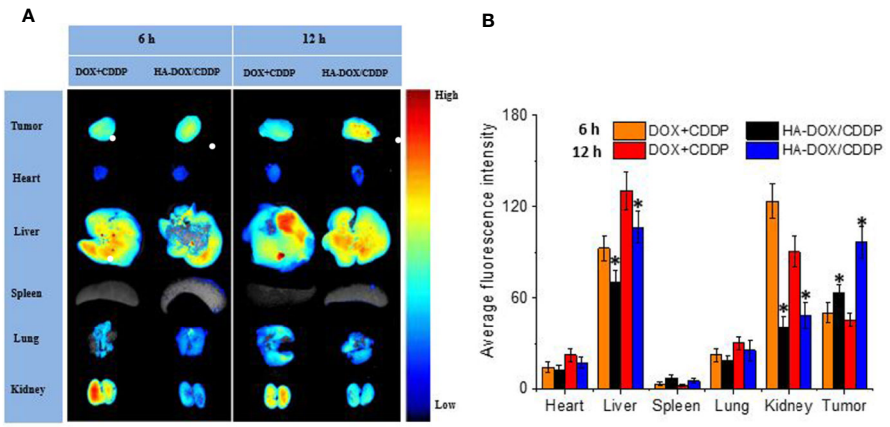

FIGURE 5 | *In vivo* DOX biodistribution. **(A)** *Ex vivo* fluorescence images of isolated organs and tumors at 6 or 12 h post-injection. **(B)** Semi-quantitative analysis of the mean fluorescence intensity in isolated organs and tumors at 6 or 12 h post-injection. Data are presented as the mean ± SD (n=3). *$P < 0.05$ compared with the DOX+CDDP group.

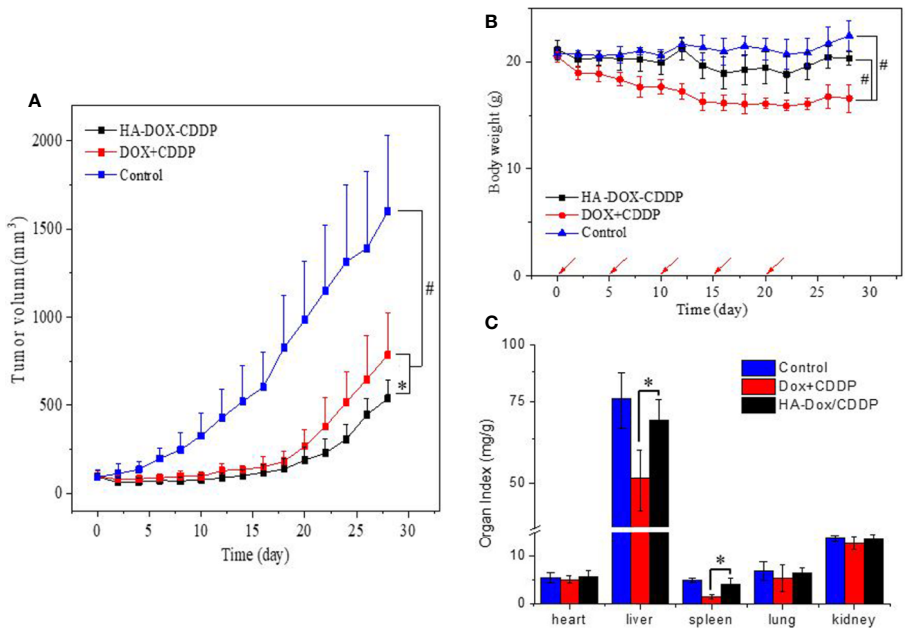

FIGURE 6 | *In vivo* safety and antitumor efficacies. **(A)** Tumor volumes and **(B)** body weights of 4T1-xenografted mice after treatment with NS as the control, DOX +CDDP, or HA-DOX-CDDP. Red arrows showed the tail-veil injection time. **(C)** Organ coefficients of isolated organs in NS, DOX +CDDP, or HA-DOX-CDDP treated groups. $^{*}P < 0.05$, $^{\#}P < 0.001$.

stage, and total body weight loss was 3.7%. Body weight did not significantly change in the control group. As shown in **Figure 6C**, organ coefficients were calculated to evaluate side effects of drug treatment. In the free DOX+CDDP group, the organ coefficients of the liver and spleen were obviously lower than in the other two groups (P<0.01). There were no significant differences in organ coefficients between the HA-DOX-CDDP and control groups.

Histopathology and Immunofluorescence Analyses

Pathological analyses of tumor tissues were performed to confirm the anticancer efficacies of the different drug formulations. As shown in **Figure 7A**, most tumor cells exhibited integrated cellular morphologies in the control group. In contrast, tumor cell necrosis was observed in the HA-DOX-CDDP and DOX+CDDP groups. Tissues in the HA-DOX-CDDP group had larger necrotic areas (56.3% ± 5.8%) than those in the free DOX+CDDP (35.65 ± 6.5%) and control groups (1.5% ± 0.8%) (**Figure 7B**).

To investigate mechanisms of apoptosis in tumor cells following treatment, immunofluorescence of PARP and survivin was evaluated in tumor tissue sections. As shown in **Figure 7C**, the fluorescence density of PARP in the control group was lower than that in the other two groups. Furthermore, PARP fluorescence intensity in the HA-DOX-CDDP group was approximately 4.15- and 2.23-fold higher than that in the free drugs and control groups, respectively (**Figure 7D**). Compared with the control group, the fluorescence intensity of survivin was lower, to differing extents, in the HA-DOX-CDDP and DOX + CDDP groups. Furthermore, the HA-DOX-CDDP groups showed significantly weaker survivin fluorescence than the free drugs group (**Figure 7E**).

DISCUSSION

Many attempts have been made to develop effective targeted anti-cancer drug delivery systems with improved safety and reduced side effects. Nanotechnology has enabled significant improvements in therapeutic efficacy (Zhou et al., 2015; Gupta et al., 2017; Youn and Bae, 2018). In the present study, an HA-modified nanoparticle was designed to encapsulate DOX and CDDP *via* side carboxyl (COOH) groups as a novel formulation for treatment of breast cancer. Doxorubicin, a chemotherapy drug that is widely used clinically, reduces DNA repair capacity, and has been shown to exert synergistic effects with CDDP for treatment of breast cancer (Roy et al., 2018; Guo et al., 2019) Previous studies used CDDP as a crosslinker for chelating HA and DOX at an optimized ratio to generate stable drug-loaded nanogels with suitable particle sizes (Harrington et al., 2000; Huang et al., 2018). The stability and pH-sensitivity of HA-DOX-CDDP were verified at pH 7.4, 6.8, and 5.5 in our study to simulate normal physiological microenvironments, acidic tumor tissue, and lysosomal microenvironments, respectively (Fan et al., 2015; Cheng et al., 2019). Extended incubation of HA-DOX-CDDP resulted in DOX release rates that increased as pH decreased from 7.4 to 5.5. This effect was likely attributable to the disruption of carboxyl groups between HA and DOX under acidic conditions. These results suggest that the pH-sensitive

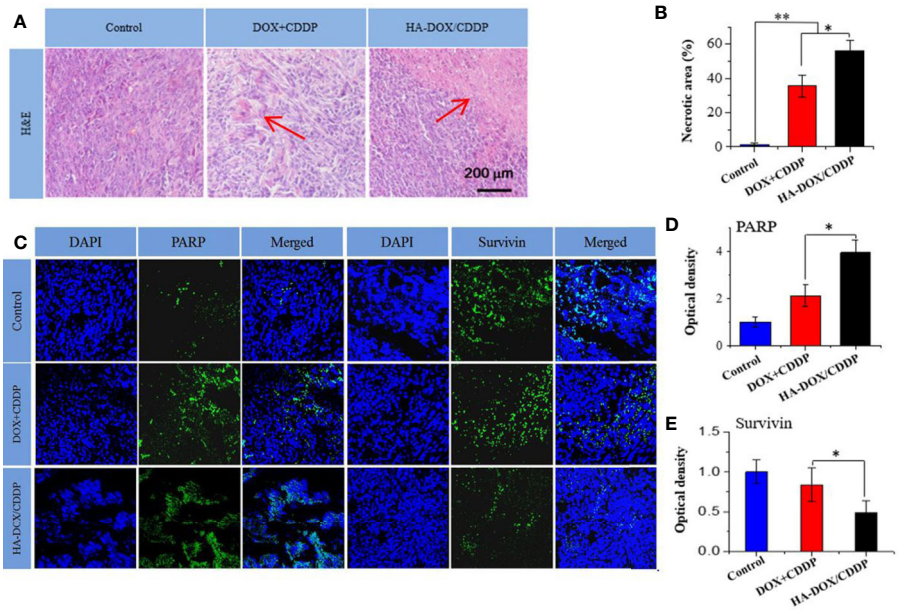

FIGURE 7 | Histopathology and immunofluorescence analyses. **(A)** Histopathological (H&E) analyses and **(B)** necrotic areas in H&E-stained tumor sections from 4T1-xenografted mice following treatment with NS as the control, DOX+CDDP, or HA-DOX-CDDP. Red arrows indicated the necrotic area. **(C)** Immunohistochemical (PARP and survivin) analyses of tumor tissue sections following treatment with NS as the control, DOX +CDDP, or HA-DOX-CDDP. **(D)** Relative optical densities of tumor sections showing PARP immunofluorescence. **(E)** Relative optical densities of tumor sections showing survivin immunofluorescence. Data are presented as the mean ± SD (n = 5). $^{*}P < 0.05$, $^{**}P < 0.01$.

nature of HA-DOX-CDDP may result in more rapid drug release in the tumor microenvironment and sustained release under normal physiological conditions, which may lead to increased antitumor activity. In addition, HA-modified nanoparticles exhibited targeted delivery to cancer cells that expressed high levels of CD44. In this study, NIH-3T3 ($CD44^{-}$) and 4T1 ($CD44^{+}$) cell lines were used to evaluate the anticancer potential of the developed formulation against breast tumors. Doxorubicin fluorescence intensity following treatment with HA-DOX-CDDP was observed in the nucleus at the same intracellular location as that observed following treatment with free DOX. In addition, fluorescence was remarkably enhanced in 4T1 cells, but only slightly in NIH-3T3 cells, compared with that in the HA-pretreated or free drug groups. These results may have been due to specific internalization of HA-DOX-CDDP through interaction with CD44 receptors on the surface of 4T1 cells. These findings indicate that DOX-loaded HA micelles exhibit optimal CD44-mediated targeting ability and pH-dependent drug release in the acidic tumor microenvironment, which could result in enhanced breast tumor-targeting efficiency and reduced drug-induced side effects.

The effects of DOX-loaded HA micelles on proliferation and growth inhibition of NIH-3T3 and 4T1cells were further confirmed the security evaluation and selective toxicity for aforesaid drug delivery systems. *In vitro* cytotoxicity assay showed that HA treatment induced negligible cytotoxicity in both cell lines, at different concentrations, which indicated good biocompatibility. Furthermore, DOX-loaded HA micelles inhibited cell growth to a greater extent than free DOX+CDDP in 4T1cells, but not in 3T3 cells, after 72 h of treatment, indicating higher cytotoxicity and selectivity of HA-DOX-CDDP. These observations are likely attributable to HA receptor-mediated endocytosis and the delayed drug release characteristic of nanosized micelles. These results agreed with those obtained using a 3D spheroid culture model, which was more representative of cellular functions and physiological responses in tissues and organs (Perin et al., 2017).

Drug distribution in tissues has been associated with therapeutic efficacy and potential organ toxicity (Salimi et al., 2018). In this study, higher accumulation of free DOX was observed in the liver and kidney in the free DOX+CDDP-treated mice. This may have been due to substantial phagocytosis by liver macrophages and rapid renal metabolism of small molecule anticancer agents (Taurin et al., 2012; Guo et al., 2018; Ding et al., 2019). In contrast, HA-DOX-CDDP treatment resulted in increased accumulation of free DOX only in breast tumor tissues. Furthermore, free DOX concentrations were lower in other organs in HA-DOX-CDDP mice than those in the free drugs-treated mice, particularly in the kidney. These results may have been due to enhanced EPR effect, excellent biocompatibility, and specific targeting to CD44 receptors. Furthermore, treatment with HA-DOX-CDDP resulted in lower tumor volume and lower loss of body weight than treatment with free DOX+CDDP. These results showed that

selective biodistribution of HA-DOX-CDDP resulted in DOX accumulation at breast tumor sites and reduced systemic toxicity following intravenous injection.

Histopathological and immunofluorescence studies were performed to evaluate drug efficacy and side effects following repeated intravenous administration. In our experiments, HA-DOX-CDDP treatment resulted in the greatest tumor necrotic areas among all of the groups, which indicated increased activity against breast cancer. Furthermore, the expression of PARP was increased and the expression of survivin was decreased in tumor sections of mice treated with HA-DOX-CDDP compared with those in mice treated with free DOX+CDDP. PARP is an important nuclear protein involved in DNA repair signaling pathways that can either maintain the structural integrality of chromosomes or mediate necrosis by inducing DNA damage (Pascal, 2018). Hyper-activation of PARP triggers DNA fragmentation and cell necrosis through enhanced release of apoptosis-inducing factor (Dale et al., 2015; Francica and Rottenberg, 2018). Survivin, an apoptosis inhibitor, plays a crucial role in tumor cell differentiation, progression, and invasion (Jaiswal et al., 2015). In particular, surviving expression has been shown to be an independent prognostic factor based on overexpression in neoplastic tissues and low expression in normal tissues (Veiga et al., 2019; Mahmoudian-Sani et al., 2019). The results of our study indicated that HA-DOX-CDDP showed greater therapeutic efficacy against breast cancer than free drugs.

In conclusion, the present CDDP-crosslinked DOX-loaded HA micelles prepared with innocuous methods and possessed an outstanding ability to control the release of DOX and CDDP for pH sensitivity and CD44 targeting.HA-DOX-CDDP exhibited synergistic anticancer effects, tumor-targeted ability, and reduced multi-organ toxicity compared with conventional anti-breast cancer agents. These results indicate that HA-DOX-CDDP may represent a multifunctional nano-drug delivery system that exhibits improved therapeutic efficacy against breast cancer. This study also provides avenues for exploring the incorporation of selective agents with biological targeting to overcome severe adverse effects in carcinoma chemotherapy.

DATA AVAILABILITY STATEMENT

All datasets generated for this study are included in the article/supplementary material.

ETHICS STATEMENT

The animal study was reviewed and approved by the Institutional Animal Care and Use Committee of Jilin University.

AUTHOR CONTRIBUTIONS

QL conceived and designed the experiments. TY and YL contributed significantly to cell culture and drug treatments, data compilation and analysis, and manuscript preparation. XG performed the mice treatments and HA-DOX-CDDP preparation.

REFERENCES

Alam, N., Koul, M., Mintoo, M. J., Khare, V., Gupta, R., Rawat, N., et al. (2017). Development and characterization of hyaluronic acid modified PLGA based nanoparticles for improved efficacy of cisplatin in solid tumor. *Biomed. Pharmacother.* 95, 856–864. doi: 10.1016/j.biopha.2017.08.108

Bahrami, B., Hojjat-Farsangi, M., Mohammadi, H., Anvari, E., Ghalamfarsa, G., Yousefi, M., et al. (2017). Nanoparticles and targeted drug delivery in cancer therapy. *Immunol. Lett.* 190, 64–83. doi: 10.1016/j.imlet

Cai, Z., Zhang, H., Wei, Y., Wei, Y., Xie, Y., and Cong, F. (2017). Reduction- and pH-Sensitive Hyaluronan Nanoparticles for Delivery of Iridium (III) Anticancer Drugs. *Biomacromolecules* 18, 2102–2117. doi: 10.1021/acs.biomac

Cheng, L., Wang, C., Feng, L. Z., Yang, K., and Liu, Z. (2014). Functional nanomaterials for phototherapies of cancer. *Chem. Rev.* 1 (14), 10869–10939. doi: 10.1021/cr400532z

Cheng, C., Meng, Y., Zhang, Z., Li, Y., Liu, C., and Zhang, Q. (2019). pH responsible and fluorescent Cy5.5-PEG-g-A-HA/CDDP complex nanoparticles: synthesis, characterization, and application for targeted drug delivery. *J. Mater. Sci. Mater. Med.* 30, 58. doi: 10.1007/s10856-019-6260-8

Cortes-Dericks, L., and Schmid, R. A. (2017). CD44 and its ligand hyaluronan as potential biomarkers in malignant pleural mesothelioma: evidence and perspectives. *Respir. Res.* 18, 58. doi: 10.1186/s12931-017-0546-5

Dale, R.II, Solberg Landsverk, K., Micci, F., Patzke, S., and Stokke, T. (2015). Replication-induced DNA damage after PARP inhibition causes G2 delay, and cell line-dependent apoptosis, necrosis and multinucleation. *Cell Cycle.* 14, 3248–3260. doi: 10.1080/15384101.2015.1085137

Ding, J., Chen, J., Gao, L., Jiang, Z., Zhang, Y., Li, M., et al. (2019). Engineered nanomedicines with enhanced tumor penetration. *Nano Today* 29, 100800. doi: 10.1016/j.nantod

Fan, X., Zhao, X., Qu, X., and Fang, J. (2015). pH sensitive polymeric complex of cisplatin with hyaluronic acid exhibits tumor-targeted delivery and improved in vivo antitumor effect. *Int. J. Pharm.* 496, 644–653. doi: 10.1016/j.ijpharm

Feng, X., Ding, J., Gref, R., and Chen, X. (2017). Poly(β-cyclodextrin)-mediated polylactide-cholesterol stereocomplex micelles for controlled drug delivery. *Chin. J. Polym. Sci.* 35, 693–699. doi: 10.1007/s10118-017-1932-7

Francica, P., and Rottenberg, S. (2018). Mechanisms of PARP inhibitor resistance in cancer and insights into the DNA damage response. *Genome Med.* 10, 101. doi: 10.1186/s13073-018-0612-8

Freitas de Freitas, L., Varca, G. H. C., Dos Santos Batista, J. G., and Benévolo Lugão, A. (2018). An Overview of the Synthesis of Gold Nanoparticles Using Radiation Technologies. *Nanomater. (Basel)* 8, 939. doi: 10.3390/nano8110939

Ganesh, S., Iyer, A. K., Gattacceca, F., Morrissey, D. V., and Amiji, M. M. (2013). In vivo biodistribution of sirna and cisplatin administered using cd44-targeted hyaluronic acid nanoparticles. *J. Control Release* 172, 699–706. doi: 10.1016/j.jconrel.2013.10.016

Girma, W. M., Tzing, S. H., Tseng, P. J., Huang, C. C., Ling, Y. C., and Chang, J. Y. (2018). Synthesis of Cisplatin(IV) Prodrug-Tethered CuFeS2 Nanoparticles in Tumor-Targeted Chemotherapy and Photothermal Therapy. *ACS Appl. Mater. Interfaces* 10, 4590–4602. doi: 10.1021/acsami.7b19640

Guo, H., Li, F., Xu, W., Chen, J., Hou, Y., Wang, C., et al. (2018). Mucoadhesive Cationic Polypeptide Nanogel with Enhanced Penetration for Efficient Intravesical Chemotherapy of Bladder Cancer. *Adv. Sci.* 5, 1800004. doi: 10.1002/advs.201800004

Guo, X. L., Kang, X. X., Wang, Y. Q., Zhang, X. J., Li, C. J., Liu, Y., et al. (2019). Co-delivery of cisplatin and doxorubicin by covalently conjugating with polyamidoamine dendrimer for enhanced synergistic cancer therapy. *Acta Biomater.* 84, 367–377. doi: 10.1016/j.actbio

Gupta, S., Gupta, P. K., Dharanivasan, G., and Verma, R. S. (2017). Current prospects and challenges of nanomedicine delivery in prostate cancer therapy. *Nanomed. (Lond).* 12, 2675–2692. doi: 10.2217/nnm-2017-0236

Harrington, K. J., Rowlinson-Busza, G., Uster, P. S., and Stewart, J. S. (2000). Pegylated liposome-encapsulated doxorubicin and cisplatin in the treatment of head and neck xenograft tumours. *Cancer Chemother. Pharmacol.* 46, 10–18. doi: 10.1007/s002800000128

Huang, W., Chen, L., Kang, L., Jin, M., Sun, P., Xin, X., et al. (2017). Nanomedicine-based combination anticancer therapy between nucleic acids and small-molecular drugs. *Adv. Drug Deliv. Rev.* 115, 82–97. doi: 10.1016/j.addr.2017.06.004

Huang, D., Qian, H., Qiao, H., Chen, W., Feijen, J., and Zhong, Z. (2018). Bioresponsive functional nanogels as an emerging platform for cancer therapy. *Expert Opin. Drug Deliv.* 15, 703–716. doi: 10.1080/17425247.2018.1497607

Jaiswal, P. K., Goel, A., and Mittal, R. D. (2015). Survivin: A molecular biomarker in cancer. *Indian J. Med. Res.* 141, 389–397. doi: 10.4103/0971-5916.159250

Katheder, N. S., Khezri, R., O'Farrell, F., Schultz, S. W., Jain, A., Rahman, M. M., et al. (2017). Microenvironmental autophagy promotes tumour growth. *Nature* 541, 417–420. doi: 10.1038/nature20815

Li, W., Ma, H., Zhang, J., Zhu, L., Wang, C., and Yang, Y. (2017). Unraveling the roles of CD44/CD24 and ALDH1 as cancer stem cell markers in tumorigenesis and metastasis. *Sci. Rep.* 7, 13856. doi: 10.1038/s41598-017-14364-2

Louhichi, T., Ziadi, S., Saad, H., Dhiab, M. B., Mestiri, S., and Trimeche, M. (2018). Clinicopathological significance of cancer stem cell markers CD44 and ALDH1 expression in breast cancer. *Breast Cancer* 25, 698–705. doi: 10.1007/s12282-018-0875-3

Mahmoudian-Sani, M. R., Alghasi, A., Saeedi-Boroujeni, A., Jalali, A., Jamshidi, M., and Khodadadi, A. (2019). Survivin as a diagnostic and therapeutic marker for thyroid cancer. *Pathol. Res. Pract.* 215, 619–625. doi: 10.1016/j.prp.2019.01.025

Mattheolabakis, G., Milane, L., Singh, A., and Amiji, M. M. (2015). Hyaluronic acid targeting of CD44 for cancer therapy: from receptor biology to nanomedicine. *J. Drug Targeting* 23, 605–618. doi: 10.3109/1061186X.2015.1052072

Michaud, T. (2018). Rheology of hyaluronic acid and dynamic facial rejuvenation: Topographical specificities. *J. Cosmet. Dermatol.* 17, 736–743. doi: 10.1111/jocd.12774

Mu, Q., Wang, H., and Zhang, M. (2017). Nanoparticles for imaging and treatment of metastatic breast cancer. *Expert Opin. Drug Deliv.* 14, 123–136. doi: 10.1080/17425247.2016.1208650

Papalia, R., Russo, F., Torre, G., Albo, E., Grimaldi, V., Papalia, G., et al. (2017). Hybrid hyaluronic acid versus high molecular weight hyaluronic acid for the treatment of osteoarthritis in obese patients. *J. Biol. Regul. Homeost. Agents* 31, 103–109.

Parashar, P., Rathor, M., Dwivedi, M., and Saraf, S. A. (2018). Hyaluronic Acid Decorated Naringenin Nanoparticles: Appraisal of Chemopreventive and Curative Potential for Lung Cancer. *Pharmaceutics* 10, 33. doi: 10.3390/pharmaceutics10010033

Pascal, J. M. (2018). The comings and goings of PARP-1 in response to DNA damage. *DNA Repair (Amst).* 71, 177–182. doi: 10.1016/j.dnarep.2018.08.022

Perin, N., Bobanović, K., Zlatar, I., Jelić, D., Kelava, V., Koštrun, S., et al. (2017). Antiproliferative activity of amino substituted benzo [b] thieno [2,3-b] pyrido [1,2-a] benzimidazoles explored by 2D and 3D cell culture system. *Eur. J. Med. Chem.* 125, 722–773. doi: 10.1016/j.ejmech.2016.09.084

Roy, A., Sarker, S., Upadhyay, P., Pal, A., Adhikary, A., Jana, K., et al. (2018). Methylglyoxal at metronomic doses sensitizes breast cancer cells to doxorubicin and cisplatin causing synergistic induction of programmed cell death and inhibition of stemness. *Biochem. Pharmacol.* 156, 322–339. doi: 10.1016/j.bcp.2018.08.041

Salimi, M., Sarkar, S., Fathi, S., Alizadeh, A. M., Saber, R., Moradi, F., et al. (2018). Biodistribution, pharmacokinetics, and toxicity of dendrimer-coated iron oxide nanoparticles in BALB/c mice. *Int. J. Nanomed.* 13, 1483–1493. doi: 10.2147/IJN.S157293. eCollection 2018.

Taurin, S., Nehoff, H., and Greish, K. (2012). Anticancer nanomedicine and tumor vascular permeability; Where is the missing link? *J. Controlled Release* 164, 265–275. doi: 10.1016/j.jconrel.2012.07.013

Veiga, G. L. D., Silva, R. D. M. D., Pereira, E. C., Azzalis, L. A., Alves, B. D. C. A., Gehrke, F. S., et al. (2019). The role of Survivin as a biomarker and potential prognostic factor for breast cancer. *Rev. Assoc. Med. Bras. (1992)* 65, 893–901. doi: 10.1590/1806-9282.65.6.893

Wang, Q., Zhang, P., Li, Z., Feng, X., Lv, C., Zhang, H., et al. (2019). Evaluation of Polymer Nanoformulations in Hepatoma Therapy by Established Rodent Models. *Theranostics* 9, 1426–1452. doi: 10.7150/thno.31683

Wang, C. (2018). Application of Hyaluronic Acid. *Zhongguo Yi Liao Qi Xie Za Zhi.* 42, 74–76. doi: 10.3969/j.issn.1671-7104.2018.01.021

Wicki, A., Witzigmann, D., Balasubramanian, V., and Huwyler, J. (2015). Nanomedicine in cancer therapy: challenges, opportunities, and clinical applications. *J. Control Release* 200, 138–157. doi: 10.1016/j.jconrel.2014.12.030

Xiao, Z., Wan, J., Nur, A. A., Dou, P., Mankin, H., Liu, T., et al. (2018). Targeting CD44 by CRISPR-Cas9 in Multi-Drug Resistant Osteosarcoma Cells. *Cell Physiol. Biochem.* 51, 1879–1893. doi: 10.1159/000495714

Youn, Y. S., and Bae, Y. H. (2018). Perspectives on the past, present, and future of cancer nanomedicine. *Adv. Drug Deliv. Rev.* 130, 3–11. doi: 10.1016/j.addr.2018.05.008

Zhang, Y., Wang, F., Li, M., Yu, Z., Qi, R., Ding, J., et al. (2018). Self-Stabilized Hyaluronate Nanogel for Intracellular Codelivery of Doxorubicin and Cisplatin to Osteosarcoma. *Adv. Sci. (Weinh).* 5, 1700821. doi: 10.1002/advs.201700821

Zhao, J., Wan, Z., Zhou, C., Yang, Q., Dong, J., Song, X., et al. (2018). Hyaluronic Acid Layer-By-Layer (LbL) Nanoparticles for Synergistic Chemo-Phototherapy. *Pharm. Res.* 35, 196. doi: 10.1007/s11095-018-2480-8

Zheng, P., Liu, Y., Chen, J., Xu, W., Li, G., and Ding, J. (2020). Targeted pH-responsive polyion complex micelle for controlled intracellular drug delivery. *Chin. Chem. Lett.* 31, 1178–1182. doi: 10.1016/j.cclet.2019.12.001

Zhou, M., Zhao, J., Tian, M., Song, S., Zhang, R., Gupta, S., et al. (2015). Radiophotothermal therapy mediated by a single compartment nanoplatform depletes tumor initiating cells and reduces lung metastasis in the orthotopic 4T1 breast tumor model. *Nanoscale* 7, 19438–19447. doi: 10.1039/c5nr04587h

Conflict of Interest: The authors declare that the research was conducted in the absence of any commercial or financial relationships that could be construed as a potential conflict of interest.

Advantages of publishing in Frontiers

OPEN ACCESS
Articles are free to read for greatest visibility and readership

FAST PUBLICATION
Around 90 days from submission to decision

HIGH QUALITY PEER-REVIEW
Rigorous, collaborative, and constructive peer-review

TRANSPARENT PEER-REVIEW
Editors and reviewers acknowledged by name on published articles

Frontiers
Avenue du Tribunal-Fédéral 34
1005 Lausanne | Switzerland

Visit us: www.frontiersin.org
Contact us: frontiersin.org/about/contact

REPRODUCIBILITY OF RESEARCH
Support open data and methods to enhance research reproducibility

DIGITAL PUBLISHING
Articles designed for optimal readership across devices

FOLLOW US
@frontiersin

IMPACT METRICS
Advanced article metrics track visibility across digital media

EXTENSIVE PROMOTION
Marketing and promotion of impactful research

LOOP RESEARCH NETWORK
Our network increases your article's readership